Springer Series in Optical Sciences 214

Hiroyuki Fujiwara
Robert W. Collins *Editors*

Spectroscopic Ellipsometry for Photovoltaics

Volume 2: Applications and Optical Data of Solar Cell Materials

Springer

Springer Series in Optical Sciences

Volume 214

Founded by

H. K. V. Lotsch

Editor-in-chief

William T. Rhodes, Florida Atlantic University, Boca Raton, FL, USA

Series editors

Ali Adibi, School of Electrical and Computer Engineering, Georgia Institute of Technology, Atlanta, GA, USA
Toshimitsu Asakura, Hokkai-Gakuen University, Sapporo, Hokkaido, Japan
Theodor W. Hänsch, Max-Planck-Institut für Quantenoptik, Garching, Bayern, Germany
Ferenc Krausz, Garching, Bayern, Germany
Barry R. Masters, Cambridge, MA, USA
Katsumi Midorikawa, Laser Technology Laboratory, RIKEN Advanced Science Institute, Saitama, Japan
Bo A. J. Monemar, Department of Physics and Measurement Technology, Linköping University, Linköping, Sweden
Herbert Venghaus, Ostseebad Binz, Germany
Horst Weber, Berlin, Germany
Harald Weinfurter, München, Germany

Springer Series in Optical Sciences is led by Editor-in-Chief William T. Rhodes, Georgia Institute of Technology, USA, and provides an expanding selection of research monographs in all major areas of optics:

- lasers and quantum optics
- ultrafast phenomena
- optical spectroscopy techniques
- optoelectronics
- information optics
- applied laser technology
- industrial applications and
- other topics of contemporary interest.

With this broad coverage of topics the series is useful to research scientists and engineers who need up-to-date reference books.

More information about this series at http://www.springer.com/series/624

Hiroyuki Fujiwara · Robert W. Collins
Editors

Spectroscopic Ellipsometry for Photovoltaics

Volume 2: Applications and Optical Data of Solar Cell Materials

Springer

Editors
Hiroyuki Fujiwara
Department of Electrical, Electronic and Computer Engineering
Gifu University
Gifu, Japan

Robert W. Collins
Department of Physics and Astronomy
The University of Toledo
Toledo, OH, USA

ISSN 0342-4111 ISSN 1556-1534 (electronic)
Springer Series in Optical Sciences
ISBN 978-3-319-95137-9 ISBN 978-3-319-95138-6 (eBook)
https://doi.org/10.1007/978-3-319-95138-6

Library of Congress Control Number: 2018931482

© Springer International Publishing AG, part of Springer Nature 2018
This work is subject to copyright. All rights are reserved by the Publisher, whether the whole or part of the material is concerned, specifically the rights of translation, reprinting, reuse of illustrations, recitation, broadcasting, reproduction on microfilms or in any other physical way, and transmission or information storage and retrieval, electronic adaptation, computer software, or by similar or dissimilar methodology now known or hereafter developed.
The use of general descriptive names, registered names, trademarks, service marks, etc. in this publication does not imply, even in the absence of a specific statement, that such names are exempt from the relevant protective laws and regulations and therefore free for general use.
The publisher, the authors and the editors are safe to assume that the advice and information in this book are believed to be true and accurate at the date of publication. Neither the publisher nor the authors or the editors give a warranty, express or implied, with respect to the material contained herein or for any errors or omissions that may have been made. The publisher remains neutral with regard to jurisdictional claims in published maps and institutional affiliations.

This Springer imprint is published by the registered company Springer Nature Switzerland AG
The registered company address is: Gewerbestrasse 11, 6330 Cham, Switzerland

Preface

There has been a strong concern for global climate change particularly in recent years, as disasters induced by extreme weathers appear to increase year by year. One solution for the environmental crisis is a clean energy source, and solar cell production increased drastically in the last decade. Although solar cells are generally viewed as pure semiconductor devices, solar cells are essentially optical devices and, for the optimization and interpretation of solar cell performance, the knowledge for the optical processes in the devices is critical. In particular, the optical characteristics of solar cell component layers and the device configurations affect the resulting conversion efficiencies directly and thus the determination of the optical properties and structures is of significant importance.

Recently, for the characterization of material optical properties and structures, spectroscopic ellipsometry (SE) technique is employed more widely in solar cell researches. In particular, ellipsometry has great advantages over other characterization techniques, including accurate optical constant determination, very fast spectral measurements within a few seconds, extremely high thickness sensitivity, and large-area characterization of optical characteristics and structures. Thus, SE has a large potential as a monitoring tool of mass production. Moreover, SE characterization can be made even for textured structures incorporated into actual devices. In fact, for the production of crystalline and amorphous Si solar cells, SE-based measurement systems have often been used.

Based on the optical constants extracted from SE characterizations, explicit device characterization/simulation can further be performed. From such analyses, we can determine the current loss mechanisms and predict the conversion efficiency of specific solar cells. In general, practical solar cell optimization relies heavily on try-and-error approach and maximizing conversion efficiencies is very time-consuming. However, the solar cell optimization using device simulation is expected to be far more effective if compared with conventional approach.

In the second volume of *Spectroscopic Ellipsometry for Photovoltaics*, we focused on SE application on solar cell characterization. In particular, this book consists of the following two major parts: spectroscopic ellipsometry applications for which more advanced instrumentation and analyses are required (Part I) and the

complete optical functions of solar cell component layers (Part II), which are crucial for ellipsometry analyses and optical simulations of devices.

Specifically, after an introductory chapter which gives (i) a general introduction for photovoltaic devices and (ii) an overview over the contents of the subsequent chapters in the book (Chap. 1), in Part I, more advanced applications for external quantum efficiency (EQE) analyses (Chaps. 2 and 3) and structural characterization (Chaps. 4–7) are described. The EQE analysis is of significant importance to find the current loss mechanism in the devices (Chap. 2) and the optical effects of each component layer (Chap. 3). By employing advanced optical modeling techniques, even textured multilayer structures can be studied by ellipsometry (Chap. 4). The examples of online monitoring of solar cell module production (Chap. 5), real-time control of thin layer growth (Chap. 6), and the mapping characterization of solar cell devices (Chap. 7) are also provided in Part I.

In Part II, tabulated optical constants and completely parameterized parameters for 148 materials used in various photovoltaic devices are summarized. The solar cell materials covered in Part II include inorganic semiconductors (Chap. 8), organic semiconductors (Chap. 9), hybrid perovskite materials (Chap. 10), transparent conductive oxides (Chap. 11), metals (Chap. 12), and substrates (Chap. 13). All the dielectric functions described in Part II are modeled using only three models, i.e., the Sellmeier, Tauc–Lorentz, and Drude models. By employing the optical data described in Part II, accurate ellipsometry characterization and optical simulation can be performed rather easily.

Gifu, Japan — Hiroyuki Fujiwara
Toledo, USA — Robert W. Collins

Acknowledgements

The editors would like to thank all authors for their great contributions and helpful suggestions. Concerning the optical data of numerous solar cell component layers, HF and RWC are especially grateful to Drs. Gerald E. Jellison Jr., James N. Hilfiker, Craig M. Herzinger, Mariano Campoy-Quiles, Nina Hong, Takashi Koida, Jian Li, Hitoshi Tampo, and Maria I. Alonso for their continuous support and encouragement during the preparation of this book that took more than 3 years. HF thanks Drs. Shigeru Niki and Koji Matsubara for their kind support. HF gratefully acknowledges Dr. Claus E. Ascheron who has supported the publication of this book. HF wishes to express sincere gratitude to Shohei Fujimoto, Akihiro Nakane, Takemasa Fujiseki, Masato Kato, Mitsutoshi Nishiwaki, and Masayuki Kozawa for their enthusiastic efforts for the preparation of this book.

RWC acknowledges data and graphics assistance from chapter contributors, Drs. Puruswottam Aryal, Dinesh Attygalle, Jie Chen, Lila Dahal, Zhiquan Huang, Abdel-Rahman Ibdah, Prakash Koirala, Puja Pradhan, and Ambalanath Shan. RWC also acknowledges the motivating collaborations with research colleagues, Profs. Hiroyuki Fujiwara, Nikolas Podraza, and Sylvain Marsillac; Drs. Miklos Fried and Peter Petrik; as well as colleagues from the photovoltaics, glass, and instrumentation industries, Jeffrey Hale, Blaine Johs, Kenneth Kormanyos, Galen Pfeiffer, and David Strickler. Finally, RWC would like to thank Linda Collins for her continuous support.

Gifu, Japan — Hiroyuki Fujiwara
Toledo, USA — Robert W. Collins

Contents

1 Introduction 1
Hiroyuki Fujiwara
1.1 Photovoltaic Devices 1
1.1.1 Principles of Solar Cell 2
1.1.2 Sunlight 3
1.1.3 Performance of Various Solar Cells 5
1.2 Optical Properties of Solar Cell Materials 7
1.2.1 Optical Constants and Dielectric Function 8
1.2.2 Optical Constants of Solar Cell Materials 9
1.2.3 Dielectric Function Modeling 12
1.3 Light Absorption in Solar Cells 17
1.3.1 Light Absorption in Absorber Layer 18
1.3.2 EQE Characteristics 19
1.3.3 Optical and Recombination Losses in Solar Cells 22
1.4 Overview of This Book 24
References 25

Part I Application of Ellipsometry Technique

2 Analysis of Optical and Recombination Losses in Solar Cells 29
Hiroyuki Fujiwara, Akihiro Nakane, Daisuke Murata, Hitoshi Tampo, Takuya Matsui and Hajime Shibata
2.1 Introduction 29
2.2 ERS and ARC Methods 35
2.2.1 Optical Admittance Method 36
2.2.2 Treatment of Glass Substrate 41
2.2.3 Analysis of a Textured Solar Cell 43
2.3 e-ARC Method 50
2.3.1 Recombination Model 50
2.3.2 Analysis of a CZTSe Solar Cell 53

2.3.3 Interpretation of EQE Spectra . . . 56
2.4 EQE Analysis Examples . . . 57
2.4.1 CZTSe and CZTS Solar Cells . . . 58
2.4.2 CdTe Solar Cell . . . 61
2.4.3 a-Si:H Solar Cell . . . 63
2.5 EQE Analysis of Textured c-Si Solar Cells . . . 66
2.5.1 Continuous Phase Approximation . . . 67
2.5.2 Analysis of Flat c-Si Solar Cells . . . 68
2.5.3 Analysis of Textured c-Si Solar Cells . . . 71
2.6 Carrier Loss Mechanisms . . . 74
2.6.1 Effect of Carrier Collection Length on J_{sc} . . . 74
2.6.2 Carrier Loss in Various Solar Cells . . . 76
2.7 Free Software for EQE Analysis . . . 78
References . . . 79

3 Optical Simulation of External Quantum Efficiency Spectra . . . 83
Prakash Koirala, Abdel-Rahman A. Ibdah, Puruswottam Aryal, Puja Pradhan, Zhiquan Huang, Nikolas J. Podraza, Sylvain Marsillac and Robert W. Collins
3.1 Introduction . . . 84
3.2 Hydrogenated Amorphous Silicon Solar Cells . . . 85
3.2.1 Solar Cell Fabrication and Performance . . . 85
3.2.2 Component Layer Dielectric Functions . . . 87
3.2.3 Spectroscopic Ellipsometry Measurement and Analysis . . . 90
3.2.4 External Quantum Efficiency Simulations . . . 94
3.3 Cadmium Telluride Solar Cells . . . 98
3.3.1 Solar Cell Fabrication and Performance . . . 98
3.3.2 Component Layer Dielectric Functions . . . 99
3.3.3 Spectroscopic Ellipsometry Analysis . . . 102
3.3.4 External Quantum Efficiency Simulations . . . 110
3.4 Copper Indium-Gallium Diselenide Solar Cells . . . 113
3.4.1 Solar Cell Fabrication and Performance . . . 113
3.4.2 Component Layer Dielectric Functions . . . 114
3.4.3 Spectroscopic Ellipsometry Analysis . . . 118
3.4.4 External Quantum Efficiency Simulations . . . 124
3.5 Summary . . . 134
References . . . 136

4 Characterization of Textured Structures . . . 139
Hiroyuki Fujiwara and Yuichiro Sago
4.1 Introduction . . . 139
4.2 Characterization of Textured Structures in a-Si:H/c-Si Solar Cells . . . 143

4.2.1 Tilt-Angle SE Measurement 143
4.2.2 Analysis of Textured a-Si:H/c-Si Structures 144
4.2.3 Effect of the Texture Size on a-Si:H Properties 146
4.2.4 Characterization of Textured Solar Cell Structures . . . 149
4.3 Characterization of Textured Structures in Thin-Film Solar Cells 150
4.3.1 EMA Multilayer and Surface Area Models 151
4.3.2 Analysis of a-Si:H Solar Cell Structures 158
4.3.3 Analysis of μc-Si:H/a-Si:H Tandem Solar-Cell Structures 161
4.3.4 Analysis of CIGSe Solar Cell Structures 164
References 166

5 On-line Monitoring of Photovoltaics Production 169
Ambalanath Shan, Jie Chen, Prakash Koirala, Kenneth R. Kormanyos, Nikolas J. Podraza and Robert W. Collins
5.1 Introduction 170
5.2 On-line Through-the-Glass SE for Rigid CdTe PV Panels in the Superstrate Configuration 173
5.2.1 Equipment Design, Development, and Measurement Procedures 174
5.2.2 Instrument Capabilities in Thin Film CdTe PV 176
5.3 On-Line SE for Roll-to-Roll Flexible PV in the Substrate Configuration 185
5.3.1 Equipment Design, Development, and Measurement Procedures 187
5.3.2 Applications in Thin Film *a*-Si:H PV 191
5.4 Summary and Future Directions 204
References 206

6 Real Time Measurement, Monitoring, and Control of $CuIn_{1-x}Ga_xSe_2$ by Spectroscopic Ellipsometry 209
Puja Pradhan, Abdel-Rahman A. Ibdah, Puruswottam Aryal, Dinesh Attygalle, Nikolas J. Podraza, Sylvain Marsillac and Robert W. Collins
6.1 Introduction 210
6.2 Dielectric Functions Relevant for Real Time SE of CIGS 214
6.3 Real Time Measurement of Three-Stage Coevaporation of CIGS 221
6.3.1 Deposition Details and Solar Cell Results 221
6.3.2 Standard CIGS Thickness in Continuous Process: Stage I $(In_{1-x}Ga_x)_2Se_3$ Deposition 226
6.3.3 Standard CIGS Thickness in Continuous Process: Stage II IGS Conversion to Cu-Rich CIGS 231

6.3.4 Standard CIGS Thickness in Continuous Process: Stage II and III Transitions Between Cu-Rich CIGS and Cu-Poor CIGS . . . 234
6.3.5 Standard CIGS Thickness in Continuous Process: Summary . . . 236
6.3.6 Standard CIGS Thickness in Shuttered Process: Summary . . . 238
6.3.7 Thin CIGS in Shuttered Process: Summary . . . 241
6.4 Issues in Real-Time Monitoring and Control . . . 247
6.5 Summary . . . 250
References . . . 252

7 Real Time and Mapping Spectroscopic Ellipsometry of Hydrogenated Amorphous and Nanocrystalline Si Solar Cells . . . 255
Zhiquan Huang, Lila R. Dahal, Sylvain Marsillac, Nikolas J. Podraza and Robert W. Collins
7.1 Introduction and Overview . . . 256
7.2 Real Time SE for Process Development: Nanocrystalline Si:H in *p-i-n* Tandem Solar Cells . . . 259
7.2.1 General Strategy and Approaches . . . 259
7.2.2 Top Cell Analysis . . . 262
7.2.3 Dielectric Functions of Nanocrystalline Si:H *n* and *p*-Layers for the Tunnel Junction . . . 265
7.2.4 Dielectric Functions of Bottom Cell Nanocrystalline Si:H *i*-Layers . . . 274
7.2.5 Real Time SE and Growth Evolution Diagram of *nc*-Si:H *i*-Layer Evolution . . . 280
7.2.6 Process-Performance Correlations for *a*-Si:H/*nc*-Si:H Tandem Solar Cells . . . 283
7.3 Mapping SE for Correlations with Device Performance: Optimization of *nc*-Si:H *n*-Layers in *a*-Si:H Solar Cells . . . 290
7.3.1 General Strategy and Approaches . . . 290
7.3.2 Dielectric Function Determination for *nc*-Si:H *n*-Layers . . . 293
7.3.3 Growth Evolution Diagram for *nc*-Si:H *n*-Layers . . . 299
7.3.4 Mapping Spectroscopic Ellipsometry of Solar Cell Structures . . . 304
7.3.5 Property-Performance Correlations for Solar Cells . . . 306
7.4 Summary . . . 312
References . . . 314

Part II Optical Data of Solar-Cell Component Materials

8 Inorganic Semiconductors and Passivation Layers 319
Akihiro Nakane, Shohei Fujimoto, Gerald E. Jellison Jr., Craig M. Herzinger, James N. Hilfiker, Jian Li, Robert W. Collins, Takashi Koida, Shinho Kim, Hitoshi Tampo and Hiroyuki Fujiwara
8.1 Introduction 320
8.2 Optical Data of Inorganic Semiconductors and Passivation Layers 322
8.2.1 Si 322
8.2.2 Ge 325
8.2.3 SiO_2 328
8.2.4 Al_2O_3 329
8.2.5 Ga_2O_3 331
8.2.6 SiN 332
8.2.7 a-Si:H 338
8.2.8 a-Si:H Layers 340
8.2.9 a-SiC:H 346
8.2.10 a-SiO:H 350
8.2.11 μc-Si:H 354
8.2.12 AlAs 356
8.2.13 GaAs 358
8.2.14 InAs 360
8.2.15 GaP 363
8.2.16 InP 365
8.2.17 AlSb 367
8.2.18 ZnS 369
8.2.19 ZnSe 370
8.2.20 ZnTe 372
8.2.21 CdS 374
8.2.22 CdSe 376
8.2.23 CdTe 378
8.2.24 $CuInSe_2$ 380
8.2.25 $CuGaSe_2$ 382
8.2.26 $CuIn_{1-x}Ga_xSe_2$ [Cu/(In + Ga) = 0.90] 384
8.2.27 $CuInGaSe_2$-Based Compound [Cu/(In + Ga) = 0.69] 397
8.2.28 $CuInGaSe_2$-Based Compound [Cu/(In + Ga) = 0.36] . . . 399
8.2.29 Cu_2ZnSnS_4 401
8.2.30 $Cu_2ZnSnSe_4$ 402
8.2.31 $Cu_2ZnSn(S_xSe_{1-x})_4$ 405
8.2.32 $Cu_2ZnGeSe_4$ 411
8.2.33 Cu_2SnSe_3 413

8.2.34 In_2S_3 . . . 418
8.2.35 MoS_2 . . . 419
8.2.36 $MoSe_2$ (Polycrystal) . . . 421
8.2.37 $MoSe_2$ (Single Crystal) . . . 423
References . . . 425

9 Organic Semiconductors . . . 427
Takemasa Fujiseki, Shohei Fujimoto, Mariano Campoy-Quiles, Maria Isabel Alonso, Takurou N. Murakami, Tetsuhiko Miyadera and Hiroyuki Fujiwara
9.1 Introduction . . . 427
9.2 Optical Data of Organic Semiconductors . . . 429
9.2.1 APFO-3 (F8TBT, PFDTBT) [Poly{2,7-(9,9-Dioctylfluorene)-alt-5,5-(4',7'-di-2-Thienyl-2',1',3'-Benzothiadiazole)}] . . . 429
9.2.2 APFO-Green9 [Poly{2,7-(9,9-Dioctylfluorene)-alt-5,5-(5,10-di-2-Thienyl-2,3,7,8-Tetraphenyl-Pyrazino-[2,3-g]Quinoxaline)}] . . . 431
9.2.3 Fluorinated CuPc (F_{16}CuPc) [Fluorinated Copper Phthalocyanine] . . . 431
9.2.4 MEH-PPV [Poly{2-Methoxy-5-(2'-Ethyl-Hexyloxy)-p-Phenylenevinylene}] . . . 435
9.2.5 P3HT [Poly(3-Hexylthiophene)] . . . 437
9.2.6 P3HT:PC_{60}BM (Blend Ratio 1:1) [Poly(3-Hexylthiophene):(6,6)-Phenyl-C_{61}-Butyric Acid Methyl Ester] . . . 439
9.2.7 P3HT:PC_{70}BM (Blend Ratio 1:1) [Poly(3-Hexylthiophene):(6,6)-Phenyl-C_{71}-Butyric Acid Methyl Ester] . . . 441
9.2.8 P3OT [Poly(3-Octylthiophene)] . . . 443
9.2.9 PC_{60}BM (Aka PCBM, [60]PCBM, PC61BM) [(6,6)-Phenyl-C_{61}-Butyric Acid Methyl Ester] . . . 445
9.2.10 PC_{70}BM (Aka [70]PCBM, PC71BM) [(6,6)-Phenyl-C_{71}-Butyric Acid Methyl Ester] . . . 447
9.2.11 PCDTBT [Poly{N-9-Heptadecanyl-2,7-Carbazole-alt-5,5-(4',7'-di-2-Thienyl-2',1',3'-Benzothiadiazole)}] . . . 449
9.2.12 PCPDTBT [Poly{2,6-(4,4-bis-(2-Ethylhexyl)-4H-Cyclopenta[2,1-b;3,4-b']-Dithiophene)-alt-4,7-(2,1,3-Benzothiadiazole)}] . . . 451
9.2.13 PEDOT:PSS [Poly(3,4-Ethylenedioxythiophene): Poly(4-Styrensulfonate)] . . . 452
9.2.14 PMMA [Poly(Methyl Methacrylate)] . . . 455

9.2.15 PTB7 [Poly{[4,8-bis[(2-Ethylhexyl)Oxy] Benzo[1,2-b:4,5-b']Dithiophene-2,6-Diyl] [3-Fluoro-2-[(2-Ethylhexyl)Carbonyl] Thieno[3,4-b]Thiophenediyl]}] 457
9.2.16 PTB7:$PC_{70}BM$ (Blend Ratio 1:1.5) [Poly{[4,8-bis [(2-Ethylhexyl)Oxy]Benzo [1,2-b:4,5-b'] Dithiophene-2,6-Diyl][3-Fluoro-2-[(2-Ethylhexyl) Carbonyl]Thieno[3,4-b]Thiophenediyl]}:(6,6)-Phenyl-C_{71}-Butyric Acid Methyl Ester] 459
9.2.17 Si-PCPDTBT [Poly{[4, 40-bis(2-Ethylhexyl) Dithieno(3,2-b:20,30-d)Silole]-2,6-Diyl-alt-[4,7-bis (2-Thienyl)-2,1,3-Benzothiadiazole]-5,50-Diyl}] 461
9.2.18 Spiro-OMeTAD [2,2',7,7'-Tetrakis-(N, N-di-p-Methoxyphenylamine) 9,9'-Spirobifluorene] 463
9.2.19 TQ1 [Poly{2,3-bis-(3-Octyloxyphenyl)Quinoxaline-5,8-Diyl-alt-Thiophene-2,5-Diyl}] 465
9.2.20 DPPTTT [Thieno(3,2-b)Thiophene-Diketopyrrolopyrrole] 467
References 469

10 Organic-Inorganic Hybrid Perovskites 471
Shohei Fujimoto, Takemasa Fujiseki, Masato Tamakoshi, Akihiro Nakane, Tetsuhiko Miyadera, Takeshi Sugita, Takurou N. Murakami, Masayuki Chikamatsu and Hiroyuki Fujiwara
10.1 Introduction 471
10.2 Optical Data of Hybrid Perovskites 473
10.2.1 $FAPbI_3$ [$HC(NH_2)_2PbI_3$] 473
10.2.2 $MAPbI_3$ ($CH_3NH_3PbI_3$) 475
10.2.3 $MAPbBr_3$ ($CH_3NH_3PbBr_3$) 477
10.2.4 $MAPb(I_{1-x}Br_x)_3$ [$CH_3NH_3Pb(I_{1-x}Br_x)_3$] 479
10.2.5 $MAPbCl_3$ ($CH_3NH_3PbCl_3$) 485
10.2.6 $FAPbI_3$ (δ Phase) 487
10.2.7 PbI_2 489
10.2.8 CH_3NH_3I 491
References 493

11 Transparent Conductive Oxides 495
Akihiro Nakane, Shohei Fujimoto, Masato Tamakoshi, Takashi Koida, James N. Hilfiker, Gerald E. Jellison Jr., Takurou N. Murakami, Tetsuhiko Miyadera and Hiroyuki Fujiwara
11.1 Introduction 496
11.2 Optical Data of Transparent Conductive Oxides 498
11.2.1 Graphene 498
11.2.2 In_2O_3 (Non-doped) 500

11.2.3 In_2O_3:H ($N_{Hall} = 2.1 \times 10^{20}$ cm^{-3}) 502
11.2.4 In_2O_3:Sn ($N_{Hall} = 4.9 \times 10^{20}$ cm^{-3}) 504
11.2.5 In_2O_3:Sn ($N_{Hall} = 7.2 \times 10^{20}$ cm^{-3}) 506
11.2.6 In_2O_3:Sn ($N_{Hall} = 1.2 \times 10^{21}$ cm^{-3}) 508
11.2.7 InZnO ($N_{Hall} = 2.5 \times 10^{20}$ cm^{-3}) 510
11.2.8 MoO_x 512
11.2.9 NiO 515
11.2.10 SnO_2 (Non-doped) 517
11.2.11 SnO_2:F (TEC-15) 519
11.2.12 TiO_2 (Polycrystal) 521
11.2.13 TiO_2 (Anatase Single Crystal) 523
11.2.14 TiO_2 (Rutile Single Crystal) 526
11.2.15 WO_3 529
11.2.16 ZnO (Non-doped) 531
11.2.17 ZnO:Ga ($N_{Hall} = 1.1 \times 10^{20}$ cm^{-3}) 533
11.2.18 ZnO:Al ($N_{opt} = 1.5 \times 10^{20}$ cm^{-3}) 535
11.2.19 ZnO:Ga ($N_{Hall} = 4.8 \times 10^{20}$ cm^{-3}) 537
11.2.20 ZnO:Ga ($N_{Hall} = 6.5 \times 10^{20}$ cm^{-3}) 539
References 541

12 Metals 543
Shohei Fujimoto, Takemasa Fujiseki and Hiroyuki Fujiwara
12.1 Introduction 543
12.2 Optical Properties and Reflectance of Metals 544
12.2.1 Optical Properties of Metals 545
12.2.2 Reflectance at Semiconductor/Metal Interface 546
12.3 Optical Data of Metals 550
12.3.1 Ag 550
12.3.2 Al 552
12.3.3 Au 554
12.3.4 C (Graphite) 556
12.3.5 Cr 558
12.3.6 Cu 560
12.3.7 Mg 562
12.3.8 Mo 564
12.3.9 Ni 566
12.3.10 Pt 568
12.3.11 Ti 570
12.3.12 W 572
References 574

13 Substrates and Coating Layers 575
Shohei Fujimoto, Takemasa Fujiseki, James N. Hilfiker, Nina Hong, Mariano Campoy-Quiles and Hiroyuki Fujiwara
13.1 Introduction 575
13.2 Optical Data of Substrates and Coating Layers 577
13.2.1 SiO_2 577
13.2.2 Stainless Steel (SUS304) 583
13.2.3 Polycarbonate 585
13.2.4 PEN [Poly(Ethylene Naphthalate)] 587
13.2.5 PET [Poly(Ethylene Terephthalate)] 591
13.2.6 PMMA [Poly(Methyl Methacrylate)] 596
13.2.7 Polyimide 597
13.2.8 Kapton HN [Poly{N,N'-(Oxydiphenylene) Pyromellitimide}] 599
13.2.9 EVA [Ethylene Vinyl Acetate] 604
13.2.10 MgF_2, LiF and NaF 605
References 608

Index 609

Contributors

Maria Isabel Alonso Institut de Ciència de Materials de Barcelona (ICMAB-CSIC), Bellaterra, Spain

Puruswottam Aryal Department of Physics & Astronomy and Center for Photovoltaics Innovation & Commercialization, University of Toledo, Toledo, OH, USA

Dinesh Attygalle Department of Physics & Astronomy and Center for Photovoltaics Innovation & Commercialization, University of Toledo, Toledo, OH, USA

Mariano Campoy-Quiles Institut de Ciència de Materials de Barcelona (ICMAB-CSIC), Bellaterra, Spain

Jie Chen Department of Physics & Astronomy and Center for Photovoltaics Innovation & Commercialization, University of Toledo, Toledo, OH, USA

Masayuki Chikamatsu Research Center for Photovoltaics, National Institute of Advanced Industrial Science and Technology, Tsukuba, Japan

Robert W. Collins Department of Physics & Astronomy and Center for Photovoltaics Innovation & Commercialization, University of Toledo, Toledo, OH, USA

Lila R. Dahal Department of Physics & Astronomy and Center for Photovoltaics Innovation & Commercialization, University of Toledo, Toledo, OH, USA

Shohei Fujimoto Gifu University, Gifu, Japan

Takemasa Fujiseki Gifu University, Gifu, Japan

Hiroyuki Fujiwara Gifu University, Gifu, Japan

Craig M. Herzinger J.A. Woollam Co., Inc., Lincoln, NE, USA

James N. Hilfiker J.A. Woollam Co., Inc., Lincoln, NE, USA

Nina Hong J.A. Woollam Co., Inc., Lincoln, NE, USA

Zhiquan Huang Department of Physics & Astronomy and Center for Photovoltaics Innovation & Commercialization, University of Toledo, Toledo, OH, USA

Abdel-Rahman A. Ibdah Department of Physics & Astronomy and Center for Photovoltaics Innovation & Commercialization, University of Toledo, Toledo, OH, USA

Gerald E. Jellison Jr. Oak Ridge National Laboratory, Oak Ridge, TN, USA

Shinho Kim Research Center for Photovoltaics, National Institute of Advanced Industrial Science and Technology, Tsukuba, Japan

Takashi Koida Research Center for Photovoltaics, National Institute of Advanced Industrial Science and Technology, Tsukuba, Japan

Prakash Koirala Department of Physics & Astronomy and Center for Photovoltaics Innovation & Commercialization, University of Toledo, Toledo, OH, USA

Kenneth R. Kormanyos Calyxo USA, Perrysburg, OH, USA

Jian Li University of Toledo, Toledo, OH, USA

Sylvain Marsillac Virginia Institute of Photovoltaics, Old Dominion University, Norfolk, VA, USA

Takuya Matsui Research Center for Photovoltaics, National Institute of Advanced Industrial Science and Technology, Tsukuba, Japan

Tetsuhiko Miyadera Research Center for Photovoltaics, National Institute of Advanced Industrial Science and Technology, Tsukuba, Japan

Takurou N. Murakami Research Center for Photovoltaics, National Institute of Advanced Industrial Science and Technology, Tsukuba, Japan

Daisuke Murata Gifu University, Gifu, Japan

Akihiro Nakane Gifu University, Gifu, Japan

Nikolas J. Podraza Department of Physics & Astronomy and Center for Photovoltaics Innovation & Commercialization, University of Toledo, Toledo, OH, USA

Puja Pradhan Department of Physics & Astronomy and Center for Photovoltaics Innovation & Commercialization, University of Toledo, Toledo, OH, USA

Yuichiro Sago Gifu University, Gifu, Japan

Ambalanath Shan Department of Physics & Astronomy and Center for Photovoltaics Innovation & Commercialization, University of Toledo, Toledo, OH, USA

Hajime Shibata Research Center for Photovoltaics, National Institute of Advanced Industrial Science and Technology, Tsukuba, Japan

Takeshi Sugita Research Center for Photovoltaics, National Institute of Advanced Industrial Science and Technology, Tsukuba, Japan

Masato Tamakoshi Gifu University, Gifu, Japan

Hitoshi Tampo Research Center for Photovoltaics, National Institute of Advanced Industrial Science and Technology, Tsukuba, Japan

Chapter 1
Introduction



Hiroyuki Fujiwara

Abstract From optical constants (refractive index n and extinction coefficient k) extracted from ellipsometry technique, advanced optical analyses, including current loss analyses and structural analyses of textured devices, can be performed. The optical response in solar cell devices is essentially governed by the optical constants of solar-cell component layers and detailed optical analysis/simulation is of significant importance in maximizing conversion efficiencies. In this chapter, I review the operating principles of practical solar cells particularly based on the view of the absorber optical properties. Specifically, the relationship between solar cell characteristics and absorber absorption properties is discussed. The critical need of the optical and recombination loss analysis based on external quantum efficiency characterization is emphasized. By comparing the absorption spectra of various solar cell materials, the optical properties of semiconductors are further discussed. This chapter will also provide an overview for the contents of subsequent chapters in this book.

1.1 Photovoltaic Devices

A solar cell is basically a simple p-n junction device and its operation is quite straightforward. However, a complex device structure is often required to minimize the power loss induced by light reflection, unfavorable parasitic absorption and carrier recombination. To understand such power loss mechanisms in the devices, accurate knowledge for optical processes in solar cells are necessary. In this section, the characteristics of various solar cells are summarized in terms of absorber (semiconductor) optical properties.

H. Fujiwara (✉)
Gifu University, 1-1 Yanagido, Gifu 501-1193, Japan
e-mail: fujiwara@gifu-u.ac.jp

© Springer International Publishing AG, part of Springer Nature 2018

H. Fujiwara and R. W. Collins (eds.), *Spectroscopic Ellipsometry for Photovoltaics*,
Springer Series in Optical Sciences 214,
https://doi.org/10.1007/978-3-319-95138-6_1

1.1.1 Principles of Solar Cell

Figure 1.1 shows (a) a simplified structure of a p-n junction solar cell with a transparent conductive oxide (TCO) front electrode and (b) the absorption coefficient (α) spectrum of $CuInSe_2$ (CISe) [1]. In Fig. 1.1a, the p layer is absorber and the photocarriers are generated within the semiconducting absorber layer under light illumination. In this case, the short-circuit current density (J_{sc}) is generated in the short-circuit condition, whereas the open-circuit voltage (V_{oc}) is obtained in the open-circuit condition. By using the fill factor (FF), the conversion efficiency is determined as

$$\eta(\%) = J_{sc}\left(\mathrm{A/cm^2}\right) \times V_{oc}(\mathrm{V}) \times FF(\%)/0.1\left(\mathrm{W/cm^2}\right) \tag{1.1}$$

For most of solar cells, FF values are 70–80% [2]. In other words, the power output is governed primarily by J_{sc} and V_{oc} (i.e., $P \propto J_{sc} \times V_{oc}$).

In Fig. 1.1b, the α value of CISe increases rapidly near the band gap ($E_g = 1.00$ eV), followed by a gradual increase above E_g. In general, V_{oc} increases with E_g, while J_{sc} is determined essentially by the product of αd, where d is the thickness of the absorber layer (Sect. 1.3). Thus, the two important parameters of solar cells (V_{oc} and J_{sc}) can be deduced from the α spectrum of the absorber. In other words, the ultimate potential of solar cell materials can be judged from the α spectrum alone, and accurate determination of absorber optical properties is therefore of significant importance.

Figure 1.2 shows more detailed optical and physical processes in a solar cell. In this figure, a hypothetical band diagram for a TCO layer/doped layer (n)/absorber (p)/metal structure is indicated. Under sunlight illumination, the reflection loss

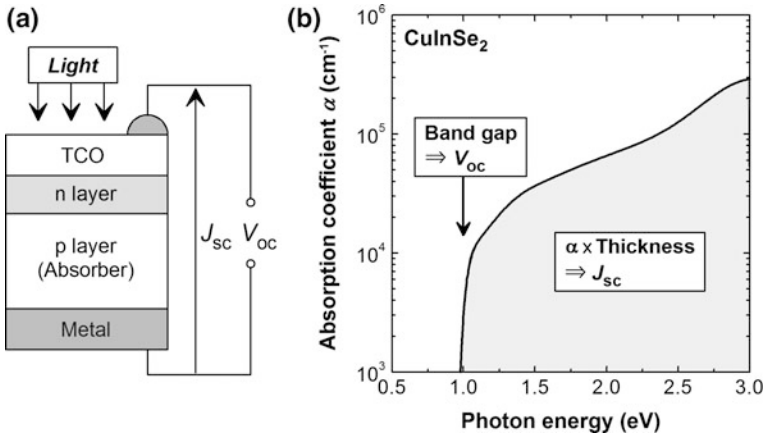


Fig. 1.1 **a** Structure of a p-n junction solar cell consisting of TCO/n layer/p layer/metal and **b** α spectrum of CISe [1]. The complete optical data of CISe are shown in Fig. 8.24

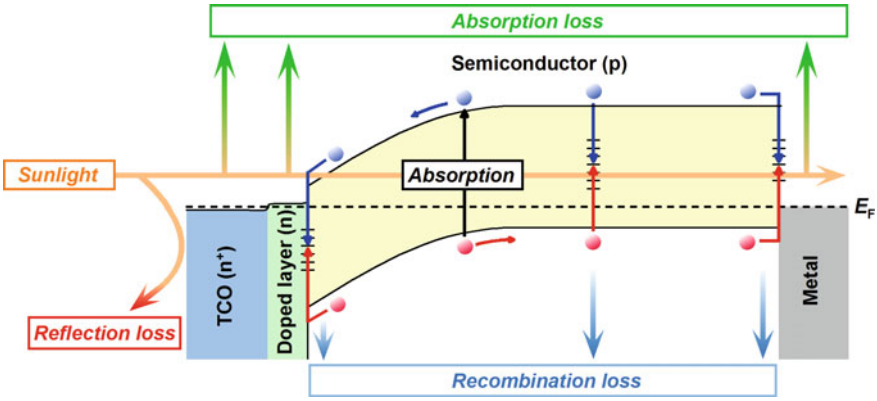


Fig. 1.2 Optical and physical processes in a solar cell with a structure of TCO/n layer/p layer/metal. The hypothetical band diagram is shown. The current losses in solar cells can be categorized into reflection, absorption and recombination losses

generally occurs by the front- and back-side reflections (see also Fig. 2.2). Some of the sunlight is absorbed in TCO, doped and metal layers, which causes the unfavorable absorption loss in the solar cell. In Fig. 1.2, the light absorption in the semiconducting p layer generates photocarriers, but some of the photocarriers recombine at defect states created within the bulk layer or at the front and rear interfaces, which constitutes the recombination loss. For the development of high-efficiency solar cells, it is necessary to minimize reflection, parasitic absorption and recombination losses. It should be emphasized that all of these losses can be determined quantitatively from detailed external quantum efficiency (EQE) analyses (Fig. 1.14 and Chap. 2).

1.1.2 Sunlight

In general, for the calculation of J_{sc}, a standard air-mass 1.5 global (AM1.5G) spectrum is used as the sunlight spectrum. Here, the "global" for AM1.5 implies that the component of scattered (diffused) light is included. Figure 1.3 shows the spectral irradiance of AM1.5G versus (a) wavelength and (b) photon energy, together with the spectral photon density of AM1.5G versus (c) wavelength and (d) photon energy. The numerical values are taken from [3]. Note that the irradiance is defined as watts per meter squared (W/m^2), whereas more conventional light intensity is defined differently as the power per unit solid angle from a point source. In Fig. 1.3, sharp drops observed in the irradiance and photon density originate from the light absorption induced by O_3, O_2, H_2O and CO_2 in the atmosphere. Although the sunlight spectrum is generally represented by Fig. 1.3a, this spectrum

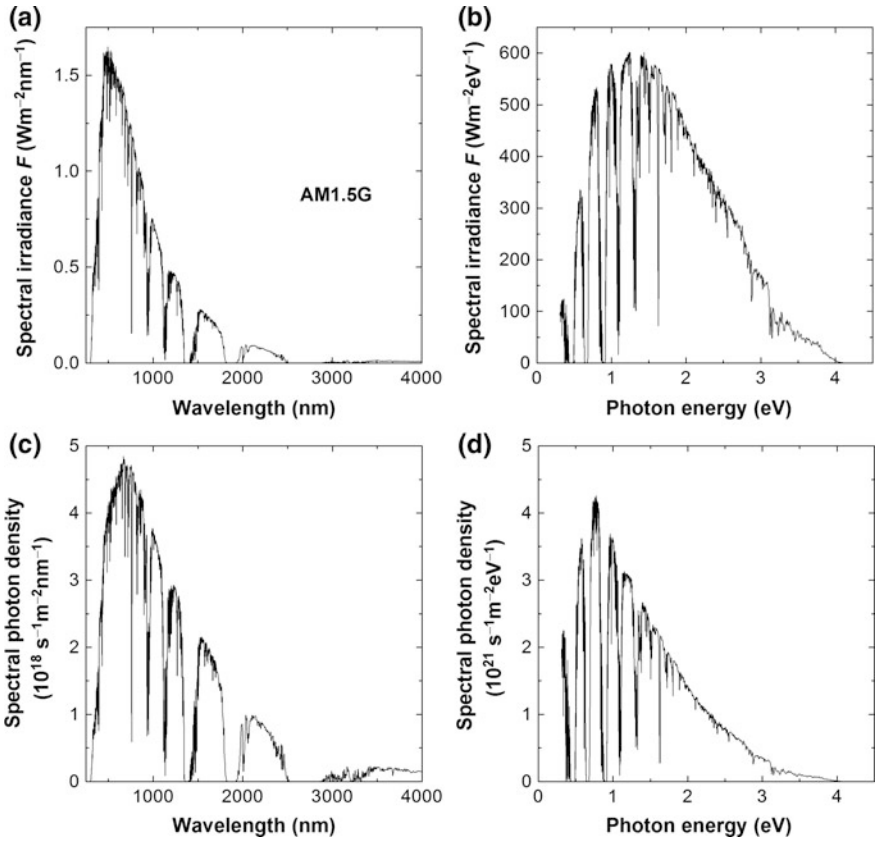


Fig. 1.3 Spectral irradiance of sunlight (AM1.5G) versus **a** wavelength and **b** photon energy, together with the spectral photon density of AM1.5G versus **c** wavelength and **d** photon energy. The numerical data are taken from [3]. The J_{sc} of solar cells is calculated from these spectra

does not correlate with actual photocarrier density generated under the sunlight illumination, as the irradiance becomes higher when the energy of photon is high.

More specifically, the photon energy E is calculated from the wavelength λ by

$$E = hc/\lambda, \tag{1.2}$$

where h and c show Planck's constant ($h = 6.62607 \times 10^{-34}$ J s) and the speed of light ($c = 2.99792 \times 10^{8}$ m/s), respectively. If electron-volt unit is used (1 eV = 1.60218×10^{-19} J), we obtain

$$E = \frac{1}{1.60218 \times 10^{-19}} \cdot \frac{hc}{\lambda} = \frac{1239.8}{\lambda(\mathrm{nm})} \ \mathrm{eV}. \tag{1.3}$$

By employing (1.2), the spectral photon density per second per meter squared is calculated as

$$\rho_{\text{photon}}(\lambda) = \frac{F(\lambda)}{E} = F(\lambda)\frac{\lambda}{hc}, \tag{1.4}$$

where $F(\lambda)$ represents the spectral irradiance shown in Fig. 1.3a. The result calculated from (1.4) has been shown in Fig. 1.3c. The ρ_{photon} versus E, obtained from a similar calculation, is also indicated in Fig. 1.3d. It can be seen that ρ_{photon} shows a maximum at 0.8 eV, while ρ_{photon} is quite low in a high energy region ($E > 3$ eV). Accordingly, the effect of the light absorption in the high-E region is negligible in solar cells. From ρ_{photon}, the current density is then determined as

$$J = q\rho_{\text{photon}}, \tag{1.5}$$

where q shows the electron charge ($q = 1.60218 \times 10^{-19}$ C). If the maximum ρ_{photon} of 4×10^{21} $\text{s}^{-1}\text{m}^{-2}\text{eV}^{-1}$ with a width of 2 eV is assumed for the spectrum of Fig. 1.3d, the upper limit of J_{sc} can be approximated by

$$J_{\text{sc}} = (1.60218 \times 10^{-19}) \cdot \frac{(4 \times 10^{21}) \times 2}{2} \cdot 10^{-4} \sim 0.064 \text{ A/cm}^2. \tag{1.6}$$

Thus, if all the sunlight ($E > 0.3$ eV) is converted to the photocurrent, we roughly obtain 64 mA/cm^2.

1.1.3 Performance of Various Solar Cells

In solar cells, photocarriers are generated when the energy of photons is higher than E_{g}, although the light absorption still occurs even below E_{g} due to the presence of tail-state absorption. If the light absorption in the absorber layer is assumed to occur only above E_{g}, the maximum J_{sc} is calculated according to the following equation using (1.5):

$$J_{\text{sc, max}} = q\int_{E_{\text{g}}}^{\infty} \rho_{\text{photon}}(E)\text{d}E. \tag{1.7}$$

In the above equation, $\rho_{\text{photon}}(E)$ corresponds to the spectrum of Fig. 1.3d.

Figure 1.4a shows the calculated $J_{\text{sc,max}}$ as a function of E_{g}, together with reported J_{sc} values of actual solar cells. The experimental J_{sc} data are taken from [2], except for CdTe [4], Cu(In,Ga)Se_2 (CIGSe) [5], $Cu_2ZnSnSe_4$ (CZTSe) [6], Cu_2ZnSnS_4 (CZTS) [7], $Cu_2ZnSn(S,Se)_4$ (CZTSSe) [8], $Cu_2Zn(Sn,Ge)Se_4$ (CZTGSe) [9], $CH_3NH_3PbI_3$ (MAPbI$_3$) [10], and $HC(NH_2)_2PbI_3$ (FAPbI$_3$) [11].

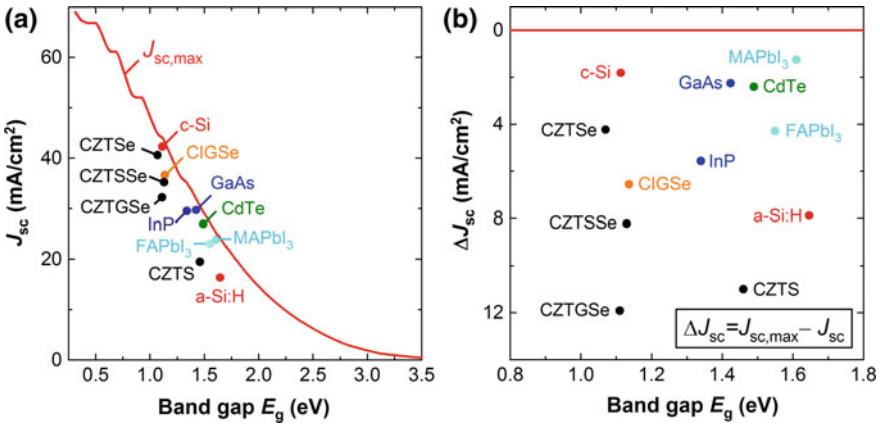


Fig. 1.4 **a** Maximum J_{sc} ($J_{sc,max}$) calculated from (1.7) as a function of E_g and **b** difference between $J_{sc,max}$ and experimental J_{sc} ($\Delta J_{sc} = J_{sc,max} - J_{sc}$). The experimental J_{sc} values are taken from [2], except for CdTe [4], $Cu(In,Ga)Se_2$ (CIGSe) [5], $Cu_2ZnSnSe_4$ (CZTSe) [6], Cu_2ZnSnS_4 (CZTS) [7], $Cu_2ZnSn(S,Se)_4$ (CZTSSe) [8], $Cu_2Zn(Sn,Ge)Se_4$ (CZTGSe) [9], $CH_3NH_3PbI_3$ ($MAPbI_3$) [10], and $HC(NH_2)_2PbI_3$ ($FAPbI_3$) [11]

The E_g values of the CZTSe, CZTS and CZTSSe were extracted from the EQE analyses [12]. In Fig. 1.4a, the experimental J_{sc} follows the trend of $J_{sc,max}$ and decreases with increasing E_g as the integrated ρ_{photon} becomes smaller.

In some solar cells, however, J_{sc} is much smaller than $J_{sc,max}$ and the difference between $J_{sc,max}$ and J_{sc} (i.e., $\Delta J_{sc} = J_{sc,max} - J_{sc}$) represents the optical and recombination losses. Figure 1.4b shows ΔJ_{sc} as a function of E_g, calculated from the result of Fig. 1.4a. As confirmed from this result, the crystalline Si (c-Si), GaAs, CdTe and $CH_3NH_3PbI_3$ solar cells show very small ΔJ_{sc} of ~2 mA/cm^2. In fact, quite high conversion efficiencies (18–29%) have been confirmed for these solar cells [2, 4, 10]. On the other hand, even though the CIGSe solar cell has a high efficiency of 21.7%, ΔJ_{sc} of this solar cell is rather large (6.6 mA/cm^2). This is due to the strong parasitic absorption in TCO (ZnO:Al), CdS and Mo layers (Fig. 2.11). It should be noted that the ΔJ_{sc} values of the CZTSe, CZTS and CZTSSe solar cells are underestimated as these solar cells exhibit relatively large tail absorption below E_g and the actual current loss is larger. The result of Fig. 1.4b shows clearly that the suppression of the J_{sc} loss is quite important to achieve high conversion efficiencies.

As mentioned above, V_{oc} shows a strong correlation with E_g. If we assume V_{oc} loss (V_{loss}) in solar cells, we can express V_{oc} as

$$V_{oc} = \frac{E_g}{q} - V_{loss}. \tag{1.8}$$

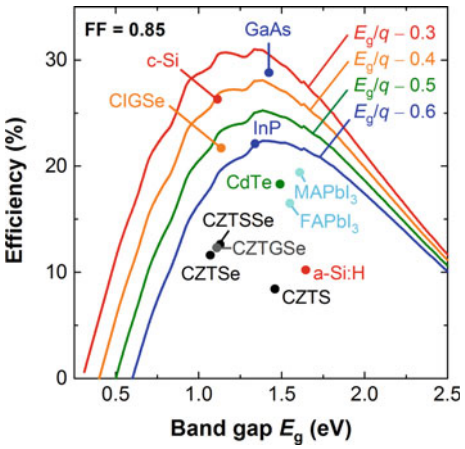


Fig. 1.5 Calculated conversion efficiency as a function of E_g, together with the experimental efficiencies of the solar cells shown in Fig. 1.4. The efficiency curves were calculated by changing V_{loss} in (1.8) in a range from 0.3 to 0.6 V assuming $FF = 0.85$

In this case, the conversion efficiency can be calculated from (1.1) by further assuming a constant FF value. Figure 1.5 shows the calculated conversion efficiency as a function of E_g, together with the experimental efficiencies of the solar cells. For the calculation, $FF = 0.85$ was assumed and several efficiency curves were calculated by changing V_{loss} in a range from 0.3 to 0.6 V. For the GaAs solar cell, FF is quite high (86.5%) and V_{loss} is quite low (0.30 V). As a result, the experimental efficiency of the GaAs solar cell is quite close to the calculation limit of $V_{loss} = 0.3$ V. In Fig. 1.5, the maximum efficiency is obtained at 1.4 eV for $V_{loss} \geq 0.4$ V, while the conversion efficiencies show high values in a range of $E_g = 1.1$–1.4 eV if $V_{loss} = 0.3$ V. It can be seen that, for most of the solar cells, the conversion efficiencies are much smaller than the calculated values. In particular, for thin-film solar cells, which have been developed mainly to realize low-cost solar cells, the overall efficiencies are quite low. Accordingly, for these solar cells, the analysis of power loss mechanism and the following optimization of solar cell structures and processing are crucial.

1.2 Optical Properties of Solar Cell Materials

As discussed in Fig. 1.1, the conversion efficiency of solar cells is ultimately governed by the absorption characteristics of solar-cell absorber layers. Thus, the understanding of the absorption properties is of utmost importance. In this section, the basic ideas of optical constants (or dielectric function) are addressed. This section will further provide the comparison of optical spectra obtained from various solar cell materials.

1.2.1 Optical Constants and Dielectric Function

The propagation of light (electromagnetic wave) in media is expressed completely by refractive index n and extinction coefficient k (Chap. 1 (Vol. 1)). In optics, the values of (n, k) are combined to yield a single complex number and we define complex refractive index N by

$$N \equiv n - ik. \tag{1.9}$$

The absolute value of N is determined from a complex dielectric constant defined by

$$\varepsilon \equiv \varepsilon_1 - i\varepsilon_2 \tag{1.10}$$

and, by Maxwell's equations, N is expressed from ε as follows [13]:

$$N^2 \equiv \varepsilon. \tag{1.11}$$

From the above equations, we get

$$\varepsilon_1 = n^2 - k^2, \tag{1.12}$$

$$\varepsilon_2 = 2nk. \tag{1.13}$$

The variation of ε with E is generally referred to as dielectric function. The ε_1 spectrum basically shows the refractive index component, whereas the ε_2 spectrum essentially shows the light absorption characteristic as the magnitude of k represents the light absorption strength. In fact, when $k = 0$, we obtain $\varepsilon_2 = 0$ ($\varepsilon_1 = n^2$) from (1.12) and (1.13). On the other hand, from (ε_1, ε_2), (n, k) can also be calculated:

$$n = \left\{ \left[\varepsilon_1 + \left(\varepsilon_1^2 + \varepsilon_2^2 \right)^{1/2} \right] /2 \right\}^{1/2}, \tag{1.14}$$

$$k = \left\{ \left[-\varepsilon_1 + \left(\varepsilon_1^2 + \varepsilon_2^2 \right)^{1/2} \right] /2 \right\}^{1/2}. \tag{1.15}$$

From k, absorption coefficient can further be obtained as

$$\alpha = \frac{4\pi k}{\lambda}. \tag{1.16}$$

The above equation shows an important relation between k and α. When there is no light absorption, it follows that $\alpha = k = \varepsilon_2 = 0$. If the unit of λ is nm, α with a conventional unit of cm^{-1} is calculated by

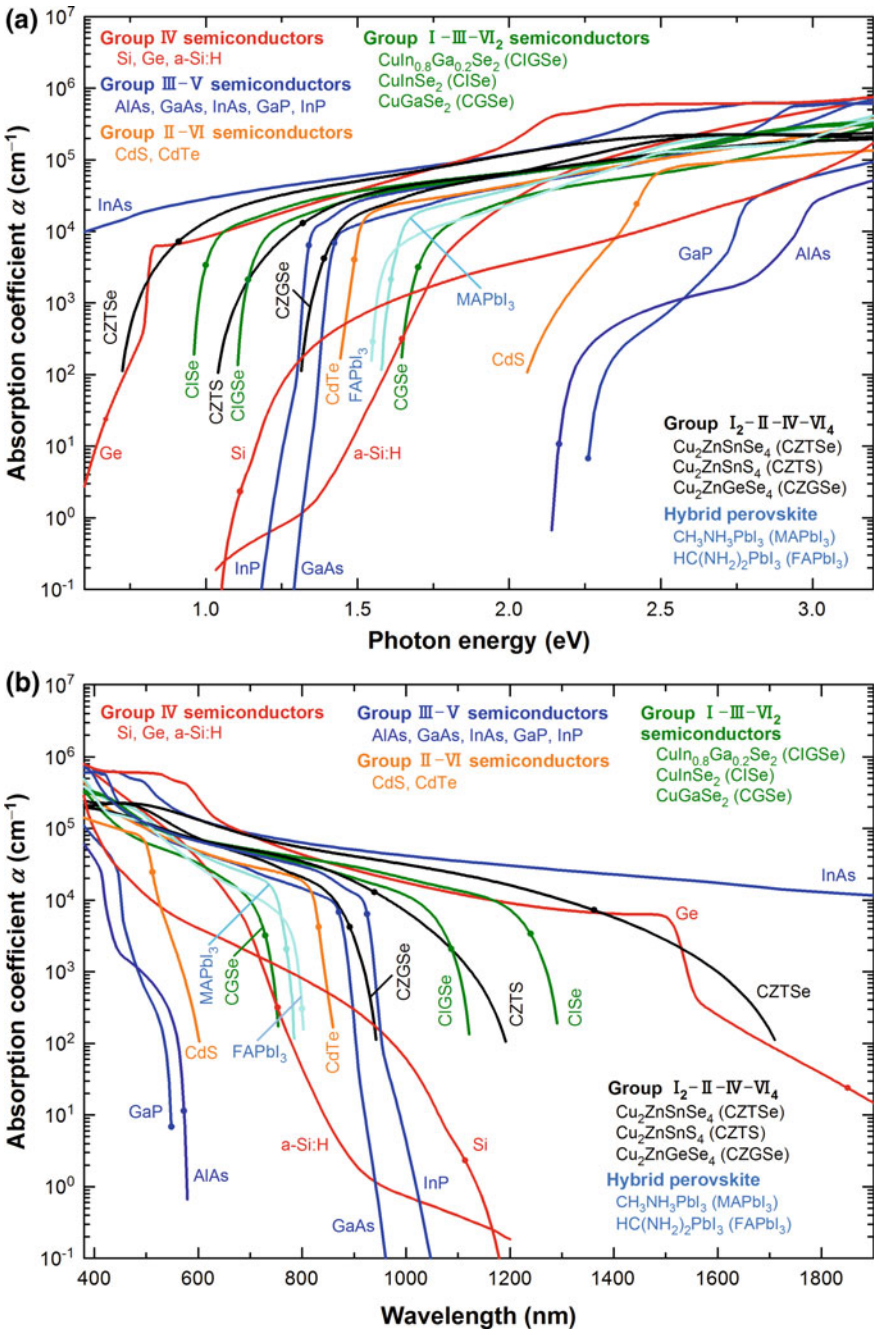
$$\alpha(\mathrm{cm}^{-1}) = \frac{4\pi k}{\lambda(\mathrm{nm})} \cdot 10^7 = \frac{4\pi k \cdot E(\mathrm{eV})}{1239.8(\mathrm{nm})} \cdot 10^7. \tag{1.17}$$

1.2.2 Optical Constants of Solar Cell Materials

Figure 1.6 summarizes the α spectra of various solar cell materials versus (a) E and (b) λ. The complete optical data of these materials can be found in Chaps. 8 and 10. In the figure, the E_g positions of each material are indicated by the closed circles. For a high efficiency CIGSe solar cell [5], the alloy composition of $CuIn_{0.8}Ga_{0.2}Se_2$ was employed and the corresponding spectrum calculated from the CIGSe optical database (Sect. 10.4 (Vol. 1)) is shown. It can be seen that many direct-transition semiconductors show similar α values of $\sim 10^4$ cm^{-1} and, at the exact E_g positions, the α values are around 5×10^3 cm^{-1}. In contrast, the indirect-transition semiconductors, including Si, Ge, GaP and AlAs, exhibit much lower values of α = 2–24 cm^{-1} at the E_g positions. Although GaP is an indirect transition semiconductor, GaInP alloys, for example, show the direct transition in a broad compositional range [14] and have been applied to concentrator/space solar cells (Chap. 14 (Vol. 1)). Except for c-Si and microcrystalline Si [15], no other indirect transition semiconductors have been investigated intensively for solar cell application due to low α values. For multi-junction devices, however, Ge substrates have been employed to widen the spectral response [16]. The hydrogenated amorphous silicon (a-Si:H) is generally considered to have a pseudo-direct band gap by zone folding [17], but α of a-Si:H at the E_g position of 1.65 eV is rather small ($\sim$100 cm^{-1}).

In earlier studies, high conversion efficiencies of $CH_3NH_3PbI_3$ solar cells were attributed to very large α values [18, 19]. However, the α values of the hybrid perovskite have been overestimated seriously (see Chap. 6 (Vol. 1)) and the actual α values are comparable to those of other direct-transition semiconductors. Detailed EQE analysis shows that high J_{sc} observed in $CH_3NH_3PbI_3$ solar cells is caused by very low parasitic absorption in the solar cells (Sect. 16.3 (Vol. 1)). Thus, solar cell structures also affect the resulting performance significantly.

As shown in Fig. 1.6, kesterite semiconductors such as CZTSe and CZTS exhibit quite large tail-state absorption and the relatively large α values are observed even below E_g [12]. The presence of the absorption tail can be confirmed more easily when α is plotted versus λ. The a-Si:H layers also show strong tail absorption due to disordered amorphous network structures [20]. In general, to characterize the tail-state absorption, the Urbach energy E_U, defined by $\alpha = \alpha_0 \exp(E/E_U)$ (i.e., $\ln \alpha \propto E/E_U$), is estimated. Figure 1.7a shows E_U of various semiconductors as a function of E_g. The E_U values were obtained from the α spectra of Fig. 1.6 in the region below E_g. In this simple analysis, however, slight ambiguity remains due to the deviation from the assumed exponential variation. In Fig. 1.7a, E_U of single crystals, denoted by the open circles, shows a low value


(a)
Group Ⅳ semiconductors
Si, Ge, a-Si:H
Group Ⅲ−Ⅴ semiconductors
AlAs, GaAs, InAs, GaP, InP
Group Ⅱ−Ⅵ semiconductors
CdS, CdTe
Group Ⅰ−Ⅲ−Ⅵ2 semiconductors
CuIn0.8Ga0.2Se2 (CIGSe)
CuInSe2 (CISe)
CuGaSe2 (CGSe)
Group Ⅰ2−Ⅱ−Ⅳ−Ⅵ4
Cu2ZnSnSe4 (CZTSe)
Cu2ZnSnS4 (CZTS)
Cu2ZnGeSe4 (CZGSe)
Hybrid perovskite
CH3NH3PbI3 (MAPbI3)
HC(NH2)2PbI3 (FAPbI3)
Absorption coefficient α (cm−1)
Photon energy (eV)
(b)
Wavelength (nm)

◀**Fig. 1.6** α spectra of various solar cell materials versus **a** photon energy and **b** wavelength. The complete optical data of these materials are shown in Chaps. 8 and 10. The closed circles indicate the E_g positions of each absorber material. For high efficiency $Cu(In,Ga)Se_2$ solar cells, the composition of $CuIn_{0.8}Ga_{0.2}Se_2$ has been used and the corresponding spectrum is shown. It should be noted that the optical constants of a-Si:H are process dependent (Sect. 9.4 (Vol. 1))

of ~9 meV, except for Ge. The polycrystalline materials, including CIGSe, CdTe and hybrid perovskites, also show very sharp absorption edges with small E_U of ~15 meV (closed circles in Fig. 1.7a). In contrast, for the CZTSe and CZTS, large E_U values of ~70 meV have been obtained, although these E_U values vary depending on the analyzed energy region. In Fig. 1.7a, the E_U values for direct and indirect semiconductors are shown, but E_U of the indirect materials (Si and Ge) could not be compared directly with those of the direct-transition absorbers.

The presence of the tail states is detrimental for solar cells and increases V_{loss} in (1.8). Figure 1.7b summarizes V_{loss} obtained from the solar cells of Fig. 1.4 as a function of E_U. The V_{loss} values were calculated from (1.8) using the experimental V_{oc} and E_g values. It can be seen that V_{loss} increases significantly with increasing E_U, as pointed out previously [21]. Unfortunately, the interpretation of V_{loss} is not straightforward and V_{loss} is also affected by carrier recombination and built-in potential. Thus, the data points of Fig. 1.7b scatter notably. However, the result of Fig. 1.7b implies that small E_U is quite important to suppress V_{loss} in solar cells.

On the other hand, when the α values near E_g are higher, the light absorption occurs more close to the front interface, and the effect of the rear-interface recombination becomes smaller (Sect. 2.6). Accordingly, the band-edge absorption characteristics directly affect the solar cell performance. For solar cell application, it is preferable if a light absorber has (i) the optimum E_g value of ~1.4 eV (Fig. 1.5),

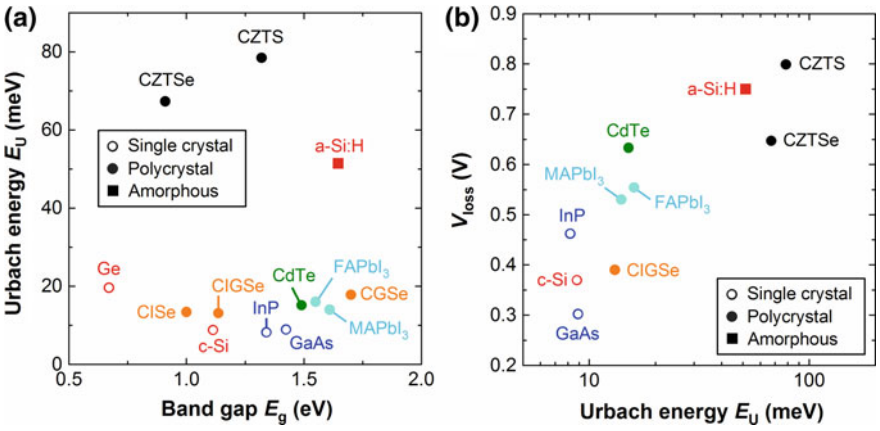


Fig. 1.7 **a** E_U determined from the α spectra of Fig. 1.6 as a function of E_g and **b** V_{loss} obtained for the solar cells of Fig. 1.4 as a function of E_U. The open circles show the E_U values of single crystalline semiconductors, whereas the closed circles indicate those extracted from polycrystalline materials. The closed square shows the value of the a-Si:H

(ii) a low Urbach energy (Fig. 1.7b) and (iii) high α values near E_g [12]. Among the existing solar-cell materials, GaAs, InP, CdTe and $CH_3NH_3PbI_3$ semiconductors fulfill these conditions relatively well.

Figure 1.8 shows (a) the ε_2 spectra and (b) the k spectra of various solar cell materials. These optical data are consistent with those of Fig. 1.6. The ε_2 values near E_g are ~0.5 for the direct-transition semiconductors, while the indirect semiconductors show almost zero ε_2 values near E_g. The corresponding k values of the direct semiconductors are ~0.1, whereas those of the indirect semiconductors are also almost zero.

1.2.3 Dielectric Function Modeling

The dielectric functions (or optical constants) modeled using theoretical expressions are particularly useful for ellipsometry analyses and optical simulations, as tabulated data have a limited number of data points. In this book, therefore, the optical data of 148 solar-cell component materials have been parameterized completely. All the model parameters and the tabulated optical data are summarized in Part II. Quite importantly, it is established in this book that the dielectric function modeling of all the solar-cell component materials can be performed using only three models: i.e., (i) the Sellmeier model, (ii) the Tauc-Lorentz (TL) model [22], and (iii) the Drude model.

Figure 1.9 summarizes the overall shapes of the dielectric functions calculated from (a) the Sellmeier, (b) TL and (c) Drude models. In general, the Sellmeier model is applied for the modeling of transparent materials and insulators, such as SiO_2 and Al_2O_3 (see Chap. 8). In this model, the light absorption in the material is assumed to be zero (i.e., $\varepsilon_2 = k = 0$) and ε_1 is calculated by

$$\varepsilon_{Sel}(\lambda) = \varepsilon_1(\lambda) = n^2(\lambda) = \frac{B_1\lambda^2}{\left(\lambda^2 - C_1\right)} + \frac{B_2\lambda^2}{\left(\lambda^2 - C_2\right)} + \frac{B_3\lambda^2}{\left(\lambda^2 - C_3\right)} + 1 \tag{1.18}$$

In this model, there are a total of six parameters (B_1, B_2, B_3, C_1, C_2, C_3) and the n spectrum can be calculated quite easily from these parameter values (see also Chap. 5 (Vol. 1)).

In the TL model [22], the dielectric function is calculated using five free parameters: the ε_1 value at high energy [$\varepsilon_1(\infty)$], the amplitude (A), width (C), band gap (E_g) and peak position (E_0) of the ε_2 peak (see Fig. 1.9b). Using these parameters, the ε_2 peak (spectrum) is calculated as

$$\varepsilon_2(E) = \frac{ACE_0(E - E_g)^2}{\left(E^2 - E_0^2\right)^2 + C^2E^2} \cdot \frac{1}{E} \quad \left(E > E_g\right), \ \varepsilon_2(E) = 0 \ \left(E \le E_g\right) \tag{1.19}$$

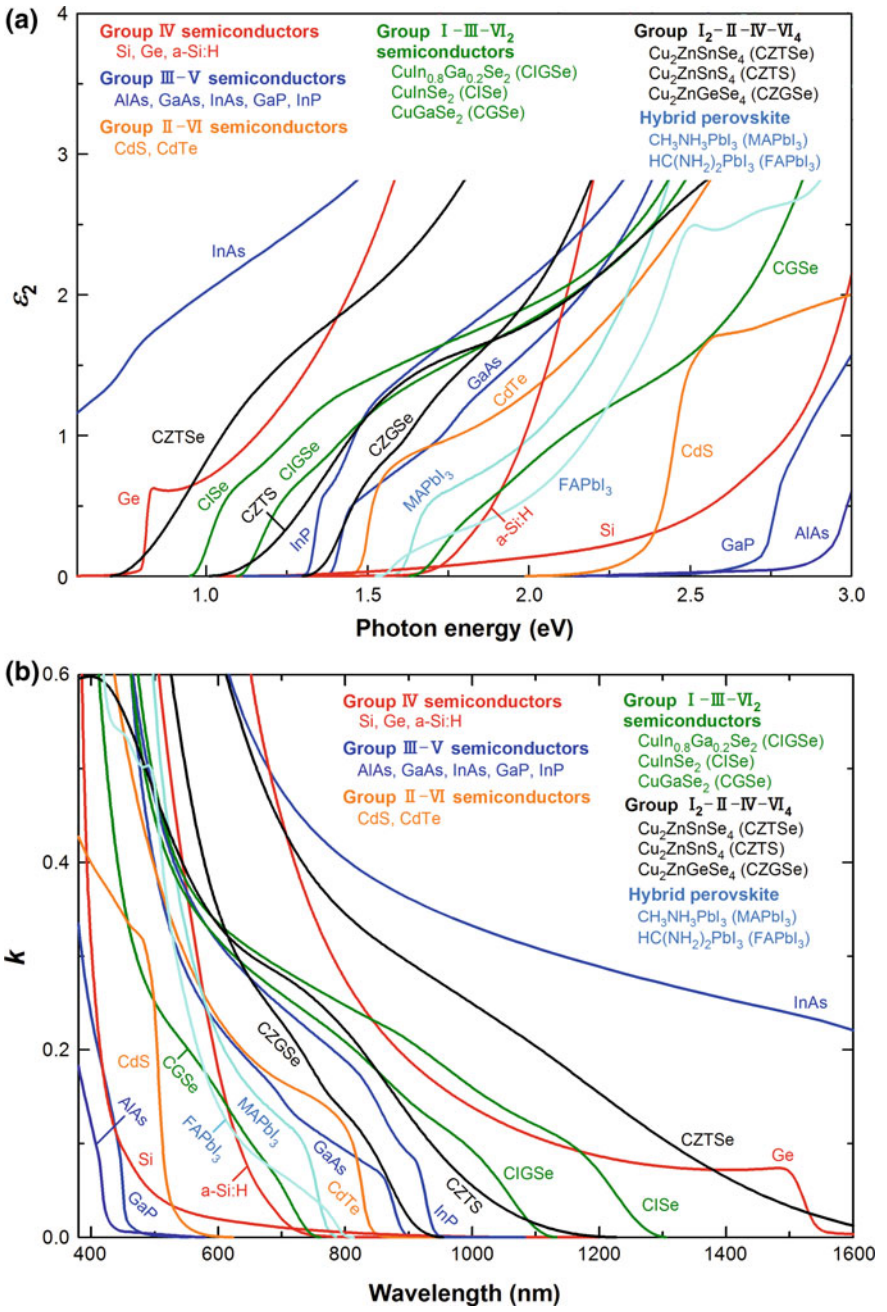


Fig. 1.8 **a** ε_2 spectra and **b** k spectra of various solar cell materials. The optical data are consistent with those shown in Fig. 1.6. The ε_2 spectra are shown for photon energy, while the k spectra are indicated for wavelength

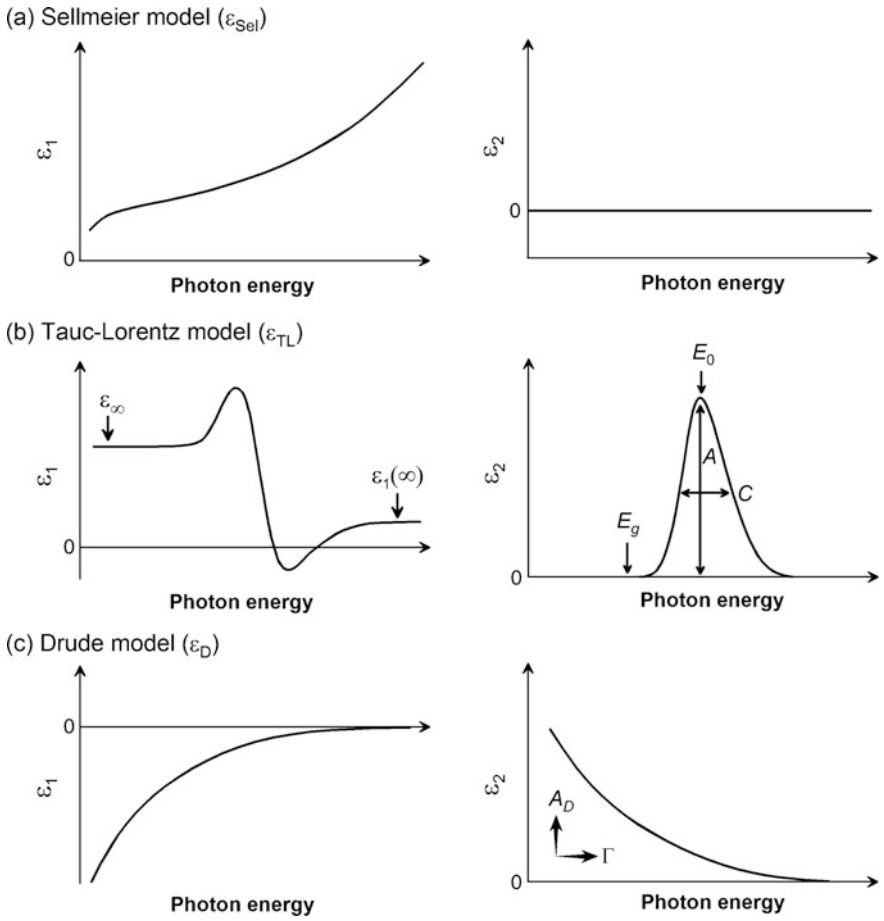


Fig. 1.9 Dielectric function models of **a** the Sellmeier model, **b** the Tauc-Lorentz (TL) model, and **c** the Drude model, which are employed for the dielectric function modeling of transparent, semiconductor, and metal (TCO) materials, respectively. The TL model is expressed by a total of five parameters: the amplitude parameter (A), broadening parameter (C), Tauc optical gap (E_g), peak transition energy (E_0), and energy-independent contribution to $\varepsilon_1(E)$ [$\varepsilon_1(\infty)$], whereas the Drude model is expressed by the amplitude parameter (A_D) and the broadening parameter (Γ). In **b**, ε_∞ represents the high-frequency dielectric constant and is not a model parameter

The corresponding $\varepsilon_1(E)$ can be obtained based on the Kramers-Kronig relations:

$$\begin{aligned}\varepsilon_1(E) = \varepsilon_1(\infty) &+ \frac{AC}{\pi\xi^4}\cdot\frac{a_{\ln}}{2\alpha E_0}\ln\left(\frac{E_0^2+E_g^2+\alpha E_g}{E_0^2+E_g^2-\alpha E_g}\right)\\ &- \frac{A}{\pi\xi^4}\cdot\frac{a_{\text{atan}}}{E_0}\left[\pi - \tan^{-1}\left(\frac{2E_g+\alpha}{C}\right) + \tan^{-1}\left(\frac{-2E_g+\alpha}{C}\right)\right]\\ &+ 2\frac{AE_0}{\pi\xi^4\alpha}E_g(E^2-\gamma^2)\left[\pi + 2\tan^{-1}\left(2\frac{\gamma^2-E_g^2}{\alpha C}\right)\right]\\ &- \frac{AE_0C}{\pi\xi^4}\cdot\frac{E^2+E_g^2}{E}\ln\left(\frac{|E-E_g|}{E+E_g}\right) + \frac{2AE_0C}{\pi\xi^4}E_g\ln\left[\frac{|E-E_g|(E+E_g)}{\sqrt{(E_0^2-E_g^2)^2+E_g^2C^2}}\right]\end{aligned} \tag{1.20}$$

where

$$a_{\ln} = (E_g^2-E_0^2)E^2 + E_g^2C^2 - E_0^2(E_0^2+3E_g^2), \tag{1.21}$$

$$a_{\text{atan}} = (E^2-E_0^2)(E_0^2+E_g^2) + E_g^2C^2, \tag{1.22}$$

$$\xi^4 = (E^2-\gamma^2)^2 + \alpha^2C^2/4, \tag{1.23}$$

$$\alpha = \sqrt{4E_0^2-C^2}, \tag{1.24}$$

$$\gamma = \sqrt{E_0^2-C^2/2}. \tag{1.25}$$

Although the above equations are rather complicated, the dielectric function of the TL model can be calculated rather easily using five parameters (A, C, E_g, E_0, $\varepsilon_1(\infty)$). For example, the dielectric function of an a-Si:H layer deposited at 230 °C has been parameterized assuming a single TL peak with parameter values of A = 214.05 eV, C = 2.33 eV, E_0 = 3.649 eV, E_g = 1.659 eV and $\varepsilon_1(\infty)$ = 0.309 (see Table 8.19). If E = 2 eV, using these parameter values, we obtain ε_2 = 0.98 directly from (1.19). For the ε_1 value, we get $a_{\ln}$ = −314.55, a_{atan} = −134.73, ξ^4 = 108.49, α = 6.92, γ = 3.26 from the assumed TL parameters using (1.21)–(1.25). With these values, (1.20) becomes

$$\begin{aligned}\varepsilon_1 &= \varepsilon_1(\infty) - 9.11\ln(6.01) + 23.19[\pi - \tan^{-1}(4.39) + \tan^{-1}(1.55)]\\ &\quad - 7.28\left[\pi + 2\tan^{-1}(0.98)\right] - 18.03\ln(0.09) + 17.72\ln(0.11)\\ &= 0.31 - 16.34 + 64.76 - 34.16 + 43.42 - 39.11\\ &= 18.88\end{aligned} \tag{1.26}$$

As a result, ε of a-Si:H at 2.0 eV is calculated to be $\varepsilon = 18.88 - i0.98$. For the $\varepsilon_1(E)$ calculation, however, E should be chosen so that $|E - E_g|$ in (1.20) does not become zero.

The Drude model shown in Fig. 1.9c is an important model, which has been employed extensively to express light absorption by free electrons (i.e., free carrier absorption) in TCO and metal materials. When the carrier concentration is high (typically $>10^{18}$ cm^{-3}), the ε_1 value becomes negative and ε_2 shows a large increase at lower energy. The theoretical expression of the Drude model is simple and is given by

$$\varepsilon_D(E) = -\frac{A_D}{E^2 - i\Gamma E} = \left(-\frac{A_D}{E^2 + \Gamma^2}\right) - i\left(\frac{A_D\Gamma}{E^3 + \Gamma^2 E}\right), \tag{1.27}$$

where A_D and Γ are the amplitude and broadening parameters, respectively. From these two parameters, carrier concentration and carrier mobility can further be obtained (Chap. 18 (Vol. 1)).

In this book, the dielectric functions of the inorganic (Chap. 8), organic (Chap. 9) and hybrid perovskite (Chap. 10) semiconductors are modeled simply by combining several TL ε_2 peaks and the corresponding $\varepsilon_1(E)$ is also calculated as a sum of the ε_1 contributions obtained from each TL peak. On the other hand, the dielectric functions of TCO materials (Chap. 11) and metals (Chap. 12) have been modeled by combining the TL model with the Drude model.

Figure 1.10 shows the examples of the dielectric function modeling performed for an indirect-transition semiconductor (c-Si), a direct-transition semiconductor (CISe), an organic semiconductor (P3HT) and a TCO (ZnO:Ga). The open circles indicate the experimental data shown in Fig. 8.1 (c-Si), Fig. 8.24 (CISe), Fig. 9.5 (P3HT) and Fig. 11.20 (ZnO:Ga), and the solid lines show the fitting results. The individual peak in Fig. 1.10 shows the TL peak and the sum of these peaks provides excellent agreement with the experimental data. In the parameterization of inorganic semiconductors, α spectra in the logarithmic scale are reproduced almost perfectly through careful modeling (Chap. 8). In the dielectric function modeling of TCO, free carrier absorption observed at low energies ($E < 3$ eV) was incorporated using the Drude model (Chaps. 5 and 18 in Vol. 1).

As confirmed from Fig. 1.10, the optical spectra of the indirect, direct and organic semiconductors are quite different. As mentioned above, near E_g, $\varepsilon_2 \sim 0$ in the indirect semiconductor, while the sharp onset of light absorption is observed in the direct CISe semiconductor. The aromatic polymer materials often exhibit sharp absorption peaks in the visible region, characterized by $\pi \rightarrow \pi^*$ transition (Chaps. 4 and 15 in Vol. 1). The ε_2 shape of the TCO can be interpreted as a sum of the TL and Drude models shown in Fig. 1.9. The free carrier absorption in TCO layers increases with free carrier concentration (Chap. 18 (Vol. 1)) and the optimization of the TCO carrier concentration is important in solar cell devices (Chap. 2).

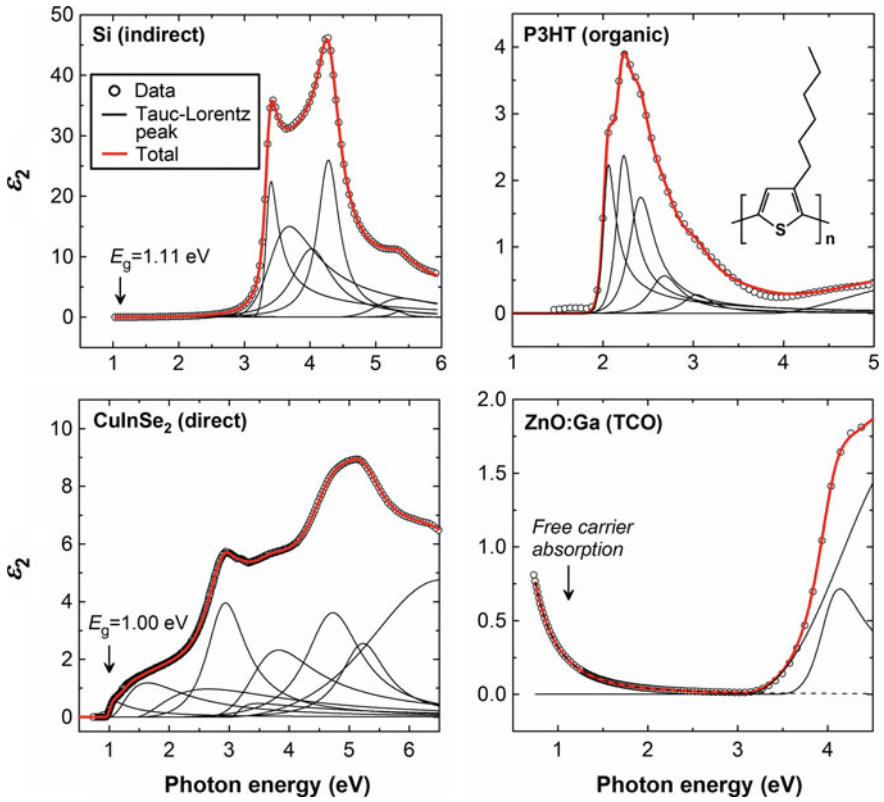


Fig. 1.10 Results of dielectric function modeling performed for Si (indirect transition), CISe (direct transition), P3HT (organic compound) and ZnO:Ga (TCO). The open circles indicate the experimental data shown in Fig. 8.1 (Si), Fig. 8.24 (CISe) [1], Fig. 9.5 (P3HT) and Fig. 11.20 (ZnO:Ga), whereas the solid lines represent the parameterization results. For P3HT, the chemical structure of the polymer is shown. The individual peaks show the TL peaks and the red lines show the sum of these peaks. For the modeling of the ZnO:Ga, the Drude model has been incorporated to express the free carrier absorption

1.3 Light Absorption in Solar Cells

The photocarrier generation by light absorption is an essential process in the operation of solar cells. The light absorption phenomena in experimental solar cells can be studied systematically based on EQE analyses. In particular, a global EQE analysis method has been established, from which all the current losses (i.e., reflection, absorption and recombination losses in Fig. 1.2) can be estimated rather easily (Chap. 2). In this section, the light absorption in photovoltaic devices is explained more quantitatively and the examples of EQE analyses performed for the state-of-the-art CIGSe and CZTSSe solar cells are introduced briefly.

1.3.1 Light Absorption in Absorber Layer

When samples consist of only substrates with infinite thickness, light absorption in the samples can be expressed by Beer's law [13]:

$$I = I_0 \exp(-\alpha d), \tag{1.28}$$

where I shows the light intensity along the sample depth d and I_0 indicates the light intensity at the material surface. Figure 1.11a shows the light intensity ratio (I/I_0) versus the depth from the surface (i.e., d), calculated from (1.28). In the figure, the calculation results for $\alpha = 10^4$ and 10^5 cm^{-1} are shown. As confirmed from Fig. 1.11a, I/I_0 decreases along d due to the light absorption, and the decay of the light intensity is more pronounced at high α because of stronger light absorption. The gray area indicated in Fig. 1.11a shows the actual light absorption in the sample, which can be expressed simply as

$$L = 1 - \exp(-\alpha d). \tag{1.29}$$

Accordingly, the extent of light absorption in media is determined by the αd product.

On the other hand, when $I/I_0 = 1/e \sim 37\%$ in (1.28), we obtain $\alpha d = 1$. This depth defines the penetration depth of light (d_p), which is given by

$$d_p \equiv 1/\alpha. \tag{1.30}$$

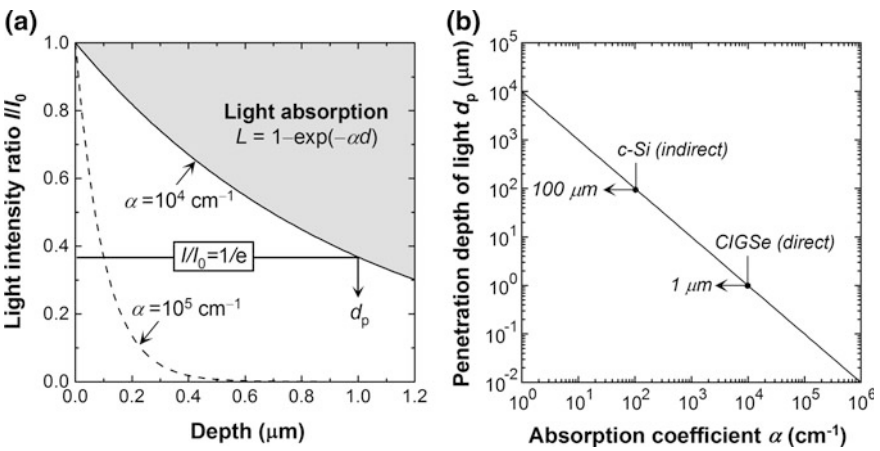


Fig. 1.11 **a** Light intensity ratio (I/I_0) versus the depth from the surface d, calculated from $I/I_0 = \exp(-\alpha d)$ and **b** penetration depth of light (d_p) versus α, determined from $d_p = 1/\alpha$. In **a**, the calculation results for $\alpha = 10^4$ and 10^5 cm^{-1} are shown and the depth at $I/I_0 = 1/e \sim 37\%$ defines d_p. The contribution of light absorption is indicated by the gray region in **a**. In **b**, the d_p values for $\alpha = 10^2$ cm^{-1} (c-Si) and 10^4 cm^{-1} (CIGSe) are indicated by the arrows

Figure 1.11b shows $_{p}$ calculated from (1.30) as a function of α. Since d_p is i*d*nversely proportional to α, the d_p value decreases rapidly with increasing α. This shows a well-known fact that the light absorption occurs more close to the surface when α is higher. As confirmed from Fig. 1.6, α of c-Si at the energy slightly above E_g is ~100 cm^{-1}. This α corresponds to d_p of 100 μm, as indicated by the arrow in Fig. 1.11b. In many direct-transition semiconductor (i.e., CIGSe, GaAs, CdTe, etc.), α above E_g is ~10^4 cm^{-1}, which is equivalent to d_p ~1 μm. These d_p values are quite consistent with the thicknesses of the absorber layers employed in the actual solar cells. Thus, high α is vital to achieve sufficient optical absorption with a limited absorber thickness.

In the above calculation, however, the infinite absorber thickness was assumed and the influence of the back-side reflection was neglected completely. The effective back-side reflection and higher optical confinement become particularly important when the thickness of the light absorbers cannot be increased due to a process limitation (spin coating, etc.) or a physical reason (high defect density, etc.). For $CH_3NH_3PbI_3$ and a-Si:H solar cells with absorber thicknesses of 200–300 nm, therefore, the high reflectivity at the rear interface is critical (see also Fig. 12.3).

Since α changes depending on λ (or E), d_p also varies with λ. By taking advantage of the λ-dependent d_p, the carrier recombinations that occur at the front and rear interfaces can be distinguished (see Fig. 2.17). It should be noted that d_p merely shows the position where the normalized light intensity becomes 37% (see Fig. 1.11a). Thus, the weaker light absorption continues to occur in the deeper region.

1.3.2 EQE Characteristics

The quantitative assessment of light absorption in solar cells can be made from EQE characterization. Here, we discuss the relation between the light absorption and the resulting EQE response observed in various solar cells.

Figure 1.12 shows (a) αd spectra of various light absorbers and (b) EQE spectra of solar cells. As we have seen in Fig. 1.11a, the light absorption in the absorber is expressed by αd. For the calculation of αd in Fig. 1.12a, the α spectra of Fig. 1.6 and the absorber thicknesses employed for the corresponding solar cells in Fig. 1.12b were employed. The EQE spectra in Fig. 1.12b show those reported for a-SiO:H/c-Si heterojunction [23] (Fig. 2.26), CIGSe [24] (Fig. 2.9), CdTe [25] (Fig. 2.21), a-Si:H (Fig. 2.23) and $CH_3NH_3PbI_3$ [26] (Fig. 16.17c in Vol. 1) solar cells. The absorber thicknesses of these solar cells were indicated in Fig. 1.12a.

Although c-Si is an indirect semiconductor with low α values, the absorber thickness (typically ~150 μm) is sufficient and the αd values are comparable to those of CIGSe and CdTe. In contrast, the a-Si:H and $CH_3NH_3PbI_3$ show smaller αd due to thin thicknesses (200–300 nm). The dotted lines for the EQE spectra indicate the results of liner fitting analyses performed in the E_g region and the λ positions of the intercepts are denoted by the orange arrows. The identical

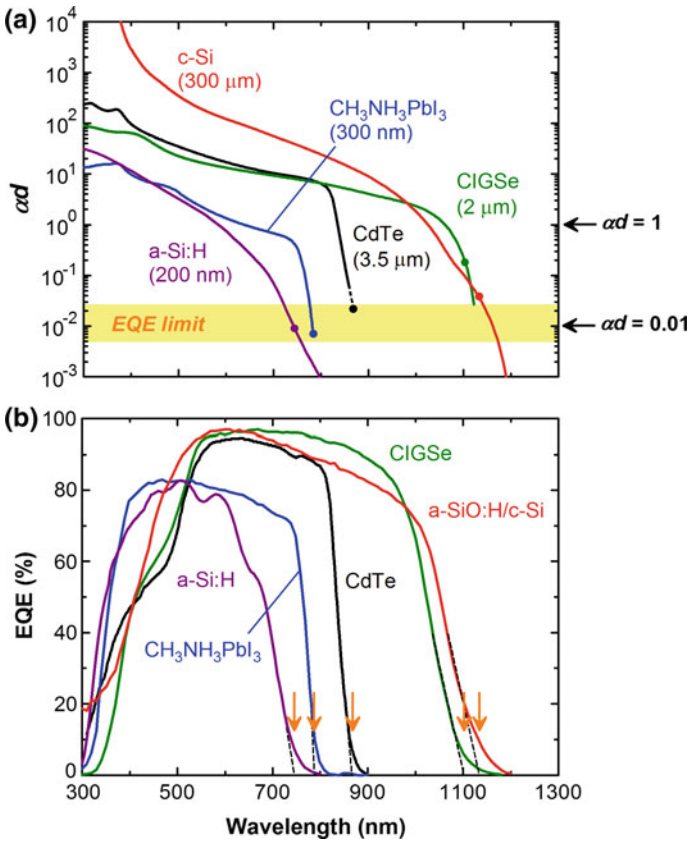


Fig. 1.12 **a** αd spectra of solar-cell light absorbers and **b** EQE spectra of corresponding solar cells. In **a**, the αd spectra were calculated using the α spectra of Fig. 1.6 and the indicated absorber thicknesses. The EQE spectra are taken from those reported for a-SiO:H/c-Si heterojunction [23] (Fig. 2.26), CIGSe [24] (Fig. 2.9), CdTe [25] (Fig. 2.21), a-Si:H (Fig. 2.23) and $CH_3NH_3PbI_3$ [26] (Fig. 16.17c (Vol. 1)) solar cells. The absorber thicknesses shown in **a** are consistent with those of the solar cells in **b**. The closed circles in **a** represent the EQE sensitivity limits obtained from the EQE linear fitting analyses denoted by the dotted lines in **b**. The positions of the EQE limits indicated by the arrows in **b** are identical to those of the closed circles in **a**

λ positions are also shown by the closed circles in Fig. 1.12a. This simple analysis reveals that the longer-λ limits observed in the EQE spectra lie at $\alpha d \sim 0.01$ and are much lower than $\alpha d = 1$ (i.e., $\alpha d_p = 1$). The CIGSe solar cell shows a slightly higher EQE limit, but this is caused by the double grading structure of the Ga composition in the solar cell (see Fig. 2.8). Even though the effect of the back-side reflection is neglected completely in the above analysis, it is obvious that the EQE response in the longer λ region is governed essentially by αd. Accordingly, the fundamental potential of a solar cell can be judged from the α spectrum and the thickness of absorber layers (Fig. 1.1b).

On the other hand, the maximum values of the EQE spectra are determined by the reflection loss as well as the absorption loss induced by the free carrier absorption in a front TCO layer (Chap. 2). The incorporation of anti-reflection layers is important to suppress the reflection loss. In fact, the anti-reflection layers have been provided to the CIGSe, CdTe, a-SiO:H/c-Si solar cells that show high EQE values of ~95% (see Fig. 1.12b).

As confirmed from Fig. 1.12b, the a-Si:H solar cell exhibits lower EQE response in the longer λ region, compared with the $CH_3NH_3PbI_3$ solar cell, even though E_g of a-Si:H (~1.65 eV) is almost the same with that of $CH_3NH_3PbI_3$ (1.61 eV). This is caused by the low αd values of the a-Si:H particularly in the longer λ region. Indeed, αd of the a-Si:H at 750 nm is almost 50 times smaller than that of $CH_3NH_3PbI_3$. Consequently, if α (or αd) near E_g is low, the carrier generation in the longer λ region becomes difficult and J_{sc} decreases.

The light absorption and the carrier generation can be determined more accurately from EQE simulations (Chap. 2). Figure 1.13 shows the partial EQE calculated for the state-of-the-art CIGSe solar cell with a structure of MgF_2/ZnO:Al/ZnO/CdS(n)/CIGSe(p)/$MoSe_2$/Mo/glass [24]. In this figure, partial EQE contributions obtained at different depths from the CdS/CIGSe interface (i.e., d) and

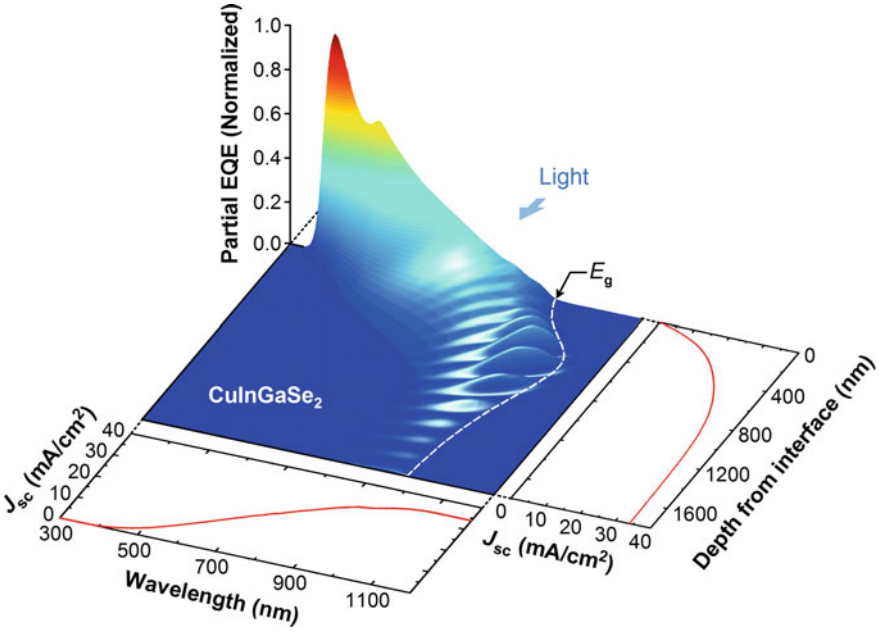


Fig. 1.13 Normalized partial EQE calculated for different depths from the CdS/CIGSe interface and wavelengths. The dotted line represents E_g of the CIGSe at each depth. The partial EQE is consistent with the EQE spectrum of the CIGSe solar cell shown in Fig. 1.12b. The integrated J_{sc} values versus d and λ, calculated from the partial EQE, are also indicated. The data are adopted from [24]

wavelengths are shown. If the partial EQE spectra obtained at different depths are integrated, the EQE spectrum shown in Fig. 1.12b is obtained. In the simulation, explicit EQE calculation has been made by incorporating the effects of the double-grading Ga profile within the CIGSe layer and the light scattering caused by the submicron textured structure (Sect. 2.2.3). In particular, the optical response of the V-shaped Ga profile, formed by conventional three-stage coevaporation, was fully simulated using a complete CIGSe optical database (Sect. 10.4 (Vol. 1)). The white dotted line in Fig. 1.13 shows the E_g positions at each depth. The EQE analysis shows that the carrier collection efficiency in the CIGSe solar cell is almost 100% and the recombination at the interfaces and grain boundaries is very small.

In Fig. 1.13, the partial EQE is quite high at $\lambda < 700$ nm and decreases rapidly versus d due to high α values in this region. In contrast, the partial EQE shows lower values at $\lambda > 700$ nm and the carrier generation occurs more uniformly in the depth direction. The oscillation pattern observed in the region of $d > 400$ nm represents the optical interference effect. In Fig. 1.13, integrated J_{sc} values versus d and λ are also indicated. Rather surprisingly, the light absorption in the 1-μm-thick CIGSe bottom layer is negligible and its contribution to J_{sc} is quite small. From this result, it has been concluded that the CIGSe bottom layer is playing a dominant role as a back surface field with conduction band grading [24]. As confirmed from the above result, device operation can be studied more precisely from EQE characterization.

1.3.3 Optical and Recombination Losses in Solar Cells

All the current losses induced by reflection, parasitic absorption, and recombination can be assessed quantitatively based on a global EQE analysis method, in which the effects of (i) light scattering induced by textured structures and (ii) carrier recombination in light absorbers are fully accounted for. By applying this technique, the optical and recombination losses in various solar cells, including c-Si, a-Si:H, CIGSe, CZTSe, CZTS, CZTSSe, CdTe and hybrid perovskite solar cells, can be determined (Chap. 16 (Vol. 1) and Chap. 2 (Vol. 2)). It has been confirmed that the developed EQE analysis method provides excellent fitting to numerous EQE spectra reported in literature [12].

Figure 1.14 shows the example of EQE analysis performed for a record-efficiency CZTSSe solar cell reported in [8]. This solar cell was fabricated by a solution-based processing and has a conversion efficiency of 12.6% (J_{sc} = 35.2 mA/cm^2, $V_{oc} = 0.513$ V, $FF = 69.8\%$). The structure of this solar cell is MgF_2 (110 nm)/ITO (50 nm)/ZnO (10 nm)/CdS (25 nm)/CZTSSe (2.0 μm)/Mo(S)Se_2 (185 nm)/Mo/glass substrate. The optical constants of these layers can be found in Part II of this book and the detailed analysis procedure is described in Sect. 2.3.

In Fig. 1.14a, the EQE and absorptance spectra of the solar-cell component layers are shown, together with the reflectance spectrum indicated as $1 - R$. The open circles show the experimental EQE and reflectance spectra reported in [8],

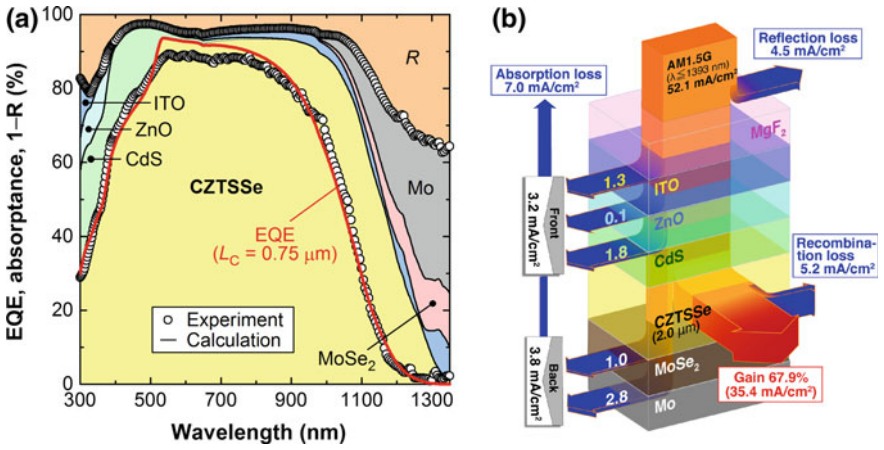


Fig. 1.14 **a** EQE analysis performed for a record-efficiency CZTSSe solar cell [8] using the global EQE analysis method and **b** optical gain and loss obtained from the analysis [12]. The EQE analysis was carried out using the optical model of MgF_2 (110 nm)/ITO (50 nm)/ZnO (10 nm)/CdS (25 nm)/CZTSSe (2.0 μm)/Mo(S)Se_2 (185 nm)/Mo/glass substrate. In **a**, the open circles show the experimental spectra reported in [8] and the red line represents the EQE spectrum calculated assuming the carrier collection length of $L_C = 0.75$ μm from the CdS/CZTSSe interface. The spectrum indicated by the yellow-colored region corresponds to the absorptance spectrum of the CZTSSe layer. In **b**, the numerical values show the corresponding current densities in units of mA/cm^2

whereas the black lines indicate the calculated absorptance spectra of the component layers. In the EQE analysis, the carrier extraction from the absorber layer was modeled by considering a carrier collection length (L_C) from the CdS/CZTSSe interface. The red line in Fig. 1.14a represents the calculated EQE spectrum obtained using L_C as an analytical parameter. The calculation result provides excellent fitting to the experimental EQE spectrum when $L_C = 0.75$ μm. This L_C value is much smaller than the CZTSSe thickness (2.0 μm), indicating that the carrier collection occurs only in a limited depth from the CdS/CZTSSe interface. In fact, the yellow-colored region in Fig. 1.14a shows the calculated absorptance of the CZTSSe layer, but the experimental EQE spectrum shows lower values particularly in the long λ region, indicating that the significant carrier loss occurs in the CZTSSe bottom region [12]. From the difference between the EQE spectrum (red line) and the absorptance spectrum of the CZTSSe (yellow-colored region), the J_{sc} loss induced by the carrier recombination can be estimated directly.

In Fig. 1.14b, the reflection, absorption and recombination losses deduced from the EQE analysis are summarized. For the CZTSSe layer, the maximum J_{sc} value attainable under the AM1.5G condition is 52.1 mA/cm^2 (see also Fig. 1.4), from which the optical gain of the CZTSSe solar cell is estimated to be 67.9% (35.4 mA/cm^2). In this solar cell, the reflection loss (4.5 mA/cm^2), total absorption loss (7.0 mA/cm^2) and recombination loss (5.2 mA/cm^2) are quite large, and the moderate efficiency of ~13% can be interpreted primarily by these losses. As confirmed from Fig. 1.14b,

major parasitic absorption occurs in the Mo layer. This originates from very low reflectance at the CZTSSe/Mo interface (see also Fig. 12.4). In this solar cell, therefore, the long-λ EQE response is limited by the carrier recombination and the parasitic light absorption in the Mo layer.

The above result demonstrates that the performance-limiting factors in solar cells can be determined quantitatively using the developed EQE analysis method. Such EQE analysis can be performed quite easily using a free EQE analysis software described in Sect. 2.7. Based on the EQE analysis result, the solar-cell processing and device structures can further be optimized quite effectively.

1.4 Overview of This Book

This volume of the book aims to provide broad understanding for the application of spectroscopic ellipsometry (SE) technique and is consisting of two major parts. In Part I, EQE analyses and advanced SE methods, which employ new optical modeling and calculation techniques, are introduced. In Part II, a quite complete optical database for numerous solar cell materials, which can be used for EQE simulations and SE analyses, is described.

More specifically, after a general introduction into the topics covered by the book (Chap. 1), Part I covers the analysis of optical and recombination losses in solar cells (Chap. 2) and the optical simulations of the EQE spectra (Chap. 3). As confirmed from Fig. 1.14, the EQE analysis is a crucial technique in revealing current loss mechanisms in solar cells. In addition to conventional material and structural characterizations, SE can be employed to assess the optical properties and structures of large-area photovoltaic modules. From this point of view, the state-of-the-art SE data analysis approaches developed for textured solar cells (Chap. 4) and on-line monitoring of photovoltaic production (Chap. 5) are introduced. Explicit SE data analyses further allow real-time control of CIGSe layers fabricated using complex coevaporation processes (Chap. 6) and mapping characterization of Si thin film devices (Chap. 7).

Part II summarizes (n, k) data for numerous solar-cell component layers (total 148 materials) incorporated into various solar cells. The dielectric functions of all the materials have been parameterized completely using only three dielectric function models mentioned above and their model parameters are also described. For inorganic semiconductors (Chap. 8), the complete optical data of group IV, III–V, II–VI, I–III–VI_2, I_2–II–IV–VI_4 semiconductors are shown. The following chapter (Chap. 9) summarizes the optical data of 20 organic semiconductors. For hybrid perovskite materials (Chap. 10), the optical constants of major absorbers and their secondary phases are described. Since TCO (Chap. 11) and metal (Chap. 12) electrodes are vital components in solar cells, the optical data of various TCO and metal layers are also summarized. In particular, for important TCO materials, the variation of optical constants with carrier concentration is indicated to show the effect of the free carrier absorption. In the final chapter (Chap. 13), the optical data of substrate

materials (glass, plastic and metal substrates) and anti-reflection coating materials are summarized.

Through the above overall descriptions, in-depth knowledge and understanding for the SE technique of solar cells can be gained.

Acknowledgements The author acknowledges Shohei Fujimoto for the preparation of Figs. 1.4, 1.5, 1.6 and 1.8. The author would like to thank Akihiro Nakane for the preparation of Figs. 1.3, 1.4 and 1.5.

References

1. S. Minoura, K. Kodera, T. Maekawa, K. Miyazaki, S. Niki, H. Fujiwara, J. Appl. Phys. **113**, 063505 (2013)
2. M.A. Green, K. Emery, Y. Hishikawa, W. Warta, E.D. Dunlop, D.H. Levi, A.W.Y. Ho-Baillie, Prog. Photovolt. **25**, 3 (2017)
3. The numerical data can be downloaded at http://pveducation.org/pvcdrom/appendices/standard-solar-spectra
4. M.A. Green, K. Emery, Y. Hishikawa, W. Warta, E.D. Dunlop, Prog. Photovolt. **21**, 1 (2013)
5. P. Jackson, D. Hariskos, R. Wuerz, O. Kiowski, A. Bauer, T.M. Friedlmeier, M. Powalla, Phys. Status Solidi RRL **9**, 28 (2015)
6. Y.S. Lee, T. Gershon, O. Gunawan, T.K. Todorov, T. Gokmen, Y. Virgus, S. Guha, Adv. Energy Mater. **5**, 1401372 (2015)
7. B. Shin, O. Gunawan, Y. Zhu, N.A. Bojarczuk, S.J. Chey, S. Guha, Prog. Photovolt. **21**, 72 (2013)
8. W. Wang, M.T. Winkler, O. Gunawan, T. Gokmen, T.K. Todorov, Y. Zhu, D.B. Mitzi, Adv. Energy Mater. **4**, 1301465 (2014)
9. S. Kim, K.M. Kim, H. Tampo, H. Shibata, S. Niki, Appl. Phys. Express **9**, 102301 (2016)
10. H.D. Kim, H. Ohkita, H. Benten, S. Ito, Adv. Mater. **28**, 917 (2016)
11. W.S. Yang, J.H. Noh, N.J. Jeon, Y.C. Kim, S. Ryu, J. Seo, S.I. Seok, Science **348**, 1234 (2015)
12. A. Nakane, H. Tampo, M. Tamakoshi, S. Fujimoto, K.M. Kim, S. Kim, H. Shibata, S. Niki, H. Fujiwara, J. Appl. Phys. **120**, 064505 (2016)
13. H. Fujiwara, *Spectroscopic Ellipsometry: Principles and Applications* (Wiley, West Sussex, UK, 2007)
14. S. Adachi, J. Appl. Phys. **53**, 8775 (1982)
15. H. Sai, K. Saito, N. Hozuki, M. Kondo, Appl. Phys. Lett. **102**, 053509 (2013)
16. A. Luque, S. Hegedus, *Handbook of Photovoltaic Science and Engineering* (Wiley, West Sussex, UK, 2011)
17. W.B. Jackson, S.M. Kelso, C.C. Tsai, J.W. Allen, S.-J. Oh, Phys. Rev. B **31**, 5187 (1985)
18. W.-J. Yin, T. Shi, Y. Yan, Adv. Mater. **26**, 4653 (2014)
19. T.M. Brenner, D.A. Egger, L. Kronik, G. Hodes, D. Cahen, Nat. Rev. Mater. **1**, 15007 (2016)
20. R.A. Street, *Hydrogenated Amorphous Silicon* (Cambridge Univ. Press, Cambride, 1991)
21. S. De Wolf, J. Holovsky, S.-J. Moon, P. Löper, B. Niesen, M. Ledinsky, F.-J. Haug, J.-H. Yum, C. Ballif, J. Phys. Chem. Lett. **5**, 1035 (2014)
22. G.E. Jellison Jr., F.A. Modine, Appl. Phys. Lett. **69**, 371 (1996). Erratum. Appl. Phys. Lett. **69**, 2137 (1996).
23. H. Fujiwara, H. Sai, M. Kondo, Jpn. J. Appl. Phys. **48**, 064506 (2009)
24. T. Hara, T. Maekawa, S. Minoura, Y. Sago, S. Niki, H. Fujiwara, Phys. Rev. Appl. **2**, 034012 (2014)

25. T. Aramoto, S. Kumazawa, H. Higuchi, T. Arita, S. Shibutani, T. Nishio, J. Nakajima, M. Tsuji, A. Hanafusa, T. Hibino, K. Omura, H. Ohyama, M. Murozono, Jpn. J. Appl. Phys. **36**, 6304 (1997)
26. J.H. Heo, D.H. Song, H.J. Han, S.Y. Kim, J.H. Kim, D. Kim, H.W. Shin, T.K. Ahn, C. Wolf, T.-W. Lee, S.H. Im, Adv. Mater. **27**, 3424 (2015)

Part I
Application of Ellipsometry Technique

Chapter 2
Analysis of Optical and Recombination Losses in Solar Cells



Hiroyuki Fujiwara, Akihiro Nakane, Daisuke Murata, Hitoshi Tampo, Takuya Matsui and Hajime Shibata

Abstract For efficient optimization of solar-cell device structures and processing, it is essential to reveal the performance-limiting optical and physical factors in solar cells. Quite fortunately, a global solar-cell characterization method has recently been developed from which the parasitic light absorption and carrier recombination in the devices are evaluated systematically based on external quantum efficiency (EQE) analysis. In this new method, the optical and recombination losses in complex solar cell structures are readily determined within the framework of a rather simple optical admittance method. The EQE analysis method described in this chapter is appropriate for a wide variety of photovoltaic devices, including crystalline Si (c-Si), hydrogenated amorphous silicon (a-Si:H), $Cu(In,Ga)Se_2$ chalcopyrite, $Cu_2ZnSn(S,Se)_4$ kesterite, CdTe zincblende and hybrid perovskite solar cells, and provides excellent fitting to numerous EQE spectra obtained experimentally. This chapter introduces the basic concept of the global EQE analysis method in which the effects of (i) light scattering by submicron textures and (ii) carrier recombination in light absorbers are fully incorporated. As examples, the EQE analyses of $Cu(In,Ga)Se_2$, $Cu_2ZnSnSe_4$, Cu_2ZnSnS_4, CdTe, a-Si:H and c-Si solar cells are described. Based on the analysis results, we will further discuss the carrier loss mechanisms in different types of photovoltaic devices.

2.1 Introduction

The performance of solar cells is affected by a variety of optical and physical characteristics of solar-cell component layers and, in developing photovoltaic devices with high efficiencies, identification and the following improvement of the

H. Fujiwara (✉) · A. Nakane · D. Murata
Gifu University, 1-1 Yanagido, Gifu 501-1193, Japan
e-mail: fujiwara@gifu-u.ac.jp

H. Tampo · T. Matsui · H. Shibata
Research Center for Photovoltaics, National Institute of Advanced Industrial Science and Technology, 1-1-1 Umezono, Tsukuba 305-8568, Japan

© Springer International Publishing AG, part of Springer Nature 2018

H. Fujiwara and R. W. Collins (eds.), *Spectroscopic Ellipsometry for Photovoltaics*,
Springer Series in Optical Sciences 214,
https://doi.org/10.1007/978-3-319-95138-6_2

limiting factors are crucial. From this point of view, the development process of solar cells can be compared to water in a barrel [1]. Figure 2.1 explains the improvement of a solar cell efficiency using this analogy. In this illustration, water is pouring into a barrel consisting of staves with different lengths, and the pouring water is an analogy of sunlight. The staves of the barrel represent the characteristics of each solar cell component and the stave length becomes shorter if the specific component shows poor characteristics. In Fig. 2.1, the examples of the important solar-cell components, including a transparent conductive oxide (TCO) layer and series resistance (R_s), are indicated.

In Fig. 2.1, the water level in the barrel corresponds to the conversion efficiency of the solar cell, and the solar-cell efficiency is governed by the most limiting factor (Law of the minimum). In other words, the solar cell performance is determined by the shortest stave and the conversion efficiency may not improve unless the characteristics of the shortest stave are improved. Even when we improve such a limiting factor, the solar cell efficiency may not show a notable increase if there is still another component that has poor properties. Unfortunately, the finding of the limiting factors of solar cells is generally quite difficult, and many researches rely on a trial and error approach to improve solar cell efficiencies. As a result, the research efforts are often ineffective, and the continuous research is necessary over a quite long period of time (often a few decades).

One quite effective method that can be applied for the accurate evaluation of performance-limiting optical and physical factors in solar cells is external quantum efficiency (EQE) analysis [2–18]. In fact, the EQE analysis is the only method that allows the quantitative assessment of unfavorable optical absorption (i.e., parasitic

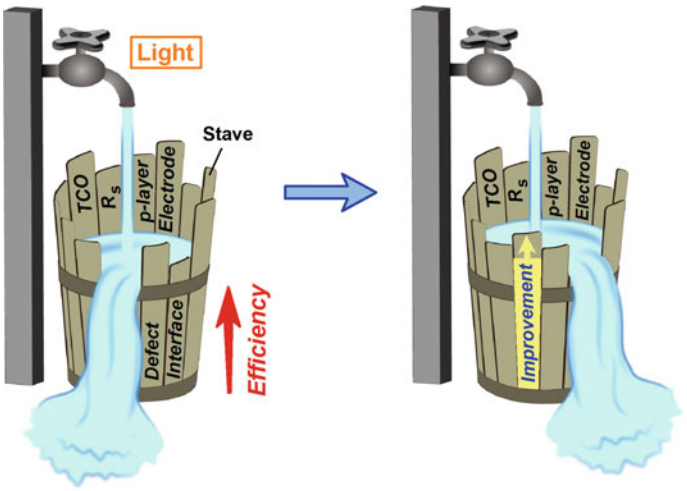


Fig. 2.1 Schematic illustration explaining the development of a high-efficiency solar cell. The pouring water is an analogy of sunlight, while the lengths of the staves indicate the characteristics of each solar cell component. The conversion efficiency is represented by the water level

absorption) in solar cells. Since the EQE spectra contain the depth information due to the wavelength (λ)-dependent penetration depth of light, the carrier recombination near the front and rear interfaces can further be determined from the EQE response in the short and long λ regions, respectively (Sect. 2.3.3).

Figure 2.2 explains how the EQE spectrum changes with the parasitic light absorption and carrier recombination in solar cells. The EQE represents the percentage of photons that actually contribute to generate the current in solar cells. In Fig. 2.2a, we assume a hypothetical situation that all the sunlight is absorbed completely in a semiconducting absorber with zero reflectance (i.e., $R = 0$). In this case, the EQE values become 100% below λ which corresponds to the band gap (E_g) of the semiconductor [λ_{Eg}(SC)]. In the example of Fig. 2.2, λ_{Eg}(SC) is assumed to locate in the infrared region.

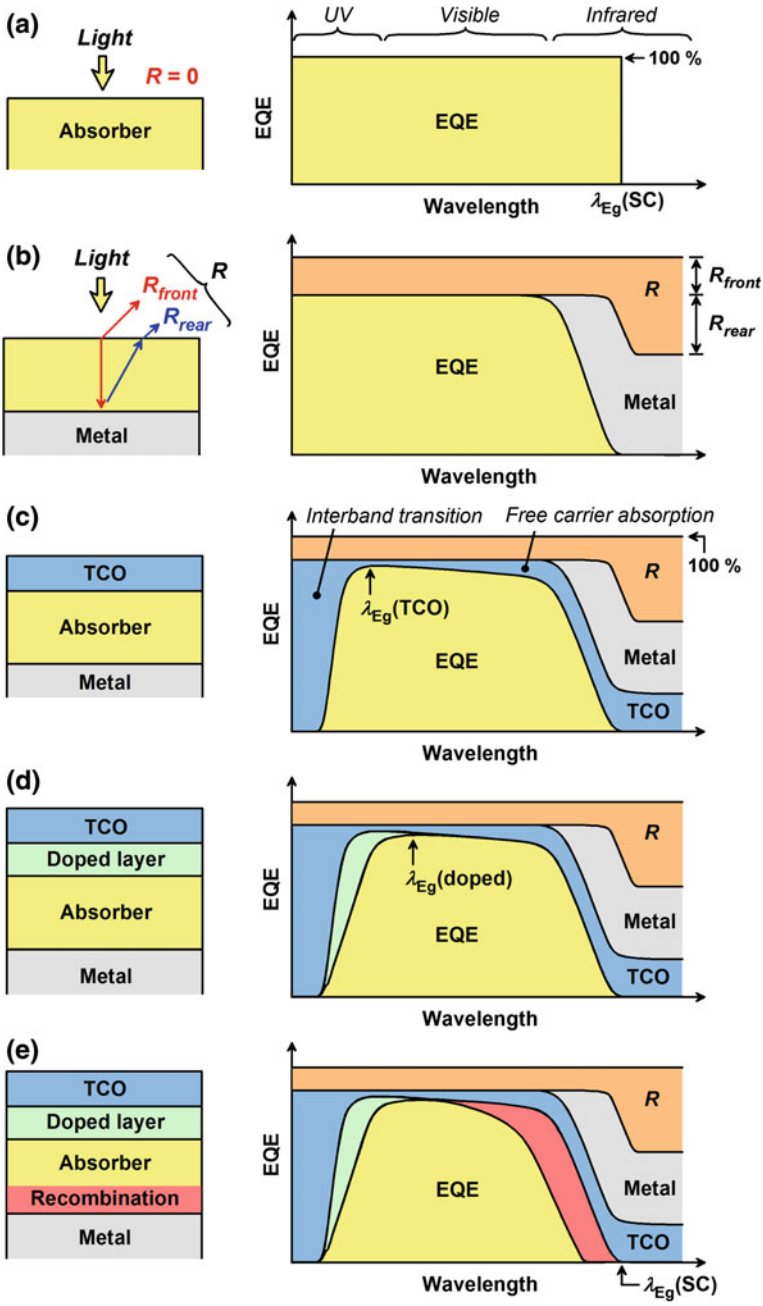
In a metal/semiconductor structure (Fig. 2.2b), the light reflection ($R > 0$) reduces the EQE response in a wide region from the ultraviolet (UV) to the visible region. The reflectance components of this structure can be categorized into the front surface (R_{front}) and rear surface (R_{rear}) contributions. The constant contribution of R in the UV/visible region is consistent with R_{front}, whereas R increases near λ_{Eg}(SC), as the light absorption within the absorber becomes weaker and R_{rear} increases. Thus, R in the transparent region is expressed by $R_{front} + R_{rear}$. In Fig. 2.2b, the onset of the light absorption in the semiconductor agrees with the position of λ_{Eg}(SC). Nevertheless, if the tail-state absorption is present, we observe non-zero EQE values even at $\lambda > \lambda_{Eg}$(SC).

It can be seen from Fig. 2.2b that the light absorption in the metal electrode layer becomes significant near λ_{Eg}(SC) due to higher light transmission in this region. However, the light absorption in the metal layer is governed by the optical constants of the semiconductor and metal and, when the reflectance at the semiconductor/metal interface is low, more light is absorbed by the metal. The reflectances of various rear metal electrodes in crystalline Si (c-Si), $Cu(In,Ga)Se_2$ (CIGSe) and hybrid perovskite [$HC(NH_2)_2PbI_3$] solar cells are summarized in Fig. 12.3.

When a front TCO electrode, such as In_2O_3:Sn (ITO) and ZnO:Al, is formed (Fig. 2.2c), the parasitic light absorption in the TCO reduces the EQE. In particular, there exist two absorption processes in TCO materials: i.e., interband transition and free carrier absorption (see Fig. 18.6 in Vol. 1). The strong reduction of the EQE in the UV region is caused by the TCO interband transition that occurs below λ corresponding to E_g of the TCO [i.e., $\lambda \leq \lambda_{Eg}$(TCO)]. On the other hand, the TCO absorption above λ_{Eg}(TCO) is attributed to the free carrier absorption (Fig. 18.8 in Vol. 1). Due to the light absorption in the TCO layer, the internal quantum efficiency (IQE) defined by the following equation also decreases.

$$\mathrm{IQE} = \mathrm{EQE}/(1 - R). \tag{2.1}$$

The IQE shows how efficiently the absorbed photons (not incident photons) are converted into the photocurrent and the IQE spectrum is obtained by normalizing the EQE spectrum using the absorption component (i.e., $1 - R$). In c-Si solar cells


(a)
Light
R = 0
Absorber
UV
Visible
Infrared
100 %
EQE
EQE
Wavelength
λEg(SC)
(b)
Light
R
Rfront
Rrear
Metal
R
Rfront
Rrear
EQE
EQE
Metal
Wavelength
(c)
TCO
Absorber
Metal
Interband transition
Free carrier absorption
100 %
R
λEg(TCO)
EQE
EQE
Metal
TCO
Wavelength
(d)
TCO
Doped layer
Absorber
Metal
R
λEg(doped)
EQE
EQE
Metal
TCO
Wavelength
(e)
TCO
Doped layer
Absorber
Recombination
Metal
R
EQE
EQE
Metal
TCO
Wavelength
λEg(SC)

◀**Fig. 2.2** Variation of EQE spectrum with solar cell structure: EQE spectra of **a** a hypothetical perfect absorber with zero reflectance ($R = 0$), **b** an absorber/metal structure, **c** a transparent conductive oxide (TCO)/absorber/metal structure, **d** a TCO/doped layer/absorber/metal structure, and **e** a TCO/doped layer/absorber/metal structure with a recombination layer within the absorber layer. The position of λ_{Eg} shows λ that corresponds to E_g of semiconductor (SC), TCO and doped layers. In the figure, λ_{Eg}(SC) is assumed to be in the infrared region. In **b**, R_{front} represents the reflectance contribution induced by the front surface reflection, while R_{rear} shows that caused by the rear-side reflection

that incorporate no TCO layers, IQE of ~100% is observed [19, 20], whereas the maximum IQE is generally limited to 80–95% for solar cells with TCO layers [5–7, 10–12, 17, 18].

In Fig. 2.2d, a doped layer is inserted at the TCO/semiconductor interface. In general, the doped layers in solar cells exhibit the intense light absorption and deteriorate the EQE response particularly in the short λ region (see Sect. 2.2.3). Since the parasitic light absorption in the TCO and doped layers occurs sequentially from the upper layer, the presence of the doped layer leads to the additional EQE reduction below λ_{Eg} of the doped layer [i.e., $\lambda \leq \lambda_{Eg}$(doped)].

In photovoltaic devices, the extraction of photo-generated carriers from the semiconductor light absorber is an essential process and the presence of recombination centers within absorber layers reduces the short-circuit current density (J_{sc}) significantly. The effect of the recombination generally becomes more severe in a solar-cell bottom region, where the generated carriers need to reach the front interface through carrier diffusion [18]. As shown in Fig. 2.2e, if the carrier recombination occurs at the semiconductor/metal rear interface, the EQE response in the longer λ region decreases. When the photogenerated carriers recombine in a solar-cell front region, the EQE values in the short λ region decrease, which is similar to the case of the doped layer in Fig. 2.2d. In other words, the carrier recombination in the front and rear interface regions can be characterized quantitatively based on detailed EQE analyses (Sect. 2.3.3). Often, E_g of the absorber layer is extracted from the EQE analysis of the longer λ region [21–25]. In this case, however, E_g will be overestimated seriously if the carrier recombination in a solar-cell bottom region is significant [18], as confirmed from Fig. 2.2e.

Unfortunately, the EQE analyses of conventional solar cells have been rather difficult due to the presence of textured structures. Figure 2.3 shows the scanning electron microscope (SEM) images of (a) CIGSe and (b) $Cu_2ZnSnSe_4$ (CZTSe) solar cells, obtained from the same samples reported in [16] and [18], respectively. The CIGSe solar cell in Fig. 2.3a, fabricated by a conventional three-stage coevaporation process [26–28], has a structure of MgF_2/ZnO:Al/ZnO/CdS/CIGSe/Mo/glass with $J_{sc} = 34.2$ mA/cm^2, a open-circuit voltage of $V_{oc} = 674$ mV and a fill factor of $FF = 0.725$ (conversion efficiency: 16.7%) [16]. The solar cell structure of CZTSe is quite similar to that of the CIGSe, although there is no MgF_2 anti-reflection layer in the solar cell. The conversion efficiency of this solar cell is 8.5% with $J_{sc} = 33.4$ mA/cm^2, $V_{oc} = 418$ mV, and $FF = 0.606$ [18]. It can be seen from Fig. 2.3 that these solar cells have submicron-size natural textures (<1 μm).

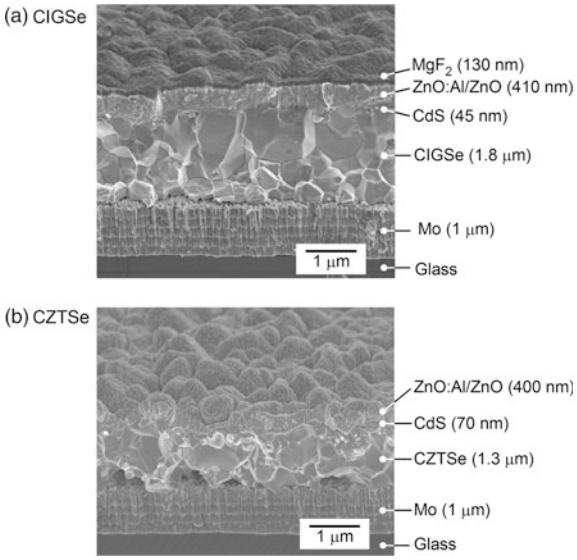


Fig. 2.3 SEM images of **a** CIGSe and **b** CZTSe solar cells, obtained from the same samples reported in [16] and [18], respectively. The CIGSe solar cell has a structure of MgF_2/ZnO:Al/ZnO (non-doped)/CdS/CIGSe/($MoSe_2$)/Mo/glass (conversion efficiency: 16.7%), whereas the CZTSe solar cell has a similar structure of ZnO:Al/ZnO(non-doped)/CdS/CZTSe/($MoSe_2$)/Mo/glass (conversion efficiency: 8.5%). The $MoSe_2$ layers are formed during the initial growth stages. Both solar cells have submicron-size natural textures (<1 μm). In the CZTSe solar cell, a complex void structure is formed in the rear interface region

In particular, the CZTSe solar cell has a complex rear interface structure due to the void formation. The generation of the void-rich structure is caused by the poor adhesion of the CZTSe layer to a $MoSe_2$ layer formed initially on the Mo layer during the CZTSe growth [18, 29].

When the texture size is comparable to λ of the incident light, light scattering occurs and its effect needs to be incorporated into the EQE analysis. Light scattering in textured solar cells has been simulated using computer intensive methods including the rigorous coupled-wave analysis [7], the ray tracing method [30], the field integration technique [8, 31], and the finite element method [32]. Nevertheless, the optical simulation by such methods is generally quite time consuming and sometimes difficult because these calculations require proper modeling of the three-dimensional random textures for all the interfaces in multilayer device structures. Moreover, the topological features of the surface/interface may depend strongly on device preparation conditions [33] and the EQE simulation based on exact modeling of surface/interface structures may have limited practical use.

Quite fortunately, a quite simple optical analysis scheme has been developed, in which the optical response in submicron-textured solar cells is calculated by imposing the anti-reflection condition assuming a flat optical model [16]. From this optical simulation method using the anti-reflection condition (ARC method),

the explicit optical simulation of the submicron-textured CIGSe solar cell shown in Fig. 2.3a has been made without considering three-dimensional structures (Sect. 2.2). The EQE analysis can also be performed by employing an experimental reflectance spectrum (ERS method) obtained from actual solar cells (Sect. 2.2.3).

Furthermore, Nakane et al. has extended the ARC method by incorporating the effect of the carrier recombination in solar cells [18]. In this extended ARC method (e-ARC method), the EQE analysis is simplified greatly by considering only the effective carrier-collection length from the absorber front interface (Sect. 2.3). The e-ARC method is a global characterization method, which can be employed to deduce J_{sc} losses induced by parasitic optical absorption and carrier recombination in a wide variety of thin-film photovoltaic devices, including CZTSe, Cu_2ZnSnS_4 (CZTS), $Cu_2ZnSn(S,Se)_4$ (CZTSSe), CdTe, and hybrid perovskite solar cells, without any restrictions [18]. By applying the e-ARC method, the performance-limiting factors in solar cells can be identified on a routine basis, which further enables us to optimize solar cell structures and processing quite effectively. From the e-ARC method, even the complex CZTSe solar-cell structure shown in Fig. 2.3b can be characterized [18].

In this chapter, the basic principles of the EQE analyses based on the ERS, ARC and e-ARC methods are explained in detail. As analysis examples, the EQE analyses of CIGSe, CZTSe, CZTS, CdTe, hydrogenated amorphous silicon (a-Si:H), and c-Si solar cells are described. To perform the EQE analysis of textured c-Si solar cells, a modified EQE calculation method that allows the treatment of incoherent light absorption in thick substrates (~200 μm) has been established (Sect. 2.5). The EQE analysis for hybrid perovskite solar cells can be found in Sect. 16.3 (Vol. 1). From these analysis results, we will further discuss the optical and recombination losses in different types of solar cells.

2.2 ERS and ARC Methods

In this section, the calculation procedures of the ERS and ARC methods are introduced. These EQE calculation methods are based on the conventional optical admittance method [34], in which optical absorption, reflection and transmission in multilayer structures are expressed rather simply assuming a flat optical model. For superstrate-type solar cells, however, the light reflection and transmission in a thick glass substrate need to be modeled properly. This section addresses the fundamental principle of the optical admittance method and the treatment of a thick glass substrate in superstrate solar cells. As an EQE analysis example, the analysis of the state-of-the-art CIGSe solar cell with a double-graded Ga profile [16], formed by a conventional three-stage process, is described.

2.2.1 Optical Admittance Method

All EQE analyses described in this chapter are implemented within the framework of the optical admittance method. Here, we will derive the important equations used in the optical admittance method based on a procedure reviewed by H. A. Macleod [34].

The calculation procedure of the optical admittance method can be understood by considering the propagation of electromagnetic waves in a thin film structure. As known well, electromagnetic waves are sinusoidal waves that have the electric field ($\boldsymbol{E}_\mathrm{f}$) and magnetic field ($\boldsymbol{H}_\mathrm{f}$) components (Fig. 2.4a). The $\boldsymbol{E}_\mathrm{f}$ and $\boldsymbol{H}_\mathrm{f}$ are perpendicular to each other, and these behaviors are consistent with Faraday's induction law and Ampère's law. The energy flow of the electromagnetic wave is described by the vector S, known as the Poynting vector: $\boldsymbol{S} = \boldsymbol{E}_\mathrm{f} \times \boldsymbol{H}_\mathrm{f}$ [34, 35]. The direction of $\boldsymbol{S}$ is consistent with the direction of the energy flow, and the irradiance (energy per unit area per unit time) of the electromagnetic wave is given by

$$I = \frac{1}{2}\mathrm{Re}\left(E_\mathrm{f} H_\mathrm{f}^{*}\right), \tag{2.2}$$

where E_f and H_f denote the amplitudes of $\boldsymbol{E}_\mathrm{f}$ and $\boldsymbol{H}_\mathrm{f}$, respectively (see Fig. 2.4a). For E_f and H_f, there is the following relation [35, 36]:

$$H_\mathrm{f} = NE_\mathrm{f}, \tag{2.3}$$

where N is the complex refractive index ($N = n - ik$) defined using the refractive index n and extinction coefficient k of the propagating medium.

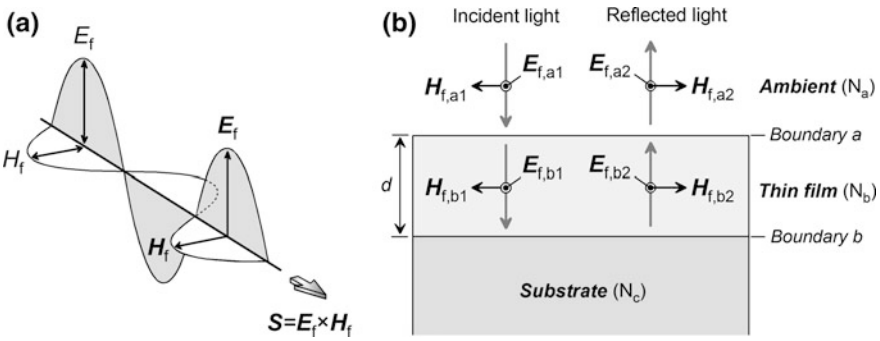


Fig. 2.4 **a** Propagation of an electromagnetic wave having electric field ($\boldsymbol{E}_\mathrm{f}$) and magnetic field ($\boldsymbol{H}_\mathrm{f}$) components and **b** propagation of the electromagnetic waves in a thin film structure consisting of ambient/thin film(thickness d)/substrate. In **a**, $\boldsymbol{S}$ denotes the Poynting vector. In **b**, the subscripts "a" and "b" show $\boldsymbol{E}_\mathrm{f}$ and $\boldsymbol{H}_\mathrm{f}$ at the boundaries a and b, whereas the subscripts "1" and "2" represent the incident and reflected waves. The $N_{\mathrm{a\text{-}c}}$ show the complex refractive indices of each layer. The direction of $\boldsymbol{E}_\mathrm{f}$ in **b** is perpendicular to the plane of the paper and is pointing to the reader

Figure 2.4b shows the propagation of the electromagnetic waves in a thin film structure consisting of ambient/thin film (thickness d)/substrate. The complex refractive indices of the ambient, thin film and substrate are N_a, N_b and N_c, respectively. In this figure, $\boldsymbol{E}_f$ and $\boldsymbol{H}_f$ at the boundary a (ambient/thin film interface) and the boundary b (thin film/substrate interface) are denoted as ($\boldsymbol{E}_{f,a}$, $\boldsymbol{H}_{f,a}$) and ($\boldsymbol{E}_{f,b}$, $\boldsymbol{H}_{f,b}$), respectively. The subscripts of "1" and "2" for $\mathbf{E}_f$ and $\boldsymbol{H}_f$ in Fig. 2.4b further indicate the incident and reflected waves, respectively. It should be noted that the direction of ($\boldsymbol{H}_{f,a2}$, $\boldsymbol{H}_{f,b2}$) is opposite to that of ($\boldsymbol{H}_{f,a1}$, $\boldsymbol{H}_{f,b1}$), as confirmed from the relation of $\boldsymbol{E}_f$ and $\boldsymbol{H}_f$ in Fig. 2.4a.

The boundary conditions for electromagnetic waves require that the components of $\boldsymbol{E}_f$ and $\boldsymbol{H}_f$ parallel to an interface (tangential components) are continuous at the interface. The tangential components at the boundary b are expressed simply by

$$E_{f,b} = E_{f,b1} + E_{f,b2}, \tag{2.4}$$

$$H_{f,b} = H_{f,b1} + H_{f,b2} = N_b E_{f,b1} + N_b(-E_{f,b2}). \tag{2.5}$$

For the transformation of (2.5), (2.3) was used. The minus sign for $E_{f,b2}$ in (2.5) shows that the direction of $\boldsymbol{E}_{f,b2}$ is opposite to that of $\boldsymbol{E}_{f,b1}$ when the vectors of $\boldsymbol{H}_{f,b1}$ and $\boldsymbol{H}_{f,b2}$ are aligned. If $E_{f,b2}$ is eliminated from (2.4) and (2.5), the following relation is obtained:

$$E_{f,b1} = \frac{1}{2}\left(E_{f,b} + \frac{H_{f,b}}{N_b}\right). \tag{2.6}$$

By applying similar procedures, we get

$$E_{f,b2} = \frac{1}{2}\left(E_{f,b} - \frac{H_{f,b}}{N_b}\right), \tag{2.7}$$

$$H_{f,b1} = N_b E_{f,b1} = \frac{1}{2}(N_b E_{f,b} + H_{f,b}), \tag{2.8}$$

$$H_{f,b2} = -N_b E_{f,b2} = \frac{1}{2}(-N_b E_{f,b} + H_{f,b}). \tag{2.9}$$

On the other hand, the phase change of the light wave in the thin layer is expressed as follows [35, 36]:

$$\delta = 2\pi(N_b/\lambda)d. \tag{2.10}$$

Thus, the relation of E_f (or H_f) between the boundaries of a and b can be described by the following relations [34, 36]:

$$E_{\mathrm{f,a1}} = E_{\mathrm{f,b1}} \exp(i\delta),\ E_{\mathrm{f,a2}} = E_{\mathrm{f,b2}} \exp(-i\delta), \tag{2.11}$$

$$H_{\mathrm{f,a1}} = H_{\mathrm{f,b1}} \exp(i\delta),\ H_{\mathrm{f,a2}} = H_{\mathrm{f,b2}} \exp(-i\delta). \tag{2.12}$$

The minus sign for δ indicates that the propagation direction is opposite to that of the incident wave. From the boundary conditions and (2.11), $E_{\mathrm{f,a}}$ can be expressed by

$$\begin{aligned} E_{\mathrm{f,a}} &= E_{\mathrm{f,a1}} + E_{\mathrm{f,a2}} = E_{\mathrm{f,b1}} \exp(i\delta) + E_{\mathrm{f,b2}} \exp(-i\delta) \\ &= E_{\mathrm{f,b}} \cos\delta + H_{\mathrm{f,b}} (i \sin\delta / N_b). \end{aligned} \tag{2.13}$$

In the above transformation, Euler's formula [i.e., $\exp(i\delta) = \cos\delta + i\sin\delta$, $\exp(-i\delta) = \cos\delta - i\sin\delta$] was used. For $H_{\mathrm{f,a}}$, we further obtain

$$H_{\mathrm{f,a}} = H_{\mathrm{f,a1}} + H_{\mathrm{f,a2}} = N_{\mathrm{b}} E_{\mathrm{f,b}} (i \sin\delta) + H_{\mathrm{f,b}} (\cos\delta). \tag{2.14}$$

In matrix form, (2.13) and (2.14) can be written as

$$\begin{bmatrix} E_{\mathrm{f,a}} \\ H_{\mathrm{f,a}} \end{bmatrix} = \begin{bmatrix} \cos\delta & i \sin\delta / N_{\mathrm{b}} \\ i N_{\mathrm{b}} \sin\delta & \cos\delta \end{bmatrix} \begin{bmatrix} E_{\mathrm{f,b}} \\ H_{\mathrm{f,b}} \end{bmatrix}. \tag{2.15}$$

Here, we define the optical admittance by $Y = H_{\mathrm{f}}/E_{\mathrm{f}}$. Since $H_{\mathrm{f}} = NE_{\mathrm{f}}$ [(2.3)], Y basically represents N. If (2.15) is divided by $E_{\mathrm{f,b}}$, we get

$$\begin{bmatrix} E_{\mathrm{f,a}}/E_{\mathrm{f,b}} \\ H_{\mathrm{f,a}}/E_{\mathrm{f,b}} \end{bmatrix} = \begin{bmatrix} B \\ C \end{bmatrix} = \begin{bmatrix} \cos\delta & i \sin\delta / N_{\mathrm{b}} \\ i N_{\mathrm{b}} \sin\delta & \cos\delta \end{bmatrix} \begin{bmatrix} 1 \\ Y_{\mathrm{b}} \end{bmatrix}, \tag{2.16}$$

where $Y_{\mathrm{b}} = H_{\mathrm{f,b}}/E_{\mathrm{f,b}} = N_{\mathrm{c}}$. Note that, at the boundary b, N of the substrate side is N_{c} and thus $Y_{\mathrm{b}} = N_{\mathrm{c}}$.

Figure 2.5 shows the calculation procedures of (a) the optical admittance and (b) the transmittance and absorptance in a multilayer structure. The optical model of Fig. 2.5a is the same as that shown in Fig. 2.4b. In this thin film structure, by applying (2.16), Y_{b} can be transferred to Y_{a} according to

$$Y_{\mathrm{a}} = \frac{C}{B} = \frac{Y_{\mathrm{b}} \cos\delta + i N_{\mathrm{b}} \sin\delta}{\cos\delta + i Y_{\mathrm{b}} \sin\delta / N_{\mathrm{b}}}. \tag{2.17}$$

It should be noted that, from (2.16), $C/B = H_{\mathrm{f,a}}/E_{\mathrm{f,a}} = Y_{\mathrm{a}}$. From Y_{a} of (2.17), the reflectance obtained assuming the flat optical model (R_{flat}) is calculated by

$$R_{\mathrm{flat}} = |N_{\mathrm{a}} - Y_{\mathrm{a}}|^2 / |N_{\mathrm{a}} + Y_{\mathrm{a}}|^2. \tag{2.18}$$

If the ambient is air, we use $N_{\mathrm{a}} = 1$.

From (2.2), on the other hand, the irradiance at the boundary a (I_{a}) is described by

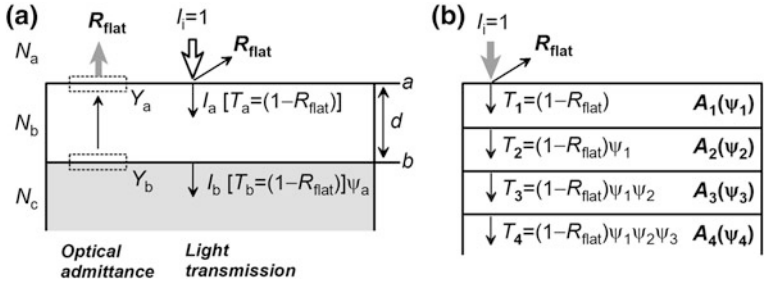


Fig. 2.5 Calculation procedures of **a** the optical admittance and **b** the transmittance and absorptance in a multilayer structure. In **a**, Y shows the optical admittance and R_{flat} indicates the reflectance obtained assuming a flat optical model, whereas I, T and ψ show the irradiance, transmittance and potential transmittance, respectively. The subscripts of "i", "a", and "b" denote the incidence, boundary a, and boundary b, respectively. In **b**, A_j shows the absorptance of the jth layer with ψ_j. The transmittance at each interface (T_j) is also indicated

$$I_a = \mathrm{Re}\left(E_{f,a}H^*_{f,a}\right)/2 \tag{2.19}$$

Since $H_{f,a} = E_{f,a}Y_a$, we get $I_a = \mathrm{Re}(Y_a)\mathrm{Re}\left(E_{f,a}E^*_{f,a}\right)/2$ using $\mathrm{Re}(Y_a) = \mathrm{Re}(Y^*_a)$. From (2.15), it can be obtained that $E_{f,a} = E_{f,b}[\cos\delta + (i\sin\delta)Y_b/N_b]$. By employing this, we further obtain

$$I_a = \frac{1}{2}\mathrm{Re}\left(E_{f,a}H^*_{f,a}\right) = \frac{1}{2}\mathrm{Re}(Y_a)\mathrm{Re}\left(E_{f,b}E^*_{f,b}\right)|\cos\delta + (i\ \sin\delta)Y_b/N_b|^2. \tag{2.20}$$

If the irradiance of the incident light is I_i, I_a is expressed as $I_a = (1 - R_{flat})I_i$. Thus, it follows from (2.19) that

$$I_i = \frac{1}{2}\cdot\frac{\mathrm{Re}\left(E_{f,a}H^*_{f,a}\right)}{(1-R_{flat})}. \tag{2.21}$$

If we assume that the irradiance at the boundary b is $I_b = \mathrm{Re}(Y_b)\mathrm{Re}\left(E_{f,b}E^*_{f,b}\right)/2$, the transmittance at the boundary b is described by $T_b = I_b/I_i = \mathrm{Re}(Y_b)\mathrm{Re}\left(E_{f,b}E^*_{f,b}\right)(1-R_{flat})/\mathrm{Re}\left(E_{f,a}H^*_{f,a}\right)$ using (2.21). By rearranging the terms, we obtain the potential transmittance defined by

$$\psi_a \equiv \frac{T_b}{(1-R_{flat})} = \mathrm{Re}(Y_b)\frac{\mathrm{Re}\left(E_{f,b}E^*_{f,b}\right)}{\mathrm{Re}\left(E_{f,a}H^*_{f,a}\right)}. \tag{2.22}$$

From the above equation and (2.20), the following equation is obtained:

$$\psi_a = \frac{\mathrm{Re}(Y_\mathrm{b})}{\mathrm{Re}(Y_\mathrm{a})\left|\cos\delta + iY_\mathrm{b}\sin\delta/N_\mathrm{b}\right|^2}. \tag{2.23}$$

It should be emphasized that, once ψ_a is known, T_b is calculated simply as $T_\mathrm{b} = (1 - R_\mathrm{flat})\psi_\mathrm{a}$ from (2.22). Since the transmittance at the boundary a is $T_\mathrm{a} = (1 - R_\mathrm{flat})$, the absorptance of the thin film (A_a) can finally be obtained by

$$A_\mathrm{a} = T_\mathrm{a} - T_\mathrm{b} = (1 - R_\mathrm{flat})(1 - \psi_\mathrm{a}). \tag{2.24}$$

In the optical admittance method, therefore, A_a is calculated from R_flat and ψ_a. Recall that R_flat and ψ_a are determined from the optical constants and the thin layer thickness of the optical model. Accordingly, if these parameters are known, A_a can readily be obtained.

The above procedure can be extended quite easily to a multilayer system. In this case, the optical admittance calculation is carried out sequentially from the bottom to the top layer. If there are a total of j layers, for example, the optical admittance of the substrate is calculated from $Y_\mathrm{j} = N_\mathrm{j+1}$. From Y_j, we can calculate $Y_\mathrm{j\text{-}1}$ by rewriting (2.17) using $Y_\mathrm{a} \rightarrow Y_\mathrm{j\text{-}1}$, $Y_\mathrm{b} \rightarrow Y_\mathrm{j}$, $\delta \rightarrow \delta_\mathrm{j}$ and $N_\mathrm{b} \rightarrow N_\mathrm{j}$. If this process is repeated in a multilayer structure, Y_0 is obtained, from which R_flat is calculated with the conversion of $Y_\mathrm{a} \rightarrow Y_0$ and $N_\mathrm{a} \rightarrow 1$ in (2.18) [16, 18]. The ψ_j values of each layer can be calculated from (2.23) using the conversion of $\psi_\mathrm{a} \rightarrow \psi_\mathrm{j}$, $Y_\mathrm{a} \rightarrow Y_\mathrm{j\text{-}1}$, $Y_\mathrm{b} \rightarrow Y_\mathrm{j}$, $\delta \rightarrow \delta_\mathrm{j}$ and $N_\mathrm{b} \rightarrow N_\mathrm{j}$.

Figure 2.5b shows the calculation of A_j in the multilayer system. As shown in this figure, T at each interface is calculated by sequentially multiplying T of the upper layer by ψ. For example, A_3 in the figure is obtained from

$$A_3 = T_3 - T_4 = (1 - R_\mathrm{flat})(1 - \psi_3)\psi_1\psi_2. \tag{2.25}$$

More generally, A_j can be expressed as follows [16, 18, 37, 38]

$$A_\mathrm{j} = (1 - R_\mathrm{flat})(1 - \psi_j)\prod_{k=1}^{j-1}\psi_k. \tag{2.26}$$

Accordingly, if R_flat is obtained, the layer absorptance is determined from the top to bottom layer ($A_1 \rightarrow A_\mathrm{j}$) using (2.26). Once the absorptance of the absorber layer in a solar cell is known, the EQE spectrum can then be simulated assuming 100% collection efficiency for the generated carriers [i.e., $A(\lambda) = \mathrm{EQE}(\lambda)$]. Finally, J_sc of the solar cell is calculated by

$$J_\mathrm{sc} = \frac{q\lambda}{hc}\int A(\lambda)F(\lambda)\mathrm{d}\lambda, \tag{2.27}$$

where q, h and c are the electron charge, Planck's constant and speed of light, respectively (see Sect. 1.1.2). In (2.27), $F(\lambda)$ indicates the irradiance in units of $\mathrm{Wcm^{-2}nm^{-1}}$ under AM1.5G illumination (see Fig. 1.3a). If the absorptance spectra of TCO, metal and doped layers, obtained simultaneously from the EQE analysis, are applied for (2.27), the J_{sc} losses induced by these layers are estimated. By replacing $A(\lambda)$ with $R(\lambda)$ in (2.27), the reflection loss can also be determined.

2.2.2 Treatment of Glass Substrate

In superstrate-type solar cells, thick glass substrates (1–6 mm) are employed and the sunlight is illuminated from the glass side (see also Fig. 18.4 in Vol. 1). Nevertheless, the thickness of the glass substrates exceeds the coherent length of light waves generated by conventional light sources (i.e., halogen and xenon lamps) and the optical calculation needs to be performed assuming the incoherent condition. More specifically, probe light employed for EQE measurements is not the perfect monochromatic light, but the quasi-monochromatic light that shows continuous variation of the phase with time. In thin film structures, an optical interference induced by the quasi-monochromatic light is essentially identical to that generated by the perfect monochromatic light because of the short optical pass length in thin film structures (coherent condition). However, when the optical pass length becomes quite long, the phase of the quasi-monochromatic light cannot be defined anymore due to the variation of the phase with time and the optical interference disappears (incoherent condition). For the optical models with thick substrates, therefore, the optical response should be calculated assuming the incoherent condition.

Figure 2.6 shows the calculation procedure used for the EQE analyses of superstrate-type solar cells with glass substrates [17, 18]. In the example of Fig. 2.6, an anti-reflection layer is provided on the front-side of the solar cell. In this case, the reflectance of the front surface (R_{front}) is calculated first using the optical admittance or a more conventional Fresnel method [36]. When $\mathrm{I_i} = 1$, the transmittance of the (anti-reflection layer)/glass front structure is given by $\mathrm{T_{front}} = 1 - R_{\mathrm{front}}$. If we neglect the light absorption within the glass substrate, the light transmits the glass substrate without any intensity change and is reflected by the rear thin-film structure with the reflectance R_{rear}. The reflected light further transmits the front structure with the transmittance T'_{front} and the reflection also occurs by the front structure (R'_{front}).

In a simple first-order approximation, the total reflectance of the whole solar cell (R_{total}) is calculated by

$$R_{\mathrm{total}} = R_{\mathrm{front}} + T_{\mathrm{front}} R_{\mathrm{rear}} = R_{\mathrm{front}} + (1 - R_{\mathrm{front}}) R_{\mathrm{rear}}. \tag{2.28}$$

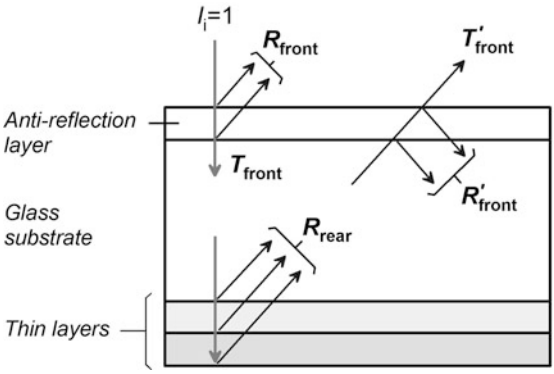


Fig. 2.6 EQE calculation procedure for superstrate-type solar cells with thick glass substrates. The R' and T' represent the reflectance and transmittance when the light propagation direction is reversed

The R_{rear} can be obtained from the optical admittance method, in which the optical constants of the glass substrate (N_{SiO2}) are used for N_a in Fig. 2.5a [i.e., $N_a \rightarrow N_{SiO2}$ and $Y_a \rightarrow Y_0$ in (2.18)]. When there is no anti-reflection layer, R_{front} is calculated by

$$R_{front} = \left(\frac{N_{SiO2} - 1}{N_{SiO2} + 1}\right)^2 \tag{2.29}$$

Since $N_{SiO2} = n_{SiO2} \sim 1.5$ (see Fig. 13.1), we observe that $R_{front} \sim 4\%$. If the anti-reflection layer is formed, R_{front} further decreases. The model of (2.28) has been applied for the EQE calculation of $CH_3NH_3PbI_3$ (Fig. 16.17 in Vol. 1) and CdTe (Fig. 2.21) solar cells.

By modifying (2.28), the multiple light reflections within the glass substrate can be calculated explicitly [36]:

$$\begin{aligned} R_{total} &= R_{front} + T_{front}R_{rear}T'_{front} + T_{front}R_{rear}T'_{front}(R'_{front}R_{rear}) \\ &\quad + T_{front}R_{rear}T'_{front}(R'_{front}R_{rear})^2 \cdots \\ &= R_{front} + \frac{T_{front}T'_{front}R_{rear}}{1 - R'_{front}R_{rear}} \end{aligned} \tag{2.30}$$

If $R'_{front} = 0$ and $T'_{front} = 1$, (2.30) reduces to (2.28). When the anti-reflection layer is not present, we obtain $R_{front} = R'_{front} = 4\%$ and $T_{front} = T'_{front} = 96\%$. Since conventional superstrate solar cells show $R_{rear} < R_{total} < 10\%$ and $R_{front} < 4\%$, we get $R'_{front}R_{rear} < 0.4\%$. Thus, the influence of the higher-order reflected beams is essentially negligible.

2.2.3 Analysis of a Textured Solar Cell

Here, the EQE analyses of a textured solar cell based on the ERS and ARC methods are explained using a CIGSe solar cell as an example. In particular, this section introduces the EQE analysis for the CIGSe solar cell with the submicron natural texture shown in Fig. 2.3a.

Figure 2.7 shows (a) the structure of a textured solar cell and (b) the optical model assumed in the ERS method. As shown in Fig. 2.7a, in non-uniform structures with rough surfaces/interfaces, light scattering occurs when the texture size is comparable to λ of the incident light. Under this condition, the light scattering changes the transmission angle (see dotted lines in Fig. 2.7a) and the transmission angle shows a broad distribution [39], which makes the calculation of $A(\lambda)$ quite difficult. However, if we apply the experimental reflectance spectrum (R_{ERS}) obtained directly from an actual device structure (ERS method), the total light absorptance in the solar cell can be determined quite easy as $\sum A_{\mathrm{j}} = 1 - R_{\mathrm{ERS}}$. Since R_{ERS} includes all the optical effects of the solar cell, this allows an accurate and simple estimation of $\sum A_{\mathrm{j}}$. Unfortunately, even in this case, the calculation of A_{j} from $\sum A_{\mathrm{j}}$ is not straightforward due to the complexity of the solar cell structure.

Nevertheless, as illustrated in Fig. 2.7a, even when the incident light is scattered, the ratio of the optical pass lengths within the solar-cell component layers may not differ significantly from the case of a flat structure, if the angular distribution of the scattered light is small. Accordingly, in the ERS method, the complicated problem of light scattering has been solved by calculating A_{j} assuming a perfectly flat structure, whereas $\sum A_{\mathrm{j}}$ itself is estimated from $(1 - R_{\mathrm{ERS}})$ (see Fig. 2.7b). The EQE analysis based on the ERS method can be conducted quite easily by simply replacing R_{flat} in (2.26) with R_{ERS}. This approach assumes that there is no change in the IQE spectra between perfectly flat and textured structures. In other words, by modifying (2.1), the EQE spectrum is deduced as

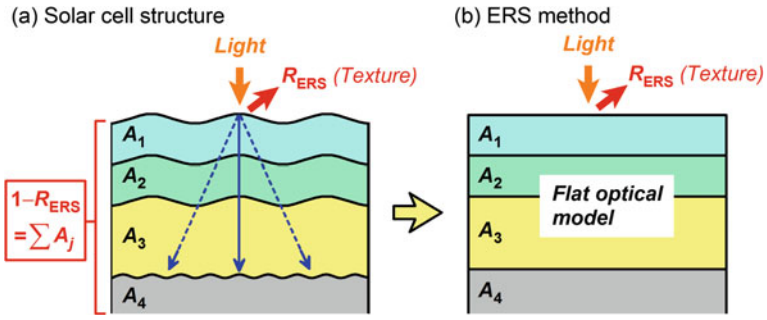


Fig. 2.7 **a** Structure of a textured solar cell and **b** optical model assumed in the ERS method. The R_{ERS} represents the reflectance obtained directly from an experimental reflectance spectrum (ERS) and A_{j} shows the absorptance of each layer. In the ERS method, A_{j} is determined assuming a flat optical model while using R_{ERS} to incorporate the effect of light scattering by submicron textures

$$\mathrm{EQE} = (1 - R_{\mathrm{ERS}})\mathrm{IQE}_{\mathrm{flat}}, \tag{2.31}$$

where $\mathrm{IQE}_{\mathrm{flat}}$ shows IQE obtained assuming a flat optical model.

By applying the ERS method, the EQE spectrum of the CIGSe solar cell shown in Fig. 2.3a has been analyzed [16]. Figure 2.8 shows (a) the optical model and (b) the variation of the Ga composition within the CIGSe layer in the solar cell [16]. For this analysis, an optical model consisting of MgF_2/ZnO:Al/ZnO/CdS/CIGSe/$MoSe_2$/Mo was constructed. In Fig. 2.8a, the thicknesses of the solar-cell component layers, determined from the transmission electron microscopy (TEM) observation, are also indicated. In conventional high-efficiency CIGSe solar cells, a double grading Ga profile is formed by a three-stage process [26–28], and the Ga composition [x = Ga/(In + Ga)] is low near the central region of the CIGSe layer, while x near the front and rear interfaces is higher (see also Fig. 10.1b in Vol. 1). To express the optical response of the compositional grading structure explicitly, the CIGSe layer was divided into 500 sublayers and the optical constants of each sublayer were obtained from a complete CIGSe optical database that allows the calculation of $Cu_yIn_{1-x}Ga_xSe_2$ optical constants in a complete two-dimensional compositional space of (x, y) (see Sect. 10.4 in Vol. 1). The optical constants of the other layers in Fig. 2.8a can be found in Part II of this book: i.e., MgF_2 (Fig. 13.10), ZnO:Al (Fig. 11.18), non-doped ZnO (Fig. 11.16), CdS (Fig. 8.21), $MoSe_2$ (Fig. 8.36) and Mo (Fig. 12.13).

In Fig. 2.8b, the depth profile of the Ga composition for the 1.8-μm-thick CIGSe layer is shown. In this figure, the x values for the depth from the CdS/CIGSe interface (d) are indicated. The open circles indicate the experimental result

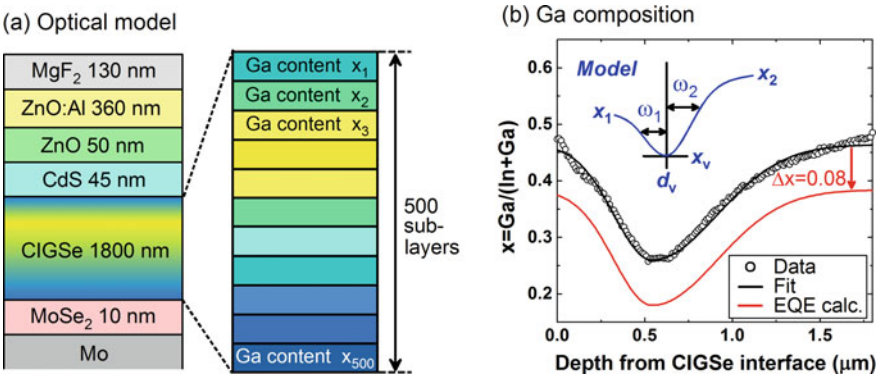


Fig. 2.8 **a** Optical model and **b** variation of the Ga composition [x = Ga/(In + Ga)] within the CIGSe layer in the CIGSe solar cell [16]. The optical model was constructed for the CIGSe solar cell shown in Fig. 2.3a. The Ga profile determined from SIMS shown in **b** was obtained from the same solar cell. The solid lines in **b** show the x values calculated from an asymmetric double-Gaussian model indicated in the inset. In the actual EQE analysis, the x values have been reduced slightly (Δx = 8 at.%) to obtain better matching with the experimental EQE spectrum

measured by secondary ion mass spectroscopy (SIMS), while the black line indicates the result obtained from fitting assuming an asymmetric double-Gaussian profile:

$$x(d) = \begin{cases} x_1 - (x_1 - x_v)\exp\left[-\{(d-d_v)/\omega_1\}^2\right] & (d \le d_v) \\ x_2 - (x_2 - x_v)\exp\left[-\{(d-d_v)/\omega_2\}^2\right] & (d > d_v) \end{cases} \tag{2.32}$$

where $x_{1,2}$ and $\omega_{1,2}$ are the Ga compositions and the broadening parameters as indicated in the inset. In addition, x_v and d_v denote x and d at the valley position in the V-shaped Ga profile, respectively. In the EQE analysis, however, the x values have been reduced slightly with a constant value of $\Delta x = 8$ at.% [i.e., $x_{EQE}(d) = x(d) - \Delta x$], so that the E_g position observed in the experimental EQE can be reproduced. The profile parameters for $x_{EQE}(d)$ are $x_1 = x_2 = 0.38$, $x_v = 0.18$, $d_v = 540$ nm, $\omega_1 = 308$ nm, and $\omega_2 = 527$ nm. On the other hand, the Cu composition in the CIGSe layer shows a constant value of 0.91.

In the actual EQE calculation, x of the CIGSe sublayer at d is calculated first by applying (2.32), from which the optical constants of the CIGSe sublayer is determined using the CIGSe optical database. By repeating this process, the optical constants of all the CIGSe sublayers are extracted. Finally, based on the ERS method, A_j of all the component layers are deduced using the optical model of Fig. 2.8a.

Figure 2.9 shows the experimental EQE spectrum (EQE_{ex}) of the CIGSe solar cell, together with the EQE spectra calculated from the conventional optical admittance and ERS methods [16]. The open circles denote EQE_{ex} and the corresponding R_{ERS} is also indicated. It can be seen that R_{flat} calculated from (2.18) is essentially similar to R_{ERS}, but the absolute values of R_{flat} are larger than those of R_{ERS}. From the comparison of these spectra, we notice the important fact that light scattering by the submicron texture suppresses the front light reflection particularly by eliminating the interference fringes [16].

In Fig. 2.9, the EQE spectrum denoted as EQE_{flat} indicates the result calculated from the optical admittance method using R_{flat}. In this analysis, the absorptance spectrum of CIGSe (A_{CIGSe}) is obtained by the summation of all the absorptance spectra of the CIGSe sublayers, and EQE_{flat} can then be deduced assuming 100% carrier collection (i.e., $EQE_{flat} = A_{CIGSe}$). Although EQE_{flat} agrees rather well with EQE_{ex}, EQE_{flat} deviates from EQE_{ex} in the range of $\lambda = 800$–1100 nm due to the interference oscillation generated by the assumed flat structure. Accordingly, if we use R_{ERS} instead of R_{flat} to remove the effect of the optical interference, a better fitting is expected to be obtained. In this case, the reflectance difference $\Delta R = R_{flat} - R_{ERS}$ is absorbed additionally within the CIGSe solar cell, and this extra light absorption is distributed among the component layers assuming a flat structure.

The EQE_{ERS} in Fig. 2.9 shows the calculation result obtained by applying R_{ERS} to (2.26). From this procedure, the interference effect is suppressed almost completely and EQE_{ERS} shows excellent agreement with EQE_{ex} in the wide spectral region. The good agreement between EQE_{ERS} and EQE_{ex} indicates that the carrier

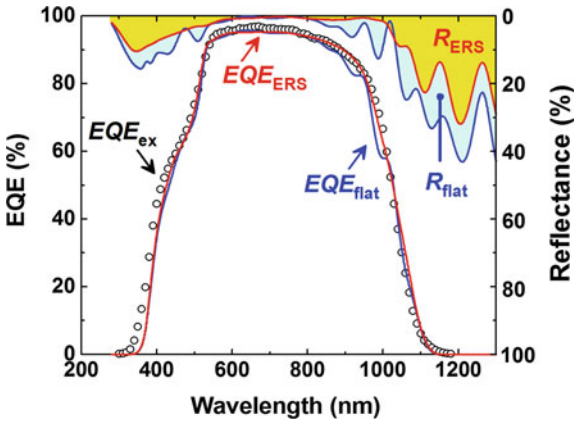


Fig. 2.9 Experimental EQE spectrum (EQE_{ex}) of the CIGSe solar cell (open circles), together with the calculated EQE results (solid lines) obtained from the optical admittance calculation assuming a flat structure (EQE_{flat}) and the ERS method (EQE_{ERS}) [16]. In this figure, the experimental reflectance spectra (R_{ERS}) and the reflectance obtained from the flat optical model (R_{flat}) are also shown. In the EQE analysis, 100% carrier collection is assumed

collection efficiency in the CIGSe light absorber is almost 100% with little carrier recombination loss. This result further confirms that the carrier recombination at grain boundaries is negligible in the polycrystalline CIGSe layer. From the EQE spectra, J_{sc} can be calculated using (2.27). The J_{sc} value obtained from EQE_{ERS} (34.0 mA/cm^2) agrees quite well with 34.2 mA/cm^2 obtained from EQE_{ex} and shows a higher value, compared with 33.4 mA/cm^2 deduced from EQE_{flat}.

When the above ERS method is used, however, R_{ERS} is always necessary, which restricts the use of this method. However, it has been found that R_{ERS} can be approximated rather easily by forcing the anti-reflection condition in the calculation of R_{flat} (ARC method) [16]. Figure 2.10 shows the EQE analysis result obtained using the ARC method [16]. In this calculation scheme, R_{ERS} is approximated by linearly connecting the minimum R positions of the inference pattern that appears in R_{flat}, as indicated by the red circles and line in Fig. 2.10. In a multilayer system, the minimum reflectance (R_{min}) position in the interference pattern represents the anti-reflection condition, in which the multiply reflected beams generated within the layered structure are out of phase, as schematically shown in the inset. In contrast, R_{flat} shows the maximum reflectance (R_{max}) when the multiple beams are in phase. As mentioned above, the optical effect of the submicron rough texture is mainly the removal of the interference fringes. In the ARC method, therefore, the anti-reflection condition is superimposed on the result of R_{flat} to reproduce the interference elimination effect by textured structures.

The minimum positions of R_{flat} can be determined by selecting λ positions where the condition $dR_{flat}(\lambda)/d\lambda = 0$ is satisfied. When the reflectance spectrum obtained from the above procedure (R_{ARC}) is employed in the calculation of (2.26), the EQE

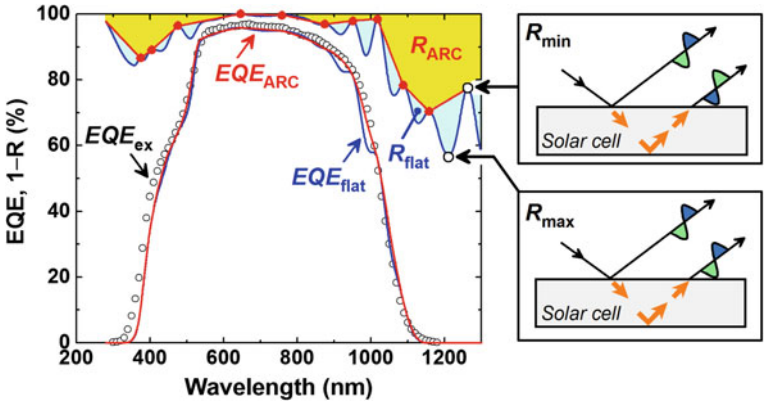


Fig. 2.10 EQE analysis result obtained from the ARC method [16]. The R_{ARC} shows the reflectance spectrum deduced by the linear approximation under the anti-reflection condition. The EQE spectrum calculated by applying R_{ARC} is indicated as EQE_{ARC}. The EQE_{ex}, EQE_{flat} and R_{flat} shown in this figure are identical to those shown in Fig. 2.9. The light reflection and transmission at the minimum reflectance (R_{min}) and maximum reflectance (R_{max}) positions are also indicated in the insets. When the multiply reflected beams are out of phase (R_{min}), the anti-reflection condition is satisfied

spectrum (EQE_{ARC}) shows excellent agreement with EQE_{ex} (Fig. 2.10). This approach simplifies the EQE analysis greatly and allows the EQE simulation of arbitrary device structures even without considering geometric textured structures. In the calculation of R_{ARC}, however, a slight ambiguity remains for the selection of the R_{min} points. This difficulty occurs particularly in the region where the interference effect is weak and the condition $dR_{Flat}(\lambda)/d\lambda = 0$ is not satisfied, although the R_{min} positions can also be selected manually to avoid this problem. In addition, for some solar cells with smaller textures, rather strong interference patterns could be generated. In such cases, the R spectra can be simulated to some extent by mixing R_{flat} and R_{ARC}.

Figure 2.11 shows (a) the absorptance spectra of the solar-cell component layers obtained from the EQE analysis using the ERS method and (b) the optical gain and loss in the CIGSe solar cell [16]. The absorptance spectrum of the CIGSe layer is identical to EQE_{ERS} in Fig. 2.9. The non-dope ZnO and $MoSe_2$ layers indicate negligible light absorption due to the small layer thicknesses. The large light absorption in the ZnO:Al layer at $\lambda < 445$ nm is caused by the interband transition, whereas the continuous light absorption in the visible/infrared regime shows the contribution of the free carrier absorption. Thus, the free carrier absorption in the TCO layer suppresses the overall EQE, and the maximum EQE at $\lambda = 800$ nm is determined preliminarily by the free carrier absorption. In the EQE analyses of Figs. 2.9 and 2.10, the free carrier absorption in the ZnO:Al layer was adjusted slightly [16] by changing A_D of the Drude model (Sect. 18.2.2 in Vol. 1).

At $\lambda = 320$–500 nm in Figs. 2.9 and 2.10, on the other hand, EQE_{ERS} and EQE_{ARC} exhibit slightly lower values, compared with EQE_{ex}. As known well,

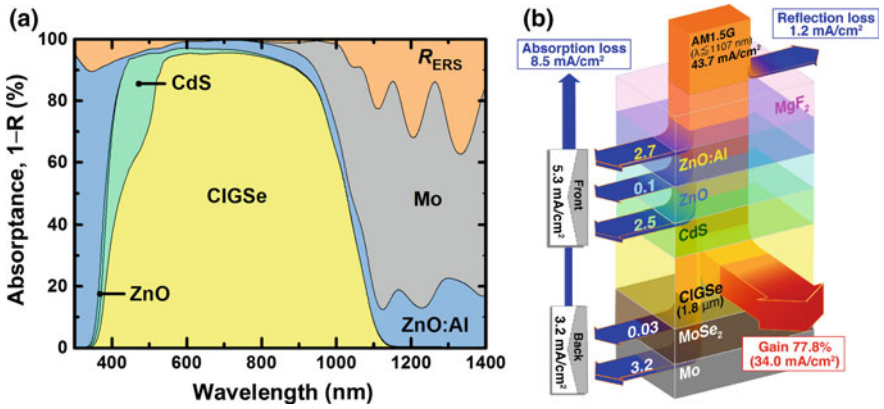


Fig. 2.11 **a** Absorptance spectra of the solar-cell component layers in the CIGSe solar cell, obtained from the EQE analysis using the ERS method and **b** optical gain and loss in the CIGSe solar cell [16]. The numerical values indicated in **b** show the corresponding current densities in units of mA/cm^2

the effective E_g of doped TCO layers increases with increasing the carrier concentration due to the Burstein-Moss shift (Sect. 18.2.1 in Vol. 1). However, this effect was not modeled properly in the above EQE analyses and the calculate EQE spectra deviate from EQE_{ex} in the short λ region. The Burstein-Moss effect can be simulated rather easily by simply shifting the onset of the interband transition toward higher energy.

In Fig. 2.11b, the optical gain and loss in the CIGSe solar cell are summarized. These values were estimated from the absorptance spectra of Fig. 2.11a using (2.27). Since E_g of the CIGSe with $x_v = 0.18$ (see Fig. 2.8) is 1.12 eV, the maximum J_{sc} value attainable under the AM1.5G condition is 43.7 mA/cm^2 (see Fig. 1.4a), from which the optical gain of the CIGSe solar cell is estimated to be 77.8% (34.0 mA/cm^2). The reflection loss calculated from R_{ERS} is rather small (1.2 mA/cm^2), whereas the total absorption loss is quite large (8.5 mA/cm^2). It can be understood from Fig. 2.11b that major parasitic light absorption occurs in the ZnO:Al, CdS, and Mo layers with optical losses of ~3 mA/cm^2 in each layer. For the ZnO:Al, the absorption loss due to the free carrier absorption (1.7 mA/cm^2) is larger than that caused by the interband transition (1.0 mA/cm^2). Although the CdS layer is quite thin (~50 nm), the J_{sc} loss attributed to this layer is quite large because of very high α of CdS (see Fig. 8.21). The result of Fig. 2.11 reveals that rather strong light absorption occurs in the metallic Mo layer. This originates from very low reflectance of R ~30% at the CIGSe/Mo interface (Fig. 12.4) and the EQE in the longer λ region is essentially limited by the parasitic light absorption in the Mo layer [16]. Thus, the result of Fig. 2.11 demonstrates that the performance-limiting factors in solar cells can be determined quite effectively based on EQE analyses.

From the EQE analysis, the operating principle of the CIGSe solar cell can further be discussed. Figure 2.12 shows (a) the cross-sectional TEM image,

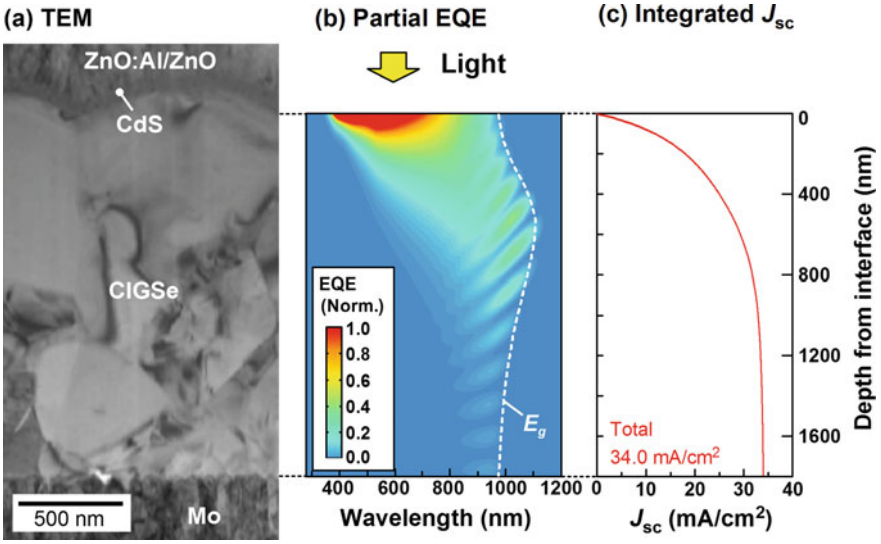


Fig. 2.12 **a** Cross-sectional TEM image, **b** normalized partial EQE calculated for different depths from the CdS/CIGSe interface and wavelengths, and **c** integrated J_{sc} for the depth [16]. In **b**, the dotted line represents E_g at each depth

(b) normalized partial EQE calculated for different depths from the CdS/CIGSe interface (i.e., d in Fig. 2.8b) and wavelengths and (c) the integrated J_{sc} for the depth [16]. If the partial EQE spectra obtained at different d positions are integrated, the absorptance spectrum shown in Fig. 2.11a is obtained. The partial EQE shown in Fig. 1.13 corresponds to that of Fig. 2.12b. It can be seen that the partial EQE is quite high at $d \sim 0$ μm and exhibits a rapid decay versus d due to the strong light absorption in the CIGSe layer. This result shows clearly that the photocarriers are generated predominantly near the CdS/CIGSe interface. The oscillation pattern of the partial EQE, observed in the region of $d > 0.4$ μm, shows the interference effect induced by the thin film structure. The dotted line represents E_g of the CIGSe at each depth determined from $x_{EQE}(d)$. In particular, at $d_v = 0.54$ μm, E_g shows the lowest value of 1.12 eV ($x_v = 0.18$) and the upper limit for the light absorption extends into the longer λ region.

In Fig. 2.12c, the partial absorptance of the CIGSe layer is integrated toward the depth to deduce the contribution of the absorptance at each depth for J_{sc}. The light absorption in the CIGSe layer occurs predominantly at $d < 600$ nm and J_{sc} increases rapidly in this thickness region. In contrast, the increase in J_{sc} is almost negligible in the CIGSe bottom region. If the CIGSe layer is divided into the two sublayers with an equal thickness of 900 nm, J_{sc} generated in the top sublayer accounts for 95% of the total J_{sc}. Based on this result, it has been concluded that the 1-μm-thick CIGSe bottom layer with the Ga-grading profile plays a dominant role as the back-surface field (BSF) layer in CIGSe solar cells [16].

As confirmed from the above analysis example, the ARC and ERS methods are quite simple but provide excellent fitting to the experimental EQE spectrum. From this method, the carrier generation within the absorber layer and the J_{sc} losses due to parasitic light absorption can be assessed quantitatively. Since the calculation cost of the ARC and ERS methods is quite low, these EQE analyses can be made using conventional computers on a routine basis.

2.3 e-ARC Method

In the above EQE analyses, the influence of the carrier recombination has been neglected. However, the photocurrent reduction by carrier recombination can be modeled quite simply by considering a carrier collection length in the absorber layer. By incorporating the effect of the carrier recombination within the framework of the ARC method, a global EQE analysis scheme has been developed [18]. From this extended ARC method (e-ARC method), optical and recombination losses in various thin-film solar cells can be estimated rather easily. In this section, the basic concept of the e-ARC method is explained.

2.3.1 Recombination Model

In solar cells, different types of recombinations occur within the semiconductor bulk layer and at the front/rear interfaces (see also Fig. 1.2). Figure 2.13 shows the carrier recombination processes in a p-n junction solar cell. In this figure, only the movement of the photogenerated electrons is shown. In this solar cell, the photocarriers created within a distance of L_C from the n/p junction interface are collected, while the carriers generated in the solar cell bottom region are lost due to the recombination at defects formed in the bulk layer or at the p layer/metal interface. In this recombination model, L_C defines the carrier collection length and all the carriers generated within L_C from the front interface are assumed to contribute to the current generation (i.e., EQE). This can be described quite simply by

$$H(\lambda) = 1 - \exp[-\alpha(\lambda)L_C], \tag{2.33}$$

where H and α show the carrier collection efficiency and the absorption coefficient of the absorber (semiconductor) layer. This model is equivalent to the light absorption expressed by the well-known Beer's law, $A(\lambda) = 1 - \exp[-\alpha(\lambda)d]$, where d is a distance from the surface or interface (see Fig. 1.11). Thus, $H(\lambda)$ represents the light absorption at the depth L_C from the surface (or interface) of materials having infinite thickness. In the model of (2.33), therefore, the optical confinement effect, induced by the back-side reflection and the resulting multiple light reflections

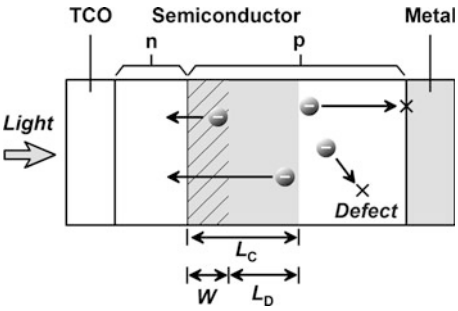


Fig. 2.13 Carrier recombination processes in a p-n junction solar cell. In this figure, only the photogenerated electrons are shown. The L_C represents the carrier collection length defined by (2.33) and, in the model, the carriers generated deeper than L_C are assumed to recombine. The L_C is further expressed as $L_C = W + L_D$ (2.34), where W and L_D are the depletion layer thickness and carrier diffusion length, respectively

within the absorber layer, has been neglected. By applying (2.33) directly to IQE spectra, simple optical simulations have also been performed [40, 41].

In the above model, the influences of the carrier diffusion and carrier drift in the space-charge region are not described separately. Moreover, the effects of the band offset and the carrier recombinations that occur in the bulk, interface and grain-boundary regions are not specifically modeled. The significance of the $H(\lambda)$ model is that all the complex effects concerning the carrier collection are represented by a single analysis parameter of L_C. As shown in Fig. 2.13, the relationship of L_C with a diffusion length (L_D) can be described by

$$L_C = W + L_D, \tag{2.34}$$

where W indicates the depletion layer thickness [40].

For $H(\lambda)$, a more exact equation has been derived by solving the carrier continuity equation [2, 3]:

$$H(\lambda) = 1 - \exp[-\alpha(\lambda)W]/[1 + \alpha(\lambda)L_D]. \tag{2.35}$$

In this model, the carrier collection is described by the two parameters (W, L_D). When the above model is applied to EQE fitting analysis, however, W and L_D show a strong correlation and it is rather difficult to obtain the unique solution [18]. In reported studies [21, 42], therefore, W has been determined from separate experiments using a capacitance-voltage technique.

Figure 2.14 explains the calculation procedure of the e-ARC method. In this calculation example, the EQE spectrum of a CZTSe solar cell is simulated assuming an optical model of ZnO:Al (350 nm)/ZnO (50 nm)/CdS (50 nm)/CZTSe (1500 nm)/Mo. The optical constants of the CZTSe were calculated assuming $E_g = 1.07$ eV based on a procedure described in Sect. 2.3.2. In the first step of the e-ARC simulation, the absorptance spectrum of the light absorber is calculated

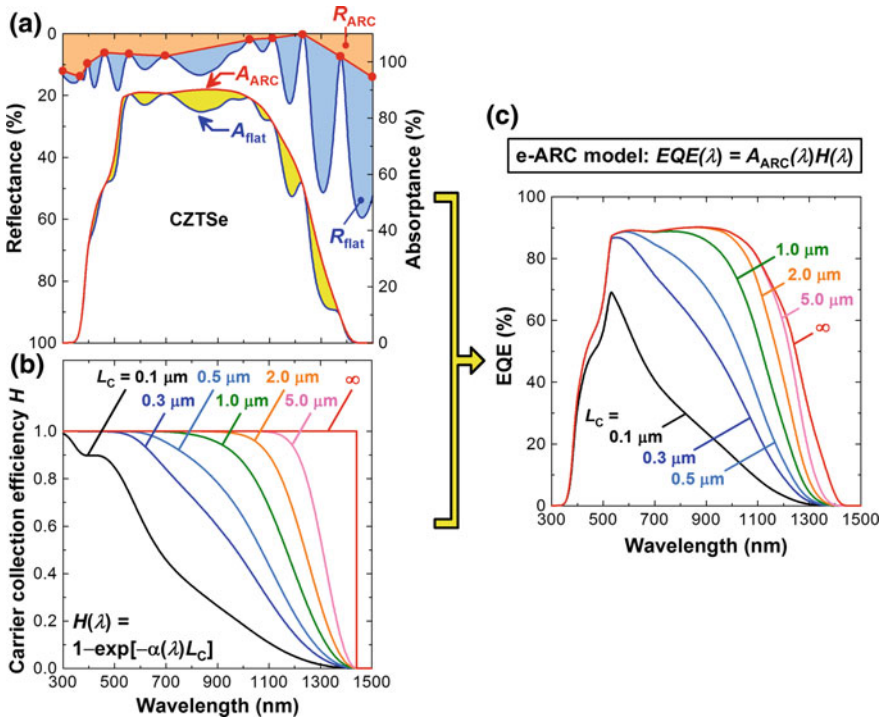


Fig. 2.14 Calculation procedure of the e-ARC method: **a** Reflectance spectra calculated assuming a flat structure (R_{flat}) and an anti-reflection condition (R_{ARC}), together with the absorptance spectra of the CZTSe layer, A_{flat} and A_{ARC}, obtained from R_{flat} and R_{ARC}, respectively, **b** carrier collection efficiency $H(\lambda)$ calculated from $\alpha(\lambda)$ of the CZTSe using different values of the carrier collection length (L_C), and **c** EQE spectra of the CZTSe solar cell calculated from the results of **a** and **b**. The EQE simulations were performed using an optical model of ZnO:Al (350 nm)/ZnO (50 nm)/CdS (50 nm)/CZTSe (1500 nm)/Mo. In **a**, the red circles correspond to the R_{min} positions indicated in Fig. 2.10

using the ARC method. In Fig. 2.14a, the obtained spectrum is shown as A_{ARC}, together with R_{ARC} as well as R_{flat} and A_{flat} determined from the optical admittance method. The calculation procedures of R_{ARC} and A_{ARC} are exactly the same as those shown in Fig. 2.10. It can be seen that the interference fringe is relatively large in the CZTSe solar cell and A_{ARC} is quite different from A_{flat}. In other words, the texture effect is rather significant in the CZTSe solar cell and the yellow-colored region indicated in Fig. 2.14a is absorbed additionally by applying the anti-reflection condition.

In the second step, $H(\lambda)$ is calculated from (2.33) by selecting L_C. In Fig. 2.14b, several $H(\lambda)$ values calculated from $\alpha(\lambda)$ of the CZTSe using different L_C values are shown. When L_C is infinite ($L_C = \infty$), we obtain $H(\lambda) = 1$ in the energy region above the absorption edge of the CZTSe ($\lambda \leq 1441$ nm in Fig. 2.14b). As L_C decreases, H in the longer λ region gradually decreases. In the calculation of $H(\lambda)$

using (2.33), however, it is necessary to use unrealistic L_C values that are far larger than the total thickness of the absorber layer (1.5 μm in Fig. 2.14). Thus, L_C defined by (2.33) should be considered as a parameter (reference) value. Nevertheless, when L_C is smaller than the absorber layer thickness, L_C approximates a real physical value.

In the e-ARC method, from $A_{ARC}(\lambda)$ and $H(\lambda)$, the EQE spectrum is calculated simply by

$$\mathrm{EQE}(\lambda) = A_{ARC}(\lambda)H(\lambda). \tag{2.36}$$

In Fig. 2.14c, the EQE spectra calculated from the e-ARC method using A_{ARC} in Fig. 2.14a and $H(\lambda)$ in Fig. 2.14b are shown. In the case of $L_C = \infty$ [i.e., $H(\lambda) = 1$], we obtain $\mathrm{EQE}(\lambda) = A_{ARC}(\lambda)$ (i.e., the ARC method in Fig. 2.10). When the EQE spectrum is calculated from the e-ARC method, the EQE response in the longer λ region decreases as L_C decreases due to the limited carrier extraction and L_C is deduced from the fitting analysis of the EQE spectrum. Based on the EQE calculation result, the J_{sc} loss due to the carrier recombination is estimated by

$$J_{loss} = \frac{q\lambda}{hc}\int [A_{ARC}(\lambda) - \mathrm{EQE}(\lambda)]F(\lambda)d\lambda. \tag{2.37}$$

In the e-ARC method, therefore, the recombination loss is calculated quantitatively using L_C as a sole parameter. It should be noted that, when the absorber layer thickness itself is modified, the optical interference and back-side reflection in solar cells change significantly [17]. Thus, it is necessary to model the carrier generation and collection separately. The above analysis scheme can also be applied for the ERS method. In this case, we employ $\mathrm{EQE}(\lambda) = A_{ERS}(\lambda)H(\lambda)$, which will be referred to as the e-ERS method.

In the e-ARC and e-ERS methods, the carrier recombination in the solar cell bottom region is assumed. In some solar cells, however, the carriers recombine predominantly near the front interface (i.e., n/p interface in Fig. 2.13). In this case, the carrier recombination can be modeled by simply dividing an absorber layer into two sublayers and treating a top sublayer near the front interface as a "dead layer" that allows no carrier extraction, as applied for the EQE analyses of hybrid perovskite solar cells (see Fig. 16.17 in Vol. 1).

2.3.2 *Analysis of a CZTSe Solar Cell*

The submicron-textured CZTSe solar cell shown in Fig. 2.3b has been analyzed by applying the e-ARC method [18]. Figure 2.15 shows (a) the EQE analysis result of the CZTSe solar cell and (b) the optical gain and loss obtained from the analysis [18]. The EQE analysis was carried out using an optical model consisting of ZnO: Al (350 nm)/ZnO (50 nm)/CdS (70 nm)/CZTSe (1260 nm)/$MoSe_2$ (150 nm)/Mo.

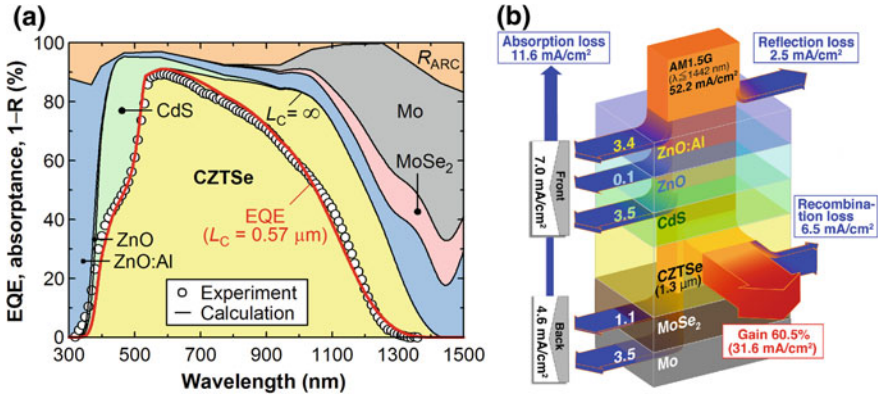


Fig. 2.15 **a** EQE analysis of the CZTSe solar cell performed by using the e-ARC method and **b** optical gain and loss obtained from the analysis [18]. The EQE analysis was carried out for the CZTSe solar cell shown in Fig. 2.3b using the optical model of ZnO:Al (350 nm)/ZnO(50 nm)/CdS (70 nm)/CZTSe (1260 nm)/$MoSe_2$ (150 nm)/Mo. In **a**, the open circles show the experimental spectrum and the red line represents the EQE spectrum calculated from the e-ARC method assuming L_C = 0.57 μm. The spectrum indicated by the yellow-colored region corresponds to the absorptance spectrum ($L_C = \infty$) of the CZTSe layer. In **b**, the numerical values show the corresponding current densities in units of mA/cm^2

The thicknesses of these layers were determined from the TEM observation. The optical effect of the void-rich CZTSe structure observed in Fig. 2.3b was also taken into account by using two sublayers for the CZTSe. In particular, for the CZTSe bottom sublayer with a thickness of 310 nm, a void volume fraction of 30 vol.% was assumed. The optical properties of this bottom sublayer were calculated by the Bruggeman effective-medium approximation [36]. For the CZTSe layer, the reported optical constants (Fig. 8.30) were used, and the change of E_g with the Cu/(Zn + Sn) ratio was further considered. This E_g shift in the CZTSe was modeled by sliding the whole spectrum toward higher energy. In this case, the ε_2 amplitude was reduced slightly so that the sum rule described by (16.1) in Vol. 1 was satisfied [18]. As a result, the EQE fitting analysis of Fig. 2.15a was implemented using two analytical parameters: i.e., L_C and E_g of the CZTSe.

In Fig. 2.15a, the open circles show the experimental EQE spectrum, whereas the black lines represent the R_{ARC} and absorptance spectra. The EQE spectrum obtained from the e-ARC fitting analysis is indicated by the red line. As confirmed from this figure, the calculated spectrum shows excellent agreement when L_C = 0.57 μm and E_g = 1.07 eV. It can be seen that, compared with A_{ARC} of the CZTSe layer ($L_C = \infty$), the experimental EQE spectrum shows quite low values particularly in the long λ region. This result indicates the significant carrier loss within the CZTSe layer. In particular, the estimated L_C value of ~0.6 μm is much smaller than the total thickness of the CZTSe absorber layer (~1.3 μm), confirming quite poor carrier collection in the solar cell bottom region.

The optical losses of the CZTSe solar cell shown in Fig. 2.15b are rather similar to those of the CIGSe solar cell in Fig. 2.11b. However, the CZTSe solar cell shows a large recombination loss of 6.5 mA/cm^2 and the resulting optical gain becomes smaller (60.5%). The result of Fig. 2.15 indicates that, based on the EQE analysis using the e-ARC method, all the reflection, absorption and recombination losses can be determined quantitatively even when solar cells have quite complex submicron textures represented by Fig. 2.3b.

Figure 2.16 summarizes the results of the EQE fitting analyses performed for the CZTSe solar cell using different optical models. The experimental data (gray open circles) correspond to those shown in Fig. 2.15a and the result of Model1 indicates that obtained from the e-ARC analysis (L_C = 0.57 μm). In Model2, the CZTSe layer is divided into active and dead layers, and the EQE fitting was implemented by adjusting the active layer thickness (d_A). In Model3, the thickness of the CZTSe layer in the optical model was changed. As shown in Fig. 2.16, all the models provide similar fittings but Model1 provides the best matching particularly in the longer λ region ($1100 < \lambda < 1300$ nm). On the other hand, d_A obtained from Model2 (0.56 μm) is almost the same as $L_C = 0.57$ μm. In other words, L_C obtained from the EQE fitting analysis is basically equivalent to the thickness of the absorber layer where the carrier extraction occurs predominantly. When the total absorber thickness is changed in the optical model (Model3), the influence of the back-side reflection becomes stronger and the effective thickness obtained from the analysis (d = 0.45 μm) becomes smaller, compared with L_C and d_A.

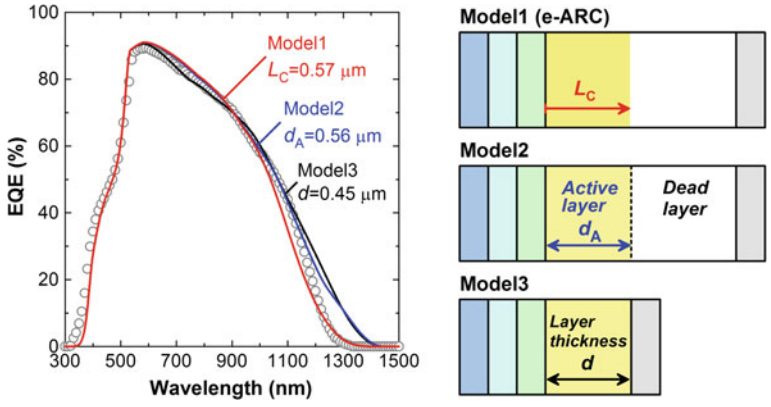


Fig. 2.16 Results of EQE fitting analyses performed for the CZTSe solar cell using different optical models: i.e., Model1: e-ARC method, Model2: two sublayer model with the bottom layer being the optical dead layer, Model3: optical model with a thinner CZTSe layer. The experimental spectrum (gray open circles) and the result of Model1 are identical to those of Fig. 2.15a

2.3.3 *Interpretation of EQE Spectra*

To understand the effects of the carrier recombinations at the front and rear interfaces of a light absorber, the partial absorptance of the above CZTSe solar cell was calculated by dividing the CZTSe layer into 1-nm-thick sublayers. Figure 2.17a shows the α spectrum of the CZTSe layer and the corresponding penetration depth of light calculated by $d_p = 1/\alpha$ (see Fig. 1.11). As confirmed from this figure, d_p is small (<200 nm) in the high α region ($\lambda < 700$ nm), but d_p increases drastically in the longer λ region. Figure 2.17b shows the normalized partial absorptance of the CZTSe layer. The partial absorptance corresponds to the absorptance spectrum of $L_C = \infty$ in Fig. 2.15a. In Fig. 2.17b, the white line represents the position of $2d_p$

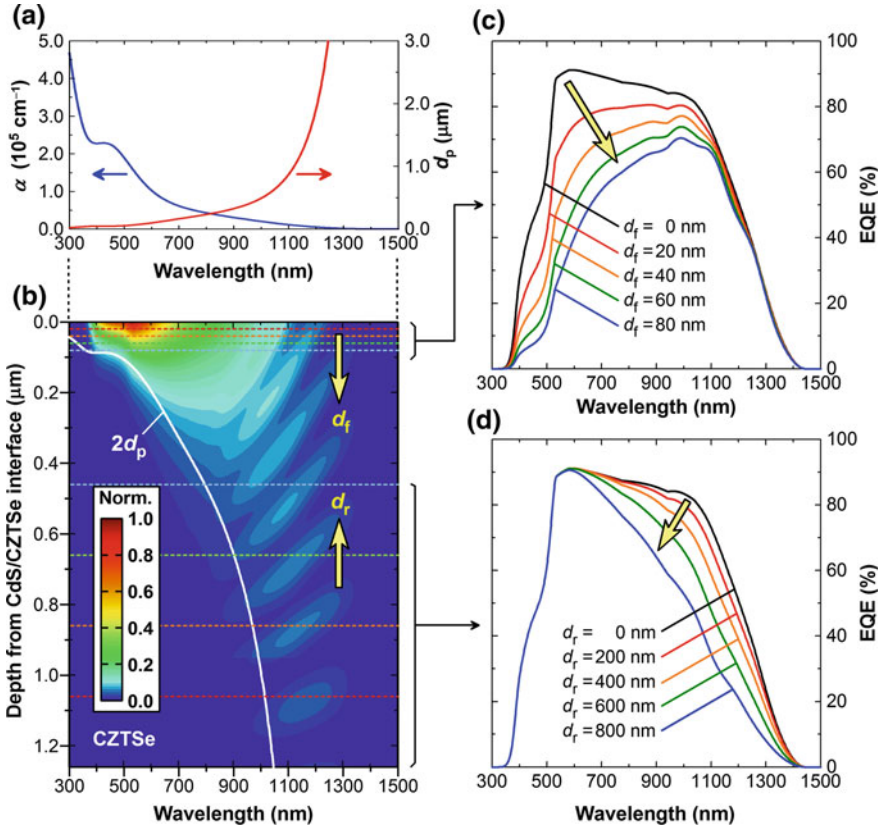


Fig. 2.17 **a** α spectrum of the CZTSe layer and the resulting penetration depth of light ($d_p = 1/\alpha$), **b** normalized partial absorptance of the CZTSe layer obtained at different depths from the CdS/CZTSe interface and wavelengths, and EQE spectra calculated with the variation of **c** the front dead-layer thickness (d_f) from 0 to 80 nm and **d** the rear dead-layer thickness (d_r) from 0 to 800 nm. In **b**, the position of $2d_p$ calculated from the result of **a** is shown, and the positions of d_f and d_r used for the calculations of **c** and **d** are also indicated

obtained from Fig. 2.17a. From the result of $2d_p$, it can be seen that the variation of the partial absorptance is determined simply by the α values. In particular, a rapid decay of the partial absorptance at $\lambda < 700$ nm is caused by the strong light absorption in the CZTSe layer, whereas the light absorption and the resulting carrier generation occur rather uniformly throughout the entire CZTSe layer in the region of $\lambda > 900$ nm due to the lower α values.

To visualize the influence of the carrier recombination, we assume a front (rear) dead layer with a thickness of d_f (d_r). The thicknesses of these dead layers used for the calculations are indicated by the dotted lines in Fig. 2.17b. By assuming no carrier extraction from these layers, the EQE spectra can be calculated. Figure 2.17c shows the EQE spectra obtained when d_f is increased from 0 to 80 nm. Since the light is absorbed strongly near the CdS/CZTSe interface, the slight increase in d_f leads to the significant reduction in the short λ response, whereas the EQE in the longer λ region shows the minor reduction as the carriers are generated uniformly in this region. In contrast, when d_r is increased in a range of 0–800 nm (Fig. 2.17d), only the longer λ response decreases, since almost no carriers are generated at the corresponding depth at $\lambda < 700$ nm. It should be emphasized that, at $\lambda \geq 900$ nm, the holes and electrons generated near the front and rear interfaces, respectively, need to travel the whole layer to generate the current in the device. Accordingly, short L_C lowers the partial EQE particularly in the longer λ region.

It is evident from the above results that the effect of the front carrier recombination appears as the EQE reduction in the short λ region, whereas the carrier recombination in the rear interface region reduces the EQE in the longer λ region. Accordingly, from the comparison with the A spectrum of the absorber layer (i.e., A_{ARC}), the carrier recombination region can be speculated rather easily. In the e-ARC analysis, the effect of d_r is expressed by L_C (see Fig. 2.16), whereas d_f is modeled directly using a sublayer. However, depending on devices, the validity of the recombination model needs to be confirmed. If the thickness of the absorber layer can be changed, several solar cells can be analyzed to confirm the consistency.

2.4 EQE Analysis Examples

The e-ARC and e-ERS methods have been applied successfully to the EQE analyses of numerous solar cells based on CZTSe, CZTS, CZTSSe, CdTe, and hybrid perovskite solar cells [18]. In this section, the EQE analyses of CZTSe, CZTS and CdTe solar cells are introduced briefly. This section further establishes the EQE analysis method for an a-Si:H p-i-n solar cell.

2.4.1 CZTSe and CZTS Solar Cells

The EQE spectra of various CZTSe and CZTS solar cells can be analyzed using the same analysis procedure described above. Figure 2.18 shows the results of the EQE fitting analyses performed for reported solar cells of (a) CZTSe [21–25] and (b) CZTS [43–47]. The open circles show the experimental EQE spectra of the reported solar cells, fabricated by coevaporation processes [21, 24, 25, 43], a solution-based processing using hydrazine [22], a selenization process [23] and sulfurization processes [44–47], whereas the solid lines indicate the fitting results obtained using the e-ARC method. For the EQE analysis of [21], however, the ERS method was applied as R_{ERS} was reported for this solar cell. To perform the above EQE analyses, the thicknesses of the solar-cell component layers were extracted from the descriptions and the SEM images of each reference. In the analyses, the TCO optical properties and the CdS thickness were adjusted slightly. Although there is slight uncertainty for the TCO optical constants in the EQE analyses for reported spectra, the TCO optical properties can still be deduced from the EQE response in the visible region (λ ~600 nm) and the analysis of L_C can be performed. In the CZTS solar cell analyses, the reported optical constants of CZTS (Fig. 8.29) were used and the variation of E_g with the Cu/(Zn + Sn) ratio was also taken into account [18]. As a result, the EQE fitting analyses of Fig. 2.18 were carried out using L_C and E_g as fitting parameters.

It can be seen that all the calculated results show excellent agreement with the experimental spectra, independent of the detailed solar cell structure and processing method. Accordingly, if the layer thicknesses are known, the quantitative EQE

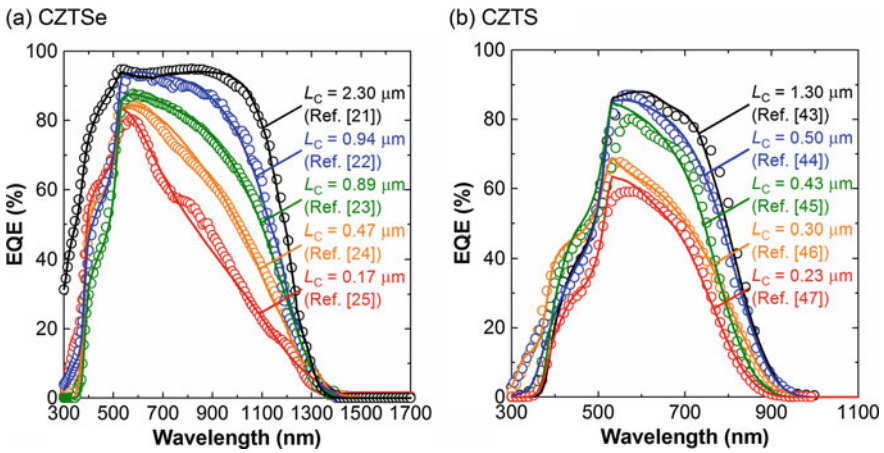


Fig. 2.18 Experimental EQE spectra of **a** CZTSe solar cells reported in [21–25] and **b** CZTS solar cells reported in [43–47] (open circles), together with the results of the EQE fitting analyses performed for these solar cells using the e-ARC and e-ERS methods (solid lines) [18]. The L_C values obtained from the EQE analyses are also shown

analysis can be performed rather easily from the e-ARC and e-ERS methods using the optical database summarized in Part II of this book. The EQE analyses of Fig. 2.18 result in the L_C values of 0.17–2.30 μm for the CZTSe solar cells and 0.23–1.30 μm for the CZTS solar cells with the E_g values in ranges of 0.98–1.07 eV (CZTSe) and 1.44–1.50 eV (CZTS). The EQE spectrum of [21] in Fig. 2.18a is obtained from a record-efficiency CZTSe solar cell with a conversion efficiency of 11.6% (J_{sc} = 40.6 mA/cm^2, V_{oc} = 423 mV, FF = 0.673). This solar cell has a very uniform thin film structure with large CZTSe grains and shows the highest L_C value of 2.3 μm. In Fig. 2.18, with decreasing L_C, the EQE response in the longer λ region decreases systematically in both CZTSe and CZTS solar cells, indicating that J_{sc} of these solar cells is limited by the carrier recombination that occurs in the solar-cell bottom region. For the CZTSe solar cells, J_{sc} increases largely from 27.0 mA/cm^2 [25] to 40.6 mA/cm^2 [21] with L_C. The L_C values extracted from the CZTS solar cells are smaller than those of the CZTSe solar cells. Moreover, in the EQE spectra of [45, 47] at λ = 500–600 nm, the experimental EQE values are slightly lower, compared with the calculated EQE values, suggesting that the carrier recombination occurs slightly near the CdS/CZTS front interface.

Other EQE spectra reported for CZTSe [48–51], CZTS [52–55] and CZTSSe [56–64] solar cells have also been characterized by the e-ARC method. To analyze the CZTSSe solar cells, a CZTSSe optical database has been developed [18], from which the $Cu_2ZnSn(S_xSe_{1-x})_4$ optical constants for the arbitrary S composition x can be extracted using the energy shift model (Sect. 10.4.1 in Vol. 1). The results calculated for selected compositions (x = 0.2, 0.4, 0.6 and 0.8) can be found in Fig. 8.31. In the EQE analyses of the CZTSSe solar cells, excellent fittings, similar to those in Fig. 2.18, have also been confirmed [18].

Figure 2.19 summarizes (a) J_{sc}, (b) V_{oc}, (c) FF and (d) efficiency of the analyzed CZTSe [21–25, 48–51], CZTS [43–47, 52–55] and CZTSSe [56–64] solar cells as a function of L_C extracted from the EQE analyses [18]. The result for J_{sc} (Fig. 2.19a) indicates clearly that the overall L_C values of the CZTS solar cells are smaller than those of the CZTSe and CZTSSe solar cells. The solid lines indicate the simulation results obtained assuming E_g of 1.04 eV (CZTSe), 1.08 eV (CZTSSe) and 1.46 eV (CZTS). These calculations were performed using the structure of ZnO:Al (350 nm)/ZnO (50 nm)/CdS (70 nm)/Absorber (CZTSe, CZTS or CZTSSe: 2.0 μm)/$MoSe_2$ (150 nm)/Mo. In Fig. 2.19a, J_{sc} increases as E_g of the absorber material decreases. The simulated J_{sc} reproduces the experimental result quite well, although the experimental data are scattered slightly due to the difference in the device structure and the material optical properties. For the variation of V_{oc} with L_C, CZTS shows the larger increase, compared with the CZTSe and CZTSSe. In particular, V_{oc} of the CZTSe is rather independent of L_C in the wide range.

From the above results, the carrier recombination mechanism can be discussed further. Figure 2.20 shows the schematic band diagram proposed for the CZTSe solar cells [18]. In this figure, the band diagram near the $MoSe_2$ is not shown, as the band diagram at the rear interface remains controversial [65, 66]. For CZTSe solar cells, a quite large conduction band offset at the CdS/CZTSe interface

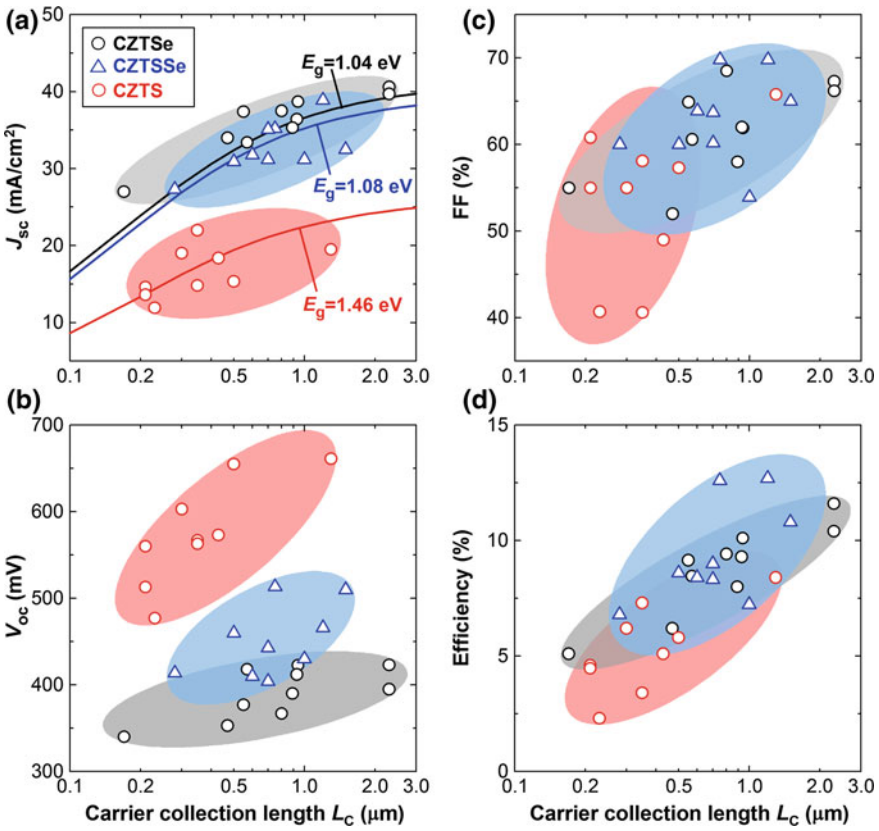


Fig. 2.19 **a** J_{sc}, **b** V_{oc}, **c** *FF* and **d** efficiency of reported CZTSe [21–25, 48–51], CZTS [43–47, 52–55] and CZTSSe [56–64] solar cells as a function of L_C deduced from the EQE analyses. The solid lines indicate the variations of J_{sc} with L_C, calculated assuming E_g of 1.04 eV (CZTSe), 1.08 eV (CZTSSe) and 1.46 eV (CZTS)

(ΔE_C = 0.48–0.6 eV) has been confirmed [67, 68]. As known well [42, 69], CZT(S)Se layers generally exhibit p-type conductivity and the depletion region is formed by the n-type CdS. It has been reported that the hole carrier concentration of a CZTSe layer is 3×10^{16} cm^{-3} and the resulting W is 0.2 μm [69]. In the CZTSe solar cells, therefore, the flat-band formation is expected to occur in the CZTSe bottom region. If we assume that W = 0.2 μm and L_C = 0.6 μm (Fig. 2.15), we obtain L_D = 0.4 μm from (2.34). As illustrated in Fig. 2.20, since the CZTSe layer thickness (>1 μm) is thicker than L_D (or L_C), many photocarriers generated in the flat band region are lost by the intense carrier recombination.

There are two possible recombination passes that are expected to lower L_D in CZTSe solar cells: i.e., the recombinations (i) at the CZTSe/$MoSe_2$ interface and (ii) within the CZTSe bulk layer, as depicted in Fig. 2.20. The low V_{oc} observed in the CZTSe solar cells is independent of L_C (Fig. 2.19b) and this can be interpreted

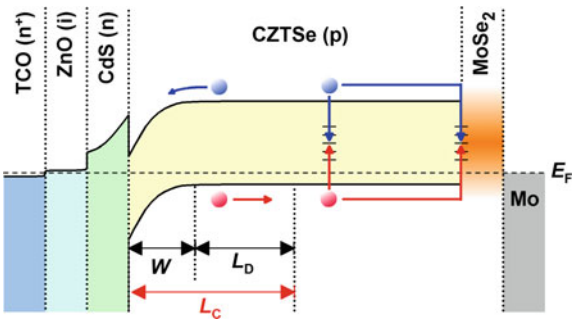


Fig. 2.20 Schematic band diagram proposed for the CZTSe solar cell [18]. The carrier recombination processes in the bulk and rear interface regions are also indicated. The rough scales of L_C, L_D and W are also shown

by the intense rear-interface recombination. In fact, when a TiN barrier layer is provided on the Mo substrate, the EQE response in the longer λ region improves significantly [70]. In the CZTSe solar cell, therefore, the insertion of a BSF structure is expected to be effective for the suppression of the carrier recombination in the bottom region.

In Fig. 2.19b, on the other hand, V_{oc} of the CZTS solar cells increases rather significantly with L_C. This result implies that V_{oc} of the CZTS solar cells is limited by the recombination within the CZTS bulk layer. The low FF values of the CZTS solar cells also support the lower quality of the CZTS absorber layers. In this way, the recombination processes in solar cells can be discussed based on the variation of solar cell characteristics with L_C. It can be seen from Fig. 2.19d that the conversion efficiency of the solar cells increases systematically with L_C, confirming that L_C is a critical parameter of solar cells.

2.4.2 CdTe Solar Cell

By applying the e-ARC method, the EQE spectrum of a reported CdTe solar cell [71], fabricated by a standard closed-space sublimation process [72, 73], has been analyzed [18]. This CdTe solar cell has a conversion efficiency of 16.0% (J_{sc} = 26.1 mA/cm^2, V_{oc} = 840 mV, FF = 0.731) with a structure consisting of MgF_2/glass/ITO/CdS/CdTe/carbon electrode [71]. Since this solar cell has a superstrate structure, the influence of the glass substrate needs to be calculated according to the procedure described in Sect. 2.2.2.

Figure 2.21 shows (a) the EQE analysis result of the CdTe solar cell and (b) the optical gain and loss obtained from the analysis [18]. The shape of the experimental EQE spectrum (open circles) is essentially similar to those of the CIGSe and CZTSe solar cells, although the longer λ response is limited in the CdTe solar cell due to a higher E_g (1.5 eV). In Fig. 2.21a, the red line represents the EQE spectrum calculated from the e-ARC method, while the EQE spectrum of $L_C = \infty$ is indicated by the yellow-colored region. For this EQE analysis, the optical model of MgF_2 (110 nm)/glass/ITO (200 nm)/CdS (50 nm)/CdTe (3.5 μm)/carbon electrode was

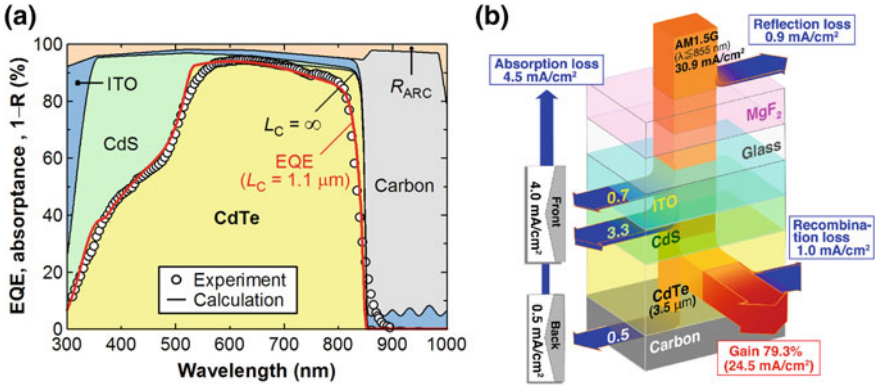


Fig. 2.21 **a** Experimental EQE spectrum (open circles) of a CdTe solar cell consisting of MgF_2/glass/ITO (200 nm)/CdS (50 nm)/CdTe (3.5 μm)/carbon electrode [71], together with the fitted EQE result (red line) obtained from the e-ARC method assuming $L_C = 1.1$ μm and **b** optical gain and loss obtained from the analysis [18]. In **a**, the absorptance spectra of the solar-cell component layers and R_{ARC} are also shown by the black lines. In **b**, the numerical values show the corresponding current densities in units of mA/cm^2

constructed by referring to the description of [71]. The EQE calculation was implemented using the reported optical constants of MgF_2 (Fig. 13.10), glass (Fig. 13.1), ITO (Fig. 11.18), CdS [16, 74], CdTe [75], and carbon (Fig. 12.9). In the EQE fitting analysis, only L_C and the free carrier absorption in the ITO layer (i.e., A_D) were adjusted. The A_D value can be optimized rather easily from the EQE values at $\lambda = 600$–700 nm and the parameters of $A_D = 1.20$ eV and $\Gamma = 0.12$ eV were used in the actual analysis, which correspond to the optical carrier concentration and mobility of $N_{opt} = 2.4 \times 10^{20}$ cm^{-3} and $\mu_{opt} = 35$ cm^2/(Vs), respectively [see (18.23)–(18.24) in Vol. 1]. It can be seen from Fig. 2.21a that the calculated EQE spectrum shows remarkable agreement with the experimental spectrum when $L_C = 1.1$ μm.

On the other hand, the experimental EQE is slightly smaller than the calculated EQE in a region of $\lambda = 520$–570 nm, indicating the small carrier loss near the CdS/CdTe interface. It has been well established that a CdS_xTe_{1-x} alloy is formed at the CdS/CdTe interface [72, 76]. Thus, the slight EQE reduction suggests the carrier recombination within the CdSTe phase. Moreover, the disagreement observed at $\lambda > 850$ nm originates from the effect of the tail-state absorption. Although polycrystalline CdTe layers are expected to show tail absorption, the CdTe dielectric function extracted from a single crystal [75] was used in the analysis of Fig. 2.21a and the calculated EQE becomes smaller at $\lambda > 850$ nm.

In Fig. 2.21b, the CdTe solar cell shows a high optical gain of ~80%. It is noteworthy that the reflection loss and the absorption loss in the ITO layer (<1 mA/cm^2) are quite small in this solar cell. This is primarily caused by the larger E_g of the CdTe. More specifically, when E_g of an absorber layer is higher, the EQE spectral range becomes narrower, and the reflection loss and the TCO absorption loss originating

from the free carrier absorption decrease. In the CdTe solar cell, the parasitic absorption by the rear electrode is also quite small and the high optical gain has been realized. The CdS layer in the CdTe solar cell exhibits the largest parasitic absorption (3.3 mA/cm^2), which is quite similar to that observed in the CIGSe and CZTSe solar cells. Although the reduction of the CdS layer thickness leads to the decrease in V_{oc}, such V_{oc} reduction can be suppressed by incorporating higher-resistive TCO layer at the CdS/TCO interface [77, 78] (see also Fig. 18.1 in Vol. 1). As confirmed from Fig. 2.21b, the analyzed CdTe shows the recombination loss of ~1 mA/cm^2. In more recent CdTe-based solar cells, a ZnTe BSF structure has been incorporated to suppress the recombination at the rear interface [79, 80].

2.4.3 a-Si:H Solar Cell

Among thin-film photovoltaic devices, the EQE analysis of a-Si:H solar cells is found to be most difficult. This difficulty arises from (i) low α values of a-Si:H and (ii) a complex solar cell structure in which a thin a-Si:H layer (~200 nm) is formed on a textured TCO structure (see Fig. 4.19). In particular, the a-Si:H shows low α values of 10–10^4 cm^{-1} in a rather extensive range of E = 1.5–1.9 eV (Fig. 1.6). Moreover, to enhance the optical confinement in the solar cell by light scattering, textured structures have commonly been employed for a-Si:H-based devices [6, 7, 9, 10] (Chap. 4). Nevertheless, due to the small texture sizes (~500 nm in Fig. 4.11), the optical interference still appears in the EQE spectra of textured a-Si:H solar cells. By the presence of both light scattering and coherent interference effects, the EQE analysis of the solar cells has been quite challenging. For the EQE analysis of a-Si:H solar cells, therefore, a slightly different approach has been developed, as described below.

Figure 2.22a shows the optical model constructed for an a-Si:H p-i-n solar cell with an initial efficiency of 9.7% (J_{sc} = 14.9 mA/cm^2, V_{oc} = 867 mV, and FF = 0.751). The optical model reflects the actual structure of glass/SnO_2:F (800 nm)/a-SiC:H p layer (8 nm)/a-SiC:H i layer (1 nm)/a-Si:H i layer (220 nm)/μc-Si:H n layer (30 nm)/ZnO:Al (100 nm)/Ag. For the fabrication of this solar cell, textured SnO_2:F-coated glass (Asahi-U) substrate was used (Sect. 18.5 in Vol. 1). In this solar cell, to suppress the influence of the photodegradation (Stabler-Wronski effect) [81], a quite thin a-Si:H layer (~200 nm) prepared by a triode plasma-deposition process [82] was incorporated, whereas a quite thin a-SiC:H p layer (8 nm) was also employed to reduce the parasitic absorption in the doped layer. The ZnO:Al layer in the device is a back reflector.

The thicknesses of each component layer used for the EQE calculation are also indicated in Fig. 2.22a. The optical constants of each component layers were extracted from separate SE analyses. The SE analyses of a-Si:H-based layers and textured SnO_2:F layers are described in Sects. 9.2 (Vol. 1) and 18.5 (Vol. 1), respectively. For the analysis of the μc-Si:H layer, the optical database shown in Fig. 8.11 [83] was employed. Since the a-Si:H solar cell has a superstrate structure,

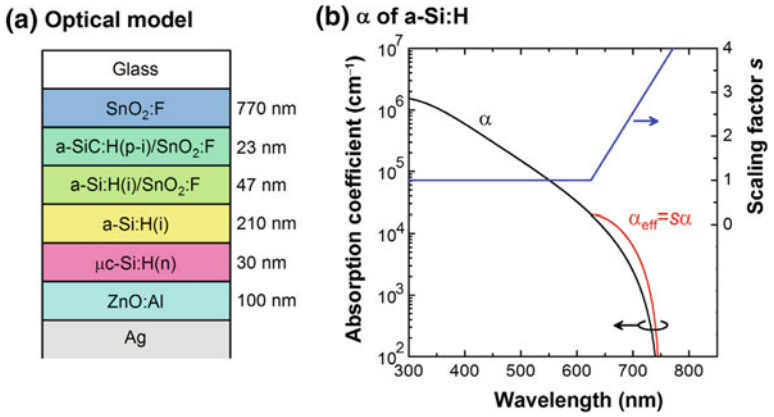


Fig. 2.22 **a** Optical model constructed for an a-Si:H p-i-n solar cell consisting of glass/SnO_2:F (800 nm)/a-SiC:H p layer (8 nm)/a-SiC:H i layer (1 nm)/a-Si:H i layer (220 nm)/μc-Si:H n layer (30 nm)/ZnO:Al (100 nm)/Ag and **b** α spectrum obtained from the SE analysis of the a-Si:H i layer (black line), together with the effective α spectrum ($\alpha_{\text{eff}} = s\alpha$) calculated using the scaling factor s (red line)

the procedure of Sect. 2.2.2 was employed to incorporate the incoherent optical effect of the thick glass substrate.

In the optical model, the a-SiC:H p-i layers were treated as a single component to simplify the analysis. More importantly, to describe the coherent optical effect of the SnO_2:F texture, two mixed-phase layers (i.e., a-SiC:H/SnO_2:F and a-Si:H/SnO_2:F) were introduced to the SnO_2:F/a-Si:H interface, and the volume fraction of the SnO_2:F component was assumed to be 70 vol.%. The presence of this layer is quite important as the mixed-phase layer also acts as the anti-reflection layer. As known well [34, 35], if the optical constants change gradually, the light reflection becomes smaller. Thus, the introduction of an interface layer having an intermediate refractive index is quite effective in suppressing the light reflection.

When the mixed-phase interface layer is incorporated, however, the calculation of the absorptance becomes difficult [9]. Specifically, in this case, once the absorptance of the mixed-phase layer is deduced, the contributions of each phase need to be separated. In the analysis of the a-SiC:H/SnO_2:F layer, for example, we have to determine the absorptances of the a-SiC:H and SnO_2:F components at each E (or λ) from the absorptance calculated for the mixed-phase layer. In general, the optical properties of such mixed-phase layers are calculated using the effective medium approximation [36] but the above separation of the absorption components becomes difficult when this model is used. Accordingly, for the calculation of the mixed-phase-layer optical properties, the following model was applied:

$$\varepsilon(E) = f_a \varepsilon_a(E) + f_b \varepsilon_b(E), \tag{2.38}$$

where $\varepsilon_{a,b}(E)$ and $f_{a,b}$ ($f_a + f_b = 1$) show the dielectric functions and the volume fractions of the materials a and b, respectively. In the above model, the interaction between the two components is neglected (i.e., the screening factor is zero) [36]. From (2.38), the contribution of $\varepsilon(E)$ can be separated into ε_a and ε_b rather easily. Even in this case, the relationship between ε and k (or α) is non-linear, and the absorptances of each component were determined assuming the linear variation of k with f_a (or f_b).

Unfortunately, for textured a-Si:H solar cells, ARC and ERS methods do not provide a satisfactory fitting. Specifically, the EQE values calculated from the ARC and ERS methods are substantially lower than the experimental values in the longer λ region, indicating the strong optical scattering effect in the solar cell. Nevertheless, if the a-Si:H layer thickness is adjusted to reproduce the increase in the effective optical-pass length by light scattering, the interference pattern deviates from the experimental spectrum. Thus, to express the enhanced light absorption in the longer λ region, the α values of the a-Si:H layer were increased using a scaling factor described below.

Figure 2.22b shows the α spectrum obtained from the SE analysis of the a-Si:H i layer (black line), together with an α spectrum calculated using a scaling factor (red line). The α spectrum denoted by the black line shows the result obtained from the dielectric function modeling using the Tauc-Lorentz model (Sect. 1.2.3), and the tail-state absorption has been neglected in the modeling. From the scaling factor s, the effective α of the a-Si:H was calculated simply as $\alpha_{\text{eff}} = s\alpha$, and s is assumed to increase linearly at $\lambda \geq 625$ nm. In this approach, the slope of s versus λ is a fitting parameter and is adjusted so that the EQE fitting in the longer λ region improves. In Fig. 2.22b, α_{eff} and s determined from the actual EQE analysis are shown and α_{eff} increases by a factor of 1–3.5, compared with α, in the range of $625 < \lambda < 750$ nm.

Figure 2.23 shows the EQE analysis result and the optical loss (gain) of the a-Si:H solar cell. The EQE analysis was performed based on the ERS method using the α_{eff} spectrum shown in Fig. 2.22b. When the ARC method is applied, the reflectance in the longer λ region is overestimated (i.e., $1 - R \sim 30\%$ at $\lambda = 700$ nm), and thus the application of the ERS method is preferable for a-Si:H solar cells. As confirmed from Fig. 2.23, the calculated EQE spectrum (red line) shows good agreement when α of the a-Si:H layer is modified. The slight disagreement observed at $\lambda > 730$ nm is caused by the insufficient modeling of the tail-state absorption. It should be emphasized that the similar good fitting can also be obtained when the a-Si:H i layer thickness is varied.

Thus, once the parameter value of s (or α_{eff}) is determined for a specific textured structure, the EQE characterization can be made rather easily. On the other hand, if the original α spectrum shown in Fig. 2.22b is applied, the calculated EQE spectrum (dotted line) deviates at $\lambda > 625$ nm and J_{sc} is underestimated by ~ 1 mA/cm^2. Thus, the approximated EQE characterization can still be made by using the ERC method. In the above analysis, since the EQE response in the longer λ region was

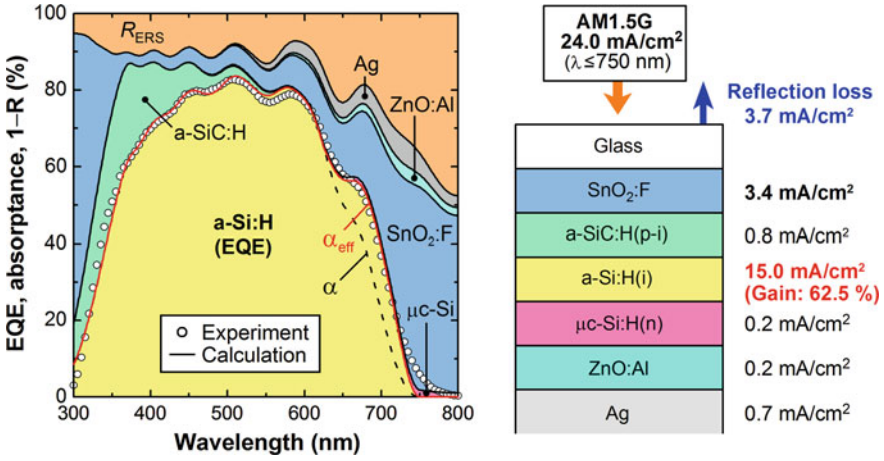


Fig. 2.23 EQE analysis result and optical loss (gain) of the analyzed a-Si:H solar cell. The open circles show the experimental EQE spectrum, whereas the black lines indicate the R_{ERS} and absorptance spectra. The red line and black dotted line represent the EQE spectra calculated using the α_{eff} and α spectra shown in Fig. 2.22b, respectively

adjusted, the determination of the recombination loss is difficult. The J_{sc} loss in the a-Si:H solar cell is attributed mainly to the reflection loss and the absorption loss in the front TCO layer. The relatively large reflection loss (~4 mA/cm^2) originates from the thin a-Si:H layer and the rather small α of a-Si:H. Because the a-Si:H solar cell is a superstrate-type solar cell, the thick SnO_2:F layer is used and the absorption loss in this TCO is relatively large. In contrast, the optical loss in the rear structure (μc-Si:H/ZnO:Al/Ag) is well suppressed. As a result, the optical gain of the a-Si:H solar cell shows a value of ~60%.

2.5 EQE Analysis of Textured c-Si Solar Cells

All the EQE analysis methods described above cannot be applied for solar cells having thick substrates ($\geq$ 10 μm) as the optical response in this case needs to be calculated under the incoherent condition (Sect. 2.2.2). Since c-Si-based solar cells are generally formed using thick c-Si wafers (~150 μm), the effect of the incoherent light absorption should be taken into account in the analysis of c-Si solar cells. However, it has been established that the coherent optical-admittance calculation can be extended to the calculation of incoherent optical systems with thick wafers by modifying the phase of propagating light waves [84]. This section introduces a new calculation scheme developed for the EQE analysis of various c-Si solar cells. It will be shown that even textured c-Si solar cells can be characterized from this method [84].

2.5.1 Continuous Phase Approximation

The calculation procedure of a coherent/incoherent optical system has long been established for the Fresnel approach (transfer matrix method) [85–87]. By adopting this calculation procedure [86, 87], a quite general calculation scheme, the continuous phase approximation (CPA) method, has been developed within the framework of the optical-admittance method [84]. In this section, this new procedure is introduced.

As described above (Sect. 2.2.2), when the thickness of layers (or substrates) exceeds the coherent length of the incoming light, the phase information (i.e., δ expressed by (2.10)) is lost and the optical interference disappears. In the CPA method, the phase δ is varied intentionally so that the coherent optical response is eliminated [86, 87].

Figure 2.24 schematically explains the CPA method. In this figure, the propagation of the incident light in a thick incoherent layer, sandwiched by coherent layers, is illustrated. The slight attenuation of the wave amplitude reflects the light absorption within the incoherent layer. In the optical admittance method, the absorptance of the layer is calculated from ψ (Sect. 2.2.1). However, if ψ of the thick incoherent layer is calculated by applying (2.23), a very sharp interference pattern is generated by the terms $\cos\delta$ and $\sin\delta$. In the CPA method, to remove the interference fringes, we change δ sequentially:

$$\delta_{\mathrm{k}} = \frac{2\pi Nd}{\lambda} + \frac{k}{m}\pi, \tag{2.39}$$

where the second term $k\pi/m$ shows the additional phase introduced to (2.10). In (2.39), m is a total number of the assumed waves, and k is the sequential number of the individual wave ($k = 0, 1, \ldots, m - 1$).

As illustrated in Fig. 2.24, when the phase is changed, the peak and valley positions of the incident wave show a shift. Thus, if all the waves are integrated, the interference effect can be eliminated. In the actual calculation, ψ of each wave (i.e., $\psi(\delta_{\mathrm{k}})$) is obtained first and, by modifying (2.26), the absorptance of the jth incoherent layer ($A_{\mathrm{inc,j}}$) is determined as follow [84]:

$$\begin{aligned} A_{\mathrm{inc,j}} &= \frac{1}{m}\sum_{k=0}^{m-1}(1-R_{\mathrm{flat}})[1-\psi(\delta_k)]\prod_{n=1}^{j-1}\psi_n \\ &= (1-R_{\mathrm{flat}})(1-\psi_{\mathrm{eff}})\prod_{n=1}^{j-1}\psi_n, \end{aligned} \tag{2.40}$$

where ψ_{eff} shows the effective ψ of the incoherent layer given by

$$\psi_{eff} = \frac{1}{m}\sum_{k=0}^{m-1}\psi(\delta_k). \tag{2.41}$$

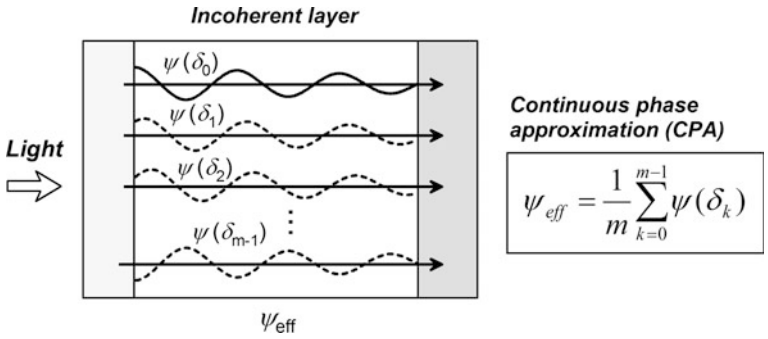


Fig. 2.24 Principle of the continuous phase approximation (CPA) method used for the calculation of solar cells with thick substrates. In this method, ψ is calculated for various δ_k given by (2.39) and the effective ψ (ψ_{eff}) is then obtained as an average of $\psi(\delta_k)$

Thus, ψ_{eff} is a simple average of different $\psi(\delta_k)$ values. Note that $\psi(\delta_0)$ corresponds to ψ obtained from (2.23). The above calculation procedure can be incorporated into the ARC and ERS (or e-ARC and e-ERS) methods quite easily and, based on the above procedure, we can calculate the optical response of a complex multilayer structure, in which coherent and incoherent layers are mixed [84].

The reflectance spectrum of the incoherent optical model can also be calculated by modifying (2.18). Specifically, in this case, we first calculate $Y_0(\delta_k)$, from which the reflectance of the flat structure is calculated by

$$R_{CPA} = \frac{1}{m}\sum_{k=0}^{m-1}\left|\frac{1-Y_0(\delta_k)}{1+Y_0(\delta_k)}\right|^2, \tag{2.42}$$

where R_{CPA} shows the reflectance obtained by applying the CPA method [84].

2.5.2 Analysis of Flat c-Si Solar Cells

Here, the EQE analysis of a flat c-Si heterojunction solar cell is described, as an example of the CPA calculation. In the analyzed c-Si solar cell [88], hydrogenated amorphous silicon oxide (a-SiO:H) layers are formed on both sides of the c-Si substrate (Sect. 9.1 in Vol. 1) with a structure of ITO (70 nm)/a-SiO:H p layer (3 nm)/a-SiO:H i layer (4 nm)/c-Si (300 μm)/a-SiO:H i layer (5 nm)/a-SiO:H n layer (15 nm)/ITO (70 nm)/Al. The conversion efficiency of this flat solar cell is 17.5% ($V_{oc} = 656$ mV, $FF = 0.75$, $J_{sc} = 35.6$ mA/cm^2). The O content in the a-SiO:H i layer is 4 at.%, whereas that of the p-n layers is 7 at.%. From these O contents, the dielectric functions of the a-SiO:H layers can be calculated using the model parameters shown

in Fig. 9.16 (Vol. 1) [89], whereas the optical constants of the c-Si (Fig. 8.1), ITO (Fig. 11.4) and Al (Fig. 12.7) are shown in Part II of this book.

Figure 2.25 shows the EQE spectrum calculated for the a-SiO:H/c-Si heterojunction solar cell. In this analysis, the absorptance of the c-Si substrate was calculated from (2.40) using $m = 13$. By assuming 100% carrier collection, the EQE spectrum was then obtained directly from the c-Si absorptance spectrum. In Fig. 2.25, the EQE spectra calculated for selected δ_k values (i.e., $k = 0$, 1, 2 and 12) are also shown. When a fixed δ_k is used, quite sharp interference fringes appear in the calculated EQE spectrum particularly in a low α region of c-Si. As confirmed from this figure, the interference pattern changes systematically with δ_k. The red line in Fig. 2.25 represents the EQE spectrum calculated from the CPA method. It can be seen that the optical interference effect induced by the c-Si is suppressed completely in the calculated spectrum. For the choice of m, the prime number is more preferable to eliminate the optical interference effectively when the m value is small.

Figure 2.26a shows the result of the EQE analysis performed for the a-SiO:H/c-Si solar cell. The open circles denote the experimental data of [88], where the black and red lines show the CPA-derived absorptance and EQE spectra, respectively. The calculated EQE spectrum, which is consistent with that in Fig. 2.25, shows the remarkable agreement with the experimental EQE spectrum in the wide λ region and J_{sc} obtained from the calculation (35.0 mA/cm^2) also agrees well with the experimental J_{sc} (35.4 mA/cm^2). The result of Fig. 2.26a reveals that the a-SiO:H layers are "dead layers" that allow negligible carrier extraction. In the a-SiO:H/c-Si solar cell, the parasitic light absorption in the front TCO layer is relatively large (1.3 mA/cm^2), while the optical loss in the rear structure (i.e., a-SiO:H(i-n)/ITO/Al)

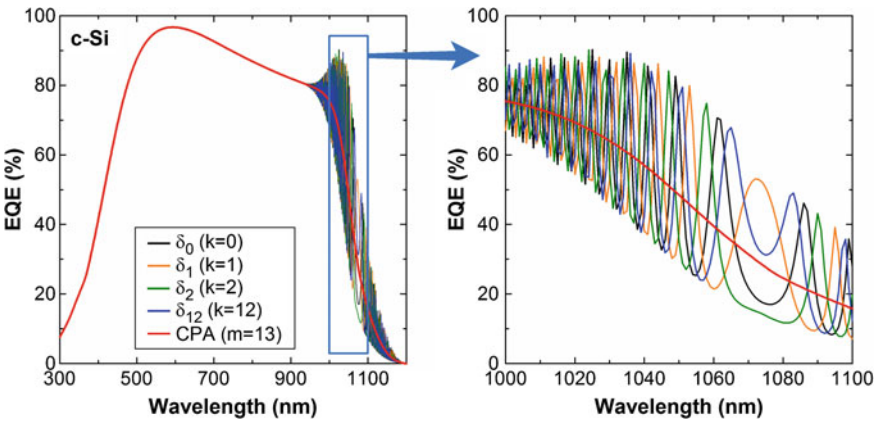


Fig. 2.25 EQE spectra calculated for the a-SiO:H/c-Si heterojunction solar cell fabricated using a flat c-Si substrate. For the EQE spectra obtained using fixed δ_k values, only the results for $k = 0$, 1, 2 and 12 ($m = 13$) are shown for clarity. The red line represents the EQE spectrum calculated by applying the CPA method. The enlarged spectra in the range of $1000 < \lambda < 1100$ nm are also shown

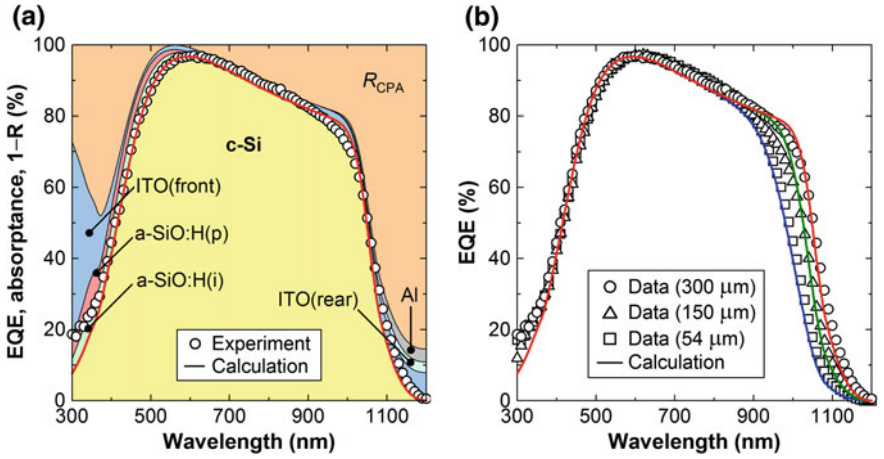


Fig. 2.26 **a** Experimental EQE spectrum (open circles) of the a-SiO:H/c-Si heterojunction solar cell having a flat structure of ITO (70 nm)/a-SiO:H p layer (3 nm)/a-SiO:H i layer (4 nm)/c-Si (300 μm)/a-SiO:H i layer (5 nm)/a-SiO:H n layer (15 nm)/ITO (70 nm)/Ag [88], together with the calculated EQE result (red line) obtained from the CPA method and **b** EQE analysis results obtained for a-SiO:H/c-Si heterojunction solar cells with different c-Si wafer thicknesses (54–300 μm) [88]. In **a**, the absorptance spectra of the solar-cell component layers and R_{CPA} are shown by the black lines

is small (0.4 mA/cm^2). Due to the flat structure, however, the reflection loss (8.8 mA/cm^2) shows the largest contribution to the current loss in the a-SiO:H/c-Si solar cell.

Figure 2.26b summarizes the results of the EQE analyses performed for similar a-SiO:H/c-Si heterojunction solar cells but with different c-Si thicknesses (54–300 μm), reported in [88]. The EQE characterization result for the 300-μm-thick substrate corresponds to that shown in Fig. 2.26a. It can be seen that the calculation results are quite consistent with the experimental EQE spectra. Thus, the carrier recombination is quite small in these solar cells. By the increase in the c-Si wafer thickness, the EQE response in the longer λ region extends gradually, increasing J_{sc} from 33.3 mA/cm^2 (54 μm) to 35.4 mA/cm^2 (300 μm). It should be emphasized that, when the c-Si substrate is thinner, accuracy of the c-Si optical constants becomes quite important to obtain good matching with the experimental result. The excellent overall agreement confirmed in Fig. 2.26b justifies the c-Si optical constants used in the calculation (see Fig. 8.2 in Vol. 1 and Table 8.2 in Vol. 2).

The results of Fig. 2.26 demonstrate that EQE analysis of solar cells with incoherent optical responses can be implemented rather easily by applying the CPA method. This calculation scheme can further be applied for the calculation of multi-junction solar cells consisting of group III–V compound semiconductors.

Figure 2.27 shows the normalized partial EQE (absorptance) for the different depths from the a-SiO:H(i)/c-Si interface and wavelengths, obtained from the analysis of Fig. 2.26a. Unlike Figs. 2.12b and 2.17b, the partial EQE values in this

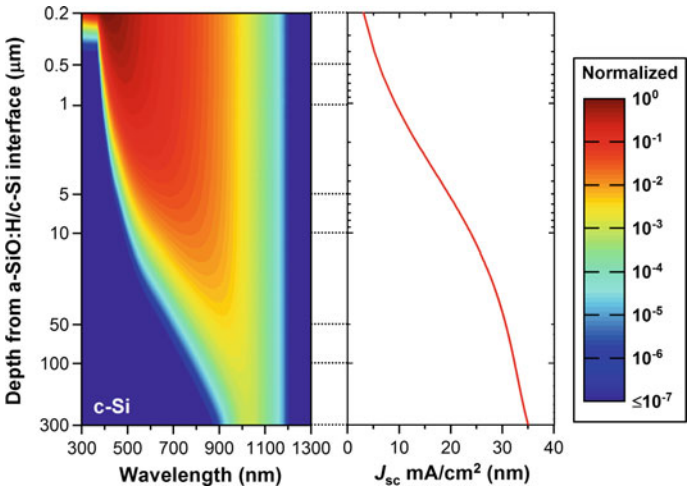


Fig. 2.27 Normalized partial EQE (absorptance) for the different depths from the a-SiO:H(i)/c-Si interface and wavelengths, and integrated J_{sc} toward depth. Note that the partial EQE values are indicated by the logarithmic scale. The results in this figure are consistent with the EQE analysis result of Fig. 2.26a

figure are shown using the logarithmic scale due to the very small α values of indirect-transition c-Si in the longer λ region (see Fig. 1.6). As shown in Fig. 2.27, the carrier generation is rather uniform up to 5 μm but the light absorption continues to occur even at 300 μm in the long λ region of $900 \leq \lambda \leq 1200$ nm.

In Fig. 2.27, the calculation result of J_{sc} for the depth is also shown. As confirmed from this result, J_{sc} increases to ~24 mA/cm^2 at the depth of 10 μm, followed by the gradual increase observed at the depth of $d > 10$ μm. For c-Si solar cells, to suppress the wafer cost, the use of thinner Si wafers is quite favorable. In this case, however, J_{sc} of the solar cells simply decreases as the light absorption becomes more difficult. To suppress the J_{sc} reduction observed in thinner c-Si solar cells, the efficient optical confinement is crucial.

2.5.3 *Analysis of Textured c-Si Solar Cells*

Rather surprisingly, the EQE analysis of textured c-Si solar cells can be performed by adopting the above calculation procedure [84]. In general, for the fabrication of c-Si solar cells, pyramid-shaped textures (see Fig. 4.1) are widely employed. As described in Sect. 4.2.4, the optical response of thin layer structures formed on the c-Si textures can be described using the coherent condition and the light scattering effect within the thin layers is very small. Furthermore, due to the shape of the specific c-Si texture, the transmission angle of the incident light in the thin film structure is close to the normal to the {111} texture-facet plane. More specifically,

the optical characterization described in Sect. 4.2.2 confirms that the top angle of the pyramid-shaped texture is 80° (see also Fig. 4.5) and the incident angle for the {111} facet is 50°, as illustrated in Fig. 2.28. Since the refractive indices of the ITO, a-Si:H and c-Si at $\lambda = 1100$ nm are $n = 1.7$ (Table 11.8), n = 3.6 (Table 8.21), and n = 3.5 (Table 8.2), the transmission angles become 27°, 12° and 12°, respectively. Consequently, the absorptance of the TCO and a-Si:H layers can be approximated assuming the normal incidence in the coherent optical model [84]. More importantly, if the suppressed light reflection by the c-Si texture is expressed by the ERS method, the light absorption in the whole structure can be deduced using a completely flat optical model [84]. The above calculation procedure for textured c-Si solar cells is exactly the same as that described in the previous section but only the experimental reflectance spectrum is used in this case to incorporate the texture effect.

Figure 2.29a shows an optical model constructed for a textured a-Si:H/c-Si heterojunction solar cell reported in [90]. This solar cell has a structure of ITO/a-Si:H(p)/a-Si:H(i)/c-Si/a-Si:H(i)/a-Si:H(n)/ITO/Ag. For the EQE analysis, the layer thicknesses described in [90] were adopted, but the thicknesses of the a-Si:H p-i layers were reduced to half to obtain good agreement with the experimental result. In Fig. 2.29a, the layer thicknesses used in the actual analysis are summarized. For the optical constants of the component layers, the optical spectra of a-Si:H p and i layers [11] and an ITO layer with a carrier concentration of 2.4×10^{20} cm^{-3} [12], reported by the same research group, were employed, while the optical constants of Fig. 8.1 were used for the c-Si. In addition, the optical constants of the a-Si:H n layer was assumed to be identical to those of the a-Si:H i layer.

Figure 2.29b shows the EQE analysis result obtained for the a-Si:H/c-Si heterojunction solar cell based on the ERS-CPA approach. It can be seen that, even

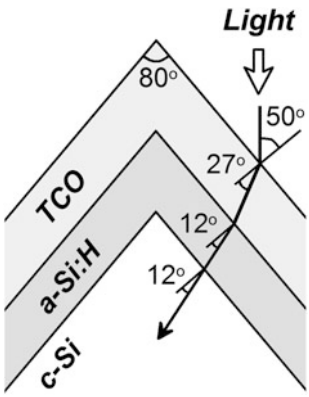


Fig. 2.28 Optical transmission in a TCO/a-Si:H thin film structure formed on a pyramid-shaped c-Si texture. The top angle of the c-Si texture is 80° (see Fig. 4.5) and the transmission angles are calculated assuming $n = 1.7$ (ITO: Table 11.8), $n = 3.6$ (a-Si:H: Table 8.21) and $n = 3.5$ (c-Si: Table 8.2) at $\lambda = 1100$ nm. As a result, the transmission angle is close to the normal to the {111} texture-facet plane

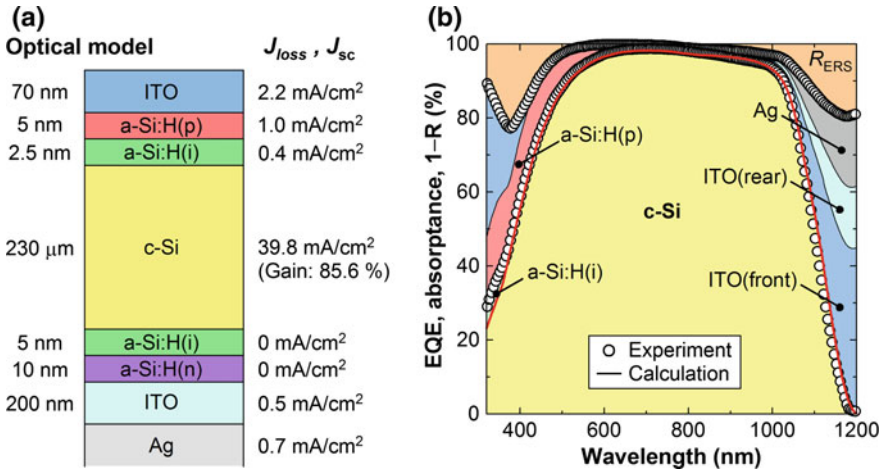


Fig. 2.29 **a** Optical model constructed for a reported a-Si:H/c-Si heterojunction solar cell [90] and **b** EQE analysis result obtained for the a-Si:H/c-Si heterojunction solar cell using the ERS-CPA method. In **a**, the current density loss (J_{loss}) and J_{sc} determined from the analysis are also shown. In **b**, the experimental reflectance and EQE spectra (open circles) and the calculated EQE and absorptance spectra (red and black lines) are indicated

though the quite simple calculation scheme has been applied, the calculated EQE spectrum (red line) shows remarkable agreement with the experimental spectrum (open circles). As mentioned above, the a-Si:H p-i layer thickness were reduced, compared with the reported thicknesses, since otherwise the calculated EQE values become notably lower than the experimental EQE values in the short λ region of $300 \leq \lambda \leq 600$ nm. In other words, the effective thicknesses of the a-Si:H p-i layers can be deduced rather easily from the EQE analysis assuming no carrier extraction from the a-Si:H layers [84] as observed in Fig. 2.26a.

The black lines in Fig. 2.29b show the absorptance spectra of the solar-cell component layers and the optical losses (gain) estimated from these spectra are also indicated in Fig. 2.29a. In the a-Si:H/c-Si heterojunction solar cells, the parasitic absorption in the a-Si:H p-i layers is relatively large (see also Fig. 9.7 in Vol. 1) and the ITO layer also induces the optical loss, but the optical gain is quite high (85.6%). However, it should be noted that J_{sc} obtained from the reported EQE spectrum of [90] (40 mA/cm^2) is higher than ~37 mA/cm^2 determined from the current density-voltage measurement [90] because the shadow loss of the front electrode is not considered in EQE.

2.6 Carrier Loss Mechanisms

In this section, from the above EQE analysis results, the carrier loss mechanisms in various solar cells are discussed. It will be emphasized that the carrier recombination is affected by not only defect creation but also the light absorption characteristics of the absorber layers.

2.6.1 *Effect of Carrier Collection Length on* J_{sc}

Figure 2.30a summarizes the α spectra of the various light absorbers applied for the above EQE analyses [18]. The α spectrum of the $CH_3NH_3PbI_3$ hybrid perovskite is also shown for comparison. In this figure, all the semiconductors show $\alpha \sim 10^4$ cm^{-1} near the E_g region. However, for CdTe and $CH_3NH_3PbI_3$, quite sharp absorption edges can be confirmed, whereas the kesterite compounds (i.e., CZTSe and CZTS) exhibit a broad optical transition near the E_g region (see Fig. 1.6). Quite importantly, the near-E_g absorption characteristics affect the carrier recombination behavior rather significantly. To understand this behavior quantitatively, the EQE simulations have been performed for the solar cell materials of Fig. 2.30a.

Figure 2.30b shows the variation of J_{sc} with L_C calculated from the e-ARC method [18]. For all the solar cells, an identical solar cell structure consisting of

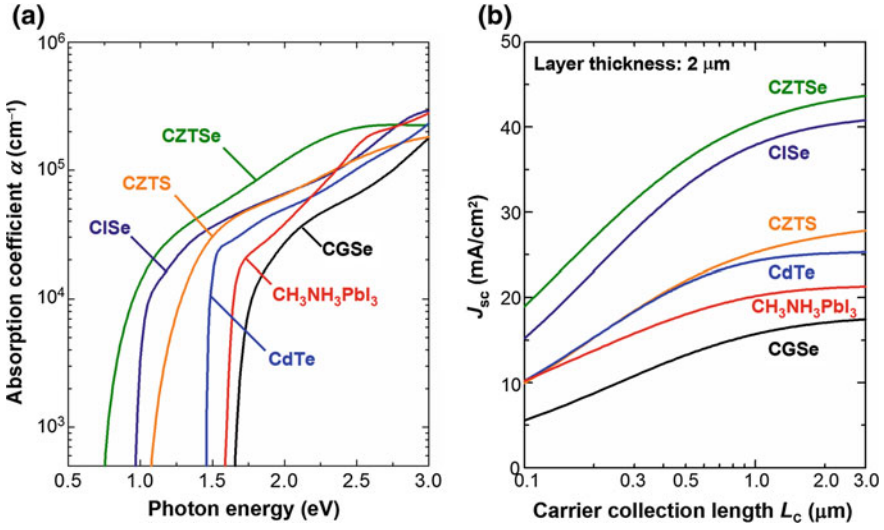


Fig. 2.30 **a** α spectra of the various light absorbers applied for the EQE analyses and **b** variation of J_{sc} with L_C calculated from the e-ARC method [18]. The optical data of **a** show reported values of CZTSe (Fig. 8.30), CZTS (Fig. 8.29), CISe (Fig. 8.24), CdTe [75], $CH_3NH_3PbI_3$ (Fig. 10.2) and CGSe (Fig. 8.25). In **b**, a fixed layer thickness of 2 μm is assumed

MgF_2 (130 nm)/ZnO:Al (360 nm)/ZnO (50 nm)/CdS (45 nm)/absorber (2.0 μm)/Mo was assumed, except for CdTe and $CH_3NH_3PbI_3$ solar cells. For these solar cells, the structures of Fig. 2.21 (CdTe) and Fig. 16.17 in Vol. 1 ($CH_3NH_3PbI_3$) were adopted, but the calculations were implemented using an identical absorber thickness of 2.0 μm. For the simulations of CZTSe and CZTS solar cells, the E_g values are increased slightly: i.e., $E_g = 1.0$ eV (CZTSe) and $E_g = 1.45$ eV (CZTS) based on the result of Fig. 2.19.

In Fig. 2.30b, J_{sc} is higher in the solar cell with a low-E_g absorber and J_{sc} increases rapidly with increasing L_C. The variations of J_{sc} with L_C are essentially similar in all the solar cells and J_{sc} tends to saturate at $L_C > 1.0$ μm because α of the absorbers is $\sim 10^4$ cm^{-1} and the resulting d_p is ~1 μm (Fig. 1.11b). Nevertheless, the J_{sc} values of the CdTe and $CH_3NH_3PbI_3$ solar cells show almost complete saturation at $L_C > 1.0$ μm. This trend originates from the sharp absorption features of these absorbers. As a result, in CdTe and $CH_3NH_3PbI_3$ solar cells, $J_{sc}J_{sc}$ is not influenced by the recombination as long as the condition of $L_C > 1.0$ μm is satisfied.

The suppressed carrier recombination in CdTe can be understood more visually from the partial absorptance. Figure 2.31 shows the partial absorptance of (a) CdTe and (b) CZTSe solar cells calculated in the simulation of Fig. 2.30b [18]. It can be seen that the carrier generation in the CdTe layer occurs more uniformly in the depth direction, compared with the CZTSe layer. This arises from the smaller penetration depth of light in the longer λ region due to higher α values. In particular, because of the sharp absorption edge of the CdTe, most of the light is absorbed in the region quite close to the CdS/CdTe interface. Thus, even when L_C is rather small (L_C ~1 μm), the carrier loss occurs only in a limited λ region of 800–850 nm (Fig. 2.31a). As a result, the influence of the carrier recombination is suppressed quite well in the CdTe solar cell. In fact, rather surprisingly, L_C of the CdTe solar cell (~1 μm in Fig. 2.21) is comparable to those of the CZTSe and CZTS solar cells

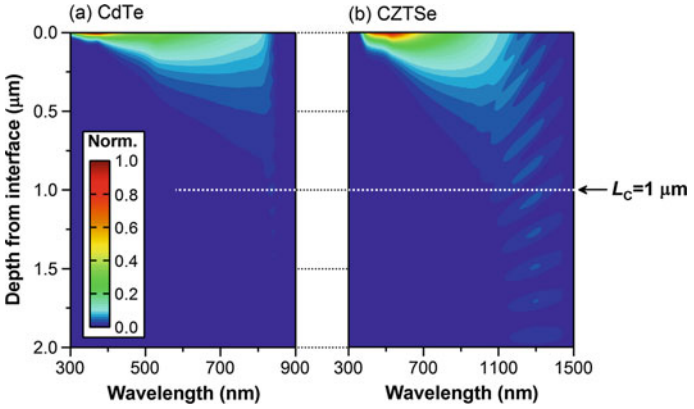


Fig. 2.31 Partial absorptance of **a** CdTe and **b** CZTSe solar cells calculated in the simulation of Fig. 2.30b [18]. The partial absorptance values are normalized by the maximum values obtained in each solar cell

(~1 μm in Fig. 2.18), even though the carrier recombination loss in the CdTe solar cell is quite small (1.0 mA/cm^2 in Fig. 2.21), compared with that in the CZTSe (~6 mA/cm^2 in Fig. 2.15).

Accordingly, carrier recombination is influenced significantly by the α spectrum of a light absorber layer and the recombination loss decreases, if $\alpha(\lambda)$ shows high values with sharp absorption edge (or a low Urbach energy). In this sense, $\alpha(\lambda)$ of CdTe and $CH_3NH_3PbI_3$ has a more ideal shape, if compared with CZTSe and CZTS.

2.6.2 Carrier Loss in Various Solar Cells

Table 2.1 summarizes J_{sc}, the optical loss and recombination loss of the various solar cells, determined from the EQE analyses in this chapter and Chap. 16 in Vol. 1. In this table, the results are ordered by decreasing E_g of the solar-cell absorber layer, and the optical gains of each solar cell are also indicated. Unfortunately, for many record efficiency solar cells, the detailed structures and optical properties of the component layers are not clear and the EQE analyses are not possible. Thus, the carrier losses and gains summarized in Table 2.1 represent reference values and the best-performing solar cells may exhibit more suppressed J_{sc} losses.

For all thin-film solar cells and c-Si heterojunction solar cells, the current losses induced by the reflection and the parasitic absorption in a front TCO layer are common problems. Although the wide-E_g a-Si:H and hybrid perovskite ($CH_3NH_3PbI_3$) solar cells exhibit the large reflection and TCO absorption losses, these optical losses tend to increase in solar cells having low-E_g absorbers due to the widening of the EQE spectral range. In fact, the reflection loss of the wide-gap CdTe solar cell is less than 1 mA/cm^2, while those of the CZTSe and CZTSSe solar cells are quite large (2.5–4.5 mA/cm^2). When low-E_g absorbers are applied, therefore, the suppression of the reflection loss and absorption loss in the front TCO becomes critical in achieving high conversion efficiencies. The high reflection losses observed in the wide-E_g a-Si:H and $CH_3NH_3PbI_3$ solar cells are caused by the quite thin absorber layers (200–300 nm).

As confirmed from Table 2.1, the J_{sc} loss induced by the TCO parasitic absorption reduces the optical gain notably. For example, Al-doped ZnO layers (~350 nm) with a carrier concentration of ~2×10^{20} cm^{-3} result in the absorption loss of ~3 mA/cm^2 (see Figs. 2.11b and 2.15b). In the CZTSSe solar cell shown in Table 2.1, the TCO absorption is suppressed by incorporating a thin ITO layer (50 nm) [14]. In the CdTe solar cell, the optical loss caused by the front ITO is only 0.7 mA/cm^2 even though the ITO thickness is 200 nm. This small optical loss in the front TCO originates from the large E_g value of CdTe, which limits the effect of the free carrier absorption, as the free carrier absorption in TCO layers increases drastically at longer wavelengths (Fig. 18.8 in Vol. 1). In contrast, the a-Si:H and $CH_3NH_3PbI_3$ solar cells having larger E_g show the relatively large front TCO losses. This is caused by strong free carrier absorption originating from a thick TCO

Table 2.1 J_{sc}, optical loss and recombination loss of various solar cells determined from the EQE analyses. The results are ordered by decreasing E_g of the solar-cell absorber layer, and the optical gains of each solar cell are also indicated. For the optical losses of the TCO, doped and metal layers, the total losses obtained by summing the contributions of related layers are indicated

Solar cell	J_{sc} (mA/cm^2)	Optical loss (mA/cm^2)				Recombination loss (mA/cm^2)	Optical gain (%)	Analysis
		Reflection loss	TCO	Doped layer	Metal			
a-Si:H	15.0	3.7	3.6	1.0	0.7	–	63	Fig. 2.23
$CH_3NH_3PbI_3$	18.7	3.2	3.4	0.1[a]	0.6	0.9	70	Fig. 16.19 (Vol. 1)
CdTe	24.5	0.9	0.7	3.3[b]	0.5	1.0	79	Fig. 2.21
CZTS	20.2	1.2	4.4	4.1[b]	8.3[c]	1.4	51	[18]
CIGSe	34.0	1.2	2.8	2.5[b]	3.2	0.0	78	Fig. 2.11
a-Si:H/c-Si	39.8 [d]	1.9	2.7	1.4[e]	0.7	0.0	86[d]	Fig. 2.29
CZTSSe	35.4	4.5	1.4	1.8[b]	3.8[c]	5.2	68	Fig. 1.14
CZTSe	31.6	2.5	3.5	3.5[b]	4.6[c]	6.5	61	Fig. 2.15

[a]Total optical loss in the electron and hole transport layers, [b]Optical loss induced by the n-type CdS layer, [c]Total optical loss of the Mo and Mo(S)Se_2 layers, [d]J_{sc} without the front electrode, [e]Total optical loss of the a-Si:H p-i layers

layer (600–900 nm) with a high carrier concentration of (3–5) × 10^{20} cm^{-3} (Asahi-U and TEC-8 substrates: see Table 18.2 in Vol. 1). The parasitic light absorption in the front TCO can be reduced by employing high-mobility TCO layers, which exhibit quite low free carrier absorption (Chap. 19 in Vol. 1).

In the CIGSe, CZTSe, CZTS and CdTe solar cells, the optical loss induced by the n-type doped CdS layer (~50 nm) is ~3 mA/cm^2. In the CZTSSe solar cell, the optical loss in the CdS layer is reduced by incorporating a quite thin CdS layer (25 nm) [14]. In high-efficiency CdTe solar cells, the parasitic absorption in the CdS layer is also reduced by adopting a thin layer [77, 78], as mentioned earlier. For CIGSe solar cells, to suppress the J_{sc} loss induced by the CdS layer, a Zn(O,S) layer has also been applied [91].

In the CIGSe and CZTSSe-based solar cells, a strong optical loss also occurs by the parasitic absorption in the Mo layer. This effect can be attributed to the very low reflectance of Mo, as mentioned above (Fig. 12.4). The strong parasitic absorption in the Mo is evident in the EQE analysis results for the CIGSe and CZTSe solar cells (Figs. 2.11a and 2.15a). In contrast, quite high reflectance can be obtained in the a-Si:H, $CH_3NH_3PbI_3$ and c-Si solar cells, which employ Al, Ag, and Au back reflectors (Fig. 12.3). Accordingly, in the Cu-Se containing semiconductors, the parasitic absorption by the CdS and Mo layers causes the large J_{sc} reduction.

It should be emphasized that the $CH_3NH_3PbI_3$ and CdTe solar cells show small overall optical losses. In particular, the parasitic absorption within the electron and hole transport layers in the hybrid perovskite solar cell is negligible (only 0.1 mA/cm^2 in Table 2.1) and the major absorption loss occurs only in the front TCO layer. Thus, a quite high conversion efficiency reported for $CH_3NH_3PbI_3$ solar cells (~20%) can be understood in part by the low parasitic absorption within the solar-cell component layers [17, 18].

In the CIGSe and a-Si:H/c-Si heterojunction solar cells, the recombination loss is negligible and high optical gains of ~80% have been realized. All the other solar cells show the recombination losses, primarily because of the lack of the BSF structures in the solar cells. The results of Table 2.1 show clearly that the reduction of the optical and recombination losses is critical in achieving high conversion efficiencies. For the determination of the performance-limiting optical and physical factors in solar cells, the EQE analysis described in this chapter provides a fast and reliable method.

2.7 Free Software for EQE Analysis

A window-based free computer software (e-ARC software), which can be applied to the EQE analysis and simulation described in this chapter, was released at EU-PVSC conference (Amsterdam, Sept. 25 in 2017) and can be downloaded from a web site (https://unit.aist.go.jp/rcpv/cie/service/index.html). Figure 2.32 shows the computer screen of the e-ARC software. In this figure, the analysis example of the CIGSe solar cell described in Sect. 2.2.3 is shown. In this software, the EQE

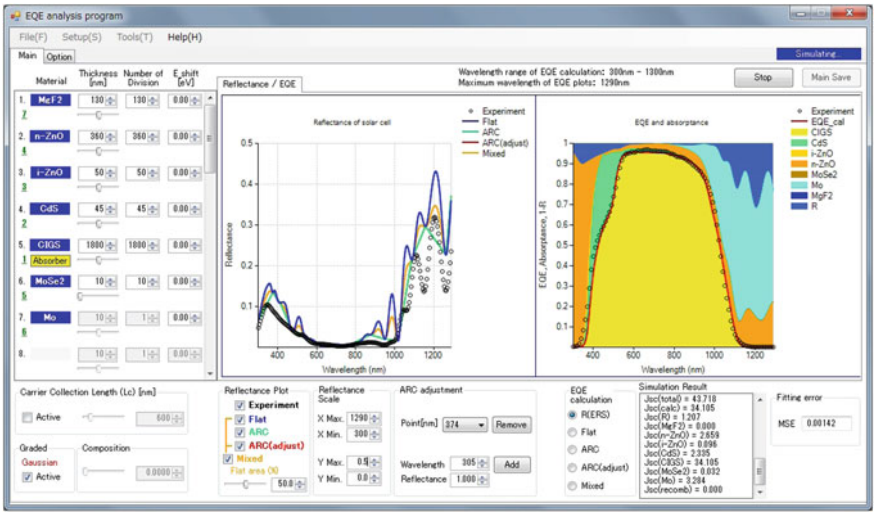


Fig. 2.32 Computer screen of the EQE analysis program (e-ARC software). The analysis example for a CIGSe solar cell is shown. This free software can be downloaded from a web site (https://unit.aist.go.jp/rcpv/cie/service/index.html)

calculation can be finished within a second. The software is quite easy to operate and is recommended particularly for students and researchers who intend to optimize solar cells.

References

1. This concept appears to be introduced first by Dr. Stefan W. Glunz, Fraunhofer ISE
2. M. Lavagna, J.P. Pique, Y. Marfaing, Solid State Electron. **20**, 235 (1977)
3. X.X. Liu, J.R. Sites, J. Appy. Phys. **75**, 577 (1994)
4. J. Sinkkonen, J. Ruokolainen, P. Uotila, A. Hovinen, Appl. Phys. Lett. **66**, 206 (1995)
5. J. Mattheis, P.J. Rostan, U. Rau, J.H. Werner, Sol. Eng. Mater. Sol. Cells **91**, 689 (2007)
6. K. Ding, T. Kirchartz, B.E. Pieters, C. Ulbrich, A.M. Ermes, S. Schicho, A. Lambertz, R. Carius, U. Rau, Sol. Eng. Mater. Sol. Cells **95**, 3318 (2011)
7. M. Agrawal, M. Frei, Prog. Photovolt. **20**, 442 (2012)
8. C. Haase, H. Stiebig, Prog. Photovolt. **14**, 629 (2006)
9. Y. Sago, H. Fujiwara, Jpn. J. Appl. Phys. **51**, 10NB01 (2012)
10. M. Zeman, O. Isabella, S. Solntsev, K. Jäger, Sol. Energy Mater. Sol. Cells **119**, 94 (2013)
11. Z.C. Holman, A. Descoeudres, L. Barraud, F.Z. Fernandez, J.P. Seif, S. De Wolf, C. Ballif, IEEE J. Photovolt. **2**, 7 (2012)
12. Z.C. Holman, M. Filipic, A. Descoeudres, S. De Wolf, F. Smole, M. Topic, C. Ballif, J. Appl. Phys. **113**, 013107 (2013)
13. D. Zhang, I.A. Digdaya, R. Santbergen, R.A.C.M.M. van Swaaij, P. Bronsveld, M. Zeman, J.A.M. van Roosmalen, A.W. Weeber, Sol. Eng. Mater. Sol. Cells **117**, 132 (2013)
14. M.T. Winkler, W. Wang, O. Gunawan, H.J. Hovel, T.K. Todorov, D.B. Mitzi, Energy Environ. Sci. **7**, 1029 (2014)

15. L. Kosyachenko, T. Toyama, Sol. Energy Mater. Sol. Cells **120**, 512 (2014)
16. T. Hara, T. Maekawa, S. Minoura, Y. Sago, S. Niki, H. Fujiwara, Phys. Rev. Appl. **2**, 034012 (2014)
17. M. Shirayama, H. Kadowaki, T. Miyadera, T. Sugita, M. Tamakoshi, M. Kato, T. Fujiseki, D. Murata, S. Hara, T.N. Murakami, S. Fujimoto, M. Chikamatsu, H. Fujiwara, Phys. Rev. Appl. **5**, 014012 (2016)
18. A. Nakane, H. Tampo, M. Tamakoshi, S. Fujimoto, K.M. Kim, S. Kim, H. Shibata, S. Niki, H. Fujiwara, J. Appl. Phys. **120**, 064505 (2016)
19. J. Zhao, A. Wang, M.A. Green, F. Ferrazza, Appl. Phys. Lett. **73**, 1991 (1998)
20. J. Benick, B. Hoex, M.C.M. van de Sanden, W.M.M. Kessels, O. Schultz, S.W. Glunz, Appl. Phys. Lett. **92**, 253504 (2008)
21. Y.S. Lee, T. Gershon, O. Gunawan, T.K. Todorov, T. Gokmen, Y. Virgus, S. Guha, Adv. Energy Mater. **5**, 1401372 (2015)
22. S. Bag, O. Gunawan, T. Gokmen, Y. Zhu, T.K. Todorov, D.B. Mitzi, Energy Environ. Sci. **5**, 7060 (2012)
23. J.-O. Jeon, K.D. Lee, L.S. Oh, S.-W. Seo, D.-K. Lee, H. Kim, J.-H. Jeong, M.J. Ko, B. Kim, H.J. Son, J.Y. Kim, Chemsuschem **7**, 1073 (2014)
24. A. Redinger, M. Mousel, M.H. Wolter, N. Valle, S. Siebentritt, Thin Solid Films **535**, 291 (2013)
25. A. Redinger, M. Mousel, R. Djemour, L. Gütay, N. Valle, S. Siebentritt, Prog. Photovolt. **22**, 51 (2014)
26. A.M. Gabor, J.R. Tuttle, D.S. Albin, M.A. Contreras, R. Noufi, A.M. Hermann, Appl. Phys. Lett. **65**, 198 (1994)
27. A.M. Gabor, J.R. Tuttle, M.H. Bode, A. Franz, A.L. Tennant, M.A. Contreras, R. Noufi, D.G. Jensen, A.M. Hermann, Sol. Eng. Mater. Sol. Cells **41/42**, 247 (1996)
28. M.A. Contreras, J. Tuttle, A. Gabor, A. Tennant, K. Ramanathan, S. Asher, A. Franz, J. Keane, L. Wang, R. Noufi, Sol. Eng. Mater. Sol. Cells **41/42**, 231 (1996)
29. B. Shin, N.A. Bojarczuk, S. Guha, Appl. Phys. Lett. **102**, 091907 (2013)
30. S.C. Baker-Finch, K.R. McIntosh, Prog. Photovolt. **19**, 406 (2011)
31. C. Haase, H. Stiebig, Appl. Phys. Lett. **91**, 061116 (2007)
32. O. Isabella, S. Solntsev, D. Caratelli, M. Zeman, Prog. Photovolt. **21**, 94 (2013)
33. M. Powalla, G. Voorwinden, D. Hariskos, P. Jackson, R. Kniese, Thin Solid Films **517**, 2111 (2009)
34. H.A. Macleod, *Thin-Film Optical Filters* (CRC Press, NY, 2010)
35. E. Hecht, *Optics*, 4th edn. (Addison Wesley, San Francisco, 2002)
36. H. Fujiwara, *Spectroscopic Ellipsometry: Principles and Applications* (Wiley, West Sussex, UK, 2007)
37. J.A. Berning, P.H. Berning, J. Opt. Soc. Am. **50**, 813 (1960)
38. F. Zhu, J. Singh, Sol. Energy Mater. Sol. Cells **31**, 119 (1993)
39. J. Krc, M. Zeman, F. Smole, M. Topic, J. Appl. Phys. **92**, 749 (2002)
40. A. Luque, S. Hegedus, *Handbook of Photovoltaic Science and Engineering* (Wiley, West Sussex, UK, 2011)
41. R. Klenk, H. Schock, W. Bloss, in *Proceeding of the 12th European Conference on Photovoltaic Solar Energy Conversion* (EUPVSEC, Amsterdam, 1994), p. 1588
42. T. Gokmen, O. Gunawan, D.B. Mitzi, J. Appl. Phys. **114**, 114511 (2013)
43. B. Shin, O. Gunawan, Y. Zhu, N.A. Bojarczuk, S.J. Chey, S. Guha, Prog. Photovolt. **21**, 72 (2013)
44. T. Fukano, S. Tajima, T. Ito, Appl. Phys. Express **6**, 062301 (2013)
45. M.G. Gang, K.V. Gurav, S.W. Shin, C.W. Hong, J.H. Min, M.P. Suryawanshi, S.A. Vanalakar, D.S. Lee, J.H. Kim, Phys. Status Solidi C **12**, 713 (2015)
46. T.P. Dhakal, C.-Y. Peng, R.R. Tobias, R. Dasharathy, C.R. Westgate, Sol. Energy **100**, 23 (2014)
47. H. Cui, X. Liu, F. Liu, X. Hao, N. Song, C. Yan, Appl. Phys. Lett. **104**, 041115 (2014)

48. I.L. Repins, H. Moutinho, S.G. Choi, A. Kanevce, D. Kuciauskas, P. Dippo, C.L. Beall, J. Carapella, C. DeHart, B. Huang, S.H. Wei, J. Appl. Phys. **114**, 084507 (2013)
49. T.K. Todorov, K.B. Reuter, D.B. Mitzi, Adv. Mater. **22**, E156 (2010)
50. I. Repins, C. Beall, N. Vora, C. DeHart, D. Kuciauskas, P. Dippo, B. To, J. Mann, W.-C. Hsu, A. Goodrich, R. Noufi, Sol. Energy Mater. Sol. Cells **101**, 154 (2012)
51. S. Oueslati, G. Brammertz, M. Buffière, H. ElAnzeery, O. Touayar, C. Köble, J. Bekaert, M. Meuris, J. Poortmans, Thin Solid Films **582**, 224 (2015)
52. A. Ennaoui, M.L. Steiner, A. Weber, D. Abou-Ras, I. Kötschau, H.-W. Schock, R. Schurr, A. Hölzing, S. Jost, R. Hock, T. Voß, J. Schulze, A. Kirbs, Thin Solid Films **517**, 2511 (2009)
53. S. Ahmed, K.B. Reuter, O. Gunawan, L. Guo, L.T. Romankiw, H. Deligianni, Adv. Energy Mater. **2**, 253 (2012)
54. J.J. Scragg, T. Ericson, X. Fontané, V. Izquierdo-Roca, A. Pérez-Rodríguez, T. Kubart, M. Edoff, C. Platzer-Björkman, Prog. Photovolt. **22**, 10 (2014)
55. F. Zhou, F. Zeng, X. Liu, F. Liu, N. Song, C. Yan, A. Pu, J. Park, K. Sun, X. Hao, A.C.S. Appl, Mater. Interfaces **7**, 22868 (2015)
56. J. Kim, H. Hiroi, T.K. Todorov, O. Gunawan, M. Kuwahara, T. Gokmen, D. Nair, M. Hopstaken, B. Shin, Y.S. Lee, W. Wang, H. Sugimoto, D.B. Mitzi, Adv. Mater. **26**, 7427 (2014)
57. W. Wang, M.T. Winkler, O. Gunawan, T. Gokmen, T.K. Todorov, Y. Zhu, D.B. Mitzi, Adv. Energy Mater. **4**, 1301465 (2014)
58. C.J. Hages, S. Levcenco, C.K. Miskin, J.H. Alsmeier, D. Abou-Ras, R.G. Wilks, M. Bär, T. Unold, R. Agrawal, Prog. Photovolt. **23**, 376 (2015)
59. G. Larramona, S. Bourdais, A. Jacob, C. Choné, T. Muto, Y. Cuccaro, B. Delatouche, C. Moisan, D. Péré, G. Dennler, J. Phys. Chem. Lett. **5**, 3763 (2014)
60. H. Xie, M. Dimitrievska, X. Fontané, Y. Sánchez, S.L. Marino, V. Izquierdo-Roca, V. Bermúdez, A. Pérez-Rodríguez, E. Saucedo, Sol. Energy Mater. Sol. Cells **140**, 289 (2015)
61. Q. Guo, G.M. Ford, W.-C. Yang, B.C. Walker, E.A. Stach, H.W. Hillhouse, R. Agrawal, J. Am. Chem. Soc. **132**, 17384 (2010)
62. H. Xin, J.K. Katahara, I.L. Braly, H.W. Hillhouse, Adv. Energy Mater. **4**, 1301823 (2014)
63. C.K. Miskin, W.-C. Yang, C.J. Hages, N.J. Carter, C.S. Joglekar, E.A. Stach, R. Agrawal, Prog. Photovolt. **23**, 654 (2015)
64. G. Larramona, S. Levcenko, S. Bourdais, A. Jacob, C. Choné, B. Delatouche, C. Moisan, J. Just, T. Unold, G. Dennler, Adv. Energy Mater. **5**, 1501404 (2015)
65. A. Chirilă, S. Buecheler, F. Pianezzi, P. Bloesch, C. Gretener, A.R. Uhl, C. Fella, L. Kranz, J. Perrenoud, S. Seyrling, R. Verma, S. Nishiwaki, Y.E. Romanyuk, G. Bilger, A.N. Tiwari, Nat. Mater. **10**, 857 (2011)
66. M. Bär, S. Nishiwaki, L. Weinhardt, S. Pookpanratana, W.N. Shafarman, C. Heske, Appl. Phys. Lett. **93**, 042110 (2008)
67. R. Haight, A. Barkhouse, O. Gunawan, B. Shin, M. Copel, M. Hopstaken, D.B. Mitzi, Appl. Phys. Lett. **98**, 253502 (2011)
68. T. Kato, H. Hiroi, N. Sakai, H. Sugimoto, in *Proceeding of the 28th European Photovoltaic Solar Energy Conference* (EUPVSEC, Paris, 2013), p. 2125
69. I.L. Repins, M.J. Romero, J.V. Li, S.-H. Wei, D. Kuciauskas, C.-S. Jiang, C. Beall, C. DeHart, J. Mann, W.-C. Hsu, G. Teeter, A. Goodrich, R. Noufi, IEEE J. Photovolt. **3**, 439 (2013)
70. B. Shin, Y. Zhu, N.A. Bojarczuk, S.J. Chey, S. Guha, Appl. Phys. Lett. **101**, 053903 (2012)
71. T. Aramoto, S. Kumazawa, H. Higuchi, T. Arita, S. Shibutani, T. Nishio, J. Nakajima, M. Tsuji, A. Hanafusa, T. Hibino, K. Omura, H. Ohyama, M. Murozono, Jpn. J. Appl. Phys. **36**, 6304 (1997)
72. C.S. Ferekides, D. Marinskiy, V. Viswanathan, B. Tetali, V. Palekis, P. Selvaraj, D.L. Morel, Thin Solid Films **361–362**, 520 (2000)
73. N. Romeo, A. Bosio, V. Canevari, A. Podestà, Sol. Energy **77**, 795 (2004)
74. J. Chen, J. Li, D. Sainju, K.D. Wells, N.J. Podraza, R.W. Collins, in *Proceedings of IEEE 4th World Conference on Photovoltaic Energy Conversion* (IEEE, New York, 2006), p. 711

75. S. Adachi, *Optical Constants of Crystalline and Amorphous Semiconductors* (Kluwer Academic Publishers, Norwell, 1999)
76. B.E. McCandless, L.V. Moulton, R.W. Birkmire, Prog. Photovolt. **5**, 249 (1997)
77. B.E. McCandless, K.D. Dobson, Sol. Energy **77**, 839 (2004)
78. B.A. Korevaar, A. Halverson, J. Cao, J. Choi, C. Collazo-Davila, W. Huber, Thin Solid Films **535**, 229 (2013)
79. J. Li, D.R. Diercks, T.R. Ohno, C.W. Warren, M.C. Lonergan, J.D. Beach, C.A. Wolden, Sol. Energy Mater. Sol. Cells **133**, 208 (2015)
80. N. Strevel, L. Trippel, C. Kotarba, I. Khan, Photovolt. Int. **22**, 66 (2014)
81. D.L. Staebler, C.R. Wronski, Appl. Phys. Lett. **31**, 292 (1977)
82. T. Matsui, A. Bidiville, K. Maejima, H. Sai, T. Koida, T. Suezaki, M. Matsumoto, K. Saito, I. Yoshida, M. Kondo, Appl. Phys. Lett. **106**, 053901 (2015)
83. T. Yuguchi, Y. Kanie, N. Matsuki, H. Fujiwara, J. Appl. Phys. **111**, 083509 (2012)
84. A. Nakane, S. Fujimoto, H. Fujiwara, J. Appl. Phys. **122**, 203101 (2017)
85. B. Harbecke, Appl. Phys. B **39**, 165 (1986)
86. M.C. Troparevsky, A.S. Sabau, A.R. Lupini, Z. Zhang, Opt. Expr. **18**, 24715 (2010)
87. R. Santbergen, A.H.M. Smets, M. Zeman, Opt. Expr. **21**, A262 (2013)
88. H. Fujiwara, H. Sai, M. Kondo, Jpn. J. Appl. Phys. **48**, 064506 (2009)
89. M. Sato, S.W. King, W.A. Lanford, P. Henry, T. Fujiseki, H. Fujiwara, J. Non-Cryst, Solids **440**, 49 (2016)
90. J.P. Seif, A. Descoeudres, M. Filipič, F. Smole, M. Topič, Z.C. Holman, S. De Wolf, C. Ballif, J. Appl. Phys. **115**, 024502 (2014)
91. S. Niki, M. Contreras, I. Repins, M. Powalla, K. Kushiya, S. Ishizuka, K. Matsubara, Prog. Photovoltaics **18**, 453 (2010)

Chapter 3
Optical Simulation of External Quantum Efficiency Spectra



Prakash Koirala, Abdel-Rahman A. Ibdah, Puruswottam Aryal, Puja Pradhan, Zhiquan Huang, Nikolas J. Podraza, Sylvain Marsillac and Robert W. Collins

Abstract Applications of ex situ spectroscopic ellipsometry (SE) are presented for determination of the parameters that describe the dielectric function and structure of thin film solar cells. Complete optical models of solar cells developed using least squares regression analysis of the SE data enable external quantum efficiency (EQE) simulations for comparison with measurements. Through this comparison, it becomes possible to understand in detail the origins of optical and electronic collection and losses in thin film photovoltaics technologies and, as a result, the underlying performance limitations. Examples of this approach are presented for the three commercialized thin film technologies of hydrogenated amorphous silicon (*a*-Si:H), cadmium telluride (CdTe), and copper indium-gallium diselenide ($CuIn_{1-x}Ga_xSe_2$; CIGS). In the studies of *a*-Si:H solar cells, a comparison between the EQE simulation based on the SE model and the measured EQE suggests electrical losses from photo-generated carriers near the *p*/*i* and *i*/*n* interfaces, the latter caused by an *i*-layer thickness greater than the hole collection length. Also demonstrated here through comparisons of EQE measurements and simulation is enhanced carrier collection near the *p*/*i* interface when a protocrystalline Si:H *i*-layer of improved electrical quality is incorporated at the interface. For a CdS/CdTe heterojunction solar cell in the superstrate configuration, SE is performed through the glass, and simulations of the EQE spectra have been generated on the basis of comprehensive optical property and multilayer analysis by SE. In this case, observed deviations between simulated and measured EQE can assist in refining the optical model of the cell. Applying these methods, the optical losses that occur when photons with above-bandgap energies are not absorbed within the cell's active layers can be

P. Koirala · A.-R. A. Ibdah · P. Aryal · P. Pradhan · Z. Huang · N. J. Podraza (✉)
R. W. Collins
Department of Physics & Astronomy and Center for Photovoltaics Innovation & Commercialization, University of Toledo, Toledo, OH 43606, USA
e-mail: Nikolas.Podraza@utoledo.edu

R. W. Collins
e-mail: robert.collins@utoledo.edu

S. Marsillac
Virginia Institute of Photovoltaics, Old Dominion University, Norfolk, VA 23529, USA

© Springer International Publishing AG, part of Springer Nature 2018

H. Fujiwara and R. W. Collins (eds.), *Spectroscopic Ellipsometry for Photovoltaics*,
Springer Series in Optical Sciences 214,
https://doi.org/10.1007/978-3-319-95138-6_3

distinguished from electronic losses that occur when electrons and holes photo-generated within these active layers are not collected. CIGS/CdS heterojunction solar cells incorporating both standard thickness and thin absorbers are also studied using SE. Data analysis is more challenging for CIGS because of the need to extract absorber layer Ga profiles for accurate optical models. For cells with standard thickness absorbers, excellent agreement is found between the simulated and measured EQE, the latter under the assumption of 100% collection from the active layers. For cells with thin absorbers, however, the difference observed between the simulated and measured EQE can be assigned to losses via electron-hole recombination near the Mo back contact. When a probability profile for carrier collection is introduced into the EQE simulation, closer agreement between this simulation and the measurement is observed. In addition to a single spot capability of SE as presented in this study, a capability also exists for high resolution mapping of multilayer thicknesses and component layer characteristics that provide short-circuit current density predictions. The mapping capability is made possible due to the high speeds [<1 s per measurement of (ψ, Δ) spectra] of multichannel ellipsometers.

3.1 Introduction

Spectroscopic ellipsometry (SE) has been applied widely in thin film photovoltaics (PV) technology for measurement of the component layer thicknesses and optical properties in multilayer PV stacks [1]. Because SE is a non-invasive, contactless method that can be used in various off-line, on-line, as well as in situ and real time modes for thin film analysis, it has been identified as a very valuable tool in PV research and development [2]. For the component layer materials of thin film PV devices, the real and imaginary parts of the complex dielectric function, given by $\varepsilon(E) = \varepsilon_1(E) - i\varepsilon_2(E)$, can be described in terms of one or more electronic oscillators [1, 3]. The layers include the metals that serve as back contacts, semiconductors that form the junctions, and transparent conducting oxides (TCOs) that serve as top contacts, SE measurements in conjunction with least squares regression for data analysis constitute an effective methodology for determining not only the thicknesses of the component layers, but also the oscillator parameters that define the (ε_1, ε_2) spectra. SE analysis of complicated multilayered PV stacks can be very challenging, however, if one seeks information on both thicknesses and layer optical properties. In addition to the conventional film-side study of solar cells in the substrate configuration, through-the-glass SE has been developed for the study of cells in the superstrate configuration [4, 5]. In through-the-glass SE, the light beam reflected from the front glass surface is blocked, as this beam sums incoherently with that reflected from the back-side films of interest. In this configuration, it may be possible to perform both film-side and through-the-glass SE and then to analyze the data together, obtaining results with greater confidence [5]. For the substrate solar cell configuration with either an opaque substrate or opaque back contacts that cover a transmitting substrate, however, only a film-side measurement is possible due to the lack of transmittance through the back side.

Once the thicknesses and (ε_1, ε_2) spectra of the component layers of the solar cells are determined by SE, additional useful information can be obtained on the solar cells. First, one can deduce the maximum external quantum efficiency (EQE) that can be achieved for the given solar cell structure and for the given thicknesses of the component layers based on the identification of the active layer or layers as well as on the assumption of specular reflection and transmission conditions [6, 7]. By simulating the EQE for variations from the deduced structure, one can optimize expeditiously the short-circuit current density in a solar cell, thus avoiding trial-and-error approaches. Second, the spectra in the reflectance from the solar illumination side can be predicted for the solar cells [5–7]. This prediction is helpful in determining the need for anti-reflection coatings, as well as in designing the optimum anti-reflection coating stack [8]. EQE simulations described here start with the assumption that all carriers photo-generated within the active layers are collected without recombination losses. Thus, a comparison between the simulated EQE and experimental EQE obtained from the measurement of a completed solar cell can provide information on electronic losses and the spectral dependence of these losses [2, 9–11]. Moreover, because only specular interfaces are assumed in the EQE model, the scattering of light at rough surfaces and interfaces is not taken into consideration in the simulation. Thus, if the measured EQE is greater than the simulated EQE in some regions of the spectrum, it will give insights regarding the collection that results from light trapping caused by scattering at rough surfaces and interfaces [5, 9].

In the following sections, selected examples will be reviewed in which EQE simulations and measurements are compared. The simulations are based on ex situ SE analysis results obtained on complete solar cells [2, 9–11]. Such ex situ SE analysis of the optical structure of the solar cell is further based on a foundation of additional SE measurements in idealized sample structures that provide (ε_1, ε_2) spectra or give insights into the oscillator models required to describe these spectra with a smaller number of variable parameters [2, 3]. This foundation is often established through measurements performed in situ and in real time. The discussion will start with a review of early SE and EQE studies of hydrogenated amorphous silicon (*a*-Si:H) solar cells [9], and will proceed to describe more recent state of the art analyses of cadmium telluride (CdTe) [10] and copper indium-gallium diselenide ($CuIn_{1-x}Ga_xSe_2$; CIGS) solar cells [11].

3.2 Hydrogenated Amorphous Silicon Solar Cells

3.2.1 Solar Cell Fabrication and Performance

A simplified schematic of the multilayered structure of an *a*-Si:H-based *p-i-n* solar cell is shown in Fig. 3.1 [12]. The two *a*-Si:H solar cells studied here were deposited in a multichamber cluster tool without vacuum breaks between the

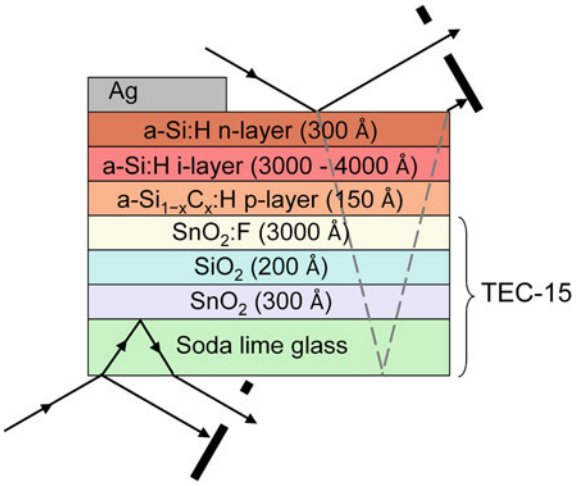


Fig. 3.1 Simplified multilayer structure and intended or nominal thicknesses for the *a*-Si:H-based solar cell in the *p-i-n* superstrate configuration on commercial TCO coated glass. Also shown are film-side (upper) and through-the-glass (lower) measurement configurations

individual layers [9]. The *a*-Si:H-based layers, both doped and undoped, were deposited by radio frequency (rf) plasma enhanced chemical vapor deposition (PECVD). The fixed PECVD parameters for the two intrinsic absorber layer (*i*-layer) depositions included a substrate temperature of 200 °C, a total silane plus hydrogen gas pressure of 450 mTorr, and a rf power of 4 W. The hydrogenated amorphous silicon-carbon alloy (a-$Si_{1-x}C_x$:H) *p*-type layer and the *a*-Si:H *n*-type layer were deposited under the same conditions for both solar cells to intended thicknesses of 150 Å and 300 Å, respectively. The intrinsic absorber layer for the first cell was deposited in a single step to an intended thickness of 4000 Å using a gas flow ratio of hydrogen to silane given by $R = [H_2]/[SiH_4] = 0.5$. The second cell was fabricated under identical conditions with the exception of a thinner two-step *i*-layer. For the two-step *i*-layer of this second cell, the component deposited in the first step, located adjacent to the *p*-layer, was intended to be protocrystalline, meaning that a high hydrogen-to-silane gas flow ratio of $R = 50$ was used in the Si:H film deposition process [13]. The intended thickness of this initially-deposited *i*-layer was 300 Å. The second step *i*-layer component, located adjacent to the *n*-layer, was deposited under identical conditions as the one-step *i*-layer of the first cell but with a reduced thickness of 3000 Å. Thus, the total intended thickness of the two-step *i*-layer for the second cell was 3300 Å.

The two cells were deposited on TEC™ 15 glass (NSG-Pilkington) in the *p-i-n* superstrate configuration as shown schematically in Fig. 3.1. In the fabrication of TEC™ 15, three different layers are deposited on the soda lime glass surface, including thin layers of SnO_2 and SiO_2 (~200–300 Å each), and the top-most SnO_2:F contact layer (~3300 Å) [10, 14]. A thin optically distinct, tin-modified region may be present on the ambient side of the soda lime glass resulting from the fact that the glass floats on molten tin during its manufacture [15].

The efficiency for the *a*-Si:H solar cell with the one-step *i*-layer is ~5.1% as indicated in Table 3.1. Because the *a*-Si:H solar cell with the one-step *i*-layer

Table 3.1 Performance parameters measured under air mass 1.5 (AM 1.5) illumination for two *a*-Si:H solar cells with different deposition processes for the absorber. In the first cell, the intrinsic layer (or *i*-layer) absorber deposition was performed to an intended ~4000 Å thickness. For the second cell, this *i*-layer was deposited in a two-step process to an intended ~3300 Å thickness. The initial step consisted of a nominal 300 Å thick protocrystalline *i*-layer deposited onto the *p*-layer at a high H_2-dilution flow ratio of $R = 50$ prior to deposition of the ~3000 Å remainder of the *i*-layer [9]

Cell	V_{OC} (mV)	J_{SC} (mA/cm^2)	FF (%)	η (%)	R_{SH} (kΩ)	R_S (Ω)
#1 One-step i-layer	734	10.1	68.7	5.10	32.9	119
#2 Two-step i-layer	886	14.5	73.3	9.43	6.9	18.1

exhibited a low efficiency, primarily due to low open-circuit voltage (V_{OC}) and low short-circuit current density (J_{SC}), a second cell with a two-step *i*-layer was fabricated. It is well known that a two-step *i*-layer with a thin high *R* *i*-layer at the *p*/*i* interface leads to improvements in the overall performance of solar cells as well as in their stability [16]. This is exemplified by the results in Table 3.1 showing that each of the cell parameters was improved and an efficiency of 9.4% was obtained for the cell with the two-step *i*-layer. Because the cells exhibit widely different performances, interesting comparisons can be made in the EQE analysis.

3.2.2 Component Layer Dielectric Functions

For the SE-EQE analyses performed in the studies of the two *a*-Si:H solar cells, dielectric functions (ε_1, ε_2) as well as selected layer thicknesses for the TEC™ 15 coated glass components were fixed from previous studies [17]. Figure 3.2 shows the (ε_1, ε_2) spectra for the thin SnO_2, the first layer of the stack, whose thickness was fixed at 294 Å in the analyses. Figure 3.3 shows (ε_1, ε_2) spectra for the SnO_2:F

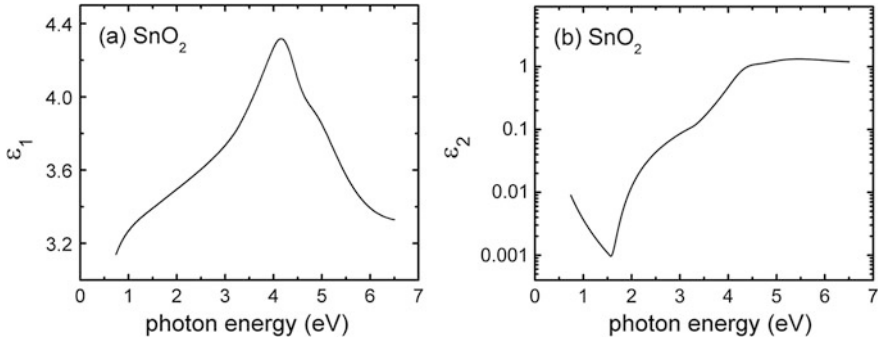


Fig. 3.2 **a** Real and **b** imaginary parts of the room temperature dielectric function $\varepsilon = \varepsilon_1 - i\varepsilon_2$ plotted versus photon energy for the thin (~300 Å) undoped SnO_2 layer adjacent to the soda lime glass for transparent conducting oxide coated glass [17]

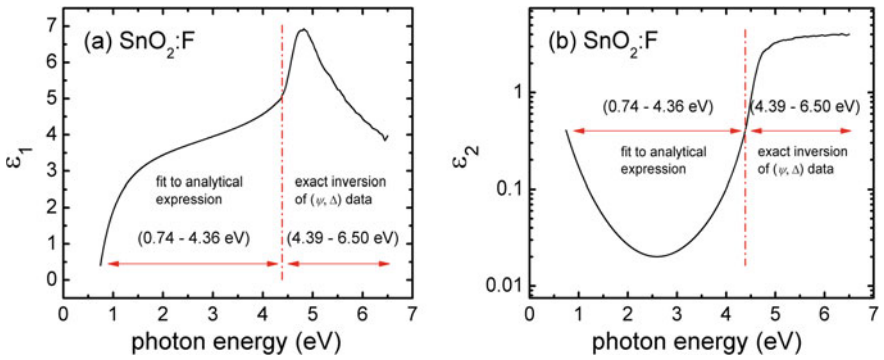


Fig. 3.3 **a** Real and **b** imaginary parts of the room temperature dielectric function $\varepsilon = \varepsilon_1 - i\,\varepsilon_2$ plotted versus photon energy for the thick (~3300 Å) SnO_2:F serving as the top conducting layer of transparent conducting oxide coated glass. These results derive from a best fit parametric expression over the low photon energy range where the film is semitransparent and from an inversion of (ψ, Δ) over the high energy range where it is essentially opaque [17]

contact layer whose thickness was allowed to vary. With the exception of the high energy data for the SnO_2:F layer, the results of Figs. 3.2 and 3.3 were obtained from least squares regression analysis fits to (ψ, Δ) spectra as well as to transmittance spectra using analytical expressions for the dielectric functions that combine Drude free electron, Sellmeier, and modified Lorentz oscillator terms. At the highest photon energies, the SnO_2:F layer is essentially opaque, and the dielectric function for energies greater than 4.4 eV was obtained by exact inversion of (ψ, Δ). In the inversion, values for the best fit thickness and void content of the roughness layer (the latter as applied in the Bruggeman effective medium approximation) were obtained from the analysis of the lower photon energy range. It should be emphasized, however, that the SE analysis results in the next sub-section do not depend on the SnO_2:F dielectric function in the high photon energy range. Through-the-glass SE is limited by absorption in the glass to energies below 3.5 eV, and for film-side SE, photon energies above 4.4 eV are absorbed by the *a*-Si:H-based layers before reaching the SnO_2:F.

For the (ε_1, ε_2) spectra of the undoped (or intrinsic), *p*-type, and *n*-type *a*-Si:H-based layer components, a single Lorentz oscillator modified by a Cody bandgap function was used [3]. The Kramers-Kronig consistent expressions for the Cody-Lorentz oscillator were first developed by Ferlauto et al. [18]. The Cody-Lorentz oscillator is similar to the Tauc-Lorentz oscillator in that it defines a bandgap energy, E_g, as well as the parameters associated with an above-gap Lorentzian absorption feature. The models behave differently in the absorption onset region, in particular at photon energies E just above E_g. In that region, the Tauc-Lorentz model follows the Tauc Law, $\varepsilon_2(E) \propto [(E - E_g)^2/E^2]$, applying the assumption of an energy independent momentum matrix element versus E, whereas the Cody-Lorentz model assumes that $\varepsilon_2(E) \propto (E - E_g)^2$, applying the assumption of an energy independent dipole matrix element first proposed by Cody [19] and

subsequently supported by electron spectroscopies [20]. Each model can also incorporate an Urbach absorption term, which generates an exponential decay of the absorption coefficient with decreasing E below the bandgap, starting from a well defined energy E_t just above E_g [18]. Thus, a modified-Lorentz oscillator expression is described by as many as eight free parameters in total. These include the constant contribution to the real part of the dielectric function (ε_{1o}), most often fixed at unity as described by Ferlauto et al.; the Lorentz oscillator amplitude (A), center energy (E_0), and broadening (Γ); the bandgap (E_g), the (band-edge)-to-oscillator transition energy (E_p), the exponential band tail (or Urbach) slope (E_u), and the (band-tail)-to-(band-edge) transition energy (E_t).

Figure 3.4 shows the analytical expressions for the real and imaginary parts of the room temperature dielectric functions of p-type a-$Si_{1-x}C_x$:H and n-type a-Si:H based on the Cody-Lorentz model. The (ε_1, ε_2) spectra for the a-$Si_{1-x}C_x$:H p-layer were extracted by depositing a thin layer of p-type a-$Si_{1-x}C_x$:H on a c-Si wafer using the same deposition conditions and time as were used for the solar cell [21]. The resulting film was modeled applying a Cody-Lorentz oscillator and allowing all parameters to vary in the fit; however, all such p-layer parameters were fixed for the analysis of the SE data obtained on the two solar cells. The (ε_1, ε_2) spectra for the n-layer were obtained from SE analysis of the complete a-Si:H solar cell with the one-step i-layer [9, 21]. The bandgap and broadening parameter for this n-layer were variables and the other parameters were linked to the bandgap as described by the model of Table 3.2. The broadening parameter for the n-layer was allowed to vary independently of the bandgap to simulate the greater disorder and potential fluctuations associated with doped a-Si:H relative to the intrinsic a-Si:H for which bandgap-linked parameters are available [18]. These resulting n-layer parameters were also used for the n-layer of the cell fabricated with the two-step i-layer. For the i-layers of the cells with one and two-step absorbers, different Cody-Lorentz

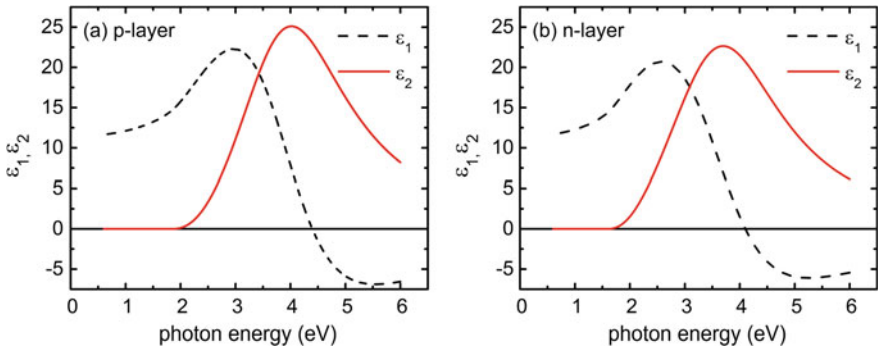


Fig. 3.4 Analytical expressions for the real and imaginary parts of the room temperature dielectric functions of **a** p-type a-$Si_{1-x}C_x$:H and **b** n-type a-Si:H based on the Cody-Lorentz model. The p-layer results were determined in a separate study of film growth on a smooth substrate and the n-layer results were obtained from the analysis of the complete a-Si:H-based solar cell in the superstrate configuration of Fig. 3.1 using the one-step i-layer [9, 21]

Table 3.2 Multilayer model used for analysis of film-side SE data collected on *a*-Si:H-based solar cell devices in the superstrate configuration. The parameters that were fixed, fit, or coupled are also shown. For coupling in the analysis, the relationships between the Cody-Lorentz (C-L) parameters are applied as given by Ferlauto et al. [18]. For through-the-glass SE, an opaque Ag layer was added at the back of the *n*-layer with Ag filling the voids in the *n*-layer roughness (Color table online)

a-Si:H *n*-layer surface/interface roughness thickness	Fit
n-layer volume fraction	Fixed (0.5)
a-Si:H *n*-layer thickness	Fit
C-L A_n	Coupled to E_{gn}
C-L E_{0n}	Coupled to E_{gn}
C-L Γ_n	Fit
C-L E_{gn}	Fit
C-L E_{pn}	Coupled to E_{gn}
a-Si:H *i*-layer thickness	Fit
C-L A_i	Coupled to E_{gi}
C-L E_{0i}	Coupled to E_{gi}
C-L Γ_i	Coupled to E_{gi}
C-L E_{gi}	Fit
C-L E_{pi}	Coupled to E_{gi}
SnO_2:F/*p*-layer/*i*-layer volume fractions	Fixed (0.25/0.25/0.50)
interface layer thickness	Fit
SnO_2:F/*p*-layer/*i*-layer volume fractions	Fixed (0.50/0.25/0.25)
interface layer thickness	Fit
SnO_2:F layer thickness	Fit
SiO_2 layer thickness	Fixed (232 Å)
SnO_2 layer	Fixed (294 Å)
Soda lime glass phase shift due to strain	Fit
Sn side layer	Fixed (610 Å)

oscillators were used with the bandgap as a single variable and all other parameters coupled to the bandgap [18]. Both absorber components of the cell with the two-step *i*-layer were assumed to have the same optical properties due to the thinness of the first-step layer and the ability of H to diffuse during completion of the cell. Due to the low sensitivity of SE for extinction coefficients $k < 0.01$, Urbach terms were not included in any of the (ε_1, ε_2) spectra of the *a*-Si:H-based layers.

3.2.3 *Spectroscopic Ellipsometry Measurement and Analysis*

The SE data for the *a*-Si:H solar cells were collected using a serially-scanning rotating-analyzer instrument (V-VASE, J.A. Woollam Company) with a potential

spectral range from 0.7 to 6.5 eV [9, 22]. As shown in Fig. 3.1, measurements were performed through the glass and from the film side, and multi-sample analysis was performed simultaneously. A focusing probe was used in through-the-glass SE along with an aperture to block the reflection from the top surface as well as higher order reflections making more than two passes through the glass. An aperture was also used to block all back surface glass reflections in film-side SE. In through-the-glass SE, the film was probed at a location coincident with the back contact electrode; in film-side SE, a location was probed slightly displaced from this spot, yielding a reflection from the *n*-layer. Thus, the multi-sample model differed in the analysis since the silver back contact was present in through-the-glass SE, but not for film-side SE. Other measurement details are provided elsewhere [9, 23]. The model used for analysis of the SE data, including the fixed parameters as well as the fitted/coupled parameters, is shown in Table 3.2.

In the model of Table 3.2, starting from the soda lime glass, a correction for stress-induced birefringence in the glass is designed to eliminate the effect of the stress on the ellipsometry angle Δ. The correction does not provide a comprehensive analysis; however, in the limit of weak stress, it provides only the product of the stress magnitude and $\cos 2\alpha$ where α is the angle between the principal axis coordinate system of the stress and the *p*-*s* coordinate system of the optical wave. Future improvements are needed to generalize the analysis, which would then provide more useful information on the glass stress itself, which is an important parameter for manufacturing [24]. As noted above, the thicknesses and dielectric functions of the SnO_2 and SiO_2 layers were fixed based on separate analyses of the uncoated TEC™ 15 [9]. For the SnO_2:F, the dielectric function was fixed, but the bulk layer thickness was allowed to vary in the analysis. From the separate SE analysis of the TEC™ 15 substrate, the surface roughness layer thickness on the SnO_2:F was found to be ~300 Å. Because the thickness of the *a*-$Si_{1-x}C_x$:H *p*-layer is ~75–150 Å for an optimized *a*-Si:H solar cell, such a thin *p*-layer is not expected to be planar, of course, but instead is fully modulated as it conforms to the rough SnO_2:F surface. Thus, the *p*-layer was not considered to exhibit any distinct bulk layer, but rather was treated as a component material of the ~300–400 Å thick roughness region located at the interface between the bulk SnO_2:F and *i*-layer. In fact, two three-component interface layers, each having different fixed volume fractions for the three components, were used in order to improve the fit to the data [5, 9]. The components of SnO_2:F, *p*-layer, and *i*-layer were used in the ratios 2:1:1, respectively, for the interface layer adjacent to the SnO_2:F layer of the TEC™ 15 coated glass. For the second interface layer, which is adjacent to the *i*-layer, these same materials were used in the ratios 1:1:2, respectively. The dielectric functions assigned to the two layers were determined using the Bruggeman effective medium approximation (EMA) [25]. Finally, the roughness layer on the surface of the *n*-layer exerts a sensitive effect on data acquired from the film-side, and this layer was also modeled using an EMA of *n*-layer and void.

Figure 3.5 shows the best fit to the SE (ψ, Δ) data obtained for the solar cell with the one-step *i*-layer applying multi-sample analysis to the data sets obtained through-the-glass and from the film side [23]. Figure 3.6 shows a comparison of the

resulting structural and dielectric function parameters obtained in the fits of the data for both solar cells [9]. For the cell with the one-step *i*-layer, a small stress birefringence correction was found for the glass in the best fit whereas the correction was fixed in the best fit for the cell with the two-step *i*-layer. The effective thicknesses or volume per area values of the SnO_2:F for the cells with one and two-step *i*-layers are 3420 Å and 3150 Å, respectively. These values differ by no more than 5% from the nominal value of 3300 Å. The corresponding results for the *p*-layer yield effective thicknesses of 76–84 Å, much thinner than the intended value of 150 Å obtained by establishing the deposition rate on thicker films. This suggests either a time-dependent deposition rate or a substrate-dependent initial rate. An excessively thin *p*-layer trades off open-circuit voltage for higher short-circuit current density. In contrast, the *n*-layer effective thicknesses of 328–333 Å were consistently larger than the intended value of 300 Å. The one and two-step total *i*-layer thicknesses were 3960 Å and 3320 Å, differing by no more 1% from the intended values.

Next, the optical parameters of the *a*-Si:H-based layers of the structure will be considered [9]. In fact, a comparison of the dielectric function parameters in Fig. 3.6 yields interesting insights into the *a*-Si:H-based material components of the solar cell. First, the *p*-layer bandgap (1.865 eV) and broadening parameter (2.667 eV) deduced from a deposition on a smooth substrate are both significantly wider than those of the one-step *i*-layer (1.632 eV and 2.273 eV, respectively). This is expected given that CH_4 is used in the *p*-layer gas mixture to generate an *a*-$Si_{1-x}C_x$:H alloy [18]. The goal of this alloying is to increase J_{SC} by suppressing absorption in the inactive, window layer of the cell and to increase the voltage of the device as a result of widening the *p*-layer bandgap. Both alloying as well as doping are expected to broaden the Lorentz component of the dielectric function due to the introduction of disorder, charged defects, and potential fluctuations that can readily scatter excited carriers [21]. In contrast to the *p*-layer serving as a window, the *n*-layer at the back of

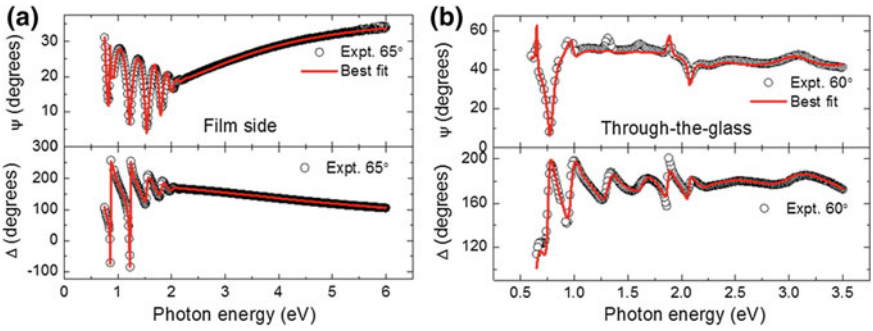


Fig. 3.5 **a** Film-side and **b** through-the-glass SE data in ψ and Δ (points) along with the corresponding best fits (lines) applying multi-sample analysis for the *a*-Si:H-based solar cell in the superstrate configuration with a single-step *i*-layer. The film-side data were collected at a location that avoids the silver back contact; the through-the-glass data were acquired at a nearby location that coincides with the silver back contact [23]

one-step i-layer		two-step i-layer
opaque	Ag	opaque
22 ± 1 Å	a-Si:H n-layer surf./interf. roughness	34 ± 1 Å
0.5	n-layer volume fraction	0.5
322 ± 11 Å	a-Si:H n-layer	311 ± 9 Å
1.611 ± 0.005 eV	Cody bandgap	1.611 eV
2.79 ± 0.02 eV	Cody-Lorentz broadening	2.79 eV
3833 ± 11 Å	a-Si:H i-layer	3198 ± 10 Å
1.632 ± 0.002 eV	Cody bandgap	1.671 ± 0.001 eV
1:1:2	SnO_2:F /p-layer/ i-layer	1:1:2
215 ± 3 Å	interface layer	168 ± 12 Å
0.25	SnO_2:F volume fraction	0.25
0.25	p-layer volume fraction	0.25
0.50	i-layer volume fraction	0.50
2:1:1	SnO_2:F /p-layer/ i-layer	2:1:1
90 ± 6 Å	interface layer	167 ± 8 Å
0.50	SnO_2:F volume fraction	0.50
0.25	p-layer volume fraction	0.25
0.25	i-layer volume fraction	0.25
3321 ± 20 Å	SnO_2:F layer	3027 ± 19 Å
232 Å	SiO_2 layer	232 Å
294 Å	SnO_2 layer	294 Å
−0.34° ± 0.16°	soda lime glass phase shift due to strain	−0.34°
610 Å	Sn side layer	610 Å

Fig. 3.6 Best fit parameters and their confidence limits deduced in the analysis of the SE data collected for *a*-Si:H solar cells with one-step (left) and two-step (right) *i*-layers. The values of the fixed thicknesses and volume fraction parameters in the analysis are also shown. Film-side SE data were analyzed simultaneously with through-the-glass SE data for each respective sample set [9]. The stress birefringence correction was fixed in the final best fit for the cell with the two-step *i*-layer

the device is not alloyed and shows a bandgap slightly narrower (1.611 eV) than that of the one-step *i*-layer (1.632 eV). This is likely an effect of doping which generates a strong sub-bandgap absorption feature that merges into the band-to-band absorption onset. The larger broadening parameter for the *n*-layer (2.79 eV) compared to the *i*-layer (2.27 eV) is consistent with the corresponding observation for the *p*-layer. Finally the bandgap deduced for the two-step *i*-layer (1.671 eV) is wider than that of the one-step *i*-layer (1.632 eV) as a result of the additional hydrogen incorporation due to the high H_2 dilution of the interface *i*-layer. The hydrogen

incorporated in the interface region can diffuse into the bulk *i*-layer during subsequent processing and modify its dielectric function [26].

3.2.4 External Quantum Efficiency Simulations

The simulation results for the low performance device with the one-step *i*-layer are shown in Fig. 3.7a along with the experimental EQE spectrum [9]. The simulation is based on the assumption that interfaces are specularly reflecting/transmitting, and that the EMA accounts for the non-ideality of interfaces relative to abrupt dielectric discontinuities. In the simulation, it is assumed that 100% collection occurs from the bulk *i*-layer with 0% collection from the *i*-layer components of the *p*/*i* interface layers. Overall reasonable agreement is observed between the simulation and experiment with the inset showing the difference between the simulated and measured spectra. The role of scattering and light trapping may be identified in the EQE when the measured spectra exceed the simulated spectra, implying that the difference in the inset of Fig. 3.7a is negative [5]. There appears to be a broad negative-trending feature that may be attributable to the beneficial effects of light scattering. This feature spans from 350 nm to 750 nm and reaches ~−0.05 in the simulated-measured EQE difference. Superimposed on this feature is a stronger positive difference of 0.08–0.12 over the range 550–650 nm, indicating reduction in measured EQE compared to the simulation. This stronger difference can be understood as described next.

Simulations were performed with various inactive *i*-layer components at the back of the *i*-layer adjacent to the *i*/*n* interface so as to improve the agreement between the simulation and experiment [9]. Although this is an over-simplified model and a carrier collection profile is expected, the approach provides insights into the origin of the discrepancy. The results of these simulations for different inactive layer thicknesses are shown in Fig. 3.7b and on an expanded scale in Fig. 3.8. Improved agreement is obtained for an inactive *i*-layer thickness of 600 Å adjacent to the *n*-layer. With this inactive layer, the maximum discrepancy between the simulated and measured EQE is decreased by approximately a factor of two. Since the bulk *i*-layer thickness determined from SE is 3833 ± 11 Å, the simulations suggest that carrier collection is most efficient within the *i*-layer thickness of ~3200 Å from the *p*/*i* interface. This indicates that ~3200 Å is likely to be the optimum *i*-layer thickness for collection in a single junction solar cell fabricated with these materials. Any further increase in thickness does not increase carrier collection due to limited hole diffusion length and a decrease in the built-in electric field that reduces the fill-factor [27, 28].

The simulated and measured EQE results for the high performance device with the two-step *i*-layer are shown in Fig. 3.9a [9]. For longer wavelengths, good agreement is observed between the two spectra, unlike the case of the lower efficiency solar cell, which was deposited with a thicker *i*-layer (~3800 Å). This supports the conclusion

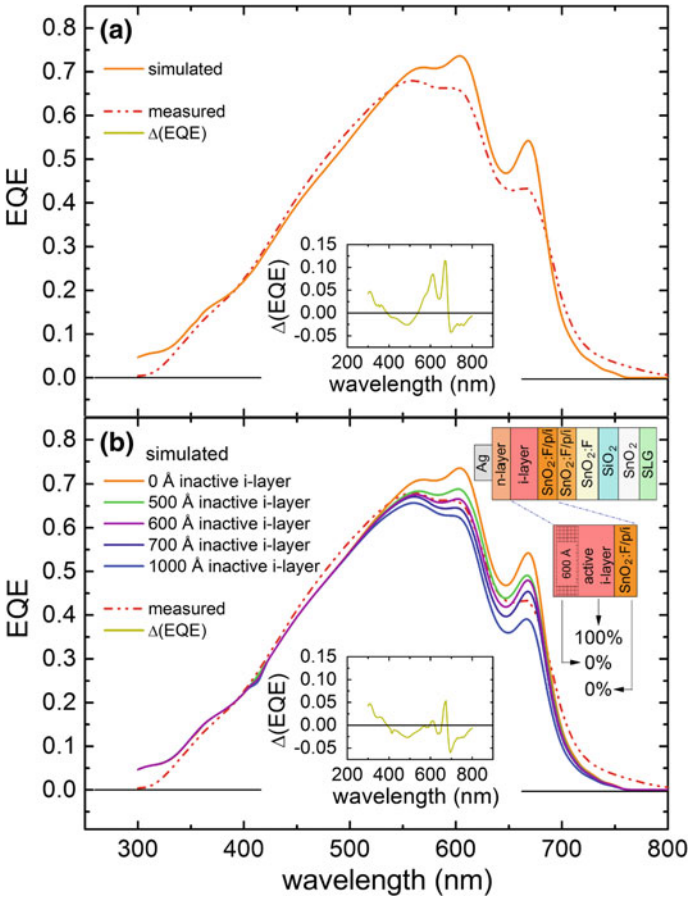


Fig. 3.7 **a** Measured external quantum efficiency (EQE) spectrum and the corresponding simulated result for the *a*-Si:H solar cell incorporating the one-step *i*-layer in the *p*-*i*-*n* superstrate configuration. The simulation is performed without any free parameters by applying the results from the SE analysis of the device as shown in Fig. 3.6 (left). In the simulation, it is assumed that only the bulk *i*-layer contributes to carrier collection. **b** Measured EQE spectrum for the solar cell with the one-step *i*-layer along with results simulated assuming inactive *i*-layer components of different thicknesses adjacent to the *i*/*n* interface. The insets in both panels show the difference ΔEQE between the simulated and the measured spectra; for the lower panel inset, the inactive layer thickness is taken as 600 Å in ΔEQE. The negative ΔEQE background can be attributed to collection via light trapping [9]

that the larger discrepancy between the simulated and measured EQE in the 550–675 nm spectral range for the lower performance cell is due to an *i*-layer thickness greater than the hole diffusion length. It should be noted, however, that in order to match the shorter wavelength range (400–550 nm) of the simulation to the experimental results for the high efficiency cell, it is necessary to assume that 50% collection occurs from the SnO_2:F/*p*/*i* interface layer adjacent to the *i*-layer.

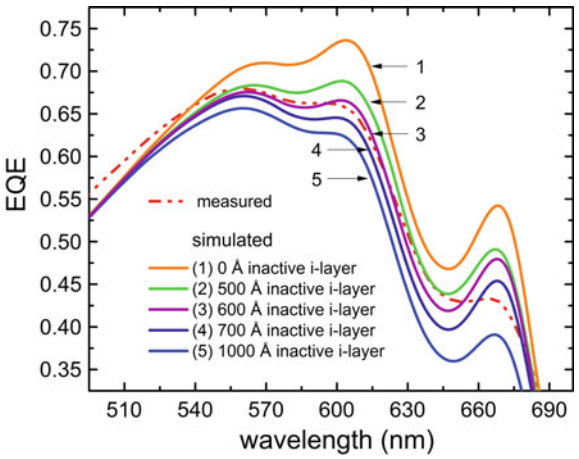


Fig. 3.8 Measured (broken line) and simulated (solid lines) EQE spectra from Fig. 3.7b on expanded scales. The simulations were computed by applying the assumption of inactive *i*-layer components of different thicknesses adjacent to the *i*/*n* interface. The goal is to achieve improved agreement between the simulated and measured spectra

This additional collection is likely to arise as a result of the 50 vol% undoped *a*-Si:H material component in the interface layer. This result is shown in Fig. 3.9b and indicates that, in a high quality *a*-Si:H solar cell with a two-step *i*-layer, the *i*-layer material in the interface layer also contributes to collection, in contrast to the observations for the cell with the one-step *i*-layer. The enhanced collection is attributed to the beneficial effect of protocrystalline Si:H incorporation at the *p*/*i* interface in the device with the two-step *i*-layer in terms of reduced recombination [13, 16]. In addition, the exposure of the *p*-layer to the high H_2-dilution deposition is likely to widen its bandgap and reduce its defect density, thereby improving its role as a doped window layer. Finally, the wider bandgap of the two-step *i*-layer suggests that additional H incorporated at the interface diffuses into the overlying bulk *i*-layer and may serve to improve its properties as well.

Figure 3.10 includes spectra in the losses for the solar cell with the one-step *i*-layer, which can also be calculated based on the best fit model of Fig. 3.6 (left) and the assumption that no carriers generated in layers other than the *i*-layer are collected [6]. These results enable a better understanding of how carrier collection can be improved through materials and thickness optimization and trade-offs. Overall, this study illustrates the usefulness of combining optical metrology based on SE with device performance simulations and EQE measurements in order to understand more fully carrier collection and the origins of optical and electronic losses in thin film Si:H. In this *a*–Si:H solar cell study, sensitivity is demonstrated for: (i) electrical losses from hole diffusion limitations near the *i*/*n* interface resulting from an overly thick *i*-layer and (ii) enhanced collection of carriers near the *p*/*i* interface resulting from the incorporation of protocrystalline Si:H with improved electronic quality at the (*p*-type *a*-$Si_{1-x}C_x$:H)/(bulk *a*-Si:H *i*-layer) interface. The application of the techniques to quantify the benefits of light trapping is also promising. The application of these SE-EQE studies to other PV technologies will be described in following sections.

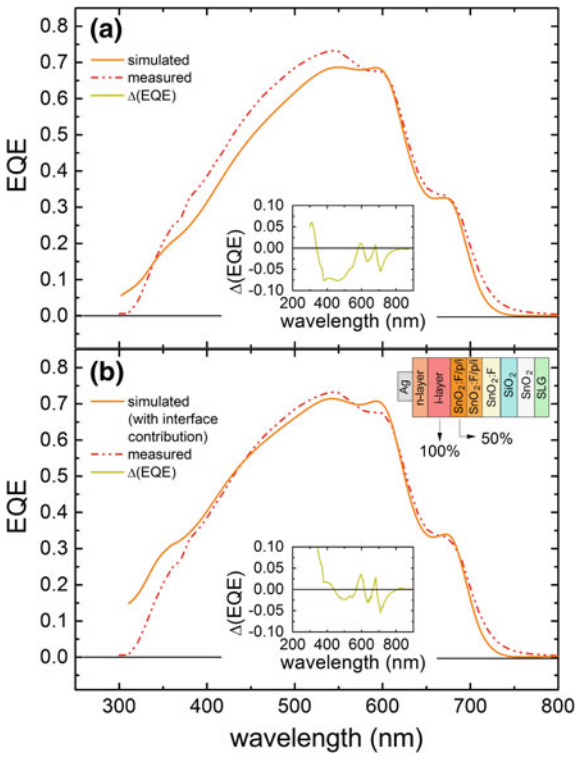


Fig. 3.9 Simulated and measured EQE results for the *a*-Si:H *p*-*i*-*n* solar cell in the superstrate configuration fabricated with the two-step *i*-layer. The simulations are based on the SE results shown in Fig. 3.6 (right). In **a**, it is assumed that only the bulk *i*-layer contributes to EQE with 100% photo-generated carrier collection from this layer; no free parameters are used. In **b**, it is assumed that, in addition to 100% collection from the bulk *i*-layer, collection also occurs from the *p*/*i* interface layer adjacent to the *i*-layer. For the interface layer, it is assumed that 50% of its spectral absorbance generates carriers that are collected. The insets show the difference between the simulated and the measured spectra (ΔEQE) [9]

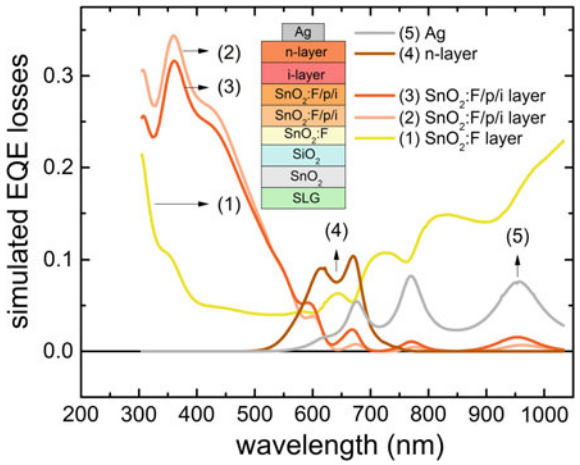


Fig. 3.10 Simulated EQE absorbance losses in the SnO_2:F layer, *n*-layer, two SnO_2:F/*p*-layer/*i*-layer interface layers, and Ag in the *a*-Si:H solar cell with a one-step *i*-layer. The simulation is based on the SE results shown in Fig. 3.6 (left)

3.3 Cadmium Telluride Solar Cells

3.3.1 Solar Cell Fabrication and Performance

A low-cost thin film photovoltaics technology utilizing polycrystalline CdTe absorbers has been established for generation of electric power with performance now competitive with or even exceeding that of multicrystalline silicon technology [29]. A superstrate configuration is applied for cells and modules, implying that the solar irradiance passes first through the soda lime glass and its coatings, the thickest being the transparent conducting oxide top contact, and then through the *n*-type window layer, before it is absorbed in the *p*-type CdTe which is typically 2–5 μm thick [30]. Thus, the solar cells assume a complicated optical structure; the solar irradiance encounters at least six thin films of different materials before absorption by the active layer. Figure 3.11 shows a schematic of a solar cell structure simplified in its depiction of the CdS/CdTe heterojunction. Recent EQE studies suggest that the most advanced devices fabricated by industry employ a graded homojunction design using II-VI alloys such as $CdTe_{1-x}Se_x$ [31]. As a result, analysis of the multilayer solar cell in terms of its layer thicknesses and their optical properties is a challenge, and the analysis of new device designs is likely to be even more challenging. Furthermore, on-line compatible solar cell characterization capabilities will be critical in the future for performance evaluations.

The coated glass used in the fabrication of the CdTe solar cell in this SE-EQE study [10] was NSG-Pilkington TEC™ 15, which is soda lime glass coated by a tri-layer in the sequence from the glass side to the film side as follows: [SnO_2 (20–30 nm)]/[SiO_2 (20–30 nm)]/[SnO_2:F (300–350 nm)], with nominal thicknesses given in parentheses. This TEC™ 15 structure was in turn coated by an additional layer of SnO_2 having a nominal thickness of 100 nm and serving as a high

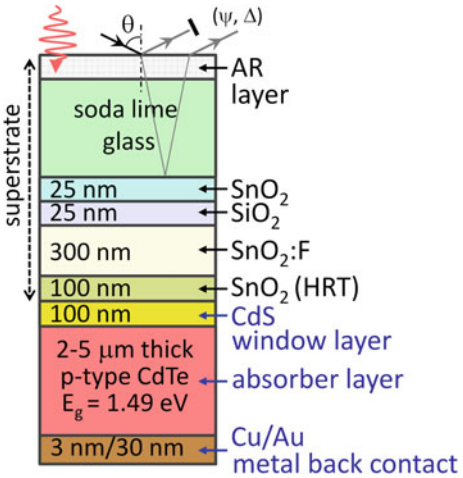


Fig. 3.11 Schematic of a CdTe solar cell of the type analyzed in this SE-EQE study. The starting structure for CdS/CdTe deposition corresponds to commercial TEC™ 15 glass coated with an anti-reflection layer and a SnO_2 high resistivity transparent (HRT) layer

Table 3.3 Performance parameters of the sputtered/$CdCl_2$-treated CdS/CdTe solar cell used for EQE measurements and simulations. The solar cell was deposited onto (TEC™ 15)/HRT transparent oxide coated soda lime glass and was completed by depositing a Cu/Au back contact and annealing the structure to promote Cu diffusion

Cell	V_{OC} (mV)	J_{SC} (mA/cm^2)	FF (%)	η (%)
(TEC™ 15)/HRT/(Sputtered CdS/CdTe)/Cu/Au	815	21.5	70.2	12.3

resistivity transparent (HRT) layer as shown in Fig. 3.11. Fabrication of the junction in this study entails depositions of CdS (~100 nm) and CdTe (~2000 nm) by magnetron sputtering on the surface of the (TEC™ 15)/HRT multilayer structure. Next, a standard 30 min $CdCl_2$ treatment step is performed on the as-deposited cell structure at a temperature of 387 °C. This step is followed by two thermal evaporation steps on the CdTe surface, resulting in an ~3 nm thick layer of Cu and an ~30 nm thick layer of Au serving as the back contact. Finally, the cell is completed by annealing the structure for 45 min at 150 °C to promote the diffusion of Cu into the underlying CdTe layer. Measurement of the solar cell performance using AM 1.5 illumination yielded an efficiency of 12.3% with parameters given in Table 3.3. Improvements in cell performance for the basic structure of Fig. 3.11 with sputtered CdS/CdTe can be made through the use of an optimized ZnO:Al top contact [32]. Improvement can also be made through the replacement of sputtering by close-space sublimation in the CdTe deposition process for higher material quality, and through additions of O_2 to the Ar gas in the CdS sputtering process for lower window layer absorbance [33]. These approaches as well as optimization of the contacts have led to efficiencies of ~16.5%, whereas the details for the highest efficiencies above 22% by industry have not been revealed.

3.3.2 *Component Layer Dielectric Functions*

The multilayer model for analysis of the CdS/CdTe solar cell structure requires identification of the complex dielectric functions $\varepsilon(E)$ of the component materials and the free parameters that may be used in analytical expressions for each [10]. In this section, the specification of $\varepsilon(E)$ as presented in Fig. 3.12 will be discussed in detail. These results are critical for the high quality fits to SE data in Sect. 3.3.3 and the EQE simulations in Sect. 3.3.4. For the CdTe and CdS semiconductors, the spectra in $\varepsilon(E)$ were expressed in parametric form through an oscillator sum [3]:

$$\varepsilon(E) = \varepsilon_{1o} + \varepsilon_{\mathrm{TL}}(E) + \sum_n \varepsilon_{\mathrm{CP},\,n}(E). \tag{3.1}$$

The first term on the right, ε_{1o}, is as a photon energy independent contribution to the real part of $\varepsilon(E)$. The complex second term, $\varepsilon_{\mathrm{TL}}(E)$, denotes a Tauc-Lorentz (TL) oscillator that generates smooth backgrounds in the real and imaginary parts of $\varepsilon(E)$. The imaginary part of $\varepsilon_{\mathrm{TL}}(E)$ is fixed to zero for energies below the bandgap

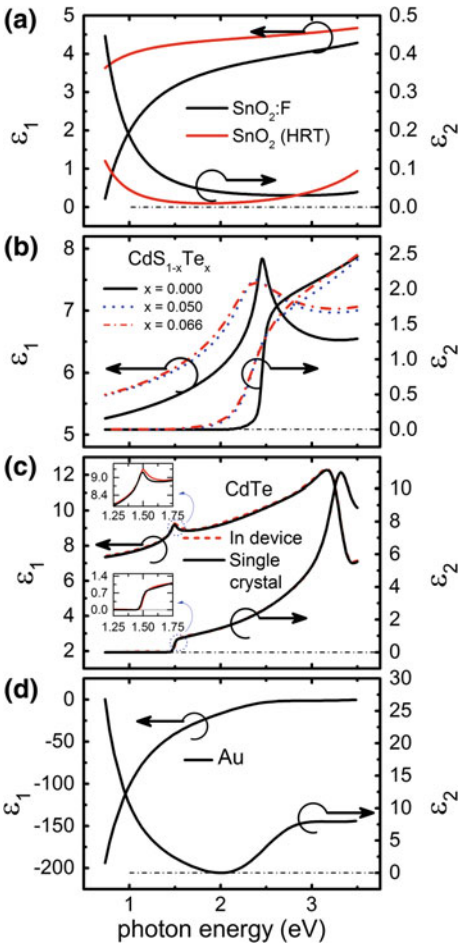


Fig. 3.12 Plots of parametric expressions describing the complex dielectric functions applied in EQE simulations of CdS/CdTe solar cells including **a** SnO_2:F front contact and SnO_2 high resistivity transparent layer; **b** $CdS_{1-x}Te_x$ alloys resulting from Te diffusion into the CdS layer; **c** CdTe in the solar cell and as a single crystal wafer; **d** Au back contact [10]. In some cases (SnO_2:F, SnO_2, $CdS_{0.95}Te_{0.05}$) best fit parameters from the solar cell structure were used for the generation of these spectra

E_0 of the lowest energy critical point (CP) by fixing the Tauc bandgap above E_0. Each of the CP oscillators in the third term of (3.1) is expressed by

$$\varepsilon_{\mathrm{CP},\,n}(E) = A_n\{\exp(i\phi_n)\}\{(\Gamma_n/2)/[E_n - E - i(\Gamma_n/2)]\}^{\mu_n}, \tag{3.2}$$

where A_n, E_n, Γ_n, μ_n, and ϕ_n denote the nth CP amplitude, resonance energy, broadening parameter, exponent, and phase, respectively. For CdTe, three critical points, E_0 [$n = 0$ in (3.2)], E_1, and $E_1 + \Delta_1$, contribute to the SE spectra over the photon energy range of 0.75–3.5 eV [34] and exhibit best fit resonance energies of 1.49 eV, 3.31 eV, and 3.89 eV, respectively, for the single crystal [35]. An Urbach tail given by $\varepsilon_2(E) = \varepsilon_2(E_0)\exp[(E\text{-}E_0)/E_u]$ is used to replace $\varepsilon_2(E)$ of (3.1) for $E < E_0$ where E_u is the Urbach energy [3]. In the SE analysis using (3.1) and (3.2) for CdTe, A_0, E_0, and Γ_0 are the variables, with all other parameters that define

$\varepsilon(E)$ being coupled to these variables. This analysis follows a methodology that has been developed to link the TL and CP oscillator parameters, the Urbach tail parameters, along with ε_{1o} for CdTe in (3.1) and (3.2) all either to E_0, which is controlled by the in-plane stress in the film [35], or to Γ_0, which is controlled by a single mean free path for excited electrons [36]. The void fraction in the CdTe can also be used as a free parameter to control the TL and CP oscillator amplitudes, as well as ε_{1o} independently. As examples, $\varepsilon(E)$ spectra for single crystal and thin film CdTe, the latter from a best fit of solar cell data, are shown in Fig. 3.12c [10].

The spectra in (ψ, Δ) for the completed CdTe solar cell are not as sensitive to $\varepsilon(E)$ of CdS due to its higher energy bandgap and a limited spectral range in through-the-glass SE. As a result, simplified $CdCl_2$-treated samples were deposited and analyzed by SE in advance of the studies of completed solar cells [10]. These samples consist of glass/CdS/CdTe with ~100 nm thick CdS layers deposited under the same conditions as the CdS in the solar cells. The layers of the (TEC™ 15)/HRT structure between the glass and the CdS show anti-reflection behavior, and by eliminating them, higher sensitivity to the $\varepsilon(E)$ spectra of CdS is possible. Equations (3.1) and (3.2) were used for these spectra with only one CP term that accounts for the CdS bandgap transition E_0. A comparison of the resulting parameters of the CdS E_0 CP with those of $CdS_{1-x}Te_x$ alloys characterized in previous studies [37] demonstrates that $\varepsilon(E)$ of the CdS of the heterojunction is affected most sensitively by the diffusion of Te from the overlying CdTe into CdS. This effect is sensitive to the thermal processing that the heterojunction undergoes. Thus, the composition x in $CdS_{1-x}Te_x$ can be adopted as a variable parameter that can then specify the E_0 CP parameters in $\varepsilon(E)$ and account for variations from as-deposited to treated CdS in the solar cell. In Fig. 3.12b, the $\varepsilon(E)$ spectra determined analytically are presented for (i) the CdS in the glass/CdS/CdTe sample after $CdCl_2$-treatment, having a Te content of $x = 0.066 \pm 0.007$ from the best fit, (ii) the CdS in the completed solar cell with $x = 0.05$, the composition that is applicable for the EQE simulation, and (iii) a CdS layer deposited individually with $x = 0$ [10]. An increase in the Te content in CdS from $x = 0$ to $x = 0.066$ leads to a decrease in the bandgap E_0 from 2.42 to 2.30 eV and an increase in the bandgap broadening Γ_0 from 0.10 to 0.43 eV.

Turning next to the glass and its coatings, procedures have been presented elsewhere that describe the measurement of $\varepsilon(E)$ used in this study for soda lime glass and for the two thinnest (TEC™ 15)/HRT components deposited first, i.e. the SnO_2 and SiO_2 [38]. The study of [38] provides the analytical expressions that best fit the spectra in $\varepsilon(E)$. The $\varepsilon(E)$ spectra for SnO_2:F and the HRT layer, the two thickest layers of the (TEC™ 15)/HRT structure, were expressed as

$$\varepsilon(E) = \varepsilon_{1o} + \varepsilon_D(E) + \sum_n \varepsilon_{\mathrm{CP},\,n}(E). \tag{3.3}$$

including the constant contribution to the real part of $\varepsilon(E)$, a term associated with intraband transitions according to the free electron description of Drude, and a sum of individual oscillators associated with interband CP transitions [3]. The free electron description is given by

$$\varepsilon_D(E) = \frac{-\hbar^2}{\varepsilon_0 \rho(\tau \cdot E^2 + i\hbar E)} \tag{3.4}$$

Here $\hbar = h/2\pi$ where h represents Planck's constant, ε_0 represents the free space permittivity, and ρ and τ represent the resistivity and mean free time associated with the free electrons, the former given by $\rho = m_e^*/Ne^2\tau = 1/e\mu N$. In this expression, m_e^* is the effective mass of the electron, and e, μ, and N represent the charge of the electron, its mobility, and its concentration, respectively. In SE analysis using (3.3) and (3.4), ε_{1o}, ρ, and τ were the variable parameters for the SnO_2:F, whereas ε_{1o} was the only variable for the HRT layer. The resulting $\varepsilon(E)$ spectra obtained in the SE analysis of the completed solar cell are given in Fig. 3.12a [10].

Finally, the $\varepsilon(E)$ spectra used to describe the Au back contact in this investigation were determined from an opaque film, deposited to a thickness of 100 nm on a glass substrate under the same conditions of evaporation as those for the back contacts in solar cells [38]. Ex situ SE was performed at multiple angles immediately after Au deposition, and the results were analyzed using a model with bulk and roughness layers. The resulting $\varepsilon(E)$ spectra were fitted using the expressions of (3.3) and (3.4), including two CP terms of (3.2) having best fit CP energies of 2.52 and 3.89 eV. The final spectra appear in Fig. 3.12d. Additional details of the models for the $\varepsilon(E)$ spectra relevant to this SE-EQE study and the resulting best fit parameters are given in the next sub-section which first addresses SE measurement and analysis.

3.3.3 *Spectroscopic Ellipsometry Analysis*

The ex situ SE data for the completed CdS/CdTe solar cell were acquired through the soda lime glass at an angle of incidence of 50° over the range of photon energy E from 0.75 to 3.5 eV [4, 10]. The limit of $E = 3.5$ eV originates from absorption in the glass. In through-the-glass SE, a focusing probe is applied with an aperture to collect only the beam that undergoes two passes through the glass, forward and backward, upon reflection. By its optical nature, this approach is non-invasive and can be applied in on-line configurations such that the ellipsometer scans the underside, i.e. glass side, of the panel moving along a conveyer [39]. Thus, with the aperture, isolation and detection of the second reflection from the glass/film-stack interface is possible. The first reflection from the ambient/glass interface is almost fully blocked as are the third and higher reflections. Thus, the polarization state changes that occur upon forward and backward transmission of the beam obliquely through the ambient/glass interface must be included in data reduction. In an ideal SE measurement through-the-glass, when only the beam reflected from the glass/film-stack interface is detected, the SE angles (ψ, Δ) in the measurement are given by: $\tan\psi \exp(i\Delta) = [(\cos\theta_0 + N_s\cos\theta_1)/(N_s\cos\theta_0 + \cos\theta_1)]^2 [\tan\psi' \exp(i\Delta')]$. In this expression, $N_s = \varepsilon_s^{1/2}$ is the index of refraction for the glass, complex in general,

with ε_s as its dielectric function; θ_0 and θ_1 are the real incidence and complex transmission angles, respectively, at the ambient/glass interface; and $\tan\psi' \exp(i\Delta') \equiv r_p/r_s$ is the complex amplitude reflection ratio for the glass/film-stack interface with glass as the semi-infinite ambient medium.

The SE data in the form of $(N, C, S) = (\cos 2\psi, \sin 2\psi \cos\Delta, \sin 2\psi \sin\Delta)$ are fitted using non-linear least squares regression analysis with the Levenberg-Marquardt algorithm. The goal is to minimize the root mean square error (MSE) which is defined according to the expression

$$\sigma_{NCS} = \sqrt{\frac{1}{3n-p}\sum_{i=1}^{n}\left[\left(\frac{N_i^{(e)}-N_i^{(c)}}{\sigma_{N,i}^{(e)}}\right)^2+\left(\frac{C_i^{(e)}-C_i^{(c)}}{\sigma_{C,i}^{(e)}}\right)^2+\left(\frac{S_i^{(e)}-S_i^{(c)}}{\sigma_{S,i}^{(e)}}\right)^2\right]}, \tag{3.5}$$

where n and p are the numbers of spectral points and fitting parameters, respectively, and the index i spans the spectra. The standard deviations in the data, denoted $\sigma_{j,i}^{(e)}$; $j = N, C, S$, are estimated as 10^{-3} for the multichannel ellipsometer used in these CdTe studies (M-2000, J.A. Woollam Co., Inc) [40].

The goal in the analysis of through-the-glass SE data for the CdS/CdTe solar cell is to determine the p photon energy independent parameters in the p-parameter model that best describes the data, while tracking σ_{NCS} and the associated confidence limits versus p [4, 10]. The p parameters include layer thicknesses, compositions in the EMA, and sample and measurement non-idealities, e.g. thickness non-uniformity. Parameters in expressions for $\varepsilon(E)$ of the component materials are also included, as emphasized in Sect. 3.3.2. Individual parameters are prioritized based on the extent to which they reduce σ_{NCS}. As a result, parameters are identified that either can be assigned fixed nominal values owing to a lack of sensitivity in the data, or can be eliminated owing to their inability to improve the fit in spite of added complexity. The initial $p = 0$ model used in SE data analysis is based on several assumptions, including fixed nominal thicknesses for all component layers of the multilayer structure: $SnO_2/SiO_2/SnO_2$:F/HRT/CdS/CdTe/Au, fixed parameters from the databases that define the $\varepsilon(E)$ spectra or fixed database $\varepsilon(E)$ spectra themselves, no interface roughness, and no optical and measurement non-idealities. For the case of CdS, for example, the database dielectric function of $CdS_{1-x}Te_x$ with fixed $x = 0.066$ was used as shown in Fig. 3.12b. For CdTe, a parametric expression for $\varepsilon(E)$ with parameters appropriate for single crystal CdTe was used as shown in Fig. 3.12c. Starting from this initial structural/optical model, 24 variable parameters are evaluated in two sets, 11 parameters predominantly related to structure and 13 parameters related to the $\varepsilon(E)$ spectra.

As demonstrated in Table 3.4 and Fig. 3.13, the first set of parameters includes only thicknesses and two optical non-idealities. The first non-ideality parameter describes possible spatial non-uniformity in the thickness of the CdTe, observed over the area of the beam and modeled assuming averages of r_p and r_s weighted according to the area [41]. The second non-ideality parameter describes a small

fraction of the reflection from the ambient/glass interface that may be collected inadvertently together with the dominant desired reflection from the glass/film-stack interface. In the analysis of this second non-ideality, an incoherent summation of the irradiances in these two reflections is performed. For the first set of parameters, Fig. 3.13a (squares) shows the sequence of steps, 62 in all, performed in the trial fits in order of decreasing best fit σ_{NCS} values. Table 3.4 shows that the best fit model having one free parameter is obtained by varying the thickness of the CdTe bulk layer, and the best two-parameter model is obtained by additionally varying the thickness of the CdS bulk layer. After completion of the multi-step analysis overall, the best fit thicknesses of the CdTe and CdS bulk layers are 1815 ± 5 nm and 67 ± 4 nm, respectively. Parameters 9 and 10 in Table 3.4 are the thicknesses of the thin SiO_2 and SnO_2 of the TEC™ 15, whose best fit values are 27 ± 1 nm and 21 ± 1 nm, respectively, after completion of the analysis. As these thicknesses are close to the nominal values, 20–30 nm, variations from the nominal values yielding the best fit values do not generate a lower σ_{NCS}. In fact, σ_{NCS} increases slightly due to the fact that p increases in (3.5). As a result, in typical analyses the thicknesses of the SnO_2 and SiO_2 layers can be fixed at nominal values. Addition of parameter 11, CdTe thickness non-uniformity which is the final parameter of the first set, is also not justifiable from Table 3.4. Thus, the nominal value (0 nm) is suitable and implies either CdTe thickness uniformity or a lack of sensitivity of the data to non-uniformity.

The second set of 13 additional photon energy independent parameters in Table 3.4 and Fig. 3.13b are generally associated with the component layer optical properties and are introduced for further improvements in the best fits. This second set enables variations in $\varepsilon(E)$ for the SnO_2:F, HRT, and CdTe component layers through analytical expressions as described in Sect. 3.3.2. Fixed $\varepsilon(E)$ spectra were used, however, for all other cell components, i.e. the soda lime glass, SnO_2, SiO_2, CdS, and back contact Au. The interface layer compositions are also included in the second set since these in turn define the $\varepsilon(E)$ spectra of the interface layers through the EMA. Finally, the stress-induced birefringence in the glass is included, modeled as a photon energy dependent shift in the SE angle Δ through the expression $\Delta[\Delta(E)] = E(a_1c_1 + a_2c_2E^2)$, where E is the photon energy in eV, $a_1 = 0.4032$ and $a_2 = 0.0655$ are unitless constants, and c_1 and c_2 are the variable parameters defining birefringence and its dispersion in the fitting.

Among the 13 variables describing the optical properties, i.e. the second set of Table 3.4, the resistivity associated with the free electron component of $\varepsilon(E)$ for SnO_2:F generates the largest reduction in σ_{NCS} starting from the best fit result in which nominal values are assigned and fixed for all 13 parameters. The best fit resistivity obtained after completion of the multistep analysis overall is (3.5 ± 0.3) × 10^{-4} Ω-cm. The optical property variables that are the second and third most effective in reducing σ_{NCS} in Table 3.4 are the compositions that control the $\varepsilon(E)$ spectra associated with the rough region at the CdTe/Au interface to the back contact. This region has been modeled assuming two layers, as indicated by the entries of Table 3.4, with starting CdTe/Au compositions of 67/33 vol% for the layer adjacent to the CdTe and 33/67 vol% for the layer adjacent to the Au contact.

Table 3.4 Two sets of variable parameters used in non-linear least squares regression analysis of SE spectra acquired through-the-glass for a CdS/CdTe solar cell. All parameters are independent of photon energy. The first set includes thicknesses and non-ideality parameters, and the second set includes parameters defining $\varepsilon(E)$ [10]. The parameters were introduced one by one in order to identify the p-parameter model that minimizes σ_{NCS}, the root mean square error

Parameter #		Parameter generating the largest reduction in σ_{NCS}	σ_{NCS}
Thickness and optical non-ideality parameters	1	CdTe: thickness of bulk layer	157.4
	2	CdS: thickness of bulk layer	117.7
	3	CdS/CdTe: thickness of interface layer (nom.: 0.5/0.5)	90.7
	4	CdTe/Au: thickness of front interface layer (nom.: 0.67/0.33)	76.3
	5	HRT: thickness of bulk layer	61.2
	6	SnO_2:F: thickness of layer	54.2
	7	Glass: fractional irradiance from top reflection (non-ideality)	52.3
	8	HRT/CdS: thickness of interface layer (nom.: 0.5/0.5)	51.0
	9	SiO_2: thickness of layer	51.1
	10	SnO_2: thickness of layer	51.2
	11	CdTe: thickness non-uniformity of bulk layer (non-ideality)	51.3
Optical property parameters	12	SnO_2:F: resistivity of layer	48.4
	13	CdTe/Au: CdTe volume fraction in front interface layer (nom.: 0.67/0.33)	46.3
	14	CdTe/Au: CdTe volume fraction in back (opaque) interface layer (nom.: 0.33/0.67)	37.3
	15	CdTe: energy of lowest energy CP (bandgap) for bulk layer	36.2
	16	Glass: first coefficient of stress birefringence	35.3
	17	Glass: second coefficient of stress birefringence	34.8
	18	CdTe: amplitude of lowest energy CP for bulk layer	34.3
	19	CdTe: broadening of lowest energy CP for bulk layer	34.1
	20	HRT: ε_1 constant offset, ε_{1o}, of bulk layer	33.8
	21	SnO_2:F: ε_1 constant offset, ε_{1o}, of layer	32.4
	22	CdS/CdTe: CdS volume fraction in interface layer (nom.: 0.5/0.5)	30.5
	23	SnO_2:F: electron mean free time of layer	30.5
	24	HRT/CdS: CdS volume fraction in interface layer (nom.: 0.5/0.5)	30.5

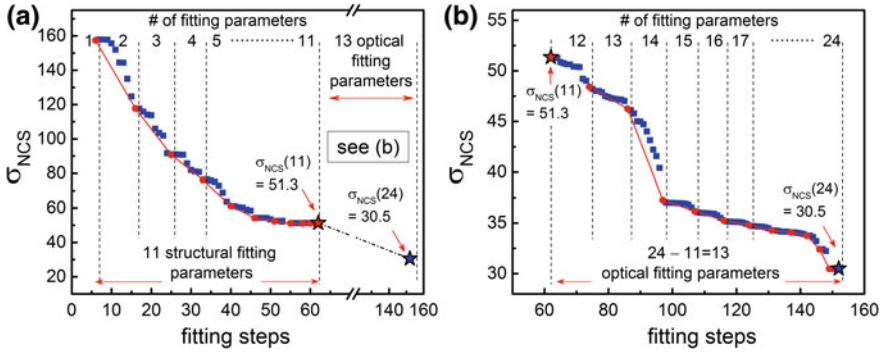


Fig. 3.13 Results from non-linear least squares regression analyses of SE data acquired in through-the-glass mode for a CdS/CdTe heterojunction solar cell. These results demonstrate step-wise improvements in the quality of fit made possible by introducing variable parameters one at a time [10]. In **a**, eleven variables related to structure and non-ideality have been identified in 62 steps (squares). In **b**, thirteen variables related to optical properties have been identified in 88 additional steps. Circles connected by lines in both plots indicate the best *p*-parameter fit for each of the two parameter sets as elaborated by the listing in Table 3.4

In the multilayer model, the latter layer acts as the semi-infinite substrate medium due to its high Au content and resulting opacity. In the complete analysis that yields the best fit overall, these CdTe/Au compositions are (88 ± 3)/(12 ± 3) vol% for the layer adjacent to the CdTe and (26 ± 2)/(74 ± 2) vol% for the opaque layer. The optical property variables that most weakly affect σ_{NCS} are the EMA compositions of the two layers at the HRT/CdS and CdS/CdTe interfaces. In the complete analysis, best fit CdS contents of 55 ± 8 vol% and 48 ± 10 vol% are obtained for the HRT/CdS and CdS/CdTe interface layers, respectively. As a result, it is suggested that these parameters can be set at their nominal starting values of 50/50 vol%. The predominant effect that generates well-defined layers at these interfaces is believed to be microscopic roughness induced by the HRT layer on which the CdS/CdTe structure is deposited since both HRT/CdS and CdS/CdTe interface layer thicknesses, 33 ± 2 nm and 31 ± 3, respectively, are close to the surface roughness thickness value deduced in an SE analysis of the uncoated HRT layer. In addition to these two CdS interface compositions, the mean free time τ associated with the free electron component of $\varepsilon(E)$ for SnO_2:F also affects σ_{NCS} only weakly, implying that τ for the solar cell structure of Table 3.4 matches that of the uncoated SnO_2:F measured to generate the dielectric function entered into the database. The value of $\tau = (7.1 \pm 0.5) \times 10^{-15}$ s is determined as the best fit result in the complete analysis.

Figure 3.14 presents experimental spectra (points) in (*N*, *C*, *S*) along with the best fit simulation (lines) for the 24 variable parameter model of Table 3.4 and Fig. 3.13 [10]. The σ_{NCS} value for this final, complete model is 30.5 as given in the table and figure. In Fig. 3.15, the complete structural/optical model for the solar cell is depicted that results upon variation of all 24 parameters, including the best fit

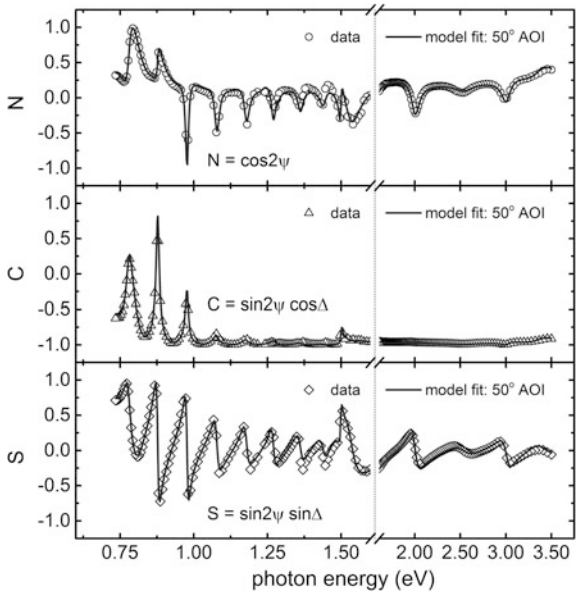


Fig. 3.14 Measured ellipsometry spectra in $(N, C, S) = (\cos 2\psi, \sin 2\psi \cos\Delta, \sin 2\psi \sin\Delta)$ and the associated best fit results for a SE study in through-the-glass mode for the CdS/CdTe solar cell [10]. The structural, optical non-ideality, and optical property parameters varied in the analysis are given in Table 3.4; values that generate the best fit along with their confidence limits are included in Fig. 3.15

thicknesses, compositional parameters, and key optical property parameters along with their confidence limits. The best fit optical property parameters from the step-by-step analysis of Table 3.4 and Fig. 3.13b provide insights into the physical and electronic properties of the materials as described in the last paragraphs of this section.

The best fit resistivity and thickness values for the SnO_2:F layer of the TEC™ 15 shown in Fig. 3.15 lead to a sheet resistance value of 11.5 ± 1.1 Ω/sq. Also from the resistivity and mean free time, an electron concentration of 5.43×10^{20} cm^{-3} and mobility of 33 cm^2/V s are obtained, assuming an electron effective mass of $m_e^* = 0.38 m_e$ for SnO_2:F [42]. In addition to the SnO_2:F free electron parameters, the constant term in $\varepsilon_1(E)$ serves as a variable for each of the SnO_2:F and SnO_2 HRT materials. The purpose of these variables is to take into account possible small differences in the concentration of electrons undergoing interband transitions in each of these materials. Figure 3.12a provides a comparison of the analytical expressions for the $\varepsilon(E)$ spectra of the SnO_2:F and HRT resulting from the best fit parameters. The differences that decrease with increasing photon energy are caused by the differences in the resistivity of the layers. The lower ε_2 in the near ultraviolet for the SnO_2:F may be attributed to a blue-shift of the optical gap due to degenerate F doping, i.e. the Burstein-Moss band filling effect [43, 44].

As listed in Table 3.4, the CP parameters A_0, E_0, and Γ_0 that characterize the $\varepsilon(E)$ spectra for the material of the CdTe bulk layer have been used as variables, and the spectra incorporating the best fit values are plotted in Fig. 3.12c together with the $\varepsilon(E)$ spectra of single crystalline CdTe. Although close agreement between the two spectra is noted, small differences in E_0 and Γ_0 are observed, highlighted by an

layer (composition, properties)	thickness
CdTe/Au intf. (0.26 ± 0.02/0.74 ± 0.02)	opaque
CdTe/Au intf. (0.88 ± 0.03/0.12 ± 0.03)	184 ± 10 nm
CdTe bulk layer stress X = 0.07 ± 0.06 GPa mean free path λ = 320 ± 130 nm	1815 ± 5 nm
CdS/CdTe intf. (0.48 ± 0.10/0.52 ± 0.10)	31 ± 3 nm
CdS bulk layer (Te content x = 0.066)	67 ± 4 nm
HRT/CdS intf. (0.45 ± 0.08/0.55 ± 0.08)	33 ± 2 nm
HRT layer	84 ± 3 nm
SnO_2:F layer resistivity ρ = (3.5 ± 0.3) x 10^{-4} Ω cm scattering time τ = (7.1 ± 0.5) x 10^{-15} s	304 ± 3 nm
SiO_2 layer	27 ± 1 nm
SnO_2 layer	21 ± 1 nm
soda lime glass stress birefringence c_1 stress birefringence dispersion c_2	3.16 mm 4.5 ± 1.2 °/eV −2.4 ± 1.0 °/eV^3

Fig. 3.15 Multilayer structure for a CdS/CdTe solar cell on SnO_2 HRT coated TEC™ 15 glass with the best fit parameters that control the structural properties and dielectric functions. The confidence limits on each of the deduced variable parameters are also provided

inset in Fig. 3.12c. The difference in E_0 is interpreted as the effect of an in-plane compressive stress of 0.07 ± 0.06 GPa, clearly near the lower limit of optical detection [35]. The difference in Γ_0 is interpreted in terms of a reduced electron mean free path of 320 ± 120 nm, likely due to grain boundary scattering, and clearly near the upper limit of optical detection in this case [36]. In fact, the mean free path provides a grain size estimate based on the assumption that grain boundary scattering limits the mean free path. The capabilities of SE analysis are more effective for characterizing the as-deposited CdTe of the solar cell in this study for which the deduced stress, 0.52 ± 0.07 GPa, is well above the lower detection limit, and the mean path, 26 ± 8 nm, is well below the upper detection limit [45].

Considering that the 24 structural and optical property parameters of Table 3.4, including the 19 highlighted in Fig. 3.15, are all determined simultaneously, corroborations of the deduced values are sought [10]. The effective thickness (or volume/area) in Fig. 3.15 for CdS is 100 ± 6 nm and that of CdTe is 1997 ± 15 nm. These values are in close agreement with the intended thicknesses of 100 nm for CdS and 2000 nm for CdTe, also serving as the nominal values in the analysis of Table 3.4 and Fig. 3.13. Figure 3.16 shows a cross-sectional transmission electron

(a)

Layer stack	SE	Eff. SE	XTEM
CdTe/Au intf. (0.26 ± 0.02 / 0.74 ± 0.02)	opaque		
CdTe/Au intf. (0.88 ± 0.03 / 0.12 ± 0.03)	184 ± 10 nm		
CdTe bulk layer stress X = 0.07 ± 0.06 GPa mean free path λ = 320 ± 130 nm	1815 ± 5 nm	1997 ± 15 nm	1932 nm
CdS/CdTe intf. (0.48 ± 0.10 / 0.52 ± 0.10)	31 ± 3 nm		
CdS bulk layer (Te content x = 0.066)	67 ± 4 nm	100 ± 6 nm	94 nm
HRT/CdS intf. (0.45 ± 0.08 / 0.55 ± 0.08)	33 ± 2 nm		
HRT layer	84 ± 3 nm		
SnO_2:F layer resistivity ρ = (3.5 ± 0.3) x 10^{-4} Ω cm scattering time τ = (7.1 ± 0.5) x 10^{-15} s	304 ± 3 nm	403 ± 6 nm	428 nm
SiO_2 layer	27 ± 1 nm	27 ± 1 nm	26 nm
SnO_2 layer	21 ± 1 nm	21 ± 1 nm	24 nm
soda lime glass stress birefringence c_1 stress birefringence dispersion c_2	3.16 mm 4.5 ± 1.2 $^{-6}$/eV −2.4 ± 1.0 $^{-6}$/eV^2		

(b)

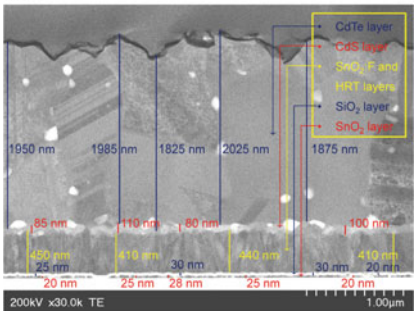


Fig. 3.16 **a** Best fit layer thicknesses and effective medium compositions for the CdS/CdTe solar cell resulting from the multilayer analysis of Fig. 3.13. The second column from the right shows the SE-determined effective thicknesses for the layers, calculated as the layer material volume/area, i.e. the product of the material volume fraction and thickness of the layer, summed over the layers that incorporate the material. The first column from the right in (**a**) lists thicknesses from (**b**) the cross-sectional transmission electron micrograph (XTEM), which shows five well-defined layers starting from the glass at the bottom of the image: (i) SnO_2; (ii) SiO_2; (iii) SnO_2:F/HRT top contact; (iv) CdS window layer; and (v) CdTe absorber. The thicknesses were obtained from the image as averages over lengths of ∼4 μm [10]

micrograph (XTEM) of the CdS/CdTe solar cell for additional corroboration of the SE-deduced thicknesses. The tabulated thicknesses of the solar cell layers from XTEM in Fig. 3.16, obtained as averages over ∼4 μm image lengths, are in reasonable accord with the effective thicknesses from SE. Because the layers of SnO_2:F and SnO_2 HRT are indistinguishable in the image, the sum of these two thicknesses is compared. In addition to these deduced thickness values, the best fit variable optical parameters are also reasonable. For example, the bandgap and broadening parameter of the bulk layer CdTe are in close agreement with the corresponding characteristics of the single crystal, an effect attributed to the $CdCl_2$ treatment. This treatment results in a low stress level and a long excited carrier mean free path, indicated in Fig. 3.15, in comparison with the as-deposited CdTe. In fact, the 320 nm mean free path is consistent with the in-plane grain size in the XTEM image of Fig. 3.16. The SnO_2:F sheet resistance value of 11.5 ± 1.1 Ω/sq, deduced from the results of Fig. 3.15, is also in reasonable agreement with the nominal value of 15 Ω/sq for (TEC™ 15)/HRT. The overall agreement of the structural and optical parameters with expected values and XTEM results demonstrates that through-the-glass SE is an effective method for non-invasive analysis of CdS/CdTe solar cells. This method is capable of measuring several key characteristics of the multilayer solar cell at a single location off-line, or at multiple locations via mapping on-line [39].

3.3.4 External Quantum Efficiency Simulations

Figure 3.17a presents the EQE spectrum and total current density J measured for the CdS/CdTe solar cell of Figs. 3.15 and 3.16, obtained under a reverse bias of −0.8 V [10]. The reverse bias is applied to promote the separation of photo-generated electrons and holes as well as their collection at the contacts. No appreciable increase in the current density occurs upon further increase of the reverse bias magnitude above 0.8 V. The best fit multilayer structural parameters in Fig. 3.15 together with the $\varepsilon(E)$ spectra of the layers, the latter from the database with best fit parameters as needed, enable prediction of the EQE spectrum and J. The prediction is performed on the basis of the assigned active layers for the cell. In the simulation of Fig. 3.17a, 100% collection is assumed for the electrons and holes photo-generated within the CdS/CdTe interface layer, the CdTe bulk layer, and the CdTe component within the layer of the CdTe/Au interface that is adjacent to the CdTe bulk layer, as shown in the inset of Fig. 3.17a. From these assumptions, it is implied that no collection at all occurs due to carriers photo-generated within the CdS bulk layer and in the CdTe/Au interface layer adjacent to the Au. Excellent agreement between the simulation and the measurement in Fig. 3.17a is observed.

For some SE-deduced parameters, however, EQE enables higher measurement and analysis sensitivity than SE because the CdTe cell itself acts as a sensitive detector for photon absorbance spectroscopy through the EQE measurement. For example, EQE appears to exhibit higher sensitivity in determining the Te content x in $CdS_{1-x}Te_x$. The CdS layer $\varepsilon(E)$ spectra selected for analysis of the SE measurements on the device of Fig. 3.15 was obtained assuming the fixed composition of $x = 0.066$ as shown in Fig. 3.12b. This result was deduced from the $\varepsilon(E)$ spectra for the CdS bulk layer in the simplified $CdCl_2$-treated glass/CdS/CdTe sample. For the EQE, however, slightly closer agreement between the simulation and the measurement is possible through the reduction of x to 0.050 in generating the $CdS_{1-x}Te_x$ $\varepsilon(E)$ spectra. In fact, this modification was incorporated in the simulation shown in Fig. 3.17a. By modifying the $\varepsilon(E)$ spectra for CdS used in the database as described, the close agreement in Fig. 3.17a is possible without the use of free parameters.

Figure 3.17b presents the EQE measurement results for the solar cell of Fig. 3.17a but at 0 V bias. Because a 1.3% decrease in collection is observed between −0.8 V and 0 V bias, a weak effect of voltage-dependent collection is identified for this cell [46]. As a result, a reduction from 100% collection found at −0.8 V, as shown in the Fig. 3.17a inset, must be incorporated into the EQE simulation to account for the results of Fig. 3.17b obtained at 0 V. In fact, the close agreement between the measured and simulated EQE in Fig. 3.17b is regained assuming 99% collection from the 1815 nm CdTe bulk layer and 30% collection from the CdTe component of the 184 nm layer of the CdTe/Au interface, as indicated in the inset of Fig. 3.17b [10]. Thus, the simulation in Fig. 3.17b represents a fit with two free parameters that identifies the origins of the electronic losses acting to reduce the short-circuit current density. From the results in both

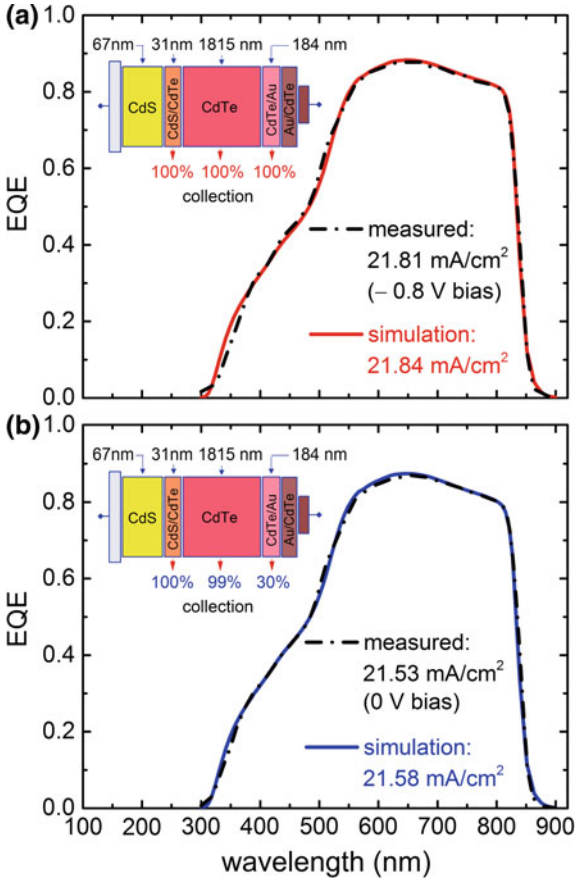


Fig. 3.17 Measured (broken lines) and simulated (solid lines) external quantum efficiency (EQE) spectra for the CdS/CdTe solar cell at bias voltages of **a** −0.8 V and **b** 0 V [10]. In (**a**) the simulation is based on the assumptions of 100% collection of photo-generated carriers from the following three layers: the CdS/CdTe interface layer 31 nm thick, the CdTe bulk layer 1815 nm thick, and the CdTe component of the CdTe/Au interface layer 184 nm thick, as depicted in the inset. In (**b**) the simulation is based on 100% collection from the CdS/CdTe interface, 99% collection from the CdTe bulk, and 30% collection from the CdTe of the CdTe/Au interface

panels of Fig. 3.17, one can conclude that the simulations developed on the basis of the SE analysis are consistent not only with the EQE spectral shapes, but also with the small changes in these shapes that occur under reverse bias. Because of the high accuracy of the model for EQE, future studies are expected to provide a greater understanding of the electronic losses at short circuit as well as the voltage dependent collection effect. Section 3.4 provides a review of advanced studies in this direction applied to thin $CuIn_{1-x}Ga_xSe_2$ solar cells.

Given this capability, the absorbance spectra for each of the device layers and the reflectance spectrum for the overall device can be calculated as shown in Fig. 3.18. Each of these spectra can be converted to a photo-generated current loss by integration over the wavelength range from 300 to 900 nm, applying AM 1.5 incident solar irradiance [38]. Figure 3.18 shows that the reflectance from the cell constitutes a 2.90 mA/cm^2 loss, and the soda lime glass 3.16 mm in thickness accounts for a 1.34 mA/cm^2 loss in terms of absorption. In addition, a total current of 1.52 mA/cm^2 is lost through absorption within the components of the TEC™ 15

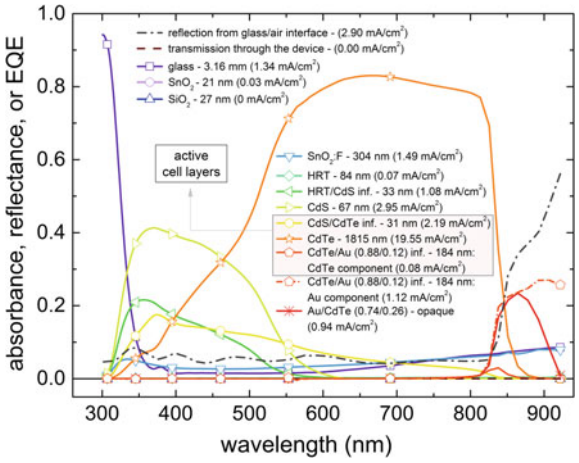


Fig. 3.18 Absorbance spectra and EQE contributions for the component layers of the CdTe solar cell structure also expressed in terms of photocurrent densities in the legend [38]. The CdS/CdTe interface layer, the CdTe bulk layer, and the CdTe component of the first CdTe/Au interface layer serve as active layers as indicated, meaning that the current can contribute to EQE (fully under reverse bias). The dot-dashed line without symbols indicates the reflectance, which represents a loss. The photocurrent densities are calculated by integrating the spectra over the wavelength range from 300 nm to 900 nm assuming AM 1.5 incident solar irradiance

including SnO_2 and SnO_2:F, and 4.10 mA/cm^2 is lost through absorption within the HRT and CdS. Finally, photocurrent of 1.12 mA/cm^2 is lost through absorption by the Au component of the 0.88/0.12 CdTe/Au interface layer adjacent to the CdTe and ~0.94 mA/cm^2 is lost within the semi-infinite CdTe/Au interface layer. Only photons of energy within or below the CdTe absorption edge enter the CdTe/Au interface layers and are absorbed as losses. Some current losses in Fig. 3.18 are quite sensitive to the choice of 900 nm as the upper wavelength limit, including the reflectance as well as the absorbance in the glass, SnO_2:F, and the two CdTe/Au interface layers. Because these losses extend above 829 nm, corresponding to the bandgap of CdTe for this device, some fraction of the lost current cannot be regained as it is in a spectral region where the CdTe absorbs only weakly or not at all for the given thickness. In general, one can conclude that the results of SE analysis for the completed CdS/CdTe solar cell, together with EQE measurements and simulations, enable characterization of all current losses in the device, and thus provide directions toward minimizing losses through improved designs for the devices.

3.4 Copper Indium-Gallium Diselenide Solar Cells

3.4.1 Solar Cell Fabrication and Performance

The two most widely commercialized thin film photovoltaics technologies include those based on CdTe absorbers in the superstrate configuration and on $CuIn_{1-x}Ga_xSe_2$ (CIGS) absorbers in the substrate configuration. Both have reached laboratory scale cell efficiencies exceeding 22% [47]. The standard CIGS solar cell of this SE-EQE study follows one approach for high efficiency, incorporating an absorber layer fabricated by three-stage coevaporation [48]. The key fabrication steps include the coevaporation of CIGS on soda lime glass (SLG) coated with molybdenum (Mo), and subsequent chemical bath deposition (CBD) of CdS on the CIGS to form the heterojunction [48]. The complete device incorporates the following layers with ranges of intended thicknesses: soda lime glass (SLG) substrate, two-step dc magnetron sputtered Mo as the back contact (~0.8–1 μm), CIGS as the absorber layer (2–3 μm), CdS as the window layer (50–100 nm), rf magnetron sputtered bi-layer of ZnO/ZnO:Al as the transparent top contact (0.2–0.4 μm), and electron beam evaporated Ni/Al/Ni for the grids. The total cell area of 0.5 cm^2 is established by mechanical scribing. An anti-reflection coating (ARC) consists of a single layer of MgF_2, optimized in this study through optical modeling and deposited in an electron beam evaporation system. The typical multilayer structure is shown in the schematic of Fig. 3.19.

The first stage of the CIGS deposition process is performed at a substrate temperature of 400 °C and includes coevaporation rates for In at 2.0 Å/s, Ga at 0.6 Å/s, and Se at 20 Å/s [23]. Once the desired $(In_{1-x}Ga_x)_2Se_3$ film thickness is reached, the first stage is terminated by reducing the source temperatures for In and Ga to cease coevaporation. The substrate temperature is then increased to a value within the range of 540–640 °C over a ramp time of 20 min to initiate the second stage. In this stage, the source temperature of Cu is increased to obtain an evaporation rate of 1.7 Å/s while continuing coevaporation of Se. As determined by end-point detection of the transition from Cu-poor CIGS to Cu-rich CIGS, the temperature of the Cu source is reduced to cease Cu evaporation. In order to obtain a final Cu-poor CIGS layer in the third stage, In and Ga are evaporated using the same rates as in the first stage, 2.0 Å/s for In and 0.6 Å/s for Ga, while maintaining a continuous flux of Se and the same substrate temperature as in the second stage. At the end of third stage, defined by the transition from Cu-rich CIGS to Cu-poor CIGS, the temperatures of the In and Ga sources are reduced to cease coevaporation. In addition, the temperature of the substrate is steadily decreased to 380 °C over a period of 20 min under continuous Se flux before shutting down the Se source and substrate heaters. During the three stages of CIGS deposition, the In, Ga, and Cu fluxes are controlled by electron impact emission spectroscopy; the evaporation crucibles are heated thermally by resistive heating coils; and the substrate temperature is measured by a thermocouple attached to the back side of the sample by physical contact.

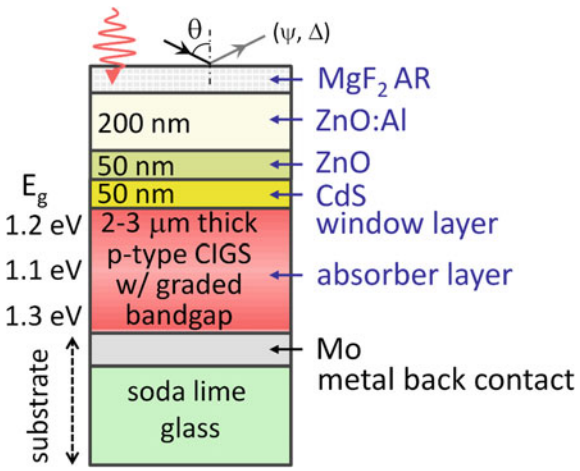


Fig. 3.19 Schematic of a CIGS/CdS solar cell of the type analyzed in this external quantum efficiency study. The substrate is soda lime glass coated with a Mo back contact layer and the top transparent conducting oxide layers consist of a ZnO/ZnO:Al bi-layer. MgF_2 is used as the anti-reflection coating

The SE-EQE study reviewed here focuses on solar cells incorporating standard and thin absorber layers before and after ARC deposition [8, 11]. The performance characteristics of the CIGS solar cell incorporating the absorber layer with standard 2.2 μm thickness are shown in Fig. 3.20 and Table 3.5. The light and dark (current density)-voltage (*J-V*) characteristics of the solar cell in Fig. 3.20 are shown before and after the deposition of the ARC. Upon application of the ARC, the solar cell efficiency increases from $\eta = 16.4$ to 17.4%. Corresponding performance parameters for a CIGS solar cell with a factor of three lower absorber layer thickness of 0.73 μm are presented in Table 3.5 as well. In this case, addition of the ARC led to an increase in efficiency from 12.4 to 13.2%. The motivation for developing CIGS solar cells with thin absorbers is to reduce materials costs and increase throughput in CIGS module manufacturing. The complete solar cells were investigated using ex situ SE, which was performed with the beam directed at the film side of the cells with a 65° angle of incidence. The ellipsometric angles (ψ, Δ) were obtained versus photon energy over the range from 0.9 to 4.0 eV (V-VASE, J. A. Woollam Co.). The ultimate goal is to develop models and an analysis methodology that can be used in on-line applications.

3.4.2 Component Layer Dielectric Functions

Starting from the Mo back contact, the interfaces and surfaces of the CIGS solar cell are very rough, yielding a complicated structural model that introduces significant uncertainties if used for the determination of the $\varepsilon(E)$ spectra of a database [49]. As a result, in CIGS studies one seeks to generate and measure sample structures that are closer to ideal, by depositing individual solar cell component materials on smooth substrates and in thinner layers that minimize roughness development.

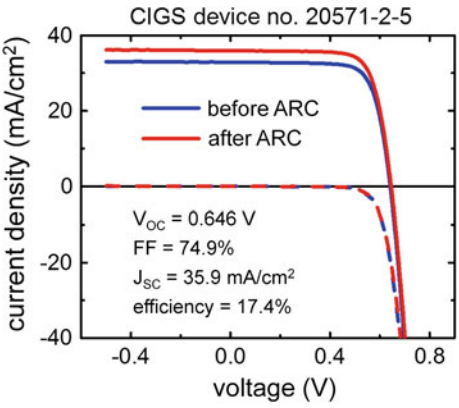


Fig. 3.20 (Current density)-voltage characteristics in the dark and under AM 1.5 illumination for a CIGS solar cell incorporating an absorber with a standard thickness of 2.2 μm. Results obtained before and after deposition of the anti-reflection coating are presented. This device was used in ex situ SE and external quantum efficiency studies [8]

Table 3.5 Performance parameters of two solar cells with CIGS absorbers fabricated by three-stage coevaporation. These cells are used for EQE measurements and simulations [8]. Devices incorporating standard 2.2 μm and thin 0.73 μm CIGS absorbers were deposited onto Mo coated soda lime glass substrates and were completed with Ni/Al/Ni grid lines. Parameters are given before and after the application of MgF_2 anti-reflection coatings for the two cells

CIGS Solar cell	V_{OC} (mV)	J_{SC} (mA/cm^2)	FF (%)	η (%)
SLG/Mo/(2.2 μm CIGS)/CdS/ZnO/ZnO:Al	646	33.8	74.9	16.4
SLG/Mo/(2.2 μm CIGS)/CdS/ZnO/ZnO:Al/MgF_2		35.9		17.4
SLG/Mo/(0.7 μm CIGS)/CdS/ZnO/ZnO:Al	551	31.9	70.8	12.4
SLG/Mo/(0.7 μm CIGS)/CdS/ZnO/ZnO:Al/MgF_2		33.8		13.2

Real time, in situ, and ex situ SE methods are used for the determination of $\varepsilon(E)$ from these structures. Possible substrate and thickness dependences must be considered, however, when following this approach. Such dependences could lead to $\varepsilon(E)$ spectra of the database that are not relevant for SE analysis of solar cell structures. This suggests the need to measure the effects of substrate and thickness on $\varepsilon(E)$ spectra in structures that are closer to ideal than the device itself. One can then incorporate a physics-based analytical form for $\varepsilon(E)$ that accounts for variations due to the substrate and thickness, examples being variable CP energies due to stress or variable broadening parameters due to grain size effects [35, 36]. Thus, significant background work is often needed in setting up an accurate and relevant dielectric function database. Confidence in the database can be obtained through studies such as the one described here that use SE-deduced models to predict solar cell performance [11].

The parametric versions of the dielectric functions $\varepsilon(E)$ measured at room temperature for the layer components of the CIGS solar cell are summarized in Fig. 3.21. The approaches for $\varepsilon(E)$ parameterization applied here are similar to those used for SE studies of the CdTe solar cell of Sect. 3.3. Investigations of the CIGS solar cells are much more challenging, however, due to the variable absorber layer composition. In fact, the three-stage deposition process leads to a notch-like Ga composition profile as a function of depth into the absorber layer of the device structure, as will be demonstrated in Sect. 3.4.3 [50]. One simplification is possible for CIGS relative to CdTe in that the CIGS deposition at high temperature occurs first. Then the CdS layer is over-deposited by low temperature chemical bath deposition, and no measurable inter-diffusion occurs at the heterojunction interface. Measurements described below to extract the $\varepsilon(E)$ spectra were performed using multichannel instruments (M-2000DI, J. A. Woollam Co.).

Sputter deposition of Mo as a back contact for CIGS solar cells is performed on soda lime glass at the elevated substrate temperature of 250 °C, which optimizes the performance of the devices [51]. The Mo is deposited in the form of a bi-layer to mitigate delamination as a result of film stress. The first layer, 50–100 nm thick, is deposited at 15 mTorr Ar pressure, and the second layer, 0.7–0.8 μm thick, is deposited at 4 mTorr Ar pressure. The Mo film used for the measurement of $\varepsilon(E)$ was deposited on a smooth c-Si substrate coated with a thermal oxide, applying conditions identical to those used for the opaque Mo top layer of the bi-layer in solar cells. After cooling the c-Si/SiO_2/Mo structure to room temperature, the $\varepsilon(E)$ spectra of relevance for the Mo top layer of the cell was obtained in situ to avoid oxidation. The surface roughness thickness correction applied to obtain the Mo bulk layer $\varepsilon(E)$ spectra was deduced from multi-time analysis of real time SE data. The parametric model for the Mo $\varepsilon(E)$ spectra includes a constant component of $\varepsilon_1(E)$, two Drude free electron components with different (ρ, τ) values, and three critical point oscillators with variable parameters of amplitude, energy, broadening, and phase, $\{A_n, E_n, \Gamma_n,$ and $\phi_n; n = 1, 2, 3\}$, respectively, whose energies E_n occur at 1.59, 2.26, and 4.25 eV. In addition, the CP exponents were fixed at unity for simplicity. Thus, the parametric model of $\varepsilon(E)$ for Mo incorporates 17 variable parameters.

The CIGS films for the determination of $\varepsilon(E)$ were deposited to thicknesses of ~60 nm using a single-stage coevaporation process. The substrates, held at 570 °C, were smooth silicon wafers with intact native oxides. Thin layers and smooth substrates were used in order to ensure compositional uniformity with depth and a relatively smooth interface and surface [52]. The SE measurements of these films were performed in situ after cooling to room temperature. A two-step process was used to extract the $\varepsilon(E)$ spectra. In the first step, a simplified model for $\varepsilon(E)$ was used to extract structural parameters, and in a second step, these structural parameters were used to extract the $\varepsilon(E)$ spectra by exact inversion. Then parametric forms for the inverted spectra were obtained using a physics-based model over the 0.7–4 eV range consisting of four CP oscillators to simulate the E_0(A, B), E_0(C), E_1(A), and E_1(B) transitions observed in the $\varepsilon(E)$ spectra of single crystal chalcopyrite alloys. Also included are ε_{1o}, the constant component of $\varepsilon_1(E)$,

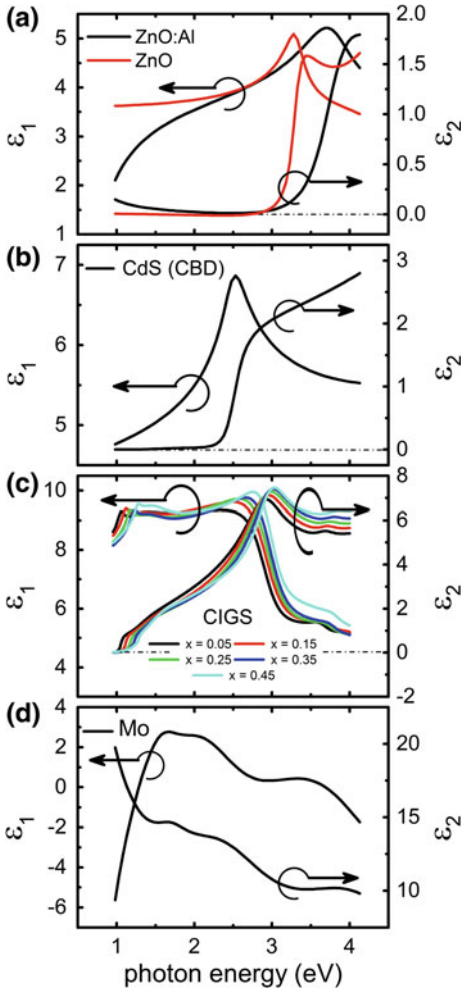


Fig. 3.21 Plots of analytical expressions for the dielectric functions applied in external quantum efficiency simulations for CIGS solar cells including **a** sputtered ZnO:Al front contact and ZnO high resistivity transparent layers; **b** CdS fabricated by chemical bath deposition; **c** $CuIn_{1-x}Ga_xSe_2$ fabricated by one-stage coevaporation for selected values of x; and **d** sputtered Mo back contact

a modified Lorentz oscillator serving as a background with a low energy onset equal to the lowest CP energy, and an Urbach tail describing the imaginary part of $\varepsilon(E)$ for energies below the lowest CP energy. For stability in the fits of the inverted $\varepsilon(E)$, the CP energies were fixed at values obtained in an analysis of the second derivative of $\varepsilon(E)$. As a result, a total of 20 variable parameters was used in the fits of $\varepsilon(E)$. Such an analysis was performed on SE data collected for samples of different Ga composition x as measured by energy dispersive X-ray spectroscopy (EDS). By plotting the parameters of $\varepsilon(E)$ as functions of x and fitting the parameters with polynomial functions, a database of polynomial coefficients is generated that allows one to compute the $\varepsilon(E)$ spectra at room temperature for a hypothetical CIGS bulk layer of any specified composition. Examples of spectra generated in this way appear in Fig. 3.21 [52].

The CdS films used in the determination of $\varepsilon(E)$ were deposited to effective thicknesses ranging from 20 to 90 nm on thermal oxide covered Si wafers using chemical bath deposition (CBD) in solutions containing 1.5 M ammonium hydroxide, 0.0075 M thiourea, and 0.0015–0.0075 M cadmium acetate at 65 °C [8]. A number of samples of different thickness were measured to assist in the modeling, and the resulting data were fitted over the range of 0.9–4.0 eV. The structural parameters in the optical model included bulk and surface roughness layer thicknesses with a variable void content in the roughness layer. A parametric expression for $\varepsilon(E)$ was included that incorporates two CP oscillators with ten parameters; the constant contribution ε_{1o} was fixed at unity. The best fit parameters were obtained by multi-sample analysis assuming a thickness independent $\varepsilon(E)$. The ZnO and ZnO:Al films for study of $\varepsilon(E)$ were deposited in standard processes at room temperature in a magnetron sputtering system from targets of pure ZnO and ZnO/Al_2O_3 (98/2 wt%), respectively. The structural and dielectric function models used for these films were similar to those used for CdS. An exception was made for the $\varepsilon(E)$ spectra of the ZnO:Al top contact layer, which incorporated a Drude term in the expression for $\varepsilon(E)$. The wider bandgap observed in Fig. 3.21b for ZnO:Al compared to ZnO is attributed to the Burstein-Moss effect of band filling due to degenerate doping [43, 44].

Future opportunities exist for improving the databases of the CdS and ZnO:Al layers applied in the analysis of the CIGS solar cell and subsequent EQE simulations, including determination of the bandgap CP parameters of the CdS window layer and the resistivity and mean free time for the ZnO:Al top contact layer. Expanded databases can be obtained by deposition of these films under different conditions, e.g. the ratio of cadmium acetate to thiourea in CdS CBD and the substrate temperature and Ar pressure in ZnO and ZnO:Al sputtering [8].

3.4.3 *Spectroscopic Ellipsometry Analysis*

For complete solar cells, film-side ex situ SE was performed at a single location on the device surface, avoiding the collection grids. The SE data were acquired using a rotating-analyzer ellipsometer (V-VASE, J.A Woollam Co.) over the photon energy range of 0.9–4 eV at a 70° angle of incidence [8]. By utilizing the component layer $\varepsilon(E)$ spectra as just described, including the accompanying database for CIGS, least squares regression was utilized for SE data analysis applying the error function σ_{NCS} defined by (3.5). The CIGS database consists of polynomial coefficients enabling calculation of the energy independent parameters defining $\varepsilon(E)$ for CIGS of any Ga content x [52]. Through least squares regression analysis, the multilayer structural information of the solar cell could be determined non-invasively including (i) the thickness of each bulk layer, (ii) the void fraction in each bulk layer, as needed, (iii) the thickness and composition for each of the interface roughness layers and for the surface roughness layer, and (iv) the Ga profile within the absorber. The model for the Ga profile includes two linear segments with four

parameters, including Ga compositions x_{HF} at the junction, x_L at the minimum within the CIGS, and x_{HB} at the back contact, along with d_L the depth of the minimum. The Ga contents of the CIGS components for the Mo/CIGS and CIGS/CdS interface layers are assumed to be x_{HB} and x_{HF}, respectively, the same as the back and front of the bulk CIGS.

Ex situ SE data in the form of (N, C, S) are shown in Fig. 3.22 (points) for the CIGS solar cell of Table 3.5 having the standard absorber thickness of 2.2 μm and no anti-reflection coating (ARC) [8]. Thus, the SE data were measured non-invasively before deposition of the ARC. The results in Figs. 3.23 and 3.24 were determined from the best fit to the data of Fig. 3.22, given as the solid lines in the figure. Figure 3.23 shows the CIGS solar cell multilayer stack and the best fit structural and composition parameters associated with the layers. Figure 3.24 depicts the SE-determined Ga profile for the CIGS absorber layer obtained in the same fitting procedure, including the four free parameters, x_{HF}, x_L, x_{HB}, and d_L.

A similar analysis was performed on a second CIGS cell with 2.2 μm absorber, again measured before ARC deposition [8]. The 15.6% efficiency of this cell is somewhat lower than that for the cell of Figs. 3.22 through 3.24; however, a secondary ion mass spectrometry (SIMS) depth profile for this sample is available for comparison with the profile deduced by SE. The final results for this sample are given in Figs. 3.25 and 3.26. First, it should be noted that the profile in Fig. 3.26 shows a stronger notch function, which may account for the lower performance of this device. As the profile indicates, the Ga content may be too low ~0.18 at the minimum, which may account for the observed lower fill-factor relative to the sample of Figs. 3.22, 3.23 and 3.24 (71.3% vs. 74.9%). This is based on the expectation that highest electronic quality CIGS is obtained at $x \sim 0.3$ [48]. In the comparison with the SE-deduced profile of Fig. 3.26, a single calibration parameter is used to scale the SIMS data. The shapes of the two profiles are found to be in good agreement, supporting the validity of the SE method for profile determination. Similarly good agreement has been obtained in a comparison of depth profiles deduced by Auger electron spectroscopy (AES) and by SE. The AES-SE comparison was made in studies of a 0.36 μm CIGS layer deposited directly on soda lime glass [52].

An additional SE measurement was performed for the solar cell of Figs. 3.22, 3.23 and 3.24 that incorporates a standard 2.2 μm thick CIGS absorber, in this case after ARC deposition [8]. By ensuring the same spot between the grids was measured on the device before and after ARC deposition, one can establish a multilayer model with fixed parameters for all layers with the exception of those incorporating the MgF_2 ARC material. Thus, the variable parameters include the ZnO:Al/MgF_2 interface, MgF_2 bulk, and MgF_2 surface roughness layer thicknesses. The compositions of these layers were determined as well, allowing for the possibility of density deficits, i.e. void volume fractions, in each of the layers applying two and three-component EMAs. Given in Fig. 3.27, these results demonstrate an effective thickness (or volume/area) for the two-layer MgF_2 bulk/roughness structure of 91 nm, close to the intended value of 94 nm.

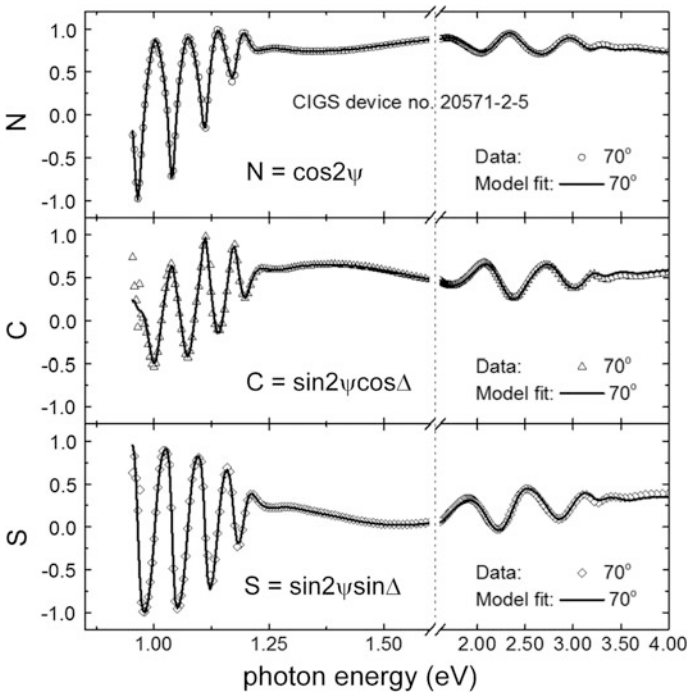


Fig. 3.22 Ex-situ SE data represented in terms of the parameters *N*, *C*, and *S* measured at an angle of incidence of 70° (symbols) for the CIGS solar cell of Table 3.5 with a standard 2.2 μm absorber. The measurement was performed before application of the anti-reflection coating. The best fit simulation (solid lines) is shown, yielding the multilayer structure and Ga composition profile in Figs. 3.23 and 3.24, respectively [8]

Fig. 3.23 Multilayer structure obtained from the best fit of the ex situ SE data in Fig. 3.22 for the solar cell of Table 3.5 incorporating a standard 2.2 μm thick CIGS absorber [8]

layer (composition, properties)	thickness
surface roughness (f_v = 38.7%)	36.31 ± 2.31 nm
ZnO:Al (f_v = 2.8%)	110.24 ± 3.04 nm
i-ZnO / ZnO:Al (f_{ZnO} = 21.9%, f_v = 2.7%)	145.10 ± 2.72 nm
i-ZnO (f_v = 0.0%)	39.32 ± 2.06 nm
CdS / i-ZnO (f_{CdS} = 49.2%, f_v = 0.0%)	45.31 ± 1.88 nm
CdS (f_v = 0.0%)	49.92 ± 1.95 nm
CIGS / CdS (f_{CIGS} = 76.1%, f_v = 0.5%)	62.42 ± 1.86 nm
CIGS (graded layer, f_v = 0.0%) (x_{HF} = 0.337 ± 0.012, x_L = 0.311 ± 0.038, x_{HB} = 0.372 ± 0.037)	2188.67 ± 2.94 nm
Mo / CIGS (f_{Mo} = 77.3%)	21.13 ± 2.57 nm
Mo (opaque)	

CIGS device no. 20571-2-5

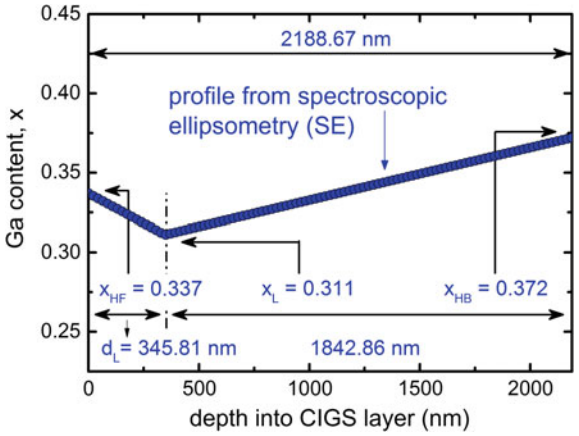


Fig. 3.24 The Ga profile for the 2.2 μm CIGS absorber obtained from the best fit of the ex situ SE data in Fig. 3.22 for the solar cell of Table 3.5 and Fig. 3.23 [8]

layer (composition, properties)	thickness
surface roughness (f_v = 30.6%)	34.29 ± 2.06 nm
ZnO:Al (f_v = 2.9%)	111.97 ± 2.79 nm
i-ZnO / ZnO:Al (f_{ZnO} = 21.8%, f_v = 2.9%)	140.08 ± 2.30 nm
i-ZnO (f_v = 0.0%)	36.23 ± 1.67 nm
CdS / i-ZnO (f_{CdS} = 48.6%, f_v = 0.0%)	44.47 ± 1.78 nm
CdS (f_v = 0.0%)	48.67 ± 1.15 nm
CIGS / CdS (f_{CIGS} = 77.5%, f_v = 0.7%)	59.12 ± 1.49 nm
CIGS (graded layer, f_v = 0.0%) (x_{HF} = 0.304 ± 0.011, x_L = 0.182 ± 0.036, x_{HB} = 0.469 ± 0.032)	2177.73 ± 2.28 nm
Mo / CIGS (f_{Mo} = 82.0%)	19.89 ± 2.31 nm
Mo (opaque)	

CIGS device no. 20565-2-20

Fig. 3.25 Multilayer structure obtained from the best fit of SE data for a solar cell incorporating a standard 2.2 μm thick CIGS absorber. The cell exhibited a lower efficiency of 15.6% relative to that of Table 3.5. No ARC was deposited on this device [8]

The ex situ SE (*N*, *C*, *S*) data are shown in Fig. 3.28 (points) for the solar cell of Table 3.5 with the thin CIGS absorber layer of 0.73 μm thickness [11]. These measurements were performed before deposition of the anti-reflection coating on the solar cell. The results in Figs. 3.29 and 3.30 were determined from the best fit to the data, given in Fig. 3.28 as the solid lines. Figure 3.29 shows the CIGS multilayer solar cell stack and the best fit structural and composition parameters, and Fig. 3.30 depicts the SE-determined Ga profile for the CIGS absorber layer obtained in the same fitting procedure. Interesting differences can be noted between the results for the thin solar cell in Fig. 3.29 and the two standard thickness cells of Figs. 3.23 and 3.25. First, it should be noted that for the cell with the thin absorber, the value of x, when an average is taken over the profile yielding $\langle x \rangle = 0.201$,

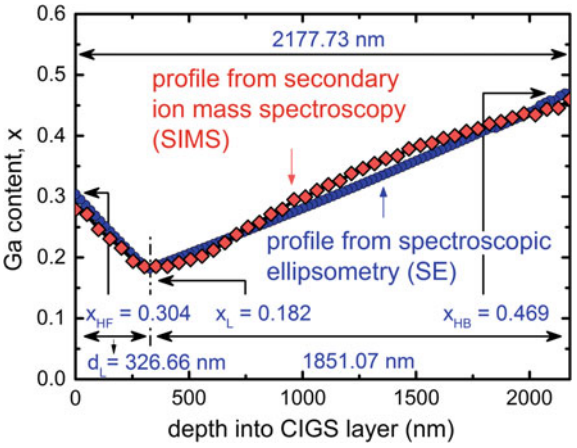


Fig. 3.26 Ga profile within the 2.2 μm thick absorber obtained from the best fit of SE data for the CIGS solar cell of Fig. 3.25 (circles). Also shown is the profile from secondary ion mass spectrometry performed on the same device (diamonds) [8]

layer (composition, properties)	thickness
surface roughness (f_v = 45.3 ± 0.6 %)	34.19 ± 1.43 nm
MgF_2 (f_v = 0.3 ± 0.5%)	72.18 ± 2.29 nm
ZnO:Al / MgF_2 (f_{MgF2} = 38.3 ± 0.3%, f_v = 0.5 ± 0.4%)	34.88 ± 2.67 nm
ZnO:Al (f_v = 2.8%)	110.24 nm
i-ZnO / ZnO: Al (f_{ZnO} = 21.9%, f_v = 2.7%)	145.10 nm
i-ZnO (f_v = 0.0%)	39.32 nm
CdS / i-ZnO (f_{CdS} = 49.2%, f_v = 0.0%)	45.31 nm
CdS (f_v = 0.0%)	49.92 nm
CIGS / CdS (f_{CIGS} = 76.1%, f_v = 0.5%)	62.42 nm
CIGS (graded layer, f_v = 0.0%) (x_{HF} = 0.337, x_L = 0.311, x_{HB} = 0.372)	2188.67 nm
Mo / CIGS (f_{Mo} = 77.3%)	21.13 nm
Mo (opaque)	

CIGS device no. 20571-2-5

Fig. 3.27 Multilayer structure for the solar cell of Table 3.5 incorporating the 2.2 μm thick CIGS absorber layer and a MgF_2 anti-reflection coating (ARC). The results obtained before ARC deposition for this cell are shown in Figs. 3.22 through 3.24 [8]

is lower than those of the cells with the 2.2 μm thick absorber in Figs. 3.24 and 3.26, $<x> = 0.339$ and $<x> = 0.313$, respectively. This is intentional since for a thin cell, it is beneficial to trade off open-circuit voltage for short-circuit current density. For a cell with a thin absorber layer, V_{OC} decreases weakly with decreasing x, whereas J_{SC} increases significantly with decreasing x. Another interesting feature is that although all Mo/CIGS interface layers are similar in thickness for the three devices, 20–24 nm, arising from the roughness on the Mo surface, the CIGS/CdS interface layer is much thinner for the cell with the thinner absorber, 38 nm versus 59–62 nm for the standard absorber. This is an indication that the roughness on the

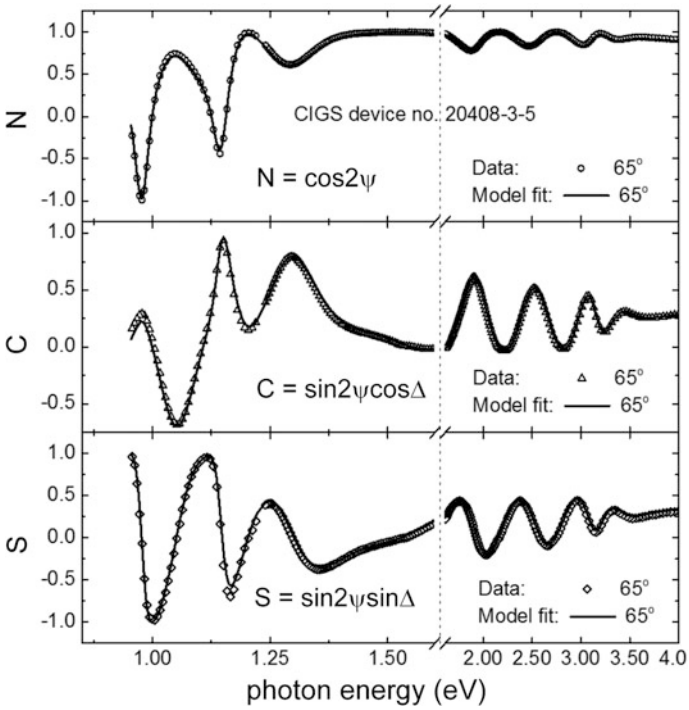


Fig. 3.28 Ex-situ SE data represented in terms of the parameters *N*, *C*, and *S* measured at an angle of incidence of 70° (symbols) for the CIGS solar cell of Table 3.5 with the thin 0.73 μm absorber. The measurement was performed before application of the anti-reflection coating. The best fit simulation (solid lines) is shown yielding the multilayer structure and Ga composition profile in Figs. 3.29 and 3.30 [11]

Fig. 3.29 Multilayer structure obtained from the best fit to the ex situ SE data of Fig. 3.28 for the solar cell of Table 3.5 incorporating a thin 0.73 μm CIGS absorber [11]

layer (composition, properties)	thickness
surface roughness (f_v = 45.2%)	32.34 ± 2.61 nm
ZnO:Al (f_v = 2.3%)	81.06 ± 2.47 nm
i-ZnO / ZnO:Al (f_{ZnO} = 19.6%, f_v = 2.2%)	195.16 ± 2.73 nm
i-ZnO (f_v = 0.0%)	65.78 ± 1.64 nm
CdS / i-ZnO (f_{CdS} = 48.6%, f_v = 0.0%)	68.31 ± 1.96 nm
CdS (f_v = 0.0%)	29.14 ± 1.55 nm
CIGS / CdS (f_{CIGS} = 77.5%, f_v = 0.7%)	38.24 ± 1.24 nm
CIGS (graded layer, f_v = 0.0%) (x_{HF} = 0.212 ± 0.014, x_L = 0.164 ± 0.033, x_{HB} = 0.243 ± 0.031)	728.19 ± 1.56 nm
Mo / CIGS (f_{Mo} = 76.6%)	24.63 ±1.93 nm
Mo (opaque)	

CIGS device no. 20408

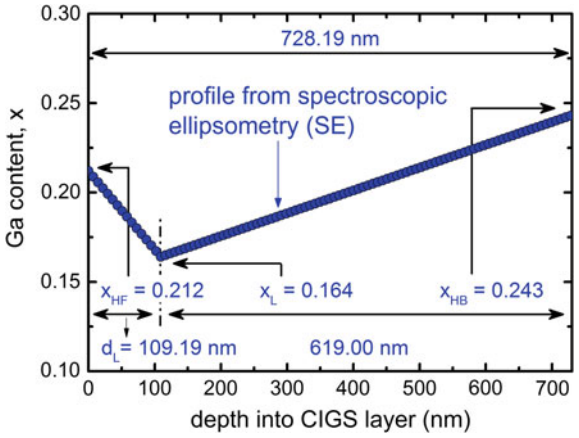


Fig. 3.30 The Ga profile within the 0.73 μm CIGS absorber obtained from the best fit to the ex situ SE data of Fig. 3.28 for the solar cell of Table 3.5 and Fig. 3.29 [11]

CIGS surface increases with increasing thickness, and this leads to a smoother heterojunction interface for thin absorbers. A smoother interface enables thinning of the CdS without shunting. This accounts for the lower CdS effective thickness of 71 nm, by design, for the cell with the thinner absorber layer, compared with effective thicknesses of 83–87 nm for the cells with standard absorber layers.

3.4.4 External Quantum Efficiency Simulations

For a better understanding of optical collection and losses in CIGS solar cells, optical simulation is performed for the solar cell structures using as inputs the results of the SE analysis. Applying the assumption of ideal collection of photo-generated carriers, i.e. no electronic losses, an EQE spectrum can be predicted simply by summing the spectra describing the absorbed photon fraction for each active layer component. In Fig. 3.31, these photon absorbance spectra associated with the layers of the CIGS/CdS interface and the CIGS bulk are simulated for the CIGS solar cell of Table 3.5 with the standard 2.2 μm absorber and no ARC, and these simulated components are summed to represent the total EQE response [8]. In Fig. 3.32, the measured EQE spectrum is compared to that simulated from the SE analysis of Fig. 3.31. Excellent agreement between the two spectra is found, including agreement in the J_{SC} values [J_{SC}(exp) = J_{SC}(sim) = 34.2 mA/cm^2]. This result demonstrates that the active layers in a CIGS solar cell are indeed the CIGS/CdS interface layer and the CIGS bulk layer. These findings are important for several reasons. First, the results suggest that the optical model used to evaluate electronic collection is accurate, and thus the losses can be evaluated accurately, as well. For demonstration, the photon absorbance spectra are presented in Fig. 3.33 as calculated for each component layer of the solar cell of Table 3.5 with the 2.2 μm absorber layer and no ARC. The photon absorbance within the opaque Mo back contact is also

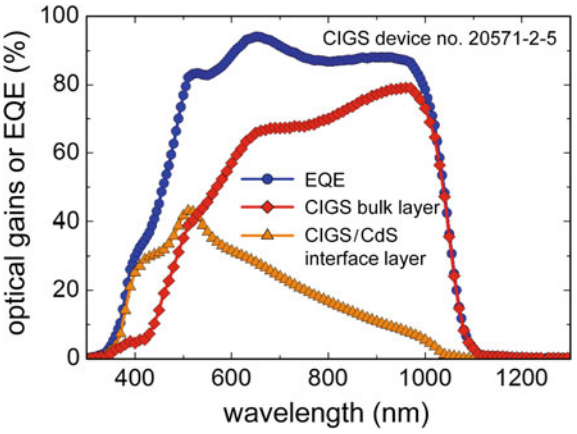


Fig. 3.31 Optically simulated EQE spectrum based on assumed 100% collection of photo-generated charge carriers for the solar cell of Figs. 3.22 through 3.24 incorporating the standard 2.2 μm CIGS absorber and no anti-reflection coating. Also shown are the simulated photon absorbance spectra for the two active layers of the device including the CIGS/CdS interface layer and the CIGS bulk layer [8]

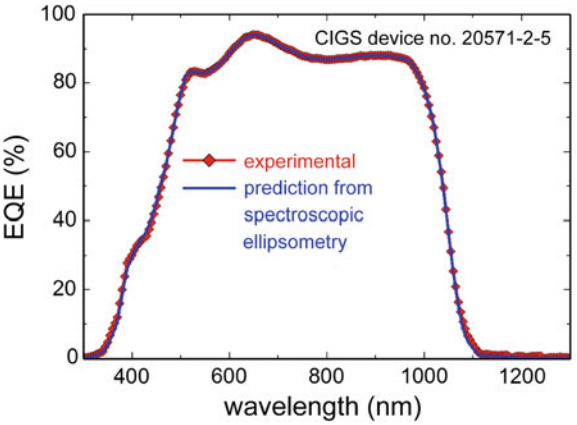


Fig. 3.32 Comparison of the EQE measurement and the optical simulation for the solar cell of Fig. 3.31 with the standard 2.2 μm CIGS absorber, based on assumed 100% collection of photo-generated charge carriers from the two active component layers [8]

included in Fig. 3.33, and the residual of the absorbance sum from unity provides the fraction of photons reflected from the cell. Second, because the short-circuit current density (J_{SC}) can be calculated directly from the EQE spectrum, J_{SC} can be used as a key parameter for optimization of current collection through device design. Thus, the established method also allows investigation of the effect of component layer thicknesses on the attainable J_{SC}, enabling further enhancement of the solar cell structure by optical means. A simple example of this approach is described in the following paragraph.

As a demonstration of the importance of the design capability made possible with an accurate optical model of the cell, deposition of a MgF_2 ARC on the CIGS cell of Figs. 3.31, 3.32 and 3.33 was performed to a thickness determined on the basis of an optimized simulation [8]. Additional details of this approach will be described when corresponding results are presented for the solar cell incorporating the 0.73 μm thick CIGS absorber. In this approach, a plot of J_{SC} increase versus

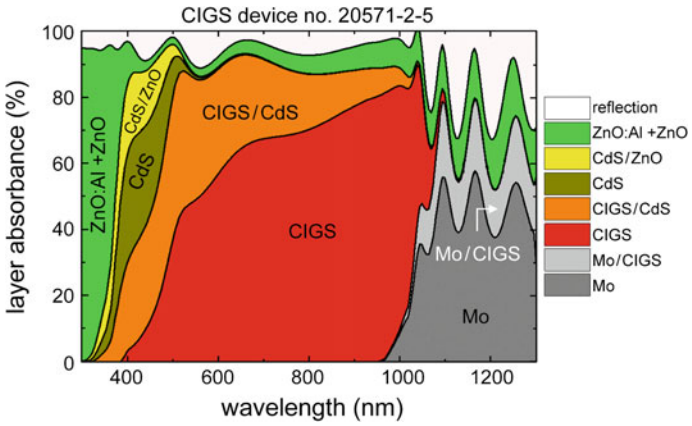


Fig. 3.33 Simulated percentage of photons absorbed (or photon absorbance) within the components of the multilayer structure that describes the solar cell of Figs. 3.31 and 3.32 incorporating a standard 2.2 μm CIGS absorber and no anti-reflection coating [8]. The deficit of the sum from 100% provides the reflectance of the solar cell

MgF_2 ARC layer thickness is generated first through a simulation designed to identify the optimum. In the simulation, it is assumed that the MgF_2 fills the modulations in the ZnO:Al surface roughness, but that the surface of the MgF_2 film is smooth. Based on these assumptions, a maximum increase of 2.1 mA/cm^2 is identified at a MgF_2 bulk layer thickness of 94 nm. Thus, an intended effective thickness of 94 nm for the bulk/roughness layers is deposited on the solar cell and measured by SE. The measurement results presented in Fig. 3.27 reveal an effective thickness of 91 nm associated with the bulk/roughness layers (excluding the interface contribution to the effective thickness), reasonably close to the intended value. Applying the assumption of ideal collection for the photo-generated carriers, i.e. no electronic losses, an EQE spectrum can be simulated optically by applying the model of Fig. 3.27 for the standard CIGS cell with the ARC by summing the optical spectra for absorption within the active layer components. In Fig. 3.34, the simulated photon absorption within the CIGS/CdS interface layer and the CIGS bulk layer is presented, and these results are added to determine the net simulated EQE for the standard CIGS solar cell that incorporates the ARC. In Fig. 3.35, the measured EQE spectrum is compared to that predicted from the SE analysis of Fig. 3.34. An experimental J_{SC} increase of 2.1 mA/cm^2 is recorded, yielding $J_{SC}(\text{exp}) = J_{SC}(\text{sim}) = 35.9$ mA/cm^2 with the ARC. Thus, the improvement is in agreement with the prediction and demonstrates the success of the ARC deposition. The resulting simulated photon absorbances for all the layers within the multilayer structure, along with the fraction of photons reflected, are shown in Fig. 3.36 for the CIGS cell with the ARC from Figs. 3.34 and 3.35.

Next, the focus is on EQE simulations and ARC design for the CIGS solar cell of Table 3.5 with the thinner absorber layer having a thickness of 0.73 μm [11]. In Fig. 3.37, photon absorbance within the CIGS/CdS interface layer and the CIGS

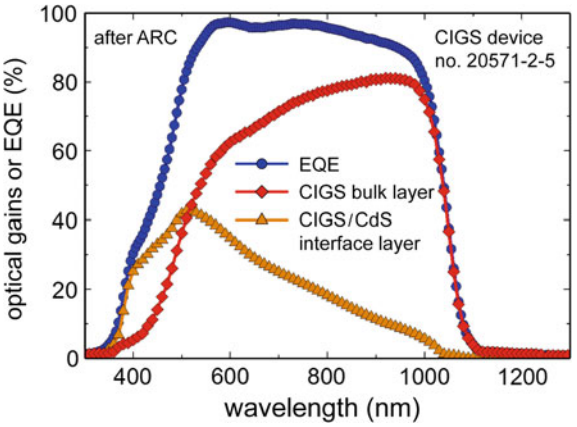


Fig. 3.34 Optically simulated EQE spectrum based on assumed 100% collection of photo-generated charge carriers for the solar cell of Fig. 3.27 incorporating the standard 2.2 μm CIGS absorber and an anti-reflection coating. Also shown are the simulated photon absorbance spectra for the active components including the CIGS/CdS interface layer and the CIGS bulk layer [8]

bulk layer are simulated by applying the SE model of Figs. 3.29 and 3.30 for the solar cell with the 0.73 μm thick CIGS absorber. The results are summed to represent the net EQE response assuming 100% collection of carriers photo-generated within these layers. In Fig. 3.38, the measured EQE spectrum is compared to that predicted from the SE analysis with ideal collection of carriers from the two active layers. Reasonable agreement overall between the simulation and the measurement is shown in Fig. 3.38; however, in this case the simulated EQE spectrum exceeds the experimentally recorded one. Integration of the simulated EQE spectrum results in $J_{SC} = 32.8$ mA/cm^2, whereas the measured EQE spectrum yields $J_{SC} = 31.9$ mA/cm^2. The deficit of 0.9 mA/cm^2 indicates that recombination of photo-generated carriers occurs within one or both of the active layers such that a fraction of these carriers exhibits collection probabilities that are less than 100%. The simulated absorbances for photons within each of the component layers of the CIGS cell incorporating the 0.73 μm thick absorber are presented in Fig. 3.39, which also includes the absorbance within the opaque Mo back contact. Because no photons are transmitted through the Mo, the deficit from unity in the absorbance sum provides the reflectance of the cell.

An understanding of the discrepancy between the simulated and measured EQE in Fig. 3.38 is possible by the introduction of a collection probability profile into the model as shown in Fig. 3.40 to simulate the effect of recombination losses [11]. The losses associated with this profile are assumed to occur within the CIGS bulk layer adjacent to the Mo back contact. As shown in Fig. 3.41, an improvement in the fit of the measured EQE spectrum is obtained by incorporating the probability profile given in Fig. 3.40 for collection from the CIGS bulk layer. CIGS solar cells with 0.5 and 0.3 μm absorbers were also fabricated by three-stage coevaporation and studied using ex situ SE to determine parameters that characterize their multilayer structures and Ga compositional profiles, as in Figs. 3.28, 3.29 and 3.30. Simulated EQE spectra were generated assuming 100% collection of photo-generated charge carriers from the two active layers. For all such solar cells with thin CIGS absorbers, the measured EQE values across the spectra were lower than

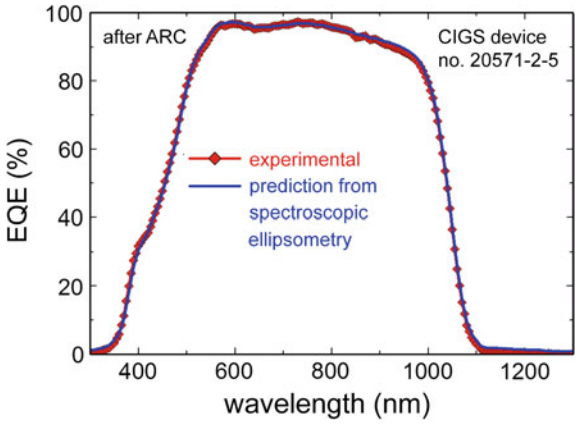


Fig. 3.35 Comparison of the EQE measurement and the optical simulation for the solar cell of Fig. 3.34 with the standard 2.2 μm CIGS absorber, based on assumed 100% collection of photo-generated charge carriers from the two active component layers [8]

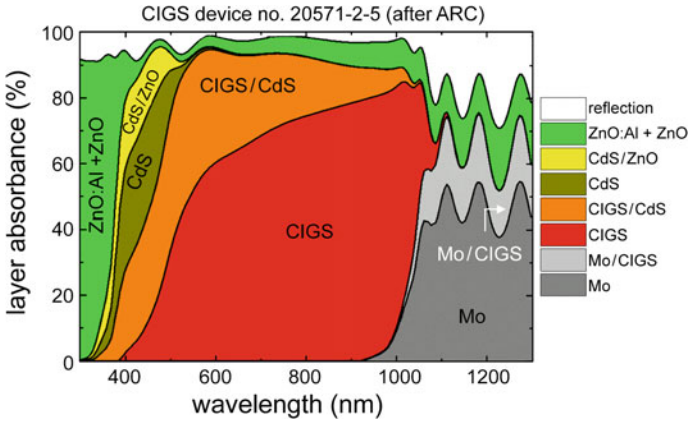


Fig. 3.36 Simulated percentage of photons absorbed (or photon absorbance) within the components of the multilayer structure that describes the solar cell of Figs. 3.34 and 3.35 incorporating a standard 2.2 μm CIGS absorber and an anti-reflection coating [8]. The deficit of the sum from 100% provides the reflectance of the solar cell

those obtained in the simulations. By introducing carrier collection probability profiles in each case to represent the actual carrier collection from different depths within the CIGS bulk layers, the differences between the EQE simulation and measurement could be understood. For the cells with thin absorbers, it was found that collection from the CIGS adjacent to the back contact is significantly reduced as is observed for the solar cell with the 0.73 μm absorber. With the decrease in absorber layer thickness, these losses due to carrier recombination increase

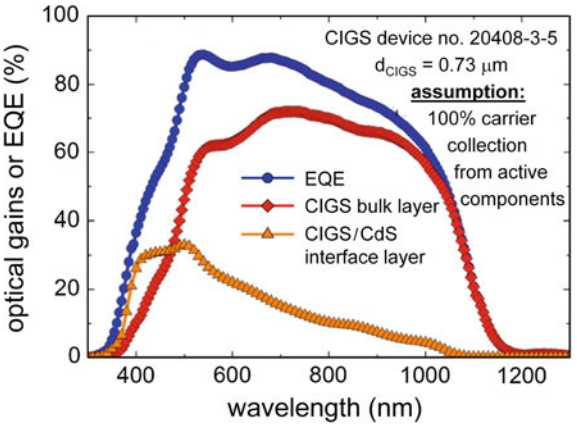


Fig. 3.37 Optically simulated EQE spectrum based on assumed 100% collection of photo-generated charge carrier for the solar cell of Figs. 3.28, 3.29 and 3.30 incorporating the thin 0.73 μm CIGS absorber and no anti-reflection coating. Also shown are the simulated photon absorbance spectra for the active components including the CIGS/CdS interface layer and the CIGS bulk layer [11]

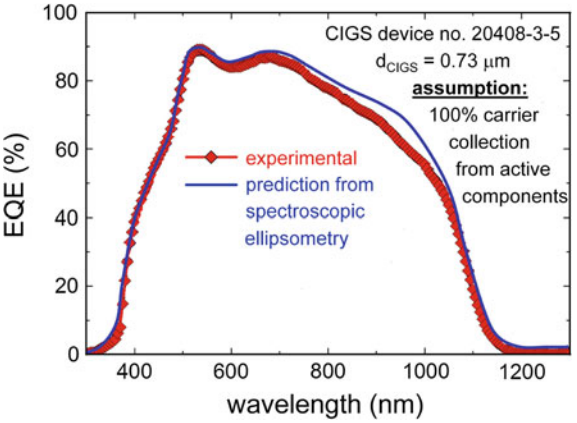


Fig. 3.38 Comparison of the EQE measurement and the optical simulation for the solar cell of Fig. 3.37 with the thin 0.73 μm CIGS absorber, based on assumed 100% collection of photo-generated charge carriers from the two active component layers [11]

monotonically. In Fig. 3.42, the experimental J_{SC} values are presented in comparison with those simulated optically assuming 100% collection of photo-generated charge carriers from the two active layers. The difference between the simulated J_{SC} value and the measured result is shown as a function of the thickness of the CIGS bulk layer in Fig. 3.43. This difference is ascribed to photo-generated carrier losses by recombination which increase from 0.0 mA/cm^2 for a high efficiency CIGS solar cell incorporating a standard 2.2 μm absorber layer to 5.4 mA/cm^2 for a solar cell incorporating an ultra-thin 0.30 μm absorber layer.

It is also of interest to design an ARC for the solar cell of Fig. 3.41 with the absorber layer thickness of 0.73 μm [8]. For this cell, thickness optimization of the MgF_2 ARC is performed as shown in Fig. 3.44 in one case based on the assumption of 100% collection of charge carriers from the active component layers and in a second case based on the assumption of reduced collection from the bulk layer of the CIGS absorber. Reduced collection is described by the collection probability profile for the solar cell in Fig. 3.40. It should be recalled also that the $\varepsilon(E)$ spectra

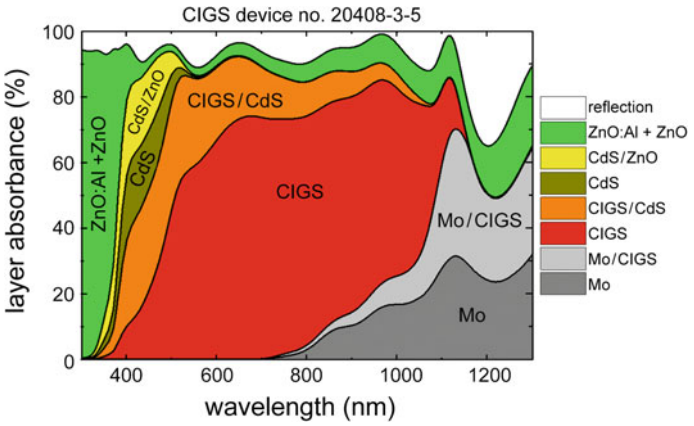


Fig. 3.39 Simulated percentage of photons absorbed (or photon absorbance) within the components of the multilayer structure that describes the solar cell of Figs. 3.37 and 3.38 incorporating the thin 0.73 μm absorber layer and no anti-reflection coating [11]. The deficit of the sum from 100% provides the reflectance of the solar cell

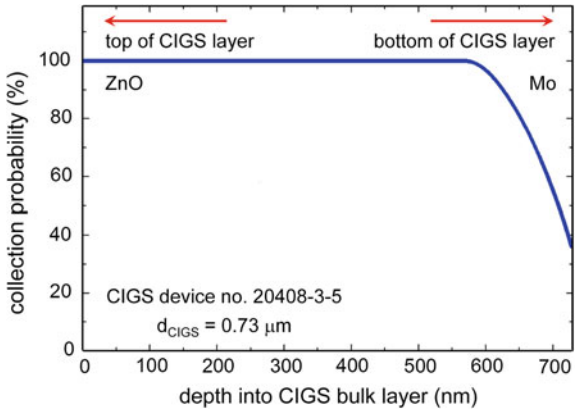


Fig. 3.40 Probability profile for photo-generated charge carrier collection applied in the EQE simulation to model losses resulting from recombination within the bulk component of the 0.73 μm thick CIGS absorber adjacent to the Mo back contact [11]

and structural parameters applied in all simulations were obtained from SE measurements and analysis results of Figs. 3.21, 3.29, and 3.30. For both cases, maxima occur at the MgF_2 bulk layer thickness of 92 nm and suggest that an enhancement in J_{SC} of 1.9 mA/cm^2 is possible via the ARC. The measured EQE spectrum for this solar cell before and after the ARC deposition with an intended 92 nm thickness is shown in Fig. 3.45. The ARC yielded an experimental J_{SC} improvement of 1.9 mA/cm^2, which is consistent with that predicted from the optical simulation. Again, the optical model for the solar cell predicts correctly the performance gain from ARC deposition.

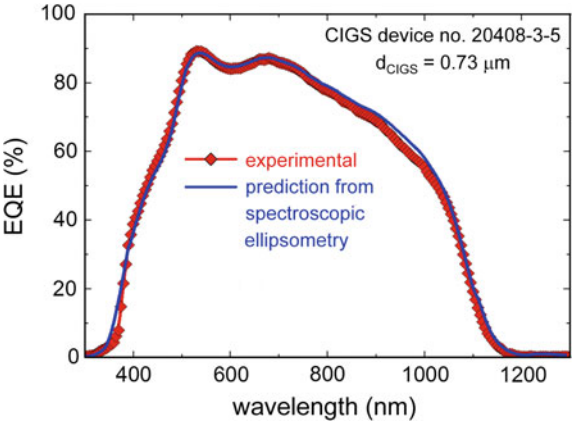


Fig. 3.41 Comparison of EQE measurement and optical simulation for the solar cell of Fig. 3.37 with the 0.73 µm thick CIGS absorber and no anti-reflection coating. The prediction is based on the assumption of 100% collection probability for photo-generated carriers from the CIGS/CdS interface layer and a reduced collection probability from the bulk layer of the CIGS absorber according to Fig. 3.40 [11]

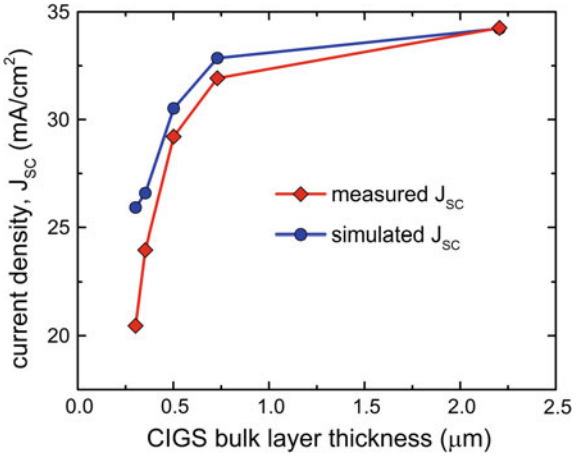


Fig. 3.42 Measured and optically simulated short-circuit current density J_{SC}, the latter based on the assumption that 100% of the charge carriers photo-generated within the CIGS/CdS interface and CIGS bulk layers are collected. These results are for solar cells incorporating standard 2.2 µm and thin CIGS absorbers without ARCs [11]

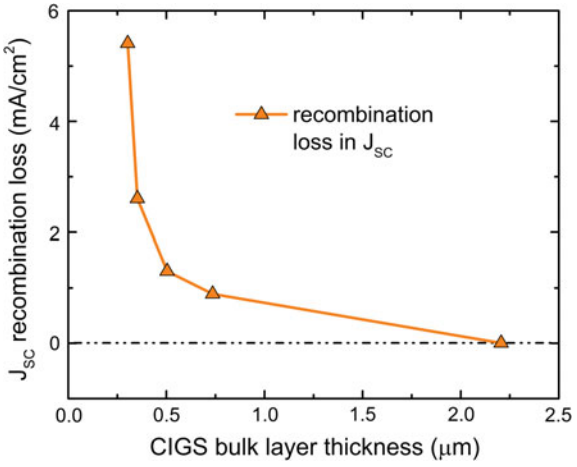


Fig. 3.43 Losses in J_{SC} due to recombination are plotted versus the CIGS bulk layer thickness corresponding to the results in Fig. 3.42 [11]

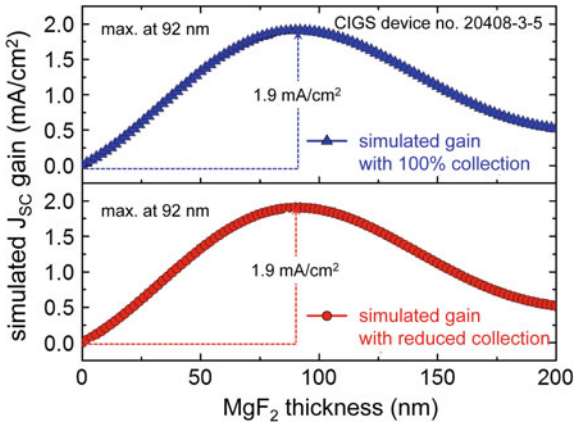


Fig. 3.44 Thickness optimization of a MgF_2 ARC for the solar cell with the 0.73 μm thick CIGS absorber layer, based on the assumption that 100% of the photo-generated charge carriers are collected (top, triangles) and based on the assumption that a reduced probability of collection occurs within the CIGS bulk layer according to the profile of Fig. 3.40 (bottom, circles) [8]

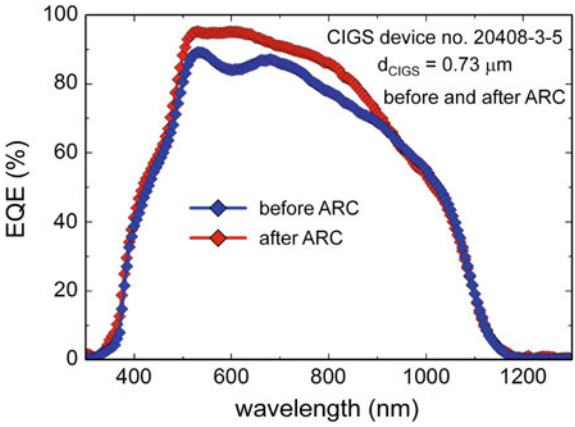


Fig. 3.45 Measured EQE spectra for the solar cell with the 0.73 μm thick CIGS absorber layer of Fig. 3.37 before and after application of the MgF_2 ARC [8]

In Fig. 3.46, photon absorbance spectra in the CIGS/CdS interface layer and the CIGS bulk layer are simulated and summed for the solar cell with a 0.73 μm reduced thickness CIGS absorber and an optimized ARC [8]. The summation is used to represent the net EQE response based on an assumed 100% collection of photo-generated charge carriers. In Fig. 3.47, the measured EQE spectrum is compared to that predicted from the SE analysis with the assumption of ideal collection of carriers from the two active layers, and the absorbance spectra are included in Fig. 3.48. Reasonable agreement overall is evident in Fig. 3.47 between the simulated EQE spectrum and that measured; however, the simulated spectrum exceeds the measured one. The simulated EQE spectrum upon integration yields J_{SC} = 34.7 mA/cm^2, whereas the measured spectrum results in J_{SC} = 33.8 mA/cm^2. The 0.9 mA/cm^2 difference again is consistent with the presence of carrier losses due to recombination in the CIGS bulk layer as discussed previously for the results obtained before the ARC deposition. The collection probability profile shown in Fig. 3.40 is expected to be relevant to collection after ARC deposition as well. By introducing this profile for the

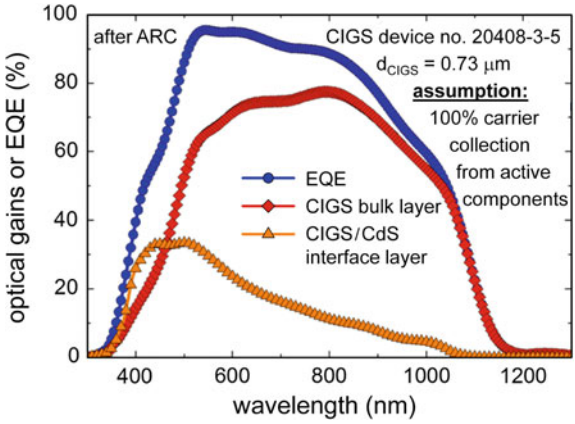


Fig. 3.46 Optically simulated EQE spectrum based on assumed 100% collection of photo-generated charge carriers for the solar cell of Figs. 3.28 through 3.30 incorporating the thin 0.73 μm CIGS absorber and an anti-reflection coating. Also shown are the simulated photon absorbance spectra for the active components including the CIGS/CdS interface layer and the CIGS bulk layer [8]

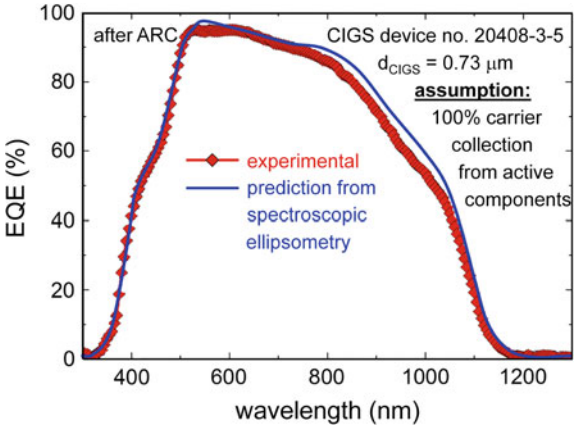


Fig. 3.47 Comparison of the EQE measurement and the optical simulation for the solar cell of Fig. 3.46 with the thin 0.73 μm CIGS absorber and an anti-reflection coating, based on assumed 100% collection of photo-generated charge carriers from the two active components, including the CIGS/CdS interface layer and the CIGS bulk layer [8]

collection probability into the simulation, an improved fit to the measured EQE spectrum is obtained. The improved EQE fit that accounts for carrier recombination losses is shown in Fig. 3.49. Thus in the analysis of the optical performance of the CIGS solar cell, the results again demonstrate the effectiveness and overall consistency of the SE-deduced model that includes the Ga profile. By comparing EQE simulations and measurement for cells with and without ARCs, an understanding of collection losses in thin cells is possible and suggests that, in thin cells, improvements in back contact performance are needed.

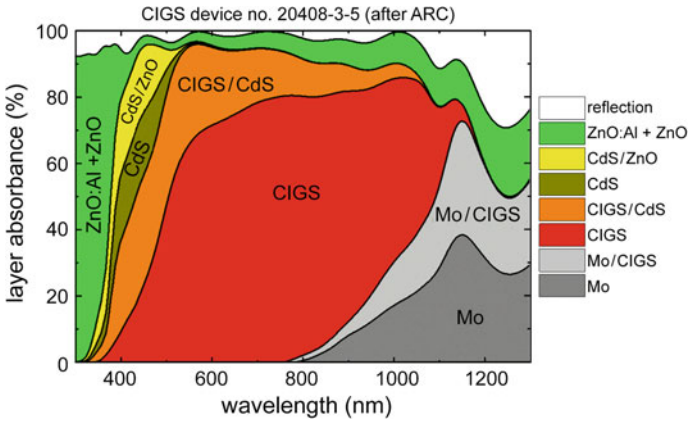


Fig. 3.48 Simulated percentage of photons absorbed (or photon absorbance) within the components of the multilayer structure that describes the solar cell of Figs. 3.46 and 3.47 incorporating the thin 0.73 μm thick CIGS absorber layer and a 92 nm thick MgF_2 ARC [8]. The deficit of the sum from 100% provides the reflectance of the solar cell

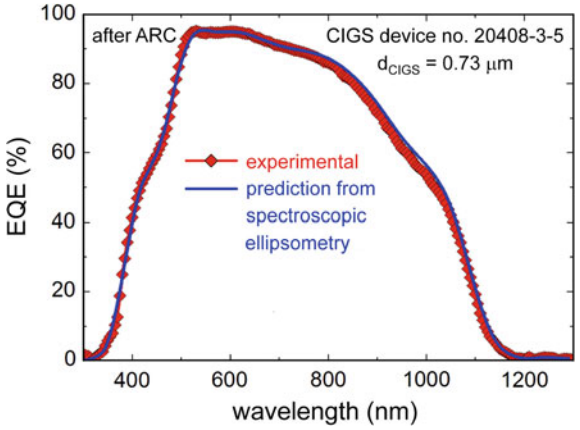


Fig. 3.49 Comparison of the EQE measurement and the optical simulation for the solar cell of Figs. 3.46 and 3.47 with the thin 0.73 μm CIGS absorber and the anti-reflection coating. The simulation is based on the assumption of 100% probability of charge carrier collection from the CIGS/CdS interface layer and reduced probability from the CIGS bulk layer according to the profile of Fig. 3.40 [8]

3.5 Summary

The results presented in this review illustrate the application of optical metrology based on spectroscopic ellipsometry (SE) in providing the foundation for external quantum efficiency (EQE) simulations of devices for comparison with measurements. The goal is to understand in greater depth the origins of optical and electronic collection and losses in thin film photovoltaics technologies, and as a result, the optical performance limitations.

In the studies of *a*-Si:H-based *p-i-n* solar cells in the superstrate configuration, sensitivity is demonstrated for electrical losses from photo-generated charge carriers near the *i*/*n* interface caused by an *i*-layer thickness greater than the collection length for holes, as imposed by their mobility limitations [9]. Also demonstrated is the enhanced collection of carriers near the *p*/*i* interface due to improved electronic quality protocrystalline Si:H in the SnO_2:F/(*p*-type *a*-$Si_{1-x}C_x$:H)/(high *R a*-Si:H) interface layer. The application of these techniques, which employ specular optical models, can be applied as well to quantify light trapping for near bandgap photon energies.

For CdS/CdTe solar cells in the superstrate configuration as well, the efficacy of SE in a through-the-glass mode has been demonstrated in-depth for non-invasive optical metrology [10]. The thicknesses deduced indirectly from the SE analysis agree well with those measured directly from XTEM images. In addition, the deduced parameters that describe the dielectric function of the bulk and interface layers provide information on the SnO_2:F transparent conductor and the CdTe absorber properties, as well as on the nature of interfaces at the heterojunction and at the contacts. Based on the results of a thorough multilayer structural and optical analysis of the CdS/CdTe solar cell by SE, optical modeling of the EQE spectra has been performed and the resulting simulations have been compared with experimental results. Observed deviations can assist in refining the inputs to the model of the solar cell, as well as in identifying and quantifying the losses. Applying these methods, the optical losses that occur when photons with energies above the bandgap are not absorbed within the active layers can be distinguished from the electronic losses when charge carriers photo-generated within the active layers are not collected from these layers.

Solar cells incorporating standard thickness and thin CIGS absorbers were also studied using SE to extract the multilayer structural and CIGS compositional parameters necessary for EQE simulation [11]. CIGS is more challenging due to the need to extract absorber layer Ga profiles for an accurate optical model. From the SE results, EQE spectra have been simulated based on the assumption that all charge carriers photo-generated within the CIGS-containing active layers, including the CIGS/CdS interface layer and the CIGS bulk layer, are collected at the contacts. For cells with standard thickness CIGS absorbers, excellent agreement between the EQE prediction from the simulation and the measured result is obtained based on this assumption. For cells with thin CIGS absorbers, however, the EQE spectra simulated under the assumption of 100% collection from the two active layers exceed the measured spectra. This indicates the occurrence of current losses by recombination of charge carriers within one or both of the active layers associated with thin absorbers. By introducing into the simulation a probability profile for charge carrier collection from the CIGS bulk layer, the EQE simulation is in closer agreement with the measured result. With step-wise decreases in the absorber layer thickness, the losses due to recombination account for an increasing fraction of the total possible current. For the cells with thin CIGS absorbers, carrier collection is reduced in the region of the CIGS bulk layer adjacent to the back contact. Applying this approach, one can determine both the origin and magnitude of current losses that in CIGS cells occur via recombination of photo-generated electrons and holes.

Although single location measurement, analysis, as well as EQE and short-circuit current density predictions for solar cells were demonstrated in this chapter, the SE-based metrology can be extended for mapping of multilayer solar cell structures. Thus, the component layer properties can be determined at each location, enabling mapping of EQE and current density, as well. This capability is enabled by the short measurement times of <1 s per (ψ, Δ) spectra made possible by a spectroscopic ellipsometer incorporating multichannel detection. As a result, multichannel SE has the potential to serve as a powerful metrology for the production line environment.

References

1. H. Fujiwara, *Spectroscopic Ellipsometry: Principles and Applications* (Wiley, Chichester, UK, 2007)
2. J. Li, R.W. Collins, M.N. Sestak, P. Koirala, N.J. Podraza, S. Marsillac, A.A. Rockett, in *Advanced Characterization Techniques for Thin Film Solar Cells,* 2nd edn, ed. by D. Abou-Ras, T. Kirchartz, U. Rau, (Wiley-VCH, Weinheim, Germany, 2016), Chapter 9, pp. 215–256
3. R.W. Collins, A.S. Ferlauto, in *Handbook of Ellipsometry*, ed. by H.G. Tompkins, E.A. Irene, (William Andrew, Norwich, NY, 2005), Chapter 2, pp. 93–235
4. J. Chen, J. Li, C. Thornberry, M.N. Sestak, R.W. Collins, J.D. Walker, S. Marsillac, A.R. Aquino, A. Rockett, in *Proceedings of the 34th IEEE Photovoltaic Specialists Conference*, Philadelphia, PA, 7–12 June 2009, (IEEE, New York, NY, 2009), pp. 1748–1753
5. P. Aryal, J. Chen, Z. Huang, L.R. Dahal, M.N. Sestak, D. Attygalle, R. Jacobs, V. Ranjan, S. Marsillac, R.W. Collins, in *Proceedings of the 37th IEEE Photovoltaic Specialists Conference*, Seattle, WA, 19–24 June 2011, (IEEE, New York, NY, 2011), pp. 2241–2246
6. A.S. Ferlauto, G.M. Ferreira, C. Chen, P.I. Rovira, C.R. Wronski, R.W. Collins, X. Deng, G. Ganguly, in *Photovoltaics for the 21st Century II*, ed. by R.D. McConnell, V.K. Kapur, (Electrochemical Society, Pennington, NJ, 2001), pp. 199–228
7. G.M. Ferreira, A.S. Ferlauto, P.I. Rovira, C. Chen, H.V. Nguyen, C.R. Wronski, R.W. Collins, in *Amorphous and Heterogeneous Silicon-Based Films - 2001, Materials Research Society Symposium Proceedings*, vol. 664, ed. by M. Stutzmann, J.B. Boyce, J.D. Cohen, R.W. Collins, J. Hanna, (MRS, Warrendale, PA, 2001), A24.6: pp. 1–6
8. A.-R. Ibdah, *Optical Physics of Cu(In, Ga)Se_2 Solar Cells and Their Layer Components*, Ph.D. Dissertation, (University of Toledo, Toledo, OH, 2016)
9. P. Aryal, Z. Huang, S. Marsillac, N. J. Podraza, R. W. Collins, in *Proceedings of the 42nd IEEE Photovoltaic Specialists Conference*, New Orleans, LA, 14–19 June 2015, (IEEE, New York, NY, 2015), Art. No. 735-6311: pp. 1–4
10. P. Koirala, J. Li, H.P. Yoon, P. Aryal, S. Marsillac, A.A. Rockett, N.J. Podraza, R.W. Collins, Prog. Photovolt. Res. Appl. **24,** 1055 (2016)
11. A.-R.A. Ibdah, P. Pradhan, P. Aryal, N.J. Podraza, S. Marsillac, R.W. Collins, in *Proceedings of the 43rd IEEE Photovoltaic Specialists Conference*, Portland, OR, 5–10 June 2016, (IEEE, New York, NY, 2016), pp. 2184–2187
12. A. Shah (ed.), *Thin Film Silicon Solar Cells* (CRC, Boca Raton, FL, 2010)
13. R.W. Collins, A.S. Ferlauto, G.M. Ferreira, C. Chen, J. Koh, R.J. Koval, Y. Lee, J.M. Pearce, C.R. Wronski, Sol. Energy Mater. Sol. Cells **78**, 143 (2003)
14. K. von Rottkay, M. Rubin, in *Thin Films for Photovoltaic and Related Device Applications*, *Materials Research Society Symposium Proceedings*, vol. 426, ed. by A. Catalano,

C. Eberspacher, D.S. Ginley, T.M. Peterson, H.W. Schock, T. Wada, (MRS, Warrendale, PA, 1996), pp. 449–454
15. R.A. Synowicki, B.D. Johs, A.C. Martin, Thin Solid Films **519**, 2907 (2011)
16. J. Koh, Y. Lee, H. Fujiwara, C.R. Wronski, R.W. Collins, Appl. Phys. Lett. **73**, 1526 (1998)
17. J. Chen, *Spectroscopic Ellipsometry Studies of II-VI Semiconductor Materials and Solar Cells*, Ph.D. Dissertation, (University of Toledo, Toledo, OH, 2010)
18. A.S. Ferlauto, G.M. Ferreira, J.M. Pearce, C.R. Wronski, R.W. Collins, X. Deng, G. Ganguly, J. Appl. Phys. **92**, 2424 (2002)
19. G.D. Cody, in *Hydrogenated Amorphous Silicon Optical Properties*; Semiconductors and Semimetals, vol. 21, Part B, ed. by J.I. Pankove, (Academic, New York, NY, 1984), Chapter 2, pp. 11–82
20. W.B. Jackson, S.M. Kelso, C.C. Tsai, J.W. Allen, S.-J. Oh, Phys. Rev. B **31**, 5187 (1985)
21. Z. Huang, *Spectroscopic Ellipsometry Studies of Thin Film a-Si:H/nc-Si:H Micromorph Solar Cell Fabrication in the p-i-n Superstrate Configuration*, Ph.D. Dissertation, (University of Toledo, Toledo, OH, 2016)
22. R.W. Collins, I. An, C. Chen, in *Handbook of Ellipsometry*, ed. by H.G. Tompkins, E.A. Irene, (William Andrew, Norwich, NY, 2005), Chapter 5, pp. 329–432
23. P. Aryal, *Optical and Photovoltaic Properties of Copper Indium-Gallium Diselenide Materials and Solar Cells*, Ph.D. Dissertation, (University of Toledo, Toledo, OH, 2014)
24. J. Li, P. Pradhan, P. Koirala, X. Tan, B. Sang, B. J. Stanbery, N.J. Podraza, R.W. Collins, in *Proceedings of the 42nd IEEE Photovoltaic Specialists Conference*, New Orleans, LA, 14–19 June 2015, (IEEE, New York, NY, 2015), Art. No. 735-5642: pp. 1–4
25. H. Fujiwara, J. Koh, P.I. Rovira, R.W. Collins, Phys. Rev. B **61**, 10832 (2000)
26. I. An, Y.M. Li, C.R. Wronski, R.W. Collins, Phys. Rev. B **48**, 4464 (1993)
27. E.A. Schiff, in *Amorphous and Polycrystalline Thin Film Silicon Science and Technology - 2009, Materials Research Society Symposium Proceedings*, vol. 1153, ed. by A. Flewitt, Q. Wang, J. Hou, A. Nathan, S. Uchikoga, (MRS, Warrendale, PA, 2009), A15-01: pp. 1-12
28. J. Liang, E.A. Schiff, S. Guha, B. Yan, J. Yang, Appl. Phys. Lett. **88**, 063512 (2006)
29. M. Gloeckler, I. Sankin, Z. Zhao, IEEE J. Photovolt. **3**, 389 (2013)
30. B.E. McCandless, J.R. Sites, in *Handbook of Photovoltaic Science and Engineering,* 2nd edn, ed. by A. Luque, S. Hegedus, (Wiley, New York, NY, 2011), pp. 600–641
31. N.R. Paudel, Y. Yan, Appl. Phys. Lett. **105**, 183510 (2014)
32. A. Gupta, A.D. Compaan, Appl. Phys. Lett. **85**, 684 (2004)
33. X. Wu, Sol. Energy **77**, 803 (2004)
34. C.C. Kim, M. Daraselia, J.W. Garland, S. Sivanathan, Phys. Rev. B **56**, 4786 (1997)
35. J. Li, J. Chen, R.W. Collins, Appl. Phys. Lett. **99**, 061905 (2011)
36. J. Li, J. Chen, R.W. Collins, Appl. Phys. Lett. **97**, 181909 (2010)
37. J. Li, N.J. Podraza, R.W. Collins, Phys. Status Solidi (a) **205**, 901 (2008)
38. P. Koirala, *Multichannel Spectroscopic Ellipsometry for CdTe Photovoltaics: From Materials and Interfaces to Solar Cells*, Ph.D. Dissertation, (University of Toledo, Toledo, OH, 2015)
39. J. Chen, P. Koirala, C. Salupo, R.W. Collins, S. Marsillac, K.R. Kormanyos, B.D. Johs, J.S. Hale, G.L. Pfeiffer, in *Proceedings of the 38th IEEE Photovoltaic Specialists Conference*, Austin, TX, 3–8 June 2012, (IEEE, New York, NY, 2012), pp. 377–381
40. B. Johs, C.M. Herzinger, Phys. Stat. Solidi (c) **5**, 1031 (2008)
41. R.H. Muller, in *Techniques for Characterization of Electrodes and Electrochemical Processes*, ed. by R. Varma, J.R. Selman, (Wiley, New York, NY, 1991), pp. 31–125
42. B. Stjerna, E. Olsson, C.G. Granqvist, J. Appl. Phys. **76**, 3797 (1994)
43. E. Burstein, Phys. Rev. **93**, 632 (1954)
44. T.S. Moss, Proc. Phys. Soc. London B **67**, 775 (1954)
45. P. Koirala, X. Tan, J. Li, N.J. Podraza, S. Marsillac, A.A. Rockett, R.W. Collins, in *Proceedings of the 40th IEEE Photovoltaic Specialists Conference*, Denver, CO, 8–13 June 2014, (IEEE, New York, NY, 2014), pp. 674–679
46. S.S. Hegedus, W.N. Shafarman, Prog. Photovolt. Res. Appl. **12,** 155 (2004)
47. http://www.nrel.gov/ncpv/images/efficiency_chart.jpg

48. W.N. Shafarman, S. Siebentritt, L. Stolt, in *Handbook of Photovoltaic Science and Engineering*, 2nd edn., ed. by A. Luque, S. Hegedus, (Wiley, New York, NY, 2011), pp. 546–599
49. P. Aryal, P. Pradhan, D. Attygalle, A.-R. Ibdah, K. Aryal, V. Ranjan, S. Marsillac, N.J. Podraza, R.W. Collins, IEEE J. Photovolt. **4**, 333 (2014)
50. A.M. Gabor, J.R. Tuttle, M.H. Bode, A. Franz, A.L. Tennant, M.A. Contreras, R. Noufi, D.G. Jensen, A.M. Hermann, Sol. Energy Mater. Sol. Cells **41–42**, 247 (1996)
51. P. Pradhan, P. Aryal, A.-R. Ibdah, P. Koirala, J. Li, N.J. Podraza, A.A. Rockett, S. Marsillac, R.W. Collins, in *Proceedings of the 42nd IEEE Photovoltaic Specialists Conference*, New Orleans, LA, 14–19 June 2015, (IEEE, New York, NY, 2015), Art. No. 735-5890: pp. 1–4
52. P. Aryal, A.-R. Ibdah, P. Pradhan, D. Attygalle, P. Koirala, N.J. Podraza, S. Marsillac, R.W. Collins, J. Li, Prog. Photovolt. Res. Appl. **24,** 1200 (2016)

Chapter 4
Characterization of Textured Structures



Hiroyuki Fujiwara and Yuichiro Sago

Abstract Various textured structures have been incorporated into photovoltaic devices to improve the short-circuit current density based on optical confinement effects. Although intense light scattering occurs in textured structures, spectroscopic ellipsometry (SE) characterization can still be made even for textured single crystalline Si (c-Si) having a pyramid size of ~10 μm. Depending on the texture size, however, different measurements and analytical approaches need to be used. It has been demonstrated that high-precision SE characterization of submicron-size rough structures can be carried out by employing advanced optical models, including (i) effective-medium-approximation multilayer model and (ii) surface area model. From such SE analyses, structural non-uniformities in large-area solar cell modules can further be determined. In this chapter, we review SE characterization performed for textured structures in c-Si heterojunction, Si thin-film and Cu(In,Ga)Se_2 solar cells.

4.1 Introduction

Incorporation of textures into solar cell devices has been a simple and straightforward approach in improving the conversion efficiencies. In particular, the textured structures in the devices enhance the short-circuit current density (J_{sc}) effectively through the reduction of the light reflection and the increase in the optical pass length within the absorber by light scattering [1–4]. However, the texture effect changes depending on the device configuration and the optical properties of solar-cell component layers. For example, if the absorption coefficient (α) of a semiconducting absorber is low and the formation of a thicker absorber is difficult, the introduction of a textured structure can be quite effective. For Si thin-film solar cells, including hydrogenated amorphous silicon (a-Si:H) and microcrystalline silicon (μc-Si:H) solar cells, rough textures are commonly used [3, 4] due to low α (see also Fig. 1.6). In crystalline Si (c-Si) solar

H. Fujiwara (✉) · Y. Sago
Gifu University, 1-1 Yanagido, 501-1193 Gifu, Japan
e-mail: fujiwara@gifu-u.ac.jp

© Springer International Publishing AG, part of Springer Nature 2018

H. Fujiwara and R. W. Collins (eds.), *Spectroscopic Ellipsometry for Photovoltaics*,
Springer Series in Optical Sciences 214,
https://doi.org/10.1007/978-3-319-95138-6_4

cells, pyramid-shaped textures are generally formed by anisotropic chemical etching [5, 6] to reduce the light reflection. In contrast, the texture effect is limited in Cu(In, Ga)Se_2 (CIGSe) solar cells since α is high and the absorber layer is sufficiently thick (Fig. 1.13) [7]. In polycrystalline semiconductors, however, natural textures are often formed by crystallographic grain growth on substrates.

Figure 4.1 shows the scanning electron microscope (SEM) images of a texture-etched single c-Si substrate [8], (b) a μc-Si:H/a-Si:H tandem solar-cell structure [9] and (c) a CIGSe solar cell structure [10]. The c-Si texture is formed by alkaline wet etching of a Si (100) substrate. In this case, due to the difference in etching rates for each crystal plane, pyramid-shaped textures with {111} facets are generated automatically, and the texture size can also be changed by controlling the etching conditions [6]. For the fabrication of a-Si:H/c-Si heterojunction solar cells, a texture size of D ~10 μm is generally employed.

For a-Si:H [3, 11] and hybrid perovskite [12, 13] solar cells, textured SnO_2:F layers formed on glass substrates have been applied quite widely, partly because

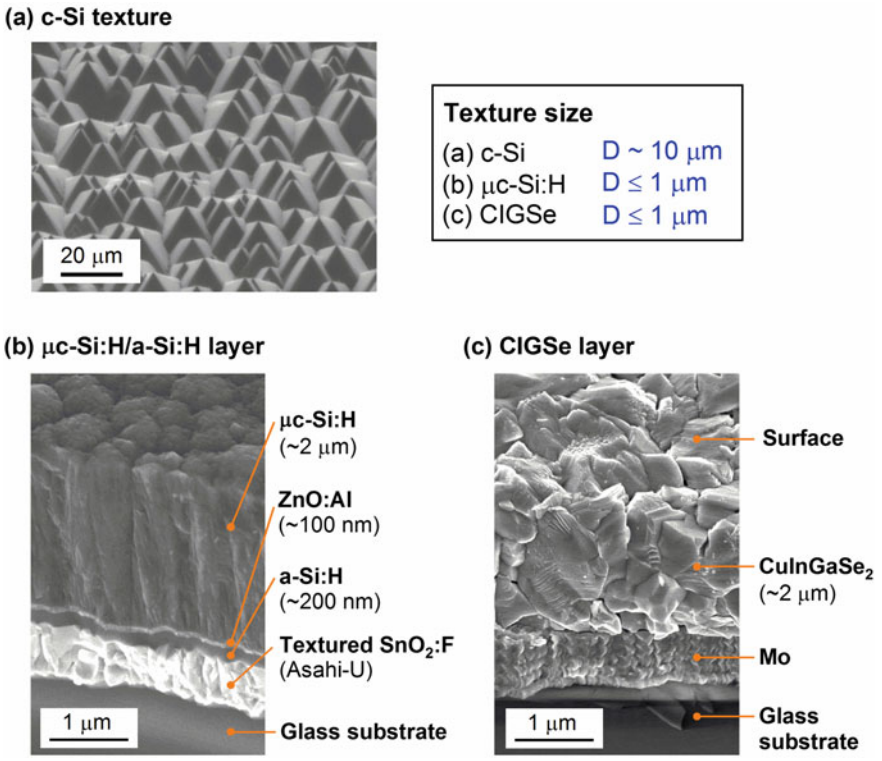


Fig. 4.1 SEM images of a texture-etched single c-Si substrate [8], **b** a μc-Si:H/a-Si:H tandem solar cell structure [9] and **c** a CIGSe solar cell structure [10]. The texture sizes of each structure are also indicated

these substrates are commercially available (Asahi-U, TEC-8 and TEC-15 substrates described in Sect. 18.5 in Vol. 1). However, the texture size of these transparent conductive oxide (TCO) layers is in a submicron range ($D < 1$ μm) and is rather small (Fig. 4.1b). In the μc-Si:H/a-Si:H tandem structure, a thin ZnO layer is introduced between the a-Si:H and μc-Si:H absorber layers to improve J_{sc} of the a-Si:H top cell [14, 15].

The CIGSe layer in Fig. 4.1c was formed by a three-stage coevaporation process in which (Cu, In Ga, Se) elemental sources are supplied with different combinations during the growth [16–18]. This process is used quite commonly to generate a V-shaped Ga profile within the CIGSe absorber with a low Ga content in the middle and higher Ga contents at the front and rear sides (Fig. 2.8). Moreover, this processing allows the formation of larger CIGSe grains of 1–2 μm while suppressing grain boundary effects, and the V-shaped profile is quite effective in reducing the carrier recombination particularly in the rear interface region [18–20].

It can be seen from Fig. 4.1 that the texture size of the c-Si ($D \sim 10$ μm) is much larger than those of the submicron natural textures ($D \leq 1$ μm) observed in μc-Si:H/a-Si:H and CIGSe solar cells. When spectroscopic ellipsometry (SE) measurements are performed for the c-Si textures, we observe no light reflection since the texture size is far larger than the wavelength (λ) of the SE light probe (typically $\lambda = 0.2$–1.5 μm). Accordingly, the SE measurement of the c-Si texture cannot be performed using a standard configuration and, in this case, the SE characterization is carried out by tilting the whole c-Si sample so that the specular light-reflection component is measured [8, 21–23]. For μc-Si:H/a-Si:H and CIGSe solar cells, on the other hand, a standard SE measurement configuration can be employed as the specular light reflection still occurs. Nevertheless, in the condition of $D \sim \lambda$, a more complex SE analysis is necessary to express the optical response of microscopically rough surface and interface structures (see also Chap. 6 in Vol. 1).

The characterization of textured solar cell structures becomes important when SE is employed as an inspection tool of large-area modules. In Fig. 4.2, the basic structure of a thin-film solar cell module is shown. This module is composed of elementary cells (μc-Si:H/a-Si:H tandem cells) having a striped shape, which are integrated by using a laser scribing technique [24, 25]. In Fig. 4.2a, the photoelectrons generated in the μc-Si:H bottom cells pass though the rear electrode/front TCO layer and recombine with the holes generated in the a-Si:H top cell. Thus, the photocurrents of the module flow as the recombination current of each elementary cell. In conventional thin-film solar cell modules, series connections are realized for all the elementary cells, and an elementary cell that shows the lowest current limits the total module current [26]. Thus, the output power of thin film modules is affected directly by the structural non-uniformity of solar-cell component layers [24, 25]. Moreover, for thin-film modules, wire-grid electrodes cannot be employed and thicker TCO layers need to be used to suppress the reduction of the fill factors. In this case, however, the TCO thickness inhomogeneity tends to increase (see Fig. 18.5 in Vol. 1), leading to a lower module output due to the variation of the free carrier absorption in the TCO layer.

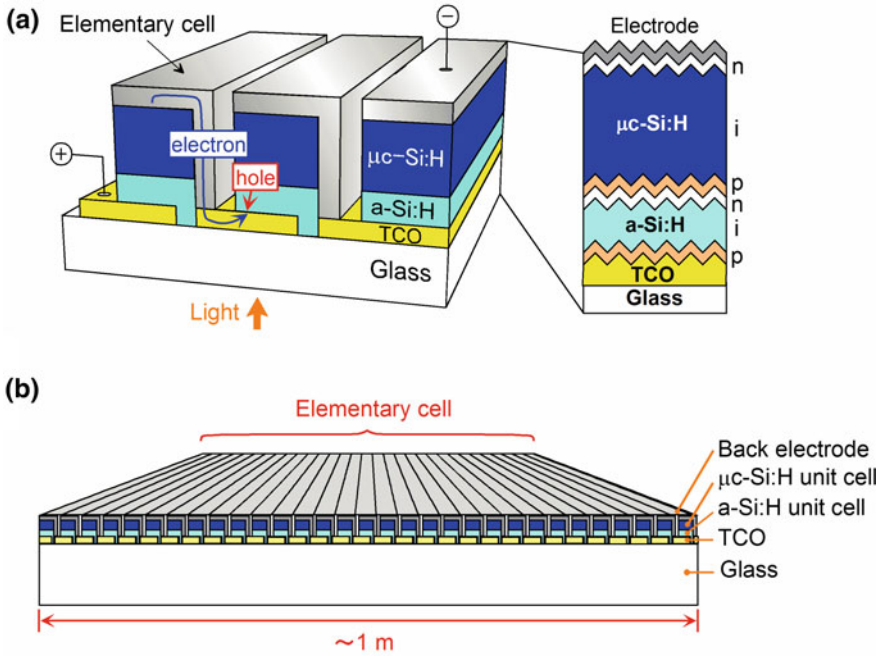


Fig. 4.2 **a** Module structure consisting of μc-Si:H/a-Si:H elementary cells and **b** structure of the large-area module for μc-Si:H/a-Si:H tandem cells

In thin-film solar cell modules, a large number of elementary cells are formed (Fig. 4.2b), and these exist ~80 elementary cells in a μc-Si:H/a-Si:H module with a size of 1.4 × 1.1 m^2. Each elementary cell further consists of the a-Si:H and μc-Si:H p-i-n cells. Accordingly, the module power is maximized when all the elementary cells (~160 cells) show the identical current. High structural uniformity of the component layers and its inspection are therefore critical to achieve the high module efficiencies. Since SE is a non-destructive characterization method with a measurement time of a few seconds, non-ideal structural inhomogeneities of solar-cell component layers can be detected rather easily by applying this technique. A SE measurement system with an effective measurement area exceeding 1.5 m^2 has already been commercialized and employed as a monitoring tool for a-Si:H-based module production.

In this chapter, SE measurement and analysis methods used for the characterization of various solar-cell textured structures are reviewed. As analysis examples of textured c-Si structures, we focused on the SE characterization of a-Si:H/c-Si heterojunction solar cells [8, 22, 23]. This chapter further introduces the structural analyses of the submicron-textured structures in Fig. 4.1 (μc-Si:H/a-Si:H and CIGSe) based on the effective-medium-approximation (EMA) multilayer model [9, 10]. The SE characterization of textured TCO structures can be found in Sect. 18.5 (Vol. 1).

4.2 Characterization of Textured Structures in a-Si:H/c-Si Solar Cells

In a-Si:H/c-Si heterojunction solar cells, quite thin a-Si:H layers with a thickness of <100 Å (Fig. 9.7 in Vol. 1) [27, 28] are formed on large c-Si textures with a scale of ~10 μm. This geometric structure makes the structural characterization of the a-Si:H layers quite difficult, even though the a-Si:H layer properties affect the a-Si:H/c-Si solar cell efficiency rather significantly (Chap. 9 in Vol. 1) [28, 29]. When a tilt-angle optical configuration is applied for the SE characterization of the textured structures, not only the thickness but also the properties of the a-Si:H layers can be determined. This section explains the basic method of the tilt-angle SE measurement and shows SE analysis examples for various a-Si:H/c-Si textured structures. The SE analysis results described in this section provide further insights into the optical response in textured c-Si solar cells.

4.2.1 Tilt-Angle SE Measurement

When c-Si textures are formed by wet alkaline etching of (100) single crystals, all the pyramid-shaped textures are oriented toward the same direction (Fig. 4.1a). Thus, if the textured c-Si substrate is aligned properly, specular reflection still occurs and the SE measurements can be performed [21]. Figure 4.3 shows the schematic diagram of the tilt-angle measurement configuration [8]. In this optical configuration, the flat plane of the c-Si {111} facets is adjusted to the normal to the incident plane by tilting a sample with the tilt angle θ_t [21]. In this configuration, therefore, each {111} facet acts as specular reflection surface and the SE

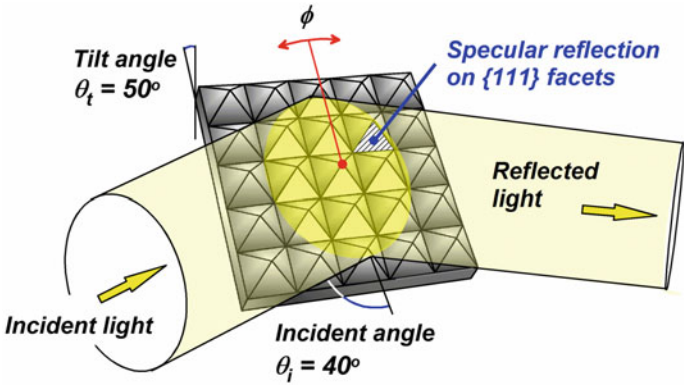


Fig. 4.3 Tilt-angle measurement configuration used for the SE measurements of textured c-Si substrates [8]. The ϕ shows the rotation angle of the sample. In this configuration, the flat surface of the c-Si {111} facets is normal to the incident plane

measurements are performed using the partially reflected light beam. In this measurement, however, the reflected light intensity decreases rather significantly, compared with flat substrates, due to light scattering. The reflection intensity of the light from the c-Si textures can be improved by applying (i) a small incident angle (θ_i) of 40° (normally ~75° for c-Si) [8], (ii) a high-intensity Xenon lamp source, and (iii) a short distance between the sample and detector [23]. In the tilt angle configuration, the precise adjustments of θ_t and the rotation angle ϕ are essential for the accurate measurements. The adjustment of θ_t and ϕ can be carried out relatively easily by simply maximizing the intensity of the reflected light [22].

From the light intensity measurement versus θ_t, the average top angle of the pyramid textures can also be evaluated using a relation of $2(90° - \theta_t)$ [8, 22]. The measurement of the c-Si texture in Fig. 4.1a leads to a texture top angle of 80° ($\theta_t = 50°$). Note that this value is different from the expected value of 70.4° determined from the Si (111) and (100) planes. The formation of the larger top angle has been attributed to the imperfect selectivity during wet etching [8]. In the actual measurement, the calibration of the SE system is carried out in the normal optical configuration ($\theta_t = 0°$) using a flat c-Si substrate, since the tilt angle configuration makes the sample calibration rather difficult because of the low intensity of reflected light. After the calibration, the sample with the texutre is placed, and the angles of θ_t and ϕ are adjusted before the SE measurement.

Based on the tilt-angle SE measurements, non-destructive characterization of SiN [21] and a-Si:H [8, 22, 23] layers has been performed. The ellipsometry system that allows the tilt angle measurements has already been commercialized and is employed widely as a characterization tool for the production of c-Si solar cells.

4.2.2 *Analysis of Textured a-Si:H/c-Si Structures*

Figure 4.4 shows (a) the (ψ, Δ) spectra obtained from the tilt-angle SE measurement of a very thin a-Si:H layer (~50 Å) formed on the textured c-Si substrate shown in Fig. 4.1a [8] and (b) the optical model for the textured a-Si:H/c-Si structure. The a-Si:H layer was deposited on the textured surface by plasma-enhanced chemical vapor deposition (PECVD). To avoid the detrimental epitaxial growth of the intended a-Si:H layer (Sect. 9.3 in Vol. 1), the low temperature growth of the a-Si:H layer (110 °C) was adopted. As confirmed from Fig. 4.4a, even for the textured structure, conventional (ψ, Δ) spectra can be obtained. However, in a short wavelength region ($\lambda < 350$ nm), the increase in the measurement noise can be seen because of low light intensities of a Xe light source and intense light scattering in the ultraviolet (UV) region.

In the tilt angle configuration, the ellipsometry analysis is simplified greatly. In particular, the SE analysis can be performed assuming a conventional flat optical model shown in Fig. 4.4b [8, 21–23], as only the specular reflection component is measured in this configuration. For the a-Si:H/c-Si analysis, an optical model with ambient/roughness layer (a-Si:H)/bulk layer (a-Si:H)/substrate (c-Si) can be

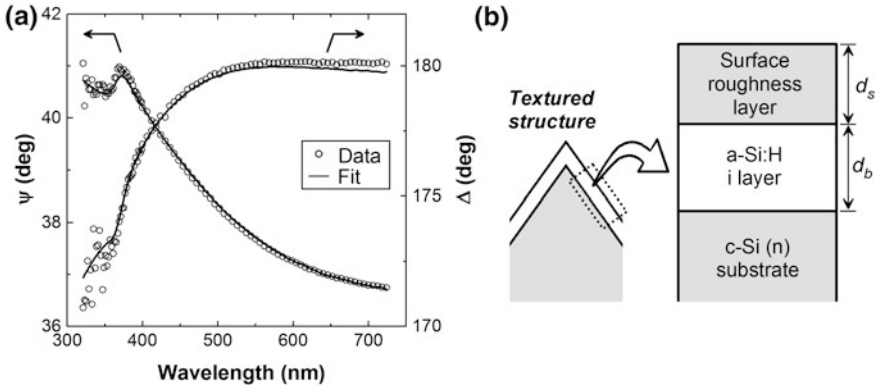


Fig. 4.4 **a** (ψ, Δ) spectra obtained from the tilt-angle SE measurement of the textured a-Si:H (~50 Å)/c-Si structure [8] and **b** optical model for the a-Si:H layer on the textured c-Si substrate

employed (Sect. 9.2.1 in Vol. 1) [30]. In this analysis, the dielectric function of an a-Si:H bulk layer, obtained in advance from a completely flat a-Si:H(200 Å)/c-Si structure, was used. The dielectric function of the surface roughness layer was calculated by applying the Bruggemman effective medium approximation (EMA) [31, 32] assuming a 50/50 vol.% mixture of the a-Si:H and voids (see Sect. 3.4.2 in Vol. 1). In the SE analysis of Fig. 4.4, therefore, only the surface roughness layer thickness (d_s) and bulk layer thickness (d_b) are characterized.

The solid lines in Fig. 4.4a show the fitting result obtained assuming the flat structure on the {111} facets. The calculated (ψ, Δ) spectra show excellent fitting to the experimental spectra in a wide λ region. From this analysis, d_b and d_s are determined to be $d_b = 58 \pm 2$ Å and $d_s = 10 \pm 1$ Å, respectively.

To justify this ellipsometry result, the same sample has been characterized by cross-sectional transmission electron microscopy (TEM). Figure 4.5 shows the TEM images of (a) the c-Si texture and (b) the a-Si:H deposited on the Si {111} facet [8]. The top angle of the Si pyramid determined from TEM (80°) is consistent with that characterized by the tilt angle measurement [$\theta_t = 50°$ in Fig. 4.4]. In Fig. 4.5b, the d_b values estimated from SE and TEM show excellent agreement, confirming the validity of the tilt-angle SE characterization. It has been found that the thicknesses of a-Si:H layers on the texture substrates (d_{tex}) and flat substrates (d_{flat}) show a clear relationship expressed by $d_{tex} = 0.69 d_{flat} + 14$ Å (Fig. 9.4 in Vol. 1). From this relation, d_{tex} can be deduced from d_{flat}. On the other hand, since the dielectric function of an a-Si:H p layer is similar to that of an a-Si:H i layer, the total thickness of a-Si:H p-i layers can also be determined using the above analysis procedure (see Sect. 9.2.2 in Vol. 1).

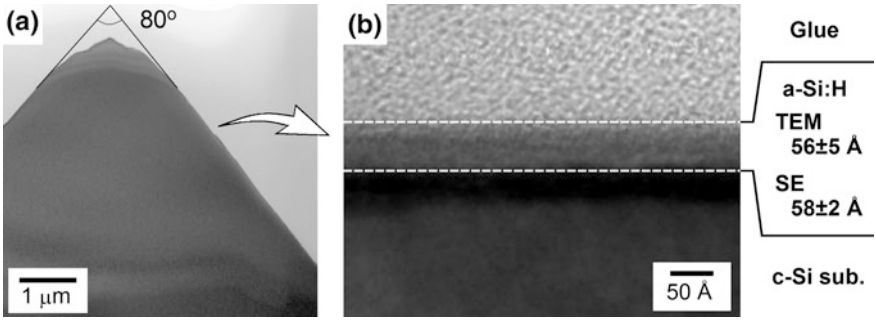


Fig. 4.5 TEM images of **a** the c-Si texture and **b** the a-Si:H layer grown on the pyramid-shaped Si {111} facet [8]. The TEM image of (**b**) shows the enlarged image of (**a**). In (**a**), the top angle of the c-Si texture (80°) is indicated

4.2.3 Effect of the Texture Size on a-Si:H Properties

The variation of the a-Si:H properties with the c-Si texture size has been investigated using the tilt angle technique [23]. In the previous section, the SE analysis was performed assuming that the textured structure does not affect the a-Si:H optical properties. However, the a-Si:H optical properties on the c-Si textures can also be studied. In particular, using the a-Si:H network model described in Sect. 9.4.1 (Vol. 1), the texture size effect on a-Si:H layer quality has been determined [23].

Figure 4.6 shows (a) the SEM images of textured c-Si substrates having different average texture sizes (A_{tex}) of 4, 8, 10, and 18 μm and (b) the normalized reflection light intensity as a function of A_{tex} [23]. Notice that the structural non-uniformity of

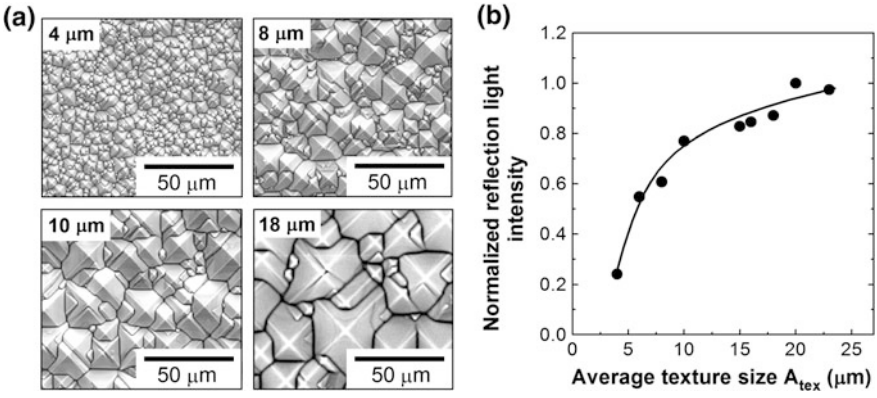


Fig. 4.6 **a** SEM images of textured c-Si substrates having different average texture sizes (A_{tex}) of 4 μm, 8 μm, 10 μm, and 18 μm and **b** normalized reflection light intensity in the tilt-angle optical configuration as a function of A_{tex} [23]

the texture increases slightly with decreasing the texture size. In Fig. 4.6b, the reflection light intensity shows a small change at $A_{tex} \geq 10$ μm, but the intensity decreases sharply at $A_{tex} < 10$ μm due to random light scattering that occurs on smaller texture surfaces. For the SE measurements of $A_{tex} < 10$ μm, therefore, a high-intensity Xe source is important to gain sufficient signal intensity.

In the SE analyses for different textures, the optical model shown in Fig. 4.4b was employed, but the optical constants of a-Si:H were obtained from the a-Si:H local network model. In this model, the a-Si:H optical properties are deduced from only two factors: i.e., the SiH_2 content (C_{SiH2}) and SiH content (C_{SiH}) of the a-Si:H (Sect. 9.4.1 in Vol. 1) [33, 34]. When this model is applied, the amplitude of the a-Si:H dielectric function is changed with C_{SiH2}, whereas the whole optical spectra move toward higher energies with increasing C_{SiH2} and C_{SiH} (Fig. 9.14 in Vol. 1). In the actual SE analysis, C_{SiH} was fixed at 9 at.%, as C_{SiH} shows a constant value at a low process temperature of $T \leq 180$ °C [33]. In addition, the incident angle (θ_i in Fig. 4.3) was also adjusted slightly in the analysis. As a result, the SE fitting analyses were carried out by using four parameters of (d_s, d_b, C_{SiH2} and θ_i).

Figure 4.7 shows the SE analyses performed for the a-Si:H(~80 Å)/c-Si textured structures of (a) $A_{tex} = 18$ μm and (b) $A_{tex} = 4$ μm [23]. In Fig. 4.7a, the calculated spectra (solid lines) show improved fitting to the experimental spectra (open circles), compared with the result of Fig. 4.4a. Moreover, the signal-to-noise ratio in the UV region is improved notably by using the high-intensity light source. From

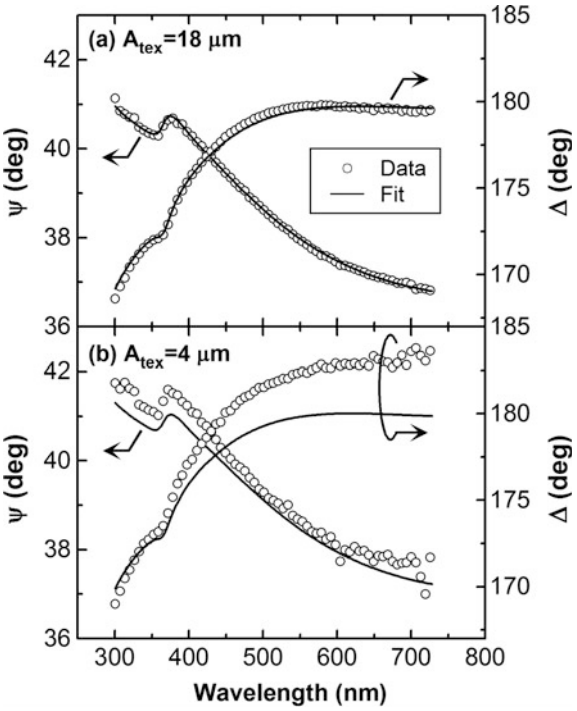


Fig. 4.7 SE analyses of the a-Si:H(~80 Å)/c-Si structures with **a** $A_{tex} = 18$ μm and **b** $A_{tex} = 4$ μm [23]. The experimental spectra (open circles) and the calculated spectra (solid lines) are shown

this analysis, the analytical parameters were determined to be $d_b = 71 \pm 2$ Å, $d_s = 25 \pm 1$ Å, and $C_{SiH2} = 6.2 \pm 0.7$ at.% with $\theta_i = 39.8 \pm 0.1°$. Accordingly, the structure and quality of quite thin a-Si:H layers (~100 Å) formed on c-Si textures can be characterized with small analysis errors.

For the a-Si:H/c-Si textured samples of $A_{tex} < 10$ μm, however, the above SE analysis is difficult due to strong light scattering and, as shown in Fig. 4.7b, the calculated spectra do not provide satisfactory fitting to the experimental spectra. Thus, a different analytical scheme has been applied for the sample characterization of $A_{tex} < 10$ μm. Specifically, in this analysis, the Stokes parameters were characterized [23], instead of (ψ, Δ) that are defined originally by $\psi = \cos^{-1}(-S_1)/2$ and $\Delta = \tan^{-1}(-S_3/S_2)$ [32]. Here, $S_{1\text{-}3}$ represent the normalized Stokes parameters. The S_1 and S_2 express the variations of light intensities between the linearly polarized states tilted at the orthogonal (0°, 90°) and (+45°, −45°) directions, respectively, while S_3 shows the light intensity difference between the left and right circular polarizations. In the actual analyses of $A_{tex} < 10$ μm, the parameters S_1 and S_2 were characterized by excluding the S_3 contribution, since for circular polarization the depolarization effect generated by light scattering is significantly larger, compared with the case of linear polarization [35, 36]. In the S_1 and S_2 spectral fitting, the effect of baseline shifts due to light scattering has also been taken into account [23].

Figure 4.8 summarizes (a) the growth rate and (b) C_{SiH2}, extracted from the SE analysis, versus A_{tex} [23]. The result obtained from the fitting analysis of conventional (ψ, Δ) is shown by closed circles, whereas the growth rate obtained from the fitting of (S_1, S_2) is indicated by squares. Moreover, the results extracted from the a-Si:H deposition on a flat c-Si substrate are shown by the dotted lines. In Fig. 4.8a, it can be seen that A_{tex} has a negligible influence on the a-Si:H growth rate, as the size of angstrom-scale SiH_3 precursors in PECVD is far smaller than the scale of the c-Si textures. The smaller a-Si:H growth rate observed on the texture surface has been attributed to the increase in the surface area (Sect. 9.2.1 in Vol. 1).

On the textures, C_{SiH2} of the a-Si:H layers shows a constant value of ~6.4 at.%. The constant growth rate also supports that no major change occurs in the a-Si:H layer with A_{tex}. The formation of SiH_2 bonds in a-Si:H network can be related to microvoid formation [33] and the material quality degrades at higher C_{SiH2}. Quite interestingly, C_{SiH2} of the textured structures (~6.4 at.%) is smaller, compared with the flat substrate (9.2 at.%). This indicates that the microvoid density decreases in the a-Si:H layers formed on the c-Si textures most likely due to the slower growth rate on the textures. In fact, when a higher rf power density was used for the a-Si:H deposition so that the a-Si:H growth rate on the texture becomes comparable to that on the flat substrate (~0.34 Å/s), the two a-Si:H layers show similar C_{SiH2} [23]. Thus, a dense a-Si:H network is formed on the {111} facets under the identical deposition conditions due to a slower deposition rate on the textures.

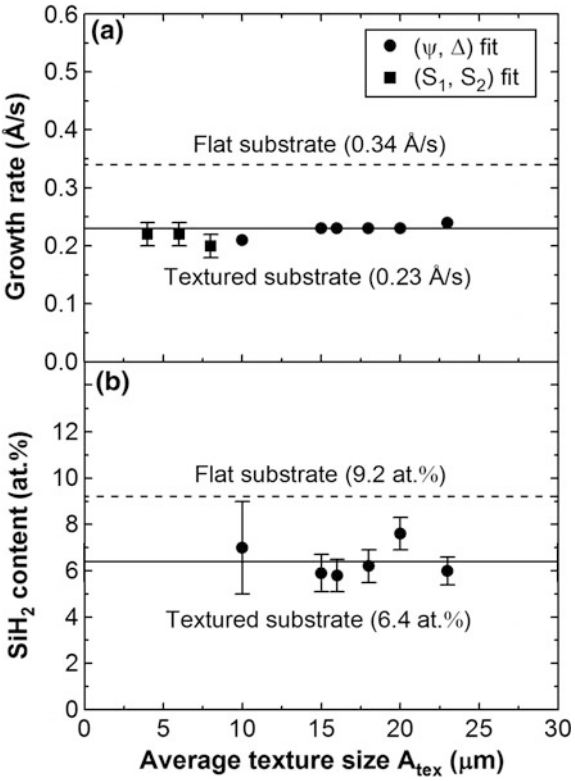


Fig. 4.8 **a** Growth rate and **b** SiH_2 hydrogen content, deduced from the SE analysis, versus A_{tex} [23]. The circles indicate the result obtained from the fitting analysis of (ψ, Δ), whereas the squares in (**a**) indicate the result extracted from the fitting analysis of (S_1, S_2). The solid lines represent the average values, whereas the values determined from the a-Si:H deposition on a flat c-Si substrate are denoted by the dotted lines

4.2.4 Characterization of Textured Solar Cell Structures

The tilt-angle SE measurements can be applied further to characterize textured TCO/a-Si:H/c-Si solar cell structures. This analysis allows the determination of the optoelectronic properties of TCO layers incorporated into actual a-Si:H/c-Si devices. From the Drude analysis of the free carrier absorption within the TCO layer, the optical carrier concentration (N_{opt}) and optical mobility (μ_{opt}) can be characterized (Sect. 18.2.2 in Vol. 1). Figure 4.9 shows the TEM images of the textured solar cell structure, together with the TEM and SE analysis results [22]. As a TCO layer, an In_2O_3:Sn (ITO) layer was prepared on an a-Si:H/c-Si texture. For this characterization, to enhance light reflection, a large c-Si texture ($A_{tex} = 28$ μm) was used. In the SE analysis, an optical model consisting of surface roughness layer (ITO)/bulk layer (ITO)/bulk layer (a-Si:H)/c-Si substrate was adopted, and the calculated (ψ, Δ) spectra show excellent agreement with the experimental spectra [22]. As confirmed from Fig. 4.9, the structural parameters extracted from SE and TEM agree well. Furthermore, N_{opt} of the ITO layer (4.7×10^{20} cm^{-3}) is consistent with a carrier concentration obtained from a flat ITO layer using the Hall measurement (4.1×10^{20} cm^{-3}) [22].

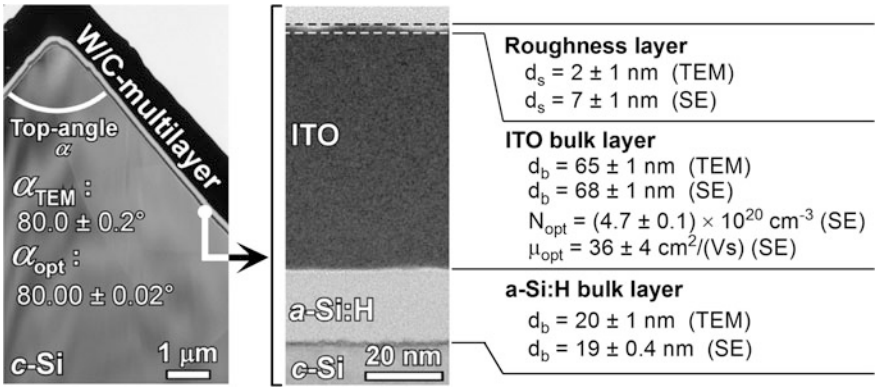


Fig. 4.9 TEM images of the textured ITO/a-Si:H/c-Si solar cell structure, together with the TEM and SE analysis results [22]. The textured structure is covered by a tungsten/carbon (W/C) protection layer. The top angles of the pyramid-shaped texture determined directly from TEM (α_{TEM}) and optically from the tilt angle measurement (α_{opt}) are also shown. For SE, the optical carrier concentration (N_{opt}) and optical mobility (μ_{opt}) determined from the free carrier absorption of the ITO layer are indicated

The above results indicate clearly that the optical response of thin film structures formed on pyramid-shaped c-Si textures can basically be expressed by a conventional coherent optical system. This explains why the external quantum efficiency of textured c-Si solar cells can be approximated assuming a coherent optical model (Sect. 2.5.3).

4.3 Characterization of Textured Structures in Thin-Film Solar Cells

For submicron-textured solar cells, conventional SE measurements can be performed as the specular reflection component still exists due to the small texture sizes. Quite fortunately, it has been found that the effect of light scattering can be neglected almost completely in the SE analyses of submicron random textures [37]. Figure 4.10 shows the schematic illustration of the submicron-texture characterization by SE. As shown in this figure, only the specular reflection component is measured in a standard SE measurement configuration, as the scattered light has different reflection angle. In general, the distance between the sample and the SE light detector is relatively long (~30 cm) and an aperture is provided in front of the light detector. Thus, the contribution of the scattered light to the SE signal intensity is small and, consequently, the SE analysis can be implemented as if no light scattering occurs on the textured surface [37].

Nevertheless, when the texture size (D in Fig. 4.10) is comparable to λ of the SE light probe, the complexity of the SE analysis increases drastically due to the

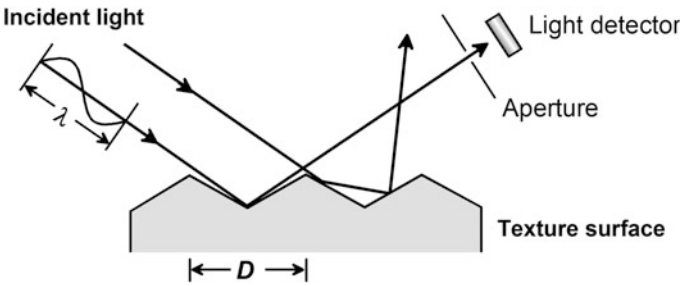


Fig. 4.10 Schematic illustration of submicron-texture characterization by SE. In this figure, λ of the SE light probe is comparable to the texture size (D ~ λ). In this configuration, the scattered light is not detected as the reflection angle is different from that of the specular light

limitation of EMA [31, 38]. More specifically, when the texture size exceeds the condition of $D \leq 0.1\lambda$, it becomes difficult to model the surface roughness layer by a single EMA layer (Fig. 6.2 in Vol. 1) and more complicated optical modeling is required to express the optical response of microscopically non-uniform structures.

In this section, we address the advanced optical modeling that can be used to describe the polarized light reflection on submicron-range rough surfaces. Here, as the SE analysis examples, the characterization of μc-Si:H/a-Si:H tandem [9] and CIGSe [10] solar cell structures are described.

4.3.1 EMA Multilayer and Surface Area Models

For the SE characterization of rough structures, Aspnes et al. employed a EMA multilayer model [39], in which surface roughness optical properties are expressed using more than two sublayers having different void volume fractions (see also Fig. 6.2 in Vol. 1). In this case, however, the number of analysis parameters increases and the complex optical model makes the whole analysis rather difficult. For the accurate and reliable SE analysis of textured structures, simplification of the model is essential.

Figure 4.11 shows the variation of the surface morphology before and after the deposition of an a-Si:H layer (~260 nm) on a textured SnO_2:F (Asahi-U) substrate [40]. These SEM images are essentially consistent with the μc-Si:H/a-Si:H structure shown in Fig. 4.1b. In Fig. 4.11, the surface morphology of the submicron texture changes drastically after the a-Si:H deposition. In the SE analyses of these textures, therefore, the change in the geometrical feature should be taken into account.

To express the optical response of the complex textured structures, a quite simple curvature model shown in Fig. 4.12 has been developed [40]. In this structural model, a cylinder geometry with a radius of r = 1 is assumed for a two-phase composite, and the change of the two-phase mixture is expressed using $d(r) = d_0(1 - r^{\alpha})$. Here, d_0 and α show the thickness of the surface roughness

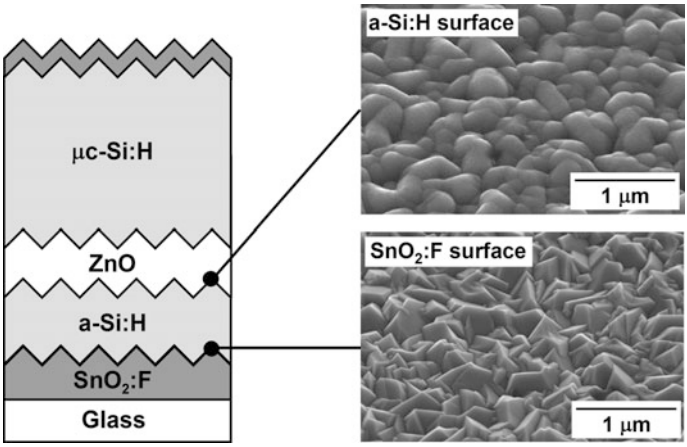


Fig. 4.11 μc-Si:H/a-Si:H tandem solar cell structure and SEM images obtained before and after the deposition of an a-Si:H layer (~260 nm) on a textured SnO_2:F (Asahi-U) substrate [40]

(or interface) layer and the curvature of d(r) at the cylinder cross-section, respectively. As shown in Fig. 4.12, when $\alpha = 1$, the two-phase composite at the cylinder cross-section changes linearly, while a round shape is created when $\alpha > 1$. Thus, using this model, the change in the surface morphology can be expressed by varying α.

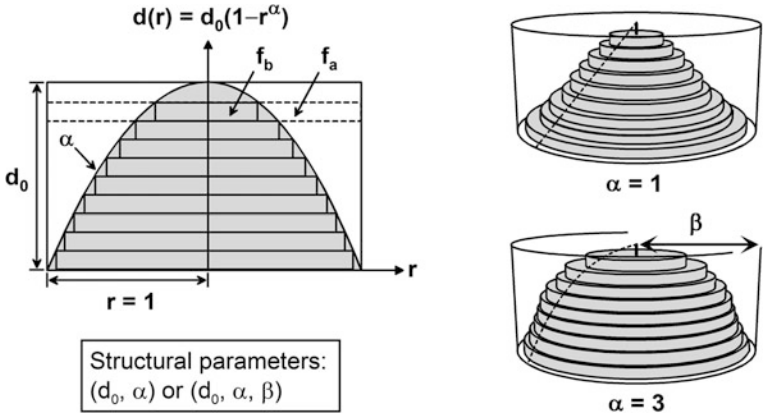


Fig. 4.12 Curvature model developed for the calculation of surface roughness and interface contributions in textured structures [40]. The r, d_0, and α of the model denote the radius, the thickness of the layer, and the curvature, respectively. The f_a and f_b show the volume fractions of the phases a and b ($f_b = 1 - f_a$), respectively. The calculation results for the two-phase composites of $\alpha = 1$ and $\alpha = 3$ are also shown. The parameter β represents the volume fraction of f_a in the top layer

In the curvature model, the volume fractions of two phases (f_a and f_b) in each layer are expressed by $r(d) = (1 - d/d_0)^{1/\alpha}$ that can be derived directly from $d = d_0(1 - r^{\alpha})$. For the jth layer at d_j, the volume of the cylinder plate can be obtained simply using $V(d_j) = \pi r(d_j)^2(d_0/m)$. Here, m shows a total number of layers used in the model (m = 10 in [40]). In the above model, f_a and f_b are estimated using the volume ratio given by

$$f_a(d_j) = \frac{V(0) - V(d_j)}{V(0)}\beta, \tag{4.1}$$

$$f_b(d_j) = 1 - f_a(d_j), \tag{4.2}$$

where $V(0)$ is the total volume of the cylinder that has a thickness of d_0/m. In addition, (4.1) includes a parameter β, which shows the volume fraction of f_a in the top layer. By the introduction of the parameter β, the structural variation can be modeled more precisely. It should be noted that, when $\beta = 1$, the volume fractions in the top layer become $f_a = 1$ and $f_b = 0$, and the actual d_0 value decreases by d_0/m. Once the volume fractions of $f_a(d_j)$ and $f_b(d_j)$ are known, the optical properties of each layer are obtained from EMA and the optical response of the whole roughness (or interface) structure is determined by considering the conventional interference effect in the EMA multilayer. Consequently, in the curvature model, microscopically rough structures are expressed by two (d_0, α) or three (d_0, α, β) parameters, and the number of the free parameters in the model is almost the same as that in a single EMA layer (i.e., d_s and f_{void}).

Figure 4.13 summarizes the SE analyses performed for the random-textured a-Si:H/SnO_2:F/glass structure shown in Fig. 4.11 using different optical models: (a) the single EMA model (Model1), (b) the curvature model (Model2), and (c) the surface area model combined with the curvature model (Model3) [40]. The experimental (ψ, Δ) spectra (open circles) were obtained using an incident angle of 55°, which corresponds to the Brewster angle of the glass substrate. When thin layers are formed on transparent (glass) substrates, the backside reflection occurs (see Fig. 18.12 in Vol. 1). In this case, it is effective to paste a semitransparent white tape (Scotch tape) onto the backside of the glass substrate [41] to suppress the influence of the backside reflection (Sect. 18.3.1 in Vol. 1).

The solid lines in Fig. 4.13 show the SE fitting results. For these analyses, the following fitting error function was used:

$$\chi^2 = \frac{1}{2N - M}\sum_{j=1}^{N}\left\{\left[\frac{\psi_{ex}(E_j) - \psi_{cal}(E_j)}{\delta\psi(E_j)}\right]^2 + \left[\frac{1}{4}\left(\frac{\Delta_{ex}(E_j) - \Delta_{cal}(E_j)}{\delta\Delta(E_j)}\right)\right]^2\right\}, \tag{4.3}$$

where N is the number of measured (ψ, Δ) pairs for photon energies and M indicates the number of analytical parameters [40]. In the above equation, the subscripts "ex" and "cal" show experimental and calculated values at the photon energy of E_j, respectively, and (δψ, δΔ) denote measurement errors in (ψ, Δ).

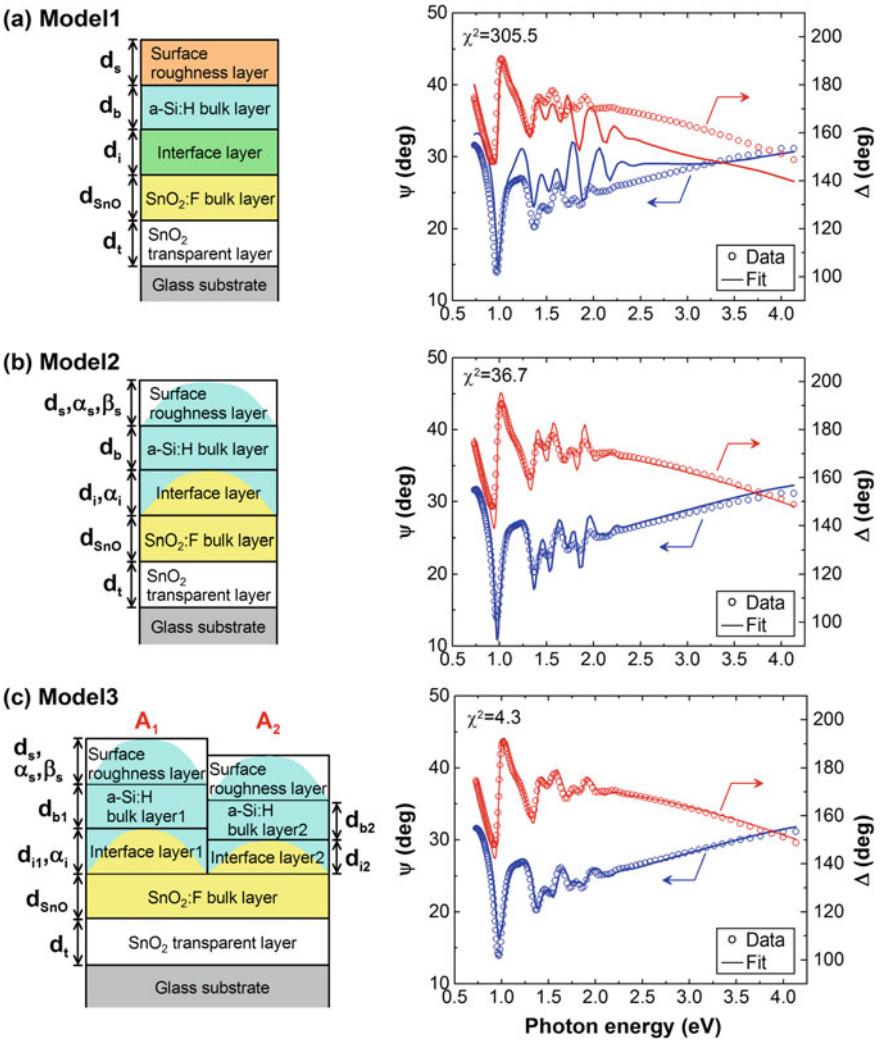


Fig. 4.13 SE analyses performed for the random-textured a-Si:H/SnO_2:F/glass structure shown in Fig. 4.11 using different optical models: **a** the single EMA model (Model1), **b** the curvature model (Model2), and **c** the surface area model combined with the curvature model (Model3) [40]. In the model, the round shape represents the curvature model, and (d, α, β) correspond to the model parameters indicated in Fig. 4.12. The open circles in the graphs show the experimental spectra obtained using an incident angle of 55° and the solid lines show the calculated spectra. The fitting errors of each analysis (χ^2) are also indicated

Equation (4.3) is almost the same as (3.20) in Vol. 1, but the fitting error for Δ is divided by four in (4.3), since the measurement range of Δ is $0° \le \Delta \le 360°$ (or $-180° \le \Delta \le 180°$) and is four times larger than that of ψ ($0° \le \psi \le 90°$). If the SE analysis of Fig. 4.13 is performed without the coefficient of 1/4 in (4.3),

the Δ spectrum is fitted predominantly, as the variation in Δ is much larger. The χ^2 values obtained from each fitting analysis are also shown in Fig. 4.13.

For the a-Si:H analysis, the Asahi-U substrate shown in Fig. 4.11 was characterized in advance (see Sect. 18.5.1 in Vol. 1). In this analysis, the SnO_2:F layer on the glass was divided into two contributions (SnO_2:F and SnO transparent layers) [40]. The SnO_2 transparent layer shows no significant free carrier absorption due to a low carrier concentration and its optical properties are different from the SnO_2:F layer. In the SE analysis of Fig. 4.13, the a-Si:H dielectric function obtained from a flat a-Si:H layer was employed assuming that the a-Si:H optical properties are independent of substrate morphology.

In Model1, the surface roughness and interface structures are expressed by single EMA layers assuming 50/50 vol.% mixtures of the a-Si:H/void and a-Si:H/SnO_2:F components, respectively. The structure of this model is described by the thicknesses of the surface roughness layer (d_s), a-Si:H bulk layer (d_b), interface layer (d_i), SnO_2:F bulk layer (d_{SnO}) and SnO_2 transparent layer (d_t). In the analysis, a fixed value of $d_t = 145$ nm was employed, and the fitting was carried out using the other four parameters. It can be seen that the overall fitting is quite poor when Model1 is applied. In particular, the calculated (ψ, Δ) spectra deviate rather significantly at high energies (E > 3.0 eV). In this energy region, due to higher absorption coefficients in the a-Si:H layer ($\alpha \sim 10^6$ cm^{-1} in Fig. 8.7), the penetration depth of light, defined by $d_p = 1/\alpha$, is quite small ($d_p \sim 10$ nm) (Fig. 1.11b). Accordingly, the large disagreement observed for Model1 particularly at the high energy indicates that the submicron rough surface cannot be expressed by a single EMA layer. This is consistent with the fact that the application of the single EMA layer becomes difficult when the texture size exceeds the limit of $D \leq 0.1\lambda$ (see Fig. 6.2 in Vol. 1).

When the curvature model is applied, the fitting improves drastically particularly at higher energies. In this analysis, the optical responses of the a-Si:H roughness and a-Si:H/SnO_2:F interface structures are described by (d_s, α_s, β_s) and (d_i, α_i), respectively. Here, the subscripts "s" and "i" denote the surface and interface layers, respectively. As shown in Fig. 4.13, the χ^2 value obtained using Model2 is almost one order of magnitude lower than that of Model1, indicating that the near-surface structure can be expressed properly by the curvature model. In the interference regime at low energies (E < 2.5 eV), however, the calculated spectra show sharp features and the fitting is rather poor.

To improve the SE fitting further, the surface area model shown in Fig. 4.13c has been applied. In this model, to express the microscopic structural inhomogeneity, the multilayer optical model is divided into two regions having different thicknesses. In this case, we can calculate the amplitude reflection coefficient by $r_{total} = A_1 r_1 + A_2 r_2$, where A_k and r_k show the surface area fractions ($A_1 + A_2 = 1$) and amplitude reflection coefficients of the two regions, respectively. By calculating r_{total} for p- and s-polarizations, (ψ, Δ) can then be obtained as $\tan\psi \exp(i\Delta) = r_{total,p}/r_{total,s}$. The surface area model has also been employed for the SE analyses of island film structures [42] and pattern-etched samples [43, 44].

In the SE analysis of Model3, the parameters indicated in Fig. 4.13c were used while using the same parameters of d_s, α_s, β_s and α_i for the two regions. To reduce the number of free parameters, fixed values of $A_1 = A_2 = 0.5$ were employed. As a result, the number of the analysis parameters becomes nine if d_t is excluded. When the surface area model is applied, the fitting quality in the low energy region shows a remarkable improvement and χ^2 decreases notably. In the surface area model, two interference fringes induced by different thicknesses overlap each other and the sharp interference structure disappears. As a result, the calculated (ψ, Δ) spectra agree quite well with the experimental spectra. The excellent agreement further confirms that the contribution of the scattered light in the SE measurement is negligible. The parameter values extracted from this SE analysis are $d_s = 104 \pm 4$ nm, $\alpha_s = 4.5 \pm 0.3$, $\beta_s = 0.41 \pm 0.01$, $d_{b1} = 255 \pm 5$ nm, $d_{b2} = 238 \pm 5$ nm, $d_{i1} = 163 \pm 7$ nm, $d_{i2} = 130 \pm 5$ nm, $\alpha_i = 3.0 \pm 0.1$, and $d_{SnO} = 627 \pm 7$ nm. It has been confirmed that the SE result obtained from Model3 agrees quite well with the structure characterized by cross-sectional TEM [40].

The above curvature model can be extended further to analyze a structure in which a thin layer is formed on a large textured structure. Figure 4.14 shows (a) the schematic illustration for a thin film on a textured structure and (b) the curvature model for the thin film on the texture. As shown in Fig. 4.14, if the same curvature is assumed for the thin layer, the geometrical structure of the thin film can be determined from the thin film thickness (d_{film}). From the cross-sectional position of the texture surface (i.e., $d_1(r)$ in Fig. 4.14b), the surface position of the thin film is described simply as $d_2(r) = d_1(r) + d_{film}$. Here, $d_1(r)$ is equivalent to d(r) in Fig. 4.12, and the radial positions of the texture (r_1) and thin layer (r_2) are expressed by $r_1 = (1 - d_1/d_0)^{1/\alpha}$ and $r_2 = \{1 - [(d_2 - d_{film})/d_0]\}^{1/\alpha}$, respectively. From these radii, the volume

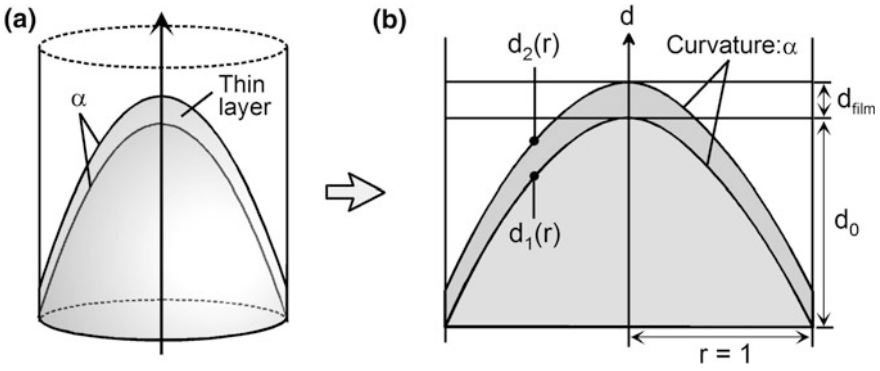


Fig. 4.14 **a** Schematic illustration of a textured structure covered uniformly by a thin film and **b** the curvature model for the thin film on the textured structure. In this model, the same curvature is assumed for the texture and thin layer. The d_{film} and d_0 denote the thicknesses of the thin film and textured structure. The cross-sections of the texture and film surface are expressed by $d_1(r)$ and $d_2(r)$, respectively

fractions of the void, thin film, texture components can be deduced. The optical properties of the three-phase layer are then calculated by EMA according to

$$\sum_{k=1}^{3} f_k \frac{\varepsilon_k - \varepsilon}{\varepsilon_k + 2\varepsilon} = 0, \tag{4.4}$$

where f_k and ε_k are the volume fraction and dielectric function of the phase k [32]. By solving (4.4), the dielectric function of the EMA layer [ε in (4.4)] is determined.

The above model has been applied to characterize a thin a-SiC:H layer (~30 nm) formed on the SnO_2:F texture (Asahi-U). Figure 4.15 shows (a) the optical model and (b) the (ψ, Δ) spectra for the a-SiC:H/SnO_2:F/glass structure. In the optical model of Fig. 4.15a, to express the optical response of the Asahi-U substrate more accurately, the SnO_2:F bulk layer is divided into two layers having slightly different optical carrier concentrations (Sect. 18.5.1 in Vol. 1). The SE fitting using the surface area model was implemented using different a-SiC:H thicknesses (d_{SiC1} and d_{SiC2}) and interface thicknesses (d_{i1} and d_{i2}) for the two regions, while a single parameter is used for the curvature α. For the TCO, the thicknesses of the SnO_2:F layer 1 and SnO_2 layer were fixed to the values indicated in Fig. 4.15a.

As shown in Fig. 4.15b, the experimental spectra are reproduced quite well using the extended surface area model of Fig. 4.15a. The values of the six structural parameters are determined to be $d_{SiC1} = 40 \pm 1$ nm, $d_{SiC2} = 24 \pm 1$ nm, $d_{i1} = 92 \pm 3$ nm, $d_{i2} = 70 \pm 4$ nm, $\alpha = 5.5 \pm 0.1$ and $d_{SnO2:F-2} = 419 \pm 5$ nm. From the average value of d_{SiC1} and d_{SiC2}, the a-SiC:H thickness is estimated to be 32 ± 1 nm. Figure 4.16 shows (a) the cross-sectional TEM image obtained from the sample of Fig. 4.15b and (b) the near surface structure of (a). In Fig. 4.16a, the roughness structure deduced from SE (d_i) agrees quite well the TEM result. More importantly, the a-SiC:H layer thicknesses deduced from SE and TEM show good

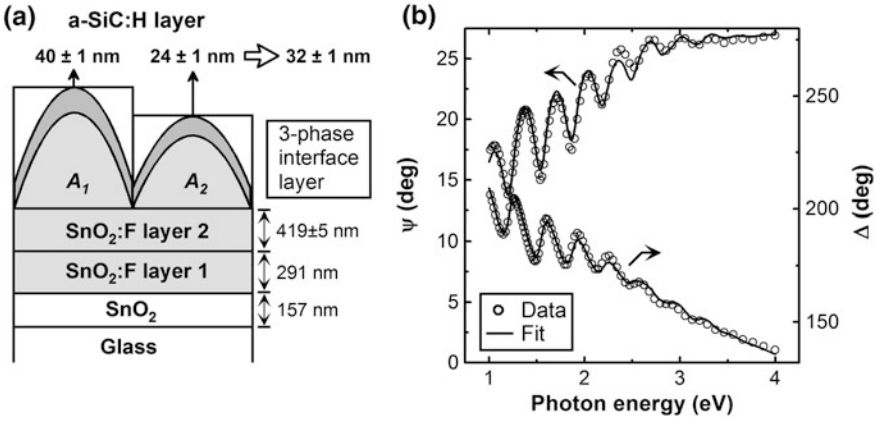


Fig. 4.15 **a** Optical model and **b** (ψ, Δ) spectra for the thin a-SiC:H layer (~30 nm) formed on the textured SnO_2:F/glass structure. The incident angle of the SE measurement is 55°

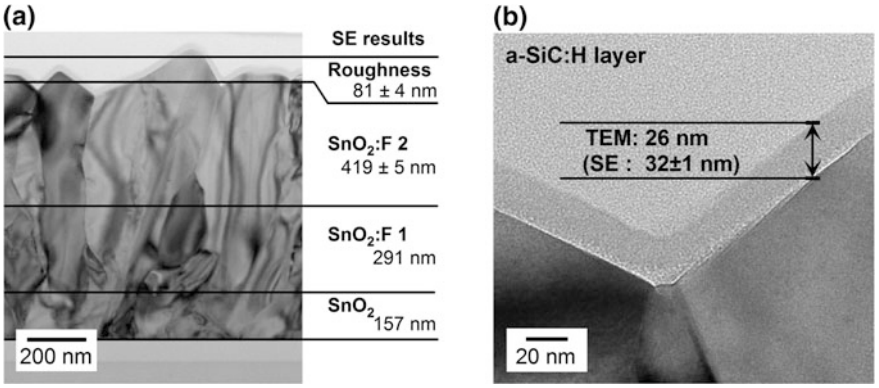


Fig. 4.16 **a** Cross-sectional TEM image obtained from the a-SiC:H/SnO_2:F/glass structure and **b** enlarged TEM image that shows the near surface structure of (**a**). The SE analysis results are also indicated

agreement with a 20% difference. If proper optical models are developed, therefore, the SE technique can be applied to characterize variety of thin-film textured structures incorporated into solar cells.

4.3.2 Analysis of a-Si:H Solar Cell Structures

By modifying the above curvature model, a more complete a-Si:H solar cell structure has been characterized [45]. Figure 4.17 illustrates (a) the optical model and measurement configuration for a glass/SnO_2:F/a-Si:H/ZnO:Al/Ag textured structure and (b) the power function model established to analyze the solar cell structure. In a-Si:H solar cells, ZnO:Al/Ag rear electrodes are generally formed. In this case, since the metal electrode prevents the optical observation of underlying structures, the light illumination from the glass-substrate side is necessary [46, 47]. In the analyzed sample, however, only the a-Si:H i layer was deposited instead of conventional p-i-n structures to test the validity of the analysis [48, 49].

In the case of the glass-side illumination, when the thickness of the glass substrate is thin, the light beam generated by the reflection at the air/glass interface overlaps with that generated by the thin film structure, as illustrated in Fig. 4.17a. Because the glass substrate thickness (~1 mm) is thicker than the coherent length of the light probe, the incoherent optical response [50–53] needs to be taken into account in the SE analysis. In the case of large-area modules, however, more simple SE analysis can be performed because of a thicker glass substrate (see Fig. 18.12 in Vol. 1) [53].

The optical model of Fig. 4.17a is essentially similar to that shown in Fig. 4.13c. In the calculation of the three-phase (a-Si:H/ZnO:Al/Ag) and two-phase

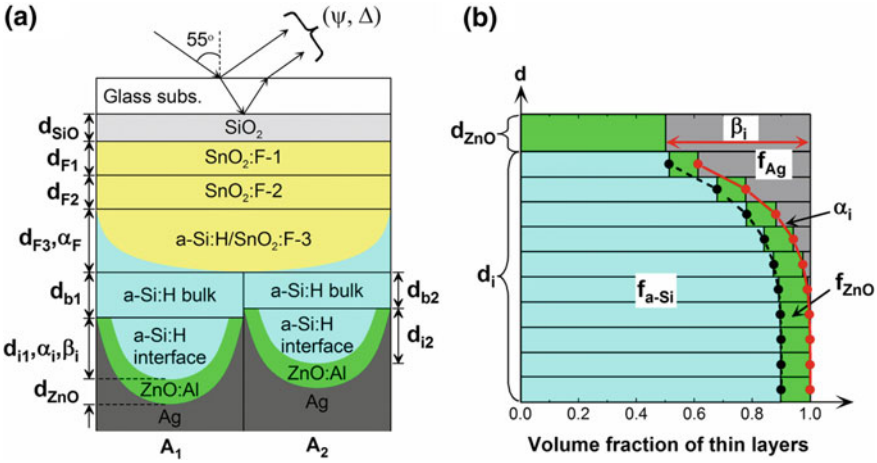


Fig. 4.17 **a** Optical model employed to express the glass/SnO_2:F/a-Si:H/ZnO:Al/Ag textured structure and **b** power function model developed for the analysis of the three-phase structure (a-Si:H/ZnO:Al/Ag) [45]. In (**a**), the SE measurement is performed using the glass-side illumination. In (**b**), d_i and d_{ZnO} indicate the interface and ZnO layer thicknesses, respectively. The red and black circles show the volume fractions of f_{Ag} and f_{ZnO} ($f_{a\text{-}Si} = 1 - f_{Ag} - f_{ZnO}$), respectively

(SnO_2:F/a-Si:H) structures, however, the power function model has been used. In this model, exact geometrical structures are not considered and the volume fractions of the mixed phases within a rough surface (or interface) are calculated directly from the expression. It should be noted that the glass-side illumination enhances the measurement sensitivity for surface and interface regions [53] and the volume fractions of minor phases become important. Unfortunately, the curvature model cannot express the gradual variation of the composite well and this is an inherent problem of the curvature model.

In the model of Fig. 4.17b, the change in a composition toward depth direction is described by a power function and, for example, the Ag volume fraction in the three-phase layer (i.e., a-Si:H/ZnO:Al/Ag mixture) is described by

$$f_{Ag}(d_j) = \beta_i (d_j/d_i)^{\alpha_i}. \tag{4.5}$$

Here, d_j and d_i denote the thickness at the middle position of the *j*th layer (see Fig. 4.17b) and the total thickness of the interface layer, respectively. The parameters that control the volume fractions of the composite are α_i and β_i, which represent a curvature parameter and a f_{Ag} value at the top position of the interface layer, respectively. The red circles in Fig. 4.17b indicate the calculation result obtained using (4.5).

In the a-Si:H solar cells, a quite thin ZnO:Al layer ($d_{ZnO} \sim 20$ nm) is inserted between the a-Si:H and Ag layers. In the optical model of Fig. 4.17b, the two-phase (ZnO:Al/Ag) layer is provided on top of the three-phase layer. The value of f_{Ag} in

this layer is controlled by β_i as $f_{Ag} = \beta_i$ at the top interface position. To estimate the ZnO volume fraction (f_{ZnO}) within the three-phase interface layer, it is assumed that the thin ZnO layer covers the a-Si:H protrusion uniformly, and f_{ZnO} is estimated from a thickness ratio of $f_{ZnO} = d_{ZnO}/d_i$. The calculation result of f_{ZnO} is indicated by the black circles in Fig. 4.17b. From f_{Ag} and f_{ZnO}, the a-Si:H volume fraction ($f_{a\text{-}Si}$) is estimated from $f_{a\text{-}Si} = 1 - f_{Ag} - f_{ZnO}$. Consequently, using the four parameters of (d_i, d_{ZnO}, α_i, β_i), the three-phase structure can be modeled completely. For the modeling of the a-Si:H/SnO_2:F two-phase layer using the power function model, on the other hand, the three analytical parameters are necessary. In the SE analysis of the solar cell structure, therefore, a total of 11 parameters indicated in Fig. 4.17a were used while fixing the thickness of a SiO_2 alkali barrier layer ($d_{SiO} = 50$ nm) formed on the glass substrate. For the optical constants of the component layers, the optical data obtained from separate characterization were employed [45].

Figure 4.18 shows the experimental ellipsometry spectra measured from the a-Si:H solar cell structure (open circles) and the fitting result calculated using the optical model of Fig. 4.17 (solid lines) [45]. The calculated spectra show quite good agreement in the analyzed energy region. Figure 4.19 shows the cross-sectional TEM image of the corresponding textured structure [45]. The layer thicknesses obtained from the SE analysis of Fig. 4.18 are also indicated by the white lines. As confirmed from Fig. 4.19, the thicknesses obtained from the SE analysis agree quite well with those observed in the TEM image. In particular, the remarkable agreement has been confirmed between the thicknesses of the ZnO:Al layers estimated from TEM (27 nm) and SE ($d_{ZnO} = 28 \pm 4$ nm), even though the ZnO layer has a complex structure. This result demonstrates that SE is a quite useful technique for the structural characterization of textured structures.

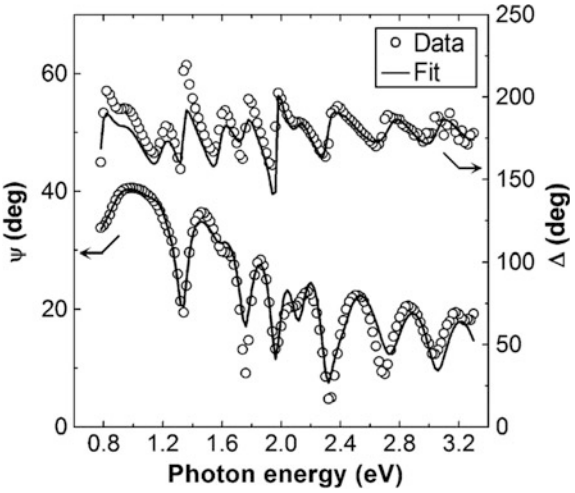


Fig. 4.18 Experimental ellipsometry spectra measured from the a-Si:H solar cell structure (open circles) and the fitting result calculated using the optical model of Fig. 4.17 (solid lines) [45]

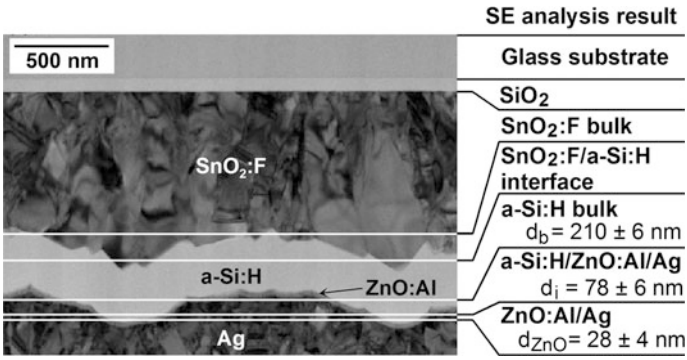


Fig. 4.19 Cross-sectional TEM image obtained from the textured solar cell structure (glass/SnO_2:F/a-Si:H/ZnO:Al/Ag) [45]. The layer thicknesses deduced from the SE analysis of Fig. 4.18 are indicated by the white lines

4.3.3 Analysis of μc-Si:H/a-Si:H Tandem Solar-Cell Structures

Based on the surface area model incorporating the curvature model, the μc-Si:H/a-Si:H tandem solar cell structure in Fig. 4.1b has been analyzed [9]. Figure 4.20a shows the optical model for the textured μc-Si:H (2000 nm)/ZnO (100 nm)/a-Si:H (200 nm)/SnO_2:F/glass structure. Although a-Si:H and μc-Si:H solar cells generally consist of p-i-n structures [48, 49], a test structure with only the a-Si:H and μc-Si:H i layers has been characterized.

In the optical model of Fig. 4.20a, the surface area model is employed for the μc-Si:H/ZnO/a-Si:H multilayer. In this model, three interface layers of μc-Si:H/ZnO:Al, ZnO:Al/a-Si:H and a-Si:H/SnO_2:F mixed phases are considered and the optical response of these structures was calculated by the curvature model in Fig. 4.12. For this analysis, a μc-Si:H optical database was applied [54]. In this database, the μc-Si:H structural factor κ is defined to express the dielectric function of μc-Si:H (see also Fig. 8.11). From the κ value, various microstructures ranging from a complete a-Si:H phase ($\kappa = 0$) to highly crystallized μc-Si:H ($\kappa = 1$) can be described.

As we have seen in Fig. 4.13, for the accurate characterization of submicron textures, optical modeling of near surface structures is of significant importance. To find the proper optical model for the μc-Si:H natural texture, the SE fitting analysis was performed using different optical models. Figure 4.20b summarizes the SE analysis results when the surface roughness is modeled by using one and three sublayers [9]. The open circles show the experimental result and the solid lines indicate the fitting results obtained from each model indicated in the inset. In the ψ spectrum, the E_1 (3.4 eV) and E_2 (4.3 eV) transitions induced by the μc-Si:H component can be seen (Fig. 8.4 in Vol. 1), and the microstructure (i.e., κ value) of the μc-Si:H is evaluated predominantly from this region [54].

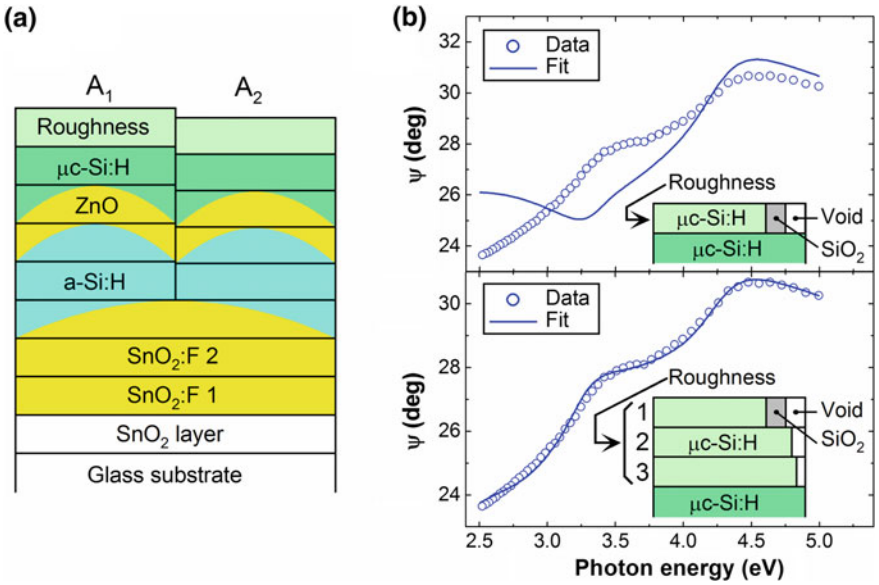


Fig. 4.20 **a** Optical model for the textured μc-Si:H/ZnO:Al/a-Si:H/SnO_2:F solar cell structure and **b** ψ spectrum obtained experimentally from the μc-Si:H/a-Si:H tandem structure (open circles) and the results of the fitting analyses (solid lines) when the number of the surface roughness sublayers is one or three [9]. In (**b**), the ellipsometry spectra were measured at an incident angle of 55°

For the μc-Si:H surface characterization, the incorporation of the SiO_2 component is important due to surface oxidation [9, 55, 56]. In the surface roughness layer, therefore, the SiO_2 component was also included. In the second and third sublayers, however, the SiO_2 contribution is neglected to simplify the analysis. Based on the volume fractions of voids (f_{void}), SiO_2 (f_{SiO2}) and μc-Si:H ($f_{Si} = 1 - f_{void} - f_{SiO2}$), the optical constants of each sublayer are calculated by EMA using (4.4).

In Fig. 4.20b, when the μc-Si:H surface is modeled by a single EMA layer, a large deviation is observed between the experimental and calculated spectra. However, with increasing the number of the surface roughness sublayers, the fitting improves drastically and a satisfactory fitting is obtained when three sublayers are used. This result confirms that textured surfaces can be described properly by simply employing the large number of the roughness sublayers with different f_{void}. Based on the three-sublayer model, a κ value of 0.60 ± 0.02 has been extracted.

Figure 4.21 shows (a) the SE analysis result and (b) the cross-sectional TEM for the μc-Si:H/a-Si:H tandem structure [9]. The SE analysis was performed using the optical model of Fig. 4.20a in which a total of 23 parameters are present. For the μc-Si:H roughness layer, the model parameters extracted from the three sublayers were used. In particular, to suppress the correlation among the analysis parameters, the SE fitting analysis of Fig. 4.21a was carried out in two steps: (i) the analysis of the UV region for the roughness characterization with eight parameters

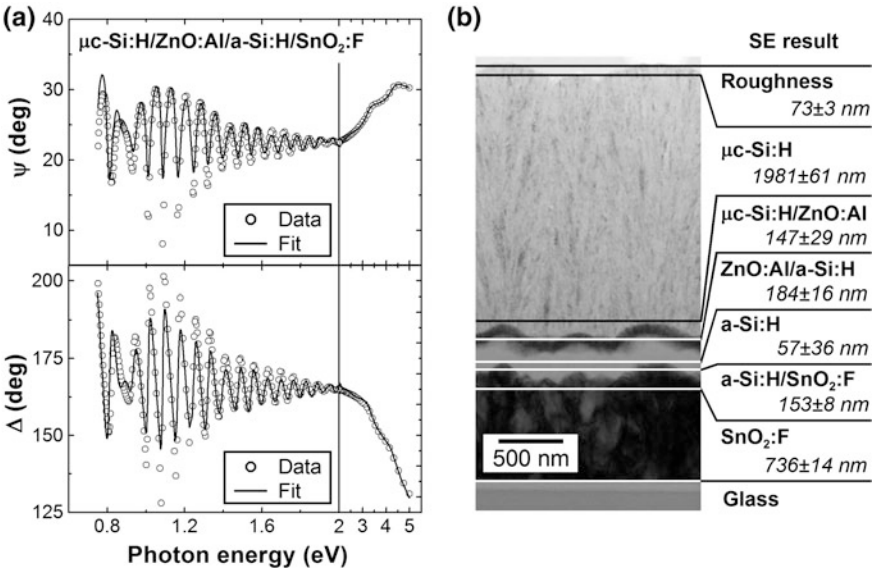


Fig. 4.21 **a** (ψ, Δ) spectra measured from the textured structure of μc-Si:H (2 μm)/ZnO:Al (100 nm)/a-Si:H (200 nm)/SnO_2:F (open circles) and the result obtained from the fitting analysis using the optical model of Fig. 4.20a (solid lines) and **b** cross-sectional TEM image measured from the same sample [9]. In (**a**), the ellipsometry spectra were measured at an incident angle of 55°. In (**b**), the thicknesses of each layer as estimated from the SE analysis of (**a**) are indicated by the white and black lines

($d_{s,1\text{-}3}$, $f_{void,1\text{-}3}$, f_{SiO2}, κ) and (ii) the analysis of the whole energy region using a total of 13 free parameters with two fixed parameters for the SnO_2:F-1 and SnO_2 layers. The fitting analyses were carried out by employing a fitting error function of (4.3). As shown in Fig. 4.21a, the (ψ, Δ) spectra calculated from the model agree well with the experimental spectra. The slight change in the interference pattern at ~0.9 eV is caused by the presence of the ZnO:Al intermediate layer and the layer thicknesses of the ZnO:Al and a-Si:H are determined mainly from the interference pattern in this region [9].

In Fig. 4.21b, the cross-sectional TEM image of the μc-Si:H/a-Si:H tandem structure is shown. The thicknesses of each layer as estimated from the SE analysis are indicated by the white and black lines, and they correspond to the average thicknesses of the two regions (A_1 and A_2) in Fig. 4.20a. The structure deduced from SE shows good agreement with that obtained from TEM. Accordingly, even when solar cell structures are complicated, quantitative characterization of random textured structures is still possible as long as the texture dimension is $D \leq 1$ μm. In such SE analyses, however, extra care is necessary to reduce the correlations among structural parameters particularly when the number of free parameters is large.

4.3.4 Analysis of CIGSe Solar Cell Structures

Using the EMA multilayer model, a CIGSe layer with a double-grading Ga profile, incorporated into the state-of-the-art CIGSe solar cell, has been characterized by SE [10]. Figure 4.22a shows the depth profile of the Ga composition x in a $Cu(In_{1-x}Ga_x)Se_2$ layer fabricated on a Mo/glass substrate using a three-stage process [10]. The SEM image of this structure has been shown in Fig. 4.1c. The x profile was measured using secondary ion mass spectroscopy, and the absolute composition was calibrated by using inductively coupled plasma-mass spectroscopy. In this Cu $(In_{1-x}Ga_x)Se_2$ layer, the x value is ~0.5 in the surface and CIGSe/Mo interface regions, whereas the x composition at the valley position is 0.26. The dotted lines in Fig. 4.22a show the compositions obtained from two SE analyses (Fit1 and Fit2) described below.

Figure 4.22b shows an optical model employed for the SE analysis. This optical model is consisting of the surface roughness, bulk, and interface layers, whereas the roughness structure is expressed by three sublayers with different d_s and f_{void} values. This surface roughness model is quite similar to that of the μc-Si:H shown in Fig. 4.20b. For the characterization of the CIGSe layer, two separate SE analyses in (i) the UV/visible region (Fit1) and (ii) the near infrared region (Fit2) have been performed to reduce the number of free parameters. The procedure of this two-step analysis is also similar to that of the μc-Si:H/a-Si:H analysis in the previous section. To simplify the SE analysis further, the x compositions in the bulk and roughness layers are expressed by single compositions of x_b and x_s, respectively, even though the CIGSe layer has a V-shaped Ga profile shown in Fig. 4.22a. For the calculation

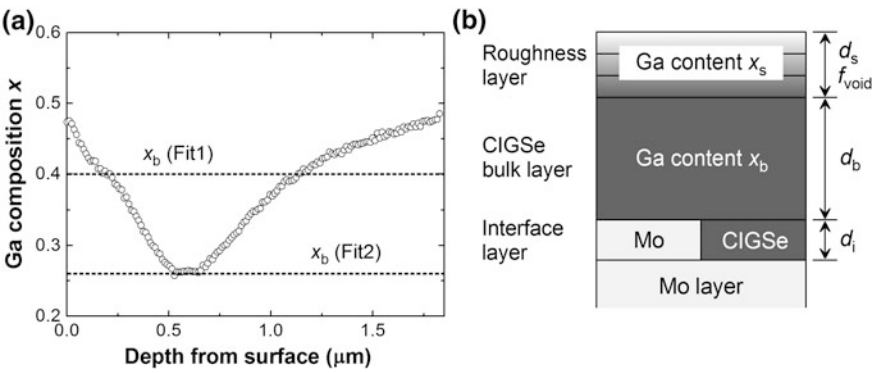


Fig. 4.22 **a** Depth profile of x in a $Cu(In_{1-x}Ga_x)Se_2$ layer fabricated on a Mo/glass substrate using a three-stage process and **b** optical model employed for the SE analysis of the CIGSe layer [10]. In (**a**), the dotted lines indicate x compositions obtained from the SE fitting analyses using different analyzed energy regions (Fit1 and Fit2) in Fig. 4.23a. In the optical model of (**b**), the CIGSe roughness layer consists of a total of three sublayers having different d_s and f_{void} values, whereas the interface layer is a 50/50 vol.% mixture of the CIGSe and Mo components. The x_b and x_s show the Ga compositions in the bulk and roughness layers, respectively

of the CIGSe dielectric function, a complete CIGSe optical database (Sect. 10.4 in Vol. 1) was used. In addition, for the CIGSe/Mo interface, a 50/50 vol.% mixture of the CIGSe/Mo components was assumed.

Figure 4.23a shows the (ψ, Δ) spectra of the CIGSe sample of Fig. 4.22a [10]. In the SE analysis of Fit1 (E = 1.6–6.0 eV), the infinite bulk layer thickness ($d_b = \infty$) is assumed, since the penetration depth of light is only ~450 nm at 1.6 eV for the optical constants of x = 0.5. For Fit1, a total of seven parameters ($d_{s,1\text{-}3}$, $f_{void,1\text{-}3}$, x_s) were used by further assuming $x_b = x_s$. As shown in Fig. 4.23a, the excellent fitting is confirmed in Fit1, even though the x composition is assumed to be constant. The SE analyses for the surface structures of the μc-Si:H (Fig. 4.20b) and CIGSe indicate that three sublayers are generally sufficient to describe the optical response of submicron textured structures. The analysis of Fig. 4.23a show that the d_s values of each sublayer are in a range of 29–47 nm and f_{void} increases systematically from 12 vol.% (bottom roughness layer) to 44 vol.% (top roughness layer). The x_s value obtained from the fitting (0.40 ± 0.02) has been indicated in Fig. 4.22a. It can be seen that x_s determined from Fit1 corresponds to the average x in the near-surface region. It should be noted that, in the analysis of Fit1, the correlation among the parameters is rather weak and the structural parameters can be estimated with small confidence limits [10].

By adopting the result of Fit1, the SE analysis of Fit2 (E = 0.7–1.6 eV) was conducted further. In this analysis, all the roughness-related parameters were fixed to the values obtained in Fit1, and only the bulk and interface layers were characterized by employing three parameters (x_b, d_b, d_i). In Fit2, the layer thicknesses of

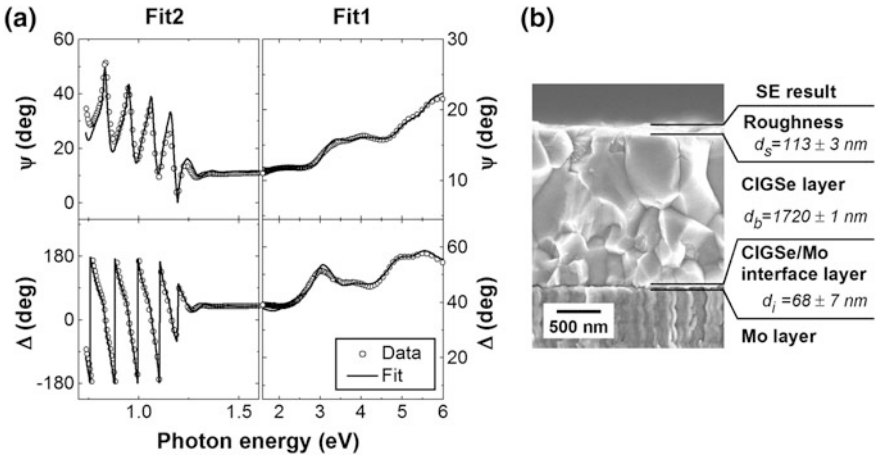


Fig. 4.23 **a** (ψ, Δ) ellipsometry spectra obtained from the CIGSe sample of Fig. 4.22a (open circles) and the results of the SE fitting analyses (solid lines) and **b** cross-sectional SEM image of the CIGSe sample [10]. In (**a**), the (ψ, Δ) spectra were obtained at an incident angle of 70° and were analyzed using two separate energy regions of 1.6–6.0 eV (Fit1) and 0.7–1.6 eV (Fit2). In Fit1, the CIGSe bulk-layer thickness was assumed to be infinite, while the result of Fit2 is obtained using the optical model of Fig. 4.22b. In (**b**), the layer thicknesses deduced from the SE analyses are indicated

d_b and d_i are determined from the strong interference pattern that appears in the low energy region. In Fig. 4.23a, the calculated (ψ, Δ) spectra provide a good fitting to the experimental data. The x_b value extracted from Fit2 is 0.26 $\pm$ 0.01, which corresponds to x of the bottom region in the V-shaped Ga profile (see Fig. 4.22a). In Fit2, x_b is essentially determined by the onset of the strong light absorption above E_g. Thus, x_b obtained in Fit2 is more influenced by x at the valley position. In the SE analysis of Fig. 4.23a, the fitting error is sufficiently low, and fitting quality does not improve significantly even when a more complicated Ga profile is assumed. The optical simulation shows that the gradual change of x (~0.2) over the ~1 μm thickness does not vary (ψ, Δ) significantly. Accordingly, the SE sensitivity for the V-shaped Ga profile appears to be low. On the other hand, more detailed characterization of the V-shaped Ga profile by SE has also been reported [57].

Figure 4.23b shows the cross-sectional SEM image of the CIGSe sample of Fig. 4.23a [10]. In this figure, the layer thicknesses deduced from the SE analyses are also indicated. For the roughness layer, a total thickness of the three sublayers is shown. It can be seen that the d_s, d_b and d_i positions deduced from SE show remarkable agreement with the actual CIGSe structure. Thus, the structural analysis of submicron-textured CIGSe layers fabricated by a conventional three-stage process can be made by SE. Such characterization is expected to be quite useful for the determination of the structural non-uniformity in large-area CIGSe modules.

References

1. A. Luque, S. Hegedus, *Handbook of Photovoltaic Science and Engineering* (Wiley, West Sussex, UK, 2011)
2. P. Campbell, M.A. Green, J. Appl. Phys. **62**, 243 (1987)
3. K. Ding, T. Kirchartz, B.E. Pieters, C. Ulbrich, A.M. Ermes, S. Schicho, A. Lambertz, R. Carius, U. Rau, Sol. Energy Mater. Sol. Cells **95**, 3318 (2011)
4. M. Zeman, O. Isabella, S. Solntsev, K. Jager, Sol. Energy Mater. Sol. Cells **119**, 94 (2013)
5. E. Vazsonyi, K. De Clercq, R. Einhaus, E. Van Kerschaver, K. Said, J. Poortmans, J. Szlufcik, J. Nijs, Sol. Energy Mater. Sol. Cells **57**, 179 (1999)
6. E. Fornies, C. Zaldo, J.M. Albella, Sol. Energy Mater. Sol. Cells **87**, 583 (2005)
7. T. Hara, T. Maekawa, S. Minoura, Y. Sago, S. Niki, H. Fujiwara, Phys. Rev. Applied **2**, 034012 (2014)
8. K. Watanabe, N. Matsuki, H. Fujiwara, Appl. Phys. Express **3**, 116604 (2010)
9. D. Murata, T. Yuguchi, H. Fujiwara, Thin Solid Films **571**, 756 (2014)
10. S. Minoura, T. Maekawa, K. Kodera, A. Nakane, S. Niki, H. Fujiwara, J. Appl. Phys. **117**, 195703 (2015)
11. Y. Sago, H. Fujiwara, Jpn. J. Appl. Phys. **51**, 10NB01 (2012)
12. M.M. Lee, J. Teuscher, T. Miyasaka, T.N. Murakami, H.J. Snaith, Science **338**, 643 (2012)
13. J. Burschka, N. Pellet, S.-J. Moon, R. Humphry-Baker, P. Gao, M.K. Nazeeruddin, M. Grätzel, Nature **499**, 316 (2013)
14. J. Meier, J. Spitznagel, U. Kroll, C. Bucher, S. Fay, T. Moriarty, A. Shah, Thin Solid Films **451–452**, 518 (2004)
15. S.Y. Myong, K. Sriprapha, S. Miyajima, M. Konagai, Appl. Phys. Lett. **90**, 263509 (2007)
16. A.M. Gabor, J.R. Tuttle, D.S. Albin, M.A. Contreras, R. Noufi, A.M. Hermann, Appl. Phys. Lett. **65**, 198 (1994)

17. A.M. Gabor, J.R. Tuttle, M.H. Bode, A. Franz, A.L. Tennant, M.A. Contreras, R. Noufi, D.G. Jensen, A.M. Hermann, Sol. Eng. Mater. Sol. Cells **41/42**, 247 (1996)
18. M.A. Contreras, J. Tuttle, A. Gabor, A. Tennant, K. Ramanathan, S. Asher, A. Franz, J. Keane, L. Wang, R. Noufi, Sol. Eng. Mater. Sol. Cells **41/42**, 231 (1996)
19. T. Dullweber, O. Lundberg, J. Malmstrom, M. Bodegard, L. Stolt, U. Rau, H.W. Schock, J.H. Werner, Thin Solid Films **387**, 11 (2001)
20. A. Chirilă, S. Buecheler, F. Pianezzi, P. Bloesch, C. Gretener, A.R. Uhl, C. Fella, L. Kranz, J. Perrenoud, S. Seyrling, R. Verma, S. Nishiwaki, Y.E. Romanyuk, G. Bilger, A.N. Tiwari, Nat. Mater. **10**, 857 (2011)
21. M.F. Saenger, J. Sun, M. Schädel, J. Hilfiker, M. Schubert, J.A. Woollam, Thin Solid Films **518**, 1830 (2010)
22. N. Matsuki, H. Fujiwara, J. Appl. Phys. **114**, 043101 (2013)
23. Y. Tanaka, N. Matsuki, H. Fujiwara, Thin Solid Films **569**, 64 (2014)
24. C. Beneking, B. Rech, S. Wieder, O. Kluth, H. Wagner, W. Frammelsberger, R. Geyer, P. Lechner, H. Rübel, H. Schade, Thin Solid Films **351**, 241 (1999)
25. Y. Tawada, H. Yamagishi, K. Yamamoto, Sol. Eng. Mater. Sol. Cells **78**, 647 (2003)
26. G.P. Willeke, Sol. Eng. Mater. Sol. Cells **72**, 191 (2002)
27. M. Tanaka, M. Taguchi, T. Matsuyama, T. Sawada, S. Tsuda, S. Nakano, H. Hanafusa, Y. Kuwano, Jpn. J. Appl. Phys. **31**, 3518 (1992)
28. H. Fujiwara, M. Kondo, J. Appl. Phys. **101**, 054516 (2007)
29. H. Fujiwara, M. Kondo, Appl. Phys. Lett. **90**, 013503 (2007)
30. H. Fujiwara, M. Kondo, Appl. Phys. Lett. **86**, 032112 (2005)
31. D.E. Aspnes, Thin Solid Films **89**, 249 (1982)
32. H. Fujiwara, *Spectroscopic Ellipsometry: Principles and Applications* (Wiley, West Sussex, UK, 2007)
33. S. Kageyama, M. Akagawa, H. Fujiwara, Phys. Rev. B **83**, 195205 (2011)
34. S. Kageyama, M. Akagawa, H. Fujiwara, J. Non-Cryst, Solids **358**, 2257 (2012)
35. S.M. Cohen, D. Eliyahu, I. Freund, M. Kaveh, Phys. Rev. A **43**, 5748 (1991)
36. G.D. Lewis, D.L. Jordan, E. Jakeman, Appl. Opt. **37**, 5985 (1998)
37. P.I. Rovira, R.W. Collins, J. Appl. Phys. **85**, 2015 (1999)
38. D.E. Aspnes, Phys. Rev. B **25**, 1358 (1982)
39. D.E. Aspnes, J.B. Theeten, F. Hottier, Phys. Rev. B **20**, 3292 (1979)
40. M. Akagawa, H. Fujiwara, J. Appl. Phys. **110**, 073518 (2011)
41. R.A. Synowicki, Phys. Status Solidi C **5**, 1085 (2008)
42. R.H. Muller, J.C. Farmer, Surf. Sci. **135**, 521 (1983)
43. H.L. Maynard, N. Layadi, J.T.C. Lee, Thin Solid Films **313–314**, 398 (1998)
44. S.-J. Cho, P.G. Snyder, C.M. Herzinger, B. Johs, J. Vac. Sci. Technol., B **20**, 197 (2002)
45. S. Yamaguchi, Y. Sugimoto, H. Fujiwara, Thin Solid Films **565**, 222 (2014)
46. J. Chen, J. Li, C. Thornberry, M.N. Sestak, R.W. Collins, J.D. Walker, S. Marsillac, A.R. Aquino, A. Rockett, in *Proceedings of 34th IEEE Photovoltaic Specialists Conference* (IEEE, New York, 2009), p. 1748
47. J. Chen, P. Koirala, C. Salupo, R.W. Collins, S. Marsillac, K.R. Kormanyos, B.D. Johs, J.S. Hale, G.L. Pfeiffer, in *Proceedings of 38th IEEE Photovoltaic Specialists Conference* (IEEE, New York, 2012), p. 377
48. A.V. Shah, H. Schade, M. Vanecek, J. Meier, E. Vallat-Sauvain, N. Wyrsch, U. Kroll, C. Droz, J. Bailat, Prog. Photovoltaics **12**, 113 (2004)
49. T. Matsui, A. Bidiville, K. Maejima, H. Sai, T. Koida, T. Suezaki, M. Matsumoto, K. Saito, I. Yoshida, M. Kondo, Appl. Phys. Lett. **106**, 053901 (2015)
50. R. Joerger, K. Forcht, A. Gombert, M. Köhl, W. Graf, Appl. Opt. **36**, 319 (1997)
51. K. Forcht, A. Gombert, R. Joerger, M. Köhl, Thin Solid Films **302**, 43 (1997)
52. M. Kildemo, R. Ossikovski, M. Stchakovsky, Thin Solid Films **313–314**, 108 (1998)
53. S. Yamaguchi, Y. Sugimoto, H. Fujiwara, Thin Solid Films **534**, 149 (2013)

54. T. Yuguchi, Y. Kanie, N. Matsuki, H. Fujiwara, J. Appl. Phys. **111**, 083509 (2012)
55. G.E. Jellison Jr., M.F. Chisholm, S.M. Gorbatkin, Appl. Phys. Lett. **62**, 3348 (1993)
56. M. Losurdo, R. Rizzoli, C. Summonte, G. Cicala, P. Capezzuto, G. Bruno, J. Appl. Phys. **88**, 2408 (2000)
57. V. Ranjan, T. Begou, S. Little, R.W. Collins, S. Marsillac, Prog. Photovoltaics **22**, 77 (2014)

Chapter 5
On-line Monitoring of Photovoltaics Production



Ambalanath Shan, Jie Chen, Prakash Koirala, Kenneth R. Kormanyos, Nikolas J. Podraza and Robert W. Collins

Abstract Two approaches are reviewed for the application of spectroscopic ellipsometry (SE) to on-line monitoring of thin film photovoltaics (PV) production. In the first approach, through-the-glass SE is applied for serial point-by-point measurements spanning the area of a thin film PV panel 60 cm × 120 cm in size. An ellipsometer detection system is used that incorporates two one-dimensional detector arrays for spectroscopy over a wide photon energy range (0.75–3.5 eV, limited by glass absorption at high energies). The PV panel in this review is fabricated starting from soda-lime glass with four oxide layers deposited on its surface, including the transparent top contact. A CdS/CdTe semiconductor bilayer is deposited subsequently on the top contact, functioning as the PV heterojunction. In the on-line analysis configuration, the coated glass panel moves along a roller conveyer with the film side facing up and passes a station designed for on-line mapping by SE. The polarization generation and detection arms of the ellipsometer located beneath the panel scan from side to side and acquire SE data in a through-the-glass measurement mode. In this approach, a maximum of ~30 locations can be measured in the one minute time period required for the 120 cm long panel to travel by the SE station; the largest fraction of the time is consumed by ellipsometer translation. The effective thickness of CdS (or CdS material volume/area), which includes bulk and interface layer components, is deduced in SE data analysis. This thickness is found to be a robust parameter that can be used in modeling to predict photo-generated charge carrier collection for the CdTe PV modules. The second approach for on-line monitoring reviewed here employs an instrument with an expanded beam for line imaging across a PV substrate/film-stack structure with a maximum image width of 15 cm. In this approach, a

A. Shan · J. Chen · P. Koirala · N. J. Podraza (✉) · R. W. Collins
Department of Physics & Astronomy and Center for Photovoltaics Innovation & Commercialization, University of Toledo, Toledo, OH 43606, USA
e-mail: Nikolas.Podraza@utoledo.edu

R. W. Collins
e-mail: robert.collins@utoledo.edu

K. R. Kormanyos
Calyxo USA, Perrysburg, OH 43551, USA

© Springer International Publishing AG, part of Springer Nature 2018

H. Fujiwara and R. W. Collins (eds.), *Spectroscopic Ellipsometry for Photovoltaics*, Springer Series in Optical Sciences 214,
https://doi.org/10.1007/978-3-319-95138-6_5

detection system is used incorporating a two-dimensional detector array; the two array indices are exploited for spectroscopy (1.3–3.3 eV) and line imaging in parallel. Thus, imaging width-wise and mapping length-wise is performed without ellipsometer translation, enabling high speed multilayer uniformity evaluations in flexible roll-to-roll PV production. The application reviewed here involves film-side analysis of multilayer fabrication on a moving length of 12.7 cm wide flexible polyimide foil substrate mounted within a cassette for roll-to-roll deposition. Maps are acquired in situ after deposition of individual Ag and ZnO layers, functioning together as the back reflector and back contact, as well as after deposition of *n*-type doped hydrogenated amorphous silicon (*a*-Si:H *n*-layer) as a component of a thin film *a*-Si:H *n-i-p* solar cell structure. Areas of the flexible coated PV panels up to 12 cm × 45 cm in size were characterized to determine layer thicknesses and optical properties. Parametric expressions incorporating Drude, critical point oscillator, and modified Lorentz oscillator terms were employed to describe the complex dielectric functions of thin film Ag and ZnO, and the *a*-Si:H *n*-layer, respectively. Currently, ~30 point line images can be collected every 20 cm of length when using an average 120 cm/min substrate speed. Prospects exist for increasing length-wise resolution significantly to ~0.5 cm, using high speed detection schemes demonstrated previously.

5.1 Introduction

Non-invasive, contactless probes are sought for production line monitoring in thin film photovoltaics (PV) technology, in particular for on-line mapping of device relevant properties that enables uniformity evaluations of large area PV panels [1]. Many challenges may be encountered upon scale-up of PV manufacturing in the early stage commercialization of new technologies. One such challenge in thin film technology involves reduction of the performance gap that inevitably exists between champion small area cells achieved in the laboratory and large area monolithically-integrated modules [2]. The efficiency difference may include a contribution due to multiple spatial non-uniformities in the properties of individual component layers originating from their deposition and processing over the full area of the module. Thus, high speed spatially-resolved measurements, typically optical in nature, that identify non-uniformities in the fundamental material properties of thin films are of great interest. In fact, if tools used for the optimization of small area cells in the laboratory can be advanced to enable optimization of large area modules in the factory, then a reduction of the observed laboratory-factory gap in efficiency may be expedited. Tools that rely on non-invasive optical probing and provide the thicknesses of component layers and key parameters that define the optical properties of the layers such as band gap serve as a very useful starting point for multilayer analysis in on-line mapping applications [3].

Component layer thickness uniformity is a desirable goal because the major thin film technologies for PV production traditionally have utilized a very thin layer

serving as an *n* or *p*-type window to the absorber layer. Such window layers include *n*-type CdS as the top semiconductor layer of CdTe and CIGS devices, or wide band gap amorphous, protocrystalline, or nanocrystalline silicon *p*-layers for the top semiconductor of thin film Si:H devices [4]. Because the window layers are electrically inactive in these thin film solar cell designs, thicknesses selected within optimum ranges sacrifice short-circuit current typically for the other two cell characteristics of open-circuit voltage and fill factor. In addition, overall performance may need to be sacrificed in favor of a high yield. The optimum thickness ranges for window layers are generally ~300–1000 Å for the CdS in CdTe and CIGS technologies, and ~50–150 Å for thin film Si:H technology. Uniformity of optical property parameters such as the band gap energies for semiconductors with amorphous, nanocrystalline, and polycrystalline thin film structure is important because, unlike the case of semiconductor single crystals, these parameters are sensitive to deposition and processing and so provide insights into key basic material characteristics. The parameters that describe the optical properties include not only band gap energies, but also the amplitudes and broadening parameters associated with the one or more oscillators describing the electronic transitions in the material [5, 6]. The amplitudes of the oscillators are affected by material density which is reduced by voids at polycrystalline grain boundaries, for example; the energy positions of the oscillators identify band gaps and are affected by in-plane strain and composition in the case of alloys; and the broadenings of oscillators are affected by the mean free path of excited carriers, which exhibits inverse relationships with respect to defect concentrations and disorder, or polycrystalline grain size.

A limitation of many important device relevant measurements for thin film mapping, for example, surface potential by scanning Kelvin probe and induced currents by scanning laser beam excitation, results from the requirements of first forming the semiconductor junction and subsequently establishing near or intimate electrical contact with the device structure [7]. Spectroscopic ellipsometry (SE) has been under development to serve as a foundation for an advanced thin film mapping metrology for large area PV panels in the early stages of the fabrication process, even before junction formation [8, 9]. As a probe based on the polarization of optical waves, SE provides the ratio (*p*:*s*) of relative (reflected/incident) optical field amplitudes $\tan\psi$ and the phase difference (*p*–*s*) shift (reflected–incident) Δ measured upon reflection of obliquely incident polarized light specularly from a substrate/film-stack sample having a planar surface and one of more planar interfaces. The SE angles (ψ, Δ) depend on both the wavelength (or photon energy) and the angle of incidence. With the development of multichannel SE that applies a linear detector array for spectroscopy in parallel [10], short spectroscopic measurement times can be achieved that enable mapping over large areas in reasonable time durations. This can be performed by translating the ellipsometer, consisting of polarization generation and detection arms, as a unit in two dimensions while maintaining the oblique specular reflection condition with respect to the panel surface. Another approach more suitable for on-line monitoring involves translating the ellipsometer in one dimension as a translating PV panel passes by a mapping station.

SE provides measurement capabilities for thin film structural parameters, including the thicknesses of bulk, interface, and roughness-related surface layers, as well as for optical parameters that define the complex dielectric functions $\varepsilon(E) = \varepsilon_1(E) - i\varepsilon_2(E)$ of the layers. In fact, analysis of the SE data acquired in the form of (ψ, Δ) enables extraction of photon energy independent parameters that control the polarization modifying properties of the sample [11]. Non-linear least-squares regression is an effective method for determining not only layer thicknesses as described, but in addition, the photon energy independent optical property parameters that include oscillator amplitudes, resonance or band gap energies, and broadening values that define expressions for $\varepsilon(E)$. From the thicknesses of all the layers and the $\varepsilon(E)$ spectra of all the component materials in the multilayer PV structure, the external quantum efficiency (EQE) can be simulated as long as the active components of the thin film PV stack are identified [12]. This simulated EQE spectrum describes the response that would be obtained if all electron-hole pairs photo-generated within the identified active components of the solar cell could be separated and the electrons and holes collected. Spatial variations detected in the SE analysis results due to non-uniformities yield associated variations in the predicted current density upon integration of the simulated EQE spectra. As a result, insights can be obtained into the origins and nature of the non-uniformities detected by mapping SE and their effect on variations in the current output from different sub-cells of the PV module, and thus, in the overall performance of the module.

Although a multichannel ellipsometer incorporating a linear detector array can provide a minimum single spectroscopic measurement time as short as ~30 ms [13], long mapping times can result from the requirement of translating the ellipsometer arms. As described in Sect. 5.2 below, such an approach limits the number of points that can be obtained on a panel in the measurement time available, and high spatial resolution is not possible. For example, in a one minute traversal time for a 120 cm long panel used in CdTe PV technology, ~30 measurement locations are possible using a 0.3 s spectroscopic measurement time, extended above the minimum due to the averaging of multiple optical cycles for signal-to-noise improvement [9]. Of the one minute traversal time, the remaining ~50 s is consumed by translation of the ellipsometer as a unit. Thus, on-line two-dimensional mapping by SE at the required speeds would benefit from an alternative approach. In Sect. 5.3 below, a measurement approach achieving higher speed with potentially high spatial resolution is described for monitoring the fabrication and processing of multilayer PV structures on-line over large areas. This approach is based on the novel concept of line imaging multichannel SE [14]. Whereas for conventional multichannel SE, a collimated white light beam is directed at the substrate/film-stack surface with a well-defined incidence angle, for line imaging multichannel SE, an expanding line-shaped white light beam spans the PV panel across its width [14–18]. The expanded beam instrument uses a two-dimensional detector array such that one array index is exploited for spectroscopy, as in standard multichannel SE, and the second array index is exploited for image location across the PV panel width. The basic design of this fundamentally different multichannel ellipsometer and its applications in thin film PV are discussed in Sect. 5.3.

5.2 On-line Through-the-Glass SE for Rigid CdTe PV Panels in the Superstrate Configuration

In this section, the capabilities of spectroscopic ellipsometry (SE) in a through-the-glass mode are reviewed for on-line mapping of full-size PV panels. The panel explored in this review was fabricated by depositing layers of CdS and CdTe, together serving as the semiconductor PV heterojunction, on the surface of a 60 cm × 120 cm soda-lime glass plate coated with a four-layer stack incorporating a transparent conducting oxide (TCO) top contact [9]. Figure 5.1 shows a generic production line sequence for CdS/CdTe PV panel fabrication in the superstrate configuration, including possible locations of real time and on-line SE instrumentation. Evaluation of on-line SE measurement capabilities for the analysis of the as-deposited structure just before post-deposition treatment has been performed in this study through comparisons with off-line mapping. In each of the on-line and off-line ellipsometers, a rotating compensator is used for modulating the polarization state of the incident beam, and linear detector arrays are used for spectroscopic measurement at high speeds [10, 19]. Because the off-line measurement capability enables greater signal averaging, it may assist in the development of accurate models and in the qualification of the on-line measurement capability.

Relative to off-line SE, on-line SE must operate at a higher speed which results in a lower signal-to-noise ratio and a limited number of data points over the area of the PV panel. For on-line analysis, the PV panel is supported on a roller conveyer, glass side facing down as shown in Fig. 5.1, and is moved by the conveyor past a station for SE mapping measurement. For this measurement the ellipsometer arms,

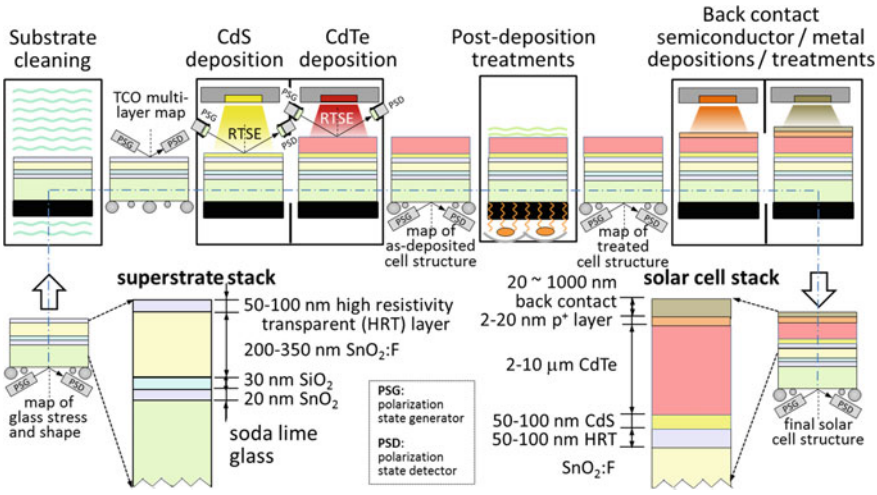


Fig. 5.1 Generic production line sequence for PV thin films of CdS, CdTe, and back contact materials on transparent conducting oxide coated glass panels in the superstrate configuration, showing possible locations of real time and on-line SE instrumentation

functioning as the polarization generator and detector, are mounted below the panel and scan from side to side in a through-the-glass ellipsometry mode. The deduced effective thickness of the CdS window layer and its spatial variations over the PV panel, as obtained by analysis of the on-line measurements, are found to be in good agreement with results obtained off-line [9]. The effective thickness of the CdS layer describes the material volume per substrate area and includes CdS contributions from the bulk layer and any interface roughness layers. This measure of thickness, useful for thin films deposited on rough surfaces, is determined as a robust parameter in both on-line and off-line analyses, and is also important for current density predictions over the areas of PV modules.

5.2.1 *Equipment Design, Development, and Measurement Procedures*

Spectroscopic ellipsometry was performed in measurement configurations designed for on-line and off-line analysis, in both cases utilizing internal reflection within glass panels [9, 20]. Thus, the light beam enters from the glass side in order to probe the opposite side which is coated by the multilayer PV structure. The polarization of the stronger light beam that reflects from the ambient/glass interface carries information only on the near-surface of the glass and its optical properties. In contrast, the polarization of the weaker beam, having undergone two ambient-glass transmissions before and after a single reflection from the glass/film-stack interface carries the desired information on the film stack. As a result, beam focusing and separation were adopted in both the on-line and off-line measurement configurations in order to isolate and detect only the single weaker glass/film-stack reflection. Given the glass panel thickness of 3.2 mm, sufficient beam displacement at a 65° angle of incidence at the ambient/glass interface makes this beam separation possible. Furthermore, in analyses of through-the-glass SE measurements, birefringence induced by strain in the soda-lime glass was taken into account along with tin-side modifications in the optical properties of the glass near-surface relative to those of the bulk [20, 21]. For these PV panels, the CdTe surface to the ambient medium was macroscopically rough such that no detectable beam was specularly reflected from the CdTe/ambient interface in through-the-glass measurements. Thus, no closely spaced oscillations arising from the interference of forward and backward reflected beams within the several micron thick CdTe layer were observable in the (ψ, Δ) spectra over the accessible photon energy range from 0.75 to 3.5 eV. Consequently, the thickness of the CdTe layer could not be measured in these studies of the PV panel in through-the-glass mode.

The off-line SE mapping performed in this study employed instrumentation based on the rotating-compensator principle with linear detector arrays (AccuMap-SE J.A. Woollam Co.) [8, 19]. Through-the-glass SE measurements spanning the 60 cm × 120 cm area of an as-deposited CdS/CdTe PV panel were

made possible by translating the ellipsometer polarization generation and detection arms as a unit in two dimensions according to a 2 cm square grid pattern of probed locations [9]. The ellipsometer light beam is ~0.65 mm in diameter at the position of the glass surface. For the fixed 65° angle of incidence, the circular beam forms an elliptical illumination area with a 1.5 mm long major axis at the ambient/glass interface. The elapsed time for ellipsometer translation and measurement at each location on the panel was ~10 s. Property maps result from the analysis of (ψ, Δ) spectra over the range 0.75–3.5 eV acquired at 1566 spatial locations in a total time of ~4 h 20 min. The spectral range above 3.5 eV is inaccessible due to glass absorption.

The instrument for on-line measurements, shown in Fig. 5.2, was developed through a collaboration with J.A. Woollam Co. [9]. Whereas a stationary PV panel is measured by the off-line SE instrumentation, as described in the previous paragraph, a moving panel is measured by this on-line instrumentation. The linear motion of the PV panel is driven by a roller conveyer so that the panel passes a fixed optical monitoring station (see Fig. 5.2) where the rotating-compensator multichannel ellipsometer performs the mapping function. The ellipsometer source and detector arms scan from side to side as a unit beneath the panel as it travels along the conveyer. Several locations on the panel are sampled along a line with a diagonal orientation that depends on the conveyer and measurement speeds. Figure 5.3 depicts the 16 spatial locations acquired on a 120 cm × 60 cm panel as it travels by the SE mapping station at a speed of ~120 cm/min (or one panel per minute). Thus, the average measurement cycle time is ~3.7 s, including 1 s for collection of raw data at a single spatial location and ~2.7 s for translation of the ellipsometer and focusing of its optics, with data analysis and real time output occurring in parallel. A second measurement mode enables acquisition of data for 31 spatial locations on the panel as it passes the mapping station. In this mode, the

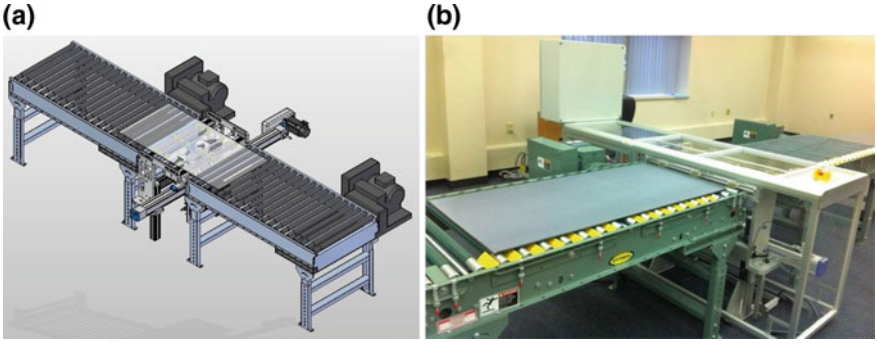


Fig. 5.2 **a** Drawing of a spectroscopic ellipsometer mounted between and beneath two PV panel conveyors for on-line SE in through-the-glass mode (courtesy of B. D. Johs, J. S. Hale, and G. L. Pfeiffer, J. A. Woollam Co.); **b** photograph of the on-line SE system conceptualized and evaluated at the University of Toledo's Wright Center for Photovoltaics Innovation and Commercialization (In-line SE, J.A. Woollam Co.) [9]

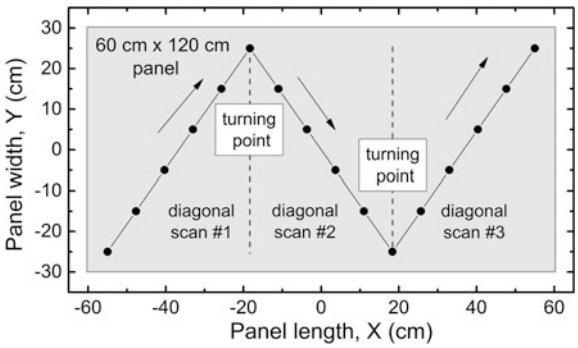


Fig. 5.3 Points sampled over a 60 cm × 120 cm panel mounted on a conveyer moving at 120 cm/min or one panel/min and passing a mapping station for on-line SE of CdTe PV production. The polarization generation and detection arms scan from side to side as the PV panel moves by the mapping station. The panel in the superstrate configuration is probed through the glass and (ψ, Δ) spectra are obtained with an acquisition time of 1 s per pair, yielding a diagonal pattern of 16 locations in this illustration [9]

average measurement cycle time is ~1.9 s per spatial location, including 0.3 s for data acquisition and ~1.6 s for the remaining processes, but without real time output. The ellipsometric spectra acquired with both on-line and off-line instruments are interpreted using the same data analysis methodology, applying least-squares regression with photon energy independent parameters.

In this study, a 60 cm × 120 cm pre-production PV panel consisting of glass/(TCO-stack)/CdS/CdTe as supplied by Calyxo USA was measured by mapping SE and the data analyzed by least-squares regression. The panel for semiconductor heterojunction deposition is NSG-Pilkington TEC™ 15 glass coated with an additional high resistivity transparent (HRT) layer on its surface. This panel is composed of a sequence of four layers on the soda-lime glass plate (3.2 mm in thickness), including thin layers of SnO_2 (~200–300 Å) and SiO_2 (~200–300 Å), and a thicker layer of SnO_2:F (~3000–3500 Å) serving as the top contact, on which a HRT layer ~800–1000 Å in thickness is deposited [22–24]. The depositions of CdS and CdTe semiconductor layers are performed sequentially by atmospheric pressure vapor deposition to thicknesses of ~700 Å and several microns, respectively [25].

5.2.2 *Instrument Capabilities in Thin Film CdTe PV*

Figures 5.4 and 5.5 show the measurement configuration together with the most detailed model used in this study for analysis of the SE mapping results obtained on-line and off-line for the PV panel structure consisting of ambient/glass/SnO_2/SiO_2/SnO_2:F/HRT/CdS/CdTe/ambient [9]. Incorporated as the first model

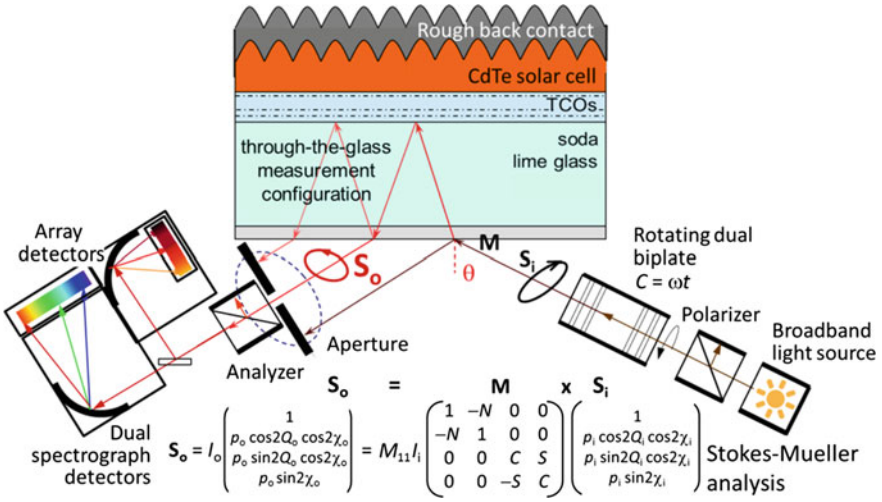


Fig. 5.4 Simplified operational schematic for through-the-glass SE of CdTe PV panels using a rotating-compensator multichannel ellipsometer with a wide spectral range (J. A. Woollam Co., Model M-2000XI). Only the beam undergoing a single reflection from the glass/film-stack interface is collected

Fig. 5.5 Details of the most general model adopted for the analysis of on-line and off-line SE data for a (TEC™ 15)/HRT panel coated with layers of CdS and CdTe in the as-deposited state. HRT designates a high resistivity transparent layer on the surface of TEC™ 15 transparent conducting oxide coated glass (NSG-Pilkington) [9]

CdTe bulk layer (semi-infinite): *avg. void volume fraction*	$[f_v\,(CdTe)]$
CdS/CdTe interface layer: *thickness*	$[d(int)]$
avg. CdTe volume fraction	$[f_{CdTe}\,(int)]$
CdS bulk layer: *thickness*	$[d(CdS)]$
avg. void volume fraction	$[f_v\,(CdS)]$
HRT layer: *thickness*	$[d(HRT)]$
constant contrib. to dielectric function	$[\varepsilon_{1o}]$
SnO_2:F layer: *thickness*	$[d(SnO_2{:}F)]$
free electron parameters	$[(A_D, \Gamma_D) \rightarrow (\rho, \tau)]$
SiO_2 layer: *thickness*	$[d(SiO_2)]$
SnO_2 layer: *thickness*	$[d(SnO_2)]$
soda lime glass: *phase shift due to strain*	$[(\delta_{s1}, \delta_{s2})]$
Sn side layer: *thickness*	$[d(Sn)]$
Ambient	

component, i.e. that for the reflecting glass/film-stack structure, are the five layers of individual materials located on the reverse side of the glass relative to the incident and reflecting light beams. In this model component, the glass is considered as a non-absorbing ambient and CdTe is considered as a semi-infinite substrate. Thus, in performing this analysis, it is assumed that the forward and backward traveling

beams within the glass are incoherent and so do not interfere. Along with the five layers, an effective medium layer can be incorporated at the CdS/CdTe interface to represent a combination of effects, including interface roughness and inter-diffusion at the heterojunction. In addition to the model component incorporating up to six layers, defining the film stack of the glass/film-stack structure, a second model component accounts for the first ambient/glass interface. This component includes a Sn-modified region at the ambient/glass interface that is incorporated due to its effect on the transmitted beam angle and polarization state within the bulk glass [21]. The effect of this layer is very weak in through-the-glass measurements that reject the top surface reflection [24]. The layer should be included in the model, however, if the bulk glass optical properties are measured by SE from the ambient/glass interface at the Sn side of the glass.

The combination of the ambient/glass and glass/film-stack model components involves as many as seven thicknesses as free parameters. Eight materials are present in the model, including the six single component layers along with the glass ambient and the CdTe substrate of the glass/film-stack model. In data analysis, the dielectric functions of these eight materials must be specified, whereas the CdS/CdTe interface layer dielectric function is determined from the Bruggeman effective medium approximation, given the volume fractions of the CdS and CdTe in the layer. The database of dielectric functions at room temperature used in this study was accumulated from a previous investigation of the TEC™ 15 glass component materials as well as those of the HRT, CdS, and CdTe layer materials [24, 26]. For the database, a series of dielectric functions for CdS was determined in situ from studies of thin films with a range of average grain sizes. These CdS films were deposited by magnetron sputtering at various substrate temperatures and cooled to room temperature for measurement. A similar database was developed for the CdTe; however for this material, a range of average grain sizes was obtained by annealing some thin film samples and by subjecting others to a standard $CdCl_2$ treatment.

For selected material components in the model, variable parameters are incorporated to describe possible variations in their optical characteristics or dielectric functions [20, 24]. These include: (i) two parameters $\delta_{sj}(j = 1, 2)$ for the soda-lime glass describing the stress-induced birefringence and its dispersion; (ii) two parameters (A_D, Γ_D) for the SnO_2:F transparent conducting layer describing the Drude amplitude and broadening associated with the free electrons; (iii) one parameter ε_{1o} for the HRT layer serving as the constant contribution to the dielectric function real part; (iv) one parameter, the void volume fraction, for the CdS layer; (v) one parameter, the CdTe fraction, for the CdS/CdTe interface layer; and (vi) one parameter, also the void fraction, for the CdTe layer. For the CdS and CdTe bulk layer materials, the void volume fractions in the model serve as averages throughout the layer thicknesses and are defined relative to those of the materials from the dielectric function database. The optical model for the entire CdS/CdTe solar cell structure continues to be a work-in-progress, and improvements have been made recently enabling an increase in the number of determined parameters, such as

CdTe stress and grain size, while retaining acceptable confidence limits on critical parameters [24].

Among the 15 possible thickness or property parameter maps in Fig. 5.5, those of the HRT and CdS thicknesses are of greatest interest [27]. The HRT thickness requires careful optimization as a trade-off between improved shunt resistance with increasing thickness, and increased series resistance when the layer becomes too thick. Typically, CdS thickness optimization represents a trade-off between increased open-circuit voltage V_{OC} and decreased short-circuit current J_{SC} with increasing thickness. Because the goal is to thin the CdS while retaining V_{OC}, the primary interest is in the effective thickness. In the limit of ultrathin CdS, the bulk layer thickness can reach zero such that the only CdS material exists as a component of the interface layers. For the model of Fig. 5.5, the CdS effective thickness d_{eff} is the volume of CdS per unit area and is obtained from the expression: $d_{\text{eff}}(\text{CdS}) = [1 - f_v(\text{CdS})]d_b(\text{CdS}) + f_{i,\text{CdS}}(\text{CdS/CdTe})d_i(\text{CdS/CdTe})$. In this expression, d_b(CdS) is the CdS bulk layer thickness, d_i(CdS/CdTe) is the CdS/CdTe interface layer thickness, f_v(CdS) is the void volume fraction in the CdS bulk layer, and $f_{i,\text{CdS}}$(CdS/CdTe) is the CdS volume fraction in the CdS/CdTe interface layer. Figure 5.6 defines the concept of effective thickness in the most general case when a HRT/CdS interface roughness layer is incorporated into the model, as in recent studies [24].

Figures 5.7a, b depict thin film property maps spanning the 50 cm × 115 cm area of the 60 cm × 120 cm panel obtained using the off-line SE instrumentation. The two critical parameters presented here are the thickness of the HRT and the effective thickness of the CdS, out of a possible ~15 available mapped parameters [9]. The HRT thickness is observed to be relatively uniform with an average thickness near 850 Å. Thinner regions are observed along the upper and lower panel edges, with thicker regions across the panel sides and a small number of apparent defects. The CdS layer exhibits an average effective thickness near 700 Å with two stripes characterized by reduced thicknesses along the panel and across its sides. Correlation between the two thicknesses appears to occur in the data analysis, and this may be minimized through the incorporation of an HRT/CdS interface roughness layer [24]. Figure 5.8 shows the measured spectra in (ψ, Δ) (points) compared with the best fits (lines) for on-line SE at the point #6 in Fig. 5.3 (counting from left to right) and the

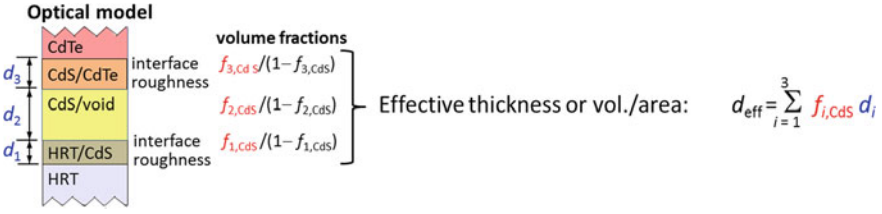


Fig. 5.6 Definition of CdS effective thickness for a HRT/CdS/CdTe PV multilayer on transparent conducting oxide coated glass. The multilayer consists of a CdS bulk layer and interface roughness layers to the underlying HRT and overlying CdTe layers

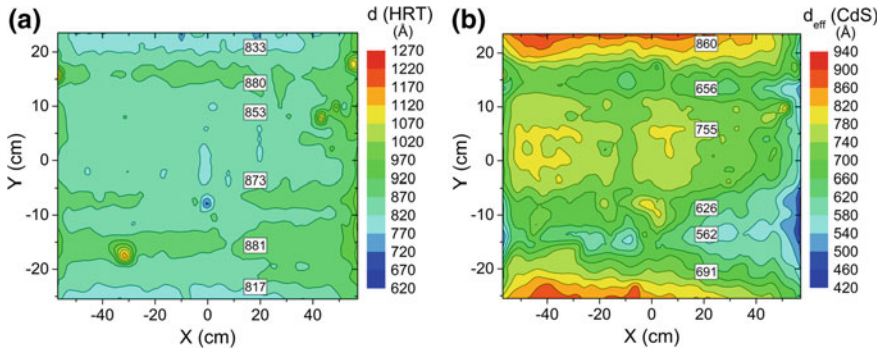


Fig. 5.7 **a** Thickness map for the SnO_2 HRT layer and **b** effective thickness map for the CdS layer, both in Ångstroms, measured off-line for a (TEC™ 15)/HRT panel 60 cm × 120 cm in size coated with CdS and CdTe layers, forming the heterojunction of a pre–production PV panel [9]

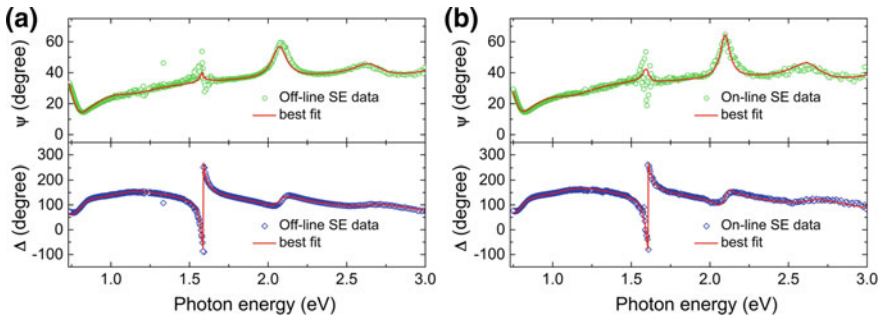


Fig. 5.8 Measured spectra in (ψ, Δ) and best fits for a single location on a pre-production panel incorporating CdS and CdTe layers on (TEC™ 15)/HRT transparent conducting oxide coated glass, including **a** an off-line SE measurement at location (−18.3, 25) in Fig. 5.7 and **b** an on-line SE measurement at the associated point #6 (from left) in Fig. 5.3 [9]

associated off-line SE result at the same point with coordinates (−18.3, 25) along the top edge of the maps of Fig. 5.7. Although the fits are reasonable, high noise in ψ is noted at the quadrant change in Δ just above the CdTe band gap.

Figure 5.9 depicts the effective thickness values of the CdS layer resulting from analysis of through-the-glass measurements performed on the as-deposited CdS/CdTe coated panel. The plot includes results from the on-line and off-line instrument configurations, both presented versus the mapping location [9]. In fact, the panel length along the abscissa corresponds to the sequence of diagonal points in Fig. 5.3, reproduced in the top panel. Thickness values from the two configurations are superimposed for the 16 points along the diagonal trajectories of the upper panel and the associated points in Fig. 5.7b. The turning points correspond to the ellipsometer translation reversal and are indicated by the vertical broken lines in Fig. 5.9. Two distinct multilayer models are also applied for the comparisons.

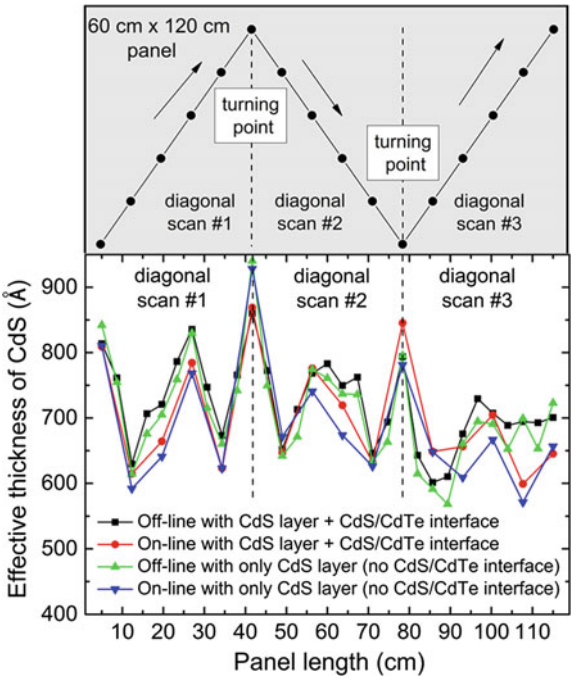


Fig. 5.9 Effective thickness values for the CdS layer obtained in analyses of data collected on-line for comparison with the associated values obtained off-line for a pre-production PV panel consisting of CdS and CdTe layers deposited on (TEC™ 15)/HRT transparent conducting oxide coated glass. Two multilayer models are applied for an additional comparison, one incorporating the roughness/interaction layer at the CdS/CdTe interface and the other neglecting this interface layer. Panel length along the abscissa is defined by the diagonal sequences of locations in Fig. 5.3, reproduced at the top [9]

One model incorporates the CdS/CdTe interface roughness/interaction layer in Fig. 5.5 and the other neglects such a layer, i.e. forces its thickness to zero, thus assuming an abrupt CdS/CdTe interface. Figure 5.10 presents the on-line values of CdS effective thickness, plotted on the ordinate, versus the associated off-line values, plotted on the abscissa, for the two multilayer models. If the few outlying points are eliminated, the on-line and off-line thicknesses are found to agree within $\sim\pm 50$ Å. Thus, in spite of the complexity of the multilayer model, which includes a total of seven layers, determination of a robust CdS thickness is possible irrespective of the selected model.

Figure 5.11 displays analysis results for the effective thickness of CdS from six repetitive on-line SE mapping measurements of the same PV panel using two modes for data collection with different acquisition times for each pair of (ψ, Δ) spectra [9]. The first data collection mode yields the thicknesses in Fig. 5.11a (lower panel) and employs an acquisition time of 1 s. In this time, 16 locations on the panel can be measured during the one minute required for the panel to pass the SE station. Given the total 16 s for data acquisition, the remaining ~44 s, i.e. ~2.7 s/location, is devoted to motion of the polarization generation and detection arms of the ellipsometer between the locations and to adjustment of the optics for a beam focus at the glass/film-stack interface before the next acquisition commences. The data are analyzed simultaneously, i.e. on-line, and the resulting

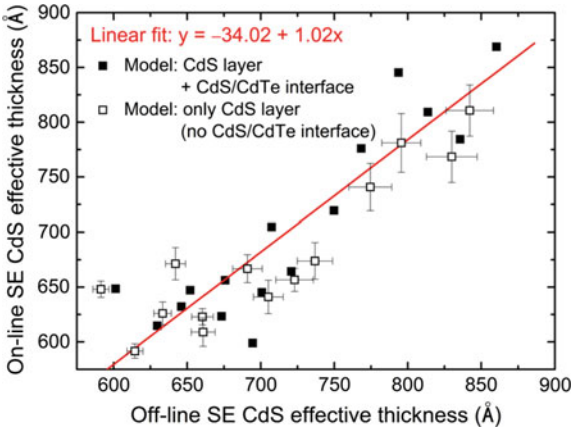


Fig. 5.10 CdS effective thickness from Fig. 5.9 measured using the on-line instrumentation plotted versus the off-line results for a pre-production panel consisting of CdS and CdTe layers deposited on (TEC™ 15)/HRT. Two multilayer models are applied, one incorporating the roughness/interaction layer at the CdS/CdTe interface (solid squares) and the other neglecting this layer (open squares). The solid line is a linear fit to both data sets [9]

effective thickness of CdS is displayed. The second mode yields the thicknesses in Fig. 5.11b (lower panel), employing an acquisition time of 0.3 s per pair of (ψ, Δ) spectra and enabling measurements at 31 locations as the panel moves by the SE station. Ellipsometer motion and beam focusing, but without on-line data analysis and output, accounts for the remaining ~51 s, i.e. 1.6 s/data-point, in this mode.

In both sets of scans in Fig. 5.11, the simplified model of the multilayer stack is applied, based on the assumptions of a single layer of CdS that incorporates voids but includes no effective medium layer at the CdS/CdTe interface [9]. The standard deviations determined from the six consecutive panel mapping runs are shown in Fig. 5.11a (top panel) for the measurements at 16 locations each performed with a 1 s acquisition time. The standard deviation is 21 Å determined as an average for the 16 locations. The corresponding value in Fig. 5.11b (upper panel) is 36 Å for the measurements at the 31 locations each performed with a 0.3 s acquisition time. When the effective medium layer is included at the CdS/CdTe interface, these standard deviations as averages increase to 38 Å for the acquisition time of 1 s and to 52 Å for that of 0.3 s, as summarized in Table 5.1. These increases in the average standard deviations are expected due to the correlations that exist among several variable parameters in the least-squares regression, including the thicknesses of interface and bulk CdS layers and the effective medium compositional parameters. Such correlations lead to larger fluctuations in the analysis results. Because all six repetitive measurements of the panel may not be probing precisely the same spatial location, the average standard deviations in Table 5.1 are believed to provide upper limits.

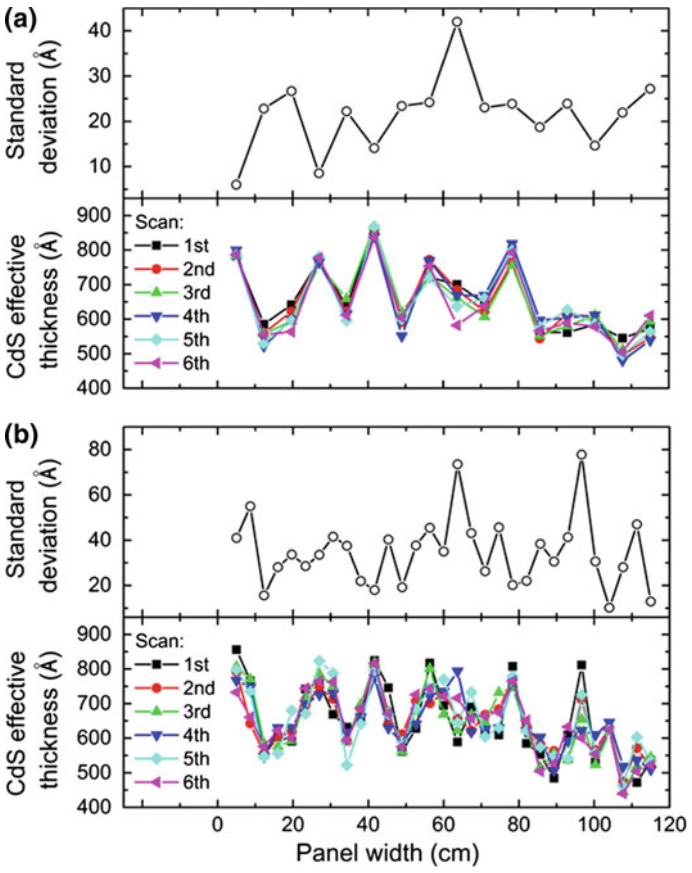


Fig. 5.11 CdS effective thickness and standard deviation for six repeated scans of the same pre-production PV panel consisting of CdS/CdTe layers on (TEC™ 15)/HRT transparent conducting oxide coated glass. Scans were performed with two data acquisition methods characterized by **a** an acquisition time of 1 s per (ψ, Δ) pair, allowing for the measurement of 16 locations on the panel and **b** an acquisition time of 0.3 s, allowing for the measurement of 31 locations [9]

Once the thicknesses and dielectric functions of the complete layer stack are available, then it becomes possible to predict the local current generated by the module under normally incident air mass 1.5 solar radiation. A simple set of assumptions appears applicable based on recent work [24]. Specifically, layers containing a dominant CdTe component are assumed to be the active components and all photons absorbed within these layers are assumed to lead to electron-hole pairs that are separated and collected. The total reflectance from the coated glass as well as the absorbance in the layers that are not active are thus considered losses. Typical values for charge carrier collection and losses, expressed in terms of

Table 5.1 Standard deviations in CdS effective thickness obtained as averages over the different locations from the two data sets of Fig. 5.11 for six scans of the same pre-production PV panel consisting of (TEC™ 15)/HRT/CdS/CdTe. Two optical models were applied, one assuming an abrupt CdS/CdTe interface (center column) and the other incorporating a distinct CdS/CdTe interface layer (right column)

Data acquisition mode	Standard deviations in CdS effective thickness	
	Only CdS layer (Å)	CdS layer + CdS/CdTe interface (Å)
16 points/min scan speed; (ψ, Δ) acquisition: 1 s	21	36
31 points/min scan speed; (ψ, Δ) acquisition: 0.3 s	38	52

Table 5.2 Typical values for charge carrier collection and losses expressed in terms of current density for a CdS/CdTe device fabricated on (TEC™ 15)/HRT coated glass. As can be observed, the dominant losses come from absorbance in the CdS bulk layer and from the total reflectance

	Layer component	J (mA/cm^2)
Collection	CdTe + CdTe/back-contact	19.63
	CdS/CdTe interface	2.19
Losses	CdS bulk	2.95
	reflection	2.90
	CdTe/back-contact	2.06
	SnO_2:F layer	1.49
	soda-lime glass	1.34
	HRT/CdS interface	1.08

current, are shown in Table 5.2 for a CdS/CdTe device fabricated by sputtering on similar (TEC™ 15)/HRT coated glass. As can be observed, the dominant loss comes from absorbance in the CdS bulk layer and in the total reflectance. The SE deduced optical parameters of the off-line map can be converted to local current generation once the nominal value is assigned to the CdTe thickness. The results are shown in Fig. 5.12 and demonstrate the potential importance of high speed, high-resolution on-line mapping for predicting the optical performance of multi-layer PV structures. The approach of translating the SE instrument, however, cannot generate a sufficiently high resolution map of the panel for typical production line speeds. As a result, a different approach is under development and evaluation as described in Sect. 5.3.

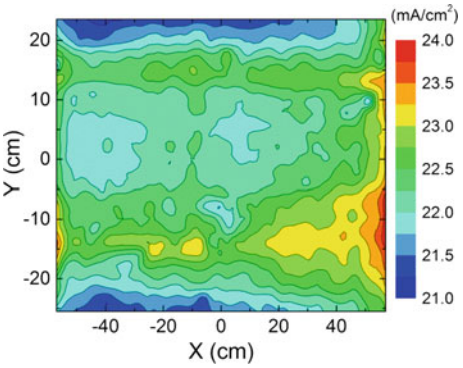


Fig. 5.12 Map of predicted current density for the panel of Fig. 5.7 obtained using the optical model deduced for the (TEC™ 15)/HRT/CdS/CdTe from the off-line SE analysis

5.3 On-Line SE for Roll-to-Roll Flexible PV in the Substrate Configuration

Continuous roll-to-roll deposition of multilayer structures is an important approach for the production of flexible thin film photovoltaic (PV) modules for various applications requiring light weight power generation. The most common PV module designs use stainless steel or polymer foil, such as polyimide, in the substrate configuration. As an example, a generic production line for co-evaporation of $CuIn_{1-x}Ga_xSe_2$ (CIGS) solar cell structures in the substrate configuration is shown in Fig. 5.13. Several possible locations are shown for real time and on-line SE instruments. These instruments can probe the moving surface along a single line on

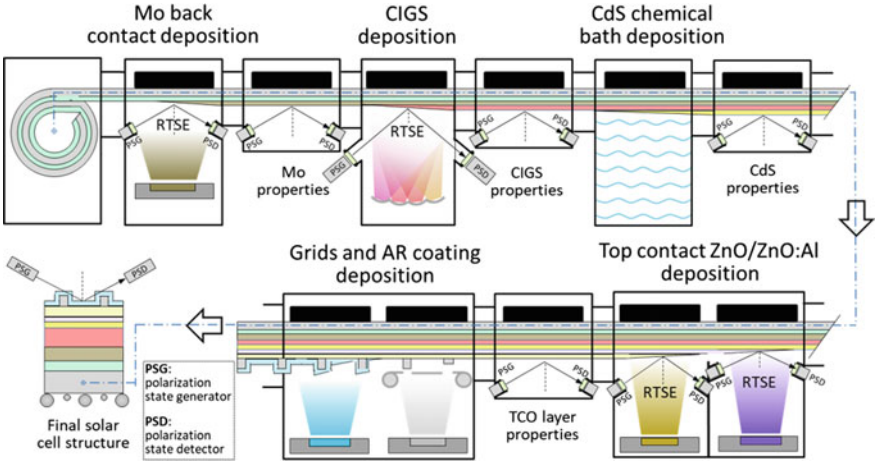


Fig. 5.13 Generic production sequence for continuous roll-to-roll $CuIn_{1-x}Ga_xSe_2$ (CIGS) PV on coated stainless steel foil in the substrate configuration, showing possible locations of real time and on-line SE instrumentation

the substrate/film-stack on-line during and after the several deposition processes as shown [28]. This CIGS technology provides one possibility for deposition of thin films on steel foil by the roll-to-roll approach. A second commercialized roll-to-roll technology was established previously based on hydrogenated silicon, which is employed here to illustrate the capabilities of on-line imaging/mapping SE instrumentation.

As reviewed next in this chapter, a spectroscopic ellipsometer integrating an expanded probe beam has been applied with the goal of in situ imaging/mapping measurements at high speeds. The instrument described here is designed for analysis of flexible substrates coated with multiple thin films deposited using roll-to-roll processes [14–18]. Thin film PV materials and device structures are characterized using this capability for evaluation of large area spatial uniformity in deposition processes using a cassette roll-to-roll flexible substrate. As described in the previous section, lower speed SE instrumentation has been developed for uniformity studies, applying a linear detector array for mapping by SE [8, 9]. Linear translation of the ellipsometer as a unit width-wise is required in order to probe the substrate/film-stack surface moving length-wise. As a result, SE measurements performed serially point-by-point on the surface are time-consuming due to translation of the optics. In contrast, the ellipsometer with an expanded beam incorporates a 2D detector array and so requires no translation of the optics. One array index is exploited for wavelength resolution and the second array index is exploited for spatial resolution, in which case a line across the width of a substrate/film-stack is imaged in reflection. Thus, the ellipsometer provides the capability of imaging the substrate/film-stack width-wise via parallel data acquisition and mapping length-wise via serial acquisition. With this instrument, the potential exists for real-time, in situ, and on-line analysis at high substrate speeds in roll-to-roll fabrication of flexible substrate/film-stack PV structures. The approach can be adapted as well to rigid PV structures on Si wafers or even on glass as in Sect. 5.2.

In this review, the expanded beam technique is illustrated for analysis of the uniformity of metallic, dielectric, and semiconductor films deposited in the sequence of an *n-i-p* hydrogenated amorphous silicon (*a*-Si:H) solar cell structure in the substrate configuration [14]. The specific layers described in this study include the Ag back contact and reflector, the ZnO dielectric spacer and diffusion barrier, and the *n*-type hydrogenated amorphous silicon layer (*a*-Si:H *n*-layer) of the *n-i-p* solar cell structure deposited on a flexible polyimide substrate 12.7 cm wide mounted in a roll-to-roll cassette. Linear images in the spectroscopic ellipsometry angles (ψ, Δ) were acquired across the width of the substrate/film-stack as it was translated by the roll-to-roll cassette drive. In this feasibility study, areas of the substrate/film-stack up to 12 cm in width and 45 cm in length were characterized for determination of thicknesses and optical property parameters of the thin films of the stack, applying relevant parametric models of the complex dielectric function spectra $\varepsilon(E)$ for the Ag, ZnO, and the *a*-Si:H *n*-layer [6].

5.3.1 Equipment Design, Development, and Measurement Procedures

Figure 5.14 depicts the (a) deposition apparatus (MV Systems, Inc.) and (b) integrated functional components of the expanded beam spectroscopic ellipsometer installed as a collaboration at University of Toledo with M. Fried et al. of the Research Institute for Technical Physics and Materials Science, Budapest, Hungary [14, 29]. Figure 5.15 depicts the instrument integrated as a component of an optical station outfitted for a roll-to-roll cassette and used for analysis of multilayer PV structures fabricated in the deposition stations of Fig. 5.14a [14]. For the in situ reflection SE configuration utilized in this study, a diverging beam of linearly-polarized, broad-band light from a source is directed onto a spherical mirror within the vacuum chamber. A converging light beam is generated upon reflection that illuminates the substrate/film-stack mounted in a roll-to-roll cassette also within the

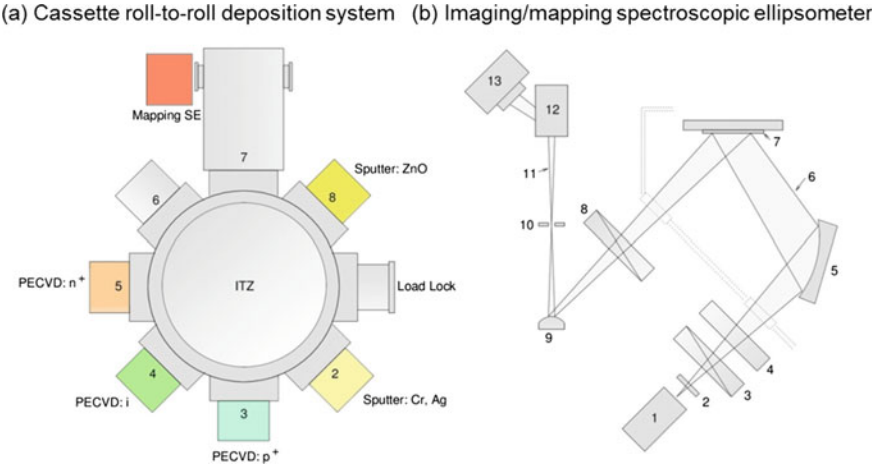


Fig. 5.14 **a** Deposition system at the University of Toledo with capabilities for rigid substrates and cassette roll-to-roll flexible substrates. Two chambers (2, 8) are outfitted for magnetron sputtering of metals and transparent conducting oxides. Dedicated RF PECVD chambers enable the deposition of Si:H *n*-, *i*-, and *p*-layers (5, 4, 3). The expanded beam spectroscopic ellipsometer (labeled 'Mapping SE') is shown at the end of chamber 7. Depositions and measurements described here were performed in situ using the roll-to-roll cassette according to the chamber sequence ($2 \rightarrow 7 \rightarrow 8 \rightarrow 7 \rightarrow 5 \rightarrow 7$). Computer controlled robotic carriers transport the substrate laden roll-to-roll cassette during the multiple trips to and from the deposition and measurement chambers. A rotary stage in the isolation and transfer zone (ITZ) positions the substrate carrier for entry into the appropriate chamber. **b** Components of a high speed imaging/mapping multichannel spectroscopic ellipsometer including (1) broad-band light source, (2) aperture in the shape of a rectangular slit, (3) broad-band polarizer, (4) rotating compensator as a polarization modulator, (5) focusing mirror, (6) converging incident beam, (7) substrate/film-stack, (8) broad-band analyzer, (9) cylindrical mirror, (10) pin-hole, (11) diverging beam, (12) correction-dispersion optics, and (13) 2D CCD detector array [18]

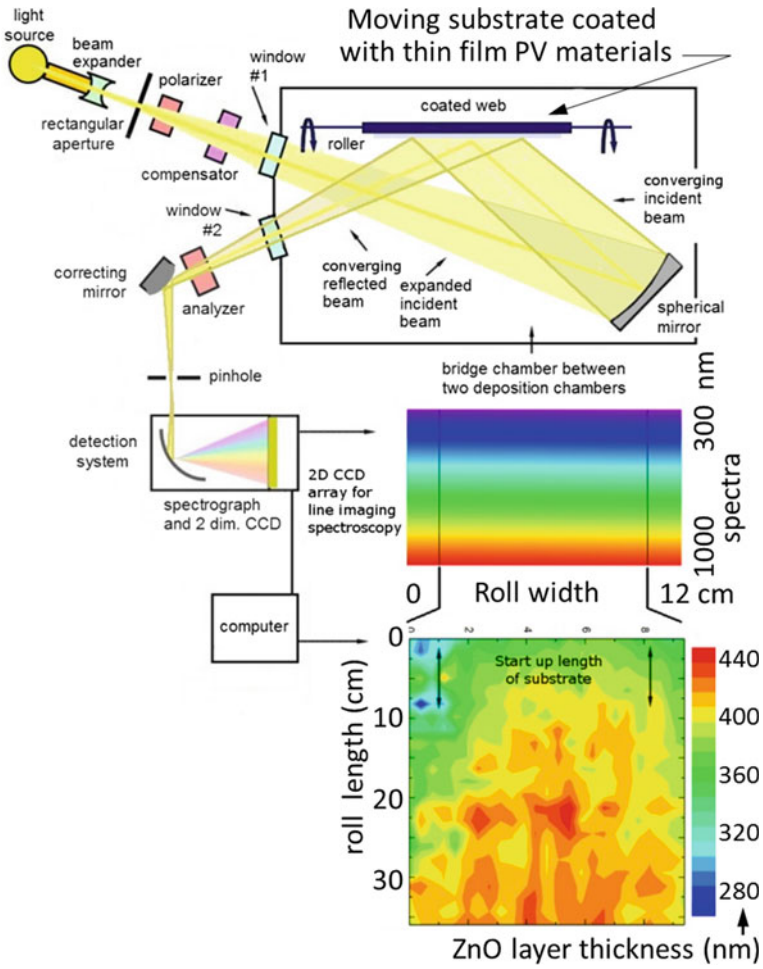


Fig. 5.15 Operational schematic of the expanded beam rotating-compensator ellipsometer for imaging/mapping spectroscopic ellipsometry mounted on-line at an optical station in a cassette roll-to-roll thin film PV deposition system. A two-dimensional array is used to perform spectroscopy along one index in parallel with line imaging along the second index

chamber. By inserting a rectangular aperture immediately following the light source, the expanded beam at the coated substrate surface is in the shape a narrow stripe which illuminates a 12.7 cm^2 area of the coated substrate, ~1 cm along its length by 12.7 cm across its width. A polarizer is mounted following the aperture for the generation of linearly-polarized diverging rays from the incident unpolarized beam. A nano-wire grid polarizer is used in this diverging beam application due its large semi-field angle. For improved accuracy in the (ψ, Δ) data, a rotating compensator, consisting of a MgF_2 biplate, is incorporated into the optical path after the polarizer as depicted in Figs. 5.14b and 5.15. This enables determination of both sinΔ and

$\cos\Delta$ (rather than $\cos\Delta$ alone as in rotating polarizer or analyzer instruments) along with $\cos 2\psi$, which in turn enables determination of the ellipsometry angles unambiguously over their full ranges of $-180° < \Delta \leq 180°$ and $0° \leq \psi \leq 90°$ [10].

The focusing mirror in Fig. 5.15 redirects the rays from the rotating compensator to the substrate/film-stack structure where they impinge at an incidence angle that depends on the location across the probed width of the structure. After reflection from from the spherical mirror and substrate/film-stack, the now converging rays pass through another polarizer (or polarization analyzer). Following polarization analysis, these rays reach their focal point coincident with a pin-hole which disperses the beam according to angle of incidence. Thus, the pin-hole acts as a camera with a spatial resolution depending on its diameter. An image of the illuminated substrate/film-stack surface is formed length-wise on the vertical slit at the entrance of an imaging spectrograph. The image along the spectrograph slit can be dispersed by a diffraction grating onto a two-dimensional silicon CCD. In this way, the pixels along the vertical dimension of the CCD array provide spatial resolution via an image measured in parallel, and the pixels along the horizontal dimension provide wavelength resolution simultaneously.

Figure 5.16 depicts the illuminated area across the full width of the substrate/film-stack and the images on the CCD. The 512 × 512 pixel CCD is binned to generate 41 × 64 pixel groups where the row index (1–41) defines the image location with the potential to cover a 15 cm substrate width, and the column index (1–64) identifies the wavelength. Of the possible 41 pixel groups, a total of 34 groups span the 12.7 cm wide roll. Due to substrate edge effects associated with this width, however, the rows are reduced to 32 pixel groups spanning 12 cm. In order to cover a wider spectral range, two sources, Xe and quartz-tungsten-halogen (QTH) lamps, and two gratings are used for successive measurements over the ranges of 376–620 nm and 620–954 nm, respectively. Overlapping spectra at the 620 nm cross-over and weak irradiance at the upper and lower limits of the range reduce the usable columns from 64 to 49 and 57 pixel groups for the two ranges, respectively, generating a 106 point spectrum. Maps of the SE data for the coated substrate can be generated by splicing together a series of images generated as the roll advances. As a result, this optical system design has no moving parts other than the rotating compensator and the source/grating switching mechanics. In future designs, a dual source and single grating can be adopted to avoid the need for sequential spectral measurements [30].

The expanded beam spectroscopic ellipsometer generates greater challenges in calibration of the instrument and reduction of the CCD data as compared to the approach of Sect. 5.2. Any optical components in the system placed between the rotating compensator and the analyzer, in addition to the substrate/film-stack of interest, have the potential to change the polarization state upon transmission or reflection and influence the measured SE images [14]. Thus, any unwanted polarization changes generated by the two chamber windows and the focusing mirror must be determined as an integral component of the calibration. In this calibration component, the polarization changes are determined as a function of the location

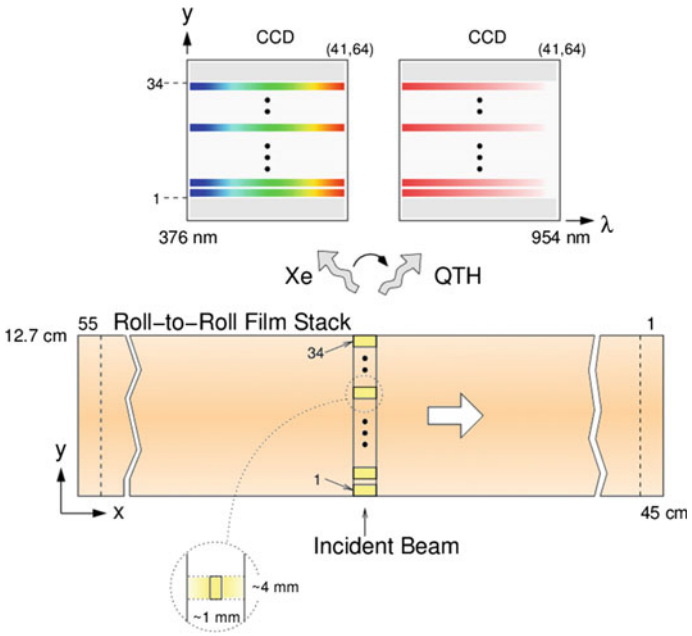


Fig. 5.16 A schematic depicting the illuminated area of the thin film coated substrate and the resulting images on the CCD. Two independent light sources are used sequentially to span the 1.30–3.30 eV photon energy range. The 512 × 512 pixel CCD is reduced by binning to 41 × 64 pixel groups. Each spatial location across the substrate roll is mapped to a CCD row, and each wavelength as dispersed by the diffraction grating of a spectrograph is associated with a CCD column. The system is capable of measuring a 15 cm wide roll, corresponding to 41 pixel group rows. A 12.7 cm wide polyimide film was used as a substrate, corresponding to 34 pixel group rows, of which 32 are usable. The images from the separate light sources are adjoined to give a total of 106 functional pixel group columns. A total of 55 line images over a 45 cm length of the substrate/film-stack are collected and analyzed. The effective unit beam spot size (~4 mm^2) is shown in the inset below the roll of substrate/film-stack

across the image, i.e. the pixel row index (1–32) of the CCD, and as a function of the wavelength, i.e. the (1–49 or 1–57) pixel column index of the final data set. In addition, a second calibration component is required in which the angle of incidence is determined as a function of the CCD pixel row index.

Performed together, the two calibration components employ samples with well-known properties mounted at the substrate/film-stack position. The samples are selected for high calibration sensitivity and include three single crystal silicon (*c*-Si) wafers with thermally-grown oxides (SiO_2) of different thicknesses. Considering only the focusing mirror in Figs. 5.14b and 5.15, its effects on the SE images are calculated starting from the product $\rho_u = \rho_k \rho_m$, which describes the measured (or uncorrected) ellipsometry angles (ψ_u, Δ_u) according to $\rho_u = r_{pu}/r_{su} = \tan\psi_u \exp(i\Delta_u)$. On the right side of the calibration equation $\rho_k = r_{pk}/r_{sk} = \tan\psi_k \exp(i\Delta_k)$ define the complex amplitude reflection ratios of the three wafers ($k = 1, 2, 3$) selected for calibration, and

$\rho_m = r_{pm}/r_{sm} = \tan\psi_m \exp(i\Delta_m)$ defines the corresponding ratio for the mirror that is to be calibrated. In these reflection ratios, r_{pj} and r_{sj} ($j = k, m$) identify the p and s complex amplitude reflection (or Fresnel) coefficients for light rays polarized linearly in directions parallel (p) and perpendicular (s) to the plane of incidence which contains the incident and reflected propagation directions. The quantities $\tan\psi_j$ and Δ_j identify the relative (reflected/incident) amplitude ratios (p:s) and phase difference (p–s) shifts (reflected–incident) that occur upon specular reflection. The calibration procedure relies on the assumption that the eigenmodes for the reflections from the spherical mirror and the substrate/film-stack shown in Figs. 5.14 and 5.15 are the same p and s linear polarizations.

In the calibration procedure using the three c-Si/SiO_2 wafer samples having different values of the oxide thickness (d_1, d_2, d_3), six spectra or $6N$ values, namely $(\psi_{u,i}, \Delta_{u,i})$, can be determined for each location across the probing width (or pixel row index), where $i = 1, \ldots, N$, defines the wavelength (or pixel column index) and $N = 106$ spans the two spectral ranges. In the procedure, $2N + 4$ unknowns $\{(\psi_{m,i}, \Delta_{m,i}), i = 1, \ldots, N; \theta, d_1, d_2, d_3\}$ must be determined according to $\rho_m = \rho_u/\rho_k$ by least-squares regression for the simultaneous calibration of the mirror parameters and the angle of incidence θ for the given location across the probing width. Thus, only two samples with well-known properties are required in theory, given the large number of wavelengths. The calibration approach also allows the c-Si/SiO_2 samples to be non-uniform since the three thicknesses are determined independently at each location. Although the procedure can be used to obtain calibration data relevant for each of the CCD pixels, a higher signal-to-noise ratio is possible by using the same pixel grouping as in the measurements. After this initial procedure with grouping, the calibration data plotted as functions of probing width and wavelength are subjected to polynomial smoothing in order to suppress statistical variations in the data. Smooth trends in the angle of incidence calibration data are expected with probing width and in the $\{\psi_m, \Delta_m\}$ calibration spectra with both probing width and wavelength. The calibration component that determines stress in the chamber windows can be performed together with that for the polarizer and analyzer azimuthal angles [31].

5.3.2 *Applications in Thin Film* a-*Si:H PV*

The capability of the expanded beam spectroscopic ellipsometer is presented first through analysis of a multilayer structure consisting of Cr/Ag/ZnO/(a-Si:H n-layer) deposited onto a flexible polyimide substrate mounted in a roll-to-roll cassette [14]. Figure 5.17 shows the deposition configuration for the roll-to-roll system, and Fig. 5.18 shows the layer sequence on the substrate and the deposition conditions for the structure of this study. The roll-to-roll speed of the flexible substrate

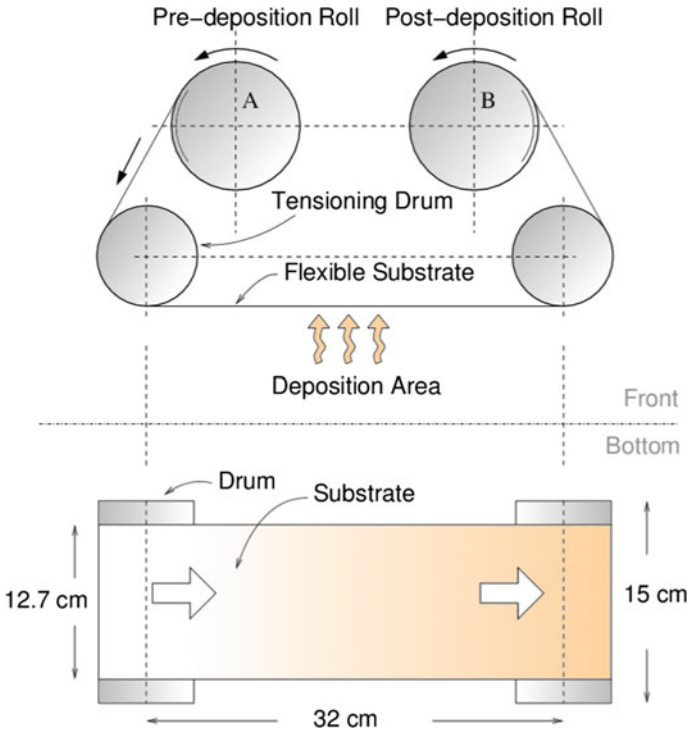


Fig. 5.17 Deposition configuration for a cassette roll-to-roll system (MVSystems, Inc.). Sputtered films including Cr, Ag, and ZnO as well as PECVD films including *n*-type *a*-Si:H are deposited on the polyimide substrate. The transfer rate is determined by the desired film thickness. Multiple layers can be deposited onto the substrate by rewinding the roll and repeating the process in different deposition chambers

v determines the steady-state deposited thickness d_0 in accordance with the simple approximate equation

$$d_0 = \frac{r}{v} L, \tag{5.1}$$

where r is the deposition rate and L is the length of the deposition zone. This equation is based on the assumptions of a deposition rate r independent of time and also location throughout the deposition zone of length L, and a deposition rate of zero outside this zone. Based on (5.1), it is clear that a thicker film is obtained by reducing the roll-to-roll speed.

Once each deposition was complete, the roll-to-roll cassette was transported to the mapping SE chamber as shown in Fig. 5.14a via internal rack and pinion tracks. The cassette was rewound and positioned to a reference point before starting the mapping measurements. Upon completion of the measurements, the cassette was rewound again and transported to the next deposition chamber. A reference point x_0

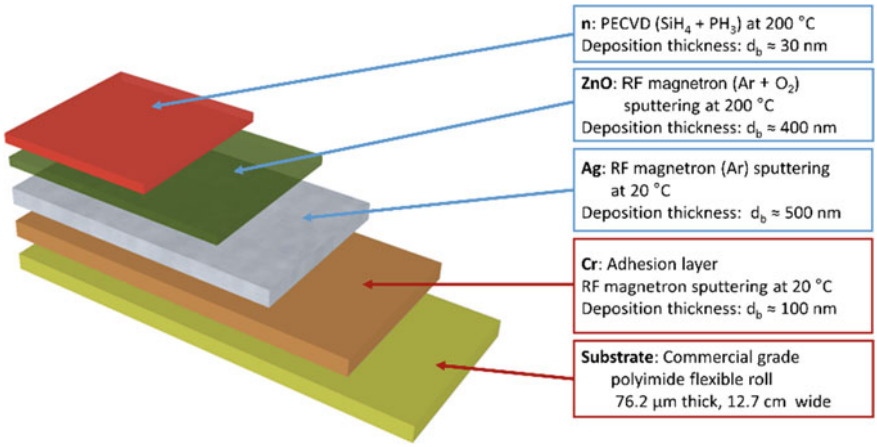


Fig. 5.18 Three-layer stack consisting of Ag/ZnO/(*a*-Si:H *n*-layer) on a Cr-coated polyimide substrate used in studies of flexible PV foil with an expanded beam rotating-compensator instrument for imaging/mapping spectroscopic ellipsometry. The multilayer is measured in situ after each film growth step at an optical station in a multi-chamber thin film deposition system accommodating the polyimide foil in a roll-to-roll cassette

for each film is defined, which is the point at the exit of the plasma zone at the plasma ignition time (which occurs simultaneously with the start of web motion). Under these conditions there exists a start-up length of roll in which the thickness d increases linearly with distance x along the roll in accordance with the approximate expression

$$d(x) = \frac{r}{v}(x - x_0); \quad x_0 \le x \le x_0 + L. \tag{5.2}$$

This thickness gradient occurs because a roll distance L of travel to the point $x = x_0 + L$ is required before the thickness saturates at the steady-state value of d_0 in (5.1). Similarly, a shut-down length of the roll exists given by

$$d(x) = \frac{r}{v}(x_f - x); \quad x_f - L \le x \le x_f. \tag{5.3}$$

This gradient is also linear because the plasma is extinguished as soon as the roll reaches its stopping point. Here x_f is a reference point at the entrance to the plasma zone at the shut-off time. Thus, for a stable deposition, the thickness is d_0 over the range $x_0 + L \le x \le x_f - L$, according to (5.1) and the associated assumptions.

The film stack incorporates a conventional metal-contact/back-reflector along with the first semiconductor layer of an *a*-Si:H-based thin film device fabricated in the *n-i-p* structure, i.e. the substrate configuration, whereby the solar radiation enters the *p*-layer first [32]. Thus, in this solar cell, the *n*-layer is the first semiconductor to be deposited in the *n-i-p*, a sequence that is used most often for

Si:H-based devices on flexible substrates that are opaque such as steel foil. The 100 nm thick Cr layer in Fig. 5.18 is for adhesion which, along with the Ag layer, was deposited by magnetron sputtering at radio frequency (RF) using a ~20 °C substrate temperature and a 5 mTorr Ar pressure. The ZnO layer was also deposited by this method but with a 200 °C setting for the substrate temperature and with an O_2 addition to the Ar gas during sputtering. The RF power densities at the sputtering targets for the Ag and ZnO depositions were selected to generate the required film thicknesses. The final values used here were 1.1 W/cm^2 for both Ag and ZnO. At a 0.02 cm/s roll speed, a total deposition time of 30 min was used in each case, yielding the final average thicknesses of ~500 nm for Ag and ~400 nm for ZnO. RF plasma enhanced chemical vapor deposition (PECVD) was used for fabrication of the *a*-Si:H *n*-layer. The gas flows of silane (SiH_4) and phosphine (PH_3) were set to maintain the ratio $D = [PH_3]/[SiH_4] = 0.005$. The following deposition conditions were used for the *n*-layer deposition: substrate temperature, 200 °C; total pressure, 350 mTorr; and RF power density, 9.5 mW/cm^2. A roll speed of 0.12 cm/s, six times higher than that of the Ag and ZnO, yielded the ~30 nm thickness desired for the *n*-layer of the solar cell. A multi-chambered, load-locked deposition system ensured that the sequence of three depositions was completed without exposure of the structure to atmosphere between the layers and during the measurement. The final output of the process was a roll 12.7 cm wide and 55 cm long consisting of polyimide/Cr/Ag/ZnO/(*a*-Si:H *n*-layer) of which 45 cm was mapped after each of the Ag, ZnO, and *n*-layer depositions.

Imaging/mapping SE with the instrument of Fig. 5.15 spans the range of photon energies from 1.3 to 3.3 eV in 106 pixel groups, as obtained from two sets of data acquisitions [14]. This corresponds to a wavelength range of 376–954 nm and a band 5.5 nm wide over a given pixel group. The spectral range possible here is valuable for analyzing many of the component layers and materials of solar cells. In fact, the structural parameters of a multilayer solar cell combined with the layer optical properties measured over the 1.3–3.3 eV range can be applied to predict the external quantum efficiency, and in addition, the losses due to absorbance within inactive layers and to the overall reflectance [12, 24]. The incidence angle of the converging beam at the surface of the substrate/film-stack varies over the range of 67.4°–72.2° across the 12 cm probed width, parallel to the plane of incidence as shown in Fig. 5.15. Thus, given the 32 pixel groups spanning the 12 cm width, the angular range is $\delta\theta = 0.15°$ for a given pixel group. The variation in the incidence angle along the 1 cm dimension of the converging beam, normal to the plane of incidence, is much smaller than $\delta\theta$ and so can be neglected. Maps spanning a 45 cm length of the coated substrate roll were generated by adjoining 55 SE images extending from the leading end to the trailing end of the flexible substrate/film-stack mounted in the roll-to-roll cassette. Thus, determination of thin film structural and optical property maps with this instrument can provide information suitable for predictions of solar cell current density output over the analyzed area and the effects of non-uniformities on that output. Each property map to be presented in the paragraphs to follow was deduced in a least-squares regression analysis applied to the corrected (ψ_c, Δ_c) maps calculated in turn from the measurements of $\rho_u = \tan\psi_u \exp(i\Delta_u)$ via the correction

for the mirror (m) reflection. The mirror correction was implemented in accordance with $\rho_c = \tan\psi_c \exp(i\Delta_c) = \rho_u/\rho_m$, where ρ_m is the complex amplitude reflection ratio that accounts for the effect of the reflection from the mirror, with the same p–s coordinate system as the substrate/film-stack.

Figure 5.19a shows a map of the mirror-corrected data Δ at the wavelength of 700 nm for the polyimide/Cr/Ag coated roll, and Fig. 5.19b shows the corresponding map for the polyimide/Cr/Ag/ZnO. Henceforth, all ellipsometry angles are mirror-corrected, and thus the subscript 'c' will be suppressed. Over the start-up length of the roll, a linear increase from zero is observed in the Ag thickness on the Cr coated polyimide. For the map in Fig. 5.19a, the start-up length for the opaque Ag deposition is not shown. As a result, the map is relatively uniform over the 45 cm length with a gradient across the width due to the angle of incidence variation. For the map in Fig. 5.19b, 5 cm of the start-up length is included on the map which leads to the length-wise non-uniformity on the left side. Again, the pattern across the width is due to the angle of incidence variation which becomes stronger from left to right as the thickness of the ZnO increases in the first 5 cm of length. In least-squares regression analysis, as will be described in the next paragraphs, maps for a collection of photon energy independent parameters are obained, including the bulk and surface roughness layer thicknesses, and in addition parameters in physics-based expressions selected to define the complex dielectric functions of the layer materials. The maps displayed for the components of the multilayer structure have been resized to ~9 cm × 35 cm, where the mean square error (MSE) values

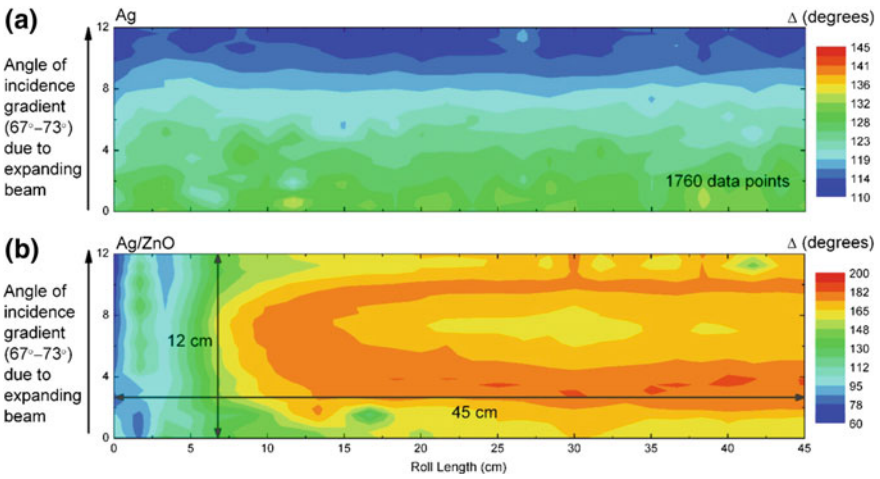


Fig. 5.19 Maps over a 12 cm × 45 cm area presented in the corrected ellipsometry angle Δ at a wavelength of 700 nm (photon energy $E = 1.77$ eV) for **a** the surface of an opaque Ag film on Cr-coated polyimide and for **b** polyimide/Cr/Ag/ZnO. The horizontal axis is the motion direction along the polyimide roll and the vertical axis is the width of the roll. In **b**, the first 5 cm from the left represents part of the start-up stretch of the polyimide/Cr/Ag/ZnO roll, depicting a gradient in the ZnO thickness

in the least-squares regression analysis are acceptable. Thus, the edge regions of the substrate/film-stack are excluded as is the start-up region at the leading end of the roll for the ZnO map in Fig. 5.19b. In future studies, it may be possible to interpret the edge regions of the roll by including layer thickness distributions in models for a single location, as well as by an analysis of the depolarization spectrum in addition to the corrected (ψ, Δ) [33]. Finally, for the various maps presented here, it should be emphasized that identical sizes correspond to the results over identical areas of the substrate/film-stack structure.

The (ψ, Δ) spectra for the opaque Ag film on the polyimide/Cr surface are analyzed by assuming a single layer model corresponding to an opaque-bulk/surface-roughness structure. The Drude free electron formula incorporating three photon energy independent variable parameters was applied for the complex dielectric function $\varepsilon = \varepsilon_1 - i\varepsilon_2$ of the bulk Ag. These three parameters include a photon energy independent value ε_{1o} as a component of the real part ε_1, the resistivity ρ of the Ag, and its electron mean free time τ [6]. The spectra in ε for the roughness layer having a thickness of d_s at the Ag surface are determined using the Bruggeman effective medium approximation (EMA), based on the assumption of a 50–50 vol% composite of the underlying bulk Ag with void [34]. Thus, analysis of the corrected experimental (ψ, Δ) spectra by least-squares regression provides $\{d_s, \varepsilon_{1o}, \rho, \tau\}$. Figure 5.20 presents illustrative experimental (ψ, Δ) spectra and the best fit results at one location on the sample, and Fig. 5.21 shows maps of d_s, ρ, and the MSE that define the best fit as in Fig. 5.20 [14]. Here, the MSE is calculated as follows

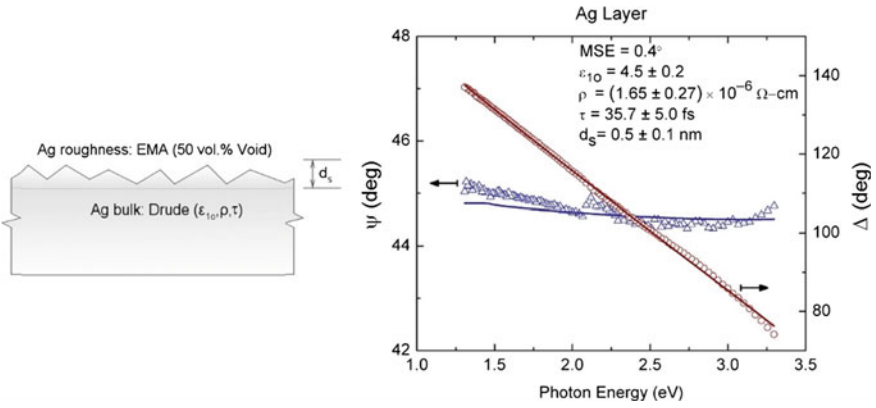


Fig. 5.20 Illustrative mirror-corrected (ψ, Δ) spectra (points) and their best fit (lines) at a single location on the map of Fig. 5.19a for thin film Ag sputtered to opacity. The best fit was obtained by least-squares regression analysis based on minimization of the mean square error (MSE) for the 1.3–3.3 eV photon energy range using a one layer model. This model consists of bulk/roughness with dielectric functions from the Drude and the Bruggeman effective medium approximation (EMA) formulas for the opaque bulk and roughness layers, respectively [14]

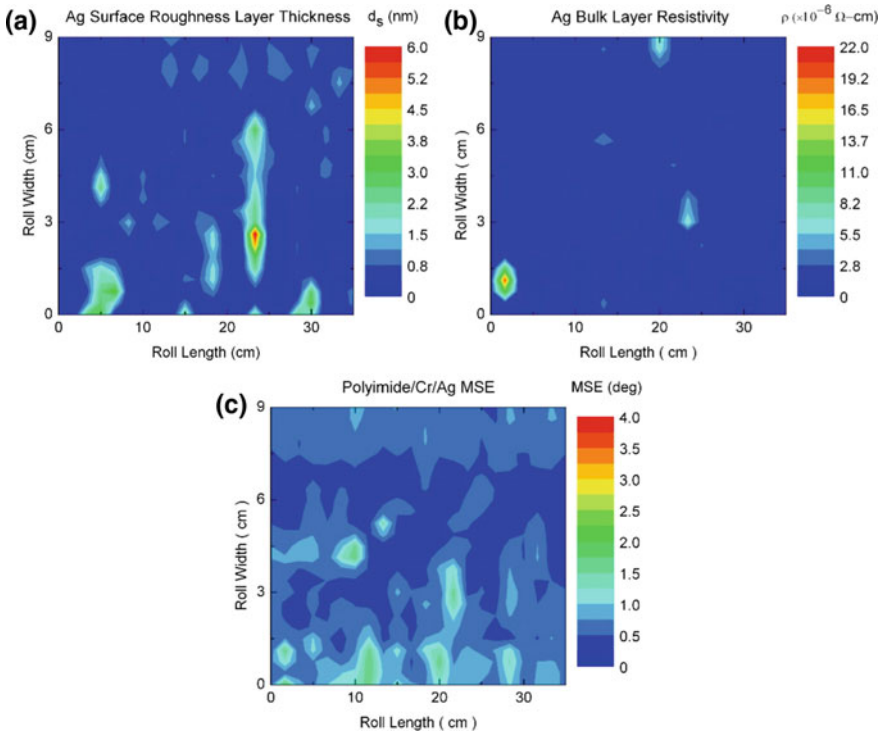


Fig. 5.21 Maps over a 35 cm length of Cr/Ag coated polyimide flexible substrate for **a** the thickness of the roughness layer on the Ag surface, **b** the Ag resistivity, and **c** the mean-square error in the best fit. The opaque layer of Ag studied here is the second thin film component of the multilayer of Fig. 5.18. The horizontal axis is parallel to the motion direction for the 35 cm length of the substrate/film-stack structure. The vertical axis defines the structure's width, across which film uniformity is assessed from edge to edge [14]

$$\sigma = \left\{ \sum_{n=1}^{N} \left[\left(\psi_n^{(c)} - \psi_n^{(m)} \right)^2 + \left(\Delta_n^{(c)} - \Delta_n^{(m)} \right)^2 \right] / (2N - p) \right\}^{1/2}, \tag{5.4}$$

where $N = 106$ denotes the number of (ψ, Δ) pairs versus photon energy and p denotes number of free parameters in the model. The superscripts '(c)' and '(m)' indicate best fit calculated and measured data values.

The resistivity in the map of Fig. 5.21b is relatively uniform, and the values are consistent with the bulk result of $1.6 \times 10^{-6}\ \Omega\,\text{cm}$ [35] within confidence limits (see also Fig. 5.20). The deduced τ indicated in Fig. 5.20 is consistent with the value of 37 fs calculated from the resistivity and atomic concentration N_a assuming a valence of unity, according to $\tau = m^*/N_a e^2 \rho$ with an effective mass of $m^* = 0.99\ m_e$, where m_e is the free electron mass. Over much of the area, the Ag film exhibits a roughness layer thickness <1 nm; however, bands having larger roughness that extend from 0 cm to as far as 7 cm across the width of the roll are observed, with one

point reaching nearly 6 nm. In addition, a few apparently defective areas are observed over the surface. The bands with larger roughness and the defective areas do not correlate with areas of higher MSE, suggesting that these mapped values are valid. The bands in the MSE may arise from a slight warping of the polyimide that arises from film stress. Definitively identifying the origin of these bands and interpreting them in greater detail requires additional investigation.

The polyimide/Cr/Ag/ZnO structure has been analyzed applying a three-layer model incorporating a Ag/ZnO interface roughness layer and ZnO bulk and surface roughness layers [36]. The thicknesses of these layers are denoted d_i, d_b, and d_s, respectively. The ε_1 and ε_2 spectra of the ZnO bulk layer are described by a complex expression that incorporates real constant and Sellmeier terms in ε_1 and a complex critical point (CP) oscillator in ε_1 and ε_2. The Sellmeier and CP terms include amplitude and resonance energies, indicated by A_j and E_j ($j = 0$ for the CP oscillator; $j = 1$ for the Sellmeier term). The CP oscillator is defined by additional variables including a broadening parameter and a phase, denoted Γ_0 and ϕ_0, respectively. In the least-squares regression, the exponent of the CP is fixed at 0.5. The dielectric function of the Ag/ZnO interface layer (i) was simulated with a Lorentz oscillator having four free parameters, $\varepsilon_{1oi}, A_i, E_i,$ and Γ_i that describe the interface plasmon resonance [36]. Here, ε_{1oi} is a constant contribution to ε_1. The properties of the opaque Ag bulk layer beneath the ZnO are fixed to the values of the previous analysis of Figs. 5.20 and 5.21 for the corresponding locations. Thus, 14 parameters are varied for analysis of the polyimide/Cr/Ag/ZnO structure, including three that describe the layered structure, and seven and four that describe the dielectric functions of the bulk ZnO and Ag/ZnO interface layer, respectively.

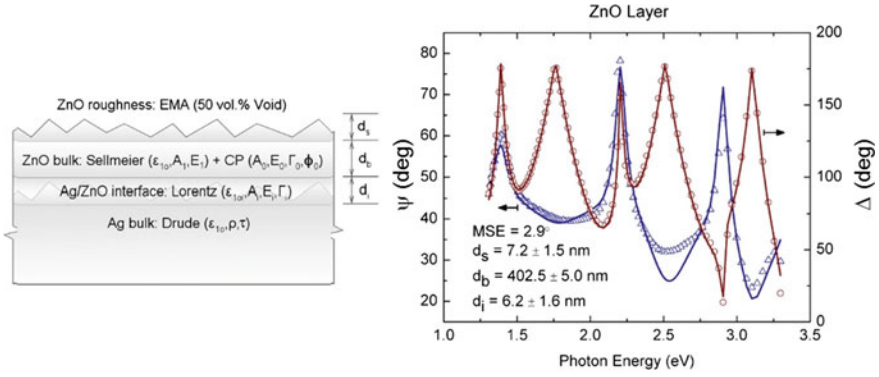


Fig. 5.22 Illustrative experimental (ψ, Δ) spectra (points) and best fit (lines) applying least-squares regression analysis with MSE minimization for a polyimide/Cr/Ag/ZnO substrate/film-stack structure at a representative location on the map presented in Fig. 5.19b. A three-layer Ag/interface/bulk/roughness model is used for the ZnO film over the range of photon energies from 1.3 to 3.3 eV. The dielectric function of the bulk layer incorporates a constant and a single photon energy dependent Sellmeier term, both contributing to the real part of the dielectric function, and a CP oscillator centered at the band gap. In this analysis, an interface roughness layer is included between the Ag and ZnO that exhibits a plasmon resonance in the form of a single Lorentz oscillator [14]

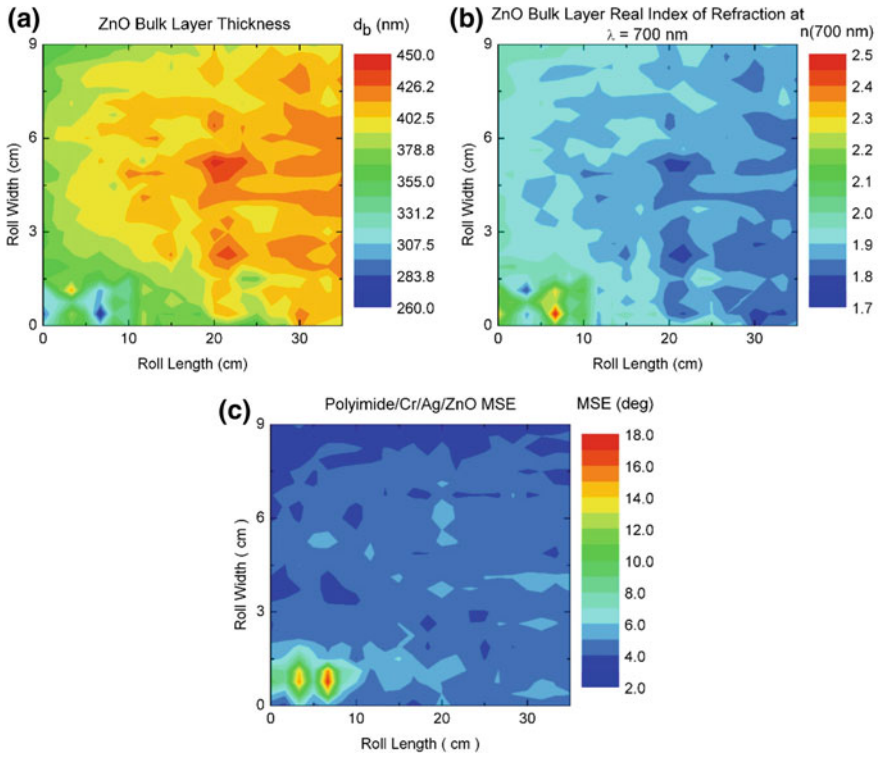


Fig. 5.23 Maps relevant for the ZnO layer on the polyimide/Cr/Ag sample structure, including **a** the thickness of the bulk layer and **b** the ZnO bulk layer index of refraction n at a wavelength of 700 nm. **c** A map of the MSE for the best fit is shown. The horizontal axis is parallel to the motion direction for the 35 cm length of the substrate/film-stack structure. The vertical axis defines the structure's width, across which film uniformity is assessed from edge to edge [14]

Based on this model, an illustrative best fit to data excerpted from the map for a representative location is provided in Fig. 5.22.

For the mapping results of the polyimide/Cr/Ag/ZnO multilayer structure as shown in Fig. 5.23, a simplified model compared to that of Fig. 5.22 was used in which case the interface layer was neglected. This enabled greater stability in the analysis as the Lorentz oscillator parameters were found to be unstable in narrow bands along the roll [14]. In Fig. 5.23a, a map for the thickness of the ZnO bulk layer is depicted based on this simplified model. Maps for the parameters that define the Sellmeier term of the dielectric function for the bulk ZnO are not presented, the reason being that the resonance energy E_1 for this term is well above the measured spectral range. Thus, the parameters A_1 and E_1 of this term do not convey useful physical information. In addition, the 3.3 eV band gap of undoped ZnO is at the upper limit of the spectral range; however, impurities can give rise to an increase in the band gap due to degenerate n-type doping [37]. Such shifts move the band gap

above the spectral range of the instrument and give rise to large uncertainties in the CP parameters. Thus, rather than mapping the Sellmeier and CP parameters, a map of n(700 nm), the index of refraction for the ZnO bulk layer at a wavelength of 700 nm is presented in Fig. 5.23b. This index value conveys useful information owing to its relevance for predicting the layer's performance as a component of the Ag/ZnO back reflector in the solar cell. In fact, the higher photon energy optical properties are of little interest since the overlying *a*-Si:H *n-i-p* layers and In_2O_3:Sn top contact layer absorb the higher energy photons before they reach the ZnO layer.

The ~9 cm × 35 cm {d_b, n(700 nm)} maps in Figs. 5.23a, b suggest that thinner films along the start-up stretch of the roll exhibit higher indices of refraction. Such behavior may arise in part from neglecting the Ag/ZnO interface layer in this analysis, as the interface region exerts a stronger effect for thinner ZnO. Along the upper side of the map, however, the increase in index of refraction from right to left occurs over a range where the MSE is low and nearly constant, suggesting that the increase is a true effect. Clear features having much higher indices of refraction occur in the lower left corner also associated with much thinner ZnO. As indicated by Fig. 5.23c, the MSE for these points appears higher than the surrounding low MSE regions. These features in both Fig. 5.23a, b may be caused by defects such as dimples in the substrate/film-stack structure that generate distortion in the reflected beam path and deviations in the resulting measurements. Additional investigation is warranted with the goal of identifying such defects and evaluating their effects on the measurement and analysis results.

In developing an appropriate model for the polyimide/Cr/Ag/ZnO structure, improvements in the MSE were obtained in the analyses such as those of Fig. 5.22 by introducing the Ag/ZnO interface layer, yielding a model with three layers. The interface layer is a key component in the evaluation of the device performance since it absorbs and dissipates photon energy, and as a result leads to losses that inhibit back reflector operation. In a previous report, the Ag/ZnO interface has been described with a single thickness d_i as a structural free parameter [36]. The ε spectra of the interface layer in [36] have been modeled over the range from 1.3 to 5.0 eV in photon energy as a superposition of a variable photon energy independent contribution to ε_1, a Drude free electron contribution, a Lorentz oscillator, and a CP oscillator representing the interband transitions in Ag with an onset near 4 eV. The Lorentz oscillator describes the dipolar plasmon resonances generated by the oscillations of free electrons within the protrusions of the Ag roughness which then appear within the Ag/ZnO interface layer after the ZnO deposition. In the present study, it is possible that a Drude component will also be needed in addition to the Lorentz oscillator in the model for the dielectric function of the layer at the Ag/ZnO interface in order to incorporate this layer into the mapping analysis yielding Fig. 5.23. Because the upper limit of the spectral range of the imaging/mapping instrument is 3.3 eV, the interband CP is not needed in this more advanced analysis. In addition to an interface layer between the Ag and ZnO, it may also be of interest to incorporate an Urbach tail absorption feature below the CP resonance energy in place of the CP oscillator tail [38, 39]. Although the two Urbach tail parameters of amplitude and slope can be fixed to ensure continuity of ε_2 and its first derivative,

respectively, it is also possible to allow the slope to vary in order to generate a variation in the sub-band-gap absorption characteristic.

Deposition of the *a*-Si:H *n*-layer on the polyimide/Cr/Ag/ZnO multilayer structure requires the introduction of an additional pair of structural parameters in the least-squares regression analysis, namely the thicknesses of the bulk and surface roughness layers, d_b and d_s, for the *n*-type a-Si:H. The ZnO/(a-Si:H *n*-layer) interface roughness region is neglected in this analysis as indicated in the structural schematic of Fig. 5.24. The *n*-layer complex dielectric function is modeled using a single Cody-Lorentz oscillator expression [39]. This expression is derived assuming densities of valence and conduction band states proportional to the square-root of the hole and electron energies, respectively, as measured relative to the band edges. A photon energy independent dipole matrix element is also assumed in describing the band-to-band transitions. This oscillator model is defined by four free parameters in the fitting, those of the Lorentz oscillator (A, E_0, Γ) as well as the band gap energy E_g. An additional possible free parameter in the Cody-Lorentz oscillator expression is the transition energy E_p that separates the behavior of ε_2 dominated by the absorption onset immediately above the band gap from that dominated by the stronger absorption associated with the Lorentz oscillator at high energies. The fits are insensitive to E_p resulting in large confidence limits. As a result, E_p can be fixed to a value consistent with the band gap E_g applying the relationships in [6]. In this model, it is also found that ε_{1o} in the Cody-Lorentz expression can be fixed at unity.

In Fig. 5.24, an example best fit to the experimental (ψ, Δ) spectra is depicted for the polyimide/Cr/Ag/ZnO/(a-Si:H *n*-layer) stack at a representative location applying the structural model shown at the left. The structural model in this case includes underlying fixed parameters associated with the polyimide/Cr/Ag/ZnO

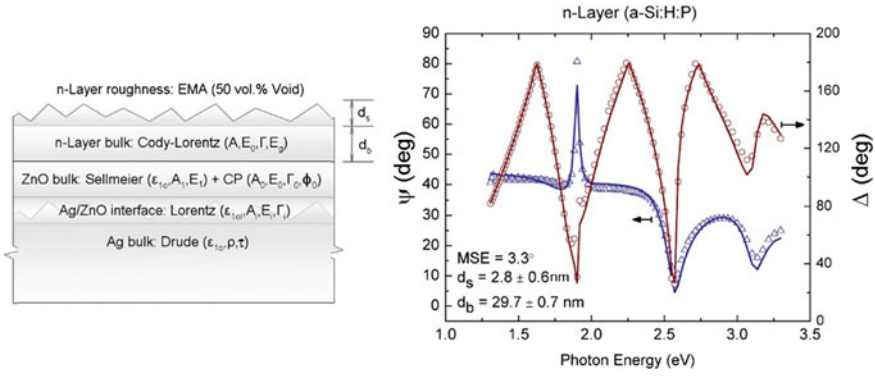


Fig. 5.24 Illustrative experimental (ψ, Δ) spectra (points) and best fit (lines) applying least-squares regression analysis with MSE minimization for a polyimide/Cr/Ag/ZnO/(*a*-Si:H *n*-layer) multilayer stack for a representative location of the 25 cm long stretch of 12 cm wide roll. A two-layer bulk/roughness model is used for the *a*-Si:H *n*-layer film over photon energy range of 1.3–3.3 eV. A single Cody-Lorentz oscillator is used as the dielectric function of the *n*-layer. In this analysis an interface roughness layer between the Ag and ZnO is included [14]

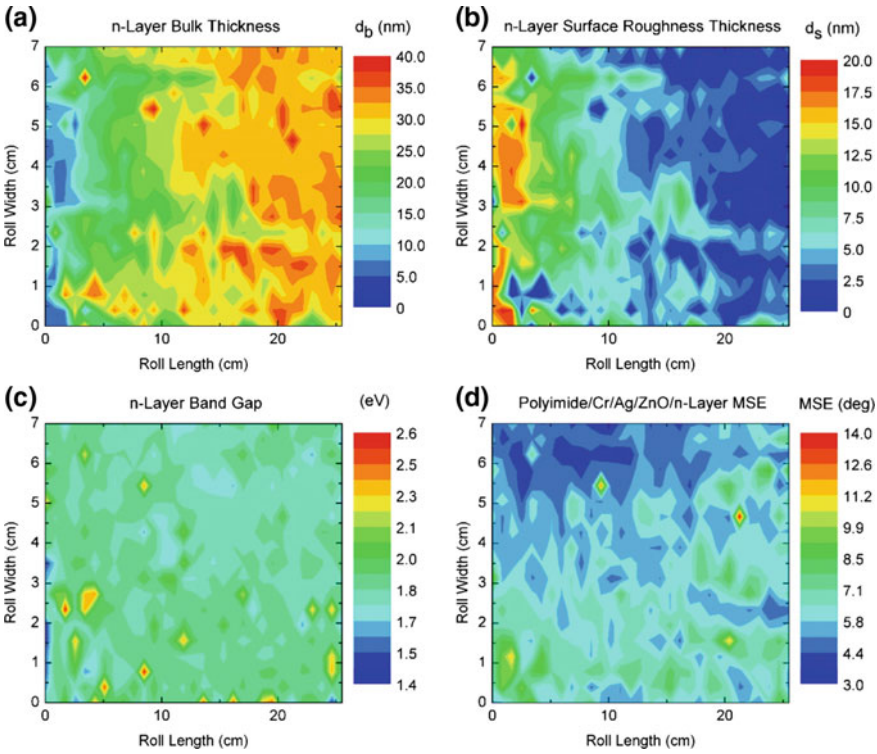


Fig. 5.25 Maps relevant to the *a*-Si:H *n*-layer on top of polyimide/Cr/Ag/ZnO thin film PV multilayer including the *n*-type a-Si:H **a** bulk layer thickness, **b** surface roughness layer thickness, and **c** band gap energy E_g, as well as the **d** MSE in the least squares regression analysis. The horizontal axis is parallel to the motion direction for the 25 cm length of the substrate/film-stack structure, which excludes the start-up lengths for the Ag and ZnO layers. The vertical axis defines the structure's width, across which film uniformity is assessed from edge to edge [14]

structure deduced from single spot analysis at the corresponding location. In Fig. 5.25a, b, the mapping results are presented for the *a*-Si:H *n*-layer bulk and surface roughness thicknesses deduced using the fixed results for the corresponding location on the underlying polyimide/Cr/Ag/ZnO according to Fig. 5.23. In this case, a more restricted area than that presented previously is mapped, due to warping of the polymer substrate which occurs as a result of the development of stress with increasing sputter layer thicknesses. In the mapping analysis of Fig. 5.25, the Ag/ZnO and the ZnO/(a-Si:H *n*-layer) interface layers are both neglected.

In Fig. 5.25, part of the start-up stretch is included, which occurs over the 0 to ~15 cm range of the roll length. The thickness over this range along the center line increases from ~5 to ~30 nm, such that the latter value is the intended thickness. The surface roughness layer thickness in Fig. 5.25b starts near 15 nm at the beginning of the start-up stretch and decreases from left to right as the *n*-layer

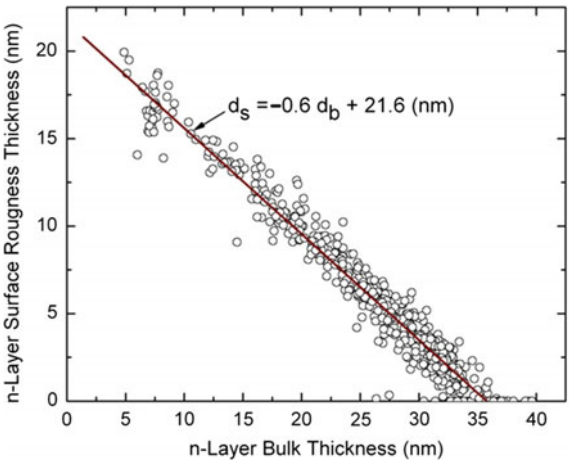


Fig. 5.26 The *a*-Si:H *n*-layer surface roughness thickness plotted as a function of the *n*-layer bulk thickness with the solid line describing the best fit linear correlation. Different data points identify the different locations on the maps of Fig. 5.25a, b. The roughness imposed by the underlying structure and the *n*-layer nucleation is smoothened in the PECVD process as the *n*-layer develops over a part of the start-up stretch of the roll

thickness increases. The close correlation between the bulk and surface roughness layer thicknesses suggests that the PECVD process generates a smoothening effect. This correlation is shown in Fig. 5.26 whereby different data points identify the different locations. At the lowest *n*-layer thicknesses, the *n*-layer surface roughness is 15–20 nm thick with contributions from the ZnO surface roughness and the *n*-layer nucleation characteristics. At sufficiently large *n*-layer thicknesses of 30–40 nm, however, the surface roughness thickness reaches negligible values. Thus, the roughness imposed by the underlying structure is smoothened in the PECVD process as the *n*-layer develops. In the stable region of film growth, after 20 cm of roll length, the roughness layer thickness is typically less than 5 nm.

The large variation in bulk layer thickness from 20 to 35 nm across the width of the roll just beyond the end of the start-up stretch at 16 cm, may occur due to warping of the substrate/film-stack. Such warping would result in certain areas of the substrate/film-stack with a smaller separation between its surface and the powered PECVD electrode, leading to a higher deposition rate, and other areas with a larger separation, leading to a lower deposition rate. As an additional or alternative explanation, the warping may generate shifts in the angle of incidence range away from that obtained in the calibration, which may then contribute to incorrect deduced thickness values over the mapped area. In this analysis, however, the MSE variation across the width at 16 cm does not appear strongly correlated with the thickness variation. This suggests that the deduced structural information in Fig. 5.25a, b is valid. In any case, the parameter maps demonstrate that deficiencies in the substrate/film-stack can be detected readily through the observed non-uniformities, and furthermore, that the possibility exists through in-depth investigations in the future to identify the origin of the deficiencies and categorize their characteristics.

The map in Fig. 5.25c depicts the band gap energy parameter E_g obtained from fits using the Cody-Lorentz oscillator. The map exhibits band gaps ranging

predominatly from ~1.75 to 1.95 eV with the lower values clustered in the upper right region where the bulk thickness is high and the surface roughness is correspondingly low. There are several locations where the *n*-type *a*-Si:H band gap is unphysically high. This problem and the fluctuations in band gap in general most likely arise from an instability of the fitting process. One possible solution is to fix Cody-Lorentz oscillator parameters in addition to E_p to values consistent with the band gap E_g applying relationships such as those in [6]. A more challenging solution is to increase the upper limit of the spectral range of the imaging/mapping spectroscopic ellipsometer. At present, the upper limit of the spectral range of the instrument is below the resonance energy of the Lorentz oscillator which likely accounts for the fitting instability in Fig. 5.25c.

5.4 Summary and Future Directions

Spectroscopic ellipsometry (SE) in a through-the-glass mode has been reviewed in Sect. 5.2, which focuses on its applications for on-line measurement and analysis of the 60 cm × 120 cm coated glass panels in the superstrate configuration for CdTe thin film PV technology [9]. For the ellipsometer used in these applications, the arms of the instrument that function as the polarization generator and detector are translated as a unit in a linear side-to-side motion below the panel as it travels along a roller conveyer film side up past a station dedicated to SE mapping. Through-the-glass data analysis capabilities have been established from earlier research and development activities, including the accumulation of a database of dielectric functions for the numerous component materials of the multilayer coated panel and the demonstration of procedures designed to correct for polarization altering artifacts unique to a through-the-glass mode [20]. For the instrument described in Sect. 5.2, 16 pairs of (ψ, Δ) spectra spanning the range 0.75–3.5 eV can be acquired for a panel 60 cm 120 cm in size during a one minute travel time of the 120 cm panel length over the SE station. Immediate feedback is provided on the effective thickness (or volume/area) of the CdS window layer in the device structure with a standard deviation based on successive conveyer runs of the same panel of ~20 Å or ~3% of the typical values for the CdS effective thickness. Agreement between on-line and off-line measurements has been demonstrated to within ~50 Å, an estimate of the absolute accuracy as an upper limit, given that precisely the same location cannot be probed in the two measurements. In addition to the effective thickness of the CdS, simultaneous determination of the transparent conducting oxide film stack properties is possible, including thicknesses and free electron characteristics. Given that the limits on the speed of this instrument have been reached due to the required time for acceleration and deceleration of the ellipsometer arms during translation, future directions must focus on new concepts relying on imaging using two-dimensional detector arrays as described in Sect. 5.3. Additional efforts in the future must be directed toward advances in the modeling and analysis of the CdS and CdTe bulk layers as well as the HRT/CdS and CdS/CdTe interface layers. Additional insights are required into the

nature of these layers and their properties, as well as the dependences on processing, as has been possible in the modeling of data collected off-line [24].

Because roll-to-roll fabrication is an important approach for the production of flexible thin film PV modules, SE instrumentation tailored for this type of process is sought. The results of Sect. 5.2 demonstrate that SE instrumentation incorporating a 1D detector array must be translated side-to-side across the width of the moving substrate/film-stack for on-line evaluations of the area uniformity of flexible substrates coated in roll-to-roll processes. Considering an ~12 cm × 12 cm area of the substrate/film-stack, for example, SE measurements at ~150 locations and ~5–10 min are required for an average spatial resolution on the cm scale. Thus, the maximum roll-to-roll speed is ~1–2 cm/min, limited by the time required for the ellipsometer translation. If a 2D detector array is adopted instead, the second array dimension enables imaging in 1D proceeding in parallel with spectroscopy via the generation of a line-shaped, broad-band light beam obliquely incident across the width of the substrate/film-stack. As a result, translation of the ellipsometer is not required for large area mapping of a flexible coated substrate in roll-to-roll motion [14]. In the demonstration reviewed here, a single ~30 point line image is acquired in situ in a time of 10 s across a 12 cm width of the substrate/film-stack in a roll-to-roll deposition system. As a result, the existing system can perform 150 measurements in a time of ~1 min, achieving an equivalent average spatial resolution at ~10–20 cm/min roll-to-roll coated substrate speed. The potential exists for significant reductions in the 10 s acquisition time for single SE images [13], reaching roll-to-roll speeds as high as 1 m/min with 0.5 cm overall mapping resolution in both length and width. Considering the capabilities of SE for determining the thicknesses of bulk, interface roughness, and surface roughness layers, as well as material phase, composition, and other characteristics that define the complex dielectric function, line imaging multichannel SE is expected to increase in analytical power through future advances. Improvements will be possible not only in the speed of the instrumentation, but also in the precision, accuracy, and image length through advanced imaging hardware as well as in the calibration, data reduction, and data analysis software [18].

Acknowledgements The authors acknowledge the contributions of Blaine D. Johs, Jeffrey S. Hale, and Galen L. Pfeiffer of J. A. Woollam Company for development of the on-line SE instrumentation for CdTe photovoltaics reviewed here. The authors also acknowledge the contributions of Miklos Fried, Gyorgy Juhász, Csaba Major, Olivér Polgár, Ágoston Németh, and Peter Petrik of the Research Institute for Technical Physics and Materials Science, Budapest, Hungary, for the development of the expanded beam SE instrumentation used in roll-to-roll photovoltaics reviewed here.

References

1. T. Ellison, D. Dodge, J. Karn, R. Kopf, R. Liu, M. Lycette, W. Messing, in *Proceedings of the 2006 IEEE 4th World Conference on Photovoltaic Energy Conversion*, Waikoloa, HI, May 7–12, 2006 (IEEE, New York, NY, 2006), pp. 1736–1739
2. M.A. Green, K. Emery, Y. Hishikawa, W. Warta, E.D. Dunlop, D.H. Levi, A.W.Y. Ho-Baillie, Prog. Photovolt.: Res. Appl. **25**, 3 (2017)
3. I.P. Herman, *Optical Diagnostics for Thin Film Processing* (Academic, New York, NY, 1996)
4. A. Luque, S. Hegedus (eds.), *Handbook of Photovoltaic Science and Engineering*, 2nd edn. (Wiley, New York, NY, 2011)
5. F. Wooten, *Optical Properties of Solids* (Academic, New York, NY, 1972)
6. R.W. Collins, A.S. Ferlauto, in *Handbook of Ellipsometry*, ed. by H.G. Tompkins, E.A. Irene (William Andrew, Norwich, NY, 2005), Chapter 2, pp. 93–235
7. D. Abou-Ras, T. Kirchartz, U. Rau (eds.), *Advanced Characterization Techniques for Thin Film Solar Cells*, 2nd edn. (Wiley-VCH, Weinheim, Germany, 2016)
8. Z. Huang, J. Chen, M.N. Sestak, D. Attygalle, L.R. Dahal, M.R. Mapes, D.A. Strickler, K.R. Kormanyos, C. Salupo, R.W. Collins, in *Proceedings of the 35th IEEE Photovoltaic Specialists Conference*, Honolulu, HI, June 20–25, 2010 (IEEE, New York, NY, 2010), pp. 1678–1683
9. J. Chen, P. Koirala, C. Salupo, R.W. Collins, S. Marsillac, K.R. Kormanyos, B.D. Johs, J.S. Hale, G.L. Pfeiffer, in *Proceedings of the 38th IEEE Photovoltaic Specialists Conference*, Austin, TX, June 3–8, 2012 (IEEE, New York, NY, 2012), pp. 377–381
10. R.W. Collins, I. An, J. Lee, J.A. Zapien, in *Handbook of Ellipsometry*, ed. by H.G. Tompkins, E.A. Irene (William Andrew, Norwich, NY, 2005), Chapter 7, pp. 481–566
11. G.E. Jellison, Jr., in *Handbook of Ellipsometry*, ed. by H.G. Tompkins, E.A. Irene (William Andrew, Norwich, NY, 2005), Chapter 3, pp. 237–296
12. P. Aryal, J. Chen, Z. Huang, L.R. Dahal, M.N. Sestak, D. Attygalle, R. Jacobs, V. Ranjan, S. Marsillac, R.W. Collins, in *Proceedings of the 37th IEEE Photovoltaic Specialists Conference*, Seattle, WA, June 19–24, 2011 (IEEE, New York, NY, 2011), pp. 2241–2246
13. I. An, Y.M. Li, H.V. Nguyen, R.W. Collins, Rev. Sci. Instrum. **63**, 3842 (1992)
14. A. Shan, M. Fried, G. Juhász, C. Major, O. Polgár, A. Németh, P. Petrik, L.R. Dahal, J. Chen, Z. Huang, N.J. Podraza, R.W. Collins, IEEE J. Photovolt. **4**, 355 (2014)
15. C. Major, G. Juhász, Z. Horváth, O. Polgár, M. Fried, Phys. Stat. Solidi (c) **5**, 1077 (2008)
16. G. Juhász, Z. Horváth, C. Major, P. Petrik, O. Polgár, M. Fried, Phys. Stat. Solidi (c) **5**, 1081 (2008)
17. C. Major, G. Juhász, P. Petrik, Z. Horváth, O. Polgár, M. Fried, Vacuum **84**, 119 (2009)
18. M. Fried, G. Juhász, C. Major, P. Petrik, O. Polgár, Z. Horváth, A. Nutsch, Thin Solid Films **519**, 2730 (2011)
19. B.D. Johs, J. Hale, N.J. Ianno, C.M. Herzinger, T. Tiwald, J.A. Woollam, in *Optical Metrology Roadmap for the Semiconductor, Optical, and Data Storage Industries II*, *Conference Proceedings of SPIE*, vol. 4449, ed. by A. Duparre, B. Singh (SPIE, Bellingham, WA, 2001), pp. 41–57
20. J. Chen, J. Li, C. Thornberry, M.N. Sestak, R.W. Collins, J.D. Walker, S. Marsillac, A.R. Aquino, A. Rockett, in *Proceedings of the 34th IEEE Photovoltaic Specialists Conference*, Philadelphia, PA, June 7–12, 2009 (IEEE, New York, NY, 2009), pp. 1748–1753
21. R.A. Synowicki, B.D. Johs, A.C. Martin, Thin Solid Films **519**, 2907 (2011)
22. K. von Rottkay, M. Rubin, in *Thin Films for Photovoltaic and Related Device Applications*, *Materials Research Society Symposium Proceedings*, vol. 426, ed. by A. Catalano, C. Eberspacher, D.S. Ginley, T.M. Peterson, H.W. Schock, T. Wada (MRS, Warrendale, PA, 1996), pp. 449–454

23. J. Chen, J. Li, D. Sainju, K.D. Wells, N.J. Podraza, R.W. Collins, in *Proceedings of the 2006 IEEE 4th World Conference on Photovoltaic Energy Conversion*, Waikoloa, HI, May 7–12, 2006 (IEEE, New York, NY, 2006), pp. 475–478
24. P. Koirala, J. Li, H.P. Yoon, P. Aryal, S. Marsillac, A.A. Rockett, N.J. Podraza, R.W. Collins, Prog. Photovolt.: Res. Appl. **24**, 1055 (2016)
25. F. Becker, H.-J. Frenck, in *Photovoltaics International*, 12th edn. (2011), p. 134
26. J. Li, J. Chen, M.N. Sestak, R.W. Collins, IEEE J. Photovolt. **1**, 187 (2011)
27. B.E. McCandless, J.R. Sites, in *Handbook of Photovoltaic Science and Engineering*, 2nd edn., ed. by A. Luque, S. Hegedus (Wiley, New York, NY, 2011), Chapter 14, pp. 600–641
28. L.R. Dahal, J. Li, J.A. Stoke, Z. Huang, A. Shan, A.S. Ferlauto, C.R. Wronski, R.W. Collins, N.J. Podraza, Sol. Energy Mater. Sol. Cells **129**, 32 (2014)
29. M. Fried, G. Juhász, C. Major, A. Németh, P. Petrik, O. Polgár, C. Salupo, L.R. Dahal, R.W. Collins, in *Advanced Materials Processing for Scalable Solar-Cell Manufacturing*, *Materials Research Society Symposium Proceedings*, vol. 1323, ed. by L. Tsakalakos, H. Ji, B. Ren (MRS, Warrenville, PA, 2011), C03-12: pp. 157–162
30. J.A. Zapien, R.W. Collins, R. Messier, Rev. Sci. Instrum. **71**, 3451 (2000)
31. R.W. Collins, I. An, C. Chen, in *Handbook of Ellipsometry*, ed. by H.G. Tompkins, E.A. Irene (William Andrew, Norwich, NY, 2005), Chapter 5, pp. 329–432
32. E.A. Schiff, S. Hegedus, X. Deng, in *Handbook of Photovoltaic Science and Engineering*, 2nd edn., ed. by A. Luque, S. Hegedus (Wiley, New York, NY, 2011), Chapter 12, pp. 487–545
33. J. Lee, P.I. Rovira, I. An, R.W. Collins, Appl. Phys. Lett. **72**, 900 (1998)
34. H. Fujiwara, J. Koh, P.I. Rovira, R.W. Collins, Phys. Rev. B **61**, 10832 (2000)
35. S.O. Kasap, *Principles of Electronic Materials and Devices*, 3rd edn. (McGraw-Hill, New York, NY, 2006), p. 129
36. L.R. Dahal, D. Sainju, N.J. Podraza, S. Marsillac, R.W. Collins, Thin Solid Films **519**, 2682 (2011)
37. A. Janotti, C.G. Van de Walle, Rep. Prog. Phys. **72**, 126501 (2009)
38. P. Aryal, A.-R. Ibdah, P. Pradhan, D. Attygalle, P. Koirala, N.J. Podraza, S. Marsillac, R.W. Collins, J. Li, Prog. Photovolt.: Res. Appl. **24**, 1200 (2016)
39. A.S. Ferlauto, G.M. Ferreira, J.M. Pearce, C.R. Wronski, R.W. Collins, X. Deng, G. Ganguly, J. Appl. Phys. **92**, 2424 (2002)

Chapter 6
Real Time Measurement, Monitoring, and Control of $CuIn_{1-x}Ga_xSe_2$ by Spectroscopic Ellipsometry

Puja Pradhan, Abdel-Rahman A. Ibdah, Puruswottam Aryal, Dinesh Attygalle, Nikolas J. Podraza, Sylvain Marsillac and Robert W. Collins

Abstract Spectroscopic ellipsometry (SE) using a rotating compensator multichannel instrument has been applied in real time for characterization of the three stages of the coevaporation process for copper indium-gallium diselenide ($CuIn_{1-x}Ga_xSe_2$; CIGS) thin films. This absorber material and the coevaporation process yield the highest small area efficiency among inorganic polycrystalline thin film solar cells. In the first deposition stage of the process, indium-gallium selenide $(In_{1-x}Ga_x)_2Se_3$ (IGS) thin film deposition is performed via coevaporation of In, Ga, and Se on a substrate consisting of Mo-coated soda lime glass held at a temperature of 400 °C. In this stage, Mo/IGS interface roughness filling can be characterized along with the subsequent evolution of the IGS bulk and surface roughness layer thicknesses. An accurate rate for the effective thickness (or volume/area) can be determined from these results, and alloy compositional analysis of the IGS has been demonstrated at the first stage endpoint. In the second deposition stage, the IGS film is converted to CIGS via coevaporation of Cu and Se fluxes at an increased substrate temperature of 570 °C. A bulk conversion model provides the best fit to the real time SE data, and this model is employed in the analysis of the second-stage data. The results include the evolution of the content of CIGS within the film, along with the thicknesses of the bulk and surface roughness layers. The formation of a copper selenide ($Cu_{2-x}Se$) component phase on the CIGS surface is detected just before the completion of the second stage. Subsequently, the evolution of the near-surface $Cu_{2-x}Se$ content is followed in terms of its effective thickness,

P. Pradhan · A.-R. A. Ibdah · P. Aryal · D. Attygalle · N. J. Podraza (✉) · R. W. Collins
Department of Physics & Astronomy and Center for Photovoltaics Innovation & Commercialization, University of Toledo, Toledo, OH 43606, USA
e-mail: Nikolas.Podraza@utoledo.edu

R. W. Collins
e-mail: robert.collins@utoledo.edu

S. Marsillac
Virginia Institute of Photovoltaics, Old Dominion University, Norfolk, VA 23529, USA

© Springer International Publishing AG, part of Springer Nature 2018

H. Fujiwara and R. W. Collins (eds.), *Spectroscopic Ellipsometry for Photovoltaics*, Springer Series in Optical Sciences 214,
https://doi.org/10.1007/978-3-319-95138-6_6

spanning the time interval from the end of the second stage through much of the third stage. In the third stage of the deposition process, In, Ga, and Se coevaporation serves to convert the Cu-rich CIGS/$Cu_{2-x}Se$ to slightly Cu-poor CIGS. In this stage, the thickness evolution can be obtained along with bulk and surface roughness layer thicknesses at the overall deposition endpoint. In the three stages, the deduced deposition rates and final thicknesses provide information on the total metallic elemental fluxes, and the roughness evolution provides information on crystalline grain growth and near-surface crystallite coalescence in the polycrystalline films. Variations in the information deduced from real time SE can lead to insights into run-to-run irreproducibility that influences the performance of the resulting solar cells. The application of these capabilities is demonstrated for the fabrication of thin film solar cells in continuous and discontinuous (shuttered) processes for standard thickness (~2.5 μm) CIGS absorber layers as well as a shuttered process deemed necessary for adequate control of the deposition of thin (~0.3 μm) absorbers.

6.1 Introduction

Among the variety of inorganic thin film absorber materials that have been developed for photovoltaics (PV), polycrystalline copper indium-gallium diselenide ($CuIn_{1-x}Ga_xSe_2$; CIGS) has yielded the highest efficiency laboratory-scale solar cells [1]. Although different approaches exist for the fabrication of CIGS absorber layers, the three-stage process of thermal coevaporation has led consistently to the highest efficiency small-area CIGS devices [2–4]. The disadvantage of the three-stage coevaporation process, however, is its complexity. Greater effort is required for process optimization, and as a result, monitoring and control capabilities are sought to expedite optimization. In addition, as a result of the complexity of the process, significant challenges are presented in process scale-up to large-area devices. Figure 6.1 shows a schematic that describes the process for continuous three-stage CIGS coevaporation from individual sources of Cu, In, Ga, and Se as applied in one of the deposition analyses reviewed here [5–8]. More generally, three-stage coevaporation involves depositing a precursor film of $(In_{1-x}Ga_x)_2Se_3$ (IGS) in the first stage and exposing it to fluxes of both Cu and Se during the second stage. By conducting the second stage at an elevated substrate temperature (~500–600 °C) relative to that of the first stage (~400 °C), the $(In_{1-x}Ga_x)_2Se_3$ (IGS) film is converted to a CIGS film throughout its typical ~1.5–3 μm thickness. Extension of the Cu and Se deposition in the second stage beyond stoichiometric CIGS results in the evolution of a Cu-rich phase on the newly converted CIGS surface. In fact, when the CIGS film becomes Cu-rich just before the end of the second stage, a semi-liquid phase of $Cu_{2-x}Se$ is believed to form on the surface and in the grain boundary regions [9]. In the third stage, the $Cu_{2-x}Se$ phase is converted to CIGS by exposing the film to In, Ga, and Se fluxes while maintaining the high substrate temperature of the second stage. The superiority of the three-stage process

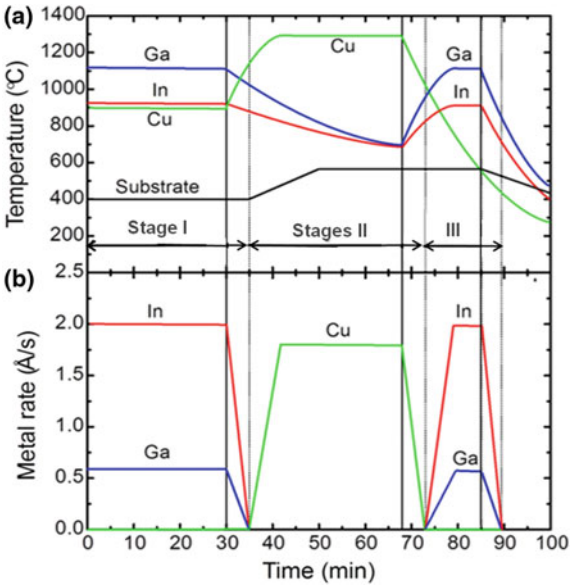


Fig. 6.1 An idealized depiction of **a** the temperatures of the individual metal evaporation sources as well as that of the substrate during the three-stage CIGS coevaporation process applied in this research and **b** the resulting rates of the individual elements. The temperature of the Se source was fixed at 263 °C for a deposition rate of 20 Å/s. The darker vertical lines indicate the times at which cooling/heating of the metal sources are initiated. The lighter vertical lines indicate the times at which the metal rates are zero to end/begin the stages; this occurs simultaneously with the onset of new fluxes to start stages II and III [8]

originates from its ability to grow CIGS with large crystalline grains and to achieve a desirable notch-like profile in the band gap, the latter due to the different diffusion characteristics of Ga as compared to In in the second and third stages. Figure 6.2 summarizes the proposed mechanisms occurring in the three-stage CIGS deposition process [10].

Real time spectroscopic ellipsometry (SE) has been applied successfully in developing and monitoring multistep thin film semiconductor deposition processes for applications in PV, including processes for hydrogenated silicon in amorphous and nanocrystalline phases (a-Si:H and nc-Si:H, respectively), CdS/CdTe, as well as CIGS, the subject of this chapter [11, 12]. The basic concept of the real time SE experiment for the CIGS absorber layer is shown in Fig. 6.3. Information extracted from real time SE includes the evolution of the bulk and surface roughness layer thicknesses, and in addition, the complex dielectric functions of the growing layers. From each dielectric function, the composition and phase structure of the individual layer can be evaluated. All this information can assist in characterizing and understanding the CIGS thin film fabrication process and in maximizing the performance of thin film solar cells [11, 12].

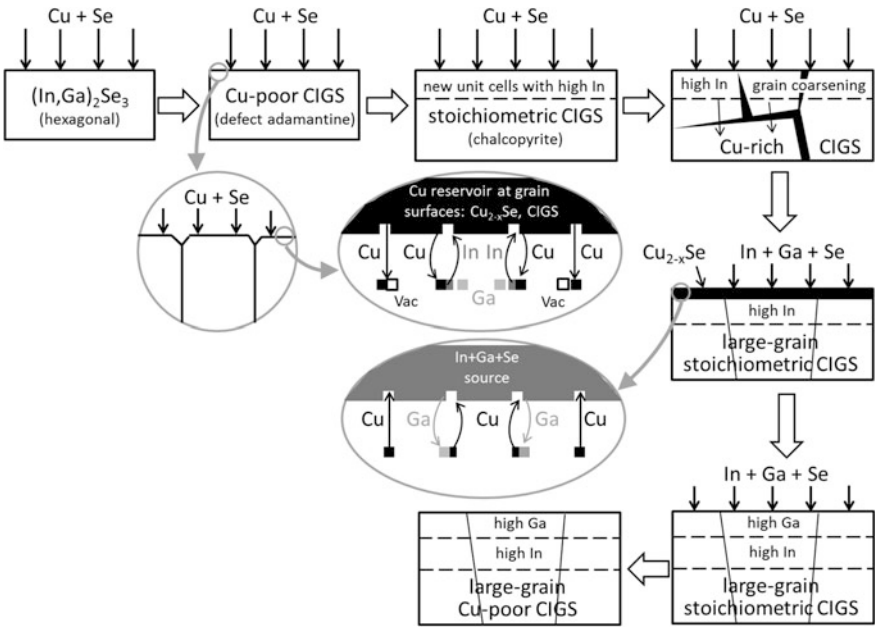


Fig. 6.2 Schematic of concepts proposed for the CIGS film growth mechanisms by three-stage coevaporation from individual sources of Cu, In, Ga, and Se [10]

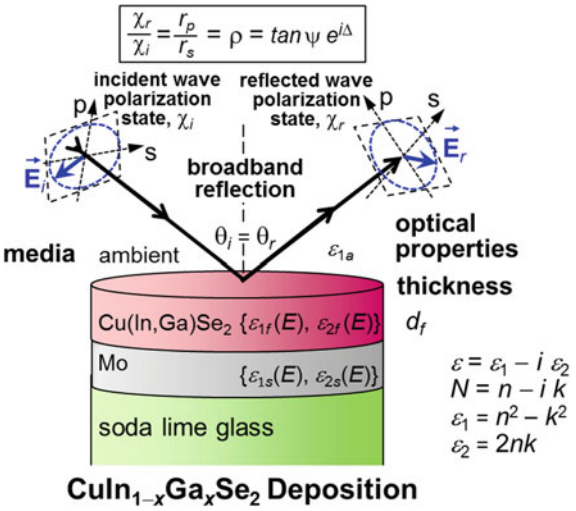


Fig. 6.3 Structure of the first two layers of the standard CIGS solar cell deposited on a soda lime glass substrate, depicting a schematic of the real time spectroscopic ellipsometry experiment performed during CIGS deposition

In the present review of the applications of real time SE to CIGS coevaporation, analysis results are presented for all stages of the three-stage process, including results that demonstrate the ability to observe Mo/IGS interface formation during

the first stage, to determine the IGS composition at the end of the first stage, and to follow the conversion of IGS to CIGS during the second stage. Furthermore, the Cu-poor to Cu-rich CIGS transition that occurs before the end of second stage, and the Cu-rich to Cu-poor CIGS transition that occurs before the end of third stage are both clearly detected upon real time SE analysis, as described in previously published studies [5–8]. Since real time SE is sensitive to monolayer-level changes at the near-surface of the CIGS film, it provides high sensitivity to the evolution of surface roughness [13]. Thus, the processes of grain growth and coalescence are revealed as crystalline grains increase in size, protrude above the surface, and interconnect with their neighbors. The high surface sensitivity also enables identification of the second stage Cu-poor to Cu-rich and third stage Cu-rich to Cu-poor transitions through the respective appearance and disappearance of the $Cu_{2-x}Se$ phase at the surface [14]. Thus, accurate endpoint detection is possible for the second and third stages. Real time SE has been reviewed in this study specifically toward applications for in situ monitoring and for evaluation of the technique in control schemes for CIGS absorber layer fabrication. The capability of in situ monitoring has been elucidated through the review of new results on the structure and phase evolution for continuous and discontinuous (or shuttered) deposition processes yielding standard thickness layers (2–3 μm) of the CIGS absorber and for the discontinuous process yielding a very thin layer (0.3 μm) of CIGS [8]. Solar cells were completed from these depositions, and the performance parameters have been reported. Figure 6.4 provides a schematic of the instrumentation used in the CIGS deposition studies by real time SE as reviewed in this chapter.

In early real time SE studies, the technique has been applied successfully to characterize the three-stage CIGS coevaporation process used most widely in PV device fabrication with a focus on endpoint detection for the second stage and on characterizing the third stage of CIGS coevaporation. It is here that $Cu_{2-x}Se$ is first

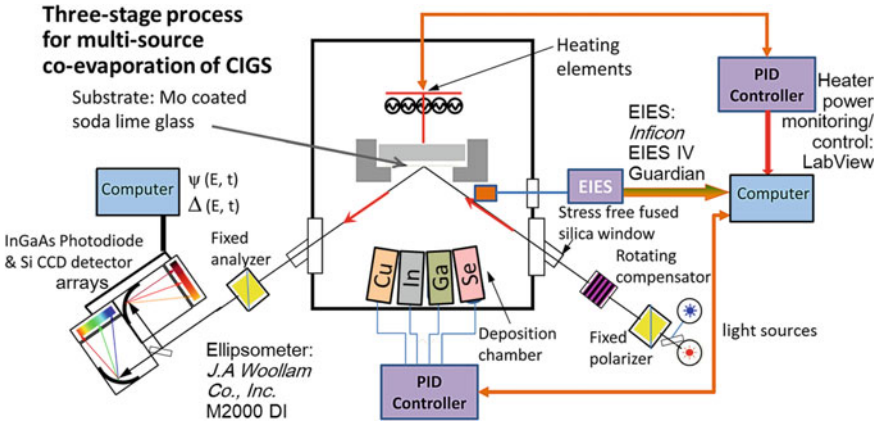


Fig. 6.4 Multisource coevaporation system and multichannel spectroscopic ellipsometer for real time SE measurement, monitoring, and control of CIGS deposition [8]

observed and is converted to CIGS, respectively [5]. More recently, real time SE has been used throughout three-stage coevaporation to determine the evolution of the film structural properties and phases, including the thickness of the bulk layer, the thickness of the surface roughness layer, the void content within the surface roughness layer, the CIGS content within the IGS film, and the effective thickness of $Cu_{2-x}Se$ near the film surface [7, 8]. The resulting structural and phase information can provide insights into the mechanisms of three-stage CIGS coevaporation and in monitoring and ultimately controlling the fabrication of CIGS solar cells [8]. The dielectric function obtained at the end of the first stage enables analysis of IGS alloy composition using a database of IGS dielectric functions. At this point, the composition is expected to be uniform with film depth. At the Cu-poor to Cu-rich and Cu-rich to Cu-poor CIGS transitions in the second and third stages, however, the stoichiometric film has developed compositional profiles with depth in which case analysis of the composition is a greater challenge. Recent ex situ mapping SE studies performed immediately after removal of the CIGS solar cell structure from the chamber and before chemical bath deposition of CdS, have enabled determination of maps in parameters that describe the Ga composition profile in the CIGS layer [15].

6.2 Dielectric Functions Relevant for Real Time SE of CIGS

Significant background studies are required before the analysis of real time SE data collected during three-stage CIGS coevaporation can proceed. These studies involve development of a dielectric function database for the thin film material components encountered in the CIGS deposition process on Mo-coated soda lime glass. Because of the sensitivity of the ellipsometry (ψ, Δ) spectra to sample surface conditions, approaches are required to avoid surface oxidation and correct for the surface roughness layers in determining the dielectric functions of the bulk layers of these films. The approach applied in these studies differs from one thin film material to the next; however, the common theme is to perform real time SE during deposition and apply multi-time data analysis over a specific time period of the deposition process [16, 17]. Multi-time analysis is based on the assumption that the properties of the accumulating film are uniform with time, yielding a well-defined dielectric function independent of depth into the film. This analysis provides the evolution of structure, including the thicknesses of the bulk and surface roughness layers, and optionally, the void content within the surface roughness expressed in terms of volume percent. Simultaneously, a point-by-point dielectric function can be obtained from an inversion of a single pair of (ψ, Δ) spectra at the center of the time period used for multi-time analysis. A second approach is to extract a point-by-point dielectric function as a best fit to the full set of (ψ, Δ) spectra collected versus time over the period of multi-time analysis. A third possible

approach is to extract a best fit dielectric function as a b-spline, selecting the nodes with a spacing sufficient to follow the features in the dielectric function [18].

The selection of an optimum time period in multi-time analysis ultimately involves a trade-off. The highest accuracy dielectric function result is most often obtained in the early period of film growth when the initial nuclei have coalesced and the surface roughness layer thickness is at a minimum [17]. The higher accuracy here arises because effective medium theories provide only an approximation to the true dielectric function of the surface roughness layer [19]. Thus, thinner roughness layers yield more accurate results for the dielectric function of the underlying bulk layer. In addition, as the film increases in thickness, variations in the dielectric function can occur with accumulated thickness, and these variations can distort the results obtained assuming that the film properties are uniform with depth [20]. This same issue generates a disadvantage in extracting the dielectric function of the thin film in the early period of growth when it is smooth. In fact, the results in this time period may not be relevant for the film later in the growth process, which is of greatest interest in the analysis of the solar cell structures. Specifically, various changes can occur in the structure of polycrystalline films as a function of thickness, including increases in grain size and in intergrain void space that account for these dielectric function changes. The best approach to deal with such a problem is to parameterize dielectric functions obtained in ranges where high accuracy is ensured, and then allow the parameters to vary in order to account for possible variations with thickness of the film [21, 22].

A second problem arises to the extent that the solar cell relevant substrates, such as glass/Mo in the case of CIGS, are generally rough [23], and this leads to an interface roughness layer and to challenges in extracting accurate dielectric functions of the overlying material. As a result, the materials whose dielectric functions are to be determined are often deposited on smooth substrates in order to avoid problems associated with underlying interface roughness [15]. It should be emphasized, however, that the dielectric function of the deposited film may depend on the chemical and structural nature of the substrate. Thus, the accurately deduced dielectric function may not be relevant for the solar cell configuration due to the same structural variations that lead to the thickness dependence, e.g. grain size and void content differences. This is another situation in which a parametric form for the dielectric function would be useful. In extreme situations, however, different film phases may evolve for the different substrates [24]. Thus, care must be taken overall in the application of dielectric function databases to ensure that the dielectric functions are relevant for analysis of real time SE in the solar cell configuration.

The starting point for database development addresses the dielectric function of the Mo bulk layer which, along with the Mo/IGS interface roughness layer arising from initial Mo surface roughness, serve as the underlying structure for the IGS bulk layer in the first stage. The Mo films used in the CIGS deposition processes analyzed in this study were deposited to opacity by magnetron sputtering onto soda lime glass with substrate temperatures ranging from room temperature to 300 °C under an otherwise standard set of conditions [8]. In order to determine the bulk Mo dielectric functions, identically prepared samples on thermally oxidized Si wafers

were studied by real time SE. For each deposition, multi-time analysis provided a Mo dielectric function in the early period of growth, as well as the evolution of the parameters that characterize the surface roughness layer, i.e. its thickness and void content, throughout the Mo deposition. After deposition and after cooling, an in situ SE measurement of (ψ, Δ) spectra was performed on the Mo film at room temperature. The parameters of the surface roughness layer for the final film were used to obtain the dielectric function at room temperature, subjecting the (ψ, Δ) spectra measured in situ to numerical inversion. For subsequent Mo samples deposited under the same conditions on soda lime glass for which real time SE is unavailable, the dielectric functions obtained from the Si wafer substrates were used as an initial database to extract the thicknesses and void volume percentages of the surface roughness layers for these samples. Inversion using these structural values for each such deposition on glass yields a new dielectric function specific to the deposition that, along with the two structural values, exactly describe the data.

Because the first stage IGS deposition on Mo is performed at 400 °C and the second and third stages are performed at 570 °C in the real time SE studies of this review, then the dielectric function specific to the given Mo sample must be obtained at both temperatures. Figure 6.5 shows typical results obtained by inversion of (ψ, Δ) spectra assuming that the structural parameters associated with the surface roughness, its layer thickness and void content, remain the same upon heating to the two elevated temperatures [8]. The validity of this assumption can be confirmed by cooling the sample and remeasuring it at room temperature. Finally, in order to avoid noise in the dielectric functions resulting from inversion, the

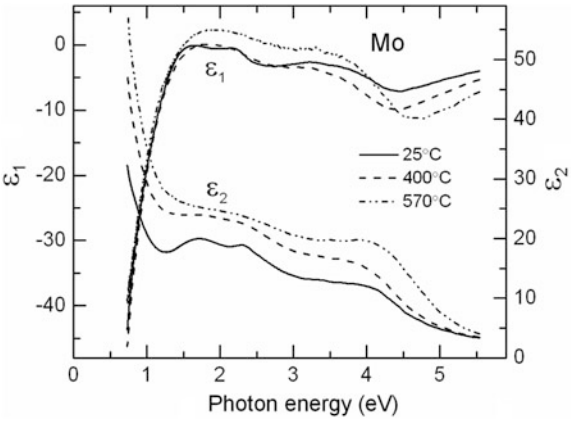


Fig. 6.5 The dielectric functions of an ~1 μm thick Mo bulk layer at three different measurement temperatures, as obtained from inversions of (ψ, Δ) that correct for the overlying surface roughness layer, characterized by its thickness and void volume percent. This Mo film, used for the ~2.7 μm CIGS deposition of Sect. 6.3.2, exhibits a value of 242 Å for the surface roughness layer thickness whereas that for the ~0.3 μm CIGS deposition of Sect. 6.3.7 exhibits a value of 231 Å. For these two CIGS depositions, the Mo layer was deposited at room temperature and at 250 °C, respectively [8]

dielectric functions can be fit using an analytical form. The analytical form for the Mo $\varepsilon(E)$ spectra includes a constant contribution to the real part of $\varepsilon(E)$, two Drude free electron components with different (ρ, τ) values, and three critical point oscillators with variable parameters of amplitude, energy, broadening, and phase, $\{A_n, E_n, \Gamma_n$, and ϕ_n; $n = 1, 2, 3\}$, respectively. The room temperature oscillator energies occur at 1.59, 2.26, and 4.25 eV. Although a parameterized version reduces statistical noise in the dielectric function, the initial mean square error (MSE) between the data and best fit deviates from zero; the value of zero would be obtained if an inverted dielectric function was used for the initial analysis, i.e. at $t = 0$ in the analysis of real time SE measured just before the first stage of IGS is initiated.

The dielectric function of $MoSe_2$ was determined in this study as well since it may develop as a possible component at the Mo/IGS and Mo/CIGS interfaces in the three-stage coevaporation process. The $MoSe_2$ in this study was fabricated by hybrid Mo-sputtering/Se-evaporation on a thermally-oxidized Si wafer held at a temperature of 490 °C [8]. This temperature was selected as it lies approximately at the center of the range between first-stage and second/third-stage deposition temperatures for CIGS. Real time SE data were collected during deposition and

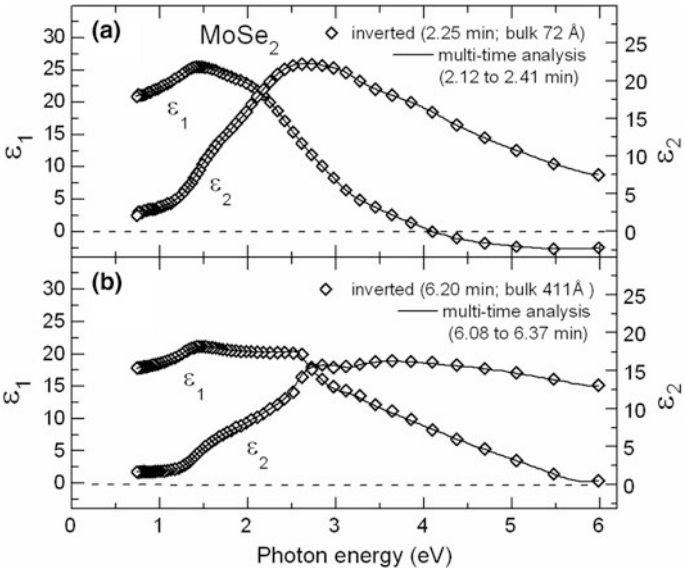


Fig. 6.6 Dielectric functions (ε_1, ε_2) measured at 490 °C for a $MoSe_2$ film deposited by hybrid Mo-sputtering/Se-evaporation. These results were obtained in an analysis of real time SE data using multi-time analysis over the time periods of **a** 2.12–2.41 min and **b** 6.08–6.37 min. For the solid lines, a Kramers-Kronig consistent b-spline dielectric function was applied with a b-spline node spacing of 0.1 eV. For the points, exact inversion was applied at 2.25 min (top), when the bulk layer thickness was 72.0 ± 3.2 Å and the surface roughness layer thickness was 7.4 ± 1.5 Å and at 6.20 min (bottom), when the bulk layer thickness was 411.3 ± 1.2 Å and the surface roughness layer thickness was 110.4 ± 0.5 Å [8]

interpreted using multi-time analysis. As shown in Fig. 6.6, multi-time analysis was performed over two different time periods of ~30 s duration each. In the initial analysis over these periods, a b-spline model was used for the dielectric function, which enables determination of the thickness evolution of the bulk and surface roughness layers assuming a 50/50 vol% mixture of $MoSe_2$/void for the latter layer. The best fit bulk and surface roughness layer thicknesses near the center of the first time period at 2.25 min were found to be 72.0 ± 3.2 Å and 7.4 ± 1.5 Å, respectively. The corresponding thicknesses near the center of the second time period of 6.20 min were found to be 411.3 ± 1.2 Å and 110.4 ± 0.5 Å, respectively. Results obtained by inversion of the (ψ, Δ) values at these near-center times are in good agreement with the best fit b-spline results.

The $MoSe_2$ dielectric functions in Fig. 6.6 show some of the features described earlier in this section. In fact, these results differ in ways consistent with a continuous evolution of polycrystalline film properties. Figure 6.6 shows that the magnitudes of the $MoSe_2$ dielectric function decrease with increasing thickness, the critical point features appear to be sharper, and the sub-bandgap absorption decreases. These observations suggest an increase in void content within the film, an increase in the grain size, and a reduction in defect density, respectively, as the $MoSe_2$ film thickness increases. In addition, the surface roughness increases significantly with increasing thickness which also suggests that the dielectric function at larger thicknesses may be subject to inaccuracies, especially at high photon energies where much of the incident SE probe is absorbed within the surface roughness layer.

The dielectric function database for IGS was obtained by real time SE starting from films deposited on Mo-coated Si wafers by one-stage coevaporation from fluxes of In, Ga, and Se. Films were deposited with different Ga contents x as determined by energy dispersive X-ray spectroscopy (EDS) [6, 8]. The conditions of the IGS depositions were the same as those used for the first stage CIGS deposition with the only variable being the In and Ga fluxes. Thermally oxidized Si wafer substrates coated with opaque Mo of reduced thickness were used as substrates to ensure smoother surfaces. The substrate temperature and thus the temperature of the dielectric function measurements was 400 °C for all IGS films. Although the total deposited thickness for each of the IGS films was ~0.9 μm, multi-time analysis was performed over time periods of 2 min duration yielding thickness increases depending on x that vary from 0.06 to 0.2 μm centered at a bulk layer thickness of ~0.4 μm. Although the IGS films were relatively rough over these time periods, with roughness thicknesses depending on x ranging from 89 to 122 Å at the center points of the analyses, these periods were selected to avoid an initial strong thickness dependence of the dielectric function. In fact, for an IGS film with $x = 0.31$, the dielectric function in the early time period of growth with a bulk layer thickness of ~300 Å exhibits the characteristics of an amorphous or nanocrystalline material with no clear evidence of the bandgap critical point. From the rapid appearance of the CP with increasing thickness, however, it appears that the grain size increases as the IGS accumulates.

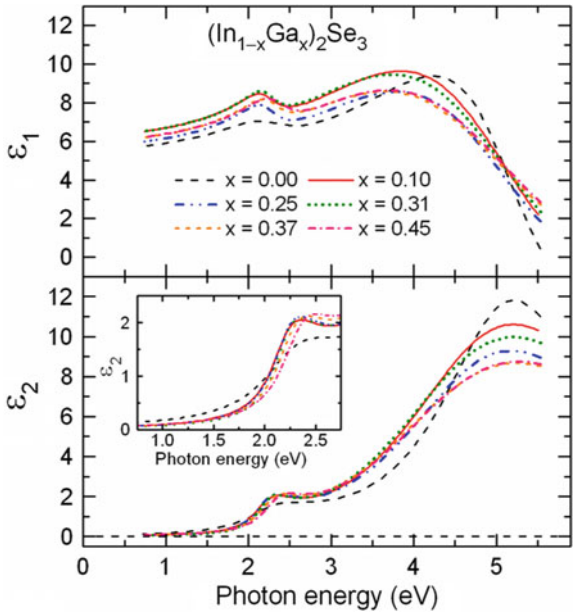


Fig. 6.7 Parameterized expressions for the dielectric functions of $(In_{1-x}Ga_x)_2Se_3$ for selected x at the deposition and measurement temperatures of 400 °C. In the parameterization, one critical point oscillator is used to model the bandgap feature at low energy (at 2.24 eV for IGS composition $x = 0.31$) and one modified Lorentz oscillator is used to model the high energy resonance (at 4.84 eV for $x = 0.31$). The absorption onset near the bandgap feature is shown in the inset and provides the highest sensitivity for compositional analysis. Associated with the database are the oscillator parameters expressed as polynomial functions of x that enable calculation of the IGS dielectric function for any composition x [6, 8]

The IGS dielectric functions that best fit the (ψ, Δ) spectra over the time period of multi-time analysis were obtained assuming a b-spline model. Inversions were also performed at the center of the time period to verify the validity of the b-spline method and node selection as in Fig. 6.6 [8]. The dielectric functions of the IGS presented in Fig. 6.7 are given in terms of parameterized expressions that best fit the inversion results obtained from multi-time analysis. In the parameterization, one critical point oscillator is used to model the bandgap feature at low energy (at 2.24 eV for the composition $x = 0.31$) and one modified Lorentz oscillator is used to model the high energy resonance (at 4.84 eV for $x = 0.31$). Parameters in the expressions are obtained as a function of the Ga content x and fit with polynomials in x. From the polynomial fits, one can determine the dielectric function for any value of x. The resulting database enables compositional analysis by least-squares regression at the end of the first stage of CIGS deposition. After the first stage, however, the temperature of the IGS is increased from 400 °C, for which the dielectric functions of Fig. 6.7 are appropriate, to 570 °C which require a modified set of dielectric functions to account for the higher measurement temperature and

possible annealing effects. The modified dielectric functions of IGS that account for the temperature increase can be deduced most accurately from the shuttered deposition process as described in the next section.

The approach for determining the dielectric functions of CIGS was somewhat different than that of IGS due to the lack of strong substrate and thickness dependences for the CIGS dielectric functions. As a result, it was possible to focus on CIGS depositions using ideal substrates that generate smooth interfaces and surfaces as well as using reduced layer thicknesses that also ensure smoother surfaces [15]. The CIGS films of different x values were deposited on native oxide covered Si wafers at a substrate temperature of 570 °C and were measured by real time SE. A one-stage coevaporation process was undertaken using continuous fluxes of Cu, In, Ga, and Se. Deposition durations of 100 s led to bulk layer thicknesses in the range of 550–700 Å. The (ψ, Δ) data were interpreted by multi-time analysis using the last 30 s time period of each 100 s deposition. Although the substrates ensured an interface of near atomic scale smoothness, however, it was necessary to incorporate a surface roughness layer into the optical model. The bulk and surface roughness layer thicknesses and the surface roughness layer void content in percent were the free parameters, and a b-spline model was used for the dielectric function with node spacings of 0.1 eV in the range of 0.75–3.00 eV and 0.2 eV in the range >3.00 eV. Figure 6.8 shows selected final results for the dielectric functions of CIGS as obtained at the measurement temperature of 570 °C. Interpolation of these results enable calculation of the CIGS dielectric function for any composition x with $0 \leq x \leq 0.48$ for use in real time SE analysis of three-stage CIGS. A more rigorous parameterization was developed for the room

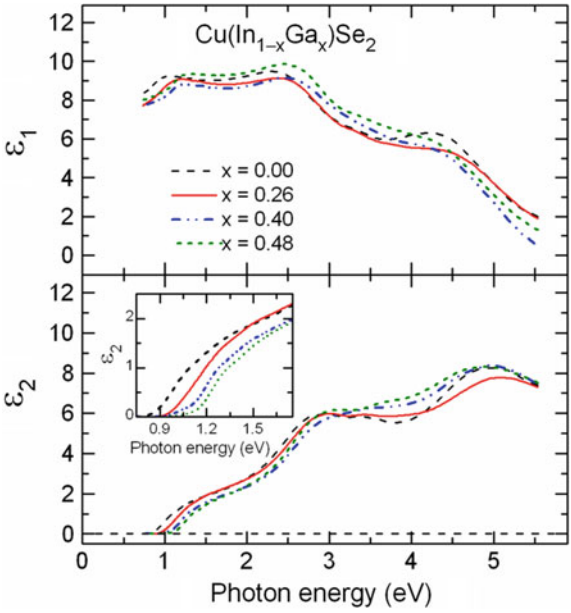


Fig. 6.8 Parameterized dielectric functions of $Cu(In_{1-x}\ Ga_x)Se_2$ for selected x obtained at the end of a one-stage coevaporation process applying in situ SE at the deposition and measurement temperatures of 570 °C. Here b-spline functions were used in the parameterization with the ability to extract the dielectric function for any x with $0 \leq x \leq 0.48$ through interpolation. The absorption onset in ε_2 shown in the inset provides the highest sensitivity for compositional analysis [15]

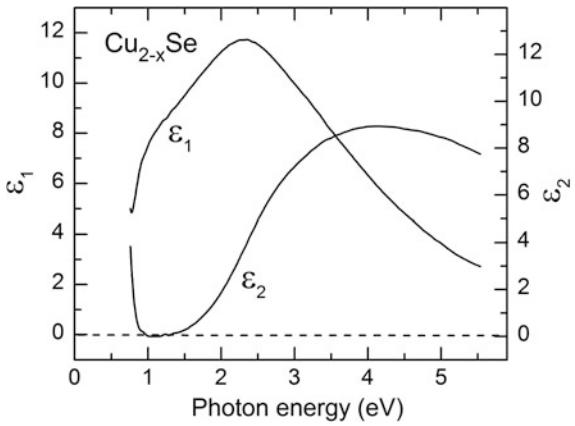


Fig. 6.9 Dielectric function of $Cu_{2-x}Se$ with $x = 0.20$ deposited by Cu and Se coevaporation under the conditions of stage II CIGS. These results were obtained at deposition and measurement temperatures of 570 °C. In situ SE data analysis was performed by inversion of (ψ, Δ) data using structural parameters deduced in real time SE analysis [8]

temperature dielectric functions of these CIGS films for use in ex situ SE analysis of absorber layers and complete solar cells [15].

Because the $Cu_{2-x}Se$ phase evolves during the Cu-rich period of film growth just before the stage II endpoint and through much of stage III, the dielectric function for $Cu_{2-x}Se$ at 570 °C is also needed. $Cu_{2-x}Se$ with stoichiometry $x \sim 0.20$, as determined by post-deposition EDS, was deposited by coevaporation of the two elements on a thermally oxidized silicon wafer under the same conditions as used for stage II CIGS coevaporation [5, 25]. Large variations of the Se/Cu atomic flux ratio during deposition, however, were found to result in cubic β-phase films with a composition range of $0.20 \leq x \leq 0.25$. In fact, $Cu_{2-x}Se$ that forms at 570 °C has been reported to exhibit a narrow stability range of $0.17 \leq x \leq 0.25$ [26, 27]. The resulting dielectric function spectra for $Cu_{2-x}Se$ with $x \sim 0.20$ as deduced by analysis of real time SE data are included in Fig. 6.9. These spectra were also obtained by multi-time analysis by inversion of (ψ, Δ) assuming a two layer (roughness/bulk) model.

6.3 Real Time Measurement of Three-Stage Coevaporation of CIGS

6.3.1 Deposition Details and Solar Cell Results

Three-stage coevaporation of CIGS was performed in a vacuum chamber outfitted with four individual sources that generate atomic fluxes of indium, gallium, copper, and selenium. The source temperatures were controlled using signals from electron impact emission spectroscopy (EIES), which enabled real time monitoring of the atomic fluxes. A multichannel ellipsometer having a design based on the rotating-compensator principle was applied for real time monitoring of the growing

film surface. Ellipsometry spectra were obtained during deposition at an angle of incidence within the range 70.6°–71.0° with an acquisition time of 3 s and a repetition time of 5 s, both for complete spectra. Solar cell substrates consisting of soda lime glass coated with optically-opaque Mo were used in this study. The results for three depositions will be discussed in this review with processing procedures given schematically in Figs. 6.10, 6.11, and 6.12. The first deposition

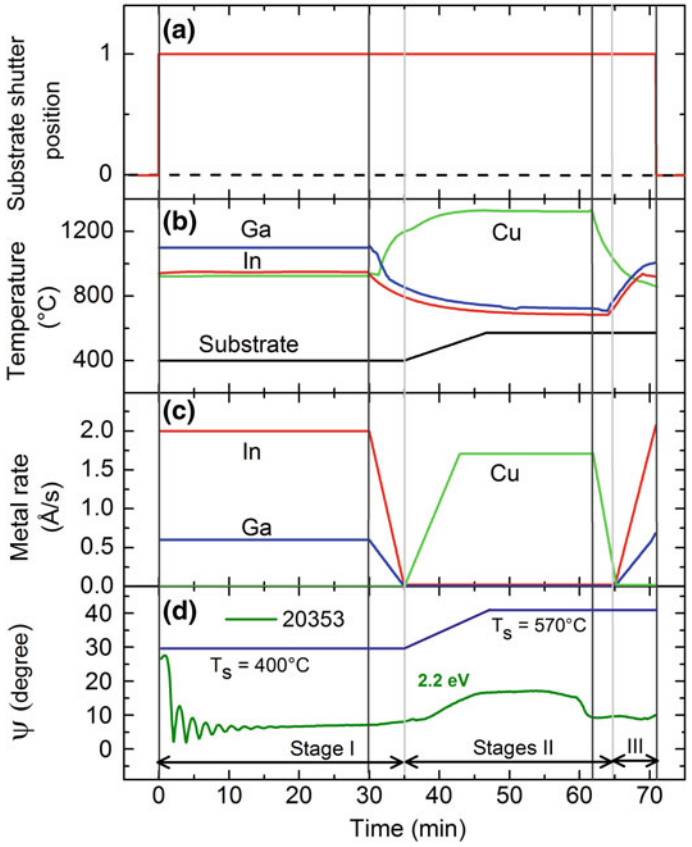


Fig. 6.10 Three-stage deposition description for the CIGS film ~2.7 μm in thickness grown on an opaque Mo film, which is in turn sputtered onto a soda lime glass substrate. For this process, the substrate shutter is open throughout the deposition. The panels depict **a** the substrate shutter position throughout the deposition (0: closed, 1: open); **b** the approximate metallic source and schematic substrate temperature profiles during the three stages; **c** schematic of the metal evaporation rates; and **d** the substrate temperature and real time SE data in ψ collected at a photon energy of 2.2 eV. The source temperature for Se was set at 263 °C for a rate of ~20 Å/s throughout the three stages. The dark vertical lines represent the shutter opening time to initiate stage I and the times at which cooling of the sources is initiated. The light vertical lines indicate the times at which the fluxes actually reach zero to end stages I and II. Stage III is terminated by closing a shutter to block the flux at the substrate/film surface [8]

yielded a 2.7 μm CIGS film in a continuous three-stage process depicted in Fig. 6.10 in which the substrate shutter is open throughout the process [7]. The second deposition process, developed specifically for thin absorber layers, is depicted in Figs. 6.11 and 6.12. The process of Fig. 6.11 was performed for a

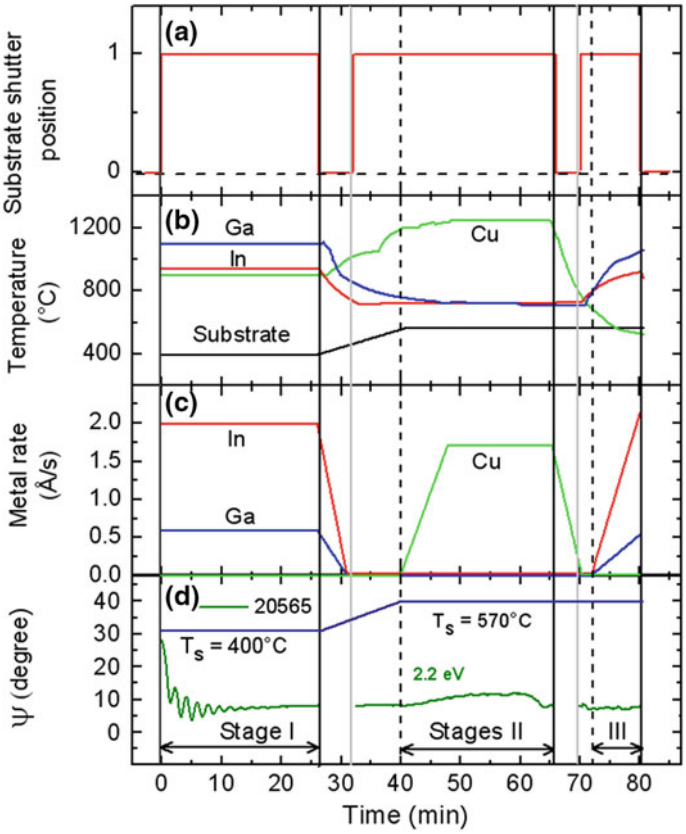


Fig. 6.11 Three-stage deposition description for the CIGS film ~2.2 μm in thickness grown on an opaque Mo film, which is in turn sputtered onto a soda lime glass substrate. For this process, the substrate shutter is closed between the different stages of the deposition to allow for source temperature stabilization. The panels depict **a** the substrate shutter position throughout the deposition (0: closed, 1: open); **b** the approximate metallic source and schematic substrate temperature profiles during the three stages; **c** schematic of the metal evaporation rates; and **d** the substrate temperature and real time SE data in ψ collected at a photon energy of 2.2 eV. The source temperature for Se was set at 263 °C for a deposition rate of ~20 Å/s throughout the three stages. The first dark vertical line indicates $t = 0$ when the shutter is open to start stage I. The subsequent dark lines indicate the onset of source cooling for the three stages. For source cooling at the end of stage III the shutter is closed. The light vertical lines indicate the times at which the flux goes to zero at the end of stages I and II and the shutter is opened before the start of stages II and III. The broken lines indicate the onset of the fluxes in stages II and III, which indicate the actual start of these stages [8]

standard 2.2 μm thick absorber layer whereas that in Fig. 6.12 was performed for a 0.3 μm absorber [7, 8]. In this second process, the substrate shutter is closed at the onset of source cooling to end stages I and II, and time delays occur between cooling and heating at the transitions between stages. The solar cell performance parameters of the three depositions to be discussed are shown in Table 6.1. Using a shutter between the stages has led to improved device performance for standard thickness absorbers, but also enables greater control in the fabrication of very thin absorbers.

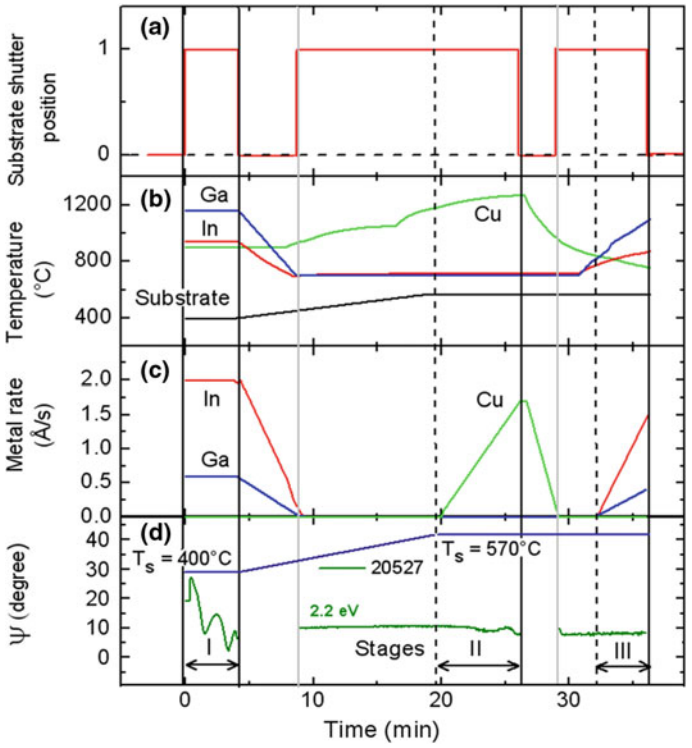


Fig. 6.12 Three-stage deposition description for the CIGS film ~0.3 μm in thickness grown on an opaque Mo film, which is in turn sputtered onto soda lime glass. For this deposition, the substrate shutter is closed between the different stages of the deposition to allow for source temperature stabilization. The panels depict **a** the substrate shutter position throughout the deposition (0: closed, 1: open); **b** the approximate metallic source and schematic substrate temperature profiles during the three stages; **c** schematic of the metal evaporation rates; and **d** the substrate temperature and real time SE data in ψ collected at a photon energy of 2.2 eV. The source temperature for Se was set at 263 °C for a deposition rate of ~20 Å/s throughout the three stages. The first dark vertical line indicates $t = 0$ when the shutter is open to start stage I. The subsequent dark lines indicate the onset of source cooling for the three stages. For source cooling at the end of stage III the shutter is closed. The light vertical lines indicate the times at which the flux goes to zero at the end of stages I and II and the shutter is opened before the start of stages II and III. The broken lines indicate the onset of the fluxes in stages II and III, which indicate the actual start of these stages [8]

Table 6.1 Characteristics of the highest performing solar cell from each deposition as studied by real time SE. Included are the Ga and Cu compositions according to the formula $Cu_y(In_{1-x}Ga_x)Se_2$ and the solar cell performance parameters of open-circuit voltage V_{oc}, short-circuit current density J_{sc}, fill factor, and efficiency. For the solar cell with the 2.2 μm absorber, results obtained after adding an anti-reflection coating (ARC) are presented [8]

CIGS thickness	x	y	V_{oc} (V)	J_{sc} (mA/cm^2)	Fill factor (%)	Efficiency (%)
2.7 μm	0.25	0.82	0.547	34.5	69.5	13.1
2.2 μm no ARC	0.29	0.86	0.638	34.2	71.3	15.6
2.2 μm ARC				36.2		16.5
0.3 μm	0.31	0.89	0.520	25.3	58.9	7.7

Further details for the continuous process in Fig. 6.10 will be provided, and then differences will be highlighted for the shuttered process of Figs. 6.11 and 6.12. To start stage I in Fig. 6.10, coevaporation of In at 2.0 Å/s, Ga at 0.6 Å/s, and Se at 20 Å/s is initiated with a substrate shutter located in front of the substrate and the substrate temperature set at 400 °C. These nominal thickness rates are assigned on the basis of measurements performed on individual elemental depositions at room temperature [8]. The deposition on the Mo-coated soda lime glass substrate in stage I is initiated with the opening of the shutter. After the deposition of an IGS film of prescribed thickness (intended as ~65% of the desired final CIGS layer thickness), serving as a precursor to the CIGS film, the temperatures of the In and Ga sources are reduced to terminate In and Ga coevaporation while maintaining Se evaporation. Next, stage II is started as soon as the In and Ga fluxes drop to zero, and here the substrate temperature is set to 570 °C. The increase in Cu source temperature causes the Cu flux to increase above zero, which defines the stage II onset. The deposition rate for Cu is set at 1.7 Å/s while the rate of Se is continued at 20 Å/s. During the first 12 min of IGS to CIGS conversion, the substrate temperature is rising which makes SE data analysis a challenge. The transition through stoichiometric CIGS, in this case a transition from Cu-poor to Cu-rich CIGS, is identified by an increase in the power to the substrate heater necessary to maintain the constant 570 °C substrate temperature. This behavior is observed due to an increase in the emissivity of the surface when it is Cu-rich. After the Cu-poor to Cu-rich transition is observed, an ~1 min waiting time is applied to ensure build-up of $Cu_{2-x}Se$ on the surface before the temperature of the Cu source is reduced in order to cease evaporation of Cu at the stage II endpoint. The start of stage III is defined by the simultaneous loss of the Cu flux and a regeneration of In and Ga flux via increases in the source temperatures. The temperatures are set to regain the stage I rates of 2.0 Å/s for In and 0.6 Å/s for Ga in stage III, while ensuring a continuous Se flux and maintaining the substrate temperature of 570 °C. Near the end of stage III, a Cu-rich to Cu-poor transition is observed in the substrate heater power. A waiting time of ~45 s after this transition ensures Cu deficient CIGS before the substrate shutter is closed and the In and Ga source temperatures are reduced in order to cease the coevaporation of these elements.

When shuttering is used during the three-stage process, as shown in Figs. 6.11 and 6.12, the substrate shutter is closed to define the end of stage I at the onset of In

and Ga source cooling [8]. In this case, stage II is initiated through an increase of the Cu source temperature sufficient to generate Cu flux, but only after the shutter is opened and the substrate temperature has reached the new set point of 570 °C. Thus, one difference between the processes with and without a shutter is that in the latter case, the substrate temperature has yet to reach the set point at the onset of stage II. The substrate shutter is also closed at the stage II endpoint when Cu source cooling begins and the Cu flux starts to decrease. This enables improved control over the amount of $Cu_{2-x}Se$ at the film surface. The shutter is reopened only after the Cu flux has reached zero; then the In and Ga sources are reheated to initiate stage III.

6.3.2 Standard CIGS Thickness in Continuous Process: Stage I $(In_{1-x}Ga_x)_2Se_3$ Deposition

The optical model used in the analysis of real time SE data throughout much of the IGS deposition in stage I is shown in Fig. 6.13. This model is general, implying that it can be used in the analysis of data obtained in all three deposition processes of Figs. 6.10 through 6.12 [6–8]. The optical model for this stage I analysis incorporates three layers associated with IGS: the interface roughness, bulk, and surface roughness layers. The interface roughness layer arises from the roughness that forms on the surface of the Mo during its deposition on the soda lime glass substrate. The roughness layer on the Mo thin films used in the solar cell deposition processes is ~250 Å in thickness as indicated in Fig. 6.13. In the initial time period of IGS film growth, the voids within the valleys of the Mo surface roughness layer fill with IGS at the same time that the IGS surface roughness itself develops on the peaks of the Mo surface roughness. Thus, in the initial period of growth, the IGS content not only within the interface roughness layer, but also within the growing



Fig. 6.13 Schematic of the optical model applied for analysis of real time SE data during stage I, which involves IGS deposition on rough Mo. The underlying Mo film is opaque. The IGS film growth is analyzed in terms of interface, bulk, and surface roughness layers. The dielectric functions of the interface and surface roughness layers are determined using the Bruggeman effective medium approximation as mixtures of underlying/overlying materials [8]

IGS surface roughness layer, vary in the analysis together with the surface roughness layer thickness. Once the interface roughness is completely filled, the bulk layer is incorporated into the model. From that point onward the model of Fig. 6.13 applies, and the bulk and surface roughness layer thicknesses, along with the void volume percent within the IGS surface roughness, are all allowed to vary with time in the analysis. The dielectric functions of interface and surface roughness layers are determined via the Bruggeman effective medium approximation (EMA) as a mixture of the materials of the two adjacent media. During the process of interface filling, however, an EMA using the three components of Mo+void+IGS must be applied.

As described in Sect. 6.2, the opaque Mo film coating the soda lime glass used as the starting substrate for the IGS deposition must be characterized by in situ SE at 400 °C, the temperature of the stage I process. The goal is to extract the characteristics of the roughness that exists on the Mo surface and the Mo dielectric function at 400 °C, in the latter case accounting for the roughness layer. As a first step toward this result, an analysis is performed on the in situ SE data acquired on the Mo-coated glass substrate at room temperature before heating [8]. This analysis applies a database dielectric function relevant to the specific deposition conditions used for the Mo film on the substrate. The results of this analysis are the thickness of the Mo surface roughness layer and the void content within this layer. It is assumed that the structure of the Mo remains the same after heating the substrate to 400 °C for an additional in situ SE measurement performed just before the IGS deposition. As a result, the same structural parameters are used in an inversion of the additional in situ SE data to deduce a Mo dielectric function at 400 °C that exactly describes the data. This Mo dielectric function can also be fit with a parametric model for application in subsequent real time SE analysis of the IGS deposition in order to suppress noise throughout the analysis generated by an exactly inverted Mo substrate dielectric function.

In addition to the dielectric function of Mo, determined as described in the previous paragraph, that of IGS is needed relevant for the deposition temperature of 400 °C and for the intended IGS composition of $x = 0.30$ based on calibrated EIES. The IGS dielectric function derives from a database established by real time SE measurements performed as described in Sect. 6.2 under the same deposition conditions as are used for solar cell fabrication. In the determination of parameters for the IGS dielectric function database, results obtained at a thickness near 4000 Å are used [6]. Thus, in the application of this database, the observed thickness dependence of the IGS dielectric function is neglected in the real time SE data analysis. This limitation has a relatively weak effect on the deduced structural evolution throughout the deposition but leads to an increase in the MSE.

Figure 6.14 shows the evolution of the film structure in the first 1.5 min during the coevaporation of IGS on a soda lime glass substrate coated in turn with an opaque layer of Mo. This deposition serves as stage I of the continuous process of Fig. 6.10 that ultimately yields a 2.7 μm CIGS absorber layer [6–8]. The roughness on the surface of the Mo measured before CIGS deposition is characterized as a 242 Å thick layer with an ~60 vol% void content. In this initial time period of IGS growth starting

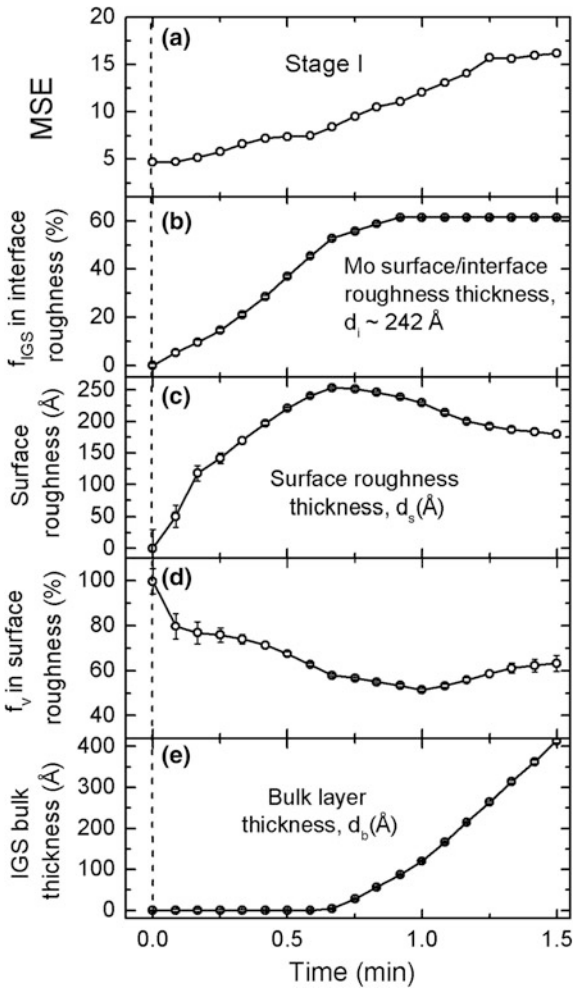


Fig. 6.14 Early stage structural evolution for $(In_{1-x}Ga_x)_2Se_3$ (IGS; $x = 0.31$) presenting results in the first ~400 Å of bulk layer growth on a soda lime glass substrate coated with opaque Mo. A 242 Å thick surface roughness layer exists on the starting Mo surface before IGS deposition. Individual panels show the time evolution of the **a** MSE; **b** IGS content in vol% filling the voids within the roughness layer on the Mo surface; **c** thickness of the IGS surface roughness layer; **d** void content in vol% within the roughness layer on the IGS surface; and **e** thickness of the IGS bulk layer. In this process, a shutter in front of the substrate was opened at $t = 0$ at the vertical broken line to initiate stage I deposition as in Fig. 6.10. Although these results were obtained during the deposition of thick (~2.7 μm) CIGS in stage I using the continuous mode of deposition with the substrate shutter open throughout, the results are relevant as well for thick (2.2 μm) and thin (~0.3 μm) CIGS using the shuttering process [8]

from $t = 0$, when the substrate shutter is opened, the voids within the Mo surface roughness layer are filled by IGS, resulting in the rapid development of the IGS content within the layer from 0 vol%, as shown in Fig. 6.14b. Concurrently, the

roughness layer on the IGS surface increases in thickness, indicated by d_s in Fig. 6.14c, and densifies with a reduction of its void content, f_v in Fig. 6.14d, as the roughness on the Mo surface is covered conformally. Once the voids within the interface roughness layer are nearly filled, which occurs when the IGS content within the layer reaches ~60 vol%, a bulk IGS layer of thickness d_b, as shown in Fig. 6.24e, can be integrated into the multilayer model. At this point, the IGS surface roughness reaches its maximum thickness of 250 Å and exhibits a ~60 vol% void content before a smoothening effect and further densification occur. Thus, during the initial growth period of the bulk layer, the roughness layer thickness on the IGS surface decreases, suggesting structural coalescence in which the substrate induced roughness is suppressed. The gradual increase in MSE in Fig. 6.14a can be attributed to the selection of a ~4000 Å thick layer for the determination of the database IGS dielectric function used in the analysis. The later period IGS structural evolution will be presented in Sect. 6.3.5 when the complete structural evolution during all three stages of CIGS deposition will be summarized. There it will be shown that the MSE versus time for the IGS analysis reaches a minimum in the range of 4000–5000 Å thickness.

In an initial analysis of the IGS deposition, an IGS dielectric function relevant for the intended composition can be selected, as described previously [8]. For the analysis of Fig. 6.14, however, a dielectric function taken directly from Fig. 6.7 was applied, the one for composition $x = 0.31$, which is sufficiently close to the intended $x = 0.30$, in consideration of possible experimental errors. As the film

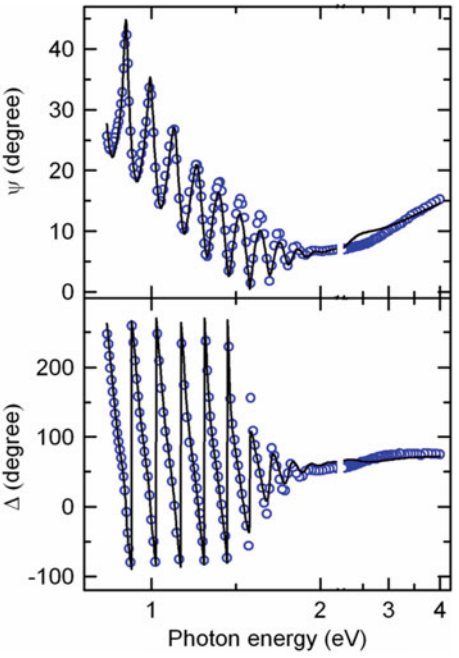


Fig. 6.15 Spectroscopic ellipsometry data (points) obtained at the end of the IGS deposition of Fig. 6.14 at a substrate temperature of 400 °C before initiation of stage II. Also shown is the best fit (solid lines) using the structural model and best fit parameters of Fig. 6.16 [8]

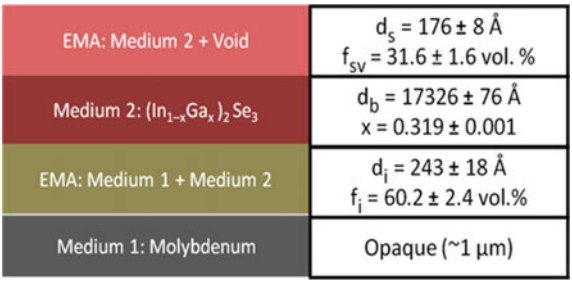


Fig. 6.16 Schematic of the structural model with best fit parameters and confidence limits obtained in the analysis of the data in Fig. 6.15. The dielectric function database for IGS at 400 °C is used for the determination of the IGS composition [8]. In this schematic, f_i is the IGS vol% in the Mo/IGS interface layer, and f_{sv} is the void vol% in the surface roughness layer

increases in thickness and the interference fringe pattern develops, the analysis becomes more sensitive to this selection of the IGS dielectric function. Then the composition can be determined accurately, as indicated by the analysis of the real time SE data at the end of the IGS deposition depicted in Figs. 6.15 and 6.16. Figure 6.15 shows the (ψ, Δ) data and the best fit using the structural parameters in the model stack of Fig. 6.16. In this analysis, the dielectric function was not fixed as that for $x = 0.31$, as in the analysis of Fig. 6.14, but rather was allowed to vary according to the composition, applying the database described in Sect. 6.2. The fit is poor at the high photon energies, likely an effect of the thickness dependence of the dielectric function and possibly the effect of the relatively thick surface roughness layer on the IGS. In spite of this, some positive indicators in the fit are observed. First, the deduced Mo/IGS interface layer thickness and IGS content within the interface layer are very close to the surface roughness thickness and void content deduced for the underlying Mo before IGS deposition. This indicates that the interface layer derives from the roughness on the Mo and that the voids in this roughness layer are completely filled with IGS in the initial time period of IGS deposition. In addition, the deduced composition x is within ~0.02 of the intended value of $x = 0.30$.

As shown in Table 6.1, the final composition of the CIGS as deduced by EDS is lower, $x = 0.25$, a difference that may result from the compositional profile of the final CIGS film and/or different probe locations for real time SE and EDS coupled with area non-uniformity in x. In addition, deviations from the intended composition may occur in stage III, which accounts for the additional deposition of ~0.3 μm thickness of CIGS. Finally, it should be noted that attempts were made to incorporate a $MoSe_2$ layer at the Mo/IGS interface in the model for real time and in situ SE analysis of stage I. Although these attempts were facilitated through the determination of a dielectric function for $MoSe_2$, as described in Sect. 6.2, they were not successful. A possible reason is the thinness of the $MoSe_2$ layer compared to the Mo roughness. This would then require incorporation of $MoSe_2$ at the Mo/IGS interface in a three component EMA of Mo+$MoSe_2$+CIGS, which may result

in a loss of sensitivity to the $MoSe_2$ content. Another possibility is that $MoSe_2$ instead forms during the higher temperature stages II and III.

6.3.3 *Standard CIGS Thickness in Continuous Process: Stage II IGS Conversion to Cu-Rich CIGS*

The model used in the analysis of stage II of CIGS deposition is given in Fig. 6.17 [7, 8]. Two differences are noted relative to the corresponding model of Fig. 6.13. First, in addition to bulk and void components of the surface roughness layer, a $Cu_{2-x}Se$ component is incorporated to simulate the development of this phase after the transition from Cu-poor to Cu-rich CIGS just before the end of stage II. When the $Cu_{2-x}Se$ first forms, IGS has already completely converted to CIGS. Thus, the roughness layer is modeled either as an IGS+void+CIGS mixture before the Cu-rich to Cu-poor transition, or as a CIGS+void+$Cu_{2-x}Se$ mixture after the transition. A second difference for the model of Fig. 6.17 is associated with the bulk layer, which is assumed to be uniform throughout the thickness and is taken as a mixture of IGS and CIGS during the entirety of stage II. For this model, $Cu_{2-x}Se$ is assumed to exist only at the surface and not within the bulk.

Thus, based on the model of Fig. 6.17 for real time SE analysis during stage II, a bulk conversion model from IGS to CIGS is applied to the CIGS growth process, meaning that the conversion occurs uniformly throughout the thickness of the IGS layer. This model is to be contrasted with one in which the conversion of IGS to CIGS occurs layer by layer. In a side-by-side comparison of the two possible models, significantly better fits to the real time SE data sets are obtained by applying the model assuming bulk IGS to CIGS conversion. In spite of this clear interpretation, corroborating results are desirable from additional analytical

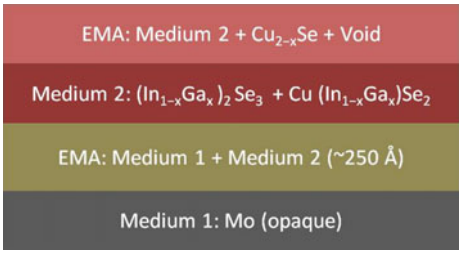


Fig. 6.17 Schematic of the optical model for analysis of real time SE data during stages II and III which encompass the processes of IGS to CIGS conversion, $Cu_{2-x}Se$ formation, and $Cu_{2-x}Se$ to CIGS conversion. In stage II, IGS (medium 2) is converted to CIGS and a surface layer component of $Cu_{2-x}Se$ develops. In stage III, the surface component of $Cu_{2-x}Se$ is converted to additional bulk and roughness layer CIGS. The dielectric functions of the roughness layers at the substrate interface and at the film surface are determined by applying the Bruggeman effective medium approximation as a mixture of the materials indicated [8]

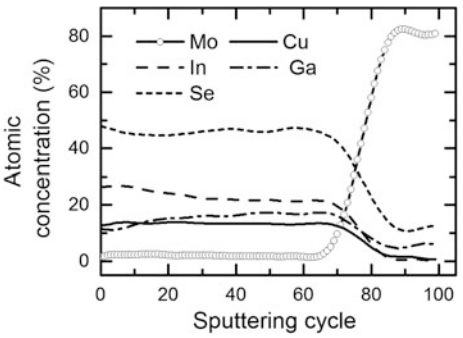


Fig. 6.18 Compositional depth profile obtained by Auger electron spectroscopy (AES) for a layer obtained after terminating the stage II process of Cu and Se coevaporation halfway through the conversion from IGS to CIGS. The thickness of the completed CIGS sample was 2.5 μm [7]

techniques. For such results, coevaporation of Cu and Se was halted approximately halfway through stage II of the CIGS deposition process. This unfinished CIGS sample was profiled throughout the thickness by Auger electron spectroscopy (AES). The resulting AES depth profile in Fig. 6.18 reveals that the Cu is uniformly distributed throughout the layer thickness with an ~12 at.% composition [7, 8]. Because the limiting form of the layer-by-layer model would predict a transition from 25 to 0 at.% Cu centered roughly halfway through the profile, this model is ruled out and instead the AES results support a bulk conversion model.

Figure 6.19 shows a summary of results for real time SE analysis of IGS to CIGS conversion in stage II during the continuous process that yields the 2.7 μm thick CIGS film [7, 8]. Thus, the IGS film from stage I at the starting point in Fig. 6.19 is that of Figs. 6.15 and 6.16. The results just before the end of stage II, extending beyond the transition from Cu-poor CIGS to Cu-rich CIGS, will be presented and discussed in Sect. 6.3.4. Figure 6.19b quantifies the IGS-CIGS conversion process in terms of the CIGS content. This analysis is based on the model of Fig. 6.17 assuming an effective medium mixture having uniform volume percentages of IGS and CIGS throughout the bulk layer. In addition to the CIGS content, the accumulation rate in terms of the effective layer thickness or volume per unit substrate area is determined as shown in Fig. 6.19c, including the bulk as well as the interface and surface roughness layer components during conversion. This figure suggests that it takes ~10 min for the CIGS accumulation rate to saturate near 1100 Å/min, the effective rate observed at the center time of stage II. Assuming that the flux of Cu is constant throughout the process, the initial rise in the rate may represent a conversion process limited by Cu concentration within a reservoir associated with all the grain boundaries [10]. After ~10 min, the supply saturates which leads to a saturation in the conversion rate limited by diffusion within the grains. A rapid decrease in the rate at 55 min occurs as the conversion to CIGS is limited by the remaining volume percentage of unconverted IGS. The inset of Fig. 6.19b shows the bulk layer thickness rate as a function of the volume percentage of CIGS within the film during conversion. A constant bulk layer thickness rate is expected as the film volume expands to accommodate the CIGS component. Variations from a constant rate may occur in the early time period if

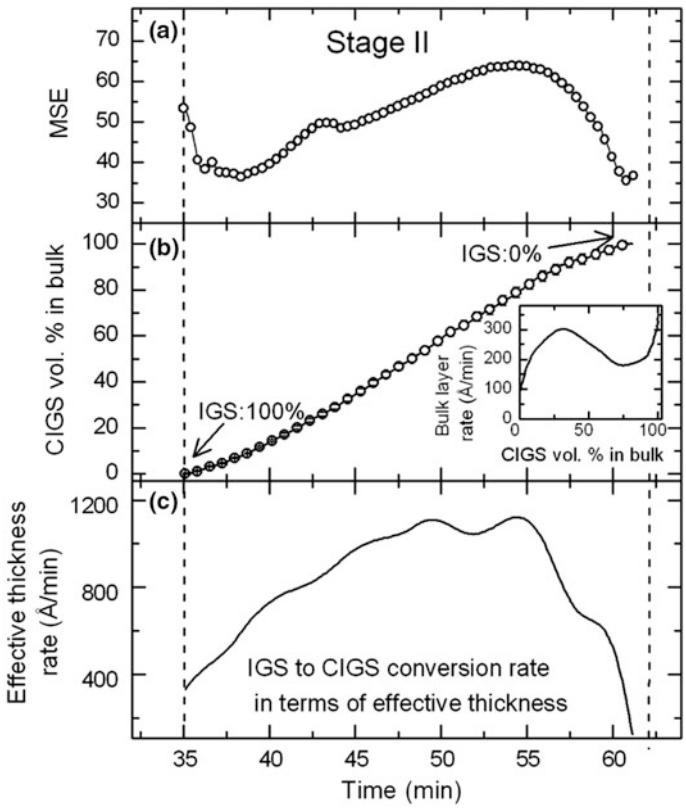


Fig. 6.19 IGS to CIGS conversion during coevaporation of Cu and Se in stage II for the 2.7 μm thick CIGS layer deposited in the continuous process of Fig. 6.10 without substrate shuttering between stages. The individual panels include the time evolution of the **a** MSE; **b** CIGS volume percent within the bulk layer that quantifies the conversion of the IGS material to CIGS; **c** the rate of IGS to CIGS conversion given in terms of the effective thickness including interface, bulk, and surface layer contributions. The inset in (**b**) shows the growth rate in terms of bulk layer thickness plotted as a function of CIGS volume percent within the bulk layer. The vertical broken lines indicate the time at which the Cu flux just increases above zero to start stage II (left) and the time at which the Cu source temperature is reduced before the end of stage II (right) in accordance with the time scale of Fig. 6.10 [8]

voids within the IGS bulk layer are filled by an expansion of the film volume. Variations may also occur due to changes in the roughness thickness and void content within the roughness layer as will be shown in Sect. 6.3.5.

The MSE obtained in the real time SE data analysis is included in Fig. 6.19a. The continuous increase in the first 20 min of stage II may be attributed in part to the increase in temperature from 400 to 570 °C which occurs in the first 10 min of stage II [8]. The database dielectric functions at 400 °C were used for IGS and those at 570 °C were used for CIGS. As a result, higher quality fits are obtained at the endpoints of the conversion where the dielectric functions are appropriate,

whereas midway through the conversion, both dielectric functions provide only approximate results. This problem has been addressed through the shuttered process to be described in Sect. 6.3.5. The fitting may also be degraded due to the development of the compositional gradient and resulting dielectric function gradient. This gradient can be observed in Fig. 6.18 which shows that the near surface is In rich according to the mechanism of Fig. 6.2, which leads to a narrower bandgap, and that the profile exhibits a linear trend in composition with depth that extends more than halfway through the film. The subsequent reduction in MSE after 55 min may also occur as the film increases in thickness during IGS conversion (from 1.8 to 2.4 μm), which serves to reduce the compositional gradient. Based on ex situ SE demonstrations [12, 15], more advanced modeling is expected to provide the time evolution of this gradient during deposition.

6.3.4 *Standard CIGS Thickness in Continuous Process: Stage II and III Transitions Between Cu-Rich CIGS and Cu-Poor CIGS*

Figure 6.20 shows the evolution of the $Cu_{2-x}Se$ effective thickness just before the endpoint of stage II and during stage III for deposition of the 2.7 μm thick absorber layer in the process of Fig. 6.10 [7, 8]. The first appearance of $Cu_{2-x}Se$ occurs at 60.8 min before the end of stage II with confidence limits on the effective thickness of ~±10 Å. The $Cu_{2-x}Se$ is first detected immediately after the transition to 100 vol% CIGS, which denotes the change from Cu-poor to Cu-rich stoichiometry given the continued deposition of Cu. The $Cu_{2-x}Se$ is assumed to exist only within the surface layer in the real time SE model; however, incorporation of $Cu_{2-x}Se$ within the grain boundaries of the bulk layer may also occur in the transition between 100 vol% CIGS and the onset of $Cu_{2-x}Se$ surface layer detection. A gradual decrease in the rate of $Cu_{2-x}Se$ deposition occurs as the Cu flux decreases to zero ending stage II. Here, the effective thickness of $Cu_{2-x}Se$ appears to decrease slightly, also suggesting that $Cu_{2-x}Se$ may be developing within the bulk CIGS. Additional evidence for this effect will be presented in Sect. 6.3.6.

Through the early part of stage III in Fig. 6.20, the $Cu_{2-x}Se$ effective thickness (volume fraction times thickness) decreases as the In, Ga, and Se react to form surface CIGS which is expected to grow epitaxially on the underlying CIGS grains as suggested by Fig. 6.2. The $Cu_{2-x}Se$ content is reduced to zero near the end of stage III. Thus, the purpose of this three-stage process is to remove the $Cu_{2-x}Se$ at the end of the deposition in order to continue to grow thin film CIGS with larger grains which appear at the junction to the CdS [10]. Upon consumption of the $Cu_{2-x}Se$, a process occurs that is opposite to that during stage II. In stage III, Cu out-diffuses from CIGS grains to react with In, Ga, and Se. In this case, the near surface becomes Ga rich rather than In rich, yielding the beneficial notch-shaped, double Ga-gradient profile of the final absorber (see Fig. 6.2).

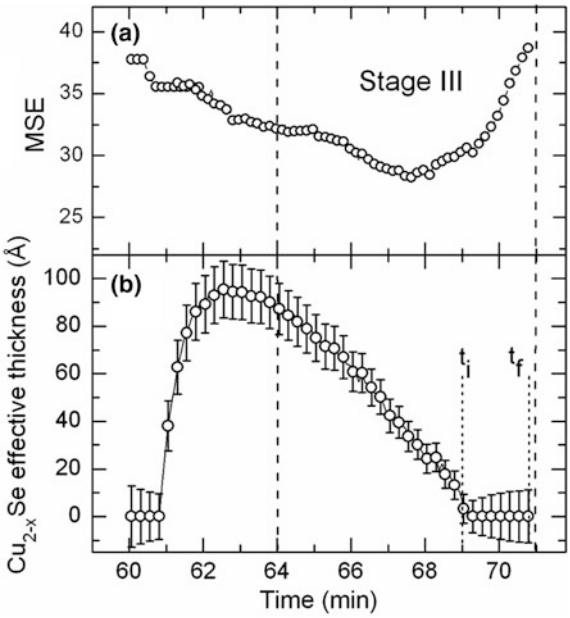


Fig. 6.20 Time evolution of the **a** MSE and **b** effective thickness of $Cu_{2-x}Se$ formed within the surface roughness modulations near the endpoint of stage II and then converted to CIGS during stage III. These results are for a 2.7 μm thick CIGS absorber layer deposited using a continuous process without substrate shuttering between the stages. The effective thickness in (**b**) is the volume of $Cu_{2-x}Se$ per unit substrate area, which is the product of the thickness of the surface layer and its volume fraction of $Cu_{2-x}Se$. The bulk thickness values obtained at time points t_i and t_f can be used to approximate the Cu composition y in $Cu_yIn_{1-x}Ga_xSe_2$. The estimated composition y obtained for this sample is 0.95, assuming a uniform distribution throughout the thickness of the final CIGS layer. The vertical broken lines across both panels indicate the time at which the Cu flux reaches zero to end stage II (left) and the end of stage III (right) in accordance with Fig. 6.10 [8]

The analysis demonstrates that real time SE can be implemented to identify the Cu-poor to Cu-rich and Cu-rich to Cu-poor transitions during three-stage coevaporation of the CIGS absorber [7, 8]. In contrast to other approaches, real time SE enables determination of the effective thickness or volume per area of the $Cu_{2-x}Se$ and, thus, improved control over the CIGS deposition process. Near the end of stage III, it is reasonable to propose that real time SE can be used to monitor and control the Cu deficiency within the film to values within the optimum range of $y = [Cu]/\{[In] + [Ga]\} \sim 0.80–0.95$. In Fig. 6.20, the Cu-rich to Cu-poor transition is identified at $t = t_i$ when the $Cu_{2-x}Se$ effective thickness reaches zero. The sample at time point t_i at which all $Cu_{2-x}Se$ has been converted to CIGS is assumed to represent stoichiometric CIGS with no excess $Cu_{2-x}Se$ and with $y(t_i) = [Cu]/\{[In] + [Ga]\} = 1$. If it is further assumed that any In or Ga and Se that is deposited after $t = t_i$ will generate the Cu-poor defect complex $2V_{Cu} + In(Ga)_{Cu}$ in CIGS [1], then at time $t = t_f$ one can estimate $y(t_f) = 3d_{eff}(t_i)/\{3d_{eff}(t_i) + 4[d_{eff}(t_f) - d_{eff}(t_i)]\}$. Using this

equation, the CIGS effective thicknesses obtained at time points t_i and t_f can be used to obtain the Cu ratio $y(t_f)$ for the final CIGS film. The y value obtained by applying this technique for the 2.7 μm CIGS deposition of Fig. 6.20 is 0.95. An ex situ EDS analysis of the CIGS layer performed after completion of the deposition, however, resulted in $y = [Cu]/\{[In] + [Ga]\} = 0.82$. The difference in this case is quite large and outside experimental and area non-uniformity errors. The difference may be attributed to a profile in Cu composition y with depth into the sample. The estimate provided by the equation above assumes that the Cu deficiency occurs uniformly throughout the thickness; however, the top-most region of the film probed by EDS may exhibit a higher deficiency than the bulk. In any case, it is expected that the predicted and EDS measured Cu compositions will scale with one another for a given CIGS thickness. As a result, real time SE is expected to be a suitable method for detecting the deposition endpoint.

Finally, it should be noted that improvements in the modeling in stage III will require incorporation of $Cu_{2-x}Se$ within the bulk layer as well as incorporation of an alloy compositional profile consisting of two linear composition gradients that form the optimum notch-like bandgap profile. The fact that a minimum in MSE occurs near the stoichiometric composition of $y \sim 1$ suggests that an improved model is needed that accounts for a depth distribution of the $Cu_{2-x}Se$.

6.3.5 *Standard CIGS Thickness in Continuous Process: Summary*

Figure 6.21 shows the structural evolution throughout the three stages of deposition for the 2.7 μm thick CIGS absorber layer using the continuous process, whereby $t = 0$ indicates the opening of the shutter to start the IGS deposition [7, 8]. In this figure, one can observe the continuation of growth that occurs after the Mo/IGS interface roughness filling and after the first 400 Å of bulk layer growth as shown in Fig. 6.14. Figure 6.21a, b depict the time evolution of the MSE and the bulk layer thickness, respectively, throughout the three stages. Average deposition rates can be determined from the latter panel, focusing on the three regions with evidently steady state processes: (i) in stage I throughout the deposition of the IGS bulk layer; (ii) in stage II after stabilization of the thickness rate and before the onset of saturation in the IGS to CIGS conversion as indicated in Fig. 6.19; and (iii) in stage III after conversion of the near-surface $Cu_{2-x}Se$ to CIGS and during fabrication of the Cu-poor CIGS. These average deposition rates can be used to assess the run-to-run reproducibility of the total rates of incorporation for In and Ga in stages I and III and for Cu in stage II. In addition to the average rates in the deposition process, the instantaneous rates can be followed as well, yielding measures of the stability of the fluxes or insights into the kinetics of the processes as they occur. For separation and characterization of the incorporation rates of the individual In and Ga elements, the compositions of the film are needed after each stage, as can be determined from the dielectric functions. This analysis is possible first at the end of

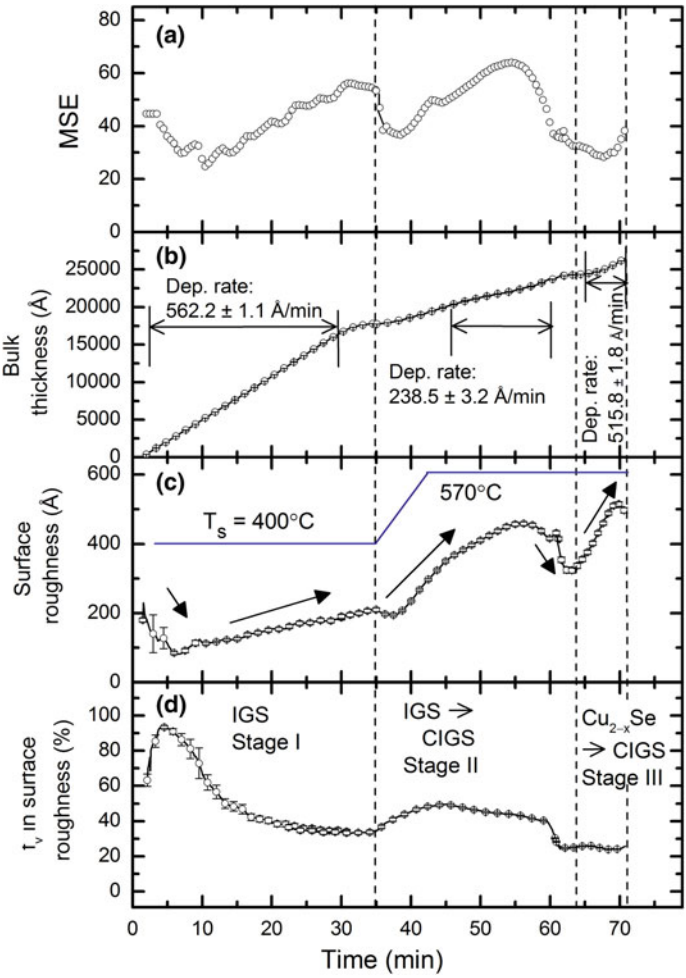


Fig. 6.21 Summary of real time SE analysis results for the 2.7 μm thick CIGS film during deposition by three-stage coevaporation using a continuous process without substrate shuttering between the stages. The individual panels include the time evolution of the **a** MSE; **b** thickness of the bulk layer; **c** thickness of the surface roughness layer; and **d** void volume percent within the surface roughness layer. The substrate temperature profile is shown in (**c**) at the top. Upward and downward arrows in (**c**) highlight surface roughening and smoothening processes. The vertical broken lines indicate the ends of stages I, II, and III in accordance with Fig. 6.10 [8]

stage I, as was shown in Figs. 6.15 and 6.16 applying the IGS database of Fig. 6.7. The dielectric function analysis is also possible at the two transitions which occur from Cu-poor to Cu-rich CIGS and from Cu-rich to Cu-poor CIGS near the end-points of stages II and III, respectively, in this case applying the CIGS database of Fig. 6.8. The results will represent an optical average through the thickness unless

bulk layer compositional profiling is incorporated in the models of Figs. 6.13 and 6.17, as has been done for ex situ measurements of the final solar cells.

Figure 6.21c, d show the evolution of the thickness of the surface roughness layer and that of the void volume percentage within the layer, respectively, throughout three-stage coevaporation of CIGS [7, 8]. As a general rule in polycrystalline film growth, surface roughening is a characteristic of grain growth in which crystallites protrude increasingly above the film surface as they develop, whereas smoothening is a characteristic of coalescence or filling of surface-connected intergrain regions. Roughening and smoothening regions are indicated by arrows in Fig. 6.21c. This figure suggests that continuous slow grain growth occurs during the deposition of IGS after a 0.3 μm bulk layer thickness has been deposited. More rapid grain growth occurs during IGS conversion to CIGS, and the most rapid growth occurs during $Cu_{2-x}Se$ conversion to CIGS as indicated in Fig. 6.21c. Figure 6.21d shows a long period of surface densification during IGS deposition as the surface structure induced by the substrate coalesces and flattens. The surface layer is also densified near the end of stage II just before and during the formation of the $Cu_{2-x}Se$ on the surface. This can be used to identify the Cu-poor to Cu-rich transition as the $Cu_{2-x}Se$, proposed to be semiliquid [9], fills the voids within the roughness layer on the surface and as a result flattens the surface. Surface layer void development is most prominent during initial IGS to CIGS conversion at the highest roughening rates when the CIGS grains that develop extend above the surface of the film.

6.3.6 *Standard CIGS Thickness in Shuttered Process: Summary*

The real time SE data acquired during the 2.2 μm CIGS deposition employing the shutter between stages were also analyzed to extract the structural and phase evolution of the film [8]. The initial time period of IGS deposition is not shown since there are no differences between the shuttered and continuous film growth processes over that time period, i.e. the first 1.5 min. The general features shown in Figs. 6.22 through 6.24 are similar to those in the continuous process depicted previously in Figs. 6.19 through 6.21. In this subsection, the results for the shuttered process will not be described in detail, but rather, the differences in the two sets of observations for continuous and shuttered processes will be highlighted.

Employing a shutter between the stages, as in the process of Fig. 6.11, enables the substrate temperature to reach the 570 °C set point before the Cu flux is initiated to start stage II, in contrast to the continuous process of Fig. 6.10 [8]. The apparent result of this effect is that the effective conversion rate of IGS to CIGS increases more rapidly to ~1200 Å/min as a result of the higher Cu diffusion coefficient at the elevated temperature that enables rapid filling of the grain boundary reservoir with Cu. In addition, the effective thickness rate decreases more gradually as the stage II endpoint is approached. The origin of the larger oscillations for the shuttered

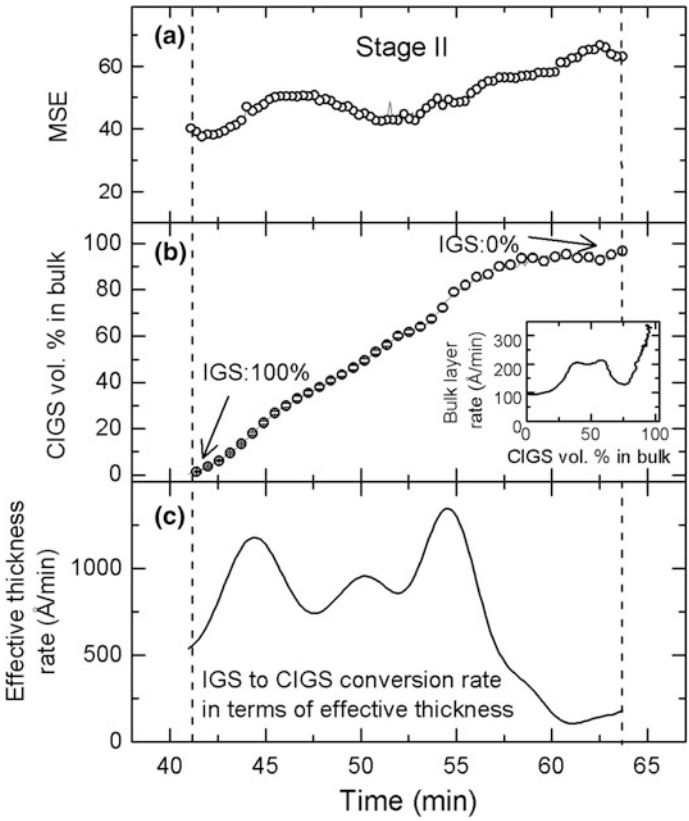


Fig. 6.22 IGS to CIGS conversion throughout stage II of the 2.2 μm thick CIGS layer deposition in a process in which a substrate shutter is closed between the stages. The individual panels include the time evolution of the **a** MSE; **b** CIGS volume percent within the bulk layer that quantifies conversion of the IGS layer to CIGS; **c** rate of IGS to CIGS conversion in terms of the effective thickness including interface, bulk, and surface layer contributions. The inset shows the growth rate in terms of bulk layer thickness plotted as a function of CIGS volume percent within the bulk layer. The vertical broken lines indicate the start of data collection after the onset of stage II and the transition from Cu-poor CIGS to Cu-rich CIGS just before the end of stage II in accordance with Fig. 6.11 [8]

process in Fig. 6.22 is unclear. One possible effect is instability in the Cu flux upon opening the shutter, which appears directly in the conversion rate due to rapid diffusion. The differences between the processes in stage II, namely the elevated substrate temperature for the shuttered process throughout stage II conversion of the IGS layer to CIGS, may account for a higher solar cell performance achievable for this process, as well. This can be noted in Table 6.1, and has been observed consistently in comparing several continuous and shuttered runs. This proposal is supported by the fact that elevated stage II and stage III temperatures even above 570 °C on specialty glass are found to result in higher performance solar cells [28].

Another observation that can be made in a comparison of Figs. 6.21 and 6.24 for stages I and II is the reduced surface roughness thickness for the shuttered process [8]. At the end of stage I, this difference is due in part to the thinner IGS layer in the shuttered process. In addition, greater smoothening occurs near the end of stage II for the shuttered process, and the smoothening continues even when the shutter is closed. This indicates that the deposited $Cu_{2-x}Se$ phase transports across the surface more readily, moving from the peaks to the valleys within the roughness layer. In fact, the surface roughness layer thickness only smoothens to a minimum of 300 Å in the beginning of stage III for the continuous process, whereas smoothening occurs extensively to 100 Å in the shuttered process. One possible conclusion is that the waiting time while the shutter is closed enables dispersal of the $Cu_{2-x}Se$ over the surface and within the grain boundaries, further enabling greater grain growth during stage III when exposed to In, Ga, and Se. Two observations support this proposal. First, the $Cu_{2-x}Se$ effective thickness at the surface decreases by a factor of two in

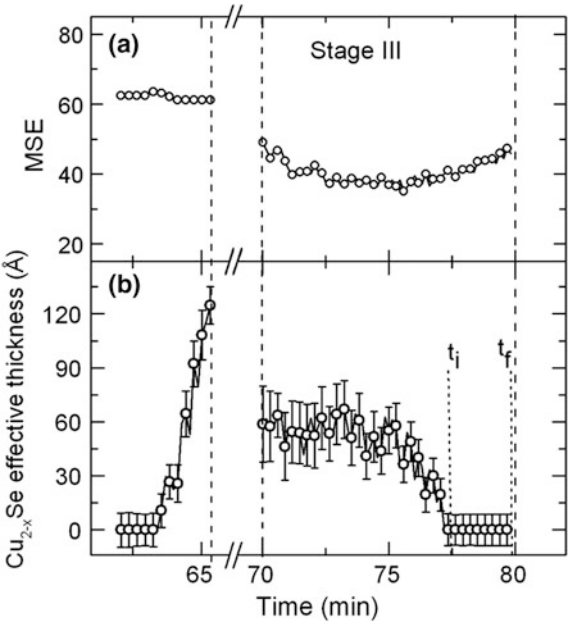


Fig. 6.23 Time evolution of the **a** MSE and **b** effective thickness of $Cu_{2-x}Se$ that develops at the CIGS surface near the stage II endpoint and converted to CIGS during stage III. These results are relevant for the 2.2 μm thick CIGS absorber layer in the deposition process with substrate shuttering between the stages. The effective thickness in (**b**) is the volume of $Cu_{2-x}Se$ per area of the substrate, or the product of the thickness and $Cu_{2-x}Se$ volume fraction associated with the surface layer. The bulk thickness values obtained at time points t_i and t_f can be used to approximate the Cu composition y in $Cu_yIn_{1-x}Ga_xSe_2$. The estimated y value obtained for this sample is 0.96, assuming a uniform distribution throughout the thickness of the final CIGS layer. The vertical broken lines extending across the panels indicate the ends of stages II and III and just before the start of stage III, defined by shutter opening in accordance with Fig. 6.11 [8]

Fig. 6.23, from 125 to 60 Å, while the shutter is closed indicating that the surface $Cu_{2-x}Se$ penetrates the grain boundaries. Second, much greater roughening occurs during the stage III for the shuttered process of Fig. 6.11, indicating enhanced grain growth. This is likely to be beneficial since a larger grain size within the CIGS is expected to enhance the cell performance due to the reduction of recombination.

Figure 6.25 serves as a summary of the instantaneous deposition rates for the CIGS film of Fig. 6.11 using the shutters between stages, presented here as a companion figure to the summary of the bulk and surface roughness layer thicknesses in Fig. 6.24 for the same deposition [8]. The deposition rates in Fig. 6.25 are given in terms of bulk layer thickness. This figure shows stabilization to a well-defined deposition rate during IGS growth in stage I, whereas the rates tend to increase as a function of time during IGS to CIGS conversion in stage II and during $Cu_{2-x}Se$ to CIGS conversion in stage III. Averages of the rates over the time periods designated by the arrows are also given in Fig. 6.25. In principle, the deposition rates in terms of effective thickness can be applied to quantify fluxes of In+Ga and Cu at the surface if one knows the phase composition and crystal structure. Such calculations would be challenging, given the complicated phase structure and microstructures of the samples, and are beyond the scope of this review.

6.3.7 *Thin CIGS in Shuttered Process: Summary*

A reduction in the absorber layer thickness without an accompanying loss of solar cell performance is important in CIGS technology owing to the potential for increasing the throughput in module manufacturing while decreasing the cost of materials [29]. For the study described in this section, the thickness of the CIGS film was reduced to 0.3 μm, which is significantly lower in comparison with the typical 2–3 μm thickness for the absorber layer used in conventional CIGS solar cells. The choice of CIGS layer thickness in general represents a compromise between a lower cost process and a reduced performance solar cell. As the thickness is reduced, all solar cell performance parameters are observed to decrease as indicated in Table 6.1 for the deposition of this review.

The complex dielectric function database for IGS and CIGS used in real time SE analysis of the CIGS layer 0.3 μm in thickness was the same as that used for the corresponding analyses of the CIGS layers ~2.7 and ~2.2 μm in thickness as described in previous sections [7, 8]. The EDS analysis of the thin CIGS absorber layer was performed ex situ after the deposition process, yielding the composition of $x = [Ga]/\{[In] + [Ga]\} = 0.31$. This is closer to the intended value most likely due to the penetration of electrons throughout the CIGS layer thickness in the EDS analysis. Based on this composition, the IGS and CIGS database dielectric functions for $x = 0.31$ are selected for this analysis. The dielectric function for $Cu_{2-x}Se$ used in the real time SE analysis for thin CIGS deposition is the same as that used in analyses for thicker CIGS, and the dielectric function for Mo is obtained from a corresponding analysis of the glass/Mo substrate used for the thin CIGS deposition.

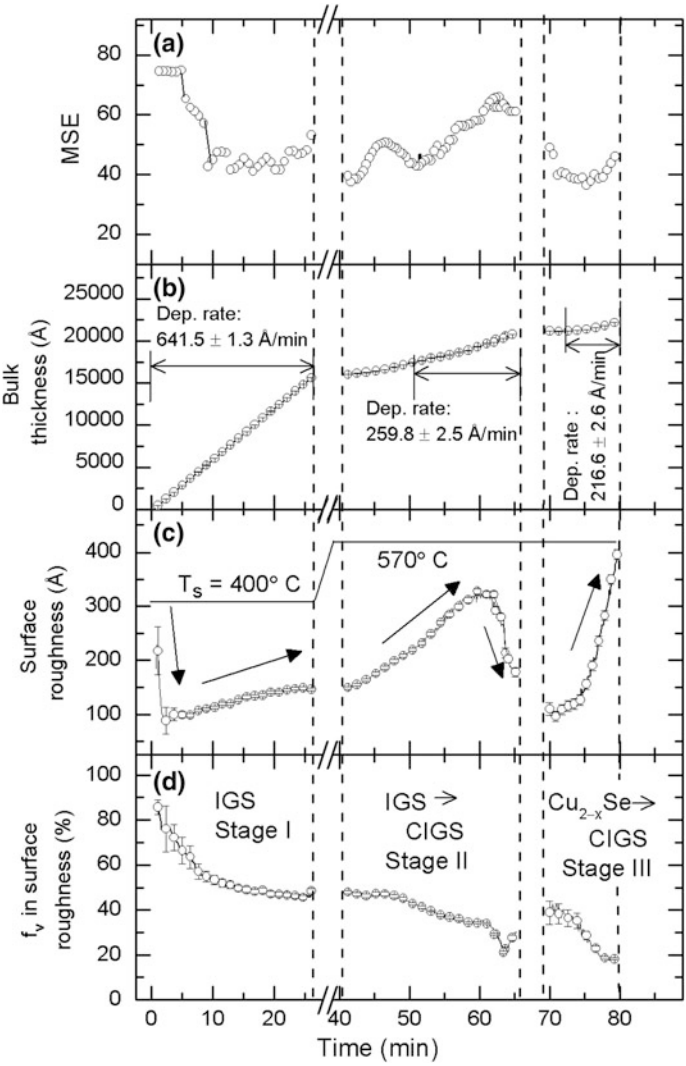


Fig. 6.24 Summary of real time SE analysis results for the 2.2 μm thick CIGS film during deposition by three-stage coevaporation using a process in which a substrate shutter is closed between the stages. The individual panels include the time evolution of the **a** MSE; **b** thickness of the bulk layer; **c** thickness of the surface roughness layer; and **d** void volume percentage within the surface roughness layer. The substrate temperature profile is shown in (**c**) at the top. Upward and downward arrows in (**c**) highlight surface roughening and smoothening processes. The vertical broken lines indicate the start and end of the stages in accordance with Fig. 6.11, with the exception of the vertical line near 70 min, which indicates the opening of the shutter before the start of stage III [8]

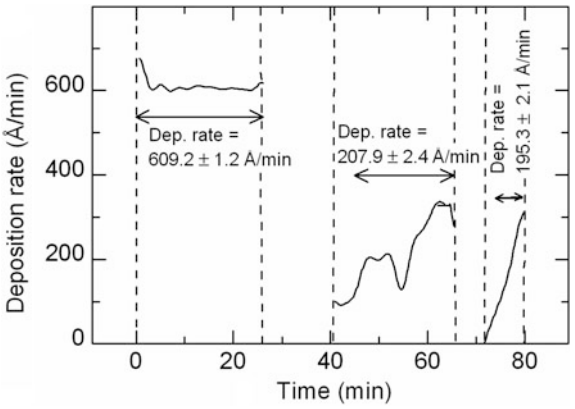


Fig. 6.25 Instantaneous deposition rates presented in terms of bulk layer thickness obtained from an analysis of real time SE data collected during the three stages of the CIGS deposition of Fig. 6.24. The values presented are obtained as an average of the rate over the time periods indicated by the arrows. The vertical broken lines indicate the stage transitions as in Fig. 6.11 [8]

Accompanying the absorber layer thickness reduction to 0.3 μm is the challenge associated with fabrication, especially in regard to the complicated three-stage process used for the CIGS films. As a result, the process in which the substrate shutter is closed between stages as indicated in Fig. 6.12 must be used. Thus, many features observed for this thin absorber layer are comparable to those observed in Figs. 6.22 through 6.25 for the 2.2 μm thick CIGS of the shuttered process with the difference simply being in the various layer thicknesses. At a thickness of 0.3 μm, however, the structural evolution of the bulk CIGS continues is found to be strongly influenced by the rough Mo substrate, as indicated by the smoothening process depicted later in this subsection. As a result, the grain size for this thin absorber is expected to be smaller than that for a conventional thickness absorber.

The conversion of the IGS layer to CIGS during the stage II process and the development of $Cu_{2-x}Se$ near the stage II endpoint are both observable in the results for the deposition of the thin CIGS absorber. These results are presented in Figs. 6.26 and 6.27, respectively, which can be compared to those for the ~2.2 μm thick CIGS in Figs. 6.22 and 6.23 [7, 8]. In Fig. 6.27, the $Cu_{2-x}Se$ that develops on the surface is very thin, reaching a maximum effective thickness of ~18 Å. This maximum thickness appears to evolve on the surface only as a result of annealing when the shutter is open. In Fig. 6.27, as in Fig. 6.23 for the thick CIGS deposition, the time point t_i at which the $Cu_{2-x}Se$ effective thickness reaches zero in stage III is assumed to represent stoichiometric CIGS with $y = [Cu]/\{[In] + [Ga]\} = 1$. For the thin CIGS of Fig. 6.27, the CIGS effective thickness at time points t_i and t_f can be used to obtain the Cu ratio y of the final CIGS film. The y value determined by applying this technique for the thin CIGS deposition is 0.93. An EDS analysis yielded $y = [Cu]/\{[In] + [Ga]\} = 0.89$, however, as performed on the thin layer ex situ after completion of the deposition. The difference in this case is smaller than that observed for the 2.2 μm thick CIGS, an observation that may be attributed to weaker effects of depth non-uniformities on EDS measurements for thinner CIGS.

Summary analysis results presented in Fig. 6.28 for the 0.3 μm CIGS film are analogous to the results for the 2.2 μm thick CIGS film in Fig. 6.24 [7, 8].

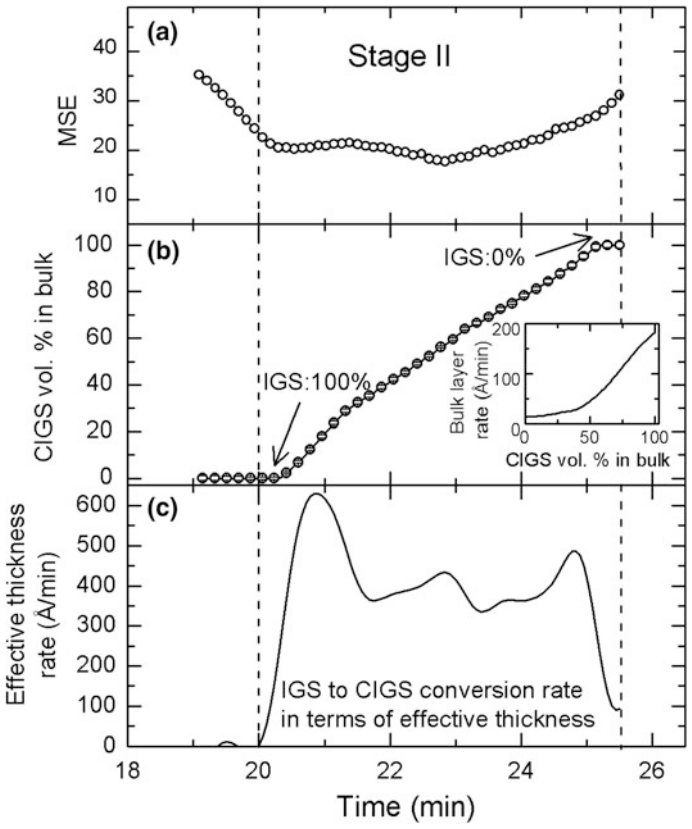


Fig. 6.26 Conversion of IGS to CIGS during stage II growth for the 0.3 μm thick CIGS layer deposited in the process of Fig. 6.12 in which a substrate shutter is closed between the stages. The individual panels include the time evolution of the **a** MSE; **b** CIGS volume percent within the bulk layer that quantifies conversion of IGS to CIGS; **c** the IGS to CIGS conversion rate in terms of the effective thickness including interface, bulk, and surface layer contributions. The inset shows the growth rate in terms of bulk thickness plotted as a function of CIGS volume percent within the bulk layer. The vertical broken lines indicate the start of the Cu flux at the onset of stage II and the Cu-poor to Cu-rich transition in accordance with Fig. 6.12 [8]

Figure 6.28a–d show the evolution of the MSE, the thickness of the bulk layer, the thickness of the surface roughness layer, and the void volume percent within the latter layer, respectively. The similarities with the 2.2 μm CIGS growth process include the clear indications of grain growth during IGS to CIGS conversion in stage II and during $Cu_{2-x}Se$ to CIGS conversion in stage III. The roughness layer thicknesses reached in the grain growth processes for thin CIGS, ~170–180 Å in Fig. 6.28, are much smaller than those reached for thick CIGS ~300–400 Å in Fig. 6.24, suggesting weaker grain growth processes for thin CIGS. Also for the thin CIGS, only weak densification of the substrate-induced voids in the surface

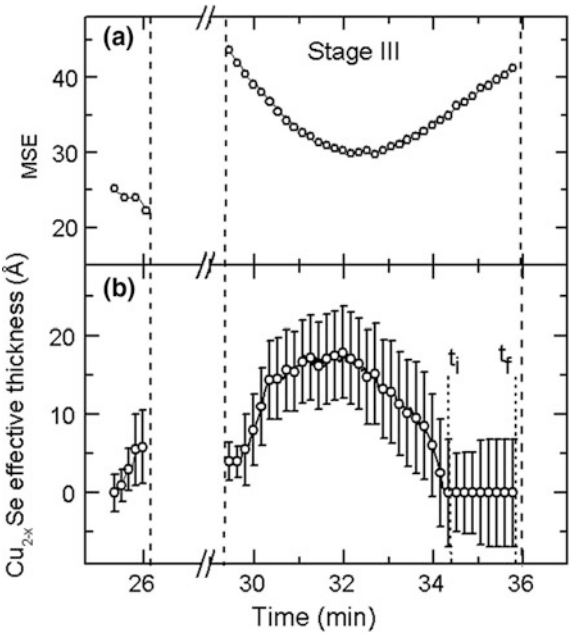


Fig. 6.27 Time evolution of the **a** MSE and **b** effective thickness of $Cu_{2-x}Se$ at the CIGS surface developing near the stage II endpoint and appearing throughout much of stage III. These results are characteristic of a 0.3 μm thick CIGS absorber layer deposited in the process of Fig. 6.12 in which a substrate shutter is closed between the stages. The effective thickness in (**b**) is the $Cu_{2-x}Se$ volume per unit substrate area, or the product of the thickness and the $Cu_{2-x}Se$ volume fraction associated with the surface layer. The bulk thickness values obtained at time points t_i and t_f can be used to approximate the Cu composition y in $Cu_yIn_{1-x}Ga_xSe_2$. The estimated composition y obtained for this sample is 0.93, assuming a uniform distribution throughout the thickness of the final CIGS layer. The left and right vertical broken lines extending across the two panels indicate the stage II and III endpoints, respectively. At the vertical line near 29 min, the shutter is opened upon termination of Cu flux before the start of stage III, in accordance with the time scale of Fig. 6.12 [8]

occurs during stage I. As a result, rapid densification occurs during IGS to CIGS conversion which suppresses the increase in the thickness of the bulk layer in the conversion process. In fact, the results in Fig. 6.28 suggest that for 0.3 μm thick CIGS, the structure of the final bulk film is influenced by the surface roughness on the Mo since the CIGS film thickness is only a factor of ~10 times larger than the thickness of the roughness layer on the underlying Mo.

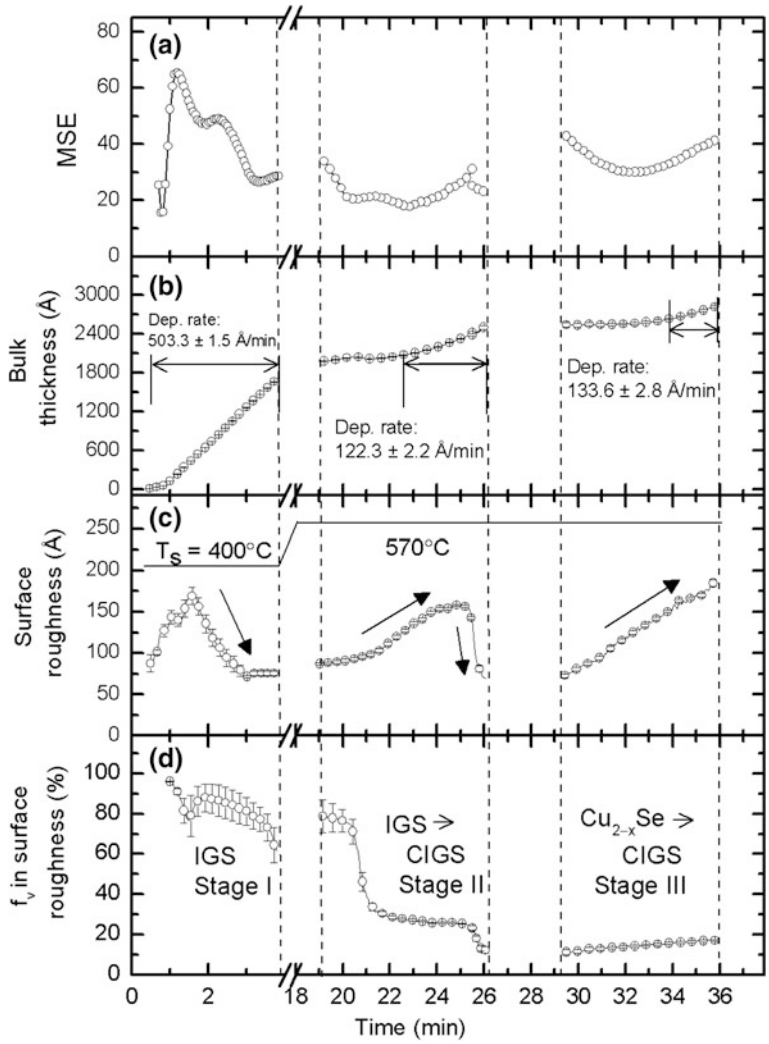


Fig. 6.28 Summary of real time SE analysis results for the CIGS film 0.3 μm in thickness during deposition by three-stage coevaporation using the process of Fig. 6.12 in which a substrate shutter is closed between the stages. The individual panels include the time evolution of the **a** MSE; **b** thickness of the bulk layer; **c** thickness of the surface roughness layer; and **d** void content in volume percent within the surface roughness layer. The substrate temperature profile is shown in (**c**) at the top. Upward and downward arrows in (**c**) highlight surface roughening and smoothening processes. The vertical broken lines indicate the start and end of the stages in accordance with Fig. 6.12, with the exception of the vertical line near 29 min, which indicates shutter opening before initiation of the In+Ga flux in stage III [8]

6.4 Issues in Real-Time Monitoring and Control

In this section, features are explored in the (ψ, Δ) values when plotted versus time during three-stage deposition of CIGS that may enable instantaneous feedback and control over the process without in-depth real time SE data analysis. In the initial investigation, a CIGS layer ~0.7 μm in thickness was deposited onto a substrate consisting of a crystalline silicon (c-Si) wafer. The continuous deposition process of Fig. 6.10 was applied without substrate shuttering [5]. The corresponding process has also been investigated here for the deposition of a CIGS film ~2.0 μm in thickness on an optically-opaque Mo film deposited onto soda lime glass, i.e. in the multilayer configuration used in solar cells.

Figure 6.29 shows the (ψ, Δ) values and their derivatives plotted versus time for the ~0.7 μm thick CIGS layer deposited on c-Si by continuous three-stage coevaporation [5]. In this figure, the stage II transition from Cu-poor to Cu-rich CIGS and the stage III transition from Cu-rich to Cu-poor CIGS are presented on an expanded time scale. From the complete spectra in (ψ, Δ), three photon energies are selected including pairs below the CIGS bandgap (0.735 eV), above the gap (1.997 eV), and well above the gap (5.697 eV). For the data in ψ acquired at 1.997 eV, a clear maximum is observed at $t = 48$ min, which corresponds to the stoichiometric CIGS composition, and immediately after this maximum an abrupt decrease is observed. Upon observation of this turning point in ψ, a waiting time of $\Delta t_1 \sim 60$ s (for $47.9 < t < 48.9$ min) is initiated during which the coevaporation of Cu and Se continues prior to the stage II endpoint. This waiting time results in the desired Cu-rich region of the CIGS film surface. A similarly abrupt turning point in ψ acquired at 1.997 eV is evident at $t = 56.3$ min, also corresponding to the stoichiometric CIGS composition. Upon identification of this turning point, an additional waiting time of $\Delta t_2 \sim 45$ s ($56.3 < t < 57.1$ min) for In, Ga, and Se coevaporation yields the desired Cu-poor CIGS at the stage III endpoint. In fact, the second waiting time produces an optimum CIGS absorber material applicable for devices, having a Cu content of ~22 at.% or $y = 0.88$ as determined post-deposition by ex situ EDS and AES. For CIGS growth on c-Si wafers in Fig. 6.29, the features in $\psi(t)$, indicative of the transitions in the near surface composition, are enhanced by tracking the derivative of ψ with respect to time. Enhanced features in $d\psi/dt$ occur for different photon energies, as exemplified by the results acquired at 1.997 eV. It should be pointed out that similar variations are exhibited in the angle $\Delta(t)$ and its time derivative; however, its high sensitivity to surface roughness implies that Δ is less useful for detecting the near surface transitions in CIGS Cu content. Finally, discontinuities in Δ can arise from angular quadrant corrections associated with changes in layer thickness that also imply less utility of Δ in monitoring applications.

Figure 6.30 shows a corresponding evaluation of the transitions analogous to that of Fig. 6.29, but for the ~2 μm thick CIGS film in the solar cell structure deposited on Mo [5]. The predominant differences in the variations of $\psi(t)$ in Fig. 6.30 relative to those in Fig. 6.29 arise due to the thicker surface roughness

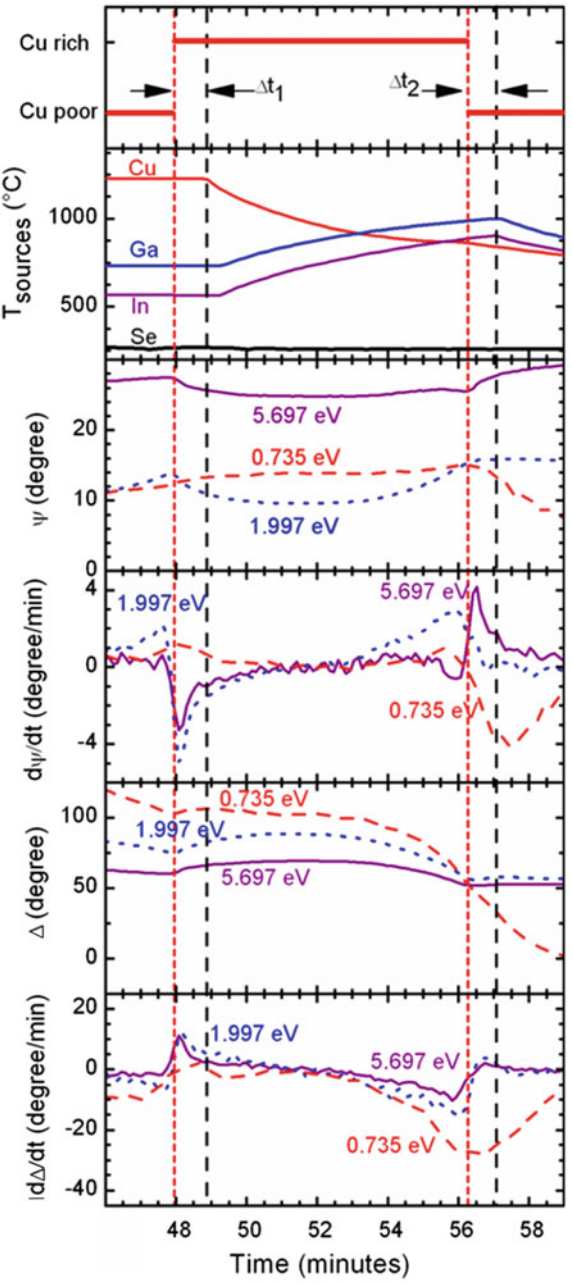


Fig. 6.29 Source temperatures and real time SE data in the ellipsometry angles (ψ, Δ) measured during three-stage coevaporation of a CIGS film ~0.7 μm in thickness on a c-Si substrate in a continuous process without substrate shuttering. The endpoints of stages II and III are shown here by long-dashed vertical lines. Short-dashed lines denote the transition from Cu-poor to Cu-rich CIGS (~47.9 min) and the transition from Cu-rich to Cu-poor CIGS (~56.3 min) as established by real time SE measurements [5]

layer for the deposition on Mo. The more extensive surface roughness of strongly absorbing CIGS contributes to the challenges in interpreting the behavior of (ψ, Δ) at photon energies above the band gap of CIGS. Here the variations in the much

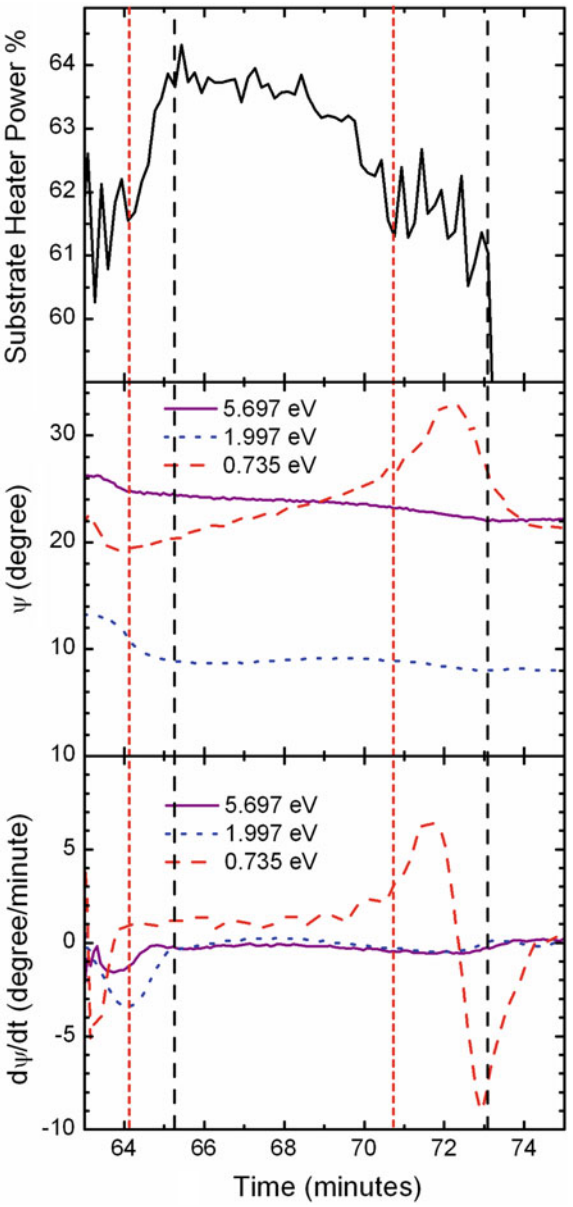


Fig. 6.30 Real time SE data obtained during three-stage coevaporation of a CIGS film ~2 μm in thickness on a substrate consisting of soda lime glass coated with optically-opaque molybdenum. The data in the ellipsometry angle ψ along with its derivative $d\psi/dt$ are presented for comparison with the relative power supplied to the substrate heater, as an indirect measure of substrate/film emissivity. The endpoints of stages II and III are shown here by long-dashed vertical lines. Short-dashed lines denote the transitions from Cu-poor to Cu-rich CIGS (~64 min) and from Cu-rich to Cu-poor (~71 min) based on the trend in the substrate heater power [5]

larger surface roughness layer thickness and the transitions in phase composition affect the (ψ, Δ) evolution simultaneously. As a result, one must focus on the real time SE data at low photon energies below the band gap to pinpoint the transitions of interest solely from the real time $\psi(t)$ data. The strong absorption of $Cu_{2-x}Se$ (with absorption coefficient $\alpha > 3 \times 10^5$ cm^{-1}) below the band gap of CIGS

generates a change in $\psi(t)$ sufficient for detection of the transitions. Basically, as more heavily absorbing $Cu_{2-x}Se$ accumulates on the surface of the CIGS bulk layer, the interference fringe pattern associated with this layer will shift in photon energy and the pattern envelope will dampen in amplitude.

Even when a thick roughness layer exists on the CIGS surface, the time evolution of the real time SE data in ψ exhibit features at the transitions from Cu-poor to Cu-rich CIGS and from Cu-rich to Cu-poor CIGS. These transitions can be identified with greater sensitivity from the time derivative $d\psi/dt$ in Fig. 6.30 [5]. For photon energies lower than the band gap of CIGS, the suppression and enhancement of optical interference amplitudes associated with the growing bulk layer pinpoints the two transitions. Considering the evolution of $d\psi/dt$, the sequence of two transitions generates a decrease in oscillations of the derivative toward zero and an increase in these oscillations above zero. The large changes in $d\psi/dt$ after the Cu-rich to Cu-poor transition near 71 min are generated by the interference fringe shift caused simply by an increase in the CIGS bulk layer thickness in the Cu-poor stage of film growth. The times associated with these optically detected transitions correlate with those at which variations in the substrate heater power occur, as shown in Fig. 6.30 (top panel). The indirect measurement of film surface emissivity through the heater power could not be applied to the deposition on the c-Si wafer substrate in Fig. 6.29 due to the thin CIGS layer and the thermal characteristics of the substrate. The results in Fig. 6.30 demonstrate the application of real time SE as a process monitor as well as for process control of three-stage CIGS deposition. This capability has been used to supplement the conventional approaches, and because of the enhanced information content provided by in-depth real time SE analysis, ultimately it may be used in the future to replace the conventional approaches [30].

6.5 Summary

Real time SE has been implemented for in situ analysis and monitoring of the three coevaporation stages applied in optimized deposition processes for $CuIn_{1-x}Ga_xSe_2$ (CIGS) thin films. These films are employed as absorber layer components incorporated into high efficiency CIGS photovoltaic devices [5–8]. Stage I of the deposition process entails coevaporation of In, Ga, and Se onto an opaque Mo-coated soda lime glass substrate held at a temperature of ~400 °C, yielding an $(In_{1-x}Ga_x)_2Se_3$ (IGS) thin film. From real time SE, the evolution of the structure of the IGS film in terms of the thicknesses of the bulk and surface roughness layers can be determined as well as the final composition of the IGS film. During stage II, coevaporation of Cu and Se converts the IGS film to CIGS. A model of uniform conversion throughout the bulk layer is substantiated for analysis of the real time SE data in stage II, resulting in time dependent and average conversion rates of IGS to CIGS in terms of layer thickness and component volume percentages. Before the stage II endpoint, the formation of a $Cu_{2-x}Se$ layer on the CIGS surface can be

observed by real time SE and tracked in terms of its effective thickness or volume per substrate area and its rate of development. The $Cu_{2-x}Se$ effective thickness at the surface of the CIGS film is determined over a time interval extending from the stage II endpoint and through much of stage III. In this stage III, the Cu-rich CIGS film and the $Cu_{2-x}Se$ at the surface are converted through the coevaporation of In, Ga, and Se to a CIGS film that is slightly Cu-poor. Real time SE can be used to identify the transition from Cu-rich to Cu-poor CIGS. Results for a continuous process of CIGS deposition in which a substrate shutter is opened/closed only at the start/end of the entire three-stage deposition are compared with results in which the shutter is used additionally to separate the stages. Detailed differences in the real time SE analysis results for the two processes suggest possible reasons for the improved solar cell performance when shuttering is performed between stages.

The three stages of the coevaporation process have been investigated in detail by applying real time SE to the fabrication of ~2.2 and ~0.3 μm thick CIGS absorber layers using a substrate shutter between stages. This analysis technique enables detailed comparison of the general features of the structural evolution, including grain growth and coalescence processes. Because real time SE enables determination of the IGS thickness and characterization of the phase conversions from IGS to CIGS and from $Cu_{2-x}Se$ to CIGS during the CIGS growth process, the analysis technique is shown to be capable of detecting the desired coevaporation endpoint in each of the three stages. Thus, this endpoint detection capability can be applied during the fabrication of the thin film absorber layer component for CIGS solar cells to complement previously-developed techniques. These techniques include electron impact emission spectroscopy (EIES) for measuring the elemental fluxes as well as pyrometry or substrate heater power monitoring for respective direct or indirect measurements of the emissivity of the film surface. The dielectric functions of the bulk IGS and CIGS layers, obtained from the real time SE analysis can provide further compositional fingerprints as well as compositional depth profiles assuming that an adequate database exists. Such a database has been developed for IGS as well as for CIGS and $Cu_{2-x}Se$ in previous work reviewed here. The composition analysis capabilities need further expansion and evaluation in future investigations.

The unprocessed data obtained by real time SE has been applied as well to follow the transitions between Cu-rich and Cu-poor states of the CIGS film surface in stages II and III of CIGS coevaporation [5]. Such an application is of interest if one seeks instantaneous feedback. In fact, variations in the amount of $Cu_{2-x}Se$ on the CIGS film surface can be inferred not only from an in-depth analysis of (ψ, Δ) spectra versus time, but also directly from the time evolution of the ellipsometry angle ψ. Here the sensitivity of $\psi(t)$ to the phase transition times was demonstrated for CIGS layers deposited on c-Si wafers and on Mo-coated glass. These transition times obtained from $\psi(t)$ correlate well with those from conventional indirect measurements of the emissivity of the substrate/film. Thus, real time SE has been demonstrated as a monitor of the presence of $Cu_{2-x}Se$ on the CIGS surface and the phase transitions that CIGS absorbers undergo during three-stage coevaporation, both in test configurations and in the solar cell device configuration. The capabilities of this non-destructive, high speed thin film analysis technique are

demonstrated for complementing or replacing existing monitoring and control techniques conventionally required for multi-stage coevaporation of CIGS in laboratory and industry applications. As a result, the technique provides insights enabling the optimization of materials and device structures as well as guidance enabling process control so that desired materials and device specifications can be met.

In final summary, it has been demonstrated in this chapter that in situ real time SE combines high thickness, phase, and compositional sensitivity with fast non-invasive data acquisition, thus providing unique insights into the dynamics of CIGS film growth. The information extracted from real time SE includes the time evolution of thicknesses that characterize bulk and surface roughness layers, as well as the evolution of the phase composition of the layers. From this information, a better understanding of the CIGS growth process throughout the three stages of deposition can be obtained. Although the results of this real time SE analysis are found to be consistent with models proposed previously, real time SE provides insights into the origins of variations in cell performance that may occur due to variations in processing. This in-depth understanding can assist in evaluating the fabrication process and thus in further enhancing the performance of optimized thin film solar cells.

References

1. W.N. Shafarman, S. Siebentritt, L. Stolt, in *Handbook of Photovoltaic Science and Engineering*, 2nd edn., ed. by A. Luque, S. Hegedus (Wiley, New York, NY, 2011), Chapter 13, pp. 546–599
2. P. Jackson, R. Wuerz, D. Hariskos, E. Lotter, W. Witte, M. Powalla, Phys. Stat. Solidi RRL **10**, 583 (2016)
3. P. Jackson, D. Hariskos, R. Wuerz, W. Wischmann, M. Powalla, Phys. Stat. Solidi RRL **9**, 28 (2015)
4. A. Chirilă, P. Reinhard, F. Pianezzi, P. Bloesch, A.R. Uhl, C. Fella, L. Kranz, D. Keller, C. Gretener, H. Hagendorfer, D. Jaeger, R. Erni, S. Nishiwaki, S. Buecheler, A.N. Tiwari, Nat. Mater. **12**, 1107 (2013)
5. D. Attygalle, V. Ranjan, P. Aryal, P. Pradhan, S. Marsillac, N.J. Podraza, R.W. Collins, IEEE J. Photovolt. **3**, 375 (2012)
6. P. Pradhan, D. Attygalle, P. Aryal, N.J. Podraza, A.S. Ferlauto, S. Marsillac, R.W. Collins, in *Proceedings of the 39th IEEE Photovoltaic Specialists Conference*, Tampa, FL, 16–21 June 2013 (IEEE, New York, NY, 2013), pp. 414–419
7. P. Pradhan, P. Aryal, A.-R. Ibdah, K. Aryal, J. Li, N.J. Podraza, S. Marsillac, R.W. Collins, in *Proceedings of the 40th IEEE Photovoltaic Specialists Conference*, Denver, CO, 8–13 June 2014 (IEEE, New York, NY, 2014), pp. 2060–2065
8. P. Pradhan, *Real Time Spectroscopic Ellipsometry Analysis of the Three Stages of* $Cu(In_{1-x}Ga_x)Se_2$ *Co-evaporation*. Ph.D. Dissertation, (University of Toledo, Toledo, OH, 2017)
9. J. Abu-Shama, R. Noufi, Y. Yan, K. Jones, B. Keyes, P. Dippo, M. Romero, M. Al-Jassim, J. Alleman, D.L. Williamson, in *II–VI Compound Semiconductor Photovoltaic Materials, Materials Research Society Symposium Proceedings*, vol. 668, ed. by R. Birkmire, R. Noufi, D. Lincot, H.-W. Schock (MRS, Warrendale, PA, 2001), Symposium H; H.7.2, pp. 1–6

10. A.M. Gabor, J.R. Tuttle, M.H. Bode, A. Franz, A.L. Tennant, M.A. Contreras, R. Noufi, D.G. Jensen, A.M. Hermann, Sol. Energy Mater. Sol. Cells **41–42**, 247 (1996)
11. S. Marsillac, R.W. Collins, in *Physics, Simulation, and Photonic Engineering of Photovoltaic Devices*, San Francisco, CA, 23–26 January 2012, Conference Proceedings of SPIE, vol. 8256, ed. by A. Freundlich, J.-F.F. Guillemoles (SPIE, Bellingham, WA, 2012), Art. No. 825613, pp. 1–11
12. J. Li, R.W. Collins, M.N. Sestak, P. Koirala, N.J. Podraza, S. Marsillac, A.A. Rockett, in *Advanced Characterization Techniques for Thin Film Solar Cells*, 2nd edn., ed. by D. Abou-Ras, T. Kirchartz, U. Rau (Wiley-VCH, Weinheim, Germany, 2016), Chapter 9, pp. 215–256
13. J.D. Walker, H. Khatri, V. Ranjan, S. Little, R. Zartman, R.W. Collins, S. Marsillac, in *Proceedings of the 34th IEEE Photovoltaic Specialists Conference*, Philadelphia, PA, 7–12 June 2009 (IEEE, New York, NY, 2009), pp. 1154–1156
14. S. Marsillac, V. Ranjan, S. Little, R.W. Collins, in *Proceedings of the 35th IEEE Photovoltaic Specialists Conference*, Honolulu, HI, 20–25 June 2010 (IEEE, New York, NY, 2010), pp. 866–868
15. P. Aryal, A.-R. Ibdah, P. Pradhan, D. Attygalle, P. Koirala, N.J. Podraza, S. Marsillac, R.W. Collins, J. Li, Prog. Photovolt.: Res. Appl. **24**, 1200 (2016)
16. Y. Cong, I. An, K. Vedam, R.W. Collins, Appl. Opt. **21**, 2692 (1991)
17. I. An, Y.M. Li, H.V. Nguyen, C.R. Wronski, R.W. Collins, Appl. Phys. Lett. **59**, 2543 (1991)
18. B. Johs, J.S. Hale, Phys. Stat. Solidi (a) **205**, 715 (2008)
19. H. Fujiwara, J. Koh, P.I. Rovira, R.W. Collins, Phys. Rev. B **61**, 10832 (2000)
20. J. Li, J. Chen, J.A. Zapien, N.J. Podraza, C. Chen, J. Drayton, A. Vasko, A. Gupta, S.L. Wang, R.W. Collins, A.D. Compaan, in *Thin-film Compound Semiconductor Photovoltaics*, *Materials Research Society Symposium Proceedings*, vol. 865, ed. by W. Shafarman, T. Gessert, S. Niki, S. Siebentritt (MRS, Warrendale, PA, 2005), Symposium F; F1.2.1, pp. 9–14
21. J. Li, J. Chen, M.N. Sestak, R.W. Collins, IEEE J. Photovolt. **1**, 187 (2011)
22. T. Begou, J.D. Walker, D. Attygalle, V. Ranjan, R.W. Collins, S. Marsillac, Phys. Stat. Solidi RRL **5**, 217 (2011)
23. J.D. Walker, H. Khatri, V. Ranjan, J. Li, R.W. Collins, S. Marsillac, Appl. Phys. Lett. **94**, 141908 (2009)
24. J. Koh, A.S. Ferlauto, P.I. Rovira, R.J. Koval, C.R. Wronski, R.W. Collins, Appl. Phys. Lett. **75**, 2286 (1999)
25. J.D. Walker, H. Khatri, S. Little, V. Ranjan, R. Collins, S. Marsillac, in *Photovoltaic Materials and Manufacturing Issues II*, *Materials Research Society Symposium Proceedings*, vol. 1210, ed. by B. Sopori, J. Yang, T. Surek, B. Dimmler (MRS, Warrendale, PA, 2009), Symposium Q; Q06-02, pp. 159–164
26. D.I. Chakrabarti, D.E. Laughlin, Bull. Alloy Phase Diagr. **2**, 305 (1981)
27. V.M. Glazov, A.S. Pashinkin, V.A. Fedorov, Inorg. Mater. **36**, 641 (2000)
28. P. Aryal, *Optical and Photovoltaic Properties of Copper Indium-gallium Diselenide Materials and Solar Cells*. Ph.D. Dissertation, (University of Toledo, Toledo, OH, 2014)
29. S. Marsillac, V. Ranjan, K. Aryal, S. Little, Y. Erkaya, G. Rajan, P. Boland, D. Attygalle, P. Aryal, P. Pradhan, R.W. Collins, in *Proceedings of the 38th IEEE Photovoltaic Specialists Conference*, Austin, TX, 3–8 June 2012 (IEEE, New York NY, 2012), pp. 1492–1494
30. J. Li, M. Contreras, J. Scharf, M. Young, T.E. Furtak, R. Noufi, D. Levi, in *Proceedings of the 39th IEEE Photovoltaic Specialists Conference*, Tampa, FL, 16–21 June 2013 (IEEE, New York, NY, 2013), pp. 2609–2611

Chapter 7
Real Time and Mapping Spectroscopic Ellipsometry of Hydrogenated Amorphous and Nanocrystalline Si Solar Cells



Zhiquan Huang, Lila R. Dahal, Sylvain Marsillac, Nikolas J. Podraza and Robert W. Collins

Abstract Real time spectroscopic ellipsometry (SE) has been applied to characterize the structural evolution and optical properties of the critical *p*-type doped and intrinsic hydrogenated silicon (Si:H) layers that comprise the nanocrystalline Si:H bottom cell of tandem photovoltaic (PV) devices. The tandem PV devices under study are fabricated in the amorphous/nanocrystalline Si:H (*a*-Si:H/*nc*-Si:H) *p-i-n* superstrate configuration in which the *nc*-Si:H cell is at the bottom of the device structure due to its narrower bandgap relative to that of the top cell *a*-Si:H. SE data collected in real time during Si:H solar cell fabrication by plasma enhanced chemical vapor deposition (PECVD) enable identification of Si crystallite development in the bottom cell *p* and *i*-layers through the evolution of surface roughness, as well as through variations in the optical properties in the form of the complex dielectric function $(\varepsilon = \varepsilon_1 - i\varepsilon_2)$. Analysis of the dielectric function permits quantification of the relative amounts of the *a*-Si-H and *nc*-Si-H components that exist during the growth of mixed-phase Si:H layers. Based on these real time SE analysis results, a PECVD growth evolution diagram has been developed for the bottom cell *i*-layer of the tandem PV cell in order to guide fabrication in this device configuration. Correlations between the *p* and *i*-layer structures and device performance are evident and can be understood on the basis of the growth evolution diagram. A second growth evolution diagram has been developed to characterize PECVD of *n*-type Si-H thin films for use as the *n*-layer component of *p-i-n a*-Si:H top cells in the same superstrate configuration. This growth evolution diagram has been established to provide guidance for PECVD of the *n*-layers over the 15 cm × 15 cm areas of glass/TCO/*p*/*i* superstrates, where TCO represents the transparent conducting oxide layer serving as the topmost contact. The goal of this study is to

Z. Huang · L. R. Dahal · N. J. Podraza (✉) · R. W. Collins
Department of Physics & Astronomy and Center for Photovoltaics Innovation & Commercialization, University of Toledo, Toledo, OH 43606, USA
e-mail: Nikolas.Podraza@utoledo.edu

S. Marsillac
Virginia Institute of Photovoltaics, Old Dominion University, Norfolk, VA 23529, USA

© Springer International Publishing AG, part of Springer Nature 2018

H. Fujiwara and R. W. Collins (eds.), *Spectroscopic Ellipsometry for Photovoltaics*, Springer Series in Optical Sciences 214,
https://doi.org/10.1007/978-3-319-95138-6_7

correlate the structural characteristics provided by the diagram with the performance parameters of single-junction *a*-Si:H solar cells that can serve as the top cell of the tandem device. A 16 × 16 array of *p-i-n* dot cells has been fabricated over the 15 cm × 15 cm area of the TCO coated glass superstrate, and this same area has been studied by mapping SE. Analysis of the SE data collected over the full area provides maps of the *p*-layer effective thickness, *i*-layer thickness and bandgap, and *n*-layer thickness and nanocrystalline volume fraction for spatial correlation with the performance parameters from current density-voltage (*J-V*) measurements of the 16 × 16 array of dot cells. The goal of the correlations that exploit mapping SE is to identify and understand the relationships between the variations in the basic materials properties and in the thin film solar cell performance over large areas. The results also enable analysis of the impacts of spatial non-uniformities on PV module performance.

7.1 Introduction and Overview

Hydrogenated amorphous silicon (*a*-Si:H) and hydrogenated nanocrystalline silicon (*nc*-Si:H) thin films fabricated by plasma enhanced chemical vapor deposition (PECVD) have been studied extensively for photovoltaics (PV) applications over many years [1, 2]. The doped forms of both *a*-Si:H and *nc*-Si:H exhibit high defect concentrations, and as a result, the solar cells based on these materials are fabricated in either *p-i-n* superstrate or *n-i-p* substrate configurations. Due to the lower mobility of holes, the light is passed first through the *p*-type hydrogenated Si (Si:H) (or *p*-layer), which serves as an inactive window layer of the cell in both configurations. As a result, these cells require a very thin Si:H *p*-layer having a wide bandgap in order to reduce collection losses due to absorption of photons in the inactive layer.

Because the accessible range of 1.6–1.8 eV for the *a*-Si:H *i*-layer bandgap is well above the optimum value of ∼1.3–1.4 eV for efficient single junction solar cells, then the highest efficiency Si:H based devices use multijunction configurations. In fact, Si:H thin films have served as the foundation for the first successful multijunction thin film PV technology. The combination of a wider bandgap *a*-Si:H top cell and a narrower bandgap *nc*-Si:H bottom cell better utilizes the solar spectrum and, in addition, reduces the impact of light induced degradation in the *a*-Si:H cell [3–8]. Thus, a common approach for the Si:H multijunction solar cell is the monolithic micromorph tandem, a two terminal device which incorporates top cell *a*-Si:H with a typical bandgap of ∼1.7 eV and bottom cell *nc*-Si:H with a bandgap of 1.1 eV. The grain size for *nc*-Si:H is generally within the range of 50–500 Å; as a result, the bandgap of this material is close to that of single crystal silicon. Because of the much lower absorption coefficient in the *nc*-Si:H *i*-layer, however, a bottom cell *nc*-Si:H *i*-layer much thicker (∼2 μm) than the thin top

cell *a*-Si:H *i*-layer (~0.1 μm) is required for current matching purposes in the *a*-Si:H/*nc*-Si:H tandem. When rigid glass plates are used to support the PV devices, then the tandem cell is most often fabricated in the *p-i-n* sequence and the resulting cell is in the superstrate configuration. In this configuration, the *p*-layer of the structure is deposited first on the transparent conducting oxide (TCO) coated glass surface. The best such devices yield stabilized cell efficiencies ~13% [9]. The single-junction and tandem *p-i-n* solar cell configurations are shown in Fig. 7.1, which provides typical thickness and bandgap values.

The dilution of silane gas by hydrogen in the PECVD process, as described by the flow ratio $R = [H_2]/[SiH_4]$, is key for controlling the microstructure of the Si:H, the volume fractions of *a*-Si:H and *nc*-Si:H phases, as well as their depth profiles in the resulting film [4, 10, 11]. As the H_2 dilution is increased, the tendency increases for nanocrystal nucleation from the growing amorphous phase or directly from the substrate, and the PECVD growth evolution diagram as deduced by real time spectroscopic ellipsometry (SE) describes this tendency quantitatively. The importance of the diagram lies in the fact that the $(a + nc)$ phase composition and its profile strongly affect the solar cell performance. Detailed real time SE studies have shown that the highest performance *a*-Si:H solar cells are obtained when the intrinsic Si:H absorber layer is fabricated with the highest possible H_2 dilution, but without crossing the $a \rightarrow (a + nc)$ transition, not only as a function of dilution

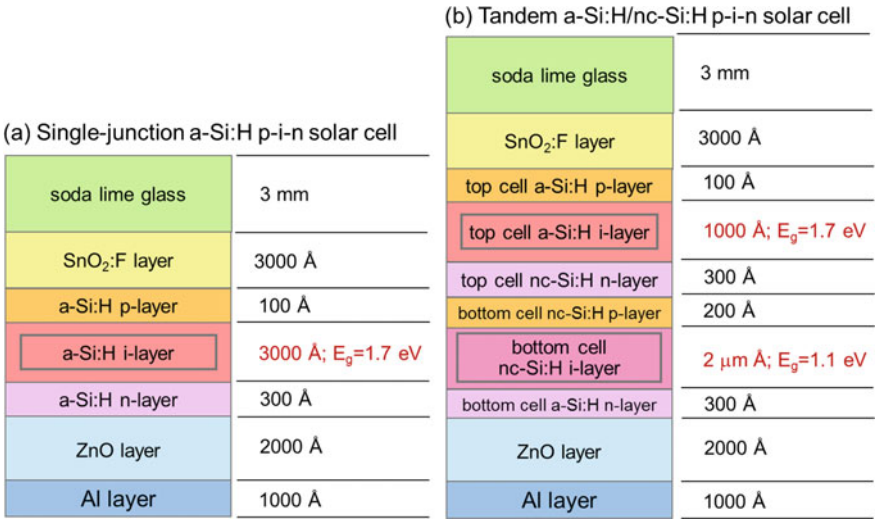


Fig. 7.1 Schematic configurations for single-junction *a*-Si:H and tandem *a*-Si:H/*nc*-Si:H solar cells in the *p-i-n* or superstrate configuration shown on rigid glass. Typical approximate thicknesses are indicated. The solar irradiance enters through the soda lime glass

ratio R in the early nucleation stage, but also as a function of thickness from the start to the end of the deposition of the device layer [11]. This observation is believed to arise from the beneficial effect of atomic H in the gas phase for passivating unstable defects, breaking weak or strained Si–Si bonds, and terminating the resulting dangling bonds. Real time SE studies have also shown that the highest performance intrinsic *nc*-Si:H for devices is obtained at the lowest possible dilution level while avoiding transitions across the $(a + nc) \rightarrow a$ boundary as a function of R and thickness [12]. This observation is believed to arise from the formation of *a*-Si:H at the grain boundaries under conditions close to the phase boundary of the deposition diagram. The *a*-Si:H is expected to passivate the grain boundaries effectively, leading to high performance *nc*-Si:H for devices.

Considering the greater complexity of Si:H based multijunction solar cells and their deposition processes compared to single junction cells, SE methods have been found to be especially useful in device characterization [13]. The abilities to characterize the structure of the films and to distinguish the *a*-Si:H and *nc*-Si:H phases based on the differences in their optical properties are particularly powerful. In this chapter, applications of two different SE methods for Si:H tandem PV technology are presented.

In Sect. 7.2, the application of real time SE will be described for the analysis of the *p* and *i*-layer components of the bottom cell *nc*-Si:H in *a*-Si:H/*nc*-Si:H tandem *p*-*i*-*n* solar cells fabricated on TCO coated glass [14, 15]. SE has been applied from the near-infrared to ultraviolet in situ and in real time during Si:H *p*-*i*-*n* tandem cell growth. The Si:H structure and phase composition characterized on the basis of the surface morphology evolution and the complex dielectric function $(\varepsilon = \varepsilon_1 - i\varepsilon_2)$ have been deduced from the analysis of the real time SE data. This structural information has been correlated with PV device performance parameters, including the open circuit voltage V_{OC}, short circuit current density J_{SC}, fill factor FF, and efficiency η. Correlations between the *p* and *i*-layer characteristics of the *nc*-Si:H bottom cell in tandem devices have been identified in this study. Specifically, the effects of plasma power density on the relative *a*-Si:H and *nc*-Si:H volume fractions in PECVD *p*-layers, H_2 dilution on the phase evolution of *i*-layers, and the impacts of these characteristics on PV performance all have been evaluated in Sect. 7.2 of this chapter.

In the second component of this chapter presented in Sect. 7.3, both real time and mapping SE are described for the optimization of the *n*-layer of the *a*-Si:H *p*-*i*-*n* solar cell used as the top cell of the tandem [15, 16]. In this study, the phase evolution of *n*-type Si:H has been analyzed in situ by real time SE during the PECVD process. In addition, mapping SE over large areas has been applied as well to study the non-uniformity of the component layers, which can be a limiting factor in Si:H module performance. Analysis of SE mapping data provides information on layer thicknesses, structure, and material optical properties. Correlations between local fundamental properties and dot cell performance parameters have been identified and provide information on the optimization of the cell performance.

7.2 Real Time SE for Process Development: Nanocrystalline Si:H in *p-i-n* Tandem Solar Cells

7.2.1 General Strategy and Approaches

It should be noted that the limitations of ex situ SE in characterizing all the layers of a tandem device motivate the need for real time or in-line measurements of the device structure at various stages in the deposition process. In this section, real time SE results will be presented on a *p-i-n* tandem cell fabricated from top/bottom cells with *a*-Si:H/*nc*-Si:H absorber materials [14, 15]. This is a particularly challenging problem because the bottom cell *nc*-Si:H exhibits a dielectric function that evolves with thickness, and so requires advanced real time SE modeling. Application of real time SE enables characterization of each layer based on measurements performed during the layer deposition. Although real time SE data sets are technically difficult to analyze, the large quantity of spectra for the sample in a continuous series of thickness states can lead to well defined solutions. Considerable challenges are encountered in the analysis of real time SE data in the actual device structures as described next.

The first challenge arises because the starting surface from which growth is initiated is inevitably rough, and as a result, the growth process and the associated real time SE analysis involve two stages. In the first stage, the voids in the surface roughness of the underlying material are filled with the depositing material; simultaneously, surface roughness develops associated with the depositing material [17]. In this first stage, no bulk layer of the depositing material is detectable. In the model for the second stage, a stable (unchanging) roughness layer exists at the interface between the underlying and depositing materials, having been filled in with deposited material in the first stage. Also in the second stage, the bulk layer grows continuously between the interface layer and the surface roughness layer of the depositing material.

In the most general models for the two stages of the deposition process, three structural parameters evolve with time during film growth. In the first stage, these include f_{mi}, the content of depositing material within the surface roughness layer of the underlying material; d_s, the surface roughness layer thickness for the depositing material; and f_{vs}, the void content in this latter roughness layer. In the second stage, after the interface composition has stabilized, the structural parameters that evolve with time for the depositing material include d_b, the bulk layer thickness; d_s; and f_{vs}. Based on the assumption that the growing film is uniform with thickness, it is best to extract the dielectric function from real time SE data collected after a thickness of bulk layer such that its properties (rather than those of the surface and interface layers) dominate the data. This analysis uses real time SE data collected at M_2 different sequential times within the second stage, yielding $2M_2N$ (ψ, Δ) values, where N is the number of spectral points [18]. In the analysis, a total of $3M_2 + 2N$ parameters, $3M_2$ structural values and $2N$ dielectric function values, must be deduced. Because $3M_2 + 2N < 2M_2N$ for any reasonable number of time

points, then a solution is possible. The critical assumption is that the dielectric function does not depend on thickness. Such a dependence would lead to a dielectric function depth profile that would invalidate the analysis. Different approaches can be used to reduce the number of values that specify the fixed dielectric function in the analysis. The complex dielectric function can be determined, not spectral point by point, but rather as a Kramers-Kronig consistent *b*-spline with node spacing that depends on the nature of the material (e.g., amorphous, nanocrystalline, or polycrystalline) [19]. Alternatively, the dielectric function can be expressed as a physics-based analytical function [20]. Once the dielectric function is determined from the real time SE data in the second stage, then it can be applied in a straightforward least squares regression analysis of the first stage in which $3M_1$ structural parameters are obtained, where M_1 is the number of time points of the first stage.

For high quality amorphous semiconductors, the complex dielectric function of the accumulating film is nearly constant with deposition time and thus uniform with depth throughout the thickness [11]. Small changes in bandgap have been observed in intrinsic *a*-Si:H absorber layers in solar cells likely due to changes in H-incorporation [21]. For *nc*-Si:H, however, considerable changes in the dielectric function occur with accumulated film growth, particularly when growth occurs from an amorphous film surface [11, 22]. As a result, a depth profile in the dielectric function is built into the sample, which generates another significant challenge in data analysis. Typically the material in the early stage of growth has the characteristics of the underlying material if it is *a*-Si:H or mixed phase *a*-Si:H+*nc*-Si-H, and the content of *nc*-Si:H increases with increasing thickness [23]. Such a film growth process is modeled using a different approach based on a virtual interface analysis as described next.

In virtual interface analysis, the growing film is modeled as an outerlayer on the surface of a semi-infinite pseudo-substrate that incorporates the past history of the non-uniform deposition [24]. The virtual interface is that between the pseudo-substrate and the outerlayer. On top of the outerlayer, a surface roughness layer is assumed with the dielectric function determined from the Bruggeman effective medium approximation (EMA) as a 50/50 vol% mixture of outerlayer material and void [25]. In this analysis, M pairs of sequential (ψ, Δ) spectra are chosen, acquired over a relatively short time period and corresponding to a deposited outerlayer thickness increment on the order of ~10 Å. During this time period, the dielectric function of the outerlayer and the surface roughness layer thickness can be approximated as constant. From these spectra, the outerlayer deposition rate R_o and the surface roughness layer thickness d_s are obtained along with a point-by-point determination of the outerlayer dielectric function. For the first of the M pairs of spectra, the outerlayer thickness is taken to be zero, and for each subsequent pair the outerlayer thickness is $d_o = jR_o\,\Delta t$, where $j = 1, 2, \ldots, M-1$, and Δt is the time duration between the collection of successive real time SE spectra. The correct pseudo-substrate dielectric function in the analysis is obtained by inversion of the initial (ψ, Δ) spectra, which applies a correction for each trial or final value of the surface roughness layer thickness [25]. In the virtual interface analysis, $2N + 2$ values are deduced from

$2(M-1)N$ data values. Once the first $j=0,1,2,\ldots,M-1$ set of spectra are analyzed, the analysis moves to the second $j=1,2,3,\ldots,M$ set of spectra. The accumulating bulk layer thickness can be determined by integrating the deposition rate. Although virtual interface analysis has its limitations, namely the evolving pseudo-substrate must be optically thick (without interference fringes) [24], it is very effective for tracking the dielectric function of an evolving thin film. As will be seen in Sect. 7.2.3, in the case of *nc*-Si:H nucleation and growth, the dielectric function obtained in virtual interface analysis can be further analyzed assuming an EMA of *a*-Si:H, *nc*-Si:H, and void. This enables determination of the phase evolution of films intended as *nc*-Si:H during deposition.

Another important goal to be achieved is the expression of the complex dielectric function of *nc*-Si:H using a physics-based analytical model with a small number of free parameters, as has been done for amorphous semiconductors [20, 26]. In many data analysis circumstances, one may seek to introduce a dielectric function with a small number of parameters, rather than determining results spectral point by point. For intrinsic and doped *nc*-Si:H, the resonance features associated with the band structure critical points are very broad, and further broadening occurs at the elevated temperatures of deposition. As a result, a simple line shape model consisting of a sum of Lorentz oscillators can be used. By using Lorentz oscillators for the three direct gap CPs over the range of 0.75–5.5 eV, one reduces the number of dielectric function parameters by six, since the Lorentz oscillator does not require phase or exponent parameters. The Lorentz oscillator sum associated with the imaginary part of the dielectric function is forced to zero according to an expression consistent with the indirect bandgap of Si [20]. Although in previous descriptions the indirect bandgap parameter was allowed to vary, in this study it is fixed at the known bandgap of *c*-Si at the deposition temperature based on the assumption that the grain size of *nc*-Si:H is sufficiently large that quantum effects do not occur. A very general complex dielectric function that covers the case of *nc*-Si:H is given by

$$\varepsilon_2(E)=\frac{\hbar\Gamma_D^2}{\varepsilon_0\rho E\left(E^2+\Gamma_D^2\right)}+G(E)\sum_{j=1}^{N_o}L_j(E) \tag{7.1}$$

$$\varepsilon_1(E)=\varepsilon_{1o}-\frac{\hbar\Gamma_D}{\varepsilon_0\rho\left(E^2+\Gamma_D^2\right)}+\frac{A_P}{E_{0P}^2-E^2}+\frac{2}{\pi}\sum_{j=1}^{N_o}\mathrm{P}\int_0^{\infty}\frac{E'G(E')L_j(E')}{E'^2-E^2}dE', \tag{7.2}$$

where

$$G(E)=\begin{cases}\left(\dfrac{E-E_g}{E}\right)^2 & E>E_g\\ 0 & E\le E_g\end{cases} \tag{7.3}$$

$$L_j(E) = \frac{A_j E_{0j} \Gamma_j E}{\left(E_{0j}^2 - E^2\right)^2 + \Gamma_j^2 E^2} \tag{7.4}$$

The first term of (7.1) is a Drude component where ρ is the resistivity and $\Gamma_D = \hbar/\tau$, with τ as the Drude free electron scattering time. In the second term, $G(E)$ represents the interband absorption onset shape in ε_2 with E_g defining the indirect bandgap. $L_j(E)$ represents the Lorentz line shape function in ε_2 for the jth oscillator with an amplitude A_j, a resonance energy E_{0j}, and a broadening parameter Γ_j [20]. As shown in (7.2), the real part of the dielectric function has four terms, the constant contribution ε_{1o}, the Drude contribution, a contribution from an oscillator with amplitude A_P and with resonance energy E_{0P} above the accessible spectral range, and a sum of Kramers-Kronig integrals one for each of the oscillators in ε_2. For *nc*-Si:H, with E_g fixed at the value for *c*-Si at the *nc*-Si:H deposition temperature and with the Drude terms and the term in A_P set to zero, then a total of ten parameters are varied in the dielectric function analysis. A goal of this work and continued future research is to reduce the number of variable parameters for intrinsic and doped *nc*-Si:H [27]. At the minimum, one might expect separate relationships to exist among the three Lorentz oscillator amplitudes, the three resonance energies, and the three broadening parameters. This could lead to a reduction in the number of parameters to four, which would be a significant improvement for analysis of multilayer stacks that include *nc*-Si:H.

7.2.2 Top Cell Analysis

Top cell characterization by real time SE starts with the analysis of the NSG-Pilkington TEC™ 15 coated glass substrate at the deposition temperature of 200 °C. In addition to a ~3000 Å thick SnO_2-F layer at the top of the TEC™ 15 substrate, ~200 Å thick layers of undoped SnO_2 and SiO_2 exist at the interface to the glass, yielding a glass/SnO_2/SiO_2/SnO_2:F structure [28, 29]. Here the focus is on the measurement of the dielectric function of the SnO_2:F layer, which is the dominant layer [15]. Figure 7.2 shows experimental (ψ, Δ) data collected for the TEC™ 15 substrate just prior to the deposition of the top cell *p*-layer in accordance with the sequence of Fig. 7.1b. A total of seven structural parameters and eleven dielectric function parameters led to the best fit shown in Fig. 7.2, and the analytical form for the dielectric function of the SnO_2:F layer is shown in Fig. 7.3. For this dielectric function, the analytical expression of (7.1)–(7.4) was used with E_g set to zero so that $G(E) \rightarrow 1$. The eleven parameters and their confidence limits are included in Table 7.1, including ε_{1o}, the two Drude parameters (ρ, τ), as well as (A_P, E_P), and the six parameters associated with two Lorentz oscillator terms. The deduced structural parameters are shown as the superstrate structure of the completed top cell in Fig. 7.4. Six layer thicknesses are used in the best fit of the TEC™ 15 substrate, including those of the SnO_2, SiO_2, and SnO_2:F films. In fact, the

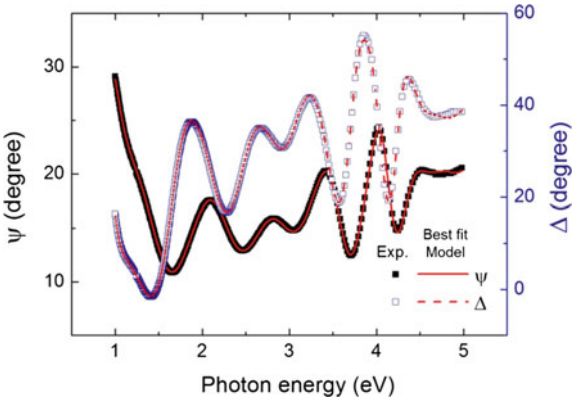


Fig. 7.2 Experimental ellipsometric spectra for a TEC™ 15 glass substrate measured in situ at the elevated temperature of 200 °C and at an angle of incidence of 70° (points). The lines represent the best fitting simulation using the dielectric function of Fig. 7.3

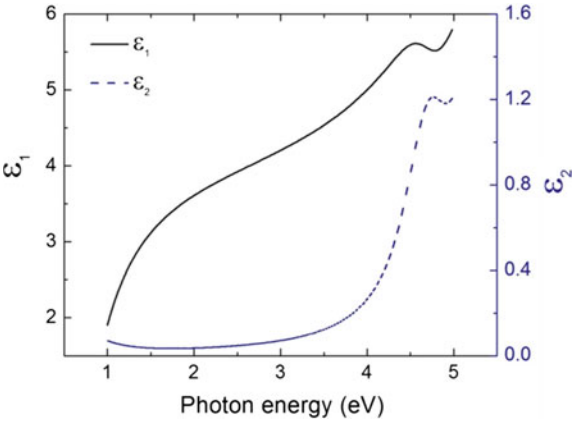


Fig. 7.3 Real (ε_1) and imaginary (ε_2) parts of the SnO_2:F dielectric function at the elevated temperature of 200 °C, as simulated using one Drude term, one oscillator with resonance energy well above the upper limit of the spectra, and two Lorentz oscillators. These results were obtained in the fit of Fig. 7.2. The best fitting parameters along with their confidence limits are given in Table 7.1

Table 7.1 Best fitting parameters along with confidence limits that describe the dielectric function of the transparent conducting oxide layer SnO_2:F as measured at 200 °C. The dielectric function was simulated assuming one Drude term, two Lorentz oscillators, and one oscillator with resonance energy well above the upper spectral limit (Sellmeier term), the latter yielding no contribution to ε_2. With a lower photon energy limit of 1 eV in this analysis, limitations exist in the ability to extract accurate Drude parameters

Dielectric function parameters for NSG Pilkington TEC™ 15 SnO_2:F at 200 °C		
ε_{1o}		2.05 ± 0.01
Drude	Resistivity (Ω cm)	(1.02 ± 0.03) × 10^{-4}
	Scattering time (fs)	22.8 ± 0.6
Lorentz 1	A_1 (eV)	0.826 ± 0.022
	Γ_1 (eV)	0.658 ± 0.015
	E_{01} (eV)	4.71 ± 0.01
Lorentz 2	A_2 (eV)	4.96 ± 0.15
	Γ_2 (eV)	0.487 ± 0.018
	E_{02} (eV)	5.57 ± 0.01
Sellmeier	A_P [$(eV)^2$]	76.3 ± 2.8
	E_{0P} (eV)	7.64 ± 0.03

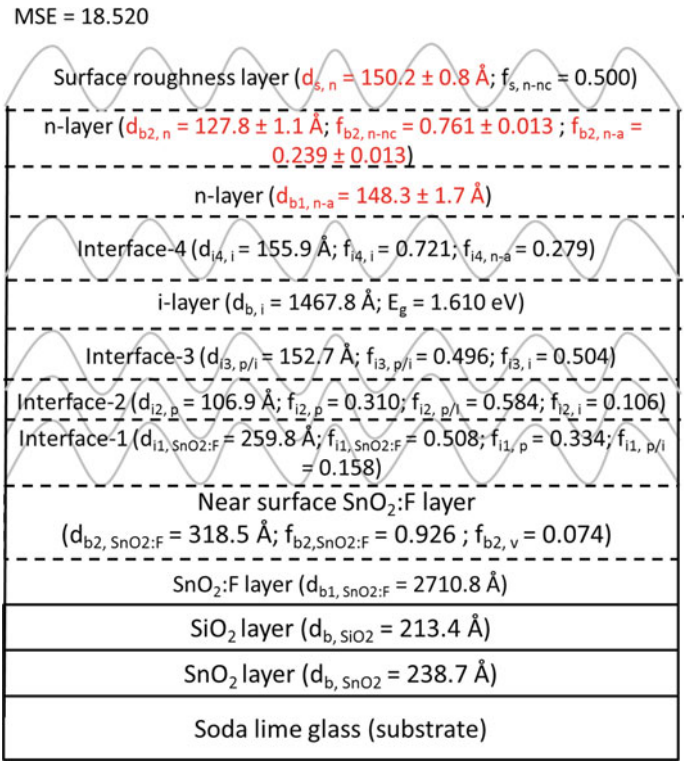


Fig. 7.4 Schematic of a completed *a*-Si:H *p*-*i*-*n* top cell on a TCO-coated glass substrate (TEC™ 15) along with the fixed and best fit structural parameters including layer thicknesses and component volume fractions. The best fit *n*-layer structural parameters obtained from the data of Fig. 7.5 are those with confidence limits. The dashed lines show the layers in the SE model, whereas the solid lines separate schematically the different thin film materials

SnO_2:F film is modeled with three layer components, a bulk layer 2711 Å thick, a near-surface layer 319 Å thick with a void content of 7 vol%, and a surface roughness layer 260 Å thick with a void content of 49 vol%. In the deposition of the overlying *a*-Si:H top solar cell on this substrate, the 49 vol% voids in the SnO_2:F roughness layer are filled in with *p*-layer and *p*/*i* interface layer materials whose target effective thicknesses are 110 Å and 150 Å, respectively.

Real time SE has been applied during the following four depositions of the *a*-Si:H top cell: the *a*-$Si_{1-x}C_x$-H *p*-type window layer, the intrinsic *a*-Si:H *p*/*i* interface layer, and the *i* and *n*-layers; as a result, details on the complete structure were obtained as shown in Fig. 7.4. For the *p* and *p*/*i* interface materials, the films were so thin that only the first deposition stage, interface roughness filling, was observed and analyzed. The *i* and *n*-layers were thicker, and for those films the second stage, bulk layer growth, was present. The *n*-layer was modeled as two layers, *a*-Si:H at the interface to the *i*-layer and mixed phase Si:H at the top with a deduced nanocrystalline volume fraction of 0.76. The best fit to the real time SE data after

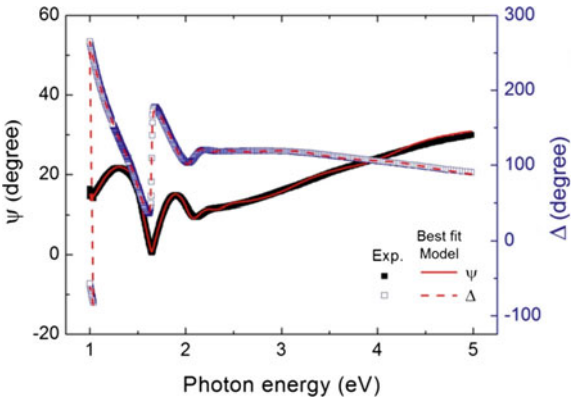


Fig. 7.5 Ellipsometric spectra of an *a*-Si:H *p*-*i*-*n* top cell on a TCO coated glass substrate (TEC™ 15) at a 70° angle of incidence (points). The lines represent the best fitting results using the Fig. 7.4 model with four free parameters. This is the top cell structure of an *a*-Si:H/*nc*-Si:H tandem

n-layer deposition is shown in Fig. 7.5 and yields the variable parameters with confidence limits in Fig. 7.4. In addition to structural parameters, the critically important *i*-layer bandgap was determined. The known temperature coefficient of -4.2×10^{-4} eV/°C enables conversion of the 1.610 eV bandgap deduced at the 200 °C deposition temperature to 1.686 eV at 20 °C [30]. The top solar cell model and parameters of Fig. 7.4 as obtained by real time SE summarize the starting point for the studies of the next sub-sections. In these sub-sections, the focus is on the deposition of the *p* and *i*-layers of the *nc*-Si:H bottom solar cell (see Fig. 7.1b) and the challenging real time SE analyses of these two depositions.

7.2.3 *Dielectric Functions of Nanocrystalline Si:H* n *and* p-*Layers for the Tunnel Junction*

For optimization of the critical bottom cell *p*-layer, a number of depositions were performed on sample structures that simulate the top solar cell structure of Fig. 7.4 [14, 15]. These structures consist of *c*-Si/SiO_2/intrinsic-(*a*-Si:H)/*n*-type-(*nc*-Si:H), as shown in Fig. 7.6, with typical ~75 Å thick surface roughness on the *n*-layers. Thus, these *n*-layers are much smoother than that of Fig. 7.4, which exhibits roughness 150 Å thick. Smoother surfaces result in more accurate dielectric functions and crystalline phase determinations for thin layers in both multi-time and virtual interface analyses. Figure 7.6 shows a schematic of a *p*-layer deposited on the *n*-layer of the smoother film stack as obtained by multi-time analysis with the parameters associated with two time points in data analysis, the second point at the end of the deposition when the bulk *p*-layer thickness is 111 Å.

In an evaluation of the crystalline phase evolution, a virtual interface analysis was also performed using real time SE data over the high photon energy range (3–5 eV). This range provides greater surface sensitivity and enables evaluation of the near-surface of the film, beneath the surface roughness layer, in terms of an EMA mixture of *a*-Si:H, *nc*-Si:H, and void as shown in Fig. 7.7. Figure 7.8 shows

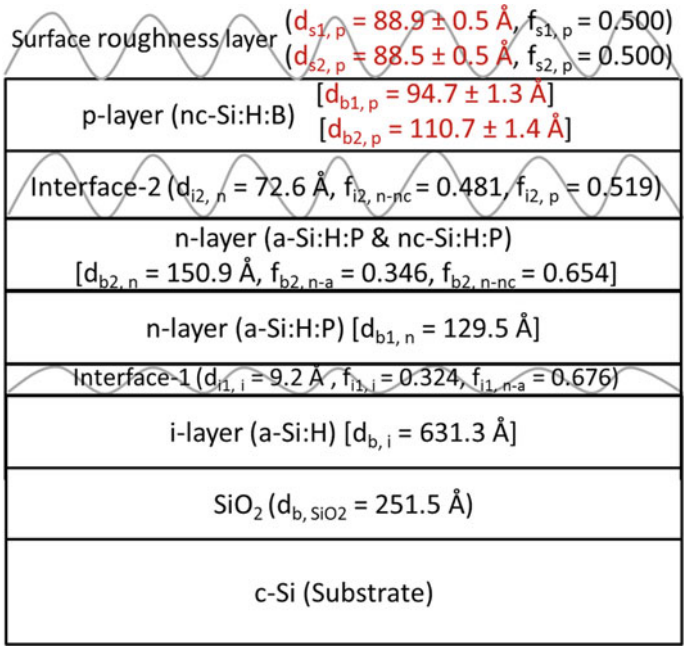


Fig. 7.6 Schematic optical model for a *nc*-Si:H:B *p*-layer deposited on a thermally oxidized *c*-Si wafer substrate which was coated in succession with an *a*-Si:H *i*-layer and an *nc*-Si:H:P *n*-layer. The *p*-layer structural parameters from two time points are shown

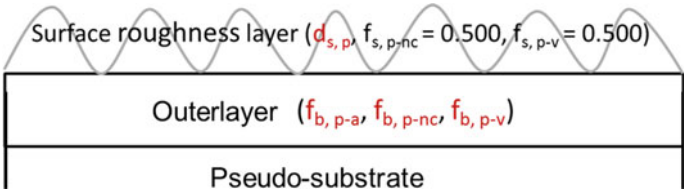


Fig. 7.7 Schematic optical model for Si:H:B *p*-layers deposited on *c*-Si/SiO_2/*i*-layer/*n*-layer structures. A mixture of *nc*-Si:H, *a*-Si:H, and voids is assumed for the outerlayer with composition determined from the dielectric function via the EMA, and virtual interface analysis is performed over the high photon energy range of 3–5 eV for surface sensitivity

the virtual interface analysis results, and Fig. 7.9 shows point-by-point representations of the dielectric functions at 200 °C deduced at the PECVD endpoint for *p*-layers deposited using three radio frequency (rf) power levels. The two higher power depositions show characteristics of a pure *nc*-Si:H phase at the end of deposition as indicated in Fig. 7.9 whereas the lower power deposition shows the characteristics of high amorphous (55 vol%) and void (11 vol%) contents. These results suggest that a higher plasma power yields a *p*-layer with continuous development of the crystalline phase, which is desirable in order to nucleate a *nc*-Si:H *i*-layer from the *p*-layer surface.

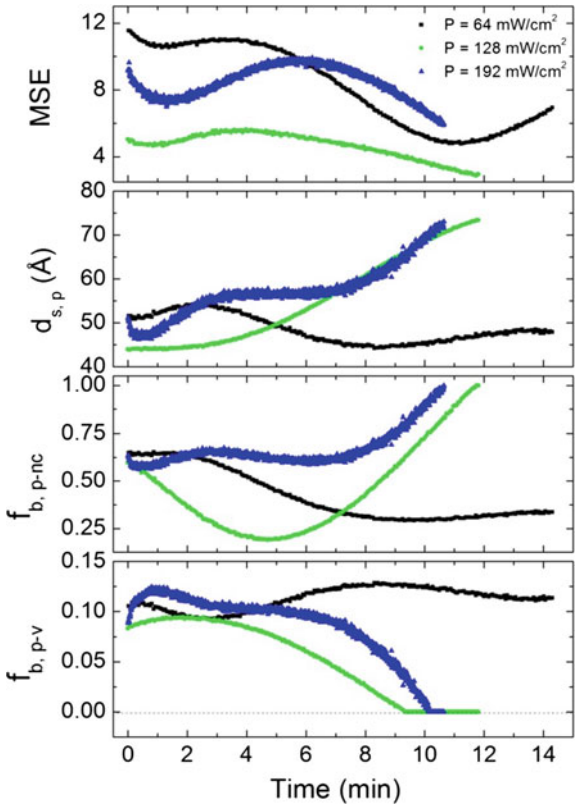


Fig. 7.8 Virtual interface analysis results for the time evolution of the mean square error (MSE), the surface roughness layer thickness $d_{s,\,p}$, and the *nc*-Si:H and void volume fractions $f_{b,\,p\text{-nc}}$, and $f_{b,\,p\text{-v}}$ for *p*-type Si:H:B depositions on *c*-Si/SiO_2/*i*-layer/*n*-layer structures simulating a top cell. These *p*-layers were prepared using different rf power densities as shown

The goal of the *p*-layer optimization is rapid nucleation and well-defined crystalline grain structure which can be evaluated based on the broadening parameter $\Gamma_2 = \hbar/\tau_2$ of the dominant E_2 optical transition observed in Fig. 7.9 as the strong feature near 4.15 eV [31]. The E_1 and E_1' transitions appear as weak shoulders on the E_2 feature, are more difficult to characterize accurately, and so are less useful for evaluating an excited state relaxation time τ_2.

The *nc*-Si:H *p*-layer dielectric functions of Fig. 7.9 were fit applying the analytical expression of (7.1)–(7.4) with three modified Lorentz oscillators. Table 7.2 summarizes the ten best fit dielectric function parameters for each of the *p*-layers of Fig. 7.9. A point-by-point representation of the dielectric function typical of the underlying top cell *n*-layers is also shown in Fig. 7.9. This result was deduced in a virtual interface analysis applied to data acquired during *n*-layer deposition and is presented for comparison with the *p*-layers. This *n*-layer dielectric function has been analyzed similarly, and the associated parameters are also included in Table 7.2. Table 7.2 provides two of the key deposition parameters of the *nc*-Si:H layers including the H_2-dilution flow ratio $R = [H_2]/[SiH_4]$ and the rf plasma power; all depositions were performed at 200 °C which also is the dielectric function measurement temperature. The parameters for the two fully *nc*-Si:H

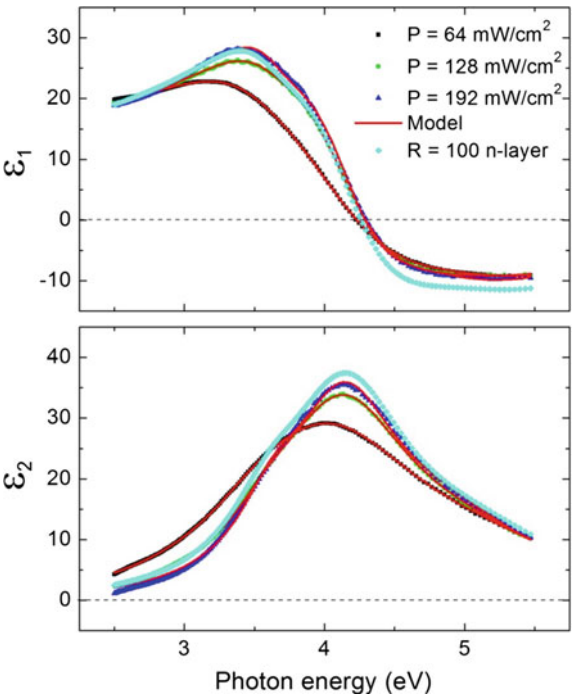


Fig. 7.9 The dielectric functions measured at 200 °C for *p*-type Si:H:B layers prepared on *c*-Si/SiO_2/*i*-layer/*n*-layer structures using three different rf power densities as indicated. The solid lines represent best fit analytical expressions for these dielectric functions. Also shown is the analytical form of the dielectric function measured at 200 °C for the $R = 100$ *n*-layer used in the analysis of the underlying sample obtained applying virtual interface analysis

p-layers in Table 7.2 are consistent with observations from Fig. 7.9. Specifically, the highest power sample exhibits the smaller values of Γ_1, Γ_2, and Γ_3, indicating larger crystalline grains, and this same sample exhibits continuous crystallite development from initial growth on the *n*-layer.

The parameters for a larger set of dielectric functions for doped *nc*-Si:H layers prepared on *n* and *i*-layer Si:H surfaces under a range of conditions are presented in Figs. 7.10, 7.11, and 7.12. The data set includes *p*-layers and *n*-layers for which variations in the hydrogen dilution ratio $R = [H_2]/[SiH_4]$ are performed. Results of *p*-layer substrate temperature T_{sub} series, and two rf plasma power series are included, the latter for the *p*-layer at substrate temperatures of 120 and 200 °C.

The purpose of these scatter plots is two-fold. First, the figures may help to identify layers with the highest crystalline quality based on evaluation of Γ_2. The second purpose is to reduce the number of free parameters in data analysis for thin layers of doped *nc*-Si:H by linking parameters. Parameter reductions can be expected based on the assumption that the resonance energies E_n are linear functions of crystallite stress X according to $E_n = E_{nb} + C_{Xn}X$ [32], where E_{nb} represents the associated single crystal Si resonance energy and C_{Xn} represents the linear stress coefficient of the energy of the *n*th oscillator. Eliminating X from the pair of equations for the *n*th and the *n*′th oscillator leads to the following linear relationship between E_n and $E_{n'}$:

Table 7.2 Parameters used in an analytical expression that represents the dielectric functions measured at 200 °C for *p*-type Si:H:B films prepared on *c*-Si/SiO_2/*i*-layer/*n*-layer structures using different rf plasma power densities. Also included are the parameters in the same analytical expression that describes the dielectric function of the underlying *nc*-Si:H:P *n*-layer. The expression is defined by three Lorentz oscillators modified by a common indirect bandgap. A constant contribution to the real part of the dielectric function ε_{1o} is also used as a free parameter

Layer type	R	P (mW/cm^2)	ε_{1o}	Parameters of the modified Lorentz oscillator			
				A (eV)	Γ (eV)	E_0 (eV)	E_g (eV)
p	250	64	1.343 ± 0.025	4.774 ± 0.953	0.828 ± 0.068	3.509 ± 0.016	1.069
				89.793 ± 1.136	1.768 ± 0.009	4.066 ± 0.008	
				3.549 ± 0.504	1.121 ± 0.101	5.140 ± 0.018	
		128	2.480 ± 0.044	8.452 ± 1.269	0.743 ± 0.042	3.604 ± 0.011	1.069
				63.723 ± 2.916	1.193 ± 0.024	4.152 ± 0.004	
				15.126 ± 2.009	1.716 ± 0.100	5.060 ± 0.035	
		192	2.841 ± 0.117	11.940 ± 2.817	0.640 ± 0.059	3.643 ± 0.019	1.069
				49.399 ± 7.523	0.952 ± 0.072	4.158 ± 0.009	
				22.978 ± 5.713	1.545 ± 0.145	4.916 ± 0.076	
n	100	100	1.438 ± 0.087	11.687 ± 2.443	0.678 ± 0.057	3.608 ± 0.016	1.069
				65.178 ± 5.185	1.103 ± 0.047	4.174 ± 0.007	
				14.968 ± 2.912	1.493 ± 0.129	5.115 ± 0.048	

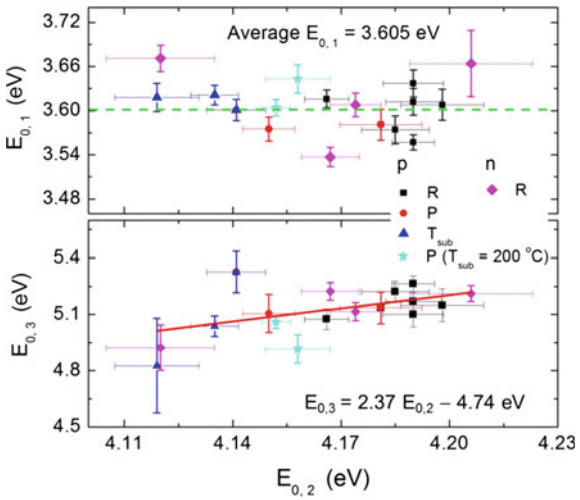


Fig. 7.10 Resonance energies of the first and third modified Lorentz oscillators that describe the dielectric functions of doped *nc*-Si:H layers. These results are plotted as functions of the resonance energy of the second oscillator. The solid line is a linear fit to $E_{0,3}$ and the broken line denotes the average of $E_{0,1}$. Results for several doped *nc*-Si:H samples are shown

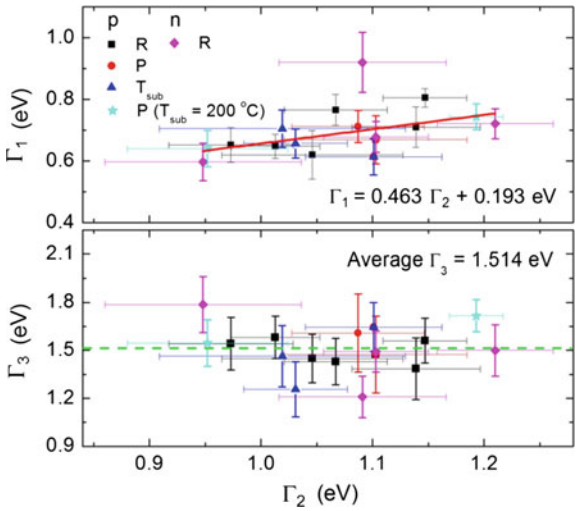


Fig. 7.11 Broadening parameters of the first and third modified Lorentz oscillators that describe the dielectric functions for several doped *nc*-Si:H layers. These results are plotted as functions of the broadening parameter of the second oscillator

$$E_n = \left(E_{nb} - \frac{C_{Xn}}{C_{Xn'}} E_{n'b}\right) + \frac{C_{Xn}}{C_{Xn'}} E_{n'}. \tag{7.5}$$

Figure 7.10 shows $E_{0,1}$ and $E_{0,3}$ in correlation with $E_{0,2}$. Associating the $E_{0,2}$ oscillator energy with the nearest crystalline Si critical point (CP), that of $E_2(X)$ located at 4.22 eV for a temperature of 200 °C [33], an increase in $E_{0,2}$ over the range of 4.12–4.20 eV would be associated with a reduction in stress. At the same time, the best fit linear correlations in $E_{0,3,}$ corresponding to the E_1' CP lead to variations over the range 4.8–5.2 eV which bring these resonance energies closer to

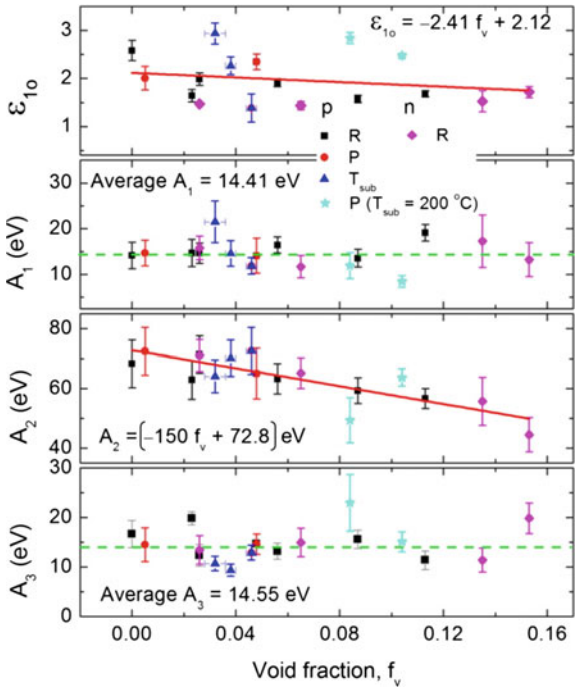


Fig. 7.12 The constant offset ε_{1o} and the amplitude parameters of the modified Lorentz oscillators that describe the dielectric functions of several doped *nc*-Si:H layers. These results are plotted as functions of the relative void volume fraction, which was obtained by using the dielectric function of the densest film of the *p*-layer H_2-dilution series with $R = 225$ and that of void in the Bruggeman EMA to simulate the dielectric functions of all other *nc*-Si:H materials. The solid lines are linear fits and the horizontal broken lines denote average values

the single crystal E_1' critical point at 5.19 eV for the substrate temperature of 200 °C [33]. All $E_{0,1}$ values are considerably higher than the associated crystalline Si E_1 CP of 3.29 eV; however, the variation is weak ~0.1 eV compared to the average ~0.3 eV difference from the *c*-Si value. The higher energy may occur if the excitonic transition associated with this lowest energy direct CP is affected by crystallite size, leading to a widening of the associated bandgap. Thus, one can conclude $E_{0,3}$ can be linked to $E_{0,2}$ through the expression in Fig. 7.10, $E_{0,3} = 2.37\ E_{0,2} - 4.74$ eV, and $E_{0,1}$ can be fixed at its average value of 3.605 eV. This can reduce the number of variable parameters in the dielectric function expression from ten to eight.

A similar analysis can be performed on the broadening parameters, correlating the parameters of the first and third oscillators with that of the second one, the strongest oscillator. Applying the assumption that each oscillator broadening parameter is controlled by the same grain boundary scattering mechanism, then the following linear relationships are expected

$$\Gamma_n = \left(\Gamma_{nb} - \frac{V_{gn}}{V_{gn'}}\Gamma_{n'b}\right) + \frac{V_{gn}}{V_{gn'}}\Gamma_{n'} \tag{7.6}$$

between the nth and the n'th parameters [31]. Here Γ_{nb} and $\Gamma_{n'b}$ represent the associated single crystal Si broadening parameters (0.16, 0.11, 0.18 eV at 200 °C for $n = 1, 2, 3$, respectively [33]) and V_{gn} and $V_{gn'}$ represent group velocities of

excited carriers that undergo scattering for the nth and the n'th oscillators. The data points for Γ_1 in Fig. 7.11 have been fit assuming a linear relationship with the result being $\Gamma_1 = 0.463\Gamma_2 + 0.193$ eV, which demonstrates behavior consistent with (7.6). The correlation for Γ_3 is unclear since the third resonance is very weak. It is reasonable to fix this third oscillator's broadening parameter at the average $\Gamma_3 = 1.514$ eV for all samples. By further applying these two results for $\Gamma_1(\Gamma_2)$ and Γ_3, one can reduce the number of free parameters in the modified Lorentz oscillator expression from eight to six.

The parameters ε_{1o} and all three oscillator amplitudes have been correlated to the relative void volume fractions obtained by EMA fits of the dielectric functions. The reference material of lowest void fraction was found to be a p-layer fabricated at $R = 225$ with a substrate temperature of $T_{sub} = 120$ °C and a plasma power of $P = 128$ mW/cm^2. This p-layer exhibited the highest amplitudes of the complex dielectric function over the measured range. Thus, the *nc*-Si:H dielectric function of this p-layer and that of void were then applied in the EMA to model all other dielectric functions in order to obtain their relative void fractions. With this approach, the least dense film is that prepared at the lowest H_2 dilution of $R = 80$, an n-layer deposition. It is noted in Fig. 7.12 that ε_{1o} and the dominant amplitude A_2 show expected linearly decreasing trends as the relative void volume fraction increases whereas the much weaker A_1 and A_3 values show no systematic trends. In the parameterization, the results in Fig. 7.12 suggest that it is possible to fix A_1 and A_3 at their average values of 14.41 and 14.55 eV and to link A_2 to the void fraction f_v through the expression of the form $A_2 = -150.0\, f_v + 72.8$ eV. Because of the large scatter in ε_{1o}, and its ability to accurately control the overall amplitude of ε_1, it is likely that this parameter is needed in addition to f_v. Thus, in summary, by applying the relations in Figs. 7.10, 7.11, and 7.12 as recommended here, one can reduce the number of parameters that define the dielectric functions of doped *nc*-Si:H materials from ten to four, including f_v, ε_{1o}, E_2, and Γ_2. The parameters are expected to provide information on the relative density via the void fraction (f_v, ε_{1o}) and measures of stress (E_2) and grain size (Γ_2).

One should be concerned with the variations in measurement temperature for the *nc*-Si:H samples in Figs. 7.10, 7.11, and 7.12. Most samples in these figures were measured in the temperature range from 120 to 200 °C. For single crystal Si, this range leads to variations of (±0.016, ±0.011, ±0.030) eV for the $E_{0,1}$, $E_{0,2}$, and $E_{0,3}$ transition energies and (±0.008, ±0.005, ±0.011) eV, for the Γ_1, Γ_2, and Γ_3 broadening parameters, respectively [33]. Thus, the effect of the temperature range is within the confidence limits, although improved statistics may be possible by adjusting all data to the same temperature using the temperature coefficients given elsewhere for p-type *nc*-Si:H [20]. It should be emphasized that the parameterization in these figures is most relevant for the temperature of ~150 °C, with a possible range of applicability of ±50 °C; thus for a room temperature dielectric function parameterization adjustments are required according to the available temperature coefficients.

The dielectric functions generated using the oscillator parameters in Table 7.2 obtained for the smoother sample structure have been applied to fit the experimental

data over the spectral range from 1 to 5 eV for bottom cell Si:H:B *p*-layers on the complete (TEC™ 15)/*p-i-n a*-Si:H top solar cell structures. In this analysis, the structural parameters of the bottom cell Si:H:B *p*-layers can be obtained. Figures 7.13 and 7.14 show the optical model and ellipsometric spectra measured at 200 °C at the end of deposition for the sample incorporating the *nc*-Si:H:B *p*-layer deposited with $P = 128$ mW/cm^2 on the (TEC™ 15)/*p-i-n* top cell structure. The final *p*-layer structural parameters as well as the effective thickness and MSE for each of the three film structures are given in Table 7.3, as determined using the optical model shown in Fig. 7.13.

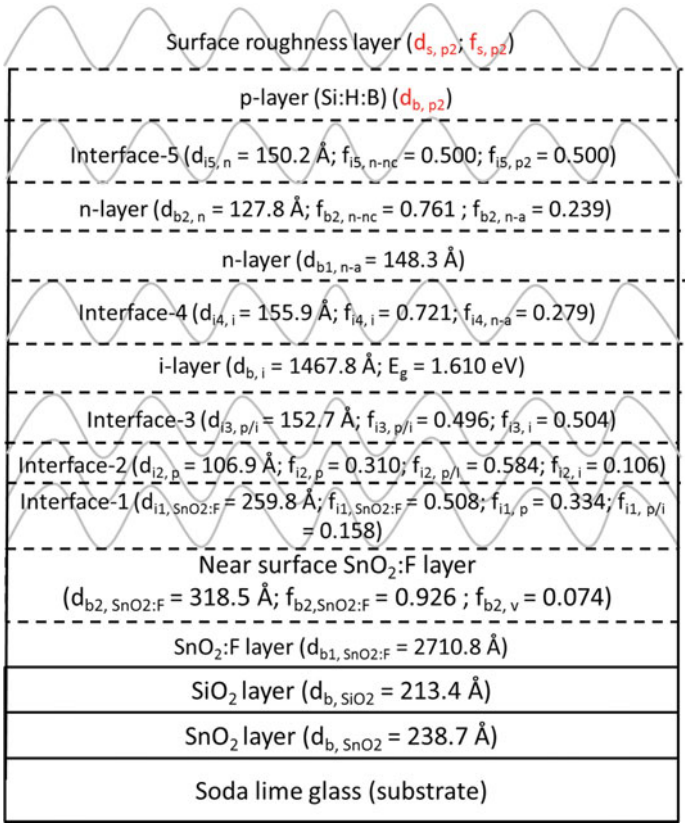


Fig. 7.13 Schematic optical model for a bottom cell Si:H:B *p*-layer deposited on a structure consisting of a (TEC™ 15)/*p-i-n a*-Si:H top solar cell. This structure describes the $P = 128$ mW/cm^2 deposition in the center column of Table 7.3. The dashed lines show the layers in the SE model, whereas the solid lines schematically demarcate the individually-deposited films

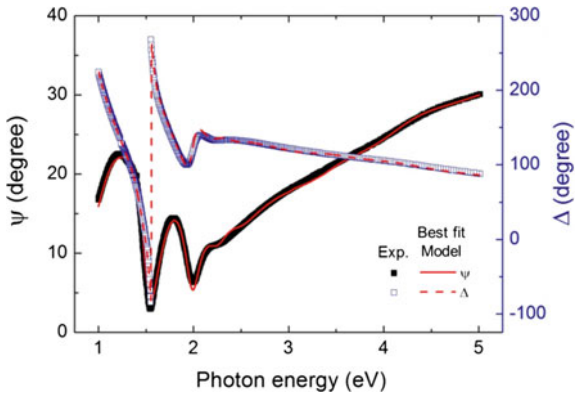


Fig. 7.14 Ellipsometric spectra at a 70° angle of incidence for a *nc*-Si:H:B *p*-layer deposited on a structure consisting of a (TEC™ 15)/*p-i-n a*-Si:H top solar cell (points). The lines represent the best fitting results using the three-parameter model shown in Fig. 7.13

Table 7.3 Best fitting structural parameters at the end of deposition along with their confidence limits for Si:H:B *p*-layers deposited on structures consisting of (TEC™ 15)/*p-i-n a*-Si:H top solar cells. The rf plasma power and deposition time are provided for each *p*-layer

Structural parameters of bottom cell *p*-layer in *a*-Si:H/*nc*-Si:H tandem			
P (mW/cm^2)	64	128	192
Time (s)	1000	600	550
MSE	17.06	18.75	17.61
Surface roughness thickness, $d_{s,p2}$ (Å)	130.0 ± 0.9	144.5 ± 0.7	137.5 ± 0.7
p-layer volume fraction in surface roughness, $f_{s,p2}$	0.512 ± 0.003	0.451 ± 0.003	0.417 ± 0.004
p-layer bulk thickness, $d_{b,p2}$ (Å)	76.5 ± 1.3	56.4 ± 1.0	44.3 ± 0.8
n/p interface thickness, $d_{i5,n}$ (Å)	129.0	150.2	173.6
p-layer volume fraction in *n/p* interface, $f_{i5,p2}$	0.500	0.500	0.500
p-layer effective thickness (Å)	207.6	196.6	188.4

7.2.4 *Dielectric Functions of Bottom Cell Nanocrystalline Si:H* i-*Layers*

In this sub-section, detailed presentation and discussion of the bottom cell *nc*-Si:H *i*-layer dielectric functions are given [14, 15]. The underlying *nc*-Si:H *p*-layer in these studies was fabricated using the intermediate power level of $P = 128$ mW/cm^2. The only *i*-layer variable is the hydrogen dilution ratio $R = [H_2]/[SiH_4]$, which is set at a value within the range from 2 to 40. The *i*-layer PECVD parameters that were held constant include a substrate temperature of 200 °C and a power density of 128 mW/cm^2. The plasma excitation frequency for the bottom cell *i*-layer was set in the very high frequency (vhf) range at 60 MHz. The higher excitation frequency promotes the formation of nanocrystallites relative to the value of 13.56 MHz used for the standard rf PECVD of the top cell and doped layers [2].

A point-by-point dielectric function for each of the bottom cell *i*-layers prepared with $R = 2$–40 on the *nc*-Si:H *p*-layer material was determined by applying

multi-time analysis to three sets of SE data acquired near the end of each deposition. The dielectric function of the *nc*-Si:H *i*-layer for each R value is assumed to have stabilized without any thickness dependence, that is, after a thick *nc*-Si:H *i*-layer has evolved. Figure 7.15 shows the best fit analytical expressions to these dielectric functions assuming three Lorentz oscillators modified by the indirect bandgap of Si of 1.069 eV at the deposition and measurement temperatures of 200 °C. The best fit parameters of the analytical expressions are shown in Table 7.4. It is evident that all five dielectric functions for *i*-layers prepared with $R = 2$–40 closely overlap and that the dielectric function amplitudes for the *i*-layers are much lower than those of the doped layers of Fig. 7.9. This may be caused by the large *i*-layer bulk and surface roughness layer thicknesses, with the possibility of surface connected microvoids, as well as voids propagating from the *p*-layer surface roughness.

Figure 7.16 presents the values of the parameters listed in Table 7.4 in plots as functions of R. The $E_{0,2}$ and $E_{0,3}$ resonance energies in Fig. 7.16 start at low R near the single crystal values of 4.22 eV and 5.19 eV at 200 °C, respectively. $E_{0,2}$ decreases to a minimum near $R = 20$, and increase again for the $R = 40$ value. This behavior suggests that film stress increases with R up to $R = 20$, and then decreases. A similar trend is observed for $E_{0,3}$, however, the confidence limits become very large at high R. The $E_{0,1}$ resonance energy shows behavior similar to that of the *p* and *n*-layers in Sect. 7.2.3. Although the $E_{0,1}$ energies for the *i*-layers, 3.48–3.50 eV, are much larger than the single crystal value of 3.29 eV at 200 °C,

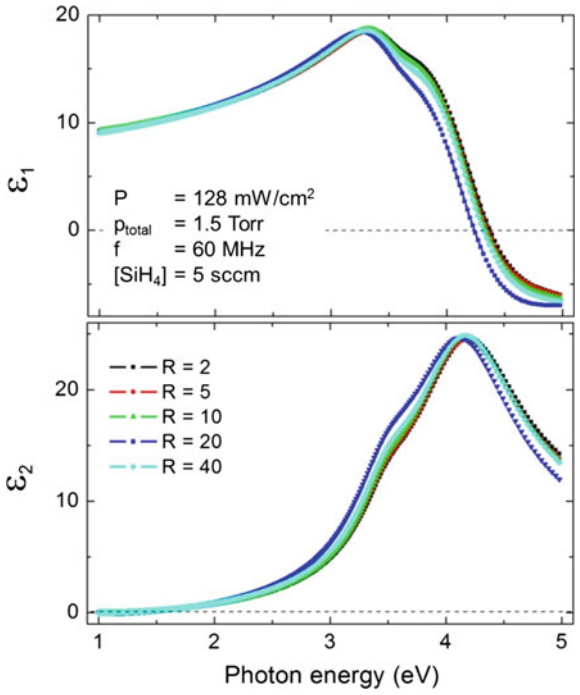


Fig. 7.15 The dielectric functions at 200 °C for bottom cell *nc*-Si:H *i*-layers, as determined by multi-sample analysis. The *i*-layers were prepared using different hydrogen dilution ratios ($R = 2$, 5, 10, 20, and 40) within a chamber dedicated to vhf-PECVD of the *i*-layers [14]

Table 7.4 Parameters used in an expression that represents the dielectric functions measured at 200 °C for nanocrystalline Si:H *i*-layers prepared using different hydrogen dilution ratios for the bottom cell. The expression is defined by three Lorentz oscillators modified by a common indirect bandgap. A constant contribution ε_{1o} to the real part of the dielectric function is also used as a free parameter

Bottom cell *nc*-Si:H *i*-layer at 200 °C					
R	ε_{1o}	Modified Lorentz oscillator			
		A (eV)	Γ (eV)	E_0 (eV)	E_g (eV)
2	0.854 ± 0.066	4.425 ± 0.578	0.562 ± 0.039	3.500 ± 0.007	1.069
		48.008 ± 2.109	1.236 ± 0.031	4.199 ± 0.004	
		17.113 ± 1.949	1.837 ± 0.113	5.253 ± 0.030	
5	0.687 ± 0.076	4.983 ± 0.654	0.584 ± 0.041	3.498 ± 0.007	1.069
		42.155 ± 2.999	1.166 ± 0.034	4.177 ± 0.004	
		24.025 ± 3.075	2.310 ± 0.148	5.152 ± 0.058	
10	0.758 ± 0.072	5.266 ± 0.638	0.586 ± 0.038	3.494 ± 0.007	1.069
		43.262 ± 2.786	1.166 ± 0.032	4.170 ± 0.004	
		22.494 ± 2.813	2.278 ± 0.142	5.152 ± 0.055	
20	0.287 ± 0.116	8.943 ± 1.469	0.705 ± 0.066	3.486 ± 0.009	1.069
		39.298 ± 6.964	1.129 ± 0.050	4.136 ± 0.005	
		26.562 ± 7.525	3.096 ± 0.463	5.077 ± 0.216	
40	0.328 ± 0.104	6.369 ± 0.948	0.618 ± 0.052	3.494 ± 0.008	1.069
		40.537 ± 5.004	1.145 ± 0.045	4.169 ± 0.005	
		27.466 ± 5.390	2.669 ± 0.263	5.112 ± 0.119	

this range is lower than the average value of 3.62 eV for the doped layers. This behavior would be expected for a larger grain size or a lower crystallite defect density in the *i*-layers compared to the doped layers. Considering next the broadening parameters in Fig. 7.16, it is noted that the broadening parameter Γ_2 of the dominant oscillator $E_{0,2}$ tends to decrease with increasing R for $R < 20$. This is an expected trend that could be attributed to an increase in grain size or an improvement in crystallite quality with increasing R to $R = 20$. In contrast, Γ_1 and Γ_3 show the opposite behavior, namely increases with increasing R over this range. This apparent inconsistency may be attributable to dielectric function inaccuracies since the $E_{0,1}$ and $E_{0,3}$ oscillators are relatively weak shoulders on the dominant $E_{0,2}$ oscillator. The similar overall amplitudes of the analytical forms of the dielectric functions for the bottom cell *i*-layers in Fig. 7.15 suggest similar void volume fractions for all *i*-layer films. In spite of this, different trends are observed versus R in the constant contribution ε_{1o} and the oscillator amplitudes. Such variations are likely to be due to correlations, since the weaker A_1 and A_3 amplitudes increase as the dominant ε_{1o} and A_2 amplitudes decrease with R, at least for the lower R values.

Because of the inconsistent trends observed in Fig. 7.16, likely caused by correlations, it seems reasonable to attempt a reduction in the number of free parameters in modeling the dielectric functions of the *nc*-Si:H *i*-layers, as was done in Sect. 7.2.3 for the doped *nc*-Si:H. The goal is to identify relationships or constants

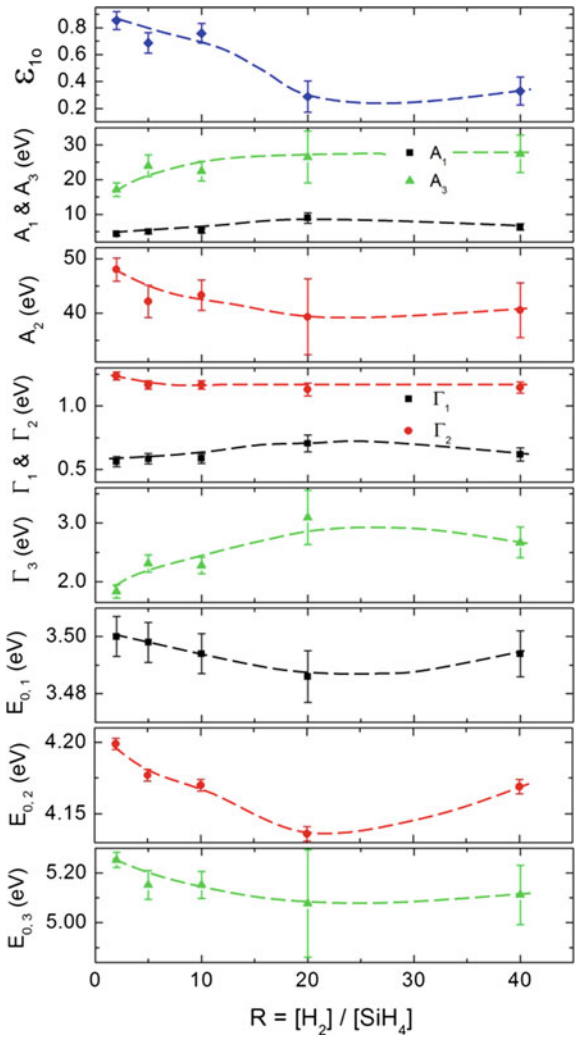


Fig. 7.16 Dielectric function parameters for bottom cell *nc*-Si:H *i*-layers measured at 200 °C and plotted versus the hydrogen dilution ratio, assuming an analytical form given by three modified Lorentz oscillators and an energy-independent contribution to ε_1. The broken lines are visual guides to the data

that may be employed for this purpose, starting with the resonance energies in Fig. 7.17. The panel for the correlation of $E_{0,3}$ with $E_{0,2}$ includes the critical point energies for single crystal silicon [33]. This correlation suggests that for the *i*-layers $E_{0,3}$ can be linked to $E_{0,2}$ in a parameterization according to $E_{0,3} = 3.71\ E_{0,2} - 10.3$ eV such that the variations in these energies are caused by stress, as was suggested for the doped *nc*-Si:H. In fact, this trend is close to that observed for the larger set of doped *nc*-Si:H and roughly consistent with the single crystal data point in Fig. 7.17, which would correspond to zero stress. In contrast, the variations in $E_{0,1}$ are much smaller, and its range of values is not understandable in terms of stressed crystallites. As a result of the smaller variations, $E_{0,1}$ can be fixed at its

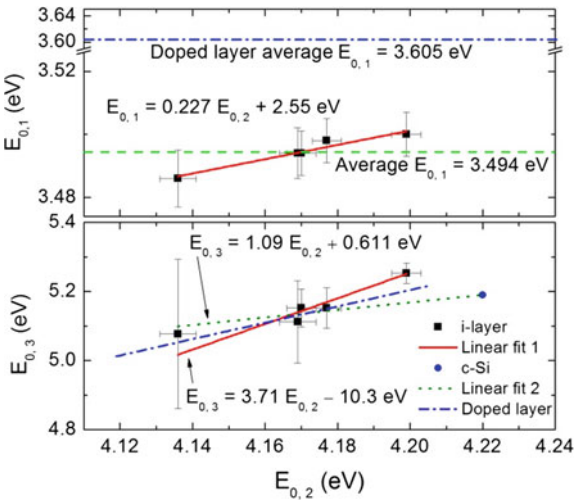


Fig. 7.17 Resonance energies of the first and third Tauc-Lorentz oscillators that describe the dielectric functions of the bottom cell *nc*-Si:H *i*-layers at 200 °C. These results are plotted as functions of the resonance energy of the second oscillator. The solid lines are the linear fits to the *i*-layer results with the equations given in each panel, and the horizontal dashed line represents the average value of $E_{0,1}$. The circular point in the lower panel identifies the values of $E_{0,2}$ and $E_{0,3}$ for single *c*-Si. The dotted line is the linear fit of the *i*-layer results, constraining the fit to pass through the point for single *c*-Si. The average value of $E_{0,1}$ and the linear fit to $E_{0,3}$ for the doped layers from Fig. 7.10 are given by the dot-dashed lines

average value of $E_{0,1} = 3.494$ eV for this series, which is considerably lower than the range of values for doped *nc*-Si:H, as shown in Fig. 7.17.

The broadening parameters of the first and third resonances are plotted as a function of the broadening of the dominant $E_{0,2}$ oscillator in Fig. 7.18. Because the same mechanism that leads to variations in broadening of the $E_{0,2}$ oscillator is not observed for the other two oscillators, the simplest consistent method for parameter reduction is to fix the broadening parameters of the two weaker oscillators to their average values, given by $\Gamma_1 = 0.611$ eV and $\Gamma_3 = 2.438$ eV. Differences may arise between the behavior observed for doped and *i*-layers since the *i*-layers have higher void fractions whereas the doped layers have higher densities of scattering centers due to defects, including the respective dopant atoms themselves.

The correlation plot of the *nc*-Si:H *i*-layer dielectric function amplitudes including the constant ε_1 offset versus the relative void fraction is given in Fig. 7.19 which uses the $R = 225$ *p*-layer as a reference. Due to the similarity of void fractions for all *i*-layers, there is no clear correlation among the *i*-layer samples in this plot. In order to obtain correlations among the *i*-layer samples similar to those for the doped layers, dielectric function measurements for *i*-layers prepared with different thicknesses or under different conditions are required. Comparing the results for the *i*-layers with the trends observed for the doped layers, the average value of A_2 is roughly consistent with the trend observed for the doped layers

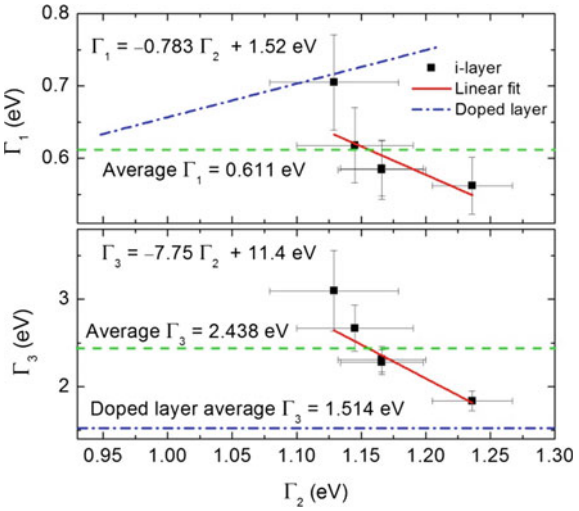


Fig. 7.18 Broadening parameters of the first and third Tauc-Lorentz oscillators that describe the dielectric functions of the bottom cell *nc*-Si:H *i*-layers at 200 °C. These results are plotted as functions of the broadening parameter of the second oscillator. The solid lines are the linear fits to the *i*-layer results with the equations given in each panel. The horizontal broken lines represent the average values of Γ_1 and Γ_3 for the *i*-layers. The dot-dashed lines describe the linear fit of Γ_1 and the average value of Γ_3 for doped layers from Fig. 7.11

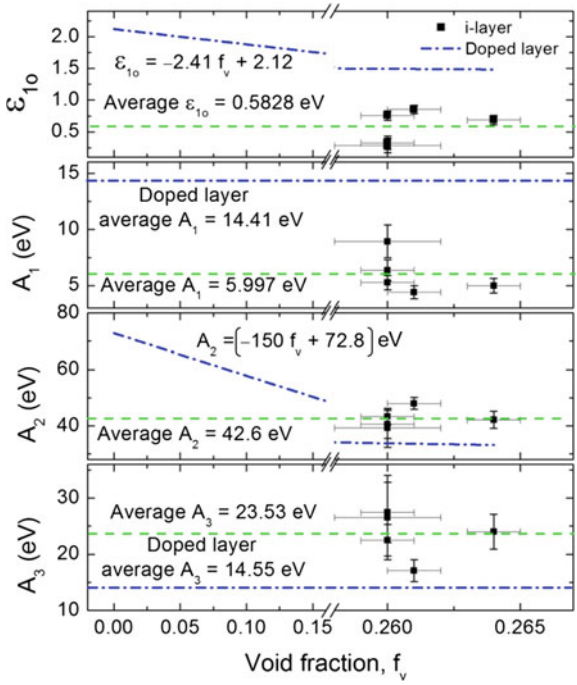


Fig. 7.19 The constant offset ε_{1o} and the amplitude parameters of the modified Lorentz oscillators that describe the dielectric functions of *nc*-Si:H *i*-layers at 200 °C. These results are plotted as functions of the relative void volume fraction, which was obtained by using the dielectric function of the densest film of the *p*-layer H_2-dilution series and that of void in the EMA to simulate the dielectric functions of all other *nc*-Si:H materials. The horizontal broken lines represent the average values from the *i*-layer series, and the dot-dashed lines represent either averages for A_1 and A_3 or linear trends for ε_{1o} and A_2 from the doped layer series of Fig. 7.12

whereas the average value of ε_{1o} for the *i*-layers is lower than the corresponding doped layer trend. Thus, a possible strategy for parameter reduction for these *i*-layers is to use (i) fixed average values for A_1 and A_3, (ii) the trend from A_2 given by the doped layers specified by the free parameter f_v, and a variable value of ε_{1o}. This approach would be consistent with that developed for *nc*-Si:H doped layers.

7.2.5 *Real Time SE and Growth Evolution Diagram of* nc-*Si:H* i-*Layer Evolution*

In the analysis of the real time SE data for the *nc*-Si:H *i*-layer of the bottom cell, plots of the bulk layer thickness versus time can be obtained by applying each of the five analytical expressions of Table 7.4 for the dielectric functions [14]. From the bulk layer thickness versus time, the deposition rate R_d can be obtained as an average over the deposition time from beginning to end. Figure 7.20 depicts R_d as a function of the H_2-dilution ratio R. The deposition rate R_d decreases rapidly as R increases over the range of $R = 2$–20 and stabilizes for $R \geq 20$.

In order to characterize the microstructural and phase evolution of each bottom cell *i*-layer, the model shown in Fig. 7.7 was applied to analyze the real time SE data over the spectral range from 3 to 5 eV. This model includes an outerlayer along with a surface roughness layer, whereby the former was simulated using a three component EMA of *a*-Si:H, *nc*-Si:H, and void. The dielectric function of *a*-Si:H used in the EMA of the semi-infinite medium is given as an analytical expression consisting of a single Cody-Lorentz oscillator with fixed $E_g = 1.68$ eV and with all other parameters linked to the bandgap with relationships adjusted for the 200 °C temperature. The resulting MSE, surface roughness layer thickness $d_{s,i\ 2}$, and *nc*-Si:H and relative void volume fractions $f_{b,i\ 2\text{-nc}}$, and $f_{b,i\ 2\text{-v}}$ are plotted versus bulk layer thickness $d_{b,i\ 2}$ in Fig. 7.21.

Considering next Fig. 7.21, a surface smoothening effect is observed in the initial stage of each *nc*-Si:H *i*-layer deposition. Such a smoothening effect is more

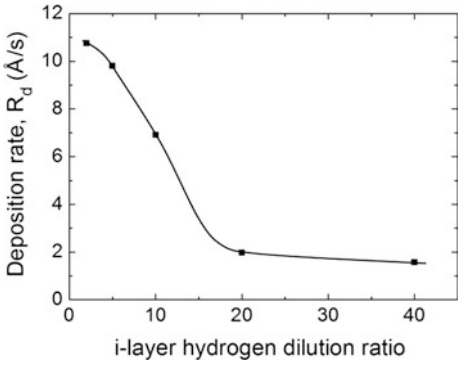


Fig. 7.20 Deposition rate R_d versus hydrogen dilution ratio $R = [H_2]/[SiH_4]$ for bottom cell Si:H *i*-layers prepared using vhf-PECVD at 60 MHz with different H_2-dilution ratios of $R = 2$, 5, 10, 20, and 40 (points). The line is a visual guide

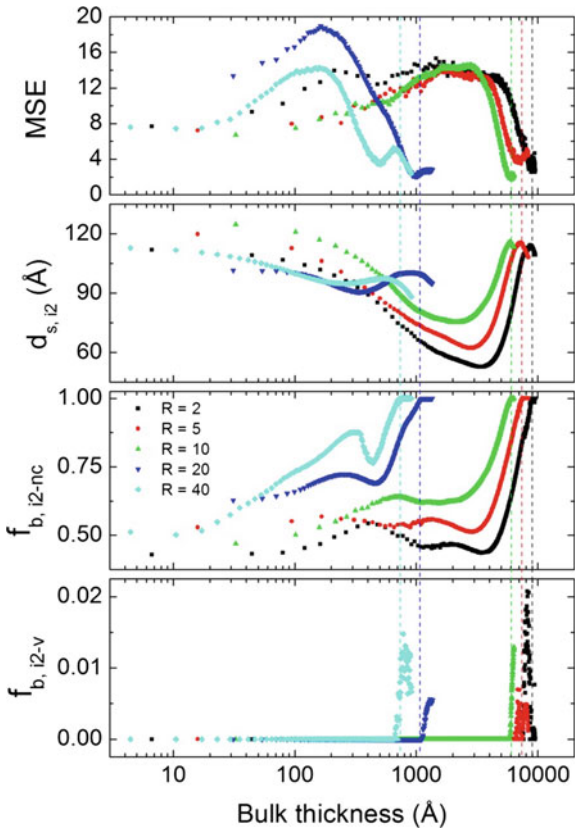


Fig. 7.21 Mean square error (MSE), surface roughness layer thickness ($d_{s,i\ 2}$), and bulk layer nanocrystalline and relative void volume fractions ($f_{b,i\ 2\text{-nc}}$ and $f_{b,i\ 2\text{-v}}$, respectively), plotted versus bulk layer thickness for Si:H *i*-layers prepared on Si:H *p*-layers in the tandem solar cell configuration. These *i*-layers were fabricated by vhf-PECVD at 60 MHz with different hydrogen dilution ratios of $R = 2$, 5, 10, 20, and 40

pronounced for the *i*-layers prepared at lower hydrogen dilution ratio. This effect is consistent with the renucleation of smaller nanocrystallites from the *p*-layer that smoothen the growing film surface. Other key features in this figure that support this interpretation include an observed subsequent roughening transition, a maximum in the surface roughness layer thickness, and a second more abrupt decrease in surface roughness. This later stage growth behavior indicates that the *i*-layers undergo a phase transition from a mixed phase which is deposited in the earlier stage of *i*-layer deposition to a coalescing nanocrystalline phase [(*a*-Si:H + *nc*-Si:H) → *nc*-Si:H] at the roughness maximum. A renucleation process and subsequent small grain growth may arise from a transient effect in the initial striking of the plasma that disrupts continued evolution of the nanocrystallites from the *p*-layer surface to the *p*/*i* interface region. This transient effect could be a gas phase compositional change with time or interface disruption that generates a damaged region. Over time, however, as the plasma stabilizes and the *p*/*i* interface is buried, the nucleating nanocrystals increase in size as indicated by the subsequent roughening effect.

Figure 7.22a shows a growth evolution diagram that depicts the bulk layer thickness at which the *nc*-Si:H volume fraction assumes specific values in plots as a function of the H_2-dilution ratio R used in the deposition process [11]. The uppermost line with $f_{b,i\ 2\text{-nc}} = 1$ represents the bulk layer thickness at which the transition occurs from mixed-phase Si:H (*a*-Si:H + *nc*-Si:H) to stable phase *nc*-Si:H. The diagram shows typical behavior in that the transition shifts to decreasing bulk layer thickness with increasing R; the most rapid shift occurs between $R = 10$ and $R = 20$.

Extensive studies have demonstrated that under specific ranges of deposition conditions, including high H_2 dilution ratio for example, Si:H films first nucleate as *a*-Si:H or mixed-phase materials and then evolve into inverted cone-like nanocrystalline structures as growth proceeds [11]. The nucleation density N_d and cone half angle θ of the nucleating nanocrystallites can be estimated from real time SE results using the difference between the bulk layer thicknesses (Δd_b) at which the coalescence and nucleation of nanocrystalline inclusions occur, as well as the associated difference in the surface roughness thickness (Δd_s). The nucleation is identified by an abrupt increase in roughness as crystallites grow preferentially relative to the surrounding material. Coalescence is identified by a clear maximum

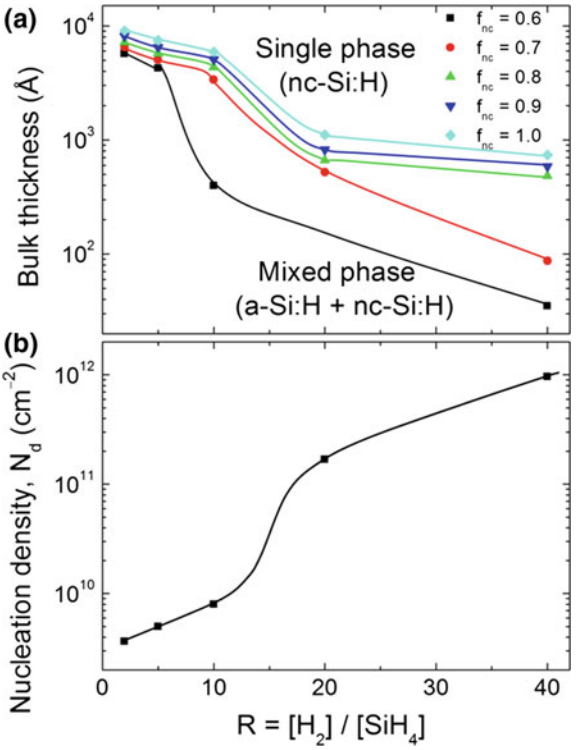


Fig. 7.22 **a** Growth evolution diagram plotted as a function of the H_2-dilution ratio for 60 MHz vhf-PECVD of bottom cell Si:H deposited on a Si:H *p*-layer in the tandem configuration (points). Depicted are the (mixed-phase)-to-(stable nanocrystalline phase) Si:H transition (diamonds) and the bulk layer thickness contours at which the *nc*-Si:H volume fraction is constant. **b** Nucleation density plotted as a function of R for the bottom cell Si:H *i*-layers (points). The lines in (**a**) and (**b**) are visual guides

in the surface roughness layer thickness. The following equations describe the nucleation geometry

$$\theta = \cos^{-1}\left(\frac{\Delta d_b}{\Delta d_b + \Delta d_s}\right), \tag{7.7}$$

$$N_d = \frac{1}{K(\Delta d_b)^2 \tan^2\theta}, \tag{7.8}$$

where K is a constant defined by the surface area fraction occupied by the bases of the nanocrystalline cones at the onset of coalescence [23]. The value of K depends on the initial distribution of the crystalline nuclei. In this study, it is assumed that the crystalline nuclei lie on a square lattice and, thus $K = 4$. Figure 7.22b shows the nucleation density determined from (7.7) and (7.8) plotted as a function of R as deduced from the data in Fig. 7.21. The nucleation density is observed to increase rapidly with increasing R with the largest step between $R = 10$ and $R = 20$.

7.2.6 *Process-Performance Correlations for* a-*Si:H*/nc-*Si:H Tandem Solar Cells*

Table 7.5 provides the deposition conditions of the individual layers of the *a*-Si:H/*nc*-Si:H tandem solar cells, where 'V' indicates the parameters that have been varied in studies of process-performance correlations [14]. One goal of this set of depositions was to explore the role of enhanced crystallinity in the bottom cell *p*-layer on the crystalline development in the overlying *i*-layer. A second goal is to explore the effects of elevated total gas pressure of 1.5 Torr on the formation of the recombination junction, the bottom cell *i*-layer, and the resulting performance of the solar cell.

Figure 7.23 shows the device performance results for tandem cells that were fabricated under identical conditions, with the exception of the bottom cell Si:H:B *p*-layers. These *p*-layers were prepared at the three different rf power levels of $P = 64$, 128, and 192 mW/cm^2 with final film structures given in Table 7.3. The H_2-dilution ratio for the bottom cell *i*-layer of these solar cell depositions was fixed at $R = 20$; all other deposition details are given in Table 7.5. The V_{OC} values of the set of cells fabricated with the lowest power *p*-layer are significantly higher and the short circuit current density values (J_{SC}) are significantly lower compared to those for the sets of cells with *p*-layers fabricated using the two higher plasma power levels. The high V_{OC} of the set of tandem cells with the bottom cell *p*-layer fabricated at low plasma power is caused by the properties of the *p*/*i* interface and its influence on subsequent *i*-layer deposition [11]. In particular, the evolution of the *i*-layer is expected to be controlled by the structure of the low plasma power *p*-layer with its higher *a*-Si:H volume fraction, resulting in the higher V_{OC}. It is clear that

Table 7.5 Deposition conditions for the component layers of the *a*-Si:H/*nc*-Si:H tandem solar cells fabricated in this investigation. The power density for the *p*-layer of the bottom cell and the hydrogen gas flow for the *i*-layer of this cell are variables in this study, as denoted "V"

Layer	T_{sub} (°C)	p_{total} (mTorr)	Plasma		Gas flow (sccm)						Time (s)	Target thickness (Å)
			f (MHz)	*P* (mW/cm^2)	Ar	SiH_4	5% B_2H_6 in H_2	5% PH_3 in H_2	CH_4	H_2		
p	200	400	13.56	9.5	–	13	1	–	8	–	50	110
p/i	200	1000	13.56	13	–	6	–	–	–	360	800	150
i	200	450	13.56	13	–	20	–	–	–	10	800	1500
n	200	1500	13.56	32	–	2	–	0.5	–	200	1000	250
p	200	1500	13.56	**V**	–	2	0.5	–	–	500	**V**	1500
i	200	1500	60	128	–	5	–	–	–	**V**	**V**	20,000
n	200	350	13.56	9.5	–	10	–	0.5	–	–	120	250
Ag	RT	5	13.56	920	10	–	–	–	–	–	1800	20,000

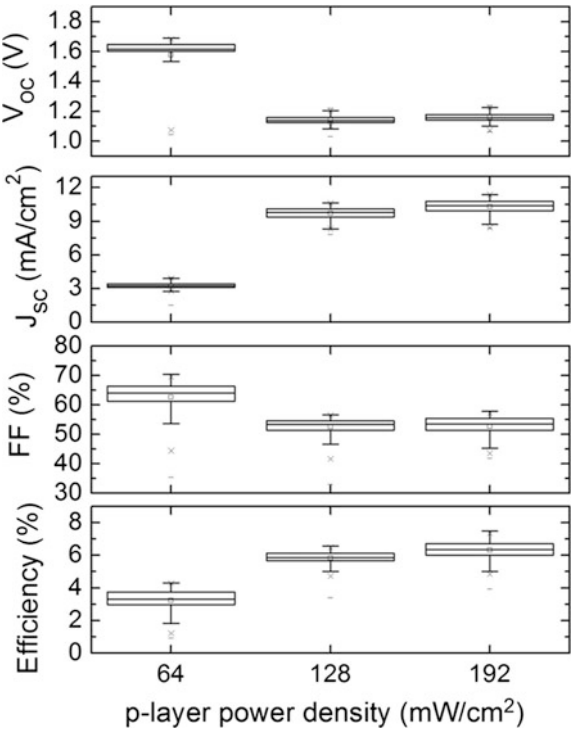


Fig. 7.23 Performance parameters of open circuit voltage (V_{OC}), short circuit current density (J_{SC}), fill factor (FF), and efficiency for Si:H tandem solar cells incorporating bottom cell Si:H:B *p*-layers prepared with different rf power density levels of $P = 64$, 128, and 192 mW/cm^2. The *i*-layer of the bottom cell used in this *p*-layer comparison was prepared using a hydrogen dilution ratio of $R = 20$

the range and maximum V_{OC} of this set of cells, the latter being $V_{OC} \sim 1.7$ V, is characteristic of a tandem device with two *a*-Si:H cells, with the top and bottom cells generating voltages of ~0.8–0.9 V. The low J_{SC} is also likely to reflect the initial amorphous phase within the *i*-layer of the bottom cell, which is not collecting sufficient current due to its inhomogeneous structure, evolving from *a*-Si:H to *nc*-Si:H. The low current generated by the bottom cell then limits current through the entire device.

For the *p*-layer prepared at the lowest plasma power, the amorphous region of the bottom cell *i*-layer adjacent to the *p*/*i* interface results from the amorphous phase of the underlying *p*-layer. Specifically, the *p*-layer suppresses the growth of nanocrystallites in the *i*-layer under the relatively low $R = 20$ H_2-dilution conditions, promoting instead the growth of the amorphous phase. The amorphous region of the bottom cell *i*-layer exerts a dominating effect on the overall tandem cell performance. A weaker effect may be related to the nature of the *n*/*p* interface formed under the low power *p*-layer conditions. Under these conditions, the interface may not serve as an effective recombination junction for the tandem solar cell. In fact, a higher density of defects may be needed at this interface. In contrast, the device performance for the sets of cells having *p*-layers prepared at $P = 128$ and 192 mW/cm^2 are similar to one another, an observation that is consistent with the similarity in the dielectric functions of the *p*-layers as shown in Fig. 7.9. For these two similar sets of cells, the V_{OC} values are consistent with an *a*-Si:H/*nc*-Si:H

tandem solar cell (as opposed to an *a*-Si:H/*a*-Si:H tandem). In fact, the observed maximum V_{OC} value of ~1.25 V from the two sets of cells is consistent with an *a*-Si:H top cell generating a voltage of ~0.85 V and a bottom cell generating a maximum voltage of ~0.4 V.

Figure 7.24 summarizes the device performance of two series of tandem solar cells that incorporate bottom cell *nc*-Si:H *p*-layers prepared at rf power levels of 128 and 192 mW/cm^2. On each of these two types of *p*-layers, a series of Si:H bottom cell *i*-layers was deposited using the H_2 dilution ratio *R* as a variable deposition parameter. Five and three different hydrogen dilution ratios of $R = 2, 5, 10, 20$, and 40, and $R = 10, 20$, and 40 were applied in *i*-layer depositions on the *nc*-Si:H *p*-layers prepared at rf power levels of 128 and 192 mW/cm^2, respectively. Considering the full set of data including cells with both *p*-layers, it is clear that the average open circuit voltage V_{OC} decreases with increasing hydrogen dilution ratio *R*. This may indicate a change in the bottom cell *p*/*i* interface region from a dominant

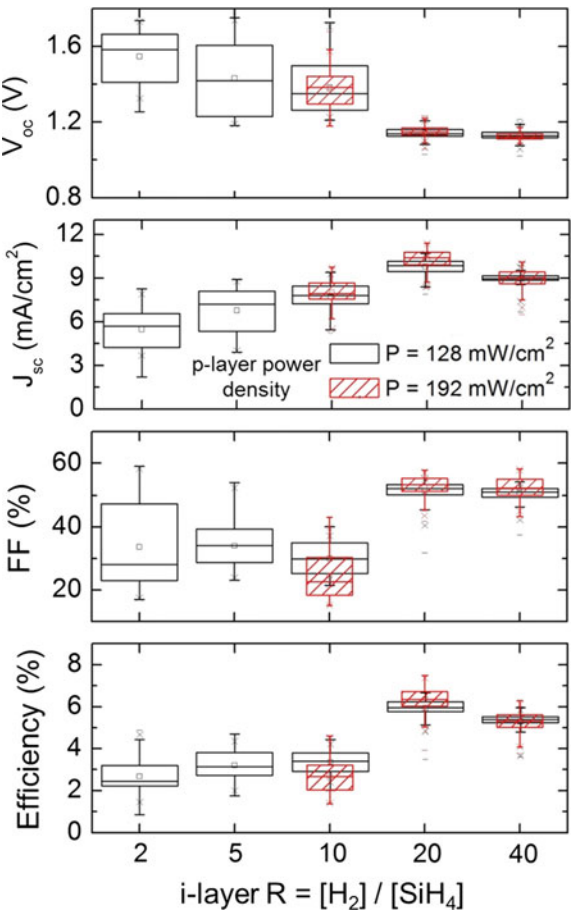


Fig. 7.24 Performance parameters of open circuit voltage (V_{OC}), short circuit current (J_{SC}), fill factor (FF), and efficiency for Si:H tandem solar cells incorporating bottom cell *i*-layers prepared with different hydrogen dilution ratios *R* enumerated along the abscissa. The bottom cell *nc*-Si:H *p*-layers used in this *i*-layer comparison were prepared at rf power density levels of $P = 128$ mW/cm^2 (black open symbols) and 192 mW/cm^2 (shaded symbols)

amorphous phase contribution to a nanocrystalline phase contribution with increasing R. In addition at low R, there is a much broader distribution of V_{OC} values, demonstrating that under these conditions there is a much stronger spatial dependence of the bottom cell i-layer structure adjacent to the p/i interface region. In contrast to V_{OC}, the average short circuit current J_{SC} increases as the H_2-dilution ratio R increases for R values from $R = 2$–20, yielding a maximum J_{SC} at $R = 20$. The maximum fill factor is highest at the lowest R value and decreases as R increases to $R = 10$. Abrupt increases in the maximum and average fill factors are observed between $R = 10$ and 20, with the maximum values nearly reaching the overall maximum possible with $R = 2$. The fill factor distribution tends to narrow with increasing R to $R = 20$, reaching a much narrower width for the two high H_2-dilution ratios of $R = 20$ and 40. This behavior again reflects a stronger spatial non-uniformity of the bottom cell structure at the lowest R values.

From the device performance shown in Fig. 7.24, the tandem solar cells separate into two groups irrespective of the rf power used in the deposition of the bottom cell p-layer. The first group includes $R = 2$, 5, and 10, whereas the second group includes $R = 20$ and 40. The transition between the two groups occurs in the same range of R as the large changes in the evolution of surface roughness and nanocrystalline fraction as determined by the real time SE data analysis shown in Fig. 7.21, the growth evolution diagram in Fig. 7.22a, and the nucleation density in Fig. 7.22b. This change is characterized by abrupt reductions in (i) the thickness at which the roughening transition occurs associated with the renucleation of crystallites starting from mixed-phase Si:H and (ii) the thickness at which the coalescence transition occurs from mixed-phase to stable-phase *nc*-Si:H. The first transition decreases from 2500 to 400 Å in the i-layer bulk thickness as R increases from $R = 10$ to 20, and the second transition decreases from ~6000 to 1000 Å in the i-layer bulk thickness as R increases from $R = 10$–20. As a result, for the low R group of cells, the volume fraction of *nc*-Si:H in the i-layer remains below 0.65 for at least the first 3000 Å of growth. Clearly, the maximum open circuit voltages V_{OC} of the first group are much higher compared to those of the second group, and the average V_{OC} for this first group is decreasing with increasing R. In fact, between the first and second groups, i.e., between $R = 10$ and 20, the average and maximum V_{OC} show a step decrease with the increase in R. In contrast, the average and maximum fill factor FF and to a lesser extent short circuit current J_{SC} exhibit step increases between $R = 10$ and 20. Overall, the trends in J_{SC} and FF dominate, and the average and maximum efficiency of the first group are lower than those of the second group.

Both average device performance and real time SE data analysis results indicate that the p/i interface of the first group has a large spread of characteristics, whereas that of the second group is dominated by the nanocrystalline phase. The large spread in V_{OC} for the first group indicates that depending on the location on the 15 cm × 15 cm sample, some cells are dominated by the amorphous phase with V_{OC} as high as 1.7 V whereas others are dominated by the nanocrystalline phase with V_{OC} as low as 1.25 V. As noted earlier, this behavior is a result of spatial non-uniformity that occurs under the deposition conditions used for the low R films.

In the following paragraphs, the further implications of the above observations will be discussed.

The open circuit voltage V_{OC} sensitively reflects the properties of the *p*/*i* interface region, in particular the phase composition and bandgap of the *i*-layer adjacent to the *p*/*i* interface [11]. Typically for mixed phase *i*-layer materials, the open circuit voltage V_{OC} increases as the volume fraction of amorphous phase in the *i*-layer at the interface increases and, for single phase *i*-layer materials, as the bandgap of the phase increases. To explore these effects, the device performance parameters of J_{SC}, FF, and efficiency, also including the series and shunt resistances R_s, and R_{shunt}, respectively, are plotted versus the open circuit voltage V_{OC} in Fig. 7.25 for all solar cell depositions. The motivation for presenting these plots is to evaluate the effect of the nature of the bottom cell *p*/*i* interface region on the performance parameters of the device.

It can be observed in Fig. 7.25 that the short circuit current J_{SC} tends to decrease continuously with increasing open circuit voltage V_{OC}. One possible reason for this behavior is the increase in the effective thickness of the amorphous component in the *i*-layer adjacent to the *p*/*i* interface as V_{OC} increases. This in turn leads to

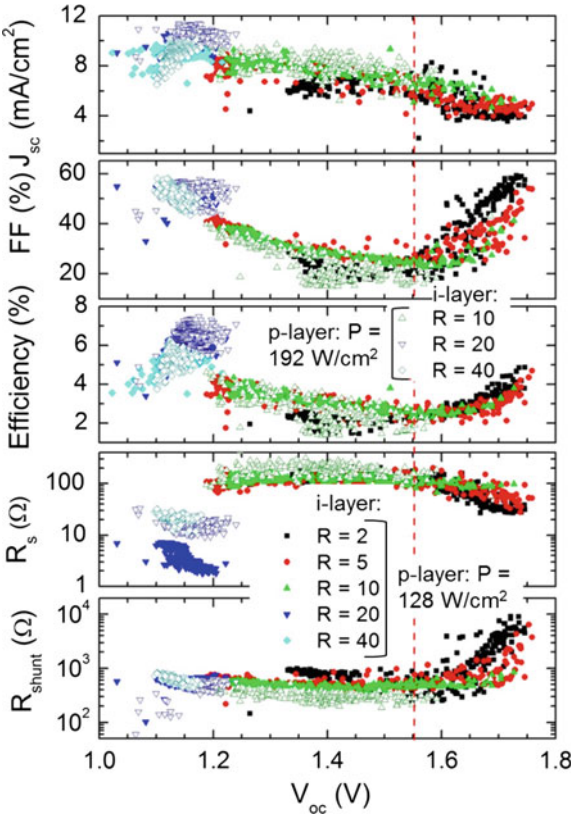


Fig. 7.25 Performance parameters of short circuit current (J_{SC}), fill factor (FF), efficiency, as well as series resistance (R_s), and shunt resistance (R_{shunt}) plotted versus the open circuit voltage (V_{OC}) for Si:H tandem solar cells incorporating bottom cell *i*-layers prepared with different hydrogen dilution ratios *R*. The bottom cell *nc*-Si:H *p*-layers used in this *i*-layer comparison were prepared at two different rf power density levels of $P = 128$ mW/cm^2 (solid symbols) and 192 mW/cm^2 (open symbols)

reduced absorption by the bottom cell since the bandgap of *a*-Si:H is wider than that of the desired *nc*-Si:H phase. The net effect is a reduction in current generated by the bottom cell and a mismatch in current generated by the two cells. The current output of the tandem device is then limited by the reduced bottom cell current.

The fill factor, on the other hand, initially decreases gradually as the open circuit voltage V_{OC} increases above 1.2 V; however, a more rapid increase in fill factor occurs when the open circuit voltage V_{OC} increases above 1.6 V. This behavior suggests that when the *i*-layer region adjacent to the *p*/*i* interface is predominantly nanocrystalline Si:H with V_{OC} being controlled by this phase, the fill-factor is relatively high. The limitation on the fill factor under these conditions is a low apparent shunt resistance in fact associated with voltage-dependent collection, characteristic of a low quality nanocrystalline bottom cell *i*-layer. A relatively high fill factor is also obtained when the *i*-layer region adjacent to the *p*/*i* interface is predominantly *a*-Si:H with V_{OC} being controlled by this phase such that the cell behaves as an *a*-Si:H same bandgap tandem cell. The limitation in this case is a high series resistance. At intermediate V_{OC} values the fill-factor is reduced when the intrinsic Si:H material transitions between amorphous and nanocrystalline phases in a thick layer adjacent to the *p*/*i* interface, or possibly when different phases co-exist locally at the *p*/*i* interface over different spatial regions of the same solar cell. Based on these considerations, one can understand a fill factor dependence on V_{OC} that is *U*-shaped as in Fig. 7.25.

A limitation to the performance of the solar cells with a *nc*-Si:H bottom cell arises due to the relatively low V_{OC}-FF product for cells in which *nc*-Si:H dominates at the *p*/*i* interface. For example, assuming a desired V_{OC} of 1.4 V with 0.85 V arising from the *a*-Si:H and 0.55 V from the *nc*-Si:H solar cell, the average fill factor is ~0.25, suggesting that for this V_{OC} value, a transition between phases occurs in the *i*-layer adjacent to the *p*/*i* interface region. Improvements in the fill-factor to a value of 0.55 require a considerable reduction in V_{OC} to the maximum of ~1.25 V which would be consistent with ~0.85 V arising from the *a*-Si:H and ~0.4 V arising from the *nc*-Si:H. This low V_{OC} of 0.4 V associated with the addition of the bottom cell may be attributable to a poor quality recombination junction, an incompletely optimized *p*-layer, or to *p*/*i* interface recombination due to either void structures or residual amorphous phase at the interface. In fact, the dielectric functions of Fig. 7.15 indicate a high void fraction in the fully *nc*-Si:H phase, and the structural evolution of Fig. 7.21 indicates a 0.5–0.6 *nc*-Si:H material fraction near the *p*/*i* interface with the remaining material being amorphous.

The real time SE results provide insights into various process changes that may assist in the improvement of the V_{OC}-FF product. A graded H_2-dilution starting from a value greater than $R = 40$ to promote initial crystallite nucleation in conjunction with a decrease in R continuously as the film increases in thickness would ensure that a high volume fraction crystallite phase forms immediately from the *p*/*i* interface and grain boundaries remain appropriately passivated with *a*-Si:H as the film evolves in thickness. The eventual evolution and coalescence of crystallites even for $R = 2$ would seem to suggest that in the grading process R can be reduced to this low value to ensure grain boundary passivation with thin *a*-Si:H material;

however, the problem associated with such low R values is the spatial non-uniformity. Thus, the final R value used in grading must avoid this problem. It is possible that spatial non-uniformity can be mitigated with a reduction in total gas pressure or an increase in SiH_4 gas flow in order to avoid SiH_4 depletion, reducing the gas residence time in the plasma.

Next the effect of preparing bottom cell p-layers at the elevated rf plasma power density of $P = 192$ mW/cm^2 on the tandem device performance parameters will be discussed, as shown in Figs. 7.24 and 7.25. For the elevated power level, three solar cell structures with $R = 10$, 20, and 40 i-layers were prepared. As noted previously, the overall performance of these cells and its dependences on R and V_{OC} are similar to those of the cell structures with the bottom cell nc-Si:H p-layer prepared at the lower rf plasma power density of $P = 128$ mW/cm^2. Incorporation of the $P = 192$ mW/cm^2 p-layer results in an improvement in device performance at $R = 20$, which for all depositions is the minimum R value while ensuring a dominant nanocrystallite phase in the p/i interface region over much of the deposition area. Apparently, the bottom cell p-layer deposited at higher power promotes greater nanocrystallinity in the i-layer region adjacent to the p-layer, leading to improvements in the maximum values of all three solar cell performance parameters. This also suggests the possibility that future improvements enhancing the nanocrystallinity of the bottom cell p-layer can lead to improvements in the i-layer and the overall cell performance. This expectation relies on the conclusions of previous real time SE studies that demonstrate the clear effects of the phase of the underlying film on the phase evolution of the overlying film [11, 12].

7.3 Mapping SE for Correlations with Device Performance: Optimization of *nc*-Si:H *n*-Layers in *a*-Si:H Solar Cells

7.3.1 General Strategy and Approaches

Two approaches exist for developing new or improved processes in thin film PV manufacturing. For thin film technologies that have yet to reach maturity, small area photovoltaic devices are optimized on the laboratory scale. Once an optimum process is achieved with sufficiently high performance, then scale up of the process is desired. The goal in scale-up is to maintain the high performance achieved in the laboratory, and this requires spatial uniformity in thickness and materials properties over large areas. Alternatively for mature technologies, one can seek to improve overall performance and yield at full-scale. In either approach, mapping SE over large areas can be a valuable capability, as it avoids cutting full-scale panels into individual pieces for single point measurements [34, 35]. Mapping SE can involve mounting the ellipsometer heads on a translation stage and either scanning the panel in two dimensions typically off-line [34] or exploiting the motion of the panel

on-line and scanning the panel in one dimension [35]. In this way, mapping SE is ideally suited for measuring non-uniformities in thickness or dielectric function and then evaluating their impact on current collection based on a summation of absorbances computed from each of the active layers.

Both ex situ multiple angle of incidence and in situ real time SE approaches have been developed for extracting both structural information and complex dielectric functions. Ex situ multi-angle SE has its limitations when more than a few structural parameters must be extracted in addition to an unknown dielectric function determined point by point versus photon energy. In many circumstances, these limitations can be overcome by expressing the dielectric function in an analytical form. As demonstrated in Sect. 7.2, real time SE also overcomes these limitations for even the most complicated multilayer structures through measurements of each deposited film for a continuous array of thicknesses. By studying each film as it is deposited, the structure and point-by-point dielectric function of a film growing uniformly with accumulated thickness can be extracted by multi-time analysis. For films having dielectric functions that are graded with accumulated thickness, virtual interface analysis becomes possible. Considering the limiting case of a film with perfect spatial uniformity, then ex situ mapping SE provides no further data analysis power over ex situ SE at a single location. If the film is spatially non-uniform with a sufficient range in thickness, however, analysis of data simultaneously at several locations spanning the range in thickness, i.e. multi-spot analysis, becomes equivalent to multi-time analysis. Thus, the requirement in multi-spot analysis is equivalent to that in multi-time analysis, namely that the dielectric function must not vary as the thickness changes.

Next a simple example will be shown to demonstrate the similarity between mapping and real time SE analysis results in studies of Si:H. Figure 7.26 shows maps of the bulk and surface roughness layer thicknesses for an intrinsic *a*-Si:H film deposited on a 15 cm × 15 cm TEC™ 15 glass substrate. The topmost layer on the glass substrate is SnO_2:F in this case having a surface roughness layer thickness of ~472 Å. As a result, the *a*-Si:H film acquires roughness imposed by conformal coverage of the underlying SnO_2:F surface as the *a*-Si:H layer is deposited. The clear statistical relation of Fig. 7.27 is found between the surface roughness and the bulk layer thicknesses from the two maps of Fig. 7.26. This behavior is consistent with substrate-induced roughness on the *a*-Si:H which is smoothened with increasing thickness due to the effects of conformal coverage and diffusion of film precursors on the *a*-Si:H surface before their incorporation into the bulk. An exponential decay of surface roughness to a stable value versus bulk thickness is predicted as a result of precursor surface diffusion [36, 37]. In fact, the data exhibit reasonable agreement with this behavior, as shown by the solid line in Fig. 7.27, which is the best two-parameter fit to an equation of the form $d_s = k_1 + \left(472\,\text{Å} - k_1\right)\exp(-ad_b)$, where k_1 is the final stable roughness value in the limit of thick film deposition. Thus, the fit is constrained such that $d_s(d_b = 0\,\text{Å}) = 472\,\text{Å}$, which is an area average of the starting roughness on the SnO_2:F, as measured before the deposition. A second set of correlations of the

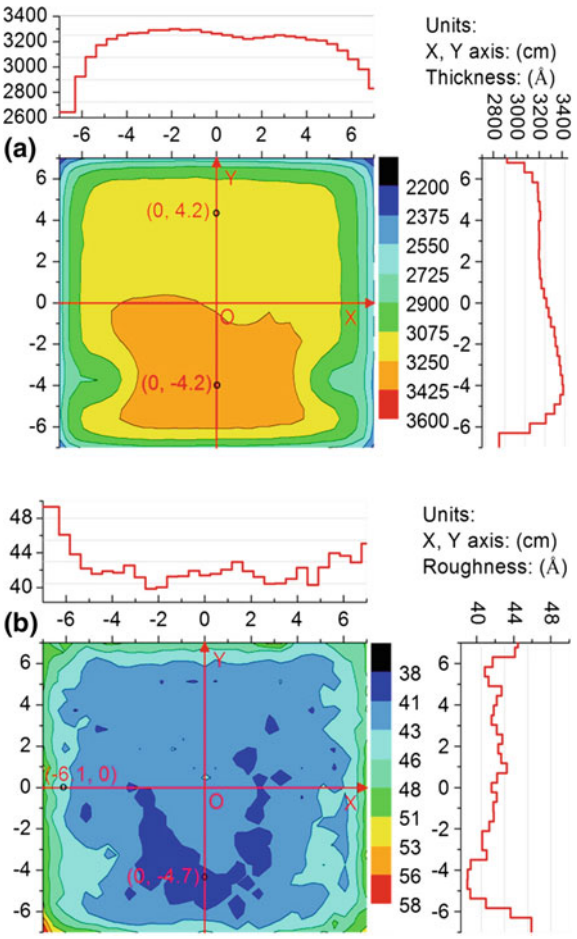


Fig. 7.26 Maps of the **a** bulk thickness and **b** surface roughness layer thickness obtained by ex situ mapping SE for an *a*-Si:H *i*-layer deposited on a 15 cm × 15 cm TEC™ 15 glass substrate. The two curves (top and right) show the thickness variations along the *X* and *Y* axes

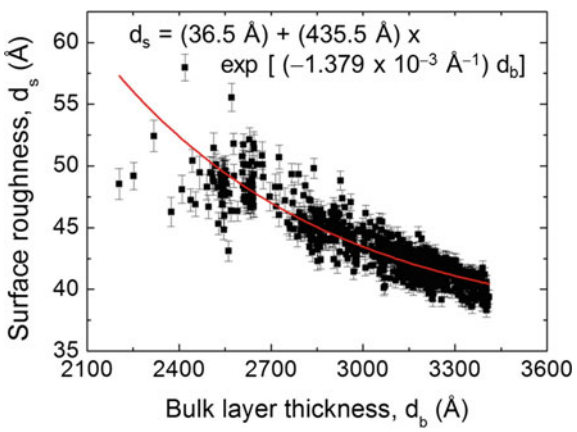


Fig. 7.27 Correlation between the surface roughness and bulk layer thicknesses for the *a*-Si:H *i*-layer obtained from ex situ mapping SE analysis of a coated TEC™ 15 glass panel 15 cm × 15 cm in size. The solid line is an exponential decay function designed to fit the data while passing through d_s = 472 Å at d_b = 0 Å, which is the thickness of the surface roughness measured for the SnO_2:F before *a*-Si:H deposition

structural properties obtained by mapping SE is provided at the very end of this section. These latter correlations provide insights into nanocrystallite evolution with bulk layer thickness.

Finally, if an array of small area cells is fabricated starting from a spatially non-uniform multilayer stack, then the performance parameters of the solar cells can be correlated with the structural and optical properties as determined by mapping SE [15, 16]. In this way, process-property-performance correlations can be established based on a single deposition. With fabrication of the array of small area devices in parallel using appropriate masks, and subsequent automated mapping and device analysis, fine tuning of the performance optimum is possible in a single deposition. This methodology will be demonstrated in the next sub-sections. With intentional spatial non-uniformities built into a process and the ability to characterize those non-uniformities by mapping SE, rapid combinatorial approaches for optimization are possible.

7.3.2 *Dielectric Function Determination for* nc-*Si:H* n-*Layers*

Single junction *p-i-n a*-Si-H solar cells have been fabricated on 15 cm × 15 cm TEC™ 15 glass in order to evaluate effects of *n*-layer crystallinity on device performance [16]. The *a*-Si:H cells under investigation apply the same basic process as those used in the top cell of the tandem *a*-Si-H/*nc*-Si-H solar cells of the previous section. The *n*-layers have been prepared on *a*-Si:H *i*-layers using a range of H_2-dilution ratios, $90 \leq R \leq 150$, in an attempt to control the crystallite evolution and its volume fraction for the range of *n*-layer thicknesses of interest used in solar cells. Because the *n*-layer film nucleates from an *a*-Si:H *i*-layer, the initial stage of growth consists of an *a*-Si:H *n*-layer that is relatively uniform with depth. As the film thickness increases, however, nanocrystals nucleate, increase in size and coalesce according to a growth evolution diagram similar in form to that of Fig. 7.22a. The initial discussion will focus on the determination of the dielectric functions of the amorphous and stable nanocrystalline phases of the *n*-layer including analyses of these spectra in terms of analytical models.

Figures 7.28 and 7.29 show structural schematics used for determination of the dielectric functions in the amorphous and stable nanocrystalline stages of *n*-layer evolution. A simplified sample configuration was used to ensure a smoother *i*-layer surface and more accurate dielectric functions. In the amorphous growth stage, multi-time analysis is performed, and the resulting point-by-point dielectric functions can be fit using the Cody-Lorentz oscillator model with A, Γ, E_0, E_g, and E_p as free parameters and with the constant offset ε_{1o} set to unity. The final results depicting the dielectric functions of the *a*-Si:H phases for the series of *n*-layers are shown in Fig. 7.30, presented as the best fit analytical expressions. Figure 7.31 depicts an example of the more challenging procedure used for dielectric function

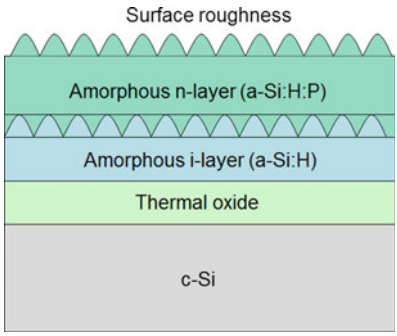


Fig. 7.28 Schematic of a single phase *a*-Si:H *n*-layer deposited on a thermally oxidized crystalline silicon wafer, pre-coated with an *a*-Si:H *i*-layer, as used for real time SE. This structure enables simulation of *n*-layer deposition in the solar cell configuration

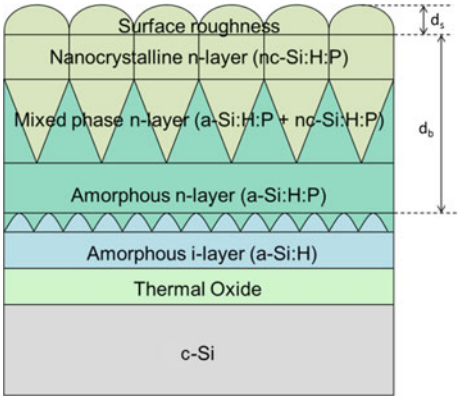


Fig. 7.29 Schematic of an *n*-layer that is non-uniform in thickness, initially growing as *a*-Si:H as in Fig. 7.28, nucleating nanocrystals, and finally becoming stable *nc*-Si:H at the surface

determination of the stable phase *nc*-Si:H, in this case *nc*-Si:H deposited with $R = 80$ [23]. In Fig. 7.31, an average MSE between the data and best fit is given versus a trial value of d_s appropriate for the time of nanocrystallite contact, which occurs at the surface smoothening onset, as will be demonstrated in the next sub-section. Each trial value generates a different *nc*-Si:H dielectric function for use in a virtual interface analysis, in which case the EMA with volume fractions of amorphous, nanocrystalline, and void components, f_a, f_{nc}, and f_v, is applied to obtain the dielectric function evolution for the top 10 Å of the bulk *n*-layer. The minimum average MSE occurs at $d_s = 100$ Å, which gives the correct dielectric function for the *nc*-Si:H via inversion of SE data at the nanocrystallite contact point (maximum d_s). The Fig. 7.31 inset gives the best fit *nc*-Si:H dielectric function obtained through point-by-point analysis with $d_s = 100$ Å along with that of *a*-Si:H from the same deposition. Figure 7.32 shows the dielectric functions of the stable

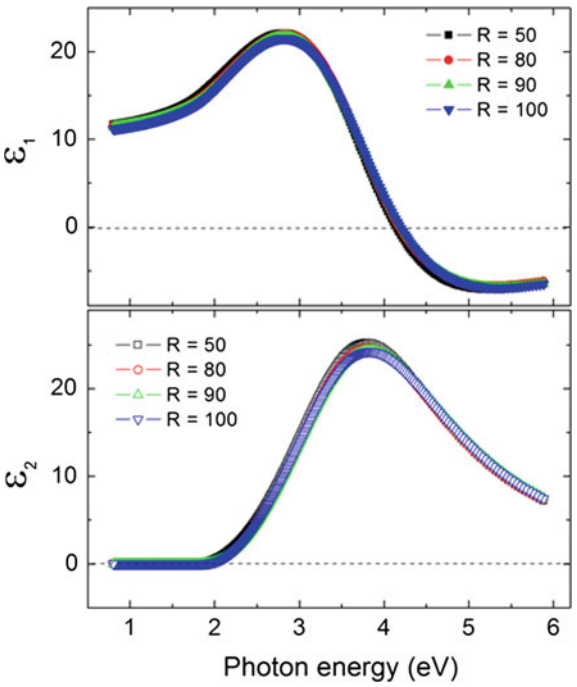


Fig. 7.30 Dielectric functions at 200 °C presented as the best fit analytical expressions for *n*-type *a*-Si:H materials obtained in the initial growth stage at four different hydrogen dilution ratios. The dielectric functions were modeled assuming a single Cody-Lorentz oscillator along with ε_{1o}, an energy-independent contribution to the real part of ε

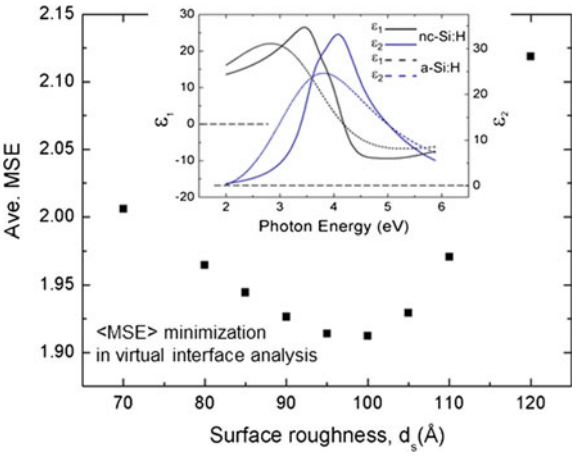


Fig. 7.31 Average mean square error (MSE) versus a trial value for the surface roughness thickness. The inset shows the amorphous (broken lines) and nanocrystalline (solid lines) complex dielectric functions ε obtained at 200 °C for an $R = 80$ *n*-type Si:H film, as determined by virtual interface analysis of real time SE data [16]

nc-Si:H for the same set of depositions as in Fig. 7.30, applying the MSE minimization procedure of Fig. 7.31 for each.

The Cody-Lorentz parameters used to model the dielectric functions of the amorphous phase of the *n*-layer before the nanocrystallite nucleation transition are plotted versus the H_2-dilution ratio in Fig. 7.33 [26]. In fact, two sets of parameters

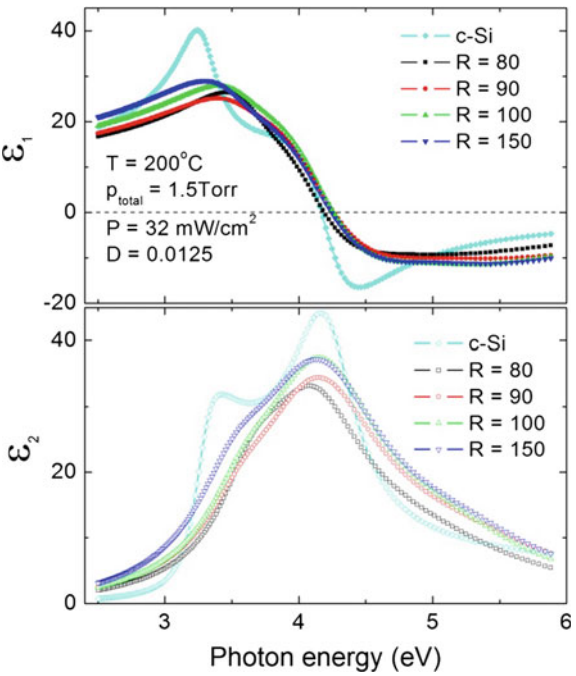


Fig. 7.32 The dielectric functions at 200 °C for nanocrystalline Si:H *n*-layers prepared using different H_2-dilution ratios along with the dielectric function at 200 °C for single crystalline silicon for comparison

are presented, the first with ε_{1o} as a variable and the second with ε_{1o} fixed at unity. The clearest parameter variation is observed in the bandgap, which increases monotonically as expected with the H_2-dilution ratio. The same trend is obtained for both sets of dielectric function parameters. Another trend is an increase in Γ with increasing H_2-dilution, which is opposite to the trends observed for *a*-Si:H *i* and *p*-layers. Such an effect may occur if the phosphorus atom incorporation increases with H_2 dilution. The Cody-Lorentz parameters shown in Fig. 7.33 are plotted versus their bandgaps, as presented in Fig. 7.34 (points). Linear fits are also provided in the figure, in order to generate a parameterization for *a*-Si:H *n*-layers based on a single bandgap variable. It should be emphasized that the *n*-layer parameters are relevant for the substrate temperature of 200 °C. An adjustment to room temperature can be applied based on the assumption that the temperature dependences of the parameters for the *n*-layers are the same as those for *i*-layers [27]. This adjustment results in the solid lines in Fig. 7.34, blue-shifted relative to the 200 °C results.

The dot-dashed lines in Fig. 7.34 are results for a set of *p*-layers deposited on *i*-layers in which case the parameters are also corrected for the substrate temperature. The dotted lines in Fig. 7.34 are the relationships reported by Ferlauto et al. for *a*-$Si_{1-x}Ge_x$:H (left) and *a*-$Si_{1-x}C_x$:H (right) *i*-layers at room temperature [26]. The results for the amplitude show consistent behavior for *n* and *p* layers that is nearly a continuation of the *a*-$Si_{1-x}Ge_x$:H *i*-layer trend of Ferlauto et al. The behaviors of the other three parameters differ between the *n* and *p* layers. Such differences for the

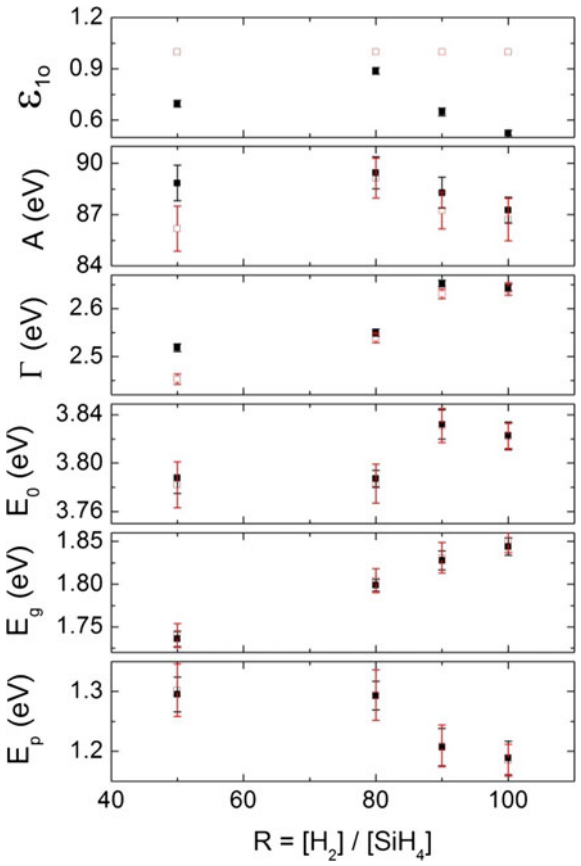


Fig. 7.33 Dielectric function parameters for *a*-Si:H *n*-layers measured at 200 °C and plotted versus the H_2-dilution ratio. For the solid and open symbols, the parameters derive from an analytical form of a single Cody-Lorentz oscillator with variable and fixed ε_{1o}, respectively

n-layer include (i) an increasing Γ with bandgap similar to the *a*-$Si_{1-x}C_x$:H *i*-layers, but differing from the *a*-Si:H *p*-layers; (ii) an increasing E_0 with bandgap, an expected trend, but one that differs from both the *a*-$Si_{1-x}C_x$:H *i*-layers and the *a*-Si:H *p*-layers; and finally, (iii) a weakly decreasing E_p with bandgap, a somewhat unexpected trend, and one that differs from the *i* and *p* layers. The results tend to suggest that the *n*-layers exhibit less disorder than the *a*-$Si_{1-x}C_x$:H *i*-layers and the *a*-Si:H *p*-layers, but that the disorder increases with increasing bandgap.

The dielectric functions of Fig. 7.32 for the *nc*-Si:H phases of the *n*-layers were parameterized as described in Sect. 7.2.3 by using three modified Lorentz oscillators that share a common bandgap. The common bandgap was fixed at 1.069 eV for all dielectric functions, since this value is the bandgap of single crystal Si at 200 °C and also can be assigned as the bandgap of the *nc*-Si:H phases of the *n*-layers. The ten Lorentz oscillator parameters A_j, $E_{0,j}$, Γ_j, including the offset ε_{1o} are given in Table 7.6, obtained by fitting the *nc*-Si:H dielectric functions of the *n*-layers. These results have been summarized as the diamond-shaped data points in Figs. 7.10, 7.11, and 7.12 along with those of the *nc*-Si:H *p*-layers. Table 7.7 shows the results

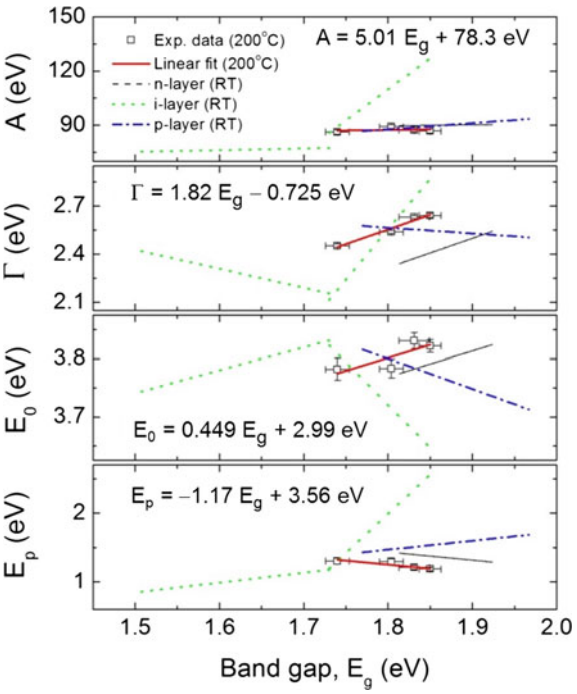


Fig. 7.34 Dielectric function parameters for *a*-Si:H *n*-layers measured at 200 °C and plotted versus the fitted bandgap. The parameters derive from an analytical form of a single Cody-Lorentz oscillator along with ε_{1o} which was fixed at unity. The solid lines shifted to higher bandgap result from corrections of the elevated temperature trends to those appropriate for room temperature (20 °C) measurement of the *n*-layers. The dot-dashed lines are the trends for *p*-layers from Sect. 7.2, and the dotted lines are the trends for *i*-layers from Ferlauto et al. [26]

Table 7.6 Parameters used in an expression that represents the dielectric functions at 200 °C for the nanocrystalline Si:H phase of *n*-layers, as described by three Lorentz oscillators modified by a common indirect bandgap, along with an energy-independent contribution to ε_1

R	ε_{1o}	Modified Lorentz oscillators			
		A (eV)	Γ (eV)	E_0 (eV)	E_g (eV)
80	1.716 ± 0.116	13.253 ± 3.688	0.597 ± 0.061	3.671 ± 0.018	1.069
		44.472 ± 5.763	0.948 ± 0.088	4.120 ± 0.015	
		19.881 ± 3.084	1.787 ± 0.175	4.923 ± 0.120	
90	1.526 ± 0.218	17.291 ± 5.757	0.920 ± 0.097	3.664 ± 0.045	1.069
		55.770 ± 8.059	1.091 ± 0.075	4.206 ± 0.017	
		11.411 ± 2.419	1.209 ± 0.130	5.211 ± 0.042	
100	1.438 ± 0.087	11.687 ± 2.443	0.678 ± 0.057	3.608 ± 0.016	1.069
		65.178 ± 5.185	1.103 ± 0.047	4.174 ± 0.007	
		14.968 ± 2.912	1.493 ± 0.129	5.115 ± 0.048	
150	1.470 ± 0.010	15.800 ± 2.570	0.721 ± 0.049	3.537 ± 0.013	1.069
		71.089 ± 5.332	1.210 ± 0.052	4.167 ± 0.008	
		13.509 ± 2.874	1.500 ± 0.160	5.224 ± 0.047	

of an analysis of the *n*-layer *nc*-Si:H dielectric functions using a model having four free parameters, including the variables f_v, $E_{0,2}$, Γ_2, and ε_{1o}, as described in Sect. 7.2.3, for a MSE comparison with the more general model having ten free

parameters. Also included are the void fraction and MSE obtained by a single-parameter EMA analysis. The material of lowest void fraction from Sect. 7.2.3 was used as the density reference in Table 7.7, namely the *p*-layer fabricated with $R = 225$, $T_{sub} = 120$ °C, and $P = 128$ mW/cm^2. Clearly the fit becomes poorer as the number of free parameters is reduced; however, the relatively small increase in MSE with the elimination of six free parameters appears to justify the parameter reduction method of Sect. 7.2.3. Such parameter reduction is likely to be needed when analyzing such films by ex situ SE in multilayer stacks. It should be pointed out, however, that these results are valid for the measurement temperature of 200 °C. For ex situ SE applications, data at room temperature for each sample would be needed. Alternatively, adjustments may be applied to shift the parameter values to those relevant for the desired temperature of measurement. The only available guidance for doing this is described in a previous study in which the temperature coefficients of eight modified-Lorentz parameters are reported (including the common value of E_g, but not the parameters of A_3, $E_{0,3}$, and Γ_3, due to the limited spectral range of that study) [20]. Such adjustments would shift each value and affect the correlations reported here.

7.3.3 *Growth Evolution Diagram for* nc-*Si:H* n-*Layers*

Figure 7.35 depicts the evolution of surface roughness layer thickness and the nanocrystalline volume fraction versus bulk layer thickness for the *n*-type Si:H films deposited with H_2-dilution flow ratios of $R = 50$, 80, and 100. These results were deduced from global MSE minimization as shown in Fig. 7.31 combined with virtual interface analyses over the mixed-phase growth regimes [16]. To extract the nanocrystalline Si:H volume fraction, the dielectric function of the outerlayer in the virtual interface analysis is modeled using the EMA as a mixture of *a*-Si:H, *nc*-Si:H, and void. The deposition rate is an outcome of the virtual interface analysis and values obtained in the amorphous and nanocrystalline growth stages, as well as an average throughout the deposition are shown in Fig. 7.36a. For the films prepared with $R = 80$ and 100, both amorphous-to-(mixed-phase) and (mixed-phase)-to-nanocrystalline transitions can be clearly identified on the surface roughness evolution plots of Fig. 7.35. For the film prepared with $R = 50$, however, a weak smoothening effect was observed indicating amorphous Si:H growth for much of the deposited range of bulk layer thickness. The surface roughness on this $R = 50$ film was found to increase after the bulk layer thickness reached ~820 Å, which indicates the film is undergoing the transition to mixed-phase material near this bulk thickness.

Using such results obtained at different H_2-dilution ratios R, a growth evolution diagram for the PECVD *n*-type Si:H can be generated [11]. In the diagram shown in Fig. 7.36b, the three phase evolution regions of amorphous, mixed phase, and nanocrystalline Si:H can be readily identified. These regions are separated by the two phase transitions designated as $[a \rightarrow (a + nc)]$ and $[(a + nc) \rightarrow nc]$, where

Table 7.7 Summary of fitting results for the nanocrystalline Si:H phase of a series of *n*-layers using a four-parameter model including ε_{1o}, Γ_2, $E_{0,2}$, and f_v. The other six parameters associated with the ten-parameter model were either fixed or linked to one of these four parameters through the expressions in Figs. 7.10, 7.11, and 7.12. A comparison of the MSE's for the one, four, and ten parameter models is included

T_{sub} (°C)	R	P (mW/cm^2)		Four parameter model					One parameter model		Ten parameter model
			ε_{1o}	Γ_2 (eV)	$E_{0,2}$ (eV)	f_v	E_g (eV)	MSE	f_v	MSE	MSE
n-layer											
200	80	32	1.855 ± 0.089	1.001 ± 0.008	4.141 ± 0.003	0.097 ± 0.001	1.069	8.222	0.146 ± 0.003	18.023	6.968
200	90	32	1.382 ± 0.044	1.125 ± 0.005	4.212 ± 0.002	0.058 ± 0.001	1.069	5.305	0.135 ± 0.002	11.601	2.689
200	100	32	1.523 ± 0.057	1.065 ± 0.005	4.202 ± 0.002	0.039 ± 0.002	1.069	6.329	0.060 ± 0.002	8.978	4.890
200	150	32	1.835 ± 0.085	1.209 ± 0.008	4.145 ± 0.003	0.011 ± 0.001	1.069	9.062	0.027 ± 0.003	16.039	6.635

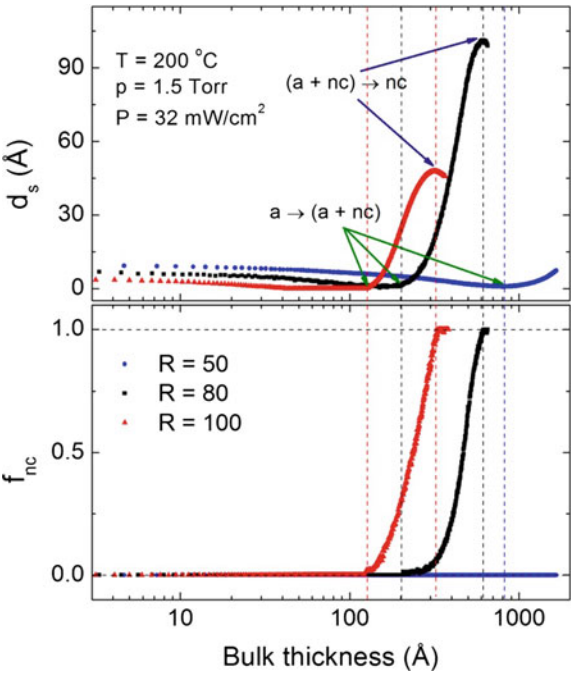


Fig. 7.35 Surface roughness layer thickness d_s and nanocrystalline Si:H volume fraction f_{nc} plotted versus bulk layer thickness for $R = 50$, 80, and 100 Si:H *n*-layers. Depositions were performed on substrates consisting of thermally oxidized crystalline silicon wafers coated with intrinsic *a*-Si:H to simulate the *p-i-n* solar cell structure, but with a smoother surface

$(a + nc)$ represents the mixed phase material. Contour lines of different nanocrystallite volume fractions are given as well, which can serve as a guide for solar cell fabrication in terms of the crystallite content at the surface of the *n*-layer. In addition to the surface roughness layer thickness, deposition rate of the outerlayer, and the nanocrystalline Si:H volume fraction of the outerlayer, the relative void volume fraction of the outerlayer serves as a fitting parameter in the SE model used for virtual interface analysis. The void fraction is a relative value since no voids are assumed in the determination of the single phase amorphous and nanocrystalline Si:H dielectric functions used in the EMA. Thus, these dielectric functions may incorporate voids implicitly that are not accounted for in the EMA analysis, existing not only in the single phase materials but also in the two-component composites.

In Fig. 7.37, the relative void volume fraction is plotted as a function of the nanocrystalline Si:H volume fraction for the *n*-layers prepared at different H_2-dilution ratios. By definition, the relative void volume fractions in the Si:H films are negligible in the initial stage when the nanocrystalline Si:H volume fraction is near zero. The film prepared at $R = 150$ is an exception, however. The large initial void volume fraction of this film is due to an $[a \rightarrow (a + nc)]$ phase transition occurring for a very thin (~45 Å) amorphous Si:H layer. Thus, the dielectric function of the amorphous phase could not be accurately obtained for this *n*-layer. As a result, the dielectric function of the pure amorphous phase used in the virtual interface analysis of the $R = 150$ deposition is the one obtained from the $R = 100$ deposition, which evidently has a lower void volume fraction than the amorphous phase of the

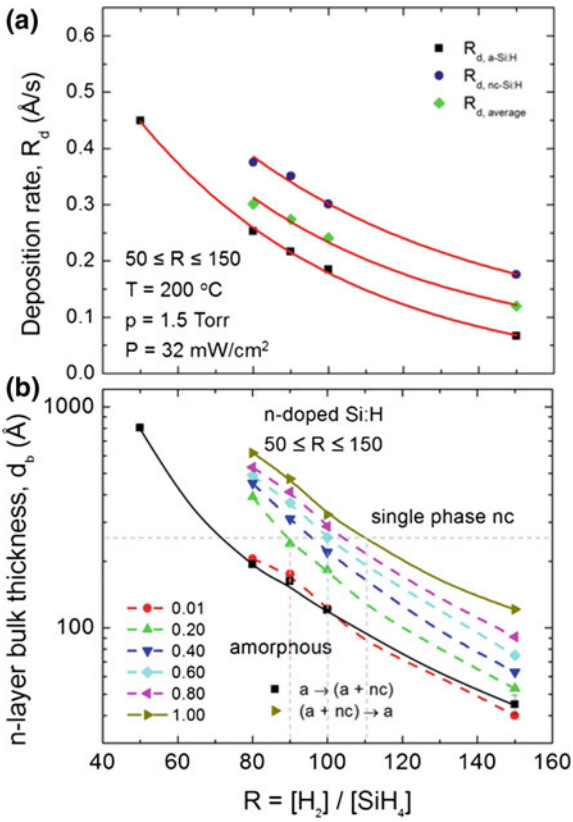


Fig. 7.36 **a** Deposition rates versus hydrogen dilution ratio $R = [H_2]/[SiH_4]$ for Si:H *n*-layers. For $R \geq 80$, the rates include those for the individual amorphous and nanocrystalline phases as well as an average throughout the deposition. **b** Growth evolution diagram for PECVD *n*-type Si:H thin films as deposited on *a*-Si:H *i*-layers, depicting the thicknesses of the $a \rightarrow (a + nc)$ transition (squares) identified from the onset of roughening and the $(a + nc) \rightarrow nc$ transition (right-pointing triangles) identified from the maximum in the surface roughness where the nanocrystalline volume fraction reaches unity. Contours defining constant volume fractions of the nanocrystalline phase are included. The horizontal line shows the 250 Å target thickness of the *n*-layer in the devices. The vertical lines show the *R* values explored in device studies designed to achieve a range of nanocrystalline volume fractions at the *n*-layer surface

$R = 150$ film. Regardless of this issue, the relative void volume fraction begins to increase and reaches its maximum when the nanocrystalline volume fraction is in the range from 0.15 to 0.26. Finally, the relative void fraction returns to zero by definition when stable phase nanocrystalline Si:H evolves.

The cone angle and the nucleation density can be calculated from (7.7) and (7.8) using structural information deduced from the real time SE data analyses of Fig. 7.35. Figure 7.38 shows these results as functions of the H_2-dilution ratio. Results for the *p*-layers deposited on *i*-layers at different *R* values are also included

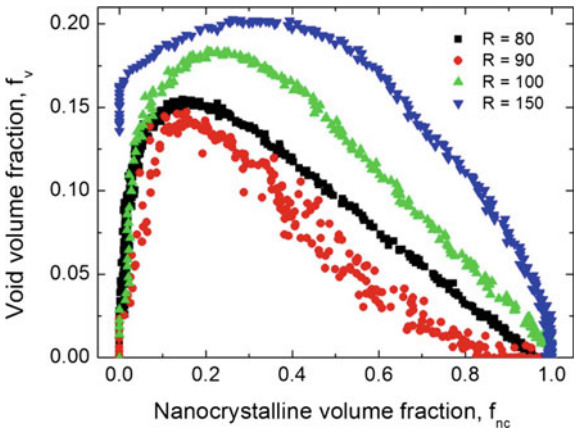


Fig. 7.37 Relative void volume fraction versus nanocrystalline volume fraction obtained by virtual interface analysis of *n*-layer depositions on substrates consisting of thermally oxidized crystalline silicon wafers coated with layers of intrinsic *a*-Si:H

for comparison. The cone half angle can be deduced not only from the surface roughness evolution via (7.7), but also from the ratio of amorphous and nanocrystalline Si:H deposition rates R_a/R_{nc} according to [23, 38]:

$$\theta = \cos^{-1}(R_a/R_{nc}). \tag{7.9}$$

Considering first the results for the cone angles of the *n* and *p*-layers in Fig. 7.38, these values increase with increasing *R*. This can be attributed to a higher growth rate ratio of the nanocrystalline phase relative to the amorphous phase. The cone angles deduced from the growth rate ratio are considerably higher, however. In fact,

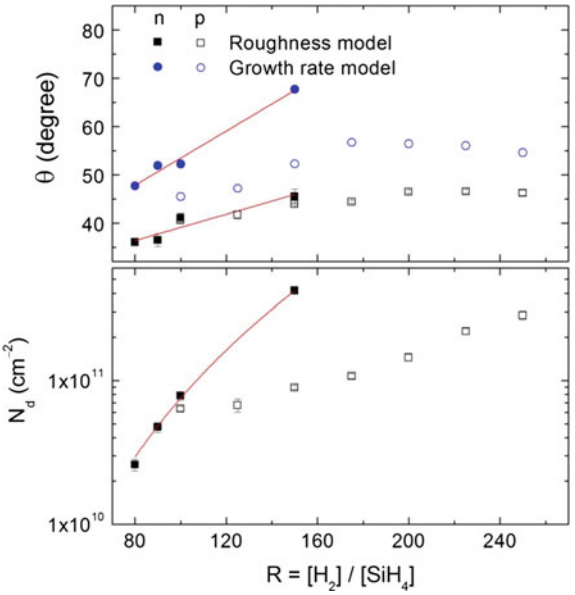


Fig. 7.38 Results for the cone half angle θ and nucleation density N_d plotted versus the H_2-dilution ratio *R* used in the deposition of a series of Si:H *n*-layers. Cone half angles were determined from the changes in the bulk and surface roughness layer thicknesses [filled squares, (7.7)] as well as from the of deposition rate ratio [filled circles, (7.9)]. Corresponding results for the *p*-layers of Sect. 7.2 are also included for comparison (open symbols)

at the highest $R = 150$, the growth rate difference would suggest almost immediate coalescence of crystallites. The cone angles of the *n*-layers from the surface roughness evolution as described by (7.7) are found to be consistent with the trend observed for the *p*-layers and are thus believed to be more reliable. Considering next the nucleation densities in Fig. 7.38, a monotonic increase is observed as the H_2-dilution ratio increases over the full range from 80 to 150. For the *n*-layers deposited with $R \leq 100$, the trend in nucleation density appears continuous with that of the *p*-layers. For the sample deposited with the highest dilution ratio of $R = 150$, however, a much higher nucleation density is observed for the *n*-layer. This indicates that, under these conditions, it is much easier to nucleate *n*-type *nc*-Si:H during *n*-layer deposition at high *R* than it is to nucleate *p*-type *nc*-Si:H.

7.3.4 *Mapping Spectroscopic Ellipsometry of Solar Cell Structures*

A 16 × 16 array of *a*-Si:H *p-i-n* dot cells has been fabricated onto 15 cm × 15 cm TEC™ 15 glass substrates using the *n*-layer process as described in the previous sub-sections. The *n*-layer H_2-dilution ratio for this cell fabrication was $R = 100$ and the doping gas ratio $[PH_3]/[SiH_4]$ was fixed at 0.0125; other *n*-layer deposition parameters include a substrate temperature of $T_{sub} = 200$ °C, a plasma power of $P = 32$ mW/cm^2, and a total pressure of $p_{total} = 1.5$ Torr. These are the same conditions as those used for the top cell *n*-layer applied in the tandem solar cell. Mapping SE was applied over the substrate area and (current-density)-voltage (*J-V*) measurements were performed on the array of dot cells in order to correlate *n*-layer material properties from SE and solar cell performance from *J-V*, as well as to characterize the role of macroscopic non-uniformities [16]. By exploiting the observed property variations over the large areas, the goal of these correlations is to identify and understand the relationships between the basic *n*-layer material properties and the single junction solar cell performance. With an appropriate optical model yielding property maps for all the layers of the device structure, one can evaluate impacts of the non-uniformities on the performance of scaled-up solar modules.

The mapping SE was performed from the film side and avoided the back contact dot cells. Thus, the topmost layer of the probed structure is the *n*-layer, which is analyzed using a two layer bulk/roughness model. Three maps of interest were obtained in the analysis. Figure 7.39a, b depict the maps of the *n*-layer bulk layer thickness and surface roughness thickness. Figure 7.39c depicts a map of the nanocrystalline volume fraction f_{nc} associated with the bulk *n*-layer, which is modeled throughout its thickness as an effective medium mixture of *a*-Si:H, *nc*-Si:H, and void. A range of $f_{nc} \sim 0.50$–0.75 is observed for the bulk layer thickness range of $d_b \sim 265$–300 Å. For this thickness range, the virtual interface analysis of

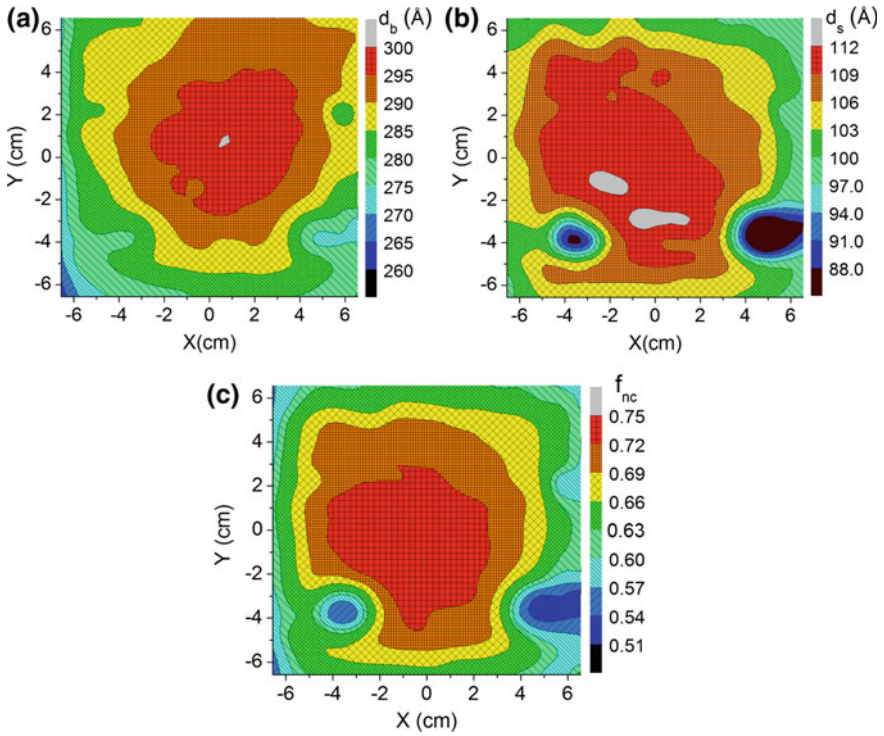


Fig. 7.39 Maps of the Si:H *n*-layer **a** bulk and **b** surface roughness layer thicknesses, and **c** nanocrystalline volume fraction over a 13 cm × 13 cm area for an *a*-Si:H *p-i-n* solar cell structure incorporating an $R = 100$ *n*-layer. Other deposition parameters include a substrate temperature of $T_{sub} = 200$ °C, a rf power of $P = 32$ mW/cm^2, and a total pressure of $p_{total} = 1.5$ Torr [16]

Figs. 7.35 and 7.36 yields top surface f_{nc} values in the range of $f_{nc} \sim 0.73$–0.86. The lower values for the maps are consistent to some extent with depth averaging of the nanocrystalline content within the *n*-layer. Given the cone-like geometry of nucleation, however, the deduced average leads to a result more closely characteristic of the top surface rather than a true average throughout the *n*-layer thickness. This is possible due to an apparently higher weighting effect of the surface in the analysis using a single bulk layer model for the graded *n*-layer.

Two observations can be made from the thickness map of Fig. 7.39a. First, the center area of the sample exhibits a greater bulk layer thickness compared with the outer area. Such a non-uniformity pattern may be caused by edge effects, meaning that the center of the anode exhibits a higher plasma density in the PECVD process relative to the edge. Second, a slight shift is observed in the non-uniformity pattern to the right side of the substrate. Apparently this asymmetry is caused by the gas flow pattern in the deposition chamber. Because the gas flow is from right to left, SiH_4 depletion is more likely to occur on the left side. Hence, a thinner *n*-layer on the left side of the substrate appears correlated with a locally increasing *R* value and

a decreasing deposition rate. Due to the local increase in R, a slightly thicker surface roughness layer is observed on the left side of the substrate, as shown in Fig. 7.39b. Because film growth is within the mixed phase (a-Si:H + nc-Si:H) region for the bulk thickness of ~270 Å, a higher hydrogen dilution ratio R will enhance nanocrystallite formation resulting in a rougher surface and a higher nanocrystalline fraction on the left side of the maps, as shown in Fig. 7.39c. In addition, it can be observed from the maps that the two cathode openings used for real time SE monitoring significantly affect the film uniformity. The effect is largest on the right side of the substrate. These two openings in the cathode appear to reduce the plasma density. As a result, the n-layer bulk and surface roughness thicknesses, as well as the nanocrystalline volume fraction in this region are observed to be lower than the surrounding substrate area.

7.3.5 *Property-Performance Correlations for Solar Cells*

The open-circuit voltage and fill-factor performance maps of solar cells incorporating $R = 100$ n-layers are shown in Fig. 7.40a, b [16]. It can be seen that the outer area gives higher V_{OC} and FF. The two circular patterns of reduced V_{OC} are observed on the map of Fig. 7.40a. These patterns are again caused by the openings in the cathode plate for real time SE monitoring. Cell performance is best evaluated from the $V_{OC} \times$ FF product rather than from the efficiency, since the short circuit current depends sensitively on the device structure (single vs. tandem) and the back-reflector design. This product is mapped in Fig. 7.40c and shows that the elevated performance occurs in an area that surrounds the center with the highest performance along the right edge. The performance parameters presented in Figs. 7.40 are difficult to interpret without correlations with fundamental properties to be presented next.

In Fig. 7.41a, the product of open circuit voltage and fill factor is presented versus the n-layer nanocrystalline volume fraction. The significant scatter in the data and variation in the envelope implies that for a given n-layer nanocrystalline volume fraction, other p, i, and n-layer properties may be varying such as their thicknesses, optical bandgaps, and depth profiles in f_{nc}. In addition, localized defects such as substrate contaminants and plasma particulates can generate shunting, leading to low shunt resistance at isolated locations on the device structure surface and reduced performance that also contributes to the scatter. The two cells with the highest individual open circuit voltage and fill factor were obtained at n-layer nanocrystalline volume fractions from 0.58 to 0.6. All data for the V_{OC}-FF product in Fig. 7.41a were fit using a second order polynomial function of nanocrystalline volume fraction (broken line parabola) which serves to identify the nanocrystalline volume fraction at which the maximum performance occurs on a statistical basis. This optimum nanocrystalline fraction for a given parameter is shown at upper right on the plots. Thus, on a statistical basis, the maximum product of open circuit voltage and fill factor is observed to occur at a nanocrystalline

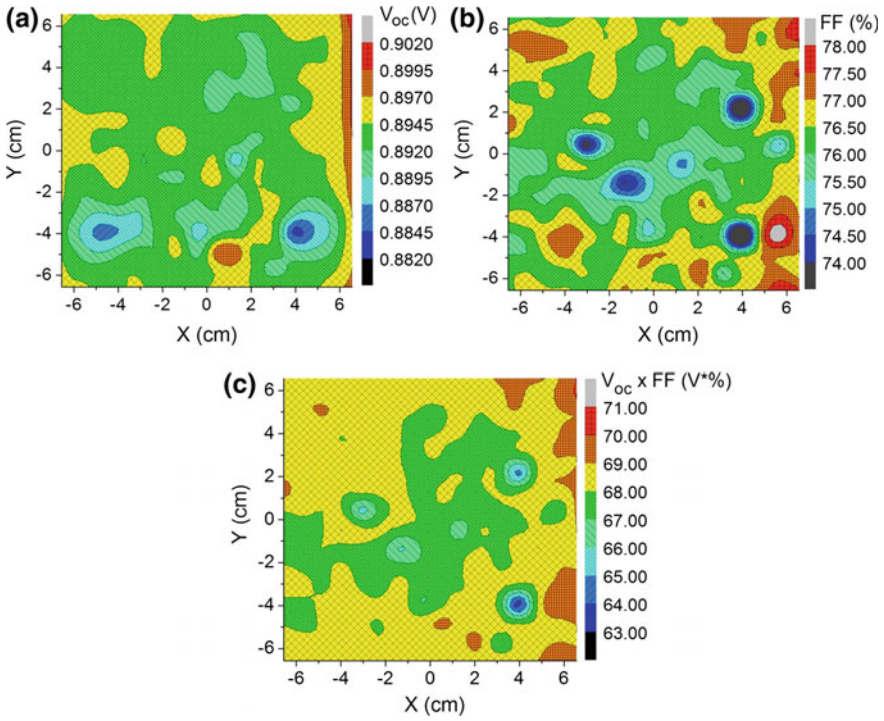


Fig. 7.40 Maps of the solar cell performance parameters of **a** V_{OC}, **b** FF, and **c** V_{OC}-FF product over a 13 cm × 13 cm substrate area for *a*-Si:H *p-i-n* devices incorporating an $R = 100$ *n*-type Si:H layer. Other *n*-layer deposition parameters include a substrate temperature of $T_{sub} = 200$ °C, a plasma power of $P = 32$ mW/cm^2, and a total pressure of $p_{total} = 1.5$ Torr

volume fraction of ~0.57, which is very close to the values for the two cells with the highest product of open circuit voltage and fill factor. One can now understand why the optimized performance on the map of Fig. 7.40c is located in the outer ring of the anode where the nanocrystalline fraction lies near ~0.6. In order to achieve the optimum conditions at the center of the anode, *R* must be decreased to reduce the volume fraction of nanocrystalline Si:H there. Alternatively, the gas pressure can be reduced to avoid depletion at the center of the anode. This latter change in the deposition process may enable the higher performance achieved on the right side of the maps to extend across the full electrode. Thus, the correlations between the solar cell and basic property maps provide directions for optimization of cell performance and improved uniformity.

Figure 7.41b, c illustrate the correlations of solar cell performance with the *n*-layer bulk and surface roughness thicknesses, respectively. Cells with the highest V_{OC}-FF product span the range of 275–290 Å in the bulk layer thickness and 95–100 Å in the surface roughness thickness. For all data in Fig. 7.41b, c, the V_{OC}-*FF* product was fit using second order polynomial functions of *n*-layer bulk and surface

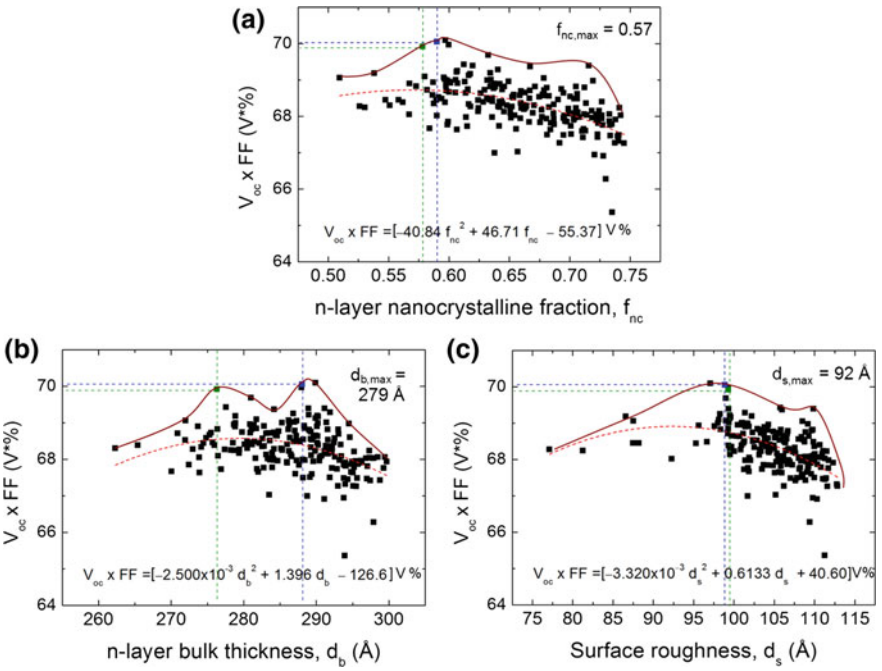


Fig. 7.41 Product of the key performance parameters of open circuit voltage and fill factor (V_{OC} × FF) correlated with the properties of the top-most $R = 100$ *n*-layer including **a** near-surface nanocrystalline volume fraction f_{nc}, **b** bulk layer thickness, and **c** surface roughness layer thickness over a 13 cm × 13 cm area for *a*-Si:H *p-i-n* solar cells. The blue and green vertical broken lines identify the cells with the highest V_{OC} and highest FF, respectively. The parabolic trends given by the red broken lines are the best fits to the complete data sets with the *n*-layer property at the maximum given at upper right. The solid lines define the maximum performance envelopes as guides to the eye

roughness thicknesses (broken line parabolas) which identify the structure at which the maximum performance occurs on a statistical basis. The thicknesses at which the maxima in the polynomial functions occur are entered into the upper right corner of each figure panel. On a statistical basis, the optimum V_{OC} × FF product occurs at ~280 Å bulk layer thickness and ~90 Å surface roughness layer thickness.

Figure 7.42a, b show plots of *n*-layer surface roughness thickness and top surface nanocrystalline volume fraction correlated with the bulk layer thickness. As expected for Si:H deposition in the mixed-phase stage of the growth evolution diagram, both the surface roughness and the nanocrystalline volume fraction increase monotonically as the bulk layer thickness increases. Figure 7.42c shows the close linear dependence of the *n*-layer surface roughness thickness on the *n*-layer nanocrystalline volume fraction. As the nanocrystalline component increases in volume fraction, protrusions above the surface increase in height, and Fig. 7.42c suggests a precise geometric relationship between the two. As a result, the optimum

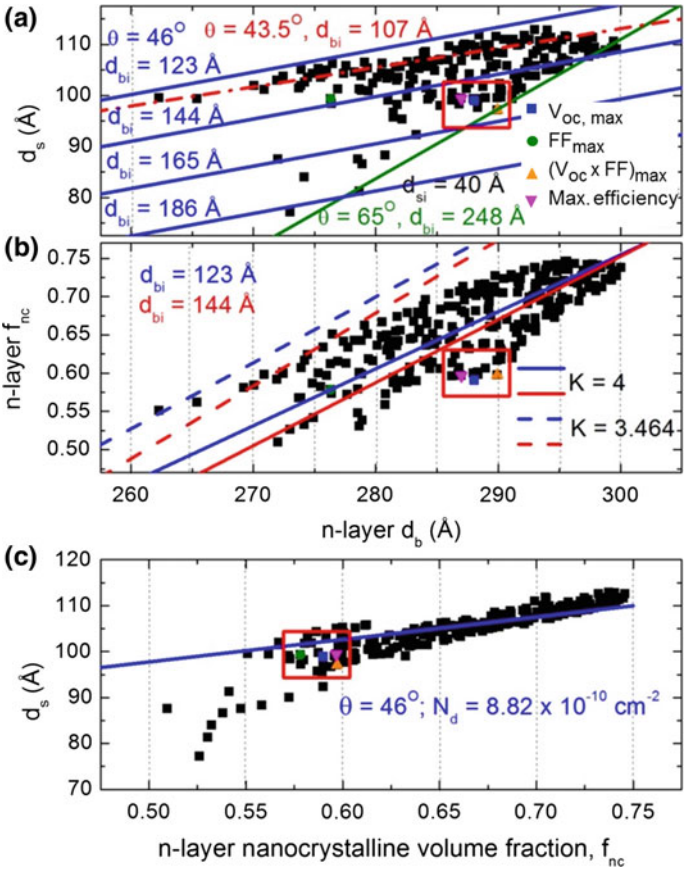


Fig. 7.42 Correlations of **a** surface roughness thickness with bulk thickness; **b** nanocrystalline volume fraction with bulk thickness; and **c** surface roughness thickness with nanocrystalline fraction, all from mapping SE for the $R = 100$ *n*-layer. The results are given for a 13 cm × 13 cm substrate area covered by a 16 × 16 array of *a*-Si:H *p*-*i*-*n* solar cells. The highest performing cells are given within the squares. The solid lines in the upper panel are the trends expected using a geometric model of nanocrystallites growing as inverted cones with spherical caps. The angle θ is the cone half-angle, and d_{bi} is the bulk layer thickness at the onset of the $[a \rightarrow (a + nc)]$ transition. The same geometric model is used to describe the data sets in (**b**) and (**c**). In (**b**), K is a constant that depends on the area distribution of conical nanocrystallites; $K = 4$ and $K = 3.46$ represent nanocrystallites on square and hexagonal close-packed grids. N_d in the bottom panel is the nucleation density of nanocrystallites

nanocrystalline volume fraction of $f_{nc} \sim 0.6$ from the statistical analysis corresponds to an optimum surface roughness thickness in the range of 95–105 Å. In the following paragraphs, the geometric relationships apparent in the three panels of Fig. 7.42 will be explored.

Considering Fig. 7.42a first, a positive correlation between the surface roughness and bulk layer thicknesses is expected within a cone growth model for the nanocrystallites. This relationship is given by

$$d_s = (\sec\theta - 1)(d_b - d_{bi}) + d_{si}, \tag{7.10}$$

where d_b and d_s are the bulk and surface roughness layer thicknesses for the n-layer, d_{bi} and d_{si} are the corresponding values at the $a \rightarrow (a + nc)$ transition, and θ is the nanocrystallite cone half-angle. Thus, d_{bi} is the bulk layer thickness from which the apices of inverted cones originate, and d_{si} is the surface roughness thickness at this bulk layer thickness. This expression is based on a model in which the conical nanocrystalline inclusions grow at a faster rate than the surrounding amorphous phase. Inverted nanocrystalline conical structures result in spherically-shaped cone caps of radius $r_c = \Delta d_b + \Delta d_s$, where $\Delta d_b = d_b - d_{bi}$ and $\Delta d_s = d_s - d_{si}$. In this simple geometric model, the cone caps form the roughness layer. For a thickness-independent cone half-angle θ and fixed values of d_{bi} and d_{si}, the d_s versus d_b relationship in (7.10) is linear. The slope of the topmost solid line in Fig. 7.42a suggests that the maximum roughness thickness envelope reflects the development of nanocrystalline cones with a fixed half-angle θ of 46° as the n-layer bulk thickness increases. This result from the mapping SE is reasonably close to the value of $\theta = 41°$ from the real time SE analysis of Fig. 7.38.

By assigning a surface roughness layer thickness d_{si} at the onset of the amorphous-to-(mixed-phase) transition, then the n-layer bulk thickness d_{bi} at the transition can be determined from the intercept of the top solid line. The initial roughness layer thickness d_{si} is set to 40 Å, based on Fig. 7.27, which shows the roughness layer thickness for a 3400 Å i-layer deposited on TEC™ 15. The parallel lines in Fig. 7.42a are associated with a fixed $\theta = 46°$ and a range of d_{bi} values from ~123 Å to 186 Å, with the majority of the data points lying within the d_{bi} range of 123–144 Å. The lower limit result of $d_{bi} \sim 123$ Å is in close consistency with the growth evolution diagram in Fig. 7.36b which exhibits $d_{bi} = 120$ Å, supporting the simple geometric interpretation of (7.10). The results also support an interpretation in which the spatial variation in data corresponds predominantly to the variation in bulk layer thickness, but with similar d_{bi} and conical geometry. This also suggests that the samples on the upper side of the distribution are from the center of the electrode where the real time SE information of Figs. 7.35 and 7.36 is obtained. A linear trend through the highest density of data points in Fig. 7.42a (dot-dashed line) yields a cone angle of 43.5°, which is closer to the real time SE result of 41°; however, this line extrapolates to $d_{bi} = 107$ Å, which is lower than the real time SE result of 120 Å for the $a \rightarrow (a + nc)$ transition. Irrespective of the line selection in Fig. 7.42a, there is agreement to within 10–20% in the geometric nucleation parameters between the real time SE and mapping SE. The data points also appear to be bounded on the lower roughness side by a line with $\theta = 65°$ and $d_{bi} = 248$ Å. This would imply that in regions where crystallites nucleate at

larger d_b, the cone angles are larger. Such behavior would be inconsistent with Fig. 7.38, however. A more likely interpretation of the spread in Fig. 7.42a is that the data just above the lower limit line correspond to the combination of a lower cone angle (shallower slope) and a larger d_{bi} value (up to ~186 Å, as indicated), behavior that would be consistent with Fig. 7.38.

Based on the assumption that the measured nanocrystalline volume fraction is associated with the top surface, the following relationship can be derived:

$$f_{\mathrm{nc}} = \frac{\pi(d_b - d_{bi})^2}{K(d_{bc} - d_{bi})^2}, \tag{7.11}$$

where d_{bc} is the bulk layer thickness at nuclei contact and K is a constant that depends on the nuclei distribution. For nucleation on square and hexagonal close packed grids, $K = 4$ and 3.464, respectively. For the deposition of interest with $R = 100$, real time SE analysis led to $d_{bc} = 305$ Å, as shown in Fig. 7.36b. Figure 7.42b shows the results of (7.11) using $d_{bc} = 305$ Å as a fixed parameter and $d_{bi} = 123$ Å, which defines the upper envelope in Fig. 7.42a and is closely consistent with the $a \rightarrow (a + nc)$ transition from real time SE. For these fixed parameters, the range of K values from 3.464 to 4, i.e. a variation in the packing of nuclei, can account for most devices of the distribution. Variations in the d_{bi} and d_{bc} values may also contribute to the variations, but to a lesser extent in the former case, as shown by the corresponding result in Fig. 7.42b for $d_{bi} = 144$ Å. More generally a closer fit to the data set is possible based on the assumption that the packing of conical structures is between that of the relatively open square grid and the close-packed patterns, i.e. for $K \sim 3.7$.

The close linear relationship between the surface roughness thickness and the nanocrystalline volume fraction as shown in Fig. 7.42c can be understood by the same assumptions and geometric model that explain the variations in Fig. 7.42a, b. In this case, the relationship between d_s and f_{nc} is given by:

$$d_s = \left(\frac{f_{\mathrm{nc}}}{\pi N_d}\right)^{1/2} \tan[(1/2)\,\theta] + d_{si}, \tag{7.12}$$

where N_d is the nucleation density. A calculation of d_s versus f_{nc} is presented in Fig. 7.42c based on the selection of $d_{si} = 40$ Å from Fig. 7.27 and $\theta = 46°$ from Fig. 7.42a. In this case, the data are consistent with a nucleation density of 8.82×10^{10} cm^{-2} which yields the solid line result in Fig. 7.42c and a reasonable fit to the data. This nucleation density is very close to that obtained from the real time SE experiment of 8×10^{10} cm^{-2}. Thus, we conclude that the thickness non-uniformity studied by mapping SE yields geometric information consistent with real time SE and the geometric aspects of nucleation and growth can be determined from mapping SE alone.

The highest performance solar cells overall are given within the squares on the three panels of Fig. 7.42. For these cells, the *n*-layer structural parameters are best described by $d_b \sim 290$ Å, $d_s \sim 100$ Å, and $f_{nc} \sim 0.60$, the latter representing the nanocrystalline volume fraction at the near surface of the *n*-layer. Among the complete collection of cells, these highest efficiency devices exhibit the lowest surface roughness thickness and the lowest nanocrystallite volume fraction for the given bulk layer thickness. This observation suggests that these cells exhibit characteristics consistent with a lower *R* value with a larger d_{bi} value relative to the devices that come from the electrode center. Thus, the highest efficiency devices exhibit thinner *n*-layers with lower crystallite contents, which then take longer to nucleate. The overall results suggest that a lower *R* and/or lower rf plasma power, as well as lower pressure to avoid depletion, would enable high performance cells over the full substrate area.

7.4 Summary

For ex situ spectroscopic ellipsometry (SE) analysis, the primary difficulty lies in distinguishing between layers whose optical properties are similar over the accessible spectral range, for example, intrinsic and doped layers of the same material. Real time SE is an important capability at both laboratory and production scales that can overcome such difficulties. One of the challenges in real time SE data interpretation relates to the modification of the underlying film structure by the depositing film. The simplest form of such modification occurs inevitably as the voids in the surface roughness on the underlying layer are filled with depositing material [17]. Analysis of real time SE data involves simultaneously analyzing the pairs of spectra collected at a number of times during which the bulk layer thickness increases typically linearly with time after the interaction with the underlying material has completely stabilized [18]. The standard multi-time analysis approach requires a dielectric function for the growing film that is thickness-independent at least until the latest time used in the multi-time analysis. The results of the analysis include the point-by-point dielectric function versus photon energy and the structural parameters of bulk and surface roughness layer thicknesses versus time. For films that are non-uniform with depth and can be broken into a small number of layers, individual multi-time analyses can be performed. It is more likely, however, that the non-uniformity leads to a graded layer structure. In this circumstance, a virtual interface analysis procedure is most appropriate for extracting the dielectric function of an outermost layer as the film grows, burying the history of the graded layer in a pseudo-substrate [25].

In this study both approaches for real time SE analysis have been applied to the successive layers of a *p-i-n* tandem solar cell consisting of *a*-Si:H/*nc*-Si:H top/bottom cells [14–16]. Multi-time analysis has been applied to the top cell *i*-layer

and virtual interface analysis has been applied to the top cell *n*-layer. Results in correlation with device performance include the optimization of both the crystalline content of the top cell *n*-layer [15, 16] and the promotion of nucleation and coalescence of the bottom cell *nc*-Si:H *p* and *i*-layers [14, 15]. Growth evolution diagrams have been developed and presented for the top cell *n*-layer and the bottom cell *i*-layer. These diagrams provide the bulk layer thickness at which the transition to stable-phase *nc*-Si:H occurs, plotted as a function of the H_2-dilution ratio, which is the primary deposition variable that controls the phase of the film [11]. In addition, contour lines of constant crystalline content are also included on the diagrams, enabling optimization of doped layer processes. Of particular interest in this study is the structural development of the bottom cell *i*-layer which exhibits a continuous evolution from mixed-phase Si:H to nanocrystalline Si:H in a process that depends sensitively on the underlying *p*-layer structure. The real time SE results for the *i*-layer phase evolution provide a clear understanding of the device performance variations and directions for improvement. Another goal of interest in these studies is the development of analytical expressions for the dielectric functions of the *nc*-Si:H layers with approaches for correlating photon energy-independent parameters so that the number of free parameters can be reduced. Simple oscillator models for *nc*-Si:H over the photon energy range from 1 to 6 eV require ten variables. Here relationships have been developed that suggest four variables may be sufficient for this purpose. The studies reviewed here suggest promising approaches for developing physics-based dielectric function parameterizations for doped and nanocrystalline Si:H layers that enable characterization of material properties beyond simply the thickness in complicated multilayer stacks.

Finally, the power of ex situ mapping SE has been described in this review with a focus on the characterization and optimization of Si:H thin films [15, 16]. All large area thin film multilayers exhibit some degree of spatial non-uniformity in the thicknesses of the component films. In Si:H-based photovoltaic structures whose properties evolve with bulk layer thickness, for example, the surface roughness layer thickness or the nanocrystalline content, multi-spot analysis exploiting the thickness non-uniformity is found to give equivalent information to multi-time and virtual interface analyses in real time SE [23, 25]. In this review, the Si:H *n*-layer in single junction *p*-*i*-*n* solar cells has been studied with the ultimate goal of incorporating such devices as the top cell in a tandem. Applying mapping SE data, nanocrystallite nucleation densities and cone angles can be determined from plots that correlate the *n*-layer surface roughness thickness, surface nanocrystallite content, and the bulk layer thickness. In correlations of solar cell performance with processing-property information that reflects the growth evolution diagram, one can identify the structural profile, from the *i*/*n*-interface to the back contact, that serves to optimize the solar cell. When intentional spatial non-uniformities are incorporated into multiple layers of the same device structure and mapped by ex situ SE, optimization using combinatorial methods is possible. This is a potentially important future direction that may expedite the development of time consuming process-property-performance correlations.

References

1. E.A. Schiff, S. Hegedus, X. Deng, in *Handbook of Photovoltaic Science and Engineering*, 2nd edn., ed. by A. Luque, S. Hegedus (Wiley, New York, NY, 2011), Chapter 12, p. 487
2. A. Shah (ed.), *Thin Film Silicon Solar Cells* (CRC, Boca Raton, FL, 2010)
3. J. Meier, S. Dubail, R. Platz, P. Torres, U. Kroll, J.A. Anna Selvan, N. Pellaton Vaucher, C. Hof, D. Fischer, H. Keppner, R. Fluckiger, A. Shah, V. Shklover, K.D. Ufert, Solar Energy Mater. Solar Cells **78**, 35 (1997)
4. A. Shah, J. Meier, E. Vallat-Sauvain, N. Wyrsch, U. Kroll, C. Droz, U. Graf, Solar Energy Mater. Solar Cells **78**, 469 (2003)
5. X. Cao, J.A. Stoke, J. Li, N.J. Podraza, W. Du, X. Yang, D. Attygalle, X. Liao, R.W. Collins, X. Deng, J. Non-Cryst. Solids **354**, 2397 (2008)
6. B. Yan, G. Yue, L. Sivec, J. Yang, S. Guha, C.-S. Jiang, Appl. Phys. Lett. **99**, 113512 (2011)
7. T. Matsui, H. Sai, K. Saito, M. Kondo, Prog. Photovolt.: Res. Appl. **21**, 1363 (2013)
8. H. Sai, T. Matsui, K. Matsubara, M. Kondo, I. Yoshida, IEEE J. Photovolt. **4**, 1349 (2014)
9. M.A. Green, K. Emery, Y. Hishikawa, W. Warta, E.D. Dunlop, D.H. Levi, A.W.Y. Ho-Baillie, Prog. Photovolt.: Res. Appl. **25**, 3 (2017)
10. O. Vetterl, F. Finger, R. Carius, P. Hapke, L. Houben, O. Kluth, A. Lambertz, A. Muck, B. Rech, H. Wagner, Solar Energy Mater. Solar Cells **62**, 97 (2000)
11. R.W. Collins, A.S. Ferlauto, G.M. Ferreira, C. Chen, J. Koh, R.J. Koval, Y. Lee, J.M. Pearce, C.R. Wronski, Solar Energy Mater. Solar Cells **78**, 143 (2003)
12. L.R. Dahal, J. Li, J.A. Stoke, Z. Huang, A. Shan, A.S. Ferlauto, C.R. Wronski, R.W. Collins, N.J. Podraza, Solar Energy Mater. Solar Cells **129**, 32 (2014)
13. H. Fujiwara, *Spectroscopic Ellipsometry: Principles and Applications* (Wiley, Chichester, UK, 2007)
14. Z. Huang, L.R. Dahal, M.M. Junda, P. Aryal, S. Marsillac, R.W. Collins, N.J. Podraza, IEEE J. Photovolt. **5**, 1516 (2015)
15. Z. Huang, in *Spectroscopic Ellipsometry Studies of Thin Film a-Si:H/nc-Si:H Micromorph Solar Cell Fabrication in the p-i-n Superstrate Configuration*. Ph.D. Dissertation (University of Toledo, Toledo, OH, 2016)
16. Z. Huang, L.R. Dahal, C. Salupo, A.S. Ferlauto, N.J. Podraza, R.W. Collins, in *Conference Record of the 39th IEEE Photovoltaics Specialists Conference*, Tampa, FL, 16–21 June 2013 (IEEE, New York, 2013), p. 1788
17. J. Koh, Y.W. Lu, S. Kim, J.S. Burnham, C.R. Wronski, R.W. Collins, Appl. Phys. Lett. **67**, 2669 (1995)
18. I. An, Y.M. Li, H.V. Nguyen, C.R. Wronski, R.W. Collins, Appl. Phys. Lett. **59**, 2543 (1991)
19. B. Johs, J.S. Hale, Phys. Stat. Solidi (a) **205**, 715 (2008)
20. R.W. Collins, A.S. Ferlauto, in *Handbook of Ellipsometry*, ed. by H.G. Tompkins, E.A. Irene (William Andrew, Norwich, NY, 2005), Chapter 2, p. 93
21. M.M. Junda, A. Shan, P. Koirala, R.W. Collins, N.J. Podraza, IEEE J. Photovolt. **5**, 307 (2015)
22. A.S. Ferlauto, G.M. Ferreira, R.J. Koval, J.M. Pearce, C.R. Wronski, R.W. Collins, M.M. Al-Jassim, K.M. Jones, Thin Solid Films **455–456**, 665 (2004)
23. J.A. Stoke, L.R. Dahal, J. Li, N.J. Podraza, X. Cao, X. Deng, R.W. Collins, in *Conference Record of the 33rd IEEE Photovoltaics Specialist Conference*, San Diego, CA, 11–16 May 2008 (IEEE, New York, 2008), Paper 413
24. D.E. Aspnes, J. Opt. Soc. Am. A **10**, 974 (1993)
25. S. Kim, R.W. Collins, Appl. Phys. Lett. **67**, 3010 (1995)
26. A.S. Ferlauto, G.M. Ferreira, J.M. Pearce, C.R. Wronski, R.W. Collins, X. Deng, G. Ganguly, J. Appl. Phys. **92**, 2424 (2002)
27. T. Yuguchi, Y. Kanie, N. Matsuki, H. Fujiwara, J. Appl. Phys. **111**, 083509 (2012)
28. K. von Rottkay, M. Rubin, *Materials Research Society Symposium Proceedings: Thin Films for Photovoltaic and Related Devices*, vol. 426 (MRS, Warrendale, PA, 1996), p. 449

29. J. Chen, J. Li, D. Sainju, K.D. Wells, N.J. Podraza, R.W. Collins, in *Conference Record of the IEEE 4th World Conference on Photovoltaic Energy Conversion 2006*, Waikoloa, HI, 7–12 May 2006 (IEEE, New York, NY, 2006), p. 475
30. N.J. Podraza, C.R. Wronski, M.W. Horn, R.W. Collins, *Materials Research Society Symposium Proceedings: Amorphous and Polycrystalline Thin-Film Silicon Science and Technology—2006*, vol. 910 (MRS, Warrendale, PA, 2006), p. 259
31. H.V. Nguyen, R.W. Collins, Phys. Rev. B **47**, 1911 (1993)
32. P. Etchegoin, J. Kircher, M. Cardona, Phys. Rev. B **47**, 10292 (1993)
33. P. Lautenschlager, M. Garriga, L. Viña, M. Cardona, Phys. Rev. B **36**, 4821 (1987)
34. Z. Huang, J. Chen, M.N. Sestak, D. Attygalle, L.R. Dahal, M.R. Mapes, D.A. Strickler, K.R. Kormanyos, C. Salupo, R.W. Collins, in *Conference Record of the 35th IEEE Photovoltaic Specialists Conference*, Honolulu, HI, 20–25 June 2010 (IEEE, New York, NY, 2010), p. 1678
35. J. Chen, P. Koirala, C. Salupo, R.W. Collins, S. Marsillac, K.R. Kormanyos, B.D. Johs, J.S. Hale, G.L. Pfeiffer, in *Conference Record of the 38th IEEE Photovoltaic Specialists Conference*, Austin, TX, 3–8 June 2012 (IEEE, New York, NY, 2012), p. 377
36. R.W. Collins, B.Y. Yang, J. Vac. Sci. Technol. B **7**, 1155 (1989)
37. Y.A. Kryukov, N.J. Podraza, R.W. Collins, J. Amar, Phys. Rev. B **80**, 085403 (2009)
38. C.W. Teplin, C.-S. Jiang, P. Stradins, H.M. Branz, Appl. Phys. Lett. **92**, 093114 (2008)

Part II
Optical Data of Solar-Cell Component Materials

Chapter 8
Inorganic Semiconductors and Passivation Layers



Akihiro Nakane, Shohei Fujimoto, Gerald E. Jellison Jr., Craig M. Herzinger, James N. Hilfiker, Jian Li, Robert W. Collins, Takashi Koida, Shinho Kim, Hitoshi Tampo and Hiroyuki Fujiwara

Abstract The dielectric functions and optical constants of various inorganic solar-cell materials, a total of 58 semiconductors, are summarized. The semiconductor materials described here include the group-IV (Si, Ge, and a-Si:H), III–V (GaAs, GaP, InP, InAs, and AlAs), II–VI (CdTe, CdS, ZnTe, ZnSe, and ZnS), I–III–VI_2 ($CuInSe_2$ and $CuGaSe_2$) and I_2–II–IV–VI_4 ($Cu_2ZnSnSe_4$, Cu_2ZnSnS_4 and $Cu_2ZnGeSe_4$) semiconductors. For a-Si:H, $Cu(In,Ga)Se_2$ and $Cu_2ZnSn(S,Se)_4$-based alloys, the variation of the optical constants with alloy composition is presented. This chapter also provides the optical properties of crystalline Si passivation layers (SiN, SiO_2, Al_2O_3, and Ga_2O_3), which are necessary for optical simulation of solar cells. Furthermore, it is established in this chapter that the dielectric functions of numerous direct and indirect transition semiconductors can be parameterized almost perfectly by assuming several transition peaks calculated from the Tauc-Lorentz model. In this chapter, the parameterization results for all the 58 semiconductors are also summarized. For the passivation layers, the parameterization results obtained using the Sellmeier model are shown.

A. Nakane · S. Fujimoto · H. Fujiwara (✉)
Gifu University, 1-1 Yanagido, Gifu 501-1193, Japan
e-mail: fujiwara@gifu-u.ac.jp

G. E. Jellison Jr.
Oak Ridge National Laboratory, Oak Ridge, TN 37830, USA
e-mail: jellisongejr@ornl.gov

C. M. Herzinger · J. N. Hilfiker
J.A. Woollam Co., Inc., 645 M Street, Suite 102, Lincoln, NE 68508, USA

J. Li · R. W. Collins
University of Toledo, Toledo, OH 43606, USA

T. Koida · S. Kim · H. Tampo
Research Center for Photovoltaics, National Institute of Advanced Industrial Science and Technology, 1-1-1 Umezono, Tsukuba 305-8568, Japan

© Springer International Publishing AG, part of Springer Nature 2018

H. Fujiwara and R. W. Collins (eds.), *Spectroscopic Ellipsometry for Photovoltaics*,
Springer Series in Optical Sciences 214,
https://doi.org/10.1007/978-3-319-95138-6_8

8.1 Introduction

The basic potential of a solar cell material is ultimately governed by the absorption characteristics and thus the absorption spectrum of the semiconducting light absorber is of paramount importance. Moreover, for optical device simulations and ellipsometry characterization of solar cell structures, the optical constants of all the solar-cell component layers are necessary. In this chapter, for the purpose of spectroscopic ellipsometry (SE) characterization and device simulation, the tabulated optical constants of various inorganic semiconductors at room temperature are provided. In particular, for most semiconductor materials, refractive index n and extinction coefficient k are shown in a wavelength (λ) range of 300–1200 nm with steps of 5 nm (300–400 nm) and 10 nm (400–1200 nm). From these numerical values, the dielectric function ($\varepsilon = \varepsilon_1 - i\varepsilon_2$) can be calculated quite easily according to $\varepsilon_1 = n^2 - k^2$ and $\varepsilon_2 = 2nk$ (see Sect. 1.2.1). The λ value can also be converted to energy (E) by $E = 1239.8/[\lambda\ (\text{nm})]$ eV [(1.3)]. From the value of k, the absorption coefficient (α) in the unit of cm^{-1} can further be obtained by $\alpha = 4\pi k \cdot 10^7/(\lambda\ [\text{nm}])$ [(1.17)]. In the tabulated data, the absolute k value is denoted as "0" when there is no observable light absorption, even though materials may have very small k (or α) values in a certain E region. It should be noted that the SE sensitivity for α is generally limited to ~500 cm^{-1} and low α values in a range of 10^{-2}–10^{2} cm^{-1} in this chapter have been determined by incorporating results obtained from transmission measurements (see Fig. 8.3 in Vol. 1).

Unfortunately, the tabulated data are sometimes insufficient for more complete SE analysis or optical simulation. Accordingly, almost all the dielectric functions of inorganic semiconductors were parameterized assuming the Tauc-Lorentz model described by (1.19)–(1.20). The Tauc-Lorentz model was developed originally to express the dielectric function of amorphous materials, but this model is found to be quite effective for the complete parameterization of crystalline-phase semiconductor materials, which exhibit complex transition peaks in the visible region. It should be emphasized that the Tauc-Lorentz model is used solely to establish the optical database of numerous solar-cell component layers. The main advantage of the Tauc-Lorentz model is the feature that $\varepsilon_2 = 0$ in an energy region below the band gap (E_g): i.e., $E \leq E_g$ [see (1.19)]. Through careful modeling, we established that all the direct and indirect transition semiconductors can be modeled almost perfectly by combining several Tauc-Lorentz transition peaks. In particular, by incorporating Tauc-Lorentz peaks with very small amplitudes, the α spectra of various inorganic semiconductors are reproduced in a quite wide range of $\alpha = 10^{-2}$–10^{6} cm^{-1} using only one dielectric function model. From the Tauc-Lorentz parameters described in this chapter, (ε_1, ε_2), (n, k) and α values at arbitrary λ and E can be calculated quite easily.

In this chapter, the ε_2 spectrum of semiconductor materials is modeled simply as a sum of the Tauc-Lorentz peaks:

$$\varepsilon_2(E) = \sum_{j=1}^{m} \frac{A_j C_j E_{0,j} (E - E_{g,j})^2}{[(E^2 - E_{0,j}^2)^2 + C_j^2 E^2] E}. \tag{8.1}$$

As confirmed from the above equation, a single Tauc-Lorentz peak is expressed by four parameters: i.e., the amplitude parameter A_j, broadening parameter C_j, peak transition energy $E_{0,j}$, and optical gap $E_{g,j}$ of the jth Tauc-Lorentz peak (see Fig. 1.19). From the parameters of (8.1), $\varepsilon_1(E)$ can then be calculated from the Kramers-Kronig integration of each Tauc-Lorentz peak:

$$\varepsilon_1(E) = \sum_{j=1}^{m} \left(\varepsilon_{1,j}(\infty) + \frac{2}{\pi} P \int_{E_g}^{\infty} \frac{E' \varepsilon_{2,j}(E')}{E'^2 - E^2} dE' \right), \tag{8.2}$$

where $\varepsilon_{1,j}(\infty)$ represents a constant contribution to $\varepsilon_1(E)$ at high energies. The second term in the parenthesis shows the Kramers-Kronig integration of the jth Tauc-Lorentz peak [$\varepsilon_{2,j}(E')$ in (8.2)]. As shown in (8.2), when a dielectric function is modeled by combining several Tauc-Lorentz peaks, $\varepsilon_1(E)$ is calculated as a sum of the ε_1 contributions obtained from each Tauc-Lorentz peak (see the example of Si shown in Fig. 8.1).

The Kramers-Kronig integration of (8.2) can be performed rather easily using the exact equation described in (1.20). In addition, the calculation example of the Tauc-Lorentz model has been indicated in (1.26). A free software described in Sect. 2.7 can further be applied to calculate the dielectric function from the Tauc-Lorentz model parameters listed in this chapter.

In the actual parameterization of the dielectric function using (8.1) and (8.2), the dielectric function fitting is performed only for $\varepsilon_2(E)$ at the initial stage. In particular, this $\varepsilon_2(E)$ fitting is carried out using a rather limited energy range of ~0.1 eV near E_g. After a satisfactory fitting is obtained, the fitting energy region is expanded slightly toward the higher energy and the $\varepsilon_2(E)$ fitting is performed again by adding new Tauc-Lorentz oscillators. This process is repeated until the intended energy region of the ε_2 spectrum is fitted. During the consecutive fittings, the Tauc-Lorentz peak parameters in the lower energy region are fixed and only the parameters of new peaks are adjusted in some cases. In the next step, the $\varepsilon_1(\infty)$ parameter is determined from the ε_1-spectrum fitting by fixing the ε_2-spectral parameters. In the final fitting performed for both $\varepsilon_1(E)$ and $\varepsilon_2(E)$, all the parameters are adjusted again, except for the parameters of the small amplitude peaks located near E_g. The above scheme is critical to obtain the reasonable fitting in a wide α range of 10^{-2}–10^{6} cm^{-1}. The parameterization of all the semiconductor dielectric functions, described in this chapter, was implemented by the group of Gifu University (A. Nakane and S. Fujimoto), unless otherwise noted.

For optically transparent passivation layers, on the other hand, the following Sellmeier model was used.

$$n^2(\lambda) = \frac{B_1\lambda^2}{(\lambda^2 - C_1)} + \frac{B_2\lambda^2}{(\lambda^2 - C_2)} + \frac{B_3\lambda^2}{(\lambda^2 - C_3)} + 1 \tag{8.3}$$

In this model, there are a total of six parameters (B_1, B_2, B_3, C_1, C_2, C_3) and the n spectrum can be calculated quite easily from these parameter values while assuming $k = 0$ (see Sect. 1.2.3).

8.2 Optical Data of Inorganic Semiconductors and Passivation Layers

8.2.1 Si

The optical data of a single Si crystal at room temperature (295 K = 22 °C) are shown. These data correspond to those in Figs. 8.2 and 8.3 (Chap. 8 in Vol. 1). Near the indirect band edge (700–1170 nm), the absorption coefficient or extinction coefficient depend significantly on temperature. If the sample temperature is different from 22 °C, then the expressions of (8.9) and (8.10) found in Chap. 8 (Vol. 1) should be used for the absorption coefficient (Tables 8.1 and 8.2).

Table 8.1 Tauc-Lorentz parameters of (8.1) and (8.2) for Si

Peak	A (eV)	C (eV)	E_0 (eV)	E_g (eV)	$\varepsilon_1(\infty)$
$j = 1$	5.446×10^{-4}	0.028	1.157	1.107	0.724
$j = 2$	7.068×10^{-3}	0.215	1.177	1.029	0
$j = 3$	0.817	1.611	1.632	1.148	0
$j = 4$	0.381	0.700	1.861	1.429	0
$j = 5$	0.837	0.488	2.810	1.658	0
$j = 6$	712.571	0.216	3.368	3.107	0
$j = 7$	237.142	0.881	3.531	2.746	0
$j = 8$	25.134	0.738	4.015	1.705	0
$j = 9$	29.911	0.402	4.277	1.751	0
$j = 10$	102.277	1.064	5.158	4.311	0
$j = 11$	0.435	0.243	5.349	1.510	0

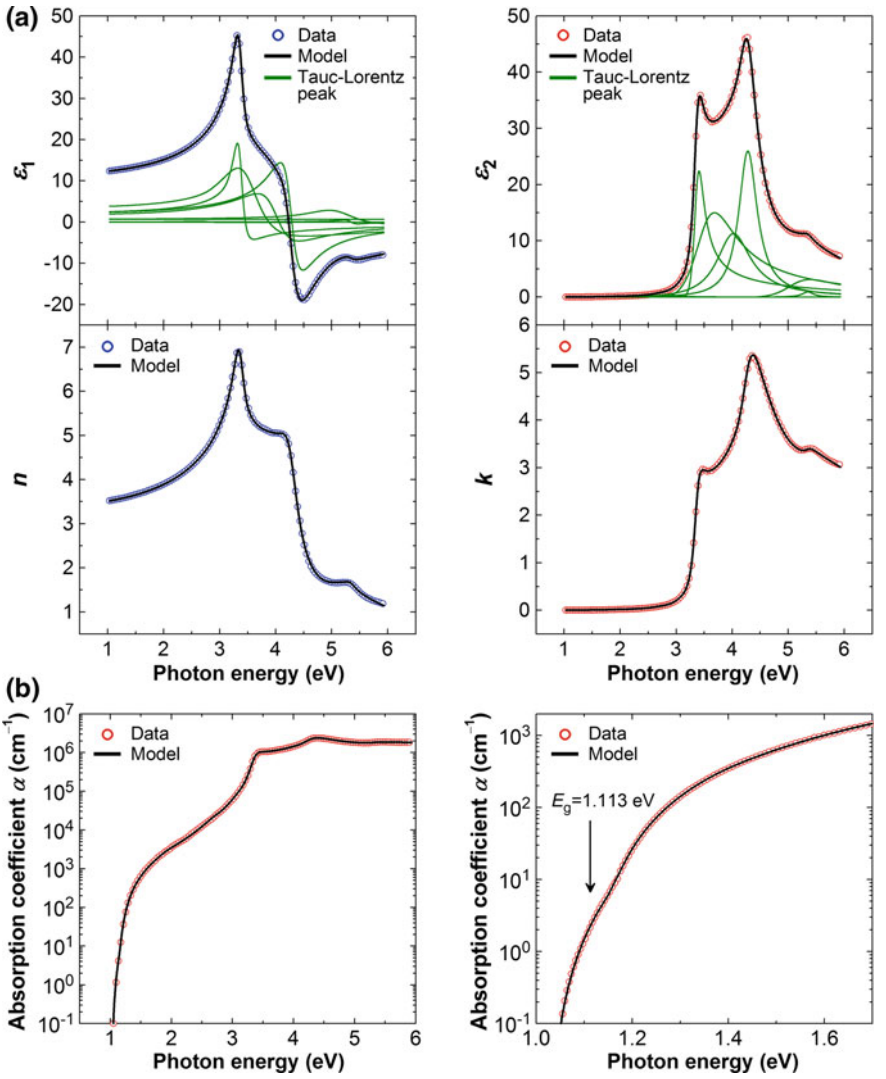


Fig. 8.1 **a** Dielectric function and optical constants and **b** absorption coefficient of a Si single crystal at room temperature. The open circles show the experimental data and the solid lines indicate the calculation result obtained from the parameterization assuming the Tauc-Lorentz model [(8.1) and (8.2)]. In (**b**), the E_g position of crystalline Si, determined from theoretical analysis (Sect. 8.2.3 in Vol. 1), is indicated

Table 8.2 Optical constants of Si. The optical data of Fig. 8.1 obtained by G. E. Jellison are shown

λ (nm)	n	k	λ (nm)	n	k	λ (nm)	n	k
210	1.190	3.067	328	5.155	3.111	630	3.874	1.59×10^{-2}
212	1.213	3.089	330	5.164	3.075	640	3.856	1.51×10^{-2}
214	1.234	3.119	332	5.193	3.05	650	3.840	1.44×10^{-2}
216	1.262	3.151	334	5.203	3.019	660	3.824	1.36×10^{-2}
218	1.291	3.182	336	5.234	2.996	670	3.810	1.23×10^{-2}
220	1.319	3.229	338	5.256	2.981	680	3.796	1.17×10^{-2}
222	1.362	3.282	340	5.28	2.958	690	3.783	1.14×10^{-2}
224	1.414	3.325	342	5.302	2.935	700	3.770	1.06×10^{-2}
226	1.468	3.368	344	5.355	2.931	710	3.759	9.50×10^{-3}
228	1.533	3.397	346	5.398	2.928	720	3.747	8.93×10^{-3}
230	1.587	3.400	348	5.449	2.931	730	3.736	8.39×10^{-3}
232	1.641	3.388	350	5.498	2.924	740	3.726	7.86×10^{-3}
234	1.665	3.376	352	5.569	2.937	750	3.716	7.37×10^{-3}
236	1.673	3.369	354	5.665	2.952	760	3.707	6.89×10^{-3}
238	1.673	3.370	356	5.782	2.965	770	3.699	6.43×10^{-3}
240	1.663	3.398	358	5.921	2.961	780	3.691	5.99×10^{-3}
242	1.660	3.429	360	6.086	2.928	790	3.683	5.58×10^{-3}
244	1.658	3.476	362	6.279	2.860	800	3.676	5.18×10^{-3}
246	1.663	3.526	364	6.473	2.737	810	3.669	4.80×10^{-3}
248	1.669	3.593	366	6.656	2.552	820	3.662	4.43×10^{-3}
250	1.683	3.671	368	6.812	2.312	830	3.655	4.09×10^{-3}
252	1.702	3.753	370	6.908	2.026	840	3.649	3.73×10^{-3}
254	1.721	3.839	372	6.924	1.724	850	3.642	3.45×10^{-3}
256	1.749	3.927	374	6.877	1.434	860	3.635	3.15×10^{-3}
258	1.778	4.014	376	6.771	1.186	870	3.630	2.87×10^{-3}
260	1.815	4.114	378	6.662	0.997	880	3.624	2.60×10^{-3}
262	1.853	4.222	380	6.522	0.843	890	3.619	2.35×10^{-3}
264	1.905	4.337	382	6.399	0.732	900	3.614	2.12×10^{-3}
266	1.971	4.458	384	6.295	0.645	910	3.609	1.89×10^{-3}
268	2.051	4.585	386	6.192	0.575	920	3.604	1.68×10^{-3}
270	2.157	4.722	388	6.087	0.515	930	3.600	1.49×10^{-3}
272	2.295	4.853	390	5.986	0.464	940	3.595	1.31×10^{-3}
274	2.459	4.973	392	5.889	0.424	950	3.591	1.14×10^{-3}
276	2.653	5.090	394	5.81	0.389	960	3.587	9.81×10^{-4}
278	2.873	5.182	396	5.736	0.357	970	3.583	8.39×10^{-4}
280	3.111	5.257	398	5.657	0.328	980	3.579	7.07×10^{-4}
282	3.363	5.306	400	5.595	0.304	990	3.575	5.89×10^{-4}
284	3.624	5.344	410	5.316	0.217	1000	3.572	4.83×10^{-4}
286	3.93	5.334	420	5.097	0.168	1010	3.568	3.88×10^{-4}

(continued)

Table 8.2 (continued)

λ (nm)	n	k	λ (nm)	n	k	λ (nm)	n	k
288	4.256	5.257	430	4.924	0.133	1020	3.565	3.06×10^{-4}
290	4.531	5.090	440	4.786	0.109	1030	3.562	2.36×10^{-4}
292	4.744	4.864	450	4.675	9.30×10^{-2}	1040	3.559	1.77×10^{-4}
294	4.882	4.647	460	4.573	7.80×10^{-2}	1050	3.556	1.30×10^{-4}
296	4.957	4.420	470	4.493	6.70×10^{-2}	1060	3.553	8.66×10^{-5}
298	5.001	4.240	480	4.413	5.93×10^{-2}	1070	3.550	6.68×10^{-5}
300	5.02	4.069	490	4.346	5.23×10^{-2}	1080	3.547	5.09×10^{-5}
302	5.033	3.930	500	4.289	4.66×10^{-2}	1090	3.545	3.92×10^{-5}
304	5.044	3.811	510	4.237	4.17×10^{-2}	1100	3.542	3.00×10^{-5}
306	5.051	3.706	520	4.19	3.76×10^{-2}	1110	3.540	2.23×10^{-5}
308	5.051	3.610	530	4.147	3.37×10^{-2}	1120	3.537	1.61×10^{-5}
310	5.055	3.535	540	4.108	3.02×10^{-2}	1130	3.535	1.15×10^{-5}
312	5.056	3.464	550	4.072	2.73×10^{-2}	1140	3.532	8.23×10^{-6}
314	5.059	3.402	560	4.039	2.52×10^{-2}	1150	3.530	5.58×10^{-6}
316	5.065	3.348	570	4.01	2.36×10^{-2}	1160	3.528	3.51×10^{-6}
318	5.077	3.304	580	3.982	2.24×10^{-2}	1170	3.526	1.93×10^{-6}
320	5.099	3.251	590	3.957	2.11×10^{-2}	1180	3.524	0
322	5.109	3.210	600	3.934	2.00×10^{-2}	1190	3.522	0
324	5.122	3.175	610	3.912	1.87×10^{-2}	1200	3.520	0
326	5.135	3.137	620	3.892	1.73×10^{-2}			

8.2.2 Ge

To express the dielectric function of a Ge single crystal, two separate data sets are used depending on the energy region:

(i) Data of G. E. Jellison, Jr. [1] for $1.94 < E \leq 3.9$ eV,
(ii) Unpublished data of C. M. Herzinger [2] for $0.2 < E \leq 1.94$ eV and $E > 3.9$ eV.

The result of [2] above was determined from a multiple data set analysis. The data sets came from values compiled in a handbook edited by E. D. Palik [3] originally from ellipsometry results [4], from another compilation [5], and from transmittance results [6]. This work also uses a parametric optical constant model [7] that allows a simultaneous analysis of different experimental results with dissimilar wavelength ranges and values. The resulting optical constants provide wide spectral coverage, continuity, and Kramers-Kronig consistency. The functional form employs Gaussian broadening and the superposition of subsections organized by critical point structures. To help reconcile differences among the experiments, the analysis model for the ellipsometric data set included an overlayer adjustment. The same basic procedure was also used for GaAs, InAs, GaP, and AlSb in this chapter (Tables 8.3 and 8.4).

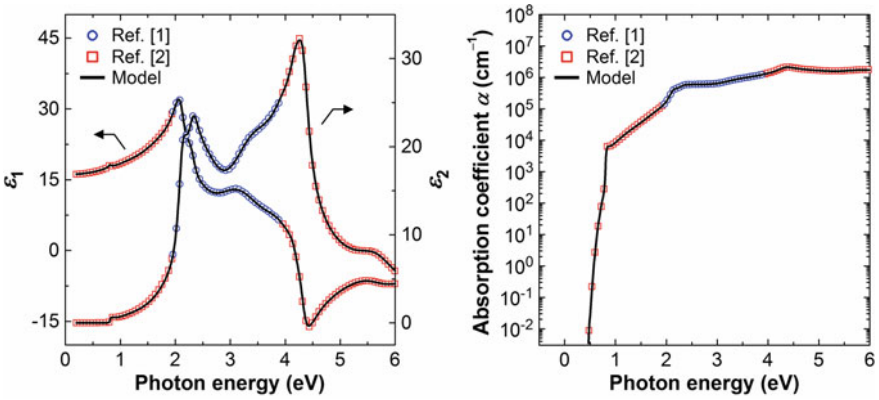


Fig. 8.2 Dielectric function and absorption coefficient of a Ge single crystal at room temperature. The open circles show the reference data and the solid lines indicate the calculation result obtained from the parameterization assuming the Tauc-Lorentz model [(8.1) and (8.2)]

Table 8.3 Tauc-Lorentz parameters of (8.1) and (8.2) for Ge

Peak	A (eV)	C (eV)	E_0 (eV)	E_g (eV)	$\varepsilon_1(\infty)$
$j = 1$	1.474×10^{-3}	0.113	0.675	0.517	1.104
$j = 2$	0.017	0.135	0.743	0.549	0
$j = 3$	30.354	0.048	0.803	0.795	0
$j = 4$	5.368×10^{-4}	1.164	0.808	0.453	0
$j = 5$	0.095	0.054	0.812	0.643	0
$j = 6$	0.097	0.011	0.842	0.800	0
$j = 7$	6.790×10^{-3}	0.436	1.014	0.499	0
$j = 8$	6.468	0.945	1.030	0.792	0
$j = 9$	95.588	0.209	2.116	1.826	0
$j = 10$	26.781	0.224	2.319	1.864	0
$j = 11$	45.081	1.113	2.475	0.945	0
$j = 12$	190.066	1.394	3.315	2.322	0
$j = 13$	9.627	0.684	4.003	0.942	0
$j = 14$	17.285	0.340	4.199	2.475	0
$j = 15$	3.688	0.244	4.325	0.900	0
$j = 16$	3.797	0.939	5.662	0.900	0

Table 8.4 Optical constants of Ge. The optical data of Fig. 8.2, obtained by G. E. Jellison and C. M. Herzinger, are shown

λ (nm)	n	k	λ (nm)	n	k	λ (nm)	n	k
300	3.969	3.749	720	4.942	0.401	1280	4.268	7.71×10^{-2}
305	4.003	3.517	730	4.909	0.380	1300	4.261	7.55×10^{-2}
310	4.017	3.340	740	4.877	0.362	1320	4.254	7.41×10^{-2}
315	4.022	3.199	750	4.847	0.344	1340	4.248	7.31×10^{-2}
320	4.019	3.098	760	4.819	0.328	1360	4.243	7.24×10^{-2}
325	4.031	3.009	770	4.793	0.313	1380	4.238	7.19×10^{-2}
330	4.038	2.932	780	4.768	0.300	1400	4.234	7.17×10^{-2}
335	4.056	2.864	790	4.745	0.287	1420	4.232	7.18×10^{-2}
340	4.067	2.802	800	4.723	0.275	1440	4.230	7.22×10^{-2}
345	4.082	2.749	810	4.701	0.264	1460	4.231	7.29×10^{-2}
350	4.101	2.697	820	4.681	0.253	1480	4.236	7.37×10^{-2}
355	4.115	2.654	830	4.662	0.243	1500	4.249	6.98×10^{-2}
360	4.137	2.610	840	4.644	0.234	1520	4.263	4.39×10^{-2}
365	4.166	2.561	850	4.627	0.226	1540	4.247	1.39×10^{-2}
370	4.190	2.514	860	4.610	0.217	1560	4.225	5.28×10^{-3}
375	4.217	2.459	870	4.595	0.210	1580	4.210	3.91×10^{-3}
380	4.232	2.401	880	4.579	0.202	1600	4.200	3.18×10^{-3}
385	4.240	2.344	890	4.565	0.196	1620	4.191	2.61×10^{-3}
390	4.247	2.285	900	4.551	0.189	1640	4.183	2.16×10^{-3}
395	4.236	2.229	910	4.538	0.183	1660	4.176	1.80×10^{-3}
400	4.223	2.181	920	4.525	0.177	1680	4.170	1.50×10^{-3}
410	4.170	2.122	930	4.513	0.171	1700	4.164	1.26×10^{-3}
420	4.130	2.102	940	4.502	0.166	1720	4.159	1.07×10^{-3}
430	4.099	2.116	950	4.490	0.161	1740	4.154	9.02×10^{-4}
440	4.102	2.143	960	4.479	0.156	1760	4.149	7.62×10^{-4}
450	4.121	2.177	970	4.469	0.152	1780	4.145	6.44×10^{-4}
460	4.158	2.214	980	4.459	0.147	1800	4.141	5.43×10^{-4}
470	4.208	2.256	990	4.449	0.143	1820	4.137	4.57×10^{-4}
480	4.273	2.291	1000	4.440	0.139	1840	4.133	3.83×10^{-4}
490	4.360	2.331	1010	4.431	0.135	1860	4.130	3.22×10^{-4}
500	4.460	2.366	1020	4.422	0.131	1880	4.126	2.68×10^{-4}
510	4.592	2.395	1030	4.414	0.128	1900	4.123	2.24×10^{-4}
520	4.756	2.414	1040	4.405	0.124	1940	4.117	1.54×10^{-4}
530	4.957	2.378	1050	4.397	0.121	1980	4.112	1.05×10^{-4}
540	5.136	2.242	1060	4.390	0.118	2020	4.106	7.09×10^{-5}
550	5.226	2.106	1070	4.382	0.115	2060	4.102	4.75×10^{-5}
560	5.300	2.019	1080	4.375	0.112	2100	4.097	3.16×10^{-5}
570	5.420	1.964	1090	4.368	0.109	2140	4.093	2.09×10^{-5}
580	5.635	1.837	1100	4.361	0.107	2180	4.090	1.37×10^{-5}

(continued)

Table 8.4 (continued)

λ (nm)	n	k	λ (nm)	n	k	λ (nm)	n	k
590	5.796	1.548	1110	4.355	0.104	2220	4.086	8.99×10^{-6}
600	5.791	1.241	1120	4.348	0.102	2260	4.083	5.85×10^{-6}
610	5.710	1.011	1130	4.342	9.97×10^{-2}	2300	4.080	3.81×10^{-6}
620	5.608	0.851	1140	4.336	9.75×10^{-2}	2340	4.077	2.47×10^{-6}
630	5.494	0.734	1150	4.330	9.55×10^{-2}	2380	4.074	1.61×10^{-6}
640	5.403	0.665	1160	4.324	9.35×10^{-2}	2420	4.071	1.04×10^{-6}
650	5.307	0.607	1170	4.319	9.16×10^{-2}	2460	4.069	6.72×10^{-7}
660	5.229	0.565	1180	4.313	8.99×10^{-2}	2500	4.067	4.37×10^{-7}
670	5.164	0.530	1190	4.308	8.82×10^{-2}	2550	4.064	2.56×10^{-7}
680	5.110	0.500	1200	4.303	8.66×10^{-2}	2600	4.061	1.48×10^{-7}
690	5.062	0.472	1220	4.294	8.37×10^{-2}	2650	4.059	8.35×10^{-8}
700	5.018	0.446	1240	4.285	8.12×10^{-2}	2700	4.057	0
710	4.979	0.422	1260	4.276	7.90×10^{-2}			

8.2.3 SiO_2

Data from C. M. Herzinger, B. Johs, W. A. McGahan, J. A. Woollam, and W. Paulson [8]. The optical data have been extracted from SiO_2 thermal oxides formed on crystalline Si (Tables 8.5 and 8.6).

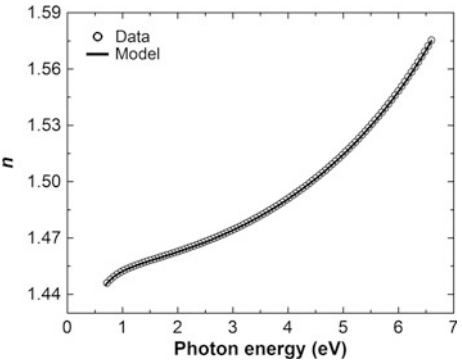


Fig. 8.3 Refractive index spectrum of SiO_2 thermal oxides at room temperature. The open circles show the reference data and the solid line indicates the refractive index spectrum calculated by the Sellmeier model of (8.3)

Table 8.5 Sellmeier parameters of (8.3) for SiO_2

Material	B_1	B_2	B_3	C_1 (μm^2)	C_2 (μm^2)	C_3 (μm^2)
SiO_2	0.633	0.486	0.647	0.00449	0.0126	63.628

Table 8.6 Refractive index of SiO_2. The optical data reported by Herzinger et al. are shown ($k = 0$)

λ (nm)	n	λ (nm)	n	λ (nm)	n	λ (nm)	n
300	1.4936	460	1.4703	720	1.4601	980	1.4557
305	1.4922	470	1.4696	730	1.4599	990	1.4555
310	1.4909	480	1.4690	740	1.4597	1000	1.4554
315	1.4897	490	1.4683	750	1.4595	1010	1.4553
320	1.4885	500	1.4678	760	1.4593	1020	1.4551
325	1.4874	510	1.4672	770	1.4590	1030	1.4550
330	1.4863	520	1.4667	780	1.4589	1040	1.4549
335	1.4853	530	1.4662	790	1.4587	1050	1.4547
340	1.4844	540	1.4657	800	1.4585	1060	1.4546
345	1.4834	550	1.4653	810	1.4583	1070	1.4544
350	1.4826	560	1.4649	820	1.4581	1080	1.4543
355	1.4817	570	1.4645	830	1.4579	1090	1.4542
360	1.4810	580	1.4641	840	1.4578	1100	1.4541
365	1.4802	590	1.4637	850	1.4576	1110	1.4539
370	1.4795	600	1.4634	860	1.4575	1120	1.4538
375	1.4788	610	1.4630	870	1.4573	1130	1.4537
380	1.4781	620	1.4627	880	1.4571	1140	1.4536
385	1.4775	630	1.4624	890	1.4570	1150	1.4534
390	1.4769	640	1.4621	900	1.4568	1160	1.4533
395	1.4763	650	1.4618	910	1.4567	1170	1.4532
400	1.4757	660	1.4616	920	1.4565	1180	1.4531
410	1.4746	670	1.4613	930	1.4564	1190	1.4529
420	1.4736	680	1.4610	940	1.4562	1200	1.4528
430	1.4727	690	1.4608	950	1.4561		
440	1.4719	700	1.4606	960	1.4559		
450	1.4711	710	1.4603	970	1.4558		

8.2.4 Al_2O_3

Data from G. Dingemans and W. M. M. Kessels [9]. The optical data have been extracted from an Al_2O_3 layer annealed at 400 °C. The Al_2O_3 sample was prepared by atomic layer deposition (Fig. 8.4, Tables 8.7 and 8.8).

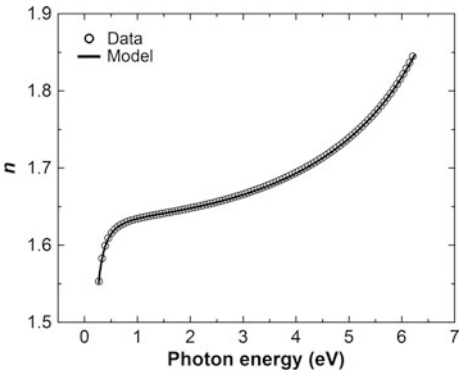


Fig. 8.4 Refractive index spectrum of Al_2O_3 at room temperature. The open circles show the reference data and the solid line indicates the refractive index spectrum calculated by the Sellmeier model of (8.3)

Table 8.7 Sellmeier parameters of (8.3) for Al_2O_3

Material	B_1	B_2	B_3	C_1 (μm^2)	C_2 (μm^2)	C_3 (μm^2)
Al_2O_3	1.125	0.555	6.747	0.00242	0.0214	550.747

Table 8.8 Refractive index of Al_2O_3. The optical data reported by Dingemans et al. are shown ($k = 0$)

λ (nm)	n	λ (nm)	n	λ (nm)	n	λ (nm)	n
300	1.6986	460	1.6595	720	1.6441	980	1.6382
305	1.6961	470	1.6584	730	1.6437	990	1.6380
310	1.6938	480	1.6573	740	1.6434	1000	1.6378
315	1.6916	490	1.6564	750	1.6432	1010	1.6377
320	1.6896	500	1.6555	760	1.6429	1020	1.6375
325	1.6876	510	1.6546	770	1.6426	1030	1.6373
330	1.6858	520	1.6538	780	1.6423	1040	1.6372
335	1.6841	530	1.6531	790	1.6421	1050	1.6370
340	1.6824	540	1.6524	800	1.6418	1060	1.6369
345	1.6809	550	1.6517	810	1.6416	1070	1.6367
350	1.6794	560	1.6511	820	1.6413	1080	1.6366
355	1.6780	570	1.6505	830	1.6411	1090	1.6364
360	1.6767	580	1.6499	840	1.6409	1100	1.6363
365	1.6754	590	1.6493	850	1.6407	1110	1.6361
370	1.6742	600	1.6488	860	1.6405	1120	1.6359
375	1.6731	610	1.6483	870	1.6402	1130	1.6358
380	1.6720	620	1.6479	880	1.6400	1140	1.6357

(continued)

Table 8.8 (continued)

λ (nm)	n	λ (nm)	n	λ (nm)	n	λ (nm)	n
385	1.6709	630	1.6474	890	1.6398	1150	1.6355
390	1.6699	640	1.6470	900	1.6396	1160	1.6354
395	1.6690	650	1.6466	910	1.6394	1170	1.6352
400	1.6680	660	1.6462	920	1.6393	1180	1.6351
410	1.6663	670	1.6458	930	1.6391	1190	1.6349
420	1.6647	680	1.6454	940	1.6389	1200	1.6348
430	1.6633	690	1.6450	950	1.6387		
440	1.6619	700	1.6447	960	1.6385		
450	1.6606	710	1.6444	970	1.6383		

8.2.5 Ga_2O_3

Data from T. Koida, Y. Kamikawa-Shimizu, A. Yamada, H. Shibata and S. Niki [10]. The optical data have been extracted from an amorphous Ga_2O_3 layer prepared by room-temperature sputtering using a Ga_2O_3 target and Ar gas (Fig. 8.5, Tables 8.9 and 8.10).

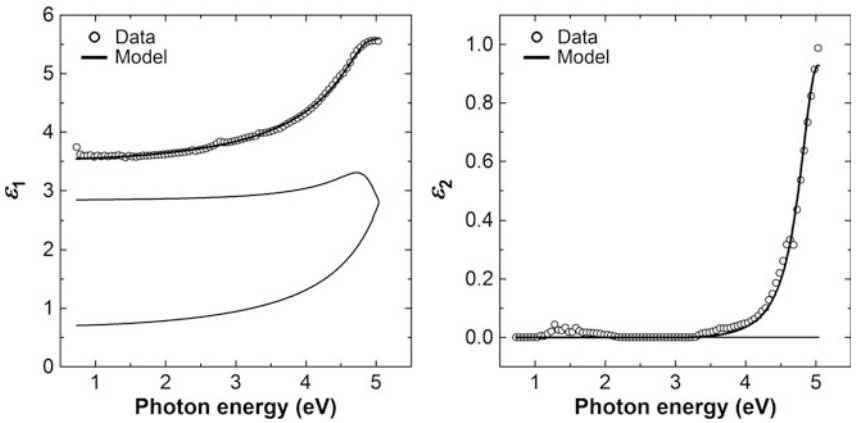


Fig. 8.5 Dielectric function of Ga_2O_3 at room temperature. The open circles show the reference data and the solid lines indicate the calculation result obtained from the parameterization assuming the Tauc-Lorentz model [(8.1) and (8.2)]

Table 8.9 Tauc-Lorentz parameters of (8.1) and (8.2) for Ga_2O_3

Peak	A (eV)	C (eV)	E_0 (eV)	E_g (eV)	$\varepsilon_1(\infty)$
$j = 1$	3.838	0.669	5.010	2.999	2.725
$j = 2$	241.918	0.009	5.803	5.058	0

Table 8.10 Refractive index of Ga_2O_3. The optical data reported by Koida et al. are shown

λ (nm)	n	k	λ (nm)	n	k	λ (nm)	n	k
300	2.113	0.015	540	1.914	0	880	1.889	0.010
305	2.096	0.013	550	1.912	0	890	1.898	0.004
310	2.081	0.012	560	1.911	0	900	1.894	0.006
315	2.069	0.011	570	1.909	0	910	1.897	0.004
320	2.057	0.01	580	1.908	0.001	920	1.897	0.006
325	2.048	0.009	590	1.907	0.002	930	1.898	0.007
330	2.039	0.008	600	1.905	0.002	940	1.895	0.005
335	2.029	0.007	610	1.904	0.002	950	1.895	0.006
340	2.017	0.008	620	1.903	0.003	960	1.895	0.014
345	2.013	0.006	630	1.902	0.003	970	1.897	0.004
350	2.008	0.005	640	1.901	0.003	980	1.897	0.003
355	2.002	0.004	650	1.900	0.003	990	1.897	0.004
360	1.998	0.004	660	1.900	0.004	1000	1.897	0.006
365	1.996	0.004	670	1.899	0.004	1010	1.895	0.004
370	1.995	0.002	680	1.898	0.004	1020	1.896	0.004
375	1.985	0	690	1.898	0.004	1030	1.893	0.009
380	1.982	0	700	1.897	0.005	1040	1.896	0.004
385	1.980	0	710	1.896	0.005	1050	1.893	0.003
390	1.977	0	720	1.895	0.005	1060	1.894	0.003
395	1.974	0	730	1.897	0.005	1070	1.895	0.003
400	1.970	0	740	1.896	0.004	1080	1.893	0.001
410	1.964	0	750	1.895	0.005	1090	1.897	0
420	1.959	0	760	1.894	0.006	1100	1.896	0.001
430	1.955	0	770	1.895	0.006	1110	1.892	0.002
440	1.957	0	780	1.892	0.007	1120	1.896	0.001
450	1.954	0	790	1.892	0.008	1130	1.898	0.001
460	1.943	0	800	1.892	0.007	1140	1.896	0
470	1.935	0	810	1.891	0.006	1150	1.897	0
480	1.929	0	820	1.889	0.009	1160	1.893	0.001
490	1.925	0	830	1.897	0.005	1170	1.889	0.001
500	1.922	0	840	1.895	0.005	1180	1.895	0
510	1.917	0	850	1.887	0.012	1190	1.897	0
520	1.921	0	860	1.886	0.013	1200	1.897	0
530	1.917	0	870	1.888	0.008			

8.2.6 SiN

Data from G. E. Jellison, Jr., F. A. Modine, P. Doshi and A. Rohatgi [11]. The optical data have been extracted from various SiN samples with different E_g, prepared by plasma-enhanced chemical vapor deposition (Tables 8.11, 8.12, 8.13, 8.14, 8.15 and 8.16).

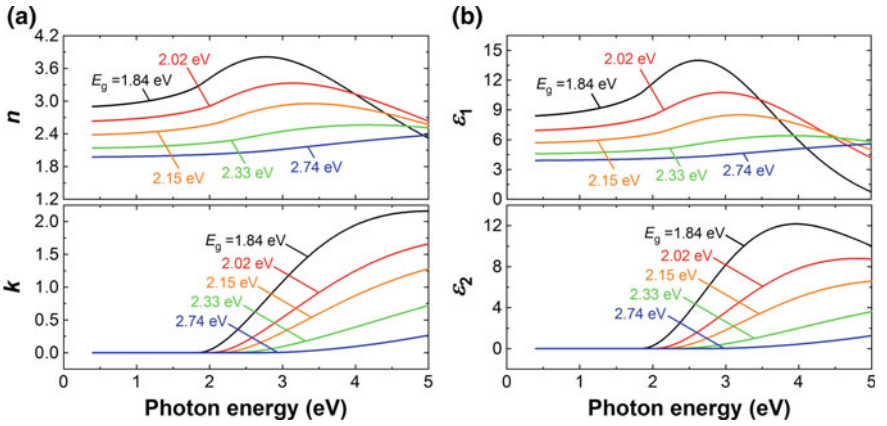


Fig. 8.6 **a** Optical constants and **b** dielectric functions of various SiN layers having different E_g. The optical functions have been calculated from the Tauc-Lorentz parameters reported by Jellison et al.

Table 8.11 Tauc-Lorentz parameters of (8.1) and (8.2) for the SiN dielectric functions in Fig. 8.6, reported by Jellison et al.

E_g (eV)	A (eV)	C (eV)	E_0 (eV)	E_g (eV)	$\varepsilon_1(\infty)$
1.84	202	4.02	3.50	1.84	1
2.02	177	5.9	4.30	2.02	1
2.15	147	7.1	4.89	2.15	1
2.33	107	9.5	6.9	2.33	1
2.74	80	7.0	8.8	2.74	1

Table 8.12 Optical constants of SiN (E_g = 1.84 eV) calculated by the Tauc-Lorentz model

λ (nm)	n	k	λ (nm)	n	k	λ (nm)	n	k
300	3.008	2.007	540	3.654	0.263	880	3.069	0
305	3.066	1.978	550	3.626	0.223	890	3.064	0
310	3.122	1.947	560	3.597	0.187	900	3.059	0
315	3.176	1.914	570	3.568	0.155	910	3.055	0
320	3.228	1.880	580	3.538	0.125	920	3.050	0
325	3.277	1.843	590	3.507	0.099	930	3.046	0
330	3.325	1.805	600	3.477	0.076	940	3.042	0
335	3.370	1.766	610	3.446	0.057	950	3.038	0
340	3.412	1.726	620	3.416	0.040	960	3.035	0
345	3.453	1.684	630	3.387	0.026	970	3.031	0
350	3.491	1.642	640	3.358	0.016	980	3.028	0
355	3.526	1.598	650	3.331	0.008	990	3.024	0

(continued)

Table 8.12 (continued)

λ (nm)	n	k	λ (nm)	n	k	λ (nm)	n	k
360	3.560	1.555	660	3.305	0.003	1000	3.021	0
365	3.590	1.510	670	3.281	0	1010	3.018	0
370	3.619	1.466	680	3.260	0	1020	3.015	0
375	3.645	1.421	690	3.242	0	1030	3.012	0
380	3.669	1.376	700	3.226	0	1040	3.010	0
385	3.691	1.331	710	3.211	0	1050	3.007	0
390	3.711	1.286	720	3.198	0	1060	3.004	0
395	3.729	1.242	730	3.186	0	1070	3.002	0
400	3.745	1.197	740	3.174	0	1080	2.999	0
410	3.770	1.110	750	3.163	0	1090	2.997	0
420	3.789	1.025	760	3.153	0	1100	2.995	0
430	3.801	0.942	770	3.144	0	1110	2.993	0
440	3.807	0.862	780	3.135	0	1120	2.991	0
450	3.808	0.786	790	3.127	0	1130	2.989	0
460	3.804	0.713	800	3.119	0	1140	2.987	0
470	3.796	0.643	810	3.112	0	1150	2.985	0
480	3.784	0.578	820	3.105	0	1160	2.983	0
490	3.768	0.516	830	3.098	0	1170	2.981	0
500	3.750	0.458	840	3.092	0	1180	2.979	0
510	3.729	0.404	850	3.086	0	1190	2.977	0
520	3.705	0.353	860	3.080	0	1200	2.976	0
530	3.680	0.306	870	3.074	0			

Table 8.13 Optical constants of SiN (E_g = 2.02 eV) calculated by the Tauc-Lorentz model

λ (nm)	n	k	λ (nm)	n	k	λ (nm)	n	k
300	3.071	1.324	540	3.084	0.067	880	2.736	0
305	3.100	1.287	550	3.060	0.050	890	2.734	0
310	3.128	1.249	560	3.035	0.035	900	2.731	0
315	3.153	1.211	570	3.011	0.023	910	2.728	0
320	3.177	1.173	580	2.988	0.014	920	2.725	0
325	3.198	1.136	590	2.965	0.007	930	2.723	0
330	3.218	1.098	600	2.944	0.002	940	2.721	0
335	3.235	1.060	610	2.924	0	950	2.718	0
340	3.251	1.023	620	2.907	0	960	2.716	0
345	3.265	0.986	630	2.893	0	970	2.714	0
350	3.278	0.949	640	2.880	0	980	2.712	0
355	3.289	0.913	650	2.868	0	990	2.710	0
360	3.298	0.877	660	2.857	0	1000	2.708	0
365	3.306	0.842	670	2.847	0	1010	2.706	0

(continued)

Table 8.13 (continued)

λ (nm)	n	k	λ (nm)	n	k	λ (nm)	n	k
370	3.313	0.808	680	2.838	0	1020	2.704	0
375	3.318	0.774	690	2.830	0	1030	2.703	0
380	3.323	0.740	700	2.822	0	1040	2.701	0
385	3.325	0.708	710	2.815	0	1050	2.699	0
390	3.327	0.676	720	2.808	0	1060	2.698	0
395	3.328	0.644	730	2.801	0	1070	2.696	0
400	3.328	0.614	740	2.795	0	1080	2.695	0
410	3.324	0.555	750	2.789	0	1090	2.693	0
420	3.317	0.499	760	2.784	0	1100	2.692	0
430	3.307	0.447	770	2.779	0	1110	2.691	0
440	3.295	0.397	780	2.774	0	1120	2.689	0
450	3.280	0.351	790	2.769	0	1130	2.688	0
460	3.263	0.307	800	2.765	0	1140	2.687	0
470	3.244	0.267	810	2.761	0	1150	2.686	0
480	3.224	0.230	820	2.757	0	1160	2.685	0
490	3.203	0.196	830	2.753	0	1170	2.684	0
500	3.180	0.164	840	2.749	0	1180	2.683	0
510	3.157	0.136	850	2.746	0	1190	2.681	0
520	3.133	0.110	860	2.743	0	1200	2.680	0
530	3.109	0.087	870	2.739	0			

Table 8.14 Optical constants of SiN (E_g = 2.15 eV) calculated by the Tauc-Lorentz model

λ (nm)	n	k	λ (nm)	n	k	λ (nm)	n	k
300	2.853	0.937	540	2.680	0.014	880	2.456	0
305	2.869	0.904	550	2.660	0.008	890	2.454	0
310	2.884	0.871	560	2.641	0.003	900	2.452	0
315	2.897	0.838	570	2.624	0	910	2.450	0
320	2.908	0.806	580	2.609	0	920	2.448	0
325	2.918	0.774	590	2.596	0	930	2.446	0
330	2.927	0.742	600	2.585	0	940	2.445	0
335	2.934	0.711	610	2.575	0	950	2.443	0
340	2.940	0.681	620	2.566	0	960	2.442	0
345	2.945	0.651	630	2.557	0	970	2.440	0
350	2.949	0.622	640	2.549	0	980	2.439	0
355	2.951	0.593	650	2.542	0	990	2.437	0
360	2.953	0.565	660	2.536	0	1000	2.436	0
365	2.953	0.538	670	2.529	0	1010	2.435	0

(continued)

Table 8.14 (continued)

λ (nm)	n	k	λ (nm)	n	k	λ (nm)	n	k
370	2.953	0.512	680	2.524	0	1020	2.433	0
375	2.952	0.486	690	2.518	0	1030	2.432	0
380	2.950	0.461	700	2.513	0	1040	2.431	0
385	2.947	0.436	710	2.508	0	1050	2.430	0
390	2.944	0.412	720	2.504	0	1060	2.429	0
395	2.940	0.389	730	2.499	0	1070	2.428	0
400	2.935	0.367	740	2.495	0	1080	2.427	0
410	2.924	0.325	750	2.492	0	1090	2.426	0
420	2.911	0.285	760	2.488	0	1100	2.425	0
430	2.896	0.248	770	2.484	0	1110	2.424	0
440	2.880	0.214	780	2.481	0	1120	2.423	0
450	2.862	0.183	790	2.478	0	1130	2.422	0
460	2.844	0.154	800	2.475	0	1140	2.421	0
470	2.824	0.128	810	2.472	0	1150	2.420	0
480	2.804	0.104	820	2.470	0	1160	2.420	0
490	2.783	0.083	830	2.467	0	1170	2.419	0
500	2.762	0.065	840	2.465	0	1180	2.418	0
510	2.741	0.049	850	2.462	0	1190	2.417	0
520	2.721	0.035	860	2.460	0	1200	2.417	0
530	2.700	0.024	870	2.458	0			

Table 8.15 Optical constants of SiN (E_g = 2.33 eV) calculated by the Tauc-Lorentz model

λ (nm)	n	k	λ (nm)	n	k	λ (nm)	n	k
300	2.561	0.435	540	2.278	0	880	2.178	0
305	2.560	0.413	550	2.270	0	890	2.177	0
310	2.558	0.391	560	2.264	0	900	2.176	0
315	2.556	0.370	570	2.257	0	910	2.175	0
320	2.553	0.350	580	2.252	0	920	2.174	0
325	2.550	0.330	590	2.246	0	930	2.173	0
330	2.546	0.312	600	2.242	0	940	2.172	0
335	2.542	0.294	610	2.237	0	950	2.171	0
340	2.538	0.276	620	2.233	0	960	2.170	0
345	2.533	0.260	630	2.229	0	970	2.169	0
350	2.527	0.244	640	2.225	0	980	2.169	0
355	2.522	0.229	650	2.222	0	990	2.168	0
360	2.516	0.214	660	2.219	0	1000	2.167	0
365	2.510	0.200	670	2.216	0	1010	2.166	0
370	2.504	0.186	680	2.213	0	1020	2.166	0
375	2.497	0.174	690	2.210	0	1030	2.165	0

(continued)

Table 8.15 (continued)

λ (nm)	n	k	λ (nm)	n	k	λ (nm)	n	k
380	2.491	0.161	700	2.208	0	1040	2.164	0
385	2.484	0.150	710	2.205	0	1050	2.164	0
390	2.477	0.138	720	2.203	0	1060	2.163	0
395	2.470	0.128	730	2.201	0	1070	2.163	0
400	2.463	0.118	740	2.199	0	1080	2.162	0
410	2.448	0.099	750	2.197	0	1090	2.161	0
420	2.434	0.082	760	2.195	0	1100	2.161	0
430	2.419	0.067	770	2.193	0	1110	2.160	0
440	2.404	0.054	780	2.191	0	1120	2.160	0
450	2.390	0.042	790	2.190	0	1130	2.159	0
460	2.375	0.032	800	2.188	0	1140	2.159	0
470	2.361	0.023	810	2.187	0	1150	2.158	0
480	2.347	0.016	820	2.185	0	1160	2.158	0
490	2.334	0.010	830	2.184	0	1170	2.158	0
500	2.321	0.006	840	2.182	0	1180	2.157	0
510	2.309	0.003	850	2.181	0	1190	2.157	0
520	2.297	0.001	860	2.180	0	1200	2.156	0
530	2.287	0	870	2.179	0			

Table 8.16 Optical constants of SiN (E_g = 2.74 eV) calculated by the Tauc-Lorentz model

λ (nm)	n	k	λ (nm)	n	k	λ (nm)	n	k
300	2.273	0.114	540	2.041	0	880	1.9953	0
305	2.264	0.104	550	2.038	0	890	1.9947	0
310	2.255	0.095	560	2.036	0	900	1.9942	0
315	2.247	0.087	570	2.033	0	910	1.9937	0
320	2.238	0.079	580	2.031	0	920	1.9932	0
325	2.230	0.072	590	2.028	0	930	1.9927	0
330	2.222	0.065	600	2.026	0	940	1.9922	0
335	2.214	0.059	610	2.024	0	950	1.9918	0
340	2.207	0.053	620	2.022	0	960	1.9913	0
345	2.199	0.047	630	2.021	0	970	1.9909	0
350	2.192	0.042	640	2.019	0	980	1.9905	0
355	2.185	0.038	650	2.017	0	990	1.9901	0
360	2.178	0.033	660	2.016	0	1000	1.9897	0
365	2.171	0.029	670	2.014	0	1010	1.9893	0
370	2.165	0.026	680	2.013	0	1020	1.9890	0
375	2.158	0.022	690	2.012	0	1030	1.9886	0
380	2.152	0.019	700	2.010	0	1040	1.9883	0
385	2.146	0.016	710	2.009	0	1050	1.9879	0

(continued)

Table 8.16 (continued)

λ (nm)	n	k	λ (nm)	n	k	λ (nm)	n	k
390	2.140	0.014	720	2.008	0	1060	1.9876	0
395	2.134	0.012	730	2.007	0	1070	1.9873	0
400	2.129	0.010	740	2.006	0	1080	1.9870	0
410	2.118	0.006	750	2.005	0	1090	1.9867	0
420	2.108	0.003	760	2.004	0	1100	1.9864	0
430	2.099	0.002	770	2.003	0	1110	1.9861	0
440	2.090	0	780	2.002	0	1120	1.9859	0
450	2.083	0	790	2.001	0	1130	1.9856	0
460	2.076	0	800	2.001	0	1140	1.9853	0
470	2.070	0	810	2	0	1150	1.9851	0
480	2.065	0	820	1.999	0	1160	1.9848	0
490	2.060	0	830	1.998	0	1170	1.9846	0
500	2.056	0	840	1.998	0	1180	1.9844	0
510	2.052	0	850	1.997	0	1190	1.9842	0
520	2.048	0	860	1.996	0	1200	1.9839	0
530	2.045	0	870	1.996	0			

8.2.7 a-Si:H

Data from R. W. Collins and K. Vedam [12]. The optical data have been extracted from a hydrogenated amorphous silicon (a-Si:H) layer prepared by conventional plasma-enhanced chemical vapor deposition (Fig. 8.7, Tables 8.17 and 8.18).

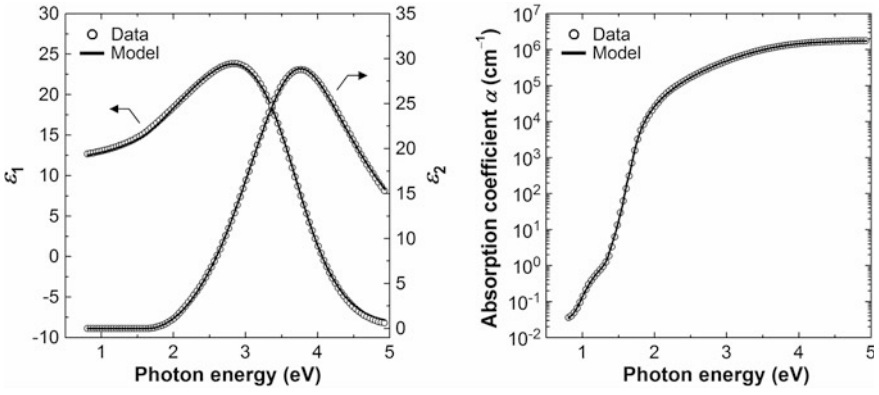


Fig. 8.7 Dielectric function and absorption coefficient of a-Si:H at room temperature. The open circles show the reference data and the solid lines indicate the calculation result obtained from the parameterization assuming the Tauc-Lorentz model [(8.1) and (8.2)]

Table 8.17 Tauc-Lorentz parameters of (8.1) and (8.2) for a-Si:H

Peak	A (eV)	C (eV)	E_0 (eV)	E_g (eV)	$\varepsilon_1(\infty)$
$j = 1$	3.497×10^{-6}	0.254	0.806	0.432	−0.411
$j = 2$	2.364×10^{-4}	0.715	1.341	0.791	0
$j = 3$	0.034	0.108	1.652	1.294	0
$j = 4$	4.268×10^{-3}	0.406	1.784	1.211	0
$j = 5$	179.062	2.351	3.458	1.637	0
$j = 6$	116.664	1.488	3.691	2.555	0

Table 8.18 Optical constants of a-Si:H. The optical data of Collins et al. are shown

λ (nm)	n	k	λ (nm)	n	k	λ (nm)	n	k
300	3.515	3.703	540	4.593	0.415	880	3.756	2.40×10^{-5}
305	3.664	3.664	550	4.551	0.371	890	3.747	1.88×10^{-5}
310	3.810	3.615	560	4.510	0.329	900	3.739	1.53×10^{-5}
315	3.952	3.555	570	4.471	0.286	910	3.731	1.27×10^{-5}
320	4.088	3.485	580	4.433	0.246	920	3.724	1.11×10^{-5}
325	4.217	3.406	590	4.396	0.212	930	3.717	9.84×10^{-6}
330	4.339	3.318	600	4.360	0.178	940	3.710	8.82×10^{-6}
335	4.452	3.224	610	4.326	0.15	950	3.704	8.02×10^{-6}
340	4.555	3.123	620	4.293	0.125	960	3.698	7.47×10^{-6}
345	4.650	3.017	630	4.260	0.103	970	3.692	6.96×10^{-6}
350	4.734	2.908	640	4.229	8.51×10^{-2}	980	3.686	6.57×10^{-6}
355	4.808	2.797	650	4.199	6.99×10^{-2}	990	3.681	6.21×10^{-6}
360	4.873	2.684	660	4.170	5.64×10^{-2}	1000	3.675	5.88×10^{-6}
365	4.928	2.571	670	4.142	4.57×10^{-2}	1010	3.670	5.57×10^{-6}
370	4.975	2.459	680	4.115	3.64×10^{-2}	1020	3.665	5.27×10^{-6}
375	5.013	2.349	690	4.089	2.79×10^{-2}	1030	3.661	5.00×10^{-6}
380	5.044	2.240	700	4.064	1.96×10^{-2}	1040	3.656	4.76×10^{-6}
385	5.067	2.135	710	4.040	1.32×10^{-2}	1050	3.652	4.50×10^{-6}
390	5.084	2.032	720	4.017	8.22×10^{-3}	1060	3.647	4.31×10^{-6}
395	5.096	1.933	730	3.995	5.26×10^{-3}	1070	3.643	4.06×10^{-6}
400	5.102	1.838	740	3.973	3.33×10^{-3}	1080	3.639	3.84×10^{-6}
410	5.102	1.659	750	3.953	2.10×10^{-3}	1090	3.635	3.66×10^{-6}
420	5.087	1.496	760	3.934	1.37×10^{-3}	1100	3.632	3.46×10^{-6}
430	5.062	1.347	770	3.915	9.14×10^{-4}	1110	3.628	3.25×10^{-6}
440	5.030	1.213	780	3.898	6.14×10^{-4}	1120	3.624	3.08×10^{-6}
450	4.992	1.092	790	3.881	4.20×10^{-4}	1130	3.621	2.88×10^{-6}
460	4.950	0.982	800	3.866	2.90×10^{-4}	1140	3.618	2.74×10^{-6}
470	4.906	0.884	810	3.853	2.03×10^{-4}	1150	3.615	2.57×10^{-6}
480	4.861	0.795	820	3.840	1.43×10^{-4}	1160	3.611	2.42×10^{-6}
490	4.815	0.715	830	3.828	1.01×10^{-4}	1170	3.608	2.27×10^{-6}
500	4.769	0.642	840	3.817	7.26×10^{-5}	1180	3.606	2.09×10^{-6}
510	4.724	0.577	850	3.806	5.39×10^{-5}	1190	3.603	1.91×10^{-6}
520	4.679	0.518	860	3.796	3.95×10^{-5}	1200	3.600	1.77×10^{-6}
530	4.635	0.464	870	3.787	3.01×10^{-5}			

8.2.8 a-Si:H Layers

Data from S. Kageyama, M. Akagawa and H. Fujiwara [13] (see also Fig. 9.11a in Vol. 1). The optical data have been extracted from various a-Si:H layers prepared by plasma-enhanced chemical vapor deposition at different substrate temperatures (T_s = 80–280 °C). The dielectric functions modeled assuming a single Tauc-Lorentz peak are summarized. In the modeling, the effect of the tail-state absorption is neglected (Tables 8.19, 8.20, 8.21, 8.22, 8.23 and 8.24).

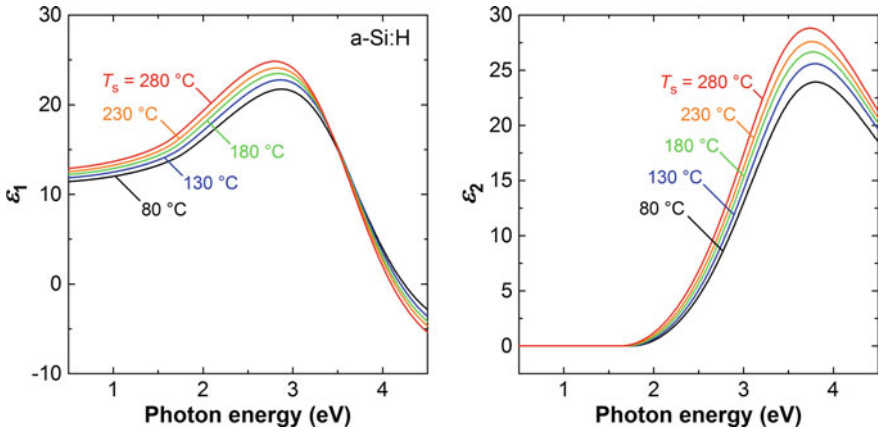


Fig. 8.8 Dielectric functions of a-Si:H layers calculated from the Tauc-Lorentz parameters reported by Kageyama et al. The results for various a-Si:H layers prepared at different substrate temperature (T_s) are shown

Table 8.19 Tauc-Lorentz parameters of (8.1) and (8.2) for the a-Si:H dielectric function in Fig. 8.8, reported by Kageyama et al.

T_s (°C)	A (eV)	C (eV)	E_0 (eV)	E_g (eV)	$\varepsilon_1(\infty)$
80	199.37	2.33	3.673	1.744	0.920
130	207.94	2.33	3.670	1.717	0.597
180	211.90	2.33	3.656	1.688	0.440
230	214.05	2.33	3.649	1.659	0.309
280	217.98	2.33	3.637	1.627	0.073

Table 8.20 Optical constants of a-Si:H (T_s = 80 °C) calculated by the Tauc-Lorentz model

λ (nm)	n	k	λ (nm)	n	k	λ (nm)	n	k
300	3.461	3.223	540	4.330	0.272	880	3.597	0
305	3.590	3.184	550	4.288	0.234	890	3.590	0
310	3.716	3.136	560	4.247	0.200	900	3.584	0
315	3.838	3.080	570	4.207	0.169	910	3.578	0
320	3.954	3.016	580	4.169	0.142	920	3.572	0
325	4.065	2.944	590	4.131	0.118	930	3.566	0
330	4.169	2.866	600	4.095	0.097	940	3.561	0
335	4.266	2.781	610	4.060	0.078	950	3.556	0
340	4.355	2.692	620	4.027	0.062	960	3.551	0
345	4.436	2.599	630	3.995	0.048	970	3.546	0
350	4.508	2.503	640	3.964	0.036	980	3.542	0
355	4.573	2.406	650	3.934	0.026	990	3.537	0
360	4.629	2.307	660	3.906	0.018	1000	3.533	0
365	4.677	2.207	670	3.879	0.011	1010	3.529	0
370	4.718	2.109	680	3.854	0.006	1020	3.525	0
375	4.752	2.011	690	3.830	0.003	1030	3.521	0
380	4.779	1.915	700	3.807	0.001	1040	3.517	0
385	4.800	1.822	710	3.787	0	1050	3.514	0
390	4.815	1.731	720	3.768	0	1060	3.510	0
395	4.825	1.642	730	3.751	0	1070	3.507	0
400	4.831	1.557	740	3.736	0	1080	3.504	0
410	4.830	1.396	750	3.722	0	1090	3.501	0
420	4.816	1.249	760	3.709	0	1100	3.498	0
430	4.792	1.114	770	3.696	0	1110	3.495	0
440	4.761	0.992	780	3.684	0	1120	3.492	0
450	4.725	0.881	790	3.673	0	1130	3.489	0
460	4.685	0.782	800	3.663	0	1140	3.487	0
470	4.642	0.692	810	3.653	0	1150	3.484	0
480	4.598	0.611	820	3.644	0	1160	3.482	0
490	4.552	0.539	830	3.635	0	1170	3.479	0
500	4.507	0.473	840	3.627	0	1180	3.477	0
510	4.462	0.415	850	3.619	0	1190	3.474	0
520	4.417	0.362	860	3.611	0	1200	3.472	0
530	4.373	0.314	870	3.604	0			

Table 8.21 Optical constants of a-Si:H (T_s = 130 °C) calculated by the Tauc-Lorentz model

λ (nm)	n	k	λ (nm)	n	k	λ (nm)	n	k
300	3.523	3.370	540	4.447	0.305	880	3.674	0
305	3.656	3.330	550	4.403	0.264	890	3.667	0
310	3.786	3.281	560	4.361	0.227	900	3.661	0
315	3.912	3.224	570	4.321	0.195	910	3.654	0
320	4.033	3.158	580	4.281	0.165	920	3.648	0
325	4.148	3.084	590	4.242	0.139	930	3.642	0
330	4.256	3.004	600	4.205	0.116	940	3.636	0
335	4.356	2.917	610	4.169	0.095	950	3.631	0
340	4.449	2.825	620	4.135	0.077	960	3.625	0
345	4.533	2.730	630	4.101	0.061	970	3.620	0
350	4.609	2.631	640	4.069	0.048	980	3.615	0
355	4.676	2.530	650	4.038	0.036	990	3.611	0
360	4.735	2.428	660	4.009	0.026	1000	3.606	0
365	4.786	2.325	670	3.981	0.018	1010	3.602	0
370	4.829	2.223	680	3.954	0.012	1020	3.597	0
375	4.865	2.122	690	3.928	0.007	1030	3.593	0
380	4.894	2.023	700	3.904	0.003	1040	3.589	0
385	4.916	1.926	710	3.882	0.001	1050	3.586	0
390	4.933	1.831	720	3.861	0	1060	3.582	0
395	4.945	1.740	730	3.842	0	1070	3.578	0
400	4.951	1.651	740	3.825	0	1080	3.575	0
410	4.952	1.484	750	3.810	0	1090	3.572	0
420	4.939	1.330	760	3.795	0	1100	3.568	0
430	4.916	1.190	770	3.781	0	1110	3.565	0
440	4.885	1.062	780	3.769	0	1120	3.562	0
450	4.849	0.947	790	3.757	0	1130	3.559	0
460	4.808	0.843	800	3.746	0	1140	3.556	0
470	4.765	0.748	810	3.735	0	1150	3.554	0
480	4.720	0.664	820	3.725	0	1160	3.551	0
490	4.674	0.587	830	3.716	0	1170	3.548	0
500	4.628	0.518	840	3.706	0	1180	3.546	0
510	4.581	0.456	850	3.698	0	1190	3.543	0
520	4.536	0.400	860	3.690	0	1200	3.541	0
530	4.491	0.350	870	3.682	0			

Table 8.22 Optical constants of a-Si:H (T_s = 180 °C) calculated by the Tauc-Lorentz model

λ (nm)	n	k	λ (nm)	n	k	λ (nm)	n	k
300	3.536	3.465	540	4.540	0.340	880	3.739	0
305	3.672	3.427	550	4.497	0.297	890	3.731	0
310	3.805	3.380	560	4.454	0.258	900	3.724	0
315	3.934	3.324	570	4.413	0.223	910	3.717	0
320	4.057	3.260	580	4.373	0.191	920	3.710	0
325	4.176	3.187	590	4.334	0.163	930	3.704	0
330	4.287	3.108	600	4.296	0.137	940	3.698	0
335	4.391	3.022	610	4.260	0.115	950	3.692	0
340	4.487	2.931	620	4.224	0.095	960	3.686	0
345	4.575	2.835	630	4.190	0.077	970	3.681	0
350	4.655	2.736	640	4.157	0.062	980	3.676	0
355	4.726	2.634	650	4.126	0.048	990	3.671	0
360	4.789	2.531	660	4.095	0.037	1000	3.666	0
365	4.843	2.428	670	4.066	0.027	1010	3.662	0
370	4.890	2.324	680	4.038	0.019	1020	3.657	0
375	4.929	2.222	690	4.012	0.012	1030	3.653	0
380	4.961	2.121	700	3.986	0.007	1040	3.649	0
385	4.987	2.022	710	3.962	0.004	1050	3.645	0
390	5.006	1.925	720	3.940	0.001	1060	3.641	0
395	5.020	1.831	730	3.919	0	1070	3.637	0
400	5.029	1.740	740	3.900	0	1080	3.633	0
410	5.034	1.569	750	3.883	0	1090	3.630	0
420	5.025	1.410	760	3.867	0	1100	3.627	0
430	5.004	1.265	770	3.853	0	1110	3.623	0
440	4.975	1.133	780	3.839	0	1120	3.620	0
450	4.940	1.013	790	3.826	0	1130	3.617	0
460	4.901	0.904	800	3.814	0	1140	3.614	0
470	4.858	0.806	810	3.803	0	1150	3.611	0
480	4.814	0.717	820	3.792	0	1160	3.608	0
490	4.768	0.637	830	3.782	0	1170	3.606	0
500	4.722	0.565	840	3.773	0	1180	3.603	0
510	4.676	0.500	850	3.763	0	1190	3.600	0
520	4.630	0.441	860	3.755	0	1200	3.598	0
530	4.585	0.388	870	3.746	0			

Table 8.23 Optical constants of a-Si:H (T_s = 230 °C) calculated by the Tauc-Lorentz model

λ (nm)	n	k	λ (nm)	n	k	λ (nm)	n	k
300	3.553	3.548	540	4.621	0.373	880	3.796	0
305	3.690	3.511	550	4.577	0.328	890	3.788	0
310	3.825	3.465	560	4.535	0.287	900	3.780	0
315	3.957	3.410	570	4.493	0.250	910	3.773	0
320	4.083	3.346	580	4.453	0.216	920	3.766	0
325	4.204	3.274	590	4.414	0.186	930	3.760	0
330	4.318	3.195	600	4.375	0.159	940	3.753	0
335	4.425	3.109	610	4.339	0.135	950	3.747	0
340	4.524	3.018	620	4.303	0.113	960	3.741	0
345	4.615	2.922	630	4.269	0.094	970	3.736	0
350	4.698	2.823	640	4.235	0.077	980	3.730	0
355	4.772	2.721	650	4.203	0.062	990	3.725	0
360	4.837	2.617	660	4.172	0.049	1000	3.720	0
365	4.894	2.512	670	4.143	0.037	1010	3.715	0
370	4.943	2.408	680	4.114	0.028	1020	3.710	0
375	4.985	2.304	690	4.087	0.020	1030	3.706	0
380	5.019	2.201	700	4.060	0.013	1040	3.702	0
385	5.047	2.101	710	4.036	0.008	1050	3.697	0
390	5.068	2.003	720	4.012	0.004	1060	3.693	0
395	5.084	1.907	730	3.990	0.002	1070	3.689	0
400	5.095	1.814	740	3.969	0	1080	3.686	0
410	5.103	1.639	750	3.950	0	1090	3.682	0
420	5.096	1.477	760	3.933	0	1100	3.678	0
430	5.077	1.328	770	3.917	0	1110	3.675	0
440	5.050	1.193	780	3.902	0	1120	3.672	0
450	5.017	1.069	790	3.889	0	1130	3.668	0
460	4.978	0.958	800	3.876	0	1140	3.665	0
470	4.937	0.857	810	3.864	0	1150	3.662	0
480	4.893	0.765	820	3.853	0	1160	3.659	0
490	4.848	0.682	830	3.842	0	1170	3.656	0
500	4.802	0.607	840	3.832	0	1180	3.654	0
510	4.756	0.540	850	3.822	0	1190	3.651	0
520	4.710	0.478	860	3.813	0	1200	3.648	0
530	4.665	0.423	870	3.804	0			

Table 8.24 Optical constants of a-Si:H (T_s = 280 °C) calculated by the Tauc-Lorentz model

λ (nm)	n	k	λ (nm)	n	k	λ (nm)	n	k
300	3.567	3.657	540	4.718	0.415	880	3.862	0
305	3.708	3.622	550	4.674	0.367	890	3.854	0
310	3.845	3.577	560	4.631	0.324	900	3.846	0
315	3.980	3.523	570	4.589	0.284	910	3.838	0
320	4.109	3.460	580	4.548	0.248	920	3.830	0
325	4.233	3.389	590	4.509	0.216	930	3.823	0
330	4.351	3.311	600	4.470	0.187	940	3.817	0
335	4.462	3.226	610	4.433	0.160	950	3.810	0
340	4.565	3.135	620	4.396	0.137	960	3.804	0
345	4.660	3.039	630	4.361	0.115	970	3.798	0
350	4.746	2.939	640	4.327	0.096	980	3.792	0
355	4.824	2.836	650	4.295	0.079	990	3.787	0
360	4.893	2.731	660	4.263	0.064	1000	3.781	0
365	4.953	2.625	670	4.232	0.051	1010	3.776	0
370	5.006	2.519	680	4.203	0.040	1020	3.771	0
375	5.051	2.413	690	4.175	0.030	1030	3.766	0
380	5.088	2.309	700	4.148	0.022	1040	3.762	0
385	5.119	2.207	710	4.122	0.015	1050	3.757	0
390	5.143	2.106	720	4.097	0.010	1060	3.753	0
395	5.162	2.008	730	4.073	0.006	1070	3.749	0
400	5.175	1.913	740	4.051	0.003	1080	3.745	0
410	5.187	1.733	750	4.030	0.001	1090	3.741	0
420	5.183	1.566	760	4.011	0	1100	3.737	0
430	5.167	1.412	770	3.993	0	1110	3.734	0
440	5.142	1.272	780	3.977	0	1120	3.730	0
450	5.110	1.144	790	3.962	0	1130	3.727	0
460	5.073	1.028	800	3.948	0	1140	3.723	0
470	5.033	0.922	810	3.935	0	1150	3.720	0
480	4.989	0.827	820	3.923	0	1160	3.717	0
490	4.945	0.740	830	3.911	0	1170	3.714	0
500	4.899	0.662	840	3.900	0	1180	3.711	0
510	4.853	0.591	850	3.890	0	1190	3.708	0
520	4.808	0.527	860	3.880	0	1200	3.705	0
530	4.762	0.468	870	3.871	0			

8.2.9 a-SiC:H

The dielectric functions of hydrogenated amorphous silicon carbide (a-$Si_{1-x}C_x$:H) alloys ($x = 0.1$–0.3) were calculated from the model parameters shown in Fig. 9.16 of Vol. 1 (see also M. Sato, S. W. King, W. A. Lanford, P. Henry, T. Fujiseki, and H. Fujiwara [14]). The original optical data were extracted from a-SiC:H layers prepared by plasma-enhanced chemical vapor deposition at 180 °C using different SiH_4/CH_4 gas flow ratios. The dielectric functions modeled assuming a single Tauc-Lorentz peak are summarized. In the modeling, the effect of the tail-state absorption is neglected (Tables 8.25, 8.26, 8.27 and 8.28).

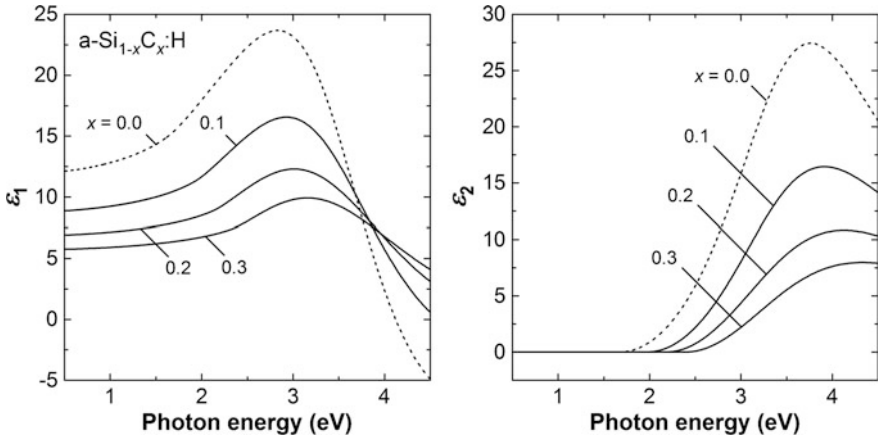


Fig. 8.9 Dielectric functions of a-$Si_{1-x}C_x$:H layers calculated from the Tauc-Lorentz parameters reported by Sato et al. The results for various a-$Si_{1-x}C_x$:H layers with different carbon content x are shown

Table 8.25 Tauc-Lorentz parameters for the a-$Si_{1-x}C_x$:H dielectric functions in Fig. 8.9, reported by Sato et al.

Alloy content x	A (eV)	C (eV)	E_0 (eV)	E_g (eV)	$\varepsilon_1(\infty)$
$x = 0.0$	213.848	2.309	3.650	1.674	0.059
$x = 0.1$	192.668	2.602	3.659	1.972	1.179
$x = 0.2$	182.601	3.082	3.667	2.182	1.359
$x = 0.3$	174.651	3.282	3.676	2.392	1.539

Table 8.26 Optical constants of a-$Si_{1-x}C_x$:H ($x = 0.1$) calculated by the Tauc-Lorentz model

λ (nm)	n	k	λ (nm)	n	k	λ (nm)	n	k
300	3.210	2.497	540	3.696	0.112	880	3.133	0
305	3.306	2.457	550	3.656	0.086	890	3.129	0
310	3.398	2.410	560	3.617	0.064	900	3.124	0
315	3.487	2.358	570	3.579	0.045	910	3.120	0
320	3.571	2.301	580	3.542	0.031	920	3.116	0
325	3.651	2.239	590	3.507	0.019	930	3.112	0
330	3.725	2.173	600	3.475	0.010	940	3.108	0
335	3.793	2.104	610	3.444	0.004	950	3.104	0
340	3.856	2.031	620	3.415	0.001	960	3.101	0
345	3.913	1.957	630	3.389	0	970	3.097	0
350	3.964	1.880	640	3.367	0	980	3.094	0
355	4.009	1.803	650	3.348	0	990	3.091	0
360	4.049	1.725	660	3.330	0	1000	3.088	0
365	4.082	1.647	670	3.314	0	1010	3.085	0
370	4.111	1.569	680	3.299	0	1020	3.082	0
375	4.134	1.492	690	3.285	0	1030	3.079	0
380	4.152	1.417	700	3.272	0	1040	3.077	0
385	4.166	1.343	710	3.260	0	1050	3.074	0
390	4.175	1.271	720	3.249	0	1060	3.072	0
395	4.181	1.201	730	3.238	0	1070	3.069	0
400	4.183	1.134	740	3.228	0	1080	3.067	0
410	4.178	1.005	750	3.219	0	1090	3.065	0
420	4.163	0.887	760	3.210	0	1100	3.063	0
430	4.140	0.778	770	3.202	0	1110	3.061	0
440	4.110	0.679	780	3.194	0	1120	3.058	0
450	4.075	0.589	790	3.186	0	1130	3.057	0
460	4.037	0.509	800	3.179	0	1140	3.055	0
470	3.996	0.436	810	3.172	0	1150	3.053	0
480	3.954	0.371	820	3.166	0	1160	3.051	0
490	3.911	0.313	830	3.160	0	1170	3.049	0
500	3.867	0.262	840	3.154	0	1180	3.047	0
510	3.824	0.217	850	3.149	0	1190	3.046	0
520	3.781	0.177	860	3.143	0	1200	3.044	0
530	3.738	0.142	870	3.138	0			

Table 8.27 Optical constants of a-$Si_{1-x}C_x$:H ($x = 0.2$) calculated by the Tauc-Lorentz model

λ (nm)	n	k	λ (nm)	n	k	λ (nm)	n	k
300	2.986	1.814	540	3.106	0.016	880	2.737	0
305	3.050	1.773	550	3.071	0.007	890	2.734	0
310	3.111	1.729	560	3.038	0.001	900	2.731	0
315	3.169	1.682	570	3.010	0	910	2.728	0
320	3.223	1.632	580	2.986	0	920	2.725	0
325	3.273	1.580	590	2.965	0	930	2.723	0
330	3.320	1.526	600	2.947	0	940	2.720	0
335	3.362	1.470	610	2.930	0	950	2.718	0
340	3.401	1.413	620	2.915	0	960	2.715	0
345	3.435	1.355	630	2.901	0	970	2.713	0
350	3.465	1.296	640	2.889	0	980	2.711	0
355	3.492	1.238	650	2.877	0	990	2.708	0
360	3.514	1.179	660	2.866	0	1000	2.706	0
365	3.533	1.120	670	2.856	0	1010	2.704	0
370	3.549	1.063	680	2.846	0	1020	2.702	0
375	3.561	1.006	690	2.838	0	1030	2.700	0
380	3.569	0.950	700	2.829	0	1040	2.699	0
385	3.575	0.895	710	2.822	0	1050	2.697	0
390	3.578	0.842	720	2.814	0	1060	2.695	0
395	3.578	0.790	730	2.807	0	1070	2.693	0
400	3.576	0.739	740	2.801	0	1080	2.692	0
410	3.565	0.644	750	2.795	0	1090	2.690	0
420	3.546	0.556	760	2.789	0	1100	2.689	0
430	3.522	0.475	770	2.783	0	1110	2.687	0
440	3.492	0.401	780	2.778	0	1120	2.686	0
450	3.459	0.334	790	2.773	0	1130	2.684	0
460	3.422	0.275	800	2.768	0	1140	2.683	0
470	3.384	0.222	810	2.764	0	1150	2.682	0
480	3.344	0.176	820	2.760	0	1160	2.681	0
490	3.304	0.136	830	2.755	0	1170	2.679	0
500	3.263	0.101	840	2.751	0	1180	2.678	0
510	3.222	0.072	850	2.748	0	1190	2.677	0
520	3.182	0.049	860	2.744	0	1200	2.676	0
530	3.143	0.030	870	2.741	0			

Table 8.28 Optical constants of a-$Si_{1-x}C_x$:H ($x = 0.3$) calculated by the Tauc-Lorentz model

λ (nm)	n	k	λ (nm)	n	k	λ (nm)	n	k
300	2.822	1.391	540	2.703	0	880	2.475	0
305	2.871	1.351	550	2.685	0	890	2.473	0
310	2.916	1.308	560	2.668	0	900	2.471	0
315	2.958	1.263	570	2.653	0	910	2.469	0
320	2.997	1.216	580	2.640	0	920	2.467	0
325	3.032	1.168	590	2.627	0	930	2.465	0
330	3.064	1.119	600	2.616	0	940	2.463	0
335	3.093	1.069	610	2.606	0	950	2.461	0
340	3.117	1.018	620	2.596	0	960	2.460	0
345	3.139	0.967	630	2.587	0	970	2.458	0
350	3.157	0.916	640	2.579	0	980	2.456	0
355	3.172	0.865	650	2.571	0	990	2.455	0
360	3.183	0.815	660	2.564	0	1000	2.453	0
365	3.192	0.765	670	2.557	0	1010	2.452	0
370	3.197	0.717	680	2.551	0	1020	2.451	0
375	3.200	0.669	690	2.545	0	1030	2.449	0
380	3.200	0.622	700	2.539	0	1040	2.448	0
385	3.198	0.577	710	2.534	0	1050	2.447	0
390	3.194	0.534	720	2.529	0	1060	2.445	0
395	3.187	0.491	730	2.524	0	1070	2.444	0
400	3.179	0.451	740	2.520	0	1080	2.443	0
410	3.156	0.375	750	2.515	0	1090	2.442	0
420	3.128	0.306	760	2.511	0	1100	2.441	0
430	3.096	0.244	770	2.508	0	1110	2.440	0
440	3.059	0.190	780	2.504	0	1120	2.439	0
450	3.020	0.143	790	2.500	0	1130	2.438	0
460	2.980	0.103	800	2.497	0	1140	2.437	0
470	2.939	0.070	810	2.494	0	1150	2.436	0
480	2.897	0.043	820	2.491	0	1160	2.435	0
490	2.857	0.023	830	2.488	0	1170	2.434	0
500	2.818	0.010	840	2.485	0	1180	2.433	0
510	2.782	0.002	850	2.483	0	1190	2.432	0
520	2.750	0	860	2.480	0	1200	2.432	0
530	2.725	0	870	2.478	0			

8.2.10 a-SiO:H

The dielectric functions of hydrogenated amorphous silicon oxide (a-$Si_{1-x}O_x$:H) alloys ($x = 0.1$–0.3) were calculated from the model parameters shown in Fig. 9.16 of Vol. 1 (see also M. Sato, S. W. King, W. A. Lanford, P. Henry, T. Fujiseki, and H. Fujiwara [14]). The original optical data were extracted from a-SiO:H layers prepared by plasma-enhanced chemical vapor deposition at 180 °C using different SiH_4/CO_2 gas mixtures. The dielectric functions modeled assuming a single Tauc-Lorentz peak are summarized. In the modeling, the effect of the tail-state absorption is neglected (Tables 8.29, 8.30, 8.31 and 8.32).

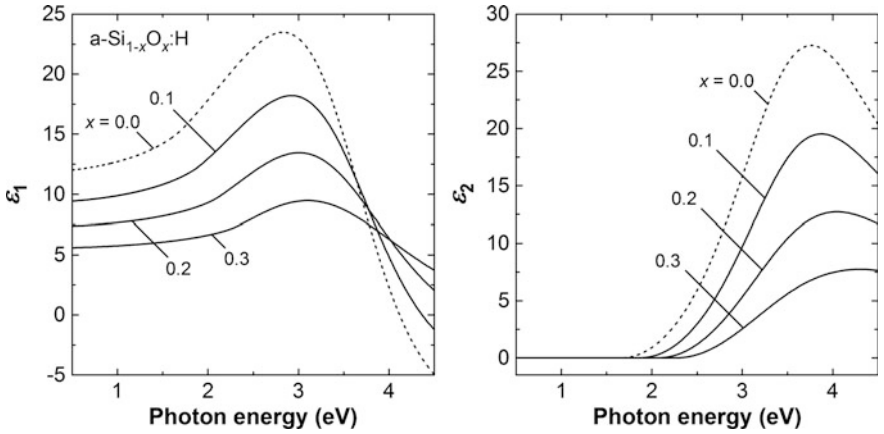


Fig. 8.10 Dielectric functions of a-$Si_{1-x}O_x$:H layers calculated from the Tauc-Lorentz parameters reported by Sato et al. The results for various a-$Si_{1-x}O_x$:H layers with different oxygen content x are shown

Table 8.29 Tauc-Lorentz parameters for the a-$Si_{1-x}O_x$:H dielectric functions in Fig. 8.10, reported by Sato et al.

Alloy content x	A (eV)	C (eV)	E_0 (eV)	E_g (eV)	$\varepsilon_1(\infty)$
$x = 0.0$	212.128	2.313	3.649	1.670	0.013
$x = 0.1$	190.950	2.435	3.691	1.873	0.708
$x = 0.2$	169.772	2.790	3.733	2.076	1.273
$x = 0.3$	148.594	3.376	3.746	2.280	1.479

Table 8.30 Optical constants of a-$Si_{1-x}O_x$:H ($x = 0.1$) calculated by the Tauc-Lorentz model

λ (nm)	n	k	λ (nm)	n	k	λ (nm)	n	k
300	3.298	2.839	540	3.893	0.170	880	3.254	0
305	3.410	2.796	550	3.852	0.139	890	3.248	0
310	3.518	2.745	560	3.811	0.112	900	3.243	0
315	3.621	2.687	570	3.773	0.089	910	3.238	0
320	3.720	2.623	580	3.735	0.069	920	3.233	0
325	3.812	2.553	590	3.699	0.052	930	3.229	0
330	3.899	2.477	600	3.664	0.038	940	3.224	0
335	3.979	2.398	610	3.631	0.026	950	3.220	0
340	4.051	2.314	620	3.600	0.016	960	3.216	0
345	4.117	2.228	630	3.570	0.009	970	3.212	0
350	4.175	2.140	640	3.542	0.004	980	3.208	0
355	4.226	2.051	650	3.516	0.001	990	3.204	0
360	4.270	1.961	660	3.492	0	1000	3.201	0
365	4.307	1.872	670	3.471	0	1010	3.197	0
370	4.338	1.783	680	3.452	0	1020	3.194	0
375	4.363	1.696	690	3.435	0	1030	3.191	0
380	4.383	1.610	700	3.419	0	1040	3.188	0
385	4.397	1.527	710	3.404	0	1050	3.185	0
390	4.406	1.446	720	3.391	0	1060	3.182	0
395	4.411	1.367	730	3.378	0	1070	3.179	0
400	4.412	1.292	740	3.366	0	1080	3.176	0
410	4.404	1.149	750	3.355	0	1090	3.174	0
420	4.386	1.018	760	3.344	0	1100	3.171	0
430	4.359	0.899	770	3.334	0	1110	3.169	0
440	4.325	0.792	780	3.325	0	1120	3.167	0
450	4.287	0.695	790	3.316	0	1130	3.164	0
460	4.246	0.607	800	3.308	0	1140	3.162	0
470	4.203	0.529	810	3.300	0	1150	3.160	0
480	4.158	0.458	820	3.292	0	1160	3.158	0
490	4.113	0.395	830	3.285	0	1170	3.156	0
500	4.068	0.339	840	3.278	0	1180	3.154	0
510	4.023	0.289	850	3.272	0	1190	3.152	0
520	3.979	0.244	860	3.265	0	1200	3.150	0
530	3.935	0.205	870	3.260	0			

Table 8.31 Optical constants of a-$Si_{1-x}O_x$:H ($x = 0.2$) calculated by the Tauc-Lorentz model

λ (nm)	n	k	λ (nm)	n	k	λ (nm)	n	k
300	3.057	2.072	540	3.277	0.049	880	2.841	0
305	3.135	2.028	550	3.241	0.033	890	2.837	0
310	3.209	1.979	560	3.206	0.020	900	2.834	0
315	3.279	1.926	570	3.174	0.010	910	2.830	0
320	3.345	1.870	580	3.143	0.004	920	2.827	0
325	3.406	1.810	590	3.115	0.001	930	2.824	0
330	3.461	1.748	600	3.090	0	940	2.821	0
335	3.512	1.684	610	3.069	0	950	2.818	0
340	3.558	1.618	620	3.050	0	960	2.815	0
345	3.598	1.550	630	3.034	0	970	2.813	0
350	3.634	1.483	640	3.018	0	980	2.810	0
355	3.664	1.415	650	3.004	0	990	2.808	0
360	3.690	1.347	660	2.991	0	1000	2.805	0
365	3.712	1.280	670	2.979	0	1010	2.803	0
370	3.729	1.214	680	2.968	0	1020	2.801	0
375	3.742	1.149	690	2.958	0	1030	2.798	0
380	3.751	1.086	700	2.948	0	1040	2.796	0
385	3.757	1.024	710	2.939	0	1050	2.794	0
390	3.759	0.965	720	2.930	0	1060	2.792	0
395	3.759	0.907	730	2.922	0	1070	2.790	0
400	3.756	0.851	740	2.914	0	1080	2.789	0
410	3.743	0.746	750	2.907	0	1090	2.787	0
420	3.722	0.649	760	2.901	0	1100	2.785	0
430	3.695	0.562	770	2.894	0	1110	2.783	0
440	3.664	0.482	780	2.888	0	1120	2.782	0
450	3.629	0.411	790	2.882	0	1130	2.780	0
460	3.591	0.347	800	2.877	0	1140	2.779	0
470	3.552	0.290	810	2.871	0	1150	2.777	0
480	3.512	0.239	820	2.866	0	1160	2.776	0
490	3.472	0.195	830	2.862	0	1170	2.774	0
500	3.432	0.156	840	2.857	0	1180	2.773	0
510	3.392	0.122	850	2.853	0	1190	2.772	0
520	3.352	0.094	860	2.849	0	1200	2.770	0
530	3.314	0.069	870	2.845	0			

Table 8.32 Optical constants of a-$Si_{1-x}O_x$:H ($x = 0.3$) calculated by the Tauc-Lorentz model

λ (nm)	n	k	λ (nm)	n	k	λ (nm)	n	k
300	2.742	1.396	540	2.697	0	880	2.445	0
305	2.790	1.357	550	2.674	0	890	2.442	0
310	2.834	1.316	560	2.654	0	900	2.440	0
315	2.876	1.274	570	2.637	0	910	2.438	0
320	2.914	1.230	580	2.621	0	920	2.436	0
325	2.949	1.184	590	2.608	0	930	2.434	0
330	2.981	1.138	600	2.595	0	940	2.432	0
335	3.010	1.090	610	2.584	0	950	2.430	0
340	3.035	1.042	620	2.573	0	960	2.428	0
345	3.057	0.994	630	2.564	0	970	2.427	0
350	3.076	0.946	640	2.555	0	980	2.425	0
355	3.092	0.898	650	2.546	0	990	2.423	0
360	3.105	0.851	660	2.539	0	1000	2.422	0
365	3.115	0.804	670	2.531	0	1010	2.420	0
370	3.122	0.758	680	2.524	0	1020	2.419	0
375	3.127	0.713	690	2.518	0	1030	2.417	0
380	3.130	0.669	700	2.512	0	1040	2.416	0
385	3.130	0.626	710	2.507	0	1050	2.415	0
390	3.128	0.585	720	2.501	0	1060	2.414	0
395	3.125	0.545	730	2.496	0	1070	2.412	0
400	3.119	0.506	740	2.491	0	1080	2.411	0
410	3.104	0.433	750	2.487	0	1090	2.410	0
420	3.083	0.365	760	2.483	0	1100	2.409	0
430	3.058	0.304	770	2.479	0	1110	2.408	0
440	3.029	0.250	780	2.475	0	1120	2.407	0
450	2.997	0.201	790	2.471	0	1130	2.406	0
460	2.964	0.158	800	2.468	0	1140	2.405	0
470	2.929	0.120	810	2.464	0	1150	2.404	0
480	2.894	0.089	820	2.461	0	1160	2.403	0
490	2.859	0.062	830	2.458	0	1170	2.402	0
500	2.824	0.040	840	2.455	0	1180	2.401	0
510	2.789	0.024	850	2.452	0	1190	2.400	0
520	2.756	0.012	860	2.450	0	1200	2.399	0
530	2.725	0.004	870	2.447	0			

8.2.11 μc-Si:H

Data from T. Yuguchi, Y. Kanie, N. Matsuki and H. Fujiwara [15]. The optical data have been extracted from microcrystalline Si (μc-Si:H) layers prepared by plasma-enhanced chemical vapor deposition at 190 °C using different SiH_4/H_2 gas flow ratios. The dielectric function of μc-Si:H is modeled by combining the Tauc-Lorentz model with the harmonic oscillator (HO) model $\left[\varepsilon_{HO}(E) = ACE_0/\left\{E_0^2 - E^2 + iCE + 0.25C^2\right\}\right]$. The variation of the model parameters with a film structure is further expressed by using a μc-Si:H structural factor κ. Depending on the μc-Si:H volume fraction, the κ value changes from zero (amorphous phase) to one (complete μc-Si:H phase). In this model, however, the optical properties in a weak absorption region ($\alpha < 10^3$ cm^{-1}) are not modeled accurately (Tables 8.33, 8.34, 8.35 and 8.36).

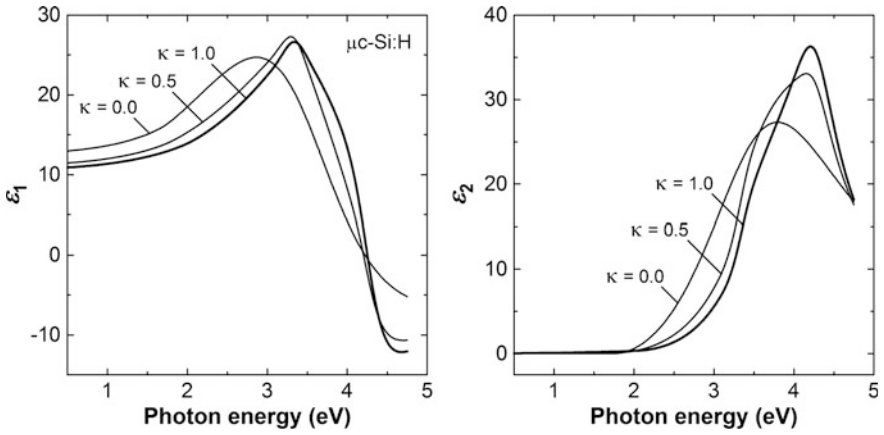


Fig. 8.11 Dielectric functions of a-Si:H (κ = 0) and μc-Si:H (κ > 0) calculated from the Tauc-Lorentz and harmonic oscillator models with the parameters reported by Yuguchi et al. The κ is a structural factor of μc-Si:H. The Tauc-Lorentz parameters of a-Si:H (κ = 0) are A = 224.9 eV, C = 2.321 eV, E_0 = 3.666 eV, E_g = 1.733 eV and $\varepsilon_1(\infty) = 1$

Table 8.33 Tauc-Lorentz (TL) and harmonic oscillator (HO) parameters for the μc-Si:H (κ = 0.5) dielectric function in Fig. 8.11, reported by Yuguchi et al.

Model	A (eV)	C (eV)	E_0 (eV)	E_g (eV)	$\varepsilon_1(\infty)$
TL peak1	137.065	1.659	3.875	1.766	1
TL peak2	202.831	0.493	3.360	3.052	0
HO peak	8.375	0.590	4.250	–	–

Table 8.34 Tauc-Lorentz (TL) and harmonic oscillator (HO) parameters for the μc-Si:H (κ = 1.0) dielectric function in Fig. 8.11, reported by Yuguchi et al.

Model	A (eV)	C (eV)	E_0 (eV)	E_g (eV)	$\varepsilon_1(\infty)$
TL peak1	135.1	1.629	3.875	2.033	1
TL peak2	203.9	0.476	3.360	3.096	0
HO peak	16.750	0.691	4.250	–	–

Table 8.35 Optical constants of μc-Si:H (κ = 0.5) calculated by the Tauc-Lorentz and harmonic oscillator models

λ (nm)	n	k	λ (nm)	n	k	λ (nm)	n	k
300	4.271	3.868	540	4.171	0.138	880	3.578	9.31×10^{-3}
305	4.429	3.690	550	4.131	0.120	890	3.573	9.17×10^{-3}
310	4.558	3.530	560	4.094	0.103	900	3.567	9.04×10^{-3}
315	4.673	3.384	570	4.059	8.86×10^{-2}	910	3.562	8.90×10^{-3}
320	4.780	3.244	580	4.026	7.58×10^{-2}	920	3.557	8.78×10^{-3}
325	4.880	3.106	590	3.995	6.46×10^{-2}	930	3.552	8.65×10^{-3}
330	4.974	2.969	600	3.966	5.48×10^{-2}	940	3.548	8.53×10^{-3}
335	5.062	2.831	610	3.938	4.63×10^{-2}	950	3.543	8.42×10^{-3}
340	5.143	2.692	620	3.911	3.90×10^{-2}	960	3.539	8.31×10^{-3}
345	5.220	2.552	630	3.886	3.27×10^{-2}	970	3.535	8.19×10^{-3}
350	5.293	2.406	640	3.862	2.75×10^{-2}	980	3.531	8.09×10^{-3}
355	5.362	2.251	650	3.840	2.32×10^{-2}	990	3.527	7.98×10^{-3}
360	5.420	2.081	660	3.819	1.97×10^{-2}	1000	3.523	7.89×10^{-3}
365	5.457	1.898	670	3.799	1.70×10^{-2}	1010	3.520	7.79×10^{-3}
370	5.465	1.709	680	3.780	1.50×10^{-2}	1020	3.516	7.69×10^{-3}
375	5.440	1.527	690	3.763	1.36×10^{-2}	1030	3.513	7.60×10^{-3}
380	5.389	1.364	700	3.746	1.29×10^{-2}	1040	3.510	7.51×10^{-3}
385	5.322	1.226	710	3.731	1.27×10^{-2}	1050	3.507	7.42×10^{-3}
390	5.250	1.113	720	3.718	1.24×10^{-2}	1060	3.503	7.33×10^{-3}
395	5.178	1.019	730	3.705	1.21×10^{-2}	1070	3.501	7.25×10^{-3}
400	5.111	0.942	740	3.693	1.19×10^{-2}	1080	3.498	7.17×10^{-3}
410	4.997	0.818	750	3.681	1.17×10^{-2}	1090	3.495	7.08×10^{-3}
420	4.902	0.713	760	3.671	1.14×10^{-2}	1100	3.492	7.01×10^{-3}
430	4.815	0.622	770	3.661	1.12×10^{-2}	1110	3.490	6.93×10^{-3}
440	4.735	0.542	780	3.651	1.10×10^{-2}	1120	3.487	6.86×10^{-3}
450	4.660	0.474	790	3.642	1.08×10^{-2}	1130	3.485	6.78×10^{-3}
460	4.590	0.414	800	3.634	1.06×10^{-2}	1140	3.482	6.71×10^{-3}
470	4.525	0.362	810	3.625	1.04×10^{-2}	1150	3.480	6.64×10^{-3}
480	4.464	0.317	820	3.618	1.03×10^{-2}	1160	3.478	6.57×10^{-3}
490	4.407	0.277	830	3.610	1.01×10^{-2}	1170	3.476	6.51×10^{-3}
500	4.354	0.242	840	3.603	9.92×10^{-3}	1180	3.474	6.44×10^{-3}
510	4.303	0.211	850	3.597	9.76×10^{-3}	1190	3.472	6.38×10^{-3}
520	4.256	0.184	860	3.590	9.61×10^{-3}	1200	3.470	6.31×10^{-3}
530	4.212	0.160	870	3.584	9.45×10^{-3}			

Table 8.36 Optical constants of μc-Si:H (κ = 1.0) calculated by the Tauc-Lorentz and harmonic oscillator models

λ (nm)	n	k	λ (nm)	n	k	λ (nm)	n	k
300	4.680	3.804	540	3.965	8.79×10^{-2}	880	3.471	2.62×10^{-2}
305	4.831	3.538	550	3.927	7.71×10^{-2}	890	3.466	2.58×10^{-2}
310	4.930	3.299	560	3.892	6.82×10^{-2}	900	3.461	2.54×10^{-2}
315	4.999	3.089	570	3.860	6.10×10^{-2}	910	3.457	2.51×10^{-2}
320	5.053	2.903	580	3.829	5.53×10^{-2}	920	3.453	2.47×10^{-2}
325	5.099	2.735	590	3.801	5.11×10^{-2}	930	3.449	2.43×10^{-2}
330	5.140	2.579	600	3.775	4.81×10^{-2}	940	3.445	2.40×10^{-2}
335	5.178	2.431	610	3.751	4.62×10^{-2}	950	3.441	2.37×10^{-2}
340	5.214	2.289	620	3.730	4.49×10^{-2}	960	3.437	2.34×10^{-2}
345	5.250	2.151	630	3.710	4.36×10^{-2}	970	3.434	2.30×10^{-2}
350	5.285	2.011	640	3.692	4.25×10^{-2}	980	3.430	2.27×10^{-2}
355	5.319	1.866	650	3.676	4.14×10^{-2}	990	3.427	2.24×10^{-2}
360	5.345	1.709	660	3.660	4.03×10^{-2}	1000	3.424	2.22×10^{-2}
365	5.355	1.541	670	3.645	3.93×10^{-2}	1010	3.421	2.19×10^{-2}
370	5.338	1.369	680	3.632	3.84×10^{-2}	1020	3.418	2.16×10^{-2}
375	5.292	1.206	690	3.619	3.75×10^{-2}	1030	3.415	2.13×10^{-2}
380	5.225	1.065	700	3.607	3.66×10^{-2}	1040	3.412	2.11×10^{-2}
385	5.146	0.948	710	3.596	3.58×10^{-2}	1050	3.409	2.08×10^{-2}
390	5.066	0.854	720	3.585	3.50×10^{-2}	1060	3.407	2.06×10^{-2}
395	4.990	0.779	730	3.575	3.43×10^{-2}	1070	3.404	2.04×10^{-2}
400	4.921	0.718	740	3.566	3.36×10^{-2}	1080	3.402	2.01×10^{-2}
410	4.807	0.615	750	3.556	3.29×10^{-2}	1090	3.399	1.99×10^{-2}
420	4.707	0.526	760	3.548	3.23×10^{-2}	1100	3.397	1.97×10^{-2}
430	4.615	0.451	770	3.540	3.17×10^{-2}	1110	3.395	1.95×10^{-2}
440	4.532	0.386	780	3.532	3.11×10^{-2}	1120	3.393	1.93×10^{-2}
450	4.454	0.332	790	3.525	3.05×10^{-2}	1130	3.391	1.90×10^{-2}
460	4.383	0.285	800	3.517	2.99×10^{-2}	1140	3.389	1.88×10^{-2}
470	4.316	0.245	810	3.511	2.94×10^{-2}	1150	3.387	1.86×10^{-2}
480	4.255	0.210	820	3.504	2.89×10^{-2}	1160	3.385	1.85×10^{-2}
490	4.197	0.181	830	3.498	2.84×10^{-2}	1170	3.383	1.83×10^{-2}
500	4.144	0.156	840	3.492	2.79×10^{-2}	1180	3.381	1.81×10^{-2}
510	4.094	0.135	850	3.486	2.75×10^{-2}	1190	3.379	1.79×10^{-2}
520	4.048	0.116	860	3.481	2.70×10^{-2}	1200	3.377	1.77×10^{-2}
530	4.005	0.101	870	3.476	2.66×10^{-2}			

8.2.12 AlAs

Data from C. M. Herzinger, H. Yao, P. G. Snyder, F. G. Celii, Y.-C. Kao, B. Johs and J. A. Woollam [16]. The optical data of an AlAs epitaxial layer formed on a GaAs substrate are shown (Fig. 8.12, Tables 8.37 and 8.38).

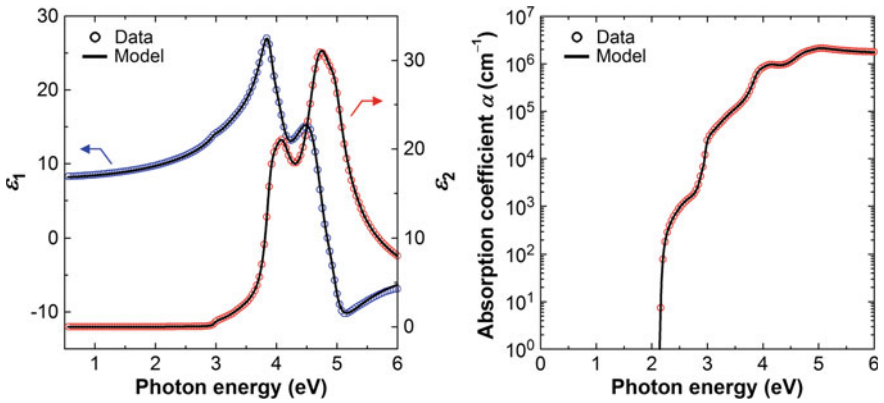


Fig. 8.12 Dielectric function and absorption coefficient of AlAs at room temperature. The open circles show the reference data and the solid lines indicate the calculation result obtained from the parameterization assuming the Tauc-Lorentz model [(8.1) and (8.2)]

Table 8.37 Tauc-Lorentz parameters of (8.1) and (8.2) for AlAs

Peak	A (eV)	C (eV)	E_0 (eV)	E_g (eV)	$\varepsilon_1(\infty)$
$j = 1$	0.599	0.177	2.152	2.151	0.378
$j = 2$	0.246	0.321	2.174	2.129	0
$j = 3$	2.871	2.198	2.179	2.178	0
$j = 4$	3.229	0.173	2.936	2.691	0
$j = 5$	135.050	0.160	2.953	2.925	0
$j = 6$	278.284	2.431	3.109	2.976	0
$j = 7$	181.787	0.242	3.893	3.492	0
$j = 8$	115.203	0.408	4.063	3.304	0
$j = 9$	165.705	0.619	4.703	3.351	0
$j = 10$	126.095	0.283	4.953	4.454	0

Table 8.38 Optical constants of AlAs. The optical data reported by Herzinger et al. are shown

λ (nm)	n	k	λ (nm)	n	k	λ (nm)	n	k
300	4.459	2.307	540	3.238	1.44×10^{-3}	880	2.978	0
305	4.714	2.228	550	3.220	9.69×10^{-4}	890	2.975	0
310	4.926	2.059	560	3.204	5.10×10^{-4}	900	2.972	0
315	5.157	1.836	570	3.188	1.22×10^{-4}	910	2.969	0
320	5.331	1.435	580	3.173	2.71×10^{-6}	920	2.967	0
325	5.265	0.986	590	3.160	0	930	2.964	0
330	5.046	0.687	600	3.148	0	940	2.962	0
335	4.829	0.532	610	3.136	0	950	2.959	0
340	4.658	0.446	620	3.125	0	960	2.957	0

(continued)

Table 8.38 (continued)

λ (nm)	n	k	λ (nm)	n	k	λ (nm)	n	k
345	4.523	0.388	630	3.115	0	970	2.955	0
350	4.412	0.344	640	3.105	0	980	2.953	0
355	4.319	0.310	650	3.096	0	990	2.951	0
360	4.240	0.281	660	3.088	0	1000	2.949	0
365	4.172	0.256	670	3.080	0	1010	2.947	0
370	4.113	0.232	680	3.072	0	1020	2.945	0
375	4.059	0.206	690	3.065	0	1030	2.943	0
380	4.005	0.183	700	3.058	0	1040	2.941	0
385	3.956	0.166	710	3.051	0	1050	2.940	0
390	3.912	0.150	720	3.045	0	1060	2.938	0
395	3.873	0.135	730	3.040	0	1070	2.937	0
400	3.837	0.121	740	3.034	0	1080	2.935	0
410	3.777	9.18×10^{-2}	750	3.029	0	1090	2.934	0
420	3.715	3.58×10^{-2}	760	3.024	0	1100	2.932	0
430	3.628	1.52×10^{-2}	770	3.019	0	1110	2.931	0
440	3.561	8.58×10^{-3}	780	3.014	0	1120	2.929	0
450	3.506	6.43×10^{-3}	790	3.010	0	1130	2.928	0
460	3.460	5.63×10^{-3}	800	3.006	0	1140	2.927	0
470	3.421	5.07×10^{-3}	810	3.002	0	1150	2.925	0
480	3.386	4.52×10^{-3}	820	2.998	0	1160	2.924	0
490	3.355	3.98×10^{-3}	830	2.994	0	1170	2.923	0
500	3.327	3.45×10^{-3}	840	2.990	0	1180	2.922	0
510	3.302	2.93×10^{-3}	850	2.987	0	1190	2.921	0
520	3.279	2.42×10^{-3}	860	2.984	0	1200	2.920	0
530	3.258	1.93×10^{-3}	870	2.981	0			

8.2.13 GaAs

To express the dielectric function of a GaAs single crystal, two separate data sets are used depending on the energy region:

(i) Data of G. E. Jellison, Jr. [1] for $E \geq 2.72$ eV,
(ii) Unpublished data of C. M. Herzinger [2] for $E < 2.72$ eV.

The result of [2] above was determined from a multiple data set analysis. The data sets include ellipsometry results [1, 2], transmittance results [17], and compiled values from a handbook edited by E. D. Palik [3] originally from ellipsometry results [18] and from prism and reflectance results [19]. The analysis procedure is described in the Ge section in this chapter (Fig. 8.13, Tables 8.39 and 8.40).

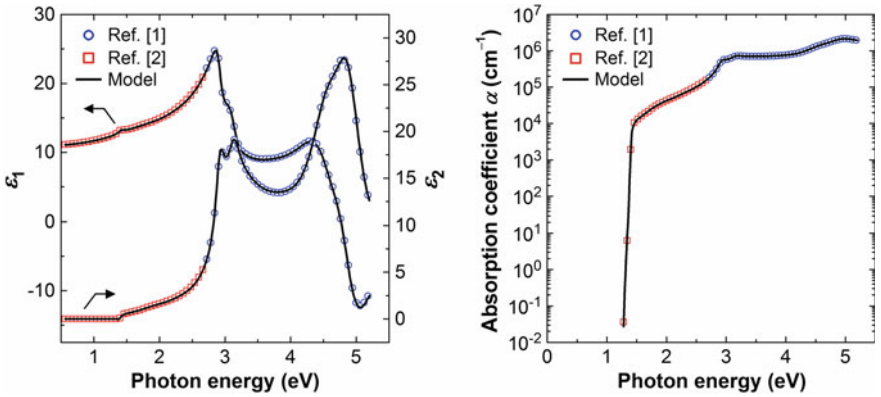


Fig. 8.13 Dielectric function and absorption coefficient of GaAs at room temperature. The open circles show the reference data and the solid lines indicate the calculation result obtained from the parameterization assuming the Tauc-Lorentz model [(8.1) and (8.2)]

Table 8.39 Tauc-Lorentz parameters of (8.1) and (8.2) for GaAs

Peak	A (eV)	C (eV)	E_0 (eV)	E_g (eV)	$\varepsilon_1(\infty)$
$j = 1$	8.732×10^{-3}	0.038	1.354	1.267	0.544
$j = 2$	39.387	0.108	1.405	1.394	0
$j = 3$	3.326	0.044	1.413	1.350	0
$j = 4$	13.956	1.054	1.744	1.360	0
$j = 5$	11.274	1.004	2.286	1.638	0
$j = 6$	38.219	0.170	2.917	2.382	0
$j = 7$	94.522	1.040	3.128	2.076	0
$j = 8$	4.161	0.229	3.134	1.561	0
$j = 9$	22.799	1.199	3.885	2.172	0
$j = 10$	18.058	0.662	4.549	1.422	0
$j = 11$	16.031	0.502	4.870	1.400	0
$j = 12$	967.771	0.599	5.084	5.103	0

Table 8.40 Optical constants of GaAs. The optical data, obtained by G. E. Jellison and C. M. Herzinger, are shown

λ (nm)	n	k	λ (nm)	n	k	λ (nm)	n	k
300	3.817	1.947	540	4.083	0.298	880	3.636	2.48×10^{-2}
305	3.735	1.908	550	4.044	0.282	890	3.619	7.53×10^{-3}
310	3.675	1.887	560	4.009	0.268	900	3.598	1.43×10^{-3}
315	3.633	1.876	570	3.978	0.256	910	3.582	2.67×10^{-4}
320	3.598	1.874	580	3.950	0.245	920	3.570	8.03×10^{-5}
325	3.579	1.879	590	3.924	0.235	930	3.559	2.89×10^{-5}
330	3.564	1.890	600	3.901	0.226	940	3.549	9.81×10^{-6}
335	3.564	1.901	610	3.880	0.217	950	3.541	3.02×10^{-6}

(continued)

Table 8.40 (continued)

λ (nm)	n	k	λ (nm)	n	k	λ (nm)	n	k
340	3.566	1.919	620	3.861	0.209	960	3.533	8.85×10^{-7}
345	3.576	1.939	630	3.843	0.201	970	3.526	2.35×10^{-7}
350	3.592	1.961	640	3.827	0.194	980	3.519	0
355	3.612	1.990	650	3.812	0.187	990	3.513	0
360	3.642	2.019	660	3.799	0.180	1000	3.507	0
365	3.682	2.050	670	3.787	0.173	1010	3.501	0
370	3.727	2.087	680	3.776	0.166	1020	3.496	0
375	3.786	2.125	690	3.766	0.157	1030	3.491	0
380	3.856	2.176	700	3.755	0.148	1040	3.486	0
385	3.962	2.232	710	3.743	0.139	1050	3.481	0
390	4.124	2.262	720	3.731	0.131	1060	3.477	0
395	4.323	2.209	730	3.719	0.125	1070	3.472	0
400	4.459	2.081	740	3.709	0.120	1080	3.468	0
410	4.557	1.902	750	3.699	0.115	1090	3.464	0
420	4.755	1.887	760	3.690	0.111	1100	3.461	0
430	5.152	1.438	770	3.682	0.106	1110	3.457	0
440	5.041	0.990	780	3.675	0.102	1120	3.453	0
450	4.858	0.755	790	3.668	9.72×10^{-2}	1130	3.450	0
460	4.688	0.631	800	3.661	9.28×10^{-2}	1140	3.447	0
470	4.557	0.541	810	3.655	8.84×10^{-2}	1150	3.444	0
480	4.452	0.480	820	3.650	8.40×10^{-2}	1160	3.441	0
490	4.367	0.434	830	3.645	7.97×10^{-2}	1170	3.438	0
500	4.294	0.396	840	3.642	7.53×10^{-2}	1180	3.435	0
510	4.232	0.365	850	3.640	7.09×10^{-2}	1190	3.432	0
520	4.176	0.339	860	3.642	6.39×10^{-2}	1200	3.429	0
530	4.127	0.317	870	3.646	4.84×10^{-2}			

8.2.14 InAs

Data: unpublished results of C. M. Herzinger. These InAs optical constants are the result of a multiple data set analysis [2]. The data sets included original ellipsometric measurements for a 1-μm epitaxial layer on GaAs (D. Chow, Hughes Research Lab, Malibu CA) [2], other ellipsometric results [4], and transmittance results [20] compiled in a handbook edited by E. D. Palik [3]. The analysis procedure is described in the Ge section in this chapter (Fig. 8.14, Tables 8.41 and 8.42).

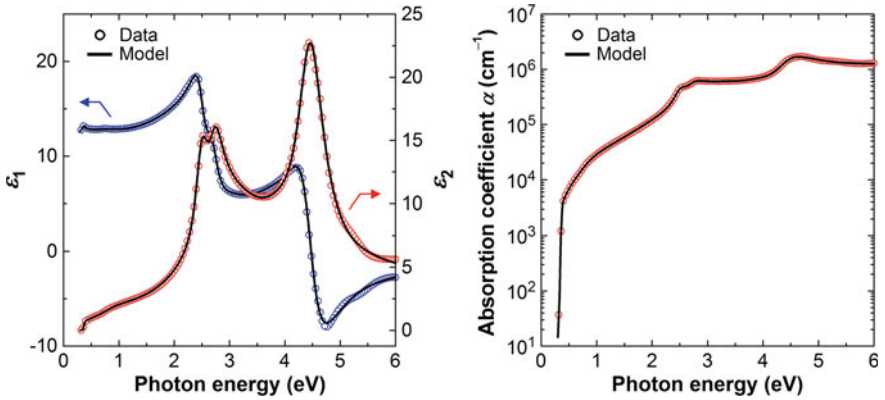


Fig. 8.14 Dielectric function and absorption coefficient of InAs at room temperature. The open circles show the reference data and the solid lines indicate the calculation result obtained from the parameterization assuming the Tauc-Lorentz model [(8.1) and (8.2)]

Table 8.41 Tauc-Lorentz parameters of (8.1) and (8.2) for InAs

Peak	A (eV)	C (eV)	E_0 (eV)	E_g (eV)	$\varepsilon_1(\infty)$
$j = 1$	0.002	0.050	0.329	0.169	0.336
$j = 2$	1.293	0.062	0.373	0.320	0
$j = 3$	2.175	0.079	0.392	0.359	0
$j = 4$	4.766	0.236	0.416	0.393	0
$j = 5$	3.647	1.030	0.623	0.622	0
$j = 6$	9.262	1.640	0.829	0.471	0
$j = 7$	18.212	0.293	2.497	1.630	0
$j = 8$	82.887	0.314	2.718	2.355	0
$j = 9$	34.752	2.500	3.144	0.720	0
$j = 10$	3.791	0.844	3.917	1.583	0
$j = 11$	250.267	4.091	4.256	4.150	0
$j = 12$	36.029	0.576	4.458	2.117	0

Table 8.42 Optical constants of InAs. The optical data obtained by C. M. Herzinger are shown

λ (nm)	n	k	λ (nm)	n	k	λ (nm)	n	k
300	3.530	1.959	680	3.845	0.498	1160	3.601	0.296
305	3.429	1.857	690	3.829	0.487	1170	3.600	0.294
310	3.342	1.790	700	3.814	0.476	1180	3.600	0.292
315	3.269	1.748	710	3.800	0.467	1190	3.599	0.291
320	3.208	1.724	720	3.787	0.457	1200	3.598	0.289
325	3.159	1.711	730	3.775	0.449	1220	3.597	0.285
330	3.120	1.706	740	3.763	0.441	1240	3.596	0.281
335	3.091	1.708	750	3.753	0.434	1260	3.595	0.278
340	3.068	1.713	760	3.743	0.427	1280	3.595	0.274
345	3.052	1.720	770	3.734	0.421	1300	3.594	0.271

(continued)

Table 8.42 (continued)

λ (nm)	n	k	λ (nm)	n	k	λ (nm)	n	k
350	3.041	1.730	780	3.725	0.414	1320	3.593	0.267
355	3.033	1.742	790	3.717	0.409	1340	3.593	0.264
360	3.029	1.756	800	3.709	0.403	1360	3.593	0.261
365	3.029	1.772	810	3.702	0.398	1380	3.593	0.258
370	3.031	1.789	820	3.695	0.393	1400	3.593	0.254
375	3.037	1.808	830	3.689	0.389	1420	3.593	0.251
380	3.046	1.830	840	3.683	0.384	1440	3.593	0.248
385	3.059	1.853	850	3.677	0.380	1460	3.593	0.245
390	3.075	1.877	860	3.672	0.376	1480	3.594	0.242
395	3.096	1.903	870	3.667	0.372	1500	3.594	0.239
400	3.120	1.929	880	3.662	0.369	1520	3.595	0.236
410	3.182	1.985	890	3.658	0.365	1540	3.596	0.233
420	3.262	2.045	900	3.653	0.362	1560	3.597	0.229
430	3.370	2.115	910	3.650	0.358	1580	3.598	0.225
440	3.553	2.176	920	3.646	0.355	1600	3.599	0.221
450	3.780	2.123	930	3.643	0.352	1650	3.599	0.210
460	3.921	1.990	940	3.639	0.349	1700	3.597	0.200
470	3.987	1.889	950	3.636	0.346	1750	3.593	0.192
480	4.056	1.848	960	3.633	0.343	1800	3.590	0.185
490	4.208	1.820	970	3.631	0.340	1850	3.588	0.180
500	4.419	1.666	980	3.628	0.338	1900	3.586	0.176
510	4.492	1.395	990	3.626	0.335	1950	3.585	0.171
520	4.448	1.186	1000	3.623	0.332	2000	3.585	0.167
530	4.385	1.045	1010	3.621	0.330	2100	3.584	0.159
540	4.322	0.940	1020	3.619	0.327	2200	3.584	0.152
550	4.262	0.859	1030	3.618	0.325	2300	3.585	0.145
560	4.206	0.795	1040	3.616	0.322	2400	3.586	0.139
570	4.155	0.744	1050	3.614	0.320	2500	3.587	0.133
580	4.109	0.702	1060	3.613	0.318	2600	3.588	0.127
590	4.068	0.668	1070	3.611	0.315	2700	3.591	0.122
600	4.032	0.640	1080	3.610	0.313	2800	3.593	0.117
610	4.000	0.615	1090	3.608	0.311	2900	3.598	0.112
620	3.971	0.593	1100	3.607	0.309	3000	3.604	0.107
630	3.945	0.574	1110	3.606	0.307	3200	3.624	8.71×10^{-2}
640	3.922	0.556	1120	3.605	0.305	3400	3.629	4.40×10^{-2}
650	3.900	0.539	1130	3.604	0.302	3650	3.597	6.00×10^{-3}
660	3.880	0.525	1140	3.603	0.300	3875	3.572	1.13×10^{-3}
670	3.862	0.511	1150	3.602	0.298	4130	3.556	4.78×10^{-4}

8.2.15 GaP

Data: unpublished results of C. M. Herzinger. The optical data of a GaP single crystal was determined from a multiple data set analysis [2]. The data sets came from values compiled in a handbook edited by E. D. Palik [3] originally from ellipsometry results [4], from prism results [21, 22], and from transmittance results [23]. The analysis procedure is described in the Ge section in this chapter (Fig. 8.15, Tables 8.43 and 8.44).

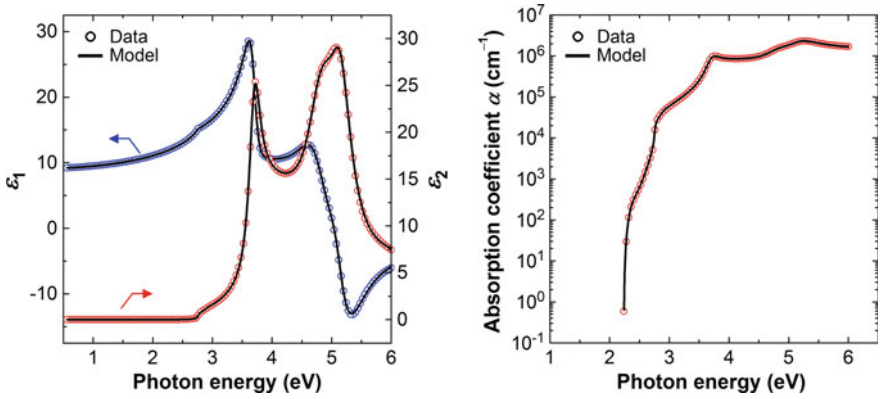


Fig. 8.15 Dielectric function and absorption coefficient of GaP at room temperature. The open circles show the reference data and the solid lines indicate the calculation result obtained from the parameterization assuming the Tauc-Lorentz model [(8.1) and (8.2)]

Table 8.43 Tauc-Lorentz parameters of (8.1) and (8.2) for GaP

Peak	A (eV)	C (eV)	E_0 (eV)	E_g (eV)	$\varepsilon_1(\infty)$
$j = 1$	1.456	0.545	2.238	2.234	0.337
$j = 2$	84.240	0.073	2.757	2.727	0
$j = 3$	6.679	0.340	2.893	2.425	0
$j = 4$	64.978	1.094	3.056	2.659	0
$j = 5$	151.903	0.233	3.696	3.117	0
$j = 6$	84.559	0.857	3.837	2.835	0
$j = 7$	33.264	0.994	4.257	2.801	0
$j = 8$	51.954	0.628	4.825	2.717	0
$j = 9$	34.165	0.440	5.143	2.900	0
$j = 10$	513.455	1.551	5.349	5.349	0

Table 8.44 Optical constants of GaP. The optical data, obtained by C. M. Herzinger, are shown

λ (nm)	n	k	λ (nm)	n	k	λ (nm)	n	k
300	3.846	2.049	540	3.469	2.63×10^{-4}	880	3.152	0
305	3.858	2.088	550	3.445	2.13×10^{-5}	890	3.149	0
310	3.892	2.142	560	3.424	0	900	3.146	0
315	3.952	2.214	570	3.405	0	910	3.142	0
320	4.048	2.317	580	3.387	0	920	3.139	0
325	4.237	2.478	590	3.371	0	930	3.136	0
330	4.671	2.604	600	3.355	0	940	3.134	0
335	5.272	2.352	610	3.341	0	950	3.131	0
340	5.555	1.736	620	3.328	0	960	3.128	0
345	5.460	1.200	630	3.315	0	970	3.126	0
350	5.247	0.881	640	3.304	0	980	3.123	0
355	5.052	0.699	650	3.293	0	990	3.121	0
360	4.892	0.579	660	3.283	0	1000	3.119	0
365	4.759	0.492	670	3.273	0	1010	3.116	0
370	4.645	0.426	680	3.264	0	1020	3.114	0
375	4.545	0.375	690	3.255	0	1030	3.112	0
380	4.457	0.335	700	3.247	0	1040	3.110	0
385	4.380	0.303	710	3.240	0	1050	3.108	0
390	4.312	0.277	720	3.232	0	1060	3.106	0
395	4.253	0.255	730	3.225	0	1070	3.104	0
400	4.200	0.236	740	3.219	0	1080	3.103	0
410	4.111	0.202	750	3.212	0	1090	3.101	0
420	4.039	0.172	760	3.206	0	1100	3.099	0
430	3.981	0.142	770	3.201	0	1110	3.098	0
440	3.931	0.108	780	3.195	0	1120	3.096	0
450	3.889	5.01×10^{-2}	790	3.190	0	1130	3.095	0
460	3.794	1.40×10^{-2}	800	3.185	0	1140	3.093	0
470	3.727	7.95×10^{-3}	810	3.180	0	1150	3.092	0
480	3.673	4.78×10^{-3}	820	3.176	0	1160	3.090	0
490	3.627	3.07×10^{-3}	830	3.172	0	1170	3.089	0
500	3.587	2.14×10^{-3}	840	3.167	0	1180	3.087	0
510	3.553	1.56×10^{-3}	850	3.163	0	1190	3.086	0
520	3.522	1.10×10^{-3}	860	3.159	0	1200	3.085	0
530	3.494	6.75×10^{-4}	870	3.156	0			

8.2.16 InP

Data from C. M. Herzinger, P. G. Snyder, B. Johs and J. A. Woollam [24]. The optical data of a single InP crystal are shown (Fig. 8.16, Tables 8.45 and 8.46).

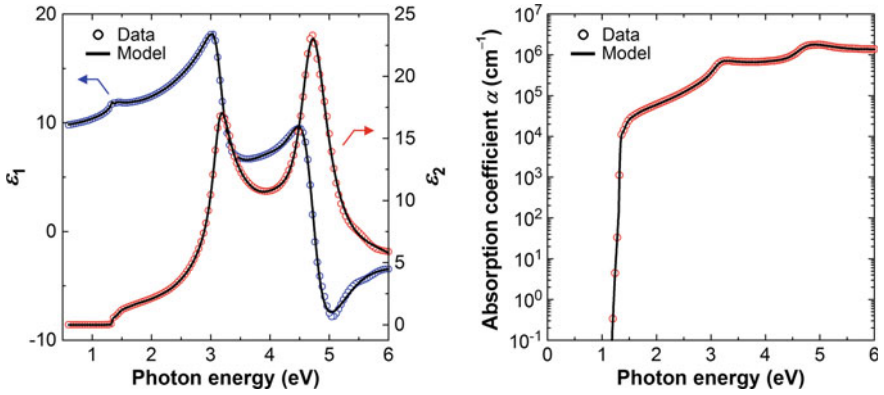


Fig. 8.16 Dielectric function and absorption coefficient of InP at room temperature. The open circles show the reference data and the solid lines indicate the calculation result obtained from the parameterization assuming the Tauc-Lorentz model [(8.1) and (8.2)]

Table 8.45 Tauc-Lorentz parameters of (8.1) and (8.2) for InP

Peak	A (eV)	C (eV)	E_0 (eV)	E_g (eV)	$\varepsilon_1(\infty)$
$j = 1$	0.058	0.078	1.318	1.200	1.355
$j = 2$	25.819	0.062	1.339	1.304	0
$j = 3$	0.011	0.549	1.342	1.161	0
$j = 4$	22.949	0.274	1.407	1.326	0
$j = 5$	7.629	0.654	1.749	1.279	0
$j = 6$	14.442	0.834	1.989	1.740	0
$j = 7$	84.556	0.349	3.143	2.574	0
$j = 8$	48.192	1.588	3.249	1.622	0
$j = 9$	10.794	1.088	4.174	1.601	0
$j = 10$	114.471	0.571	4.707	3.320	0
$j = 11$	121.715	1.686	5.584	4.830	0

Table 8.46 Optical constants of InP. The optical data reported by Herzinger et al. are shown

λ (nm)	n	k	λ (nm)	n	k	λ (nm)	n	k
300	3.257	1.698	540	3.679	0.384	880	3.441	0.106
305	3.212	1.691	550	3.655	0.369	890	3.437	9.67×10^{-2}
310	3.180	1.693	560	3.633	0.356	900	3.434	8.97×10^{-2}
315	3.157	1.699	570	3.613	0.344	910	3.437	8.22×10^{-2}
320	3.143	1.711	580	3.595	0.333	920	3.442	6.38×10^{-2}
325	3.135	1.727	590	3.578	0.324	930	3.434	3.09×10^{-2}
330	3.133	1.748	600	3.563	0.315	940	3.413	7.52×10^{-3}
335	3.138	1.774	610	3.550	0.306	950	3.389	1.23×10^{-3}
340	3.151	1.805	620	3.538	0.298	960	3.370	4.37×10^{-4}
345	3.171	1.840	630	3.527	0.291	970	3.356	2.38×10^{-4}
350	3.200	1.879	640	3.517	0.284	980	3.344	1.30×10^{-4}
355	3.239	1.922	650	3.508	0.277	990	3.334	6.90×10^{-5}
360	3.288	1.970	660	3.499	0.270	1000	3.325	3.48×10^{-5}
365	3.350	2.028	670	3.492	0.264	1010	3.317	1.71×10^{-5}
370	3.444	2.100	680	3.485	0.258	1020	3.309	7.99×10^{-6}
375	3.595	2.157	690	3.479	0.252	1030	3.303	3.64×10^{-6}
380	3.775	2.157	700	3.473	0.246	1040	3.296	1.60×10^{-6}
385	3.950	2.115	710	3.468	0.240	1050	3.290	6.76×10^{-7}
390	4.135	2.042	720	3.464	0.234	1060	3.284	0
395	4.321	1.899	730	3.460	0.228	1070	3.279	0
400	4.446	1.686	740	3.456	0.223	1080	3.274	0
410	4.450	1.278	750	3.453	0.217	1090	3.269	0
420	4.343	1.032	760	3.451	0.212	1100	3.265	0
430	4.237	0.876	770	3.449	0.206	1110	3.260	0
440	4.144	0.769	780	3.447	0.200	1120	3.256	0
450	4.066	0.690	790	3.446	0.195	1130	3.252	0
460	4.000	0.628	800	3.446	0.189	1140	3.249	0
470	3.943	0.578	810	3.446	0.182	1150	3.245	0
480	3.893	0.535	820	3.447	0.175	1160	3.242	0
490	3.847	0.499	830	3.450	0.167	1170	3.238	0
500	3.807	0.469	840	3.451	0.156	1180	3.235	0
510	3.770	0.443	850	3.452	0.143	1190	3.232	0
520	3.736	0.420	860	3.451	0.130	1200	3.229	0
530	3.706	0.401	870	3.447	0.117			

8.2.17 AlSb

Data: unpublished results of C. M. Herzinger. These AlSb optical constants are the result of a multiple data set analysis [2]. The data sets came from values compiled in a handbook edited by E. D. Palik [3] originally from ellipsometry results [25] and another compilation [19]. The analysis procedure is described in the Ge section in this chapter (Fig. 8.17, Tables 8.47 and 8.48).

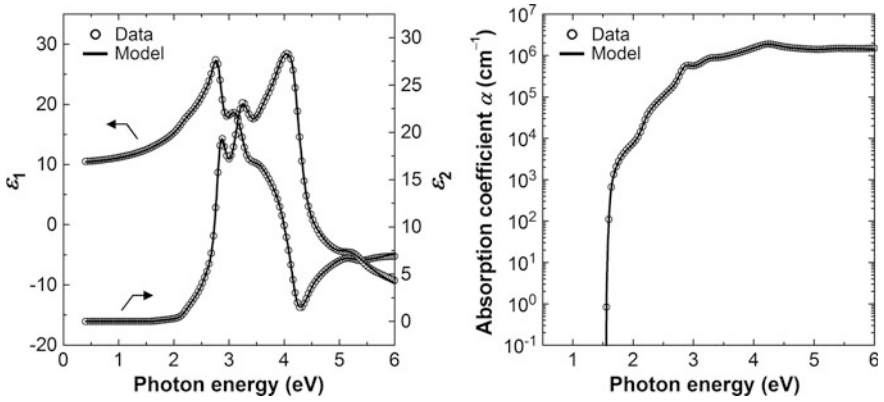


Fig. 8.17 Dielectric function and absorption coefficient of AlSb at room temperature. The open circles show the reference data and the solid lines indicate the calculation result obtained from the parameterization assuming the Tauc-Lorentz model [(8.1) and (8.2)]

Table 8.47 Tauc-Lorentz parameters of (8.1) and (8.2) for AlSb

Peak	A (eV)	C (eV)	E_0 (eV)	E_g (eV)	$\varepsilon_1(\infty)$
$j = 1$	2.833	0.289	1.628	1.584	0.921
$j = 2$	0.374	0.114	1.630	1.549	0
$j = 3$	2.848	0.651	1.851	1.562	0
$j = 4$	3.397	0.286	2.244	1.719	0
$j = 5$	39.236	0.500	2.370	2.071	0
$j = 6$	9.944	0.332	2.598	1.964	0
$j = 7$	170.565	0.259	2.829	2.435	0
$j = 8$	58.527	0.437	3.210	2.230	0
$j = 9$	47.559	0.818	3.681	1.918	0
$j = 10$	23.300	0.510	3.999	2.000	0
$j = 11$	10.187	0.324	4.166	2.000	0
$j = 12$	230.634	0.507	4.517	4.337	0
$j = 13$	84.958	0.766	5.127	4.466	0

Table 8.48 Optical constants of AlSb. The optical data, obtained by C. M. Herzinger, are shown

λ (nm)	n	k	λ (nm)	n	k	λ (nm)	n	k
300	3.236	4.236	540	4.311	0.213	880	3.485	0
305	3.543	3.997	550	4.259	0.177	890	3.478	0
310	3.740	3.756	560	4.211	0.140	900	3.471	0
315	3.867	3.539	570	4.155	0.101	910	3.464	0
320	3.951	3.350	580	4.094	7.45×10^{-2}	920	3.458	0
325	4.005	3.188	590	4.038	5.84×10^{-2}	930	3.452	0
330	4.042	3.054	600	3.989	4.85×10^{-2}	940	3.446	0
335	4.074	2.941	610	3.945	4.20×10^{-2}	950	3.441	0
340	4.102	2.841	620	3.906	3.76×10^{-2}	960	3.436	0
345	4.123	2.749	630	3.872	3.43×10^{-2}	970	3.430	0
350	4.132	2.671	640	3.842	3.15×10^{-2}	980	3.425	0
355	4.133	2.616	650	3.814	2.89×10^{-2}	990	3.421	0
360	4.138	2.589	660	3.789	2.64×10^{-2}	1000	3.416	0
365	4.163	2.590	670	3.765	2.39×10^{-2}	1010	3.412	0
370	4.225	2.608	680	3.744	2.14×10^{-2}	1020	3.407	0
375	4.339	2.617	690	3.724	1.90×10^{-2}	1030	3.403	0
380	4.492	2.576	700	3.705	1.66×10^{-2}	1040	3.399	0
385	4.640	2.465	710	3.687	1.42×10^{-2}	1050	3.395	0
390	4.737	2.305	720	3.670	1.19×10^{-2}	1060	3.392	0
395	4.770	2.141	730	3.654	9.66×10^{-3}	1070	3.388	0
400	4.756	2.004	740	3.639	7.44×10^{-3}	1080	3.385	0
410	4.671	1.859	750	3.624	5.26×10^{-3}	1090	3.381	0
420	4.659	1.899	760	3.610	3.16×10^{-3}	1100	3.378	0
430	4.937	1.951	770	3.596	1.40×10^{-3}	1110	3.375	0
440	5.319	1.619	780	3.582	3.77×10^{-4}	1120	3.372	0
450	5.338	1.090	790	3.570	5.01×10^{-5}	1130	3.369	0
460	5.118	0.763	800	3.558	2.61×10^{-6}	1140	3.366	0
470	4.921	0.616	810	3.547	0	1150	3.363	0
480	4.784	0.525	820	3.536	0	1160	3.361	0
490	4.676	0.451	830	3.527	0	1170	3.358	0
500	4.584	0.388	840	3.518	0	1180	3.356	0
510	4.503	0.335	850	3.509	0	1190	3.353	0
520	4.431	0.290	860	3.501	0	1200	3.351	0
530	4.368	0.250	870	3.493	0			

8.2.18 ZnS

Data from S. Adachi [26]. The optical data extracted from a zincblende ZnS crystal are shown (Fig. 8.18, Tables 8.49 and 8.50).

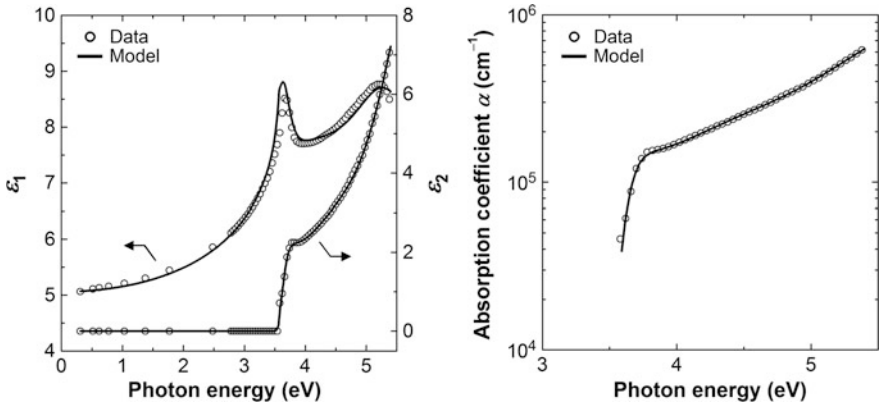


Fig. 8.18 Dielectric function and absorption coefficient of a zincblende ZnS crystal at room temperature. The open circles show the reference data and the solid lines indicate the calculation result obtained from the parameterization assuming the Tauc-Lorentz model [(8.1) and (8.2)]

Table 8.49 Tauc-Lorentz parameters of (8.1) and (8.2) for ZnS (zincblende)

Peak	A (eV)	C (eV)	E_0 (eV)	E_g (eV)	$\varepsilon_1(\infty)$
$j = 1$	536.939	0.030	3.560	3.560	2.044
$j = 2$	163.081	0.306	3.638	3.492	0
$j = 3$	124.994	2.128	3.789	3.532	0
$j = 4$	65.058	1.435	5.689	3.565	0
$j = 5$	16.558	0.028	5.820	4.054	0

Table 8.50 Optical constants of ZnS (zincblende) calculated by the Tauc-Lorentz model

λ (nm)	n	k	λ (nm)	n	k	λ (nm)	n	k
300	2.825	0.447	540	2.380	0	880	2.293	0
305	2.820	0.431	550	2.374	0	890	2.292	0
310	2.817	0.417	560	2.369	0	900	2.291	0
315	2.820	0.406	570	2.364	0	910	2.290	0
320	2.830	0.399	580	2.359	0	920	2.289	0
325	2.853	0.389	590	2.355	0	930	2.288	0
330	2.894	0.368	600	2.351	0	940	2.287	0
335	2.945	0.315	610	2.347	0	950	2.286	0
340	2.974	0.220	620	2.343	0	960	2.285	0

(continued)

Table 8.50 (continued)

λ (nm)	n	k	λ (nm)	n	k	λ (nm)	n	k
345	2.958	0.114	630	2.340	0	970	2.285	0
350	2.871	0.014	640	2.337	0	980	2.284	0
355	2.789	0	650	2.334	0	990	2.283	0
360	2.738	0	660	2.331	0	1000	2.282	0
365	2.700	0	670	2.328	0	1010	2.282	0
370	2.670	0	680	2.325	0	1020	2.281	0
375	2.645	0	690	2.323	0	1030	2.280	0
380	2.623	0	700	2.321	0	1040	2.280	0
385	2.604	0	710	2.318	0	1050	2.279	0
390	2.586	0	720	2.316	0	1060	2.279	0
395	2.571	0	730	2.314	0	1070	2.278	0
400	2.557	0	740	2.312	0	1080	2.278	0
410	2.532	0	750	2.310	0	1090	2.277	0
420	2.510	0	760	2.309	0	1100	2.276	0
430	2.492	0	770	2.307	0	1110	2.276	0
440	2.476	0	780	2.305	0	1120	2.276	0
450	2.461	0	790	2.304	0	1130	2.275	0
460	2.448	0	800	2.302	0	1140	2.275	0
470	2.437	0	810	2.301	0	1150	2.274	0
480	2.426	0	820	2.300	0	1160	2.274	0
490	2.417	0	830	2.298	0	1170	2.273	0
500	2.408	0	840	2.297	0	1180	2.273	0
510	2.400	0	850	2.296	0	1190	2.272	0
520	2.393	0	860	2.295	0	1200	2.272	0
530	2.386	0	870	2.294	0			

8.2.19 ZnSe

To express the dielectric function of a ZnSe zincblende crystal, two separate data sets are used depending on the energy region:

(i) Data of J. Lee, R. W. Collins, A. R. Heyd, F. Flack and N. Samarth [27] for $E \geq 1.5$ eV,
(ii) Data of D. T. F. Marple [28] for $E < 1.5$ eV.

The optical data have been extracted from an epitaxial ZnSe layer formed on a GaAs substrate [27] and a ZnSe crystal formed by sublimation [28] (Fig. 8.19, Tables 8.51 and 8.52).

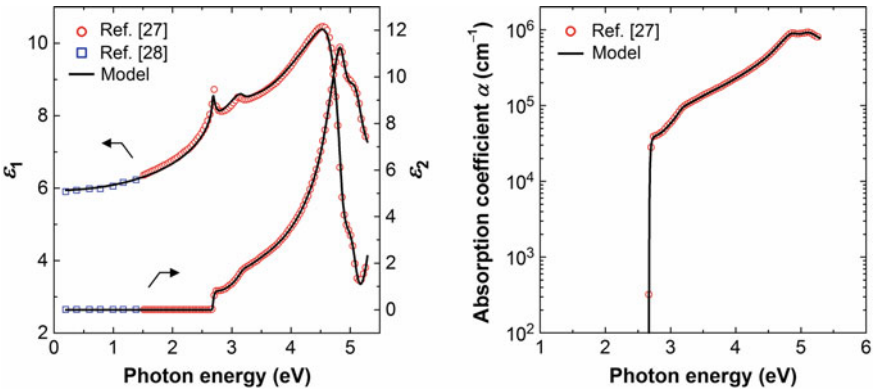


Fig. 8.19 Dielectric function and absorption coefficient of ZnSe at room temperature. The open circles show the reference data and the solid lines indicate the calculation result obtained from the parameterization assuming the Tauc-Lorentz model [(8.1) and (8.2)]

Table 8.51 Tauc-Lorentz parameters of (8.1) and (8.2) for ZnSe

Peak	A (eV)	C (eV)	E_0 (eV)	E_g (eV)	$\varepsilon_1(\infty)$
$j = 1$	447.567	0.051	2.672	2.667	2.473
$j = 2$	37.872	1.332	3.113	2.667	0
$j = 3$	1.492	0.211	3.181	2.667	0
$j = 4$	10.447	0.492	4.770	2.667	0
$j = 5$	1.016	0.171	4.833	2.667	0
$j = 6$	53.016	2.193	4.836	2.667	0
$j = 7$	3.281	0.273	5.086	3.081	0
$j = 8$	228.551	0.113	5.622	5.004	0

Table 8.52 Optical constants of ZnSe calculated by the Tauc-Lorentz model

λ (nm)	n	k	λ (nm)	n	k	λ (nm)	n	k
300	3.174	0.641	540	2.655	0	880	2.501	0
305	3.144	0.600	550	2.643	0	890	2.500	0
310	3.117	0.564	560	2.632	0	900	2.498	0
315	3.092	0.533	570	2.623	0	910	2.497	0
320	3.069	0.506	580	2.614	0	920	2.495	0
325	3.049	0.482	590	2.606	0	930	2.494	0
330	3.031	0.460	600	2.598	0	940	2.492	0
335	3.015	0.441	610	2.591	0	950	2.491	0

(continued)

Table 8.52 (continued)

λ (nm)	n	k	λ (nm)	n	k	λ (nm)	n	k
340	3.000	0.424	620	2.585	0	960	2.490	0
345	2.988	0.408	630	2.579	0	970	2.489	0
350	2.978	0.392	640	2.573	0	980	2.488	0
355	2.968	0.378	650	2.568	0	990	2.487	0
360	2.960	0.364	660	2.563	0	1000	2.485	0
365	2.953	0.350	670	2.558	0	1010	2.484	0
370	2.946	0.337	680	2.554	0	1020	2.483	0
375	2.941	0.326	690	2.550	0	1030	2.482	0
380	2.938	0.315	700	2.546	0	1040	2.482	0
385	2.939	0.304	710	2.542	0	1050	2.481	0
390	2.944	0.287	720	2.539	0	1060	2.480	0
395	2.944	0.262	730	2.536	0	1070	2.479	0
400	2.937	0.238	740	2.532	0	1080	2.478	0
410	2.914	0.201	750	2.529	0	1090	2.477	0
420	2.890	0.175	760	2.527	0	1100	2.476	0
430	2.870	0.157	770	2.524	0	1110	2.476	0
440	2.857	0.146	780	2.521	0	1120	2.475	0
450	2.863	0.140	790	2.519	0	1130	2.474	0
460	2.919	9.04×10^{-2}	800	2.517	0	1140	2.474	0
470	2.824	0	810	2.514	0	1150	2.473	0
480	2.776	0	820	2.512	0	1160	2.472	0
490	2.744	0	830	2.510	0	1170	2.472	0
500	2.720	0	840	2.508	0	1180	2.471	0
510	2.700	0	850	2.506	0	1190	2.470	0
520	2.683	0	860	2.505	0	1200	2.470	0
530	2.668	0	870	2.503	0			

8.2.20 ZnTe

Data from S. Adachi [26]. The optical data of a single ZnTe crystal are shown (Fig. 8.20, Tables 8.53 and 8.54).

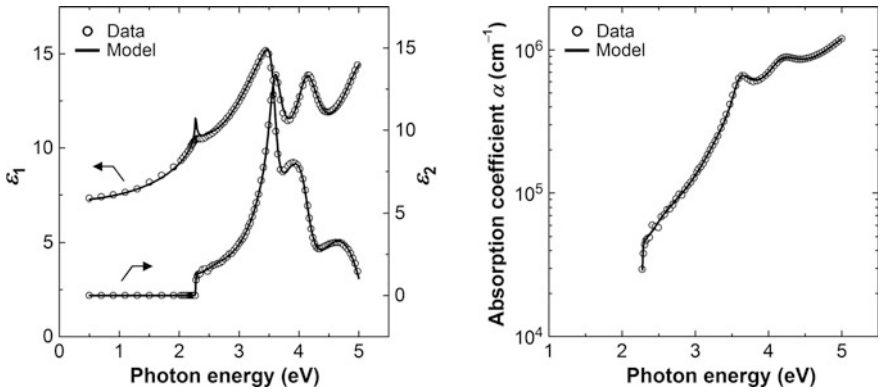


Fig. 8.20 Dielectric function and absorption coefficient of ZnTe at room temperature. The open circles show the reference data and the solid lines indicate the calculation result obtained from the parameterization assuming the Tauc-Lorentz model [(8.1) and (8.2)]

Table 8.53 Tauc-Lorentz parameters of (8.1) and (8.2) for ZnTe

Peak	A (eV)	C (eV)	E_0 (eV)	E_g (eV)	$\varepsilon_1(\infty)$
$j = 1$	1687.93	0.017	2.267	2.267	1.061
$j = 2$	81.164	1.094	2.267	2.267	0
$j = 3$	89.180	1.315	3.491	2.659	0
$j = 4$	11.054	0.257	3.584	2.267	0
$j = 5$	11.900	0.474	4.137	2.267	0
$j = 6$	56.504	1.419	5.172	2.430	0

Table 8.54 Optical constants of ZnTe calculated by the Tauc-Lorentz model

λ (nm)	n	k	λ (nm)	n	k	λ (nm)	n	k
300	3.331	1.998	540	3.335	0.189	880	2.819	0
305	3.435	1.862	550	3.291	0	890	2.815	0
310	3.461	1.726	560	3.204	0	900	2.812	0
315	3.437	1.632	570	3.156	0	910	2.808	0
320	3.400	1.588	580	3.120	0	920	2.805	0
325	3.372	1.592	590	3.091	0	930	2.802	0
330	3.375	1.642	600	3.067	0	940	2.799	0
335	3.446	1.728	610	3.045	0	950	2.796	0
340	3.632	1.792	620	3.026	0	960	2.794	0
345	3.896	1.709	630	3.009	0	970	2.791	0
350	4.064	1.470	640	2.994	0	980	2.788	0
355	4.085	1.227	650	2.980	0	990	2.786	0
360	4.039	1.049	660	2.967	0	1000	2.784	0
365	3.979	0.924	670	2.955	0	1010	2.781	0
370	3.921	0.829	680	2.944	0	1020	2.779	0

(continued)

Table 8.54 (continued)

λ (nm)	n	k	λ (nm)	n	k	λ (nm)	n	k
375	3.869	0.754	690	2.933	0	1030	2.777	0
380	3.821	0.691	700	2.924	0	1040	2.775	0
385	3.776	0.636	710	2.915	0	1050	2.773	0
390	3.734	0.589	720	2.906	0	1060	2.771	0
395	3.694	0.547	730	2.898	0	1070	2.769	0
400	3.656	0.511	740	2.891	0	1080	2.767	0
410	3.586	0.453	750	2.884	0	1090	2.766	0
420	3.524	0.408	760	2.877	0	1100	2.764	0
430	3.471	0.375	770	2.871	0	1110	2.762	0
440	3.426	0.349	780	2.865	0	1120	2.761	0
450	3.389	0.328	790	2.859	0	1130	2.759	0
460	3.359	0.311	800	2.854	0	1140	2.758	0
470	3.336	0.295	810	2.849	0	1150	2.756	0
480	3.318	0.279	820	2.844	0	1160	2.755	0
490	3.303	0.262	830	2.839	0	1170	2.753	0
500	3.289	0.245	840	2.835	0	1180	2.752	0
510	3.279	0.229	850	2.830	0	1190	2.751	0
520	3.273	0.217	860	2.826	0	1200	2.750	0
530	3.281	0.207	870	2.822	0			

8.2.21 CdS

Data from J. Li, J. Chen and R. W. Collins [29]. The optical data of a polycrystalline CdS layer prepared by sputtering at 310 °C are shown (Fig. 8.21, Tables 8.55 and 8.56).

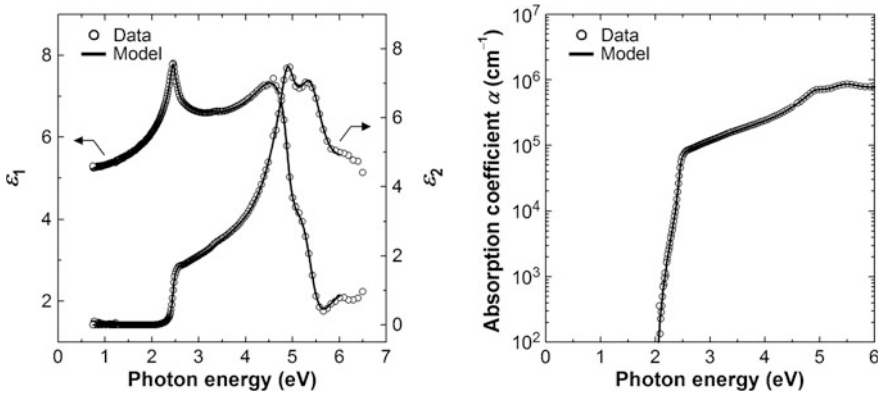


Fig. 8.21 Dielectric function and absorption coefficient of CdS at room temperature. The open circles show the reference data and the solid lines indicate the calculation result obtained from the parameterization assuming the Tauc-Lorentz model [(8.1) and (8.2)]

Table 8.55 Tauc-Lorentz parameters of (8.1) and (8.2) for CdS

Peak	A (eV)	C (eV)	E_0 (eV)	E_g (eV)	$\varepsilon_1(\infty)$
$j = 1$	28.655	0.124	2.463	2.342	0.968
$j = 2$	7.388	0.307	2.583	1.985	0
$j = 3$	147.591	0.440	2.588	2.585	0
$j = 4$	162.769	5.572	2.980	2.775	0
$j = 5$	0.093	0.200	3.395	2.397	0
$j = 6$	28.082	1.044	4.772	3.404	0
$j = 7$	2.059	0.349	4.888	2.408	0
$j = 8$	16.217	0.638	5.366	3.789	0
$j = 9$	251.674	1.963	5.781	5.601	0

Table 8.56 Optical constants of CdS calculated by the Tauc-Lorentz model

λ (nm)	n	k	λ (nm)	n	k	λ (nm)	n	k
300	2.718	0.630	540	2.622	1.92×10^{-2}	880	2.349	0
305	2.701	0.607	550	2.591	1.21×10^{-2}	890	2.347	0
310	2.686	0.587	560	2.566	7.52×10^{-3}	900	2.345	0
315	2.673	0.570	570	2.544	4.54×10^{-3}	910	2.343	0
320	2.662	0.554	580	2.526	2.61×10^{-3}	920	2.341	0
325	2.652	0.540	590	2.509	1.37×10^{-3}	930	2.340	0
330	2.644	0.527	600	2.495	6.10×10^{-4}	940	2.338	0
335	2.637	0.514	610	2.482	1.92×10^{-4}	950	2.336	0
340	2.631	0.503	620	2.471	0	960	2.335	0
345	2.625	0.492	630	2.461	0	970	2.333	0
350	2.620	0.483	640	2.452	0	980	2.332	0
355	2.616	0.474	650	2.443	0	990	2.330	0
360	2.614	0.466	660	2.436	0	1000	2.329	0
365	2.614	0.458	670	2.429	0	1010	2.328	0
370	2.614	0.447	680	2.422	0	1020	2.326	0
375	2.612	0.437	690	2.416	0	1030	2.325	0
380	2.609	0.427	700	2.411	0	1040	2.324	0
385	2.607	0.419	710	2.405	0	1050	2.323	0
390	2.605	0.412	720	2.400	0	1060	2.322	0
395	2.603	0.405	730	2.396	0	1070	2.321	0
400	2.602	0.399	740	2.391	0	1080	2.320	0
410	2.602	0.388	750	2.387	0	1090	2.319	0
420	2.605	0.378	760	2.383	0	1100	2.318	0
430	2.610	0.367	770	2.380	0	1110	2.317	0
440	2.617	0.356	780	2.376	0	1120	2.316	0
450	2.626	0.345	790	2.373	0	1130	2.315	0

(continued)

Table 8.56 (continued)

λ (nm)	n	k	λ (nm)	n	k	λ (nm)	n	k
460	2.635	0.334	800	2.370	0	1140	2.314	0
470	2.650	0.327	810	2.367	0	1150	2.313	0
480	2.677	0.319	820	2.364	0	1160	2.312	0
490	2.720	0.294	830	2.361	0	1170	2.312	0
500	2.776	0.241	840	2.359	0	1180	2.311	0
510	2.781	0.120	850	2.356	0	1190	2.310	0
520	2.714	5.30×10^{-2}	860	2.354	0	1200	2.309	0
530	2.660	3.02×10^{-2}	870	2.351	0			

8.2.22 CdSe

Data from S. Adachi [26]. The optical data of a wurtzite CdSe single crystal are shown. The wurtzite CdSe crystal has uniaxial optical anisotropy, but the optical properties are almost isotropic at $E < 4$ eV. Here, the optical constants for the electric field perpendicular to the c axis ($E \perp c$: ordinary ray) are indicated. The optical constants of the cubic CdSe phase are quite similar to those of the wurtzite phase described here (Fig. 8.22, Tables 8.57 and 8.58).

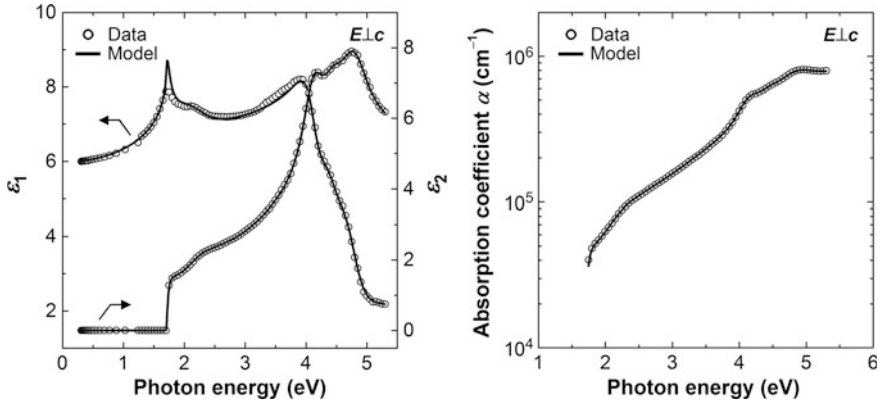


Fig. 8.22 Dielectric function and absorption coefficient of CdSe (wurtzite) at room temperature. The optical data for ordinary ray ($E \perp c$) in CdSe are shown. The open circles show the reference data and the solid lines indicate the calculation result obtained from the parameterization assuming the Tauc-Lorentz model [(8.1) and (8.2)]

Table 8.57 Tauc-Lorentz parameters for the ordinary ray in CdSe (wurtzite)

Peak	A (eV)	C (eV)	E_0 (eV)	E_g (eV)	$\varepsilon_1(\infty)$
$j = 1$	324.484	0.063	1.700	1.700	0.376
$j = 2$	22.872	1.364	2.160	1.706	0
$j = 3$	15.818	4.567	2.285	1.700	0
$j = 4$	2.913	0.438	4.119	1.700	0
$j = 5$	4.050	0.454	4.434	2.874	0
$j = 6$	3.212	0.608	4.789	1.700	0
$j = 7$	137.812	9.534	5.539	2.391	0

Table 8.58 Optical constants for the ordinary ray in CdSe (wurtzite) calculated by the Tauc-Lorentz model

λ (nm)	n	k	λ (nm)	n	k	λ (nm)	n	k
300	2.919	1.240	540	2.735	0.401	880	2.618	0
305	2.990	1.147	550	2.742	0.390	890	2.612	0
310	3.016	1.036	560	2.747	0.378	900	2.606	0
315	3.006	0.940	570	2.752	0.366	910	2.601	0
320	2.980	0.866	580	2.756	0.353	920	2.596	0
325	2.952	0.812	590	2.760	0.341	930	2.592	0
330	2.925	0.770	600	2.762	0.330	940	2.588	0
335	2.901	0.737	610	2.765	0.319	950	2.583	0
340	2.880	0.710	620	2.767	0.309	960	2.580	0
345	2.862	0.686	630	2.770	0.301	970	2.576	0
350	2.847	0.666	640	2.774	0.294	980	2.572	0
355	2.833	0.648	650	2.780	0.287	990	2.569	0
360	2.821	0.631	660	2.788	0.282	1000	2.566	0
365	2.810	0.616	670	2.800	0.276	1010	2.563	0
370	2.800	0.601	680	2.817	0.269	1020	2.560	0
375	2.791	0.588	690	2.842	0.259	1030	2.557	0
380	2.782	0.576	700	2.877	0.240	1040	2.554	0
385	2.774	0.565	710	2.923	0.196	1050	2.552	0
390	2.767	0.554	720	2.954	9.51×10^{-2}	1060	2.549	0
395	2.761	0.544	730	2.866	0	1070	2.547	0
400	2.755	0.535	740	2.807	0	1080	2.544	0
410	2.744	0.518	750	2.773	0	1090	2.542	0
420	2.734	0.504	760	2.748	0	1100	2.540	0
430	2.727	0.491	770	2.728	0	1110	2.538	0

(continued)

Table 8.58 (continued)

λ (nm)	n	k	λ (nm)	n	k	λ (nm)	n	k
440	2.720	0.480	780	2.711	0	1120	2.536	0
450	2.716	0.470	790	2.697	0	1130	2.534	0
460	2.713	0.462	800	2.684	0	1140	2.532	0
470	2.711	0.454	810	2.673	0	1150	2.530	0
480	2.711	0.446	820	2.663	0	1160	2.529	0
490	2.712	0.439	830	2.654	0	1170	2.527	0
500	2.714	0.432	840	2.645	0	1180	2.525	0
510	2.717	0.425	850	2.638	0	1190	2.524	0
520	2.722	0.418	860	2.630	0	1200	2.522	0
530	2.728	0.410	870	2.624	0			

8.2.23 CdTe

Data: unpublished results of J. Li and R. W. Collins. The optical data of a polycrystalline CdTe layer processed with post $CdCl_2$/annealing treatments are shown (see also Chap. 13 in Vol. 1) (Fig. 8.23, Tables 8.59 and 8.60).

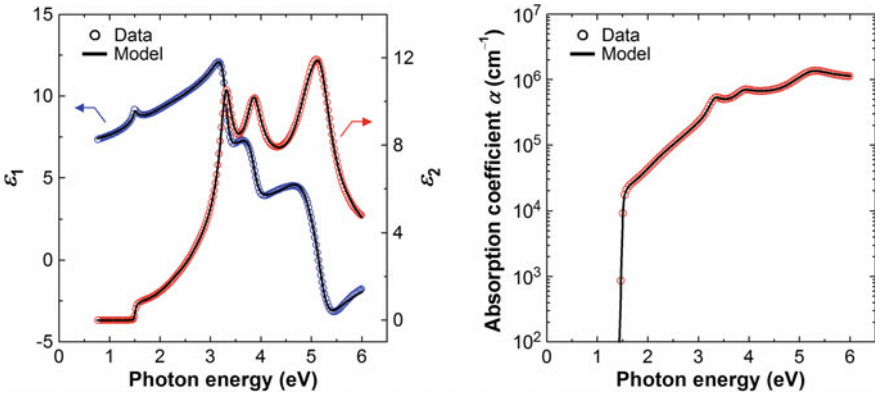


Fig. 8.23 Dielectric function and absorption coefficient of CdTe at room temperature. The open circles show the reference data and the solid lines indicate the calculation result obtained from the parameterization assuming the Tauc-Lorentz model [(8.1) and (8.2)]

Table 8.59 Tauc-Lorentz parameters of (8.1) and (8.2) for CdTe

Peak	A (eV)	C (eV)	E_0 (eV)	E_g (eV)	$\varepsilon_1(\infty)$
$j = 1$	0.396×10^{-3}	0.039	1.379	1.262	1.329
$j = 2$	19.762	0.479	1.479	1.458	0
$j = 3$	0.681	0.036	1.489	1.369	0
$j = 4$	93.077	0.060	1.489	1.483	0
$j = 5$	4.023	0.276	3.301	1.481	0
$j = 6$	85.342	5.904	3.432	1.671	0
$j = 7$	41.876	1.791	3.506	2.382	0
$j = 8$	2.648	0.352	3.858	1.604	0
$j = 9$	6.673	0.715	4.962	1.795	0
$j = 10$	5.554	0.480	5.181	2.224	0

Table 8.60 Optical constants of CdTe. The optical data obtained by J. Li and R. W. Collins are shown

λ (nm)	n	k	λ (nm)	n	k	λ (nm)	n	k
300	2.560	1.611	540	3.144	0.314	880	2.915	1.25×10^{-4}
305	2.586	1.667	550	3.129	0.297	890	2.902	4.17×10^{-5}
310	2.652	1.732	560	3.115	0.282	900	2.892	1.55×10^{-5}
315	2.770	1.773	570	3.102	0.269	910	2.882	5.67×10^{-6}
320	2.911	1.746	580	3.090	0.256	920	2.874	2.08×10^{-6}
325	3.010	1.659	590	3.078	0.244	930	2.866	6.87×10^{-7}
330	3.055	1.566	600	3.067	0.233	940	2.859	3.16×10^{-7}
335	3.066	1.490	610	3.056	0.224	950	2.852	1.15×10^{-7}
340	3.060	1.437	620	3.046	0.215	960	2.846	0
345	3.045	1.407	630	3.036	0.206	970	2.841	0
350	3.030	1.403	640	3.028	0.199	980	2.836	0
355	3.025	1.427	650	3.019	0.192	990	2.831	0
360	3.049	1.479	660	3.012	0.186	1000	2.826	0
365	3.126	1.544	670	3.005	0.180	1010	2.821	0
370	3.270	1.577	680	2.998	0.175	1020	2.817	0
375	3.447	1.523	690	2.993	0.170	1030	2.813	0
380	3.581	1.385	700	2.988	0.166	1040	2.809	0
385	3.637	1.221	710	2.984	0.162	1050	2.806	0
390	3.636	1.077	720	2.981	0.159	1060	2.802	0
395	3.607	0.967	730	2.979	0.156	1070	2.799	0
400	3.570	0.883	740	2.978	0.152	1080	2.796	0
410	3.498	0.768	750	2.979	0.148	1090	2.793	0
420	3.440	0.691	760	2.980	0.144	1100	2.790	0
430	3.394	0.632	770	2.983	0.140	1110	2.787	0

(continued)

Table 8.60 (continued)

λ (nm)	n	k	λ (nm)	n	k	λ (nm)	n	k
440	3.357	0.584	780	2.988	0.134	1120	2.784	0
450	3.325	0.543	790	2.994	0.127	1130	2.782	0
460	3.297	0.507	800	3.003	0.117	1140	2.779	0
470	3.272	0.474	810	3.015	0.103	1150	2.777	0
480	3.250	0.445	820	3.029	7.73×10^{-2}	1160	2.774	0
490	3.229	0.418	830	3.030	3.50×10^{-2}	1170	2.772	0
500	3.210	0.394	840	3.003	1.10×10^{-2}	1180	2.770	0
510	3.192	0.371	850	2.972	3.52×10^{-3}	1190	2.768	0
520	3.175	0.350	860	2.948	1.08×10^{-3}	1200	2.766	0
530	3.159	0.331	870	2.930	3.76×10^{-4}			

8.2.24 $CuInSe_2$

Data from S. Minoura, T. Maekawa, K. Kodera, A. Nakane, S. Niki and H. Fujiwara [30] (see also Fig. 10.7a in Vol. 1). The optical data of a chalcopyrite $CuInSe_2$ polycrystal (Cu/In = 0.86) prepared by a single co-evaporation process at 520 °C are shown. Although a $CuInSe_2$ single crystal exhibits notable uniaxial anisotropy at $E > 2.5$ eV, the optical properties are isotropic in $CuInSe_2$ polycrystals.

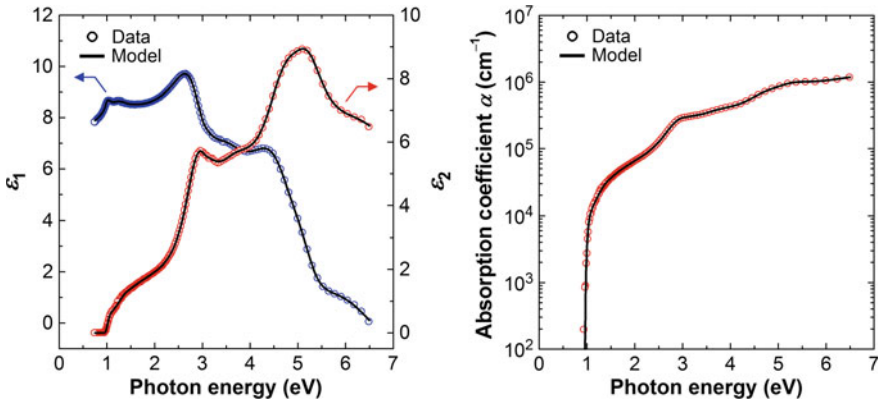


Fig. 8.24 Dielectric function and absorption coefficient of $CuInSe_2$ (chalcopyrite) at room temperature. The open circles show the reference data and the solid lines indicate the calculation result obtained from the parameterization assuming the Tauc-Lorentz model [(8.1) and (8.2)]

Table 8.61 Tauc-Lorentz parameters of (8.1) and (8.2) for $CuInSe_2$ (chalcopyrite). The model parameters reported by Minoura et al. are summarized

Peak	A (eV)	C (eV)	E_0 (eV)	E_g (eV)	$\varepsilon_1(\infty)$
$j = 1$	12.255	0.175	0.996	0.947	1.342
$j = 2$	14.580	1.087	1.281	1.001	0
$j = 3$	21.014	2.446	1.860	1.438	0
$j = 4$	13.185	0.802	2.909	1.485	0
$j = 5$	58.905	0.425	3.050	3.017	0
$j = 6$	35.077	1.332	3.599	2.593	0
$j = 7$	12.440	1.129	4.709	2.013	0
$j = 8$	7.692	0.928	5.216	2.324	0
$j = 9$	54.873	3.381	6.399	2.948	0

Table 8.62 Optical constants of $CuInSe_2$ calculated by the Tauc-Lorentz model

λ (nm)	n	k	λ (nm)	n	k	λ (nm)	n	k
300	2.812	1.082	560	3.017	0.368	920	2.939	0.200
305	2.799	1.065	570	3.005	0.358	930	2.940	0.195
310	2.791	1.053	580	2.995	0.350	940	2.941	0.190
315	2.787	1.044	590	2.985	0.342	950	2.941	0.185
320	2.787	1.036	600	2.977	0.335	960	2.942	0.180
325	2.790	1.029	610	2.970	0.329	970	2.942	0.175
330	2.796	1.020	620	2.964	0.324	980	2.942	0.170
335	2.803	1.011	630	2.959	0.318	990	2.942	0.165
340	2.811	1.000	640	2.954	0.313	1000	2.942	0.160
345	2.817	0.989	650	2.950	0.308	1010	2.941	0.155
350	2.822	0.977	660	2.946	0.304	1020	2.941	0.150
355	2.826	0.967	670	2.943	0.299	1030	2.940	0.146
360	2.829	0.959	680	2.941	0.295	1040	2.939	0.142
365	2.832	0.953	690	2.938	0.291	1050	2.938	0.138
370	2.836	0.950	700	2.937	0.286	1060	2.938	0.134
375	2.841	0.949	710	2.935	0.282	1070	2.937	0.130
380	2.849	0.949	720	2.933	0.278	1080	2.937	0.126
385	2.860	0.951	730	2.932	0.274	1090	2.936	0.123
390	2.873	0.952	740	2.931	0.270	1100	2.936	0.120
395	2.889	0.952	750	2.931	0.266	1110	2.937	0.116
400	2.906	0.953	760	2.930	0.263	1120	2.937	0.113
410	2.951	0.956	770	2.930	0.259	1130	2.938	0.110
420	3.020	0.945	780	2.929	0.255	1140	2.939	0.106
430	3.089	0.902	790	2.929	0.251	1150	2.941	0.102

(continued)

Table 8.62 (continued)

λ (nm)	n	k	λ (nm)	n	k	λ (nm)	n	k
440	3.143	0.836	800	2.929	0.247	1160	2.942	9.68×10^{-2}
450	3.174	0.761	810	2.929	0.244	1170	2.944	9.14×10^{-2}
460	3.184	0.687	820	2.929	0.240	1180	2.946	8.52×10^{-2}
470	3.178	0.621	830	2.929	0.236	1190	2.947	7.80×10^{-2}
480	3.163	0.565	840	2.930	0.233	1200	2.948	7.00×10^{-2}
490	3.144	0.520	850	2.930	0.229	1220	2.947	5.19×10^{-2}
500	3.123	0.483	860	2.931	0.226	1240	2.940	3.31×10^{-2}
510	3.102	0.453	870	2.932	0.222	1260	2.928	1.68×10^{-2}
520	3.082	0.429	880	2.934	0.219	1280	2.912	5.60×10^{-3}
530	3.063	0.409	890	2.935	0.214	1300	2.895	0
540	3.046	0.393	900	2.937	0.210			
550	3.031	0.379	910	2.938	0.205			

8.2.25 $CuGaSe_2$

Data from S. Minoura, T. Maekawa, K. Kodera, A. Nakane, S. Niki and H. Fujiwara [30] (see also Fig. 10.7a in Vol. 1). The optical data of a chalcopyrite $CuGaSe_2$ polycrystal (Cu/Ga = 0.84) prepared by a single co-evaporation process at 520 °C are shown. Although a $CuGaSe_2$ single crystal exhibits uniaxial anisotropy, the optical properties are isotropic in $CuGaSe_2$ polycrystals.

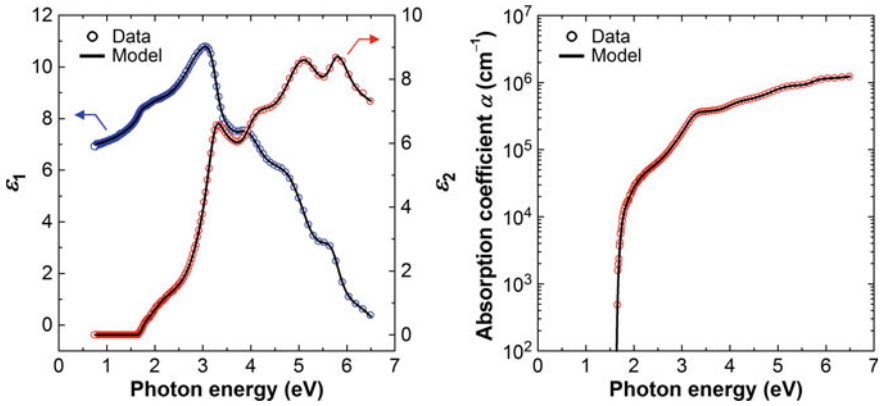


Fig. 8.25 Dielectric function and absorption coefficient of $CuGaSe_2$ (chalcopyrite) at room temperature. The open circles show the reference data and the solid lines indicate the calculation result obtained from the parameterization assuming the Tauc-Lorentz model [(8.1) and (8.2)]

Table 8.63 Tauc-Lorentz parameters of (8.1) and (8.2) for $CuGaSe_2$ (chalcopyrite). The model parameters reported by Minoura et al. are summarized

Peak	A (eV)	C (eV)	E_0 (eV)	E_g (eV)	$\varepsilon_1(\infty)$
$j = 1$	13.966	0.252	1.713	1.626	1.202
$j = 2$	34.567	1.162	1.855	1.728	0
$j = 3$	22.058	0.946	3.024	2.098	0
$j = 4$	41.486	0.487	3.227	2.678	0
$j = 5$	18.203	0.733	3.582	2.659	0
$j = 6$	107.550	0.955	3.970	3.441	0
$j = 7$	14.859	1.286	5.104	1.946	0
$j = 8$	55.933	0.592	5.759	4.973	0
$j = 9$	51.600	3.063	6.729	3.245	0

Table 8.64 Optical constants of $CuGaSe_2$ calculated by the Tauc-Lorentz model

λ (nm)	n	k	λ (nm)	n	k	λ (nm)	n	k
300	2.899	1.197	540	3.002	0.212	880	2.750	0
305	2.922	1.163	550	2.993	0.203	890	2.745	0
310	2.937	1.126	560	2.985	0.194	900	2.742	0
315	2.942	1.089	570	2.978	0.185	910	2.738	0
320	2.939	1.060	580	2.972	0.175	920	2.734	0
325	2.931	1.040	590	2.966	0.165	930	2.731	0
330	2.925	1.031	600	2.961	0.155	940	2.728	0
335	2.924	1.030	610	2.956	0.144	950	2.725	0
340	2.930	1.034	620	2.950	0.133	960	2.722	0
345	2.943	1.038	630	2.944	0.122	970	2.719	0
350	2.962	1.043	640	2.937	0.112	980	2.716	0
355	2.986	1.050	650	2.930	0.102	990	2.714	0
360	3.018	1.057	660	2.924	9.28×10^{-2}	1000	2.711	0
365	3.061	1.062	670	2.918	8.39×10^{-2}	1010	2.709	0
370	3.116	1.057	680	2.912	7.50×10^{-2}	1020	2.707	0
375	3.179	1.038	690	2.907	6.54×10^{-2}	1030	2.704	0
380	3.242	1.000	700	2.902	5.46×10^{-2}	1040	2.702	0
385	3.297	0.942	710	2.895	4.22×10^{-2}	1050	2.700	0
390	3.335	0.872	720	2.886	2.95×10^{-2}	1060	2.698	0
395	3.355	0.800	730	2.874	1.74×10^{-2}	1070	2.696	0
400	3.359	0.731	740	2.860	7.91×10^{-3}	1080	2.694	0
410	3.341	0.618	750	2.845	2.20×10^{-3}	1090	2.693	0
420	3.310	0.532	760	2.830	0	1100	2.691	0
430	3.275	0.463	770	2.819	0	1110	2.689	0
440	3.239	0.407	780	2.809	0	1120	2.688	0
450	3.202	0.363	790	2.801	0	1130	2.686	0
460	3.167	0.329	800	2.793	0	1140	2.685	0
470	3.135	0.302	810	2.786	0	1150	2.683	0
480	3.107	0.281	820	2.780	0	1160	2.682	0
490	3.082	0.264	830	2.774	0	1170	2.680	0
500	3.060	0.251	840	2.769	0	1180	2.679	0
510	3.041	0.239	850	2.763	0	1190	2.678	0
520	3.026	0.229	860	2.758	0	1200	2.676	0
530	3.013	0.220	870	2.754	0			

8.2.26 $CuIn_{1-x}Ga_xSe_2$ [Cu/(In + Ga) = 0.90]

The dielectric functions of $CuIn_{1-x}Ga_xSe_2$ chalcopyrite polycrystalline alloys with different Ga composition x are summarized. These dielectric functions were obtained originally from an established optical database in which the Cu(In,Ga)Se_2 optical constants for arbitrary Cu and Ga compositions can be deduced by applying the energy shift model and spectral averaging method [Sect. 10.4 (Fig. 10.18) in Vol. 1] (see also S. Minoura, T. Maekawa, K. Kodera, A. Nakane, S. Niki and H. Fujiwara [30]). Based on this method, various $CuIn_{1-x}Ga_xSe_2$ dielectric functions (x = 0.1–0.9) with a fixed Cu composition [Cu/(In + Ga) = 0.90] were calculated using the dielectric functions of $CuInSe_2$ (Fig. 8.24) and $CuGaSe_2$ (Fig. 8.25). The dielectric functions obtained from this procedure have been parameterized further using the Tauc-Lorentz model and the modeled results are described here. The Tauc-Lorentz parameters and optical constants of x = 0.0 ($CuInSe_2$) and x = 1.0 ($CuGaSe_2$) are shown in Tables 8.61, 8.62, 8.63 and 8.64 (Fig. 8.26, Tables 8.65, 8.66, 8.67, 8.68, 8.69, 8.70, 8.71, 8.72, 8.73, 8.74, 8.75, 8.76, 8.77, 8.78, 8.79, 8.80, 8.81 and 8.82).

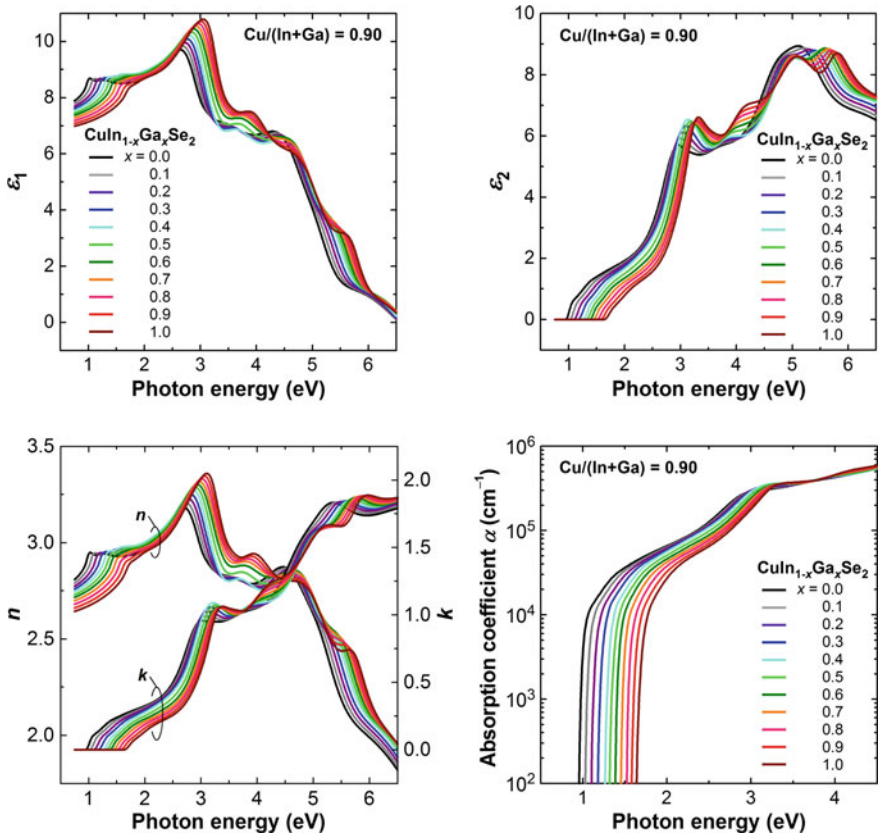


Fig. 8.26 Dielectric functions, optical constants and absorption coefficients of various polycrystalline $CuIn_{1-x}Ga_xSe_2$ alloys [Cu/(In + Ga) = 0.90] calculated by the Tauc-Lorentz model [(8.1) and (8.2)]. The dielectric functions of x = 0.0 and x = 1.0 correspond to those shown in Figs. 8.24 and 8.25, respectively

Table 8.65 Tauc-Lorentz parameters of (8.1) and (8.2) for $CuIn_{1-x}Ga_xSe_2$ ($x = 0.1$)

Peak	A (eV)	C (eV)	E_0 (eV)	E_g (eV)	$\varepsilon_1(\infty)$
$j = 1$	14.853	0.219	1.068	1.020	1.369
$j = 2$	18.161	1.014	1.318	1.123	0
$j = 3$	21.968	2.512	2.002	1.503	0
$j = 4$	14.544	0.783	2.943	1.593	0
$j = 5$	22.096	0.350	3.145	3.039	0
$j = 6$	33.335	1.253	3.632	2.626	0
$j = 7$	9.890	1.114	4.777	1.659	0
$j = 8$	7.383	0.840	5.299	2.615	0
$j = 9$	46.334	3.437	6.478	2.523	0

Table 8.66 Tauc-Lorentz parameters of (8.1) and (8.2) for $CuIn_{1-x}Ga_xSe_2$ ($x = 0.2$)

Peak	A (eV)	C (eV)	E_0 (eV)	E_g (eV)	$\varepsilon_1(\infty)$
$j = 1$	15.475	0.246	1.145	1.093	1.380
$j = 2$	10.059	0.610	1.370	1.194	0
$j = 3$	33.548	3.756	2.294	1.334	0
$j = 4$	19.566	0.735	2.970	1.886	0
$j = 5$	3.749	0.404	3.251	2.789	0
$j = 6$	38.388	1.074	3.642	2.902	0
$j = 7$	9.945	1.062	4.822	1.845	0
$j = 8$	6.285	0.781	5.374	2.621	0
$j = 9$	37.065	3.364	6.561	2.149	0

Table 8.67 Tauc-Lorentz parameters of (8.1) and (8.2) for $CuIn_{1-x}Ga_xSe_2$ ($x = 0.3$)

Peak	A (eV)	C (eV)	E_0 (eV)	E_g (eV)	$\varepsilon_1(\infty)$
$j = 1$	21.463	0.321	1.207	1.171	1.382
$j = 2$	15.793	0.652	1.415	1.363	0
$j = 3$	17.913	2.320	2.815	1.291	0
$j = 4$	30.709	0.703	2.977	2.204	0
$j = 5$	3.545	0.580	3.252	2.394	0
$j = 6$	60.430	0.983	3.650	3.141	0
$j = 7$	8.539	1.049	4.873	1.577	0
$j = 8$	8.083	0.750	5.441	3.021	0
$j = 9$	40.809	3.286	6.564	2.319	0

Table 8.68 Tauc-Lorentz parameters of (8.1) and (8.2) for $CuIn_{1-x}Ga_xSe_2$ ($x = 0.4$)

Peak	A (eV)	C (eV)	E_0 (eV)	E_g (eV)	$\varepsilon_1(\infty)$
$j = 1$	20.119	0.292	1.311	1.254	1.374
$j = 2$	17.816	0.636	1.504	1.430	0
$j = 3$	17.292	2.088	2.769	1.366	0
$j = 4$	31.278	0.677	3.008	2.272	0
$j = 5$	4.029	0.860	3.336	1.746	0
$j = 6$	91.535	0.901	3.662	3.302	0
$j = 7$	7.514	1.019	4.919	1.436	0
$j = 8$	7.366	0.727	5.511	2.970	0
$j = 9$	40.931	3.189	6.588	2.367	0

Table 8.69 Tauc-Lorentz parameters of (8.1) and (8.2) for $CuIn_{1-x}Ga_xSe_2$ ($x = 0.5$)

Peak	A (eV)	C (eV)	E_0 (eV)	E_g (eV)	$\varepsilon_1(\infty)$
$j = 1$	15.363	0.245	1.381	1.308	1.336
$j = 2$	19.581	0.825	1.623	1.411	0
$j = 3$	36.688	2.475	2.677	1.741	0
$j = 4$	42.958	0.762	3.056	2.328	0
$j = 5$	3.898	0.594	3.403	2.904	0
$j = 6$	81.053	0.918	3.712	3.342	0
$j = 7$	9.899	1.056	4.936	1.852	0
$j = 8$	6.757	0.739	5.564	2.832	0
$j = 9$	45.498	3.084	6.615	2.776	0

Table 8.70 Tauc-Lorentz parameters of (8.1) and (8.2) for $CuIn_{1-x}Ga_xSe_2$ ($x = 0.6$)

Peak	A (eV)	C (eV)	E_0 (eV)	E_g (eV)	$\varepsilon_1(\infty)$
$j = 1$	16.750	0.184	1.419	1.377	1.316
$j = 2$	19.946	0.958	1.644	1.413	0
$j = 3$	22.586	1.661	2.554	1.795	0
$j = 4$	55.205	0.900	3.086	2.375	0
$j = 5$	3.644	0.659	3.142	2.224	0
$j = 6$	79.176	1.037	3.773	3.296	0
$j = 7$	7.673	1.081	4.960	1.392	0
$j = 8$	3.544	0.752	5.623	1.708	0
$j = 9$	48.704	3.193	6.655	2.777	0

Table 8.71 Tauc-Lorentz parameters of (8.1) and (8.2) for $CuIn_{1-x}Ga_xSe_2$ ($x = 0.7$)

Peak	A (eV)	C (eV)	E_0 (eV)	E_g (eV)	$\varepsilon_1(\infty)$
$j = 1$	21.037	0.213	1.489	1.444	1.283
$j = 2$	35.604	0.889	1.554	1.552	0
$j = 3$	22.060	1.682	2.809	1.852	0
$j = 4$	50.790	0.771	3.120	2.435	0
$j = 5$	3.847	0.857	3.420	2.488	0
$j = 6$	81.395	1.056	3.828	3.306	0
$j = 7$	8.338	1.101	4.988	1.491	0
$j = 8$	5.241	0.725	5.668	2.541	0
$j = 9$	51.167	3.227	6.663	2.889	0

Table 8.72 Tauc-Lorentz parameters of (8.1) and (8.2) for $CuIn_{1-x}Ga_xSe_2$ ($x = 0.8$)

Peak	A (eV)	C (eV)	E_0 (eV)	E_g (eV)	$\varepsilon_1(\infty)$
$j = 1$	29.218	0.229	1.526	1.514	1.247
$j = 2$	37.482	1.205	1.623	1.617	0
$j = 3$	20.700	1.226	2.953	1.967	0
$j = 4$	44.971	0.637	3.157	2.533	0
$j = 5$	8.127	0.642	3.491	2.624	0
$j = 6$	99.920	1.059	3.858	3.328	0
$j = 7$	11.027	1.147	5.021	1.827	0
$j = 8$	14.165	0.676	5.699	3.924	0
$j = 9$	52.886	3.202	6.666	3.053	0

Table 8.73 Tauc-Lorentz parameters of (8.1) and (8.2) for $CuIn_{1-x}Ga_xSe_2$ ($x = 0.9$)

Peak	A (eV)	C (eV)	E_0 (eV)	E_g (eV)	$\varepsilon_1(\infty)$
$j = 1$	28.319	0.321	1.594	1.572	1.243
$j = 2$	38.663	1.173	1.731	1.735	0
$j = 3$	24.561	1.109	3.045	2.056	0
$j = 4$	31.780	0.512	3.194	2.597	0
$j = 5$	13.690	0.726	3.536	2.602	0
$j = 6$	104.073	0.979	3.916	3.405	0
$j = 7$	15.900	1.246	5.068	2.122	0
$j = 8$	51.960	0.633	5.708	4.851	0
$j = 9$	43.761	3.092	6.785	2.935	0

Table 8.74 Optical constants of $CuIn_{1-x}Ga_xSe_2$ ($x = 0.1$) calculated by the Tauc-Lorentz model

λ (nm)	n	k	λ (nm)	n	k	λ (nm)	n	k
300	2.794	1.079	540	3.049	0.384	880	2.950	0.192
305	2.784	1.067	550	3.035	0.371	890	2.950	0.186
310	2.779	1.058	560	3.023	0.361	900	2.950	0.180
315	2.778	1.051	570	3.012	0.351	910	2.950	0.174
320	2.782	1.045	580	3.003	0.343	920	2.950	0.169
325	2.788	1.038	590	2.994	0.335	930	2.950	0.163
330	2.797	1.029	600	2.987	0.328	940	2.949	0.157
335	2.805	1.018	610	2.981	0.321	950	2.948	0.152
340	2.813	1.006	620	2.975	0.315	960	2.947	0.147
345	2.818	0.993	630	2.970	0.309	970	2.946	0.142
350	2.822	0.982	640	2.966	0.304	980	2.945	0.137
355	2.824	0.973	650	2.962	0.298	990	2.945	0.132
360	2.825	0.967	660	2.958	0.293	1000	2.944	0.128
365	2.827	0.964	670	2.955	0.288	1010	2.943	0.123
370	2.831	0.965	680	2.953	0.283	1020	2.943	0.119
375	2.838	0.969	690	2.951	0.279	1030	2.942	0.115
380	2.850	0.975	700	2.949	0.274	1040	2.942	0.110
385	2.865	0.980	710	2.947	0.269	1050	2.943	0.106
390	2.885	0.984	720	2.946	0.265	1060	2.943	0.101
395	2.907	0.987	730	2.945	0.261	1070	2.944	9.61×10^{-2}
400	2.933	0.990	740	2.944	0.256	1080	2.945	9.04×10^{-2}
410	3.001	0.985	750	2.943	0.252	1090	2.945	8.41×10^{-2}
420	3.079	0.951	760	2.943	0.248	1100	2.946	7.72×10^{-2}
430	3.146	0.887	770	2.943	0.243	1110	2.946	6.96×10^{-2}
440	3.188	0.807	780	2.943	0.239	1120	2.946	6.11×10^{-2}
450	3.205	0.725	790	2.943	0.235	1130	2.944	5.19×10^{-2}
460	3.203	0.651	800	2.943	0.231	1140	2.941	4.24×10^{-2}
470	3.189	0.589	810	2.943	0.226	1150	2.937	3.30×10^{-2}
480	3.169	0.538	820	2.944	0.222	1160	2.931	2.41×10^{-2}
490	3.146	0.497	830	2.945	0.218	1170	2.924	1.63×10^{-2}
500	3.124	0.464	840	2.946	0.213	1180	2.916	9.85×10^{-3}
510	3.103	0.438	850	2.947	0.208	1190	2.907	4.98×10^{-3}
520	3.083	0.416	860	2.948	0.203	1200	2.898	1.79×10^{-3}
530	3.065	0.399	870	2.949	0.197	1210	2.890	0

Table 8.75 Optical constants of $CuIn_{1-x}Ga_xSe_2$ ($x = 0.2$) calculated by the Tauc-Lorentz model

λ (nm)	n	k	λ (nm)	n	k	λ (nm)	n	k
300	2.778	1.080	540	3.054	0.375	880	2.957	0.158
305	2.771	1.071	550	3.041	0.363	890	2.955	0.152
310	2.769	1.065	560	3.030	0.352	900	2.954	0.146
315	2.772	1.060	570	3.020	0.342	910	2.953	0.140
320	2.779	1.054	580	3.011	0.333	920	2.951	0.134
325	2.789	1.046	590	3.003	0.325	930	2.949	0.129
330	2.799	1.035	600	2.997	0.318	940	2.948	0.124
335	2.808	1.022	610	2.991	0.310	950	2.947	0.120
340	2.814	1.008	620	2.985	0.304	960	2.947	0.115
345	2.818	0.995	630	2.980	0.297	970	2.947	0.110
350	2.819	0.985	640	2.976	0.291	980	2.946	0.104
355	2.818	0.978	650	2.972	0.285	990	2.947	9.88×10^{-2}
360	2.818	0.977	660	2.969	0.280	1000	2.947	9.27×10^{-2}
365	2.820	0.980	670	2.966	0.275	1010	2.947	8.61×10^{-2}
370	2.827	0.988	680	2.964	0.269	1020	2.947	7.88×10^{-2}
375	2.839	0.997	690	2.962	0.264	1030	2.946	7.08×10^{-2}
380	2.856	1.006	700	2.960	0.259	1040	2.945	6.22×10^{-2}
385	2.879	1.014	710	2.959	0.254	1050	2.943	5.29×10^{-2}
390	2.906	1.020	720	2.957	0.249	1060	2.940	4.33×10^{-2}
395	2.938	1.023	730	2.957	0.244	1070	2.935	3.37×10^{-2}
400	2.976	1.022	740	2.956	0.240	1080	2.929	2.46×10^{-2}
410	3.059	0.998	750	2.956	0.235	1090	2.922	1.65×10^{-2}
420	3.139	0.941	760	2.956	0.230	1100	2.913	9.84×10^{-3}
430	3.195	0.859	770	2.956	0.225	1110	2.904	4.86×10^{-3}
440	3.224	0.770	780	2.956	0.219	1120	2.894	1.64×10^{-3}
450	3.227	0.687	790	2.956	0.214	1130	2.886	0
460	3.215	0.615	800	2.957	0.209	1140	2.878	0
470	3.194	0.558	810	2.957	0.203	1150	2.872	0
480	3.170	0.512	820	2.958	0.197	1160	2.867	0
490	3.146	0.476	830	2.958	0.191	1170	2.862	0
500	3.123	0.448	840	2.958	0.184	1180	2.857	0
510	3.103	0.424	850	2.958	0.178	1190	2.853	0
520	3.084	0.405	860	2.958	0.171	1200	2.849	0
530	3.068	0.389	870	2.958	0.165			

Table 8.76 Optical constants of $CuIn_{1-x}Ga_xSe_2$ ($x = 0.3$) calculated by the Tauc-Lorentz model

λ (nm)	n	k	λ (nm)	n	k	λ (nm)	n	k
300	2.764	1.086	540	3.059	0.364	880	2.956	0.125
305	2.761	1.080	550	3.047	0.352	890	2.954	0.120
310	2.763	1.076	560	3.036	0.342	900	2.953	0.115
315	2.770	1.071	570	3.027	0.332	910	2.952	0.110
320	2.781	1.064	580	3.020	0.323	920	2.952	0.104
325	2.792	1.053	590	3.012	0.314	930	2.952	9.77×10^{-2}
330	2.803	1.040	600	3.006	0.306	940	2.952	9.04×10^{-2}
335	2.811	1.025	610	3.000	0.298	950	2.952	8.22×10^{-2}
340	2.815	1.011	620	2.995	0.291	960	2.952	7.32×10^{-2}
345	2.815	0.999	630	2.990	0.284	970	2.950	6.35×10^{-2}
350	2.813	0.992	640	2.986	0.277	980	2.947	5.33×10^{-2}
355	2.810	0.991	650	2.982	0.271	990	2.943	4.29×10^{-2}
360	2.811	0.996	660	2.979	0.265	1000	2.937	3.28×10^{-2}
365	2.816	1.006	670	2.976	0.260	1010	2.930	2.34×10^{-2}
370	2.828	1.020	680	2.974	0.254	1020	2.921	1.52×10^{-2}
375	2.847	1.033	690	2.972	0.249	1030	2.912	8.51×10^{-3}
380	2.874	1.045	700	2.971	0.243	1040	2.902	3.64×10^{-3}
385	2.907	1.053	710	2.970	0.238	1050	2.891	0
390	2.945	1.057	720	2.969	0.232	1060	2.882	0
395	2.987	1.054	730	2.969	0.226	1070	2.875	0
400	3.033	1.044	740	2.968	0.221	1080	2.869	0
410	3.124	0.996	750	2.968	0.214	1090	2.863	0
420	3.197	0.917	760	2.969	0.208	1100	2.858	0
430	3.239	0.821	770	2.969	0.201	1110	2.853	0
440	3.251	0.727	780	2.969	0.194	1120	2.849	0
450	3.241	0.647	790	2.969	0.187	1130	2.845	0
460	3.220	0.581	800	2.968	0.180	1140	2.841	0
470	3.195	0.530	810	2.967	0.173	1150	2.837	0
480	3.170	0.490	820	2.967	0.165	1160	2.834	0
490	3.146	0.459	830	2.965	0.158	1170	2.831	0
500	3.124	0.433	840	2.964	0.151	1180	2.827	0
510	3.105	0.411	850	2.962	0.144	1190	2.824	0
520	3.088	0.393	860	2.960	0.138	1200	2.822	0
530	3.072	0.378	870	2.958	0.131			

Table 8.77 Optical constants of $CuIn_{1-x}Ga_xSe_2$ ($x = 0.4$) calculated by the Tauc-Lorentz model

λ (nm)	n	k	λ (nm)	n	k	λ (nm)	n	k
300	2.752	1.093	540	3.065	0.353	880	2.957	9.29×10^{-2}
305	2.753	1.090	550	3.054	0.341	890	2.957	8.44×10^{-2}
310	2.760	1.086	560	3.044	0.329	900	2.957	7.45×10^{-2}
315	2.771	1.081	570	3.036	0.319	910	2.955	6.35×10^{-2}
320	2.784	1.071	580	3.028	0.309	920	2.952	5.17×10^{-2}
325	2.797	1.058	590	3.021	0.300	930	2.946	3.96×10^{-2}
330	2.806	1.042	600	3.014	0.291	940	2.939	2.82×10^{-2}
335	2.811	1.026	610	3.008	0.283	950	2.929	1.81×10^{-2}
340	2.811	1.012	620	3.003	0.276	960	2.918	9.92×10^{-3}
345	2.807	1.004	630	2.998	0.269	970	2.907	4.14×10^{-3}
350	2.802	1.003	640	2.994	0.262	980	2.895	0
355	2.800	1.011	650	2.991	0.256	990	2.885	0
360	2.804	1.024	660	2.988	0.249	1000	2.876	0
365	2.816	1.041	670	2.986	0.243	1010	2.869	0
370	2.837	1.059	680	2.984	0.237	1020	2.863	0
375	2.867	1.075	690	2.983	0.231	1030	2.857	0
380	2.906	1.086	700	2.982	0.224	1040	2.852	0
385	2.950	1.089	710	2.981	0.217	1050	2.847	0
390	2.998	1.085	720	2.981	0.210	1060	2.843	0
395	3.047	1.072	730	2.981	0.203	1070	2.838	0
400	3.097	1.050	740	2.981	0.195	1080	2.835	0
410	3.187	0.978	750	2.980	0.187	1090	2.831	0
420	3.247	0.880	760	2.979	0.179	1100	2.827	0
430	3.271	0.777	770	2.978	0.170	1110	2.824	0
440	3.268	0.684	780	2.976	0.162	1120	2.821	0
450	3.248	0.609	790	2.974	0.154	1130	2.818	0
460	3.221	0.551	800	2.972	0.145	1140	2.815	0
470	3.194	0.506	810	2.969	0.138	1150	2.812	0
480	3.169	0.471	820	2.966	0.131	1160	2.809	0
490	3.146	0.442	830	2.964	0.124	1170	2.807	0
500	3.126	0.419	840	2.961	0.117	1180	2.804	0
510	3.108	0.398	850	2.959	0.112	1190	2.802	0
520	3.092	0.381	860	2.957	0.106	1200	2.799	0
530	3.077	0.366	870	2.957	9.99×10^{-2}			

Table 8.78 Optical constants of $CuIn_{1-x}Ga_xSe_2$ ($x = 0.5$) calculated by the Tauc-Lorentz model

λ (nm)	n	k	λ (nm)	n	k	λ (nm)	n	k
300	2.787	1.113	540	3.055	0.321	880	2.941	5.10×10^{-2}
305	2.793	1.106	550	3.044	0.310	890	2.936	3.91×10^{-2}
310	2.804	1.098	560	3.034	0.299	900	2.928	2.74×10^{-2}
315	2.817	1.086	570	3.025	0.289	910	2.918	1.70×10^{-2}
320	2.830	1.071	580	3.017	0.280	920	2.907	8.89×10^{-3}
325	2.840	1.053	590	3.010	0.272	930	2.894	3.45×10^{-3}
330	2.846	1.035	600	3.003	0.264	940	2.883	0
335	2.847	1.018	610	2.997	0.257	950	2.873	0
340	2.844	1.007	620	2.992	0.250	960	2.864	0
345	2.840	1.002	630	2.988	0.244	970	2.857	0
350	2.838	1.005	640	2.984	0.237	980	2.851	0
355	2.840	1.014	650	2.981	0.231	990	2.845	0
360	2.850	1.027	660	2.979	0.225	1000	2.840	0
365	2.868	1.043	670	2.977	0.218	1010	2.835	0
370	2.895	1.058	680	2.976	0.212	1020	2.830	0
375	2.931	1.068	690	2.974	0.205	1030	2.826	0
380	2.974	1.072	700	2.973	0.198	1040	2.822	0
385	3.021	1.068	710	2.972	0.191	1050	2.818	0
390	3.071	1.054	720	2.972	0.184	1060	2.815	0
395	3.120	1.030	730	2.971	0.175	1070	2.811	0
400	3.167	0.997	740	2.970	0.167	1080	2.808	0
410	3.240	0.907	750	2.969	0.158	1090	2.805	0
420	3.279	0.804	760	2.967	0.150	1100	2.802	0
430	3.287	0.704	770	2.965	0.141	1110	2.799	0
440	3.272	0.619	780	2.962	0.133	1120	2.796	0
450	3.247	0.552	790	2.959	0.125	1130	2.794	0
460	3.218	0.499	800	2.956	0.118	1140	2.791	0
470	3.189	0.458	810	2.954	0.111	1150	2.789	0
480	3.163	0.426	820	2.951	0.104	1160	2.787	0
490	3.139	0.400	830	2.950	9.73×10^{-2}	1170	2.784	0
500	3.117	0.379	840	2.948	9.00×10^{-2}	1180	2.782	0
510	3.098	0.361	850	2.947	8.19×10^{-2}	1190	2.780	0
520	3.082	0.345	860	2.946	7.26×10^{-2}	1200	2.778	0
530	3.067	0.332	870	2.944	6.23×10^{-2}			

Table 8.79 Optical constants of $CuIn_{1-x}Ga_xSe_2$ ($x = 0.6$) calculated by the Tauc-Lorentz model

λ (nm)	n	k	λ (nm)	n	k	λ (nm)	n	k
300	2.825	1.128	540	3.044	0.291	880	2.901	8.01×10^{-3}
305	2.836	1.117	550	3.033	0.281	890	2.887	1.98×10^{-3}
310	2.848	1.103	560	3.023	0.272	900	2.874	0
315	2.861	1.086	570	3.014	0.263	910	2.864	0
320	2.872	1.066	580	3.006	0.255	920	2.856	0
325	2.879	1.046	590	2.999	0.247	930	2.848	0
330	2.882	1.027	600	2.993	0.240	940	2.842	0
335	2.881	1.012	610	2.987	0.233	950	2.836	0
340	2.877	1.003	620	2.982	0.227	960	2.831	0
345	2.875	1.001	630	2.978	0.221	970	2.826	0
350	2.876	1.006	640	2.975	0.214	980	2.821	0
355	2.883	1.016	650	2.972	0.208	990	2.816	0
360	2.898	1.028	660	2.970	0.202	1000	2.812	0
365	2.923	1.041	670	2.968	0.195	1010	2.808	0
370	2.955	1.051	680	2.967	0.188	1020	2.805	0
375	2.996	1.056	690	2.966	0.181	1030	2.801	0
380	3.044	1.052	700	2.965	0.174	1040	2.798	0
385	3.094	1.037	710	2.964	0.165	1050	2.795	0
390	3.143	1.012	720	2.963	0.157	1060	2.792	0
395	3.188	0.977	730	2.962	0.148	1070	2.789	0
400	3.227	0.934	740	2.960	0.139	1080	2.786	0
410	3.281	0.833	750	2.957	0.130	1090	2.783	0
420	3.301	0.730	760	2.954	0.122	1100	2.781	0
430	3.295	0.636	770	2.951	0.113	1110	2.778	0
440	3.273	0.558	780	2.948	0.105	1120	2.776	0
450	3.243	0.497	790	2.945	9.75×10^{-2}	1130	2.774	0
460	3.212	0.449	800	2.942	9.00×10^{-2}	1140	2.771	0
470	3.181	0.412	810	2.939	8.25×10^{-2}	1150	2.769	0
480	3.153	0.383	820	2.937	7.45×10^{-2}	1160	2.767	0
490	3.128	0.360	830	2.935	6.57×10^{-2}	1170	2.765	0
500	3.106	0.341	840	2.933	5.54×10^{-2}	1180	2.764	0
510	3.086	0.326	850	2.930	4.35×10^{-2}	1190	2.762	0
520	3.069	0.313	860	2.924	3.05×10^{-2}	1200	2.760	0
530	3.056	0.302	870	2.914	1.79×10^{-2}			

Table 8.80 Optical constants of $CuIn_{1-x}Ga_xSe_2$ ($x = 0.7$) calculated by the Tauc-Lorentz model

λ (nm)	n	k	λ (nm)	n	k	λ (nm)	n	k
300	2.844	1.148	540	3.034	0.268	880	2.845	0
305	2.858	1.132	550	3.023	0.259	890	2.838	0
310	2.874	1.114	560	3.013	0.250	900	2.831	0
315	2.888	1.092	570	3.004	0.242	910	2.825	0
320	2.897	1.068	580	2.996	0.234	920	2.819	0
325	2.902	1.045	590	2.990	0.227	930	2.814	0
330	2.901	1.025	600	2.984	0.221	940	2.809	0
335	2.898	1.012	610	2.979	0.214	950	2.804	0
340	2.895	1.006	620	2.975	0.207	960	2.800	0
345	2.894	1.007	630	2.972	0.200	970	2.796	0
350	2.899	1.014	640	2.969	0.193	980	2.792	0
355	2.911	1.025	650	2.966	0.186	990	2.788	0
360	2.932	1.036	660	2.964	0.179	1000	2.785	0
365	2.962	1.046	670	2.962	0.171	1010	2.782	0
370	3.000	1.051	680	2.961	0.163	1020	2.778	0
375	3.044	1.050	690	2.959	0.154	1030	2.775	0
380	3.094	1.038	700	2.957	0.145	1040	2.772	0
385	3.145	1.016	710	2.954	0.136	1050	2.770	0
390	3.193	0.982	720	2.951	0.126	1060	2.767	0
395	3.235	0.940	730	2.948	0.117	1070	2.765	0
400	3.269	0.890	740	2.944	0.109	1080	2.762	0
410	3.310	0.780	750	2.941	0.100	1090	2.760	0
420	3.315	0.674	760	2.937	9.20×10^{-2}	1100	2.758	0
430	3.297	0.584	770	2.934	8.40×10^{-2}	1110	2.755	0
440	3.267	0.513	780	2.930	7.59×10^{-2}	1120	2.753	0
450	3.234	0.458	790	2.928	6.72×10^{-2}	1130	2.751	0
460	3.202	0.415	800	2.925	5.76×10^{-2}	1140	2.749	0
470	3.171	0.382	810	2.922	4.59×10^{-2}	1150	2.747	0
480	3.143	0.355	820	2.916	3.22×10^{-2}	1160	2.746	0
490	3.118	0.334	830	2.907	1.88×10^{-2}	1170	2.744	0
500	3.096	0.316	840	2.893	7.97×10^{-3}	1180	2.742	0
510	3.077	0.302	850	2.878	1.63×10^{-3}	1190	2.741	0
520	3.061	0.290	860	2.864	0	1200	2.739	0
530	3.047	0.278	870	2.854	0			

Table 8.81 Optical constants of $CuIn_{1-x}Ga_xSe_2$ ($x = 0.8$) calculated by the Tauc-Lorentz model

λ (nm)	n	k	λ (nm)	n	k	λ (nm)	n	k
300	2.857	1.170	540	3.024	0.249	880	2.808	0
305	2.876	1.150	550	3.013	0.240	890	2.803	0
310	2.894	1.126	560	3.004	0.232	900	2.797	0
315	2.907	1.098	570	2.996	0.225	910	2.792	0
320	2.915	1.070	580	2.989	0.217	920	2.788	0
325	2.916	1.046	590	2.983	0.210	930	2.784	0
330	2.912	1.027	600	2.978	0.202	940	2.779	0
335	2.907	1.017	610	2.974	0.194	950	2.776	0
340	2.904	1.016	620	2.970	0.186	960	2.772	0
345	2.908	1.020	630	2.967	0.178	970	2.768	0
350	2.918	1.029	640	2.964	0.169	980	2.765	0
355	2.937	1.038	650	2.961	0.161	990	2.762	0
360	2.963	1.046	660	2.958	0.151	1000	2.759	0
365	2.996	1.052	670	2.954	0.142	1010	2.756	0
370	3.036	1.054	680	2.951	0.133	1020	2.753	0
375	3.085	1.048	690	2.947	0.123	1030	2.751	0
380	3.138	1.031	700	2.943	0.114	1040	2.748	0
385	3.191	1.001	710	2.939	0.105	1050	2.745	0
390	3.240	0.959	720	2.935	9.61×10^{-2}	1060	2.743	0
395	3.280	0.906	730	2.930	8.73×10^{-2}	1070	2.741	0
400	3.309	0.847	740	2.926	7.84×10^{-2}	1080	2.739	0
410	3.331	0.727	750	2.922	6.92×10^{-2}	1090	2.737	0
420	3.320	0.623	760	2.918	5.94×10^{-2}	1100	2.735	0
430	3.292	0.541	770	2.914	4.89×10^{-2}	1110	2.733	0
440	3.259	0.477	780	2.909	3.67×10^{-2}	1120	2.731	0
450	3.225	0.427	790	2.900	2.34×10^{-2}	1130	2.729	0
460	3.192	0.388	800	2.888	1.11×10^{-2}	1140	2.727	0
470	3.162	0.356	810	2.873	2.62×10^{-3}	1150	2.725	0
480	3.133	0.331	820	2.857	0	1160	2.724	0
490	3.108	0.311	830	2.846	0	1170	2.722	0
500	3.087	0.295	840	2.836	0	1180	2.721	0
510	3.068	0.281	850	2.828	0	1190	2.719	0
520	3.051	0.269	860	2.821	0	1200	2.718	0
530	3.037	0.258	870	2.814	0			

Table 8.82 Optical constants of $CuIn_{1-x}Ga_xSe_2$ ($x = 0.9$) calculated by the Tauc-Lorentz model

λ (nm)	n	k	λ (nm)	n	k	λ (nm)	n	k
300	2.876	1.186	540	3.013	0.228	880	2.776	0
305	2.898	1.160	550	3.003	0.220	890	2.772	0
310	2.917	1.129	560	2.994	0.211	900	2.767	0
315	2.927	1.096	570	2.987	0.203	910	2.763	0
320	2.929	1.066	580	2.980	0.195	920	2.759	0
325	2.925	1.042	590	2.974	0.186	930	2.756	0
330	2.919	1.028	600	2.969	0.178	940	2.752	0
335	2.914	1.023	610	2.965	0.169	950	2.749	0
340	2.916	1.025	620	2.961	0.160	960	2.745	0
345	2.925	1.030	630	2.956	0.150	970	2.742	0
350	2.940	1.037	640	2.952	0.140	980	2.739	0
355	2.962	1.044	650	2.947	0.130	990	2.736	0
360	2.991	1.051	660	2.942	0.120	1000	2.734	0
365	3.027	1.056	670	2.937	0.111	1010	2.731	0
370	3.074	1.055	680	2.931	0.102	1020	2.729	0
375	3.128	1.044	690	2.926	9.28×10^{-2}	1030	2.726	0
380	3.187	1.020	700	2.921	8.42×10^{-2}	1040	2.724	0
385	3.243	0.978	710	2.916	7.56×10^{-2}	1050	2.722	0
390	3.290	0.923	720	2.912	6.69×10^{-2}	1060	2.720	0
395	3.323	0.858	730	2.908	5.64×10^{-2}	1070	2.717	0
400	3.341	0.791	740	2.903	4.43×10^{-2}	1080	2.716	0
410	3.341	0.671	750	2.895	3.13×10^{-2}	1090	2.714	0
420	3.317	0.575	760	2.885	1.88×10^{-2}	1100	2.712	0
430	3.285	0.501	770	2.871	8.47×10^{-3}	1110	2.710	0
440	3.250	0.442	780	2.856	1.88×10^{-3}	1120	2.708	0
450	3.215	0.395	790	2.841	0	1130	2.707	0
460	3.181	0.357	800	2.830	0	1140	2.705	0
470	3.150	0.328	810	2.821	0	1150	2.703	0
480	3.122	0.305	820	2.813	0	1160	2.702	0
490	3.097	0.286	830	2.805	0	1170	2.700	0
500	3.075	0.271	840	2.799	0	1180	2.699	0
510	3.056	0.258	850	2.792	0	1190	2.698	0
520	3.039	0.247	860	2.787	0	1200	2.696	0
530	3.025	0.237	870	2.781	0			

8.2.27 $CuInGaSe_2$-Based Compound [Cu/(In + Ga) = 0.69]

Data from S. Minoura, T. Maekawa, K. Kodera, A. Nakane, S. Niki and H. Fujiwara [30] (see also Fig. 10.9a in Vol. 1). The optical data of a low-Cu $CuIn_{1-x}Ga_xSe_2$-based polycrystalline layer [Cu/(In + Ga) = 0.69, $x = 0.42$] prepared by a single co-evaporation process at 520 °C are shown (Fig. 8.27, Tables 8.83 and 8.84).

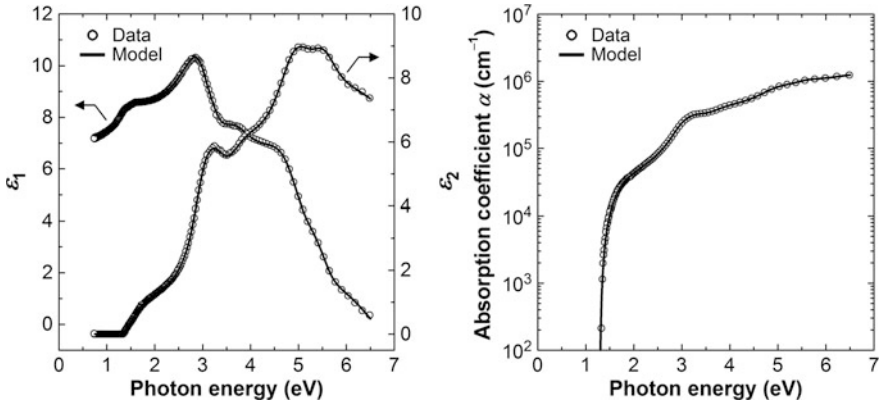


Fig. 8.27 Dielectric function and absorption coefficient of a $CuIn_{1-x}Ga_xSe_2$-based compound [Cu/(In + Ga) = 0.69, $x = 0.42$] at room temperature. The open circles show the reference data and the solid lines indicate the calculation result obtained from the parameterization assuming the Tauc-Lorentz model [(8.1) and (8.2)]

Table 8.83 Tauc-Lorentz parameters of (8.1) and (8.2) for a $CuIn_{1-x}Ga_xSe_2$-based compound [Cu/(In + Ga) = 0.69, $x = 0.42$]. The model parameters reported by Minoura et al. are summarized

Peak	A (eV)	C (eV)	E_0 (eV)	E_g (eV)	$\varepsilon_1(\infty)$
$j = 1$	15.013	0.612	1.355	1.287	1.203
$j = 2$	23.516	1.791	1.595	1.453	0
$j = 3$	18.503	1.439	2.948	1.901	0
$j = 4$	21.522	0.591	2.986	2.395	0
$j = 5$	3.420	0.687	3.332	1.428	0
$j = 6$	148.907	1.126	3.563	3.284	0
$j = 7$	7.182	1.102	4.950	1.415	0
$j = 8$	3.674	0.775	5.532	2.477	0
$j = 9$	48.984	3.519	6.509	2.553	0

Table 8.84 Optical constants of a $CuIn_{1-x}Ga_xSe_2$-based compound [Cu/(In + Ga) = 0.69, $x = 0.42$] calculated by the Tauc-Lorentz model

λ (nm)	n	k	λ (nm)	n	k	λ (nm)	n	k
300	2.887	1.118	540	3.024	0.264	880	2.875	2.98×10^{-2}
305	2.893	1.101	550	3.011	0.255	890	2.868	2.38×10^{-2}
310	2.901	1.084	560	3.000	0.247	900	2.862	1.81×10^{-2}
315	2.911	1.067	570	2.989	0.239	910	2.855	1.31×10^{-2}
320	2.921	1.047	580	2.980	0.233	920	2.847	8.77×10^{-3}
325	2.930	1.027	590	2.972	0.226	930	2.840	5.24×10^{-3}
330	2.936	1.006	600	2.966	0.220	940	2.832	2.58×10^{-3}
335	2.939	0.986	610	2.960	0.215	950	2.825	0
340	2.939	0.968	620	2.954	0.209	960	2.817	0
345	2.938	0.956	630	2.950	0.204	970	2.811	0
350	2.937	0.949	640	2.946	0.199	980	2.806	0
355	2.938	0.947	650	2.943	0.193	990	2.801	0
360	2.945	0.950	660	2.940	0.188	1000	2.797	0
365	2.958	0.954	670	2.938	0.182	1010	2.793	0
370	2.978	0.957	680	2.936	0.176	1020	2.789	0
375	3.003	0.958	690	2.935	0.17	1030	2.785	0
380	3.034	0.955	700	2.933	0.163	1040	2.782	0
385	3.068	0.944	710	2.932	0.156	1050	2.778	0
390	3.101	0.927	720	2.931	0.149	1060	2.775	0
395	3.134	0.906	730	2.929	0.142	1070	2.772	0
400	3.166	0.879	740	2.927	0.135	1080	2.770	0
410	3.223	0.811	750	2.926	0.127	1090	2.767	0
420	3.261	0.725	760	2.924	0.119	1100	2.764	0
430	3.271	0.634	770	2.922	0.111	1110	2.762	0
440	3.259	0.553	780	2.919	0.103	1120	2.759	0
450	3.235	0.487	790	2.916	9.55×10^{-2}	1130	2.757	0
460	3.205	0.435	800	2.913	8.74×10^{-2}	1140	2.755	0
470	3.175	0.394	810	2.910	7.94×10^{-2}	1150	2.753	0
480	3.147	0.362	820	2.906	7.15×10^{-2}	1160	2.751	0
490	3.120	0.337	830	2.901	6.38×10^{-2}	1170	2.749	0
500	3.096	0.316	840	2.896	5.64×10^{-2}	1180	2.747	0
510	3.074	0.299	850	2.891	4.94×10^{-2}	1190	2.745	0
520	3.055	0.286	860	2.886	4.28×10^{-2}	1200	2.744	0
530	3.039	0.274	870	2.881	3.62×10^{-2}			

8.2.28 $CuInGaSe_2$-Based Compound [Cu/(In + Ga) = 0.36]

Data from S. Minoura, T. Maekawa, K. Kodera, A. Nakane, S. Niki and H. Fujiwara [30] (see also Fig. 10.9a in Vol. 1). The optical data of a low-Cu $CuIn_{1-x}Ga_xSe_2$-based polycrystalline layer [Cu/(In + Ga) = 0.36, $x = 0.40$] prepared by a single co-evaporation process at 520 °C are shown (Fig. 8.28, Tables 8.85 and 8.86).

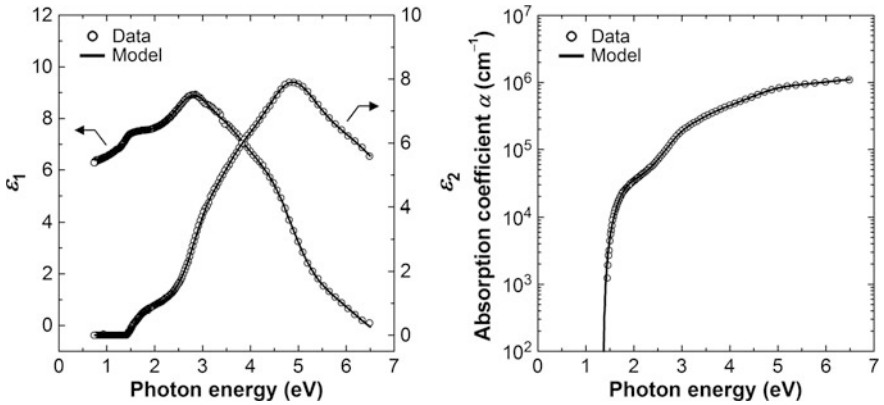


Fig. 8.28 Dielectric function and absorption coefficient of a $CuIn_{1-x}Ga_xSe_2$-based compound [Cu/(In + Ga) = 0.36, $x = 0.40$] at room temperature. The open circles show the reference data and the solid lines indicate the calculation result obtained from the parameterization assuming the Tauc-Lorentz model [(8.1) and (8.2)]

Table 8.85 Tauc-Lorentz parameters of (8.1) and (8.2) for a $CuIn_{1-x}Ga_xSe_2$-based compound [Cu/(In + Ga) = 0.36, $x = 0.40$]. The model parameters reported by S. Minoura et al. are summarized

Peak	A (eV)	C (eV)	E_0 (eV)	E_g (eV)	$\varepsilon_1(\infty)$
$j = 1$	22.696	1.305	1.449	1.349	1.288
$j = 2$	28.043	1.269	3.059	2.019	0
$j = 3$	54.974	1.389	3.553	2.986	0
$j = 4$	23.104	2.081	4.918	1.455	0
$j = 5$	88.140	2.956	6.020	4.315	0

Table 8.86 Optical constants of a $CuIn_{1-x}Ga_xSe_2$-based compound [Cu/(In + Ga) = 0.36, $x = 0.40$] calculated by the Tauc-Lorentz model

λ (nm)	n	k	λ (nm)	n	k	λ (nm)	n	k
300	2.796	1.180	540	2.839	0.214	880	2.667	6.04×10^{-3}
305	2.810	1.149	550	2.825	0.206	890	2.660	3.38×10^{-3}
310	2.825	1.120	560	2.812	0.199	900	2.653	1.47×10^{-3}
315	2.839	1.092	570	2.801	0.193	910	2.646	0
320	2.853	1.066	580	2.791	0.188	920	2.639	0
325	2.867	1.039	590	2.783	0.184	930	2.634	0
330	2.880	1.012	600	2.776	0.180	940	2.629	0
335	2.893	0.986	610	2.770	0.176	950	2.625	0
340	2.905	0.959	620	2.766	0.173	960	2.621	0
345	2.916	0.933	630	2.763	0.169	970	2.617	0
350	2.926	0.907	640	2.760	0.164	980	2.613	0
355	2.934	0.881	650	2.758	0.159	990	2.610	0
360	2.942	0.857	660	2.757	0.154	1000	2.607	0
365	2.949	0.834	670	2.755	0.148	1010	2.604	0
370	2.957	0.812	680	2.754	0.141	1020	2.601	0
375	2.964	0.790	690	2.752	0.135	1030	2.598	0
380	2.972	0.768	700	2.751	0.128	1040	2.595	0
385	2.979	0.747	710	2.749	0.120	1050	2.593	0
390	2.987	0.725	720	2.748	0.113	1060	2.590	0
395	2.995	0.702	730	2.746	0.105	1070	2.588	0
400	3.003	0.679	740	2.743	9.69×10^{-2}	1080	2.586	0
410	3.015	0.630	750	2.740	8.88×10^{-2}	1090	2.584	0
420	3.023	0.580	760	2.737	8.08×10^{-2}	1100	2.582	0
430	3.026	0.528	770	2.733	7.27×10^{-2}	1110	2.580	0
440	3.021	0.476	780	2.729	6.48×10^{-2}	1120	2.578	0
450	3.010	0.429	790	2.725	5.71×10^{-2}	1130	2.576	0
460	2.993	0.386	800	2.720	4.96×10^{-2}	1140	2.574	0
470	2.974	0.349	810	2.714	4.24×10^{-2}	1150	2.573	0
480	2.953	0.318	820	2.708	3.56×10^{-2}	1160	2.571	0
490	2.932	0.292	830	2.702	2.93×10^{-2}	1170	2.569	0
500	2.911	0.270	840	2.695	2.34×10^{-2}	1180	2.568	0
510	2.891	0.251	850	2.689	1.81×10^{-2}	1190	2.566	0
520	2.872	0.237	860	2.682	1.35×10^{-2}	1200	2.565	0
530	2.855	0.224	870	2.674	9.41×10^{-3}			

8.2.29 Cu_2ZnSnS_4

Data from J. Li, H. Du, J. Yarbrough, A. Norman, K. Jones, G. Teeter, F. L. Terry Jr., and D. Levi [31]. The optical data of a polycrystalline Cu_2ZnSnS_4 layer (Cu:Zn:Sn = 1.94:1.06:1.01) prepared by a single co-evaporation process at 450 °C are shown.

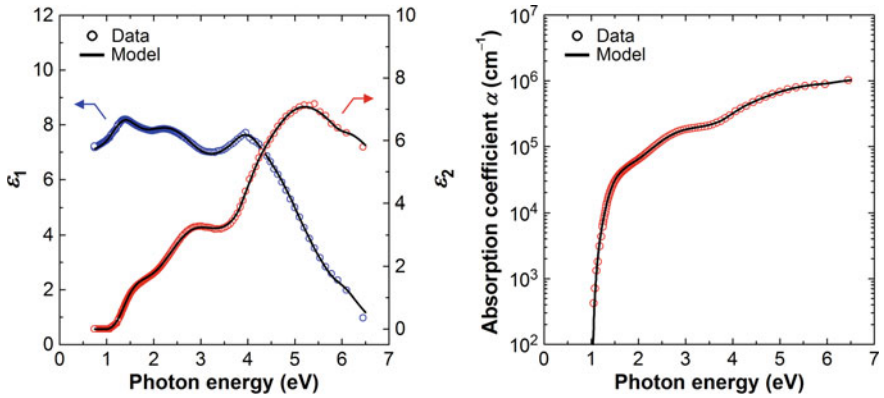


Fig. 8.29 Dielectric function and absorption coefficient of Cu_2ZnSnS_4 at room temperature. The open circles show the reference data and the solid lines indicate the calculation result obtained from the parameterization assuming the Tauc-Lorentz model [(8.1) and (8.2)]

Table 8.87 Tauc-Lorentz parameters of (8.1) and (8.2) for Cu_2ZnSnS_4

Peak	A (eV)	C (eV)	E_0 (eV)	E_g (eV)	$\varepsilon_1(\infty)$
$j = 1$	10.562	1.013	1.540	1.009	1.730
$j = 2$	32.722	2.448	2.790	1.548	0
$j = 3$	36.534	1.303	4.055	2.967	0
$j = 4$	195.722	2.801	4.674	3.683	0
$j = 5$	103.461	0.885	5.994	5.823	0

Table 8.88 Optical constants of Cu_2ZnSnS_4 calculated by the Tauc-Lorentz model

λ (nm)	n	k	λ (nm)	n	k	λ (nm)	n	k
300	2.869	0.878	540	2.837	0.405	880	2.864	0.149
305	2.873	0.832	550	2.836	0.390	890	2.863	0.140
310	2.870	0.788	560	2.834	0.376	900	2.861	0.131
315	2.862	0.746	570	2.832	0.364	910	2.860	0.122
320	2.848	0.708	580	2.830	0.353	920	2.857	0.113
325	2.830	0.676	590	2.827	0.342	930	2.855	0.104
330	2.809	0.651	600	2.824	0.333	940	2.851	9.64×10^{-2}
335	2.789	0.633	610	2.822	0.325	950	2.848	8.86×10^{-2}

(continued)

Table 8.88 (continued)

λ (nm)	n	k	λ (nm)	n	k	λ (nm)	n	k
340	2.771	0.621	620	2.819	0.318	960	2.844	8.11×10^{-2}
345	2.756	0.611	630	2.817	0.312	970	2.840	7.40×10^{-2}
350	2.742	0.604	640	2.816	0.306	980	2.836	6.73×10^{-2}
355	2.731	0.600	650	2.815	0.301	990	2.832	6.10×10^{-2}
360	2.721	0.597	660	2.815	0.296	1000	2.827	5.51×10^{-2}
365	2.713	0.595	670	2.815	0.292	1010	2.822	4.95×10^{-2}
370	2.708	0.595	680	2.816	0.288	1020	2.817	4.43×10^{-2}
375	2.704	0.595	690	2.817	0.284	1030	2.813	3.95×10^{-2}
380	2.702	0.596	700	2.819	0.280	1040	2.808	3.50×10^{-2}
385	2.702	0.597	710	2.821	0.275	1050	2.803	3.08×10^{-2}
390	2.703	0.598	720	2.824	0.271	1060	2.798	2.70×10^{-2}
395	2.706	0.598	730	2.827	0.266	1070	2.793	2.34×10^{-2}
400	2.710	0.598	740	2.830	0.261	1080	2.788	2.02×10^{-2}
410	2.720	0.597	750	2.834	0.255	1090	2.783	1.73×10^{-2}
420	2.734	0.593	760	2.837	0.249	1100	2.779	1.46×10^{-2}
430	2.749	0.585	770	2.841	0.242	1110	2.774	1.22×10^{-2}
440	2.764	0.574	780	2.844	0.236	1120	2.770	1.00×10^{-2}
450	2.779	0.561	790	2.848	0.229	1130	2.765	8.13×10^{-3}
460	2.793	0.545	800	2.851	0.221	1140	2.761	6.45×10^{-3}
470	2.804	0.528	810	2.854	0.213	1150	2.756	4.99×10^{-3}
480	2.814	0.510	820	2.857	0.205	1160	2.752	3.74×10^{-3}
490	2.822	0.492	830	2.859	0.196	1170	2.748	2.68×10^{-3}
500	2.828	0.473	840	2.861	0.187	1180	2.744	1.81×10^{-3}
510	2.833	0.455	850	2.863	0.178	1190	2.740	1.13×10^{-3}
520	2.835	0.438	860	2.864	0.168	1200	2.737	0
530	2.837	0.421	870	2.864	0.159			

8.2.30 $Cu_2ZnSnSe_4$

Data from Y. Hirate, H. Tampo, S. Minoura, H. Kadowaki, A. Nakane, K. M. Kim, H. Shibata, S. Niki and H. Fujiwara [32]. The optical data of a polycrystalline $Cu_2ZnSnSe_4$ layer (Cu:Zn:Sn:Se = 1.95:1.08:0.97:3.99) prepared by a single co-evaporation process at 370 °C are shown.

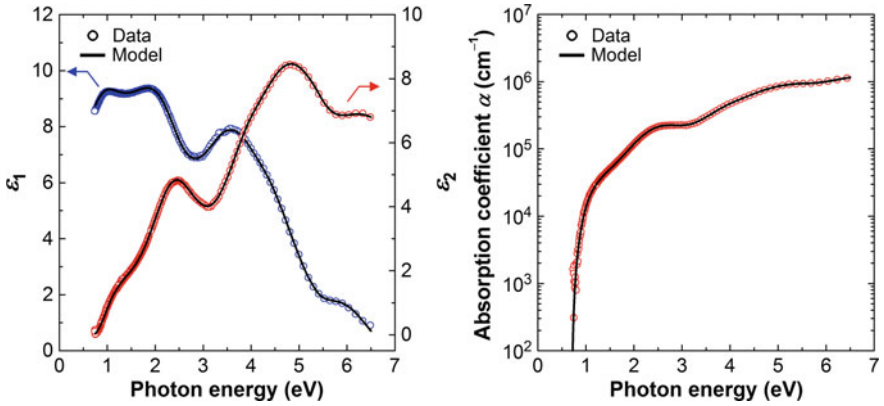


Fig. 8.30 Dielectric function and absorption coefficient of $Cu_2ZnSnSe_4$ at room temperature. The open circles show the reference data and the solid lines indicate the calculation result obtained from the parameterization assuming the Tauc-Lorentz model [(8.1) and (8.2)]

Table 8.89 Tauc-Lorentz parameters of (8.1) and (8.2) for $Cu_2ZnSnSe_4$. The model parameters reported by Hirate et al. are summarized

Peak	A (eV)	C (eV)	E_0 (eV)	E_g (eV)	$\varepsilon_1(\infty)$
$j = 1$	11.122	1.330	1.177	0.700	0.770
$j = 2$	25.139	1.664	2.401	1.150	0
$j = 3$	63.399	1.563	3.789	2.598	0
$j = 4$	173.079	2.205	4.549	3.566	0
$j = 5$	231.270	2.009	5.886	5.455	0

Table 8.90 Optical constants of $Cu_2ZnSnSe_4$ calculated by the Tauc-Lorentz model

λ (nm)	n	k	λ (nm)	n	k	λ (nm)	n	k
300	2.895	1.239	720	3.086	0.414	1240	3.056	0.134
305	2.911	1.200	730	3.082	0.403	1250	3.055	0.129
310	2.925	1.162	740	3.079	0.393	1260	3.054	0.124
315	2.938	1.123	750	3.075	0.383	1270	3.053	0.119
320	2.949	1.083	760	3.072	0.374	1280	3.051	0.114
325	2.956	1.043	770	3.069	0.366	1290	3.050	0.11
330	2.959	1.003	780	3.066	0.359	1300	3.048	0.105
335	2.958	0.965	790	3.063	0.352	1310	3.047	0.101
340	2.954	0.928	800	3.061	0.345	1320	3.045	9.61×10^{-2}
345	2.946	0.894	810	3.058	0.339	1330	3.043	9.17×10^{-2}
350	2.936	0.863	820	3.056	0.333	1340	3.041	8.75×10^{-2}
355	2.924	0.834	830	3.055	0.327	1350	3.039	8.33×10^{-2}

(continued)

Table 8.90 (continued)

λ (nm)	n	k	λ (nm)	n	k	λ (nm)	n	k
360	2.910	0.807	840	3.053	0.322	1360	3.037	7.92×10^{-2}
365	2.894	0.785	850	3.052	0.317	1370	3.035	7.53×10^{-2}
370	2.876	0.765	860	3.051	0.312	1380	3.033	7.14×10^{-2}
375	2.858	0.750	870	3.050	0.307	1390	3.031	6.76×10^{-2}
380	2.839	0.738	880	3.049	0.303	1400	3.028	6.39×10^{-2}
385	2.821	0.730	890	3.049	0.298	1410	3.026	6.04×10^{-2}
390	2.803	0.726	900	3.049	0.294	1420	3.023	5.69×10^{-2}
395	2.788	0.724	910	3.048	0.289	1430	3.021	5.36×10^{-2}
400	2.773	0.725	920	3.048	0.285	1440	3.018	5.03×10^{-2}
410	2.751	0.734	930	3.049	0.280	1450	3.016	4.72×10^{-2}
420	2.737	0.749	940	3.049	0.276	1460	3.013	4.41×10^{-2}
430	2.732	0.767	950	3.049	0.272	1470	3.011	4.12×10^{-2}
440	2.736	0.786	960	3.049	0.267	1480	3.008	3.84×10^{-2}
450	2.748	0.805	970	3.050	0.263	1490	3.005	3.56×10^{-2}
460	2.766	0.821	980	3.050	0.258	1500	3.003	3.30×10^{-2}
470	2.790	0.833	990	3.051	0.254	1510	3.000	3.05×10^{-2}
480	2.819	0.841	1000	3.051	0.249	1520	2.997	2.81×10^{-2}
490	2.850	0.842	1010	3.052	0.245	1530	2.994	2.58×10^{-2}
500	2.883	0.838	1020	3.053	0.240	1540	2.992	2.36×10^{-2}
510	2.914	0.829	1030	3.053	0.236	1550	2.989	2.15×10^{-2}
520	2.945	0.815	1040	3.054	0.231	1560	2.986	1.95×10^{-2}
530	2.973	0.798	1050	3.054	0.227	1570	2.983	1.77×10^{-2}
540	2.998	0.777	1060	3.055	0.222	1580	2.980	1.59×10^{-2}
550	3.021	0.755	1070	3.055	0.218	1590	2.978	1.42×10^{-2}
560	3.040	0.731	1080	3.056	0.213	1600	2.975	1.26×10^{-2}
570	3.057	0.706	1090	3.057	0.209	1610	2.972	1.11×10^{-2}
580	3.070	0.680	1100	3.057	0.204	1620	2.969	9.76×10^{-3}
590	3.081	0.655	1110	3.058	0.199	1630	2.967	8.47×10^{-3}
600	3.090	0.630	1120	3.058	0.194	1640	2.964	7.28×10^{-3}
610	3.096	0.606	1130	3.059	0.189	1650	2.961	6.18×10^{-3}
620	3.100	0.583	1140	3.059	0.184	1660	2.959	5.18×10^{-3}
630	3.103	0.561	1150	3.059	0.179	1670	2.956	4.27×10^{-3}
640	3.104	0.539	1160	3.059	0.174	1680	2.954	3.45×10^{-3}
650	3.104	0.520	1170	3.059	0.169	1690	2.951	2.72×10^{-3}
660	3.103	0.501	1180	3.059	0.164	1700	2.949	2.08×10^{-3}
670	3.101	0.484	1190	3.059	0.159	1710	2.946	1.53×10^{-3}
680	3.099	0.467	1200	3.059	0.154	1720	2.944	1.07×10^{-3}
690	3.096	0.452	1210	3.058	0.149	1730	2.941	0
700	3.093	0.439	1220	3.057	0.144			
710	3.089	0.426	1230	3.057	0.139			

8.2.31 $Cu_2ZnSn(S_xSe_{1-x})_4$

The dielectric functions of $Cu_2ZnSn(S_xSe_{1-x})_4$ with different S composition of $x = S/(S + Se)$ are summarized. These dielectric functions were obtained from an $Cu_2ZnSn(S_xSe_{1-x})_4$ optical database (A. Nakane, H. Tampo, M. Tamakoshi, S. Fujimoto, K. M. Kim, S. Kim, H. Shibata, S. Niki and H. Fujiwara [33]), in which the $Cu_2ZnSn(S,Se)_4$ optical constants for arbitrary S content are deduced by applying the energy shift model (Sect. 10.4.1 in Vol. 1). Based on this method, various $Cu_2ZnSn(S,Se)_4$ dielectric functions ($x = 0.2$–0.8) with a constant Cu composition [Cu/(Zn + Sn) ~ 0.95] were calculated using the dielectric functions of Cu_2ZnSnS_4 (Fig. 8.29) and $Cu_2ZnSnSe_4$ (Fig. 8.30). The dielectric functions obtained from this procedure have been parameterized further using the Tauc-Lorentz model and the modeled results are described here. The Tauc-Lorentz parameters and optical constants of $x = 0.0$ ($Cu_2ZnSnSe_4$) and $x = 1.0$ (Cu_2ZnSnS_4) are shown in Tables 8.87, 8.88, 8.89 and 8.90 (Fig. 8.31, Tables 8.91, 8.92, 8.93, 8.94, 8.95, 8.96, 8.97 and 8.98).

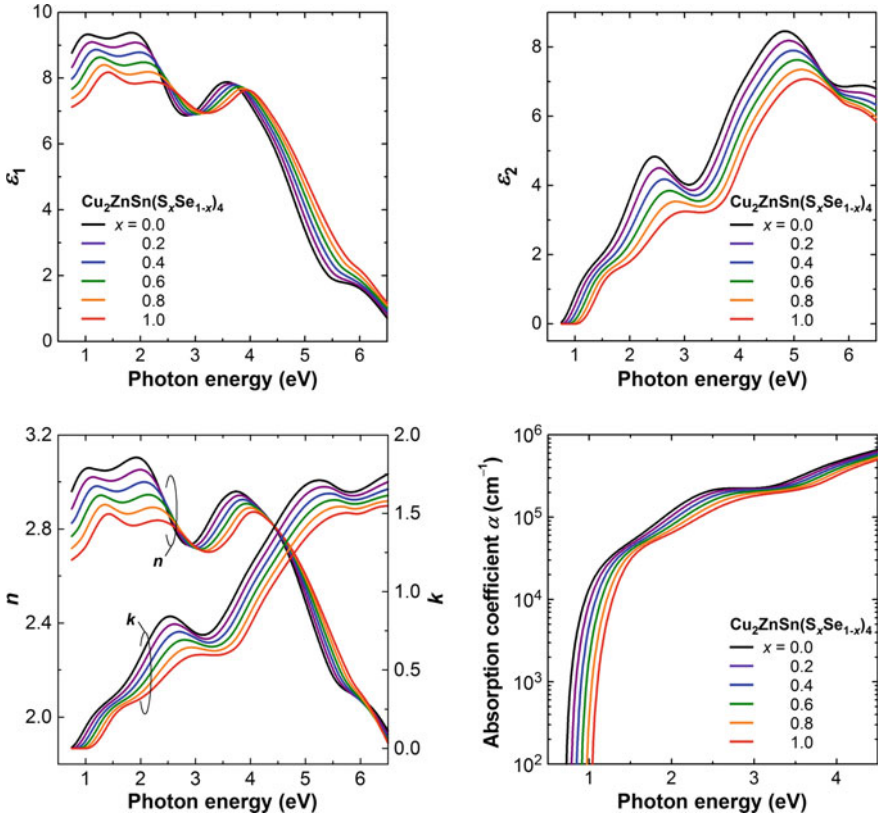


Fig. 8.31 Dielectric functions, optical constants and absorption coefficients of various $Cu_2ZnSn(S_xSe_{1-x})_4$ calculated by the Tauc-Lorentz model [(8.1) and (8.2)]. The $Cu_2ZnSn(S_xSe_{1-x})_4$ dielectric functions in a range of $x = 0.2$–0.8 represent those calculated from the energy shift model, whereas the dielectric functions of $x = 0.0$ and $x = 1.0$ correspond to those shown in Figs. 8.30 and 8.29, respectively

Table 8.91 Tauc-Lorentz parameters of (8.1) and (8.2) for $Cu_2ZnSn(S_xSe_{1-x})_4$ ($x = 0.2$)

Peak	A (eV)	C (eV)	E_0 (eV)	E_g (eV)	$\varepsilon_1(\infty)$
$j = 1$	11.278	1.265	1.245	0.762	0.979
$j = 2$	25.951	1.728	2.467	1.229	0
$j = 3$	57.917	1.499	3.852	2.653	0
$j = 4$	181.771	2.271	4.582	3.614	0
$j = 5$	205.806	1.942	5.906	5.515	0

Table 8.92 Tauc-Lorentz parameters of (8.1) and (8.2) for $Cu_2ZnSn(S_xSe_{1-x})_4$ ($x = 0.4$)

Peak	A (eV)	C (eV)	E_0 (eV)	E_g (eV)	$\varepsilon_1(\infty)$
$j = 1$	11.031	1.179	1.313	0.823	1.184
$j = 2$	26.614	1.825	2.542	1.295	0
$j = 3$	55.577	1.521	3.872	2.740	0
$j = 4$	158.392	2.463	4.683	3.532	0
$j = 5$	194.914	1.862	5.881	5.575	0

Table 8.93 Tauc-Lorentz parameters of (8.1) and (8.2) for $Cu_2ZnSn(S_xSe_{1-x})_4$ ($x = 0.6$)

Peak	A (eV)	C (eV)	E_0 (eV)	E_g (eV)	$\varepsilon_1(\infty)$
$j = 1$	11.010	1.132	1.391	0.884	1.374
$j = 2$	27.995	1.941	2.612	1.384	0
$j = 3$	49.458	1.481	3.934	2.799	0
$j = 4$	162.760	2.580	4.718	3.560	0
$j = 5$	185.419	1.631	5.824	5.656	0

Table 8.94 Tauc-Lorentz parameters of (8.1) and (8.2) for $Cu_2ZnSn(S_xSe_{1-x})_4$ ($x = 0.8$)

Peak	A (eV)	C (eV)	E_0 (eV)	E_g (eV)	$\varepsilon_1(\infty)$
$j = 1$	10.868	1.080	1.467	0.946	1.558
$j = 2$	29.936	2.123	2.690	1.471	0
$j = 3$	42.757	1.401	3.997	2.867	0
$j = 4$	177.685	2.689	4.710	3.620	0
$j = 5$	167.614	1.240	5.817	5.750	0

Table 8.95 Optical constants of $Cu_2ZnSn(S_xSe_{1-x})_4$ ($x = 0.2$) calculated by the Tauc-Lorentz model

λ (nm)	n	k	λ (nm)	n	k	λ (nm)	n	k
300	2.893	1.170	670	3.043	0.427	1140	3.019	0.141
305	2.908	1.130	680	3.039	0.414	1150	3.018	0.136
310	2.922	1.091	690	3.036	0.402	1160	3.017	0.130
315	2.933	1.050	700	3.032	0.391	1170	3.015	0.124
320	2.940	1.008	710	3.029	0.381	1180	3.014	0.119
325	2.943	0.967	720	3.025	0.372	1190	3.012	0.114
330	2.942	0.927	730	3.022	0.363	1200	3.011	0.108
335	2.936	0.889	740	3.019	0.355	1210	3.009	0.103
340	2.926	0.854	750	3.017	0.348	1220	3.007	9.78×10^{-2}
345	2.914	0.824	760	3.014	0.341	1230	3.005	9.28×10^{-2}
350	2.901	0.796	770	3.012	0.335	1240	3.003	8.80×10^{-2}
355	2.886	0.771	780	3.010	0.329	1250	3.000	8.32×10^{-2}
360	2.869	0.749	790	3.009	0.323	1260	2.998	7.86×10^{-2}
365	2.851	0.732	800	3.007	0.318	1270	2.995	7.41×10^{-2}
370	2.832	0.718	810	3.006	0.313	1280	2.993	6.97×10^{-2}
375	2.814	0.708	820	3.006	0.308	1290	2.990	6.55×10^{-2}
380	2.797	0.702	830	3.005	0.303	1300	2.987	6.14×10^{-2}
385	2.781	0.699	840	3.005	0.298	1310	2.985	5.75×10^{-2}
390	2.766	0.699	850	3.005	0.293	1320	2.982	5.36×10^{-2}
395	2.754	0.701	860	3.005	0.289	1330	2.979	5.00×10^{-2}
400	2.744	0.705	870	3.005	0.284	1340	2.976	4.64×10^{-2}
410	2.730	0.718	880	3.006	0.279	1350	2.973	4.30×10^{-2}
420	2.725	0.734	890	3.006	0.275	1360	2.970	3.98×10^{-2}
430	2.729	0.750	900	3.007	0.270	1370	2.967	3.67×10^{-2}
440	2.741	0.766	910	3.008	0.265	1380	2.964	3.37×10^{-2}
450	2.758	0.779	920	3.008	0.260	1390	2.960	3.08×10^{-2}
460	2.781	0.788	930	3.009	0.256	1400	2.957	2.81×10^{-2}
470	2.808	0.793	940	3.010	0.251	1410	2.954	2.56×10^{-2}
480	2.838	0.792	950	3.011	0.246	1420	2.951	2.31×10^{-2}
490	2.868	0.785	960	3.012	0.241	1430	2.948	2.08×10^{-2}
500	2.897	0.774	970	3.013	0.236	1440	2.945	1.87×10^{-2}
510	2.924	0.758	980	3.014	0.231	1450	2.941	1.66×10^{-2}
520	2.949	0.740	990	3.015	0.226	1460	2.938	1.47×10^{-2}
530	2.971	0.719	1000	3.015	0.221	1470	2.935	1.29×10^{-2}
540	2.991	0.696	1010	3.016	0.215	1480	2.932	1.13×10^{-2}
550	3.007	0.672	1020	3.017	0.210	1490	2.929	9.72×10^{-3}
560	3.020	0.647	1030	3.018	0.205	1500	2.926	8.30×10^{-3}
570	3.031	0.623	1040	3.019	0.199	1510	2.923	7.00×10^{-3}

(continued)

Table 8.95 (continued)

λ (nm)	n	k	λ (nm)	n	k	λ (nm)	n	k
580	3.039	0.598	1050	3.020	0.194	1520	2.920	5.82×10^{-3}
590	3.045	0.575	1060	3.020	0.188	1530	2.917	4.75×10^{-3}
600	3.049	0.552	1070	3.021	0.182	1540	2.914	3.80×10^{-3}
610	3.051	0.531	1080	3.021	0.176	1550	2.911	2.96×10^{-3}
620	3.052	0.510	1090	3.021	0.171	1560	2.908	2.23×10^{-3}
630	3.052	0.491	1100	3.021	0.165	1570	2.905	1.60×10^{-3}
640	3.050	0.473	1110	3.021	0.159	1580	2.903	1.08×10^{-3}
650	3.048	0.457	1120	3.020	0.153	1590	2.900	0
660	3.046	0.441	1130	3.020	0.147			

Table 8.96 Optical constants of $Cu_2ZnSn(S_xSe_{1-x})_4$ ($x = 0.4$) calculated by the Tauc-Lorentz model

λ (nm)	n	k	λ (nm)	n	k	λ (nm)	n	k
300	2.889	1.099	630	2.996	0.432	1060	2.981	0.145
305	2.903	1.058	640	2.993	0.417	1070	2.980	0.139
310	2.914	1.017	650	2.990	0.404	1080	2.979	0.132
315	2.921	0.975	660	2.986	0.392	1090	2.978	0.126
320	2.925	0.933	670	2.983	0.381	1100	2.976	0.119
325	2.924	0.892	680	2.980	0.371	1110	2.974	0.113
330	2.918	0.853	690	2.976	0.361	1120	2.972	0.107
335	2.908	0.816	700	2.973	0.353	1130	2.970	0.101
340	2.894	0.784	710	2.971	0.345	1140	2.968	9.56×10^{-2}
345	2.877	0.757	720	2.968	0.338	1150	2.965	9.00×10^{-2}
350	2.859	0.734	730	2.966	0.332	1160	2.963	8.46×10^{-2}
355	2.841	0.716	740	2.964	0.325	1170	2.960	7.93×10^{-2}
360	2.824	0.701	750	2.963	0.320	1180	2.957	7.43×10^{-2}
365	2.807	0.690	760	2.961	0.314	1190	2.954	6.93×10^{-2}
370	2.790	0.682	770	2.961	0.309	1200	2.951	6.46×10^{-2}
375	2.775	0.677	780	2.960	0.304	1210	2.948	6.01×10^{-2}
380	2.761	0.675	790	2.960	0.299	1220	2.945	5.57×10^{-2}
385	2.749	0.675	800	2.960	0.295	1230	2.941	5.15×10^{-2}
390	2.738	0.677	810	2.960	0.290	1240	2.938	4.75×10^{-2}
395	2.730	0.681	820	2.961	0.285	1250	2.934	4.37×10^{-2}
400	2.724	0.687	830	2.962	0.280	1260	2.931	4.00×10^{-2}
410	2.719	0.699	840	2.963	0.275	1270	2.927	3.66×10^{-2}
420	2.722	0.713	850	2.964	0.270	1280	2.924	3.33×10^{-2}

(continued)

Table 8.96 (continued)

λ (nm)	n	k	λ (nm)	n	k	λ (nm)	n	k
430	2.733	0.726	860	2.965	0.265	1290	2.920	3.02×10^{-2}
440	2.749	0.736	870	2.967	0.260	1300	2.917	2.72×10^{-2}
450	2.771	0.742	880	2.968	0.255	1310	2.913	2.44×10^{-2}
460	2.796	0.744	890	2.969	0.250	1320	2.910	2.18×10^{-2}
470	2.823	0.740	900	2.971	0.244	1330	2.906	1.94×10^{-2}
480	2.851	0.731	910	2.972	0.239	1340	2.902	1.71×10^{-2}
490	2.876	0.718	920	2.973	0.233	1350	2.899	1.50×10^{-2}
500	2.900	0.701	930	2.975	0.227	1360	2.895	1.30×10^{-2}
510	2.922	0.682	940	2.976	0.222	1370	2.892	1.12×10^{-2}
520	2.940	0.661	950	2.977	0.216	1380	2.888	9.54×10^{-3}
530	2.956	0.638	960	2.978	0.210	1390	2.885	8.02×10^{-3}
540	2.969	0.615	970	2.979	0.204	1400	2.882	6.64×10^{-3}
550	2.980	0.591	980	2.980	0.198	1410	2.878	5.41×10^{-3}
560	2.988	0.568	990	2.981	0.191	1420	2.875	4.31×10^{-3}
570	2.994	0.545	1000	2.982	0.185	1430	2.872	3.34×10^{-3}
580	2.997	0.523	1010	2.982	0.178	1440	2.869	2.50×10^{-3}
590	2.999	0.503	1020	2.982	0.172	1450	2.865	1.79×10^{-3}
600	3.000	0.483	1030	2.982	0.165	1460	2.862	1.20×10^{-3}
610	2.999	0.465	1040	2.982	0.158	1470	2.860	0
620	2.998	0.448	1050	2.982	0.152			

Table 8.97 Optical constants of $Cu_2ZnSn(S_xSe_{1-x})_4$ ($x = 0.6$) calculated by the Tauc-Lorentz model

λ (nm)	n	k	λ (nm)	n	k	λ (nm)	n	k
300	2.886	1.027	600	2.944	0.423	1000	2.942	0.141
305	2.897	0.984	610	2.941	0.408	1010	2.940	0.134
310	2.905	0.941	620	2.938	0.394	1020	2.939	0.127
315	2.908	0.898	630	2.935	0.382	1030	2.937	0.120
320	2.906	0.856	640	2.932	0.371	1040	2.935	0.113
325	2.899	0.816	650	2.929	0.361	1050	2.933	0.106
330	2.888	0.779	660	2.926	0.352	1060	2.930	9.95×10^{-2}
335	2.873	0.747	670	2.923	0.343	1070	2.928	9.31×10^{-2}
340	2.855	0.720	680	2.920	0.336	1080	2.925	8.69×10^{-2}
345	2.836	0.699	690	2.918	0.329	1090	2.922	8.10×10^{-2}
350	2.817	0.683	700	2.916	0.323	1100	2.919	7.53×10^{-2}
355	2.800	0.670	710	2.915	0.317	1110	2.915	6.98×10^{-2}
360	2.784	0.660	720	2.914	0.312	1120	2.912	6.45×10^{-2}
365	2.769	0.654	730	2.913	0.306	1130	2.908	5.95×10^{-2}
370	2.755	0.650	740	2.913	0.302	1140	2.905	5.46×10^{-2}

(continued)

Table 8.97 (continued)

λ (nm)	n	k	λ (nm)	n	k	λ (nm)	n	k
375	2.743	0.649	750	2.913	0.297	1150	2.901	5.01×10^{-2}
380	2.733	0.649	760	2.913	0.292	1160	2.897	4.57×10^{-2}
385	2.725	0.651	770	2.914	0.287	1170	2.893	4.16×10^{-2}
390	2.719	0.655	780	2.915	0.283	1180	2.889	3.77×10^{-2}
395	2.715	0.659	790	2.917	0.278	1190	2.885	3.40×10^{-2}
400	2.714	0.664	800	2.918	0.273	1200	2.881	3.06×10^{-2}
410	2.716	0.674	810	2.920	0.268	1210	2.877	2.73×10^{-2}
420	2.725	0.683	820	2.922	0.262	1220	2.873	2.43×10^{-2}
430	2.740	0.689	830	2.924	0.257	1230	2.869	2.15×10^{-2}
440	2.759	0.692	840	2.926	0.251	1240	2.865	1.88×10^{-2}
450	2.782	0.691	850	2.928	0.246	1250	2.861	1.64×10^{-2}
460	2.806	0.685	860	2.930	0.240	1260	2.857	1.42×10^{-2}
470	2.829	0.675	870	2.932	0.234	1270	2.853	1.21×10^{-2}
480	2.851	0.660	880	2.933	0.227	1280	2.850	1.02×10^{-2}
490	2.871	0.643	890	2.935	0.221	1290	2.846	8.54×10^{-3}
500	2.889	0.624	900	2.937	0.215	1300	2.842	7.01×10^{-3}
510	2.904	0.603	910	2.938	0.208	1310	2.838	5.65×10^{-3}
520	2.917	0.581	920	2.940	0.201	1320	2.835	4.44×10^{-3}
530	2.927	0.559	930	2.941	0.194	1330	2.831	3.39×10^{-3}
540	2.935	0.537	940	2.942	0.186	1340	2.828	2.49×10^{-3}
550	2.940	0.515	950	2.943	0.179	1350	2.824	1.74×10^{-3}
560	2.944	0.495	960	2.943	0.171	1360	2.821	1.13×10^{-3}
570	2.945	0.475	970	2.943	0.164	1370	2.818	0
580	2.946	0.456	980	2.943	0.156			
590	2.945	0.439	990	2.942	0.149			

Table 8.98 Optical constants of $Cu_2ZnSn(S_xSe_{1-x})_4$ ($x = 0.8$) calculated by the Tauc-Lorentz model

λ (nm)	n	k	λ (nm)	n	k	λ (nm)	n	k
300	2.879	0.953	570	2.891	0.414	940	2.902	0.142
305	2.887	0.909	580	2.890	0.399	950	2.901	0.134
310	2.890	0.865	590	2.887	0.385	960	2.900	0.126
315	2.888	0.822	600	2.885	0.373	970	2.898	0.118
320	2.880	0.781	610	2.882	0.361	980	2.895	0.110
325	2.868	0.744	620	2.879	0.351	990	2.893	0.103
330	2.851	0.712	630	2.876	0.342	1000	2.890	9.56×10^{-2}
335	2.832	0.686	640	2.873	0.334	1010	2.887	8.86×10^{-2}
340	2.812	0.666	650	2.870	0.327	1020	2.883	8.19×10^{-2}

(continued)

Table 8.98 (continued)

λ (nm)	n	k	λ (nm)	n	k	λ (nm)	n	k
345	2.794	0.651	660	2.868	0.320	1030	2.880	7.55×10^{-2}
350	2.777	0.640	670	2.867	0.314	1040	2.876	6.94×10^{-2}
355	2.762	0.632	680	2.865	0.309	1050	2.872	6.36×10^{-2}
360	2.749	0.627	690	2.865	0.303	1060	2.868	5.81×10^{-2}
365	2.737	0.624	700	2.865	0.299	1070	2.864	5.29×10^{-2}
370	2.727	0.623	710	2.865	0.294	1080	2.860	4.79×10^{-2}
375	2.719	0.623	720	2.865	0.290	1090	2.855	4.33×10^{-2}
380	2.713	0.625	730	2.867	0.285	1100	2.851	3.89×10^{-2}
385	2.710	0.627	740	2.868	0.280	1110	2.847	3.48×10^{-2}
390	2.708	0.630	750	2.870	0.276	1120	2.842	3.10×10^{-2}
395	2.708	0.633	760	2.872	0.271	1130	2.838	2.74×10^{-2}
400	2.710	0.636	770	2.875	0.266	1140	2.833	2.41×10^{-2}
410	2.718	0.641	780	2.877	0.260	1150	2.829	2.11×10^{-2}
420	2.731	0.643	790	2.880	0.255	1160	2.824	1.83×10^{-2}
430	2.747	0.643	800	2.882	0.249	1170	2.820	1.57×10^{-2}
440	2.766	0.639	810	2.885	0.243	1180	2.816	1.34×10^{-2}
450	2.786	0.630	820	2.888	0.236	1190	2.812	1.12×10^{-2}
460	2.806	0.618	830	2.890	0.230	1200	2.807	9.32×10^{-3}
470	2.824	0.603	840	2.892	0.223	1210	2.803	7.60×10^{-3}
480	2.840	0.586	850	2.895	0.216	1220	2.799	6.08×10^{-3}
490	2.854	0.567	860	2.897	0.208	1230	2.795	4.74×10^{-3}
500	2.865	0.547	870	2.899	0.201	1240	2.792	3.59×10^{-3}
510	2.875	0.526	880	2.901	0.193	1250	2.788	2.61×10^{-3}
520	2.882	0.506	890	2.902	0.184	1260	2.784	1.79×10^{-3}
530	2.887	0.486	900	2.903	0.176	1270	2.781	1.14×10^{-3}
540	2.890	0.466	910	2.904	0.168	1280	2.777	0
550	2.892	0.448	920	2.904	0.159			
560	2.892	0.430	930	2.903	0.151			

8.2.32 $Cu_2ZnGeSe_4$

Data: unpublished results of S. Fujimoto, S. Kim and H. Tampo. The optical data of a polycrystalline $Cu_2ZnGeSe_4$ layer (Cu:Zn:Ge:Se = 2.00:1.11:0.96:3.93), prepared by a single co-evaporation process at a low temperature (200 °C) and the following thermal annealing at 500–550 °C under $GeSe_2$ + Se atmosphere, are shown. The preparation and characterization results are described in [34] (Fig. 8.32, Tables 8.99 and 8.100).

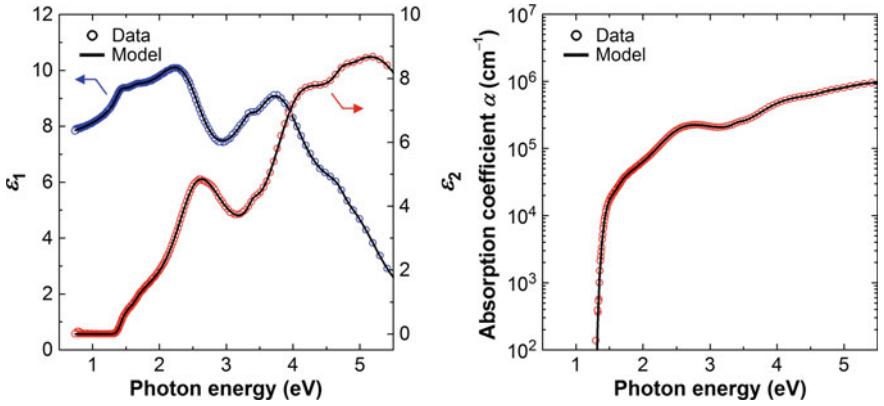


Fig. 8.32 Dielectric function and absorption coefficient of $Cu_2ZnGeSe_4$ at room temperature. The open circles show the experimental data and the solid lines indicate the calculation result obtained from the parameterization assuming the Tauc-Lorentz model [(8.1) and (8.2)]

Table 8.99 Tauc-Lorentz parameters of (8.1) and (8.2) for $Cu_2ZnGeSe_4$

Peak	A (eV)	C (eV)	E_0 (eV)	E_g (eV)	$\varepsilon_1(\infty)$
$j = 1$	9.595	0.256	1.418	1.296	1.319
$j = 2$	20.178	0.892	1.556	1.358	0
$j = 3$	8.758	0.216	1.593	1.586	0
$j = 4$	28.586	1.056	2.535	1.583	0
$j = 5$	0.724	0.253	3.400	2.032	0
$j = 6$	54.292	1.310	3.995	2.585	0
$j = 7$	0.350	0.321	4.736	1.998	0
$j = 8$	91.874	2.053	5.140	3.309	0
$j = 9$	204.022	1.204	6.253	5.506	0
$j = 10$	647.965	0.040	6.759	6.577	0

Table 8.100 Optical constants of $Cu_2ZnGeSe_4$. The optical data obtained by S. Fujimoto, S. Kim and H. Tampo are shown

λ (nm)	n	k	λ (nm)	n	k	λ (nm)	n	k
300	3.030	1.257	540	3.217	0.533	880	3.047	4.44×10^{-2}
305	3.070	1.211	550	3.214	0.491	890	3.036	3.13×10^{-2}
310	3.104	1.159	560	3.209	0.455	900	3.025	2.06×10^{-2}
315	3.130	1.103	570	3.199	0.423	910	3.012	1.34×10^{-2}
320	3.149	1.041	580	3.189	0.394	920	3.000	7.63×10^{-3}
325	3.158	0.977	590	3.178	0.370	930	2.989	2.52×10^{-3}
330	3.154	0.911	600	3.166	0.351	940	2.979	0
335	3.135	0.851	610	3.157	0.332	950	2.969	0
340	3.105	0.803	620	3.146	0.317	960	2.959	0
345	3.072	0.767	630	3.138	0.304	970	2.951	0
350	3.047	0.743	640	3.130	0.288	980	2.943	0

(continued)

Table 8.100 (continued)

λ (nm)	n	k	λ (nm)	n	k	λ (nm)	n	k
355	3.021	0.729	650	3.122	0.278	990	2.936	0
360	3.007	0.719	660	3.115	0.268	1000	2.929	0
365	3.002	0.703	670	3.112	0.257	1010	2.924	0
370	2.993	0.678	680	3.106	0.247	1020	2.920	0
375	2.965	0.658	690	3.103	0.240	1030	2.914	0
380	2.935	0.652	700	3.100	0.228	1040	2.909	0
385	2.917	0.644	710	3.098	0.220	1050	2.903	0
390	2.892	0.646	720	3.096	0.212	1060	2.900	0
395	2.872	0.651	730	3.095	0.201	1070	2.895	0
400	2.856	0.661	740	3.095	0.189	1080	2.892	0
410	2.828	0.690	750	3.090	0.176	1090	2.889	0
420	2.820	0.727	760	3.086	0.167	1100	2.886	0
430	2.834	0.760	770	3.081	0.157	1110	2.882	0
440	2.865	0.791	780	3.076	0.148	1120	2.879	0
450	2.911	0.808	790	3.073	0.139	1130	2.876	0
460	2.959	0.807	800	3.068	0.133	1140	2.873	0
470	3.005	0.802	810	3.065	0.124	1150	2.871	0
480	3.055	0.791	820	3.065	0.118	1160	2.868	0
490	3.105	0.761	830	3.065	0.107	1170	2.867	0
500	3.148	0.721	840	3.064	9.82×10^{-2}	1180	2.863	0
510	3.179	0.676	850	3.062	8.46×10^{-2}	1190	2.862	0
520	3.201	0.627	860	3.059	7.27×10^{-2}	1200	2.859	0
530	3.210	0.580	870	3.054	5.94×10^{-2}			

8.2.33 Cu_2SnSe_3

Two optical data sets extracted from cubic and monoclinic Cu_2SnSe_3 polycrystals are summarized:

(i) Cubic Cu_2SnSe_3: Y. Hirate, H. Tampo, S. Minoura, H. Kadowaki, A. Nakane, K. M. Kim, H. Shibata, S. Niki and H. Fujiwara [32].
(ii) Monoclinic Cu_2SnSe_3: S. G. Choi, J. Kang, J. Li, H. Haneef, N. J. Podraza, C. Beall, S.-H. Wei, S. T. Christensen and I. L. Repins [35].

The optical data have been extracted from Cu_2SnSe_3 layers prepared by a single co-evaporation process at 370 °C (cubic) and 455 °C (monoclinic), and the composition of the cubic phase is Cu:Sn:Se = 2.06:0.99:2.95. The optical functions parameterized by the Tauc-Lorentz model are summarized. For the dielectric function of the cubic phase, the contribution of the free carrier absorption has been removed based on the analysis using the Drude model (Fig. 8.33, Tables 8.101, 8.102, 8.103 and 8.104).

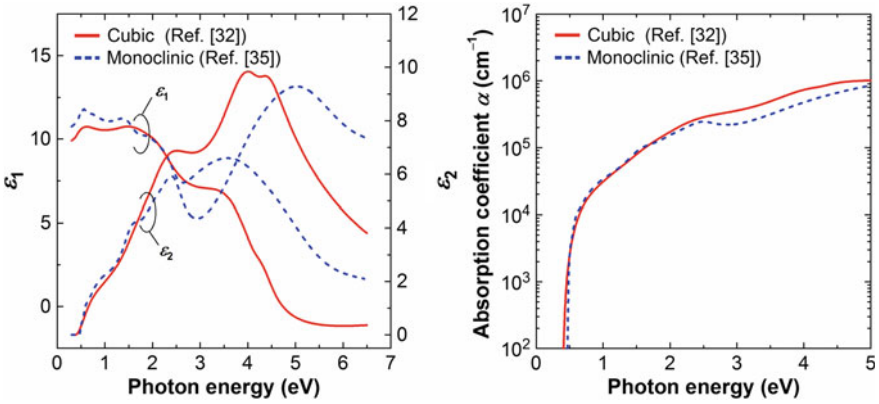


Fig. 8.33 Dielectric functions and absorptions coefficient of Cu_2SnSe_3 at room temperature. The solid lines indicate the calculation result obtained from the parameterization assuming the Tauc-Lorentz model [(8.1) and (8.2)]

Table 8.101 Tauc-Lorentz parameters of (8.1) and (8.2) for Cu_2SnSe_3 (cubic). The model parameters reported by Hirate et al. are summarized

Peak	A (eV)	C (eV)	E_0 (eV)	E_g (eV)	$\varepsilon_1(\infty)$
$j = 1$	5.268	1.084	0.684	0.387	1.294
$j = 2$	7.194	1.491	1.768	0.411	0
$j = 3$	28.799	1.467	2.257	1.249	0
$j = 4$	89.533	4.499	3.216	1.908	0
$j = 5$	49.140	1.508	3.917	2.517	0
$j = 6$	93.356	0.544	4.333	4.093	0

Table 8.102 Tauc-Lorentz parameters of (8.1) and (8.2) for Cu_2SnSe_3 (monoclinic). The model parameters reported by Choi et al. are summarized

Peak	A (eV)	C (eV)	E_0 (eV)	E_g (eV)	$\varepsilon_1(\infty)$
$j = 1$	2.84	0.06	0.49	0.46	1.0
$j = 2$	0.94	0.12	0.58	0.46	0
$j = 3$	9.41	1.13	0.75	0.46	0
$j = 4$	1.55	0.53	1.57	0.46	0
$j = 5$	3.21	0.90	2.10	0.46	0
$j = 6$	1.84	0.57	2.44	0.46	0
$j = 7$	7.16	2.12	4.20	0.46	0
$j = 8$	16.06	2.56	5.21	0.46	0
$j = 9$	33.09	5.12	8.23	0.46	0

Table 8.103 Optical constants of Cu_2SnSe_3 (cubic) calculated by the Tauc-Lorentz model

λ (nm)	n	k	λ (nm)	n	k	λ (nm)	n	k
300	2.605	1.869	750	3.323	0.620	1400	3.261	0.267
305	2.663	1.845	760	3.324	0.605	1420	3.262	0.263
310	2.721	1.809	770	3.324	0.592	1440	3.263	0.258
315	2.774	1.766	780	3.324	0.578	1460	3.263	0.254
320	2.820	1.718	790	3.323	0.565	1480	3.264	0.250
325	2.858	1.666	800	3.323	0.553	1500	3.265	0.246
330	2.889	1.614	810	3.322	0.541	1520	3.266	0.242
335	2.911	1.562	820	3.321	0.529	1540	3.267	0.237
340	2.927	1.512	830	3.319	0.518	1560	3.268	0.233
345	2.937	1.466	840	3.318	0.507	1580	3.269	0.229
350	2.943	1.423	850	3.316	0.496	1600	3.270	0.225
355	2.944	1.385	860	3.314	0.486	1620	3.271	0.220
360	2.944	1.351	870	3.312	0.477	1640	3.272	0.216
365	2.941	1.320	880	3.310	0.467	1660	3.273	0.212
370	2.937	1.294	890	3.307	0.459	1680	3.274	0.208
375	2.933	1.271	900	3.305	0.450	1700	3.274	0.203
380	2.929	1.251	910	3.303	0.442	1720	3.275	0.199
385	2.925	1.235	920	3.300	0.435	1740	3.276	0.194
390	2.921	1.220	930	3.297	0.428	1760	3.277	0.190
395	2.918	1.208	940	3.295	0.421	1780	3.277	0.186
400	2.916	1.198	950	3.292	0.415	1800	3.278	0.181
410	2.914	1.182	960	3.290	0.408	1820	3.279	0.177
420	2.917	1.172	970	3.288	0.403	1840	3.279	0.173
430	2.923	1.164	980	3.285	0.398	1860	3.279	0.168
440	2.933	1.159	990	3.283	0.393	1880	3.280	0.164
450	2.948	1.155	1000	3.282	0.388	1900	3.280	0.160
460	2.965	1.151	1010	3.280	0.383	1920	3.280	0.155
470	2.986	1.146	1020	3.278	0.379	1940	3.280	0.151
480	3.010	1.140	1030	3.277	0.374	1960	3.280	0.147
490	3.035	1.132	1040	3.276	0.370	1980	3.280	0.142
500	3.063	1.122	1050	3.275	0.366	2000	3.280	0.138
510	3.091	1.108	1060	3.273	0.362	2050	3.280	0.127
520	3.119	1.091	1070	3.272	0.358	2100	3.278	0.117
530	3.145	1.071	1080	3.271	0.354	2150	3.277	0.107
540	3.170	1.049	1090	3.270	0.350	2200	3.274	9.73×10^{-2}
550	3.193	1.025	1100	3.269	0.346	2250	3.272	8.79×10^{-2}
560	3.213	1.000	1110	3.268	0.343	2300	3.269	7.89×10^{-2}
570	3.231	0.974	1120	3.267	0.339	2350	3.265	7.03×10^{-2}
580	3.246	0.947	1130	3.267	0.336	2400	3.262	6.22×10^{-2}

(continued)

Table 8.103 (continued)

λ (nm)	n	k	λ (nm)	n	k	λ (nm)	n	k
590	3.259	0.921	1140	3.266	0.333	2450	3.257	5.45×10^{-2}
600	3.269	0.895	1150	3.265	0.330	2500	3.253	4.73×10^{-2}
610	3.278	0.870	1160	3.264	0.326	2550	3.248	4.06×10^{-2}
620	3.284	0.847	1170	3.264	0.323	2600	3.243	3.44×10^{-2}
630	3.290	0.824	1180	3.263	0.320	2650	3.238	2.87×10^{-2}
640	3.294	0.804	1190	3.263	0.318	2700	3.233	2.35×10^{-2}
650	3.298	0.785	1200	3.262	0.315	2750	3.228	1.89×10^{-2}
660	3.302	0.766	1220	3.261	0.309	2800	3.222	1.48×10^{-2}
670	3.306	0.748	1240	3.261	0.304	2850	3.217	1.12×10^{-2}
680	3.309	0.731	1260	3.260	0.299	2900	3.211	8.10×10^{-3}
690	3.313	0.713	1280	3.260	0.294	2950	3.206	5.56×10^{-3}
700	3.315	0.697	1300	3.260	0.289	3000	3.201	3.53×10^{-3}
710	3.318	0.680	1320	3.260	0.285	3050	3.196	2.00×10^{-3}
720	3.319	0.664	1340	3.260	0.280	3100	3.191	0
730	3.321	0.649	1360	3.260	0.276			
740	3.322	0.634	1380	3.261	0.271			

Table 8.104 Optical constants of Cu_2SnSe_3 (monoclinic) calculated by the Tauc-Lorentz model

λ (nm)	n	k	λ (nm)	n	k	λ (nm)	n	k
300	3.096	1.256	720	3.273	0.652	1280	3.353	0.327
305	3.110	1.216	730	3.278	0.649	1300	3.356	0.323
310	3.120	1.176	740	3.284	0.646	1320	3.358	0.319
315	3.128	1.138	750	3.292	0.643	1340	3.360	0.315
320	3.132	1.100	760	3.302	0.638	1360	3.363	0.311
325	3.135	1.064	770	3.312	0.633	1380	3.366	0.307
330	3.134	1.029	780	3.323	0.626	1400	3.368	0.303
335	3.131	0.996	790	3.334	0.617	1420	3.371	0.298
340	3.127	0.965	800	3.345	0.607	1440	3.374	0.294
345	3.120	0.936	810	3.355	0.596	1460	3.376	0.289
350	3.112	0.909	820	3.363	0.583	1480	3.379	0.285
355	3.102	0.884	830	3.371	0.569	1500	3.381	0.280
360	3.092	0.861	840	3.377	0.555	1520	3.384	0.275
365	3.080	0.841	850	3.381	0.541	1540	3.386	0.270
370	3.067	0.822	860	3.384	0.527	1560	3.388	0.265
375	3.054	0.805	870	3.386	0.514	1580	3.390	0.260
380	3.040	0.790	880	3.387	0.501	1600	3.392	0.255

(continued)

Table 8.104 (continued)

λ (nm)	n	k	λ (nm)	n	k	λ (nm)	n	k
385	3.026	0.778	890	3.387	0.488	1620	3.394	0.250
390	3.012	0.767	900	3.386	0.477	1640	3.395	0.245
395	2.997	0.758	910	3.385	0.466	1660	3.397	0.240
400	2.982	0.752	920	3.383	0.456	1680	3.398	0.235
410	2.953	0.744	930	3.381	0.447	1700	3.399	0.230
420	2.924	0.745	940	3.378	0.438	1720	3.400	0.226
430	2.898	0.754	950	3.376	0.430	1740	3.401	0.221
440	2.875	0.771	960	3.373	0.423	1760	3.402	0.216
450	2.858	0.798	970	3.371	0.416	1780	3.403	0.212
460	2.850	0.833	980	3.368	0.410	1800	3.403	0.208
470	2.856	0.874	990	3.366	0.404	1820	3.404	0.204
480	2.877	0.915	1000	3.363	0.399	1840	3.404	0.200
490	2.915	0.951	1010	3.361	0.394	1860	3.405	0.196
500	2.965	0.972	1020	3.359	0.390	1880	3.405	0.193
510	3.019	0.977	1030	3.357	0.386	1900	3.406	0.189
520	3.069	0.965	1040	3.355	0.382	1920	3.407	0.186
530	3.110	0.944	1050	3.354	0.378	1940	3.408	0.183
540	3.141	0.918	1060	3.352	0.375	1960	3.409	0.181
550	3.163	0.893	1070	3.351	0.372	1980	3.411	0.178
560	3.181	0.870	1080	3.350	0.369	2000	3.413	0.175
570	3.195	0.850	1090	3.349	0.366	2050	3.420	0.167
580	3.208	0.831	1100	3.348	0.364	2100	3.428	0.155
590	3.220	0.812	1110	3.347	0.361	2150	3.434	0.139
600	3.231	0.795	1120	3.347	0.359	2200	3.436	0.121
610	3.241	0.777	1130	3.346	0.356	2250	3.433	0.104
620	3.249	0.759	1140	3.346	0.354	2300	3.428	8.98×10^{-2}
630	3.255	0.742	1150	3.346	0.352	2350	3.423	7.91×10^{-2}
640	3.260	0.726	1160	3.346	0.350	2400	3.420	7.02×10^{-2}
650	3.263	0.711	1170	3.346	0.348	2450	3.420	5.99×10^{-2}
660	3.265	0.697	1180	3.346	0.346	2500	3.420	4.46×10^{-2}
670	3.266	0.685	1190	3.347	0.344	2550	3.414	2.53×10^{-2}
680	3.266	0.675	1200	3.347	0.342	2600	3.399	9.72×10^{-3}
690	3.267	0.667	1220	3.348	0.338	2650	3.382	1.81×10^{-3}
700	3.268	0.661	1240	3.350	0.335	2700	3.368	0
710	3.270	0.656	1260	3.351	0.331			

8.2.34 In_2S_3

Data from S. Marsillac, N. Barreau, H. Khatri, J. Li, D. Sainju, A. Parikh, N. J. Podraza and R. W. Collins [36]. The optical data of a polycrystalline In_2S_3 layer prepared by co-evaporation at 200 °C are shown (Fig. 8.34, Tables 8.105 and 8.106).

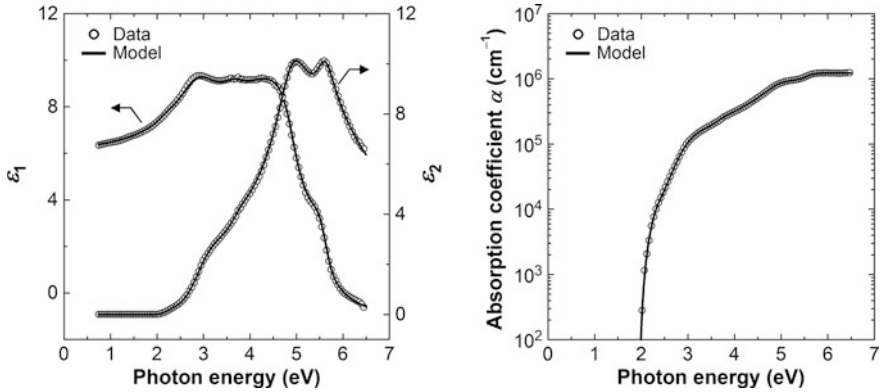


Fig. 8.34 Dielectric function and absorption coefficient of In_2S_3 at room temperature. The open circles show the reference data and the solid lines indicate the calculation result obtained from the parameterization assuming the Tauc-Lorentz model [(8.1) and (8.2)]

Table 8.105 Tauc-Lorentz parameters of (8.1) and (8.2) for In_2S_3

Peak	A (eV)	C (eV)	E_0 (eV)	E_g (eV)	$\varepsilon_1(\infty)$
$j = 1$	8.470	0.890	2.359	1.950	1.570
$j = 2$	63.324	1.467	3.014	2.394	0
$j = 3$	13.276	0.681	3.735	3.155	0
$j = 4$	142.697	3.045	4.869	3.145	0
$j = 5$	14.782	0.777	4.899	3.156	0
$j = 6$	47.434	0.481	5.584	4.868	0

Table 8.106 Optical constants of In_2S_3. The optical data obtained by S. Marsillac are shown

λ (nm)	n	k	λ (nm)	n	k	λ (nm)	n	k
300	3.140	0.837	540	2.820	3.88×10^{-2}	880	2.589	0
305	3.131	0.803	550	2.804	3.08×10^{-2}	890	2.587	0
310	3.124	0.773	560	2.788	2.34×10^{-2}	900	2.585	0
315	3.116	0.746	570	2.771	1.58×10^{-2}	910	2.582	0
320	3.104	0.720	580	2.757	1.09×10^{-2}	920	2.580	0
325	3.111	0.691	590	2.743	8.25×10^{-3}	930	2.578	0
330	3.112	0.670	600	2.732	5.01×10^{-3}	940	2.575	0
335	3.099	0.633	610	2.720	1.72×10^{-3}	950	2.573	0

(continued)

Table 8.106 (continued)

λ (nm)	n	k	λ (nm)	n	k	λ (nm)	n	k
340	3.091	0.606	620	2.709	0	960	2.571	0
345	3.092	0.585	630	2.699	0	970	2.570	0
350	3.083	0.565	640	2.690	0	980	2.567	0
355	3.075	0.547	650	2.681	0	990	2.566	0
360	3.069	0.530	660	2.672	0	1000	2.564	0
365	3.063	0.513	670	2.666	0	1010	2.562	0
370	3.059	0.497	680	2.660	0	1020	2.561	0
375	3.057	0.481	690	2.654	0	1030	2.559	0
380	3.056	0.468	700	2.648	0	1040	2.557	0
385	3.058	0.451	710	2.643	0	1050	2.556	0
390	3.061	0.434	720	2.639	0	1060	2.554	0
395	3.062	0.416	730	2.634	0	1070	2.553	0
400	3.065	0.399	740	2.630	0	1080	2.553	0
410	3.069	0.363	750	2.625	0	1090	2.552	0
420	3.070	0.320	760	2.622	0	1100	2.551	0
430	3.067	0.268	770	2.618	0	1110	2.550	0
440	3.053	0.221	780	2.615	0	1120	2.549	0
450	3.035	0.182	790	2.612	0	1130	2.549	0
460	3.008	0.154	800	2.608	0	1140	2.548	0
470	2.979	0.127	810	2.605	0	1150	2.547	0
480	2.948	0.106	820	2.603	0	1160	2.547	0
490	2.919	8.84×10^{-2}	830	2.600	0	1170	2.546	0
500	2.893	7.47×10^{-2}	840	2.598	0	1180	2.546	0
510	2.872	6.36×10^{-2}	850	2.596	0	1190	2.545	0
520	2.853	5.42×10^{-2}	860	2.594	0	1200	2.545	0
530	2.837	4.67×10^{-2}	870	2.592	0			

8.2.35 MoS_2

Data from A. R. Beal and H. P. Hughes [37]. The optical data of a MoS_2 single crystal are shown (Fig. 8.35, Tables 8.107 and 8.108).

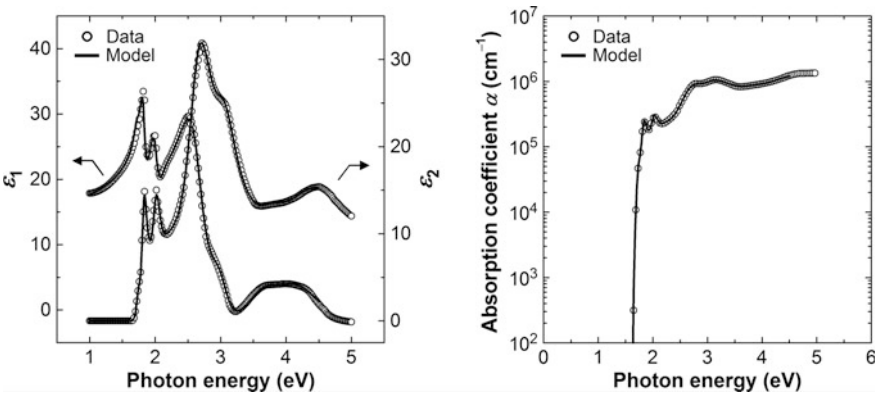


Fig. 8.35 Dielectric function and absorption coefficient of MoS_2 (single crystal) at room temperature. The open circles show the reference data and the solid lines indicate the calculation result obtained from the parameterization assuming the Tauc-Lorentz model [(8.1) and (8.2)]

Table 8.107 Tauc-Lorentz parameters of (8.1) and (8.2) for MoS_2 (single crystal)

Peak	A (eV)	C (eV)	E_0 (eV)	E_g (eV)	$\varepsilon_1(\infty)$
$j = 1$	82.008	0.105	1.729	1.630	1.770
$j = 2$	193.604	0.095	1.824	1.688	0
$j = 3$	106.419	0.163	2.007	1.760	0
$j = 4$	315.846	0.314	2.101	2.057	0
$j = 5$	175.565	0.490	2.655	1.962	0
$j = 6$	91.133	0.437	3.043	2.424	0
$j = 7$	57.615	0.820	3.844	2.732	0
$j = 8$	562.577	1.142	4.132	3.798	0

Table 8.108 Optical constants of MoS_2 (single crystal) calculated by the Tauc-Lorentz model

λ (nm)	n	k	λ (nm)	n	k	λ (nm)	n	k
300	3.052	2.321	540	5.101	1.096	880	4.527	0
305	3.037	2.287	550	5.009	1.062	890	4.508	0
310	3.021	2.270	560	4.928	1.040	900	4.490	0
315	3.010	2.264	570	4.845	1.033	910	4.474	0
320	3.002	2.261	580	4.753	1.062	920	4.458	0
325	2.995	2.260	590	4.680	1.165	930	4.443	0
330	2.986	2.258	600	4.716	1.344	940	4.429	0
335	2.963	2.257	610	4.945	1.453	950	4.416	0
340	2.925	2.272	620	5.196	1.314	960	4.403	0

(continued)

Table 8.108 (continued)

λ (nm)	n	k	λ (nm)	n	k	λ (nm)	n	k
345	2.883	2.310	630	5.234	1.059	970	4.391	0
350	2.845	2.372	640	5.104	0.919	980	4.380	0
355	2.819	2.457	650	4.959	0.950	990	4.369	0
360	2.811	2.560	660	4.928	1.133	1000	4.358	0
365	2.825	2.676	670	5.175	1.344	1010	4.349	0
370	2.865	2.800	680	5.640	1.188	1020	4.339	0
375	2.932	2.926	690	5.747	0.716	1030	4.330	0
380	3.028	3.048	700	5.584	0.449	1040	4.321	0
385	3.154	3.157	710	5.471	0.340	1050	4.313	0
390	3.306	3.243	720	5.408	0.217	1060	4.305	0
395	3.476	3.297	730	5.293	9.15×10^{-2}	1070	4.297	0
400	3.651	3.311	740	5.158	2.77×10^{-2}	1080	4.290	0
410	3.941	3.243	750	5.046	4.97×10^{-3}	1090	4.283	0
420	4.113	3.168	760	4.958	0	1100	4.276	0
430	4.267	3.182	770	4.891	0	1110	4.270	0
440	4.516	3.231	780	4.836	0	1120	4.263	0
450	4.871	3.206	790	4.788	0	1130	4.257	0
460	5.258	3.027	800	4.746	0	1140	4.251	0
470	5.565	2.694	810	4.709	0	1150	4.246	0
480	5.717	2.288	820	4.676	0	1160	4.240	0
490	5.717	1.906	830	4.646	0	1170	4.235	0
500	5.622	1.602	840	4.618	0	1180	4.230	0
510	5.484	1.385	850	4.593	0	1190	4.225	0
520	5.342	1.242	860	4.569	0	1200	4.220	0
530	5.212	1.151	870	4.547	0			

8.2.36 *$MoSe_2$ (Polycrystal)*

Data from M. Richter, C. Schubbert, P. Eraerds, I. Riedel, J. Keller, J. Parisi, T. Dalibor, and A. Avellan-Hampe [38]. The optical data have been extracted from a $MoSe_2$ layer formed by selenization of a Mo layer during rapid thermal processing (Tables 8.109 and 8.110).

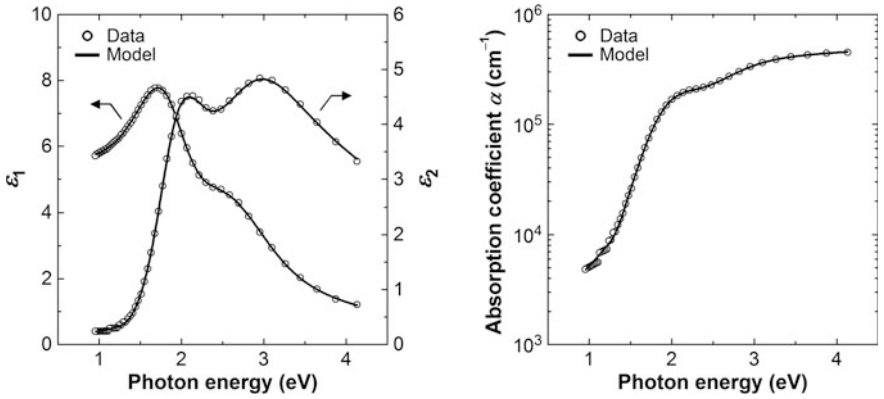


Fig. 8.36 Dielectric function and absorption coefficient of $MoSe_2$ (polycrystal) at room temperature. The open circles show the reference data and the solid lines indicate the calculation result obtained from the parameterization assuming the Tauc-Lorentz model [(8.1) and (8.2)]

Table 8.109 Tauc-Lorentz parameters of (8.1) and (8.2) for $MoSe_2$ (polycrystal)

Peak	A (eV)	C (eV)	E_0 (eV)	E_g (eV)	$\varepsilon_1(\infty)$
$j = 1$	22.010	0.855	1.915	1.250	1.448
$j = 2$	103.004	3.880	2.281	2.276	0
$j = 3$	1.676	5.317	2.910	0.107	0
$j = 4$	9.249	1.646	2.936	1.002	0

Table 8.110 Optical constants of $MoSe_2$ (polycrystal) calculated by the Tauc-Lorentz model

λ (nm)	n	k	λ (nm)	n	k	λ (nm)	n	k
300	1.544	1.091	540	2.393	0.897	880	2.617	0.110
305	1.566	1.101	550	2.416	0.899	890	2.604	0.103
310	1.590	1.111	560	2.443	0.900	900	2.592	9.63×10^{-2}
315	1.613	1.120	570	2.475	0.898	910	2.581	9.07×10^{-2}
320	1.637	1.129	580	2.510	0.893	920	2.570	8.58×10^{-2}
325	1.661	1.137	590	2.547	0.883	930	2.559	8.16×10^{-2}
330	1.686	1.145	600	2.585	0.868	940	2.549	7.79×10^{-2}
335	1.711	1.152	610	2.624	0.848	950	2.539	7.48×10^{-2}
340	1.737	1.159	620	2.661	0.823	960	2.530	7.23×10^{-2}
345	1.763	1.165	630	2.696	0.793	970	2.521	7.02×10^{-2}
350	1.789	1.170	640	2.728	0.759	980	2.513	6.85×10^{-2}
355	1.816	1.174	650	2.756	0.721	990	2.506	6.72×10^{-2}
360	1.844	1.177	660	2.780	0.680	1000	2.499	6.62×10^{-2}
365	1.871	1.179	670	2.798	0.638	1010	2.493	6.52×10^{-2}
370	1.900	1.180	680	2.812	0.595	1020	2.487	6.43×10^{-2}
375	1.928	1.180	690	2.820	0.552	1030	2.481	6.34×10^{-2}
380	1.956	1.178	700	2.824	0.510	1040	2.476	6.25×10^{-2}

(continued)

Table 8.110 (continued)

λ (nm)	n	k	λ (nm)	n	k	λ (nm)	n	k
385	1.984	1.175	710	2.825	0.470	1050	2.471	6.17×10^{-2}
390	2.012	1.170	720	2.821	0.431	1060	2.466	6.08×10^{-2}
395	2.039	1.164	730	2.815	0.395	1070	2.462	6.01×10^{-2}
400	2.066	1.157	740	2.807	0.361	1080	2.457	5.93×10^{-2}
410	2.117	1.138	750	2.796	0.330	1090	2.453	5.86×10^{-2}
420	2.164	1.114	760	2.784	0.302	1100	2.449	5.79×10^{-2}
430	2.205	1.086	770	2.771	0.275	1110	2.445	5.73×10^{-2}
440	2.240	1.057	780	2.758	0.251	1120	2.442	5.66×10^{-2}
450	2.269	1.027	790	2.743	0.230	1130	2.438	5.60×10^{-2}
460	2.292	0.998	800	2.729	0.210	1140	2.435	5.55×10^{-2}
470	2.310	0.971	810	2.714	0.192	1150	2.432	5.49×10^{-2}
480	2.324	0.948	820	2.699	0.176	1160	2.429	5.44×10^{-2}
490	2.335	0.928	830	2.685	0.162	1170	2.426	5.39×10^{-2}
500	2.344	0.914	840	2.670	0.149	1180	2.423	5.34×10^{-2}
510	2.353	0.903	850	2.656	0.138	1190	2.420	5.30×10^{-2}
520	2.364	0.897	860	2.643	0.127	1200	2.418	5.26×10^{-2}
530	2.376	0.895	870	2.629	0.118			

8.2.37 $MoSe_2$ (Single Crystal)

Data from A. R. Beal and H. P. Hughes [37]. The optical data of a $MoSe_2$ single crystal are shown. Unlike a $MoSe_2$ polycrystalline layer (Fig. 8.36), the light absorption is negligible below $E < 1.3$ eV in a $MoSe_2$ single crystal (Fig. 8.37, Tables 8.111 and 8.112).

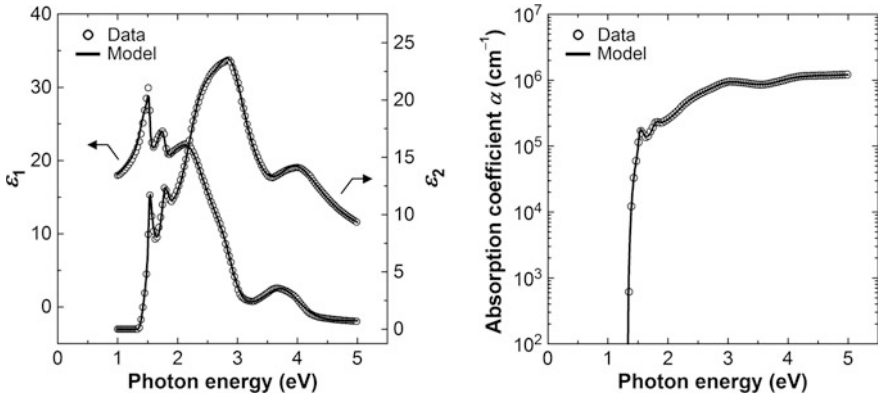


Fig. 8.37 Dielectric function and absorption coefficient of $MoSe_2$ (single crystal) at room temperature. The open circles show the reference data and the solid lines indicate the calculation result obtained from the parameterization assuming the Tauc-Lorentz model [(8.1) and (8.2)]

Table 8.111 Tauc-Lorentz parameters of (8.1) and (8.2) for $MoSe_2$ (single crystal)

Peak	A (eV)	C (eV)	E_0 (eV)	E_g (eV)	$\varepsilon_1(\infty)$
$j = 1$	109.854	0.255	1.444	1.325	1.292
$j = 2$	133.264	0.072	1.525	1.441	0
$j = 3$	25.093	0.171	1.777	1.456	0
$j = 4$	140.873	1.224	2.175	1.490	0
$j = 5$	189.347	0.813	2.218	2.041	0
$j = 6$	27.496	0.625	2.879	1.721	0
$j = 7$	119.412	1.062	3.875	3.040	0
$j = 8$	72.551	3.313	5.199	3.432	0

Table 8.112 Optical constants of $MoSe_2$ (single crystal) calculated by the Tauc-Lorentz model

λ (nm)	n	k	λ (nm)	n	k	λ (nm)	n	k
300	2.605	2.637	540	4.904	1.927	880	5.058	0.144
305	2.685	2.615	550	4.936	1.812	890	4.995	9.16×10^{-2}
310	2.755	2.580	560	4.951	1.700	900	4.930	5.20×10^{-2}
315	2.810	2.535	570	4.950	1.595	910	4.866	2.47×10^{-2}
320	2.847	2.485	580	4.936	1.500	920	4.806	8.41×10^{-3}
325	2.865	2.437	590	4.911	1.418	930	4.752	1.01×10^{-3}
330	2.864	2.398	600	4.881	1.351	940	4.706	0
335	2.851	2.373	610	4.850	1.298	950	4.669	0
340	2.830	2.365	620	4.821	1.254	960	4.636	0
345	2.807	2.375	630	4.790	1.219	970	4.607	0
350	2.787	2.402	640	4.759	1.197	980	4.580	0
355	2.775	2.443	650	4.731	1.193	990	4.556	0
360	2.773	2.496	660	4.716	1.207	1000	4.533	0
365	2.783	2.557	670	4.726	1.237	1010	4.513	0
370	2.806	2.622	680	4.778	1.267	1020	4.494	0
375	2.841	2.691	690	4.873	1.260	1030	4.476	0
380	2.889	2.760	700	4.968	1.184	1040	4.459	0
385	2.949	2.828	710	5.008	1.063	1050	4.443	0
390	3.022	2.892	720	4.986	0.952	1060	4.428	0
395	3.108	2.950	730	4.932	0.878	1070	4.414	0
400	3.205	3.000	740	4.872	0.842	1080	4.401	0
410	3.428	3.065	750	4.818	0.836	1090	4.388	0
420	3.669	3.067	760	4.777	0.856	1100	4.376	0
430	3.896	3.005	770	4.755	0.899	1110	4.365	0
440	4.081	2.899	780	4.762	0.967	1120	4.354	0
450	4.217	2.780	790	4.823	1.060	1130	4.343	0
460	4.318	2.671	800	4.990	1.145	1140	4.333	0

(continued)

Table 8.112 (continued)

λ (nm)	n	k	λ (nm)	n	k	λ (nm)	n	k
470	4.402	2.578	810	5.271	1.078	1150	4.324	0
480	4.481	2.495	820	5.424	0.794	1160	4.315	0
490	4.562	2.416	830	5.371	0.556	1170	4.306	0
500	4.643	2.334	840	5.285	0.428	1180	4.298	0
510	4.722	2.244	850	5.219	0.344	1190	4.290	0
520	4.795	2.146	860	5.165	0.273	1200	4.282	0
530	4.857	2.039	870	5.114	0.206			

References

1. G.E. Jellison Jr., Opt. Mat. **1**, 151 (1992)
2. C.M. Herzinger, University of Nebraska-Lincoln (unpublished) (1994)
3. E.D. Palik (ed.), *Handbook of Optical Constants of Solids* (Academic, New York, 1985)
4. D.E. Aspnes, A.A. Studna, Phys. Rev. B **27**, 985 (1983)
5. N.P. Barnes, M.S. Piltch, J. Opt. Soc. Am. **69**, 178 (1979)
6. W.C. Dash, R. Newman, Phys. Rev. **99**, 1151 (1955)
7. B. Johs, C.M. Herzinger, J.H. Dinan, A. Cornfeld, J.B. Benson, Thin Solid Films **313–314**, 137 (1998)
8. C.M. Herzinger, B. Johs, W.A. McGahan, J.A. Woollam, W. Paulson, J. Appl. Phys. **83**, 3323 (1998)
9. G. Dingemans, W.M.M. Kessels, J. Vac. Sci. Technol. A **30**, 040802 (2012)
10. T. Koida, Y. Kamikawa-Shimizu, A. Yamada, H. Shibata, S. Niki, IEEE J. Photovolt. **5**, 956 (2015)
11. G.E. Jellison Jr., F.A. Modine, P. Doshi, A. Rohatgi, Thin Solid Films **313–314**, 193 (1998)
12. R.W. Collins, K. Vedam, in *Encyclopedia of Applied Physics*, vol. 12 (Wiley-VCH, Berlin, 1995), pp. 285–336
13. S. Kageyama, M. Akagawa, H. Fujiwara, Phys. Rev. B **83**, 195205 (2011)
14. M. Sato, S.W. King, W.A. Lanford, P. Henry, T. Fujiseki, H. Fujiwara, J. Non-Cryst. Solids **440**, 49–58 (2016)
15. T. Yuguchi, Y. Kanie, N. Matsuki, H. Fujiwara, J. Appl. Phys. **111**, 083509 (2012)
16. C.M. Herzinger, H. Yao, P.G. Snyder, F.G. Celii, Y.-C. Kao, B. Johs, J.A. Woollam, J. Appl. Phys. **77**, 4677 (1995)
17. D.S. Gerber, G.N. Maracas, IEEE J. Quant. Elect. **29**, 2589 (1993)
18. J.B. Theeten, D.E. Aspnes, R.P.H. Chang, J. Appl. Phys. **49**, 6097 (1978)
19. A.N. Pikhtin, A.D. Yas'kov, Sov. Phys. Semicond. **12**, 622 (1978)
20. J.R. Dixon, J.M. Ellis, Phys. Rev. **123**, 1560 (1961)
21. D.F. Nelson, E.H. Turner, J. Appl. Phys. **39**, 3337 (1968)
22. W.L. Bond, J. Appl. Phys. **36**, 1674 (1965)
23. B.O. Seraphin, H.E. Bennet, in *Semiconductors and Semimetals*, vol. 3 (Academic, New York, 1967), p. 219
24. C.M. Herzinger, P.G. Snyder, B. Johs, J.A. Woollam, J. Appl. Phys. **77**, 1715 (1995)
25. S. Zollner, C. Lin, E. Schoenherr, A. Boehringer, M. Cardona, J. Appl. Phys. **66**, 383 (1989)
26. S. Adachi, *Optical Constants of Crystalline and Amorphous Semiconductors: Numerical Data and Graphical Information* (Kluwer Academic Publishers, Norwell, USA, 1999)
27. J. Lee, R.W. Collins, A.R. Heyd, F. Flack, N. Samarth, Appl. Phys. Lett. **69**, 2273 (1996)

28. D.T.F. Marple, J. Appl. Phys. **35**, 539 (1964)
29. J. Li, J. Chen, R.W. Collins, Appl. Phys. Lett. **97**, 181909 (2010)
30. S. Minoura, T. Maekawa, K. Kodera, A. Nakane, S. Niki, H. Fujiwara, J. Appl. Phys. **117**, 195703 (2015)
31. J. Li, H. Du, J. Yarbrough, A. Norman, K. Jones, G. Teeter, F.L. Terry Jr., D. Levi, Opt. Express **20**, A327 (2012)
32. Y. Hirate, H. Tampo, S. Minoura, H. Kadowaki, A. Nakane, K.M. Kim, H. Shibata, S. Niki, H. Fujiwara, J. Appl. Phys. **117**, 015702 (2015)
33. A. Nakane, H. Tampo, M. Tamakoshi, S. Fujimoto, K.M. Kim, S. Kim, H. Shibata, S. Niki, H. Fujiwara, J. Appl. Phys. **120**, 064505 (2016)
34. S. Kim, K.M. Kim, H. Tampo, H. Shibata, K. Matsubara, S. Niki, Sol. Energy Mater. Sol. Cells **144**, 488 (2016)
35. S.G. Choi, J. Kang, J. Li, H. Haneef, N.J. Podraza, C. Beall, S.-H. Wei, S.T. Christensen, I.L. Repins, Appl. Phys. Lett. **106**, 043902 (2015)
36. S. Marsillac, N. Barreau, H. Khatri, J. Li, D. Sainju, A. Parikh, N.J. Podraza, R.W. Collins, Phys. Stat. Sol. C **5**, 1244 (2008)
37. A.R. Beal, H.P. Hughes, J. Phys. C **12**, 881 (1979)
38. M. Richter, C. Schubbert, P. Eraerds, I. Riedel, J. Keller, J. Parisi, T. Dalibor, A. Avellan-Hampe, Thin Solid Films **535**, 331 (2013)

Chapter 9
Organic Semiconductors



Takemasa Fujiseki, Shohei Fujimoto, Mariano Campoy-Quiles, Maria Isabel Alonso, Takurou N. Murakami, Tetsuhiko Miyadera and Hiroyuki Fujiwara

Abstract The dielectric functions and optical constants of various organic solar-cell materials, a total of 20 semiconductors, are summarized. The organic materials described here include CuPc (fluorinated), MEH-PPV, P3HT, $PC_{60}BM$, $PC_{70}BM$, PCDTBT, PEDOT:PSS, PMMA, PTB7, and spiro-OMeTAD. For P3HT and PTB7 semiconductors, the optical properties of those polymers blended with $PC_{60}BM$ and $PC_{70}BM$ are shown. For CuPc (fluorinated), MEH-PPV, P3OT, and PEDOT:PSS layers, the anisotropic optical properties are also indicated. Furthermore, it is established that all the dielectric functions described in this chapter can be parameterized by using several transition peaks calculated from the Tauc-Lorentz model, except for PEDOT:PSS, which is modeled further by incorporating the Drude term.

9.1 Introduction

So far, in an attempt to realize highly efficient solar cells based on organic semiconductors, numerous organic materials have been developed. In general, the organic semiconductors exhibit strong absorption peaks in the visible region and their absorption characteristics are quite important for the interpretation and prediction of the solar cell performance. In organic and organic-inorganic hybrid

T. Fujiseki · S. Fujimoto · H. Fujiwara (✉)
Gifu University, 1-1 Yanagido, Gifu 501-1193, Japan
e-mail: fujiwara@gifu-u.ac.jp

M. Campoy-Quiles · M. I. Alonso
Institut de Ciència de Materials de Barcelona (ICMAB-CSIC), Campus UAB, 08193 Bellaterra, Spain
e-mail: isabel.alonso@icmab.es

T. N. Murakami · T. Miyadera
Research Center for Photovoltaics, National Institute of Advanced Industrial Science and Technology, 1-1-1 Higashi, Tsukuba 305-8568, Japan

© Springer International Publishing AG, part of Springer Nature 2018

H. Fujiwara and R. W. Collins (eds.), *Spectroscopic Ellipsometry for Photovoltaics*, Springer Series in Optical Sciences 214,
https://doi.org/10.1007/978-3-319-95138-6_9

perovskite solar cells, on the other hand, organic layers such as P3HT, PCBM, PEDOT:PSS, PCDTBT and spiro-OMeTAD are applied widely as doped layers.

For the ellipsometry characterization of the device structures and the optical simulation, it is necessary to have the optical constants of all the solar-cell component layers. In this chapter, therefore, for the purpose of spectroscopic ellipsometry (SE) characterization and device simulation, the tabulated optical constants of various organic semiconductors at room temperature are provided. In particular, for almost all organic semiconductors, refractive index n and extinction coefficient k are shown in a wavelength (λ) range of 300–1200 nm with steps of 5 nm (300–400 nm) and 10 nm (400–1200 nm). From these numerical values, the dielectric function ($\varepsilon = \varepsilon_1 - i\varepsilon_2$) and the absorption coefficient (α) can be calculated quite easily according to $\varepsilon_1 = n^2 - k^2$, $\varepsilon_2 = 2nk$ and $\alpha = 4\pi k/\lambda$ (Sect. 1.2.1). The λ value can also be converted to energy (E) by $E = 1239.8/[\lambda\ (\text{nm})]$ eV (1.3). It should be noted that, in the tabulated data, the absolute k value is denoted as "0" when there is no observable light absorption, even though materials may show very small k (or α) values in a certain E region.

Often, organic polymer materials consisting of sp^2-carbon aromatic chains exhibit strong optical anisotropy. Specifically, when the oscillation direction of the electric field of incident light is parallel to the polymer chains, the light absorption increases significantly due to the optical transition induced by the sp^2 π electrons ($\pi \rightarrow \pi^*$ transition in Sect. 4.5.2 (Vol. 1)). In spin-coated polymer films, the polymer chains are preferentially aligned parallel to the film surface. Thus, for the electric-field oscillation parallel to the film surface (i.e., ordinary ray), the light absorption is much higher than that when the electric-field oscillation is perpendicular to the film surface (i.e., extraordinary ray). This type of optical anisotropy is classified as uniaxial anisotropy, with the optic (optical) axis perpendicular to the film surface in this case [1]. Consequently, the in-plane optical constants (ordinary ray) are different from the optical constants for the perpendicular direction (extraordinary ray). In this chapter, the complex dielectric constant for the ordinary ray is represented by $\varepsilon_{\parallel}$ ($\varepsilon_{\parallel} = \varepsilon_{1,\parallel} - i\varepsilon_{2,\parallel}$), whereas that for the extraordinary ray is denoted by $\varepsilon_{\perp}$ ($\varepsilon_{\perp} = \varepsilon_{1,\perp} - i\varepsilon_{2,\perp}$). For the tabulated data of uniaxial polymer materials (MEH-PPV, P3OT, and PEDOT:PSS), however, only the $\varepsilon_{\parallel}$ data are shown since the $\varepsilon_{\parallel}$ component is more important for solar cell devices in which the electric-field oscillation of the incident light is parallel to the device (film) surface.

Unfortunately, the tabulated optical data are sometimes insufficient for more complete SE analysis or optical simulation. Accordingly, the dielectric functions of the semiconductors were parameterized assuming the Tauc-Lorentz model described by (1.19)–(1.20). The Tauc-Lorentz model was developed originally to express the dielectric function of amorphous semiconductors [2]. In particular, we found that this model is quite effective for the complete parameterization of almost all organic semiconductors. By combining several Tauc-Lorentz peaks, the dielectric functions of various organic semiconductors are reproduced almost perfectly in a wide photon energy range (E = 1–5 eV) using only one dielectric function model. From the Tauc-Lorentz parameters described in this chapter, (ε_1, ε_2), (n, k) and α values at arbitrary λ and E can be calculated quite easily. It should be emphasized

that the Tauc-Lorentz model is used solely to establish the optical database of various solar-cell component layers. When only limited spectral information is available, however, the Tauc-Lorentz model is also applied to extrapolate the spectrum beyond experimental data to cover the consistent spectral range of 300–1200 nm.

In the actual modeling, the dielectric functions of organic semiconductors were calculated using (8.1) and (8.2), while the dielectric function of PEDOT:PSS was modeled by further incorporating the Drude term (1.27). The calculation example of the Tauc-Lorentz model is shown in (1.26). A free software described in Sect. 2.7 can further be applied to calculate the dielectric function from the Tauc-Lorentz model parameters listed in this chapter. All the parameterizations of the dielectric functions described in this chapter were implemented by the group of Gifu University (T. Fujiseki and S. Fujimoto), unless otherwise noted.

9.2 Optical Data of Organic Semiconductors

9.2.1 APFO-3 (F8TBT, PFDTBT) [Poly{2,7-(9,9-Dioctylfluorene)-alt-5,5-(4',7'-di-2-Thienyl-2',1',3'-Benzothiadiazole)}]

Data from C. Müller, J. Bergqvist, K. Vandewal, K. Tvingstedt, A. S. Anselmo, R. Magnusson, M. I. Alonso, E. Moons, H. Arwin, M. Campoy-Quiles and O. Inganäs [3]. The optical data have been extracted from a sample fabricated by a spin-coating process (Fig. 9.1 and Tables 9.1, 9.2).

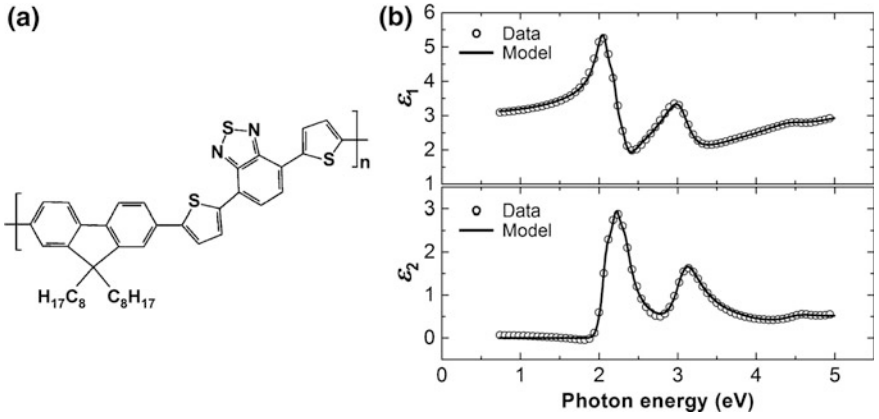


Fig. 9.1 **a** Chemical structure and **b** dielectric function of APFO-3 at room temperature. The open circles show the experimental data and the solid lines indicate the calculation result obtained from the parameterization assuming the Tauc-Lorentz model [(8.1) and (8.2)]

Table 9.1 Tauc-Lorentz parameters of (8.1) and (8.2) for APFO-3

Peak	A (eV)	C (eV)	E_0 (eV)	E_g (eV)	$\varepsilon_1(\infty)$
$j = 1$	25.678	0.192	2.079	1.849	0.021
$j = 2$	11.055	0.173	2.210	1.872	0
$j = 3$	4.061	0.182	2.326	1.872	0
$j = 4$	24.971	0.393	3.065	2.645	0
$j = 5$	6.125	0.584	4.472	3.978	0
$j = 6$	78.248	6.832	11.350	3.579	0

Table 9.2 Optical constants of APFO-3. The optical data reported by Müller et al. are shown

λ (nm)	n	k	λ (nm)	n	k	λ (nm)	n	k
300	1.615	0.131	540	1.773	0.742	880	1.830	0.005
305	1.601	0.135	550	1.910	0.744	890	1.827	0.005
310	1.587	0.140	560	2.035	0.704	900	1.825	0.006
315	1.574	0.147	570	2.136	0.637	910	1.822	0.006
320	1.562	0.156	580	2.216	0.555	920	1.819	0.007
325	1.550	0.166	590	2.277	0.459	930	1.817	0.007
330	1.538	0.178	600	2.314	0.347	940	1.815	0.008
335	1.527	0.193	610	2.311	0.229	950	1.813	0.008
340	1.518	0.209	620	2.271	0.130	960	1.810	0.009
345	1.509	0.229	630	2.211	0.063	970	1.808	0.009
350	1.502	0.251	640	2.152	0.025	980	1.807	0.009
355	1.498	0.276	650	2.101	0.005	990	1.805	0.010
360	1.498	0.304	660	2.060	0	1000	1.803	0.010
365	1.503	0.336	670	2.027	0	1010	1.802	0.010
370	1.515	0.370	680	2.001	0	1020	1.800	0.011
375	1.536	0.404	690	1.978	0	1030	1.798	0.011
380	1.567	0.436	700	1.960	0	1040	1.797	0.011
385	1.609	0.462	710	1.944	0	1050	1.796	0.011
390	1.662	0.476	720	1.930	0	1060	1.794	0.012
395	1.721	0.472	730	1.918	0	1070	1.793	0.012
400	1.777	0.449	740	1.908	0	1080	1.792	0.012
410	1.848	0.356	750	1.899	0	1090	1.791	0.012
420	1.845	0.253	760	1.890	0	1100	1.790	0.013
430	1.796	0.184	770	1.883	0	1110	1.788	0.013
440	1.734	0.153	780	1.876	0	1120	1.787	0.013
450	1.672	0.150	790	1.869	0	1130	1.786	0.013
460	1.615	0.166	800	1.864	0	1140	1.785	0.013
470	1.565	0.200	810	1.858	0	1150	1.784	0.014
480	1.522	0.251	820	1.853	0.001	1160	1.783	0.014
490	1.491	0.320	830	1.849	0.002	1170	1.783	0.014
500	1.478	0.406	840	1.845	0.002	1180	1.782	0.014
510	1.495	0.506	850	1.841	0.003	1190	1.781	0.014
520	1.550	0.608	860	1.837	0.004	1200	1.780	0.014
530	1.646	0.694	870	1.834	0.004			

9.2.2 APFO-Green9 [Poly{2,7-(9,9-Dioctylfluorene)-alt-5,5-(5,10-di-2-Thienyl-2,3,7,8-Tetraphenyl-Pyrazino-[2,3-g]Quinoxaline)}]

Data: unpublished results of M. Campoy-Quiles. The characterization results are described in [4] and refractive index data at different temperatures are shown in the supplementary information of [4]. Data for blends of APFO-Green9 and PC70BM can be found in [5] (Fig. 9.2 and Tables 9.3, 9.4).

9.2.3 Fluorinated CuPc (F_{16}CuPc) [Fluorinated Copper Phthalocyanine]

The optical data correspond to those shown in Fig. 15.3a (Chap. 15 in Vol. 1). Partial data can also be found in M. I. Alonso, M. Garriga, J. O. Ossó, F. Schreiber, E. Barrena, and H. Dosch [6]. The optical data have been extracted from a

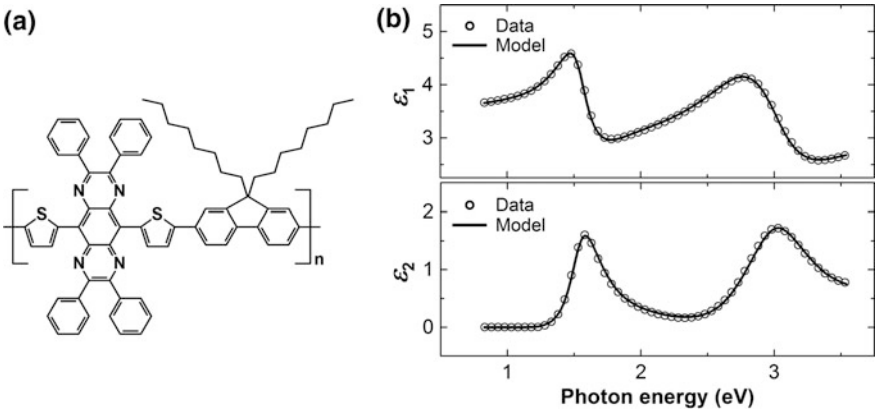


Fig. 9.2 **a** Chemical structure and **b** dielectric function of APFO-Green9 at room temperature. The open circles show the experimental data and the solid lines indicate the calculation result obtained from the parameterization assuming the Tauc-Lorentz model [(8.1) and (8.2)]

Table 9.3 Tauc-Lorentz parameters of (8.1) and (8.2) for APFO-Green9

Peak	A (eV)	C (eV)	E_0 (eV)	E_g (eV)	$\varepsilon_1(\infty)$
$j = 1$	5.582	0.259	1.553	1.155	2.762
$j = 2$	0.492	0.312	1.670	1.092	0
$j = 3$	6.766	0.627	2.823	2.218	0
$j = 4$	8.439	0.539	2.999	2.200	0
$j = 5$	33.773	1.698	3.348	3.343	0

Table 9.4 Optical constants of APFO-Green9. The optical data obtained by Campoy-Quiles et al. are shown

λ (nm)	n	k	λ (nm)	n	k	λ (nm)	n	k
350	1.654	0.233	610	1.778	0.085	920	2.063	0.032
355	1.645	0.243	620	1.770	0.095	930	2.052	0.025
360	1.637	0.258	630	1.763	0.105	940	2.042	0.019
365	1.633	0.278	640	1.756	0.117	950	2.033	0.014
370	1.634	0.302	650	1.749	0.131	960	2.024	0.010
375	1.641	0.330	660	1.744	0.145	970	2.016	0.007
380	1.656	0.360	670	1.740	0.162	980	2.009	0.005
385	1.681	0.390	680	1.738	0.181	990	2.003	0.003
390	1.714	0.417	690	1.737	0.202	1000	1.996	0.002
395	1.753	0.440	700	1.740	0.225	1010	1.990	0.001
400	1.801	0.454	710	1.745	0.251	1020	1.985	0
410	1.898	0.454	720	1.759	0.278	1030	1.981	0
420	1.981	0.416	730	1.775	0.308	1040	1.976	0
430	2.031	0.351	740	1.806	0.336	1050	1.972	0
440	2.049	0.279	750	1.839	0.364	1060	1.969	0
450	2.044	0.214	760	1.885	0.386	1070	1.966	0
460	2.028	0.162	770	1.939	0.400	1080	1.963	0
470	2.006	0.123	780	1.988	0.403	1090	1.960	0
480	1.981	0.093	790	2.040	0.391	1100	1.957	0
490	1.957	0.073	800	2.086	0.365	1110	1.955	0
500	1.933	0.059	810	2.117	0.329	1120	1.953	0
510	1.912	0.050	820	2.134	0.287	1130	1.950	0
520	1.892	0.045	830	2.150	0.242	1140	1.948	0
530	1.874	0.044	840	2.150	0.201	1150	1.946	0
540	1.857	0.044	850	2.143	0.164	1160	1.945	0
550	1.843	0.047	860	2.137	0.132	1170	1.943	0
560	1.829	0.051	870	2.125	0.106	1180	1.942	0
570	1.817	0.056	880	2.112	0.084	1190	1.940	0
580	1.806	0.062	890	2.099	0.066	1200	1.939	0
590	1.796	0.069	900	2.087	0.052			
600	1.787	0.076	910	2.075	0.041			

perfluorinated CuPc film (see Fig. 9.3a) fabricated by evaporation at 49 °C. Although the optical properties have been obtained from a perfluorinated CuPc sample, conventional hydrogenated CuPc shows similar optical properties. The uniaxial anisotropy of the film was originated both by the molecular anisotropy and by the ordering, resulting in an optic axis in the plane of the film. In this case, the ordinary component, $\varepsilon_{\|}$, represents an optical response related to the plane of the molecules, which is not the plane of the film (Tables 9.5, 9.6 and 9.7).

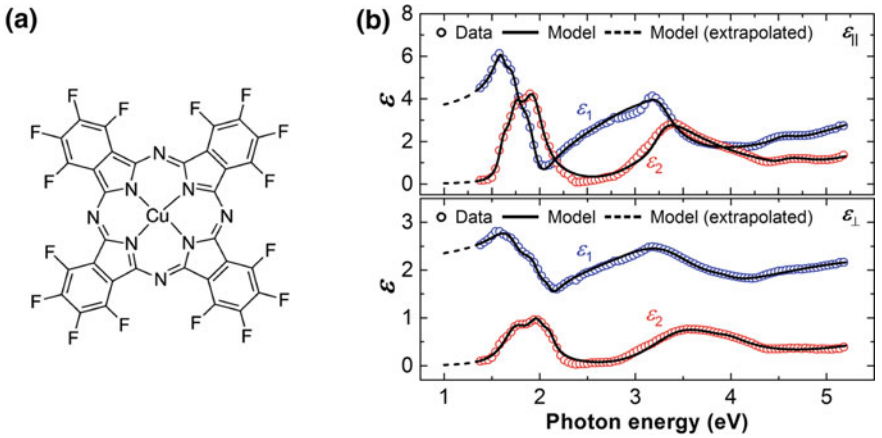


Fig. 9.3 **a** Chemical structure and **b** dielectric function of perfluorinated CuPc at room temperature. In (**b**), $\varepsilon_{\parallel}$ and $\varepsilon_{\perp}$ show the ordinary and extraordinary dielectric function components of the film, although in this case the subindices $_{\parallel}$ and $_{\perp}$ do not refer to the film but are related to contributions nearly parallel or perpendicular to the molecular planes, respectively. The open circles show the experimental data and the solid lines indicate the calculation result obtained from the parameterization assuming the Tauc-Lorentz model [(8.1) and (8.2)]. The dotted lines show the extrapolated result obtained from the Tauc-Lorentz model

Table 9.5 Tauc-Lorentz parameters of (8.1) and (8.2) for $\varepsilon_{\parallel}$ of perfluorinated CuPc

Peak	A (eV)	C (eV)	E_0 (eV)	E_g (eV)	$\varepsilon_1(\infty)$
$j = 1$	6.882	0.125	1.615	1.376	0.725
$j = 2$	4.208	0.191	1.747	1.177	0
$j = 3$	1.359	0.262	1.933	0.388	0
$j = 4$	22.538	1.140	3.242	2.338	0
$j = 5$	46.863	0.362	3.259	3.022	0
$j = 6$	44.611	0.380	4.550	4.377	0
$j = 7$	114.552	2.537	5.932	4.629	0

Table 9.6 Tauc-Lorentz parameters of (8.1) and (8.2) for $\varepsilon_{\perp}$ of perfluorinated CuPc

Peak	A (eV)	C (eV)	E_0 (eV)	E_g (eV)	$\varepsilon_1(\infty)$
$j = 1$	0.713	0.337	1.743	0.753	0.890
$j = 2$	0.150	0.234	1.973	1×10^{-4}	0
$j = 3$	0.043	0.146	2.102	1×10^{-4}	0
$j = 4$	8.831	1.100	3.419	2.432	0
$j = 5$	0.082	0.343	3.994	1.796	0
$j = 6$	82.689	14.454	7.275	4.269	0

Table 9.7 Optical constants for the ordinary ray ($N_{\|} = n_{\|} - ik_{\|}$) in perfluorinated CuPc calculated by the Tauc-Lorentz model

λ (nm)	$n_{\|}$	$k_{\|}$	λ (nm)	$n_{\|}$	$k_{\|}$	λ (nm)	$n_{\|}$	$k_{\|}$
300	1.421	0.496	540	1.334	0.233	880	2.163	0.048
305	1.423	0.528	550	1.282	0.288	890	2.145	0.043
310	1.431	0.559	560	1.231	0.359	900	2.129	0.040
315	1.443	0.591	570	1.187	0.452	910	2.115	0.037
320	1.461	0.621	580	1.160	0.569	920	2.102	0.034
325	1.483	0.650	590	1.164	0.706	930	2.090	0.031
330	1.510	0.677	600	1.209	0.854	940	2.080	0.029
335	1.542	0.702	610	1.303	0.995	950	2.069	0.027
340	1.580	0.724	620	1.445	1.106	960	2.060	0.026
345	1.622	0.742	630	1.619	1.163	970	2.051	0.024
350	1.671	0.755	640	1.794	1.154	980	2.043	0.023
355	1.725	0.762	650	1.931	1.092	990	2.035	0.022
360	1.786	0.760	660	2.017	1.015	1000	2.028	0.021
365	1.852	0.746	670	2.063	0.953	1010	2.022	0.020
370	1.921	0.713	680	2.098	0.922	1020	2.015	0.019
375	1.984	0.659	690	2.151	0.910	1030	2.009	0.018
380	2.027	0.585	700	2.231	0.889	1040	2.004	0.017
385	2.043	0.505	710	2.320	0.832	1050	1.998	0.016
390	2.035	0.434	720	2.382	0.743	1060	1.993	0.016
395	2.015	0.377	730	2.405	0.653	1070	1.988	0.015
400	1.991	0.334	740	2.406	0.586	1080	1.984	0.015
410	1.945	0.274	750	2.413	0.543	1090	1.979	0.014
420	1.906	0.228	760	2.443	0.501	1100	1.975	0.014
430	1.865	0.188	770	2.480	0.429	1110	1.971	0.013
440	1.821	0.157	780	2.486	0.333	1120	1.968	0.013
450	1.775	0.134	790	2.457	0.247	1130	1.964	0.012
460	1.729	0.119	800	2.413	0.185	1140	1.961	0.012
470	1.682	0.110	810	2.367	0.143	1150	1.957	0.012
480	1.634	0.108	820	2.326	0.114	1160	1.954	0.011
490	1.586	0.111	830	2.289	0.094	1170	1.951	0.011
500	1.538	0.121	840	2.257	0.079	1180	1.948	0.011
510	1.488	0.137	850	2.229	0.068	1190	1.946	0.010
520	1.438	0.160	860	2.204	0.060	1200	1.943	0.010
530	1.386	0.191	870	2.182	0.053			

9.2.4 MEH-PPV [Poly{2-Methoxy-5-(2'-Ethyl-Hexyloxy)-p-Phenylenevinylene}]

Data from M. Tammer and A. P. Monkman [7]. The optical data have been extracted from a sample fabricated by a spin-coating process (Fig. 9.4 and Tables 9.8, 9.9, 9.10).

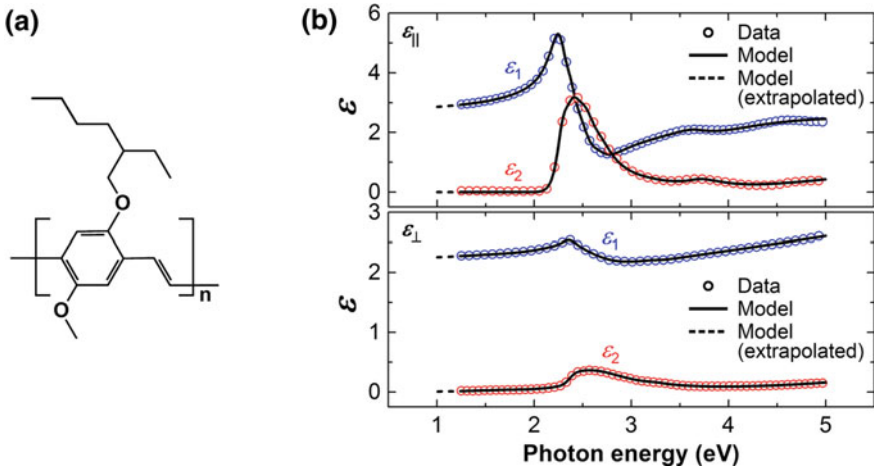


Fig. 9.4 **a** Chemical structure and **b** dielectric functions of MEH-PPV at room temperature. In (**b**), $\varepsilon_{\parallel}$ and $\varepsilon_{\perp}$ show the dielectric functions parallel (ordinary) and perpendicular (extraordinary) to the thin film surface, respectively. The open circles show the experimental data and the solid lines indicate the calculation result obtained from the parameterization assuming the Tauc-Lorentz model [(8.1) and (8.2)]. The dotted lines show the extrapolated result obtained from the Tauc-Lorentz model

Table 9.8 Tauc-Lorentz parameters of (8.1) and (8.2) for $\varepsilon_{\parallel}$ of MEH-PPV

Peak	A (eV)	C (eV)	E_0 (eV)	E_g (eV)	$\varepsilon_1(\infty)$
$j = 1$	26.539	0.188	2.281	2.025	1.591
$j = 2$	10.150	0.205	2.397	1.998	0
$j = 3$	5.165	0.253	2.524	1.915	0
$j = 4$	1.735	0.289	2.693	1.950	0
$j = 5$	3.807	0.424	3.680	3.179	0
$j = 6$	74.534	9.432	4.750	4.005	0

Table 9.9 Tauc-Lorentz parameters of (8.1) and (8.2) for $\varepsilon_{\perp}$ of MEH-PPV

Peak	A (eV)	C (eV)	E_0 (eV)	E_g (eV)	$\varepsilon_1(\infty)$
$j = 1$	0.047	0.960	1.734	0.382	0.527
$j = 2$	7.471	0.233	2.372	2.242	0
$j = 3$	0.894	0.766	2.622	1.448	0
$j = 4$	0.057	0.246	3.258	2.352	0
$j = 5$	43.389	4.682	11.406	3.214	0

Table 9.10 Optical constants for the ordinary ray ($N_{\parallel} = n_{\parallel} - ik_{\parallel}$) in MEH-PPV calculated by the Tauc-Lorentz model

λ (nm)	$n_{\parallel}$	$k_{\parallel}$	λ (nm)	$n_{\parallel}$	$k_{\parallel}$	λ (nm)	$n_{\parallel}$	$k_{\parallel}$
300	1.470	0.092	540	2.271	0.550	880	1.731	0
305	1.458	0.098	550	2.328	0.364	890	1.729	0
310	1.448	0.107	560	2.279	0.193	900	1.727	0
315	1.441	0.118	570	2.191	0.092	910	1.725	0
320	1.437	0.130	580	2.110	0.042	920	1.723	0
325	1.438	0.141	590	2.045	0.017	930	1.721	0
330	1.443	0.149	600	1.993	0.006	940	1.719	0
335	1.450	0.150	610	1.954	0.002	950	1.718	0
340	1.454	0.144	620	1.923	0.001	960	1.716	0
345	1.450	0.136	630	1.899	0	970	1.715	0
350	1.440	0.129	640	1.879	0	980	1.714	0
355	1.426	0.127	650	1.863	0	990	1.712	0
360	1.412	0.129	660	1.849	0	1000	1.711	0
365	1.398	0.134	670	1.836	0	1010	1.710	0
370	1.384	0.141	680	1.825	0	1020	1.708	0
375	1.370	0.150	690	1.816	0	1030	1.707	0
380	1.356	0.160	700	1.807	0	1040	1.706	0
385	1.343	0.172	710	1.799	0	1050	1.705	0
390	1.330	0.185	720	1.792	0	1060	1.704	0
395	1.316	0.201	730	1.786	0	1070	1.703	0
400	1.303	0.218	740	1.780	0	1080	1.702	0
410	1.276	0.260	750	1.775	0	1090	1.701	0
420	1.250	0.315	760	1.770	0	1100	1.701	0
430	1.231	0.389	770	1.765	0	1110	1.700	0
440	1.232	0.485	780	1.761	0	1120	1.699	0
450	1.270	0.589	790	1.757	0	1130	1.698	0
460	1.342	0.675	800	1.753	0	1140	1.697	0
470	1.419	0.744	810	1.750	0	1150	1.697	0
480	1.522	0.817	820	1.747	0	1160	1.696	0
490	1.663	0.852	830	1.744	0	1170	1.695	0
500	1.793	0.841	840	1.741	0	1180	1.695	0
510	1.922	0.823	850	1.738	0	1190	1.694	0
520	2.061	0.756	860	1.736	0	1200	1.693	0
530	2.163	0.664	870	1.733	0			

9.2.5 P3HT [Poly(3-Hexylthiophene)]

Data from M. Campoy-Quiles, J. Nelson, D. D. C. Bradley and P. G. Etchegoin [8]. The optical data have been extracted from a P3HT layer formed on a fused silica substrate using a spin-coating process (Fig. 9.5 and Tables 9.11, 9.12).

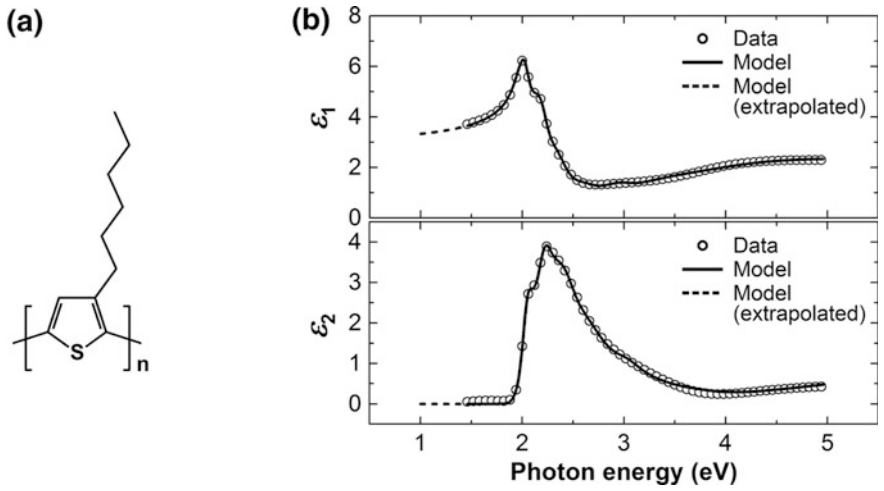


Fig. 9.5 **a** Chemical structure and **b** dielectric function of P3HT at room temperature. The open circles show the experimental data and the solid lines indicate the calculation result obtained from the parameterization assuming the Tauc-Lorentz model [(8.1) and (8.2)]. The dotted lines show the extrapolated result obtained from the Tauc-Lorentz model

Table 9.11 Tauc-Lorentz parameters of (8.1) and (8.2) for P3HT

Peak	A (eV)	C (eV)	E_0 (eV)	E_g (eV)	$\varepsilon_1(\infty)$
$j = 1$	29.026	0.158	2.039	1.824	1.875
$j = 2$	15.858	0.224	2.209	1.813	0
$j = 3$	7.716	0.347	2.393	1.730	0
$j = 4$	1.957	0.412	2.659	1.748	0
$j = 5$	0.721	0.395	3.025	1.842	0
$j = 6$	58.901	6.156	3.863	3.862	0

Table 9.12 Optical constants of P3HT calculated by the Tauc-Lorentz model

λ (nm)	n	k	λ (nm)	n	k	λ (nm)	n	k
300	1.450	0.101	540	1.975	0.938	880	1.896	0
305	1.436	0.101	550	2.091	0.930	890	1.891	0
310	1.422	0.104	560	2.224	0.862	900	1.888	0
315	1.407	0.108	570	2.302	0.742	910	1.884	0
320	1.393	0.114	580	2.312	0.647	920	1.880	0
325	1.379	0.122	590	2.328	0.612	930	1.877	0
330	1.367	0.131	600	2.410	0.579	940	1.874	0
335	1.354	0.140	610	2.510	0.453	950	1.871	0
340	1.342	0.150	620	2.514	0.272	960	1.868	0
345	1.329	0.162	630	2.440	0.141	970	1.865	0
350	1.317	0.174	640	2.353	0.068	980	1.863	0
355	1.304	0.188	650	2.276	0.031	990	1.860	0
360	1.292	0.203	660	2.215	0.013	1000	1.858	0
365	1.279	0.220	670	2.165	0.004	1010	1.856	0
370	1.267	0.239	680	2.126	0.001	1020	1.854	0
375	1.256	0.261	690	2.095	0.001	1030	1.852	0
380	1.246	0.285	700	2.070	0	1040	1.850	0
385	1.238	0.313	710	2.049	0	1050	1.848	0
390	1.234	0.342	720	2.031	0	1060	1.846	0
395	1.235	0.373	730	2.015	0	1070	1.844	0
400	1.241	0.403	740	2.000	0	1080	1.842	0
410	1.263	0.449	750	1.988	0	1090	1.841	0
420	1.275	0.482	760	1.977	0	1100	1.839	0
430	1.275	0.523	770	1.966	0	1110	1.838	0
440	1.279	0.584	780	1.957	0	1120	1.836	0
450	1.304	0.655	790	1.949	0	1130	1.835	0
460	1.349	0.718	800	1.941	0	1140	1.834	0
470	1.400	0.768	810	1.934	0	1150	1.832	0
480	1.449	0.816	820	1.927	0	1160	1.831	0
490	1.508	0.874	830	1.921	0	1170	1.830	0
500	1.594	0.931	840	1.915	0	1180	1.829	0
510	1.703	0.961	850	1.910	0	1190	1.828	0
520	1.809	0.956	860	1.905	0	1200	1.827	0
530	1.893	0.940	870	1.900	0			

9.2.6 P3HT:$PC_{60}BM$ (Blend Ratio 1:1) [Poly (3-Hexylthiophene):(6,6)-Phenyl-C_{61}-Butyric Acid Methyl Ester]

Data from C. J. M. Emmott, J. A. Röhr, M. Campoy-Quiles, T. Kirchartz, A. Urbina, N. J. Ekins-Daukes, and J. Nelson [9] (Supplementary Information) (Fig. 9.6 and Tables 9.13, 9.14).

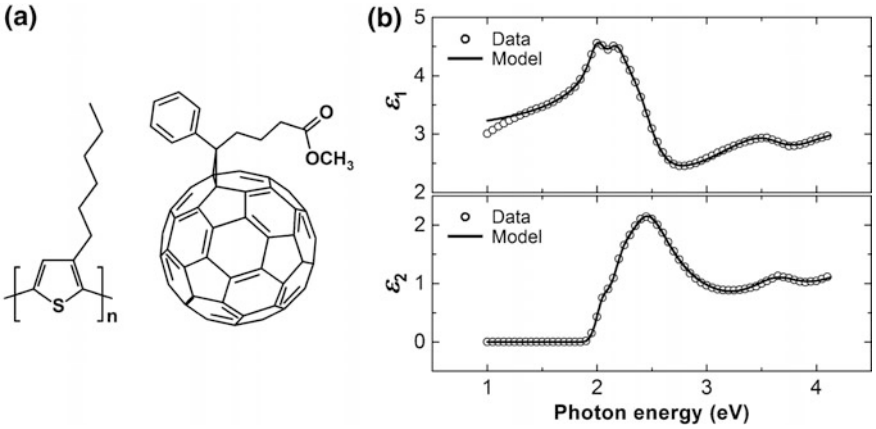


Fig. 9.6 **a** Chemical structure and **b** dielectric function of P3HT:$PC_{60}BM$ at room temperature. The open circles show the reference data and the solid lines indicate the calculation result obtained from the parameterization assuming the Tauc-Lorentz model [(8.1) and (8.2)]

Table 9.13 Tauc-Lorentz parameters of (8.1) and (8.2) for P3HT:$PC_{60}BM$

Peak	A (eV)	C (eV)	E_0 (eV)	E_g (eV)	$\varepsilon_1(\infty)$
$j = 1$	16.475	0.199	2.024	1.856	1.494
$j = 2$	24.496	0.274	2.189	2.016	0
$j = 3$	11.627	0.500	2.429	1.866	0
$j = 4$	1.794	0.687	3.619	1.860	0
$j = 5$	77.305	3.771	4.448	3.449	0

Table 9.14 Optical constants of P3HT:$PC_{60}BM$. The optical data reported by Emmott et al. are shown

λ (nm)	n	k	λ (nm)	n	k	λ (nm)	n	k
300	1.757	0.323	540	2.074	0.437	880	1.845	0
305	1.745	0.312	550	2.102	0.398	890	1.842	0
310	1.733	0.301	560	2.135	0.356	900	1.839	0
315	1.720	0.299	570	2.148	0.291	910	1.836	0
320	1.707	0.298	580	2.135	0.239	920	1.833	0
325	1.703	0.309	590	2.120	0.214	930	1.830	0
330	1.700	0.320	600	2.126	0.196	940	1.827	0
335	1.713	0.323	610	2.141	0.156	950	1.824	0
340	1.727	0.327	620	2.137	0.099	960	1.821	0
345	1.733	0.312	630	2.112	0.054	970	1.817	0
350	1.740	0.298	640	2.075	0.023	980	1.814	0
355	1.735	0.285	650	2.039	0.006	990	1.811	0
360	1.730	0.273	660	2.009	0.001	1000	1.808	0
365	1.722	0.268	670	1.985	0	1010	1.805	0
370	1.714	0.264	680	1.965	0	1020	1.802	0
375	1.704	0.262	690	1.951	0	1030	1.799	0
380	1.695	0.261	700	1.940	0	1040	1.796	0
385	1.686	0.262	710	1.931	0	1050	1.793	0
390	1.677	0.262	720	1.923	0	1060	1.789	0
395	1.668	0.267	730	1.915	0	1070	1.786	0
400	1.659	0.271	740	1.908	0	1080	1.783	0
410	1.640	0.287	750	1.900	0	1090	1.780	0
420	1.625	0.312	760	1.894	0	1100	1.777	0
430	1.615	0.343	770	1.888	0	1110	1.774	0
440	1.613	0.385	780	1.881	0	1120	1.771	0
450	1.623	0.428	790	1.876	0	1130	1.768	0
460	1.647	0.475	800	1.872	0	1140	1.765	0
470	1.688	0.518	810	1.868	0	1150	1.761	0
480	1.741	0.551	820	1.864	0	1160	1.758	0
490	1.807	0.568	830	1.860	0	1170	1.755	0
500	1.876	0.568	840	1.858	0	1180	1.752	0
510	1.940	0.553	850	1.855	0	1190	1.749	0
520	1.999	0.520	860	1.852	0	1200	1.746	0
530	2.042	0.479	870	1.849	0			

9.2.7 P3HT:$PC_{70}BM$ (Blend Ratio 1:1) [Poly (3-Hexylthiophene):(6,6)-Phenyl-C_{71}-Butyric Acid Methyl Ester]

Data from C. J. M. Emmott, J. A. Röhr, M. Campoy-Quiles, T. Kirchartz, A. Urbina, N. J. Ekins-Daukes, and J. Nelson [9] (Supplementary Information) (Fig. 9.7 and Tables 9.15, 9.16).

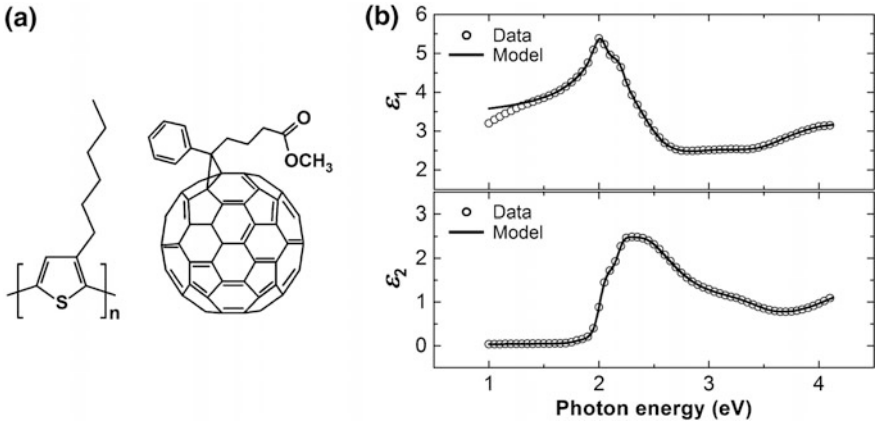


Fig. 9.7 **a** Chemical structure and **b** dielectric function of P3HT:$PC_{70}BM$ at room temperature. The open circles show the reference data and the solid lines indicate the calculation result obtained from the parameterization assuming the Tauc-Lorentz model [(8.1) and (8.2)]

Table 9.15 Tauc-Lorentz parameters of (8.1) and (8.2) for P3HT:$PC_{70}BM$

Peak	A (eV)	C (eV)	E_0 (eV)	E_g (eV)	$\varepsilon_1(\infty)$
$j = 1$	30.647	0.199	2.025	1.880	1.772
$j = 2$	14.683	0.190	2.199	2.016	0
$j = 3$	9.281	0.703	2.387	1.572	0
$j = 4$	0.171	3.986	2.644	1×10^{-4}	0
$j = 5$	1.300	0.920	3.247	1.672	0
$j = 6$	85.280	3.141	4.061	3.474	0

Table 9.16 Optical constants of P3HT:$PC_{70}BM$. The optical data reported by Emmott et al. are shown

λ (nm)	n	k	λ (nm)	n	k	λ (nm)	n	k
300	1.804	0.313	540	2.076	0.599	880	1.941	0.012
305	1.795	0.291	550	2.133	0.580	890	1.936	0.012
310	1.786	0.269	560	2.200	0.541	900	1.932	0.011
315	1.770	0.254	570	2.242	0.467	910	1.928	0.011
320	1.753	0.239	580	2.245	0.411	920	1.924	0.011
325	1.734	0.233	590	2.257	0.382	930	1.919	0.011
330	1.715	0.227	600	2.291	0.346	940	1.915	0.011
335	1.697	0.229	610	2.326	0.278	950	1.911	0.011
340	1.679	0.231	620	2.327	0.188	960	1.907	0.011
345	1.663	0.240	630	2.288	0.114	970	1.903	0.011
350	1.648	0.248	640	2.236	0.071	980	1.898	0.011
355	1.638	0.262	650	2.191	0.050	990	1.894	0.011
360	1.628	0.275	660	2.156	0.041	1000	1.890	0.011
365	1.623	0.291	670	2.128	0.036	1010	1.886	0.011
370	1.619	0.307	680	2.108	0.033	1020	1.881	0.011
375	1.623	0.320	690	2.092	0.030	1030	1.877	0.011
380	1.626	0.334	700	2.077	0.024	1040	1.873	0.011
385	1.628	0.340	710	2.062	0.019	1050	1.869	0.011
390	1.630	0.346	720	2.048	0.017	1060	1.865	0.011
395	1.630	0.356	730	2.035	0.015	1070	1.860	0.011
400	1.629	0.366	740	2.024	0.014	1080	1.856	0.011
410	1.632	0.386	750	2.014	0.014	1090	1.852	0.011
420	1.635	0.407	760	2.006	0.013	1100	1.848	0.010
430	1.638	0.432	770	1.998	0.013	1110	1.843	0.010
440	1.643	0.462	780	1.990	0.013	1120	1.839	0.010
450	1.656	0.499	790	1.984	0.012	1130	1.835	0.010
460	1.680	0.538	800	1.978	0.012	1140	1.831	0.010
470	1.716	0.573	810	1.972	0.012	1150	1.827	0.010
480	1.760	0.602	820	1.967	0.012	1160	1.822	0.010
490	1.811	0.622	830	1.962	0.012	1170	1.818	0.010
500	1.866	0.632	840	1.957	0.012	1180	1.814	0.010
510	1.921	0.633	850	1.953	0.012	1190	1.810	0.010
520	1.975	0.626	860	1.949	0.012	1200	1.805	0.010
530	2.026	0.614	870	1.945	0.012			

9.2.8 P3OT [Poly(3-Octylthiophene)]

Data from U. Zhokhavets, G. Gobsch, H. Hoppe and N. S. Sariciftci [10]. The optical data have been extracted from a P3OT layer fabricated by a spin-coating process (Fig. 9.8 and Tables 9.17, 9.18, 9.19).

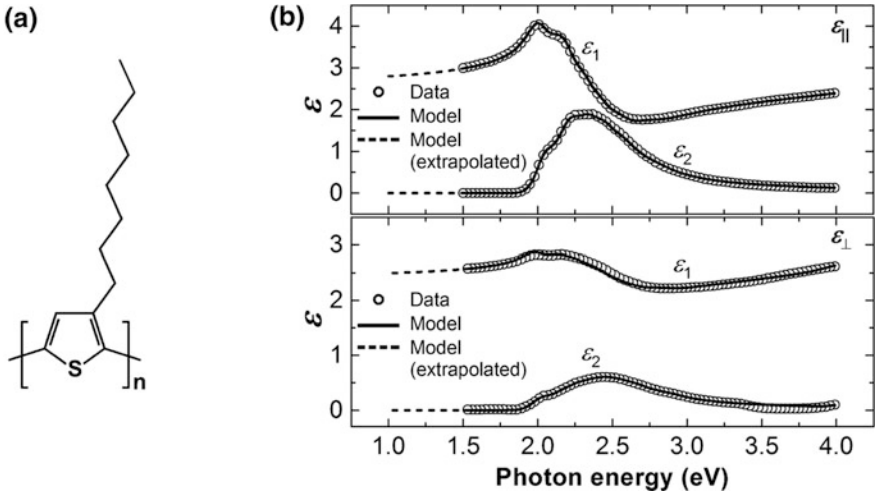


Fig. 9.8 **a** Chemical structure and **b** dielectric functions of P3OT at room temperature. In (**b**), $\varepsilon_{\|}$ and $\varepsilon_{\perp}$ show the dielectric functions parallel (ordinary) and perpendicular (extraordinary) to the thin film surface, respectively. The open circles show the experimental data and the solid lines indicate the calculation result obtained from the parameterization assuming the Tauc-Lorentz model [(8.1) and (8.2)]. The dotted lines show the extrapolated results obtained from the Tauc-Lorentz model

Table 9.17 Tauc-Lorentz parameters of (8.1) and (8.2) for $\varepsilon_{\|}$ of P3OT

Peak	A (eV)	C (eV)	E_0 (eV)	E_g (eV)	$\varepsilon_1(\infty)$
$j = 1$	14.417	0.191	2.024	1.830	1.884
$j = 2$	8.118	0.221	2.201	1.830	0
$j = 3$	2.993	0.210	2.334	1.830	0
$j = 4$	1.738	0.210	2.445	1.830	0
$j = 5$	1.248	0.255	2.575	1.830	0
$j = 6$	0.503	0.356	2.772	1.828	0
$j = 7$	21.870	0.199	6.018	3.947	0

Table 9.18 Tauc-Lorentz parameters of (8.1) and (8.2) for $\varepsilon_{\perp}$ of P3OT

Peak	A (eV)	C (eV)	E_0 (eV)	E_g (eV)	$\varepsilon_1(\infty)$
$j = 1$	4.054	0.207	1.990	1.815	1.776
$j = 2$	0.236	0.141	2.152	1.815	0
$j = 3$	2.077	0.328	2.239	1.815	0
$j = 4$	1.854	0.440	2.442	1.735	0
$j = 5$	0.732	0.339	2.633	2.078	0
$j = 6$	0.100	0.278	2.886	1.813	0
$j = 7$	81.090	3.543	3.852	3.850	0

Table 9.19 Optical constants for the ordinary ray ($N_{\parallel} = n_{\parallel} - ik_{\parallel}$) in P3OT calculated by the Tauc-Lorentz model

λ (nm)	$n_{\parallel}$	$k_{\parallel}$	λ (nm)	$n_{\parallel}$	$k_{\parallel}$	λ (nm)	$n_{\parallel}$	$k_{\parallel}$
310	1.549	0.041	550	1.847	0.500	880	1.714	0
315	1.540	0.044	560	1.913	0.467	890	1.711	0
320	1.532	0.046	570	1.965	0.400	900	1.709	0
325	1.524	0.049	580	1.976	0.332	910	1.707	0
330	1.516	0.052	590	1.974	0.291	920	1.705	0
335	1.508	0.055	600	1.988	0.263	930	1.703	0
340	1.500	0.058	610	2.016	0.217	940	1.702	0
345	1.493	0.062	620	2.024	0.147	950	1.700	0
350	1.485	0.066	630	1.999	0.081	960	1.699	0
355	1.478	0.070	640	1.958	0.039	970	1.697	0
360	1.470	0.074	650	1.918	0.016	980	1.696	0
365	1.463	0.079	660	1.884	0.005	990	1.694	0
370	1.455	0.084	670	1.857	0.001	1000	1.693	0
375	1.447	0.089	680	1.836	0	1010	1.692	0
380	1.439	0.095	690	1.820	0	1020	1.691	0
385	1.431	0.102	700	1.807	0	1030	1.690	0
390	1.422	0.109	710	1.796	0	1040	1.688	0
395	1.414	0.118	720	1.786	0	1050	1.687	0
400	1.405	0.127	730	1.777	0	1060	1.686	0
410	1.387	0.150	740	1.770	0	1070	1.685	0
420	1.371	0.180	750	1.763	0	1080	1.685	0
430	1.359	0.218	760	1.757	0	1090	1.684	0
440	1.356	0.260	770	1.752	0	1100	1.683	0
450	1.359	0.302	780	1.747	0	1110	1.682	0
460	1.364	0.349	790	1.742	0	1120	1.681	0
470	1.383	0.409	800	1.738	0	1130	1.680	0
480	1.428	0.461	810	1.734	0	1140	1.680	0
490	1.477	0.496	820	1.731	0	1150	1.679	0
500	1.532	0.532	830	1.727	0	1160	1.678	0
510	1.604	0.549	840	1.724	0	1170	1.678	0
520	1.667	0.550	850	1.721	0	1180	1.677	0
530	1.735	0.545	860	1.719	0	1190	1.676	0
540	1.795	0.521	870	1.716	0	1200	1.676	0

9.2.9 $PC_{60}BM$ (Aka PCBM, [60]PCBM, PC61BM) [(6,6)-Phenyl-C_{61}-Butyric Acid Methyl Ester]

Data from M. Campoy-Quiles, J. Nelson, D. D. C. Bradley and P. G. Etchegoin [8]. The optical data have been extracted from a $PC_{60}BM$ layer formed on a fused silica substrate using a spin-coating process (Fig. 9.9 and Tables 9.20, 9.21).

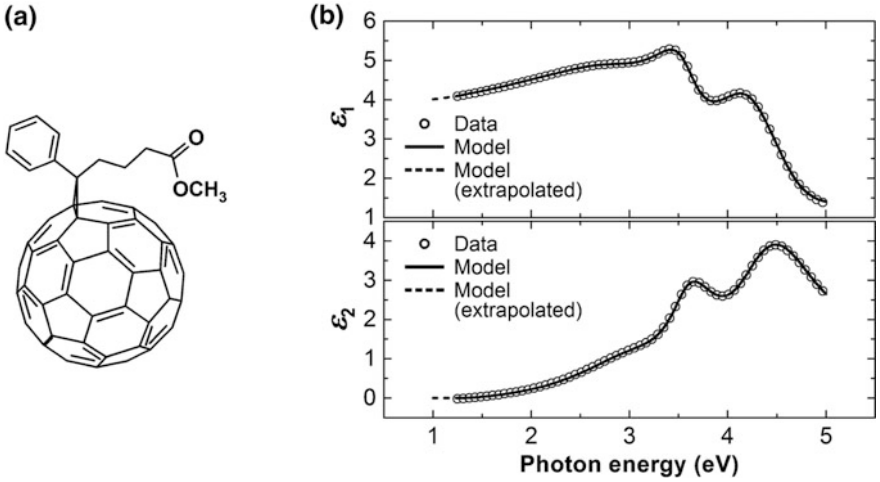


Fig. 9.9 **a** Chemical structure and **b** dielectric function of $PC_{60}BM$ at room temperature. The open circles show the experimental data and the solid lines indicate the calculation result obtained from the parameterization assuming the Tauc-Lorentz model [(8.1) and (8.2)]. The dotted lines show the extrapolated result obtained from the Tauc-Lorentz model

Table 9.20 Tauc-Lorentz parameters of (8.1) and (8.2) for $PC_{60}BM$

Peak	A (eV)	C (eV)	E_0 (eV)	E_g (eV)	$\varepsilon_1(\infty)$
$j = 1$	4.497	1.366	3.011	1.649	2.249
$j = 2$	16.877	0.550	3.593	2.771	0
$j = 3$	7.436	0.723	4.318	2.593	0
$j = 4$	45.755	0.787	4.501	3.840	0
$j = 5$	11.350	10.278	5.140	1.232	0

Table 9.21 Optical constants of $PC_{60}BM$ calculated by the Tauc-Lorentz model

λ (nm)	n	k	λ (nm)	n	k	λ (nm)	n	k
300	2.150	0.681	540	2.170	0.100	880	2.043	0.004
305	2.131	0.642	550	2.164	0.092	890	2.041	0.003
310	2.109	0.622	560	2.158	0.085	900	2.040	0.003
315	2.093	0.621	570	2.152	0.079	910	2.038	0.002
320	2.088	0.633	580	2.146	0.073	920	2.036	0.002
325	2.099	0.652	590	2.141	0.067	930	2.034	0.001
330	2.129	0.669	600	2.135	0.062	940	2.032	0.001
335	2.175	0.676	610	2.130	0.057	950	2.031	0.001
340	2.230	0.664	620	2.125	0.053	960	2.029	0.001
345	2.283	0.629	630	2.121	0.049	970	2.027	0
350	2.322	0.578	640	2.116	0.045	980	2.026	0
355	2.341	0.521	650	2.112	0.042	990	2.024	0
360	2.343	0.467	660	2.107	0.039	1000	2.023	0
365	2.334	0.422	670	2.103	0.036	1010	2.022	0
370	2.320	0.387	680	2.099	0.033	1020	2.020	0
375	2.304	0.360	690	2.096	0.030	1030	2.019	0
380	2.289	0.339	700	2.092	0.028	1040	2.018	0
385	2.276	0.324	710	2.088	0.026	1050	2.017	0
390	2.265	0.312	720	2.085	0.024	1060	2.016	0
395	2.256	0.301	730	2.081	0.022	1070	2.015	0
400	2.249	0.292	740	2.078	0.020	1080	2.014	0
410	2.240	0.276	750	2.075	0.018	1090	2.013	0
420	2.234	0.261	760	2.072	0.017	1100	2.012	0
430	2.230	0.244	770	2.069	0.015	1110	2.012	0
440	2.227	0.228	780	2.067	0.014	1120	2.011	0
450	2.223	0.212	790	2.064	0.013	1130	2.010	0
460	2.219	0.195	800	2.062	0.011	1140	2.009	0
470	2.215	0.180	810	2.059	0.010	1150	2.009	0
480	2.209	0.165	820	2.057	0.009	1160	2.008	0
490	2.203	0.152	830	2.054	0.008	1170	2.007	0
500	2.196	0.139	840	2.052	0.007	1180	2.007	0
510	2.190	0.128	850	2.050	0.006	1190	2.006	0
520	2.183	0.118	860	2.048	0.005	1200	2.005	0
530	2.177	0.108	870	2.046	0.005			

9.2.10 $PC_{70}BM$ (Aka [70]PCBM, PC71BM) [(6,6)-Phenyl-C_{71}-Butyric Acid Methyl Ester]

Data from A. Guerrero, B. Dörling, T. Ripolles-Sanchis, M. Aghamohammadi, E. Barrena, M. Campoy-Quiles and G. Garcia-Belmonte [11] (Supplementary Information) (Fig. 9.10 and Tables 9.22, 9.23).

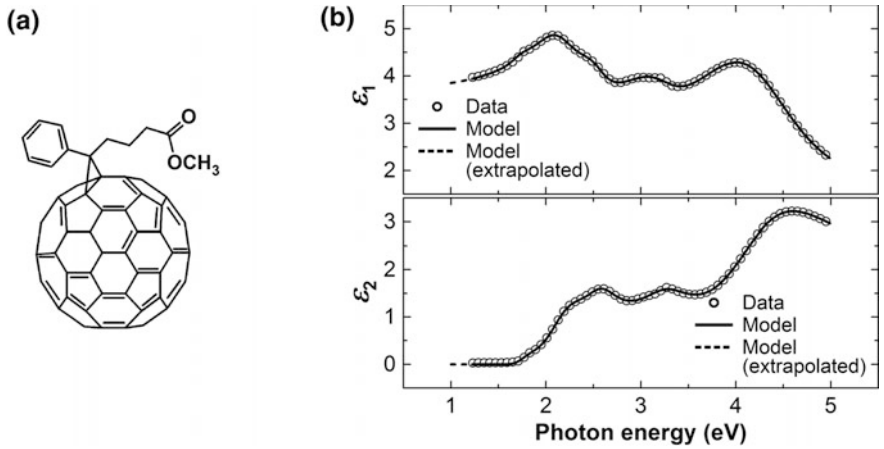


Fig. 9.10 **a** Chemical structure and **b** dielectric function of $PC_{70}BM$ at room temperature. The open circles show the experimental data and the solid lines indicate the calculation result obtained from the parameterization assuming the Tauc-Lorentz model [(8.1) and (8.2)]. The dotted lines show the extrapolated result obtained from the Tauc-Lorentz model

Table 9.22 Tauc-Lorentz parameters of (8.1) and (8.2) for $PC_{70}BM$

Peak	A (eV)	C (eV)	E_0 (eV)	E_g (eV)	$\varepsilon_1(\infty)$
$j = 1$	4.363	0.346	1.766	1.581	1.615
$j = 2$	15.347	0.679	2.160	1.740	0
$j = 3$	4.593	0.422	2.558	2.015	0
$j = 4$	3.568	0.818	3.256	1.722	0
$j = 5$	90.660	4.935	3.948	3.945	0
$j = 6$	43.177	1.588	4.295	3.032	0

Table 9.23 Optical constants of $PC_{70}BM$ calculated by the Tauc-Lorentz model

λ (nm)	n	k	λ (nm)	n	k	λ (nm)	n	k
300	2.134	0.578	540	2.161	0.302	880	2.013	0
305	2.134	0.532	550	2.176	0.286	890	2.010	0
310	2.127	0.491	560	2.191	0.267	900	2.007	0
315	2.115	0.456	570	2.203	0.243	910	2.005	0
320	2.099	0.426	580	2.210	0.217	920	2.003	0
325	2.080	0.403	590	2.213	0.190	930	2.000	0
330	2.060	0.385	600	2.211	0.164	940	1.998	0
335	2.041	0.374	610	2.205	0.140	950	1.996	0
340	2.022	0.368	620	2.196	0.120	960	1.994	0
345	2.006	0.367	630	2.185	0.103	970	1.992	0
350	1.994	0.370	640	2.174	0.089	980	1.991	0
355	1.986	0.376	650	2.164	0.078	990	1.989	0
360	1.982	0.383	660	2.155	0.068	1000	1.987	0
365	1.984	0.390	670	2.146	0.060	1010	1.986	0
370	1.989	0.395	680	2.139	0.052	1020	1.984	0
375	1.997	0.397	690	2.133	0.043	1030	1.983	0
380	2.006	0.395	700	2.125	0.035	1040	1.981	0
385	2.015	0.390	710	2.117	0.027	1050	1.980	0
390	2.021	0.382	720	2.109	0.019	1060	1.979	0
395	2.026	0.372	730	2.099	0.013	1070	1.978	0
400	2.027	0.362	740	2.090	0.008	1080	1.976	0
410	2.023	0.346	750	2.080	0.004	1090	1.975	0
420	2.014	0.336	760	2.071	0.002	1100	1.974	0
430	2.004	0.335	770	2.063	0.001	1110	1.973	0
440	1.997	0.343	780	2.056	0	1120	1.972	0
450	1.997	0.357	790	2.049	0	1130	1.971	0
460	2.008	0.374	800	2.044	0	1140	1.970	0
470	2.032	0.386	810	2.039	0	1150	1.969	0
480	2.063	0.388	820	2.034	0	1160	1.968	0
490	2.092	0.376	830	2.030	0	1170	1.967	0
500	2.112	0.358	840	2.026	0	1180	1.967	0
510	2.125	0.340	850	2.022	0	1190	1.966	0
520	2.135	0.327	860	2.019	0	1200	1.965	0
530	2.147	0.315	870	2.016	0			

9.2.11 PCDTBT [Poly{N-9-Heptadecanyl-2,7-Carbazole-alt-5,5-(4',7'-di-2-Thienyl-2',1',3'-Benzothiadiazole)}]

Data: unpublished results of M. Campoy-Quiles. The preparation and analysis of a PCDTBT layer are described in [11]. The extinction coefficient data have been shown in [12] (Fig. 9.11 and Tables 9.24, 9.25).

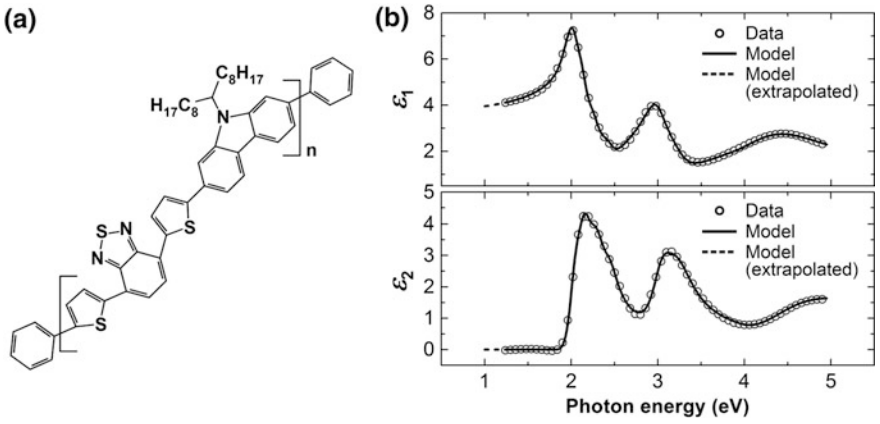


Fig. 9.11 **a** Chemical structure and **b** dielectric function of PCDTBT at room temperature. The open circles show the experimental data and the solid lines indicate the calculation result obtained from the parameterization assuming the Tauc-Lorentz model [(8.1) and (8.2)]. The dotted lines show the extrapolated result obtained from the Tauc-Lorentz model

Table 9.24 Tauc-Lorentz parameters of (8.1) and (8.2) for PCDTBT

Peak	A (eV)	C (eV)	E_0 (eV)	E_g (eV)	$\varepsilon_1(\infty)$
$j = 1$	47.521	0.210	2.028	1.829	2.020
$j = 2$	17.312	0.199	2.144	1.834	0
$j = 3$	7.933	0.225	2.287	1.832	0
$j = 4$	2.754	0.219	2.448	1.833	0
$j = 5$	33.209	0.320	3.022	2.640	0
$j = 6$	9.082	0.403	3.220	2.512	0
$j = 7$	83.250	1.495	4.327	3.941	0

Table 9.25 Optical constants of PCDTBT calculated by the Tauc-Lorentz model

λ (nm)	n	k	λ (nm)	n	k	λ (nm)	n	k
300	1.589	0.254	540	2.036	0.948	880	2.071	0
305	1.549	0.253	550	2.139	0.932	890	2.066	0
310	1.509	0.264	560	2.225	0.925	900	2.062	0
315	1.475	0.286	570	2.345	0.918	910	2.058	0
320	1.448	0.313	580	2.483	0.855	920	2.054	0
325	1.425	0.342	590	2.586	0.751	930	2.050	0
330	1.406	0.375	600	2.664	0.638	940	2.047	0
335	1.390	0.412	610	2.726	0.495	950	2.043	0
340	1.377	0.453	620	2.732	0.328	960	2.040	0
345	1.370	0.500	630	2.674	0.185	970	2.037	0
350	1.369	0.551	640	2.589	0.091	980	2.034	0
355	1.376	0.609	650	2.504	0.039	990	2.031	0
360	1.396	0.670	660	2.431	0.013	1000	2.029	0
365	1.431	0.732	670	2.372	0.002	1010	2.026	0
370	1.484	0.789	680	2.326	0	1020	2.024	0
375	1.553	0.834	690	2.292	0	1030	2.021	0
380	1.633	0.859	700	2.264	0	1040	2.019	0
385	1.714	0.863	710	2.240	0	1050	2.017	0
390	1.789	0.851	720	2.220	0	1060	2.015	0
395	1.860	0.830	730	2.203	0	1070	2.013	0
400	1.931	0.798	740	2.187	0	1080	2.011	0
410	2.055	0.666	750	2.173	0	1090	2.009	0
420	2.061	0.480	760	2.161	0	1100	2.008	0
430	1.965	0.362	770	2.149	0	1110	2.006	0
440	1.854	0.326	780	2.139	0	1120	2.004	0
450	1.758	0.341	790	2.130	0	1130	2.003	0
460	1.681	0.388	800	2.121	0	1140	2.001	0
470	1.625	0.461	810	2.113	0	1150	2.000	0
480	1.594	0.559	820	2.106	0	1160	1.998	0
490	1.606	0.677	830	2.099	0	1170	1.997	0
500	1.676	0.784	840	2.092	0	1180	1.996	0
510	1.770	0.835	850	2.087	0	1190	1.994	0
520	1.837	0.870	860	2.081	0	1200	1.993	0
530	1.918	0.922	870	2.076	0			

9.2.12 PCPDTBT [Poly{2,6-(4,4-bis-(2-Ethylhexyl)-4H-Cyclopenta[2,1-b;3,4-b']-Dithiophene)-alt-4,7-(2,1,3-Benzothiadiazole)}]

Data from A. Guerrero, B. Dörling, T. Ripolles-Sanchis, M. Aghamohammadi, E. Barrena, M. Campoy-Quiles and G. Garcia-Belmonte [11] (Supplementary Information) (Fig. 9.12 and Tables 9.26, 9.27).

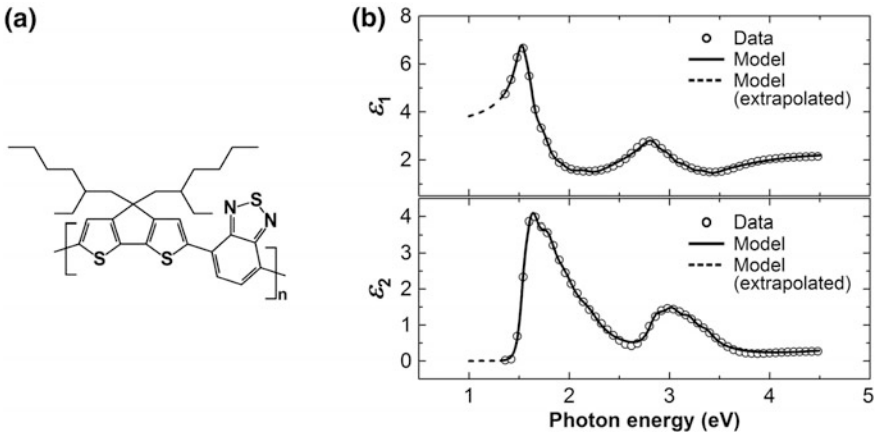


Fig. 9.12 **a** Chemical structure and **b** dielectric function of PCPDTBT at room temperature. The open circles show the experimental data and the solid lines indicate the calculation result obtained from the parameterization assuming the Tauc-Lorentz model [(8.1) and (8.2)]. The dotted lines show the extrapolated result obtained from the Tauc-Lorentz model

Table 9.26 Tauc-Lorentz parameters of (8.1) and (8.2) for PCPDTBT

Peak	A (eV)	C (eV)	E_0 (eV)	E_g (eV)	$\varepsilon_1(\infty)$
$j = 1$	16.531	0.116	1.539	1.396	2.157
$j = 2$	15.494	0.189	1.615	1.326	0
$j = 3$	5.166	0.239	1.776	1.289	0
$j = 4$	1.233	0.296	1.959	1.084	0
$j = 5$	0.269	0.300	2.189	0.631	0
$j = 6$	8.980	0.216	2.853	2.477	0
$j = 7$	0.334	0.232	3.197	1.325	0
$j = 8$	2.847	0.229	3.017	2.320	0
$j = 9$	0.063	0.212	3.374	1×10^{-4}	0
$j = 10$	21.461	4.019	4.290	3.723	0

Table 9.27 Optical constants of PCPDTBT calculated by the Tauc-Lorentz model

λ (nm)	n	k	λ (nm)	n	k	λ (nm)	n	k
300	1.441	0.084	540	1.309	0.414	880	2.284	0.020
305	1.429	0.084	550	1.316	0.475	890	2.250	0.014
310	1.415	0.085	560	1.338	0.528	900	2.222	0.010
315	1.401	0.088	570	1.366	0.566	910	2.197	0.007
320	1.386	0.092	580	1.387	0.596	920	2.176	0.005
325	1.369	0.098	590	1.402	0.629	930	2.156	0.004
330	1.351	0.107	600	1.417	0.671	940	2.140	0.003
335	1.333	0.119	610	1.444	0.720	950	2.125	0.003
340	1.313	0.133	620	1.485	0.765	960	2.111	0.003
345	1.292	0.153	630	1.532	0.799	970	2.099	0.003
350	1.270	0.179	640	1.579	0.824	980	2.088	0.002
355	1.249	0.217	650	1.620	0.847	990	2.078	0.002
360	1.240	0.270	660	1.663	0.875	1000	2.069	0.002
365	1.258	0.324	670	1.715	0.908	1010	2.060	0.002
370	1.290	0.353	680	1.783	0.936	1020	2.052	0.002
375	1.305	0.371	690	1.862	0.945	1030	2.044	0.002
380	1.317	0.405	700	1.936	0.934	1040	2.037	0.001
385	1.351	0.442	710	1.995	0.914	1050	2.031	0.001
390	1.397	0.455	720	2.040	0.900	1060	2.025	0.001
395	1.426	0.454	730	2.086	0.899	1070	2.019	0.001
400	1.445	0.464	740	2.150	0.907	1080	2.014	0.001
410	1.531	0.486	750	2.239	0.905	1090	2.008	0.001
420	1.599	0.439	760	2.342	0.873	1100	2.004	0.001
430	1.653	0.407	770	2.438	0.807	1110	1.999	0.001
440	1.703	0.307	780	2.511	0.721	1120	1.995	0.001
450	1.656	0.212	790	2.567	0.629	1130	1.991	0.001
460	1.587	0.176	800	2.614	0.523	1140	1.987	0.001
470	1.528	0.172	810	2.634	0.396	1150	1.983	0.001
480	1.479	0.183	820	2.608	0.271	1160	1.979	0.001
490	1.437	0.203	830	2.550	0.175	1170	1.976	0.001
500	1.400	0.229	840	2.485	0.112	1180	1.973	0.001
510	1.367	0.263	850	2.423	0.072	1190	1.970	0.001
520	1.339	0.304	860	2.370	0.046	1200	1.967	0.001
530	1.318	0.355	870	2.323	0.030			

9.2.13 PEDOT:PSS [Poly(3,4-Ethylenedioxythiophene): Poly(4-Styrensulfonate)]

Data from L. A. A. Pettersson, S. Ghosh and O. Inganäs [13]. The optical data have been extracted from the multi-sample analysis of PEDOT:PSS layers formed on

SiO_2-covered crystalline Si and fused silica substrates using a spin-coating process. The thermal annealing of the PEDOT:PSS samples were also perfomred at 120 °C for 2 min to enhance the conductivity. The electrical conductivity of the PEDOT:PSS layer in the direction parallel to the sample surface is 0.94 S/cm (Fig. 9.13 and Tables 9.28, 9.29, 9.30).

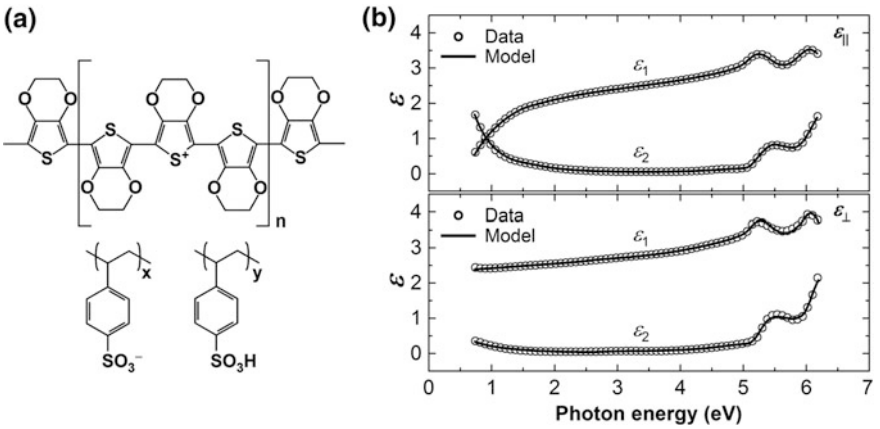


Fig. 9.13 **a** Chemical structure and **b** dielectric functions of PEDOT:PSS at room temperature. In (**b**), $\varepsilon_\parallel$ and $\varepsilon_\perp$ show the dielectric functions parallel (ordinary) and perpendicular (extraordinary) to the thin film surface, respectively. The open circles show the experimental data and the solid lines indicate the calculation result obtained from the parameterization assuming the Tauc-Lorentz model combined with the Drude model [(11.1) and (11.2)]

Table 9.28 Tauc-Lorentz (TL) peak and Drude parameters of (11.1) and (11.2) for $\varepsilon_\parallel$ of PEDOT:PSS

Model	A/A_D (eV)	C/Γ (eV)	E_0 (eV)	E_g (eV)	$\varepsilon_1(\infty)$
TL peak1	0.446	0.532	1.520	1.204	1.822
TL peak2	100.873	0.613	5.169	5.004	0
TL peak3	0.678	1.893	5.240	1.815	0
TL peak4	1.302	0.285	5.439	4.730	0
TL peak5	188.455	0.880	6.073	5.736	0
Drude	1.810	0.631	–	–	–

Table 9.29 Tauc-Lorentz (TL) peak and Drude parameters of (11.1) and (11.2) for $\varepsilon_\perp$ of PEDOT:PSS

Model	A/A_D (eV)	C/Γ (eV)	E_0 (eV)	E_g (eV)	$\varepsilon_1(\infty)$
TL peak1	2.203	0.740	2.547	2.652	1.594
TL peak2	0.845	1.654	5.226	1.443	0
TL peak3	124.649	0.581	5.239	5.047	0
TL peak4	336.897	0.946	5.942	5.941	0
TL peak5	54.486	0.507	6.124	5.602	0
Drude	0.459	1.512	–	–	–

Table 9.30 Optical constants for the ordinary ray ($N_{\parallel} = n_{\parallel} - ik_{\parallel}$) in PEDOT:PSS. The optical data reported by Pettersson et al. are shown

λ (nm)	$n_{\parallel}$	$k_{\parallel}$	λ (nm)	$n_{\parallel}$	$k_{\parallel}$	λ (nm)	$n_{\parallel}$	$k_{\parallel}$
300	1.642	2.03×10^{-2}	540	1.488	3.70×10^{-2}	880	1.339	0.133
305	1.636	1.90×10^{-2}	550	1.483	3.96×10^{-2}	890	1.334	0.136
310	1.631	1.84×10^{-2}	560	1.477	4.12×10^{-2}	900	1.329	0.140
315	1.624	1.76×10^{-2}	570	1.473	4.37×10^{-2}	910	1.323	0.143
320	1.620	1.76×10^{-2}	580	1.468	4.54×10^{-2}	920	1.317	0.146
325	1.616	1.67×10^{-2}	590	1.463	4.79×10^{-2}	930	1.312	0.150
330	1.611	1.68×10^{-2}	600	1.458	5.04×10^{-2}	940	1.307	0.154
335	1.607	1.68×10^{-2}	610	1.453	5.29×10^{-2}	950	1.302	0.158
340	1.602	1.68×10^{-2}	620	1.449	5.55×10^{-2}	960	1.296	0.162
345	1.598	1.68×10^{-2}	630	1.445	5.88×10^{-2}	970	1.289	0.167
350	1.593	1.68×10^{-2}	640	1.44	6.19×10^{-2}	980	1.283	0.171
355	1.590	1.68×10^{-2}	650	1.437	6.47×10^{-2}	990	1.278	0.176
360	1.585	1.68×10^{-2}	660	1.432	6.82×10^{-2}	1000	1.272	0.181
365	1.582	1.68×10^{-2}	670	1.428	7.06×10^{-2}	1010	1.267	0.186
370	1.579	1.68×10^{-2}	680	1.424	7.33×10^{-2}	1020	1.260	0.191
375	1.575	1.76×10^{-2}	690	1.420	7.70×10^{-2}	1030	1.254	0.197
380	1.572	1.76×10^{-2}	700	1.416	7.98×10^{-2}	1040	1.248	0.203
385	1.568	1.76×10^{-2}	710	1.412	8.26×10^{-2}	1050	1.242	0.209
390	1.565	1.76×10^{-2}	720	1.408	8.57×10^{-2}	1060	1.236	0.215
395	1.563	1.76×10^{-2}	730	1.404	8.91×10^{-2}	1070	1.230	0.220
400	1.559	1.77×10^{-2}	740	1.400	9.20×10^{-2}	1080	1.224	0.225
410	1.555	1.85×10^{-2}	750	1.396	9.49×10^{-2}	1090	1.219	0.229
420	1.549	1.94×10^{-2}	760	1.393	9.77×10^{-2}	1100	1.213	0.234
430	1.543	2.02×10^{-2}	770	1.388	0.102	1110	1.208	0.240
440	1.538	2.10×10^{-2}	780	1.383	0.104	1120	1.202	0.249
450	1.533	2.19×10^{-2}	790	1.380	0.107	1130	1.197	0.257
460	1.527	2.27×10^{-2}	800	1.375	0.11	1140	1.192	0.267
470	1.523	2.44×10^{-2}	810	1.371	0.113	1150	1.186	0.276
480	1.517	2.61×10^{-2}	820	1.367	0.115	1160	1.180	0.282
490	1.512	2.77×10^{-2}	830	1.363	0.118	1170	1.176	0.287
500	1.508	2.95×10^{-2}	840	1.358	0.121	1180	1.170	0.296
510	1.503	3.11×10^{-2}	850	1.354	0.124	1190	1.166	0.306
520	1.498	3.28×10^{-2}	860	1.349	0.127	1200	1.162	0.315
530	1.493	3.44×10^{-2}	870	1.343	0.13			

9.2.14 PMMA [Poly(Methyl Methacrylate)]

Data from M. Campoy-Quiles, J. Nelson, D. D. C. Bradley and P. G. Etchegoin [8]. The optical data have been extracted from a PMMA layer formed on a fused silica substrate using a spin-coating process. While PMMA is not per se a photovoltaic material, this material is often used within the field. The optical data of a thick PMMA substrate are shown in Fig. 13.6 (Chap. 13) (Fig. 9.14 and Tables 9.31, 9.32).

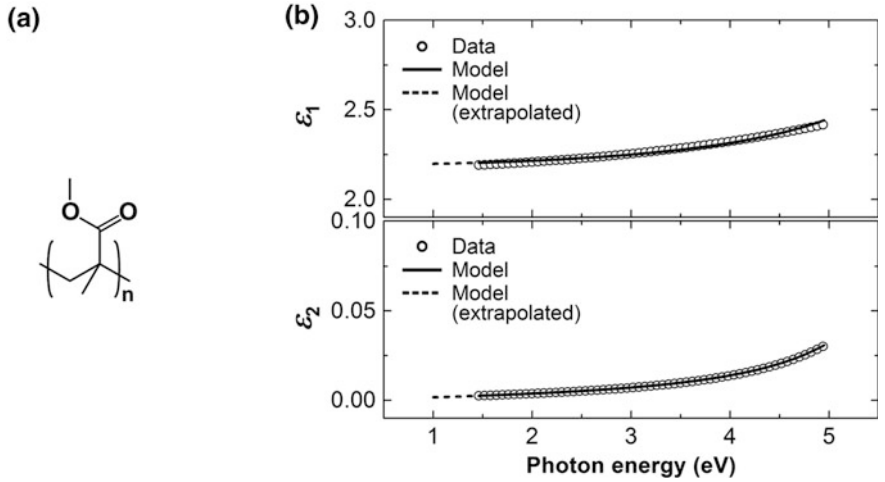


Fig. 9.14 **a** Chemical structure and **b** dielectric function of PMMA at room temperature. The open circles show the experimental data and the solid lines indicate the calculation result obtained from the parameterization assuming the Tauc-Lorentz model [(8.1) and (8.2)]. The dotted lines show the extrapolated result obtained from the Tauc-Lorentz model

Table 9.31 Tauc-Lorentz parameters of (8.1) and (8.2) for PMMA

Peak	A (eV)	C (eV)	E_0 (eV)	E_g (eV)	$\varepsilon_1(\infty)$
$j = 1$	1.819	0.311	7.043	0.027	1.937

Table 9.32 Optical constants of PMMA calculated by the Tauc-Lorentz model

λ (nm)	n	k	λ (nm)	n	k	λ (nm)	n	k
300	1.526	0.005	540	1.491	0.002	880	1.485	0.001
305	1.523	0.005	550	1.491	0.001	890	1.484	0.001
310	1.521	0.005	560	1.490	0.001	900	1.484	0.001
315	1.520	0.004	570	1.490	0.001	910	1.484	0.001
320	1.518	0.004	580	1.490	0.001	920	1.484	0.001
325	1.516	0.004	590	1.489	0.001	930	1.484	0.001
330	1.515	0.004	600	1.489	0.001	940	1.484	0.001
335	1.514	0.004	610	1.489	0.001	950	1.484	0.001
340	1.512	0.004	620	1.489	0.001	960	1.484	0.001
345	1.511	0.003	630	1.488	0.001	970	1.484	0.001
350	1.510	0.003	640	1.488	0.001	980	1.484	0.001
355	1.509	0.003	650	1.488	0.001	990	1.484	0.001
360	1.508	0.003	660	1.488	0.001	1000	1.484	0.001
365	1.507	0.003	670	1.487	0.001	1010	1.484	0.001
370	1.506	0.003	680	1.487	0.001	1020	1.484	0.001
375	1.505	0.003	690	1.487	0.001	1030	1.484	0.001
380	1.504	0.003	700	1.487	0.001	1040	1.483	0.001
385	1.504	0.003	710	1.487	0.001	1050	1.483	0.001
390	1.503	0.003	720	1.486	0.001	1060	1.483	0.001
395	1.502	0.003	730	1.486	0.001	1070	1.483	0.001
400	1.502	0.003	740	1.486	0.001	1080	1.483	0.001
410	1.500	0.002	750	1.486	0.001	1090	1.483	0.001
420	1.499	0.002	760	1.486	0.001	1100	1.483	0.001
430	1.498	0.002	770	1.486	0.001	1110	1.483	0.001
440	1.497	0.002	780	1.486	0.001	1120	1.483	0.001
450	1.496	0.002	790	1.485	0.001	1130	1.483	0.001
460	1.496	0.002	800	1.485	0.001	1140	1.483	0.001
470	1.495	0.002	810	1.485	0.001	1150	1.483	0.001
480	1.494	0.002	820	1.485	0.001	1160	1.483	0.001
490	1.494	0.002	830	1.485	0.001	1170	1.483	0.001
500	1.493	0.002	840	1.485	0.001	1180	1.483	0.001
510	1.493	0.002	850	1.485	0.001	1190	1.483	0.001
520	1.492	0.002	860	1.485	0.001	1200	1.483	0.001
530	1.492	0.002	870	1.485	0.001			

9.2.15 PTB7 [Poly{[4,8-bis[(2-Ethylhexyl)Oxy]Benzo [1,2-b:4,5-b']Dithiophene-2,6-Diyl][3-Fluoro-2-[(2-Ethylhexyl)Carbonyl]Thieno[3,4-b] Thiophenediyl]}]

Data from M. R. Hammond, R. J. Kline, A. A. Herzing, L. J. Richter, D. S. Germack, H.-W. Ro, C. L. Soles, D. A. Fischer, T. Xu, L. Yu, M. F. Toney and D. M. DeLongchamp [14]. Although PTB7 films formed by a spin-coating process exhibit optical anisotropy, only the dielectric function parallel to the thin film surface (ordinary, $\varepsilon_{\|}$) is shown (Fig. 9.15 and Tables 9.33, 9.34).

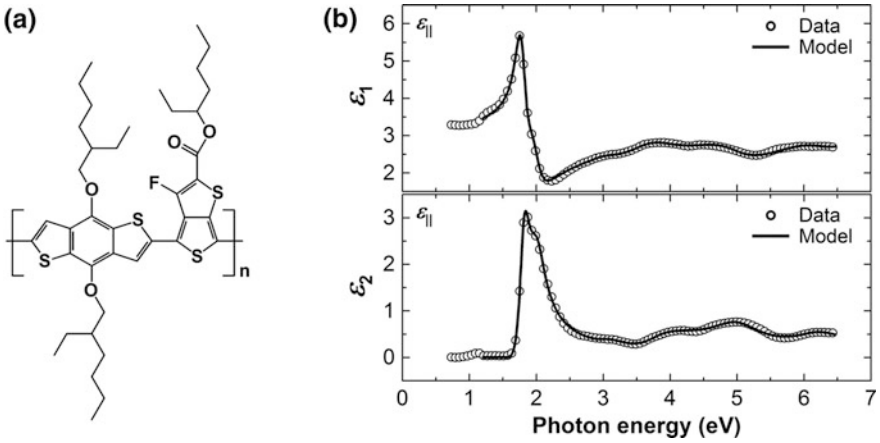


Fig. 9.15 **a** Chemical structure and **b** dielectric function of PTB7 at room temperature. In (**b**), only the dielectric function for ordinary ray ($\varepsilon_{\|}$) is shown. The open circles show the experimental data and the solid lines indicate the calculation result obtained from the parameterization assuming the Tauc-Lorentz model [(8.1) and (8.2)]

Table 9.33 Tauc-Lorentz parameters of (8.1) and (8.2) for PTB7

Peak	A (eV)	C (eV)	E_0 (eV)	E_g (eV)	$\varepsilon_1(\infty)$
$j = 1$	31.263	0.191	1.800	1.574	0.783
$j = 2$	6.497	0.284	1.997	1.532	0
$j = 3$	1.350	0.451	3.068	2.595	0
$j = 4$	14.175	0.926	3.777	3.346	0
$j = 5$	0.425	0.932	5.005	1×10^{-4}	0
$j = 6$	2.103	1.002	6.233	3.713	0
$j = 7$	146.963	9.858	10.718	6.224	0

Table 9.34 Optical constants of PTB7. The optical data reported by Hammond et al. are shown

λ (nm)	n	k	λ (nm)	n	k	λ (nm)	n	k
300	1.671	0.174	540	1.398	0.373	880	1.942	0.010
305	1.676	0.169	550	1.404	0.427	890	1.934	0.010
310	1.679	0.164	560	1.420	0.482	900	1.932	0.012
315	1.682	0.157	570	1.445	0.536	910	1.925	0.010
320	1.683	0.148	580	1.478	0.589	920	1.921	0.010
325	1.682	0.139	590	1.523	0.645	930	1.919	0.010
330	1.679	0.130	600	1.585	0.695	940	1.917	0.011
335	1.676	0.120	610	1.665	0.729	950	1.911	0.011
340	1.670	0.109	620	1.748	0.739	960	1.909	0.010
345	1.660	0.098	630	1.819	0.730	970	1.905	0.009
350	1.647	0.091	640	1.875	0.723	980	1.902	0.009
355	1.633	0.088	650	1.933	0.729	990	1.897	0.009
360	1.622	0.089	660	2.011	0.741	1000	1.894	0.008
365	1.612	0.094	670	2.121	0.729	1010	1.889	0.008
370	1.605	0.099	680	2.242	0.680	1020	1.881	0.009
375	1.598	0.104	690	2.353	0.566	1030	1.873	0.012
380	1.592	0.109	700	2.405	0.418	1040	1.867	0.012
385	1.588	0.115	710	2.395	0.276	1050	1.862	0.015
390	1.585	0.120	720	2.343	0.169	1060	1.854	0.020
395	1.584	0.123	730	2.279	0.100	1070	1.848	0.023
400	1.582	0.123	740	2.219	0.058	1080	1.843	0.025
410	1.572	0.127	750	2.169	0.035	1090	1.838	0.025
420	1.563	0.131	760	2.128	0.022	1100	1.836	0.025
430	1.552	0.135	770	2.095	0.015	1110	1.832	0.027
440	1.537	0.142	780	2.068	0.012	1120	1.829	0.026
450	1.523	0.150	790	2.047	0.011	1130	1.827	0.025
460	1.511	0.155	800	2.027	0.010	1140	1.825	0.024
470	1.497	0.162	810	2.011	0.009	1150	1.823	0.023
480	1.479	0.177	820	1.996	0.009	1160	1.822	0.022
490	1.463	0.192	830	1.986	0.008	1170	1.820	0.020
500	1.445	0.215	840	1.975	0.009	1180	1.820	0.019
510	1.430	0.243	850	1.964	0.009	1190	1.819	0.017
520	1.415	0.280	860	1.954	0.009	1200	1.818	0.016
530	1.403	0.323	870	1.947	0.009			

9.2.16 PTB7:$PC_{70}BM$ (Blend Ratio 1:1.5) [Poly{[4,8-bis [(2-Ethylhexyl)Oxy]Benzo [1,2-b:4,5-b'] Dithiophene-2,6-Diyl][3-Fluoro-2-[(2-Ethylhexyl) Carbonyl]Thieno[3,4-b]Thiophenediyl]}:(6,6)-Phenyl-C_{71}-Butyric Acid Methyl Ester]

Data from C. J. M. Emmott, J. A. Röhr, M. Campoy-Quiles, T. Kirchartz, A. Urbina, N. J. Ekins-Daukes, and J. Nelson [9] (Supplementary Information) (Fig. 9.16 and Tables 9.35, 9.36).

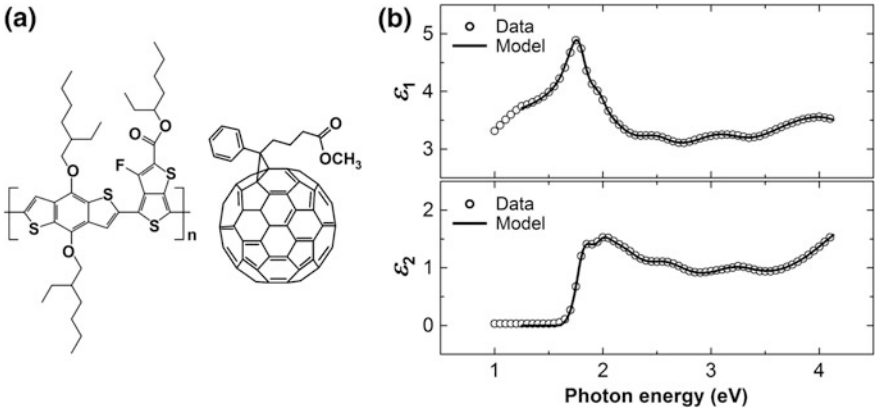


Fig. 9.16 **a** Chemical structure and **b** dielectric function of PTB7:$PC_{70}BM$ at room temperature. The open circles show the experimental data and the solid lines indicate the calculation result obtained from the parameterization assuming the Tauc-Lorentz model [(8.1) and (8.2)]

Table 9.35 Tauc-Lorentz parameters of (8.1) and (8.2) for PTB7:$PC_{70}BM$

Peak	A (eV)	C (eV)	E_0 (eV)	E_g (eV)	$\varepsilon_1(\infty)$
$j = 1$	15.800	0.237	1.796	1.564	1.695
$j = 2$	3.565	0.230	1.991	1.657	0
$j = 3$	7.477	0.526	2.120	1.694	0
$j = 4$	3.653	0.507	2.558	2.009	0
$j = 5$	1.609	0.705	3.231	1.624	0
$j = 6$	73.603	4.011	4.209	3.129	0
$j = 7$	0.290	0.592	4.212	1.555	0

Table 9.36 Optical constants of PTB7:$PC_{70}BM$. The optical data reported by Emmott et al. are shown

λ (nm)	n	k	λ (nm)	n	k	λ (nm)	n	k
300	1.920	0.412	540	1.832	0.333	880	1.966	0.008
305	1.920	0.384	550	1.842	0.348	890	1.962	0.008
310	1.920	0.356	560	1.857	0.360	900	1.959	0.008
315	1.912	0.334	570	1.876	0.368	910	1.955	0.008
320	1.905	0.312	580	1.894	0.375	920	1.952	0.008
325	1.893	0.297	590	1.913	0.382	930	1.949	0.008
330	1.882	0.282	600	1.938	0.389	940	1.946	0.008
335	1.870	0.272	610	1.968	0.390	950	1.943	0.008
340	1.858	0.263	620	2.000	0.382	960	1.941	0.008
345	1.845	0.259	630	2.025	0.366	970	1.939	0.008
350	1.833	0.255	640	2.041	0.350	980	1.937	0.008
355	1.823	0.258	650	2.056	0.342	990	1.935	0.008
360	1.814	0.260	660	2.077	0.341	1000	1.932	0.008
365	1.811	0.268	670	2.114	0.334	1010	1.929	0.008
370	1.808	0.275	680	2.157	0.315	1020	1.924	0.008
375	1.814	0.280	690	2.200	0.269	1030	1.920	0.008
380	1.820	0.284	700	2.221	0.206	1040	1.915	0.008
385	1.822	0.278	710	2.216	0.143	1050	1.910	0.008
390	1.824	0.273	720	2.191	0.094	1060	1.905	0.008
395	1.823	0.270	730	2.161	0.060	1070	1.901	0.008
400	1.822	0.267	740	2.131	0.039	1080	1.896	0.008
410	1.818	0.261	750	2.105	0.027	1090	1.891	0.008
420	1.811	0.256	760	2.082	0.020	1100	1.886	0.008
430	1.801	0.254	770	2.063	0.015	1110	1.882	0.008
440	1.789	0.260	780	2.047	0.012	1120	1.877	0.008
450	1.784	0.274	790	2.033	0.011	1130	1.872	0.008
460	1.787	0.290	800	2.022	0.009	1140	1.868	0.008
470	1.798	0.301	810	2.012	0.008	1150	1.863	0.008
480	1.810	0.306	820	2.002	0.008	1160	1.858	0.008
490	1.820	0.305	830	1.995	0.008	1170	1.853	0.008
500	1.824	0.303	840	1.988	0.008	1180	1.849	0.008
510	1.826	0.305	850	1.981	0.008	1190	1.844	0.008
520	1.826	0.310	860	1.975	0.008	1200	1.839	0.008
530	1.827	0.321	870	1.971	0.008			

9.2.17 Si-PCPDTBT [Poly{[4, 40-bis(2-Ethylhexyl) Dithieno (3,2-b:20,30-d)Silole]-2,6-Diyl-alt-[4,7-bis (2-Thienyl)-2,1,3-Benzothiadiazole]-5,50-Diyl}]

Data: unpublished results of M. Campoy-Quiles. The preparation and analysis of a Si-PCPDTBT layer are described in [15]. Data for the Si-PCPDTBT:PC70BM are shown in the supplementary information of [15]. Extinction coefficient data have been shown in [12] (Fig. 9.17 and Tables 9.37, 9.38).

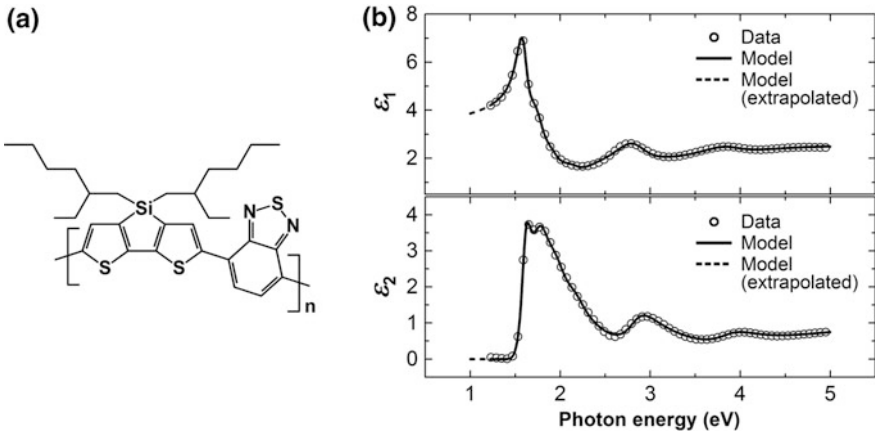


Fig. 9.17 **a** Chemical structure and **b** dielectric function of Si-PCPDTBT at room temperature. The open circles show the experimental data and the solid lines indicate the calculation result obtained from the parameterization assuming the Tauc-Lorentz model [(8.1) and (8.2)]. The dotted lines show the extrapolated result obtained from the Tauc-Lorentz model

Table 9.37 Tauc-Lorentz parameters of (8.1) and (8.2) for Si-PCPDTBT

Peak	A (eV)	C (eV)	E_0 (eV)	E_g (eV)	$\varepsilon_1(\infty)$
$j = 1$	32.524	0.146	1.606	1.422	1.696
$j = 2$	12.197	0.265	1.765	1.395	0
$j = 3$	3.292	0.299	1.945	1.390	0
$j = 4$	1.033	0.292	2.167	1.398	0
$j = 5$	18.709	0.435	2.846	2.498	0
$j = 6$	11.818	0.577	3.870	3.408	0
$j = 7$	70.597	8.627	4.603	3.785	0

Table 9.38 Optical constants of Si-PCPDTBT calculated by the Tauc-Lorentz model

λ (nm)	n	k	λ (nm)	n	k	λ (nm)	n	k
300	1.555	0.231	540	1.371	0.472	880	2.216	0
305	1.561	0.236	550	1.382	0.532	890	2.193	0
310	1.571	0.238	560	1.409	0.588	900	2.174	0
315	1.581	0.233	570	1.444	0.631	910	2.156	0
320	1.588	0.220	580	1.477	0.661	920	2.141	0
325	1.587	0.204	590	1.503	0.691	930	2.128	0
330	1.578	0.190	600	1.529	0.728	940	2.115	0
335	1.563	0.180	610	1.563	0.771	950	2.104	0
340	1.546	0.177	620	1.610	0.811	960	2.094	0
345	1.529	0.179	630	1.667	0.842	970	2.085	0
350	1.514	0.185	640	1.725	0.861	980	2.076	0
355	1.500	0.194	650	1.780	0.873	990	2.068	0
360	1.489	0.206	660	1.833	0.886	1000	2.060	0
365	1.480	0.219	670	1.892	0.900	1010	2.053	0
370	1.473	0.234	680	1.961	0.909	1020	2.047	0
375	1.468	0.249	690	2.038	0.902	1030	2.041	0
380	1.466	0.265	700	2.110	0.876	1040	2.035	0
385	1.465	0.283	710	2.167	0.839	1050	2.030	0
390	1.468	0.301	720	2.206	0.806	1060	2.025	0
395	1.473	0.319	730	2.240	0.790	1070	2.020	0
400	1.483	0.338	740	2.288	0.791	1080	2.015	0
410	1.515	0.370	750	2.371	0.792	1090	2.011	0
420	1.565	0.383	760	2.491	0.758	1100	2.007	0
430	1.618	0.362	770	2.612	0.656	1110	2.003	0
440	1.644	0.311	780	2.678	0.498	1120	1.999	0
450	1.630	0.258	790	2.672	0.338	1130	1.996	0
460	1.591	0.227	800	2.618	0.214	1140	1.992	0
470	1.545	0.219	810	2.547	0.129	1150	1.989	0
480	1.501	0.230	820	2.478	0.075	1160	1.986	0
490	1.463	0.253	830	2.415	0.042	1170	1.983	0
500	1.433	0.284	840	2.361	0.021	1180	1.980	0
510	1.408	0.321	850	2.315	0.010	1190	1.977	0
520	1.388	0.365	860	2.275	0.003	1200	1.975	0
530	1.375	0.415	870	2.243	0.001			

9.2.18 Spiro-OMeTAD [2,2',7,7'-Tetrakis-(N, N-di-p-Methoxyphenylamine) 9,9'-Spirobifluorene]

Data from M. Shirayama, H. Kadowaki, T. Miyadera, T. Sugita, M. Tamakoshi, M. Kato, T. Fujiseki, D. Murata, S. Hara, T. N. Murakami, S. Fujimoto, M. Chikamatsu and H. Fujiwara [16]. The optical data have been extracted from a spiro-OMeTAD layer formed on a ZnO-coated crystalline Si substrate using a spin-coating process. The thermal annealing of the sample was performed at 100 °C. The spiro-OMeTAD layer doped with Li (LiTFSI) has been characterized (Fig. 9.18 and Tables 9.39, 9.40).

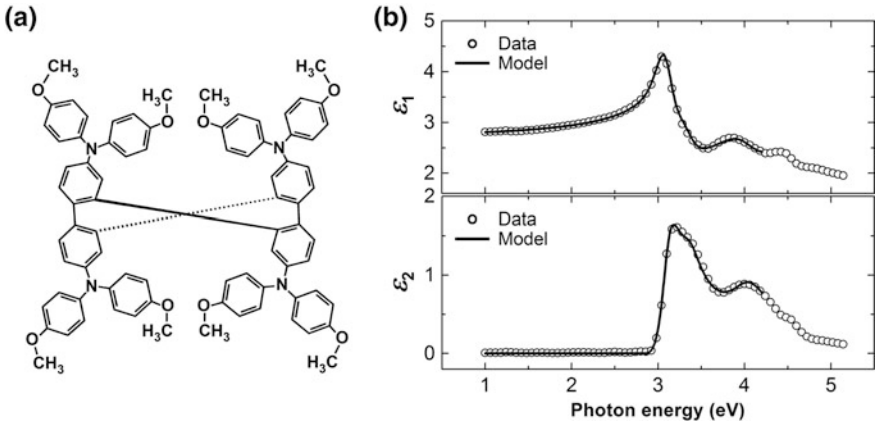


Fig. 9.18 **a** Chemical structure and **b** dielectric function of spiro-OMeTAD at room temperature. The open circles show the experimental data and the solid lines indicate the calculation result obtained from the parameterization assuming the Tauc-Lorentz model [(8.1) and (8.2)]

Table 9.39 Tauc-Lorentz parameters of (8.1) and (8.2) for spiro-OMeTAD reported by Shirayama et al.

Peak	A (eV)	C (eV)	E_0 (eV)	E_g (eV)	$\varepsilon_1(\infty)$
$j = 1$	55.872	0.283	3.102	2.855	2.256
$j = 2$	4.914	0.303	3.358	2.826	0
$j = 3$	3.033	0.555	4.035	2.850	0
$j = 4$	4.482	0.001	5.183	2.850	0

Table 9.40 Optical constants of spiro-OMeTAD calculated by the Tauc-Lorentz model

λ (nm)	n	k	λ (nm)	n	k	λ (nm)	n	k
300	1.592	0.269	540	1.742	0	880	1.686	0
305	1.617	0.280	550	1.738	0	890	1.686	0
310	1.640	0.276	560	1.734	0	900	1.685	0
315	1.653	0.262	570	1.730	0	910	1.685	0
320	1.654	0.249	580	1.727	0	920	1.684	0
325	1.647	0.241	590	1.723	0	930	1.684	0
330	1.637	0.240	600	1.721	0	940	1.684	0
335	1.625	0.247	610	1.718	0	950	1.683	0
340	1.616	0.261	620	1.716	0	960	1.683	0
345	1.609	0.282	630	1.713	0	970	1.682	0
350	1.609	0.310	640	1.711	0	980	1.682	0
355	1.619	0.344	650	1.710	0	990	1.682	0
360	1.643	0.379	660	1.708	0	1000	1.681	0
365	1.682	0.407	670	1.706	0	1010	1.681	0
370	1.729	0.419	680	1.705	0	1020	1.681	0
375	1.770	0.421	690	1.703	0	1030	1.680	0
380	1.809	0.425	700	1.702	0	1040	1.680	0
385	1.859	0.432	710	1.700	0	1050	1.680	0
390	1.929	0.426	720	1.699	0	1060	1.679	0
395	2.010	0.386	730	1.698	0	1070	1.679	0
400	2.073	0.305	740	1.697	0	1080	1.679	0
410	2.068	0.120	750	1.696	0	1090	1.679	0
420	1.980	0.027	760	1.695	0	1100	1.678	0
430	1.907	0.002	770	1.694	0	1110	1.678	0
440	1.862	0	780	1.693	0	1120	1.678	0
450	1.834	0	790	1.692	0	1130	1.678	0
460	1.814	0	800	1.692	0	1140	1.677	0
470	1.799	0	810	1.691	0	1150	1.677	0
480	1.786	0	820	1.690	0	1160	1.677	0
490	1.776	0	830	1.689	0	1170	1.677	0
500	1.767	0	840	1.689	0	1180	1.677	0
510	1.760	0	850	1.688	0	1190	1.676	0
520	1.753	0	860	1.688	0	1200	1.676	0
530	1.747	0	870	1.687	0			

9.2.19 TQ1 [Poly{2,3-bis-(3-Octyloxyphenyl) Quinoxaline-5,8-Diyl-alt-Thiophene-2,5-Diyl}]

Data for TQ1 and its blends with PC70BM are described in M. Campoy-Quiles, C. Müller, M. Garriga, E. Wang, O. Inganäs, M. I. Alonso [5]. The preparation and analysis of a TQ1 layer can be found in [17] (Fig. 9.19 and Tables 9.41, 9.42).

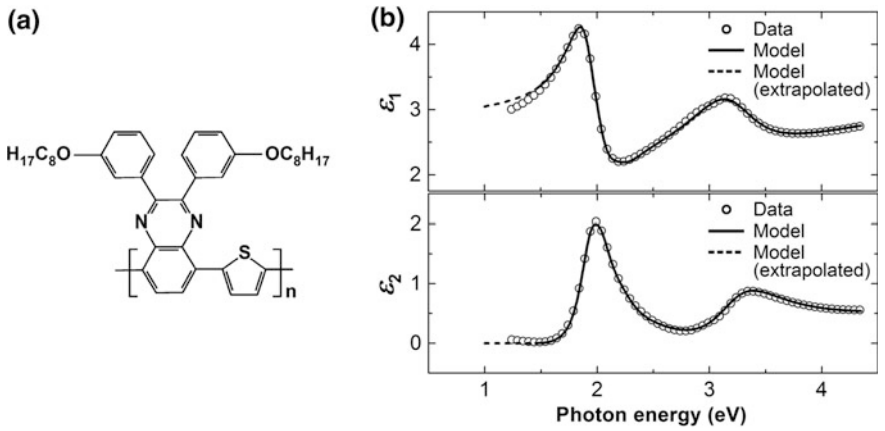


Fig. 9.19 **a** Chemical structure and **b** dielectric function of TQ1 at room temperature. The open circles show the experimental data and the solid lines indicate the calculation result obtained from the parameterization assuming the Tauc-Lorentz model [(8.1) and (8.2)]. The dotted lines show the extrapolated result obtained from the Tauc-Lorentz model

Table 9.41 Tauc-Lorentz parameters of (8.1) and (8.2) for TQ1

Peak	A (eV)	C (eV)	E_0 (eV)	E_g (eV)	$\varepsilon_1(\infty)$
$j = 1$	7.453	0.287	1.938	1.448	0.003
$j = 2$	1.494	0.227	2.045	1.516	0
$j = 3$	0.384	0.260	2.215	1.514	0
$j = 4$	14.465	0.714	3.233	2.674	0
$j = 5$	66.752	10.063	13.570	2.549	0

Table 9.42 Optical constants of TQ1 calculated by the Tauc-Lorentz model

λ (nm)	n	k	λ (nm)	n	k	λ (nm)	n	k
300	1.650	0.171	540	1.507	0.239	880	1.807	0
305	1.646	0.175	550	1.508	0.282	890	1.804	0
310	1.642	0.180	560	1.517	0.325	900	1.800	0
315	1.639	0.187	570	1.532	0.369	910	1.796	0
320	1.637	0.194	580	1.556	0.421	920	1.793	0
325	1.636	0.202	590	1.599	0.476	930	1.790	0
330	1.637	0.211	600	1.667	0.522	940	1.788	0
335	1.639	0.220	610	1.751	0.544	950	1.785	0
340	1.644	0.230	620	1.840	0.540	960	1.783	0
345	1.652	0.239	630	1.926	0.512	970	1.780	0
350	1.662	0.247	640	2.001	0.459	980	1.778	0
355	1.676	0.254	650	2.053	0.387	990	1.776	0
360	1.692	0.258	660	2.078	0.309	1000	1.774	0
365	1.711	0.258	670	2.079	0.238	1010	1.772	0
370	1.730	0.253	680	2.065	0.179	1020	1.771	0
375	1.749	0.243	690	2.043	0.134	1030	1.769	0
380	1.765	0.227	700	2.019	0.100	1040	1.767	0
385	1.777	0.208	710	1.996	0.075	1050	1.766	0
390	1.784	0.186	720	1.974	0.056	1060	1.764	0
395	1.785	0.164	730	1.953	0.041	1070	1.763	0
400	1.782	0.142	740	1.935	0.031	1080	1.762	0
410	1.763	0.107	750	1.918	0.023	1090	1.760	0
420	1.737	0.084	760	1.904	0.017	1100	1.759	0
430	1.708	0.071	770	1.890	0.012	1110	1.758	0
440	1.681	0.067	780	1.878	0.008	1120	1.757	0
450	1.656	0.069	790	1.868	0.006	1130	1.756	0
460	1.633	0.074	800	1.858	0.004	1140	1.755	0
470	1.613	0.084	810	1.849	0.002	1150	1.754	0
480	1.594	0.095	820	1.841	0.001	1160	1.753	0
490	1.576	0.109	830	1.834	0.001	1170	1.752	0
500	1.559	0.125	840	1.828	0	1180	1.751	0
510	1.543	0.145	850	1.822	0	1190	1.750	0
520	1.527	0.170	860	1.816	0	1200	1.749	0
530	1.514	0.202	870	1.812	0			

9.2.20 DPPTTT [Thieno(3,2-b)Thiophene-Diketopyrrolopyrrole]

Data from M. S. Vezie, S. Few, I. Meager, G. Pieridou, B. Dörling, R. S. Ashraf, A. R. Goñi, H. Bronstein, I. McCulloch, S. C. Hayes, M. Campoy-Quiles and J. Nelson [12] (Fig. 9.20 and Tables 9.43, 9.44).

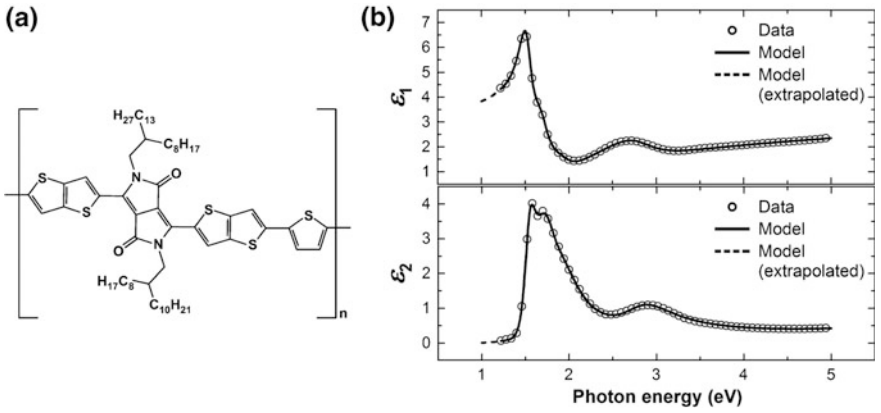


Fig. 9.20 **a** Chemical structure and **b** dielectric function of DPPTTT at room temperature. The open circles show the experimental data and the solid lines indicate the calculation result obtained from the parameterization assuming the Tauc-Lorentz model [(8.1) and (8.2)]. The dotted lines show the extrapolated result obtained from the Tauc-Lorentz model

Table 9.43 Tauc-Lorentz parameters of (8.1) and (8.2) for DPPTTT

Peak	A (eV)	C (eV)	E_0 (eV)	E_g (eV)	$\varepsilon_1(\infty)$
$j = 1$	26.722	0.168	1.536	1.329	1.325
$j = 2$	2.368	0.288	1.731	0.866	0
$j = 3$	4.202	0.443	1.921	1.304	0
$j = 4$	7.090	0.727	2.822	2.095	0
$j = 5$	15.258	4.552	9.949	1.563	0

Table 9.44 Optical constants of DPPTTT calculated by the Tauc-Lorentz model

λ (nm)	n	k	λ (nm)	n	k	λ (nm)	n	k
300	1.460	0.147	540	1.354	0.366	880	2.367	0.079
305	1.454	0.150	550	1.337	0.403	890	2.325	0.060
310	1.447	0.155	560	1.326	0.446	900	2.288	0.047
315	1.440	0.160	570	1.321	0.494	910	2.255	0.037
320	1.434	0.165	580	1.324	0.545	920	2.227	0.031
325	1.427	0.171	590	1.335	0.598	930	2.202	0.027
330	1.421	0.178	600	1.357	0.650	940	2.181	0.025
335	1.415	0.185	610	1.386	0.699	950	2.162	0.022
340	1.410	0.193	620	1.423	0.742	960	2.146	0.020
345	1.404	0.201	630	1.464	0.779	970	2.131	0.019
350	1.400	0.211	640	1.505	0.810	980	2.118	0.017
355	1.396	0.221	650	1.547	0.838	990	2.105	0.015
360	1.392	0.232	660	1.589	0.866	1000	2.094	0.014
365	1.390	0.243	670	1.634	0.896	1010	2.084	0.013
370	1.388	0.256	680	1.687	0.926	1020	2.074	0.012
375	1.388	0.269	690	1.751	0.952	1030	2.065	0.011
380	1.389	0.282	700	1.825	0.966	1040	2.057	0.010
385	1.391	0.296	710	1.903	0.964	1050	2.049	0.009
390	1.396	0.310	720	1.974	0.946	1060	2.041	0.008
395	1.402	0.323	730	2.033	0.918	1070	2.034	0.008
400	1.411	0.336	740	2.078	0.892	1080	2.028	0.007
410	1.435	0.357	750	2.116	0.874	1090	2.022	0.006
420	1.464	0.369	760	2.158	0.868	1100	2.016	0.006
430	1.495	0.367	770	2.214	0.869	1110	2.010	0.005
440	1.519	0.353	780	2.294	0.865	1120	2.005	0.005
450	1.532	0.331	790	2.396	0.836	1130	2.000	0.004
460	1.531	0.308	800	2.503	0.764	1140	1.995	0.004
470	1.520	0.289	810	2.585	0.650	1150	1.991	0.004
480	1.500	0.277	820	2.621	0.514	1160	1.986	0.003
490	1.476	0.274	830	2.612	0.386	1170	1.982	0.003
500	1.450	0.278	840	2.574	0.281	1180	1.978	0.003
510	1.423	0.290	850	2.522	0.203	1190	1.974	0.002
520	1.398	0.309	860	2.467	0.147	1200	1.971	0.002
530	1.375	0.334	870	2.415	0.107			

References

1. H. Fujiwara, *Spectroscopic Ellipsometry: Principles and Applications* (Wiley, West Sussex, UK, 2007)
2. G.E. Jellison Jr., F.A. Modine, Appl. Phys. Lett. **69**, 371 (1996); Erratum, Appl. Phys. Lett. **69**, 2137 (1996)
3. C. Müller, J. Bergqvist, K. Vandewal, K. Tvingstedt, A.S. Anselmo, R. Magnusson, M.I. Alonso, E. Moons, H. Arwin, M. Campoy-Quiles, O. Inganäs, J. Mater. Chem. **21**, 10676 (2011)
4. C. Müller, L.M. Andersson, O. Peña-Rodríguez, M. Garriga, O. Inganäs, M. Campoy-Quiles, Macromolecules **46**, 7325 (2013)
5. M. Campoy-Quiles, C. Müller, M. Garriga, E. Wang, O. Inganäs, M.I. Alonso, Thin Solid Films **571**, 371 (2014)
6. M.I. Alonso, M. Garriga, J.O. Ossó, F. Schreiber, E. Barrena, H. Dosch, J. Chem. Phys. **119**, 6335 (2003)
7. M. Tammer, A.P. Monkman, Adv. Mater. **14**, 210 (2002)
8. M. Campoy-Quiles, J. Nelson, D.D.C. Bradley, P.G. Etchegoin, Phys. Rev. B **76**, 235206 (2007)
9. C.J.M. Emmott, J.A. Röhr, M. Campoy-Quiles, T. Kirchartz, A. Urbina, N.J. Ekins-Daukes, J. Nelson, Energy Environ. Sci. **8**, 1317 (2015)
10. U. Zhokhavets, G. Gobsch, H. Hoppe, N.S. Sariciftci, Thin Solid Films **451–452**, 69 (2004)
11. A. Guerrero, B. Dörling, T. Ripolles-Sanchis, M. Aghamohammadi, E. Barrena, M. Campoy-Quiles, G. Garcia-Belmonte, ACS Nano **7**, 4637 (2013)
12. M.S. Vezie, S. Few, I. Meager, G. Pieridou, B. Dörling, R.S. Ashraf, A.R. Goñi, H. Bronstein, I. McCulloch, S.C. Hayes, M. Campoy-Quiles, J. Nelson, Nat. Mater. **15**, 746 (2016)
13. L.A.A. Pettersson, S. Ghosh, O. Inganäs, Org. Electron. **3**, 143 (2002)
14. M.R. Hammond, R.J. Kline, A.A. Herzing, L.J. Richter, D.S. Germack, H.-W. Ro, C.L. Soles, D.A. Fischer, T. Xu, L. Yu, M.F. Toney, D.M. DeLongchamp, ACS Nano **5**, 8248 (2011)
15. T. Kirchartz, T. Agostinelli, M. Campoy-Quiles, W. Gong, J. Nelson, J. Phys. Chem. Lett. **3**, 3470 (2012)
16. M. Shirayama, H. Kadowaki, T. Miyadera, T. Sugita, M. Tamakoshi, M. Kato, T. Fujiseki, D. Murata, S. Hara, T.N. Murakami, S. Fujimoto, M. Chikamatsu, H. Fujiwara, Phys. Rev. Appl. **5**, 014012 (2016)
17. L. Hou, E. Wang, J. Bergqvist, B.V. Andersson, Z. Wang, C. Müller, M. Campoy-Qulies, M.R. Andersson, F. Zhang, O. Inganäs, Adv. Funct. Mater. **21**, 3169 (2011)

Chapter 10
Organic-Inorganic Hybrid Perovskites



Shohei Fujimoto, Takemasa Fujiseki, Masato Tamakoshi, Akihiro Nakane, Tetsuhiko Miyadera, Takeshi Sugita, Takurou N. Murakami, Masayuki Chikamatsu and Hiroyuki Fujiwara

Abstract The dielectric functions and optical constants of various organic-inorganic hybrid perovskite semiconductors, including $HC(NH_2)_2PbI_3$, $CH_3NH_3PbI_3$, $CH_3NH_3PbBr_3$ and $CH_3NH_3PbCl_3$, are summarized. For $CH_3NH_3Pb(I, Br)_3$ alloys, the variation of the dielectric function with Br content, calculated by applying the energy shift model, is presented. This chapter also provides the optical constants of perovskite secondary phases, such as semitransparent δ-phase $HC(NH_2)_2PbI_3$, PbI_2 and CH_3NH_3I. It has been established that the dielectric functions of all the hybrid perovskite compounds can be parameterized by assuming several transition peaks calculated from the Tauc-Lorentz model. In particular, by incorporating Tauc-Lorentz peaks with very small amplitudes, the absorption coefficient spectra of the hybrid perovskites are reproduced almost perfectly in a quite wide range of $\alpha = 10^2$–10^6 cm^{-1}. In this chapter, the Tauc-Lorentz parameters obtained from the above parameterization scheme are summarized, together with the tabulated optical constants.

10.1 Introduction

The methylammonium lead iodide ($MAPbI_3$; $CH_3NH_3PbI_3$) and formamidinium lead iodide [$FAPbI_3$; $HC(NH_2)_2PbI_3$] are direct transition semiconductors with band gaps of 1.61 eV and 1.55 eV, respectively [1], and hybrid perovskite solar cells

S. Fujimoto · T. Fujiseki · M. Tamakoshi · A. Nakane · H. Fujiwara (✉)
Gifu University, 1-1 Yanagido, Gifu 501-1193, Japan
e-mail: fujiwara@gifu-u.ac.jp

T. Miyadera · T. Sugita · T. N. Murakami · M. Chikamatsu
Research Center for Photovoltaics, National Institute of Advanced Industrial Science and Technology, 1-1-1 Higashi, Tsukuba 305-8568, Japan

© Springer International Publishing AG, part of Springer Nature 2018

H. Fujiwara and R. W. Collins (eds.), *Spectroscopic Ellipsometry for Photovoltaics*,
Springer Series in Optical Sciences 214,
https://doi.org/10.1007/978-3-319-95138-6_10

with these absorbers exhibit a short-circuit current density (J_{sc}) of ~20 mA/cm^2 (Chap. 16 in Vol. 1). The optimal device design basically relies on the optical constants of component layers and, particularly in tandem solar cells with hybrid perovskites, accurate optical data are necessary in optimizing complex device structures [2]. Furthermore, the reliable absorber optical constants are of paramount importance in interpreting carrier recombination dynamics in hybrid perovskite solar cells [3].

In this chapter, for the purpose of spectroscopic ellipsometry (SE) characterization and device simulation, the tabulated optical constants of various hybrid perovskite materials at room temperature are provided. The dielectric functions of $FAPbI_3$ and $MAPbI_3$ have been extracted from thin layers fabricated by a laser evaporation technique, in which PbI_2 and $HC(NH_2)_2I$ [or CH_3NH_3I] source materials are heated by a near-infrared laser [2]. In particular, this technique allows the formation of the smoother perovskite layers, which is critical for accurate determination of optical constants [1] (Chap. 6 in Vol. 1). Unfortunately, solution-processed hybrid perovskites often exhibit quite roughness surfaces with a dimension comparable to the wavelength (λ) of SE light probe and, therefore, extra care is necessary for the SE analysis of these samples (Chap. 6 in Vol. 1). Moreover, since $FAPbI_3$ and $MAPbI_3$ show rather significant phase change in humid air (Chap. 16 in Vol. 1), the SE measurements of laser-evaporated $FAPbI_3$ and $MAPbI_3$ layers were carried out in a N_2-filled glove bag without exposing the samples to air, although the $MAPbI_3$ spectra in a high energy region ($E \geq 4.75$ eV) were obtained from the measurements in air [2]. The optical properties of δ-phase $FAPbI_3$, PbI_2 and CH_3NH_3I secondary phases, fabricated by laser evaporation, are also determined without air exposure. On the other hand, for $MAPb(I_{1-x}Br_x)_3$, the full optical data sets are provided for different Br contents in a complete range of $x = 0$–1.0.

For all the materials described here, refractive index n and extinction coefficient k are shown in a λ range of 300–1200 nm with steps of 5 nm (300–400 nm) and 10 nm (400–1200 nm). From these numerical values, the dielectric function ($\varepsilon = \varepsilon_1 - i\varepsilon_2$) and the absorption coefficient (α) can be calculated quite easily according to $\varepsilon_1 = n^2 - k^2$, $\varepsilon_2 = 2nk$ and $\alpha = 4\pi k/\lambda$ (Sect. 1.2.1). The λ value can also be converted to energy (E) by $E = 1239.8/[\lambda \text{ (nm)}]$ eV (1.3).

Unfortunately, the tabulated optical data are sometimes insufficient for more complete SE analysis or optical simulation. Accordingly, all the dielectric functions are parameterized assuming the Tauc-Lorentz model described by (1.19)–(1.20). Although the Tauc-Lorentz model was developed originally to express the dielectric function of amorphous semiconductors [4], this model is quite effective for the complete parameterization of the dielectric functions. In particular, by combining several Tauc-Lorentz peaks, the dielectric functions described in this chapter can be reproduced almost perfectly in a wide photon energy range ($E = 1$–5 eV) using only one dielectric function model. From the Tauc-Lorentz parameters described in

this chapter, (ε_1, ε_2), (n, k) and α values at arbitrary λ and E can be calculated quite easily. It should be emphasized that the Tauc-Lorentz model is used solely to establish the optical database of various solar-cell component layers. When only limited spectral information is available, however, the Tauc-Lorentz model is also applied to extrapolate the spectrum beyond experimental data to cover the consistent spectral range of 300–1200 nm.

In the actual modeling, the dielectric functions were calculated using (8.1) and (8.2). The calculation example of the Tauc-Lorentz model is also shown in (1.26). A free software described in Sect. 2.7 can further be applied to calculate the dielectric function from the Tauc-Lorentz model parameters listed in this chapter. All the parameterizations of the dielectric functions described in this chapter were implemented by the group of Gifu University, unless otherwise noted.

10.2 Optical Data of Hybrid Perovskites

10.2.1 $FAPbI_3$ [$HC(NH_2)_2PbI_3$]

Data from M. Kato, T. Fujiseki, T. Miyadera, T. Sugita, S. Fujimoto, M. Tamakoshi, M. Chikamatsu, and H. Fujiwara [5] (see also Fig. 16.5 in Vol. 1). The optical data have been determined by multi-sample SE analysis of cubic $FAPbI_3$ (α phase), formed on SiO_2-covered crystalline Si substrates by laser evaporation at room temperature (Fig. 10.1 and Tables 10.1, 10.2).

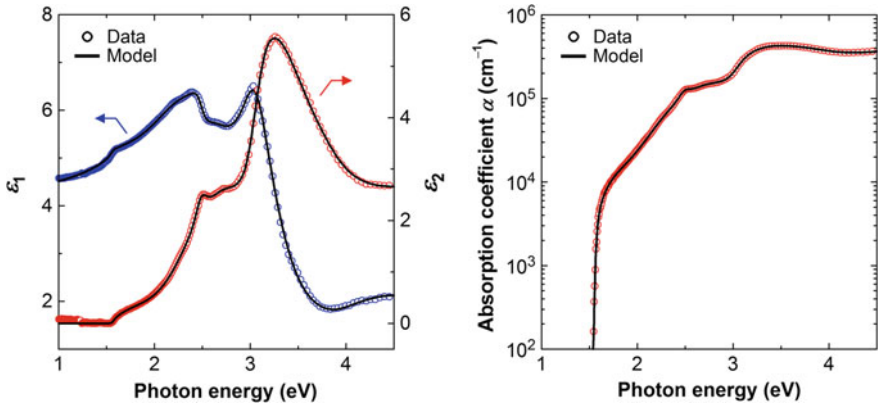


Fig. 10.1 Dielectric function and absorption coefficient of $FAPbI_3$ (α phase) at room temperature. The open circles show the experimental data and the solid lines indicate the calculation result obtained from the parameterization assuming the Tauc-Lorentz model [(8.1) and (8.2)]

Table 10.1 Tauc-Lorentz parameters of (8.1) and (8.2) for $FAPbI_3$ (α phase). The model parameters reported by Kato et al. are summarized

Peak	A (eV)	C (eV)	E_0 (eV)	E_g (eV)	$\varepsilon_1(\infty)$
$j = 1$	10.018	0.099	1.557	1.543	1.462
$j = 2$	8.849	0.498	1.566	1.521	0
$j = 3$	9.041	0.794	2.344	1.618	0
$j = 4$	1.028	0.171	2.486	1.740	0
$j = 5$	20.435	0.755	2.712	2.093	0
$j = 6$	66.516	0.417	3.083	2.726	0
$j = 7$	98.353	0.657	3.190	2.918	0
$j = 8$	131.316	3.018	3.897	3.882	0

Table 10.2 Optical constants of $FAPbI_3$ (α phase) calculated by the Tauc-Lorentz model

λ (nm)	n	k	λ (nm)	n	k	λ (nm)	n	k
300	1.646	0.855	540	2.518	0.279	880	2.201	0
305	1.645	0.882	550	2.504	0.248	890	2.197	0
310	1.649	0.914	560	2.490	0.221	900	2.193	0
315	1.658	0.951	570	2.475	0.196	910	2.189	0
320	1.677	0.992	580	2.458	0.175	920	2.186	0
325	1.704	1.032	590	2.442	0.156	930	2.182	0
330	1.738	1.069	600	2.426	0.141	940	2.179	0
335	1.778	1.104	610	2.411	0.128	950	2.176	0
340	1.824	1.136	620	2.396	0.117	960	2.173	0
345	1.876	1.164	630	2.383	0.107	970	2.170	0
350	1.934	1.188	640	2.370	9.91×10^{-2}	980	2.168	0
355	1.997	1.206	650	2.359	9.22×10^{-2}	990	2.165	0
360	2.066	1.218	660	2.349	8.62×10^{-2}	1000	2.163	0
365	2.139	1.221	670	2.339	8.09×10^{-2}	1010	2.160	0
370	2.215	1.214	680	2.331	7.60×10^{-2}	1020	2.158	0
375	2.293	1.197	690	2.324	7.14×10^{-2}	1030	2.156	0
380	2.372	1.168	700	2.317	6.68×10^{-2}	1040	2.154	0
385	2.449	1.126	710	2.311	6.21×10^{-2}	1050	2.152	0
390	2.522	1.068	720	2.306	5.73×10^{-2}	1060	2.150	0
395	2.584	0.993	730	2.301	5.23×10^{-2}	1070	2.148	0
400	2.627	0.903	740	2.296	4.71×10^{-2}	1080	2.147	0
410	2.633	0.717	750	2.292	4.16×10^{-2}	1090	2.145	0
420	2.560	0.596	760	2.288	3.57×10^{-2}	1100	2.143	0
430	2.490	0.554	770	2.284	2.89×10^{-2}	1110	2.142	0
440	2.453	0.543	780	2.279	2.02×10^{-2}	1120	2.140	0
450	2.441	0.538	790	2.271	9.61×10^{-3}	1130	2.139	0

(continued)

Table 10.2 (continued)

λ (nm)	n	k	λ (nm)	n	k	λ (nm)	n	k
460	2.443	0.527	800	2.258	1.79×10^{-3}	1140	2.137	0
470	2.447	0.512	810	2.246	0	1150	2.136	0
480	2.451	0.502	820	2.237	0	1160	2.135	0
490	2.472	0.503	830	2.229	0	1170	2.133	0
500	2.525	0.479	840	2.223	0	1180	2.132	0
510	2.552	0.411	850	2.217	0	1190	2.131	0
520	2.544	0.354	860	2.211	0	1200	2.130	0
530	2.531	0.313	870	2.206	0			

10.2.2 $MAPbI_3$ ($CH_3NH_3PbI_3$)

Data from M. Shirayama, H. Kadowaki, T. Miyadera, T. Sugita, M. Tamakoshi, M. Kato, T. Fujiseki, D. Murata, S. Hara, T. N. Murakami, S. Fujimoto, M. Chikamatsu, and H. Fujiwara [2] (see also Fig. 16.5 in Vol. 1). The optical data have been determined by multi-sample SE analysis of quite smooth $MAPbI_3$ layers, formed on ZnO-coated crystalline Si substrates by laser evaporation at room temperature.

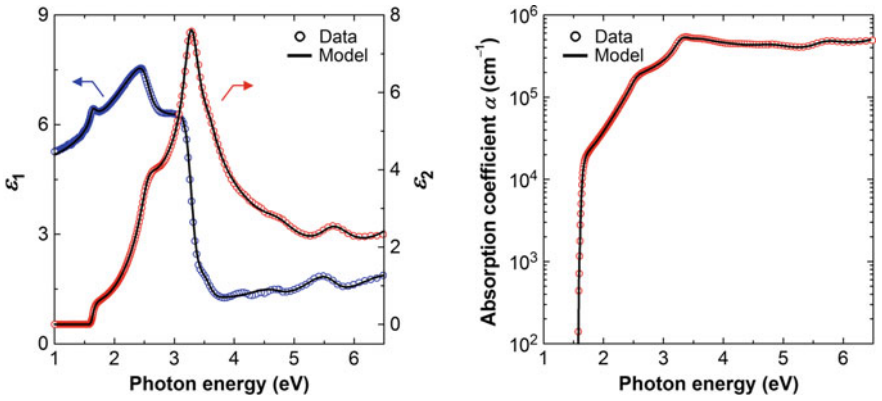


Fig. 10.2 Dielectric function and absorption coefficient of $MAPbI_3$ at room temperature. The open circles show the experimental data and the solid lines indicate the calculation result obtained from the parameterization assuming the Tauc-Lorentz model [(8.1) and (8.2)]

Table 10.3 Tauc-Lorentz parameters of (8.1) and (8.2) for $MAPbI_3$. The model parameters reproted by Shirayama et al. are summarized

Peak	A (eV)	C (eV)	E_0 (eV)	E_g (eV)	$\varepsilon_1(\infty)$
$j = 1$	1.621	0.024	1.593	1.565	0
$j = 2$	47.677	0.137	1.607	1.593	1.486
$j = 3$	2.909	0.349	2.553	1.684	0
$j = 4$	39.202	2.391	3.046	1.563	0

(continued)

Table 10.3 (continued)

Peak	A (eV)	C (eV)	E_0 (eV)	E_g (eV)	$\varepsilon_1(\infty)$
$j = 5$	4.955	0.329	3.278	1.764	0
$j = 6$	1.369	0.354	3.581	2.246	0
$j = 7$	1.622	0.745	4.726	2.823	0
$j = 8$	4.137	0.666	5.648	3.839	0
$j = 9$	11.256	2.053	7.408	2.276	0

Table 10.4 Optical constants of $MAPbI_3$ calculated by the Tauc-Lorentz model

λ (nm)	n	k	λ (nm)	n	k	λ (nm)	n	k
300	1.580	1.075	540	2.738	0.360	880	2.376	0
305	1.596	1.107	550	2.718	0.327	890	2.370	0
310	1.614	1.141	560	2.699	0.299	900	2.365	0
315	1.636	1.177	570	2.680	0.274	910	2.360	0
320	1.660	1.215	580	2.663	0.252	920	2.355	0
325	1.689	1.256	590	2.646	0.233	930	2.350	0
330	1.725	1.299	600	2.630	0.216	940	2.346	0
335	1.771	1.344	610	2.615	0.201	950	2.342	0
340	1.828	1.384	620	2.601	0.188	960	2.338	0
345	1.892	1.413	630	2.588	0.177	970	2.334	0
350	1.951	1.434	640	2.576	0.167	980	2.331	0
355	2.007	1.460	650	2.564	0.158	990	2.328	0
360	2.072	1.499	660	2.554	0.150	1000	2.324	0
365	2.164	1.542	670	2.546	0.144	1010	2.321	0
370	2.293	1.568	680	2.538	0.138	1020	2.318	0
375	2.447	1.545	690	2.533	0.132	1030	2.316	0
380	2.587	1.461	700	2.529	0.127	1040	2.313	0
385	2.677	1.339	710	2.527	0.122	1050	2.310	0
390	2.714	1.217	720	2.528	0.115	1060	2.308	0
395	2.718	1.117	730	2.531	0.105	1070	2.305	0
400	2.707	1.041	740	2.536	8.99×10^{-2}	1080	2.303	0
410	2.678	0.941	750	2.538	6.73×10^{-2}	1090	2.301	0
420	2.658	0.878	760	2.531	3.80×10^{-2}	1100	2.299	0
430	2.647	0.834	770	2.508	1.27×10^{-2}	1110	2.297	0
440	2.644	0.800	780	2.483	3.42×10^{-3}	1120	2.295	0
450	2.647	0.774	790	2.461	0	1130	2.293	0
460	2.660	0.755	800	2.446	0	1140	2.291	0
470	2.688	0.737	810	2.433	0	1150	2.289	0
480	2.731	0.705	820	2.422	0	1160	2.287	0
490	2.773	0.648	830	2.412	0	1170	2.286	0
500	2.793	0.575	840	2.404	0	1180	2.284	0
510	2.792	0.505	850	2.396	0	1190	2.283	0
520	2.777	0.447	860	2.389	0	1200	2.281	0
530	2.758	0.399	870	2.382	0			

10.2.3 $MAPbBr_3$ ($CH_3NH_3PbBr_3$)

Data from A. M. A. Leguy, P. Azarhoosh, M. I. Alonso, M. Campoy-Quiles, O. J. Weber, J. Yao, D. Bryant, M. T. Weller, J. Nelson, A. Walsh, M. van Schilfgaarde, and P. R. F. Barnes [6] (see also Fig. 16.5 in Vol. 1). The optical data have been extracted from a $MAPbBr_3$ single crystal (Fig. 10.3, Tables 10.5 and 10.6).

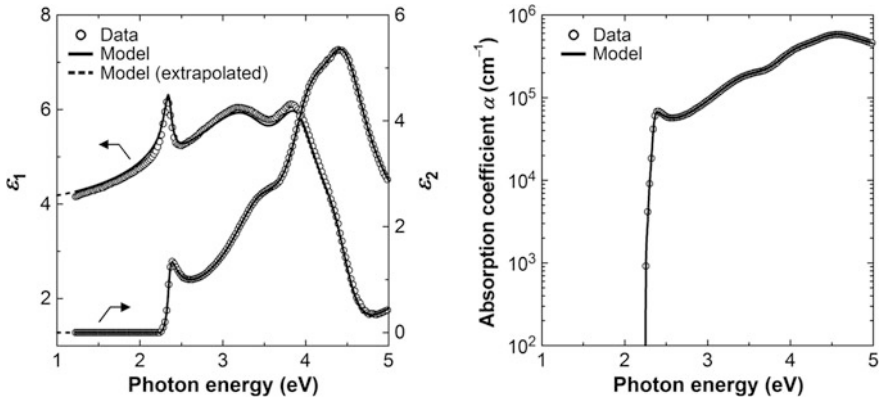


Fig. 10.3 Dielectric function and absorption coefficient of $MAPbBr_3$ at room temperature. The open circles show the experimental data and the solid lines indicate the calculation result obtained from the parameterization assuming the Tauc-Lorentz model [(8.1) and (8.2)]

Table 10.5 Tauc-Lorentz parameters of (8.1) and (8.2) for $MAPbBr_3$

Peak	A (eV)	C (eV)	E_0 (eV)	E_g (eV)	$\varepsilon_1(\infty)$
$j = 1$	14.194	0.022	2.258	2.245	0.011
$j = 2$	50.951	0.110	2.298	2.257	0
$j = 3$	140.251	0.090	2.343	2.305	0
$j = 4$	48.060	2.641	2.425	2.382	0
$j = 5$	14.262	1.002	3.416	2.412	0
$j = 6$	78.865	0.663	3.949	3.489	0
$j = 7$	6.204	0.620	4.466	2.428	0
$j = 8$	41.650	0.070	8.469	2.905	0

Table 10.6 Optical constants of $MAPbBr_3$ calculated by the Tauc-Lorentz model

λ (nm)	n	k	λ (nm)	n	k	λ (nm)	n	k
300	2.427	1.009	540	2.439	3.24×10^{-2}	880	2.088	0
305	2.478	0.955	550	2.370	2.06×10^{-3}	890	2.086	0
310	2.521	0.886	560	2.323	0	900	2.084	0
315	2.546	0.808	570	2.293	0	910	2.082	0
320	2.548	0.731	580	2.271	0	920	2.080	0
325	2.531	0.666	590	2.253	0	930	2.078	0
330	2.505	0.619	600	2.237	0	940	2.076	0
335	2.479	0.589	610	2.224	0	950	2.075	0
340	2.459	0.571	620	2.212	0	960	2.073	0
345	2.447	0.560	630	2.202	0	970	2.072	0
350	2.442	0.551	640	2.192	0	980	2.070	0
355	2.445	0.542	650	2.184	0	990	2.069	0
360	2.452	0.528	660	2.176	0	1000	2.067	0
365	2.460	0.510	670	2.168	0	1010	2.066	0
370	2.466	0.489	680	2.162	0	1020	2.065	0
375	2.471	0.465	690	2.156	0	1030	2.064	0
380	2.472	0.440	700	2.150	0	1040	2.062	0
385	2.471	0.415	710	2.145	0	1050	2.061	0
390	2.467	0.391	720	2.139	0	1060	2.060	0
395	2.461	0.369	730	2.135	0	1070	2.059	0
400	2.453	0.348	740	2.130	0	1080	2.058	0
410	2.435	0.312	750	2.126	0	1090	2.057	0
420	2.415	0.283	760	2.122	0	1100	2.056	0
430	2.395	0.260	770	2.118	0	1110	2.055	0
440	2.376	0.242	780	2.115	0	1120	2.054	0
450	2.358	0.229	790	2.112	0	1130	2.053	0
460	2.341	0.220	800	2.108	0	1140	2.052	0
470	2.327	0.216	810	2.105	0	1150	2.051	0
480	2.316	0.217	820	2.103	0	1160	2.051	0
490	2.310	0.224	830	2.100	0	1170	2.050	0
500	2.314	0.239	840	2.097	0	1180	2.049	0
510	2.340	0.262	850	2.095	0	1190	2.048	0
520	2.421	0.273	860	2.092	0	1200	2.048	0
530	2.516	0.142	870	2.090	0			

10.2.4 $MAPb(I_{1-x}Br_x)_3$ $[CH_3NH_3Pb(I_{1-x}Br_x)_3]$

Data: unpublished results of Gifu University. The dielectric functions of MAPb $(I_{1-x}Br_x)_3$ alloys with different Br content x are summarized. These dielectric functions have been obtained by applying the energy shift model [7], in which the dielectric function of an alloy is "synthesized" from two known dielectric functions (see also Sect. 10.4.1 in Vol. 1). For this calculation, the dielectric functions of $MAPbI_3$ and $MAPbBr_3$, reported by M. Shirayama et al. [2] and J.-S. Park et al. [8], respectively, were adopted as the end point compositions.

In the actual calculation, the band gap bowing effect in the $MAPb(I_{1-x}Br_x)_3$ alloy system has also been taken into account. The dielectric functions obtained from this procedure have been parameterized further using the Tauc-Lorentz model and the modeled results are described here. The Tauc-Lorentz parameters and optical constants of $x = 0.0$ ($MAPbI_3$) are shown in Tables 10.3 and 10.4 (Fig. 10.4, Tables 10.7, 10.8, 10.9, 10.10, 10.11, 10.12, 10.13 and 10.14).

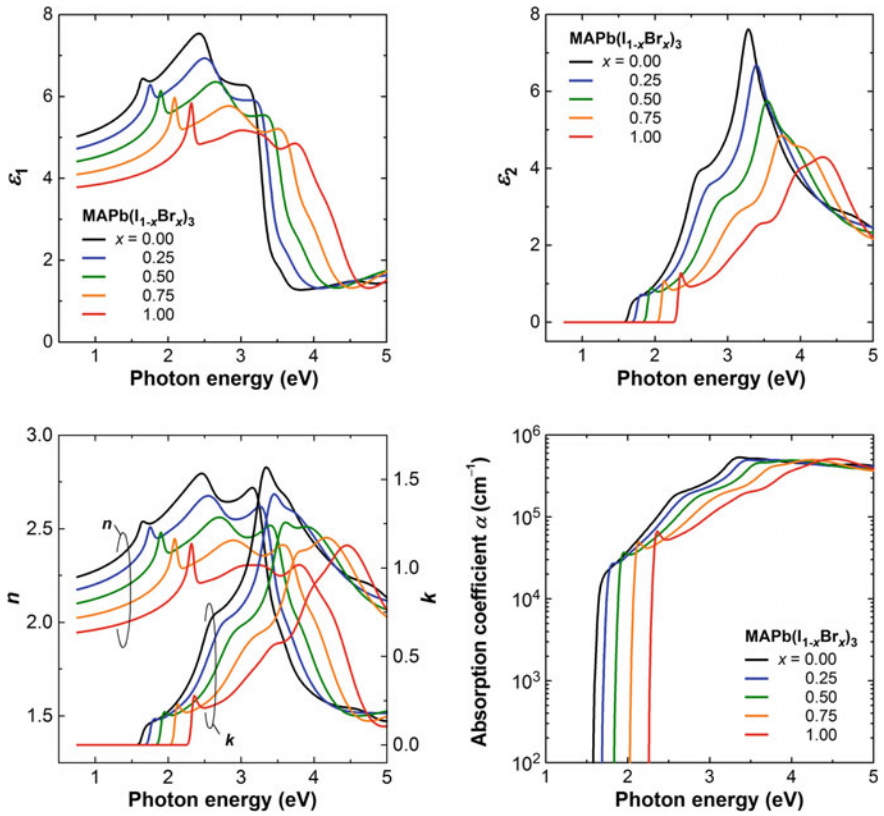


Fig. 10.4 Dielectric functions, optical constants and absorption coefficients of various MAPb $(I_{1-x}Br_x)_3$ alloys calculated by the Tauc-Lorentz model [(8.1) and (8.2)]. The $MAPb(I_{1-x}Br_x)_3$ dielectric functions in a range of $x = 0.25$–0.75 represent those calculated from the energy shift model, where the dielectric function of $x = 0.0$ corresponds to that shown in Fig. 10.2

Table 10.7 Tauc-Lorentz parameters of (8.1) and (8.2) for $MAPb(I_{1-x}Br_x)_3$ ($x = 0.25$)

Peak	A (eV)	C (eV)	E_0 (eV)	E_g (eV)	$\varepsilon_1(\infty)$
$j = 1$	11.185	0.089	1.700	1.677	1.287
$j = 2$	44.013	0.113	1.750	1.704	0
$j = 3$	30.150	0.659	1.792	1.791	0
$j = 4$	24.972	0.846	2.707	1.887	0
$j = 5$	88.842	0.823	2.973	2.763	0
$j = 6$	30.875	0.379	3.368	2.733	0
$j = 7$	88.986	0.425	3.584	3.444	0
$j = 8$	124.162	6.451	4.089	4.072	0

Table 10.8 Tauc-Lorentz parameters of (8.1) and (8.2) for $MAPb(I_{1-x}Br_x)_3$ ($x = 0.50$)

Peak	A (eV)	C (eV)	E_0 (eV)	E_g (eV)	$\varepsilon_1(\infty)$
$j = 1$	14.467	0.083	1.843	1.827	1.283
$j = 2$	52.571	0.100	1.903	1.847	0
$j = 3$	24.250	0.838	1.993	1.881	0
$j = 4$	24.333	0.889	2.864	2.032	0
$j = 5$	60.788	0.822	3.198	2.895	0
$j = 6$	26.191	0.377	3.509	2.869	0
$j = 7$	57.244	0.620	3.791	3.405	0
$j = 8$	142.483	4.840	4.366	4.365	0

Table 10.9 Tauc-Lorentz parameters of (8.1) and (8.2) for $MAPb(I_{1-x}Br_x)_3$ ($x = 0.75$)

Peak	A (eV)	C (eV)	E_0 (eV)	E_g (eV)	$\varepsilon_1(\infty)$
$j = 1$	24.343	0.112	2.045	2.019	1.191
$j = 2$	32.193	0.606	2.092	2.099	0
$j = 3$	62.145	0.088	2.098	2.036	0
$j = 4$	24.011	1.093	3.083	2.139	0
$j = 5$	34.346	0.647	3.636	3.005	0
$j = 6$	5.746	0.307	3.709	2.985	0
$j = 7$	39.177	0.752	4.046	3.345	0
$j = 8$	161.085	4.956	4.730	4.556	0

Table 10.10 Tauc-Lorentz parameters of (8.1) and (8.2) for $MAPb(I_{1-x}Br_x)_3$ ($x = 1.00$). The model parameters reported by Park et al. are summarized

Peak	A (eV)	C (eV)	E_0 (eV)	E_g (eV)	$\varepsilon_1(\infty)$
$j = 1$	70.13	0.09	2.33	2.25	1.0
$j = 2$	30.02	0.60	2.34	2.25	0
$j = 3$	8.69	0.83	3.10	2.25	0
$j = 4$	2.76	0.47	3.42	2.25	0
$j = 5$	5.03	0.58	3.92	2.25	0
$j = 6$	11.13	0.90	4.36	2.25	0
$j = 7$	4.70	1.41	5.88	2.25	0
$j = 8$	18.53	0.77	9.65	2.25	0

Table 10.11 Optical constants of $MAPb(I_{1-x}Br_x)_3$ ($x = 0.25$) calculated by the Tauc-Lorentz model

λ (nm)	n	k	λ (nm)	n	k	λ (nm)	n	k
300	1.587	1.095	540	2.591	0.279	880	2.286	0
305	1.616	1.137	550	2.572	0.257	890	2.281	0
310	1.652	1.177	560	2.554	0.239	900	2.277	0
315	1.694	1.216	570	2.539	0.224	910	2.273	0
320	1.742	1.251	580	2.525	0.211	920	2.269	0
325	1.796	1.282	590	2.513	0.199	930	2.265	0
330	1.856	1.306	600	2.502	0.188	940	2.262	0
335	1.917	1.322	610	2.492	0.178	950	2.259	0
340	1.974	1.333	620	2.483	0.168	960	2.255	0
345	2.027	1.347	630	2.474	0.160	970	2.252	0
350	2.087	1.374	640	2.466	0.152	980	2.249	0
355	2.173	1.406	650	2.458	0.147	990	2.247	0
360	2.294	1.416	660	2.452	0.145	1000	2.244	0
365	2.430	1.375	670	2.450	0.145	1010	2.242	0
370	2.539	1.283	680	2.456	0.146	1020	2.239	0
375	2.601	1.170	690	2.474	0.142	1030	2.237	0
380	2.620	1.065	700	2.501	0.117	1040	2.235	0
385	2.614	0.983	710	2.507	6.41×10^{-2}	1050	2.232	0
390	2.599	0.922	720	2.477	2.08×10^{-2}	1060	2.230	0
395	2.585	0.878	730	2.441	4.09×10^{-3}	1070	2.228	0
400	2.573	0.844	740	2.412	0	1080	2.226	0
410	2.558	0.794	750	2.393	0	1090	2.225	0
420	2.551	0.757	760	2.378	0	1100	2.223	0
430	2.552	0.732	770	2.365	0	1110	2.221	0
440	2.566	0.712	780	2.354	0	1120	2.219	0
450	2.593	0.690	790	2.344	0	1130	2.218	0

(continued)

Table 10.11 (continued)

λ (nm)	*n*	*k*	λ (nm)	*n*	*k*	λ (nm)	*n*	*k*
460	2.630	0.652	800	2.335	0	1140	2.216	0
470	2.658	0.598	810	2.327	0	1150	2.215	0
480	2.673	0.538	820	2.320	0	1160	2.213	0
490	2.675	0.479	830	2.313	0	1170	2.212	0
500	2.667	0.424	840	2.307	0	1180	2.210	0
510	2.651	0.377	850	2.301	0	1190	2.209	0
520	2.632	0.338	860	2.296	0	1200	2.208	0
530	2.611	0.305	870	2.290	0			

Table 10.12 Optical constants of $MAPb(I_{1-x}Br_x)_3$ ($x = 0.50$) calculated by the Tauc-Lorentz model

λ (nm)	*n*	*k*	λ (nm)	*n*	*k*	λ (nm)	*n*	*k*
300	1.667	1.157	540	2.439	0.223	880	2.190	0
305	1.726	1.192	550	2.427	0.210	890	2.187	0
310	1.791	1.217	560	2.416	0.199	900	2.183	0
315	1.859	1.230	570	2.406	0.188	910	2.180	0
320	1.925	1.232	580	2.397	0.179	920	2.177	0
325	1.982	1.228	590	2.387	0.172	930	2.174	0
330	2.031	1.227	600	2.379	0.168	940	2.172	0
335	2.082	1.236	610	2.373	0.169	950	2.169	0
340	2.152	1.252	620	2.373	0.174	960	2.167	0
345	2.248	1.255	630	2.387	0.183	970	2.164	0
350	2.360	1.219	640	2.428	0.182	980	2.162	0
355	2.455	1.138	650	2.478	0.125	990	2.160	0
360	2.506	1.035	660	2.456	3.98×10^{-2}	1000	2.158	0
365	2.517	0.943	670	2.403	5.83×10^{-3}	1010	2.156	0
370	2.509	0.872	680	2.363	0	1020	2.154	0
375	2.494	0.821	690	2.338	0	1030	2.152	0
380	2.481	0.784	700	2.319	0	1040	2.150	0
385	2.469	0.755	710	2.304	0	1050	2.149	0
390	2.461	0.733	720	2.291	0	1060	2.147	0
395	2.456	0.715	730	2.280	0	1070	2.145	0
400	2.453	0.701	740	2.270	0	1080	2.144	0
410	2.459	0.679	750	2.260	0	1090	2.142	0
420	2.478	0.657	760	2.252	0	1100	2.141	0
430	2.507	0.626	770	2.245	0	1110	2.139	0
440	2.537	0.581	780	2.238	0	1120	2.138	0
450	2.556	0.525	790	2.232	0	1130	2.137	0

(continued)

Table 10.12 (continued)

λ (nm)	*n*	*k*	λ (nm)	*n*	*k*	λ (nm)	*n*	*k*
460	2.561	0.467	800	2.226	0	1140	2.136	0
470	2.555	0.414	810	2.220	0	1150	2.134	0
480	2.541	0.368	820	2.215	0	1160	2.133	0
490	2.523	0.330	830	2.210	0	1170	2.132	0
500	2.504	0.299	840	2.206	0	1180	2.131	0
510	2.485	0.274	850	2.202	0	1190	2.130	0
520	2.468	0.254	860	2.197	0	1200	2.129	0
530	2.453	0.237	870	2.194	0			

Table 10.13 Optical constants of $MAPb(I_{1-x}Br_x)_3$ ($x = 0.75$) calculated by the Tauc-Lorentz model

λ (nm)	*n*	*k*	λ (nm)	*n*	*k*	λ (nm)	*n*	*k*
300	1.888	1.168	540	2.303	0.187	880	2.092	0
305	1.961	1.152	550	2.295	0.184	890	2.090	0
310	2.020	1.129	560	2.289	0.188	900	2.087	0
315	2.068	1.110	570	2.294	0.204	910	2.085	0
320	2.116	1.100	580	2.337	0.228	920	2.083	0
325	2.177	1.095	590	2.437	0.173	930	2.081	0
330	2.257	1.075	600	2.413	4.16×10^{-2}	940	2.079	0
335	2.341	1.020	610	2.338	1.97×10^{-3}	950	2.077	0
340	2.394	0.936	620	2.294	0	960	2.075	0
345	2.413	0.853	630	2.266	0	970	2.073	0
350	2.410	0.785	640	2.246	0	980	2.071	0
355	2.397	0.734	650	2.229	0	990	2.070	0
360	2.382	0.697	660	2.215	0	1000	2.068	0
365	2.368	0.672	670	2.203	0	1010	2.067	0
370	2.358	0.656	680	2.192	0	1020	2.065	0
375	2.355	0.644	690	2.183	0	1030	2.064	0
380	2.358	0.633	700	2.174	0	1040	2.062	0
385	2.365	0.623	710	2.166	0	1050	2.061	0
390	2.375	0.610	720	2.159	0	1060	2.060	0
395	2.387	0.594	730	2.152	0	1070	2.058	0
400	2.399	0.576	740	2.146	0	1080	2.057	0
410	2.420	0.533	750	2.141	0	1090	2.056	0
420	2.434	0.483	760	2.136	0	1100	2.055	0
430	2.438	0.433	770	2.131	0	1110	2.054	0
440	2.432	0.385	780	2.126	0	1120	2.053	0
450	2.420	0.344	790	2.122	0	1130	2.052	0

(continued)

Table 10.13 (continued)

λ (nm)	n	k	λ (nm)	n	k	λ (nm)	n	k
460	2.405	0.310	800	2.118	0	1140	2.051	0
470	2.388	0.282	810	2.114	0	1150	2.050	0
480	2.372	0.259	820	2.110	0	1160	2.049	0
490	2.357	0.241	830	2.107	0	1170	2.048	0
500	2.344	0.226	840	2.104	0	1180	2.047	0
510	2.332	0.214	850	2.101	0	1190	2.046	0
520	2.322	0.203	860	2.098	0	1200	2.046	0
530	2.312	0.194	870	2.095	0			

Table 10.14 Optical constants of $MAPb(I_{1-x}Br_x)_3$ ($x = 1.00$) calculated by the Tauc-Lorentz model

λ (nm)	n	k	λ (nm)	n	k	λ (nm)	n	k
300	2.122	0.974	540	2.379	4.67×10^{-2}	880	1.998	0
305	2.163	0.939	550	2.276	0	890	1.996	0
310	2.209	0.903	560	2.226	0	900	1.995	0
315	2.255	0.856	570	2.195	0	910	1.993	0
320	2.290	0.796	580	2.172	0	920	1.991	0
325	2.306	0.730	590	2.153	0	930	1.990	0
330	2.303	0.672	600	2.138	0	940	1.988	0
335	2.287	0.627	610	2.125	0	950	1.987	0
340	2.269	0.599	620	2.114	0	960	1.985	0
345	2.254	0.584	630	2.104	0	970	1.984	0
350	2.249	0.577	640	2.095	0	980	1.983	0
355	2.253	0.573	650	2.086	0	990	1.981	0
360	2.267	0.563	660	2.079	0	1000	1.980	0
365	2.282	0.546	670	2.072	0	1010	1.979	0
370	2.295	0.523	680	2.066	0	1020	1.978	0
375	2.302	0.498	690	2.060	0	1030	1.977	0
380	2.305	0.474	700	2.055	0	1040	1.976	0
385	2.306	0.452	710	2.050	0	1050	1.975	0
390	2.306	0.432	720	2.045	0	1060	1.974	0
395	2.306	0.413	730	2.041	0	1070	1.973	0
400	2.305	0.394	740	2.037	0	1080	1.972	0
410	2.303	0.357	750	2.033	0	1090	1.971	0
420	2.294	0.322	760	2.029	0	1100	1.970	0

(continued)

Table 10.14 (continued)

λ (nm)	n	k	λ (nm)	n	k	λ (nm)	n	k
430	2.282	0.292	770	2.026	0	1110	1.969	0
440	2.268	0.268	780	2.023	0	1120	1.968	0
450	2.254	0.250	790	2.020	0	1130	1.968	0
460	2.242	0.236	800	2.017	0	1140	1.967	0
470	2.233	0.226	810	2.014	0	1150	1.966	0
480	2.226	0.217	820	2.011	0	1160	1.965	0
490	2.219	0.211	830	2.009	0	1170	1.965	0
500	2.213	0.210	840	2.007	0	1180	1.964	0
510	2.211	0.222	850	2.004	0	1190	1.963	0
520	2.238	0.260	860	2.002	0	1200	1.963	0
530	2.380	0.244	870	2.000	0			

10.2.5 $MAPbCl_3$ ($CH_3NH_3PbCl_3$)

Data from A. M. A. Leguy, P. Azarhoosh, M. I. Alonso, M. Campoy-Quiles, O. J. Weber, J. Yao, D. Bryant, M. T. Weller, J. Nelson, A. Walsh, M. van Schilfgaarde, and P. R. F. Barnes [6] (see also Fig. 16.5 in Vol. 1). The optical data have been extracted from a $MAPbCl_3$ single crystal (Fig. 10.5, Tables 10.15 and 10.16).

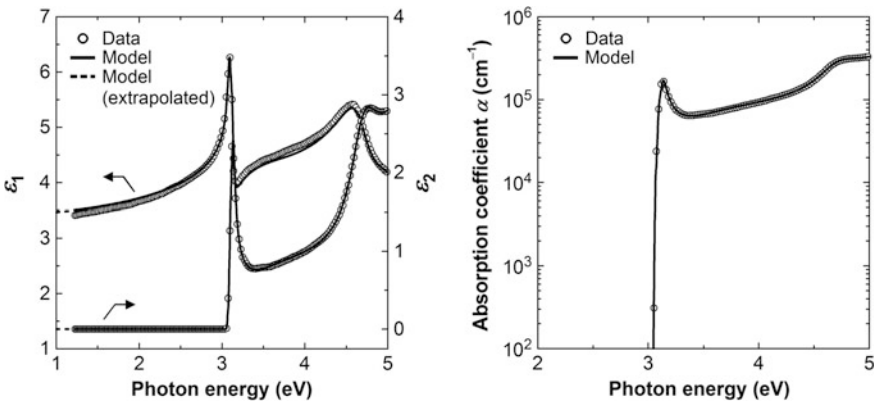


Fig. 10.5 Dielectric function and absorption coefficient of $MAPbCl_3$ at room temperature. The open circles show the experimental data and the solid lines indicate the calculation result obtained from the parameterization assuming the Tauc-Lorentz model [(8.1) and (8.2)]

Table 10.15 Tauc-Lorentz parameters of (8.1) and (8.2) for $MAPbCl_3$

Peak	A (eV)	C (eV)	E_0 (eV)	E_g (eV)	$\varepsilon_1(\infty)$
$j = 1$	24.330	0.012	3.065	3.045	0.076
$j = 2$	177.556	0.046	3.096	3.043	0
$j = 3$	219.273	0.052	3.125	3.071	0
$j = 4$	34.078	1.516	3.199	3.099	0
$j = 5$	10.013	0.397	4.695	3.733	0
$j = 6$	17.475	1.421	5.279	3.051	0
$j = 7$	209.001	0.053	9.718	6.544	0

Table 10.16 Optical constants of $MAPbCl_3$ calculated by the Tauc-Lorentz model

λ (nm)	n	k	λ (nm)	n	k	λ (nm)	n	k
300	2.189	0.248	540	1.965	0	880	1.882	0
305	2.173	0.239	550	1.959	0	890	1.882	0
310	2.159	0.232	560	1.954	0	900	1.881	0
315	2.148	0.226	570	1.949	0	910	1.880	0
320	2.138	0.220	580	1.944	0	920	1.879	0
325	2.129	0.215	590	1.940	0	930	1.878	0
330	2.122	0.209	600	1.936	0	940	1.877	0
335	2.115	0.204	610	1.932	0	950	1.877	0
340	2.108	0.199	620	1.929	0	960	1.876	0
345	2.101	0.195	630	1.926	0	970	1.875	0
350	2.094	0.191	640	1.923	0	980	1.875	0
355	2.086	0.187	650	1.920	0	990	1.874	0
360	2.077	0.186	660	1.917	0	1000	1.873	0
365	2.067	0.186	670	1.915	0	1010	1.873	0
370	2.056	0.190	680	1.912	0	1020	1.872	0
375	2.043	0.200	690	1.910	0	1030	1.871	0
380	2.028	0.221	700	1.908	0	1040	1.871	0
385	2.013	0.263	710	1.906	0	1050	1.870	0
390	2.015	0.358	720	1.904	0	1060	1.870	0
395	2.209	0.532	730	1.902	0	1070	1.869	0
400	2.496	0.292	740	1.900	0	1080	1.869	0
410	2.243	0	750	1.899	0	1090	1.868	0
420	2.156	0	760	1.897	0	1100	1.868	0
430	2.112	0	770	1.896	0	1110	1.867	0

(continued)

Table 10.16 (continued)

λ (nm)	n	k	λ (nm)	n	k	λ (nm)	n	k
440	2.082	0	780	1.894	0	1120	1.867	0
450	2.060	0	790	1.893	0	1130	1.867	0
460	2.042	0	800	1.891	0	1140	1.866	0
470	2.028	0	810	1.890	0	1150	1.866	0
480	2.015	0	820	1.889	0	1160	1.865	0
490	2.004	0	830	1.888	0	1170	1.865	0
500	1.994	0	840	1.887	0	1180	1.865	0
510	1.986	0	850	1.885	0	1190	1.864	0
520	1.978	0	860	1.884	0	1200	1.864	0
530	1.971	0	870	1.883	0			

10.2.6 $FAPbI_3$ (δ Phase)

Data from M. Kato, T. Fujiseki, T. Miyadera, T. Sugita, S. Fujimoto, M. Tamakoshi, M. Chikamatsu, and H. Fujiwara [5] (see also Fig. 16.6 in Vol. 1). The optical data have been determined by multi-sample SE analysis of $FAPbI_3$ crystals (δ phase), formed on a PCDTBT(5 nm)/ZnO(50 nm)/crystalline Si substrate structure by laser evaporation at room temperature (Fig. 10.6, Tables 10.17 and 10.18).

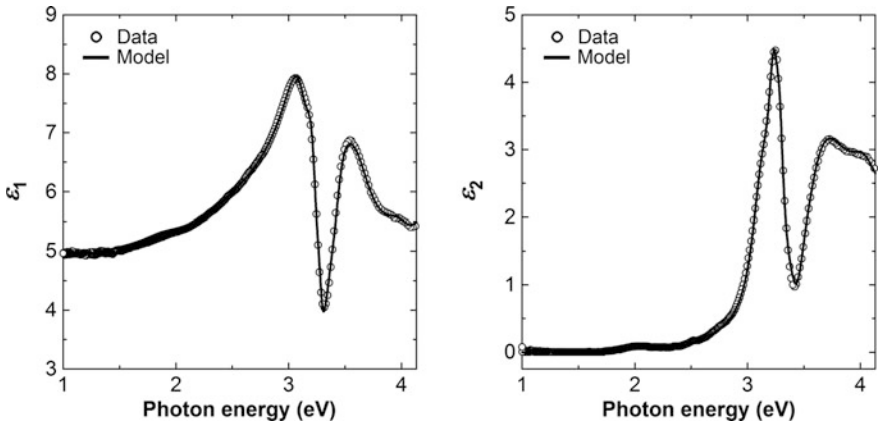


Fig. 10.6 Dielectric function of $FAPbI_3$ (δ phase) at room temperature. The open circles show the experimental data and the solid lines indicate the calculation result obtained from the parameterization assuming the Tauc-Lorentz model [(8.1) and (8.2)]

Table 10.17 Tauc-Lorentz parameters of (8.1) and (8.2) for $FAPbI_3$ (δ phase). The model parameters reproted by Kato et al. are summarized

Peak	A (eV)	C (eV)	E_0 (eV)	E_g (eV)	$\varepsilon_1(\infty)$
$j = 1$	1.573	0.404	1.893	1.667	2.455
$j = 2$	15.657	1.898	2.291	2.288	0
$j = 3$	2.182	0.232	3.127	1.690	0
$j = 4$	1.563	0.118	3.232	1.803	0
$j = 5$	0.411	0.078	3.285	1.695	0
$j = 6$	367.887	0.233	3.439	3.411	0
$j = 7$	72.513	0.366	3.611	3.398	0
$j = 8$	3.777	0.291	4.021	3.305	0
$j = 9$	776.547	0.202	4.638	4.388	0

Table 10.18 Optical constants of $FAPbI_3$ (δ phase) calculated by the Tauc-Lorentz model

λ (nm)	n	k	λ (nm)	n	k	λ (nm)	n	k
300	2.408	0.550	540	2.378	1.50×10^{-2}	880	2.242	0
305	2.408	0.593	550	2.366	1.53×10^{-2}	890	2.240	0
310	2.429	0.609	560	2.356	1.57×10^{-2}	900	2.239	0
315	2.441	0.608	570	2.347	1.63×10^{-2}	910	2.237	0
320	2.447	0.613	580	2.340	1.69×10^{-2}	920	2.236	0
325	2.466	0.624	590	2.334	1.75×10^{-2}	930	2.235	0
330	2.502	0.629	600	2.328	1.80×10^{-2}	940	2.233	0
335	2.553	0.616	610	2.324	1.82×10^{-2}	950	2.232	0
340	2.606	0.572	620	2.320	1.80×10^{-2}	960	2.231	0
345	2.639	0.498	630	2.317	1.71×10^{-2}	970	2.230	0
350	2.640	0.406	640	2.314	1.56×10^{-2}	980	2.229	0
355	2.595	0.299	650	2.311	1.35×10^{-2}	990	2.228	0
360	2.464	0.216	660	2.307	1.09×10^{-2}	1000	2.227	0
365	2.286	0.253	670	2.303	8.26×10^{-3}	1010	2.226	0
370	2.143	0.393	680	2.299	5.83×10^{-3}	1020	2.225	0
375	2.117	0.704	690	2.295	3.82×10^{-3}	1030	2.224	0
380	2.414	0.872	700	2.290	2.29×10^{-3}	1040	2.223	0
385	2.685	0.814	710	2.285	1.22×10^{-3}	1050	2.223	0
390	2.778	0.634	720	2.281	0	1060	2.222	0
395	2.800	0.543	730	2.277	0	1070	2.221	0
400	2.836	0.455	740	2.273	0	1080	2.220	0
410	2.815	0.267	750	2.270	0	1090	2.220	0
420	2.734	0.163	760	2.267	0	1100	2.219	0
430	2.663	0.113	770	2.264	0	1110	2.218	0
440	2.609	8.52×10^{-2}	780	2.262	0	1120	2.217	0
450	2.567	6.77×10^{-2}	790	2.259	0	1130	2.217	0

(continued)

Table 10.18 (continued)

λ (nm)	n	k	λ (nm)	n	k	λ (nm)	n	k
460	2.533	5.52×10^{-2}	800	2.257	0	1140	2.216	0
470	2.505	4.54×10^{-2}	810	2.254	0	1150	2.216	0
480	2.481	3.73×10^{-2}	820	2.252	0	1160	2.215	0
490	2.460	3.07×10^{-2}	830	2.250	0	1170	2.214	0
500	2.440	2.52×10^{-2}	840	2.248	0	1180	2.214	0
510	2.423	2.08×10^{-2}	850	2.247	0	1190	2.213	0
520	2.406	1.76×10^{-2}	860	2.245	0	1200	2.213	0
530	2.391	1.56×10^{-2}	870	2.243	0			

10.2.7 PbI_2

Data from M. Shirayama, H. Kadowaki, T. Miyadera, T. Sugita, M. Tamakoshi, M. Kato, T. Fujiseki, D. Murata, S. Hara, T. N. Murakami, S. Fujimoto, M. Chikamatsu, and H. Fujiwara [2] (see also Fig. 16.6 in Vol. 1). The optical data have been determined by multi-sample SE analysis of PbI_2 layers, formed on crystalline Si substrates by laser evaporation at room temperature (Fig. 10.7, Tables 10.19 and 10.20).

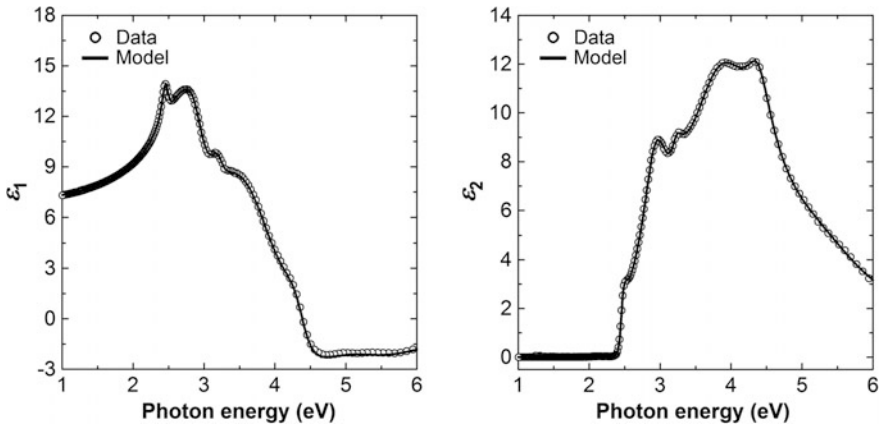


Fig. 10.7 Dielectric function of PbI_2 at room temperature. The open circles show the experimental data and the solid lines indicate the calculation result obtained from the parameterization assuming the Tauc-Lorentz model [(8.1) and (8.2)]

Table 10.19 Tauc-Lorentz parameters of (8.1) and (8.2) for PbI_2. The model parameters reproted by Shirayama et al. are summarized

Peak	A (eV)	C (eV)	E_0 (eV)	E_g (eV)	$\varepsilon_1(\infty)$
$j = 1$	1.087	0.794	1.820	1.720	1.812
$j = 2$	162.630	0.124	2.462	2.374	0
$j = 3$	38.741	0.415	2.644	2.335	0
$j = 4$	55.440	0.453	2.902	2.316	0
$j = 5$	61.819	0.200	3.208	3.023	0
$j = 6$	75.977	1.428	3.829	2.211	0
$j = 7$	24.014	0.441	4.364	3.376	0
$j = 8$	3.436	1.381	5.313	1.800	0

Table 10.20 Optical constants of PbI_2 calculated by the Tauc-Lorentz model

λ (nm)	n	k	λ (nm)	n	k	λ (nm)	n	k
300	2.747	2.158	540	3.312	7.54×10^{-3}	880	2.788	0
305	2.813	2.121	550	3.255	5.99×10^{-3}	890	2.784	0
310	2.887	2.082	560	3.207	5.36×10^{-3}	900	2.780	0
315	2.965	2.034	570	3.167	5.19×10^{-3}	910	2.777	0
320	3.040	1.976	580	3.133	4.96×10^{-3}	920	2.773	0
325	3.108	1.909	590	3.104	4.68×10^{-3}	930	2.769	0
330	3.164	1.835	600	3.077	4.35×10^{-3}	940	2.766	0
335	3.209	1.759	610	3.054	3.96×10^{-3}	950	2.763	0
340	3.241	1.684	620	3.032	3.53×10^{-3}	960	2.760	0
345	3.260	1.612	630	3.013	3.06×10^{-3}	970	2.757	0
350	3.270	1.548	640	2.995	2.56×10^{-3}	980	2.754	0
355	3.272	1.492	650	2.979	2.07×10^{-3}	990	2.751	0
360	3.269	1.449	660	2.964	1.58×10^{-3}	1000	2.748	0
365	3.265	1.418	670	2.950	1.14×10^{-3}	1010	2.746	0
370	3.267	1.401	680	2.936	0	1020	2.743	0
375	3.283	1.393	690	2.924	0	1030	2.741	0
380	3.321	1.381	700	2.912	0	1040	2.738	0
385	3.367	1.340	710	2.902	0	1050	2.736	0
390	3.380	1.278	720	2.891	0	1060	2.734	0
395	3.363	1.245	730	2.882	0	1070	2.732	0
400	3.356	1.247	740	2.873	0	1080	2.730	0
410	3.427	1.274	750	2.865	0	1090	2.728	0
420	3.575	1.237	760	2.857	0	1100	2.726	0
430	3.712	1.101	770	2.849	0	1110	2.724	0
440	3.771	0.919	780	2.842	0	1120	2.722	0
450	3.764	0.757	790	2.836	0	1130	2.721	0
460	3.730	0.630	800	2.829	0	1140	2.719	0

(continued)

Table 10.20 (continued)

λ (nm)	n	k	λ (nm)	n	k	λ (nm)	n	k
470	3.686	0.530	810	2.823	0	1150	2.717	0
480	3.637	0.462	820	2.818	0	1160	2.716	0
490	3.621	0.437	830	2.812	0	1170	2.714	0
500	3.712	0.363	840	2.807	0	1180	2.713	0
510	3.677	0.115	850	2.802	0	1190	2.711	0
520	3.499	1.97×10^{-2}	860	2.797	0	1200	2.710	0
530	3.387	1.03×10^{-2}	870	2.793	0			

10.2.8 CH_3NH_3I

Data from M. Shirayama, H. Kadowaki, T. Miyadera, T. Sugita, M. Tamakoshi, M. Kato, T. Fujiseki, D. Murata, S. Hara, T. N. Murakami, S. Fujimoto, M. Chikamatsu, and H. Fujiwara [2] (see also Fig. 16.6 in Vol. 1). The optical data have been extracted from a CH_3NH_3I layer, formed on ZnO-coated crystalline Si substrates by laser evaporation at room temperature (Fig. 10.8, Tables 10.21 and 10.22).

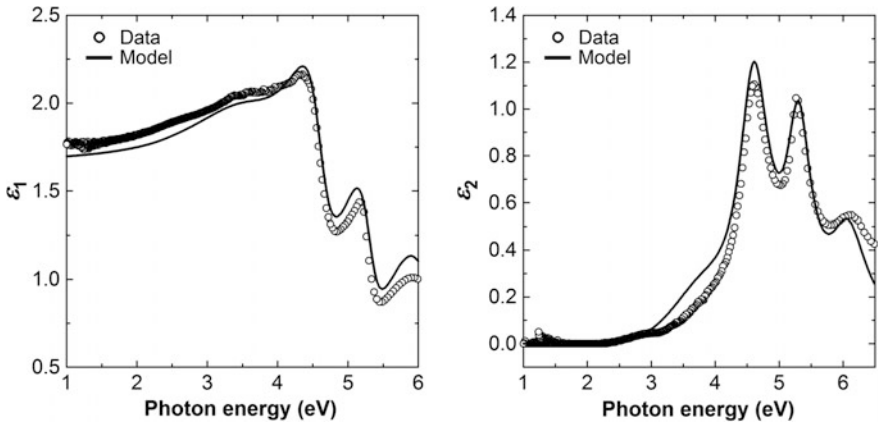


Fig. 10.8 Dielectric function of CH_3NH_3I at room temperature. The open circles show the experimental data and the solid lines indicate the calculation result obtained from the parameterization assuming the Tauc-Lorentz model [(8.1) and (8.2)]

Table 10.21 Tauc-Lorentz parameters of (8.1) and (8.2) for CH_3NH_3I. The model parameters reproted by Shirayama et al. are summarized

Peak	A (eV)	C (eV)	E_0 (eV)	E_g (eV)	$\varepsilon_1(\infty)$
$j = 1$	2.018	1.556	3.743	2.200	1.405
$j = 2$	1.994	0.547	4.601	2.200	0
$j = 3$	0.967	0.444	5.302	2.200	0
$j = 4$	0.608	0.671	6.083	2.200	0

Table 10.22 Optical constants of CH_3NH_3I calculated by the Tauc-Lorentz model

λ (nm)	n	k	λ (nm)	n	k	λ (nm)	n	k
300	1.463	0.150	540	1.335	0	880	1.308	0
305	1.452	0.137	550	1.333	0	890	1.308	0
310	1.443	0.128	560	1.331	0	900	1.308	0
315	1.436	0.120	570	1.329	0	910	1.307	0
320	1.431	0.114	580	1.327	0	920	1.307	0
325	1.428	0.108	590	1.326	0	930	1.307	0
330	1.425	0.103	600	1.325	0	940	1.307	0
335	1.423	9.68×10^{-2}	610	1.323	0	950	1.307	0
340	1.422	9.08×10^{-2}	620	1.322	0	960	1.306	0
345	1.420	8.48×10^{-2}	630	1.321	0	970	1.306	0
350	1.419	7.87×10^{-2}	640	1.320	0	980	1.306	0
355	1.417	7.27×10^{-2}	650	1.319	0	990	1.306	0
360	1.415	6.68×10^{-2}	660	1.319	0	1000	1.306	0
365	1.413	6.11×10^{-2}	670	1.318	0	1010	1.305	0
370	1.410	5.57×10^{-2}	680	1.317	0	1020	1.305	0
375	1.407	5.06×10^{-2}	690	1.316	0	1030	1.305	0
380	1.404	4.58×10^{-2}	700	1.316	0	1040	1.305	0
385	1.401	4.14×10^{-2}	710	1.315	0	1050	1.305	0
390	1.398	3.73×10^{-2}	720	1.315	0	1060	1.305	0
395	1.395	3.36×10^{-2}	730	1.314	0	1070	1.304	0
400	1.392	3.02×10^{-2}	740	1.313	0	1080	1.304	0
410	1.386	2.43×10^{-2}	750	1.313	0	1090	1.304	0
420	1.380	1.94×10^{-2}	760	1.312	0	1100	1.304	0
430	1.375	1.54×10^{-2}	770	1.312	0	1110	1.304	0
440	1.369	1.22×10^{-2}	780	1.312	0	1120	1.304	0
450	1.365	9.53×10^{-3}	790	1.311	0	1130	1.304	0
460	1.360	7.36×10^{-3}	800	1.311	0	1140	1.304	0
470	1.356	5.60×10^{-3}	810	1.310	0	1150	1.303	0
480	1.352	4.18×10^{-3}	820	1.310	0	1160	1.303	0
490	1.349	3.04×10^{-3}	830	1.310	0	1170	1.303	0
500	1.345	2.14×10^{-3}	840	1.309	0	1180	1.303	0
510	1.342	1.44×10^{-3}	850	1.309	0	1190	1.303	0
520	1.340	0	860	1.309	0	1200	1.303	0
530	1.337	0	870	1.308	0			

References

1. H. Fujiwara, M. Kato, M. Tamakoshi, T. Miyadera, M. Chikamatsu, Phys. Status Solidi A **215**, 1700730 (2018)
2. M. Shirayama, H. Kadowaki, T. Miyadera, T. Sugita, M. Tamakoshi, M. Kato, T. Fujiseki, D. Murata, S. Hara, T.N. Murakami, S. Fujimoto, M. Chikamatsu, H. Fujiwara, Phys. Rev. Appl. **5**, 014012 (2016)
3. A. Nakane, H. Tampo, M. Tamakoshi, S. Fujimoto, K.M. Kim, S. Kim, H. Shibata, S. Niki, H. Fujiwara, J. Appl. Phys. **120**, 064505 (2016)
4. G. E. Jellison, Jr., F. A. Modine, Appl. Phys. Lett. **69**, 371 (1996). Erratum, Appl. Phys. Lett. **69**, 2137 (1996)
5. M. Kato, T. Fujiseki, T. Miyadera, T. Sugita, S. Fujimoto, M. Tamakoshi, M. Chikamatsu, H. Fujiwara, J. Appl. Phys. **121**, 115501 (2017)
6. A.M.A. Leguy, P. Azarhoosh, M.I. Alonso, M. Campoy-Quiles, O.J. Weber, J. Yao, D. Bryant, M.T. Weller, J. Nelson, A. Walsh, M. van Schilfgaarde, P.R.F. Barnes, Nanoscale **8**, 6317 (2016)
7. P.G. Snyder, J.A. Woollam, S.A. Alterovitz, B. Johs, J. Appl. Phys. **68**, 5925 (1990)
8. J.-S. Park, S. Choi, Y. Yan, Y. Yang, J.M. Luther, S.-H. Wei, P. Parilla, K. Zhu, J. Phys. Chem. Lett. **6**, 4304 (2015)

Chapter 11
Transparent Conductive Oxides



Akihiro Nakane, Shohei Fujimoto, Masato Tamakoshi, Takashi Koida, James N. Hilfiker, Gerald E. Jellison Jr., Takurou N. Murakami, Tetsuhiko Miyadera and Hiroyuki Fujiwara

Abstract The dielectric functions and optical constants of various transparent conductive oxide (TCO) materials, which have been incorporated into solar cell devices, are summarized. The TCO materials described here include In_2O_3:Sn (ITO), In_2O_3:H, InZnO, SnO_2:F, TiO_2, and ZnO:Al (or Ga). Oxide layers such as MoO_x, NiO, and WO_3 are often employed to improve electronic properties at semiconductor interfaces and the optical data of these TCO layers are also described. In conventional solar cells, the free carrier absorption that occurs within the TCO layers reduces the photocurrent largely, and the characterization of the parasitic absorption within the solar cell is quite important. Accordingly, for ITO and doped ZnO layers, the variation of the dielectric function with carrier concentration is presented. Since non-doped TCO layers are widely employed as high-resistive buffer layers, the dielectric functions of non-doped In_2O_3, SnO_2 and ZnO are also described. It is established in this chapter that all the TCO dielectric functions in the whole near-infrared/visible/ultraviolet region (1–5 eV) can be parameterized by the combined use of the Tauc-Lorentz and Drude models. For the modeling with the Tauc-Lorentz model, several transition peaks are assumed in the ultraviolet region to describe the interband transition above the band gap. In this chapter, the parameterization results for all the TCO materials are summarized, together with the tabulated optical constants.

A. Nakane · S. Fujimoto · M. Tamakoshi · H. Fujiwara (✉)
Gifu University, 1-1 Yanagido, Gifu 501-1193, Japan
e-mail: fujiwara@gifu-u.ac.jp

T. Koida · T. N. Murakami · T. Miyadera
Research Center for Photovoltaics, National Institute of Advanced Industrial Science and Technology, 1-1-1 Umezono, Tsukuba 305-8568, Japan

J. N. Hilfiker
J.A. Woollam Co., Inc., 645 M Street, Suite 102, Lincoln, NE 68508, USA

G. E. Jellison Jr.
Oak Ridge National Laboratory, Oak Ridge, TN 37830, USA

© Springer International Publishing AG, part of Springer Nature 2018

H. Fujiwara and R. W. Collins (eds.), *Spectroscopic Ellipsometry for Photovoltaics*,
Springer Series in Optical Sciences 214,
https://doi.org/10.1007/978-3-319-95138-6_11

11.1 Introduction

Transparent conductive oxide (TCO) layers are commonly used as front electrodes in almost all thin-film photovoltaic devices. Unfortunately, these TCO layers exhibit rather strong light absorption due to free carrier absorption, induced by free electrons present within the TCO (Chap. 18 in Vol. 1). In particular, the parasitic light absorption in the TCO reduces the short-circuit current density by ~3 mA/cm^2 (Table 2.1) and thus the suppression of the TCO free carrier absorption is crucial for maximizing the conversion efficiencies (Chap. 2). For the estimation and interpretation of optical losses caused by TCO layers, however, the optical constants of TCO layers need to be characterized.

In this chapter, for the purpose of spectroscopic ellipsometry (SE) characterization and device simulation, the tabulated optical constants of various TCO materials at room temperature are provided. In addition, graphene (C), which can be employed as an alternative TCO layer, is also treated here. For all the materials, refractive index n and extinction coefficient k are shown in a wavelength (λ) range of 300–1200 nm with steps of 5 nm (300–400 nm) and 10 nm (400–1200 nm). From these numerical values, the dielectric function ($\varepsilon = \varepsilon_1 - i\varepsilon_2$) and the absorption coefficient (α) can be calculated quite easily according to $\varepsilon_1 = n^2 - k^2$, $\varepsilon_2 = 2nk$ and $\alpha = 4\pi k/\lambda$ (Sect. 1.2.1). The λ value can also be converted to energy (E) by $E = 1239.8/[\lambda\ (\text{nm})]$ eV (1.3). It should be noted that, in the tabulated data, the absolute k value is denoted as "0" when there is no observable light absorption, even though materials may have very small k (or α) values in a certain E region.

Unfortunately, the tabulated data are sometimes insufficient for more complete SE analysis or optical simulation. Accordingly, all the TCO dielectric functions were parameterized using the Tauc-Lorentz model described by (1.19)–(1.20). When the TCO exhibited free carrier absorption, the dielectric function was parameterized by further combining the Drude model [see (1.27)]. The Tauc-Lorentz model was developed originally to express the dielectric function of amorphous materials [1], but we found that this model is quite effective for the complete parameterization of light absorption that occurs above the band gap (E_g) of TCO materials. It should be emphasized that the Tauc-Lorentz model is used solely to establish the optical database of numerous solar-cell component layers.

In this chapter, the dielectric function of TCO materials is modeled by combining several Tauc-Lorentz peaks with the Drude model:

$$\varepsilon_2(E) = \sum_{j=1}^{m} \frac{A_j C_j E_{0,j} (E - E_{g,j})^2}{[(E^2 - E_{0,j}^2)^2 + C_j^2 E^2]E} + \frac{A_D \Gamma}{E^3 + \Gamma^2 E}. \tag{11.1}$$

In (11.1), the first and second terms on the right side show the Tauc-Lorentz and Drude contributions, respectively. As confirmed from this equation, a single Tauc-Lorentz peak is expressed by four parameters: i.e., the amplitude parameter A_j,

broadening parameter C_j, peak transition energy $E_{0,j}$, and optical gap $E_{g,j}$ of the jth Tauc-Lorentz peak (see Fig. 1.9).

On the other hand, the Drude contribution can also be described by the amplitude parameter A_D and broadening parameter Γ. From the Drude parameters of (A_D, Γ), the optical carrier concentration (N_{opt}) and optical mobility (μ_{opt}) can be estimated further if the effective mass m^* is known (see Sect. 18.3.3 in Vol. 1). In general, N_{opt} shows quite good agreement with the carrier concentration obtained from Hall measurements (N_{Hall}), while μ_{opt} is generally larger than μ_{Hall} (Sect. 18.4 in Vol. 1). Since the free carrier absorption increases significantly with N_{opt} and N_{Hall}, the values of (N_{opt}, μ_{opt}) and (N_{Hall}, μ_{Hall}) are described whenever possible. For SnO_2:F, In_2O_3:Sn and doped ZnO in this chapter, the calculation of (N_{opt}, μ_{opt}) from (A_D, Γ) was performed using (18.24)–(18.25) in Vol. 1 and the result of Table 18.1 in Vol. 1 by taking the effect of nonparabolic TCO conduction band into account. In this chapter, the carrier concentration of various TCO materials is basically represented by N_{Hall}, as the calculation of N_{opt} is not possible when m^* is unknown.

Using the parameters of (11.1), $\varepsilon_1(E)$ can then be calculated from the Kramers-Kronig integration of each Tauc-Lorentz ε_2 peak and the ε_1 contribution of the Drude term:

$$\varepsilon_1(E) = \sum_{j=1}^{m} \left(\varepsilon_{1,j}(\infty) + \frac{2}{\pi} P \int_{E_g}^{\infty} \frac{E' \varepsilon_{2,j}(E')}{E'^2 - E^2} dE' \right) - \frac{A_D}{E^2 + \Gamma^2}, \tag{11.2}$$

where $\varepsilon_{1,j}(\infty)$ represents a constant contribution to $\varepsilon_1(E)$ at high energies. The first term on the right side shows the Kramers-Kronig integration of the jth Tauc-Lorentz peak [$\varepsilon_{2,j}(E')$ in (11.2)] and this integration can be performed rather easily using the exact equations shown in (1.20). As confirmed from (11.2), when a dielectric function is modeled by combining several Tauc-Lorentz peaks, $\varepsilon_1(E)$ is calculated as a sum of the ε_1 contributions obtained from each Tauc-Lorentz peak (see the example of graphene in Fig. 11.1). The calculation example of the Tauc-Lorentz model is also given by (1.26). On the other hand, the second term on the right side of (11.2) represents the ε_1 contribution of the Drude model (Sects. 5.3.4 in Vol. 1 and 18.2.3 in Vol. 1). A free software described in Sect. 2.7 can further be applied to calculate the dielectric function from the Tauc-Lorentz and Drude parameters listed in this chapter.

In the actual $\varepsilon_1(E)$ and $\varepsilon_2(E)$ calculation, however, E should be chosen so that $|E - E_g|$ in (1.20) does not become zero. The parameterization of all the TCO dielectric functions using (11.1) and (11.2), described in this chapter, was implemented by the group of Gifu University (A. Nakane, S. Fujimoto, and M. Tamakoshi), unless otherwise noted.

11.2 Optical Data of Transparent Conductive Oxides

11.2.1 Graphene

Data from M. Losurdo, M. M. Giangregorio, G. V. Bianco, P. Capezzuto, G. Bruno [2]. The optical data have been extracted from chemical-vapor-deposited monolayer graphene (polycrystal) on glass substrate. This graphene layer shows p-type conductivity with $N_{\mathrm{Hall}} = 6 \times 10^{11}$ cm^{-2} and $\mu_{\mathrm{Hall}} = 1200$ cm^2/(Vs) (Fig. 11.1, Tables 11.1 and 11.2).

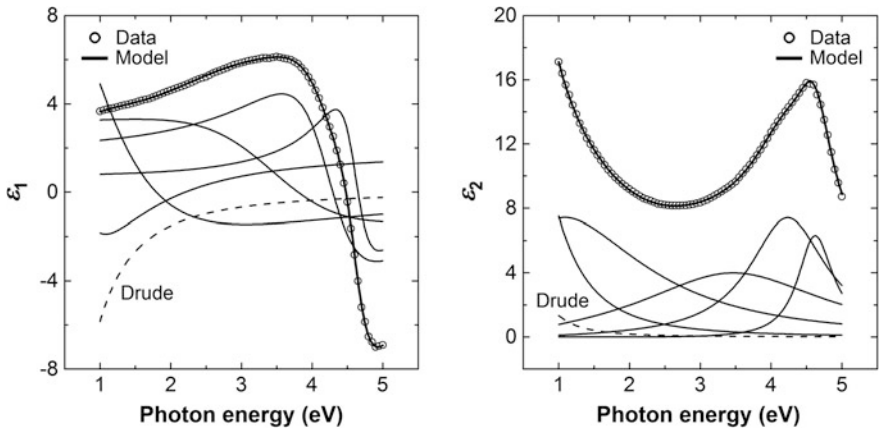


Fig. 11.1 Dielectric function of graphene at room temperature. The open circles show the reference data and the lines indicate the calculation result obtained from the parameterization assuming the Tauc-Lorentz (solid lines) and Drude (dotted line) models [(11.1) and (11.2)]

Table 11.1 Tauc-Lorentz (TL) peak and Drude parameters of (11.1) and (11.2) for graphene

Model	A/A_{D} (eV)	C/Γ (eV)	E_0 (eV)	E_{g} (eV)	$\varepsilon_1(\infty)$
TL peak1	41.068	0.819	0.435	0.174	1.777
TL peak2	22.262	3.360	1.706	0.071	0
TL peak3	12.222	3.205	3.801	1×10^{-4}	0
TL peak4	11.461	1.330	4.278	0.319	0
TL peak5	14.500	0.613	4.614	2.232	0
Drude	6.155	0.230	–	–	–

Table 11.2 Optical constants of graphene calculated by the Tauc-Lorentz and Drude models

λ (nm)	n	k	λ (nm)	n	k	λ (nm)	n	k
300	3.012	2.257	540	2.720	1.546	880	2.912	2.118
305	3.035	2.169	550	2.717	1.561	890	2.921	2.133
310	3.049	2.084	560	2.716	1.577	900	2.931	2.149
315	3.055	2.006	570	2.715	1.592	910	2.940	2.164
320	3.053	1.935	580	2.715	1.609	920	2.949	2.179
325	3.046	1.872	590	2.716	1.625	930	2.959	2.195
330	3.035	1.816	600	2.718	1.642	940	2.968	2.210
335	3.022	1.767	610	2.720	1.660	950	2.977	2.225
340	3.007	1.724	620	2.723	1.677	960	2.987	2.240
345	2.992	1.688	630	2.726	1.695	970	2.996	2.254
350	2.977	1.656	640	2.730	1.712	980	3.005	2.269
355	2.962	1.628	650	2.735	1.730	990	3.015	2.284
360	2.948	1.604	660	2.740	1.748	1000	3.024	2.299
365	2.934	1.583	670	2.745	1.766	1010	3.034	2.313
370	2.921	1.565	680	2.751	1.783	1020	3.043	2.328
375	2.909	1.549	690	2.757	1.801	1030	3.052	2.342
380	2.897	1.535	700	2.763	1.819	1040	3.062	2.356
385	2.886	1.523	710	2.770	1.836	1050	3.071	2.371
390	2.876	1.512	720	2.777	1.854	1060	3.081	2.385
395	2.866	1.503	730	2.784	1.871	1070	3.090	2.399
400	2.857	1.495	740	2.792	1.888	1080	3.100	2.413
410	2.839	1.482	750	2.800	1.905	1090	3.109	2.427
420	2.824	1.474	760	2.807	1.922	1100	3.118	2.441
430	2.809	1.468	770	2.816	1.939	1110	3.128	2.455
440	2.796	1.465	780	2.824	1.956	1120	3.137	2.469
450	2.784	1.466	790	2.832	1.973	1130	3.147	2.483
460	2.772	1.468	800	2.841	1.989	1140	3.156	2.497
470	2.762	1.472	810	2.849	2.006	1150	3.166	2.510
480	2.753	1.479	820	2.858	2.022	1160	3.175	2.524
490	2.745	1.487	830	2.867	2.038	1170	3.185	2.538
500	2.738	1.496	840	2.876	2.054	1180	3.194	2.551
510	2.732	1.507	850	2.885	2.070	1190	3.204	2.565
520	2.727	1.519	860	2.894	2.086	1200	3.213	2.578
530	2.723	1.532	870	2.903	2.102			

11.2.2 In_2O_3 (Non-doped)

Data: unpublished results of T. Koida. The preparation and characterization of In_2O_3 layers can be found in [3]. The optical data have been extracted from a polycrystalline In_2O_3 layer formed by rf sputtering at room temperature using an Ar/O_2 gas mixture and an In_2O_3 target. The electrical characteristics of this layer are $N_{Hall} = 5.3 \times 10^{18}$ cm^{-3} and $\mu_{Hall} = 13.2$ cm^2/(Vs) (Tables 11.3, 11.4 and Fig. 11.2).

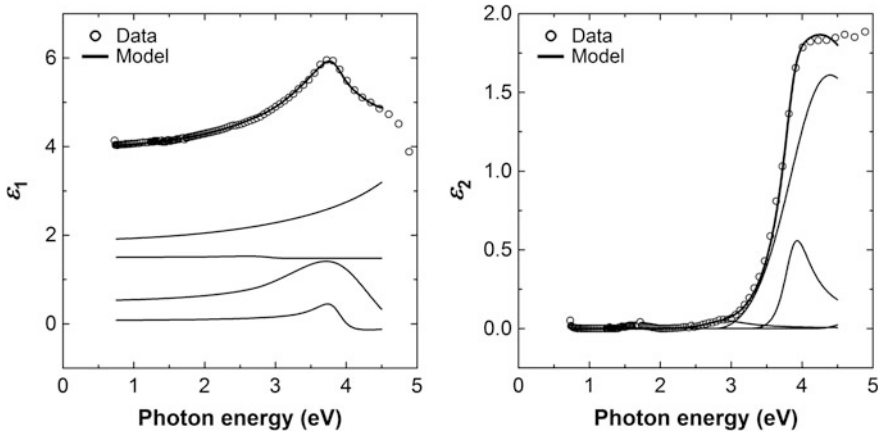


Fig. 11.2 Dielectric function of non-doped In_2O_3 at room temperature. The open circles show the experimental data and the solid lines indicate the calculation result obtained from the parameterization assuming the Tauc-Lorentz model [(8.1) and (8.2)]

Table 11.3 Tanc-Lorentz parameters of (8.1) and (8.2) for non-doped In_2O_3

Peak	A (eV)	C (eV)	E_0 (eV)	E_g (eV)	$\varepsilon_1(\infty)$
$j = 1$	0.263	0.706	2.855	1.823	1.489
$j = 2$	9.740	0.463	3.865	3.260	0
$j = 3$	22.790	1.707	4.163	2.773	0
$j = 4$	93.634	1.459	6.986	4.191	0

Table 11.4 Optical constants of non-doped In_2O_3 calculated by the Tauc-Lorentz model

λ (nm)	n	k	λ (nm)	n	k	λ (nm)	n	k
300	2.323	0.398	540	2.100	1.13×10^{-3}	880	2.031	0
305	2.345	0.390	550	2.095	0	890	2.030	0
310	2.371	0.378	560	2.091	0	900	2.029	0
315	2.400	0.357	570	2.087	0	910	2.028	0
320	2.428	0.323	580	2.083	0	920	2.028	0
325	2.444	0.279	590	2.080	0	930	2.027	0
330	2.445	0.232	600	2.076	0	940	2.026	0
335	2.435	0.190	610	2.073	0	950	2.026	0
340	2.419	0.157	620	2.070	0	960	2.025	0
345	2.400	0.130	630	2.068	0	970	2.024	0
350	2.382	0.109	640	2.065	0	980	2.024	0
355	2.363	9.17×10^{-2}	650	2.063	0	990	2.023	0
360	2.346	7.74×10^{-2}	660	2.060	0	1000	2.023	0
365	2.329	6.56×10^{-2}	670	2.058	0	1010	2.022	0
370	2.314	5.57×10^{-2}	680	2.056	0	1020	2.022	0
375	2.299	4.76×10^{-2}	690	2.054	0	1030	2.021	0
380	2.285	4.08×10^{-2}	700	2.052	0	1040	2.021	0
385	2.272	3.52×10^{-2}	710	2.051	0	1050	2.020	0
390	2.260	3.04×10^{-2}	720	2.049	0	1060	2.020	0
395	2.248	2.65×10^{-2}	730	2.047	0	1070	2.019	0
400	2.238	2.32×10^{-2}	740	2.046	0	1080	2.019	0
410	2.218	1.84×10^{-2}	750	2.044	0	1090	2.018	0
420	2.202	1.52×10^{-2}	760	2.043	0	1100	2.018	0
430	2.188	1.28×10^{-2}	770	2.042	0	1110	2.018	0
440	2.175	1.09×10^{-2}	780	2.041	0	1120	2.017	0
450	2.165	9.43×10^{-3}	790	2.039	0	1130	2.017	0
460	2.155	7.88×10^{-3}	800	2.038	0	1140	2.017	0
470	2.146	6.36×10^{-3}	810	2.037	0	1150	2.016	0
480	2.138	5.03×10^{-3}	820	2.036	0	1160	2.016	0
490	2.130	3.94×10^{-3}	830	2.035	0	1170	2.016	0
500	2.123	3.07×10^{-3}	840	2.034	0	1180	2.015	0
510	2.117	2.39×10^{-3}	850	2.033	0	1190	2.015	0
520	2.111	1.86×10^{-3}	860	2.032	0	1200	2.015	0
530	2.105	1.45×10^{-3}	870	2.031	0			

11.2.3 In_2O_3:H ($N_{Hall} = 2.1 \times 10^{20}$ cm^{-3})

Data from T. Koida, M. Kondo, K. Tsutsumi, A. Sakaguchi, M. Suzuki and H. Fujiwara [4] [see also Fig. 19.9 (poly-In_2O_3:H) in Chap. 19 (Vol. 1)]. The optical data have been extracted from a high-mobility In_2O_3:H polycrystal formed by a two-step process: (i) rf sputtering at room temperature using an In_2O_3 target and an Ar/O_2 gas mixture with H_2O vapor and (ii) thermal annealing at 200 °C. The electrical characteristics of this layer are $N_{Hall} = 2.1 \times 10^{20}$ cm^{-3} and $\mu_{Hall} = 108$ $cm^2/(Vs)$ with $N_{opt} = 1.85 \times 10^{20}$ cm^{-3} and $\mu_{opt} = 104$ $cm^2/(Vs)$ (Table 19.2 in Vol. 1) (Tables 11.5, 11.6 and Fig. 11.3).

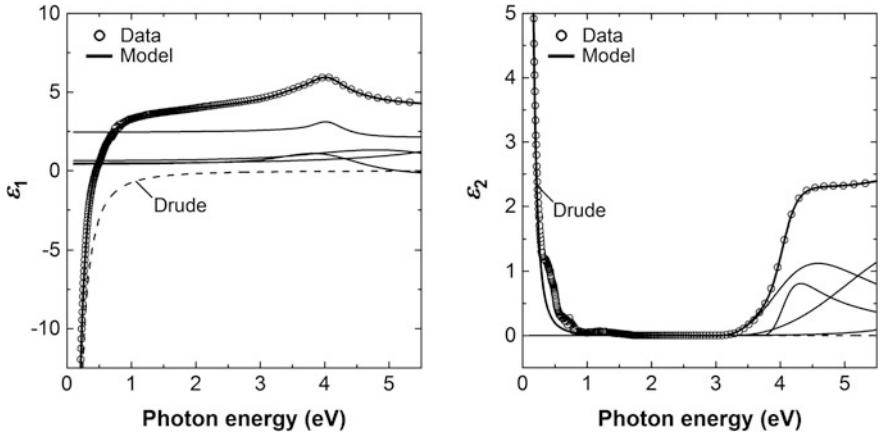


Fig. 11.3 Dielectric function of In_2O_3:H at room temperature. The open circles show the reference data and the lines indicate the calculation result obtained from the parameterization assuming the Tauc-Lorentz (solid lines) and Drude (dotted line) models [(11.1) and (11.2)]

Table 11.5 Tauc-Lorentz (TL) peak and Drude parameters of (11.1) and (11.2) for In_2O_3:H

Model	A/A_D (eV)	C/Γ (eV)	E_0 (eV)	E_g (eV)	$\varepsilon_1(\infty)$
TL peak1	45.989	0.684	4.061	3.714	2.236
TL peak2	25.507	1.971	4.162	3.054	0
TL peak3	27.441	4.016	5.892	3.285	0
TL peak4	10.891	0.436	7.095	3.069	0
Drude	0.759	0.033	–	–	–

Table 11.6 Optical constants of In_2O_3:H calculated by the Tauc-Lorentz and Drude models

λ (nm)	n	k	λ (nm)	n	k	λ (nm)	n	k
300	2.436	0.357	540	2.032	5.09×10^{-4}	880	1.919	2.33×10^{-3}
305	2.450	0.303	550	2.027	5.39×10^{-4}	890	1.916	2.42×10^{-3}
310	2.449	0.247	560	2.023	5.70×10^{-4}	900	1.913	2.50×10^{-3}
315	2.435	0.198	570	2.018	6.03×10^{-4}	910	1.910	2.59×10^{-3}
320	2.413	0.158	580	2.014	6.36×10^{-4}	920	1.907	2.68×10^{-3}
325	2.388	0.127	590	2.010	6.71×10^{-4}	930	1.904	2.77×10^{-3}
330	2.364	0.104	600	2.006	7.07×10^{-4}	940	1.901	2.87×10^{-3}
335	2.342	8.66×10^{-2}	610	2.002	7.45×10^{-4}	950	1.898	2.97×10^{-3}
340	2.323	7.19×10^{-2}	620	1.999	7.83×10^{-4}	960	1.895	3.07×10^{-3}
345	2.305	5.88×10^{-2}	630	1.995	8.23×10^{-4}	970	1.892	3.17×10^{-3}
350	2.288	4.73×10^{-2}	640	1.991	8.65×10^{-4}	980	1.889	3.27×10^{-3}
355	2.272	3.73×10^{-2}	650	1.988	9.07×10^{-4}	990	1.886	3.38×10^{-3}
360	2.256	2.88×10^{-2}	660	1.985	9.52×10^{-4}	1000	1.883	3.49×10^{-3}
365	2.241	2.17×10^{-2}	670	1.981	9.97×10^{-4}	1010	1.880	3.60×10^{-3}
370	2.226	1.58×10^{-2}	680	1.978	1.04×10^{-3}	1020	1.877	3.71×10^{-3}
375	2.212	1.12×10^{-2}	690	1.975	1.09×10^{-3}	1030	1.874	3.83×10^{-3}
380	2.199	7.61×10^{-3}	700	1.972	1.14×10^{-3}	1040	1.871	3.95×10^{-3}
385	2.187	4.84×10^{-3}	710	1.969	1.19×10^{-3}	1050	1.868	4.07×10^{-3}
390	2.176	2.79×10^{-3}	720	1.966	1.25×10^{-3}	1060	1.865	4.19×10^{-3}
395	2.165	1.37×10^{-3}	730	1.963	1.30×10^{-3}	1070	1.861	4.32×10^{-3}
400	2.155	5.33×10^{-4}	740	1.960	1.36×10^{-3}	1080	1.858	4.45×10^{-3}
410	2.138	2.12×10^{-4}	750	1.957	1.42×10^{-3}	1090	1.855	4.58×10^{-3}
420	2.124	2.29×10^{-4}	760	1.954	1.48×10^{-3}	1100	1.852	4.72×10^{-3}
430	2.112	2.47×10^{-4}	770	1.951	1.54×10^{-3}	1110	1.849	4.86×10^{-3}
440	2.101	2.66×10^{-4}	780	1.948	1.60×10^{-3}	1120	1.845	5.00×10^{-3}
450	2.091	2.86×10^{-4}	790	1.945	1.67×10^{-3}	1130	1.842	5.14×10^{-3}
460	2.082	3.07×10^{-4}	800	1.942	1.73×10^{-3}	1140	1.839	5.29×10^{-3}
470	2.074	3.29×10^{-4}	810	1.939	1.80×10^{-3}	1150	1.835	5.44×10^{-3}
480	2.067	3.52×10^{-4}	820	1.936	1.87×10^{-3}	1160	1.832	5.59×10^{-3}
490	2.060	3.75×10^{-4}	830	1.933	1.94×10^{-3}	1170	1.828	5.75×10^{-3}
500	2.054	4.00×10^{-4}	840	1.930	2.02×10^{-3}	1180	1.825	5.91×10^{-3}
510	2.048	4.26×10^{-4}	850	1.927	2.09×10^{-3}	1190	1.822	6.07×10^{-3}
520	2.042	4.52×10^{-4}	860	1.925	2.17×10^{-3}	1200	1.818	6.24×10^{-3}
530	2.037	4.80×10^{-4}	870	1.922	2.25×10^{-3}			

11.2.4 In_2O_3:Sn ($N_{Hall} = 4.9 \times 10^{20}$ cm^{-3})

Data from H. Fujiwara and M. Kondo [5]. The optical data have been extracted from an ITO layer formed by rf sputtering at room temperature using an Ar gas and an ITO target (In_2O_3:SnO_2 = 90:10 wt.%). The electrical characteristics of this layer are $N_{Hall} = 4.9 \times 10^{20}$ cm^{-3} and $\mu_{Hall} = 23.0$ $cm^2/(Vs)$ with $N_{opt} = 4.6 \times 10^{20}$ cm^{-3} and $\mu_{opt} = 23.7$ $cm^2/(Vs)$ (Tables 11.7, 11.8 and Fig. 11.4).

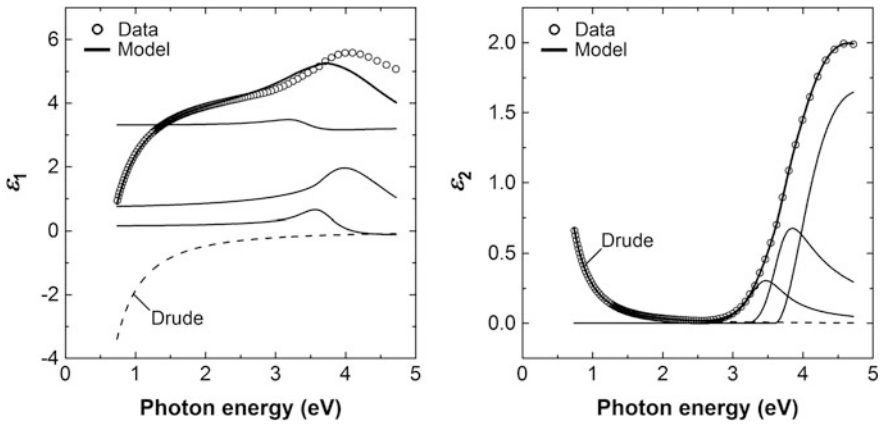


Fig. 11.4 Dielectric function of In_2O_3:Sn ($N_{Hall} = 4.9 \times 10^{20}$ cm^{-3}) at room temperature. The open circles show the reference data and the lines indicate the calculation result obtained from the parameterization assuming the Tauc-Lorentz (solid lines) and Drude (dotted line) models [(11.1) and (11.2)]

Table 11.7 Tauc-Lorentz (TL) peak and Drude parameters of (11.1) and (11.2) for In_2O_3:Sn ($N_{Hall} = 4.9 \times 10^{20}$ cm^{-3})

Model	A/A_D (eV)	C/Γ (eV)	E_0 (eV)	E_g (eV)	$\varepsilon_1(\infty)$
TL peak1	2.247	0.684	3.410	2.389	3.253
TL peak2	20.530	0.689	3.672	3.184	0
TL peak3	127.242	1.583	3.753	3.596	0
Drude	1.909	0.147	–	–	–

Table 11.8 Optical constants of In_2O_3:Sn ($N_{Hall} = 4.9 \times 10^{20}$ cm^{-3}). The optical data reported by Fujiwara et al. are shown

λ (nm)	n	k	λ (nm)	n	k	λ (nm)	n	k
300	2.386	0.347	540	2.013	5.74×10^{-3}	880	1.830	2.72×10^{-2}
305	2.386	0.327	550	2.007	6.09×10^{-3}	890	1.823	2.82×10^{-2}
310	2.381	0.306	560	2.002	6.44×10^{-3}	900	1.817	2.93×10^{-2}
315	2.373	0.283	570	1.997	6.81×10^{-3}	910	1.811	3.03×10^{-2}
320	2.361	0.261	580	1.992	7.19×10^{-3}	920	1.804	3.14×10^{-2}
325	2.347	0.237	590	1.987	7.59×10^{-3}	930	1.798	3.26×10^{-2}
330	2.330	0.214	600	1.982	8.00×10^{-3}	940	1.791	3.38×10^{-2}
335	2.309	0.189	610	1.977	8.42×10^{-3}	950	1.784	3.50×10^{-2}
340	2.284	0.164	620	1.972	8.87×10^{-3}	960	1.778	3.62×10^{-2}
345	2.267	0.145	630	1.967	9.32×10^{-3}	970	1.771	3.75×10^{-2}
350	2.251	0.128	640	1.962	9.80×10^{-3}	980	1.764	3.88×10^{-2}
355	2.235	0.112	650	1.957	1.03×10^{-2}	990	1.757	4.02×10^{-2}
360	2.222	9.65×10^{-2}	660	1.952	1.08×10^{-2}	1000	1.750	4.15×10^{-2}
365	2.208	8.40×10^{-2}	670	1.946	1.13×10^{-2}	1010	1.743	4.30×10^{-2}
370	2.194	7.34×10^{-2}	680	1.941	1.19×10^{-2}	1020	1.736	4.44×10^{-2}
375	2.179	5.89×10^{-2}	690	1.936	1.24×10^{-2}	1030	1.728	4.59×10^{-2}
380	2.168	5.13×10^{-2}	700	1.931	1.30×10^{-2}	1040	1.721	4.75×10^{-2}
385	2.156	4.32×10^{-2}	710	1.926	1.36×10^{-2}	1050	1.714	4.90×10^{-2}
390	2.145	3.61×10^{-2}	720	1.921	1.42×10^{-2}	1060	1.706	5.07×10^{-2}
395	2.135	3.02×10^{-2}	730	1.915	1.49×10^{-2}	1070	1.698	5.24×10^{-2}
400	2.126	2.55×10^{-2}	740	1.910	1.55×10^{-2}	1080	1.691	5.40×10^{-2}
410	2.110	1.81×10^{-2}	750	1.905	1.62×10^{-2}	1090	1.683	5.58×10^{-2}
420	2.096	1.32×10^{-2}	760	1.899	1.69×10^{-2}	1100	1.675	5.76×10^{-2}
430	2.084	1.01×10^{-2}	770	1.894	1.76×10^{-2}	1110	1.667	5.95×10^{-2}
440	2.076	8.13×10^{-3}	780	1.888	1.84×10^{-2}	1120	1.659	6.14×10^{-2}
450	2.069	6.58×10^{-3}	790	1.883	1.91×10^{-2}	1130	1.650	6.33×10^{-2}
460	2.062	5.44×10^{-3}	800	1.877	1.99×10^{-2}	1140	1.642	6.53×10^{-2}
470	2.055	4.68×10^{-3}	810	1.871	2.08×10^{-2}	1150	1.634	6.74×10^{-2}
480	2.048	4.29×10^{-3}	820	1.865	2.16×10^{-2}	1160	1.625	6.95×10^{-2}
490	2.041	4.26×10^{-3}	830	1.860	2.25×10^{-2}	1170	1.616	7.17×10^{-2}
500	2.035	4.51×10^{-3}	840	1.854	2.33×10^{-2}	1180	1.608	7.39×10^{-2}
510	2.029	4.80×10^{-3}	850	1.848	2.43×10^{-2}	1190	1.599	7.62×10^{-2}
520	2.023	5.10×10^{-3}	860	1.842	2.52×10^{-2}	1200	1.590	7.85×10^{-2}
530	2.018	5.42×10^{-3}	870	1.836	2.62×10^{-2}			

11.2.5 In_2O_3:Sn ($N_{Hall} = 7.2 \times 10^{20}$ cm^{-3})

Data from H. Fujiwara and M. Kondo [5]. The optical data have been extracted from an ITO layer formed by rf sputtering at 200 °C using an Ar gas and an ITO target (In_2O_3:SnO_2 = 90:10 wt.%). The electrical characteristics of this layer are $N_{Hall} = 7.2 \times 10^{20}$ cm^{-3} and $\mu_{Hall} = 43.4$ $cm^2/(Vs)$ with $N_{opt} = 7.0 \times 10^{20}$ cm^{-3} and $\mu_{opt} = 22.9$ $cm^2/(Vs)$ (Tables 11.9, 11.10 and Fig. 11.5).

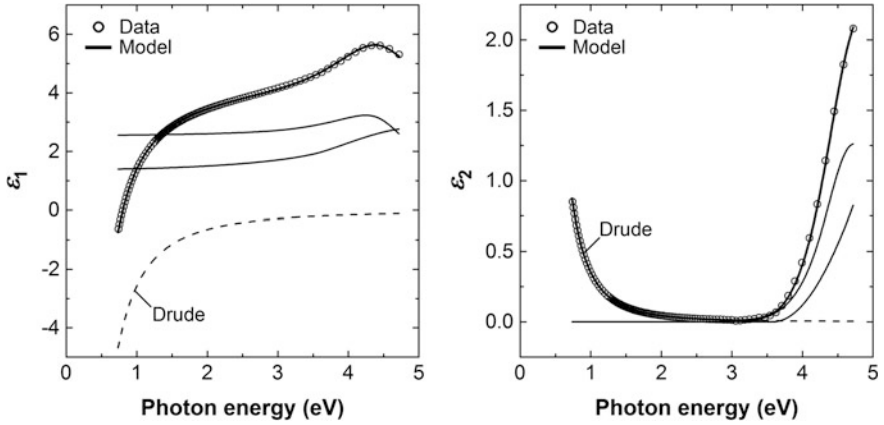


Fig. 11.5 Dielectric function of In_2O_3:Sn ($N_{Hall} = 7.2 \times 10^{20}$ cm^{-3}) at room temperature. The open circles show the reference data and the lines indicate the calculation result obtained from the parameterization assuming the Tauc-Lorentz (solid lines) and Drude (dotted line) models [(11.1) and (11.2)]

Table 11.9 Tauc-Lorentz (TL) peak and Drude parameters of (11.1) and (11.2) for In_2O_3:Sn ($N_{Hall} = 7.2 \times 10^{20}$ cm^{-3})

Model	A/A_D (eV)	C/Γ (eV)	E_0 (eV)	E_g (eV)	$\varepsilon_1(\infty)$
TL peak1	12.267	1.159	4.635	3.059	2.275
TL peak2	73.547	4.751	6.042	3.579	0
Drude	2.620	0.137	–	–	–

Table 11.10 Optical constants of In_2O_3:Sn ($N_{Hall} = 7.2 \times 10^{20}$ cm^{-3}). The optical data reported by Fujiwara et al. are shown

λ (nm)	n	k	λ (nm)	n	k	λ (nm)	n	k
300	2.335	0.141	540	1.917	7.71×10^{-3}	880	1.639	3.88×10^{-2}
305	2.312	0.115	550	1.909	8.18×10^{-3}	890	1.629	4.04×10^{-2}
310	2.290	9.32×10^{-2}	560	1.901	8.67×10^{-3}	900	1.620	4.20×10^{-2}
315	2.269	7.46×10^{-2}	570	1.894	9.18×10^{-3}	910	1.610	4.37×10^{-2}
320	2.250	5.89×10^{-2}	580	1.886	9.71×10^{-3}	920	1.600	4.54×10^{-2}
325	2.233	4.50×10^{-2}	590	1.878	1.03×10^{-2}	930	1.590	4.72×10^{-2}
330	2.213	3.33×10^{-2}	600	1.871	1.08×10^{-2}	940	1.579	4.90×10^{-2}
335	2.192	2.48×10^{-2}	610	1.863	1.14×10^{-2}	950	1.569	5.09×10^{-2}
340	2.173	1.77×10^{-2}	620	1.855	1.20×10^{-2}	960	1.559	5.29×10^{-2}
345	2.161	1.40×10^{-2}	630	1.848	1.27×10^{-2}	970	1.548	5.49×10^{-2}
350	2.148	1.06×10^{-2}	640	1.840	1.34×10^{-2}	980	1.537	5.70×10^{-2}
355	2.136	9.26×10^{-3}	650	1.833	1.40×10^{-2}	990	1.526	5.92×10^{-2}
360	2.126	7.54×10^{-3}	660	1.825	1.48×10^{-2}	1000	1.515	6.14×10^{-2}
365	2.116	7.09×10^{-3}	670	1.817	1.55×10^{-2}	1010	1.503	6.38×10^{-2}
370	2.106	6.30×10^{-3}	680	1.809	1.63×10^{-2}	1020	1.492	6.62×10^{-2}
375	2.095	4.57×10^{-3}	690	1.802	1.71×10^{-2}	1030	1.480	6.87×10^{-2}
380	2.088	4.57×10^{-3}	700	1.794	1.79×10^{-2}	1040	1.469	7.12×10^{-2}
385	2.079	3.51×10^{-3}	710	1.786	1.88×10^{-2}	1050	1.457	7.39×10^{-2}
390	2.071	3.23×10^{-3}	720	1.778	1.97×10^{-2}	1060	1.444	7.66×10^{-2}
395	2.064	2.22×10^{-3}	730	1.770	2.06×10^{-2}	1070	1.432	7.95×10^{-2}
400	2.057	2.71×10^{-3}	740	1.762	2.15×10^{-2}	1080	1.419	8.24×10^{-2}
410	2.043	2.44×10^{-3}	750	1.754	2.25×10^{-2}	1090	1.407	8.55×10^{-2}
420	2.030	3.43×10^{-3}	760	1.745	2.35×10^{-2}	1100	1.394	8.86×10^{-2}
430	2.018	3.70×10^{-3}	770	1.737	2.46×10^{-2}	1110	1.380	9.20×10^{-2}
440	2.007	3.99×10^{-3}	780	1.729	2.57×10^{-2}	1120	1.367	9.53×10^{-2}
450	1.997	4.29×10^{-3}	790	1.720	2.68×10^{-2}	1130	1.353	9.89×10^{-2}
460	1.987	4.61×10^{-3}	800	1.712	2.80×10^{-2}	1140	1.340	0.103
470	1.977	4.94×10^{-3}	810	1.703	2.92×10^{-2}	1150	1.326	0.106
480	1.968	5.28×10^{-3}	820	1.694	3.04×10^{-2}	1160	1.311	0.110
490	1.959	5.64×10^{-3}	830	1.685	3.17×10^{-2}	1170	1.297	0.114
500	1.950	6.02×10^{-3}	840	1.676	3.30×10^{-2}	1180	1.282	0.119
510	1.942	6.42×10^{-3}	850	1.667	3.44×10^{-2}	1190	1.267	0.123
520	1.933	6.83×10^{-3}	860	1.658	3.58×10^{-2}	1200	1.252	0.128
530	1.925	7.26×10^{-3}	870	1.648	3.73×10^{-2}			

11.2.6 In_2O_3:Sn ($N_{Hall} = 1.2 \times 10^{21}$ cm^{-3})

Data from H. Fujiwara and M. Kondo [5] (see also Fig. 18.14 in Vol. 1). The optical data have been extracted from an ITO layer formed by rf sputtering at 240 °C using an Ar gas and an ITO target (In_2O_3:SnO_2 = 90:10 wt%). The electrical characteristics of this layer are $N_{Hall} = 1.2 \times 10^{21}$ cm^{-3} and $\mu_{Hall} = 31$ $cm^2/(Vs)$ with $N_{opt} = 1.2 \times 10^{21}$ cm^{-3} and $\mu_{opt} = 27.0$ $cm^2/(Vs)$ (Tables 11.11, 11.12 and Fig. 11.6).

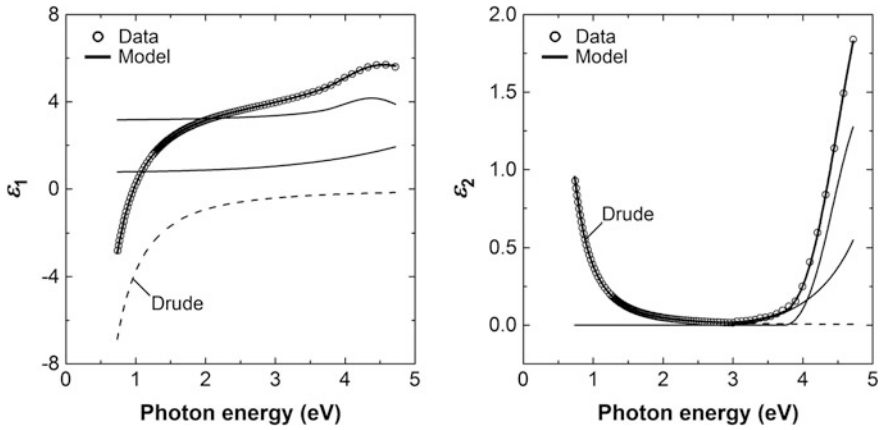


Fig. 11.6 Dielectric function of In_2O_3:Sn ($N_{Hall} = 1.2 \times 10^{21}$ cm^{-3}) at room temperature. The open circles show the reference data and the lines indicate the calculation result obtained from the parameterization assuming the Tauc-Lorentz (solid lines) and Drude (dotted line) models [(11.1) and (11.2)]

Table 11.11 Tauc-Lorentz (TL) peak and Drude parameters of (11.1) and (11.2) for In_2O_3:Sn ($N_{Hall} = 1.2 \times 10^{21}$ cm^{-3})

Model	A/A_D (eV)	C/Γ (eV)	E_0 (eV)	E_g (eV)	$\varepsilon_1(\infty)$
TL peak1	53.445	1.741	4.580	3.731	2.635
TL peak2	18.514	1.534	6.039	2.761	0
Drude	3.786	0.102	–	–	–

Table 11.12 Optical constants of In_2O_3:Sn ($N_{Hall} = 1.2 \times 10^{21}$ cm^{-3}). The optical data reported by Fujiwara et al. are shown

λ (nm)	n	k	λ (nm)	n	k	λ (nm)	n	k
300	2.309	9.95×10^{-2}	540	1.854	8.57×10^{-3}	880	1.451	4.72×10^{-2}
305	2.287	7.69×10^{-2}	550	1.844	9.10×10^{-3}	890	1.435	4.94×10^{-2}
310	2.263	5.66×10^{-2}	560	1.834	9.66×10^{-3}	900	1.420	5.16×10^{-2}
315	2.234	3.93×10^{-2}	570	1.824	1.02×10^{-2}	910	1.404	5.40×10^{-2}
320	2.207	3.29×10^{-2}	580	1.815	1.08×10^{-2}	920	1.387	5.64×10^{-2}
325	2.186	2.86×10^{-2}	590	1.805	1.15×10^{-2}	930	1.370	5.90×10^{-2}
330	2.168	2.51×10^{-2}	600	1.794	1.21×10^{-2}	940	1.353	6.17×10^{-2}
335	2.151	2.14×10^{-2}	610	1.784	1.28×10^{-2}	950	1.336	6.45×10^{-2}
340	2.133	1.80×10^{-2}	620	1.774	1.36×10^{-2}	960	1.318	6.75×10^{-2}
345	2.120	1.55×10^{-2}	630	1.764	1.43×10^{-2}	970	1.299	7.06×10^{-2}
350	2.108	1.34×10^{-2}	640	1.753	1.51×10^{-2}	980	1.281	7.38×10^{-2}
355	2.096	1.25×10^{-2}	650	1.743	1.59×10^{-2}	990	1.261	7.72×10^{-2}
360	2.085	1.16×10^{-2}	660	1.732	1.67×10^{-2}	1000	1.242	8.09×10^{-2}
365	2.074	1.07×10^{-2}	670	1.721	1.76×10^{-2}	1010	1.222	8.47×10^{-2}
370	2.065	9.54×10^{-3}	680	1.710	1.85×10^{-2}	1020	1.201	8.87×10^{-2}
375	2.053	8.25×10^{-3}	690	1.699	1.95×10^{-2}	1030	1.180	9.30×10^{-2}
380	2.045	7.35×10^{-3}	700	1.688	2.05×10^{-2}	1040	1.158	9.75×10^{-2}
385	2.036	6.45×10^{-3}	710	1.676	2.15×10^{-2}	1050	1.136	0.102
390	2.027	6.25×10^{-3}	720	1.665	2.26×10^{-2}	1060	1.114	0.107
395	2.020	5.96×10^{-3}	730	1.653	2.37×10^{-2}	1070	1.090	0.113
400	2.012	5.85×10^{-3}	740	1.641	2.49×10^{-2}	1080	1.066	0.119
410	1.996	6.00×10^{-3}	750	1.629	2.61×10^{-2}	1090	1.041	0.125
420	1.983	3.77×10^{-3}	760	1.617	2.73×10^{-2}	1100	1.016	0.131
430	1.970	4.08×10^{-3}	770	1.604	2.87×10^{-2}	1110	0.990	0.139
440	1.958	4.39×10^{-3}	780	1.591	3.00×10^{-2}	1120	0.963	0.146
450	1.947	4.73×10^{-3}	790	1.579	3.14×10^{-2}	1130	0.935	0.155
460	1.936	5.08×10^{-3}	800	1.565	3.29×10^{-2}	1140	0.906	0.164
470	1.925	5.44×10^{-3}	810	1.552	3.45×10^{-2}	1150	0.876	0.174
480	1.915	5.83×10^{-3}	820	1.538	3.61×10^{-2}	1160	0.846	0.185
490	1.904	6.24×10^{-3}	830	1.524	3.77×10^{-2}	1170	0.814	0.197
500	1.894	6.66×10^{-3}	840	1.510	3.95×10^{-2}	1180	0.782	0.211
510	1.884	7.11×10^{-3}	850	1.496	4.13×10^{-2}	1190	0.748	0.226
520	1.874	7.57×10^{-3}	860	1.481	4.32×10^{-2}	1200	0.713	0.243
530	1.864	8.06×10^{-3}	870	1.466	4.52×10^{-2}			

11.2.7 *InZnO ($N_{Hall} = 2.5 \times 10^{20}$ cm^{-3})*

Data: unpublished results of T. Koida. The optical data have been extracted from an amorphous InZnO layer (non-doped) formed by rf sputtering at room temperature using an Ar/O_2 gas mixture and an InZnO target (In_2O_3:ZnO = 90.6:9.4 wt.%) [6]. The electrical characteristics of this layer are $N_{Hall} = 2.5 \times 10^{20}$ cm^{-3} and $\mu_{Hall} = 50.4$ cm^2/(Vs) (Fig. 19.4b in Vol. 1) (Tables 11.13, 11.14 and Fig. 11.7).

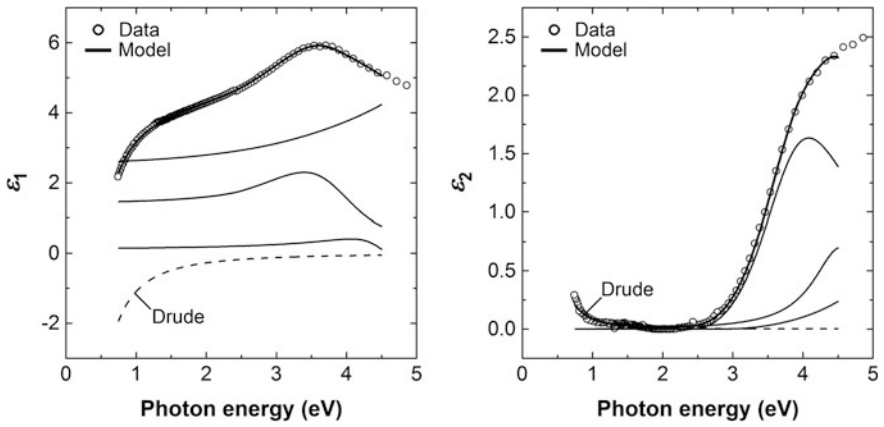


Fig. 11.7 Dielectric function of InZnO ($N_{Hall} = 2.5 \times 10^{20}$ cm^{-3}) at room temperature. The open circles show the reference data and the lines indicate the calculation result obtained from the parameterization assuming the Tauc-Lorentz (solid lines) and Drude (dotted line) models [(11.1) and (11.2)]

Table 11.13 Tauc-Lorentz (TL) peak and Drude parameters of (11.1) and (11.2) for InZnO ($N_{Hall} = 2.5 \times 10^{20}$ cm^{-3})

Model	A/A_D (eV)	C/Γ (eV)	E_0 (eV)	E_g (eV)	$\varepsilon_1(\infty)$
TL peak1	18.352	1.719	3.893	2.410	0.892
TL peak2	0.992	0.979	4.561	0.766	0
TL peak3	56.582	1.250	7.483	2.874	0
Drude	1.099	0.081	–	–	–

Table 11.14 Optical constants of InZnO ($N_{Hall} = 2.5 \times 10^{20}$ cm^{-3}) calculated by the Tauc-Lorentz and Drude models

λ (nm)	n	k	λ (nm)	n	k	λ (nm)	n	k
300	2.389	0.453	540	2.127	6.04×10^{-3}	880	1.947	9.08×10^{-3}
305	2.402	0.437	550	2.119	5.91×10^{-3}	890	1.943	9.35×10^{-3}
310	2.413	0.419	560	2.111	5.80×10^{-3}	900	1.938	9.62×10^{-3}
315	2.424	0.400	570	2.103	5.71×10^{-3}	910	1.934	9.90×10^{-3}
320	2.433	0.379	580	2.096	5.64×10^{-3}	920	1.930	1.02×10^{-2}
325	2.440	0.357	590	2.090	5.59×10^{-3}	930	1.925	1.05×10^{-2}
330	2.445	0.333	600	2.083	5.55×10^{-3}	940	1.921	1.08×10^{-2}
335	2.448	0.310	610	2.077	5.53×10^{-3}	950	1.916	1.11×10^{-2}
340	2.449	0.286	620	2.071	5.53×10^{-3}	960	1.912	1.14×10^{-2}
345	2.447	0.262	630	2.065	5.54×10^{-3}	970	1.907	1.18×10^{-2}
350	2.443	0.240	640	2.059	5.56×10^{-3}	980	1.903	1.21×10^{-2}
355	2.437	0.218	650	2.054	5.59×10^{-3}	990	1.898	1.25×10^{-2}
360	2.430	0.197	660	2.048	5.63×10^{-3}	1000	1.894	1.28×10^{-2}
365	2.421	0.178	670	2.043	5.69×10^{-3}	1010	1.889	1.32×10^{-2}
370	2.412	0.160	680	2.038	5.75×10^{-3}	1020	1.885	1.36×10^{-2}
375	2.401	0.144	690	2.033	5.83×10^{-3}	1030	1.880	1.40×10^{-2}
380	2.391	0.129	700	2.028	5.92×10^{-3}	1040	1.876	1.44×10^{-2}
385	2.379	0.115	710	2.023	6.02×10^{-3}	1050	1.871	1.48×10^{-2}
390	2.368	0.103	720	2.018	6.12×10^{-3}	1060	1.866	1.53×10^{-2}
395	2.357	9.19×10^{-2}	730	2.014	6.24×10^{-3}	1070	1.862	1.57×10^{-2}
400	2.345	8.17×10^{-2}	740	2.009	6.37×10^{-3}	1080	1.857	1.62×10^{-2}
410	2.323	6.44×10^{-2}	750	2.004	6.50×10^{-3}	1090	1.852	1.66×10^{-2}
420	2.301	5.04×10^{-2}	760	2.000	6.65×10^{-3}	1100	1.848	1.71×10^{-2}
430	2.280	3.94×10^{-2}	770	1.995	6.80×10^{-3}	1110	1.843	1.76×10^{-2}
440	2.260	3.06×10^{-2}	780	1.991	6.96×10^{-3}	1120	1.838	1.81×10^{-2}
450	2.242	2.36×10^{-2}	790	1.986	7.14×10^{-3}	1130	1.833	1.86×10^{-2}
460	2.225	1.82×10^{-2}	800	1.982	7.32×10^{-3}	1140	1.828	1.91×10^{-2}
470	2.209	1.41×10^{-2}	810	1.978	7.51×10^{-3}	1150	1.823	1.97×10^{-2}
480	2.194	1.10×10^{-2}	820	1.973	7.70×10^{-3}	1160	1.818	2.02×10^{-2}
490	2.181	8.80×10^{-3}	830	1.969	7.91×10^{-3}	1170	1.813	2.08×10^{-2}
500	2.168	7.39×10^{-3}	840	1.964	8.13×10^{-3}	1180	1.808	2.13×10^{-2}
510	2.156	6.64×10^{-3}	850	1.960	8.35×10^{-3}	1190	1.803	2.19×10^{-2}
520	2.146	6.37×10^{-3}	860	1.956	8.59×10^{-3}	1200	1.798	2.25×10^{-2}
530	2.136	6.19×10^{-3}	870	1.951	8.83×10^{-3}			

11.2.8 MoO_x

Data: unpublished results of S. Fujimoto. The optical data have been extracted from an amorphous MoO_x layer ($x = 2$–3) formed by rf sputtering at room temperature using an Ar/O_2 gas mixture and a Mo target. The results obtained by varying the Ar/O_2 flow ratio are shown (Tables 11.15, 11.16, 11.17, 11.18 and Fig. 11.8).

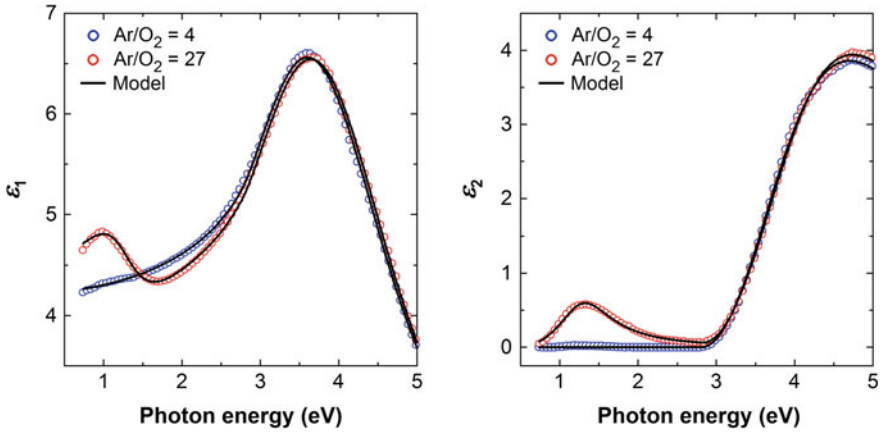


Fig. 11.8 Dielectric function of MoO_x layers at room temperature. The results for MoO_x layers prepared using different Ar/O_2 flow ratios are shown. The open circles show the experimental data and the solid lines indicate the calculation result obtained from the parameterization assuming the Tauc-Lorentz model [(8.1) and (8.2)]

Table 11.15 Tauc-Lorentz parameters of (8.1) and (8.2) for MoO_x ($Ar/O_2 = 4$)

Peak	A (eV)	C (eV)	E_0 (eV)	E_g (eV)	$\varepsilon_1(\infty)$
$j = 1$	100.142	3.008	3.994	2.808	0.791
$j = 2$	43.743	0.239	11.570	4.051	0

Table 11.16 Tauc-Lorentz parameters of (8.1) and (8.2) for MoO_x ($Ar/O_2 = 27$)

Peak	A (eV)	C (eV)	E_0 (eV)	E_g (eV)	$\varepsilon_1(\infty)$
$j = 1$	1.250	0.870	1.320	0.469	0.436
$j = 2$	98.965	3.037	4.065	2.817	0
$j = 3$	76.640	0.254	12.474	5.445	0

Table 11.17 Optical constants of MoO_x ($Ar/O_2 = 4$). The optical data obtained by S. Fujimoto are shown

λ (nm)	n	k	λ (nm)	n	k	λ (nm)	n	k
300	2.487	0.663	540	2.187	0	880	2.0956	0.005
305	2.519	0.63	550	2.180	0	890	2.0954	0.004
310	2.543	0.593	560	2.175	0	900	2.0943	0.005
315	2.561	0.554	570	2.169	0	910	2.0944	0.005
320	2.573	0.511	580	2.163	0	920	2.0932	0.005
325	2.586	0.467	590	2.159	0	930	2.0912	0.005
330	2.590	0.427	600	2.154	0	940	2.0901	0.005
335	2.593	0.386	610	2.150	0	950	2.0918	0.005
340	2.592	0.348	620	2.146	0	960	2.0899	0.005
345	2.589	0.309	630	2.142	0	970	2.0901	0.005
350	2.582	0.278	640	2.139	0	980	2.0890	0.005
355	2.573	0.244	650	2.135	0	990	2.0893	0.005
360	2.562	0.215	660	2.134	0	1000	2.0899	0.005
365	2.549	0.185	670	2.129	0	1010	2.0877	0.005
370	2.532	0.159	680	2.127	0	1020	2.0872	0.005
375	2.515	0.133	690	2.125	0	1030	2.0852	0.006
380	2.497	0.112	700	2.122	0.001	1040	2.0868	0.005
385	2.481	0.095	710	2.120	0.001	1050	2.0845	0.005
390	2.464	0.077	720	2.118	0.001	1060	2.0855	0.005
395	2.446	0.062	730	2.116	0.001	1070	2.0847	0.006
400	2.431	0.05	740	2.114	0.001	1080	2.0840	0.005
410	2.398	0.028	750	2.112	0.002	1090	2.0839	0.004
420	2.370	0.013	760	2.110	0.002	1100	2.0846	0.004
430	2.344	0.005	770	2.109	0.002	1110	2.0838	0.004
440	2.319	0	780	2.108	0.002	1120	2.0838	0.004
450	2.299	0	790	2.105	0.003	1130	2.0830	0.004
460	2.278	0	800	2.104	0.003	1140	2.0821	0.004
470	2.260	0	810	2.103	0.004	1150	2.0813	0.004
480	2.248	0	820	2.102	0.004	1160	2.0819	0.003
490	2.236	0	830	2.100	0.004	1170	2.0816	0.003
500	2.222	0	840	2.099	0.004	1180	2.0823	0.003
510	2.213	0	850	2.098	0.005	1190	2.0805	0.002
520	2.203	0	860	2.098	0.004	1200	2.0794	0.002
530	2.195	0	870	2.097	0.004			

Table 11.18 Optical constants of MoO_x ($Ar/O_2 = 27$). The optical data obtained by S. Fujimoto are shown

λ (nm)	n	k	λ (nm)	n	k	λ (nm)	n	k
300	2.505	0.655	540	2.155	0.027	880	2.117	0.133
305	2.530	0.615	550	2.146	0.028	890	2.121	0.134
310	2.554	0.577	560	2.139	0.031	900	2.124	0.135
315	2.564	0.538	570	2.133	0.034	910	2.127	0.135
320	2.581	0.494	580	2.127	0.036	920	2.131	0.136
325	2.586	0.454	590	2.121	0.040	930	2.134	0.136
330	2.589	0.414	600	2.116	0.043	940	2.136	0.136
335	2.589	0.375	610	2.111	0.046	950	2.143	0.134
340	2.584	0.338	620	2.106	0.051	960	2.146	0.134
345	2.576	0.301	630	2.103	0.053	970	2.147	0.133
350	2.571	0.271	640	2.100	0.058	980	2.148	0.133
355	2.560	0.238	650	2.096	0.061	990	2.155	0.132
360	2.551	0.213	660	2.094	0.067	1000	2.160	0.131
365	2.536	0.184	670	2.091	0.069	1010	2.159	0.130
370	2.519	0.159	680	2.089	0.073	1020	2.160	0.129
375	2.500	0.135	690	2.088	0.077	1030	2.164	0.127
380	2.483	0.115	700	2.086	0.081	1040	2.168	0.126
385	2.468	0.099	710	2.086	0.085	1050	2.170	0.124
390	2.450	0.083	720	2.085	0.089	1060	2.173	0.123
395	2.432	0.069	730	2.086	0.093	1070	2.176	0.121
400	2.415	0.056	740	2.086	0.097	1080	2.178	0.118
410	2.384	0.037	750	2.086	0.101	1090	2.180	0.116
420	2.353	0.024	760	2.088	0.104	1100	2.183	0.114
430	2.326	0.019	770	2.088	0.108	1110	2.185	0.111
440	2.300	0.016	780	2.090	0.111	1120	2.188	0.108
450	2.277	0.018	790	2.092	0.115	1130	2.188	0.106
460	2.256	0.015	800	2.094	0.118	1140	2.190	0.104
470	2.238	0.016	810	2.096	0.121	1150	2.191	0.101
480	2.220	0.018	820	2.099	0.123	1160	2.192	0.098
490	2.210	0.019	830	2.102	0.126	1170	2.195	0.095
500	2.193	0.021	840	2.105	0.128	1180	2.196	0.092
510	2.183	0.022	850	2.107	0.129	1190	2.196	0.089
520	2.173	0.023	860	2.111	0.130	1200	2.197	0.086
530	2.164	0.025	870	2.115	0.132			

11.2.9 NiO

Data from H. L. Lu, G. Scarel, M. Alia, M. Fanciulli, S.-J. Ding and D. W. Zhang [7]. The optical data have been extracted from an as-deposited NiO layer prepared by atomic layer deposition using $Ni(C_5H_5)_2$ and O_3 sources at 300 °C (Tables 11.19, 11.20 and Fig. 11.9).

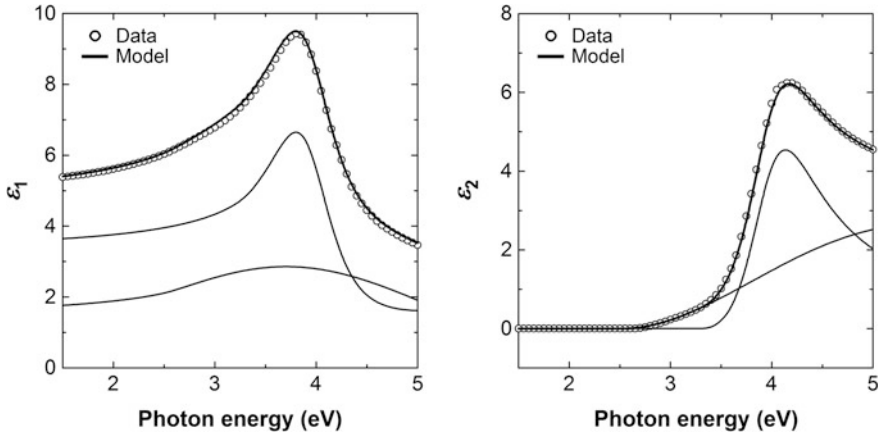


Fig. 11.9 Dielectric function of NiO at room temperature. The open circles show the reference data and the solid lines indicate the calculation result obtained from the parameterization assuming the Tauc-Lorentz model [(8.1) and (8.2)]

Table 11.19 Tauc-Lorentz parameters of (8.1) and (8.2) for NiO. The model parameters reported by Lu et al. are summarized

Peak	A (eV)	C (eV)	E_0 (eV)	E_g (eV)	$\varepsilon_1(\infty)$
$j = 1$	111.89	0.82	3.96	3.30	2.50
$j = 2$	59.10	5.83	5.09	2.53	0

Table 11.20 Optical constants of NiO calculated by the Tauc-Lorentz model

λ (nm)	n	k	λ (nm)	n	k	λ (nm)	n	k
300	2.852	1.086	540	2.420	0	880	2.318	0
305	2.954	1.014	550	2.413	0	890	2.317	0
310	3.040	0.916	560	2.406	0	900	2.316	0
315	3.101	0.800	570	2.400	0	910	2.315	0
320	3.130	0.677	580	2.394	0	920	2.314	0
325	3.130	0.559	590	2.389	0	930	2.313	0
330	3.109	0.455	600	2.384	0	940	2.312	0
335	3.072	0.367	610	2.380	0	950	2.311	0
340	3.029	0.297	620	2.375	0	960	2.310	0
345	2.983	0.242	630	2.371	0	970	2.309	0
350	2.937	0.199	640	2.368	0	980	2.309	0
355	2.894	0.166	650	2.364	0	990	2.308	0
360	2.855	0.141	660	2.361	0	1000	2.307	0
365	2.819	0.122	670	2.358	0	1010	2.306	0
370	2.786	0.108	680	2.355	0	1020	2.306	0
375	2.758	9.73×10^{-2}	690	2.352	0	1030	2.305	0
380	2.734	8.87×10^{-2}	700	2.349	0	1040	2.304	0
385	2.714	8.05×10^{-2}	710	2.347	0	1050	2.304	0
390	2.695	7.27×10^{-2}	720	2.344	0	1060	2.303	0
395	2.678	6.53×10^{-2}	730	2.342	0	1070	2.302	0
400	2.662	5.82×10^{-2}	740	2.340	0	1080	2.302	0
410	2.632	4.54×10^{-2}	750	2.338	0	1090	2.301	0
420	2.606	3.43×10^{-2}	760	2.336	0	1100	2.301	0
430	2.581	2.48×10^{-2}	770	2.334	0	1110	2.300	0
440	2.559	1.70×10^{-2}	780	2.332	0	1120	2.300	0
450	2.538	1.07×10^{-2}	790	2.330	0	1130	2.299	0
460	2.519	5.94×10^{-3}	800	2.329	0	1140	2.299	0
470	2.501	2.60×10^{-3}	810	2.327	0	1150	2.298	0
480	2.484	0	820	2.326	0	1160	2.298	0
490	2.470	0	830	2.324	0	1170	2.297	0
500	2.457	0	840	2.323	0	1180	2.297	0
510	2.447	0	850	2.322	0	1190	2.296	0
520	2.437	0	860	2.320	0	1200	2.296	0
530	2.428	0	870	2.319	0			0

11.2.10 SnO_2 (Non-doped)

Data from H. S. So, J.-W. Park, D. H. Jung, K. H. Ko and H. Lee [8]. The optical data have been extracted from a polycrystalline SnO layer, which is prepared by sputtering using an Ar gas and a non-doped SnO_2 target, followed by thermal annealing at 800 °C. The electrical characteristics of this layer are $N_{Hall} = 2.6 \times 10^{19}$ cm^{-3} and $\mu_{Hall} = 1.0$ cm^2/(Vs) (Tables 11.21, 11.22 and Fig. 11.10).

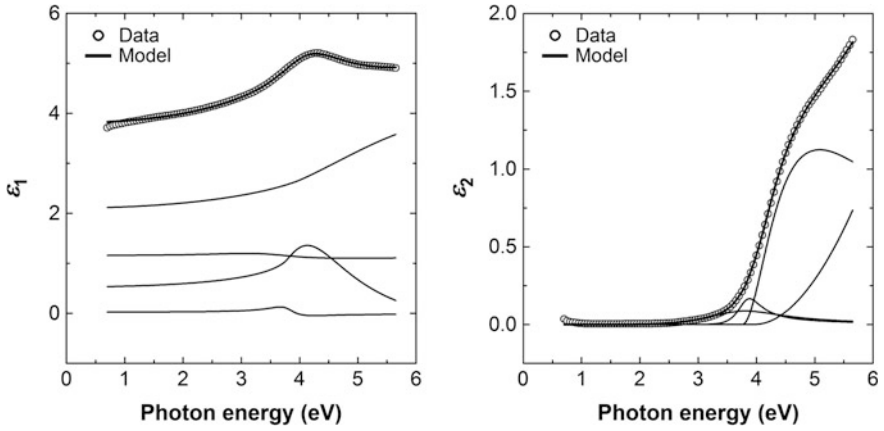


Fig. 11.10 Dielectric function of SnO_2 (non-doped) at room temperature. The open circles show the reference data and the solid lines indicate the calculation result obtained from the parameterization assuming the Tauc-Lorentz model [(8.1) and (8.2)]

Table 11.21 Tauc-Lorentz parameters of (8.1) and (8.2) for SnO_2 (non-doped)

Peak	A (eV)	C (eV)	E_0 (eV)	E_g (eV)	$\varepsilon_1(\infty)$
$j = 1$	0.492	1.660	3.744	1.729	1.128
$j = 2$	110.633	1.569	3.758	3.757	0
$j = 3$	1.947	0.505	3.825	3.051	0
$j = 4$	94.303	7.390	9.121	3.959	0

Table 11.22 Optical constants of SnO_2 (non-doped) calculated by the Tauc-Lorentz model

λ (nm)	n	k	λ (nm)	n	k	λ (nm)	n	k
300	2.277	0.138	540	2.018	1.17×10^{-3}	880	1.974	0
305	2.268	0.117	550	2.015	0	890	1.973	0
310	2.257	9.93×10^{-2}	560	2.012	0	900	1.973	0
315	2.246	8.38×10^{-2}	570	2.010	0	910	1.972	0
320	2.234	7.01×10^{-2}	580	2.008	0	920	1.972	0
325	2.220	5.79×10^{-2}	590	2.005	0	930	1.971	0
330	2.206	4.88×10^{-2}	600	2.003	0	940	1.971	0
335	2.195	4.18×10^{-2}	610	2.001	0	950	1.971	0
340	2.183	3.52×10^{-2}	620	2.000	0	960	1.970	0
345	2.172	2.99×10^{-2}	630	1.998	0	970	1.970	0
350	2.161	2.57×10^{-2}	640	1.996	0	980	1.969	0
355	2.152	2.25×10^{-2}	650	1.995	0	990	1.969	0
360	2.143	2.00×10^{-2}	660	1.993	0	1000	1.969	0
365	2.134	1.79×10^{-2}	670	1.992	0	1010	1.968	0
370	2.127	1.62×10^{-2}	680	1.991	0	1020	1.968	0
375	2.120	1.47×10^{-2}	690	1.989	0	1030	1.968	0
380	2.113	1.35×10^{-2}	700	1.988	0	1040	1.967	0
385	2.107	1.23×10^{-2}	710	1.987	0	1050	1.967	0
390	2.102	1.14×10^{-2}	720	1.986	0	1060	1.967	0
395	2.096	1.05×10^{-2}	730	1.985	0	1070	1.966	0
400	2.091	9.67×10^{-3}	740	1.984	0	1080	1.966	0
410	2.082	8.32×10^{-3}	750	1.983	0	1090	1.966	0
420	2.074	7.16×10^{-3}	760	1.982	0	1100	1.966	0
430	2.067	6.17×10^{-3}	770	1.981	0	1110	1.965	0
440	2.060	5.31×10^{-3}	780	1.980	0	1120	1.965	0
450	2.054	4.57×10^{-3}	790	1.980	0	1130	1.965	0
460	2.049	3.94×10^{-3}	800	1.979	0	1140	1.965	0
470	2.044	3.40×10^{-3}	810	1.978	0	1150	1.964	0
480	2.039	2.93×10^{-3}	820	1.977	0	1160	1.964	0
490	2.035	2.52×10^{-3}	830	1.977	0	1170	1.964	0
500	2.031	2.17×10^{-3}	840	1.976	0	1180	1.964	0
510	2.027	1.86×10^{-3}	850	1.976	0	1190	1.963	0
520	2.024	1.60×10^{-3}	860	1.975	0	1200	1.963	0
530	2.021	1.37×10^{-3}	870	1.974	0			

11.2.11 SnO_2:F (TEC-15)

Data from J. Chen, J. Li, C. Thornberry, M. N. Sestak, R. W. Collins, J. D. Walker, S. Marsillac, A. R. Aquino and A. Rockett [9]. The optical data of SnO_2:F (TEC-15, Pilkington) have been extracted from a SnO_2:F/SiO_2/SnO_2/glass structure (see also Sect. 18.5 in Vol. 1). The electrical characteristics of the SnO_2:F layer (300 nm) have been reported to be $N_{Hall} = 5.6 \times 10^{20}$ cm^{-3} and $\mu_{Hall} = 21$ cm^2/(Vs) [10]. The Drude analysis of the SnO_2:F dielectric function shown here leads to $N_{opt} = 3.5 \times 10^{20}$ cm^{-3} and $\mu_{opt} = 55.6$ cm^2/(Vs). The structure and electrical properties of TEC-8 are quite similar but a thicker SnO_2:F layer (520 nm) is incorporated to lower sheet resistance (see Table 18.2 in Vol. 1) (Tables 11.23, 11.24 and Fig. 11.11).

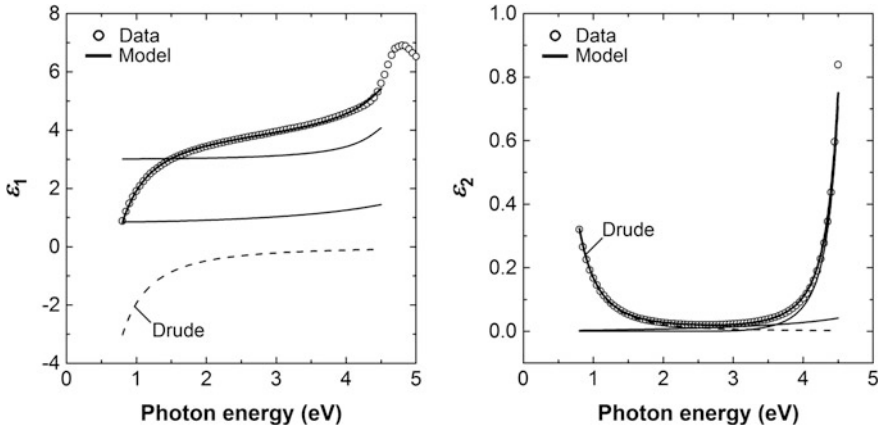


Fig. 11.11 Room-temperature dielectric function of a SnO_2:F layer incorporated into TEC-15. The open circles show the reference data and the lines indicate the calculation result obtained from the parameterization assuming the Tauc-Lorentz (solid lines) and Drude (dotted line) models [(11.1) and (11.2)]

Table 11.23 Tauc-Lorentz (TL) peak and Drude parameters of (11.1) and (11.2) for SnO_2:F (TEC-15)

Model	A/A_D (eV)	C/Γ (eV)	E_0 (eV)	E_g (eV)	$\varepsilon_1(\infty)$
TL peak1	4.853	0.380	4.763	2.708	2.820
TL peak2	5.728	0.173	6.897	1×10^{-4}	0
Drude	1.956	0.085	–	–	–

Table 11.24 Optical constants of SnO_2:F (TEC-15) calculated by the Tauc-Lorentz and Drude models

λ (nm)	n	k	λ (nm)	n	k	λ (nm)	n	k
300	2.173	3.68×10^{-2}	540	1.902	5.91×10^{-3}	880	1.703	1.87×10^{-2}
305	2.153	3.02×10^{-2}	550	1.896	6.07×10^{-3}	890	1.696	1.94×10^{-2}
310	2.136	2.52×10^{-2}	560	1.891	6.24×10^{-3}	900	1.689	2.01×10^{-2}
315	2.121	2.15×10^{-2}	570	1.886	6.43×10^{-3}	910	1.682	2.08×10^{-2}
320	2.107	1.86×10^{-2}	580	1.880	6.62×10^{-3}	920	1.675	2.15×10^{-2}
325	2.095	1.63×10^{-2}	590	1.875	6.83×10^{-3}	930	1.668	2.23×10^{-2}
330	2.084	1.44×10^{-2}	600	1.870	7.05×10^{-3}	940	1.660	2.30×10^{-2}
335	2.075	1.29×10^{-2}	610	1.864	7.28×10^{-3}	950	1.653	2.38×10^{-2}
340	2.066	1.17×10^{-2}	620	1.859	7.52×10^{-3}	960	1.645	2.46×10^{-2}
345	2.057	1.06×10^{-2}	630	1.854	7.77×10^{-3}	970	1.638	2.55×10^{-2}
350	2.049	9.75×10^{-3}	640	1.848	8.04×10^{-3}	980	1.630	2.63×10^{-2}
355	2.042	9.01×10^{-3}	650	1.843	8.32×10^{-3}	990	1.622	2.72×10^{-2}
360	2.035	8.39×10^{-3}	660	1.837	8.61×10^{-3}	1000	1.614	2.81×10^{-2}
365	2.029	7.85×10^{-3}	670	1.832	8.92×10^{-3}	1010	1.606	2.91×10^{-2}
370	2.023	7.39×10^{-3}	680	1.826	9.24×10^{-3}	1020	1.598	3.01×10^{-2}
375	2.017	7.00×10^{-3}	690	1.821	9.57×10^{-3}	1030	1.589	3.11×10^{-2}
380	2.012	6.66×10^{-3}	700	1.815	9.91×10^{-3}	1040	1.581	3.21×10^{-2}
385	2.007	6.37×10^{-3}	710	1.810	1.03×10^{-2}	1050	1.572	3.32×10^{-2}
390	2.002	6.12×10^{-3}	720	1.804	1.06×10^{-2}	1060	1.564	3.42×10^{-2}
395	1.997	5.90×10^{-3}	730	1.798	1.10×10^{-2}	1070	1.555	3.54×10^{-2}
400	1.993	5.72×10^{-3}	740	1.792	1.14×10^{-2}	1080	1.546	3.65×10^{-2}
410	1.984	5.44×10^{-3}	750	1.786	1.18×10^{-2}	1090	1.537	3.77×10^{-2}
420	1.976	5.24×10^{-3}	760	1.780	1.23×10^{-2}	1100	1.528	3.90×10^{-2}
430	1.968	5.12×10^{-3}	770	1.774	1.27×10^{-2}	1110	1.518	4.02×10^{-2}
440	1.961	5.06×10^{-3}	780	1.768	1.32×10^{-2}	1120	1.509	4.15×10^{-2}
450	1.954	5.05×10^{-3}	790	1.762	1.37×10^{-2}	1130	1.499	4.29×10^{-2}
460	1.948	5.09×10^{-3}	800	1.756	1.42×10^{-2}	1140	1.490	4.43×10^{-2}
470	1.942	5.14×10^{-3}	810	1.750	1.47×10^{-2}	1150	1.480	4.57×10^{-2}
480	1.936	5.22×10^{-3}	820	1.743	1.52×10^{-2}	1160	1.470	4.72×10^{-2}
490	1.930	5.30×10^{-3}	830	1.737	1.57×10^{-2}	1170	1.460	4.87×10^{-2}
500	1.924	5.40×10^{-3}	840	1.730	1.63×10^{-2}	1180	1.450	5.03×10^{-2}
510	1.918	5.51×10^{-3}	850	1.724	1.69×10^{-2}	1190	1.439	5.19×10^{-2}
520	1.913	5.63×10^{-3}	860	1.717	1.75×10^{-2}	1200	1.429	5.35×10^{-2}
530	1.907	5.77×10^{-3}	870	1.710	1.81×10^{-2}			

11.2.12 TiO_2 (Polycrystal)

Data from M. Shirayama, H. Kadowaki, T. Miyadera, T. Sugita, M. Tamakoshi, S. Fujimoto, M. Chikamatsu and H. Fujiwara [11]. The optical data have been extracted from a polycrystalline TiO_2 (anataze) layer formed by a spray pyrolysis method at 450 °C. This TiO_2 polycrystal shows isotropic optical properties (Tables 11.25, 11.26 and Fig. 11.12).

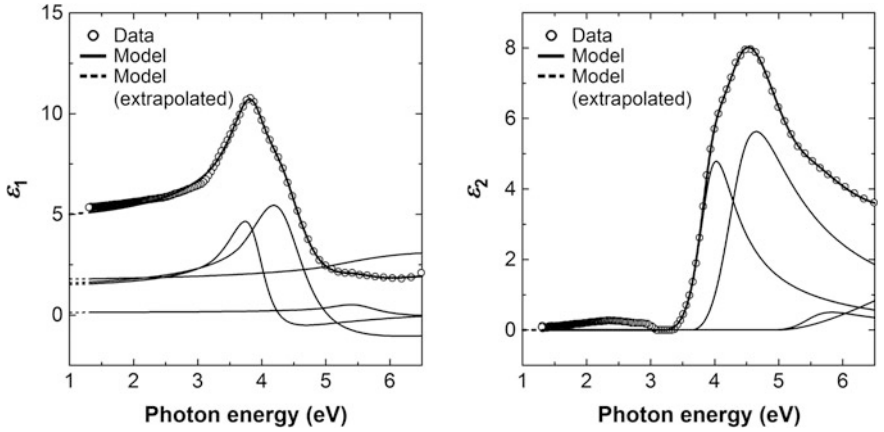


Fig. 11.12 Dielectric function of polycrystalline TiO_2 (anatase) at room temperature. The open circles show the reference data and the solid lines indicate the calculation result obtained from the parameterization assuming the Tauc-Lorentz model [(8.1) and (8.2)]. The dotted lines show the extrapolated result obtained from the Tauc-Lorentz model

Table 11.25 Tauc-Lorentz parameters of (8.1) and (8.2) for polycrystalline TiO_2 (anatase). The model parameters reported by Shirayama et al. are summarized

Peak	A (eV)	C (eV)	E_0 (eV)	E_g (eV)	$\varepsilon_1(\infty)$
$j = 1$	94.341	0.693	3.904	3.215	0.537
$j = 2$	177.870	1.127	4.359	3.636	0
$j = 3$	28.662	1.028	5.514	4.894	0
$j = 4$	153.220	11.861	8.603	4.950	0

Table 11.26 Optical constants of polycrystalline TiO_2 (anatase) calculated by the Tauc-Lorentz model

λ (nm)	n	k	λ (nm)	n	k	λ (nm)	n	k
300	3.119	1.050	540	2.381	0	880	2.265	0
305	3.174	0.976	550	2.373	0	890	2.264	0
310	3.233	0.888	560	2.366	0	900	2.263	0
315	3.286	0.779	570	2.359	0	910	2.262	0
320	3.316	0.650	580	2.353	0	920	2.260	0
325	3.315	0.516	590	2.347	0	930	2.259	0
330	3.282	0.390	600	2.342	0	940	2.258	0
335	3.227	0.285	610	2.337	0	950	2.257	0
340	3.161	0.203	620	2.332	0	960	2.256	0
345	3.093	0.142	630	2.327	0	970	2.255	0
350	3.028	9.61×10^{-2}	640	2.323	0	980	2.254	0
355	2.966	6.27×10^{-2}	650	2.319	0	990	2.253	0
360	2.910	3.90×10^{-2}	660	2.315	0	1000	2.252	0
365	2.859	2.26×10^{-2}	670	2.312	0	1010	2.251	0
370	2.813	1.16×10^{-2}	680	2.308	0	1020	2.250	0
375	2.772	4.86×10^{-3}	690	2.305	0	1030	2.250	0
380	2.736	1.24×10^{-3}	700	2.302	0	1040	2.249	0
385	2.704	0	710	2.299	0	1050	2.248	0
390	2.677	0	720	2.296	0	1060	2.247	0
395	2.653	0	730	2.294	0	1070	2.247	0
400	2.631	0	740	2.291	0	1080	2.246	0
410	2.595	0	750	2.289	0	1090	2.245	0
420	2.563	0	760	2.286	0	1100	2.245	0
430	2.537	0	770	2.284	0	1110	2.244	0
440	2.514	0	780	2.282	0	1120	2.243	0
450	2.493	0	790	2.280	0	1130	2.243	0
460	2.475	0	800	2.278	0	1140	2.242	0
470	2.459	0	810	2.276	0	1150	2.241	0
480	2.445	0	820	2.275	0	1160	2.241	0
490	2.432	0	830	2.273	0	1170	2.240	0
500	2.420	0	840	2.271	0	1180	2.240	0
510	2.409	0	850	2.270	0	1190	2.239	0
520	2.399	0	860	2.268	0	1200	2.239	0
530	2.390	0	870	2.267	0			

11.2.13 TiO_2 (Anatase Single Crystal)

Data from G. E. Jellison, Jr., L. A. Boatner and J. D. Budai [12]. A TiO_2 anataze single crystal shows uniaxial optical anisotropy and the optical data for the ordinary and extraordinary rays are summarized (Tables 11.27, 11.28, 11.29, 11.30 and Fig. 11.13).

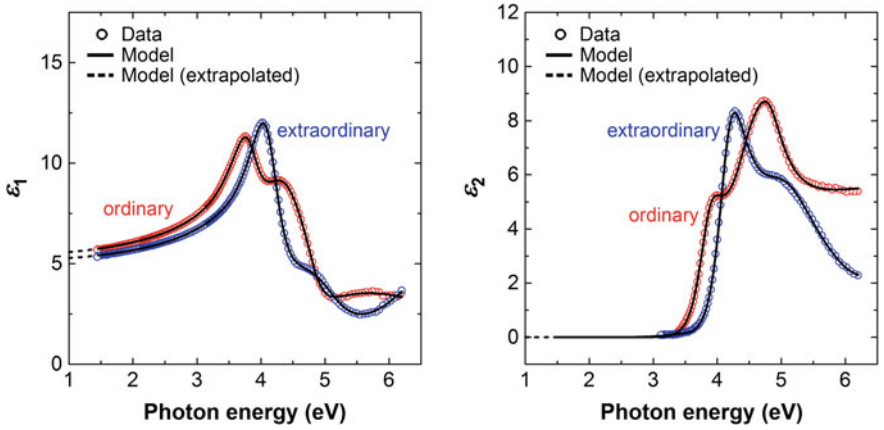


Fig. 11.13 Dielectric function of a TiO_2 anatase single crystal at room temperature. The open circles show the reference data and the solid lines indicate the calculation result obtained from the parameterization assuming the Tauc-Lorentz model [(8.1) and (8.2)]. The dotted lines show the extrapolated result obtained from the Tauc-Lorentz model

Table 11.27 Tauc-Lorentz parameters of (8.1) and (8.2) for the ordinary ray in TiO_2 (anatase single crystal)

Peak	A (eV)	C (eV)	E_0 (eV)	E_g (eV)	$\varepsilon_1(\infty)$
$j = 1$	67.736	0.522	3.852	3.197	0.309
$j = 2$	31.185	0.885	4.536	2.962	0
$j = 3$	5.331	0.561	4.804	2.593	0
$j = 4$	330.100	9.403	4.998	3.685	0

Table 11.28 Tauc-Lorentz parameters of (8.1) and (8.2) for the extraordinary ray in TiO_2 (anatase single crystal)

Peak	A (eV)	C (eV)	E_0 (eV)	E_g (eV)	$\varepsilon_1(\infty)$
$j = 1$	172.533	0.573	4.157	3.545	0.018
$j = 2$	17.915	1.325	5.079	2.542	0
$j = 3$	424.332	5.651	7.775	5.918	0

Table 11.29 Optical constants for the ordinary ray in TiO_2 (anatase single crystal), calculated by the Tauc-Lorentz model

λ (nm)	n	k	λ (nm)	n	k	λ (nm)	n	k
300	3.130	0.844	540	2.514	0	880	2.392	0
305	3.140	0.833	550	2.505	0	890	2.391	0
310	3.182	0.823	560	2.498	0	900	2.389	0
315	3.254	0.789	570	2.491	0	910	2.388	0
320	3.333	0.710	580	2.484	0	920	2.387	0
325	3.385	0.590	590	2.478	0	930	2.385	0
330	3.391	0.454	600	2.472	0	940	2.384	0
335	3.356	0.332	610	2.467	0	950	2.383	0
340	3.298	0.236	620	2.462	0	960	2.382	0
345	3.232	0.165	630	2.457	0	970	2.381	0
350	3.167	0.114	640	2.453	0	980	2.380	0
355	3.105	7.80×10^{-2}	650	2.449	0	990	2.379	0
360	3.049	5.28×10^{-2}	660	2.445	0	1000	2.378	0
365	2.999	3.52×10^{-2}	670	2.441	0	1010	2.377	0
370	2.955	2.30×10^{-2}	680	2.437	0	1020	2.376	0
375	2.915	1.47×10^{-2}	690	2.434	0	1030	2.375	0
380	2.879	9.34×10^{-3}	700	2.431	0	1040	2.374	0
385	2.848	6.11×10^{-3}	710	2.428	0	1050	2.374	0
390	2.820	4.41×10^{-3}	720	2.425	0	1060	2.373	0
395	2.795	3.19×10^{-3}	730	2.422	0	1070	2.372	0
400	2.773	2.24×10^{-3}	740	2.419	0	1080	2.371	0
410	2.735	1.03×10^{-3}	750	2.417	0	1090	2.371	0
420	2.703	0	760	2.414	0	1100	2.370	0
430	2.675	0	770	2.412	0	1110	2.369	0
440	2.651	0	780	2.410	0	1120	2.369	0
450	2.630	0	790	2.408	0	1130	2.368	0
460	2.611	0	800	2.406	0	1140	2.367	0
470	2.594	0	810	2.404	0	1150	2.367	0
480	2.579	0	820	2.402	0	1160	2.366	0
490	2.566	0	830	2.400	0	1170	2.365	0
500	2.554	0	840	2.398	0	1180	2.365	0
510	2.542	0	850	2.397	0	1190	2.364	0
520	2.532	0	860	2.395	0	1200	2.364	0
530	2.522	0	870	2.394	0			

Table 11.30 Optical constants for the extraordinary ray in TiO_2 (anatase single crystal), calculated by the Tauc-Lorentz model

λ (nm)	n	k	λ (nm)	n	k	λ (nm)	n	k
300	3.478	0.975	540	2.425	0	880	2.323	0
305	3.525	0.731	550	2.418	0	890	2.322	0
310	3.490	0.514	560	2.412	0	900	2.321	0
315	3.408	0.348	570	2.406	0	910	2.320	0
320	3.310	0.231	580	2.400	0	920	2.319	0
325	3.213	0.152	590	2.395	0	930	2.318	0
330	3.124	0.101	600	2.391	0	940	2.317	0
335	3.046	6.77×10^{-2}	610	2.386	0	950	2.316	0
340	2.979	4.74×10^{-2}	620	2.382	0	960	2.315	0
345	2.921	3.57×10^{-2}	630	2.378	0	970	2.314	0
350	2.873	3.00×10^{-2}	640	2.374	0	980	2.313	0
355	2.833	2.67×10^{-2}	650	2.371	0	990	2.312	0
360	2.800	2.37×10^{-2}	660	2.367	0	1000	2.311	0
365	2.770	2.09×10^{-2}	670	2.364	0	1010	2.310	0
370	2.744	1.85×10^{-2}	680	2.361	0	1020	2.310	0
375	2.720	1.63×10^{-2}	690	2.358	0	1030	2.309	0
380	2.699	1.43×10^{-2}	700	2.355	0	1040	2.308	0
385	2.679	1.26×10^{-2}	710	2.353	0	1050	2.308	0
390	2.662	1.10×10^{-2}	720	2.350	0	1060	2.307	0
395	2.645	9.53×10^{-3}	730	2.348	0	1070	2.306	0
400	2.630	8.24×10^{-3}	740	2.346	0	1080	2.306	0
410	2.602	6.07×10^{-3}	750	2.344	0	1090	2.305	0
420	2.578	4.34×10^{-3}	760	2.342	0	1100	2.304	0
430	2.557	2.98×10^{-3}	770	2.340	0	1110	2.304	0
440	2.538	1.93×10^{-3}	780	2.338	0	1120	2.303	0
450	2.521	1.14×10^{-3}	790	2.336	0	1130	2.303	0
460	2.506	0	800	2.334	0	1140	2.302	0
470	2.492	0	810	2.333	0	1150	2.302	0
480	2.479	0	820	2.331	0	1160	2.301	0
490	2.468	0	830	2.330	0	1170	2.301	0
500	2.458	0	840	2.328	0	1180	2.300	0
510	2.448	0	850	2.327	0	1190	2.300	0
520	2.440	0	860	2.326	0	1200	2.299	0
530	2.432	0	870	2.324	0			

11.2.14 TiO_2 (Rutile Single Crystal)

Data from G. E. Jellison, Jr., F. A. Modine, and L. A. Boatner [13]. A TiO_2 rutile single crystal shows uniaxial optical anisotropy and the optical data for the ordinary and extraordinary rays are summarized (Tables 11.31, 11.32, 11.33, 11.34 and Fig. 11.14).

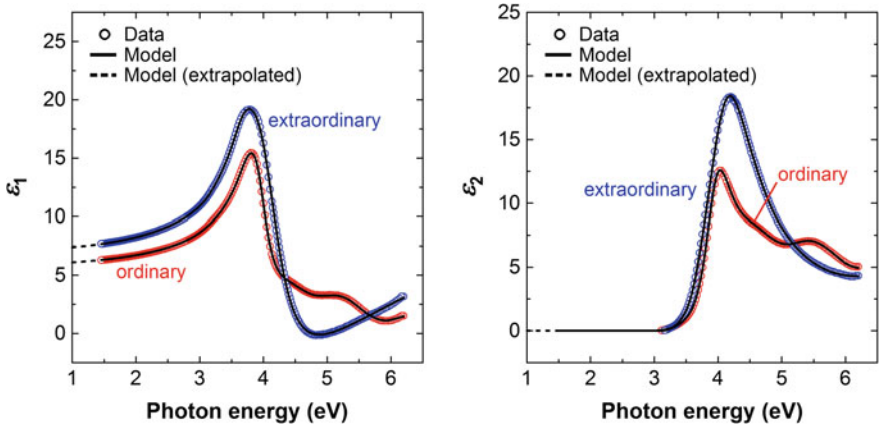


Fig. 11.14 Dielectric function of a TiO_2 rutile single crystal at room temperature. The open circles show the reference data and the solid lines indicate the calculation result obtained from the parameterization assuming the Tauc-Lorentz model [(8.1) and (8.2)]. The dotted lines show the extrapolated result obtained from the Tauc-Lorentz model

Table 11.31 Tauc-Lorentz parameters of (8.1) and (8.2) for the ordinary ray in TiO_2 (rutile single crystal)

Peak	A (eV)	C (eV)	E_0 (eV)	E_g (eV)	$\varepsilon_1(\infty)$
$j = 1$	44.205	0.575	3.888	2.898	1.444
$j = 2$	237.420	0.462	3.952	3.542	0
$j = 3$	32.207	1.152	4.562	2.928	0
$j = 4$	94.318	1.225	5.381	4.281	0
$j = 5$	407.216	1.635	6.036	5.942	0

Table 11.32 Tauc-Lorentz parameters of (8.1) and (8.2) for the extraordinary ray in TiO_2 (rutile single crystal)

Peak	A (eV)	C (eV)	E_0 (eV)	E_g (eV)	$\varepsilon_1(\infty)$
$j = 1$	98.921	0.466	3.698	3.469	0.734
$j = 2$	255.549	0.922	4.065	3.090	0
$j = 3$	159.686	3.028	7.900	4.930	0

Table 11.33 Optical constants for the ordinary ray in TiO_2 (rutile single crystal), calculated by the Tauc-Lorentz model

λ (nm)	n	k	λ (nm)	n	k	λ (nm)	n	k
300	3.202	1.842	540	2.655	0	880	2.506	0
305	3.454	1.808	550	2.645	0	890	2.504	0
310	3.720	1.669	560	2.635	0	900	2.503	0
315	3.926	1.424	570	2.626	0	910	2.501	0
320	4.023	1.129	580	2.618	0	920	2.500	0
325	4.017	0.851	590	2.611	0	930	2.498	0
330	3.946	0.624	600	2.604	0	940	2.497	0
335	3.843	0.452	610	2.597	0	950	2.495	0
340	3.732	0.329	620	2.591	0	960	2.494	0
345	3.625	0.242	630	2.585	0	970	2.493	0
350	3.529	0.183	640	2.579	0	980	2.492	0
355	3.447	0.140	650	2.574	0	990	2.490	0
360	3.375	0.108	660	2.569	0	1000	2.489	0
365	3.311	8.21×10^{-2}	670	2.565	0	1010	2.488	0
370	3.253	6.24×10^{-2}	680	2.560	0	1020	2.487	0
375	3.202	4.70×10^{-2}	690	2.556	0	1030	2.486	0
380	3.155	3.50×10^{-2}	700	2.552	0	1040	2.485	0
385	3.113	2.56×10^{-2}	710	2.549	0	1050	2.484	0
390	3.075	1.83×10^{-2}	720	2.545	0	1060	2.483	0
395	3.040	1.27×10^{-2}	730	2.542	0	1070	2.482	0
400	3.009	8.36×10^{-3}	740	2.538	0	1080	2.481	0
410	2.953	2.86×10^{-3}	750	2.535	0	1090	2.481	0
420	2.906	0	760	2.532	0	1100	2.480	0
430	2.867	0	770	2.530	0	1110	2.479	0
440	2.834	0	780	2.527	0	1120	2.478	0
450	2.806	0	790	2.525	0	1130	2.477	0
460	2.781	0	800	2.522	0	1140	2.477	0
470	2.759	0	810	2.520	0	1150	2.476	0
480	2.739	0	820	2.518	0	1160	2.475	0
490	2.722	0	830	2.515	0	1170	2.474	0
500	2.706	0	840	2.513	0	1180	2.474	0
510	2.691	0	850	2.511	0	1190	2.473	0
520	2.678	0	860	2.510	0	1200	2.473	0
530	2.666	0	870	2.508	0			

Table 11.34 Optical constants for the extraordinary ray in TiO_2 (rutile single crystal), calculated by the Tauc-Lorentz model

λ (nm)	n	k	λ (nm)	n	k	λ (nm)	n	k
300	4.061	2.239	540	2.951	0	880	2.763	0
305	4.255	2.023	550	2.938	0	890	2.761	0
310	4.394	1.779	560	2.926	0	900	2.759	0
315	4.475	1.525	570	2.915	0	910	2.757	0
320	4.506	1.281	580	2.905	0	920	2.755	0
325	4.498	1.053	590	2.895	0	930	2.753	0
330	4.460	0.844	600	2.886	0	940	2.752	0
335	4.395	0.655	610	2.878	0	950	2.750	0
340	4.304	0.492	620	2.870	0	960	2.748	0
345	4.198	0.362	630	2.863	0	970	2.747	0
350	4.089	0.264	640	2.856	0	980	2.745	0
355	3.984	0.192	650	2.849	0	990	2.744	0
360	3.890	0.141	660	2.843	0	1000	2.742	0
365	3.806	0.101	670	2.837	0	1010	2.741	0
370	3.729	6.94×10^{-2}	680	2.832	0	1020	2.739	0
375	3.659	4.56×10^{-2}	690	2.827	0	1030	2.738	0
380	3.594	2.79×10^{-2}	700	2.822	0	1040	2.737	0
385	3.536	1.53×10^{-2}	710	2.817	0	1050	2.736	0
390	3.483	6.89×10^{-3}	720	2.813	0	1060	2.734	0
395	3.434	2.00×10^{-3}	730	2.808	0	1070	2.733	0
400	3.391	0	740	2.804	0	1080	2.732	0
410	3.321	0	750	2.800	0	1090	2.731	0
420	3.264	0	760	2.797	0	1100	2.730	0
430	3.217	0	770	2.793	0	1110	2.729	0
440	3.176	0	780	2.790	0	1120	2.728	0
450	3.140	0	790	2.787	0	1130	2.727	0
460	3.109	0	800	2.784	0	1140	2.726	0
470	3.082	0	810	2.781	0	1150	2.725	0
480	3.057	0	820	2.778	0	1160	2.724	0
490	3.035	0	830	2.775	0	1170	2.723	0
500	3.015	0	840	2.773	0	1180	2.723	0
510	2.997	0	850	2.770	0	1190	2.722	0
520	2.980	0	860	2.768	0	1200	2.721	0
530	2.965	0	870	2.765	0			

11.2.15 WO_3

Data: unpublished results of J.A. Woollam Co., Inc. (Tables 11.35, 11.36 and Fig. 11.15).

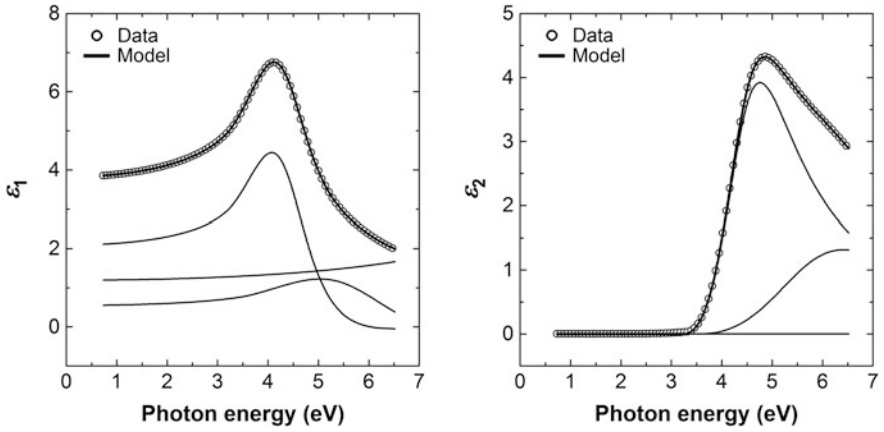


Fig. 11.15 Dielectric function of WO_3 at room temperature. The open circles show the reference data and the solid lines indicate the calculation result obtained from the parameterization assuming the Tauc-Lorentz model [(8.1) and (8.2)]

Table 11.35 Tauc-Lorentz parameters of (8.1) and (8.2) for WO_3

Peak	A (eV)	C (eV)	E_0 (eV)	E_g (eV)	$\varepsilon_1(\infty)$
$j = 1$	81.565	1.725	4.435	3.249	0.821
$j = 2$	28.205	3.591	5.943	3.602	0
$j = 3$	43.097	0.100	12.220	5.104	0

Table 11.36 Optical constants of WO_3 obtained by J.A. Woollam Co., Inc

λ (nm)	n	k	λ (nm)	n	k	λ (nm)	n	k
300	2.632	0.405	540	2.060	0	880	1.9891	0
305	2.620	0.342	550	2.055	0	890	1.9883	0
310	2.602	0.285	560	2.051	0	900	1.9875	0
315	2.579	0.234	570	2.047	0	910	1.9867	0
320	2.552	0.189	580	2.043	0	920	1.9859	0
325	2.523	0.151	590	2.040	0	930	1.9852	0
330	2.494	0.119	600	2.036	0	940	1.9845	0
335	2.464	0.092	610	2.033	0	950	1.9838	0
340	2.434	0.069	620	2.030	0	960	1.9832	0
345	2.405	0.051	630	2.027	0	970	1.9826	0
350	2.377	0.037	640	2.025	0	980	1.9819	0
355	2.351	0.026	650	2.022	0	990	1.9814	0
360	2.326	0.018	660	2.020	0	1000	1.9808	0
365	2.303	0.012	670	2.018	0	1010	1.9802	0
370	2.282	0.009	680	2.016	0	1020	1.9797	0
375	2.263	0.007	690	2.014	0	1030	1.9792	0
380	2.247	0	700	2.012	0	1040	1.9787	0
385	2.233	0	710	2.010	0	1050	1.9782	0
390	2.221	0	720	2.008	0	1060	1.9777	0
395	2.209	0	730	2.007	0	1070	1.9772	0
400	2.199	0	740	2.005	0	1080	1.9768	0
410	2.180	0	750	2.004	0	1090	1.9764	0
420	2.163	0	760	2.002	0	1100	1.9759	0
430	2.149	0	770	2.001	0	1110	1.9755	0
440	2.136	0	780	2.000	0	1120	1.9751	0
450	2.125	0	790	1.998	0	1130	1.9748	0
460	2.115	0	800	1.997	0	1140	1.9744	0
470	2.106	0	810	1.996	0	1150	1.9740	0
480	2.097	0	820	1.995	0	1160	1.9737	0
490	2.090	0	830	1.994	0	1170	1.9733	0
500	2.083	0	840	1.993	0	1180	1.9730	0
510	2.076	0	850	1.992	0	1190	1.9727	0
520	2.071	0	860	1.991	0	1200	1.9723	0
530	2.065	0	870	1.990	0			

11.2.16 ZnO (Non-doped)

Data from T. Hara, T. Maekawa, S. Minoura, Y. Sago, S. Niki and H. Fujiwara [14]. The optical data have been extracted from a sputter-deposited ZnO layer (Tables 11.37, 11.38 and Fig. 11.16).

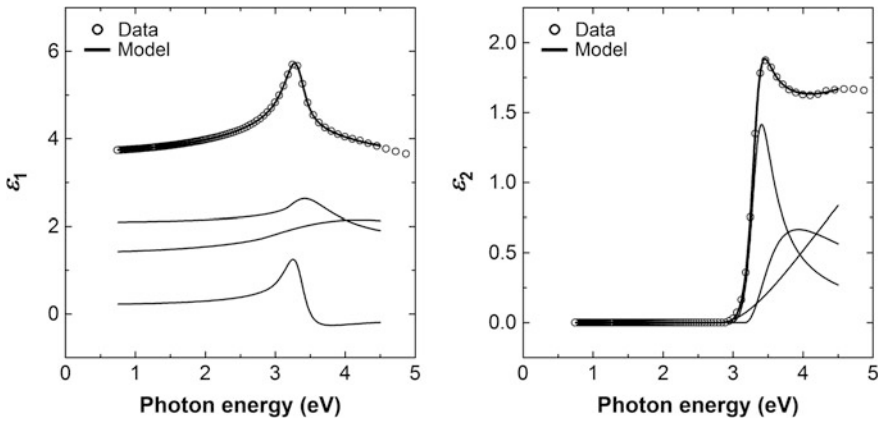


Fig. 11.16 Dielectric function of ZnO (non-doped) at room temperature. The open circles show the reference data and the solid lines indicate the calculation result obtained from the parameterization assuming the Tauc-Lorentz model [(8.1) and (8.2)]

Table 11.37 Tauc-Lorentz parameters of (8.1) and (8.2) for ZnO (non-doped)

Peak	A (eV)	C (eV)	E_0 (eV)	E_g (eV)	$\varepsilon_1(\infty)$
$j = 1$	50.215	0.887	3.308	3.171	1.830
$j = 2$	35.907	0.369	3.334	2.961	0
$j = 3$	61.700	12.953	7.212	2.806	0

Table 11.38 Optical constants of ZnO (non-doped). The optical data reported by Hara et al. are shown

λ (nm)	n	k	λ (nm)	n	k	λ (nm)	n	k
300	2.036	0.398	540	2.024	0	880	1.956	0
305	2.042	0.397	550	2.019	0	890	1.956	0
310	2.050	0.397	560	2.015	0	900	1.955	0
315	2.059	0.397	570	2.011	0	910	1.954	0
320	2.068	0.398	580	2.007	0	920	1.954	0
325	2.079	0.399	590	2.004	0	930	1.953	0
330	2.091	0.401	600	2.001	0	940	1.952	0
335	2.105	0.405	610	1.998	0	950	1.952	0
340	2.122	0.410	620	1.995	0	960	1.951	0
345	2.144	0.415	630	1.992	0	970	1.950	0
350	2.172	0.420	640	1.99	0	980	1.950	0
355	2.209	0.422	650	1.987	0	990	1.949	0
360	2.257	0.415	660	1.985	0	1000	1.949	0
365	2.314	0.390	670	1.983	0	1010	1.948	0
370	2.369	0.341	680	1.981	0	1020	1.948	0
375	2.401	0.263	690	1.979	0	1030	1.947	0
380	2.400	0.184	700	1.977	0	1040	1.947	0
385	2.375	0.120	710	1.976	0	1050	1.947	0
390	2.338	7.52×10^{-2}	720	1.974	0	1060	1.946	0
395	2.301	4.65×10^{-2}	730	1.973	0	1070	1.946	0
400	2.269	2.80×10^{-2}	740	1.971	0	1080	1.945	0
410	2.214	1.02×10^{-2}	750	1.97	0	1090	1.945	0
420	2.174	3.13×10^{-3}	760	1.969	0	1100	1.944	0
430	2.145	0	770	1.967	0	1110	1.944	0
440	2.123	0	780	1.966	0	1120	1.944	0
450	2.104	0	790	1.965	0	1130	1.943	0
460	2.088	0	800	1.964	0	1140	1.943	0
470	2.077	0	810	1.963	0	1150	1.943	0
480	2.065	0	820	1.962	0	1160	1.942	0
490	2.055	0	830	1.961	0	1170	1.942	0
500	2.048	0	840	1.96	0	1180	1.942	0
510	2.041	0	850	1.959	0	1190	1.941	0
520	2.035	0	860	1.958	0	1200	1.941	0
530	2.029	0	870	1.957	0			

11.2.17 ZnO:Ga ($N_{Hall} = 1.1 \times 10^{20}$ cm^{-3})

Data from H. Fujiwara and M. Kondo [5] (see also Fig. 18.8 in Vol. 1). The optical data have been extracted from a ZnO:Ga layer formed by dc sputtering at 170 °C using an Ar gas and a ZnO target (Ga_2O_3: 3.4 wt.%). The electrical characteristics of this layer are $N_{Hall} = 1.1 \times 10^{20}$ cm^{-3} and $\mu_{Hall} = 15.7$ cm^2/(Vs) with $N_{opt} = 1.5 \times 10^{20}$ cm^{-3} and $\mu_{opt} = 26.1$ cm^2/(Vs) (Tables 11.39, 11.40 and Fig. 11.17).

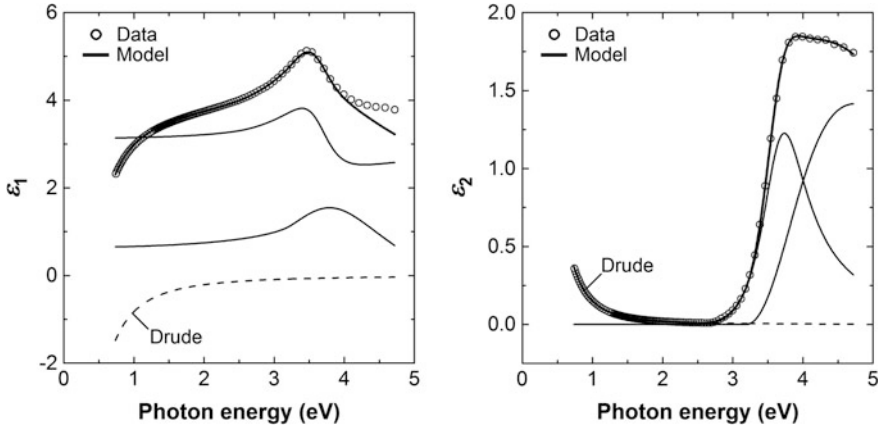


Fig. 11.17 Dielectric function of ZnO:Ga ($N_{Hall} = 1.1 \times 10^{20}$ cm^{-3}) at room temperature. The open circles show the reference data and the lines indicate the calculation result obtained from the parameterization assuming the Tauc-Lorentz (solid lines) and Drude (dotted line) models [(11.1) and (11.2)]

Table 11.39 Tauc-Lorentz (TL) peak and Drude parameters of (11.1) and (11.2) for ZnO:Ga ($N_{Hall} = 1.1 \times 10^{20}$ cm^{-3})

Model	A/A_D (eV)	C/Γ (eV)	E_0 (eV)	E_g (eV)	$\varepsilon_1(\infty)$
TL peak1	9.975	0.799	3.662	2.534	2.889
TL peak2	55.423	2.327	3.875	3.198	0
Drude	0.852	0.183	–	–	–

Table 11.40 Optical constants of ZnO:Ga ($N_{Hall} = 1.1 \times 10^{20}$ cm^{-3}). The optical data reported by Fujiwara et al. are shown

λ (nm)	n	k	λ (nm)	n	k	λ (nm)	n	k
300	2.046	0.448	540	1.973	3.24×10^{-3}	880	1.847	1.48×10^{-2}
305	2.061	0.447	550	1.967	3.43×10^{-3}	890	1.844	1.53×10^{-2}
310	2.079	0.444	560	1.962	3.63×10^{-3}	900	1.841	1.59×10^{-2}
315	2.100	0.440	570	1.957	3.84×10^{-3}	910	1.838	1.64×10^{-2}
320	2.123	0.433	580	1.953	4.05×10^{-3}	920	1.834	1.70×10^{-2}
325	2.152	0.422	590	1.948	4.27×10^{-3}	930	1.831	1.76×10^{-2}
330	2.182	0.407	600	1.944	4.50×10^{-3}	940	1.828	1.82×10^{-2}
335	2.209	0.378	610	1.939	4.74×10^{-3}	950	1.825	1.88×10^{-2}
340	2.233	0.341	620	1.935	4.99×10^{-3}	960	1.821	1.94×10^{-2}
345	2.256	0.304	630	1.931	5.24×10^{-3}	970	1.818	2.01×10^{-2}
350	2.272	0.263	640	1.928	5.51×10^{-3}	980	1.815	2.07×10^{-2}
355	2.274	0.222	650	1.924	5.78×10^{-3}	990	1.812	2.14×10^{-2}
360	2.269	0.182	660	1.920	6.06×10^{-3}	1000	1.808	2.21×10^{-2}
365	2.257	0.149	670	1.916	6.35×10^{-3}	1010	1.805	2.28×10^{-2}
370	2.241	0.121	680	1.913	6.65×10^{-3}	1020	1.801	2.35×10^{-2}
375	2.219	9.53×10^{-2}	690	1.909	6.96×10^{-3}	1030	1.798	2.43×10^{-2}
380	2.203	7.82×10^{-2}	700	1.906	7.27×10^{-3}	1040	1.795	2.50×10^{-2}
385	2.185	6.32×10^{-2}	710	1.902	7.60×10^{-3}	1050	1.791	2.58×10^{-2}
390	2.169	5.22×10^{-2}	720	1.899	7.94×10^{-3}	1060	1.788	2.65×10^{-2}
395	2.154	4.22×10^{-2}	730	1.896	8.29×10^{-3}	1070	1.784	2.74×10^{-2}
400	2.139	3.56×10^{-2}	740	1.892	8.64×10^{-3}	1080	1.781	2.82×10^{-2}
410	2.113	2.45×10^{-2}	750	1.889	9.01×10^{-3}	1090	1.777	2.90×10^{-2}
420	2.092	1.70×10^{-2}	760	1.886	9.39×10^{-3}	1100	1.774	2.98×10^{-2}
430	2.074	1.16×10^{-2}	770	1.883	9.78×10^{-3}	1110	1.770	3.07×10^{-2}
440	2.060	7.73×10^{-3}	780	1.879	1.02×10^{-2}	1120	1.767	3.16×10^{-2}
450	2.047	4.21×10^{-3}	790	1.876	1.06×10^{-2}	1130	1.763	3.25×10^{-2}
460	2.034	2.37×10^{-3}	800	1.873	1.10×10^{-2}	1140	1.760	3.34×10^{-2}
470	2.023	2.09×10^{-3}	810	1.870	1.14×10^{-2}	1150	1.756	3.44×10^{-2}
480	2.014	2.23×10^{-3}	820	1.866	1.19×10^{-2}	1160	1.752	3.53×10^{-2}
490	2.005	2.38×10^{-3}	830	1.863	1.23×10^{-2}	1170	1.748	3.63×10^{-2}
500	1.998	2.54×10^{-3}	840	1.860	1.28×10^{-2}	1180	1.745	3.73×10^{-2}
510	1.991	2.71×10^{-3}	850	1.857	1.33×10^{-2}	1190	1.741	3.83×10^{-2}
520	1.984	2.88×10^{-3}	860	1.854	1.38×10^{-2}	1200	1.737	3.94×10^{-2}
530	1.978	3.06×10^{-3}	870	1.851	1.43×10^{-2}			

11.2.18 ZnO:Al (N_{opt} = 1.5 × 10^{20} cm^{-3})

Data from T. Hara, T. Maekawa, S. Minoura, Y. Sago, S. Niki and H. Fujiwara [14]. The optical data have been extracted from a sputter-deposited ZnO:Al layer. The electrical characteristics of this layer are N_{opt} = 1.5 × 10^{20} cm^{-3} and μ_{opt} = 41.9 cm^2/(Vs) (Tables 11.41, 11.42 and Fig. 11.18).

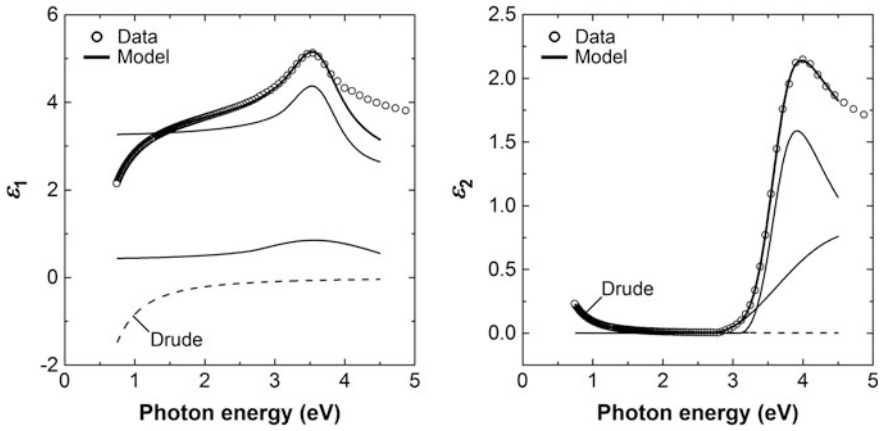


Fig. 11.18 Dielectric function of ZnO:Al (N_{opt} = 1.5 × 10^{20} cm^{-3}) at room temperature. The open circles show the reference data and the lines indicate the calculation result obtained from the parameterization assuming the Tauc-Lorentz (solid lines) and Drude (dotted line) models [(11.1) and (11.2)]

Table 11.41 Tauc-Lorentz (TL) peak and Drude parameters of (11.1) and (11.2) for ZnO:Al (N_{opt} = 1.5 × 10^{20} cm^{-3})

Model	A/A_D (eV)	C/Γ (eV)	E_0 (eV)	E_g (eV)	$\varepsilon_1(\infty)$
TL peak1	45.155	0.937	3.663	3.087	2.816
TL peak2	20.531	3.849	4.139	2.702	0
Drude	0.850	0.114	–	–	–

Table 11.42 Optical constants of ZnO:Al ($N_{opt} = 1.5 \times 10^{20}$ cm^{-3}). The optical data reported by Hara et al. are shown

λ (nm)	n	k	λ (nm)	n	k	λ (nm)	n	k
300	2.111	0.492	540	1.952	2.04×10^{-3}	880	1.821	9.43×10^{-3}
305	2.125	0.498	550	1.947	2.16×10^{-3}	890	1.817	9.77×10^{-3}
310	2.139	0.501	560	1.941	2.29×10^{-3}	900	1.814	1.01×10^{-2}
315	2.156	0.491	570	1.936	2.42×10^{-3}	910	1.810	1.05×10^{-2}
320	2.174	0.475	580	1.931	2.55×10^{-3}	920	1.807	1.08×10^{-2}
325	2.194	0.454	590	1.927	2.69×10^{-3}	930	1.803	1.12×10^{-2}
330	2.221	0.422	600	1.922	2.84×10^{-3}	940	1.800	1.16×10^{-2}
335	2.245	0.383	610	1.918	2.99×10^{-3}	950	1.797	1.20×10^{-2}
340	2.262	0.338	620	1.913	3.15×10^{-3}	960	1.793	1.24×10^{-2}
345	2.273	0.287	630	1.909	3.31×10^{-3}	970	1.790	1.28×10^{-2}
350	2.277	0.240	640	1.905	3.48×10^{-3}	980	1.786	1.33×10^{-2}
355	2.271	0.196	650	1.901	3.65×10^{-3}	990	1.783	1.37×10^{-2}
360	2.260	0.156	660	1.897	3.83×10^{-3}	1000	1.779	1.41×10^{-2}
365	2.245	0.122	670	1.893	4.01×10^{-3}	1010	1.775	1.46×10^{-2}
370	2.225	9.55×10^{-2}	680	1.890	4.20×10^{-3}	1020	1.772	1.51×10^{-2}
375	2.204	7.19×10^{-2}	690	1.886	4.40×10^{-3}	1030	1.768	1.55×10^{-2}
380	2.183	5.56×10^{-2}	700	1.882	4.60×10^{-3}	1040	1.765	1.60×10^{-2}
385	2.165	4.40×10^{-2}	710	1.879	4.81×10^{-3}	1050	1.761	1.65×10^{-2}
390	2.148	3.48×10^{-2}	720	1.875	5.03×10^{-3}	1060	1.757	1.70×10^{-2}
395	2.132	2.76×10^{-2}	730	1.872	5.25×10^{-3}	1070	1.754	1.75×10^{-2}
400	2.118	2.17×10^{-2}	740	1.868	5.48×10^{-3}	1080	1.750	1.81×10^{-2}
410	2.093	1.38×10^{-2}	750	1.865	5.71×10^{-3}	1090	1.746	1.86×10^{-2}
420	2.072	8.81×10^{-3}	760	1.861	5.95×10^{-3}	1100	1.742	1.92×10^{-2}
430	2.056	5.29×10^{-3}	770	1.858	6.20×10^{-3}	1110	1.739	1.97×10^{-2}
440	2.042	2.69×10^{-3}	780	1.854	6.46×10^{-3}	1120	1.735	2.03×10^{-2}
450	2.026	9.56×10^{-4}	790	1.851	6.72×10^{-3}	1130	1.731	2.09×10^{-2}
460	2.014	1.22×10^{-3}	800	1.847	6.99×10^{-3}	1140	1.727	2.15×10^{-2}
470	2.003	1.31×10^{-3}	810	1.844	7.27×10^{-3}	1150	1.723	2.21×10^{-2}
480	1.994	1.40×10^{-3}	820	1.841	7.55×10^{-3}	1160	1.719	2.28×10^{-2}
490	1.986	1.50×10^{-3}	830	1.837	7.84×10^{-3}	1170	1.715	2.34×10^{-2}
500	1.978	1.60×10^{-3}	840	1.834	8.14×10^{-3}	1180	1.711	2.41×10^{-2}
510	1.971	1.70×10^{-3}	850	1.831	8.45×10^{-3}	1190	1.707	2.47×10^{-2}
520	1.964	1.81×10^{-3}	860	1.827	8.77×10^{-3}	1200	1.703	2.54×10^{-2}
530	1.958	1.92×10^{-3}	870	1.824	9.10×10^{-3}			

11.2.19 ZnO:Ga ($N_{Hall} = 4.8 \times 10^{20}$ cm^{-3})

Data from H. Fujiwara and M. Kondo [5] (see also Fig. 18.8 in Vol. 1). The optical data have been extracted from a ZnO:Ga layer formed by dc sputtering at 240 °C using an Ar gas and a ZnO target (Ga_2O_3: 3.4 wt.%). The electrical characteristics of this layer are $N_{Hall} = 4.8 \times 10^{20}$ cm^{-3} and $\mu_{Hall} = 15.5$ cm^2/(Vs) with $N_{opt} = 4.2 \times 10^{20}$ cm^{-3} and $\mu_{opt} = 27.1$ cm^2/(Vs) (Tables 11.43, 11.44 and Fig. 11.19).

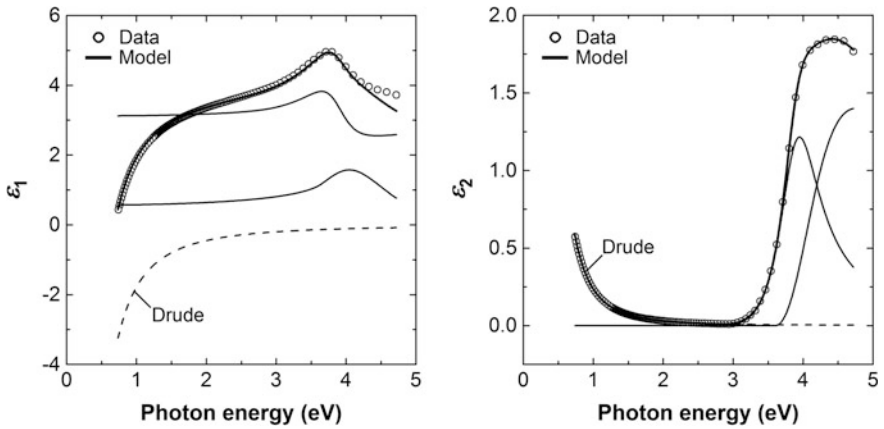


Fig. 11.19 Dielectric function of ZnO:Ga ($N_{Hall} = 4.8 \times 10^{20}$ cm^{-3}) at room temperature. The open circles show the reference data and the lines indicate the calculation result obtained from the parameterization assuming the Tauc-Lorentz (solid lines) and Drude (dotted line) models [(11.1) and (11.2)]

Table 11.43 Tauc-Lorentz (TL) peak and Drude parameters of (11.1) and (11.2) for ZnO:Ga ($N_{Hall} = 4.8 \times 10^{20}$ cm^{-3})

Model	A/A_D (eV)	C/Γ (eV)	E_0 (eV)	E_g (eV)	$\varepsilon_1(\infty)$
TL peak1	11.894	0.706	3.877	2.857	2.906
TL peak2	77.627	1.548	4.019	3.605	0
Drude	1.811	0.133	–	–	–

Table 11.44 Optical constants of ZnO:Ga ($N_{Hall} = 4.8 \times 10^{20}$ cm^{-3}). The optical data reported by Fujiwara et al. are shown

λ (nm)	n	k	λ (nm)	n	k	λ (nm)	n	k
300	2.098	0.426	540	1.882	5.28×10^{-3}	880	1.670	2.56×10^{-2}
305	2.129	0.412	550	1.875	5.60×10^{-3}	890	1.663	2.66×10^{-2}
310	2.161	0.39	560	1.869	5.93×10^{-3}	900	1.656	2.76×10^{-2}
315	2.196	0.359	570	1.862	6.28×10^{-3}	910	1.649	2.87×10^{-2}
320	2.222	0.317	580	1.856	6.63×10^{-3}	920	1.642	2.97×10^{-2}
325	2.240	0.267	590	1.850	7.01×10^{-3}	930	1.635	3.09×10^{-2}
330	2.242	0.218	600	1.843	7.39×10^{-3}	940	1.628	3.20×10^{-2}
335	2.231	0.172	610	1.837	7.79×10^{-3}	950	1.621	3.32×10^{-2}
340	2.212	0.132	620	1.831	8.21×10^{-3}	960	1.614	3.44×10^{-2}
345	2.195	0.104	630	1.825	8.64×10^{-3}	970	1.606	3.56×10^{-2}
350	2.178	8.13×10^{-2}	640	1.819	9.09×10^{-3}	980	1.599	3.69×10^{-2}
355	2.158	6.35×10^{-2}	650	1.813	9.55×10^{-3}	990	1.591	3.82×10^{-2}
360	2.140	4.95×10^{-2}	660	1.807	1.00×10^{-2}	1000	1.583	3.96×10^{-2}
365	2.122	3.88×10^{-2}	670	1.801	1.05×10^{-2}	1010	1.576	4.09×10^{-2}
370	2.105	3.13×10^{-2}	680	1.795	1.10×10^{-2}	1020	1.568	4.24×10^{-2}
375	2.087	2.23×10^{-2}	690	1.789	1.16×10^{-2}	1030	1.560	4.38×10^{-2}
380	2.073	1.77×10^{-2}	700	1.783	1.21×10^{-2}	1040	1.552	4.54×10^{-2}
385	2.060	1.35×10^{-2}	710	1.777	1.27×10^{-2}	1050	1.544	4.69×10^{-2}
390	2.048	1.02×10^{-2}	720	1.771	1.33×10^{-2}	1060	1.536	4.85×10^{-2}
395	2.037	7.73×10^{-3}	730	1.765	1.39×10^{-2}	1070	1.527	5.02×10^{-2}
400	2.027	6.20×10^{-3}	740	1.759	1.45×10^{-2}	1080	1.519	5.18×10^{-2}
410	2.007	3.49×10^{-3}	750	1.753	1.51×10^{-2}	1090	1.510	5.36×10^{-2}
420	1.992	2.35×10^{-3}	760	1.747	1.58×10^{-2}	1100	1.502	5.54×10^{-2}
430	1.979	2.54×10^{-3}	770	1.741	1.65×10^{-2}	1110	1.493	5.72×10^{-2}
440	1.967	2.74×10^{-3}	780	1.735	1.72×10^{-2}	1120	1.484	5.91×10^{-2}
450	1.956	2.95×10^{-3}	790	1.729	1.79×10^{-2}	1130	1.475	6.11×10^{-2}
460	1.946	3.16×10^{-3}	800	1.722	1.87×10^{-2}	1140	1.466	6.31×10^{-2}
470	1.937	3.39×10^{-3}	810	1.716	1.95×10^{-2}	1150	1.457	6.52×10^{-2}
480	1.928	3.62×10^{-3}	820	1.710	2.03×10^{-2}	1160	1.447	6.73×10^{-2}
490	1.919	3.87×10^{-3}	830	1.703	2.11×10^{-2}	1170	1.438	6.95×10^{-2}
500	1.911	4.13×10^{-3}	840	1.697	2.20×10^{-2}	1180	1.428	7.17×10^{-2}
510	1.904	4.40×10^{-3}	850	1.690	2.28×10^{-2}	1190	1.419	7.40×10^{-2}
520	1.896	4.68×10^{-3}	860	1.684	2.37×10^{-2}	1200	1.409	7.64×10^{-2}
530	1.889	4.98×10^{-3}	870	1.677	2.47×10^{-2}			

11.2.20 ZnO:Ga ($N_{Hall} = 6.5 \times 10^{20}$ cm^{-3})

Data from H. Fujiwara and M. Kondo [5] (see also Fig. 18.8 in Vol. 1). The optical data have been extracted from a ZnO:Ga layer formed by dc sputtering at 240 °C using an Ar gas and a ZnO target (Ga_2O_3: 5.7 wt.%). The electrical characteristics of this layer are $N_{Hall} = 6.5 \times 10^{20}$ cm^{-3} and $\mu_{Hall} = 23.1$ cm^2/(Vs) with $N_{opt} = 6.8 \times 10^{20}$ cm^{-3} and $\mu_{opt} = 24.1$ cm^2/(Vs) (Tables 11.45, 11.46 and Fig. 11.20).

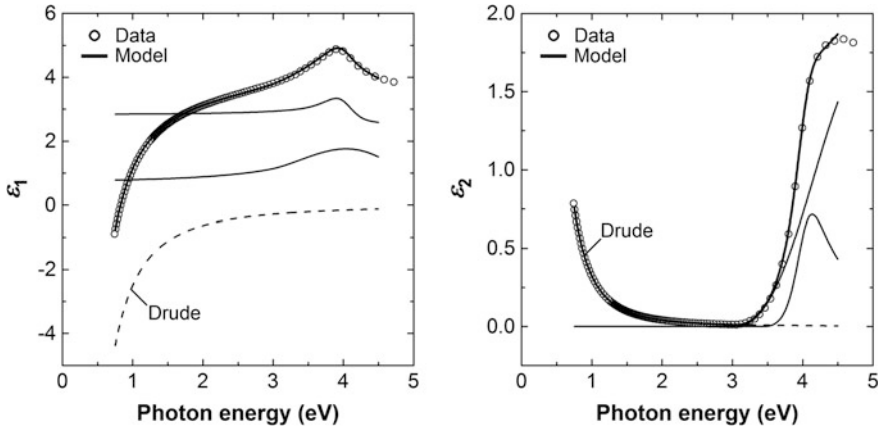


Fig. 11.20 Dielectric function of ZnO:Ga ($N_{Hall} = 6.5 \times 10^{20}$ cm^{-3}) at room temperature. The open circles show the reference data and the lines indicate the calculation result obtained from the parameterization assuming the Tauc-Lorentz (solid lines) and Drude (dotted line) models [(11.1) and (11.2)]

Table 11.45 Tauc-Lorentz (TL) peak and Drude parameters of (11.1) and (11.2) for ZnO:Ga ($N_{Hall} = 6.5 \times 10^{20}$ cm^{-3})

Model	A/A_D (eV)	C/Γ (eV)	E_0 (eV)	E_g (eV)	$\varepsilon_1(\infty)$
TL peak1	17.420	0.571	4.029	3.452	2.718
TL peak2	39.381	2.849	4.603	3.071	0
Drude	2.537	0.130	–	–	–

Table 11.46 Optical constants of ZnO:Ga ($N_{Hall} = 6.5 \times 10^{20}$ cm^{-3}). The optical data reported by Fujiwara et al. are shown

λ (nm)	n	k	λ (nm)	n	k	λ (nm)	n	k
300	2.161	0.377	540	1.827	7.44×10^{-3}	880	1.543	3.79×10^{-2}
305	2.190	0.340	550	1.819	7.90×10^{-3}	890	1.533	3.95×10^{-2}
310	2.212	0.290	560	1.811	8.37×10^{-3}	900	1.523	4.11×10^{-2}
315	2.220	0.236	570	1.803	8.86×10^{-3}	910	1.513	4.28×10^{-2}
320	2.212	0.185	580	1.796	9.38×10^{-3}	920	1.503	4.45×10^{-2}
325	2.196	0.143	590	1.788	9.91×10^{-3}	930	1.492	4.63×10^{-2}
330	2.175	0.113	600	1.780	1.05×10^{-2}	940	1.481	4.81×10^{-2}
335	2.153	8.90×10^{-2}	610	1.773	1.10×10^{-2}	950	1.471	5.00×10^{-2}
340	2.131	7.00×10^{-2}	620	1.765	1.16×10^{-2}	960	1.459	5.20×10^{-2}
345	2.113	5.50×10^{-2}	630	1.757	1.23×10^{-2}	970	1.448	5.40×10^{-2}
350	2.096	4.28×10^{-2}	640	1.750	1.29×10^{-2}	980	1.437	5.61×10^{-2}
355	2.079	3.35×10^{-2}	650	1.742	1.36×10^{-2}	990	1.425	5.83×10^{-2}
360	2.064	2.59×10^{-2}	660	1.734	1.43×10^{-2}	1000	1.414	6.06×10^{-2}
365	2.049	2.01×10^{-2}	670	1.726	1.50×10^{-2}	1010	1.402	6.30×10^{-2}
370	2.036	1.51×10^{-2}	680	1.718	1.58×10^{-2}	1020	1.390	6.54×10^{-2}
375	2.018	1.13×10^{-2}	690	1.710	1.66×10^{-2}	1030	1.377	6.79×10^{-2}
380	2.009	9.16×10^{-3}	700	1.702	1.74×10^{-2}	1040	1.365	7.06×10^{-2}
385	1.998	6.75×10^{-3}	710	1.694	1.82×10^{-2}	1050	1.352	7.33×10^{-2}
390	1.988	5.32×10^{-3}	720	1.686	1.91×10^{-2}	1060	1.339	7.61×10^{-2}
395	1.980	3.99×10^{-3}	730	1.678	2.00×10^{-2}	1070	1.326	7.90×10^{-2}
400	1.970	3.30×10^{-3}	740	1.670	2.09×10^{-2}	1080	1.313	8.21×10^{-2}
410	1.956	3.05×10^{-3}	750	1.661	2.19×10^{-2}	1090	1.299	8.52×10^{-2}
420	1.942	3.30×10^{-3}	760	1.653	2.29×10^{-2}	1100	1.286	8.85×10^{-2}
430	1.930	3.56×10^{-3}	770	1.644	2.39×10^{-2}	1110	1.271	9.19×10^{-2}
440	1.918	3.84×10^{-3}	780	1.636	2.50×10^{-2}	1120	1.257	9.55×10^{-2}
450	1.907	4.13×10^{-3}	790	1.627	2.61×10^{-2}	1130	1.243	9.92×10^{-2}
460	1.897	4.43×10^{-3}	800	1.618	2.72×10^{-2}	1140	1.228	0.103
470	1.887	4.75×10^{-3}	810	1.609	2.84×10^{-2}	1150	1.213	0.107
480	1.878	5.09×10^{-3}	820	1.600	2.96×10^{-2}	1160	1.197	0.111
490	1.869	5.44×10^{-3}	830	1.591	3.09×10^{-2}	1170	1.182	0.116
500	1.860	5.80×10^{-3}	840	1.582	3.22×10^{-2}	1180	1.166	0.12
510	1.851	6.19×10^{-3}	850	1.572	3.36×10^{-2}	1190	1.150	0.125
520	1.843	6.59×10^{-3}	860	1.563	3.50×10^{-2}	1200	1.133	0.13
530	1.835	7.01×10^{-3}	870	1.553	3.64×10^{-2}			

References

1. G. E. Jellison Jr., F. A. Modine, Appl. Phys. Lett. **69**, 371 (1996); Erratum, Appl. Phys. Lett. **69**, 2137 (1996)
2. M. Losurdo, M.M. Giangregorio, G.V. Bianco, P. Capezzuto, G. Bruno, Thin Solid Films **571**, 389 (2014)
3. T. Koida, H. Fujiwara, M. Kondo, Jpn. J. Appl. Phys. **46**, L685 (2007)
4. T. Koida, M. Kondo, K. Tsutsumi, A. Sakaguchi, M. Suzuki, H. Fujiwara, J. Appl. Phys. **107**, 033514 (2010)
5. H. Fujiwara, M. Kondo, Phys. Rev. B **71**, 075109 (2005)
6. T. Koida, H. Sai, H. Shibata, M. Kondo, Jpn. J. Appl. Phys. **53**, 05FA08 (2014)
7. H.L. Lu, G. Scarel, M. Alia, M. Fanciulli, S.-J. Ding, D. W. Zhang, Appl. Phys. Lett. **92**, 222907 (2008)
8. H.S. So, J.-W. Park, D.H. Jung, K.H. Ko, H. Lee, J. Appl. Phys. **118**, 085303 (2015)
9. J. Chen, J. Li, C. Thornberry, M.N. Sestak, R.W. Collins, J.D. Walker, S. Marsillac, A.R. Aquino, A. Rockett, in *Proceedings of the 34th IEEE PVSC* (IEEE, New York, 2009), p. 1748
10. D.S. Bhachu, M.R. Waugh, K. Zeissler, W.R. Branford, I.P. Parkin, Chem. Eur. J. **17**, 11613 (2011)
11. M. Shirayama, H. Kadowaki, T. Miyadera, T. Sugita, M. Tamakoshi, S. Fujimoto, M. Chikamatsu, H. Fujiwara, Phys. Rev. Appl. **5**, 014012 (2016)
12. G.E. Jellison Jr., L.A. Boatner, J.D. Budai, J. Appl. Phys. **93**, 9537 (2003)
13. G.E. Jellison Jr., F.A. Modine, L.A. Boatner, Opt. Lett. **22**, 1808 (1997)
14. T. Hara, T. Maekawa, S. Minoura, Y. Sago, S. Niki, H. Fujiwara, Phys. Rev. Appl. **2**, 034012 (2014)

Chapter 12
Metals



Shohei Fujimoto, Takemasa Fujiseki and Hiroyuki Fujiwara

Abstract The dielectric functions and optical constants of various metals, which have been incorporated into solar cell devices as front and rear electrodes, are summarized. The metals described here include the group-Ib (Cu, Ag, Au), IIa (Mg), IIIb (Al), IVa (Ti), VIa (Cr, Mo, W), and VIII (Ni, Pt) metals. The optical constants of C (graphite), which has been applied widely for CdTe solar cells, are also shown. It is established in this chapter that the metal dielectric functions in the whole near-infrared/visible/ultraviolet region (1–5 eV) can be parameterized almost perfectly by the combined use of the Tauc-Lorentz and Drude models. For the modeling with the Tauc-Lorentz model, several transition peaks are assumed in the analyzed region. In this chapter, the parameterization results for all the metals are summarized, together with the tabulated optical constants. The dielectric function and optical constants of various metals are also compared. Moreover, the reflectances at semiconductor/metal interfaces in crystalline Si, Cu(In,Ga)Se_2 and hybrid perovskite [$HC(NH_2)_2PbI_3$] solar cells are calculated and their results are discussed.

12.1 Introduction

Metal electrodes are a vital component in photovoltaic devices, serving also as optical back reflector in the case of rear electrodes. In solar cells, the reduction of the short-circuit current density (J_{sc}) occurs by the parasitic optical absorption in metal back electrodes, and the optical loss increases rather significantly when the reflectance at absorber/metal interfaces is low. Since the back-side reflection is determined essentially by the optical properties of the rear metal contact, the optical constants of rear metals are of particular concern for the optimization of device structures. In Cu(In,Ga)Se_2 (CIGSe) and $Cu_2ZnSn(S,Se)_4$ (CZTSSe) solar cells, for example, Mo layers formed on soda-lime glass substrates show weak reflectance (Sect. 12.2) and the necessity of using Mo rear electrodes in these solar cells leads

S. Fujimoto · T. Fujiseki · H. Fujiwara (✉)
Gifu University, 1-1 Yanagido, Gifu 501-1193, Japan
e-mail: fujiwara@gifu-u.ac.jp

© Springer International Publishing AG, part of Springer Nature 2018

H. Fujiwara and R. W. Collins (eds.), *Spectroscopic Ellipsometry for Photovoltaics*,
Springer Series in Optical Sciences 214,
https://doi.org/10.1007/978-3-319-95138-6_12

to the J_{sc} loss of ~3 mA/cm^2 (Sect. 2.6). In optical simulations, if a metal layer is sufficiently thick (typically >10 nm), this layer should be treated as a substrate material, as there is negligible light transmission though the metal layer.

In this chapter, for the purpose of spectroscopic ellipsometry (SE) characterization and device simulation, the tabulated optical constants of various metals at room temperature are provided. In addition, the optical properties of C graphite, which can also be employed as a rear electrode, are described here. For all the metals and semimetal, refractive index n and extinction coefficient k are shown in a wavelength (λ) range of 300–1200 nm with steps of 5 nm (300–400 nm) and 10 nm (400–1200 nm). From these numerical values, the dielectric function ($\varepsilon = \varepsilon_1 - i\varepsilon_2$) and the absorption coefficient (α) can be calculated quite easily according to $\varepsilon_1 = n^2 - k^2$, $\varepsilon_2 = 2nk$ and $\alpha = 4\pi k/\lambda$ (Sect. 1.2.1). The λ value can also be converted to energy (E) by $E = 1239.8/[\lambda\ (\text{nm})]$ eV (1.3).

Unfortunately, the tabulated data are sometimes insufficient for more complete SE analysis or optical simulation. Accordingly, all the dielectric functions of the metals and semimetal were parameterized by combining the Tauc-Lorentz model with the Drude model (see Sect. 1.2.3). The Tauc-Lorentz model was developed originally to express the dielectric function of amorphous materials [1], but we found that the combination of the Tauc-Lorentz model with the Drude model is quite effective for the complete parameterization of metal dielectric functions. However, it should be emphasized that the Tauc-Lorentz model is used solely to establish the optical database of various solar-cell component layers.

By combining several Tauc-Lorentz peaks with a single Drude term, the dielectric functions of various metals are reproduced almost perfectly in a wide photon energy range ($E = 1-5$ eV) using an unified parameterization scheme. In the actual modeling, the dielectric functions of the metals and semimetal were calculated using (11.1) and (11.2). The calculation example of the Tauc-Lorentz model is also shown in (1.26). A free software described in Sect. 2.7 can further be applied to calculate the dielectric function from the Tauc-Lorentz and Drude parameters listed in this chapter.

In this chapter, in addition to the optical data of metals, the basic optical properties of metals are explained. Moreover, for crystal Si (c-Si), CIGSe and hybrid perovskite solar cells, the reflectances at semiconductor/metal interfaces are calculated for different metal materials. Based on the results obtained from the calculations, we further discuss the parasitic light absorption in metal electrodes.

12.2 Optical Properties and Reflectance of Metals

In this section, the optical constants of metals are compared to understand the optical properties of metals. The various reflectance spectra calculated for different semiconductor/metal interfaces are also presented.

12.2.1 Optical Properties of Metals

Figure 12.1 shows the dielectric functions (ε_1, ε_2) and the optical constants (n, k) of selected metals versus photon energy. The optical data of each material can be found in Sect. 12.3. As confirmed from the figure, all the metals show negative ε_1 values at low energies, whereas many metals exhibit very large ε_2 values in the low-E region. The decrease in ε_1 and the increase in ε_2 with reducing energy are the specific feature of the free carrier absorption (see Fig. 1.9c), which is induced by the light absorption of free electrons (Chap. 18 in Vol. 1). The free carrier absorption can be expressed rather simply using the Drude model described by (1.27). In metals, however, the optical transitions from the d bands also occur [2] and each metal shows different features.

The negative ε_1 values observed in metal materials can be related to the reflectance at metal interfaces. In particular, when a metal has a large negative value, the propagation of an electromagnetic wave into the metal is hindered strongly and the reflectance at the metal interface increases. For example, Ag and Al exhibit large negative ε_1 values in a wide region in Fig. 12.1. In this case, all

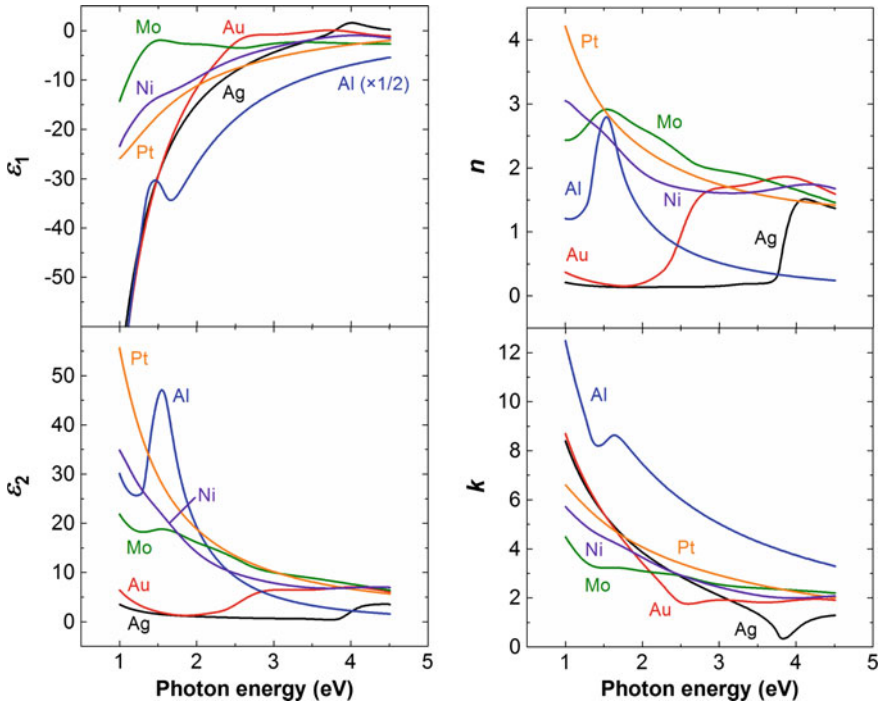


Fig. 12.1 Dielectric functions (ε_1, ε_2) and optical constants (n, k) of selected metals (Ag, Al, Au, Mo, Ni, and Pt) versus photon energy. The optical data described in this chapter are summarized. Note that the ε_1 values of Al are reduced to half for clarity

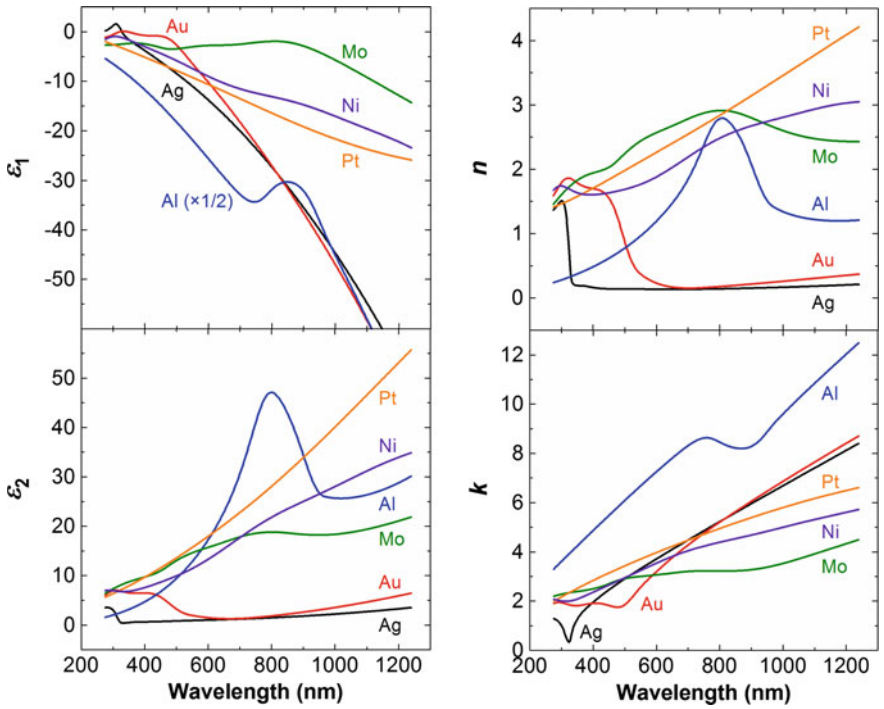


Fig. 12.2 Dielectric functions (ε_1, ε_2) and optical constants (n, k) of selected metals versus wavelength. The optical data described in this chapter are summarized. Note that the ε_1 values of Al are reduced to half for clarity

near-infrared, visible and ultraviolet light is reflected strongly, resulting in a whitish color on Ag and Al metal surfaces. In contrast, ε_1 of Au shows a drop in the visible region ($E < 2.5$ eV) and the reflectance for the green/blue light is weaker. This is the reason why the color of Au looks yellowish (or reddish). In (n, k) spectra, on the other hand, n shows a positive value and the (n, k) values increase at lower energies due to the effect of free carrier absorption. Notice that the overall k values of the metals are quite large, indicating strong light absorption in the materials. Figure 12.2 shows the same optical data as in Fig. 12.1, but the optical spectra are shown versus λ. From the above spectra, the reflectance spectra at semiconductor/metal interfaces can be calculated.

12.2.2 Reflectance at Semiconductor/Metal Interface

The reflectance R at material interfaces can be calculated rather easily by applying the Fresnel equations assuming the normal incidence [i.e., $\theta_i = 0°$ in (3.15) in Vol. 1]:

$$R = \left|r_p\right|^2 = \left|r_s\right|^2 = \left|\frac{N_M - N_i}{N_M + N_i}\right|^2 \tag{12.1}$$

where r_p and r_s show the amplitude reflection coefficients for p- and s-polarizations. In the above equation, N_M and N_i represent the complex refractive indices ($N \equiv n - ik$) of a metal and an incident medium (i.e., air, semiconductor, etc.). By inserting $N_M = n_M - ik_M$ and $N_i = n_i - ik_i$ into (12.1), we obtain

$$R = \left|\frac{(n_M - n_i) - i(k_M - k_i)}{(n_M + n_i) - i(k_M + k_i)}\right|^2 = \frac{(n_M - n_i)^2 + (k_M - k_i)^2}{(n_M + n_i)^2 + (k_M + k_i)^2} \tag{12.2}$$

Thus, R simply increases if the differences in n and k at the interface become larger.

Figure 12.3 shows the R spectra calculated for air/metal, c-Si/metal, $CuIn_{0.6}Ga_{0.4}Se_2$/metal and hybrid perovskite/metal interfaces using different metal materials (i.e., Al, Ag, Au, Pt, Ni and Mo). For N_i, we employed $N_i = n_i = 1$ (air) and the optical data shown in Fig. 8.1(c-Si), Fig. 8.26 ($CuIn_{0.6}Ga_{0.4}Se_2$) and Fig. 10.1 [α-$FAPbI_3$, $HC(NH_2)_2PbI_3$], whereas the optical functions in Fig. 12.2 were applied for N_M. Note that, in CIGSe solar cells prepared by conventional three-stage coevaporation, the Ga composition is modified continuously toward the growth direction and the double-grading Ga profile is formed. The Ga composition of $CuIn_{1-x}Ga_xSe_2$ at the rear interface is typically $x \sim 0.4$ (see Fig. 2.8). Thus, the calculation result for $CuIn_{0.6}Ga_{0.4}Se_2$ is shown in Fig. 12.3. It can be confirmed that Al, Ag and Au show high R values in a wide spectral region, compared with the other metals. Since R increases when the "optical contrast" between the two interface materials is larger, the R values obtained for the air/metal interfaces are higher than those for the semiconductor/metal interfaces.

Figure 12.4 compares the R spectra for the rear interfaces in actual solar cells. For c-Si solar cells, Al and Ag rear electrodes are generally employed (Sect. 2.5.2), whereas Au and Ag metals are used for hybrid perovskite solar cells (Sect. 16.3 in Vol. 1). In solar cells, external quantum efficiency (EQE) response in a longer λ region is quite important and high R near the band gap (E_g) is crucial to suppress the parasitic absorption in rear metal electrodes (Chap. 2). In the c-Si and hybrid perovskite solar cells, R near E_g (1100 nm in c-Si and 800 nm in α-$FAPbI_3$) is sufficiently high. In contrast, at the $CuIn_{0.6}Ga_{0.4}Se_2$/Mo interface, R is only 36% near E_g (1100 nm) and the EQE response in the longer λ region reduces by the light absorption in the Mo layer (Fig. 2.11). The lower R at the CIGSe/Mo interface is caused by the optical properties of Mo. Specifically, Mo shows $\varepsilon_1 \sim 0$ in a broad region of $E > 1.5$ eV (see Fig. 12.1). Since R increases when ε_1 shows a large negative value, Mo is not a good reflector. As a result, Cu-Se containing solar cells (i.e., CIGSe and CZTSSe solar cells), which use Mo rear electrodes, suffer from relatively large parasitic absorption in Mo (Table 2.1).

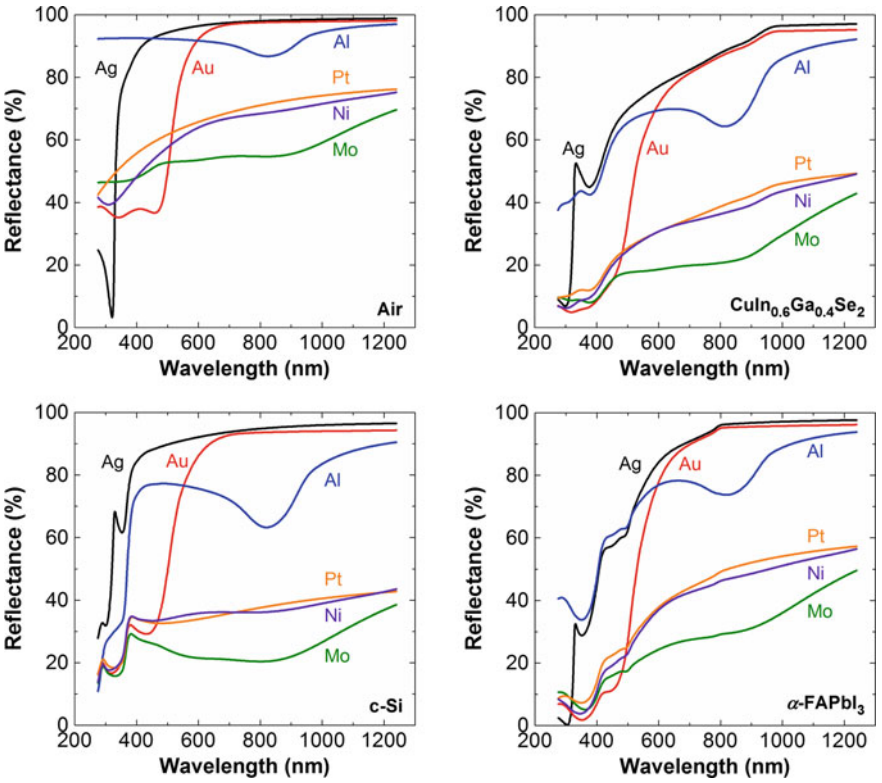


Fig. 12.3 *R* spectra calculated for air/metal, c-Si/metal, $CuIn_{0.6}Ga_{0.4}Se_2$/metal and hybrid perovskite/metal interfaces using different metal materials (Al, Ag, Au, Pt, Ni and Mo)

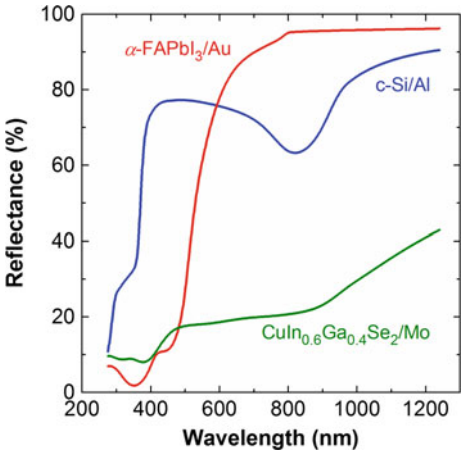


Fig. 12.4 *R* spectra calculated for c-Si/Al, $CuIn_{0.6}Ga_{0.4}Se_2$/Mo and α-$FAPbI_3$/Au interfaces formed in actual solar cells. The results are consistent with those shown in Fig. 12.3

As confirmed from (12.2), the contribution of R at the interface can be separated into two factors concerning n and k:

$$R = R_n + R_k. \tag{12.3}$$

Here, R_n and R_k show the R factors induced by the difference in n and k, respectively. If $A = (n_M + n_i)^2 + (k_M + k_i)^2$ is applied for (12.2), R_n and R_k are expressed by

$$R_n = (n_M - n_i)^2/A,\ R_k = (k_M - k_i)^2/A. \tag{12.4}$$

Figure 12.5 summarizes R_n and R_k spectra calculated for (a) the $CuIn_{0.6}Ga_{0.4}Se_2$/metal and (b) the α-$FAPbI_3$/metal interfaces. If we focus on R in the E_g region, R is determined predominantly by R_k and the contribution of R_n is low ($R_n < 15\%$). To achieve high R at the rear interface, therefore, high-k metals are important. Unfortunately, for Cu-Se containing solar cells, the current fabrication processes favor the use of Mo layers. Accordingly, to enhance R at the rear interface of these solar cells, Mo alloys including Mo-Al, Mo-Ag and Mo-Au could be applied.

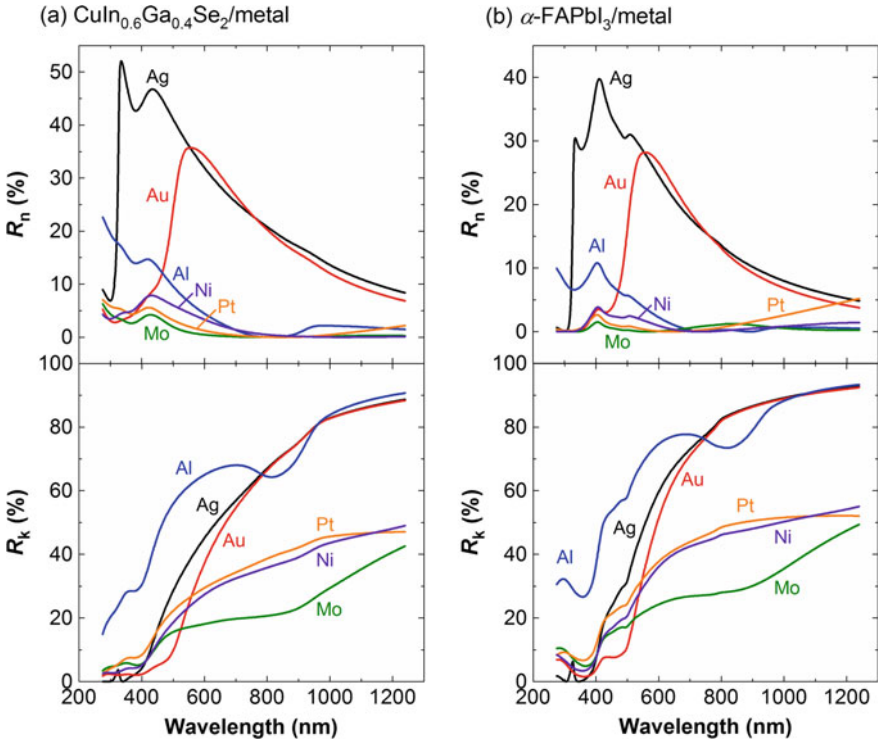


Fig. 12.5 R_n and R_k spectra calculated for **a** the $CuIn_{0.6}Ga_{0.4}Se_2$/metal and **b** the α-$FAPbI_3$/metal interfaces using (12.4)

12.3 Optical Data of Metals

12.3.1 Ag

Data: unpublished results of Gifu University. The optical data have been extracted from a dc sputtered Ag layer (Fig. 12.6, Tables 12.1 and 12.2).

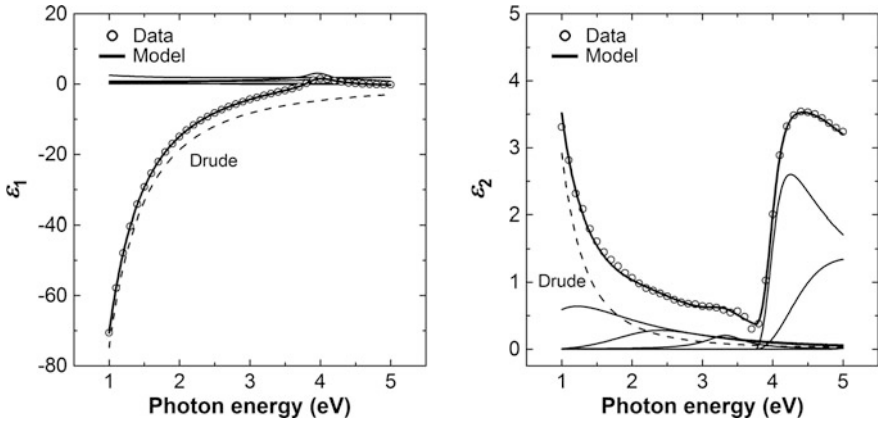


Fig. 12.6 Dielectric function of Ag at room temperature. The open circles show the experimental data and the lines indicate the calculation result obtained from the parameterization assuming the Tauc-Lorentz (solid lines) and Drude (dotted line) models [(11.1) and (11.2)]

Table 12.1 Tauc-Lorentz (TL) peak and Drude parameters of (11.1) and (11.2) for Ag

Model	A/A_D (eV)	C/Γ (eV)	E_0 (eV)	E_g (eV)	$\varepsilon_1(\infty)$
TL peak1	3.671	2.344	1.179	0.427	1.928
TL peak2	1.305	1.904	2.381	0.863	0
TL peak3	0.162	0.700	3.339	0.217	0
TL peak4	233.000	0.572	3.949	3.748	0
TL peak5	85.379	1.825	4.130	3.766	0
TL peak6	23.454	1.256	5.322	4.840	0
Drude	74.909	0.039	–	–	–

Table 12.2 Optical constants of Ag calculated by the Tauc-Lorentz and Drude models

λ (nm)	n	k	λ (nm)	n	k	λ (nm)	n	k
300	1.508	1.008	540	0.137	3.237	880	0.148	5.814
305	1.499	0.867	550	0.136	3.317	890	0.150	5.887
310	1.432	0.694	560	0.136	3.397	900	0.151	5.960
315	1.280	0.516	570	0.136	3.477	910	0.152	6.033
320	1.027	0.376	580	0.135	3.556	920	0.153	6.106
325	0.667	0.343	590	0.135	3.634	930	0.155	6.178
330	0.320	0.579	600	0.134	3.712	940	0.156	6.251
335	0.234	0.843	610	0.134	3.790	950	0.157	6.324
340	0.207	1.022	620	0.134	3.868	960	0.159	6.396
345	0.195	1.159	630	0.133	3.945	970	0.160	6.469
350	0.190	1.272	640	0.133	4.022	980	0.162	6.541
355	0.189	1.369	650	0.133	4.099	990	0.163	6.613
360	0.188	1.454	660	0.133	4.175	1000	0.165	6.685
365	0.187	1.530	670	0.133	4.252	1010	0.166	6.758
370	0.186	1.599	680	0.133	4.328	1020	0.168	6.830
375	0.183	1.663	690	0.133	4.404	1030	0.169	6.902
380	0.180	1.724	700	0.134	4.479	1040	0.171	6.974
385	0.175	1.783	710	0.134	4.555	1050	0.173	7.046
390	0.170	1.841	720	0.135	4.630	1060	0.174	7.118
395	0.165	1.898	730	0.135	4.705	1070	0.176	7.190
400	0.160	1.954	740	0.136	4.780	1080	0.178	7.262
410	0.152	2.063	750	0.136	4.855	1090	0.180	7.334
420	0.147	2.169	760	0.137	4.929	1100	0.181	7.405
430	0.143	2.270	770	0.138	5.004	1110	0.183	7.477
440	0.141	2.369	780	0.138	5.078	1120	0.185	7.549
450	0.140	2.464	790	0.139	5.152	1130	0.187	7.620
460	0.139	2.556	800	0.140	5.226	1140	0.189	7.692
470	0.139	2.647	810	0.141	5.300	1150	0.191	7.764
480	0.138	2.735	820	0.142	5.374	1160	0.193	7.835
490	0.138	2.822	830	0.143	5.447	1170	0.195	7.907
500	0.138	2.907	840	0.144	5.521	1180	0.197	7.978
510	0.138	2.991	850	0.145	5.594	1190	0.199	8.050
520	0.137	3.074	860	0.146	5.668	1200	0.201	8.121
530	0.137	3.156	870	0.147	5.741			

12.3.2 Al

Data from S. Adachi [3] (Fig. 12.7, Tables 12.3 and 12.4).

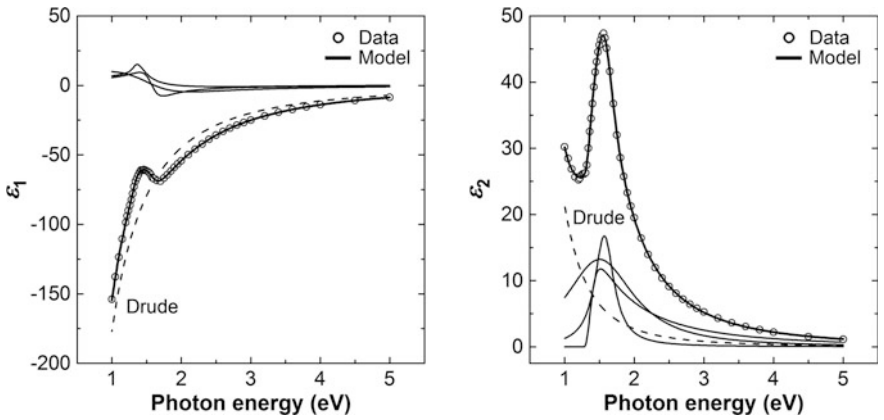


Fig. 12.7 Dielectric function of Al at room temperature. The open circles show the reference data and the lines indicate the calculation result obtained from the parameterization assuming the Tauc-Lorentz (solid lines) and Drude (dotted line) models [(11.1) and (11.2)]

Table 12.3 Tauc-Lorentz (TL) peak and Drude parameters of (11.1) and (11.2) for Al

Model	A/A_D (eV)	C/Γ (eV)	E_0 (eV)	E_g (eV)	$\varepsilon_1(\infty)$
TL peak1	369.196	0.269	1.341	1.280	0.885
TL peak2	5.604	0.335	1.578	1×10^{-4}	0
TL peak3	15.459	1.214	1.616	1×10^{-4}	0
Drude	179.505	0.121	–	–	–

Table 12.4 Optical constants of Al calculated by the Tauc-Lorentz and Drude models

λ (nm)	n	k	λ (nm)	n	k	λ (nm)	n	k
300	0.279	3.614	540	0.923	6.561	880	2.323	8.205
305	0.287	3.678	550	0.963	6.678	890	2.204	8.232
310	0.296	3.741	560	1.006	6.795	900	2.076	8.280
315	0.305	3.804	570	1.049	6.911	910	1.943	8.353
320	0.314	3.867	580	1.095	7.026	920	1.813	8.451
325	0.324	3.930	590	1.142	7.140	930	1.694	8.574
330	0.333	3.993	600	1.191	7.253	940	1.592	8.716
335	0.342	4.055	610	1.241	7.365	950	1.511	8.870
340	0.352	4.118	620	1.294	7.477	960	1.452	9.029
345	0.362	4.181	630	1.350	7.587	970	1.414	9.183
350	0.372	4.243	640	1.408	7.696	980	1.385	9.326
355	0.382	4.306	650	1.469	7.804	990	1.360	9.462
360	0.393	4.368	660	1.534	7.911	1000	1.338	9.595
365	0.404	4.430	670	1.603	8.015	1010	1.319	9.726
370	0.414	4.493	680	1.677	8.118	1020	1.301	9.854
375	0.425	4.555	690	1.757	8.217	1030	1.285	9.981
380	0.437	4.617	700	1.844	8.311	1040	1.271	10.106
385	0.448	4.679	710	1.937	8.399	1050	1.259	10.231
390	0.459	4.741	720	2.039	8.477	1060	1.248	10.354
395	0.471	4.803	730	2.147	8.544	1070	1.238	10.477
400	0.483	4.865	740	2.262	8.595	1080	1.229	10.599
410	0.508	4.988	750	2.380	8.625	1090	1.222	10.721
420	0.533	5.111	760	2.494	8.632	1100	1.215	10.841
430	0.560	5.234	770	2.599	8.615	1110	1.210	10.962
440	0.587	5.357	780	2.686	8.576	1120	1.205	11.082
450	0.616	5.479	790	2.749	8.521	1130	1.202	11.201
460	0.645	5.601	800	2.784	8.456	1140	1.199	11.320
470	0.676	5.723	810	2.791	8.391	1150	1.197	11.439
480	0.707	5.844	820	2.773	8.331	1160	1.195	11.557
490	0.740	5.965	830	2.734	8.281	1170	1.195	11.675
500	0.774	6.085	840	2.678	8.242	1180	1.194	11.792
510	0.809	6.205	850	2.608	8.215	1190	1.195	11.910
520	0.846	6.324	860	2.525	8.199	1200	1.196	12.027
530	0.883	6.443	870	2.430	8.195			

12.3.3 Au

To express the dielectric function of Au, two separate data sets are used depending on the energy region: (i) S. Adachi [3] for $E \geq 1.6$ eV and (ii) E. D. Palik [4] for $E \leq 1.5$ eV (Fig. 12.8, Tables 12.5 and 12.6).

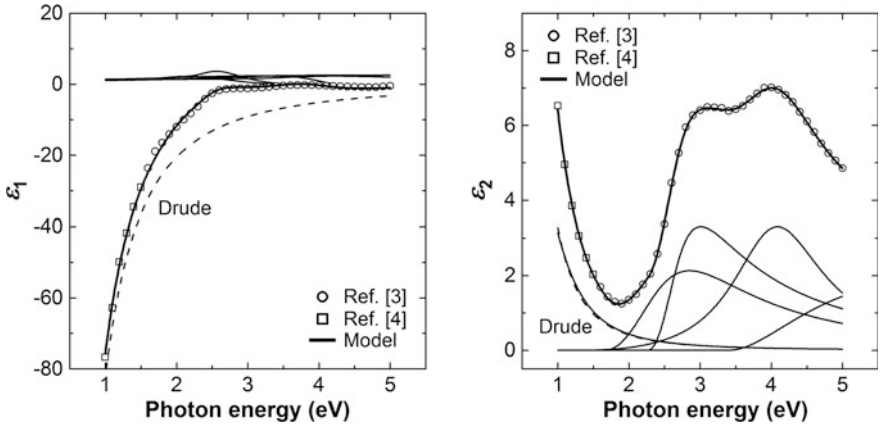


Fig. 12.8 Dielectric function of Au at room temperature. The plots show the reference data and the lines indicate the calculation result obtained from the parameterization assuming the Tauc-Lorentz (solid lines) and Drude (dotted line) models [(11.1) and (11.2)]

Table 12.5 Tauc-Lorentz (TL) peak and Drude parameters of (11.1) and (11.2) for Au

Model	A/A_D (eV)	C/Γ (eV)	E_0 (eV)	E_g (eV)	$\varepsilon_1(\infty)$
TL peak1	4.485	0.933	0.774	1×10^{-4}	2.710
TL peak2	31.570	1.884	2.444	1.669	0
TL peak3	104.771	0.997	2.574	2.267	0
TL peak4	150.616	6.282	3.489	3.414	0
TL peak5	12.628	1.566	4.077	1.468	0
Drude	82.101	0.040	–	–	–

Table 12.6 Optical constants of Au calculated by the Tauc-Lorentz and Drude models

λ (nm)	n	k	λ (nm)	n	k	λ (nm)	n	k
300	1.790	1.936	540	0.421	2.413	880	0.206	5.886
305	1.818	1.922	550	0.373	2.561	890	0.210	5.969
310	1.840	1.903	560	0.335	2.697	900	0.214	6.052
315	1.853	1.883	570	0.302	2.827	910	0.218	6.134
320	1.859	1.863	580	0.274	2.953	920	0.222	6.216
325	1.858	1.845	590	0.249	3.075	930	0.227	6.297
330	1.851	1.830	600	0.229	3.195	940	0.231	6.379
335	1.839	1.819	610	0.211	3.312	950	0.235	6.460
340	1.824	1.812	620	0.197	3.427	960	0.240	6.540
345	1.807	1.809	630	0.185	3.540	970	0.244	6.620
350	1.790	1.812	640	0.175	3.651	980	0.248	6.700
355	1.773	1.818	650	0.167	3.759	990	0.253	6.780
360	1.757	1.827	660	0.160	3.866	1000	0.257	6.860
365	1.744	1.838	670	0.156	3.971	1010	0.262	6.939
370	1.734	1.850	680	0.153	4.075	1020	0.266	7.018
375	1.724	1.862	690	0.151	4.177	1030	0.271	7.097
380	1.717	1.873	700	0.150	4.277	1040	0.276	7.176
385	1.710	1.884	710	0.150	4.375	1050	0.280	7.254
390	1.705	1.893	720	0.151	4.473	1060	0.285	7.332
395	1.700	1.900	730	0.153	4.569	1070	0.289	7.410
400	1.696	1.906	740	0.155	4.663	1080	0.294	7.488
410	1.687	1.909	750	0.158	4.756	1090	0.299	7.565
420	1.673	1.902	760	0.162	4.848	1100	0.303	7.643
430	1.650	1.884	770	0.165	4.938	1110	0.308	7.720
440	1.612	1.855	780	0.168	5.028	1120	0.313	7.797
450	1.553	1.819	790	0.172	5.116	1130	0.317	7.874
460	1.468	1.783	800	0.175	5.204	1140	0.322	7.951
470	1.353	1.756	810	0.179	5.292	1150	0.327	8.027
480	1.210	1.750	820	0.182	5.378	1160	0.331	8.104
490	1.045	1.779	830	0.186	5.464	1170	0.336	8.180
500	0.876	1.851	840	0.190	5.550	1180	0.341	8.256
510	0.719	1.963	850	0.194	5.634	1190	0.345	8.332
520	0.590	2.104	860	0.198	5.719	1200	0.350	8.408
530	0.492	2.258	870	0.202	5.803			

12.3.4 C (Graphite)

Data from S. Adachi [3]. Graphite single crystals exhibit uniaxial optical anisotropy with the optical axis perpendicular to the basal (graphite C) plane. Here, the optical data for the ordinary ray ($\varepsilon_\perp$: the electric field parallel to the basal plane) are summarized (Fig. 12.9, Tables 12.7 and 12.8).

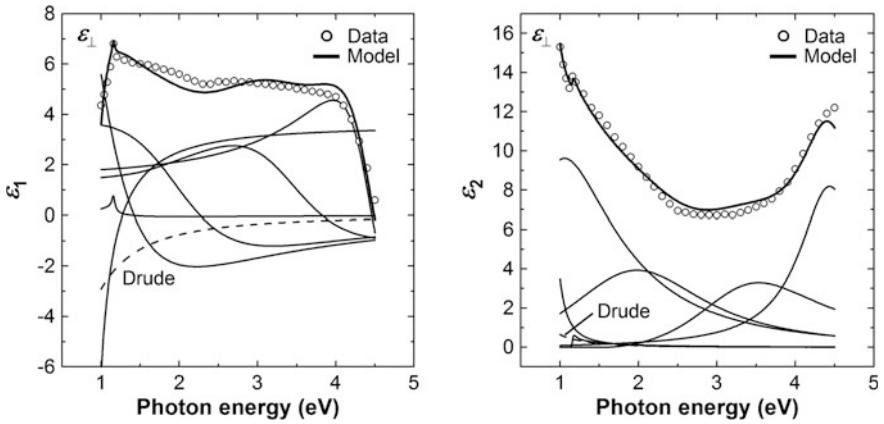


Fig. 12.9 Dielectric function of C (graphite). The $\varepsilon_\perp$ represents the dielectric function parallel to the basal plane (ordinary ray). The open circles show the reference data and the lines indicate the calculation result obtained from the parameterization assuming the Tauc-Lorentz (solid lines) and Drude (dotted line) models [(11.1) and (11.2)]

Table 12.7 Tauc-Lorentz (TL) peak and Drude parameters of (11.1) and (11.2) for $\varepsilon_\perp$ of C (graphite)

Model	A/A_D (eV)	C/Γ (eV)	E_0 (eV)	E_g (eV)	$\varepsilon_1(\infty)$
TL peak1	10.191	0.091	0.830	0.311	3.544
TL peak2	44.915	1.535	0.959	0.416	0
TL peak3	38.793	0.049	1.155	1.133	0
TL peak4	9.322	2.208	2.216	0.127	0
TL peak5	21.746	2.053	3.449	1.532	0
TL peak6	7.683	0.941	4.460	1×10^{-4}	0
Drude	3.058	0.222	–	–	–

Table 12.8 Optical constants for the ordinary ray in C (graphite) calculated by the Tauc-Lorentz and Drude models ($N_\perp = n_\perp - \mathrm{i}k_\perp$)

λ (nm)	$n_\perp$	$k_\perp$	λ (nm)	$n_\perp$	$k_\perp$	λ (nm)	$n_\perp$	$k_\perp$
300	2.792	1.768	540	2.669	1.498	880	3.132	1.903
305	2.787	1.674	550	2.682	1.517	890	3.143	1.912
310	2.771	1.601	560	2.695	1.536	900	3.153	1.921
315	2.752	1.545	570	2.710	1.553	910	3.164	1.930
320	2.732	1.504	580	2.724	1.570	920	3.174	1.940
325	2.715	1.473	590	2.740	1.586	930	3.183	1.949
330	2.701	1.450	600	2.755	1.602	940	3.193	1.958
335	2.690	1.432	610	2.771	1.616	950	3.202	1.968
340	2.682	1.419	620	2.787	1.630	960	3.211	1.977
345	2.677	1.407	630	2.803	1.644	970	3.220	1.987
350	2.674	1.398	640	2.818	1.656	980	3.228	1.997
355	2.673	1.389	650	2.834	1.669	990	3.237	2.008
360	2.672	1.381	660	2.849	1.681	1000	3.245	2.018
365	2.673	1.373	670	2.864	1.692	1010	3.254	2.029
370	2.673	1.365	680	2.878	1.703	1020	3.264	2.040
375	2.674	1.357	690	2.893	1.714	1030	3.275	2.051
380	2.674	1.350	700	2.907	1.725	1040	3.289	2.060
385	2.674	1.343	710	2.921	1.736	1050	3.305	2.066
390	2.673	1.337	720	2.935	1.746	1060	3.323	2.061
395	2.672	1.331	730	2.949	1.757	1070	3.327	2.042
400	2.670	1.327	740	2.962	1.767	1080	3.306	2.029
410	2.665	1.320	750	2.975	1.777	1090	3.280	2.040
420	2.658	1.317	760	2.988	1.787	1100	3.266	2.061
430	2.650	1.318	770	3.001	1.797	1110	3.257	2.081
440	2.643	1.324	780	3.014	1.807	1120	3.249	2.101
450	2.637	1.333	790	3.026	1.817	1130	3.241	2.121
460	2.632	1.346	800	3.039	1.827	1140	3.233	2.143
470	2.629	1.361	810	3.051	1.837	1150	3.225	2.166
480	2.629	1.378	820	3.063	1.847	1160	3.216	2.190
490	2.630	1.397	830	3.075	1.856	1170	3.206	2.216
500	2.634	1.417	840	3.087	1.866	1180	3.196	2.245
510	2.640	1.437	850	3.099	1.875	1190	3.185	2.276
520	2.648	1.458	860	3.110	1.884	1200	3.174	2.309
530	2.658	1.478	870	3.121	1.894			

12.3.5 Cr

Data from S. Adachi [3] (Fig. 12.10, Tables 12.9 and 12.10).

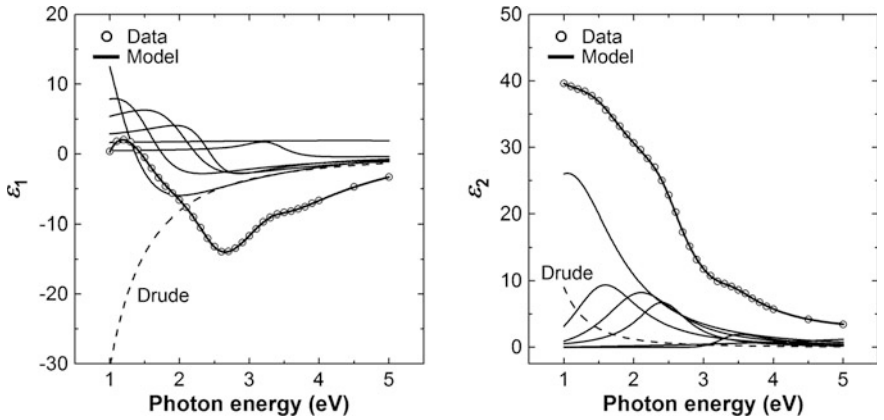


Fig. 12.10 Dielectric function of Cr at room temperature. The open circles show the reference data and the lines indicate the calculation result obtained from the parameterization assuming the Tauc-Lorentz (solid lines) and Drude (dotted line) models [(11.1) and (11.2)]

Table 12.9 Tauc-Lorentz (TL) peak and Drude parameters of (11.1) and (11.2) for Cr

Model	A/A_D (eV)	C/Γ (eV)	E_0 (eV)	E_g (eV)	$\varepsilon_1(\infty)$
TL peak1	40.348	1.727	1.325	1×10^{-4}	1.137
TL peak2	22.164	1.221	1.618	0.456	0
TL peak3	18.218	1.320	2.147	0.492	0
TL peak4	6.058	0.907	2.445	8×10^{-4}	0
TL peak5	34.747	0.789	3.365	2.713	0
TL peak6	18.194	6.730	8.473	0.623	0
Drude	33.203	0.295	–	–	–

Table 12.10 Optical constants of Cr calculated by the Tauc-Lorentz and Drude models

λ (nm)	n	k	λ (nm)	n	k	λ (nm)	n	k
300	0.982	2.663	540	3.036	4.434	880	4.370	4.311
305	1.007	2.724	550	3.117	4.419	890	4.387	4.307
310	1.034	2.784	560	3.189	4.405	900	4.402	4.304
315	1.064	2.843	570	3.255	4.392	910	4.417	4.300
320	1.096	2.900	580	3.314	4.381	920	4.431	4.297
325	1.130	2.954	590	3.370	4.372	930	4.443	4.294
330	1.166	3.006	600	3.422	4.365	940	4.455	4.292
335	1.205	3.054	610	3.471	4.359	950	4.466	4.290
340	1.243	3.098	620	3.518	4.355	960	4.475	4.289
345	1.282	3.138	630	3.563	4.353	970	4.484	4.287
350	1.319	3.173	640	3.606	4.351	980	4.492	4.287
355	1.352	3.204	650	3.648	4.351	990	4.499	4.286
360	1.380	3.233	660	3.690	4.351	1000	4.505	4.287
365	1.402	3.261	670	3.730	4.352	1010	4.510	4.287
370	1.418	3.291	680	3.770	4.353	1020	4.515	4.288
375	1.430	3.326	690	3.809	4.354	1030	4.519	4.290
380	1.439	3.367	700	3.847	4.355	1040	4.522	4.292
385	1.448	3.414	710	3.885	4.356	1050	4.524	4.294
390	1.460	3.468	720	3.923	4.357	1060	4.526	4.297
395	1.475	3.526	730	3.959	4.357	1070	4.527	4.300
400	1.495	3.587	740	3.995	4.357	1080	4.528	4.304
410	1.550	3.714	750	4.029	4.356	1090	4.528	4.308
420	1.624	3.841	760	4.063	4.355	1100	4.527	4.313
430	1.715	3.962	770	4.096	4.353	1110	4.526	4.319
440	1.820	4.075	780	4.127	4.350	1120	4.524	4.324
450	1.938	4.176	790	4.157	4.347	1130	4.522	4.331
460	2.066	4.264	800	4.186	4.344	1140	4.519	4.338
470	2.200	4.336	810	4.214	4.340	1150	4.515	4.345
480	2.338	4.391	820	4.240	4.336	1160	4.511	4.353
490	2.475	4.429	830	4.265	4.332	1170	4.507	4.361
500	2.606	4.451	840	4.289	4.328	1180	4.502	4.370
510	2.730	4.459	850	4.311	4.324	1190	4.497	4.380
520	2.844	4.457	860	4.332	4.319	1200	4.491	4.390
530	2.946	4.447	870	4.351	4.315			

12.3.6 Cu

To express the dielectric function of Cu, two separate data sets are used depending on the energy region:

(i) A. D. Rakic, A. B. Djurisic, J. M. Elazar, and M. L. Majewski [5] for $E \geq 1$ eV,
(ii) E. D. Palik [4] for $0.616 \leq E < 1$ eV (Fig. 12.11, Tables 12.11 and 12.12).

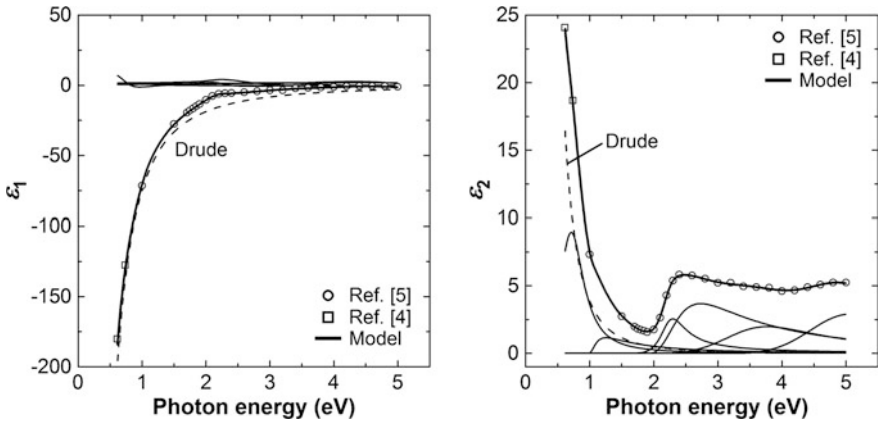


Fig. 12.11 Dielectric function of Cu at room temperature. The plots show the reference data and the lines indicate the calculation result obtained from the parameterization assuming the Tauc-Lorentz (solid lines) and Drude (dotted line) models [(11.1) and (11.2)]

Table 12.11 Tauc-Lorentz (TL) peak and Drude parameters of (11.1) and (11.2) for Cu

Model	A/A_D (eV)	C/Γ (eV)	E_0 (eV)	E_g (eV)	$\varepsilon_1(\infty)$
TL peak1	4.912	0.472	0.744	0.060	1.968
TL peak2	32.533	0.289	0.998	0.987	0
TL peak3	19.338	0.477	2.234	1.694	0
TL peak4	97.523	1.112	2.257	1.952	0
TL peak5	24.330	1.922	3.514	2.182	0
TL peak6	54.887	1.980	4.789	3.317	0
Drude	74.866	0.052	–	–	–

Table 12.12 Optical constants of Cu calculated by the Tauc-Lorentz and Drude models

λ (nm)	n	k	λ (nm)	n	k	λ (nm)	n	k
300	1.364	1.712	540	1.014	2.633	880	0.290	5.719
305	1.346	1.732	550	0.941	2.629	890	0.295	5.797
310	1.331	1.756	560	0.840	2.639	900	0.301	5.874
315	1.319	1.780	570	0.718	2.679	910	0.306	5.952
320	1.309	1.805	580	0.593	2.755	920	0.311	6.029
325	1.301	1.829	590	0.481	2.864	930	0.316	6.105
330	1.295	1.853	600	0.390	2.993	940	0.321	6.181
335	1.289	1.876	610	0.323	3.132	950	0.326	6.257
340	1.284	1.899	620	0.277	3.272	960	0.332	6.332
345	1.279	1.920	630	0.247	3.408	970	0.337	6.408
350	1.273	1.942	640	0.231	3.537	980	0.342	6.482
355	1.267	1.963	650	0.221	3.657	990	0.347	6.557
360	1.260	1.984	660	0.215	3.771	1000	0.352	6.631
365	1.253	2.005	670	0.212	3.881	1010	0.357	6.705
370	1.246	2.027	680	0.210	3.986	1020	0.361	6.779
375	1.238	2.049	690	0.211	4.088	1030	0.366	6.853
380	1.230	2.072	700	0.212	4.187	1040	0.371	6.926
385	1.222	2.095	710	0.214	4.284	1050	0.375	6.999
390	1.214	2.119	720	0.218	4.378	1060	0.379	7.072
395	1.206	2.143	730	0.221	4.470	1070	0.383	7.145
400	1.198	2.168	740	0.225	4.560	1080	0.387	7.218
410	1.184	2.219	750	0.229	4.649	1090	0.391	7.291
420	1.172	2.271	760	0.233	4.736	1100	0.394	7.363
430	1.163	2.322	770	0.238	4.822	1110	0.397	7.436
440	1.155	2.372	780	0.242	4.908	1120	0.400	7.509
450	1.150	2.419	790	0.247	4.992	1130	0.403	7.583
460	1.145	2.463	800	0.251	5.075	1140	0.406	7.656
470	1.140	2.504	810	0.256	5.158	1150	0.408	7.730
480	1.134	2.540	820	0.261	5.240	1160	0.411	7.804
490	1.127	2.573	830	0.265	5.321	1170	0.414	7.879
500	1.118	2.600	840	0.270	5.401	1180	0.417	7.954
510	1.106	2.622	850	0.275	5.481	1190	0.420	8.030
520	1.088	2.635	860	0.280	5.561	1200	0.424	8.106
530	1.060	2.638	870	0.285	5.640			

12.3.7 Mg

To express the dielectric function of Mg, three separate data sets are used: (i) S. Adachi [3], (ii) E. D. Palik [6], and (iii) R. Machorro, J. M. Siqueiros, and S. Wang [7] (Fig. 12.12, Tables 12.13 and 12.14).

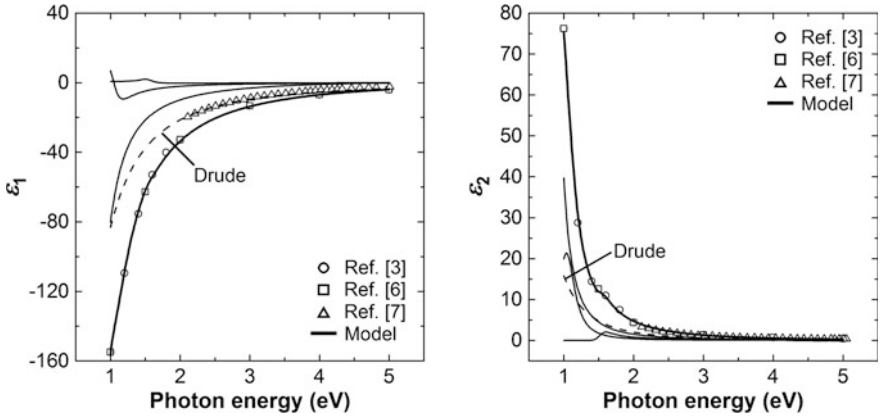


Fig. 12.12 Dielectric function of Mg at room temperature. The plots show the reference data and the lines indicate the calculation result obtained from the parameterization assuming the Tauc-Lorentz (solid lines) and Drude (dotted line) models [(11.1) and (11.2)]

Table 12.13 Tauc-Lorentz (TL) peak and Drude parameters of (11.1) and (11.2) for Mg

Model	A/A_D (eV)	C/Γ (eV)	E_0 (eV)	E_g (eV)	$\varepsilon_1(\infty)$
TL peak1	83.530	0.164	0.781	0.185	1.545
TL peak2	6.007	0.282	1.048	1×10^{-4}	0
TL peak3	28.474	0.253	1.538	1.357	0
Drude	86.155	0.190	–	–	–

Table 12.14 Optical constants of Mg calculated by the Tauc-Lorentz and Drude models

λ (nm)	n	k	λ (nm)	n	k	λ (nm)	n	k
300	0.099	2.534	540	0.301	4.991	880	0.835	8.575
305	0.102	2.587	550	0.313	5.094	890	0.861	8.702
310	0.105	2.640	560	0.325	5.196	900	0.890	8.829
315	0.108	2.692	570	0.338	5.299	910	0.921	8.956
320	0.111	2.744	580	0.351	5.402	920	0.953	9.083
325	0.114	2.796	590	0.364	5.505	930	0.988	9.210
330	0.117	2.848	600	0.378	5.608	940	1.024	9.337
335	0.120	2.900	610	0.392	5.712	950	1.063	9.465
340	0.124	2.952	620	0.407	5.815	960	1.103	9.593
345	0.127	3.004	630	0.423	5.919	970	1.146	9.722
350	0.130	3.055	640	0.439	6.024	980	1.190	9.851
355	0.134	3.107	650	0.456	6.128	990	1.238	9.980
360	0.137	3.158	660	0.473	6.232	1000	1.288	10.110
365	0.141	3.209	670	0.491	6.337	1010	1.340	10.240
370	0.144	3.261	680	0.510	6.442	1020	1.396	10.370
375	0.148	3.312	690	0.530	6.546	1030	1.455	10.499
380	0.151	3.363	700	0.551	6.650	1040	1.516	10.628
385	0.155	3.414	710	0.572	6.754	1050	1.581	10.755
390	0.159	3.465	720	0.595	6.857	1060	1.650	10.882
395	0.163	3.516	730	0.618	6.959	1070	1.721	11.007
400	0.167	3.567	740	0.642	7.060	1080	1.795	11.129
410	0.175	3.669	750	0.666	7.159	1090	1.872	11.249
420	0.183	3.771	760	0.689	7.256	1100	1.951	11.366
430	0.191	3.872	770	0.710	7.350	1110	2.031	11.480
440	0.200	3.974	780	0.728	7.443	1120	2.113	11.590
450	0.209	4.075	790	0.741	7.536	1130	2.194	11.696
460	0.218	4.177	800	0.749	7.632	1140	2.275	11.799
470	0.227	4.278	810	0.753	7.733	1150	2.354	11.899
480	0.237	4.380	820	0.755	7.840	1160	2.431	11.997
490	0.247	4.482	830	0.759	7.954	1170	2.505	12.093
500	0.257	4.583	840	0.766	8.074	1180	2.575	12.189
510	0.268	4.685	850	0.777	8.197	1190	2.642	12.286
520	0.278	4.787	860	0.793	8.322	1200	2.705	12.386
530	0.290	4.889	870	0.812	8.448			

12.3.8 Mo

Data from T. Hara, T. Maekawa, S. Minoura, Y. Sago, S. Niki and H. Fujiwara [8]. The optical data have been extracted from a Mo layer formed by sputtering (Fig. 12.13, Tables 12.15 and 12.16).

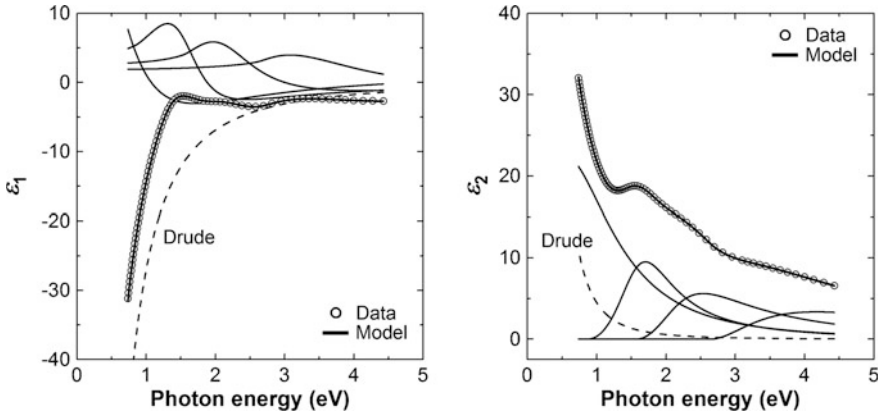


Fig. 12.13 Dielectric function of Mo at room temperature. The open circles show the reference data and the lines indicate the calculation result obtained from the parameterization assuming the Tauc-Lorentz (solid lines) and Drude (dotted line) models [(11.1) and (11.2)]

Table 12.15 Tauc-Lorentz (TL) peak and Drude parameters of (11.1) and (11.2) for Mo

Model	A/A_D (eV)	C/Γ (eV)	E_0 (eV)	E_g (eV)	$\varepsilon_1(\infty)$
TL peak1	34.298	1.871	0.961	0.021	1.261
TL peak2	42.314	1.005	1.616	0.851	0
TL peak3	86.182	1.520	2.144	1.562	0
TL peak4	196.919	2.390	2.642	2.639	0
Drude	27.947	0.168	–	–	–

Table 12.16 Optical constants of Mo. The optical data reported by Hara et al. are shown

λ (nm)	n	k	λ (nm)	n	k	λ (nm)	n	k
300	1.601	2.281	540	2.404	2.986	880	2.835	3.250
305	1.628	2.295	550	2.437	2.999	890	2.817	3.262
310	1.655	2.308	560	2.468	3.011	900	2.797	3.276
315	1.680	2.320	570	2.496	3.023	910	2.777	3.292
320	1.704	2.332	580	2.521	3.036	920	2.756	3.310
325	1.727	2.343	590	2.545	3.048	930	2.735	3.331
330	1.750	2.353	600	2.567	3.062	940	2.714	3.354
335	1.771	2.363	610	2.588	3.076	950	2.693	3.380
340	1.790	2.372	620	2.609	3.092	960	2.673	3.407
345	1.809	2.381	630	2.630	3.107	970	2.653	3.436
350	1.826	2.390	640	2.651	3.123	980	2.634	3.466
355	1.843	2.399	650	2.672	3.139	990	2.616	3.498
360	1.858	2.408	660	2.693	3.155	1000	2.598	3.532
365	1.871	2.417	670	2.715	3.169	1010	2.581	3.567
370	1.884	2.427	680	2.737	3.183	1020	2.565	3.603
375	1.896	2.437	690	2.759	3.195	1030	2.550	3.640
380	1.906	2.448	700	2.781	3.205	1040	2.537	3.677
385	1.916	2.459	710	2.802	3.213	1050	2.524	3.716
390	1.925	2.472	720	2.822	3.220	1060	2.512	3.755
395	1.933	2.485	730	2.841	3.225	1070	2.501	3.795
400	1.941	2.499	740	2.857	3.228	1080	2.491	3.835
410	1.955	2.531	750	2.872	3.230	1090	2.481	3.876
420	1.969	2.568	760	2.884	3.231	1100	2.473	3.917
430	1.985	2.610	770	2.894	3.231	1110	2.466	3.958
440	2.005	2.656	780	2.902	3.230	1120	2.459	4.000
450	2.029	2.706	790	2.907	3.230	1130	2.453	4.041
460	2.060	2.757	800	2.910	3.229	1140	2.448	4.083
470	2.099	2.807	810	2.910	3.228	1150	2.443	4.125
480	2.146	2.849	820	2.908	3.227	1160	2.439	4.167
490	2.194	2.883	830	2.902	3.226	1170	2.436	4.208
500	2.241	2.912	840	2.893	3.227	1180	2.434	4.250
510	2.286	2.935	850	2.882	3.230	1190	2.432	4.292
520	2.328	2.955	860	2.868	3.235	1200	2.430	4.333
530	2.367	2.972	870	2.852	3.241			

12.3.9 Ni

Data from S. Adachi [3] (Fig. 12.14, Tables 12.17 and 12.18).

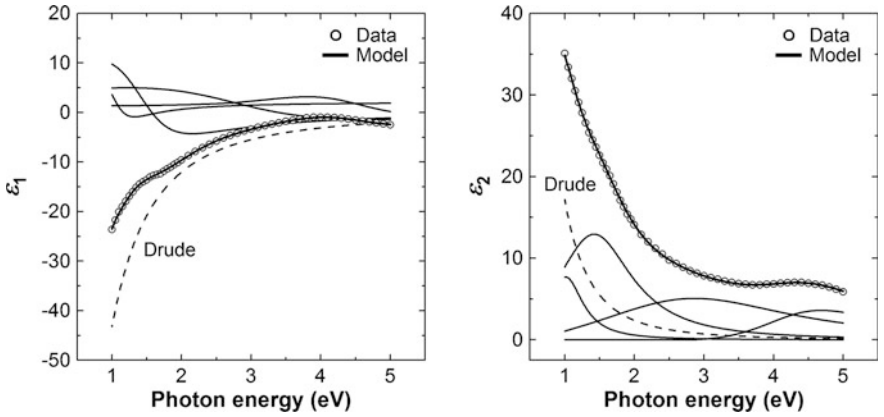


Fig. 12.14 Dielectric function of Ni at room temperature. The open circles show the reference data and the lines indicate the calculation result obtained from the parameterization assuming the Tauc-Lorentz (solid lines) and Drude (dotted line) models [(11.1) and (11.2)]

Table 12.17 Tauc-Lorentz (TL) peak and Drude parameters of (11.1) and (11.2) for Ni

Model	A/A_D (eV)	C/Γ (eV)	E_0 (eV)	E_g (eV)	$\varepsilon_1(\infty)$
TL peak1	4.525	0.600	1.058	1×10^{-4}	2.082
TL peak2	17.513	1.366	1.565	0.027	0
TL peak3	22.171	3.617	3.221	0.352	0
TL peak4	49.193	2.198	4.429	2.701	0
Drude	50.010	0.398	–	–	–

Table 12.18 Optical constants of Ni calculated by the Tauc-Lorentz and Drude models

λ (nm)	n	k	λ (nm)	n	k	λ (nm)	n	k
300	1.737	1.999	540	1.746	3.187	880	2.642	4.623
305	1.733	1.990	550	1.765	3.247	890	2.658	4.652
310	1.725	1.986	560	1.785	3.307	900	2.673	4.681
315	1.715	1.986	570	1.806	3.367	910	2.688	4.711
320	1.703	1.990	580	1.829	3.426	920	2.702	4.742
325	1.690	1.998	590	1.854	3.485	930	2.715	4.772
330	1.677	2.011	600	1.880	3.543	940	2.729	4.803
335	1.664	2.026	610	1.907	3.599	950	2.742	4.835
340	1.653	2.045	620	1.935	3.655	960	2.755	4.866
345	1.642	2.065	630	1.965	3.709	970	2.768	4.898
350	1.633	2.088	640	1.995	3.761	980	2.780	4.931
355	1.625	2.113	650	2.026	3.812	990	2.793	4.963
360	1.618	2.138	660	2.058	3.862	1000	2.806	4.995
365	1.612	2.165	670	2.090	3.910	1010	2.819	5.028
370	1.608	2.193	680	2.123	3.956	1020	2.832	5.060
375	1.605	2.221	690	2.156	4.000	1030	2.845	5.093
380	1.603	2.249	700	2.189	4.043	1040	2.858	5.125
385	1.601	2.277	710	2.221	4.084	1050	2.871	5.157
390	1.601	2.306	720	2.253	4.123	1060	2.884	5.189
395	1.601	2.335	730	2.285	4.161	1070	2.897	5.220
400	1.602	2.364	740	2.316	4.197	1080	2.909	5.252
410	1.605	2.422	750	2.346	4.232	1090	2.922	5.282
420	1.610	2.480	760	2.375	4.266	1100	2.934	5.313
430	1.616	2.538	770	2.404	4.299	1110	2.946	5.343
440	1.623	2.596	780	2.431	4.331	1120	2.957	5.373
450	1.631	2.654	790	2.457	4.361	1130	2.968	5.402
460	1.641	2.713	800	2.482	4.391	1140	2.979	5.432
470	1.651	2.771	810	2.506	4.421	1150	2.988	5.461
480	1.662	2.829	820	2.529	4.450	1160	2.998	5.490
490	1.674	2.888	830	2.550	4.479	1170	3.006	5.519
500	1.686	2.947	840	2.571	4.508	1180	3.014	5.547
510	1.699	3.006	850	2.590	4.536	1190	3.021	5.576
520	1.714	3.066	860	2.608	4.565	1200	3.028	5.605
530	1.729	3.127	870	2.626	4.594			

12.3.10 Pt

Data from S. Adachi [3] (Fig. 12.15, Tables 12.19 and 12.20).

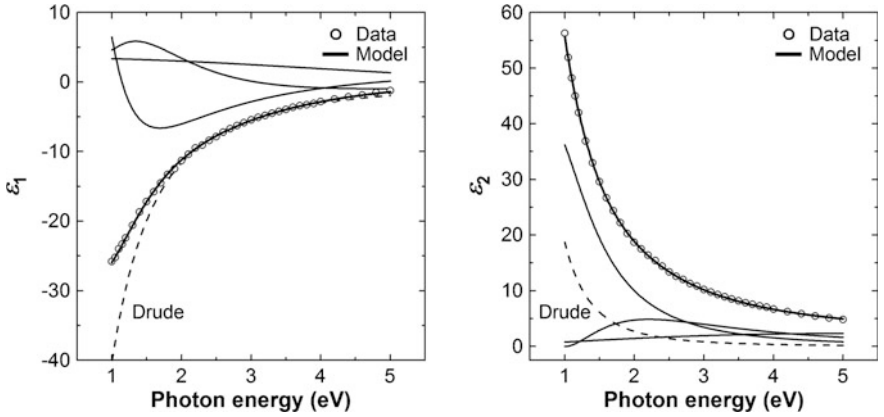


Fig. 12.15 Dielectric function of Pt at room temperature. The open circles show the reference data and the lines indicate the calculation result obtained from the parameterization assuming the Tauc-Lorentz (solid lines) and Drude (dotted line) models [(11.1) and (11.2)]

Table 12.19 Tauc-Lorentz (TL) peak and Drude parameters of (11.1) and (11.2) for Pt

Model	A/A_D (eV)	C/Γ (eV)	E_0 (eV)	E_g (eV)	$\varepsilon_1(\infty)$
TL peak1	93.659	1.362	0.880	0.216	2.282
TL peak2	76.972	3.016	1.601	1.011	0
TL peak3	29.551	16.080	8.477	1×10^{-4}	0
Drude	49.047	0.464	–	–	–

Table 12.20 Optical constants of Pt calculated by the Tauc-Lorentz and Drude models

λ (nm)	n	k	λ (nm)	n	k	λ (nm)	n	k
300	1.462	2.174	540	2.093	3.653	880	3.080	5.307
305	1.472	2.209	550	2.121	3.707	890	3.111	5.350
310	1.483	2.243	560	2.149	3.760	900	3.142	5.393
315	1.494	2.278	570	2.177	3.813	910	3.173	5.435
320	1.505	2.312	580	2.205	3.866	920	3.204	5.477
325	1.516	2.346	590	2.233	3.918	930	3.236	5.519
330	1.528	2.380	600	2.261	3.970	940	3.267	5.560
335	1.539	2.414	610	2.290	4.022	950	3.299	5.601
340	1.551	2.448	620	2.318	4.073	960	3.330	5.641
345	1.563	2.482	630	2.346	4.124	970	3.362	5.681
350	1.575	2.515	640	2.374	4.175	980	3.394	5.721
355	1.587	2.548	650	2.402	4.226	990	3.425	5.760
360	1.600	2.581	660	2.431	4.276	1000	3.457	5.799
365	1.612	2.614	670	2.459	4.326	1010	3.489	5.837
370	1.625	2.647	680	2.487	4.375	1020	3.521	5.875
375	1.638	2.679	690	2.516	4.424	1030	3.553	5.913
380	1.651	2.712	700	2.545	4.474	1040	3.584	5.950
385	1.664	2.744	710	2.573	4.522	1050	3.616	5.987
390	1.677	2.776	720	2.602	4.571	1060	3.648	6.023
395	1.690	2.807	730	2.631	4.619	1070	3.680	6.059
400	1.703	2.839	740	2.660	4.667	1080	3.712	6.095
410	1.730	2.901	750	2.689	4.715	1090	3.744	6.130
420	1.757	2.963	760	2.718	4.762	1100	3.775	6.165
430	1.784	3.024	770	2.748	4.809	1110	3.807	6.199
440	1.812	3.084	780	2.777	4.856	1120	3.839	6.233
450	1.840	3.144	790	2.807	4.903	1130	3.870	6.267
460	1.868	3.203	800	2.837	4.949	1140	3.902	6.300
470	1.896	3.261	810	2.867	4.995	1150	3.933	6.333
480	1.924	3.319	820	2.897	5.040	1160	3.965	6.365
490	1.952	3.376	830	2.927	5.086	1170	3.996	6.397
500	1.980	3.432	840	2.957	5.130	1180	4.027	6.429
510	2.008	3.488	850	2.988	5.175	1190	4.058	6.460
520	2.036	3.543	860	3.018	5.219	1200	4.090	6.491
530	2.064	3.598	870	3.049	5.263			

12.3.11 Ti

Data from E. D. Palik [6] (Fig. 12.16, Tables 12.21 and 12.22).

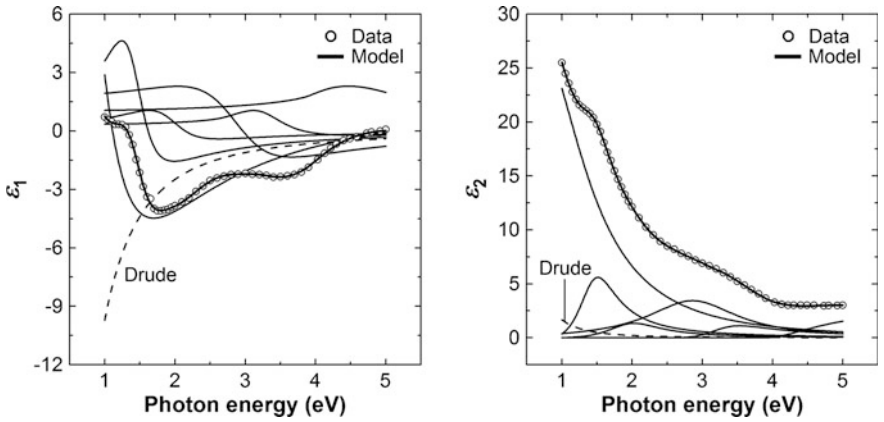


Fig. 12.16 Dielectric function of Ti at room temperature. The open circles show the reference data and the lines indicate the calculation result obtained from the parameterization assuming the Tauc-Lorentz (solid lines) and Drude (dotted line) models [(11.1) and (11.2)]

Table 12.21 Tauc-Lorentz (TL) peak and Drude parameters of (11.1) and (11.2) for Ti

Model	A/A_D (eV)	C/Γ (eV)	E_0 (eV)	E_g (eV)	$\varepsilon_1(\infty)$
TL peak1	51.696	1.560	0.924	0.127	1.343
TL peak2	18.731	0.670	1.460	0.816	0
TL peak3	4.457	0.941	1.987	0.934	0
TL peak4	5.288	1.563	2.965	1×10^{-4}	0
TL peak5	21.875	1.031	3.296	2.616	0
TL peak6	167.447	3.032	3.899	3.878	0
Drude	9.997	0.172	–	–	–

Table 12.22 Optical constants of Ti calculated by the Tauc-Lorentz and Drude models

λ (nm)	n	k	λ (nm)	n	k	λ (nm)	n	k
300	1.045	1.500	540	1.863	2.568	880	3.153	3.290
305	1.038	1.559	550	1.888	2.609	890	3.176	3.283
310	1.040	1.621	560	1.914	2.651	900	3.197	3.276
315	1.051	1.684	570	1.943	2.692	910	3.215	3.270
320	1.071	1.745	580	1.974	2.732	920	3.231	3.265
325	1.099	1.800	590	2.005	2.771	930	3.245	3.261
330	1.131	1.849	600	2.038	2.809	940	3.258	3.259
335	1.165	1.893	610	2.072	2.845	950	3.270	3.258
340	1.200	1.932	620	2.106	2.881	960	3.281	3.259
345	1.237	1.966	630	2.141	2.916	970	3.291	3.261
350	1.274	1.995	640	2.177	2.950	980	3.301	3.264
355	1.310	2.020	650	2.212	2.983	990	3.310	3.269
360	1.345	2.041	660	2.249	3.016	1000	3.320	3.275
365	1.378	2.059	670	2.287	3.049	1010	3.329	3.282
370	1.408	2.074	680	2.325	3.080	1020	3.339	3.290
375	1.436	2.087	690	2.365	3.111	1030	3.349	3.298
380	1.462	2.099	700	2.406	3.141	1040	3.359	3.307
385	1.485	2.111	710	2.448	3.170	1050	3.370	3.317
390	1.506	2.122	720	2.492	3.197	1060	3.381	3.328
395	1.526	2.134	730	2.537	3.222	1070	3.392	3.338
400	1.545	2.145	740	2.584	3.245	1080	3.404	3.349
410	1.579	2.170	750	2.631	3.265	1090	3.416	3.360
420	1.612	2.194	760	2.679	3.283	1100	3.429	3.372
430	1.642	2.217	770	2.727	3.298	1110	3.441	3.383
440	1.669	2.241	780	2.774	3.309	1120	3.455	3.395
450	1.693	2.264	790	2.822	3.318	1130	3.468	3.406
460	1.714	2.289	800	2.868	3.323	1140	3.482	3.418
470	1.733	2.316	810	2.912	3.326	1150	3.496	3.429
480	1.751	2.346	820	2.955	3.326	1160	3.510	3.440
490	1.768	2.377	830	2.995	3.323	1170	3.524	3.451
500	1.784	2.411	840	3.032	3.319	1180	3.539	3.462
510	1.802	2.448	850	3.067	3.313	1190	3.554	3.472
520	1.820	2.486	860	3.099	3.306	1200	3.568	3.483
530	1.841	2.526	870	3.128	3.298			

12.3.12 W

Data from S. Adachi [3] (Fig. 12.17, Table 12.23 and 12.24).

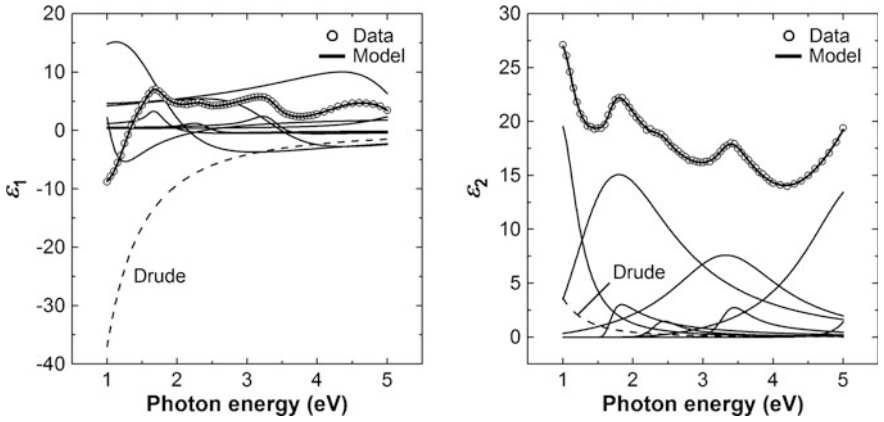


Fig. 12.17 Dielectric function of W at room temperature. The open circles show the reference data and the lines indicate the calculation result obtained from the parameterization assuming the Tauc-Lorentz (solid lines) and Drude (dotted line) models [(11.1) and (11.2)]

Table 12.23 Tauc-Lorentz (TL) peak and Drude parameters of (11.1) and (11.2) for W

Model	A/A_D (eV)	C/Γ (eV)	E_0 (eV)	E_g (eV)	$\varepsilon_1(\infty)$
TL peak1	11.433	0.585	1.000	1×10^{-4}	2.240
TL peak2	70.027	0.381	1.680	1.524	0
TL peak3	74.001	1.900	1.755	0.665	0
TL peak4	15.009	0.468	2.372	1.889	0
TL peak5	54.766	0.527	3.343	2.838	0
TL peak6	19.398	1.947	3.418	0.447	0
TL peak7	27.618	0.495	5.236	3.910	0
TL peak8	67.404	2.014	5.270	1.802	0
Drude	37.346	0.098	–	–	–

Table 12.24 Optical constants of W calculated by the Tauc-Lorentz and Drude models

λ (nm)	n	k	λ (nm)	n	k	λ (nm)	n	k
300	2.987	2.359	540	3.489	2.725	880	3.308	2.937
305	2.968	2.389	550	3.495	2.736	890	3.278	2.971
310	2.958	2.425	560	3.500	2.753	900	3.249	3.007
315	2.957	2.464	570	3.507	2.776	910	3.221	3.044
320	2.965	2.505	580	3.518	2.801	920	3.194	3.084
325	2.982	2.546	590	3.534	2.827	930	3.168	3.125
330	3.008	2.586	600	3.554	2.852	940	3.143	3.169
335	3.043	2.622	610	3.577	2.875	950	3.120	3.213
340	3.086	2.654	620	3.603	2.896	960	3.099	3.260
345	3.138	2.679	630	3.631	2.913	970	3.080	3.307
350	3.196	2.694	640	3.661	2.926	980	3.063	3.356
355	3.260	2.696	650	3.693	2.934	990	3.048	3.406
360	3.323	2.682	660	3.725	2.937	1000	3.036	3.456
365	3.380	2.650	670	3.757	2.934	1010	3.026	3.506
370	3.422	2.605	680	3.787	2.924	1020	3.018	3.556
375	3.446	2.554	690	3.814	2.906	1030	3.012	3.606
380	3.450	2.505	700	3.835	2.881	1040	3.008	3.656
385	3.441	2.467	710	3.847	2.850	1050	3.007	3.705
390	3.424	2.439	720	3.849	2.815	1060	3.007	3.753
395	3.405	2.423	730	3.839	2.779	1070	3.010	3.799
400	3.386	2.415	740	3.816	2.747	1080	3.014	3.845
410	3.355	2.416	750	3.783	2.720	1090	3.020	3.888
420	3.332	2.432	760	3.742	2.703	1100	3.027	3.930
430	3.317	2.455	770	3.697	2.697	1110	3.035	3.970
440	3.309	2.484	780	3.651	2.699	1120	3.044	4.009
450	3.307	2.517	790	3.607	2.710	1130	3.054	4.045
460	3.311	2.552	800	3.565	2.728	1140	3.064	4.079
470	3.321	2.590	810	3.527	2.750	1150	3.074	4.110
480	3.338	2.628	820	3.494	2.774	1160	3.084	4.140
490	3.364	2.663	830	3.462	2.798	1170	3.094	4.167
500	3.395	2.690	840	3.431	2.823	1180	3.103	4.192
510	3.429	2.708	850	3.400	2.849	1190	3.112	4.215
520	3.458	2.716	860	3.369	2.876	1200	3.119	4.237
530	3.478	2.720	870	3.339	2.906			

References

1. G.E. Jellison, Jr., F.A. Modine. Appl. Phys. Lett. **69**, 371 (1996); Erratum. Appl. Phys. Lett. **69**, 2137 (1996)
2. H. Fujiwara, *Spectroscopic Ellipsometry: Principles and Applications* (Wiley, West Sussex, UK, 2007)
3. S. Adachi, *The Handbook on Optical Constants of Metals: in Tables and Figures* (World Scientific, Singapore, 2012)
4. E.D. Palik, *Handbook of Optical Constants of Solids* (Academic, New York, 1985)
5. A.D. Rakic, A.B. Djurisic, J.M. Elazar, M.L. Majewski. Appl. Opt. **37**, 5271 (1998)
6. E.D. Palik, *Handbook of Optical Constants of Solids III* (Academic, San Diego, 1998)
7. R. Machorro, J.M. Siqueiros, S. Wang, Thin solid films **269**, 1 (1995)
8. T. Hara, T. Maekawa, S. Minoura, Y. Sago, S. Niki, H. Fujiwara, Phys. Rev. Appl. **2**, 034012 (2014)

Chapter 13
Substrates and Coating Layers



Shohei Fujimoto, Takemasa Fujiseki, James N. Hilfiker, Nina Hong, Mariano Campoy-Quiles and Hiroyuki Fujiwara

Abstract The optical constants of various substrates and coating materials employed widely for solar-cell fabrication are summarized. The substrate materials described here include various SiO_2 (soda-lime glass, borosilicate glass, fused silica, and quartz), metal (stainless) and plastic (polycarbonate, PEN, PET, PMMA, Kapton HN) substrates. For PEN, PET and Kapton HN substrates, which exhibit strong biaxial optical anisotropy, full data sets are provided. In solar cell devices, a protection coating (EVA) and anti-reflection (MgF_2/LiF) layers are quite important, and the optical constants of these coating layers are also described here. The refractive index spectra of the transparent materials were parameterized using the Sellmeier model, whereas the parameterization of absorbing polymer substrates was carried out assuming several transition peaks calculated by the Tauc-Lorentz model. In this chapter, the model parameters for all the substrates and coating materials are summarized, together with the tabulated optical constants.

13.1 Introduction

For the preparation of solar cells, various substrates made of glass, metal and polymer have been used. In particular, for light-weight flexible solar cells, thin stainless steel and polymer substrates have been applied. The optical properties of

S. Fujimoto · T. Fujiseki · H. Fujiwara (✉)
Gifu University, 1-1 Yanagido, Gifu 501-1193, Japan
e-mail: fujiwara@gifu-u.ac.jp

J. N. Hilfiker · N. Hong
J.A. Woollam Co., Inc., 645 M Street, Suite 102, Lincoln, NE 68508, USA

M. Campoy-Quiles
Institut de Ciència de Materials de Barcelona (ICMAB-CSIC), Campus UAB,
08193 Bellaterra, Spain

© Springer International Publishing AG, part of Springer Nature 2018

H. Fujiwara and R. W. Collins (eds.), *Spectroscopic Ellipsometry for Photovoltaics*,
Springer Series in Optical Sciences 214,
https://doi.org/10.1007/978-3-319-95138-6_13

solar-cell substrates are quite important particularly for superstrate-type solar cells in which sunlight passes through the thick substrates. To reduce the front light reflection of solar cells, on the other hand, MgF_2 and LiF anti-reflection layers are employed widely. Moreover, in crystalline-Si modules, an organic protection layer (EVA) is generally formed on the solar-cell front surface.

For spectroscopic ellipsometry (SE) characterization and optical simulation of solar cell devices, it is necessary to have all the optical constants of the solar-cell component layers. In this chapter, therefore, the tabulated optical constants of various substrates and anti-reflection/protection layers at room temperature are provided. In particular, for most materials, refractive index n and extinction coefficient k are shown in a wavelength (λ) range of 300–1200 nm with steps of 5 nm (300–400 nm) and 10 nm (400–1200 nm). From these numerical values, the dielectric function ($\varepsilon = \varepsilon_1 - i\varepsilon_2$) and the absorption coefficient (α) can be calculated quite easily according to $\varepsilon_1 = n^2 - k^2$, $\varepsilon_2 = 2nk$ and $\alpha = 4\pi k/\lambda$ (Sect. 1.2.1). The λ value can also be converted to energy (E) by $E = 1239.8/[\lambda\ (\text{nm})]$ eV (1.3). It should be noted that, in the tabulated data, the absolute k value is denoted as "0" when there is no observable light absorption, even though materials may have very small k (or α) value in a certain E region. For some substrates (soda-lime glass, polycarbonate, PMMA, Kapton HN) and EVA, however, the k values in a range of $10^{-5} \sim 10^{-4}$ are shown, as rather strong light absorption still occurs in these materials even with the small k values due to large thicknesses of the substrate (~5 mm) and the EVA film (~100 μm).

Unfortunately, the tabulated data are sometimes insufficient for more complete SE analysis or optical simulation. Accordingly, all the optical constants of substrates and coating layers were parameterized assuming (i) the Sellmeier model or (ii) the Tauc-Lorentz model (see Fig. 1.9). Specifically, for optically transparent materials, the following Sellmeier model was used.

$$n^2(\lambda) = \frac{B_1\lambda^2}{\left(\lambda^2 - C_1\right)} + \frac{B_2\lambda^2}{\left(\lambda^2 - C_2\right)} + \frac{B_3\lambda^2}{\left(\lambda^2 - C_3\right)} + 1 \tag{13.1}$$

In this model, there are a total of six parameters (B_1, B_2, B_3, C_1, C_2, C_3) and the n spectrum can be calculated quite easily from these parameter values while assuming $k = 0$.

On the other hand, the Tauc-Lorentz model (Sect. 1.2.3) is quite effective for the parameterization of organic materials (Chap. 9) and metals (Chap. 12). In particular, by combining several Tauc-Lorentz peaks, the dielectric functions of isotropic/anisotropic plastic substrates can be expressed, although the Tauc-Lorentz model is used solely to establish the optical database for various solar-cell component materials. When only limited spectral information is available, however, the

Tauc-Lorentz model is also applied to extrapolate the spectrum beyond experimental data to cover the consistent spectral range of 300–1200 nm.

In the actual modeling of plastic substrates (polycarbonate, PEN, PET and Kapton HN), the dielectric functions were calculated using (8.1) and (8.2), while the dielectric function of a stainless substrate was modeled by further incorporating the Drude term [see (11.1) and (11.2)]. The calculation example of the Tauc-Lorentz model is shown in (1.26). A free software described in Sect. 2.7 can further be applied to calculate the dielectric function from the model parameters listed in this chapter. All the parameterizations of the optical constants described in this chapter were implemented by the group of Gifu University (S. Fujimoto and T. Fujiseki), unless otherwise noted.

13.2 Optical Data of Substrates and Coating Layers

13.2.1 SiO_2

The refractive index spectra of various SiO_2 substrates reported in the following references are summarized:

(i) Soda-lime glass: R. A. Synowicki, B. D. Johs, and A. C. Martin [1],
(ii) Eagle XG glass: unpublished results of Gifu university,
(iii) Borosilicate (BK7) glass: SCHOTT optical glass data sheets [2],
(iv) Fused silica: I. H. Malitson [3],
(v) Quartz: G. Gosh [4].

The refractive index spectra of soda-lime, Eagle XG and quartz substrates are parameterized using the Sellmeier model of (13.1). For borosilicate and fused silica substrates, however, the Sellmeier parameters are taken from the above references.

In general, soda-lime glass substrates are produced by floating molten SiO_2 on liquid Sn. As a result, the Sn-side and air-side of the soda-lime glass show slightly different optical properties. Here, the optical constants that correspond to the bulk component of a soda-lime glass substrate are indicated. On the other hand, quartz substrates exhibit small optical anisotropy and the optical data for ordinary and extraordinary rays are summarized (Fig. 13.1, Tables 13.1, 13.2, 13.3, 13.4, 13.5, 13.6 and 13.7).

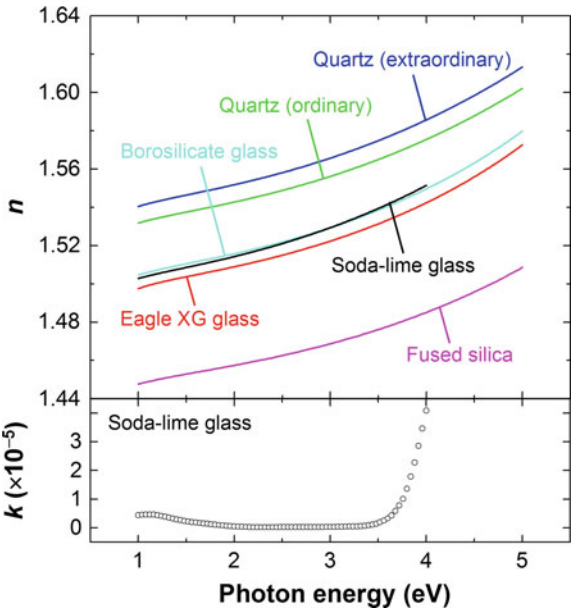


Fig. 13.1 Optical constants of SiO_2 at room temperature. The refractive index spectra (solid lines) represent the calculation results obtained from the Sellmeier model expressed by (13.1) and the extinction-coefficient spectrum for the soda-lime glass (open circles) shows the experimental data reported by Synowicki et al. [1]

Table 13.1 Sellmeier parameters of (13.1) for various SiO_2 substrates. The reported parameter values are adopted for the substrates of borosilicate glass [2] and fused silica [3]

Material	B_1	B_2	B_3	C_1 (μm^2)	C_2 (μm^2)	C_3 (μm^2)
Soda-lime glass	1.263	0.334	–	9.90×10^{-3}	43.346	–
Eagle XG glass	1.132	0.120	8.85×10^{-2}	6.81×10^{-3}	2.48×10^{-2}	10.105
Borosilicate glass	1.040	0.232	1.010	6.00×10^{-3}	2.00×10^{-2}	103.561
Fused silica	0.696	0.408	0.897	4.68×10^{-3}	1.35×10^{-2}	97.935
Quartz (ordinary)	1.353	0.212	–	8.41×10^{-3}	24.647	–
Quartz (extraordinary)	1.380	0.223	–	8.57×10^{-3}	24.647	–

Table 13.2 Optical constants of soda-lime glass. The optical data of the bulk component reported by Synowicki et al. are shown

λ (nm)	n	k ($\times 10^{-5}$)	λ (nm)	n	k ($\times 10^{-5}$)	λ (nm)	n	k ($\times 10^{-5}$)
305	1.5514	5.1791	550	1.5177	0.0196	890	1.5072	0.2955
310	1.5504	4.0846	560	1.5172	0.0196	900	1.5071	0.3076
315	1.5490	3.0913	570	1.5167	0.0221	910	1.5069	0.3189
320	1.5478	2.1865	580	1.5162	0.0270	920	1.5067	0.3313
325	1.5465	1.4904	590	1.5157	0.0319	930	1.5066	0.3414
330	1.5451	0.9815	600	1.5152	0.0370	940	1.5063	0.3534
335	1.5438	0.6739	610	1.5148	0.0393	950	1.5061	0.3632
340	1.5426	0.4446	620	1.5143	0.0467	960	1.5060	0.3753

(continued)

Table 13.2 (continued)

345	1.5415	0.3106	630	1.5138	0.0564	970	1.5058	0.3853
350	1.5404	0.2206	640	1.5134	0.0662	980	1.5057	0.3951
355	1.5393	0.1518	650	1.5131	0.0737	990	1.5055	0.4042
360	1.5381	0.1104	660	1.5127	0.0809	1000	1.5054	0.4120
365	1.5373	0.0859	670	1.5123	0.0883	1010	1.5052	0.4221
370	1.5364	0.0652	680	1.5119	0.0982	1020	1.5051	0.4294
375	1.5356	0.0517	690	1.5116	0.1055	1030	1.5050	0.4368
380	1.5348	0.0466	700	1.5113	0.1154	1040	1.5048	0.4417
385	1.5340	0.0442	710	1.5110	0.1251	1050	1.5047	0.4466
390	1.5331	0.0417	720	1.5108	0.1374	1060	1.5045	0.4515
395	1.5323	0.0392	730	1.5105	0.1445	1070	1.5044	0.4564
400	1.5315	0.0344	740	1.5102	0.1546	1080	1.5043	0.4589
410	1.5301	0.0294	750	1.5099	0.1619	1090	1.5043	0.4589
420	1.5287	0.0270	760	1.5097	0.1693	1100	1.5041	0.4613
430	1.5275	0.0245	770	1.5095	0.1767	1110	1.5040	0.4613
440	1.5264	0.0222	780	1.5093	0.1839	1120	1.5040	0.4613
450	1.5254	0.0221	790	1.5091	0.1939	1130	1.5039	0.4613
460	1.5245	0.0245	800	1.5089	0.2012	1140	1.5038	0.4613
470	1.5235	0.0245	810	1.5087	0.2087	1150	1.5037	0.4590
480	1.5226	0.0245	820	1.5085	0.2208	1160	1.5037	0.4589
490	1.5218	0.0221	830	1.5083	0.2307	1170	1.5036	0.4564
500	1.5211	0.0220	840	1.5081	0.2405	1180	1.5035	0.4540
510	1.5203	0.0196	850	1.5079	0.2501	1190	1.5034	0.4515
520	1.5196	0.0172	860	1.5078	0.2625	1200	1.5034	0.4491
530	1.5190	0.0172	870	1.5076	0.2724			
540	1.5184	0.0196	880	1.5074	0.2849			

Table 13.3 Refractive index of Eagle XG glass calculated by the Sellmeier model ($k = 0$)

λ (nm)	n	λ (nm)	n	λ (nm)	n	λ (nm)	n
300	1.5458	460	1.5178	720	1.5061	980	1.5013
305	1.5441	470	1.5170	730	1.5058	990	1.5012
310	1.5425	480	1.5162	740	1.5056	1000	1.5010
315	1.5409	490	1.5155	750	1.5054	1010	1.5009
320	1.5395	500	1.5148	760	1.5052	1020	1.5007
325	1.5381	510	1.5142	770	1.5050	1030	1.5006
330	1.5369	520	1.5136	780	1.5047	1040	1.5005
335	1.5356	530	1.5130	790	1.5045	1050	1.5003
340	1.5345	540	1.5125	800	1.5043	1060	1.5002
345	1.5334	550	1.5120	810	1.5041	1070	1.5000
350	1.5323	560	1.5115	820	1.5040	1080	1.4999

(continued)

Table 13.3 (continued)

λ (nm)	n	λ (nm)	n	λ (nm)	n	λ (nm)	n
355	1.5313	570	1.5110	830	1.5038	1090	1.4998
360	1.5304	580	1.5106	840	1.5036	1100	1.4996
365	1.5295	590	1.5102	850	1.5034	1110	1.4995
370	1.5286	600	1.5098	860	1.5032	1120	1.4994
375	1.5278	610	1.5094	870	1.5031	1130	1.4992
380	1.5270	620	1.5090	880	1.5029	1140	1.4991
385	1.5262	630	1.5087	890	1.5027	1150	1.4989
390	1.5255	640	1.5084	900	1.5026	1160	1.4988
395	1.5248	650	1.5080	910	1.5024	1170	1.4987
400	1.5241	660	1.5077	920	1.5022	1180	1.4985
410	1.5228	670	1.5074	930	1.5021	1190	1.4984
420	1.5217	680	1.5071	940	1.5019	1200	1.4983
430	1.5206	690	1.5069	950	1.5018		
440	1.5196	700	1.5066	960	1.5016		
450	1.5187	710	1.5063	970	1.5015		

Table 13.4 Refractive index of borosilicate glass calculated by the Sellmeier model ($k = 0$)

λ (nm)	n	λ (nm)	n	λ (nm)	n	λ (nm)	n
300	1.5530	460	1.5246	720	1.5127	980	1.5080
305	1.5512	470	1.5238	730	1.5125	990	1.5078
310	1.5496	480	1.5230	740	1.5123	1000	1.5077
315	1.5481	490	1.5223	750	1.5120	1010	1.5076
320	1.5466	500	1.5216	760	1.5118	1020	1.5074
325	1.5452	510	1.5210	770	1.5116	1030	1.5073
330	1.5439	520	1.5204	780	1.5114	1040	1.5072
335	1.5427	530	1.5198	790	1.5112	1050	1.5070
340	1.5415	540	1.5192	800	1.5110	1060	1.5069
345	1.5404	550	1.5187	810	1.5108	1070	1.5068
350	1.5394	560	1.5182	820	1.5106	1080	1.5066
355	1.5384	570	1.5178	830	1.5104	1090	1.5065
360	1.5374	580	1.5173	840	1.5102	1100	1.5064
365	1.5365	590	1.5169	850	1.5100	1110	1.5062
370	1.5356	600	1.5165	860	1.5099	1120	1.5061
375	1.5347	610	1.5161	870	1.5097	1130	1.5060
380	1.5339	620	1.5157	880	1.5095	1140	1.5059
385	1.5332	630	1.5154	890	1.5094	1150	1.5057
390	1.5324	640	1.5150	900	1.5092	1160	1.5056
395	1.5317	650	1.5147	910	1.5090	1170	1.5055

(continued)

Table 13.4 (continued)

λ (nm)	n	λ (nm)	n	λ (nm)	n	λ (nm)	n
400	1.5310	660	1.5144	920	1.5089	1180	1.5054
410	1.5298	670	1.5141	930	1.5087	1190	1.5052
420	1.5286	680	1.5138	940	1.5086	1200	1.5051
430	1.5275	690	1.5135	950	1.5084		
440	1.5265	700	1.5133	960	1.5083		
450	1.5255	710	1.5130	970	1.5081		

Table 13.5 Refractive index of fused silica calculated by the Sellmeier model ($k = 0$)

λ (nm)	n	λ (nm)	n	λ (nm)	n	λ (nm)	n
300	1.4877	460	1.4648	720	1.4548	980	1.4506
305	1.4864	470	1.4641	730	1.4546	990	1.4505
310	1.4851	480	1.4635	740	1.4544	1000	1.4504
315	1.4838	490	1.4629	750	1.4542	1010	1.4503
320	1.4827	500	1.4623	760	1.4540	1020	1.4501
325	1.4816	510	1.4617	770	1.4538	1030	1.4500
330	1.4805	520	1.4612	780	1.4536	1040	1.4499
335	1.4795	530	1.4608	790	1.4535	1050	1.4498
340	1.4786	540	1.4603	800	1.4533	1060	1.4496
345	1.4777	550	1.4599	810	1.4531	1070	1.4495
350	1.4768	560	1.4595	820	1.4529	1080	1.4494
355	1.4760	570	1.4591	830	1.4528	1090	1.4493
360	1.4752	580	1.4587	840	1.4526	1100	1.4492
365	1.4745	590	1.4583	850	1.4525	1110	1.4490
370	1.4738	600	1.4580	860	1.4523	1120	1.4489
375	1.4731	610	1.4577	870	1.4522	1130	1.4488
380	1.4724	620	1.4574	880	1.4520	1140	1.4487
385	1.4718	630	1.4571	890	1.4519	1150	1.4486
390	1.4712	640	1.4568	900	1.4517	1160	1.4485
395	1.4706	650	1.4565	910	1.4516	1170	1.4484
400	1.4701	660	1.4562	920	1.4514	1180	1.4482
410	1.4690	670	1.4560	930	1.4513	1190	1.4481
420	1.4680	680	1.4557	940	1.4512	1200	1.4480
430	1.4671	690	1.4555	950	1.4510		
440	1.4663	700	1.4553	960	1.4509		
450	1.4655	710	1.4550	970	1.4508		

Table 13.6 Refractive index of quartz (ordinary) calculated by the Sellmeier model ($k = 0$)

λ (nm)	n	λ (nm)	n	λ (nm)	n	λ (nm)	n
300	1.5785	460	1.5515	720	1.5397	980	1.5350
305	1.5769	470	1.5507	730	1.5395	990	1.5349
310	1.5754	480	1.5499	740	1.5392	1000	1.5348
315	1.5740	490	1.5492	750	1.5390	1010	1.5346
320	1.5726	500	1.5485	760	1.5388	1020	1.5345
325	1.5713	510	1.5479	770	1.5386	1030	1.5344
330	1.5701	520	1.5473	780	1.5384	1040	1.5342
335	1.5690	530	1.5467	790	1.5382	1050	1.5341
340	1.5679	540	1.5462	800	1.5380	1060	1.5340
345	1.5668	550	1.5457	810	1.5378	1070	1.5338
350	1.5658	560	1.5452	820	1.5376	1080	1.5337
355	1.5648	570	1.5447	830	1.5374	1090	1.5336
360	1.5639	580	1.5443	840	1.5372	1100	1.5335
365	1.5630	590	1.5438	850	1.5371	1110	1.5333
370	1.5622	600	1.5434	860	1.5369	1120	1.5332
375	1.5614	610	1.5431	870	1.5367	1130	1.5331
380	1.5606	620	1.5427	880	1.5365	1140	1.5330
385	1.5598	630	1.5423	890	1.5364	1150	1.5329
390	1.5591	640	1.5420	900	1.5362	1160	1.5327
395	1.5584	650	1.5417	910	1.5361	1170	1.5326
400	1.5578	660	1.5414	920	1.5359	1180	1.5325
410	1.5565	670	1.5411	930	1.5358	1190	1.5324
420	1.5554	680	1.5408	940	1.5356	1200	1.5323
430	1.5543	690	1.5405	950	1.5355		
440	1.5533	700	1.5402	960	1.5353		
450	1.5524	710	1.5400	970	1.5352		

Table 13.7 Refractive index of quartz (extraordinary) calculated by the Sellmeier model ($k = 0$)

λ (nm)	n	λ (nm)	n	λ (nm)	n	λ (nm)	n
300	1.5888	460	1.5609	720	1.5487	980	1.5438
305	1.5872	470	1.5600	730	1.5484	990	1.5437
310	1.5856	480	1.5592	740	1.5482	1000	1.5435
315	1.5842	490	1.5585	750	1.5479	1010	1.5434
320	1.5828	500	1.5578	760	1.5477	1020	1.5433
325	1.5814	510	1.5571	770	1.5475	1030	1.5431
330	1.5802	520	1.5565	780	1.5473	1040	1.5430
335	1.5789	530	1.5559	790	1.5471	1050	1.5428
340	1.5778	540	1.5554	800	1.5469	1060	1.5427
345	1.5767	550	1.5548	810	1.5467	1070	1.5426
350	1.5757	560	1.5543	820	1.5465	1080	1.5424

(continued)

Table 13.7 (continued)

λ (nm)	n	λ (nm)	n	λ (nm)	n	λ (nm)	n
355	1.5747	570	1.5538	830	1.5463	1090	1.5423
360	1.5737	580	1.5534	840	1.5461	1100	1.5422
365	1.5728	590	1.5529	850	1.5459	1110	1.5421
370	1.5719	600	1.5525	860	1.5457	1120	1.5419
375	1.5711	610	1.5521	870	1.5456	1130	1.5418
380	1.5703	620	1.5518	880	1.5454	1140	1.5417
385	1.5695	630	1.5514	890	1.5452	1150	1.5415
390	1.5688	640	1.5510	900	1.5450	1160	1.5414
395	1.5681	650	1.5507	910	1.5449	1170	1.5413
400	1.5674	660	1.5504	920	1.5447	1180	1.5412
410	1.5661	670	1.5501	930	1.5446	1190	1.5410
420	1.5649	680	1.5498	940	1.5444	1200	1.5409
430	1.5638	690	1.5495	950	1.5443		
440	1.5627	700	1.5492	960	1.5441		
450	1.5618	710	1.5489	970	1.5440		

13.2.2 Stainless Steel (SUS304)

Data: unpublished results of T. Fujiseki. The optical data have been extracted from a mirror-polished stainless substrate (SUS304). No particular surface treatment of the sample was made before the ellipsometry measurement (Fig. 13.2, Tables 13.8 and 13.9).

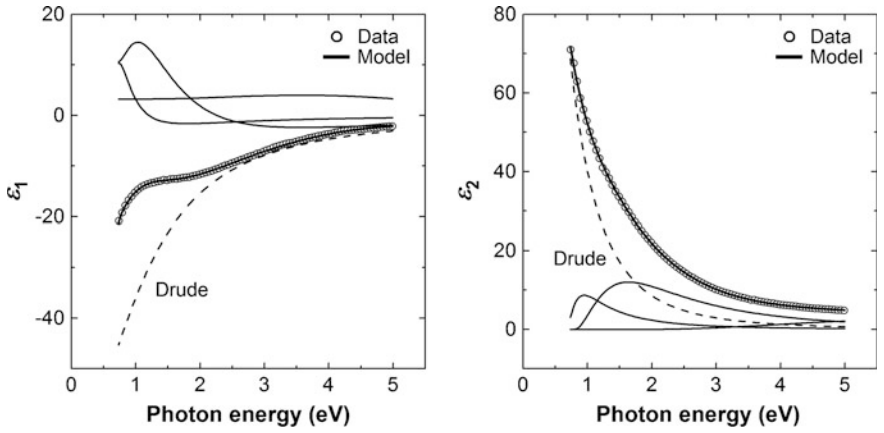


Fig. 13.2 Dielectric function of stainless steel at room temperature. The open circles show the experimental data and the solid lines indicate the calculation result obtained from the parameterization assuming the Tauc-Lorentz and Drude models expressed by (11.1) and (11.2)

Table 13.8 Tauc-Lorentz and Drude parameters for stainless steel

Model	A/A_D (ΓL)	C/Γ (eV)	E_0 (eV)	E_g (eV)	$\varepsilon_1(\infty)$
TL peak1	132.086	0.392	0.660	0.656	1.816
TL peak2	172.262	1.967	1.068	0.805	0
TL peak3	29.284	5.569	5.695	1.935	0
Drude	80.655	1.114	–	–	–

Table 13.9 Optical constants of stainless steel calculated by the Tauc-Lorentz and Drude models

λ (nm)	n	k	λ (nm)	n	k	λ (nm)	n	k
300	1.323	2.265	540	2.192	3.896	880	3.559	5.059
305	1.329	2.302	550	2.238	3.946	890	3.590	5.083
310	1.336	2.340	560	2.284	3.995	900	3.620	5.107
315	1.344	2.378	570	2.331	4.043	910	3.650	5.130
320	1.353	2.416	580	2.377	4.089	920	3.679	5.154
325	1.362	2.455	590	2.423	4.134	930	3.708	5.178
330	1.372	2.494	600	2.469	4.178	940	3.736	5.201
335	1.383	2.533	610	2.514	4.221	950	3.764	5.224
340	1.395	2.572	620	2.559	4.263	960	3.791	5.247
345	1.407	2.612	630	2.604	4.303	970	3.818	5.270
350	1.420	2.651	640	2.649	4.343	980	3.844	5.293
355	1.433	2.690	650	2.693	4.381	990	3.870	5.316
360	1.448	2.729	660	2.737	4.418	1000	3.896	5.339
365	1.463	2.767	670	2.780	4.454	1010	3.921	5.362
370	1.478	2.806	680	2.823	4.490	1020	3.946	5.385
375	1.494	2.844	690	2.866	4.524	1030	3.971	5.408
380	1.511	2.882	700	2.907	4.558	1040	3.995	5.431
385	1.528	2.919	710	2.949	4.590	1050	4.019	5.454
390	1.545	2.957	720	2.989	4.622	1060	4.042	5.477
395	1.563	2.994	730	3.029	4.653	1070	4.065	5.500
400	1.581	3.030	740	3.069	4.684	1080	4.088	5.523
410	1.619	3.102	750	3.108	4.714	1090	4.111	5.546
420	1.659	3.173	760	3.146	4.743	1100	4.133	5.569
430	1.699	3.242	770	3.184	4.772	1110	4.156	5.592
440	1.741	3.309	780	3.221	4.800	1120	4.177	5.616
450	1.784	3.375	790	3.257	4.828	1130	4.199	5.639
460	1.827	3.439	800	3.293	4.855	1140	4.221	5.662
470	1.871	3.502	810	3.328	4.882	1150	4.242	5.685
480	1.916	3.563	820	3.363	4.908	1160	4.263	5.709
490	1.961	3.622	830	3.397	4.934	1170	4.284	5.732
500	2.007	3.680	840	3.431	4.959	1180	4.305	5.755
510	2.053	3.736	850	3.464	4.985	1190	4.326	5.779
520	2.099	3.791	860	3.496	5.009	1200	4.346	5.802
530	2.145	3.844	870	3.528	5.034			

13.2.3 Polycarbonate

Data: unpublished results of J. N. Hilfiker. The optical data of a 3-mm-thick polycarbonate substrate have been extracted by analyzing three SE spectra measured at three different incident angles (55°, 65°, 75°) and a transmittance spectrum simultaneously (Fig. 13.3, Tables 13.10 and 13.11).

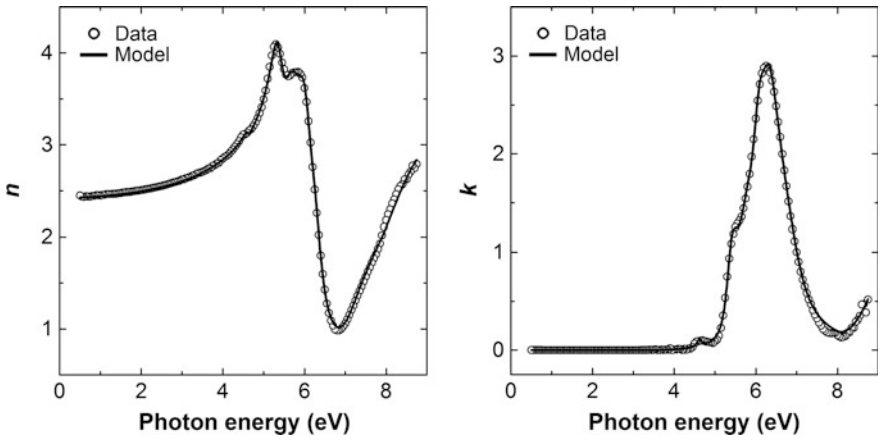


Fig. 13.3 Optical constants of polycarbonate at room temperature. The open circles show the experimental data and the solid lines indicate the calculation result obtained from the parameterization assuming the Tauc-Lorentz model [(8.1) and (8.2)]

Table 13.10 Tauc-Lorentz parameters of (8.1) and (8.2) for polycarbonate

Peak	A (eV)	C (eV)	E_0 (eV)	E_g (eV)	$\varepsilon_1(\infty)$
$j = 1$	4.01×10^{-5}	0.513	2.108	1.252	0.828
$j = 2$	3.03×10^{-4}	0.490	3.693	1.717	0
$j = 3$	3.022	0.150	4.606	3.935	0
$j = 4$	170.307	0.333	5.378	4.791	0
$j = 5$	14.504	0.528	5.771	3.099	0
$j = 6$	26.397	0.419	6.053	3.499	0
$j = 7$	12.430	0.409	6.280	3.500	0
$j = 8$	885.063	2.927	9.052	7.963	0

Table 13.11 Optical constants of polycarbonate calculated by the Tauc-Lorentz model

λ (nm)	n	k	λ (nm)	n	k	λ (nm)	n	k
300	2.896	1.15×10^{-2}	540	2.527	2.19×10^{-6}	880	2.465	0
305	2.870	9.34×10^{-3}	550	2.524	2.38×10^{-6}	890	2.465	0
310	2.846	7.56×10^{-3}	560	2.520	2.55×10^{-6}	900	2.464	0
315	2.824	6.10×10^{-3}	570	2.517	2.67×10^{-6}	910	2.463	0
320	2.805	4.90×10^{-3}	580	2.513	2.71×10^{-6}	920	2.462	0
325	2.786	3.90×10^{-3}	590	2.510	2.64×10^{-6}	930	2.462	0
330	2.770	3.08×10^{-3}	600	2.507	2.48×10^{-6}	940	2.461	0
335	2.755	2.40×10^{-3}	610	2.505	2.25×10^{-6}	950	2.460	0
340	2.740	1.86×10^{-3}	620	2.502	1.98×10^{-6}	960	2.460	0
345	2.727	1.42×10^{-3}	630	2.500	1.72×10^{-6}	970	2.459	0
350	2.715	1.08×10^{-3}	640	2.497	1.46×10^{-6}	980	2.459	0
355	2.704	8.26×10^{-4}	650	2.495	1.24×10^{-6}	990	2.458	0
360	2.693	6.27×10^{-4}	660	2.493	1.04×10^{-6}	1000	2.458	0
365	2.683	4.63×10^{-4}	670	2.491	8.78×10^{-7}	1010	2.457	0
370	2.674	3.29×10^{-4}	680	2.489	7.39×10^{-7}	1020	2.457	0
375	2.665	2.22×10^{-4}	690	2.488	6.23×10^{-7}	1030	2.456	0
380	2.657	1.39×10^{-4}	700	2.486	5.26×10^{-7}	1040	2.456	0
385	2.649	7.79×10^{-5}	710	2.484	4.45×10^{-7}	1050	2.455	0
390	2.642	3.61×10^{-5}	720	2.483	3.78×10^{-7}	1060	2.455	0
395	2.635	1.20×10^{-5}	730	2.481	3.22×10^{-7}	1070	2.454	0
400	2.628	3.78×10^{-6}	740	2.48	2.74×10^{-7}	1080	2.454	0
410	2.616	3.00×10^{-6}	750	2.479	2.34×10^{-7}	1090	2.453	0
420	2.605	2.46×10^{-6}	760	2.477	2.00×10^{-7}	1100	2.453	0
430	2.595	2.09×10^{-6}	770	2.476	1.70×10^{-7}	1110	2.453	0
440	2.586	1.84×10^{-6}	780	2.475	1.44×10^{-7}	1120	2.452	0
450	2.578	1.66×10^{-6}	790	2.474	1.23×10^{-7}	1130	2.452	0
460	2.570	1.55×10^{-6}	800	2.473	1.05×10^{-7}	1140	2.451	0
470	2.564	1.50×10^{-6}	810	2.472	0	1150	2.451	0
480	2.557	1.49×10^{-6}	820	2.471	0	1160	2.451	0
490	2.551	1.52×10^{-6}	830	2.470	0	1170	2.450	0
500	2.546	1.58×10^{-6}	840	2.469	0	1180	2.450	0
510	2.541	1.69×10^{-6}	850	2.468	0	1190	2.450	0
520	2.536	1.83×10^{-6}	860	2.467	0	1200	2.450	0
530	2.532	2.00×10^{-6}	870	2.466	0			

13.2.4 PEN [Poly(Ethylene Naphthalate)]

Data from N. Hong, R. A. Synowicki, and J. N. Hilfiker [5]. The biaxial optical anisotropy of a PEN substrate (DuPont Teijin Films) has been characterized by Mueller-matrix SE in reflection and transmission modes. Full SE data sets obtained at different incident and sample rotation angles were analyzed to extract the optical data. The biaxial material has different optical constants for polarizations along the x, y, and z axes: i.e., $N_x = n_x - ik_x$, $N_y = n_y - ik_y$, and $N_z = n_z - ik_z$. For the z direction, however, only the non-absorbing region has been characterized assuming $k_z = 0$. In the case of a PEN substrate, the light absorption in the substrate can be estimated as an average of k_x and k_y, as the electric fields of incident light can be decomposed into the components parallel to the x and y axes (see also Fig. 13.4b) (Tables 13.12, 13.13, 13.14, 13.15, 13.16 and 13.17).

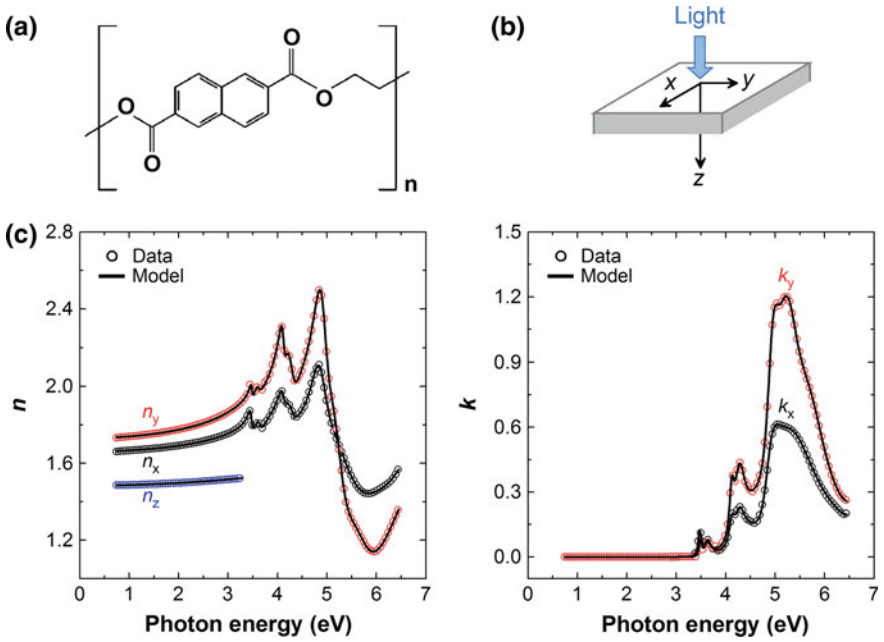


Fig. 13.4 **a** Chemical structure, **b** coordinate system, and **c** room-temperature optical constants of PEN. For the light polarization along the x, y, and z axes in **b**, the optical constants are defined by $N_x = n_x - ik_x$, $N_y = n_y - ik_y$ and $N_z = n_z - ik_z$. For the k spectra, only the in-plane components are shown. In **c**, the open circles show the experimental data and the solid lines indicate the calculation results obtained from the parameterization assuming the Tauc-Lorentz model expressed by (8.1) and (8.2). For the refractive index spectrum of n_z, however, the Sellmeier model expressed by (13.1) was applied

Table 13.12 Tauc-Lorentz parameters of (8.1) and (8.2) for $\varepsilon_x = (N_x)^2$ of PEN

Peak	A (eV)	C (eV)	E_0 (eV)	E_g (eV)	$\varepsilon_1(\infty)$
$j = 1$	4.630	8.58×10^{-2}	3.467	3.169	1.741
$j = 2$	0.468	0.132	3.635	2.742	0
$j = 3$	1.446	0.136	4.116	3.269	0
$j = 4$	4.053	0.249	4.266	3.497	0
$j = 5$	3.593	0.889	4.504	3.404	0
$j = 6$	97.800	0.375	4.868	4.533	0
$j = 7$	4.202	0.954	5.317	2.831	0
$j = 8$	205.741	2.240	6.301	6.301	0

Table 13.13 Tauc-Lorentz parameters of (8.1) and (8.2) for $\varepsilon_y = (N_y)^2$ of PEN

Peak	A (eV)	C (eV)	E_0 (eV)	E_g (eV)	$\varepsilon_1(\infty)$
$j = 1$	6.379	6.58×10^{-2}	3.477	3.284	1.936
$j = 2$	10.167	0.132	3.605	3.423	0
$j = 3$	0.734	0.116	4.116	2.414	0
$j = 4$	14.971	0.248	4.257	3.634	0
$j = 5$	5.572	0.711	4.569	3.320	0
$j = 6$	49.304	0.304	4.921	4.214	0
$j = 7$	8.273	0.475	5.193	3.323	0
$j = 8$	2.092	0.764	5.646	2.658	0
$j = 9$	71.440	1.278	7.060	6.084	0

Table 13.14 Sellmeier parameters of (13.1) for n_z of PEN

Material	B_1	B_2	B_3	C_1 (μm^2)	C_2 (μm^2)	C_3 (μm^2)
PEN	1.202	0.207	–	1.28×10^{-2}	604.127	–

Table 13.15 Optical constants of $N_x = n_x - ik_x$ for PEN reported by Hong et al.

λ (nm)	n_x	k_x	λ (nm)	n_x	k_x	λ (nm)	n_x	k_x
300	1.932	0.202	540	1.705	1.08×10^{-4}	880	1.675	5.4×10^{-5}
305	1.976	0.121	550	1.703	1.04×10^{-4}	890	1.675	5.4×10^{-5}
310	1.932	6.54×10^{-2}	560	1.701	1.01×10^{-4}	900	1.674	5.3×10^{-5}
315	1.898	4.41×10^{-2}	570	1.699	9.8×10^{-5}	910	1.674	5.2×10^{-5}
320	1.865	2.99×10^{-2}	580	1.698	9.5×10^{-5}	920	1.674	5.1×10^{-5}
325	1.832	3.20×10^{-2}	590	1.696	9.2×10^{-5}	930	1.673	5.1×10^{-5}
330	1.817	3.90×10^{-2}	600	1.695	9.0×10^{-5}	940	1.673	5.0×10^{-5}
335	1.788	4.74×10^{-2}	610	1.694	8.8×10^{-5}	950	1.673	5.0×10^{-5}
340	1.802	8.09×10^{-2}	620	1.692	8.6×10^{-5}	960	1.672	4.9×10^{-5}

(continued)

Table 13.15 (continued)

λ (nm)	n_x	k_x	λ (nm)	n_x	k_x	λ (nm)	n_x	k_x
345	1.809	6.78×10^{-2}	630	1.691	8.4×10^{-5}	970	1.672	4.8×10^{-5}
350	1.800	5.58×10^{-2}	640	1.690	8.2×10^{-5}	980	1.672	4.8×10^{-5}
355	1.794	0.11	650	1.689	8.0×10^{-5}	990	1.672	4.7×10^{-5}
360	1.872	8.02×10^{-2}	660	1.688	7.8×10^{-5}	1000	1.671	4.7×10^{-5}
365	1.853	2.16×10^{-2}	670	1.687	7.7×10^{-5}	1010	1.671	4.6×10^{-5}
370	1.827	7.68×10^{-3}	680	1.686	7.5×10^{-5}	1020	1.671	4.6×10^{-5}
375	1.810	2.66×10^{-3}	690	1.685	7.4×10^{-5}	1030	1.671	4.5×10^{-5}
380	1.797	1.06×10^{-3}	700	1.685	7.2×10^{-5}	1040	1.670	4.5×10^{-5}
385	1.787	6.97×10^{-4}	710	1.684	7.1×10^{-5}	1050	1.670	4.4×10^{-5}
390	1.779	5.82×10^{-4}	720	1.683	7.0×10^{-5}	1060	1.670	4.4×10^{-5}
395	1.773	5.07×10^{-4}	730	1.683	6.8×10^{-5}	1070	1.670	4.3×10^{-5}
400	1.767	4.47×10^{-4}	740	1.682	6.7×10^{-5}	1080	1.670	4.3×10^{-5}
410	1.758	3.55×10^{-4}	750	1.681	6.6×10^{-5}	1090	1.669	4.2×10^{-5}
420	1.750	2.90×10^{-4}	760	1.681	6.5×10^{-5}	1100	1.669	4.2×10^{-5}
430	1.743	2.45×10^{-4}	770	1.680	6.4×10^{-5}	1110	1.669	4.1×10^{-5}
440	1.737	2.12×10^{-4}	780	1.680	6.3×10^{-5}	1120	1.669	4.1×10^{-5}
450	1.732	1.87×10^{-4}	790	1.679	6.2×10^{-5}	1130	1.669	4.1×10^{-5}
460	1.728	1.69×10^{-4}	800	1.678	6.1×10^{-5}	1140	1.668	4.0×10^{-5}
470	1.724	1.55×10^{-4}	810	1.678	6.0×10^{-5}	1150	1.668	4.0×10^{-5}
480	1.720	1.44×10^{-4}	820	1.678	5.9×10^{-5}	1160	1.668	3.9×10^{-5}
490	1.717	1.35×10^{-4}	830	1.677	5.8×10^{-5}	1170	1.668	3.9×10^{-5}
500	1.714	1.28×10^{-4}	840	1.677	5.7×10^{-5}	1180	1.668	3.9×10^{-5}
510	1.712	1.21×10^{-4}	850	1.676	5.7×10^{-5}	1190	1.667	3.8×10^{-5}
520	1.709	1.16×10^{-4}	860	1.676	5.6×10^{-5}	1200	1.667	3.8×10^{-5}
530	1.707	1.12×10^{-4}	870	1.675	5.5×10^{-5}			

Table 13.16 Optical constants of $N_y = n_y - ik_y$ for PEN reported by Hong et al.

λ (nm)	n_y	k_y	λ (nm)	n_y	k_y	λ (nm)	n_y	k_y
300	2.203	0.381	540	1.794	2.11×10^{-4}	880	1.751	8.8×10^{-5}
305	2.308	0.21	550	1.791	2.03×10^{-4}	890	1.750	8.7×10^{-5}
310	2.215	0.105	560	1.789	1.95×10^{-4}	900	1.750	8.6×10^{-5}
315	2.154	6.61×10^{-2}	570	1.786	1.87×10^{-4}	910	1.749	8.4×10^{-5}
320	2.098	4.10×10^{-2}	580	1.784	1.80×10^{-4}	920	1.749	8.3×10^{-5}
325	2.044	4.17×10^{-2}	590	1.782	1.74×10^{-4}	930	1.749	8.2×10^{-5}
330	2.029	4.78×10^{-2}	600	1.780	1.68×10^{-4}	940	1.748	8.1×10^{-5}
335	1.984	4.86×10^{-2}	610	1.778	1.63×10^{-4}	950	1.748	7.9×10^{-5}
340	1.991	6.40×10^{-2}	620	1.776	1.58×10^{-4}	960	1.747	7.8×10^{-5}

(continued)

Table 13.16 (continued)

λ (nm)	n_y	k_y	λ (nm)	n_y	k_y	λ (nm)	n_y	k_y
345	1.995	6.53×10^{-2}	630	1.774	1.53×10^{-4}	970	1.747	7.7×10^{-5}
350	1.976	3.39×10^{-2}	640	1.773	1.48×10^{-4}	980	1.746	7.6×10^{-5}
355	1.971	7.92×10^{-2}	650	1.771	1.44×10^{-4}	990	1.746	7.5×10^{-5}
360	2.013	3.40×10^{-2}	660	1.770	1.40×10^{-4}	1000	1.746	7.4×10^{-5}
365	1.965	1.85×10^{-3}	670	1.768	1.36×10^{-4}	1010	1.745	7.3×10^{-5}
370	1.943	1.47×10^{-3}	680	1.767	1.33×10^{-4}	1020	1.745	7.2×10^{-5}
375	1.928	1.21×10^{-3}	690	1.766	1.29×10^{-4}	1030	1.745	7.1×10^{-5}
380	1.916	1.02×10^{-3}	700	1.765	1.26×10^{-4}	1040	1.744	7.0×10^{-5}
385	1.906	8.74×10^{-4}	710	1.764	1.23×10^{-4}	1050	1.744	7.0×10^{-5}
390	1.897	7.66×10^{-4}	720	1.763	1.20×10^{-4}	1060	1.744	6.9×10^{-5}
395	1.889	6.82×10^{-4}	730	1.762	1.18×10^{-4}	1070	1.743	6.8×10^{-5}
400	1.882	6.17×10^{-4}	740	1.761	1.15×10^{-4}	1080	1.743	6.7×10^{-5}
410	1.870	5.23×10^{-4}	750	1.760	1.13×10^{-4}	1090	1.743	6.6×10^{-5}
420	1.859	4.60×10^{-4}	760	1.759	1.10×10^{-4}	1100	1.743	6.6×10^{-5}
430	1.850	4.14×10^{-4}	770	1.758	1.08×10^{-4}	1110	1.742	6.5×10^{-5}
440	1.841	3.78×10^{-4}	780	1.757	1.06×10^{-4}	1120	1.742	6.4×10^{-5}
450	1.834	3.49×10^{-4}	790	1.757	1.04×10^{-4}	1130	1.742	6.3×10^{-5}
460	1.828	3.25×10^{-4}	800	1.756	1.02×10^{-4}	1140	1.741	6.3×10^{-5}
470	1.822	3.04×10^{-4}	810	1.755	1.00×10^{-4}	1150	1.741	6.2×10^{-5}
480	1.817	2.86×10^{-4}	820	1.755	9.8×10^{-5}	1160	1.741	6.1×10^{-5}
490	1.812	2.70×10^{-4}	830	1.754	9.6×10^{-5}	1170	1.741	6.1×10^{-5}
500	1.808	2.56×10^{-4}	840	1.753	9.5×10^{-5}	1180	1.740	6.0×10^{-5}
510	1.804	2.43×10^{-4}	850	1.753	9.3×10^{-5}	1190	1.740	5.9×10^{-5}
520	1.800	2.31×10^{-4}	860	1.752	9.1×10^{-5}	1200	1.740	5.9×10^{-5}
530	1.797	2.21×10^{-4}	870	1.752	9.0×10^{-5}			

Table 13.17 Refractive index of n_z for PEN reported by Hong et al. ($k = 0$)

λ (nm)	n_z	λ (nm)	n_z	λ (nm)	n_z	λ (nm)	n_z
380	1.5223	580	1.4996	800	1.4918	1020	1.4886
385	1.5213	590	1.4990	810	1.4916	1030	1.4885
390	1.5202	600	1.4985	820	1.4914	1040	1.4884
395	1.5193	610	1.4980	830	1.4912	1050	1.4883
400	1.5183	620	1.4975	840	1.4911	1060	1.4882
410	1.5166	630	1.4971	850	1.4909	1070	1.4881
420	1.5149	640	1.4967	860	1.4907	1080	1.4880
430	1.5134	650	1.4962	870	1.4905	1090	1.4879
440	1.5120	660	1.4959	880	1.4904	1100	1.4879
450	1.5107	670	1.4955	890	1.4902	1110	1.4878

(continued)

Table 13.17 (continued)

λ (nm)	n_z	λ (nm)	n_z	λ (nm)	n_z	λ (nm)	n_z
460	1.5095	680	1.4951	900	1.4901	1120	1.4877
470	1.5084	690	1.4948	910	1.4899	1130	1.4876
480	1.5073	700	1.4945	920	1.4898	1140	1.4876
490	1.5063	710	1.4941	930	1.4896	1150	1.4875
500	1.5054	720	1.4938	940	1.4895	1160	1.4874
510	1.5045	730	1.4936	950	1.4894	1170	1.4874
520	1.5037	740	1.4933	960	1.4893	1180	1.4873
530	1.5029	750	1.4930	970	1.4891	1190	1.4872
540	1.5022	760	1.4928	980	1.4890	1200	1.4872
550	1.5015	770	1.4925	990	1.4889		
560	1.5008	780	1.4923	1000	1.4888		
570	1.5002	790	1.4921	1010	1.4887		

13.2.5 PET [Poly(Ethylene Terephthalate)]

Data from N. Hong, R. A. Synowicki, and J. N. Hilfiker [5]. The biaxial optical anisotropy of a 50-μm-thick PET substrate (DuPont Teijin Films) has been characterized by Mueller-matrix SE in reflection and transmission modes. Full SE data sets obtained at different incident and sample rotation angles were analyzed to extract the optical data. The biaxial material has different optical constants for polarizations along the x, y, and z axes: i.e., $N_x = n_x - ik_x$, $N_y = n_y - ik_y$, and $N_z = n_z - ik_z$. For the z direction, however, only the non-absorbing region has been characterized assuming $k_z = 0$. In the case of a PET substrate, the light absorption in the substrate can be estimated as an average of k_x and k_y, as the electric fields of incident light can be decomposed into the components parallel to the x and y axes (see also Fig. 13.5b) (Tables 13.18, 13.19, 13.20, 13.21, 13.22 and 13.23).

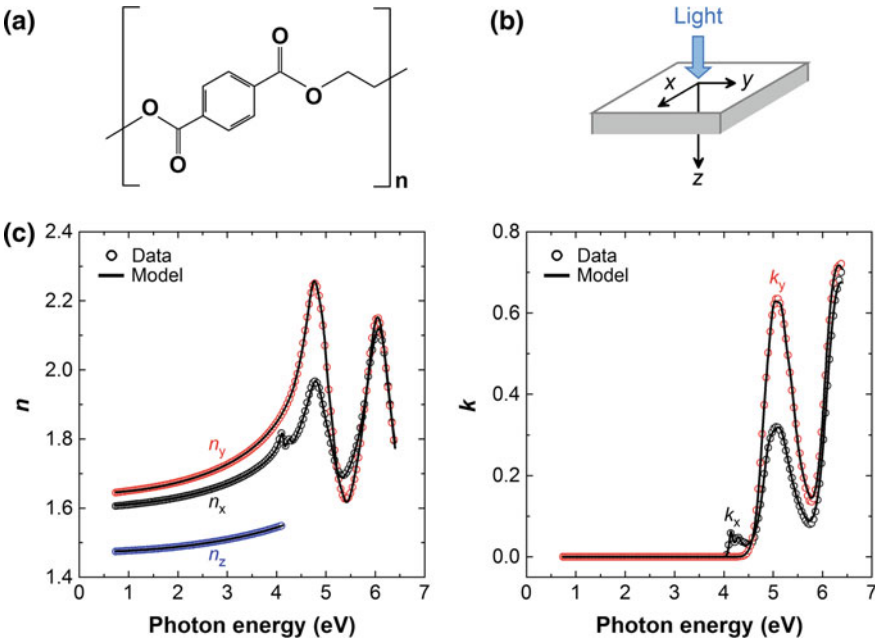


Fig. 13.5 **a** Chemical structure, **b** coordinate system, and **c** room-temperature optical constants of PET. For the light polarization along the x, y, and z axes in **b**, the optical constants are defined by $N_x = n_x - ik_x$, $N_y = n_y - ik_y$ and $N_z = n_z - ik_z$. For the k spectra, only the in-plane components are shown. In **c**, the open circles show the experimental data and the solid lines indicate the calculation results obtained from the parameterization assuming the Tauc-Lorentz model expressed by (8.1) and (8.2). For the refractive index spectrum of n_z, however, the Sellmeier model expressed by (13.1) was applied

Table 13.18 Tauc-Lorentz parameters of (8.1) and (8.2) for $\varepsilon_x = (N_x)^2$ of PET

Peak	A (eV)	C (eV)	E_0 (eV)	E_g (eV)	$\varepsilon_1(\infty)$
$j = 1$	0.295	5.03×10^{-2}	4.090	3.796	9.81×10^{-2}
$j = 2$	13.827	7.41×10^{-2}	4.133	3.999	0
$j = 3$	3.754	0.136	4.280	3.999	0
$j = 4$	13.448	0.378	4.871	4.177	0
$j = 5$	6.856	0.489	5.116	3.994	0
$j = 6$	187.902	0.627	6.126	5.654	0
$j = 7$	208.764	6.05×10^{-2}	16.633	10.135	0

Table 13.19 Tauc-Lorentz parameters of (8.1) and (8.2) for $\varepsilon_y = (N_y)^2$ of PET

Peak	A (eV)	C (eV)	E_0 (eV)	E_g (eV)	$\varepsilon_1(\infty)$
$j = 1$	5.75×10^{-3}	0.133	4.258	3.991	1.368
$j = 2$	1.41×10^{-2}	7.66×10^{-2}	4.309	3.953	0
$j = 3$	37.036	0.343	4.808	4.293	0
$j = 4$	19.367	0.294	4.982	4.300	0
$j = 5$	8.444	0.285	5.152	4.300	0
$j = 6$	2.571	0.278	5.341	4.299	0
$j = 7$	261.342	0.576	6.069	5.702	0
$j = 8$	231.353	9.52×10^{-2}	8.982	7.661	0

Table 13.20 Sellmeier parameters of (13.1) for n_z of PET

Material	B_1	B_2	B_3	C_1 (μm^2)	C_2 (μm^2)	C_3 (μm^2)
PET	0.888	0.282	–	9.18×10^{-3}	2.87×10^{-2}	–

Table 13.21 Optical constants of $N_x = n_x - \mathrm{i}k_x$ for PET reported by Hong et al.

λ (nm)	n_x	k_x	λ (nm)	n_x	k_x	λ (nm)	n_x	k_x
300	1.806	5.65×10^{-2}	540	1.640	0	880	1.617	0
305	1.802	6.61×10^{-3}	550	1.638	0	890	1.616	0
310	1.775	3.00×10^{-4}	560	1.637	0	900	1.616	0
315	1.760	5.3×10^{-5}	570	1.636	0	910	1.616	0
320	1.749	9×10^{-6}	580	1.635	0	920	1.615	0
325	1.740	2×10^{-6}	590	1.633	0	930	1.615	0
330	1.733	0	600	1.632	0	940	1.615	0
335	1.726	0	610	1.631	0	950	1.615	0
340	1.720	0	620	1.630	0	960	1.614	0
345	1.715	0	630	1.630	0	970	1.614	0
350	1.710	0	640	1.629	0	980	1.614	0
355	1.705	0	650	1.628	0	990	1.614	0
360	1.701	0	660	1.627	0	1000	1.614	0
365	1.698	0	670	1.626	0	1010	1.613	0
370	1.694	0	680	1.626	0	1020	1.613	0
375	1.691	0	690	1.625	0	1030	1.613	0
380	1.688	0	700	1.624	0	1040	1.613	0
385	1.685	0	710	1.624	0	1050	1.613	0
390	1.682	0	720	1.623	0	1060	1.612	0
395	1.679	0	730	1.623	0	1070	1.612	0
400	1.677	0	740	1.622	0	1080	1.612	0
410	1.672	0	750	1.622	0	1090	1.612	0
420	1.668	0	760	1.621	0	1100	1.612	0

(continued)

Table 13.21 (continued)

λ (nm)	n_x	k_x	λ (nm)	n_x	k_x	λ (nm)	n_x	k_x
430	1.665	0	770	1.621	0	1110	1.612	0
440	1.661	0	780	1.620	0	1120	1.611	0
450	1.658	0	790	1.620	0	1130	1.611	0
460	1.656	0	800	1.619	0	1140	1.611	0
470	1.653	0	810	1.619	0	1150	1.611	0
480	1.651	0	820	1.619	0	1160	1.611	0
490	1.649	0	830	1.618	0	1170	1.611	0
500	1.647	0	840	1.618	0	1180	1.610	0
510	1.645	0	850	1.618	0	1190	1.610	0
520	1.643	0	860	1.617	0	1200	1.610	0
530	1.641	0	870	1.617	0			

Table 13.22 Optical constants of $N_y = n_y - ik_y$ for PET reported by Hong et al.

λ (nm)	n_y	k_y	λ (nm)	n_y	k_y	λ (nm)	n_y	k_y
300	1.878	7×10^{-6}	540	1.687	0	880	1.658	0
305	1.861	1×10^{-6}	550	1.685	0	890	1.658	0
310	1.847	0	560	1.683	0	900	1.657	0
315	1.834	0	570	1.682	0	910	1.657	0
320	1.823	0	580	1.680	0	920	1.657	0
325	1.813	0	590	1.679	0	930	1.656	0
330	1.804	0	600	1.678	0	940	1.656	0
335	1.796	0	610	1.676	0	950	1.656	0
340	1.789	0	620	1.675	0	960	1.656	0
345	1.782	0	630	1.674	0	970	1.655	0
350	1.776	0	640	1.673	0	980	1.655	0
355	1.771	0	650	1.672	0	990	1.655	0
360	1.765	0	660	1.671	0	1000	1.654	0
365	1.760	0	670	1.670	0	1010	1.654	0
370	1.756	0	680	1.669	0	1020	1.654	0
375	1.752	0	690	1.669	0	1030	1.654	0
380	1.748	0	700	1.668	0	1040	1.653	0
385	1.744	0	710	1.667	0	1050	1.653	0
390	1.740	0	720	1.666	0	1060	1.653	0
395	1.737	0	730	1.666	0	1070	1.653	0
400	1.734	0	740	1.665	0	1080	1.653	0
410	1.728	0	750	1.664	0	1090	1.652	0
420	1.723	0	760	1.664	0	1100	1.652	0

(continued)

Table 13.22 (continued)

λ (nm)	n_y	k_y	λ (nm)	n_y	k_y	λ (nm)	n_y	k_y
430	1.718	0	770	1.663	0	1110	1.652	0
440	1.714	0	780	1.663	0	1120	1.652	0
450	1.710	0	790	1.662	0	1130	1.652	0
460	1.707	0	800	1.662	0	1140	1.651	0
470	1.703	0	810	1.661	0	1150	1.651	0
480	1.700	0	820	1.661	0	1160	1.651	0
490	1.698	0	830	1.660	0	1170	1.651	0
500	1.695	0	840	1.660	0	1180	1.651	0
510	1.693	0	850	1.659	0	1190	1.651	0
520	1.691	0	860	1.659	0	1200	1.650	0
530	1.689	0	870	1.659	0			

Table 13.23 Refractive index of n_z for PET reported by Hong et al. ($k = 0$)

λ (nm)	n_z	λ (nm)	n_z	λ (nm)	n_z	λ (nm)	n_z
300	1.5500	460	1.5015	720	1.4841	980	1.4789
305	1.5468	470	1.5001	730	1.4837	990	1.4788
310	1.5439	480	1.4989	740	1.4834	1000	1.4787
315	1.5411	490	1.4978	750	1.4832	1010	1.4786
320	1.5386	500	1.4967	760	1.4829	1020	1.4785
325	1.5361	510	1.4958	770	1.4826	1030	1.4784
330	1.5338	520	1.4948	780	1.4824	1040	1.4783
335	1.5317	530	1.4940	790	1.4821	1050	1.4782
340	1.5296	540	1.4931	800	1.4819	1060	1.4781
345	1.5277	550	1.4924	810	1.4817	1070	1.4780
350	1.5258	560	1.4916	820	1.4815	1080	1.4779
355	1.5241	570	1.4910	830	1.4813	1090	1.4778
360	1.5225	580	1.4903	840	1.4811	1100	1.4777
365	1.5209	590	1.4897	850	1.4809	1110	1.4776
370	1.5194	600	1.4891	860	1.4807	1120	1.4775
375	1.5180	610	1.4886	870	1.4805	1130	1.4775
380	1.5166	620	1.4881	880	1.4803	1140	1.4774
385	1.5153	630	1.4876	890	1.4802	1150	1.4773
390	1.5141	640	1.4871	900	1.4800	1160	1.4772
395	1.5129	650	1.4866	910	1.4799	1170	1.4772
400	1.5118	660	1.4862	920	1.4797	1180	1.4771
410	1.5097	670	1.4858	930	1.4796	1190	1.4770
420	1.5078	680	1.4854	940	1.4794	1200	1.4770
430	1.5060	690	1.4851	950	1.4793		
440	1.5044	700	1.4847	960	1.4792		
450	1.5029	710	1.4844	970	1.4790		

13.2.6 PMMA [Poly(Methyl Methacrylate)]

Data from N. Hong, R. A. Synowicki, and J. N. Hilfiker [5]. The optical data have been extracted from a commercial 130-μm-thick PMMA substrate (Plexiglas). The SE analysis has been performed assuming isotropic optical properties. The optical data of a PMMA thin film are shown in Fig. 9.14 (Fig. 13.6, Tables 13.24 and 13.25).

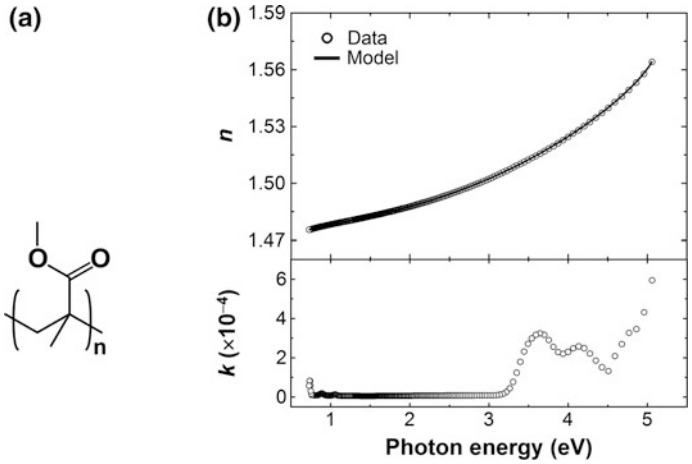


Fig. 13.6 **a** Chemical structure and **b** room-temperature optical constants of PMMA. The open circles show the reference data and the solid line indicates the refractive index spectrum calculated by the Sellmeier model of (13.1)

Table 13.24 Sellmeier parameters of (13.1) for PMMA

Material	B_1	B_2	B_3	C_1 (μm^2)	C_2 (μm^2)	C_3 (μm^2)
PMMA	1.179	2.56×10^{-3}	3.67×10^{-2}	1.02×10^{-2}	5.42×10^{-2}	14.528

Table 13.25 Optical constants of PMMA. The optical data reported by Hong et al. are shown

λ (nm)	n	k ($\times 10^{-4}$)	λ (nm)	n	k ($\times 10^{-4}$)	λ (nm)	n	k ($\times 10^{-4}$)
300	1.5281	2.57	540	1.4913	0.06	880	1.4817	0.04
305	1.5262	2.47	550	1.4907	0.06	890	1.4815	0.04
310	1.5244	2.29	560	1.4902	0.06	900	1.4814	0.04
315	1.5227	2.19	570	1.4897	0.06	910	1.4813	0.05
320	1.5211	2.28	580	1.4892	0.06	920	1.4811	0.05
325	1.5196	2.55	590	1.4888	0.06	930	1.4810	0.05

(continued)

Table 13.25 (continued)

λ (nm)	n	k ($\times 10^{-4}$)	λ (nm)	n	k ($\times 10^{-4}$)	λ (nm)	n	k ($\times 10^{-4}$)
330	1.5182	2.90	600	1.4884	0.06	940	1.4809	0.05
335	1.5168	3.16	610	1.4880	0.05	950	1.4808	0.05
340	1.5156	3.24	620	1.4876	0.05	960	1.4807	0.05
345	1.5144	3.16	630	1.4872	0.05	970	1.4805	0.05
350	1.5133	2.98	640	1.4869	0.05	980	1.4804	0.05
355	1.5122	2.71	650	1.4866	0.05	990	1.4803	0.05
360	1.5112	2.31	660	1.4862	0.05	1000	1.4802	0.05
365	1.5102	1.78	670	1.4859	0.05	1010	1.4801	0.05
370	1.5092	1.23	680	1.4857	0.05	1020	1.4800	0.05
375	1.5083	0.76	690	1.4854	0.05	1030	1.4799	0.05
380	1.5074	0.43	700	1.4851	0.05	1040	1.4798	0.05
385	1.5065	0.24	710	1.4849	0.05	1050	1.4797	0.05
390	1.5057	0.15	720	1.4846	0.05	1060	1.4796	0.05
395	1.5049	0.11	730	1.4844	0.05	1070	1.4795	0.05
400	1.5041	0.09	740	1.4842	0.05	1080	1.4794	0.05
410	1.5027	0.08	750	1.4839	0.05	1090	1.4794	0.05
420	1.5014	0.08	760	1.4837	0.05	1100	1.4793	0.05
430	1.5002	0.08	770	1.4835	0.05	1110	1.4792	0.06
440	1.4991	0.07	780	1.4833	0.05	1120	1.4791	0.06
450	1.4980	0.07	790	1.4831	0.05	1130	1.4790	0.06
460	1.4971	0.07	800	1.4830	0.04	1140	1.4789	0.08
470	1.4962	0.07	810	1.4828	0.04	1150	1.4788	0.09
480	1.4953	0.07	820	1.4826	0.04	1160	1.4788	0.11
490	1.4945	0.07	830	1.4824	0.04	1170	1.4787	0.13
500	1.4938	0.07	840	1.4823	0.04	1180	1.4786	0.13
510	1.4931	0.06	850	1.4821	0.04	1190	1.4785	0.12
520	1.4924	0.06	860	1.4820	0.04	1200	1.4785	0.10
530	1.4918	0.06	870	1.4818	0.04			

13.2.7 Polyimide

Data from M. Campoy-Quiles, J. Nelson, D. D. C. Bradley and P. G. Etchegoin [6]. The optical data have been extracted from a polyimide thin film prepared by a spin coating process. In this process, a precursor solution (polyamic acid) was coated onto a fused silica substrate, followed by thermal annealing. The SE analysis has been performed assuming isotropic optical properties (Fig. 13.7, Tables 13.26 and 13.27).

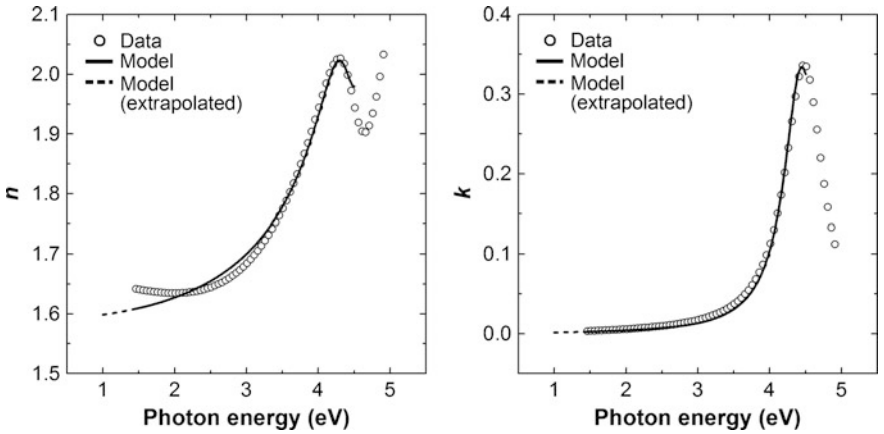


Fig. 13.7 Optical constants of polyimide at room temperature. The open circles show the reference data and the solid lines indicate the calculation result obtained from the parameterization assuming the Tauc-Lorentz model [(8.1) and (8.2)]

Table 13.26 Tauc-Lorentz parameters of (8.1) and (8.2) for polyimide

Peak	A (eV)	C (eV)	E_0 (eV)	E_g (eV)	$\varepsilon_1(\infty)$
$j = 1$	0.693	0.570	4.434	1×10^{-4}	1.947
$j = 2$	10.639	0.109	5.036	2.756	0

Table 13.27 Optical constants of polyimide calculated by the Tauc-Lorentz model

λ (nm)	n	k	λ (nm)	n	k	λ (nm)	n	k
300	1.985	0.159	540	1.642	5.86×10^{-3}	880	1.607	2.45×10^{-3}
305	1.957	0.128	550	1.640	5.62×10^{-3}	890	1.607	2.41×10^{-3}
310	1.930	0.104	560	1.638	5.40×10^{-3}	900	1.606	2.38×10^{-3}
315	1.905	8.63×10^{-2}	570	1.636	5.19×10^{-3}	910	1.606	2.34×10^{-3}
320	1.883	7.27×10^{-2}	580	1.634	5.00×10^{-3}	920	1.606	2.30×10^{-3}
325	1.862	6.22×10^{-2}	590	1.632	4.82×10^{-3}	930	1.605	2.27×10^{-3}
330	1.844	5.38×10^{-2}	600	1.630	4.66×10^{-3}	940	1.605	2.24×10^{-3}
335	1.828	4.72×10^{-2}	610	1.629	4.51×10^{-3}	950	1.605	2.20×10^{-3}
340	1.813	4.17×10^{-2}	620	1.627	4.36×10^{-3}	960	1.604	2.17×10^{-3}
345	1.800	3.72×10^{-2}	630	1.626	4.23×10^{-3}	970	1.604	2.14×10^{-3}
350	1.788	3.35×10^{-2}	640	1.625	4.11×10^{-3}	980	1.604	2.11×10^{-3}
355	1.777	3.03×10^{-2}	650	1.623	3.99×10^{-3}	990	1.603	2.09×10^{-3}
360	1.767	2.76×10^{-2}	660	1.622	3.88×10^{-3}	1000	1.603	2.06×10^{-3}
365	1.758	2.53×10^{-2}	670	1.621	3.78×10^{-3}	1010	1.603	2.03×10^{-3}
370	1.750	2.33×10^{-2}	680	1.620	3.68×10^{-3}	1020	1.603	2.01×10^{-3}

(continued)

Table 13.27 (continued)

λ (nm)	n	k	λ (nm)	n	k	λ (nm)	n	k
375	1.742	2.16×10^{-2}	690	1.619	3.59×10^{-3}	1030	1.602	1.98×10^{-3}
380	1.735	2.00×10^{-2}	700	1.618	3.50×10^{-3}	1040	1.602	1.96×10^{-3}
385	1.729	1.87×10^{-2}	710	1.617	3.41×10^{-3}	1050	1.602	1.93×10^{-3}
390	1.723	1.75×10^{-2}	720	1.616	3.34×10^{-3}	1060	1.602	1.91×10^{-3}
395	1.717	1.64×10^{-2}	730	1.616	3.26×10^{-3}	1070	1.601	1.89×10^{-3}
400	1.712	1.55×10^{-2}	740	1.615	3.19×10^{-3}	1080	1.601	1.86×10^{-3}
410	1.703	1.38×10^{-2}	750	1.614	3.12×10^{-3}	1090	1.601	1.84×10^{-3}
420	1.695	1.25×10^{-2}	760	1.614	3.05×10^{-3}	1100	1.601	1.82×10^{-3}
430	1.687	1.14×10^{-2}	770	1.613	2.99×10^{-3}	1110	1.601	1.80×10^{-3}
440	1.681	1.05×10^{-2}	780	1.612	2.93×10^{-3}	1120	1.600	1.78×10^{-3}
450	1.675	9.72×10^{-3}	790	1.612	2.88×10^{-3}	1130	1.600	1.76×10^{-3}
460	1.670	9.06×10^{-3}	800	1.611	2.82×10^{-3}	1140	1.600	1.74×10^{-3}
470	1.665	8.48×10^{-3}	810	1.610	2.77×10^{-3}	1150	1.600	1.72×10^{-3}
480	1.661	7.97×10^{-3}	820	1.610	2.72×10^{-3}	1160	1.600	1.70×10^{-3}
490	1.657	7.52×10^{-3}	830	1.609	2.67×10^{-3}	1170	1.600	1.69×10^{-3}
500	1.654	7.11×10^{-3}	840	1.609	2.62×10^{-3}	1180	1.599	1.67×10^{-3}
510	1.650	6.75×10^{-3}	850	1.608	2.58×10^{-3}	1190	1.599	1.65×10^{-3}
520	1.647	6.43×10^{-3}	860	1.608	2.53×10^{-3}	1200	1.599	1.63×10^{-3}
530	1.645	6.13×10^{-3}	870	1.608	2.49×10^{-3}			

13.2.8 Kapton HN [Poly{N,N'-(Oxydiphenylene) Pyromellitimide}]

Data from N. Hong, R. A. Synowicki, and J. N. Hilfiker [5]. Kapton HN (DuPont Teijin Films) is a polyimide-based compound (see Fig. 13.8a) and the biaxial optical anisotropy of a 50-μm-thick Kapton HN substrate has been characterized by Mueller-matrix SE in reflection and transmission modes. Full SE data sets obtained at different incident and sample rotation angles were analyzed to extract the optical data. The biaxial material has different optical constants for polarizations along the x, y, and z axes: i.e., $N_x = n_x - ik_x$, $N_y = n_y - ik_y$, and $N_z = n_z - ik_z$. For the z direction, however, only the non-absorbing region has been characterized assuming $k_z = 0$. In the case of a Kapton HN substrate, the light absorption in the substrate can be estimated as an average of k_x and k_y, as the electric fields of incident light can be decomposed into the components parallel to the x and y axes (see also Fig. 13.8b). The optical properties of a Kapton H film [7] are quite similar to those of the Kapton HN (Tables 13.28, 13.29, 13.30, 13.31, 13.32 and 13.33).

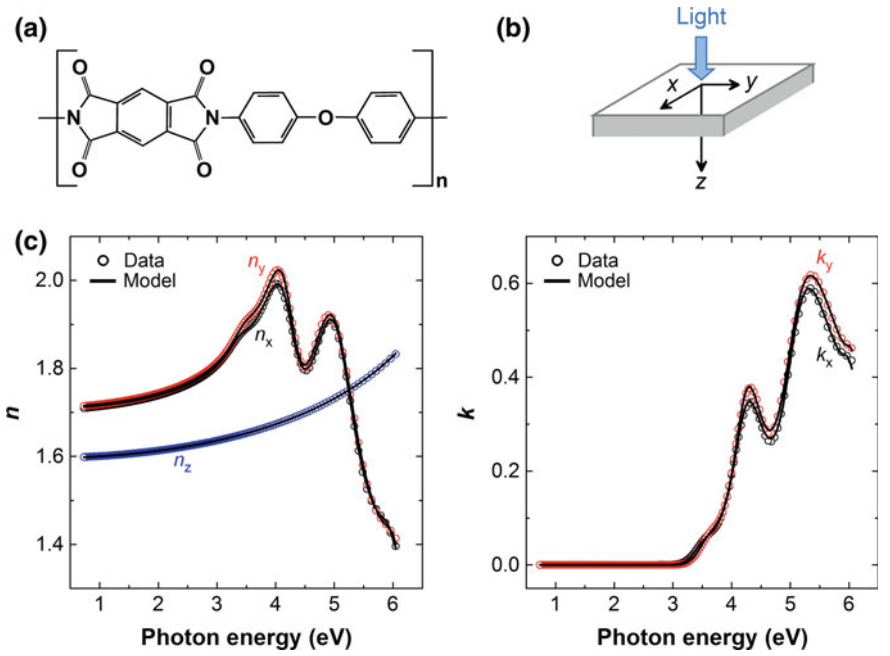


Fig. 13.8 **a** Chemical structure, **b** coordinate system, and **c** room-temperature optical constants of Kapton HN. For the light polarization along the x, y, and z axes in **b**, the optical constants are defined by $N_x = n_x - ik_x$, $N_y = n_y - ik_y$ and $N_z = n_z - ik_z$. For the k spectra, only the in-plane components are shown. In **c**, the open circles show the experimental data and the solid lines indicate the calculation results obtained from the parameterization assuming the Tauc-Lorentz model expressed by (8.1) and (8.2). For the refractive index spectrum of n_z, however, the Sellmeier model expressed by (13.1) was applied

Table 13.28 Tauc-Lorentz parameters of (8.1) and (8.2) for $\varepsilon_x = (N_x)^2$ of Kapton HN

Peak	A (eV)	C (eV)	E_0 (eV)	E_g (eV)	$\varepsilon_1(\infty)$
$j = 1$	6.16×10^{-2}	0.210	3.046	2.793	2.322
$j = 2$	4.77×10^{-2}	0.303	3.201	2.654	0
$j = 3$	4.912	0.600	3.440	3.007	0
$j = 4$	14.727	0.720	4.205	3.200	0
$j = 5$	60.075	0.888	5.059	4.338	0
$j = 6$	0.647	0.273	5.967	4.525	0

Table 13.29 Tauc-Lorentz parameters of (8.1) and (8.2) for $\varepsilon_y = (N_y)^2$ of Kapton HN

Peak	A (eV)	C (eV)	E_0 (eV)	E_g (eV)	$\varepsilon_1(\infty)$
$j = 1$	1.29×10^{-2}	0.162	3.053	2.727	2.283
$j = 2$	4.268	0.608	3.543	3.014	0
$j = 3$	13.826	0.645	4.216	3.175	0
$j = 4$	61.403	0.986	5.053	4.272	0
$j = 5$	2.757	0.240	6.006	5.425	0

Table 13.30 Sellmeier parameters of (13.1) for n_z of Kapton HN

Material	B_1	B_2	B_3	C_1 (μm^2)	C_2 (μm^2)	C_3 (μm^2)
Kapton HN	0.752	0.795	–	5.83×10^{-3}	1.96×10^{-2}	–

Table 13.31 Optical constants of $N_x = n_x - ik_x$ for Kapton HN reported by Hong et al.

λ (nm)	n_x	k_x	λ (nm)	n_x	k_x	λ (nm)	n_x	k_x
300	1.971	0.281	540	1.757	0	880	1.726	0
305	1.989	0.236	550	1.754	0	890	1.725	0
310	1.992	0.192	560	1.753	0	900	1.725	0
315	1.984	0.152	570	1.751	0	910	1.725	0
320	1.969	0.121	580	1.749	0	920	1.724	0
325	1.951	9.94×10^{-2}	590	1.747	0	930	1.724	0
330	1.934	8.50×10^{-2}	600	1.746	0	940	1.724	0
335	1.919	7.58×10^{-2}	610	1.745	0	950	1.724	0
340	1.909	6.91×10^{-2}	620	1.743	0	960	1.723	0
345	1.901	6.29×10^{-2}	630	1.742	0	970	1.723	0
350	1.895	5.60×10^{-2}	640	1.741	0	980	1.723	0
355	1.890	4.82×10^{-2}	650	1.740	0	990	1.722	0
360	1.884	3.98×10^{-2}	660	1.739	0	1000	1.722	0
365	1.877	3.16×10^{-2}	670	1.738	0	1010	1.722	0
370	1.869	2.40×10^{-2}	680	1.737	0	1020	1.722	0
375	1.861	1.76×10^{-2}	690	1.736	0	1030	1.722	0
380	1.853	1.24×10^{-2}	700	1.735	0	1040	1.721	0
385	1.844	8.40×10^{-3}	710	1.735	0	1050	1.721	0
390	1.836	5.52×10^{-3}	720	1.734	0	1060	1.721	0
395	1.829	3.52×10^{-3}	730	1.733	0	1070	1.721	0
400	1.822	2.18×10^{-3}	740	1.733	0	1080	1.721	0
410	1.810	7.78×10^{-4}	750	1.732	0	1090	1.720	0
420	1.801	2.55×10^{-4}	760	1.731	0	1100	1.720	0

(continued)

Table 13.31 (continued)

λ (nm)	n_x	k_x	λ (nm)	n_x	k_x	λ (nm)	n_x	k_x
430	1.793	7.8×10^{-5}	770	1.731	0	1110	1.720	0
440	1.787	2.2×10^{-5}	780	1.730	0	1120	1.720	0
450	1.781	6×10^{-6}	790	1.730	0	1130	1.720	0
460	1.776	2×10^{-6}	800	1.729	0	1140	1.719	0
470	1.772	0	810	1.729	0	1150	1.719	0
480	1.768	0	820	1.728	0	1160	1.719	0
490	1.764	0	830	1.728	0	1170	1.719	0
500	1.761	0	840	1.727	0	1180	1.719	0
510	1.758	0	850	1.727	0	1190	1.719	0
520	1.756	0	860	1.727	0	1200	1.719	0
530	1.753	0	870	1.726	0			

Table 13.32 Optical constants of $N_y = n_y - ik_y$ for Kapton HN reported by Hong et al.

λ (nm)	n_y	k_y	λ (nm)	n_y	k_y	λ (nm)	n_y	k_y
300	2.003	0.3	540	1.687	0	880	1.658	0
305	2.021	0.247	550	1.685	0	890	1.658	0
310	2.021	0.196	560	1.683	0	900	1.657	0
315	2.008	0.153	570	1.682	0	910	1.657	0
320	1.988	0.122	580	1.680	0	920	1.657	0
325	1.968	0.101	590	1.679	0	930	1.656	0
330	1.950	8.86×10^{-2}	600	1.678	0	940	1.656	0
335	1.938	7.99×10^{-2}	610	1.676	0	950	1.656	0
340	1.929	7.19×10^{-2}	620	1.675	0	960	1.656	0
345	1.922	6.29×10^{-2}	630	1.674	0	970	1.655	0
350	1.916	5.27×10^{-2}	640	1.673	0	980	1.655	0
355	1.908	4.21×10^{-2}	650	1.672	0	990	1.655	0
360	1.899	3.20×10^{-2}	660	1.671	0	1000	1.654	0
365	1.890	2.31×10^{-2}	670	1.670	0	1010	1.654	0
370	1.879	1.59×10^{-2}	680	1.669	0	1020	1.654	0
375	1.869	1.04×10^{-2}	690	1.669	0	1030	1.654	0
380	1.859	6.57×10^{-3}	700	1.668	0	1040	1.653	0
385	1.850	3.99×10^{-3}	710	1.667	0	1050	1.653	0
390	1.841	2.33×10^{-3}	720	1.666	0	1060	1.653	0
395	1.834	1.32×10^{-3}	730	1.666	0	1070	1.653	0
400	1.827	7.25×10^{-4}	740	1.665	0	1080	1.653	0
410	1.816	2.02×10^{-4}	750	1.664	0	1090	1.652	0
420	1.807	5.1×10^{-5}	760	1.664	0	1100	1.652	0

(continued)

Table 13.32 (continued)

λ (nm)	n_y	k_y	λ (nm)	n_y	k_y	λ (nm)	n_y	k_y
430	1.799	1.2×10^{-5}	770	1.663	0	1110	1.652	0
440	1.793	3×10^{-6}	780	1.663	0	1120	1.652	0
450	1.787	1×10^{-6}	790	1.662	0	1130	1.652	0
460	1.782	0	800	1.662	0	1140	1.651	0
470	1.778	0	810	1.661	0	1150	1.651	0
480	1.774	0	820	1.661	0	1160	1.651	0
490	1.770	0	830	1.660	0	1170	1.651	0
500	1.767	0	840	1.660	0	1180	1.651	0
510	1.764	0	850	1.659	0	1190	1.651	0
520	1.761	0	860	1.659	0	1200	1.650	0
530	1.759	0	870	1.659	0			

Table 13.33 Refractive index of n_z for Kapton HN reported by Hong et al. ($k = 0$)

λ (nm)	n_z	λ (nm)	n_z	λ (nm)	n_z	λ (nm)	n_z
300	1.6792	460	1.6276	720	1.6084	980	1.6027
305	1.6759	470	1.6262	730	1.6081	990	1.6026
310	1.6728	480	1.6248	740	1.6077	1000	1.6024
315	1.6700	490	1.6236	750	1.6074	1010	1.6023
320	1.6673	500	1.6224	760	1.6071	1020	1.6022
325	1.6647	510	1.6213	770	1.6068	1030	1.6021
330	1.6623	520	1.6203	780	1.6066	1040	1.6019
335	1.6600	530	1.6194	790	1.6063	1050	1.6018
340	1.6578	540	1.6185	800	1.6060	1060	1.6017
345	1.6558	550	1.6176	810	1.6058	1070	1.6016
350	1.6538	560	1.6168	820	1.6055	1080	1.6015
355	1.6520	570	1.6161	830	1.6053	1090	1.6014
360	1.6502	580	1.6154	840	1.6051	1100	1.6013
365	1.6486	590	1.6147	850	1.6049	1110	1.6012
370	1.6470	600	1.6140	860	1.6047	1120	1.6011
375	1.6455	610	1.6134	870	1.6045	1130	1.6011
380	1.6440	620	1.6129	880	1.6043	1140	1.6010
385	1.6426	630	1.6123	890	1.6041	1150	1.6009
390	1.6413	640	1.6118	900	1.6039	1160	1.6008
395	1.6400	650	1.6113	910	1.6037	1170	1.6007
400	1.6388	660	1.6108	920	1.6036	1180	1.6006
410	1.6366	670	1.6104	930	1.6034	1190	1.6006
420	1.6345	680	1.6099	940	1.6033	1200	1.6005
430	1.6325	690	1.6095	950	1.6031		
440	1.6308	700	1.6091	960	1.6030		
450	1.6291	710	1.6088	970	1.6028		

13.2.9 EVA [Ethylene Vinyl Acetate]

Data from

(i) K. R. McIntosh, G. Lau, J. N. Cotsell, K. Hanton, D. L. Bätzner, F. Bettiol and B. S. Richards [8],
(ii) K. R. McIntosh, J. N. Cotsell, J. S. Cumpston, A. W. NorrisN. E. Powell, and B. M. Ketola [9] (Fig. 13.9, Tables 13.34 and 13.35).

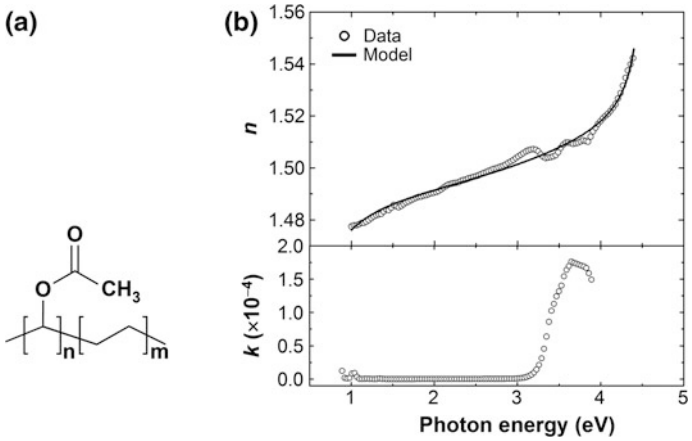


Fig. 13.9 **a** Chemical structure and **b** room-temperature optical constants of EVA. The open circles show the reference data and the solid line indicates the refractive index spectrum calculated by the Sellmeier model of (13.1)

Table 13.34 Sellmeier parameters of (13.1) for EVA

Material	B_1	B_2	B_3	C_1 (μm^2)	C_2 (μm^2)	C_3 (μm^2)
EVA	1.210	7.65×10^{-3}	16.358	4.84×10^{-3}	7.35×10^{-2}	580.829

Table 13.35 Refractive index of EVA calculated by the Sellmeier model. The extinction coefficient reported by McIntosh et al. is also shown

λ (nm)	n	k ($\times 10^{-5}$)	λ (nm)	n	k ($\times 10^{-5}$)	λ (nm)	n	k ($\times 10^{-5}$)
300	1.5225		540	1.4941	0.0243	880	1.4847	0.0146
305	1.5199		550	1.4937	0.0236	890	1.4844	0.0245
310	1.5179		560	1.4934	0.0230	900	1.4842	0.0337
315	1.5162		570	1.4930	0.0228	910	1.4840	0.0483
320	1.5147	15.3840	580	1.4926	0.0223	920	1.4837	0.0807

(continued)

Table 13.35 (continued)

λ (nm)	n	k ($\times 10^{-5}$)	λ (nm)	n	k ($\times 10^{-5}$)	λ (nm)	n	k ($\times 10^{-5}$)
325	1.5134	16.8150	590	1.4923	0.0216	930	1.4835	0.1038
330	1.5122	17.0840	600	1.4920	0.0210	940	1.4833	0.0661
335	1.5111	17.3430	610	1.4916	0.0205	950	1.4830	0.0296
340	1.5102	17.5670	620	1.4913	0.0200	960	1.4828	0.0181
345	1.5093	16.4910	630	1.4910	0.0196	970	1.4826	0.0146
350	1.5085	14.5010	640	1.4907	0.0193	980	1.4823	0.0137
355	1.5077	12.9930	650	1.4904	0.0190	990	1.4821	0.0161
360	1.5070	11.4320	660	1.4901	0.0185	1000	1.4819	0.0220
365	1.5063	9.7343	670	1.4899	0.0177	1010	1.4816	0.0321
370	1.5057	6.4349	680	1.4896	0.0169	1020	1.4814	0.0402
375	1.5051	3.8936	690	1.4893	0.0160	1030	1.4812	0.0490
380	1.5045	2.2007	700	1.4890	0.0146	1040	1.4809	0.0576
385	1.5039	1.2961	710	1.4888	0.0137	1050	1.4807	0.0529
390	1.5034	0.7669	720	1.4885	0.0135	1060	1.4804	0.0415
395	1.5029	0.4565	730	1.4883	0.0136	1070	1.4802	0.0323
400	1.5025	0.2822	740	1.4880	0.0135	1080	1.4800	0.0273
410	1.5016	0.1237	750	1.4878	0.0134	1090	1.4797	0.0230
420	1.5008	0.0701	760	1.4875	0.0124	1100	1.4795	0.0215
430	1.5000	0.0480	770	1.4873	0.0114	1110	1.4792	0.0249
440	1.4993	0.0403	780	1.4870	0.0105	1120	1.4790	0.0342
450	1.4986	0.0360	790	1.4868	0.0095	1130	1.4787	0.0545
460	1.4980	0.0330	800	1.4865	0.0088	1140	1.4785	0.0990
470	1.4974	0.0312	810	1.4863	0.0087	1150	1.4782	0.1821
480	1.4969	0.0299	820	1.4861	0.0086	1160	1.4780	0.3301
490	1.4964	0.0287	830	1.4858	0.0087	1170	1.4777	0.4595
500	1.4959	0.0275	840	1.4856	0.0088	1180	1.4775	0.6129
510	1.4954	0.0264	850	1.4854	0.0089	1190	1.4772	0.8518
520	1.4950	0.0256	860	1.4851	0.0093	1200	1.4770	1.2670
530	1.4945	0.0249	870	1.4849	0.0106			

13.2.10 MgF_2, LiF and NaF

The refractive index spectra of MgF_2, LiF and NaF materials reported in the following references are parameterized by the Sellmeier model of (13.1) and the modeled results are summarized:

(i) MgF_2: unpublished results of S. Fujimoto,
(ii) LiF: E. D. Palik [10],
(iii) NaF: E. D. Palik [11] (Fig. 13.10, Tables 13.36, 13.37, 13.38 and 13.39).

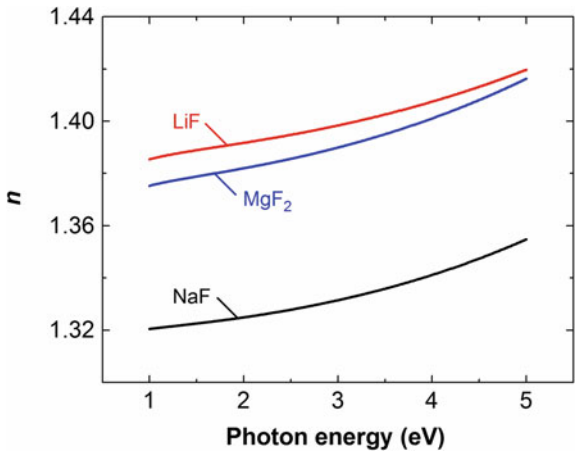


Fig. 13.10 Refractive index spectra of MgF_2, LiF and NaF calculated by the Sellmeier model of (13.1)

Table 13.36 Sellmeier parameters of (13.1) for MgF_2, LiF and NaF

Material	B_1	B_2	B_3	C_1 (μm^2)	C_2 (μm^2)	C_3 (μm^2)
MgF_2	0.896	0.699	–	6.73×10^{-3}	127.462	–
LiF	0.926	7.045	–	5.44×10^{-3}	1087.014	–
NaF	0.207	0.536	0.424	1.07×10^{-5}	9.05×10^{-3}	251.444

Table 13.37 Refractive index of MgF_2 calculated by the Sellmeier model ($k = 0$)

λ (nm)	n	λ (nm)	n	λ (nm)	n	λ (nm)	n
300	1.4028	460	1.3872	720	1.3802	980	1.3773
305	1.4019	470	1.3867	730	1.3800	990	1.3772
310	1.4011	480	1.3863	740	1.3799	1000	1.3772
315	1.4002	490	1.3858	750	1.3798	1010	1.3771
320	1.3995	500	1.3854	760	1.3796	1020	1.3770
325	1.3987	510	1.3851	770	1.3795	1030	1.3769
330	1.3980	520	1.3847	780	1.3794	1040	1.3768
335	1.3973	530	1.3844	790	1.3792	1050	1.3767
340	1.3967	540	1.3840	800	1.3791	1060	1.3767
345	1.3961	550	1.3837	810	1.3790	1070	1.3766
350	1.3955	560	1.3834	820	1.3789	1080	1.3765
355	1.3949	570	1.3832	830	1.3788	1090	1.3764
360	1.3944	580	1.3829	840	1.3787	1100	1.3763
365	1.3939	590	1.3827	850	1.3786	1110	1.3763
370	1.3934	600	1.3824	860	1.3785	1120	1.3762

(continued)

Table 13.37 (continued)

λ (nm)	n	λ (nm)	n	λ (nm)	n	λ (nm)	n
375	1.3929	610	1.3822	870	1.3784	1130	1.3761
380	1.3925	620	1.3820	880	1.3783	1140	1.3760
385	1.3920	630	1.3818	890	1.3782	1150	1.3760
390	1.3916	640	1.3816	900	1.3781	1160	1.3759
395	1.3912	650	1.3814	910	1.3780	1170	1.3758
400	1.3909	660	1.3812	920	1.3779	1180	1.3757
410	1.3901	670	1.3810	930	1.3778	1190	1.3757
420	1.3895	680	1.3808	940	1.3777	1200	1.3756
430	1.3888	690	1.3807	950	1.3776		
440	1.3882	700	1.3805	960	1.3775		
450	1.3877	710	1.3803	970	1.3774		

Table 13.38 Refractive index of LiF calculated by the Sellmeier model ($k = 0$)

λ (nm)	n	λ (nm)	n	λ (nm)	n	λ (nm)	n
300	1.4089	460	1.3961	720	1.3901	980	1.3875
305	1.4082	470	1.3957	730	1.3900	990	1.3874
310	1.4075	480	1.3953	740	1.3899	1000	1.3873
315	1.4068	490	1.3950	750	1.3897	1010	1.3872
320	1.4062	500	1.3946	760	1.3896	1020	1.3871
325	1.4056	510	1.3943	770	1.3895	1030	1.3870
330	1.4050	520	1.3940	780	1.3894	1040	1.3870
335	1.4044	530	1.3937	790	1.3893	1050	1.3869
340	1.4039	540	1.3935	800	1.3892	1060	1.3868
345	1.4034	550	1.3932	810	1.3891	1070	1.3867
350	1.4029	560	1.3930	820	1.3890	1080	1.3866
355	1.4025	570	1.3927	830	1.3888	1090	1.3866
360	1.4020	580	1.3925	840	1.3887	1100	1.3865
365	1.4016	590	1.3923	850	1.3886	1110	1.3864
370	1.4012	600	1.3921	860	1.3885	1120	1.3863
375	1.4008	610	1.3919	870	1.3885	1130	1.3862
380	1.4005	620	1.3917	880	1.3884	1140	1.3862
385	1.4001	630	1.3915	890	1.3883	1150	1.3861
390	1.3998	640	1.3913	900	1.3882	1160	1.3860
395	1.3994	650	1.3912	910	1.3881	1170	1.3859
400	1.3991	660	1.3910	920	1.3880	1180	1.3859
410	1.3985	670	1.3908	930	1.3879	1190	1.3858
420	1.3980	680	1.3907	940	1.3878	1200	1.3857
430	1.3975	690	1.3905	950	1.3877		
440	1.3970	700	1.3904	960	1.3876		
450	1.3965	710	1.3903	970	1.3875		

Table 13.39 Refractive index of NaF calculated by the Sellmeier model ($k = 0$)

λ (nm)	n	λ (nm)	n	λ (nm)	n	λ (nm)	n
300	1.3427	460	1.3291	720	1.3235	980	1.3215
305	1.3419	470	1.3287	730	1.3234	990	1.3215
310	1.3411	480	1.3284	740	1.3233	1000	1.3214
315	1.3404	490	1.3280	750	1.3232	1010	1.3214
320	1.3397	500	1.3277	760	1.3231	1020	1.3213
325	1.3391	510	1.3274	770	1.3230	1030	1.3213
330	1.3384	520	1.3271	780	1.3229	1040	1.3212
335	1.3379	530	1.3268	790	1.3228	1050	1.3212
340	1.3373	540	1.3265	800	1.3227	1060	1.3212
345	1.3368	550	1.3263	810	1.3226	1070	1.3211
350	1.3363	560	1.3260	820	1.3226	1080	1.3211
355	1.3358	570	1.3258	830	1.3225	1090	1.3210
360	1.3353	580	1.3256	840	1.3224	1100	1.3210
365	1.3349	590	1.3254	850	1.3223	1110	1.3209
370	1.3344	600	1.3252	860	1.3223	1120	1.3209
375	1.3340	610	1.3250	870	1.3222	1130	1.3209
380	1.3336	620	1.3249	880	1.3221	1140	1.3208
385	1.3333	630	1.3247	890	1.3221	1150	1.3208
390	1.3329	640	1.3245	900	1.3220	1160	1.3207
395	1.3326	650	1.3244	910	1.3219	1170	1.3207
400	1.3322	660	1.3243	920	1.3219	1180	1.3207
410	1.3316	670	1.3241	930	1.3218	1190	1.3206
420	1.3311	680	1.3240	940	1.3218	1200	1.3206
430	1.3305	690	1.3239	950	1.3217		
440	1.3300	700	1.3237	960	1.3216		
450	1.3296	710	1.3236	970	1.3216		

References

1. R.A. Synowicki, B.D. Johs, A.C. Martin, Thin Solid Films **519**, 2907 (2011)
2. SCHOTT optical glass data sheets (2012)
3. I.H. Malitson, J. Opt. Soc. Am. **55**, 1205 (1965)
4. G. Gosh, Opt. Commun. **163**, 95 (1999)
5. N. Hong, R.A. Synowicki, J.N. Hilfiker, Appl. Surf. Sci. **421**, 518 (2017)
6. M. Campoy-Quiles, J. Nelson, D.D.C. Bradley, P.G. Etchegoin, Phys. Rev. B **76**, 235206 (2007)
7. E.T. Arakawa, M.W. Williams, J.C. Ashley, L.R. Painter, J. Appl. Phys. **52**, 3579 (1981)
8. K.R. McIntosh, G. Lau, J.N. Cotsell, K. Hanton, D.L. Bätzner, F. Bettiol, B.S. Richards, Prog. Photovoltaics **17**, 191 (2009)
9. K.R. McIntosh, J.N. Cotsell, J.S. Cumpston, A.W. Norris, N.E. Powell, B.M. Ketola, in *Proceeding of the 34th IEEE PVSC* (IEEE, New York, 2009), p. 544
10. E.D. Palik, *Handbook of Optical Constants of Solids* (Academic Press, New York, 1985)
11. E.D. Palik, *Handbook of Optical Constants of Solids II* (Academic Press, New York, 1991)

Index

A
Absorbance, 183
Absorbance spectroscopy, 110
Absorber layer thickness, 241
Absorber layer thickness reduction, 243
Absorptance, 22, 40
Absorption coefficient, 8, 89, 256
Absorption loss, 23, 48, 76
Absorption onset, 88
Absorption spectrum, 320
Absorption tail, 9
AES depth profile, 232
Ag, 170, 545, 550
Air-mass 1.5 global, 3
Al, 545, 552
Al_2O_3, 329
AlAs, 9, 356
Alloy composition, 214
AlSb, 367
Ambient/glass interface, 103
AM1.5G, 3, 41
Amorphous semiconductor, 260
Amorphous silicon (a-Si:H), 338, 340
Amorphous silicon carbide (a-SiC:H), 346
Amorphous silicon oxide (a-SiO:H), 350
Amorphous-to-(mixed-phase) transition, 310
Angle of incidence, 191, 222
Angle of incidence calibration, 191
Anisotropy, 428
Annealing, 99
Anti-Reflection Coating (ARC), 85, 225
Anti-reflection layer, 21, 575
APFO-3, 429
APFO-Green9, 431
ARC method, 35, 46
Asahi-U, 63, 151
A-Si:H, 9, 19, 83, 170, 225, 338, 340
A-Si:H/c-Si heterojunction solar cell, 72, 143
A-Si:H local network model, 147
A-Si:H n-i-p solar cell, 170
A-Si:H n-layer, 170
A-Si:H solar cell, 63, 158
A-SiO:H/c-Si, 19
A-$Si_{1-x}C_x$:H, 264, 346
Asymmetric double-Gaussian profile, 45
Atmospheric pressure vapor deposition, 176
Au, 545, 554
Au back contact, 102
Auger Electron Spectroscopy (AES), 119, 232

B
Back contact, 84
Back reflector, 78, 170
Back-side reflection, 543
Back-Surface Field (BSF), 22, 49, 78
Band filling, 107
Band gap, 89, 199, 256
Band gap energies, 172
Band gap profile, 236
Band offset, 59
Band structure critical points, 261
Beam focusing, 174
Beer's law, 50
Biaxial optical anisotropy, 575
Birefringence, 174
Borosilicate glass, 577
Broadening, 172
Broadening parameter, 89, 270

© Springer International Publishing AG, part of Springer Nature 2018

H. Fujiwara and R. W. Collins (eds.), *Spectroscopic Ellipsometry for Photovoltaics*,
Springer Series in Optical Sciences 214,
https://doi.org/10.1007/978-3-319-95138-6

Bruggeman Effective Medium Approximation (EMA), 88, 178, 227
B-spline, 215
Built-in electric field, 94
Bulk layer, 104, 214
Bulk layer thickness, 179, 259
Burstein-Moss effect, 118
Burstein-Moss shift, 48

C
Cadmium telluride, 83
Calibration, 189
Camera, 189
Carrier collection, 83
Carrier collection efficiency, 50
Carrier collection length, 23, 50
Carrier collection profile, 94
Carrier continuity equation, 51
Carrier diffusion, 51
Carrier drift, 51
Carrier loss, 76
Carrier loss mechanism, 74
Carrier recombination, 31, 50
$CdCl_2$ treatment, 99
CdS, 99, 174, 374
CdS/CdTe heterojunction, 98
CdS/CdTe interface, 106, 178
CdS/CdTe PV panel, 174
CdSe, 376
CdS effective thickness, 181
CdS layer, 174
CdS window layer, 174
$CdS_{1-x}Te_x$, 101
CdTe, 5, 11, 19, 83, 169, 378
CdTe PV module, 169
CdTe solar cell, 61, 178
C (graphite), 556
$CH_3NH_3PbI_3$, 5, 9, 19, 475
$CH_3NH_3PbI_3$ solar cell, 75
CH_3NH_3I, 491
Characterization of Textured Structures, 139
Charge carrier collection, 183
Chemical bath deposition, 113
CIGS, 83, 209
CIGS/CdS interface, 122
CIGS deposition process, 214
CIGSe, 9, 19, 547
CIGSe solar cell, 21, 43, 140, 164
CIGS solar cell, 113, 212
CISe, 16
Close-space sublimation, 99
Coalescence, 229
Coating layer, 575
Cody-Lorentz oscillator, 88, 201, 280
Coevaporation, 209
Coherent condition, 41
Coherent length, 41, 67
Collection grids, 118
Collection probability profile, 127
Complex amplitude reflection ratio, 103
Complex dielectric constant, 8
Complex dielectric function, 84, 186, 211, 255
Complex refractive index, 8
Composition, 230
Compositional gradient, 234
Composition profile, 116, 214
Compressive stress, 108
Confidence limits, 103
Conical nanocrystallites, 309
Continuous Phase Approximation (CPA), 67
Conversion efficiency, 2
Copper indium-gallium diselenide, 83, 209
Copper Phthalocyanine (CuPc), 431
Copper selenide, 209
Cr, 194, 558
Critical point, 100
Critical Point (CP) oscillator, 116, 198, 217
Cross-sectional transmission electron micrograph, 109
Crystalline grain structure, 267
Crystalline silicon, 296
C-Si, 548
C-Si heterojunction solar cell, 69
C-Si solar cell, 66
Cu, 560
$CuGaSe_2$, 382
$Cu(In,Ga)Se_2$ (CIGSe), 5
$CuIn_{1-x}Ga_xSe_2$, 83, 209, 384, 547
$CuIn_{1-x}Ga_xSe_2$ (CIGS) solar cell, 185
$CuInSe_2$, 380
Cu_2SnSe_3, 413
$Cu_2ZnGeSe_4$, 411
Cu_2ZnSnS_4 (CZTS), 5, 401
$Cu_2ZnSnSe_4$ (CZTSe), 5, 402
$Cu_2ZnSn(S,Se)_4$ (CZTSSe), 5
$Cu_2ZnSn(S_xSe_{1-x})_4$, 405
$Cu_{2-x}Se$, 209
Cu deficient CIGS, 225
Cu-poor CIGS, 232
Cu-rich CIGS, 232

Current density, 110
Current-density-voltage (J-V) measurements, 304
Curvature model, 151
CZTS, 9
CZTSe, 9
CZTSe solar cell, 53
CZTSSe solar cell, 22
CZTS solar cell, 58

D
Data analysis, 84
Database dielectric function, 227
Dead layer, 57
Defect complex, 235
Degenerate doping, 118
Depletion layer thickness, 51
Deposition rate, 210, 260
Deposition system, 194
Depth profile, 260
Dielectric function, 8, 83, 178, 255
Dielectric function database, 115
Dielectric function gradient, 234
Dielectric function modeling, 12
Diffusion barrier, 186
Diffusion coefficient, 238
Diffusion length, 51
Dipolar plasmon, 200
Dipole matrix element, 201
Direct-transition semiconductor, 9
Disorder, 92, 171
Doped window layer, 96
Doping, 92
DPPTTT, 467
Drude component, 262
Drude free electron, 116, 217
Drude free electron formula, 196
Drude model, 47, 496

E
Eagle XG glass, 577
e-ARC method, 50
e-ERS, 53
Effective mass, 497
Effective medium approximation, 260
Effective medium layer, 182
Effective thickness, 92, 174, 256
Efficiency, 7, 86, 225
Electromagnetic wave, 36
Electron, 102
Electron beam evaporation, 113
Electron concentration, 107
Electron-hole recombination, 84
Electronic loss, 85
Electronic transition, 171
Electron impact emission spectroscopy, 113
Electron mean free time, 196
Electron-volt, 4
Elementary cell, 141
Ellipsometer translation, 180
Ellipsometry angles, 189
EMA multilayer model, 151
Emissivity, 225
End-point detection, 113, 213
Energy Dispersive X-ray Spectroscopy (EDS), 117, 218
Energy shift model, 384, 405, 479
EQE analysis, 30
EQE characteristics, 19
EQE limit, 20
Error function, 118
ERS method, 35, 43
Ethylene Vinyl Acetate (EVA), 604
Evaporation rate, 222
Exact inversion, 88
Excited carrier mean free path, 109
Expanded beam spectroscopic ellipsometer, 187
Expanded probe beam, 186
Ex-situ spectroscopic ellipsometry, 83
Extended ARC method, 50
External Quantum Efficiency (EQE), 29, 83, 172
Extinction coefficient, 8
Extraordinary ray, 428

F
$FAPbI_3$ (α phase), 473
$FAPbI_3$ (δ phase), 487
F doping, 107
Fill-factor, 2, 94, 225, 289
Fitting error function, 153
Flexible substrate, 186
Flexible thin film photovoltaic (PV) modules, 185
Formamidinium lead iodide $FAPbI_3$($HC(NH_2)_2PbI_3$), 471, 473, 547
Free carrier absorption, 47, 496, 545
Fresnel coefficients, 191
F8TBT, 429
Full-size PV panel, 173
Fused silica, 577

G
GaAs, 6, 12, 358
Ga_2O_3, 331
GaP, 9, 363
Ge, 9, 325
Glass/film-stack interface, 103
Glass-side illumination, 158
Grain boundaries, 232, 258
Grain boundary scattering, 108
Grain growth, 213
Grain size, 108
Graphene, 498
Grids, 113
Growth evolution diagram, 255
Growth mechanism, 212

H
H_2 dilution, 93
Heterojunction, 178
Heterojunction interface, 124
Heterojunction solar cell, 68
High Resistivity Transparent (HRT) layer, 99, 176
Hole diffusion length, 94
HRT layer, 106
Hybrid perovskite, 471, 548
Hydrogenated amorphous, 86
Hydrogenated amorphous silicon, 83, 170, 256
Hydrogenated nanocrystalline silicon, 256
Hydrogenated silicon, 186, 255
Hydrogen incorporation, 93

I
Ideal collection, 124
Imaging, 186
Imaging/mapping SE, 186
Imaging multichannel SE, 172
Imaging spectrograph, 189
Inactive layer, 94
InAs, 360
Incoherent condition, 41
Incoherent light absorption, 66
Incoherent summation, 104
Index of refraction, 200
Indirect bandgap, 261
Indirect-transition semiconductor, 9
Indium-gallium selenide, 209
Inorganic Semiconductor, 319
InP, 12, 365
In-plane strain, 171
In_2S_3, 418
In_2O_3:H, 502
In_2O_3 (non-doped), 500
In_2O_3:Sn, 504, 506, 508
In situ monitoring, 213
In situ SE, 216
Instantaneous deposition rate, 241
Interband CP transition, 102
Inter-diffusion, 178
Interface, 83, 259
Interface formation, 212
Interface layer, 91, 179, 264
Interface layer composition, 104
Interface roughness, 118, 178, 198, 215, 264
Interference fringe pattern, 230
Internal quantum efficiency, 31
Intraband transition, 101
Intrinsic absorber layer, 86
Inversion, 214, 260
$(In_{1-x}Ga_x)_2Se_3$, 113, 209
InZnO, 510
IQE, 31
Irradiance, 3, 36
ITO, 504, 506, 508

J
Junction, 84
(J-V) characteristic, 114

K
Kapton HN [poly{N,N'-(oxydiphenylene) pyromellitimide}], 599
Kramers-Kronig consistent, 217
Kramers-Kronig integration, 321, 497

L
Lamp, 189
Law of the minimum, 30
Layer thickness, 172
Least-squares regression, 219
Least squares regression analysis, 83, 260
Levenberg-Marquardt algorithm, 103
LiF, 605
Light absorption, 18
Light scattering, 34, 94
Light trapping, 85
Light trapping gain, 96
Linear detector array, 171
Lorentz oscillator, 88, 198, 219, 261

M
Magnetron sputtering, 99, 178
Maximum J_{sc}, 5
$MAPbBr_3$ ($CH_3NH_3PbBr_3$), 477
$MAPbCl_3$ ($CH_3NH_3PbCl_3$), 485
$MAPb(I_{1-x}Br_x)_3$ ($CH_3NH_3Pb(I_{1-x}Br_x)_3$), 479
Mapping, 136
Mapping SE, 192, 304
Material density, 171
Matrix element, 88
Maximum efficiency, 7
Maxwell's equations, 8
Mean free time, 102
Mean Square Error (MSE), 103, 195, 217, 281
Metal, 84, 543
Methylammonium lead iodide $MAPbI_3$($CH_3NH_3PbI_3$), 471, 475
Mg, 562
MgF_2, 119, 605
MgF_2 ARC, 119
MgF_2 biplate, 188
Microcrystalline Si (μc-Si:H), 354
Micromorph tandem, 256
Mixed phase a-Si-H + nc-Si:H, 260
Mixed-phase-to-nanocrystalline transition, 299
Mo, 545, 564
Mo back contact, 114
Mobility, 102
Mo-coated, 209
Molybdenum, 113, 249
MoS_2, 217, 419
$MoSe_2$ (polycrystal), 421
$MoSe_2$ (single crystal), 423
MoO_x, 512
Mueller-matrix SE, 587
Multichannel ellipsometer, 84, 175
Multichannel spectroscopic ellipsometer, 171, 213
Multijunction thin film PV, 256
Multilayer analysis, 83
Multilayer model, 181
Multi-sample analysis, 91
Multi-sample model, 91
Multi-step analysis, 104
Multi-time analysis, 116, 214, 265

N
NaF, 605
Nanocrystalline material, 218
Nanocrystalline volume fraction, 256
Nanocrystals, 281
Nc-Si:H, 255
Ni, 545, 566
NiO, 515
Non-doped TCO, 495
Non-invasive analysis, 109
Non-linear least-squares regression, 172
Nonparabolic TCO conduction band, 497
n-type a-Si:H, 88
n-type hydrogenated amorphous silicon, 186
n-type nc-Si-H, 304
n-type Si-H, 255
Nucleation, 257
Nucleation density, 282

O
Off-line SE mapping, 174
One-stage coevaporation, 220
On-line mapping, 169
On-line monitoring, 169
On-line SE, 173
Open-circuit voltage, 2, 92, 179, 225, 306
Optical admittance, 38
Optical admittance method, 36
Optical carrier concentration, 497
Optical constants, 8
Optical gain, 47
Optical loss, 76, 83
Optical mobility, 497
Optical model, 226
Optical properties, 84
Optical properties of metal, 545
Optical simulation, 83
Ordinary ray, 428
Organic-inorganic hybrid perovskite, 471
Organic semiconductors, 427
Oscillator amplitude, 172
Oscillator model, 85
Oxidation, 214

P
Parameterization, 220
Parameter map, 203
Parameter reduction, 268
Parametric model, 227
Parasitic absorption, 24, 547
Parasitic light absorption, 31
Partial EQE, 21, 49
Passivation layer, 319
PbI_2, 489
$PC_{60}BM$, 445
$PC_{70}BM$, 447

PCDTBT, 449
PCPDTBT, 451
Penetration depth, 18
Penetration depth of light, 56
PFDTBT, 429
Phase evolution, 213
Phosphine, 194
Photo-generated electrons and holes, 110
Photon density, 5
Photon energy, 4
Photovoltaics, 256
Photovoltaics (PV) production, 169
Photovoltaics (PV) technology, 170
P3HT, 16, 437
P3HT:$PC_{60}BM$, 439
P3HT:$PC_{70}BM$, 441
p/i interface, 87
p-i-n a-Si-H solar cells, 293
Pin-hole, 189
P-i-n solar cell, 85
Planck's constant, 4
Plasma Enhanced Chemical Vapor Deposition (PECVD), 86, 194, 256
Plasma ignition, 193
Plasmon resonance, 198
Plastic substrate, 576
Polarization analyzer, 189
Polarizer, 188
Polarizer and analyzer azimuthal angle, 191
Poly (3,4-EthyleneDioxyThiophene):Poly (4-StyrenSulfonate) (PEDOT:PSS), 452
Poly (Ethylene Naphthalate) (PEN), 587
Poly (Ethylene Terephthalate) (PET), 591
Poly (3-HexylThiophene) (P3HT), 437
Poly (Methyl MethAcrylate) (PMMA), 455
Poly (Methyl Methacrylate) (PMMA), 596
Poly (3-OctylThiophene) (P3OT), 443
Polycarbonate, 585
Polycrystalline CdTe absorber, 98
Polycrystalline film, 215
Polycrystalline film growth, 238
Polycrystalline grain size, 171
Polycrystalline thin film solar cell, 209
Polyimide, 170, 597
Polymer foil, 185
Polymer substrate, 202, 575
Poly {2-Methoxy-5-(2′-Ethyl-Hexyloxy)-P-PhenyleneVinylene} (MEH-PPV), 435
Potential transmittance, 39
Power function model, 158
Poynting vector, 36
P-parameter model, 103
Principles of solar cell, 2
Process control, 250
Process monitor, 250
Process-performance correlations, 283
Process-property-performance correlations, 293
Property map, 179
Protection coating, 575
Protocrystalline Si:H, 83
Pseudo-substrate, 260
Pt, 545, 568
PTB7, 457
PTB7:$PC_{70}BM$, 459
p-type a-$Si_{1-x}C_x$:H, 89
p-type nc-Si-H, 304
PV manufacturing, 170
Pyramid-shaped texture, 140

Q
Quartz, 577
Quartz-tungsten-halogen, 189
Quasi-monochromatic, 41

R
Real time SE, 116, 211, 255
Recombination junction, 283
Recombination loss, 23, 53, 55, 76
Recombination model, 50
Reflectance, 38, 85, 183
Reflectance of metal, 544
Reflectance spectrum, 111
Reflection loss, 23, 48, 76
Refractive index, 8
Resistivity, 102, 196
Resonance energy, 100
Reverse bias, 110
Roll-to-roll cassette, 186
Roll-to-roll PV, 170
Roll-to-roll speed, 192
Roll-to-roll technology, 186
Rotating-analyzer, 90
Rotating-analyzer ellipsometer, 118
Rotating compensator, 173, 221
Roughening, 238
Roughness layer, 196
Rough surface, 85

S
Scaling factor, 65
Secondary ion mass spectrometry, 119
Sellmeier model, 576

Sellmeier term, 198
SE mapping, 181
SE mapping station, 175
Semiconductor, 84
Semiconductor deposition, 211
Sheet resistance, 107
Short-circuit current, 179
Short-circuit current density, 2, 84, 225
Si, 6, 9, 16, 322
Si-H-B p-layer, 266
Silane, 194
Silicon-carbon alloy, 86
Silver back contact, 91
SIMS, 119
SiN, 332
Single crystal CdTe, 103
Single crystal chalcopyrite, 116
Single junction solar cell, 256
Single-stage coevaporation, 116
SiO_2, 86, 176, 328, 577
Si-PCPDTBT, 461
Si texture, 140
Smoothening, 238
SnO_2, 86, 176
SnO_2:F, 86, 176, 262, 519
SnO_2 (non-doped), 517
Soda-lime glass, 86, 173, 212, 577
Solar cell, 1, 83, 210, 256
Solar cell performance, 256
Solar cell substrates, 222
Source temperature, 221
Space-charge region, 51
Spatial non-uniformities, 170, 256
Spatial resolution, 189
Spectral range, 204
Spectroscopic Ellipsometry (SE), 84, 169, 209, 255
Specular reflection component, 150
Speed of light, 4
Spiro-OMeTAD, 463
Stabler-Wronski effect, 63
Stainless steel (SUS304), 583
Standard deviation, 103
Steel foil, 186
Stoichiometric CIGS, 235
Stoichiometry, 221
Stokes parameters, 148
Stress-induced birefringence, 91
Structural evolution, 227, 255
Sub-bandgap absorption, 93
Submicron natural textures, 141
Submicron rough texture, 46
Substrate, 575
Substrate configuration, 84
Substrate shutter, 223
Substrate temperature, 225
Sunlight, 3
Superstrate configuration, 84, 257
Surface area model, 153
Surface roughness, 91, 198, 213, 255
Surface structure, 238

T
Tail absorption, 9
Tail-state absorption, 62
Tandem a-Si:H/nc-Si:H solar cells, 293
Tandem p-i-n solar cells, 258
Tandem PV devices, 255
Tandem solar cell, 259
Tandem solar-cell structures, 161
Tauc-Lorentz model, 12, 320, 496
Tauc-Lorentz oscillator, 88, 278
TCO absorption loss, 76
TEC-15, 519
TEC-8, 519
Textured c-Si Solar Cell, 71
Textured solar cell, 43
Textured structure, 139
Thermal evaporation, 99
Thickness, 84, 256
Thickness evolution, 218
Thickness non-uniformity, 103
Thickness uniformity, 170
Thin absorber, 84
Thin film analysis, 84
Thin film photovoltaics, 83
Thin film solar cell, 83
Thin-film solar cell module, 141
Thinner absorber layer, 124
Three-stage coevaporation, 113, 210
Three-stage process, 44
Through-the-glass SE, 84, 169
Ti, 570
Tilt-angle SE Measurement, 143
TiO_2 (anatase single crystal), 523
TiO_2 (polycrystal), 521
TiO_2 (rutile single crystal), 526
Top contact, 84
TQ1, 465
Transmittance, 40, 88
Transparent Conductive Oxide (TCO), 84, 173, 263, 495
Transparent material, 575
Tunnel junction, 265
Two-dimensional detector array, 170
Two-dimensional silicon CCD, 189
Two-step absorber, 89

U
Uniaxial anisotropy, 428
Urbach absorption, 89
Urbach energy, 9, 100
Urbach tail, 100

V
Virtual interface analysis, 260
Void content, 214, 259
Void fraction, 101
Void volume fraction, 178
Voltage-dependent collection, 110

W
W, 572
Window layer, 92, 171
WO_3, 529

X
Xe, 189
XTEM, 109

Z
ZnO, 113, 170
ZnO:Al, 113, 535
ZnO:Ga, 16, 533, 537, 539
ZnO (non-doped), 531
ZnS, 369
ZnSe, 370
ZnTe, 372